Investigation of noncovalent interactions to construct supramolecular switches

Inaugural-Dissertation
to obtain the academic degree
Doctor rerum naturalium (Dr. rer. nat.)

submitted to the Department of Biology, Chemistry, Pharmacy
of Freie Universität Berlin

by

Henrik Hupatz, M.Sc.

from Berlin

Berlin, 2023

The present research was carried out under the supervision of Prof. Dr. Christoph A. Schalley from January 2016 until February 2022 at the Department of Biology, Chemistry and Pharmacy of Freie Universität Berlin and the Bundesanstalt für Materialfoschung und -prüfung (BAM).

Hereby, I declare that the submitted thesis is my own work and was prepared without the aid of other sources or people than the ones cited and acknowledged. This dissertation has not yet been presented to any other examination authority in the same or a similar form and has not yet been published.

_____

Henrik Hupatz Berlin, den 06.01.2023

1. Reviwer:	Prof. Dr. Christoph A. Schalley
2. Reviewer:	Prof. Dr. Beate Paulus
Date of defence:	07.02.2023

Acknowledgements

First and foremost, I want to thank my academic supervisor Christoph A. Schalley for offering me the freedom and resources to develop my research project. It was a pleasure to learn from you how to ask the right questions, and your question 'What would an *advocatus diaboli* say to these results?' greatly improved my critical thinking. Also, I want to express my deepest gratitude for you being very understanding and supportive during difficult times.

Furthermore, I want to thank Beate Paulus for being my second reviewer as well as for the years of very constructive collaboration and discussions.

A special gratitude is dedicated to the "TTF subgroup", Hendrik V. Schröder and Marius Gaedke. It was a great pleasure to develop and evolve this project together with you both. Thank you for the very fun atmosphere and for all the things I learnt from you, guys!

I want to thank Wolfgang E. S. Unger and Vasile-Dan Hodoroaba for welcoming me as a guest scientist in their research group at BAM, and for allowing me to conduct surface analysis. I want to thank Jörg Radnik and Andreas Wagner for their help with measuring at the HE-SGM beamline at BESSY II. I learnt a lot from immersing myself into a totally different research environment, and I enjoyed the time with you during our shifts.

I am also thankful to all my other collaboration partners. I would like to mention Andreas J. Achazi, Fei Jia, Wei Jiang, Amel Mekic, Sebastian Sobottka, Biprajit Sarkar and Felix Witte, among others. This thesis benefitted greatly from your diverse expertise and constructive input.

I also want to thank all current and past members of the AG Schalley for the very productive and supportive work atmosphere, but also for the many fun evenings together at barbecues and other enjoyable activities. I am grateful that I have got to know Larissa Kapp, Tuğrul Kaynak, Anneli Kruve, Marta da Pian, Stefan Schoder, and Daniel Stares.

Additionally, I want to mention Larissa von Krbek, who introduced me to the miracles of ITC, and Thomas Heinrich, who showed me the wonders of surface analysis. I am very thankful that I could learn from both of you!

I want to thank Silke Benndorf, who always made sure that no one got lost in the university bureaucracy jungle!

I am very grateful to Fabian Klautzsch, who supported me with conducting the ITC experiments, and shared with me the pleasure of working with a very temperamental instrument placed in a 'sauna' room. I would like to thank Andreas Springer for his great

patience in teaching me how to handle the MS instruments, and for his aura, which magically made mistakes vanish.

I am very grateful for the funding of my research offered by the CRC 765, and for conference funding by the GdCh.

I want to thank Sebastian Müller for the help with the syntheses. I am also very thankful for the excellent work of my students Felix Witte, Susanne Rupf, and Julian Hille.

I would like to thank Volker Schmiedel and Ulrike Warzok, who had a great impact on my professional and personal development since I met you during the bachelor, for their great friendship and support.

Volker Schmiedel, Marius Gaedke, Konstantin Simon, and Cristina Mozaceanu are gratefully acknowledged for helping me to proof-read and correct this thesis.

I want to express my deepest gratitude to my friends and family for their support over all these years. Especially, I want to thank Jenny, Sophia, Konstantin, Alex, Marwin, and Nici for being friends who have my back since many years and who made sure that I did not lose my mind, after all.

Finally, I would like to express my deepest gratitude to my beloved partner Cristina, for her immense personal and professional support throughout my last few years and during the process of writing this thesis. Thank you for believing in me and supporting me to get back up again!

Abstract

Molecular switches can interconvert between two stable states controlled by an external stimulus. They are applied in adaptive materials, molecular electronics, and are needed to develop artificial molecular machines. Molecular switches can be assembled and operated based on noncovalent interactions. A detailed understanding of the involved noncovalent interactions is fundamental to develop new switching functions and operation modes.

In this thesis, the redox-switchable units tetrathiafulvalene (TTF) and naphthalene diimide (NDI) are incorporated into crown ethers. The thermodynamic binding properties of crown ethers and *sec*-ammonium ions were investigated through isothermal titration calorimetry (ITC). The effects of the counterion as well as the structural changes both in the macrocycle and in the axle on the noncovalent interactions in the pseudorotaxanes were identified.

Additionally, an organic cage was developed, which can adopt a self-inclusion complex. The cage showed a very strong enthalpy driven binding ($K_a > 10^9$ M^{-1}) of cations such as acetylcholine. Interestingly, the binding was also entropically favoured.

Based on a toolbox of molecular components of redox-switchable crown ethers and *sec*-ammonium axles, different functions of molecular switches were constructed using the concepts of self-assembly, self-sorting, mechanical bonding, and multivalency. Switching of a kinetically hindered pseudorotaxane revealed differences in the disassembly timeframe depending on the type of the applied stimulus.

Five redox-switchable monovalent rotaxanes with different switching modes were assembled. In two of these rotaxanes a shuttling motion of the wheel along the axle was observed upon switching. In a planar chiral rotaxane, redox-switching resulted in a sign inversion in the electronic circular dichroism spectrum.

In a homo[3]rotaxane, attractive noncovalent interactions between two extended TTF units which are incorporated in both wheels were identified. When both TTFs were oxidised to TTF^{2+}, Coulomb repulsion triggers a 180° rotation of the wheels in relation to each other.

By applying integrative self-sorting, two different wheels were combined on one axle to form hetero[3]pseudorotaxanes. The self-sorting equilibrium was studied and it revealed a major impact of the smaller second wheel on the hetero[3]pseudorotaxane properties. The construction of four hetero[3]rotaxanes was achieved.

The formation of a divalent pseudorotaxane containing TTF and NDI showed positive chelate cooperativity and an emerging intramolecular charge-transfer band confirmed the donor-acceptor interaction between TTF and NDI. The investigation of the redox-switching of a divalent donor-acceptor rotaxane revealed interesting optoelectronic properties.

Kurzzusammenfassung

Molekulare Schalter können reversibel zwischen zwei stabilen Zuständen wechseln und werden dabei von einem externen Stimulus kontrolliert. Sie finden Anwendung in adaptiven Materialen, in molekularer Elektronik und sind notwendig in der Entwicklung von künstlichen molekularen Maschinen. Nicht-kovalente Wechselwirkungen können zum Zusammenbau von molekularen Schaltern verwendet werden und diese haben einen Einfluss auf ihren Betrieb. Ein genaues Verständnis der zugrunde liegenden nicht-kovalenten Wechselwirkungen ist fundamental, um neue Schalterfunktionen zu entwickeln.

In dieser Dissertation wurden die elektrochemisch schaltbaren molekularen Einheiten Tetrathiafulvalen (TTF) und Naphtalendiimid (NDI) in Kronenether eingebaut. Die thermodynamischen Bindungseigenschaften dieser Kronenether zu *sec*-Ammoniumionen wurden durch isothermale Titrationskalorimetrie (ITC) detailliert untersucht. Die Effekte von Gegenionen und von strukturellen Änderungen im Makrozyklus, sowie in der Ammoniumachse auf die nicht-kovalenten Wechselwirkungen im Pseudorotaxan wurden offengelegt.

Zusätzlich wurde ein organischer Käfig entwickelt, der einen selbst-Einschlusskomplex bilden kann. Es wurde gezeigt, dass die starke Bindung des Käfigs von Kationen, wie Acetylcholin, ($K_a > 10^9$ M^{-1}) Enthalpie-getrieben ist. Interessanterweise ist diese Bindung aber auch entopisch günstig.

Ausgehend von den molekularen Komponenten, bestehend aus elektrochemisch schaltbaren Kronenethern und *sec*-Ammoniumachsen, wurde durch die Anwendung der Konzepte der Selbstassemblierung, der Selbstsortierung, der Multivalenz und der mechanischen Bindung eine Vielzahl von molekularen Schaltern mit verschiedenen Funktionen konstruiert. Bei der Schaltung eines kinetisch gehemmten Pseudorotaxans mit zwei unterschiedlichen Arten von Stimuli zeigten sich Unterschiede beim Zeitraum, in dem der Reif von der Achse abfädelte.

Es wurden fünf elektrochemisch schaltbare Rotaxane mit unterschiedlichen Schaltungsmechanismen zusammengebaut. In zwei dieser Rotaxane konnte eine Translationsbewegung des Makrozyklus entlang der Achse festgestellt werden, die durch die Schaltung ausgelöst wurde. In einem planar chiralen Rotaxan führte die elektrochemische Schaltung zu einem Vorzeichenwechsel des elektronischen Zirkulardichroismus.

In einem Homo[3]rotaxan konnten anziehende, nicht-kovalente Wechselwirkung zwischen zwei verlängerten TTF-Einheiten, die sich jeweils in den beiden Reifen befanden, nachgewiesen werden. Sobald beide TTF-Einheiten zum Dikation oxidiert wurden, löste die Coulomb-Abstoßung eine 180° Rotation der beiden Reifen zueinander aus.

Durch die Anwendung von integraler Selbstsortierung konnten zwei verschiedene Reifen auf eine Achse gefädelt werden und so Hetero[3]pseudorotaxane gebildet werden. Das

Selbstsortierungsgleichgewicht wurde untersucht und es konnte gezeigt werden, dass der kleinere zweite Reif den größeren Einfluss auf die Eigenschaften des Hetero[3]pseudorotaxane hatte als der größere Reif. Davonausgehend wurden vier Hetero[3]rotaxane hergestellt.

Die Bildung eines divalenten Pseudorotaxans, das TTF- und NDI-Einheiten enthält zeigte positive Chelatkooperativität und eine intramolekulare Ladungstransferbande entstand, welche die Bildung eines Donor-Akzeptor-Komplexes zwischen TTF und NDI belegte. Die elektrochemische Schaltung eines daraus hergestellten Donor-Akzpetor-Rotaxans zeigte interessante optoelektronische Eigenschaften.

Abbreviations

AFM	atomic force microscopy
AMM	artificial molecular machine
CCS	collision cross section
CD	circular dichroism
CID	collision induced dissociation
COSY	correlation spectroscopy
CV	cyclic voltammetry
DCE	1,2-dichloroethane
DFT	density functional theory
DMC	double mutant cycle
DNA	desoxyribonucleic acid
DPV	differential pulse voltammetry
ECD	electrical circular dichroism
EM	effective molarity
EPR	electron paramagnetic resonance
ESI	electrospray ionisation
exTTF	extended tetrathiafulvalene
HPLC	high performance liquid chromatography
HRMS	high resolution mass spectrometry
IMS	ion mobility spectrometry
ITC	isothermal titration calorimetry
ITO	indium tin oxide
NDI	naphthalene diimide
NIR	near-infrared
NMR	nuclear magnetic resonance
NP	naphthalene
MIM	mechanically interlocked molecule
MS	mass spectrometry
MV	methylviologen
TTF	tetrathiafulvalene
TW	travelling wave
UV/Vis	ultraviolet/visible

Table of Contents

1 Introduction

According to the *Cambridge Dictionary* a device is defined as "an object or machine that has been invented for a particular purpose",[1] which holds true for an innumerable number of artificial objects in human daily life. The number of devices grows daily with the technological progress of mankind and problems found to be solved by new-developed devices. Most of these devices contain at least one adaptive component: a *switch*, which allows the device to interact with its environment, *i.e.*, a human using a lever to switch the power connection of the device on or off.

Along with the progress in molecular design and chemical synthesis, the exploration of molecular devices began in the second half of the 20th century. Interestingly, the initial idea was not envisioned first by a chemist, but rather a lecture of the theoretical physicist FEYNMAN is considered to be the starting point of this research area, which was later called *molecular nanotechnology.*[2-4] In his lecture, FEYNMAN discussed the miniaturisation of information, devices and machines, and outlined how infinitesimally small devices or machines could be assembled directly from their atoms.[2] Recently, a visual representation of this vision was achieved by the development of nanocars (Figure 1.1a, right).[5,6] Though, in comparison to their macroscopic analogues they are very slow (Figure 1.1a, left), as the "fastest" nanocar required 2 h to reach the goal line after 150 nm on a track made of specifically prepared metal surfaces under ultra-high vacuum conditions.[6,7] This example for a molecular device will, in all likelihood, remain a scientific curiosity without having any direct application, but it challenged scientific methods and shifted the limits of molecular nanotechnology.

Molecular devices were defined as an "assembly of a discrete number of molecular components designed to achieve a specific function".[4,8] Hereby, not the individual components, but the molecular assembly as a whole produces the emergent function. For example, in nanocar **1** components for wheels, axle, and chassis are connected to one molecule.

Similarly to their macroscopic counterparts, a key feature which is present in molecular devices is an adaptive component, the *molecular switch.*[4,8-11] These switchable moieties can be transformed between at least two stable states by an external stimulus.[10-12] For example, 8,8'-biindeno[2,1-*b*]thiophenylidene **BTP** can be reversibly oxidised to the dicationic redox state **BTP^{2+}** (Figure 1.1b left).[13,14] **BTP** can be classified as an *electrochromic molecular switch*, because of a change in the optical properties when switching to the **BTP^{2+}**-state. Additionally, this molecular switch was investigated as a molecular break junction and exhibited an increased conductance by the factor of 70 upon oxidation.[13]

In contrast, if the switching results in a molecular motion, the molecule can be categorised as a *mechanical molecular switch*.[15-19] For example, azobenzene *trans*-**2** can isomerise to its *cis*-form controlled by light (Figure 1.1b right).[18,20] Upon switching, the mechanical motion brings the two crown ethers in close proximity in *cis*-**2**, which also alters the cation binding properties. While *trans*-**2** binds Na^+ cations, *cis*-**2** binds larger Rb^+ cations in a sandwich complex.[20]

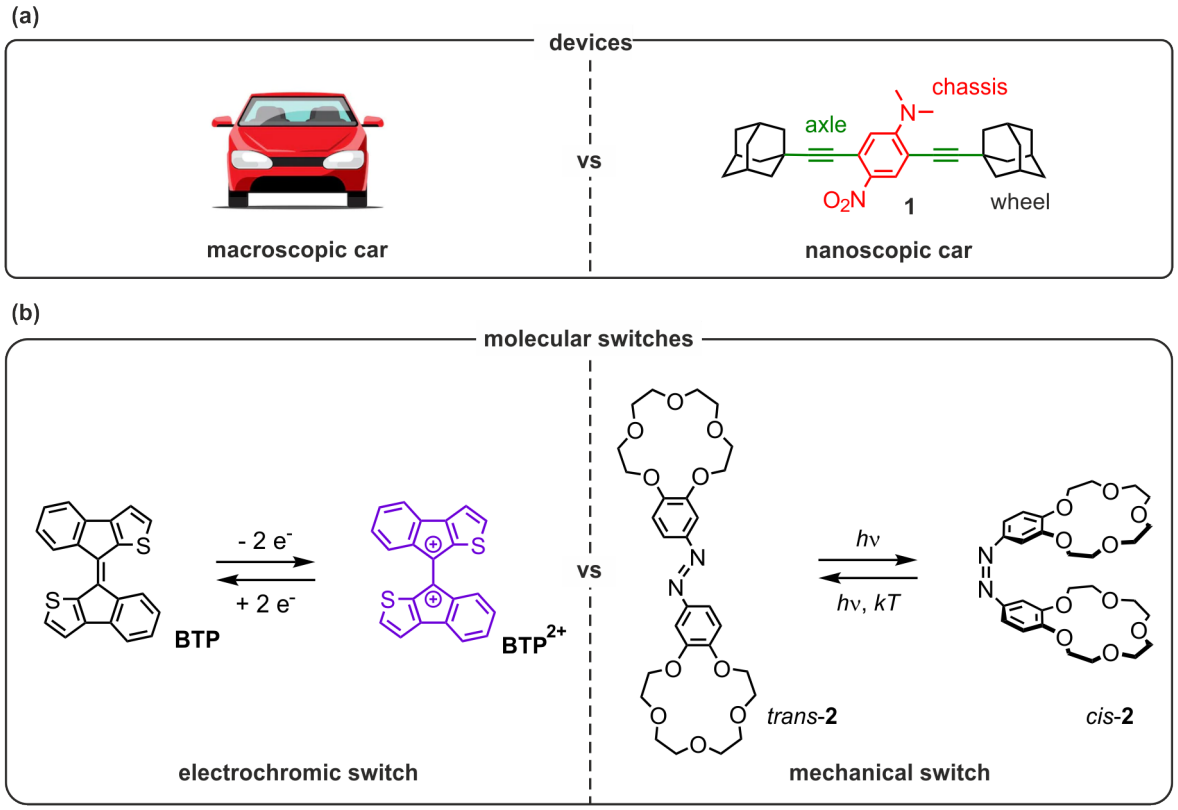

Figure 1.1. (a) Comparison of macroscopic (left) and nanoscopic (right) devices on the example of a car; depicted nanocar **1** was the winner of the nanocar race in 2017.[5-7] (b) Comparison between types of molecular switches: left: electrochromic redox-switch **BTP**[13,14]; right: light-switchable azobenzene **2** as an example for a mechanical switch.[18,20]

These mechanical motions on the molecular level are the integral part of *artificial molecular machines* (AMM), which were defined as molecular assemblies that can undergo changes in the relative positions of their components to perform a "useful task"[3] upon addition of an external stimulus.[3,4,8,17-19,21] This research field has seen a growing interest in recent years, which was recognised by the Nobel Prize in chemistry for Jean-Pierre Sauvage, Sir J. Fraser Stoddart and Bernard L. Feringa in 2016.[22-24] In the literature it is debated if the mere presence of a controlled molecular motion[4,18,25] or performed work is the critical criterion to qualify a molecule to be a molecular machine.[26,27] For example, the mechanical molecular switch **2** can be considered a molecular machine according to the first criterion,[18] but does not perform any work.

Additional to being components of AMMs and molecular devices, molecular switches have been utilised for controlling drug delivery[28-31] or the properties of polymers,[9,32] in molecular

electronics,[14,33-35] as switchable catalysts[36] or as molecular logic gates.[37,38] Therefore, the development of novel switching modes and functions along with the analytical understanding of the assembly processes and operation of molecular switches are worthwhile endeavours.

The two examples of molecular switches in Figure 1.1 are constructed by covalent synthesis. Yet, the more complex the structure and functions of the molecular switches are, the more difficult it becomes to synthesise such compounds directly by forming covalent bonds. Therefore, a supramolecular approach is often employed, which allows to assemble different components by reversible *noncovalent interactions*. As long as the types and positions of the noncovalent interactions in the molecular components are well designed, complex molecules with emerging functions can be *self-assembled* in a "lego-type" fashion.[39]

A simple example of a switchable supramolecular complex is the inclusion complex **TTF@3**, which forms due to noncovalent donor-acceptor interactions between the electron-rich tetrathiafulvalene **TTF** and the electron-poor viologen units of host **3** (Figure 1.2 left).[40] When **TTF** is oxidised, it becomes cationic and is repelled from the cavity of host **3**. Consequently, the complex of **TTF** and **3** disassembles and $\mathbf{TTF^{2+}@4}$ is formed, instead. In this complex, the electron-poor $\mathbf{TTF^{2+}}$ forms a donor-acceptor interaction with the electron-rich host **4**. This process can be reversed by the reduction to the neutral **TTF**.

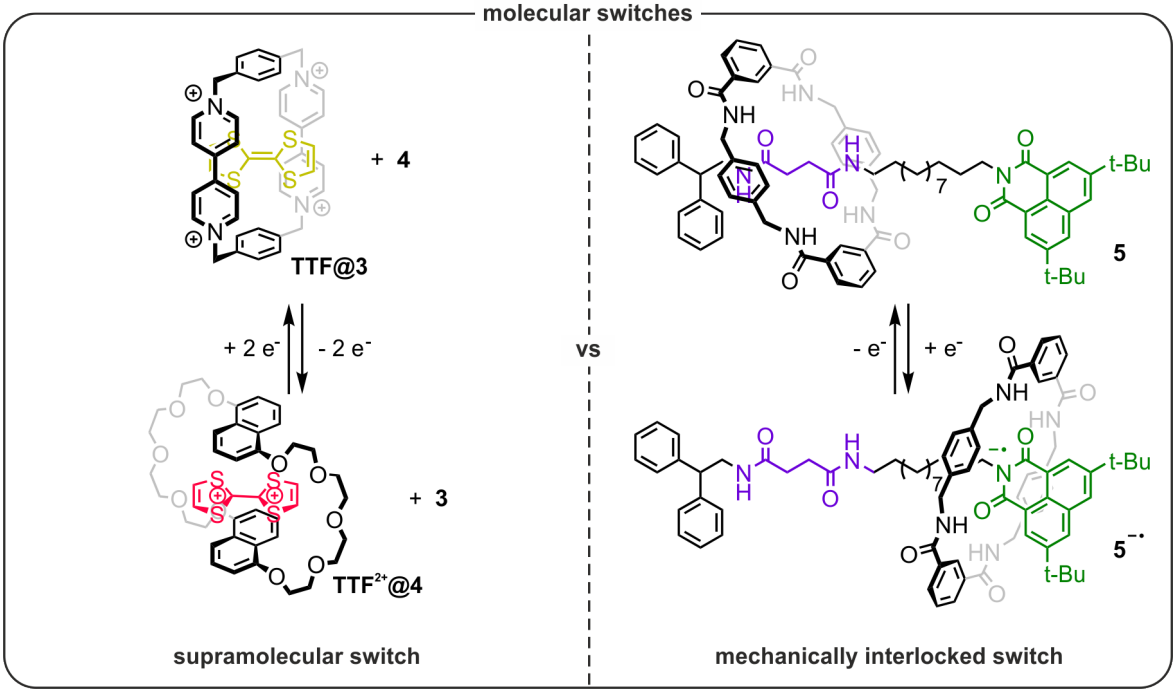

Figure 1.2. Comparison between redox-switchable supramolecular and mechanically interlocked switches. left: supramolecular switch **TTF@3** can be reversibly interconverted by oxidation to the inclusion complex $\mathbf{TTF^{2+}@4}$;[40,41] right: rotaxane **5** as an example for a mechanically interlocked switchable shuttle.[42]

To prevent the disassembly of supramolecular switches, complexes can be mechanically interlocked.[43] In *mechanically interlocked molecules* (MIMs), the switching may result in a motion of one component with respect to the other component. For example, in rotaxane **5**

the macrocyclic component can reversibly undergo a movement along the axle component from the diamide (violet) to the naphthalimide (green) moiety (Figure 1.2 right).[42] The macrocycle populates the diamide binding unit more in the neutral state **5** and the naphthalimide unit more in the reduced state $\mathbf{5}^{-\bullet}$, as the strengths of the hydrogen bonds are higher in the anionic naphthalene unit.

While noncovalent interactions cohere the assembly and compensate for the negative entropy of complex formation in supramolecular complexes, in MIMs noncovalent interactions determine the most stable co-conformation in each of the different switching states.

Both switches shown in Figure 1.2 are redox-switchable since the switching by an electrical potential is advantageous due to no production of chemical waste. Additionally, electrochemical analytical techniques can be applied to investigate the operation of the switch and be effector and detector at the same time.[44]

Generally, the noncovalent interactions need to be designed in a tailor-made manner for the molecular switch or machine to be assembled and to perform its desired function. Therefore, this thesis emphasises the analytical tools used for understanding these noncovalent interactions, which are fundamental for the successful development of novel supramolecular as well as mechanically interlocked switches. Additional analytical techniques are developed to investigate the assembly process and the operation of molecular switches.

The specific goals of this thesis are:

- Introduction of redox-switchable components into a well-known supramolecular system, which allows the construction of rotaxanes
- Investigation of the thermodynamic parameters of the complexes in dependence on structural changes in the macrocycle and axle
- Detailed understanding of noncovalent interactions in the involved complexes at different conditions and upon switching
- Development of a new host for strong binding of cationic guests
- Design of novel molecular switches based on the interpretation of thermodynamic properties of their components
- Construction of molecular switches applying the fundamental concepts self-assembly, mechanical bonding, self-sorting, and multivalency
- Analytical investigations of the assembly process and operation of molecular switches

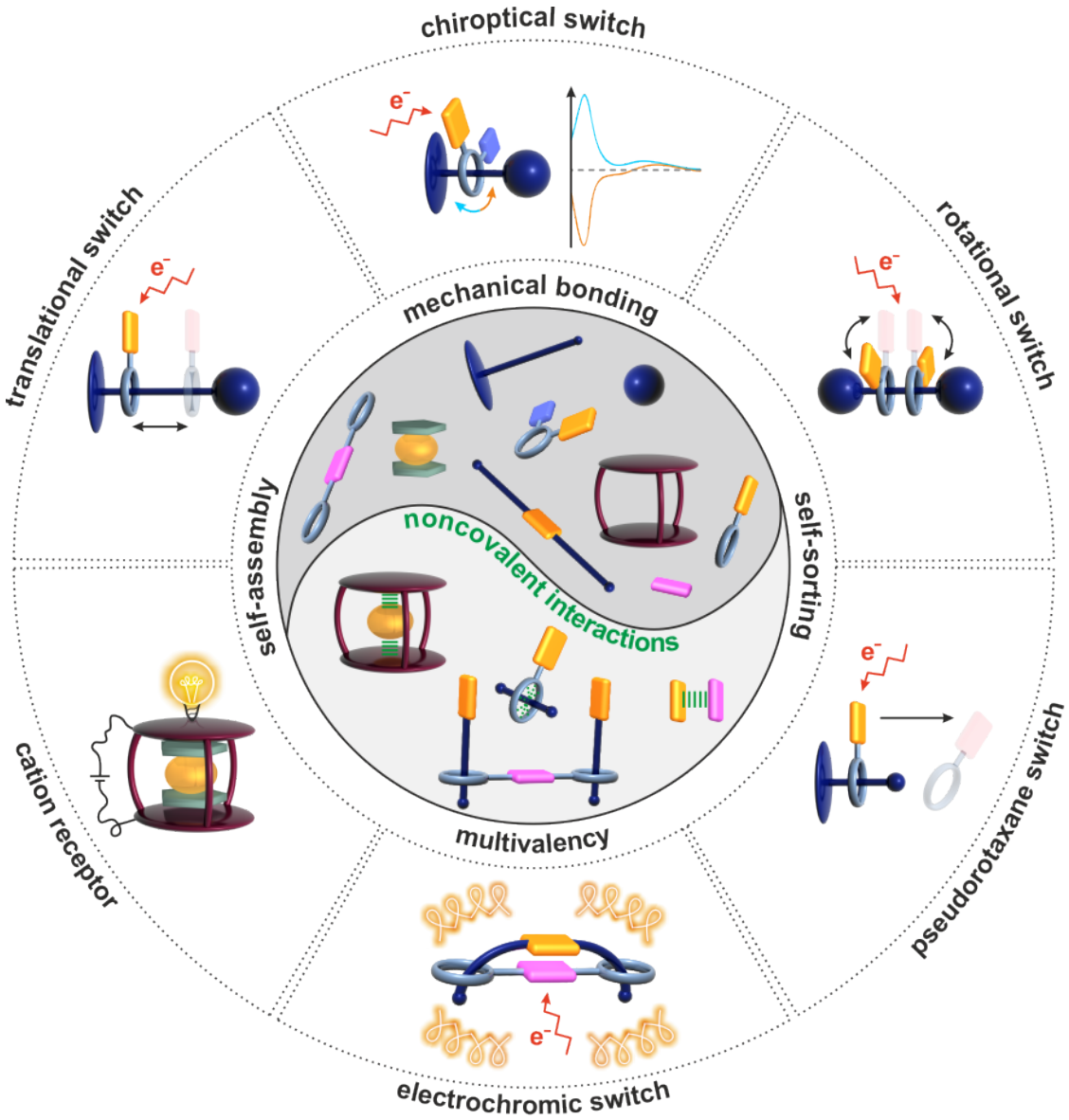

Figure 1.3. Schematic outline of the topics discussed in this thesis: Noncovalent interactions (green) are investigated and then applied using the fundamental concepts of self-assembly, self-sorting, multivalency and mechanical bonding to construct various functional supramolecular complexes and molecular switches.

The results of this thesis are mainly analytical and benefitted from close collaboration with other researchers, who synthesised some of the molecules or building blocks, contributed to the scientific understanding with other analytical techniques or theoretical calculations. Detailed author contributions are outlined for each peer-reviewed article in Section 6.

2 Theoretical background

2.1 Introduction to supramolecular chemistry

2.1.1 Noncovalent interactions

Supramolecular chemistry has been defined as the "chemistry of molecular assemblies and of the intermolecular bond" by JEAN-MARIE LEHN in 1988 in his Nobel Lecture.[45,46] LEHN received the Nobel prize together with CHARLES J. PEDERSEN[47] and DONALD J. CRAM[48] "for their development and use of molecules with structure-specific interactions of high selectivity". Based on the definition given by LEHN, the intermolecular bonds, more specifically *noncovalent interactions*, are a fundamental pillar and a distinguishing factor of supramolecular chemistry from other chemical research fields. These intermolecular interactions are generally considered to be weaker than their covalent counterparts. In covalent bonds, electrons are shared between two atoms and classical examples are C-C or C-H bonds exhibiting dissociation energies of 346 kJ mol^{-1} and 411 kJ mol^{-1}, respectively.[49] But there are also weaker covalent bonds, such as C-I bonds with a dissociation energy of 213 kJ mol^{-1}.[49] Yet, for noncovalent interactions the electron and charge distributions of the involved atoms barely change and their strengths range from very low 1 kJ mol^{-1} to comparably high dissociation energies around 350 kJ mol^{-1} in specific cases.[50-54] This wide variety of bond strengths and their common feature of reversibility make noncovalent interactions crucial for the three-dimensional structure of biomolecules, such as proteins or DNA,[55] as well as impacting the properties and functions of polymers.[50]

An overview on the types and strengths of noncovalent interactions is given in Figure 2.1. *Coulomb interactions* between two oppositely charged ions are the strongest bonds, which can reach binding energies of similar strengths as covalent bonds depending on the environment. *Coordinative bonds* between metal atoms and ligands exhibit medium to high dissociation energies in the range of 40–125 kJ mol^{-1} and are extensively utilised in supramolecular assemblies,[56,57] however they are considered more as covalent and are not used in the following thesis.

Hydrogen bonds are key interactions in DNA, as they hold together the DNA base pairs. Their strengths span over a wide range, with *ionic hydrogen bonds* being the subcategory with higher binding energies. The strongest example for ionic hydrogen bonds with a dissociation energy of 160 kJ mol^{-1} corresponds to a hydrogen bond formed between a fluoride anion and a hydrofluoric acid molecule.[51,52,58] An example for the weaker *neutral hydrogen bonds* are hydrogen bonds between two amide units in a protein core with dissociation energies of 2–10

kJ mol^{-1}.[51] Furthermore, hydrogen bonds exhibit a specific angle of 90°–180° with the stronger ones coming closer to linearity, because of their higher covalent character.[52,53] *Halogen bonds* exhibit also more a covalent characer and are the most directional of the interactions discussed here, as all halogen bonds form an angle of nearly 180°.[54] The directionality of noncovalent interactions can be utilised to facilitate a higher selectivity in a supramolecular assembly process. The other electrostatic noncovalent interactions mentioned exhibit a lower degree of directionality, *i.e.,* dipole-dipole interactions or no directionality, *i.e.,* Van der Waals interactions.

Van der Waals interactions are the weakest on the list of noncovalent forces. They are significant for nonpolar molecules where other interactions are absent. Van der Waals interactions occur when the fluctuating electron cloud of one molecule polarises the electron cloud of another molecule causing an attractive electrostatic interaction (induced dipole interaction).[53]

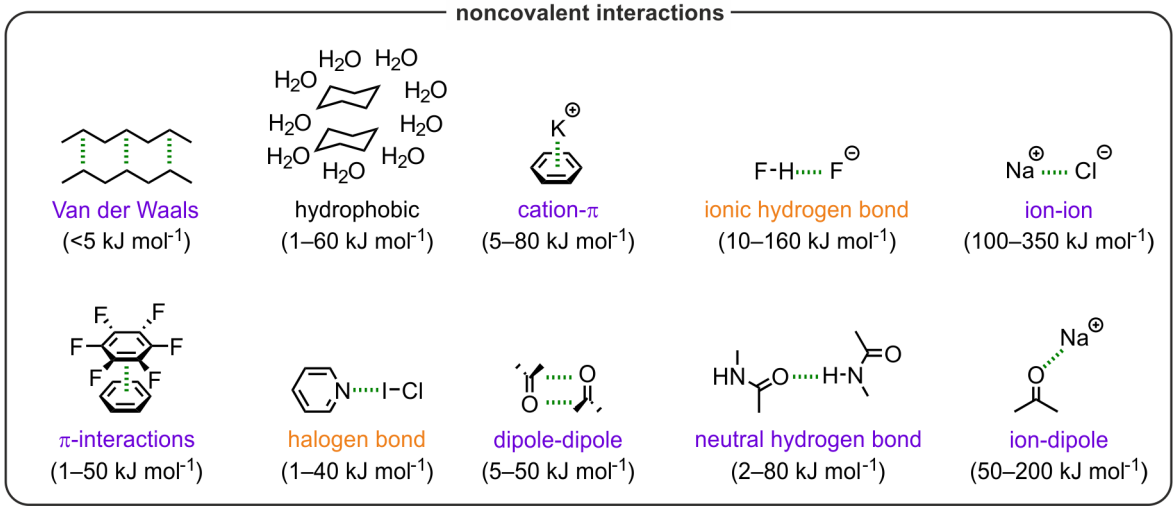

Figure 2.1. Examples of noncovalent interactions with their estimated binding strengths given as bond dissociation energies.[51-54] The binding strength increases from left to right. The electrostatic noncovalent interactions are highlighted in violet and noncovalent interaction with a more covalent character in orange. The hydrophobic effect does not fit in any of these two categories.

Noncovalent interactions differ not just in their strength, but also their interaction range. Whereas Coulomb interactions become weaker over the distance r with r^{-2} and ion-dipole interactions with r^{-4}, Van der Waals and dipole-dipole interactions lose strength with r^{-6}.

A simple description for *cation-π interactions* is the electrostatic attraction of a negatively charged π-electron cloud and a positively charged cation. However, all π-interactions can be more accurately described when the quadrupole of the aromatic molecule is considered. Terms like "π-π-stacking" have been shown to be misleading and describing only a few systems accurately.[59,60]

In Figure 2.2 the quadrupole of electron-rich and electron-poor aromatic systems are schematically shown. For two electron-rich aromatic systems a face-centred stacking results

in repulsion of the two negatively polarised electron clouds. Instead, an off-centre parallel stacking is observed or edge-to-face interactions which can also be described as C-H-π interactions formed between the positively polarised hydrogen of one benzene and the π-electrons of another.

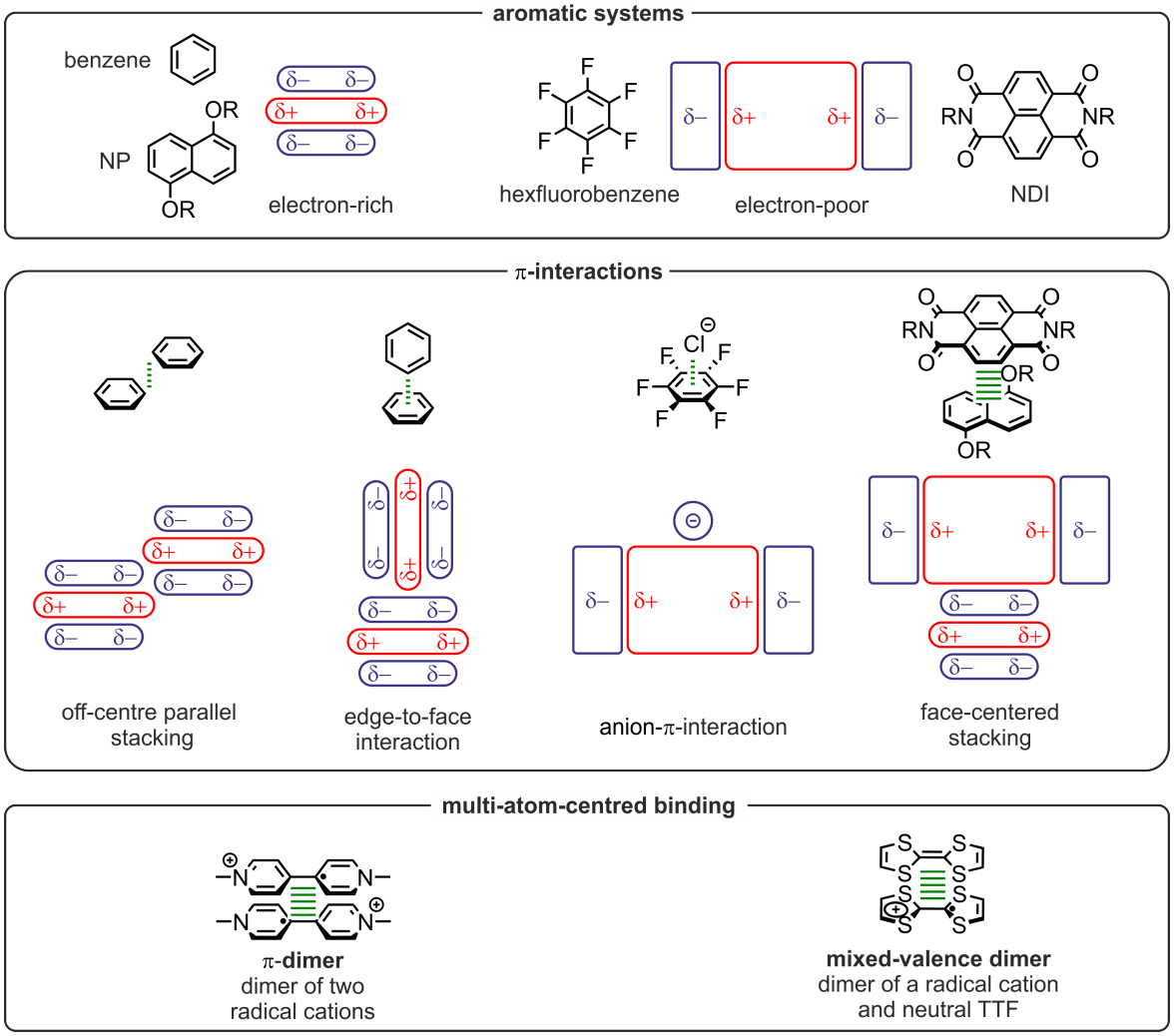

Figure 2.2. (top) Examples of electron-rich and electron-poor aromatic systems with a schematic representation of the molecule's quadrupole. For the electron rich-system, the quadrupole is depicted with the aromatic plane orthogonal to the paper plane and for the electron-poor system the aromatic plane is in the paper plane;[59] (middle) Examples of attractive interactions of aromatic molecules involving π-electrons; (bottom) multi-atom-centred π-bonding of two MV radical cations (π-dimer) and between a TTF cation and a neutral TTF (mixed-valence dimer).[41,61]

Electron-poor aromatic systems such as hexafluorobenzene have most of their electron density located on the peripheral fluorine atoms and the centre of the aromatic system is positively polarised instead. This allows *anion-π interactions* to be formed, which are the newest discovered noncovalent forces.[62,63] In contrast, classical face-centred stacking can be observed for the combination of one electron-rich and one electron-poor aromatic system, as shown in Figure 2.1 for benzene and hexafluorobenzene and in Figure 2.2 for naphthalene diimide (NDI) and 1,5-dialkoxynaphthalene (NP). In these so-called *donor-acceptor complexes*, a *charge*

transfer interaction is possible, which can typically be observed by a characteristic absorption band in the UV/vis spectrum.[52,64]

Aromatic radicals are a special case where face-centred stacking is observed, as shown for organic radical cations of methylviologen (MV), TTF and others.[61] When two organic radicals are interacting, a diamagnetic π-dimer can be observed, where the two unpaired electrons engage in a *multi-atom-centred bonding* overcoming even the repulsion of the two cationic charges.[41,61] A related interaction can also be found for a radical cation and a nonaromatic neutral TTF. This attractive force is referred to as *mixed-valence interaction* and the spin density of the radical is equally shared between both TTF molecules.[41,61,65]

Outstanding from the noncovalent interactions is the *hydrophobic effect*, as it represents not a direct interaction between two atoms or molecules, but rather the absence of interactions:[51,66] Hydrophobic molecules do not have significant attractive interactions with water, while water molecules can form hydrogen bonds with each other. Therefore, hydrophobic molecules aggregate to reduce the surface which is in contact with the surrounding water molecules. The energy gained in this interaction arises from more hydrogen bonds formed between water molecules, as well as a higher entropy state of the water molecules that are not in contact with the hydrophobic molecules. In case another polar solvent instead of water is present, this interaction is then referred to as the *solvophobic effect*.

Generally, the high dependence of all noncovalent interactions on their environment needs to be highlighted. For instance, ion-ion interactions become stronger as the environment becomes less polar and are the strongest in the gas-phase. Additionally, hydrogen bonds become weaker, if the solvent is protic, as solvent molecules can compete with the binding partners.

The full applicability and importance of noncovalent interactions cannot be found in individual bonds, but in the combination of multiple and different types of noncovalent interactions in the same supramolecular system, allowing researchers to control the assembly process and function of molecules and supermolecules in detail.

2.1.2 Host-guest complexes

The prototype of a supramolecular system is the *host-guest complex* and is usually composed of a small guest **G** and a large host molecule **H** (Figure 2.3).[48] If there are different guests competing for the host as shown in Figure 2.3, the host-guest combination with the highest affinity forms, this concept is called *molecular recognition*.[67] Molecular recognition is based on the *complementarity* of the geometrical shapes and noncovalent interactions of both binding partners. In the schematic example the shape of guest **G** fits well in the cavity of host **H**.

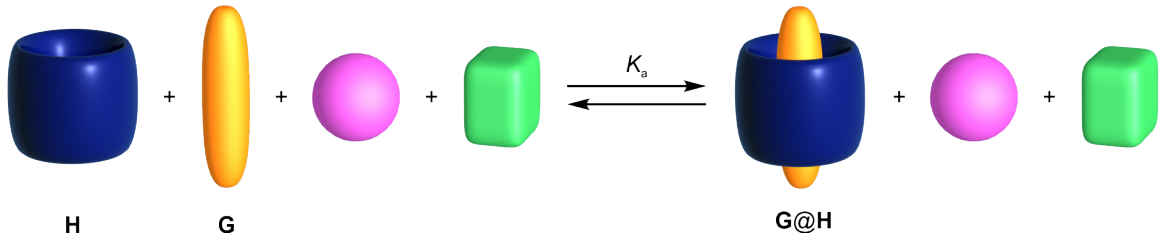

Figure 2.3. Schematic representation of a host-guest equilibrium with three different guests. The orange guest **G** exhibits the highest affinity for the host **H**.

Binding constants for complexes can be translated into free energy changes $\triangle G^0$ (free Gibbs energy) by Equation 2.1 which is derived from the van't Hoff equation considering the temperature T and the ideal gas constant R. $\triangle G^0$ will be referred to as *binding energy* in this thesis and exhibits negative values for exergonic processes, thus complexes with attractive binding energies and a binding constant > 1.

$$\Delta G^0 = -RT \ln K_a \tag{2.1}$$

$$= \Delta H^0 - T \Delta S^0 \tag{2.2}$$

For a full thermodynamic description and understanding of a host-guest complex the binding energy $\triangle G^0$ can be divided into an enthalpic and entropic contribution, according to the *Gibbs-Helmholtz equation* (Equation 2.2). The binding enthalpy $\triangle H^0$ depends on the sum of all attractive and non-attractive forces formed or broken during the assembly process. Hence, in case of a supramolecular complex, $\triangle H^0$ contains the sum of all noncovalent interactions broken and formed upon complex formation. If the sum of all interactions is attractive, $\triangle H^0$ exhibits negative values. In contrast, the binding entropy $\triangle S^0$ is positive if $\triangle S^0$ contributes favourably to the overall binding energy $\triangle G^0$, which occurs when the disorder of the system is increased upon complex formation. Usually, for a host-guest complex such as the schematic example in Figure 2.3 the order in the system is increased upon binding due to the lower particle number. Methods for determining the binding constants, energies, enthalpies, and entropies for a system will be discussed in Section 2.3.

The entropic penalty upon binding can be lowered by *preorganising* the host's structure to recognise a specific guest.[68] Flexible hosts loose more degrees of freedom upon guest binding than rigid hosts. In Figure 2.4a HAMILTON receptor **6** binding diethylbarbital **5** is shown.[69] Here, the structure of the macrocycle is preorganised to bind the guest with overall six hydrogen bonds. Increasing the flexibility of the receptor **7** by opening the macrocycle lowers the binding constant significantly.[70] Introducing a more flexible alkyl spacer in the receptor **8** instead of an aryl spacer lowers the binding constant further. In contrast, for another guest 3-methyl-7-propylxanthine **9** the opposite observation can be made. Here the preorganised host **6** does not fit to the shape of the guest, therefore the more flexible receptor **9** exhibits the highest binding constant compared to the other two receptors.[70] Overall, preorganisation leads to a higher guest selectivity and a lower entropic penalty upon guest binding.

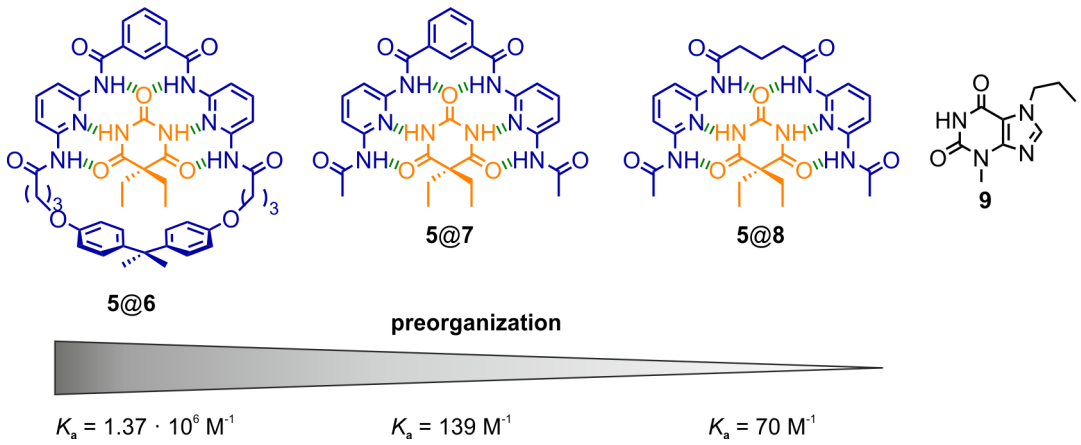

Figure 2.4. Three receptors for diethylbarbital **5** with different degrees of preorganisation and their binding constants are shown in chloroform.[69,70]

A similar trend can be observed for host molecules, when moving from *macrocycles* to three-dimensional structures (Figure 2.5). For example, the two-dimensional tetralactam macrocycle exhibits less preorganisation and thereby enthalpy-driven binding, *i.e.*, it binds diamide guests through four hydrogen bonds.[71] For hosts with three-dimensional structures, as cucurbit[n]urils, a more entropy-driven guest-binding can be observed due to higher preorganisation of the host and these hosts are also referred to as molecular cavitands or containers. Cucurbiturils are mainly utilised in water, where they bind guests driven by the hydrophobic effect and dipolar interactions with the negatively polarised portals of cucurbiturils.[72,73] For polycyclic host molecules with a defined cavity, the term *cage* was coined. These highly preorganised structures show a high selectivity for a small guest number. Here, a resorcinarene-based hemicarcerand is shown which binds *p*-xylene due to hydrophobic interactions, but *o*- and *m*-xylene do not fit the cavity anymore.[74] In fact, the hemicarcerand does not form without a suitable guest, as an empty cavity is energetically unfavourable. This widely applied approach to facilitate the formation of a specific host by its guest, is called the *template-effect*. The largest number of cages described in the literature are metal-organic cages,[57,75-77] yet many solely organic cages are known, as well.[78,79]

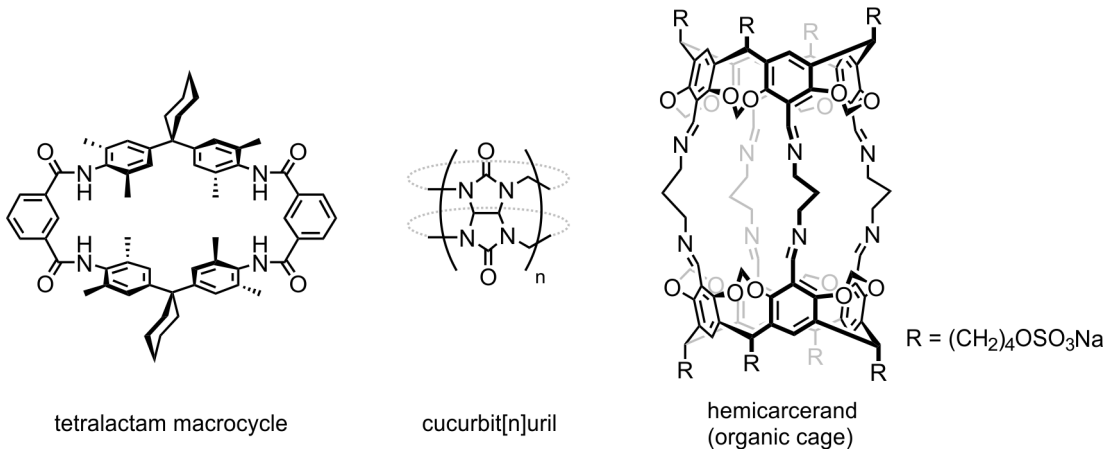

Figure 2.5. Examples of host molecules.[74]

So far, we have considered the host-guest equilibrium as a singular interaction between two molecules. However, the environment, specifically the solvent, needs to be considered, as well. The nature of the solvent has a considerable effect on the binding strength of all host-guest complexes. Both the host **H** and the guest **G** are surrounded by a solvation shell in solution, which needs to be disrupted and then reformed around the complex **H@G** (Figure 2.6). On the one hand, the molecules **H** and **G** form noncovalent interactions to solvent molecules which need to be broken. On the other hand, the solvent molecules released from the solvation shell can form noncovalent interactions with bulk solvent leading to an overall higher binding energy. Considering entropic effects, the release of solvent molecules from the solvent shell into the bulk solution increases the disorder of the system. Here, a special case are solvent molecules which are released from the host's cavity, as these molecules are in an entropically unfavourable state and form fewer attractive interactions with other solvent molecules (Figure 2.6, light grey spheres). If the solvent is water the term of *high-energy water* was coined for water molecules trapped in the host's cavity.[66] For example, it was shown for cucurbiturils[80] and metal-organic cages[81] among other hosts[66] that the release of high-energy water molecules is a major determinant for guest binding in aqueous solutions.

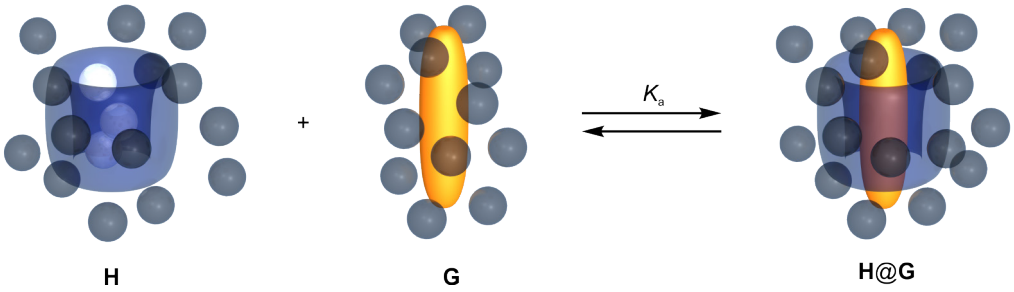

Figure 2.6. Schematical representation of the host-guest equilibrium considering the solvation shell (grey) of host **H** and guest **G**. Solvent molecules bound in the host's cavity are highlighted in light grey.

A careful consideration of the role of the solvent for each host-guest system is crucial from a practical point of view, as the solvent needs to solvate the guest, host, and host-guest complex, but also not to compete with one of the binding partners for the desired host-guest interaction. For most host-guest systems, which are not based on the solvophobic effect, nonpolar solvents with a low dielectric constant (*e.g.,* chloroform, dichloromethane) provide the highest binding energies, although for insoluble polar guests or hosts more polar solvents (*e.g.,* acetonitrile, dimethylformamide) or protic solvents (*e.g.,* methanol or water) may be preferable.[53] For each host-guest system a fine balance between these effects needs to be maintained, often resulting in the necessity to employ solvent mixtures.

2.1.3 Crown ether/ammonium complexes

Cyclic polyethers, called *crown ethers,* were among the first host structures studied by supramolecular chemists. The synthesis and the affinity of crown ethers for a wide range of cations, *e.g.*, Li^+, Na^+ or Pb^{2+} were published by Nobel laureate PEDERSEN in 1967.[47,82,83]

[3*n*]Crown-*n* ethers are classified by the number of oxygen or other chalcogen atoms *n* and the overall atom number 3*n* in the macrocycle. Depending on the size of the crown ether, the binding energy for various cations changes.[84] For example, potassium cations exhibit the highest binding energy for [18]crown-6 (**C6**), as the cations fit in the macrocyclic plane and form cation-dipole interactions with all six oxygen atoms (Figure 2.7a). In contrast, caesium cations are too large for the diameter of the cavity of **C6** and bind stronger to [21]crown-7 (**C7**), instead.[84]

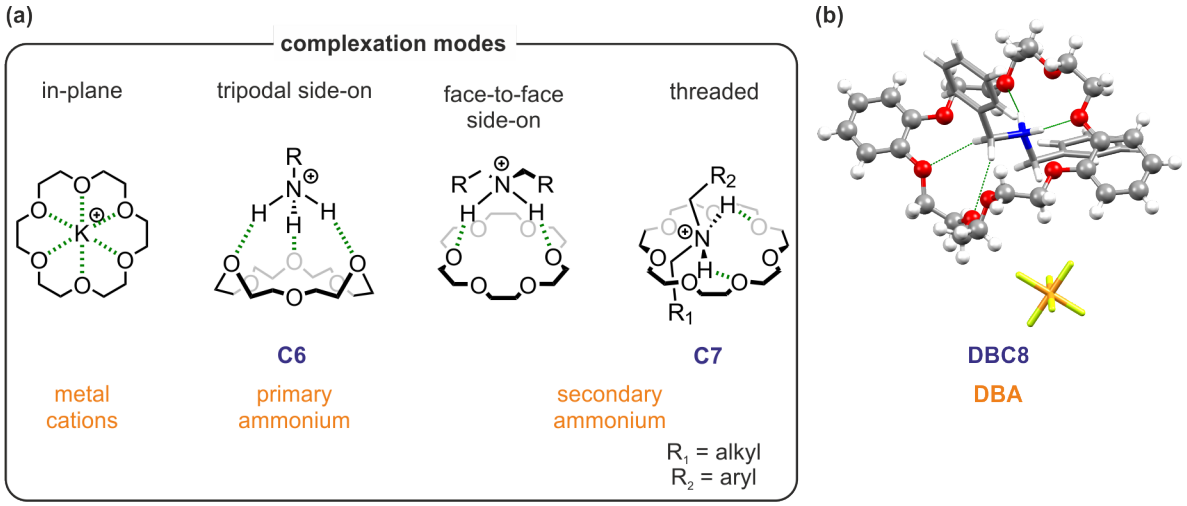

Figure 2.7. (a) Different complexation modes of crown ethers. The host is given in blue and the guest in orange. (b) Crystal structure of the dibenzylammonium (**DBA**) hexafluorophosphate and dibenzo-[24]crown-8 (**DBC8**) complex.[85] The attractive interactions (cation-dipole and hydrogen bonds) are highlighted in green.

Since 1995, special attention was directed to the complexes of crown ethers with ammonium ions.[43] While primary ammonium ions form tripodal side-on complexes,[86] for example with **C6**, secondary ammonium ions can form a face-to-face side-on complex with smaller crown ethers, but also a threaded complex with **C7** and [24]crown-8 (**C8**).[43,85,87] These complexes are of a particular interest, as they allow the formation of mechanically interlocked molecules, that will be discussed in Section 2.1.6. In the crystal structure of the complex of dibenzo[24]crown-8 (**DBC8**) and dibenzylammonium (**DBA**) hexafluorophosphate the Z-shape of the crown ether and the additional C-H···O hydrogen bonds can be observed which make the threaded complex energetically more favoured over a side-on complex (Figure 2.7b).[85] In contrast, the smaller **C7** cannot form a threaded complex with **DBA** as the *sec*-ammonium ion is required to bear at least one alkyl substituent to allow threading through the cavity of **C7**.[88] Additionally, other crown ethers larger than **C7** show stable complexes with quaternary ammonium ions, such as pyridinium ions, but they will not be discussed in detail here.[43,89]

There is a large variety of crown ethers and *sec*-ammonium ions described which form threaded complexes.[43] The binding energies for these complexes are higher in nonpolar solvents, such as $CHCl_3$ and CH_2Cl_2, and they decrease with an increasing polarity over

CH_3CN to acetone.[43,85] But, many *sec*-ammonium ions are not soluble in pure $CHCl_3$. Consequently, mixtures are often utilised, for example $CHCl_3/CH_3CN$.

Generally, a higher binding energy is observed for dialkyl substituted ammonium ions compared to aryl substituted *sec*-ammonium ions, due to a steric disruption of the hydrogen bonding pattern.[43,90] The higher hydrogen bond donor property of the benzylic methylene groups compared to the aliphatic ones does not compensate for this steric effect. Yet, there are aromatic systems, i.e. anthracene, which form additional π-interactions or donor-acceptor interactions with the crown ether and exhibit comparably higher binding constants as dialkylammonium ions.[43,91] For aryl substituted *sec*-ammonium ions electron withdrawing substituents lead to higher binding energies.[43]

Crown ethers are functionalised to endow the resulting complex with additional properties.[43,92] However, the functionalisation can alter the interactions of the crown/*sec*-ammonium complex significantly and may even prohibit the complex formation. For example, expanding the crown ether ring by an additional atom as in **DB25C8** in which a resorcinol was incorporated instead of the catechol results in a dramatic decrease of the binding constant (Figure 2.8a). **DBC8** binds approximately one order of magnitude stronger than **DB25C8** for the same conditions and guest.[93] If both catechols are exchanged with resorcinol no threaded complex is observed in solution.[93] For the crown ether ***i*-DBC8**, where two catechol units are incorporated in the ring asymmetrically, a slightly weaker binding than for the symmetrical isomer **DBC8** is observed.[87]

In contrast, exchanging two of the oxygen atoms in the crown ether with sulphur in dithiacrown **DTC8** results in a drop of the binding constant by a factor of 60, due to the weaker hydrogen bond acceptor strength of sulphur, and also due to the increased crown ether ring size caused by the higher radius of sulphur (Figure 2.8a, b).[94] The binding energies are given for the hexafluorophosphate counterion, which has become the gold standard for crown/*sec*-ammonium complexes, because of the synthetic accessibility, solubility and strength of binding of the hexafluorophosphate salts.[43] For weakly binding crown ethers as **DTC8**, the use of less coordinating anions results in an increase of the binding constant (Figure 2.8b). For instance, the use of tetrakis[3,5-bis(trifluoromethyl)phenyl]borate $BArF_{24}^-$ as an anion for **DBA** raises the binding constant by a factor higher than 25.[94] This effect of the counterion on the binding constant in **DBA@DTC8** can be rationalised by the poor stabilisation of the ammonium cation by weak coordinating anions. In other words, the binding energy of the cation and anion is low and, therefore, they compete less with the crown ether which stabilises the ammonium cation in the complex.

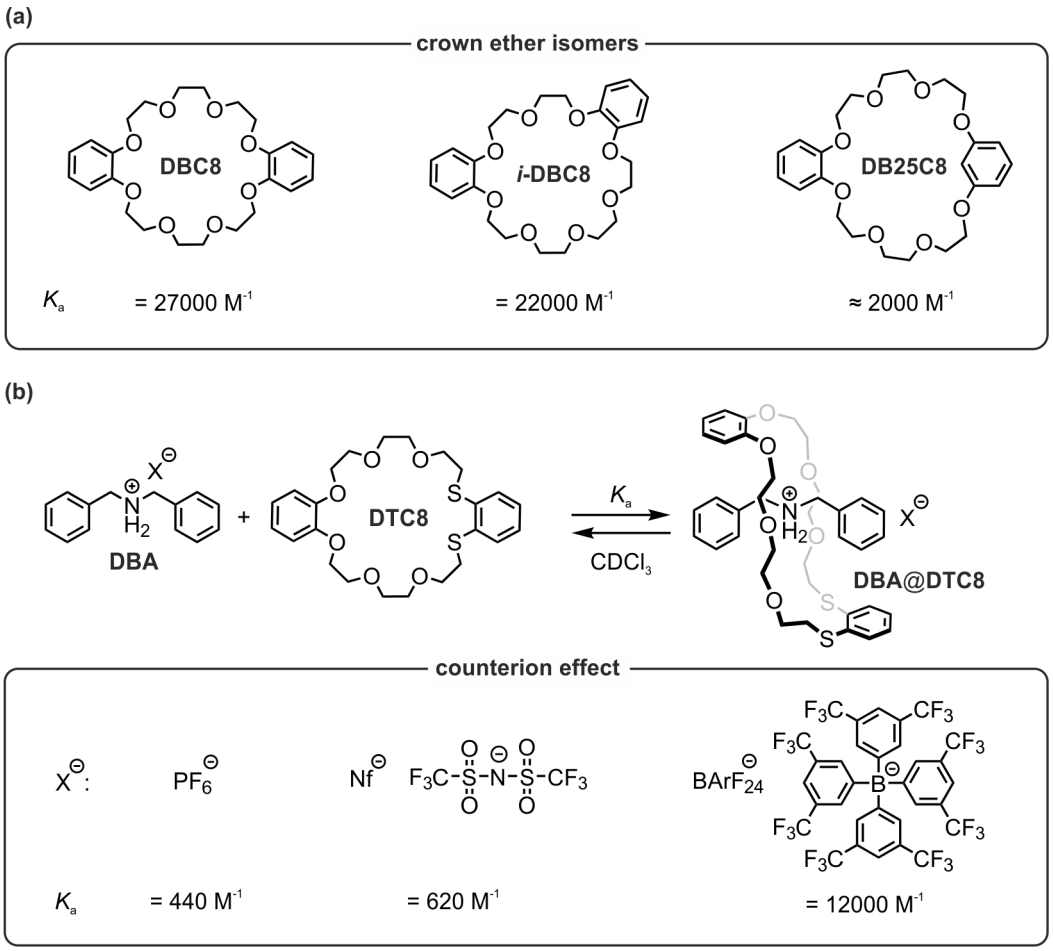

Figure 2.8. (a) **DBC8** and two of its isomers, along with their binding constants to **DBA**PF6 in $CDCl_3$.[87] The value for **DB25C8** is estimated from a slightly different system (CH_2Cl_2 as a solvent and bis(4-methoxycarbonylbenzyl)ammonium hexafluorophosphate as a guest) based on the binding constant of **DBC8** for the same system.[93] (b) Binding of dithiacrown **DTC8** to **DBA** with different weakly coordinating anions.[94]

The effect of counterions was studied in more detail for **DBA** and **DBC8** by GIBSON and coworkers.[95,96] In their works, the complexation equilibrium shown in Figure 2.8b is separated in a two-step process. Firstly, the dissociation of the ion pair occurs followed by the binding of the crown ether and the dissociated cation. For stronger coordinating anions, such as tosylate, tetrafluoroborate or trifluoroacetate, the ammonium salts exist as ion pairs in nonpolar solvents, while the complex does not appear as ion pairs.[95] The differences in the observed binding constants for these salts are determined by the differences in the salt dissociation energies. In this thesis, only weak coordinating anions will be utilised, which lead to a highly dissociative character of the ammonium salts in nonpolar solvents. Consequently, the ion dissociation will not be considered separately for the determination of the binding constants.

2.1.4 Self-assembly, self-organisation and self-sorting

The process of formation of a host-guest complex under thermodynamic control is a simple two-component example of *self-assembly*.[97] Yet, more complex ordered structures can also

form spontaneously from multicomponent mixtures by self-assembly.[98] Self-assembly can be observed at the molecular, as well as the nanoscopic or macroscopic scale.[39] At the molecular level, the free movement of the molecules involved and the reversibility of interactions between components, that allow for the error-correction of structures which are not the thermodynamically most stable ones, are key requirements for a successful self-assembly process.[52] Hence, noncovalent interactions are commonly used to form self-assembled complexes. Yet, the position and the type of the involved noncovalent interactions in the molecular components need to be precisely designed to allow the formation of the desired structure. According to the Gibbs-Helmholtz equation, the binding enthalpy of the newly formed interactions is required to overcome the entropic loss in the self-assembly process to allow the formation of ordered structures (Figure 2.9a).[39] Consequently, a closed system already at its thermodynamic minimum cannot form ordered structures.

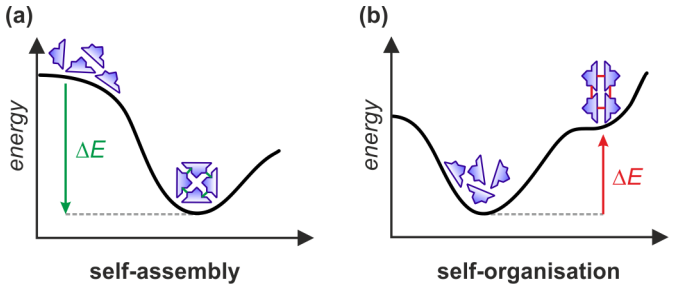

Figure 2.9. Schematic representation of the energy profiles for: (a) a self-assembled system with released energy in green and (b) a self-organised system with dissipated energy in red.

In contrast, open systems, as most biological systems, exhibit complex ordered structures that are not in a thermodynamic minimum state. If a constant energy flow maintains the ordered state, this process is called *self-organisation* (Figure 2.9b).[98] For example, this energy flow can be generated by a chemical fuel or light. If this flow stops the system returns to a less ordered state in the thermodynamic minimum. For biological systems, such a state may be the death of the living organism. Artificial non-equilibrium, also called dissipative systems, are of rising interest on the topic of molecular machines.[99] While self-organised systems consume energy, self-assembled systems release energy. Overall, both self-assembly and self-organisation are key concepts in supramolecular chemistry to control the formation of complex structures from disordered mixtures of simple components.[100]

Another concept allowing the understanding and prediction of complex emerging structures from multicomponent mixtures is *self-sorting*.[101-104] For solutions containing multiple binding partners, self-sorting describes the process when from the library of virtual complexes only specific combinations are formed. If molecules recognise themselves and form dimers, trimers, and higher oligomers, *narcissistic self-sorting* is occurring. In contrast, *social self-sorting* describes the formation of specific combinations, as shown in Figure 2.10 top. In the schematic example, the cubic host **H2** recognises the cubic guest **G2**, whereas the blue host **H1** recognises the orange guest **G1**. Hereby, the self-sorting of complexes can occur

thermodynamically based on their respective binding energies. Additionally, kinetic self-sorting was applied, when not the thermodynamically most stable complexes are formed.[104,105] In Figure 2.10 top, a small four component self-sorted system is shown. As this concept can be translated to big mixtures, including libraries of hundreds of virtually possible complexes, self-sorting represents a key concept in the field of *systems chemistry*, as well.[101,102,106,107] In the human body, self-sorting occurs in between the DNA bases, where adenine recognises thymine, as guanine does with cytosine.

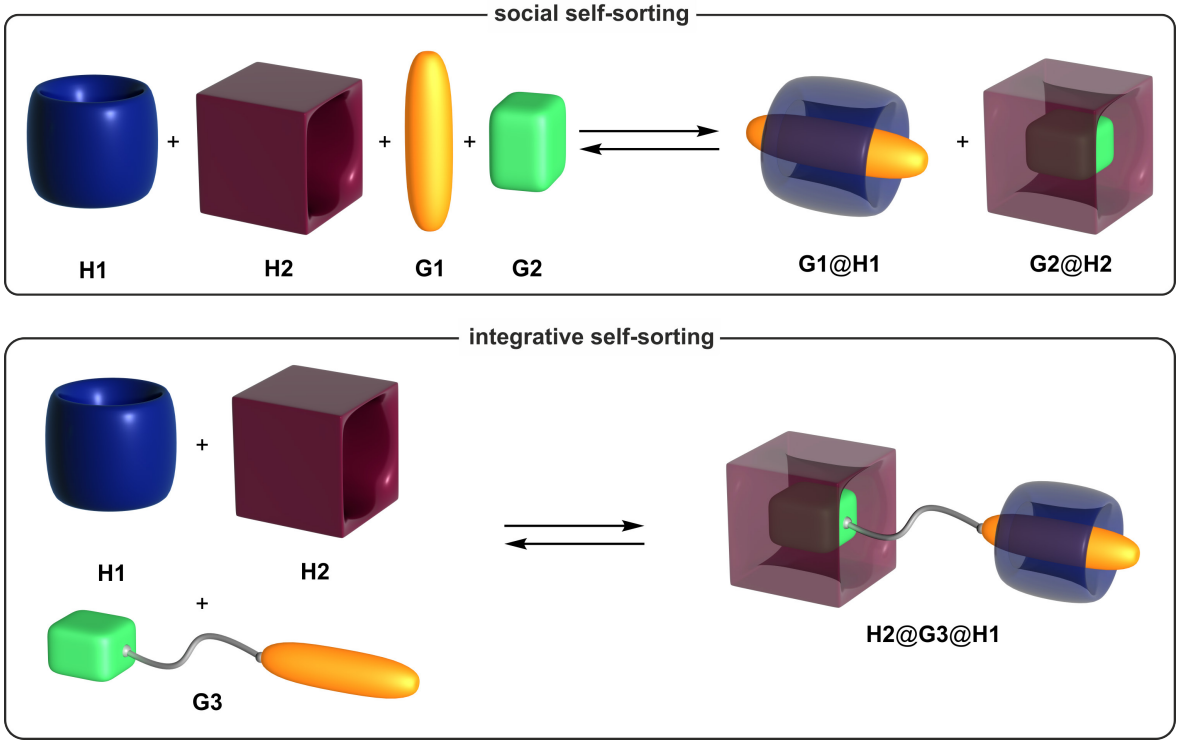

Figure 2.10. Schematic representation of a social and an integrative self-sorting system. The red host **H2** has a high affinity for the green guest **G2** and the blue host **H1** for the orange guest **G1**.

Self-sorting can also be applied to assemble multiple different components into one molecule. Therefore, two or more binding units are combined into the same molecule and thereby, dictate the assembly of one complex. This process known as *integrative self-sorting* is shown for the combination of the cubic and round shaped units combined to one guest molecule **G3** that forms one complex with both hosts **H1** and **H2** (Figure 2.10 bottom).[102]

For self-sorting to be successful often, an orthogonal binding approach is taken, where the undesired structures not only exhibit a low binding constant or form slowly, but are thermodynamically unstable or kinetically impossible to form. Consequently, self-sorting is a tool for supramolecular chemists to "write" into the molecular code of designed components in mixtures and, thereby, program the resulting molecular assemblies.[101]

2.1.5 Multivalency and cooperativity

Considering the heterodivalent guest **G3** mentioned in Figure 2.10, another fundamental concept of supramolecular chemistry was introduced, which is *multivalency*. This term describes how many singular weak interactions combine to maximise the interaction energy for the whole multivalent complex.[108,109] A simple example that illustrates multivalent binding at a macroscopic level is a burr which sticks to a surface only when many of its hooks are in contact with that surface (Figure 2.11a).[108] One hook alone does not have a sufficiently strong interaction strength to hold the weight of the burr on a surface. At a molecular level, multivalency describes the interaction of at least two molecules with m and n numbers of binding sites (m, n > 1).[108,110] The interactions in a multivalent complex need to be reversible to allow for error-correction. In Figure 2.11b, a hexavalent porphyrin macrocycle is shown which binds a hexavalent pyridine guest.[111] In this example, the *effective molarity EM* for each binding step describes the concentration level below which the multivalent binding (ring closure between the same two molecules) is preferred over the oligomeric binding to a third molecule (Figure 2.11c and Figure 2.12c).

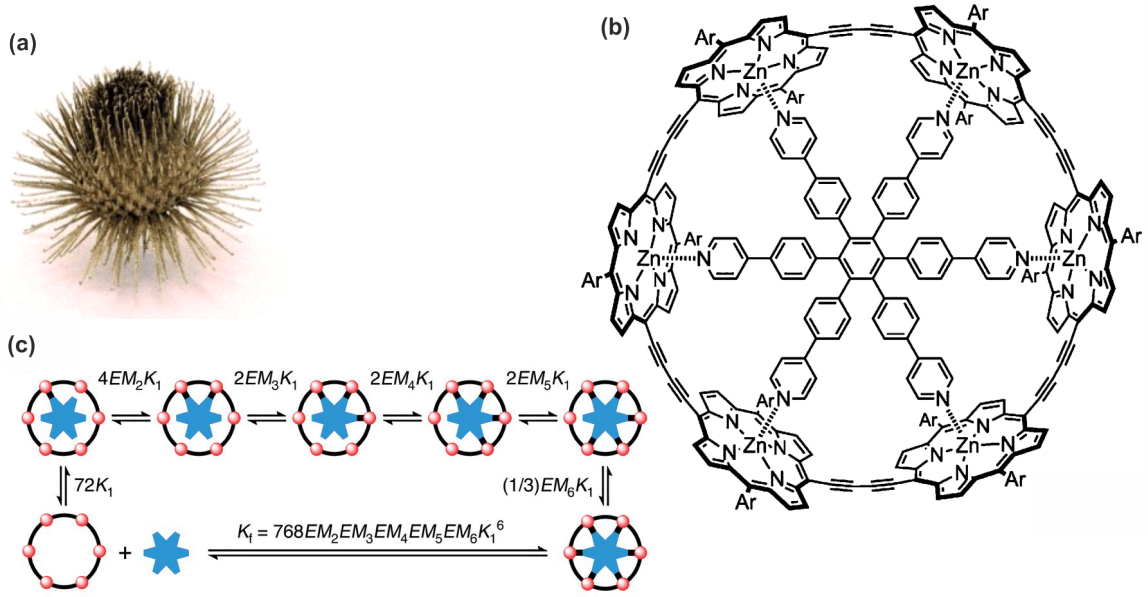

Figure 2.11. (a) A burr illustrating multivalency in the macroscopic world. Adapted with permission from C. Fasting *et al.*[108] Copyright © 2012 WILEY-VCH Verlag GmbH & Co. KGaA, Weinheim. (b) Hexavalent porphyrin-pyridine complex.[111] (c) Scheme of the stepwise binding in the hexavalent porphyrin-pyridine complex with effective molarities of *EM* = 280 –1700 M. Adapted with permission from H. J. Hogben *et al.*[111] Copyright © 2011 American Chemical Society.

If the individual binding events are dependent of each other, multivalent systems are characterised with respect to their *cooperativity* of binding.[112-114] Generally, cooperativity describes for a given system, whether the multivalent binding energy is higher or lower compared to the binding energy of the same amount and type of independent bonds (Figure 2.12a-c). The binding in the hexavalent complex above is highly positively cooperative due to the preorganisation of the two rigid hexavalent components. It is worth noting that

cooperativity does not need to be positive. For example, when two binding sites are in proximity, steric repulsion might cause negative cooperativity. Quantification of cooperative events is performed by *cooperativity factors*, which can be determined from binding constants. Over the course of this thesis, only divalent systems will be investigated, therefore, cooperativity factors will be discussed based on a divalent model system (Figure 2.12). All statistical correction factors were determined according to literature methods and are already included in Figure 2.12 and Equations 2.3 – 2.7.[113,115]

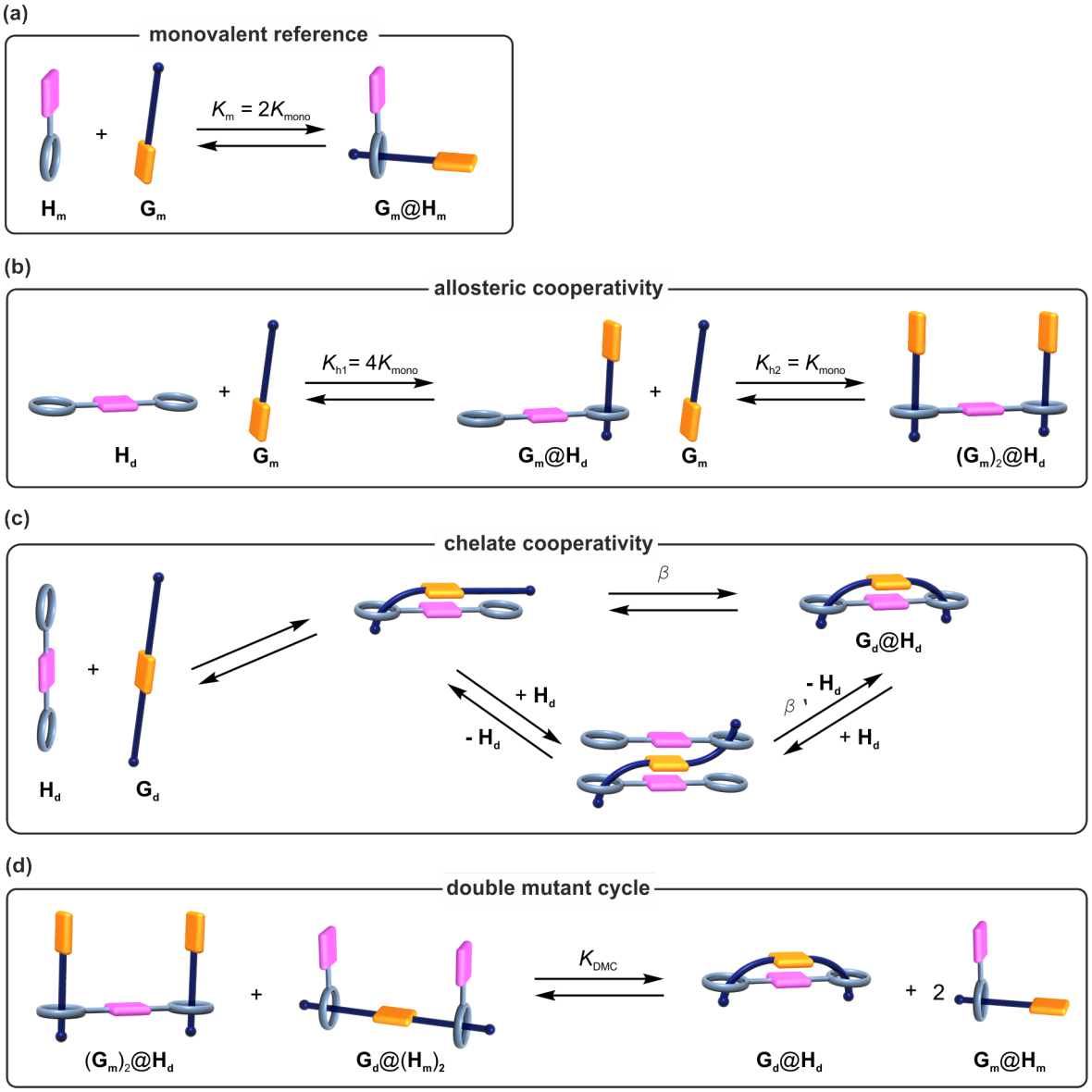

Figure 2.12. Divalent model system for the description of cooperativity factors and double mutant cycle analysis: (a) Monovalent reference system and definition of K_{mono}, as a statistically corrected monovalent binding constant. (b) Binding of two monovalent guests to a divalent host that illustrate allosteric cooperativity. (c) Stepwise binding of a divalent host and a divalent guest, showing the equilibrium steps, where the chelate cooperativity factors β and β' originate from.[112,114] (d) Disproportionation equilibrium to determine *EM* with a double mutant cycle (DMC) analysis.[113,115]

First, *allosteric cooperativity* characterises the *intermolecular* binding of multivalent molecules. For example, allosteric cooperativity can be investigated for 1:n complexes, where

a multivalent molecule exhibits n binding stations, even though 1:n complexes are technically not multivalent complexes. For a 1:2 complex, allosteric cooperativity describes if the first binding event facilitates or hampers the second binding event (Figure 2.12b). It can be considered separately for both a divalent host and a divalent guest. The allosteric cooperativity factor α can be expressed by Equation 2.3.[113,114]

$$\alpha = \frac{K_{\mathrm{h}}}{(K_{\mathrm{mono}})^2} = \frac{K_{\mathrm{h1}} \cdot K_{\mathrm{h2}}}{(K_{\mathrm{mono}})^2} \tag{2.3}$$

The binding constants K_{h1} and K_{h2} correspond to the two binding events of a monovalent guest and a divalent host $(\mathbf{G_m})_2@\mathbf{H_d}$, K_{h} is the product of both binding steps and K_{mono} is the statistically corrected binding constant of a monovalent model compound (Figure 2.12a, b). If the monovalent binding constant K_{mono} is not known, an allosteric cooperativity factor α' can also be calculated using only the two binding constants K_{h1} and K_{h2} (Equation 2.4).[113] For both definitions of allosteric cooperativity factors, the system is positively allosteric cooperative for $\alpha > 1$ and negatively allosteric cooperative for $\alpha < 1$.

$$\alpha' = \frac{K_{\mathrm{h1}}}{K_{\mathrm{h2}}} \tag{2.4}$$

In contrast, chelate cooperativity is considered for the complex between two multivalent, here divalent, compounds. A complex exhibits positive chelate cooperativity if the cyclic 1:1 complex is preferred over the oligomeric open complex. Consequently, HUNTER and ANDERSON defined a chelate cooperativity factor β based on the equilibrium between the singly bound state and the doubly bound product $\mathbf{G_d}@\mathbf{H_d}$ of a divalent host and a divalent guest (Figure 2.12c and Equation 2.5).[112]

$$\beta = K_{\mathrm{mono}} \cdot EM \tag{2.5}$$

By including the monovalent binding constant K_{mono} in the calculation of β, the chelate cooperativity of the multivalent binding event becomes dependent on the binding strength of the chosen monovalent binding motif. In contrast, ERCOLANI and SCHIAFFINO considered the equilibrium between the oligomeric and the cyclic doubly bound states, and normalised their cooperativity factor β' in relation to the host concentration $[\mathbf{H_d}]$ (Figure 2.12c and Equation 2.6).[114]

$$\beta' = \frac{EM}{4\ [\mathbf{H_d}]} \tag{2.6}$$

Both chelate cooperativity factors β and β' reflect a positive cooperativity if they are larger than 1 and are defined by the effective molarity *EM* which can be determined by a *double mutant cycle* analysis in which *EM* is separated from the overall binding constant of the divalent complex. The two 1:2 complexes $(\mathbf{G_m})_2@\mathbf{H_d}$ and $\mathbf{G_d}@(\mathbf{H_m})_2$ are called mutations and are utilised to correct for allosteric cooperativity. With these two mutations $(\mathbf{G_m})_2@\mathbf{H_d}$ and $\mathbf{G_d}@(\mathbf{H_m})_2$, as well as the divalent and monovalent complexes $\mathbf{G_d}@\mathbf{H_d}$ and $\mathbf{G_m}@\mathbf{H_m}$ the

disproportionation equilibrium as shown in Figure 2.12d can be formulated. If the monovalent model compounds are chosen correctly, all interactions occur with the same frequency on both sides of the equilibrium, apart from the interactions unique to the divalent complex $\mathbf{G_d@H_d}$, *i.e.,* linker-linker interaction between the orange and pink units. In the case of positive chelate cooperativity, the disproportionation equilibrium is shifted to the right side, and for negative chelate cooperativity to the left side.[113]

For the divalent model system, Equation 2.7 is used to calculate *EM*, provided the binding constants for all four complexes are known. Hereby, K_m is the binding constant of the monovalent complex $\mathbf{G_m@H_m}$ and K_d of the divalent complex $\mathbf{G_d@H_d}$. K_g represents the binding constant of a complex between two monovalent hosts and a divalent guest $\mathbf{G_d@(H_m)_2}$.

$$K_\mathrm{DMC} = \frac{K_\mathrm{d} \cdot (K_\mathrm{m})^2}{K_\mathrm{h} \cdot K_\mathrm{g}} = EM \tag{2.7}$$

For complexes of divalent *sec*-ammonium ions **10** and divalent crown-8 **11**, the DMC analysis revealed a positive chelate cooperativity only for the shortest alkyl-linker **10@11** (Figure 2.13, n = 0, $\beta = 40$).[116] A detailed thermodynamic analysis and the crystal structure revealed that *sec*-ammonium **10** with n = 0 exhibited the best preorganisation for the divalent crown ether by having the most suitable length. Longer linkers need to adopt a geometrically compressed conformation to fit the two crown cavities and lose more degrees of freedom, which is entropically disfavoured. Additionally, an attractive interaction between the crown ether's anthracene unit and the benzene in the ammonium ions was identified, showing that the positive chelate cooperativity can be an indicator for attractive linker-linker interactions. This concept was further investigated for the aryl-linked divalent ammonium ion **12** which exhibits a significantly higher positive chelate cooperativity β of 164.[117]

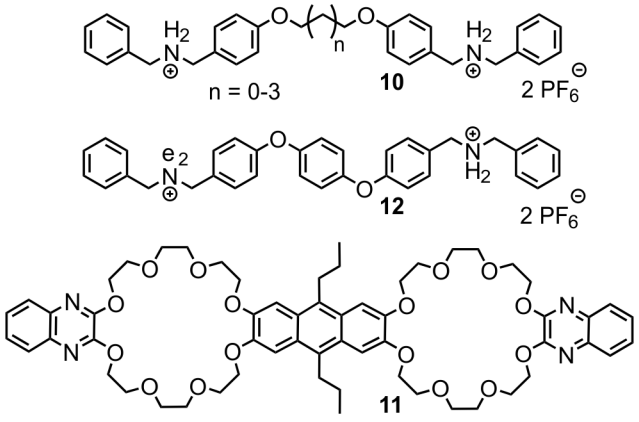

Figure 2.13. Divalent *sec*-ammonium guests and divalent crown ethers for studying chelate cooperativity.[116,117]

The interplay of matching linker length and chelate cooperativity depending on the linker's flexibility was investigated for divalent a crown-6 host and divalent primary ammonium guests.[115,118] In these works it was shown that slight structural mismatches between rigid spacers can cause a significant decrease in chelate cooperativity and, consequently, the

divalent binding constant. For more flexible linkers, structural mismatches can be compensated for. Therefore, the more flexible linkers show higher chelate cooperativities for similar linker lengths.[118] These results emphasise that it has to be considered if reducing the degree of preorganisation by increasing the linkers flexibility is beneficial for the overall binding constant.

2.1.6 Mechanically interlocked molecules

The final concept covered in this thesis to construct switchable architectures is the *mechanical bond.*[43,119] It describes how two molecular parts are bound to each other not by a covalent or noncovalent bond, but by an interlocked structure. These *mechanically interlocked molecules* (MIM) can only be separated by breaking a covalent bond.[43] For example, two macrocyclic molecules can be interlocked to form a [2]*catenane* and two macrocyclic molecules can be interlocked around a dumbbell-shaped molecule with two bulky *stopper* groups, also called *axle,* to form a [3]*rotaxane* (Figure 2.14).[120,121] Hereby, the total number of components which are interlocked in the MIM is given in brackets.

A macroscopic analogue of a polycatenane is a chain mail and it can be utilised to visualise the advantage of MIMs: While the wearer of a chain mail benefits from the mechanical stability of the metal rings against incoming sword attacks, the individual rings can still move and grant the wearer of the chain mail a mobility advantage over a knight in a full metal armour. Analogously, the components of MIMs held together similarly strongly by covalent bonds, and still undergo motions in relation to one another, as it will be discussed in Section 2.2.2.

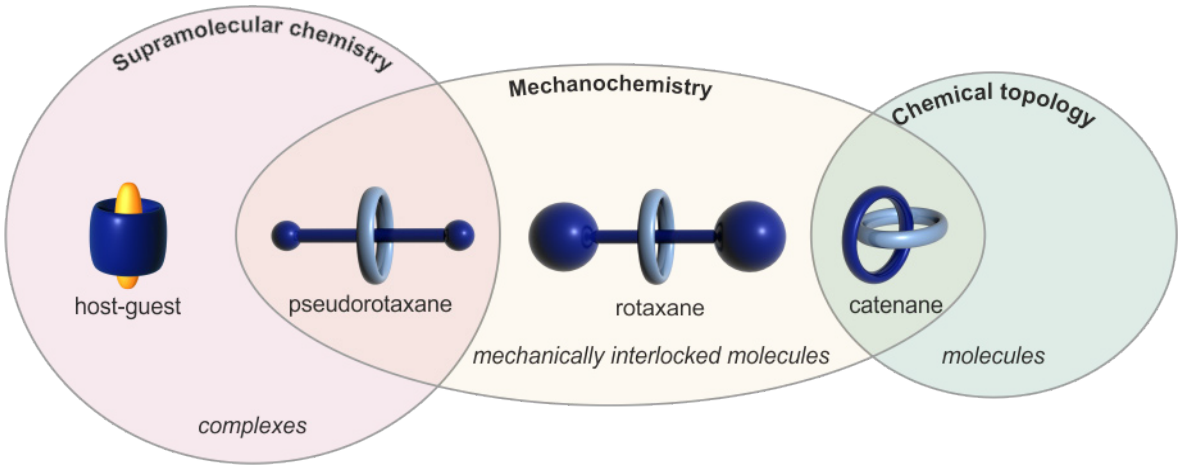

Figure 2.14. Venn diagram showing the relation of supramolecular chemistry, mechanochemistry and chemical topology.[43]

Yet, rotaxanes and catenanes possess a major different property with respect to topology: According to the rules of topology, bonds can be stretched, and specifically, for a rotaxane the macrocycle can be stretched to surpass the stoppers. Consequently, rotaxanes are not

topologically interlocked, while catenanes are (Figure 2.14).[43,122,123] Another example for topologically interlocked molecules are *molecular knots*.[123]

A rotaxane-like assembly where the ring can pass over the stopper groups is called a *pseudorotaxane*, which is in turn a specific type of host-guest complex.[120] Even though the research on MIMs branched from the field of supramolecular chemistry, rotaxanes are by definition no supermolecules or complexes, but molecules (Figure 2.14).[43]

The transition from pseudorotaxane to rotaxane can be continuous and depends on external factors as a change in temperature, solvent or the addition of a chemical reagent.[124-126] If at least one stopper and the macrocycle exhibit a complementary size, the assembly is called *size-complementary* rotaxane and possesses properties of rotaxanes and pseudorotaxanes at distinct conditions, respectively (Figure 2.15).[125,127] The closer the sizes of one stopper unit and the macrocycle are, the slower the macrocycle exchange rate becomes. For size-complementary rotaxanes this property can be employed to control the disassembly of the rotaxane by triggering the dethreading/deslipping of the macrocycle through deprotonation,[125] heating[128,129] or solvent change.[124,127,128]

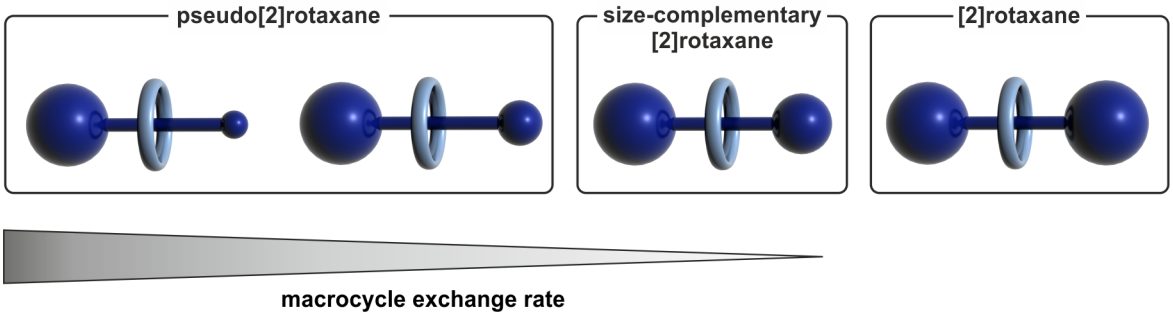

Figure 2.15. Schematic representation of (pseudo)[2]rotaxanes with increasing stopper sizes, which lowers the macrocycle exchange rate.[130] The macrocycle exchange rate describes how fast a macrocycle dethreads and rethreads on the axle of a pseudorotaxane. By definition, for a [2]rotaxane this exchange rate is zero.

In contrast, the slipping of a macrocycle over a size-complementary stopper represents one strategy to synthesise rotaxanes (Figure 2.16).[131,132] However, the approach of *capping* is more common, which involves the formation of a pseudorotaxane, followed by a reaction where one or both stopper units are connected with the pseudorotaxane (Figure 2.16). Hereby, the formed pseudorotaxane acts as a passive *template*. In the *clipping* approach the macrocycle is closed around the preformed axle (Figure 2.16). Another more recently developed approach is the *active template* synthesis, where, for example, a metal ion is bound in the cavity of the macrocycle and catalyses the reaction of two axle components inside the cavity of the macrocycle to form the desired rotaxane.[133,134] The metal ion can be removed after the successful synthesis.[43,120]

In the synthesis of crown/*sec*-ammonium rotaxanes, capping is commonly utilised to attach the stopper units, due to their ability to form stable pseudorotaxanes (Section 2.1.3).[135] Commonly avoided chemicals in the synthesis of crown/ *sec*-ammonium rotaxanes are basic

reagents, which can deprotonate the *sec*-ammonium ion, and protic solvents, which compete with the hydrogen bonding of the crown/ammonium pseudorotaxane.[135] Various chemical reactions are applied to connect the pseudorotaxane with the stopper, of which 1,3-dipolar cycloadditions[136-138] or ester formation[88] are the most common ones.

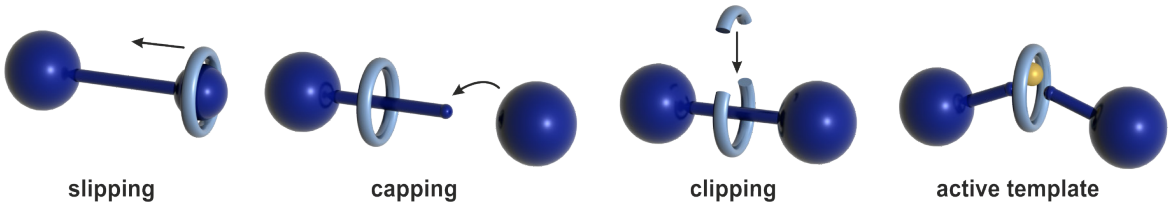

Figure 2.16. General approaches for rotaxane synthesis.[43,120] For the active template approach the template is depicted in yellow.

For all synthetic approaches mentioned above, attractive noncovalent interactions are crucial to hold the components of the desired rotaxanes in place to facilitate the reaction forming the mechanical bond. The position on the axle where the macrocycle forms noncovalent interactions is also referred to as the *binding station*. The mechanical bond increases the strength of the noncovalent interactions in the formed MIMs,[121] as it was observed for crown/*sec*-ammonium rotaxanes with an increased pK_a of the *sec*-ammonium unit compared to the one of the pseudorotaxane.[139] Also, metal ions were found to be more difficult to remove from the interlocked catenane compared to from the precursor complex.[140] This strengthening of the noncovalent interactions can be explained by the loss of degrees of freedom in the interlocked molecule.[121]

The question of how strong a mechanical bond is, may be broadly answered by the dissociation energy of the weakest covalent bond which opens the mechanically interlocked structure. This can be observed in gas-phase experiments by tandem mass spectrometry where typically the weakest covalent bonds break first upon increasing fragmentation energy (see Section 2.3.3).[141] However, studying the mechanochemical properties of MIMs through atomic force spectroscopy (AFM) or ultrasound-induced activation showed that this answer concerning the strength of a mechanical bond is only partially true.[142,143] DE BO and coworkers showed for a crown/*sec*-ammonium [2]rotaxane in an ultrasound-induced activation experiment by applying force in opposite directions on the macrocycle and the axle, that indeed the weakest ester bond broke. In comparison, a similar experiment performed on both sides of the pristine axle emphasised that the [2]rotaxane broke at lower forces. Theoretical calculations suggested that the macrocycle accumulated bending and torsional stress that facilitated the bond cleavage.[143] These results display, that the mechanical bond can weaken the covalent bonds of the MIM.

Higher order rotaxanes containing multiple rings and/or axle components are synthetically more challenging, but have the potential for exhibiting more sophisticated functions due to their increased structural complexity.[144,145] In this regard, homo[n]rotaxanes bearing multiple

identical macrocycles on one axle are among the most commonly studied higher order rotaxanes, as their synthesis can be controlled *via* an oligomeric axle bearing multiple of the same binding stations.[146-149] Additionally, polyhomorotaxanes were described for different macrocycles and polymers.[150-152]

Synthetically more challenging is the formation of hetero[n]rotaxanes with different macrocycles threaded onto the axle.[145] For the case of two different macrocycles, the formation of the desired hetero[3]rotaxane, the two [2]rotaxanes, and the two homo[3]rotaxanes are theoretically possible (Figure 2.17). With a directional axle, the hetero[3]rotaxane can form additional sequence isomers (Figure 2.17).[153,154] Typically, all these rotaxanes have a similar polarity and solubility making the purification of the mixture tedious. Consequently, more sophisticated synthetic approaches are necessary to favour the formation of the desired hetero[3]rotaxane.[155]

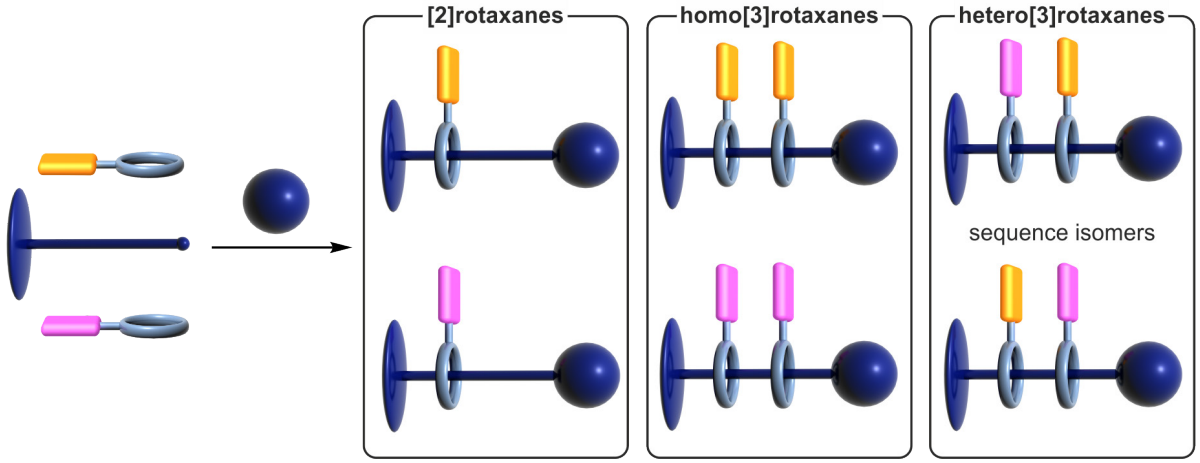

Figure 2.17. Rotaxanes which can theoretically be formed for a divalent directional axle and two macrocycles in a capping reaction.

A sequential synthesis is frequently applied, where the [2]rotaxane is formed and purified in a first step, followed by the incorporation of the second macrocycle in the interlocked structure.[153,156,157] Even the first heterorotaxane synthesis by STODDART and coworkers was based on this method.[156] More recently, LOEB and coworkers synthesised the hetero[3]rotaxane **R1** which introduces a new switching mode by sequential capping and clipping approach (Figure 2.18).[157]

In Section 2.1.4, integrative self-sorting as described by SCHALLEY and coworkers was introduced, which allows for the synthesis of hetero[n]rotaxanes in one pot.[102,158] In this method, orthogonal binding stations are incorporated in the axle, so that one macrocycle binds selectively to one binding station and the second macrocycle to another one. In the synthesis of rotaxane **R2,** benzo [21]crown-7 **BC7** (Figure 2.18 orange) cannot thread over the phenyl spacer and exhibits the higher binding constant than **DBC8** (Figure 2.18 pink), when bound to the alkylammonium ion. Consequently**, DBC8** can thread over the phenyl spacer and binds to the dibenzylammonium ion. After the desired heteropseudo[3]rotaxane is formed the

hetero[3]rotaxane can be synthesised by capping.[158] It was shown that error-correction of dead-end structures and kinetic path selection are critical to form the self-sorted structure.[159] The method was expanded to higher order crown/*sec*-ammonium hetero[n]rotaxanes[160-162] and to other macrocycles.[163] GOLDUP and coworkers introduced a different kinetic self-sorting approach for the construction of hetero[3]rotaxanes.[164]

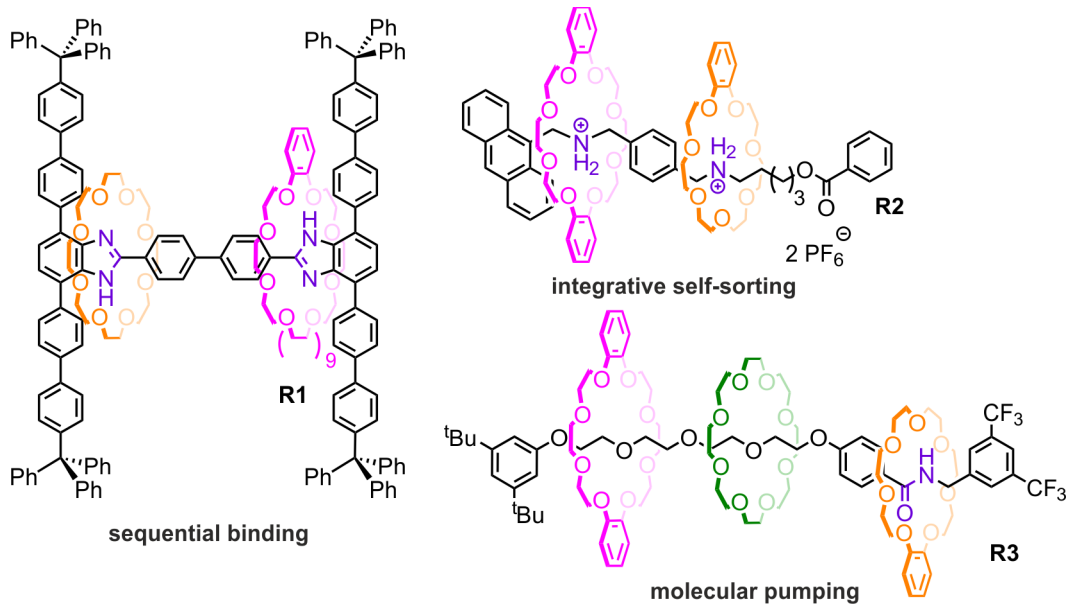

Figure 2.18. Examples for heterorotaxanes with their respective synthesis method: **R1**,[157] **R2**,[158] **R3**[165] Binding stations are marked in violet.

Recently, LEIGH and coworkers synthesised the hetero[4]rotaxane **R3** which bears only one binding station on the axle but three macrocycles which are trapped in a higher energetic state by molecular pumping (Figure 2.18c).[165] Molecular pumps are a type of AMMs (Section 2.2.3), which were also shown to be suitable to synthesise homo[n]rotaxanes.[166,167]

2.2 Switchable supramolecular complexes and rotaxanes

2.2.1 Classification of molecular switches

Molecular switches are chemical species which can interconvert reversibly between at least two stable or metastable states triggered by an external stimulus.[4,9,11] Hereby, the switching of the bistable molecule must not occur spontaneously but in a controlled manner. The energy expended to control the state of the molecular switch can originate from light, as well as electrical or chemical sources.[43] Molecular switches contain distinct adaptive moieties, which can undergo chemical changes and can be classified by the stimulus they are responsive to (Figure 2.19).

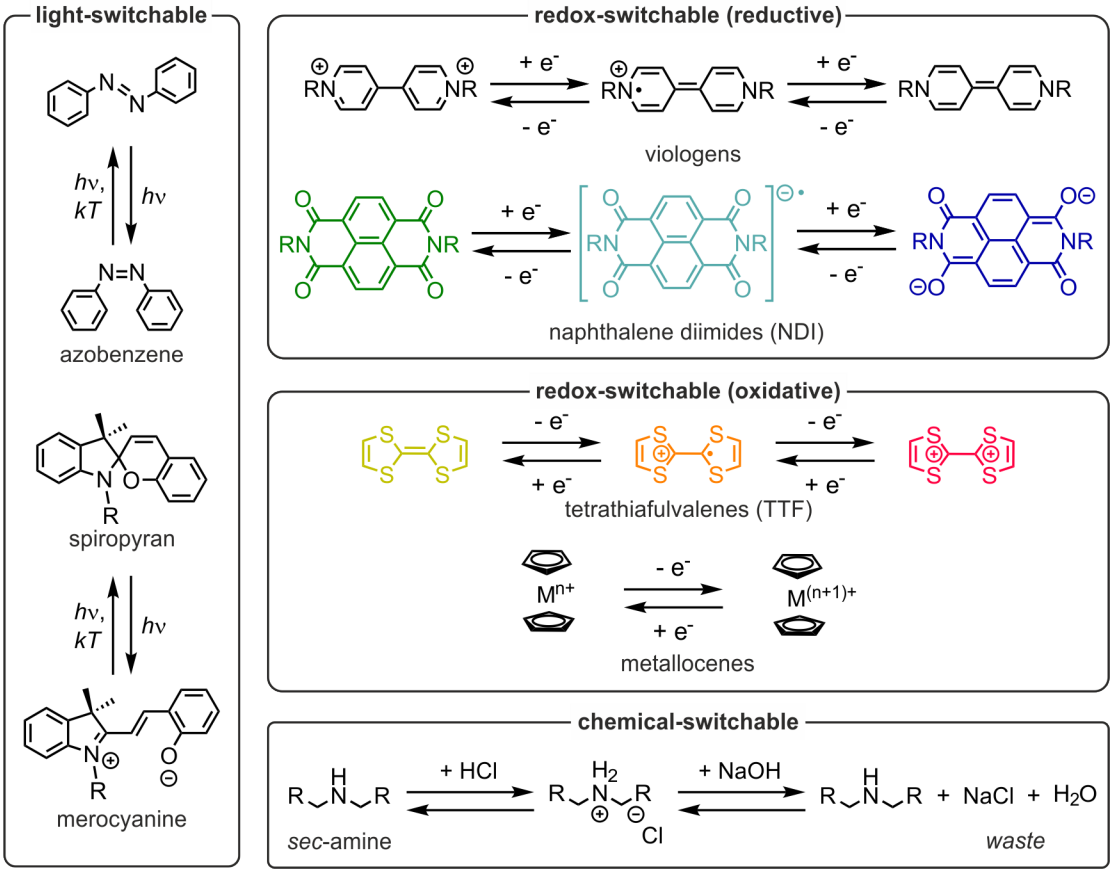

Figure 2.19. Examples for light-, redox- and chemical-switchable moieties: azobenzene,[11,168,169] spiropyran,[170] viologens,[171] NDI,[172-174] TTF,[41,175,176] metallocene[177] and *sec*-ammonium.[43] TTF, NDI and their redox states play a central role in this thesis and are highlighted in colours.

Azobenzene is an example for a light-switchable moiety, where the central *trans* double bond is isomerised to its *cis* form upon irradiation with light of a specific wavelength (Figure 2.19). This isomerisation is reversible by irradiating with light of another wavelength or thermal relaxation.[168] Many different azobenzene derivatives have been incorporated in molecular switches.[11,168,169] Furthermore, in spiropyran a double bond can be isomerised by light, as well.

In a spiropyran this isomerisation comes along with a ring-opening reaction of the central six-membered ring yielding the merocyanine form (Figure 2.19).[170]

Switching with light brings major advantages, such as no waste is produced and light is easily accessible.[11,19,178] Additionally, light allows to push the switchable system out of its thermodynamic minimum, as the excited state is typically metastable. Yet, a disadvantage of photo-switches is the photostationary state. For a specific wavelength, the photostationary state of a photochemical reaction describes the equilibrium ratio between the ground and excited states. This may prevent a full conversion to the desired state of the switch.

Another, potentially waste-free stimulus is switching with an electrical potential.[41,177,178] The state of a redox-switchable moiety with no potential being applied or oxidising or reducing agent being present, will be called *pristine redox state* in this thesis. Hereby, *reductive* redox-active moieties can be reversibly reduced from their pristine redox states and *oxidative* redox-switchable moieties can be oxidised from their pristine redox state. Commonly, redox-switches contain metal centres, such as in metallocenes or large delocalised π-systems, such as in viologens. The pristine redox state is the viologen dication, which can undergo two consecutive one-electron reduction steps to the radical cation and the neutral state (Figure 2.19).[171] The well-known "bluebox" macrocycle developed by Stoddart and coworkers contains two viologen units and, thereby, can be reduced with four electrons, overall.[179,180] Yet, viologens are poorly soluble in organic solvents and labile to base.[181]

In contrast, NDI is another reductive redox-switchable moiety, which is neutral in its pristine redox state and stable under basic and acidic conditions. It is an electron-poor aromatic system and can be reduced twice to its radical anion and dianion (Figure 2.19).[172-174] In the radical anion, EPR measurements show that the spin density is delocalised in the whole NDI-unit and the NDI radical anion can be isolated.[174] The negative charges are delocalised over the four oxygen atoms in the NDI dianion.[182,183] Additionally, the neutral NDI shows a weak fluorescence emission, which is quenched upon reduction.[173,174] NDIs and viologens are π-electron acceptors, which readily form donor-acceptor complexes with π-electron donors, such as dialkoxynaphthalenes or TTF.[184-186]

TTF is an oxidative electron-rich system, which can undergo two consecutive one-electron oxidations, where both pro-aromatic five-membered rings become aromatic (Figure 2.19).[41,175,176] The radical cation $TTF^{+\bullet}$ can be isolated and the spin-density is delocalised over both five-membered rings, as it can be observed in the planar structure of the radical cation.[187,188] All three oxidation states are stable in organic solvents when exposed to air and moisture. The two oxidation processes have comparably low oxidation potentials (0.37 and 0.74 V vs Ag/AgCl in CH_3CN),[189] which makes them easily accessible. Yet, TTF and its oxidation states are sensitive towards acids and nucleophiles.[190]

Redox-switching can also be performed by the addition of a chemical oxidising or reducing agent, not only by an electrical source. However, chemical-switching accumulates a *waste* as a side-product with each switching cycle. Other chemical stimuli are, for example, the addition of ions or acid/base.[18,43] In the case of reversible protonation and deprotonation of *sec*-amines, a salt is produced as waste (Figure 2.19).

So far, molecular switches were discussed focussing on their stimulus, yet the output of each switching state is equally important. The output does not only allow to characterise and identify the operation of the molecular switch, but it also paves the way for potential applications of the respective molecular switches. For example, a *photochromic* molecular switch changes its colour and absorption spectra when triggered by light,[11] and an *electrochromic* molecular switch changes its colour as a function of the electric potential.[191,192] A switchable electrochromic material was obtained by the combination of π-donor thiophene and π-acceptor benzothiadiazole in block copolymer **P1** (Figure 2.20a, left).[192] Polymer **P1** exhibits a broad homogenous absorption of visible light, which is bleached by the reversible oxidation of the thiophene units, as it was shown in spectroelectrochemical measurements and can be seen by eye (Figure 2.20a, right).

Feringa and coworkers developed overcrowded alkene *cis*-**13**, which can be reversibly switched by light to *trans*-**13** (Figure 2.20b).[193-195] In the circular dichroism (CD) spectra of both switching states a reverse of the sign is observed.[195] For molecules which can invert their chirality and change the direction along which they interact with circularly polarised light, the term *chiroptical switch* was coined.[11,193,196]

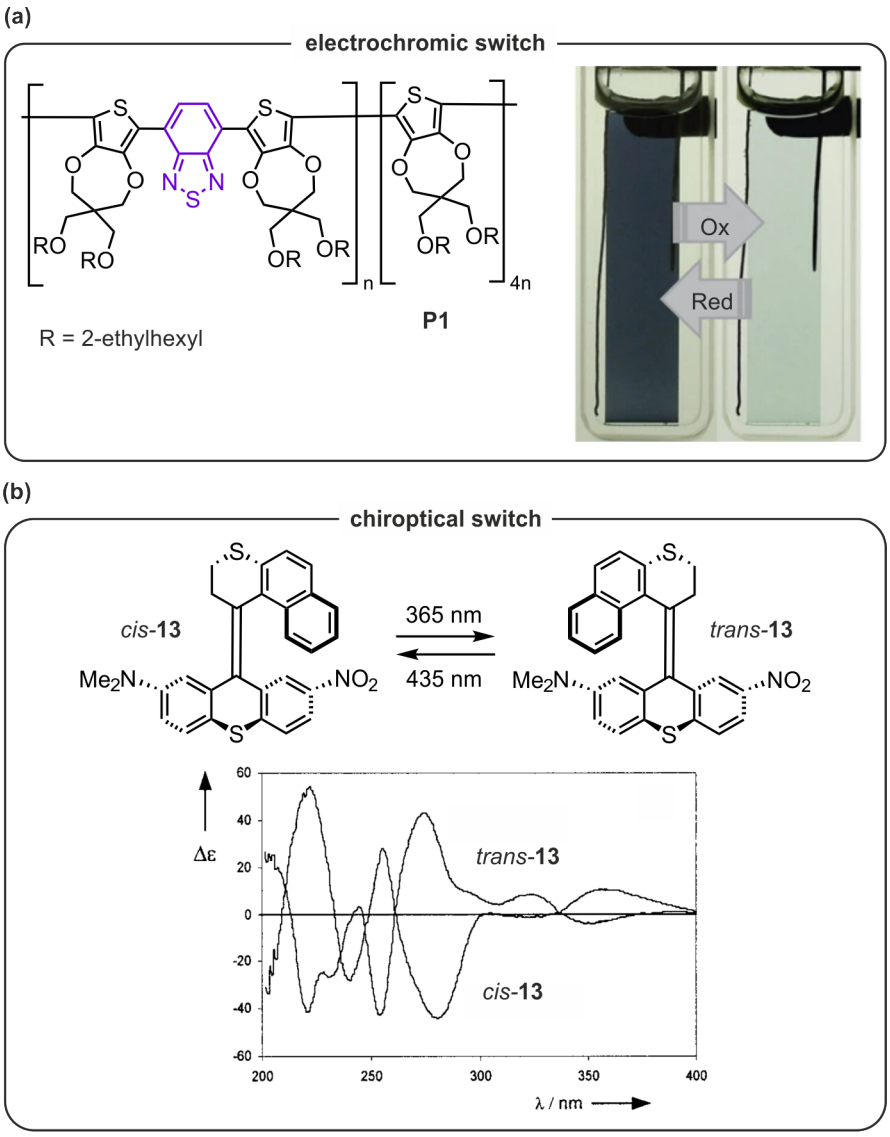

Figure 2.20. Examples for molecular switches: (a) Redox-switchable electrochromic polymer based on thiophene and benzothiadiazole (violet). A polymeric film of **P1** was spray-casted onto glass coated with indium tin oxide in a spectroelectrochemical setup (right). After the potential was increased to 0.74 V the polymeric film bleached. Reproduced with permission from Springer Nature. Copyright © 2008, Nature Publishing Group.[192] (b) Chiroptical photo-switch *cis*-**13**.[193-195] CD spectrum is given for pure trans-**13** and cis-**13**. The ratio of cis/trans-isomers in their photostationary states at 365 nm is 70:30, and at 435 nm is 10:90. Adapted with permission from B. L. Feringa *et al.*[195] Copyright 2000 American Chemical Society.

A common approach is to combine switchable moieties with receptor molecules, such as hosts.[176,197,198] In this case, the assembly and disassembly of a host-guest complex or pseudorotaxane can be controlled by the external stimulus of the molecular switch and monitored by its output.

BECHER, SALLÉ and coworkers incorporated TTF in crown ether macrocycles and studied their cation binding properties (Figure 2.21a).[176,199-201] Depending on the size of the macrocycle, different cations were selectively bound. The thiacrown **14** showed a higher binding constant for softer cations, such as Ag^+.[201] The binding of cations in the crown ether's cavity impacts the redox properties of the TTF and therefore, can be monitored through cyclic voltammetry

(CV). For instance, the addition of barium perchlorate to a solution of crown ether **16** resulted in a positive shift of the first oxidation potential $E_{1/2}{}^1$ of the TTF unit (Figure 2.21b).[199] These redox and guest-binding properties make these crown ethers excellent candidates to be exploited as cation sensors.[176,202]

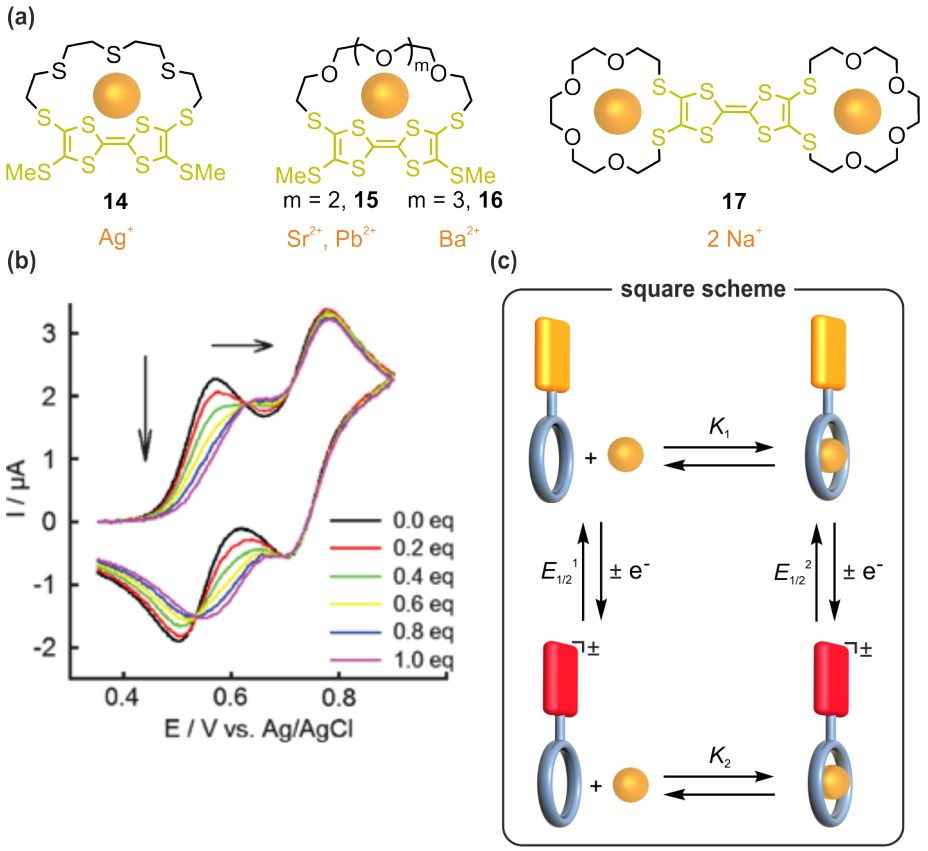

Figure 2.21. Redox-switchable macrocycles: (a) TTF incorporated into crown ethers with their respective metal ion guests in orange.[176,199-201] Crown ethers **14**, **15** and **16** were obtained as *Z*/*E* mixtures. Only the *Z*-isomer binds to the cations. (b) CV of crown ether **16** with increasing amounts of barium perchlorate (1 mmol l^{-1} in CH_2Cl_2/CH_3CN (1:1), Bu_4NPF_6 (0.1 mmol l^{-1}), at 293 K and 100 mV s^{-1}).[199] Used with permission of Royal Society of Chemistry, from D. Canevet *et al.*[176], permission conveyed through Copyright Clearance Center, Inc. (c) Electrochemical square scheme for the oxidation/reduction of a redox-switchable macrocycle in the presence of a guest.[44]

This redox-sensing can be explained by considering a square scheme of the redox process and the host-guest equilibrium (Figure 2.21c). The binding of the cation in the cavity reduces the π-electron density of the TTF unit, thus it requires a higher potential to be oxidised to its radical cation $E_{1/2}{}^1$. Following from the NERNST equation, Equation 2.8 can be derived to estimate the binding constant K_2 of the cation to the oxidised macrocycle, if K_1 is known. ΔG_{el} refers to the difference in free Gibbs energy of the two host-guest equilibria, F is the Faraday constant and z the number of electrons transmitted in the redox process.

$$\Delta G_{el} = -zF\Delta E_{1/2} \tag{2.8}$$

The higher the difference of the two binding constants, the larger the difference of the electrochemical potentials $\Delta E_{1/2}$. No potential shift is observed for the second oxidation to TTF^{2+} of the crown ether **16** when binding barium cations, which emphasises that the cation

was expelled from the cavity after the first oxidation (Figure 2.21b). Therefore, the redox-controlled disassembly of the host-guest complex can be applied to control the release of cationic guests.[200]

The controlled disassembly of a pseudorotaxane was applied in a dye-sensitised solar cell which mimics the function of natural photosynthesis (Figure 2.22).[203] The so-called "P1 dye" (orange) is functionalised with two alkoxynaphthalene units (red) in the axle **18**. Both can form a pseudorotaxane complex with the NDI crown ether **19** due to donor-acceptor interactions (Figure 2.22a). The P1 dye acts as a photosensitiser for the NiO electrode. Photo-emitted electrons are transferred to the NDI ring **19** reducing it. The newly formed electron-rich radical-anion **19**$^{\bullet-}$ dethreads and a neutral ring **19** binds to the open binding station. By this dethreading, the negative charge is separated from the NiO-interface preventing charge recombination, which is a major obstacle for dye-sensitised solar cells. The ring **19**$^{\bullet-}$ diffuses to the counter electrode, where it is reoxidised to its neutral form (Figure 2.22b). This is a suitable example of a molecular switch being combined with other functional molecular units to yield a *molecular device* with the emerging function of acting as a photosensitiser and charge carrier in a solar cell.

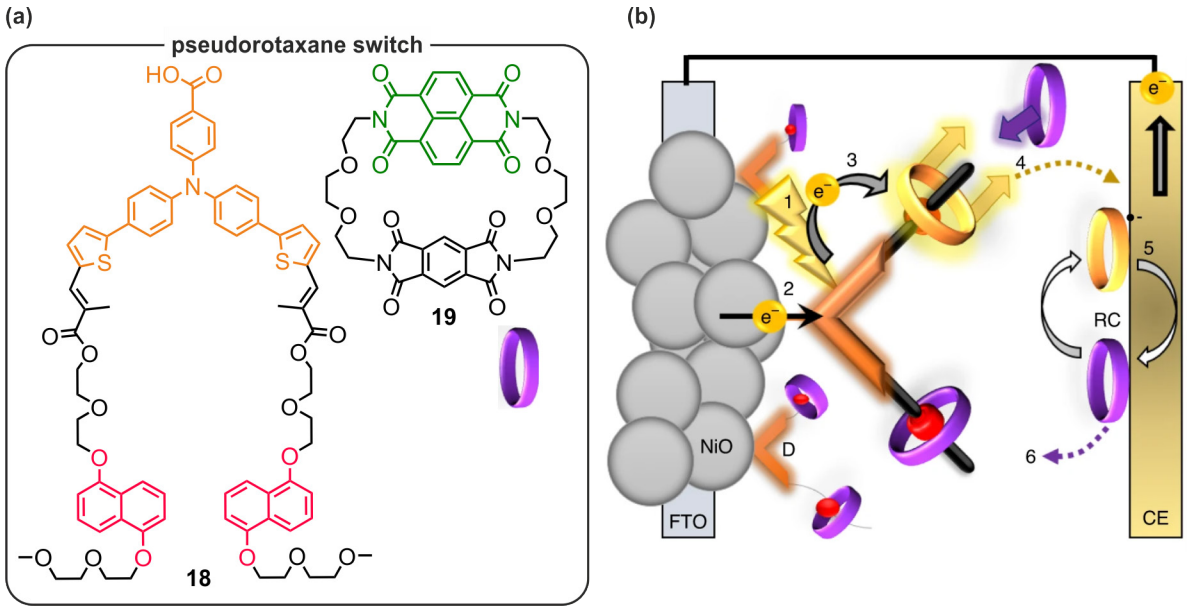

Figure 2.22. Example of a pseudorotaxane switch applied in a dye-sensitised solar cell. (a) Chemical structures for the divalent axle **18** with the P1 dye in orange and binding stations in red, and the NDI macrocycle **19**. (b) Schematic representation of the operational mechanism of the dye-sensitised solar cell.[203] Photoexcitation of the Dye D (1) and subsequent hole injection into NiO (2). The electron e^- is transferred to the NDI ring **19** (3), which dethreads and is replaced by a neutral ring (4). At the counter electrode CE, the neutral NDI ring **19** is regenerated (5-6). FTO is fluorine-doped tin oxide; RC is redox couple. Reproduced with permission from Springer Nature. Copyright © 2022 T. Bouwens *et al.*[203], under exclusive licence to Springer Nature Limited.

In this example, a switchable pseudorotaxane is disassembled by removing the attractive noncovalent interactions between the binding station and the macrocycle, and the free macrocycle is utilised to transport an electron. In contrast, a mechanically interlocked

rotaxane cannot disassemble, and consequently, a similar disruption of the attractive noncovalent interactions may result in a molecular motion.

2.2.2 Mechanical motion in switchable rotaxanes

At the molecular level, all molecules are permanently moving due to *Brownian motion*, hence the criterion for molecular motion is that it is observable and controlled. For a [2]rotaxane, the axle is considered static and limits the types of motion the macrocycle can undergo to three (Figure 2.23). Specifically, rocking motions occur very fast and uncontrolled. For most rotaxanes and analytical techniques, rotational or pirouetting motions are too fast to be observed in solution, and they play a more significant role in the solid state.[204,205] Therefore, in rotaxane-based mechanical switches a translational motion is frequently utilised.[44,206]

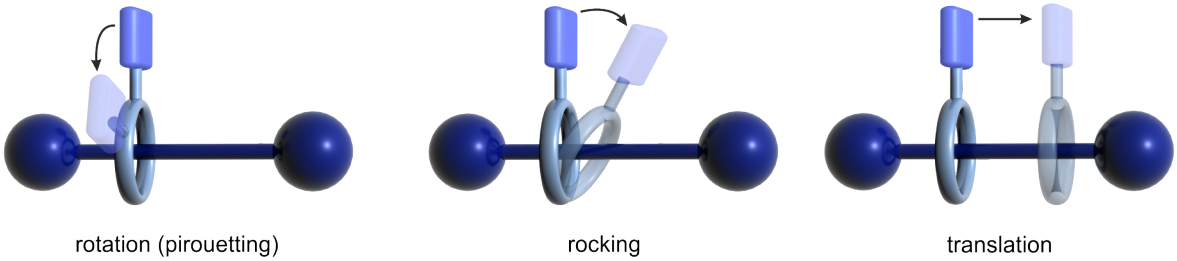

Figure 2.23. Schematic representation of modes of motion for a [2]rotaxane.[206]

To allow a translational motion in a rotaxane, two binding stations are incorporated into the axle, commonly. If the two binding stations (Figure 2.24a, violet) are the same, a *degenerate molecular shuttle* is present, where the macrocycle spontaneously moves back and forth between the two binding stations driven by Brownian motion. Hereby, the shuttling rate depends on the activation energy $\triangle G^{\ddagger}$ and the molecular motion is not controlled. It was shown for crown/*sec*-ammonium rotaxanes that the shuttling rate does not depend on the length of the axle between the two binding stations,[207,208] but folding or different sterically demanding groups can have an impact.[209]

In the non-degenerate case, the two binding stations are different, and the macrocycle binds to each binding station in a ratio dependent on the relative binding energies of the two co-conformations $\triangle G^{0}$ (Figure 2.24b, left). The intramolecular equilibrium constant K_i which describes the ratio of the two co-conformations can be calculated according to Equation 2.9.[44] Though, this ratio represents the time-average for all rotaxane molecules. For an individual rotaxane the ring shuttles back and forth between the two stations, depending on the activation energy as for the degenerate shuttle. If this activation barrier is so high that it cannot be overcome at a given temperature, the rotaxanes are kinetically trapped in one state and do not shuttle back and forth.

$$K_i = e^{\frac{-\Delta G^0}{RT}} \tag{2.9}$$

With the incorporation of a switchable moiety in the [2]rotaxane the binding energy for one or both binding stations can be altered.[25] Therefore, the equilibrium ratio of the macrocycle changes and a translational motion is triggered (Figure 2.24b, state II). In this switching process a meta-stable co-conformation is created when the potential energy surface is changed by the stimulus, but the motion did not occur yet (Figure 2.24b, metastable state). Whether this motion occurs only on average for all rotaxanes or occurs controlled for each individual molecule, depends on the height of the kinetic barrier. Nevertheless, this controlled mechanical motion is undone upon back-switching and, thereby, no continuous work is performed.

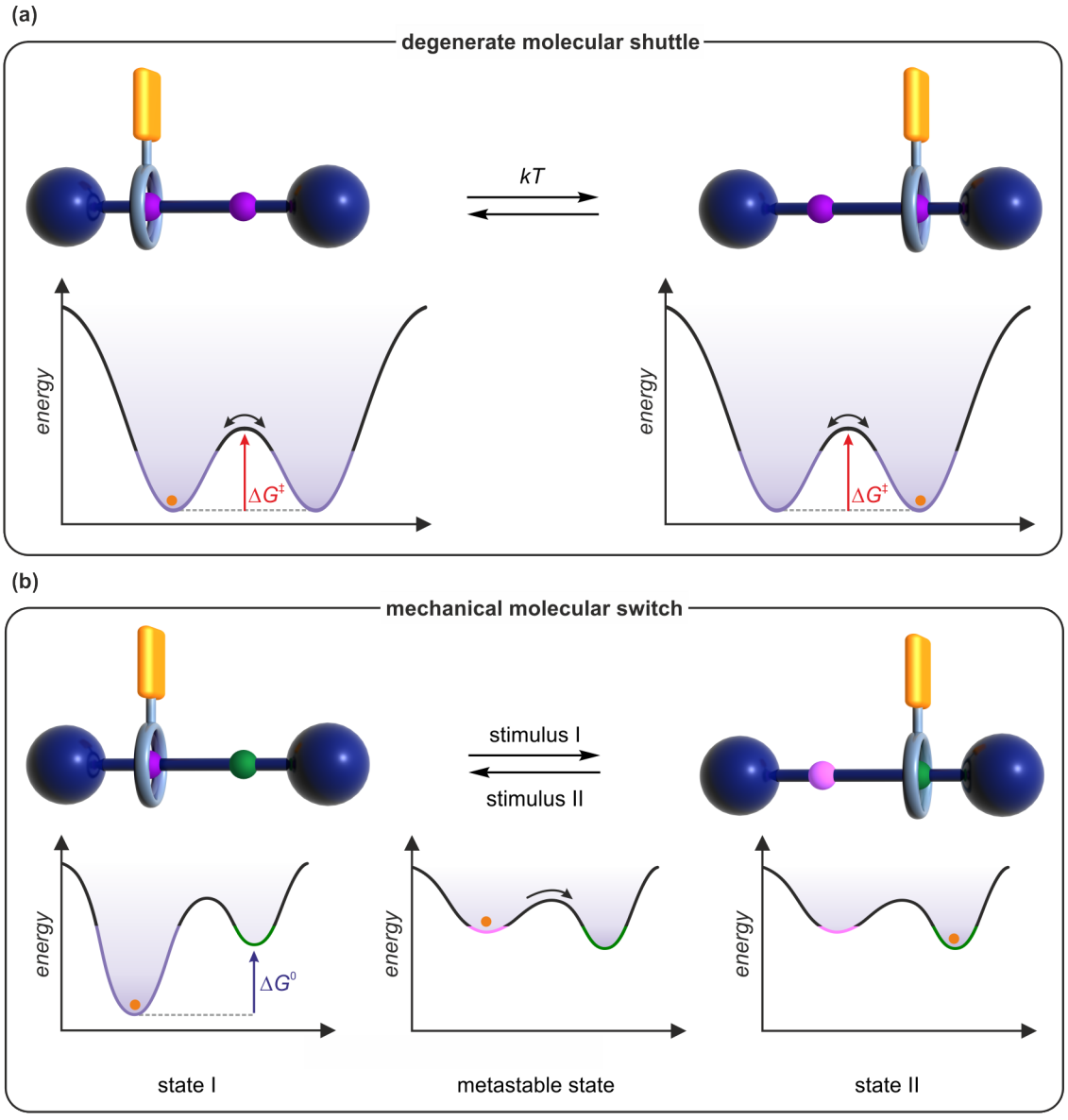

Figure 2.24. Translational molecular motion in a [2]rotaxane with two binding stations.[44,206] (a) Degenerate molecular shuttle, where the macrocycle shuttles between two equal binding stations (violet), with potential energy surfaces indicating the activation energy of shuttling in red. (b) For the non-degenerate case (state I) with two binding stations in violet and green, the potential energy surface is given with the relative binding energies of the two co-confirmations in blue. Upon switching with a stimulus, the binding energy of one station is lowered (pink) and a metastable state is created. If the kinetic barrier can be overcome, a molecular motion to the second binding station occurs.

In crown/*sec*-ammonium rotaxanes, the deprotonation of the *sec*-ammonium binding station can trigger a translational motion, if a second binding station is present. A viologen dication was introduced as a second binding station, as it exhibits a lower binding constant to the dibenzo crown ethers as the *sec*-ammonium ion, but higher as for the *sec*-amine (Figure 2.25).[210,211] In rotaxane **20·H**$^+$, the co-conformation with the crown ether binding to the *sec*-ammonium is preferred.[211] However, in deprotonated rotaxane **20** the co-conformation with the crown ether residing on the viologen unit becomes thermodynamically more stable, as there are no attractive cation-dipole interactions with the *sec*-amine.

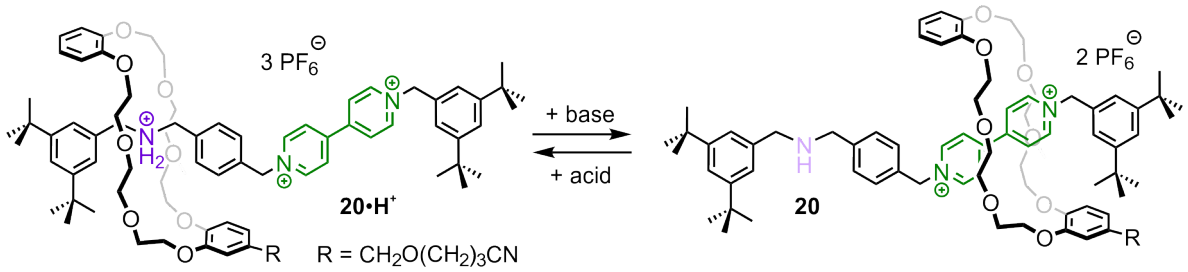

Figure 2.25. Dual-stimuli switchable rotaxane **20•H**$^+$.[211] By deprotonation of the *sec*-ammonium ion (violet) with a base (*i.e.*, P1 base) a translational motion of the crown ether to the viologen binding station (green) is triggered.

Additionally, CREDI and coworkers demonstrated that this translational switch can be influenced by a second stimulus with the reduction of the viologen.[211] The two consecutive one-electron reductions of the viologen lower the binding constant of the crown ether to the viologen stepwise. It was shown that the binding strengths of the viologen unit in the different redox states have an impact on what base was needed to deprotonate the *sec*-ammonium of the dual-switchable rotaxane **20·H**$^+$. The *sec*-amine in **20** was shown to exhibit redox state dependent pK_a values of 18.1, 22.0, and 25.0, respectively.[211]

Typically, the molecules are oriented randomly in solution, thus the overall molecular motion does not have a direction. Researchers put great effort into coupling these molecular motions to create a macroscopic effect by mounting the molecular switches on surfaces, or incorporating them into polymers or other soft materials.[9,206,212,213] For example, the switchable crown/ammonium [*c2*] daisy chain rotaxane **21·2H**$^+$ was incorporated into a gel (Figure 2.26).[214] Again, the *sec*-ammonium binding station can be deprotonated to induce a translational motion of approximately 1 nm; here, triazolium ions act as second binding stations (Figure 2.26a green). GIUSEPPONE and coworkers demonstrated that the translational motion at the molecular level could be amplified to cause a macroscopic contraction of the soft material of 60% (Figure 2.26b).[214]

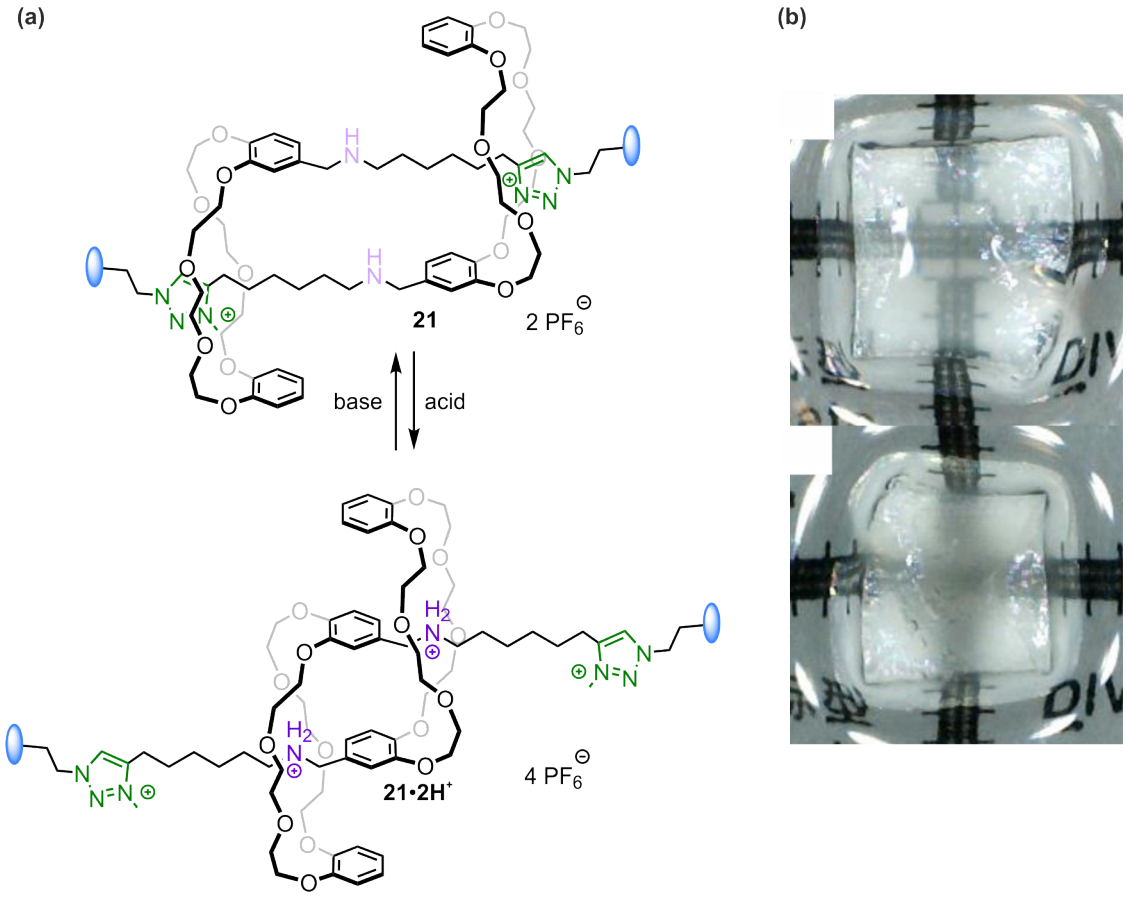

Figure 2.26. (a) Structure of the [*c2*] daisy chain rotaxane, which was incorporated into a cross-linked polyethylene glycol gel (light blue). Switching was performed by the addition of NaOH as a base, and NH_4PF_6 as an acid.[214] (b) Pictures of the soft material showing the expanded deprotonated state (top) and contracted protonated state (bottom). This is an unofficial adaptation of an article that appeared in an ACS publication.[214] ACS has not endorsed the content of this adaptation or the context of its use. It is an open access article published under an ACS AuthorChoice licence, Copyright © 2017 American Chemical Society.

2.2.3 Artificial molecular machines

The mechanical molecular switches described in Figure 2.25 and Figure 2.26 are considered to be *artificial molecular machines* by researchers, due to their ability to undergo a molecular motion.[18,19] However, only the interfaced mechanical switch **21·2H**$^+$ performs work, while the total energy transmitted by the switching stimulus in the mechanical switch **20·H**$^+$ is transformed into background heat. APRAHAMIAN discussed how the definition for AMMs based on the molecular motion is "too lax" and the definition based on the performed work may be "too restrictive".[26] Additionally, he emphasised that the environment influences if a molecule can be considered a molecular machine or not. For example, the [*c2*] daisy chain rotaxane **21·2H**$^+$ would not perform any work in solution. For this thesis, a more restrictive definition for AMMs based on the performed work will be applied and all other molecules allowing a mechanical molecular motion are considered mechanical molecular switches.

Nonetheless, for the gel-mounted molecular switch **21·2H**$^+$, all performed work is undone by the addition of the second stimulus and the system remains a function of the state. Instead,

to perform continuous work, the system needs to be a function of the trajectory, which means that the order of the applied stimuli has an impact on the outcome of the system. This can be achieved by implementing a directional potential energy surface, this general mechanism being called *ratcheting*.[9] For a gearwheel, this can be visualised as followed: Instead of turning the wheel left by the stimulus I and right by the stimulus II, the wheel is constantly turned in one direction. Macroscopically, this direction can be achieved by asymmetric teeth on the wheel (Figure 2.27). Here, the mechanical work is not undone and can be harvested, as in a macroscopic car, for example.

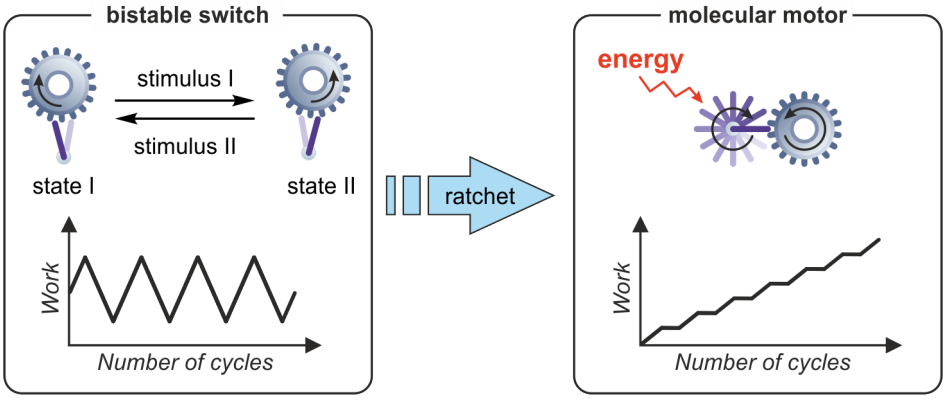

Figure 2.27. Comparison of the operational mechanism of a bistable molecular switch and a directional molecular motor, using the macroscopic example of a gearwheel.[9]

Analogously, AMMs applying a ratchet mechanism are constructed by introducing directionality in molecular switches, and are called *molecular motors*.[169,215] There are two types of ratchet mechanisms which were shown to operate molecular motors (Figure 2.28).[9,18]

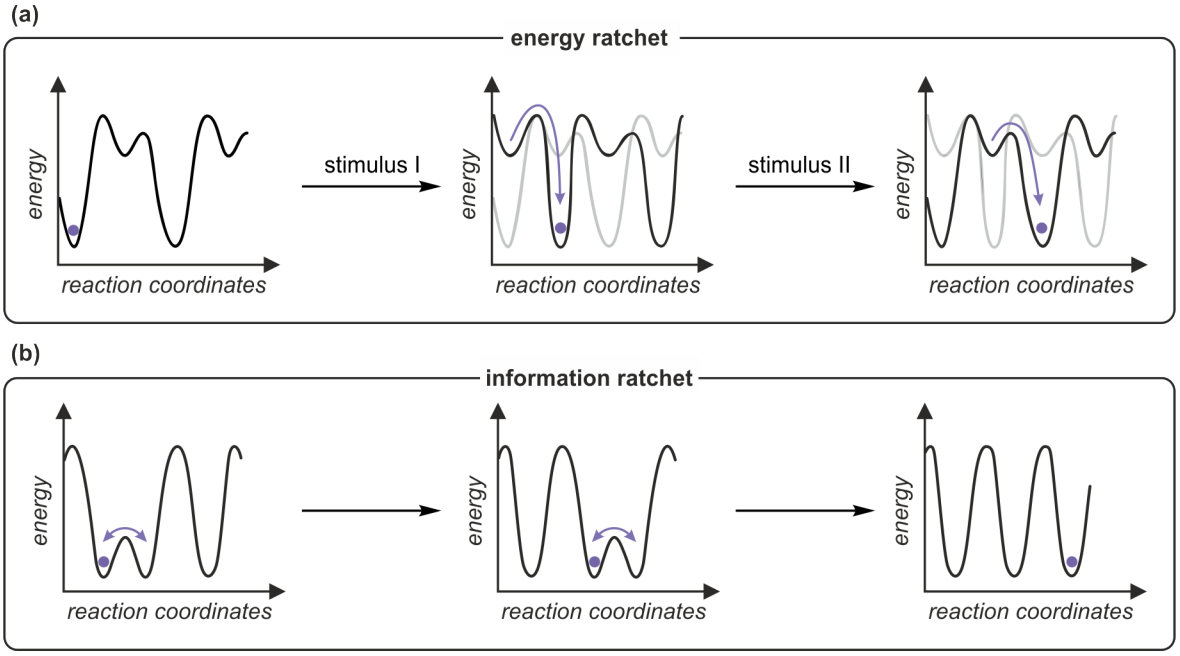

Figure 2.28. Potential energy surfaces for ratchetting mechanisms with the position of the system on the potential energy surface indicated in violet:[9,18] (a) Energy ratchet with a biased potential energy surface in dependence of external stimuli. (b) Information ratchet, where the potential energy surface depends on the position of the system on the potential energy surface.

In an *energy ratchet*, the system transitions on an asymmetrical potential energy surface, which is modulated by an external stimulus (Figure 2.28a). The potential energy surface changes its shape in dependence of the two stimuli and does not depend on the co-conformation of the motor molecule. In contrast, the potential energy surface in an *information ratchet* changes its shape depending on the position of the system on the potential energy surface (Figure 2.28b). LEIGH and coworkers have published examples for molecular motors for both information ratchet[216] and energy ratchet mechanisms (Figure 2.29).[217]

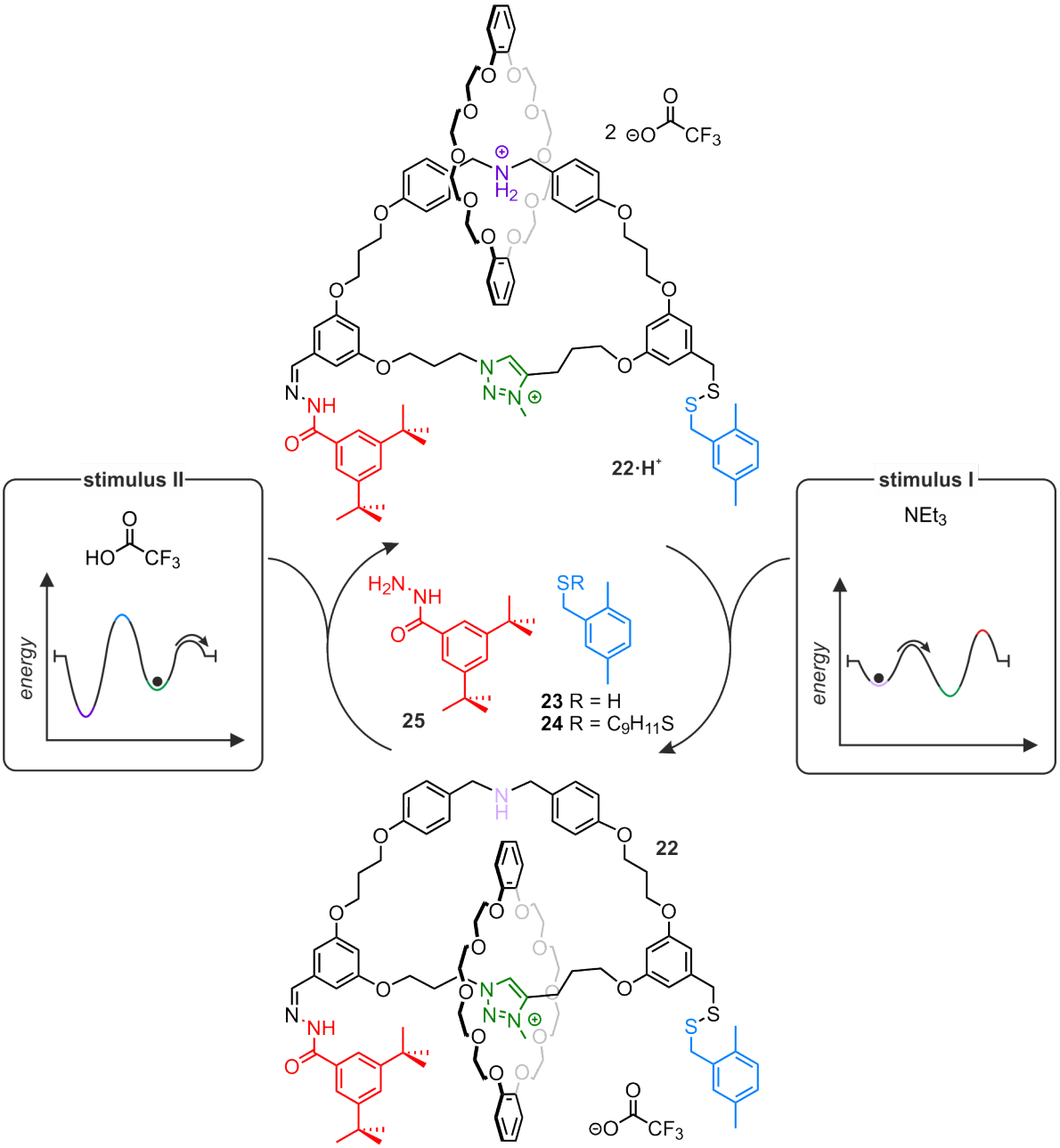

Figure 2.29. Example of a molecular rotary motor with an energy ratchet mechanism.[217] Molecules **23**, **24** and **25** allow exchange of the blocking groups in basic and acidic conditions, respectively. For both stimuli, a schematic potential energy surface is shown to illustrate the energy ratchet mechanism facilitating the unidirectional rotation. The black circle represents the position of the dibenzo crown-10 macrocycle before the stimulus is applied.

[2]Catenane **22**·$\mathbf{H}^+$ is a rotary motor, where the dibenzo crown-10 macrocycle resides on the *sec*-ammonium ion (Figure 2.29, violet).[217] Again, a triazolium ion acts as a second binding station (Figure 2.29, green). However, the macrocycle can follow two trajectories to translocate to the triazolium ion. On the right trajectory, the macrocycle needs to pass a base-labile disulphide blocking group (Figure 2.29, blue), whereas on the left trajectory an acid-labile hydrazone blocking group (Figure 2.29, red).

Both blocking groups are labile at orthogonal conditions. In the presence of the first stimulus, triethylamine, the *sec*-ammonium is deprotonated, and the disulphide becomes labile. Therefore, in basic conditions, the macrocycle passes on the right trajectory to bind to the thermodynamically preferred triazolium moiety in the deprotonated catenane **22**. In contrast, in acidic conditions, the hydrazone becomes labile. Consequently, the macrocycle passes the hydrazone unit on the left pathway upon the addition of the second stimulus, trifluoracetic acid. Overall, a unidirectional rotational motion of the macrocycle is achieved after the addition of both stimuli.[217] This molecular motor follows an energy ratchet mechanism, as the potential energy surfaces do not depend on the position of the crown ether macrocycle on the bigger macrocycle, but only the external stimulus.

Another type of AMMs are molecular pumps, which transport ions or small molecules energetically uphill in a non-equilibrium state.[99] This allows to create concentration gradients or to form rotaxanes with more macrocycles than binding stations. An example was shown in Figure 2.18 in the previous subchapter.[165]

Sec-ammonium/crown ether complexes and rotaxanes have been used as examples, from the simple pseudo[2]rotaxane (Figure 2.7) to the complex molecular rotary motor (Figure 2.29), to visualise the scientific journey from understanding of the noncovalent interactions of a simple two-component supramolecular complex to complex functional molecular architectures. The construction of sophisticated AMMs would not be possible without a detailed understanding of the thermodynamic properties in crown/*sec*-ammonium complexes and how these are influenced by a stimulus, in this case acid/base.

2.3 Analytical methods

2.3.1 Analytical techniques for engineering molecular switches

The process of constructing molecular switches and machines was described as *molecular engineering*.[26,193,218] It is a multi-step process, which requires to be characterised and monitored at all stages by various complementary analytical techniques. To give an overview on the applied analytical techniques, the molecular engineering process is structured around four general steps:

I) *Design*: The desired function of the molecular switch is envisioned. The molecular components for binding, switching and additional functional molecular units, such as anchoring units for mounting are chosen. Noncovalent interactions are studied.

II) *Assembly*: The components are assembled according to the blueprint created in the design step, the fundamental concepts of supramolecular chemistry mentioned in Section 2.1 are applied.

III) *Operation*: The molecular switch is operated in solution, as well as its input and output are tested. Switching kinetics are investigated.

IV) *Mounting*: Molecular switches are mounted and subsequently operated at an interface.

The analytical methods which are utilised in this thesis are assigned to the four steps of molecular engineering in Figure 2.30. The results of this thesis concern the first three steps, yet the fourth step is included for the example of mounting on surfaces in Figure 2.30.

In the design step, it is of particular importance that the noncovalent interactions of the involved complexes are quantified. Commonly, the design step undergoes multiple iteration cycles of building block synthesis and quantification of their noncovalent interactions, especially, when novel binding motifs are studied.

Many methods, such as NMR, UV/Vis absorption and fluorescence spectroscopies allow the determination of binding constants with the non-linear regression of titration data applying equations which are derived from Equation 2.10.[52,219]

$$[\mathbf{G@H}] = \frac{1}{2}\left\{\left([\mathbf{G}]_0 + [\mathbf{H}]_0 + \frac{1}{K_a}\right) - \sqrt{\left([\mathbf{G}]_0 + [\mathbf{H}]_0 + \frac{1}{K_a}\right)^2 - 4[\mathbf{H}]_0[\mathbf{G}]_0}\right\} \quad (2.10)$$

$[\mathbf{G@H}]$ represents the equilibrium concertation of the studied complex, whilst $[\mathbf{G}]_0$ and $[\mathbf{H}]_0$ are the total concentrations of guest and host. Equation 2.10 is given for a 1:1 binding model. Which analytical method is suitable for a specific complex depends on what physical property changes upon complexation and on the magnitude of the binding constant.[52]

Nonetheless, these analytical methods do not obtain the values of the binding enthalpy $\triangle H^0$ and entropy $\triangle S^0$. A van't Hoff analysis of titration data acquired at different temperatures allows to determine these values. Yet, due to the boiling or melting point of the solvent or restrictions of the analytical methods a sufficient temperature range cannot always be covered, which limits the van't Hoff method. Therefore, isothermal titration calorimetry (ITC) is advantageous over the van't Hoff method, as it yields both the binding enthalpy $\triangle H^0$ and entropy $\triangle S^0$ in one measurement at room temperature. ITC will be discussed in detail in the following chapter. Additionally in the design step, the switching of simple model compounds is examined. For example, redox-switchable moieties are characterised by CV.

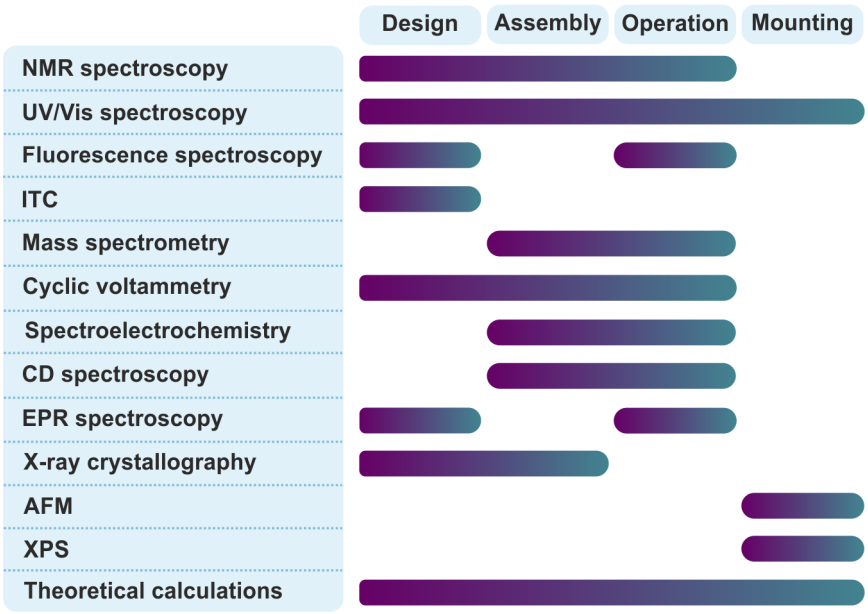

Figure 2.30. Analytical methods considered in this thesis and assigned to the four steps of engineering molecular switches. X-ray photoelectron spectroscopy (XPS) and AFM are used to characterise molecular switches deposited on surfaces.[212]

The assembly of molecular switches is investigated by archetypal methods of compound characterisation, such as NMR spectroscopy and high-resolution mass spectrometry (HRMS). Additionally, MS facilitates the investigation of complex mixtures, for example, originating from a self-sorting process. To distinguish a mechanically interlocked from a non-interlocked structure can be tedious with common methods. Tandem MS allows to distinguish both based on their gas-phase fragmentation pathways, as will be discussed in Section 2.3.3.

NMR spectroscopy is also an important tool to probe the operation of molecular switches and is complemented by methods suitable for the respective stimulus of the molecular switch. For example, CV and spectroelectrochemical measurements have a high importance for redox-switches.[44] However, distinguishing the different co-conformations of switchable rotaxanes can be a major obstacle and only a combination of several different methods allows to resolve the switching process in detail.[220] For instance, CD spectroscopy can be applied in the case of chiral molecular switches, and electron paramagnetic resonance (EPR) spectroscopy for

paramagnetic substances. Additionally, time-dependent measurements may allow to investigate switching kinetics.

Theoretical calculations are a powerful and versatile method for all four engineering steps, as they can fill analytical gaps or facilitate the evaluation of analytical results.[115] GRIMME introduced dispersion-corrected functionals to improve the quantification of noncovalent interactions in density functional theory.[221]

2.3.2 Isothermal titration calorimetry

Generally, *isothermal titration calorimetry* measures heat changes during the titration of one solution to another solution. Therefore, it allows to quantify all exothermal and endothermal processes.[222,223] In Figure 2.31, the twin-calorimeter setup of a *heat conduction* calorimeter is depicted.[113,223,224] Such a calorimeter was used to obtain the majority of the experimental data included in this thesis. In the sample cell, the heat generated by a *thermal event* is directly exchanged with the surrounding heat sink maintaining the isothermal conditions. A thermal event can be caused by dilution, covalent or noncovalent bond formation, but also the decomposition of one of the analytes. A heat detector (*i.e.*, a thermoelectric module) directly measures the heat absorbed or evolved in the sample cell. This so-called *heat flow* is corrected against the heat flow in the reference cell. Hence, an exothermic process results in a positive heat flow (Figure 2.32a).

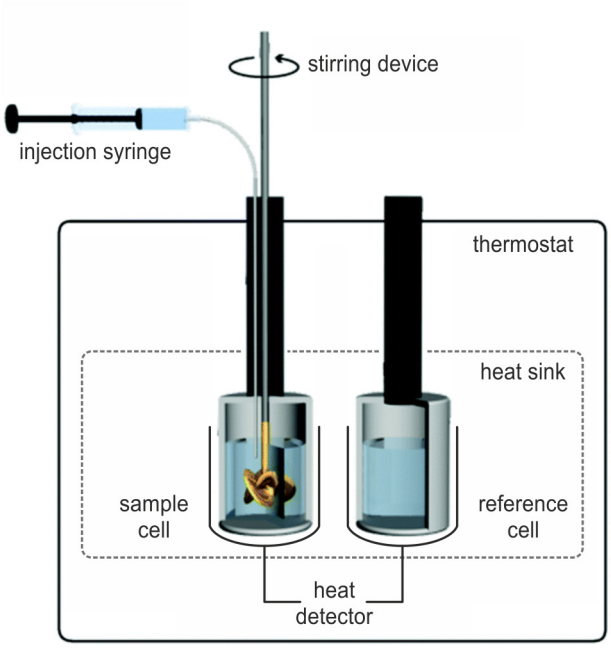

Figure 2.31. Heat conduction calorimeter setup for ITC titrations performed in this thesis. This scheme was adapted with permission of the Royal Society of Chemistry, from L. K. S. von Krbek *et al.*[113], permission conveyed through Copyright Clearance Center, Inc.

The second calorimeter type operates on *differential power compensation*, which has the advantage of a faster response time to thermal events and is applied by most of the current

commercially available calorimeters.[223,225] Technically, this calorimeter type does not maintain isothermal conditions and heaters apply a constant thermal gradient to both cells. A thermal event is measured as a differential temperature signal. In this setup, an exothermic process in the sample cell results in a negative signal.

To obtain binding constants with an ITC titration, one component is placed in the sample cell to which the binding partner is added in consecutive steps via a syringe. The reference cell is filled with the pure solvent. A thermal event caused by the interactions of both binding partners results in a heat flow signal increasing from the baseline (Figure 2.32a). Between the titration steps, a time delay of several minutes needs to be left to allow the solution to equilibrate chemically and the calorimeter thermally. For each titration step, the corresponding heat flow signal above the baseline is integrated and plotted against the molar ratio of the concentrations of both binding partners to yield the binding isotherm (Figure 2.32b).[113]

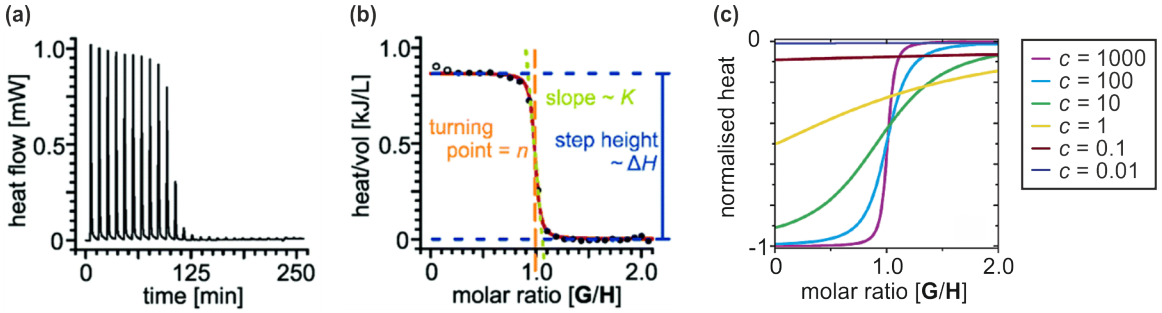

Figure 2.32. (a) Typical titration curve for an exothermic complex formation in a heat conduction calorimeter.[113] (b) Binding isotherm obtained for the titration data in (a).The fitting curve is marked in red. Additionally, a visual representation of how the binding constant *K* (green), the enthalpy ΔH^0 (blue) and the stoichiometry *n* (orange) can be extracted from the graphical plot is shown. Used with with permission of the Royal Society of Chemistry, from L. K. S. von Krbek *et al.*[113], permission conveyed through Copyright Clearance Center, Inc. (c) Wiseman isotherms obtained with a differential power compensation calorimeter for $n = 1$.[226] The Wiseman value *c* is given by Equation 2.12. Adapted with permission from W. B. Turnbull and A. H. Daranas[226] Copyright 2003 American Chemical Society.

For a bimolecular complex formation reaction of a guest **G** and a host **H** with a stoichiometry $n = 1$, the isotherm is described by Equation 2.11. For this WISEMAN isotherm, $\mathrm{d}Q_\mathrm{s}/\mathrm{d}[\mathbf{G}]_\mathrm{t}$ is the heat change for each titration step, V_0 is the effective volume of the sample cell, and $[\mathbf{H}]_\mathrm{t}$ and $[\mathbf{G}]_\mathrm{t}$ are the concentrations of guest and host at a certain titration step t in the titration experiment.[226,227]

$$\frac{\mathrm{d}Q_\mathrm{s}}{\mathrm{d}[\mathbf{G}]_\mathrm{t}} = \frac{\Delta H^0 \cdot V_0}{2} \left(1 + \frac{1 - \frac{[\mathbf{G}]_\mathrm{t}}{[\mathbf{H}]_\mathrm{t}} - (K_a[\mathbf{H}]_\mathrm{t})^{-1}}{\sqrt{\left(1 + \frac{[\mathbf{G}]_\mathrm{t}}{[\mathbf{H}]_\mathrm{t}} + (K_a[\mathbf{H}]_\mathrm{t})^{-1}\right)^2 - 4\frac{[\mathbf{G}]_\mathrm{t}}{[\mathbf{H}]_\mathrm{t}}}} \right) \tag{2.11}$$

A non-linear curve fitting with Equation 2.11 yields the binding constant K_a, corresponding to the slope, the binding enthalpy ΔH^0 to the step height, and the stoichiometry n to the

turning point of the isotherm (Figure 2.32b). Subsequently, the binding energy $\triangle G^0$ and the binding entropy $\triangle S^0$ can be calculated using Equations 2.1 and 2.2.

The maximum binding constant which can be determined with ITC depends on the host concentration $[\mathbf{H}]_0$ in the sample cell. TURNBULL and DARANAS discuss different curve shapes based on the WISEMAN value c (Figure 2.32c and Equation 2.12).[226] For low errors of the binding constant K_a and enthalpy $\triangle H^0$, a sigmoidal curve shape is recommended, which applies for values of c between 10 and 1000.[226] For values lower than 10, $\triangle H^0$ exhibits a high error, yet reliable values for K_a can still be obtained. In contrast, for values higher than 1000, $\triangle H^0$ yields accurate values, while K_a carries large errors.

$$c = n\ K_a[\mathbf{H_0}] \tag{2.12}$$

For high binding constants such as $K_a > 10^6$ M^{-1}, very low concentrations (µM) are necessary to meet the c-value criterium. Depending on the used calorimeter, the heat change for each titration step may not be distinguishable from the noise at these concentrations. The setup used in this thesis exhibited an upper limit of $K_a \approx 1{\cdot}10^6$ M^{-1}. To determine higher binding constants, a competition experiment can be used, where the host **H** is placed together with a guest **G1** in the sample cell. Subsequently, a stronger binding guest **G2** is titrated to this solution.[228] This *displacement* ITC yields an apparent binding constant K_{comp} and a binding enthalpy $\triangle H^0_{comp}$ according to the chemical equilibrium in Equation 2.13.[229]

$$\mathbf{G1@H} + \mathbf{G2} \underset{\longleftarrow}{\overset{K_{comp}}{\longrightarrow}} \mathbf{G2@H} + \mathbf{G1} \tag{2.13}$$

SIGURSKJOLD derived Equations 2.14 and 2.15 to determine the binding constant K_{G2} and enthalpy $\triangle H^0_{G2}$ of the stronger binding guest **G2**.[229] The binding constant K_{G1} and enthalpy $\triangle H^0_{G1}$ of the weaker binding guest need to be determined in a separate experiment and the equations are based on the approximation that the concentration [**G1**] remains constant. Consequently, Equations 2.14 and 2.15 are most accurate for high excess of **G1**.[229]

$$K_{G2} = K_{comp} \cdot (K_{G1}[\mathbf{G1}] + 1) \tag{2.14}$$

$$\Delta H^0_{G2} = \Delta H^0_{comp} + \Delta H^0_{G2} \cdot \frac{K_{G1}[\mathbf{G1}]}{K_{G1}[\mathbf{G1}] + 1} \tag{2.15}$$

For displacement ITC to yield reasonable results, a significant difference between the two binding enthalpies $\triangle H^0_{G1}$ and $\triangle H^0_{G2}$ is essential. Additionally, the measured K_{comp} and $\triangle H^0_{comp}$ depend on the concentration [**G1**], which allows the fine tuning of the optimal experimental conditions for a sigmoidal curve shape of the titration data.

For multivalent complexes, a DMC analysis can be applied using binding constants obtained by ITC (Section 2.1.5). For the thermodynamic analysis of 1:n complexes, the stoichiometry n is included in the non-linear curve fitting to obtain n binding constants and binding enthalpies.[113]

Generally, ITC does not consider any structural information. Instead, it determines the overall enthalpy balance of the reaction. What complexes are formed, whether multiple complexes are formed or if a side-reaction occurs must be investigated by other analytical methods. Therefore, all ITC titration data need to be supported with structural data, usually from NMR spectroscopy, or, in more complex cases, from MS as well.

2.3.3 Mass spectrometry of (pseudo)rotaxanes

Mass spectrometry is a very versatile analytical technique which is applied in many different scientific fields. It does not only allow to characterise pure compounds and compound mixtures by their mass-to-charge ratio m/z and fragmentation pattern, but also can be coupled to various chromatographic or other analytical tools, generating huge amounts of data in a short timeframe.

For this thesis, MS was applied to investigate mixtures of supramolecular complexes and study mechanically interlocked rotaxanes.[230] At a first glance, MS can be employed in supramolecular chemistry to characterise compounds based on their exact masses, isotopic patterns, charge states, stoichiometries, elemental compositions or impurities.

In the first experimental step, the supramolecular complexes and rotaxanes need to be transferred into the gas-phase. This process is called *ionisation* and may exhibit relatively harsh conditions. For example, electron ionisation results directly in the fragmentation of analyte ions. Only with the development of *electrospray ionisation* (ESI), a mild ionisation technique, supramolecular complexes could be transferred into the gas-phase without their dissociation. J. B. Fenn received the Nobel Prize in Chemistry in 2002 for substantial contributions to the development of ESI in the study of biomacromolecules, such as proteins, in the gas-phase.[231] In ESI, a micromolar solution of the analyte is pumped through a capillary held in a strong electrical field, which leads to charge separation. At the tip of the capillary charged droplets are formed, that further shrink due to the solvent evaporation facilitated by the flow of a nebulizer gas.[232] Ultimately, ESI produces analyte ions as proton or alkali cation adducts in the positive mode, or deprotonated ions or adducts of small anions, mainly chloride, in the negative mode. Intrinsically charged ions, such as crown/ammonium complexes, tend to lose their counterion. In general, the higher the mass of the analyte, the more charge states are observed. But also, structural features of the analyte ions have an impact on the number of observed charge states.

After their ionisation, the analyte ions are isolated from other ions and solvent molecules due to the vacuum and charge repulsion; thus, their gas-phase reactivity and intrinsic properties can be studied.[141,233] In the gas-phase, the noncovalent interactions of supramolecular complexes change dramatically compared to solution (Section 2.1.1), which may cause changes in the binding strength, mode, and geometry.[141,233,234]

MS displays its full potential in the investigation of complex mixtures, where a distinct number of species are formed, *i.e.*, in self-sorting processes or systems chemistry. While other methods may struggle with the signal overlap of impure compounds, MS allows to identify the formed species by their *m/z* ratios.[159] However, the ion count does not correlate equally for all analyte ions with the concentrations of the analytes in solution. Additionally, time-dependent measurements can be easily conducted, as MS is a quick method that allows the qualitative characterisation of the kinetics of self-sorting or self-assembly processes.[159]

For a further investigation in the gas-phase, the ions are separated through a method of ion selection, such as the use of a quadrupole (Figure 2.33a). Subsequently, in *tandem mass spectrometry* or *MS/MS*, the ions are activated by light or collision with particles. In collision induced dissociation (CID), the accelerated analyte ions collide with stationary inert gas molecules, such as argon, helium, or nitrogen (Figure 2.33b).[212] The collision energy can be adjusted by the external electrical field which accelerates the ions. Upon an increasing activation energy, the ions may undergo intramolecular reactions or fragment. The occurring fragmentation pathways may yield structural information about the analyte ion. For supramolecular complexes, such as pseudorotaxanes, the first bonds to break are the noncovalent ones, leading to the disassembly of the complex. However, for some very strong bound noncovalent complexes, it was observed that covalent bonds break before dissociation of the complex.[233] Comparatively in MIMs, such as rotaxanes, the fragmentation occurs always with the breaking of covalent bonds. Differences in the fragmentation pathways allows to distinguish mechanically interlocked from non-interlocked structures, with the observed fragments yielding additional structural information of the ionised MIMs.[141,235,236]

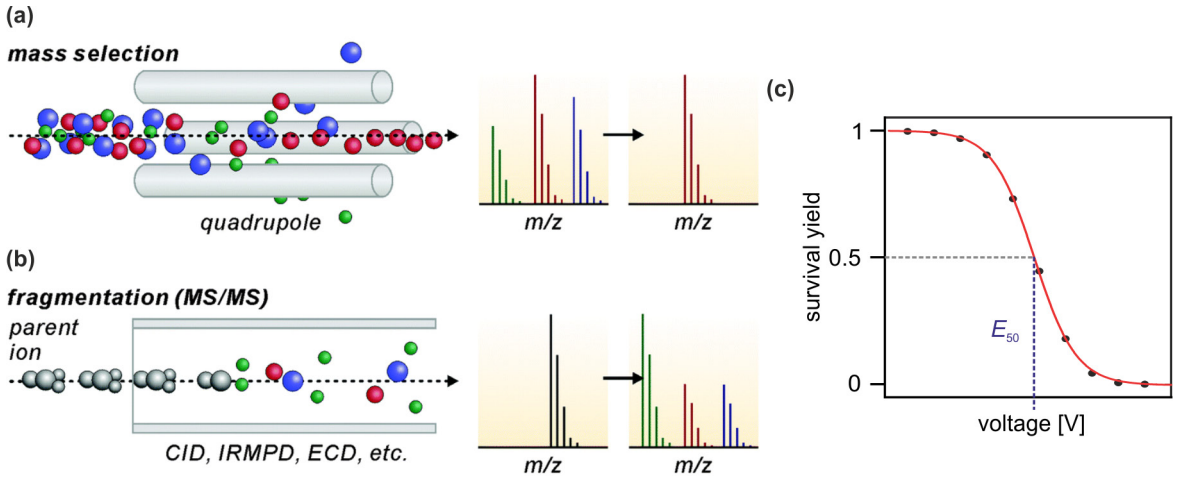

Figure 2.33. Schematic setup and *m/z* ratios in mass techniques: (a) mass selection and (b) tandem mass spectrometry. Adapted with permission from Z. Qi *et al.*[234], published by the Royal Society of Chemistry, under the CC BY-NC 3.0 licence. (c) Survival yield curve, with fitted curve in red and 50% survival yield voltage E_{50} in blue.

To quantify the gas phase stabilities of analyte ions, the survival yield can be plotted over the collision voltage (Figure 2.33c). The survival yield SY of an analyte ion can be calculated

for each voltage in a CID experiment by Equation 2.16, with I_P the integral of the intensity of the parent ion and I_F the integral of the intensity for each fragment ion.

$$SY = \frac{\int I_P}{\int I_P + \sum_i \int I_{F_i}} \tag{2.16}$$

The 50% survival yield voltage E_{50} describes the voltage where 50% of the parent ions are fragmented (Figure 2.33c). These voltages can be directly transformed into survival yield energies E_{SY}, according to Equation 2.17, considering the charge of the ion z and the elemental charge of an electron e.

$$E_{SY} = e \cdot z \cdot E_{50} \tag{2.17}$$

The non-linear curve fitting of the survival yield data over both the voltages or energies with a sigmoidal curve allows for an accurate determination of E_{SY} and E_{50}, respectively. Equation 2.18 is given for the determination of the 50% survival yield energy E_{SY} of the parent ion. Herein, E_C is the collision energy, a, b, and d the empirical constants, with $a \approx 1$, $b \approx 0$, and d the steepest part of the sigmoidal curve.[237]

$$SY = \frac{a - b}{1 + e^{(E_C - E_{SY})/d}} + b \tag{2.18}$$

To compare gas-phase stabilities, the energy E_{SY} needs to be normalised by the reduced mass.[238,239] E_{SY} may be converted into the *center-of-mass frame* E_{cm} by Equation 2.19, which involves the masses of the neutral gas m_{gas} and parent ion m_{ion}.[238,239] When the sizes of the analyte ions differ significantly, an additional correction that includes the degrees of freedom of the ions should be applied to compare the gas-phase stabilities of ions.[239,240]

$$E_{cm} = E_{SY}\left(\frac{m_{gas}}{m_{gas} + m_{ion}}\right) \tag{2.19}$$

Another possibility to gain structural information of the ionised analytes is through ion mobility spectrometry (IMS). In IMS the ions are separated by their collision cross section (CCS), which is dependent on the three-dimensional shape, size and m/z value of the ions (Figure 2.34).[230,234,241] The CCS represents the averaged geometric area of an ion that tumbles through a neutral gas in an ion mobility cell.[241] Consequently, smaller ions travel faster, and structural or conformational information can be obtained.

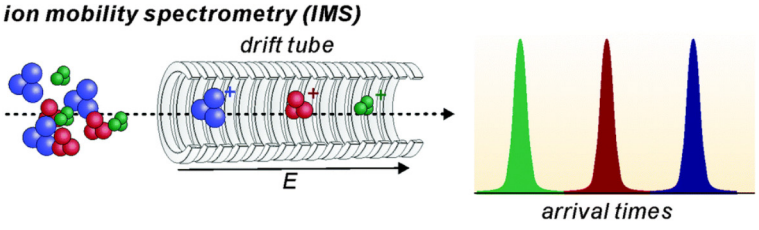

Figure 2.34. Schematical setup and arrival times in an IMS experiment, particular for a drift tube cell. Adapted with permission from Z. Qi *et al.*[234], published by the Royal Society of Chemistry, under the CC BY-NC 3.0 licence.

The experimental data of this thesis were acquired using a Synapt G2-Si mass spectrometer by Waters, with its setup being depicted in Figure 2.35. The instrument was equipped with an ESI source and the ions were focused in an ion guide, and transferred to a quadrupole, where mass selection can be performed. This Synapt is equipped with two collision cells, namely the trap and transfer cells. Ion mobility is performed in a travelling wave (TW) IMS cell. In a TW-IMS setup, the ions are pushed through the IMS cell by symmetric potential waves.[242] In the IMS cell, collisions with a buffer gas slow down the ions, allowing the separation by their CCS. Ultimately, the ions are channelled through a time-of-flight mass analyser and reach the detector.

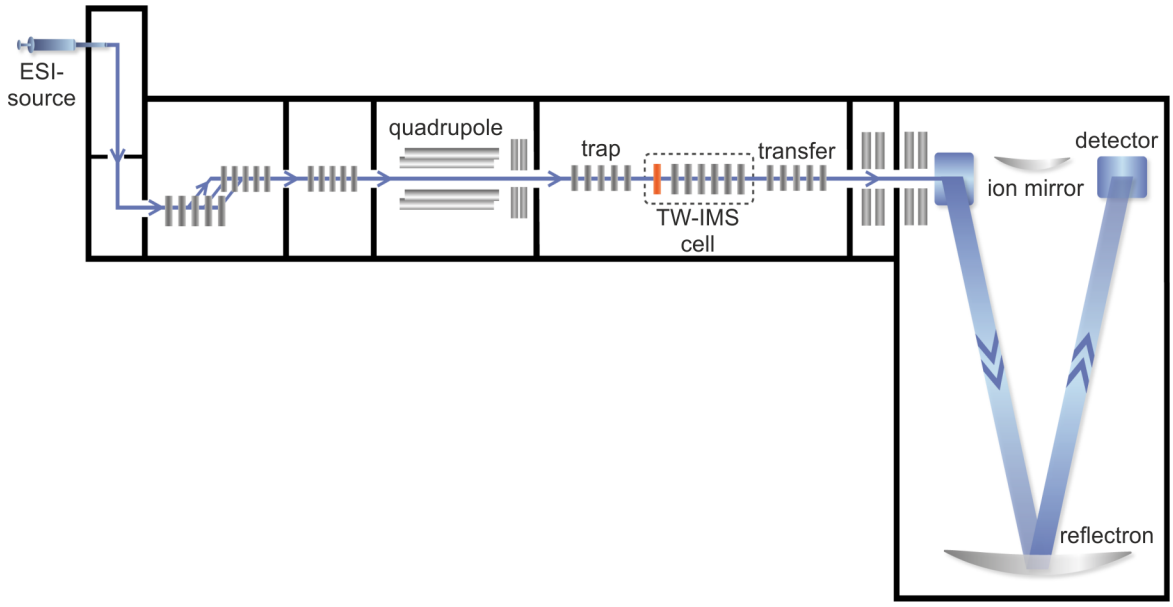

Figure 2.35. Instrumental setup of the Synapt G2-Si (from Waters Corporation) mass spectrometer used in this thesis.[243]

3 Summarised Results

3.1 General remarks

The results of this thesis are published in eight peer-reviewed publications. Here, the results are divided into two chapters. In the first subchapter, the thermodynamic properties of the involved supramolecular complexes are studied. The focus is put on crown/*sec*-ammonium pseudorotaxanes with crown ethers, which incorporate redox-switchable TTF and NDI units. Additionally, the guest binding of an organic cage is introduced which was investigated in collaboration with the group of Wei Jiang (SUSTech Shenzhen).

In the second subchapter, the analytical characterisation of the assembly and the operation of different supramolecular and mechanically interlocked molecular switches are summarised. The results are structured with respect to their mechanically interlocked structures, starting from pseudo[2]rotaxanes, to [2]rotaxanes, a divalent [2]rotaxane and divalent [3]rotaxanes. These results were obtained in collaboration with: the group of Bipraijit Sarkar (Universität Stuttgart), who performed EPR and specialised electrochemical measurements; the groups of Kari Rissannen (University of Jyväskylä) and Moritz Malischewski (Freie Universität Berlin), who conducted crystal structure analysis; the group of Arne Lützen (Friedrich-Wilhelms-Universität Bonn), who purified chiral rotaxanes; and the group of Beate Paulus (Freie Universität Berlin), who performed and evaluated theoretical calculations.

3.2 Thermodynamic analysis of supramolecular complexes

3.2.1 Redox-switchable crown/*sec*-ammonium pseudorotaxanes

The results discussed in this subchapter are part of six publications.[130,244-248]

While others introduced TTF containing crown ethers for metal binding,[176,198,200,201] we envisioned the TTF unit to render a switchable unit in mechanically interlocked switches. A divalent pseudo[3]rotaxane with a TTF containing crown ether was described by Stoddart and coworkers, but no rotaxane was constructed or redox-switching was investigated there.[249]

The crown ether **TTFC8** was synthesised as the prototype macrocycle, and it forms a pseudorotaxane complex with axle **A1**·PF_6 as shown by ^{1}H NMR spectroscopy (Figure 3.1). ITC revealed the binding between the crown ether and the axle to be enthalpy driven and exhibit a significant negative entropy of binding, leading to a total binding energy

$\triangle G^0$ = (-25.7 ± 0.2) kJ mol^{-1} and binding constant K_a = (33 ± 3) M^{-1} (Figure 3.1 and Section 6.6). In comparison to the **DBC8** macrocycle, the binding of **TTFC8** to **A1**·PF_6 is weaker by more than 9 kJ mol^{-1} (K_a lower by a factor of ≈ 40) due to the presence of two sulphur atoms in the ring of the macrocycle, which are weaker hydrogen bond acceptors and are less negatively polarised compared to oxygen atoms. Additionally, we observed in the crystal structure of **TTFC8** that the wheel is larger than **DBC8** (Section 6.7), which worsens the hydrogen bonding pattern as well. Additional noncovalent interactions of the π-systems of the TTF or naphthalene unit minorly contribute to the total binding energy.

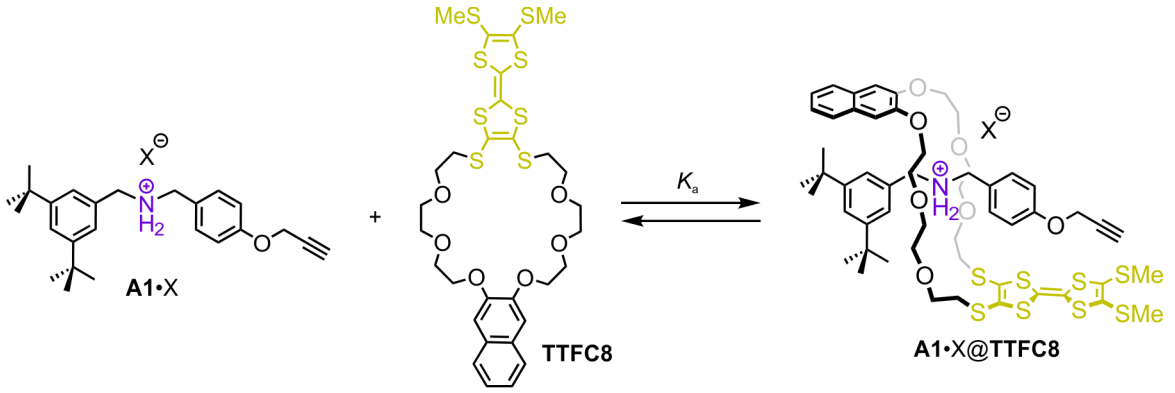

thermodynamic binding data

	K_a [10^3 M^{-1}]	ΔG^0 [kJ mol^{-1}]	ΔH^0 [kJ mol^{-1}]	$T\Delta S^0$ [kJ mol^{-1}]
X = PF_6^-:	33 ± 3	-25.7 ± 0.2	-51.5 ± 0.9	-25.9 ± 1.1
= $BArF_{24}^-$:	440 ± 40	-32.2 ± 0.3	-46.2 ± 0.7	-14.0 ± 1.0

Figure 3.1. Pseudorotaxane formation of **TTFC8** and **A1**·X with different counter ions and thermodynamic binding properties obtained by ITC in DCE at 298 K (details in Section 6.6). Synthesis is described in Section 6.2.

To compensate for the lower binding constant, we used the non-polar solvent 1,2-dichloroethane (DCE) which stabilises the *sec*-ammonium salt poorly and, thereby, facilitates the formation of the complex. Furthermore, using the weaker coordinating anion $BArF_{24}^-$, increased the binding energy by 6.5 kJ mol^{-1} (K_a increased by a factor of ≈ 13, Section 6.6). Interestingly, this binding enhancement is no enthalpic effect, as it might be expected when considering the ion pairing of both axle salts competing with the pseudorotaxane formation. In fact, the binding enthalpy $\triangle H^0$ of **A1**·$BArF_{24}$@**TTFC8** is lower than for **A1**·PF_6@**TTFC8** (Figure 3.1). Instead, the binding entropy $\triangle S^0$ is significantly less negative, which is the reason for the overall higher binding energy $\triangle G^0$. We proposed that these differences in the binding entropies originate from a favourable change in the solvation entropies from **A1**·PF_6@**TTFC8** to **A1**·$BArF_{24}$@**TTFC8** (Section 6.6).

Based on **TTFC8**, we prepared three additional TTF containing crown ethers and introduced two extended TTF containing crown ethers as well. TTF sits directly in the crown ether's cavity, which we designed to experience Coulomb repulsion from the ammonium unit upon oxidation to TTF^{2+}. Instead, the extended TTF (exTTF) unit is more remote from the cavity of the crown ether and, due to its larger π-system, also facilitates mixed-valence or π-dimer

interactions, as it was shown for the exTTF monomer.[250] Additionally, two reductive NDI-containing crown ether macrocycles were introduced. An overview on the crown ether macrocycles and monovalent axles used for ITC titrations in this thesis are depicted with their respective binding constants in Figure 3.2. The crown-7 analogues form a threaded complex only with alkylammonium axle **A2**·PF_6, as discussed in Section 2.1.3.

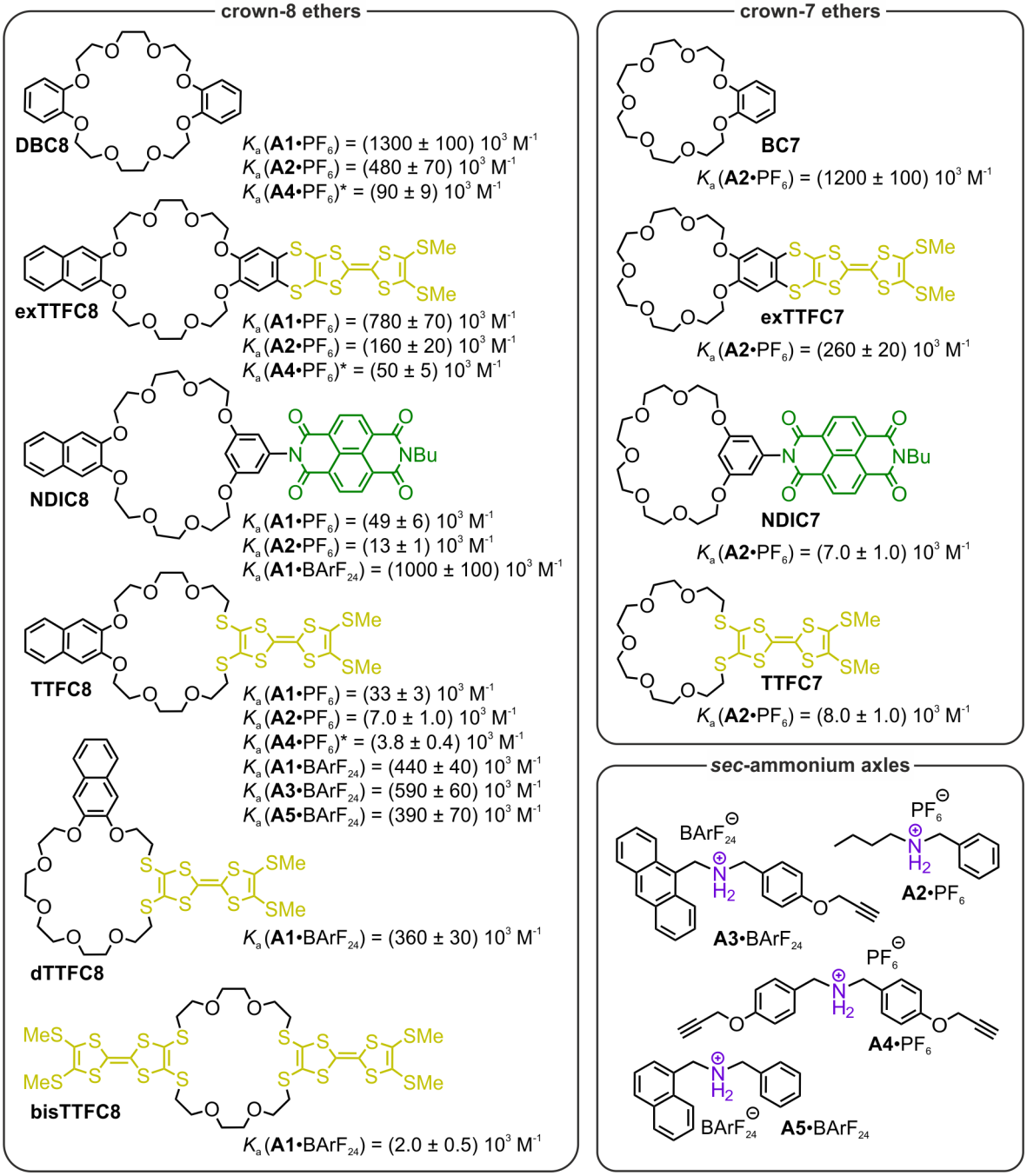

Figure 3.2. Overview on the toolbox of monovalent axles, crown-8 and crown-7 ethers studied in this thesis. Binding constants were obtained with ITC and are given for DCE at 298 K. Values marked with * were obtained in DCE/CH_3CN (10:1), as **A4**·PF_6 is poorly soluble in pure DCE. The crown-8 ethers are sorted by their binding constant from high (top) to low (bottom). The full thermodynamic binding data and syntheses are given: for **NDIC8**, **bisTTFC8**, **exTTFC7**, **TTFC7**, **A1**·PF_6 and **A2**·PF_6 in Section 6.6, for **TTFC8** and **A3**·$BArF_{24}$ in Section 6.2, for **exTTFC8** and **A4**·PF_6 in Section 6.3, for **NDIC7** in Section 6.8, for **dTTFC8** in Section 6.5 and **A5**·$BArF_{24}$ in Section 6.7.

The major conclusions drawn from the thermodynamic binding data of the crown ether macrocycles and *sec*-ammonium axles are:

- **exTTFC8** binds slightly weaker than **DBC8** (K_a is lower by a factor of ≈ 2 and $\triangle G^0$ by ≈ 1-2 kJ mol^{-1}) and significantly stronger than **TTFC8**.
- **NDIC8** binds to all three ammonium axles similarly strong as **TTFC8**. For **NDIC8** the weaker binding compared to **DBC8** arises from the crown ether being one carbon atom larger, which weakens the hydrogen bonding pattern.[93]
- **NDIC8** exhibits a lower $\triangle H^0$ by ≈ 5 kJ mol^{-1} than **TTFC8** when binding to **A1**·PF_6, and an increased $\triangle S^0$. The more flexible **TTFC8** macrocycle adopts a more optimal conformation for hydrogen bonding and additional π-interactions than the rigid **NDIC8**, resulting in a higher enthalpy and a stronger conformational fixation in the complex corroborated with a less favorable binding entropy (Section 6.6).
- Changing the positions of the naphthalene and TTF units in the crown ether ring while keeping the same crown ether size in **dTTFC8** has only a minor impact on the binding constant.
- Incorporation of a second TTF in the crown ether in **bisTTFC8** results in a strong drop of K_a by a factor of ≈ 220 ($\triangle G^0$ lower by 13.5 kJ mol^{-1}) compared to **TTFC8**.
- Structural changes in the aromatic units of the axle in **A1**·$BArF_{24}$, **A3**·$BArF_{24}$, **A5**·$BArF_{24}$ have only a minor impact on the binding constants to **TTFC8**.
- The symmetrical axle **A4**·PF_6 was not soluble in pure DCE, hence it was studied in a solvent mixture of DCE/CH_3CN (10:1). The binding to **DBC8**, **exTTFC8** and **TTFC8** followed similar trends compared to **A1**·PF_6 in DCE, though a decrease of K_a by a factor of ≈ 10 was observed, which is reasoned by an increase in solvent polarity.
- Alkylammonium axle **A2**·PF_6 binds to all crown-8 ether with a significantly lower binding constant K_a than **A1**·PF_6. Due to a higher flexibility in the alkyl chain of axle **A2**·PF_6, which is reduced upon complexation, the complex formation is more entropically disfavoured. Additionally, there are more favourable π-interactions possible in **A1**·PF_6.
- Crown-7 ethers bind to **A2**·PF_6 slightly stronger than their crown-8 analogues, except for **NDIC7** which binds to **A2**·PF_6 slightly weaker than **NDIC8**.

The redox potentials of the switching of the NDI, TTF and exTTF units were only minorly impacted by the incorporation in the crown ether and not impacted by the crown ether size, as shown by voltametric measurements (Section 6.6). The UV/Vis absorption spectra of each

switching state of the three redox-switchable units were also not changed by the incorporation in the crown ether (Section 6.2, 6.3 and 6.6).

3.2.2 A cation binding organic cage

The results discussed in this subchapter are part of one publication.[251]

The low preorganisation in the crown/*sec*-ammonium complexes limits the binding energy, as additional attractive noncovalent interactions come together with entropic penalties originating from the conformational fixation upon complexation. We developed the organic naphthocage **NC** with three naphthalene walls. It exhibits a higher degree of preorganisation, yet it maintains some flexibility due to the benzyl ether bridges (Figure 3.3). This flexibility allows the formation of a self-inclusion complex in the solid state (Figure 3.3 middle). In solution at room temperature, the cage interconverts between different conformations, but at 218 K the **NC** cage also exhibits signals in the ^{1}H NMR spectrum consistent with a self-inclusion complex.

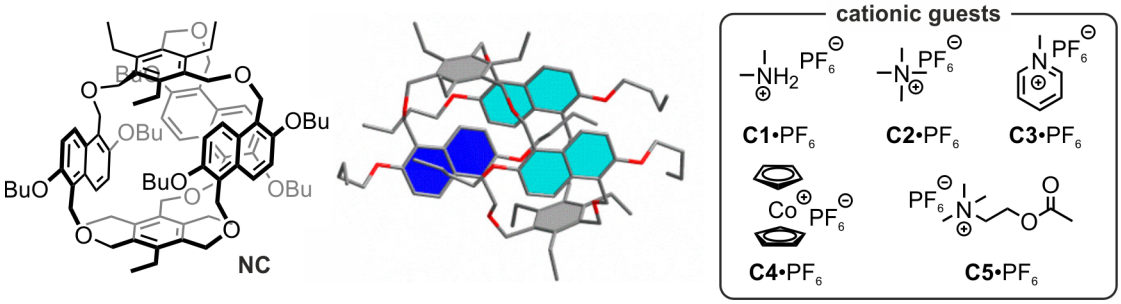

Figure 3.3. Structures of organic cage **NC** and some of its guest. In the middle the crystal structure of **NC** is shown. The self-included naphthalene wall is highlighted in dark blue. Reprinted with permission from Jia *et al*.[251] Copyright © 2019 American Chemical Society.

Due to the electron-rich aromatic systems in its walls, this cage is an excellent candidate to bind cations. We found that it binds small tetraalkyammonium PF_6 salts, such as tetraethylammonium PF_6. In contrast, tetrapropylammonium PF_6 did not bind inside the cavity. The thermodynamic binding data were obtained by a Nano ITC setup, which allows measurements at low concentrations (0.16 mM). However, for $K_a > 10^7$ M^{-1} the Wiseman c value is above 10000.[226] To measure such extreme binding constants, we employed an ITC displacement method[229] with a moderately strong binding guest **C1**·PF_6 as a competing guest. We obtained the highest binding constant of $K_a = (6.7 \pm 2.1)\ 10^9$ M^{-1} for acetylcholine **C5**·PF_6 (Table 3.1 and Section 6.4).

Considering that **NC** is a rather flexible cage and adopts even a self-inclusion conformation in its free state, the binding constants are high. The binding energies for all guests are enthalpy dominated due to strong cation-π interactions. However, the binding enthalpies ΔH^0 of all complexes of **NC** are lower than for some crown/*sec*-ammonium complexes. Instead, the binding inside **NC** is entropically favoured for all guests except for **C1**·PF_6. A highly positive

entropic contribution $\triangle S^0$ comes along with a comparably lower binding enthalpy $\triangle H^0$ in the smaller guests **C2**·PF_6 and **C3**·PF_6. This trend shows that smaller guests have weaker covalent interactions, but the conformational flexibility of **NC** is maintained, and the binding is more entropically favoured. The strongest binding is observed for larger guests, which fit the cavity well (*i.e.*, **C4**·PF_6) or have some conformational flexibility (*i.e.*, **C5**·PF_6). Such large guests form very strong interactions, while mildly affecting the conformational flexibility of **NC**.

Table 3.1. Thermodynamic binding data of cage **NC** with different cationic guests by ITC titrations in DCE at 298 K (for the full data set and titration curves, see Section 6.4).

entry	guest	K_a [M^{-1}]	ΔG^0 [kJ mol^{-1}]	ΔH^0 / [kJ mol^{-1}]	$T\Delta S^0$ / [kJ mol^{-1}]
1	**C1**·PF_6	$(4.1 \pm 0.4) \cdot 10^5$	-32.0 ± 0.3	-37.1 ± 1.4	-5.1 ± 1.7
2	**C2**·PF_6	$(1.6 \pm 0.3) \cdot 10^7$	-41.2 ± 0.3	-23.8 ± 0.5	17.4 ± 0.8
3[a]	**C3**·PF_6	$(7.6 \pm 2.4) \cdot 10^8$	-50.7 ± 0.3	-30.4 ± 0.2[b]	20.3 ± 0.9
4[a]	**C4**·PF_6	$(6.1 \pm 1.9) \cdot 10^9$	-55.8 ± 0.7	-45.7 ± 0.3[b]	10.1 ± 1.0
5[a]	**C5**·PF_6	$(6.7 \pm 2.1) \cdot 10^9$	-56.1 ± 0.7	-45.5 ± 0.3[b]	10.6 ± 1.0

[a]Data obtained by ITC displacement method with **C1**·PF_6. [b]ΔH^0 was taken from direct ITC titrations.

These high affinities of **NC** for cationic guests were applied for detecting acetylcholine **C5**·PF_6 with ion-selective electrodes. Besides, a very high shift of the oxidation potential of ferrocene was observed in the presence of **NC** as only the oxidised cationic ferrocenium binds into the cavity. These interesting redox properties were applied in another study for switchable supramolecular complexes of **NC** with TTF and viologen.[252]

3.3 Assembly and operation of molecular switches

3.3.1 Pseudorotaxane switches

The results discussed in this subchapter are part of three publications.[130,246,248]

The proof-of-concept for the redox-switching of TTF-containing pseudorotaxanes was demonstrated for **A3**·$BArF_{24}$@**TTFC8** (Figure 3.4 left and Section 6.3). Upon oxidation the macrocycle dethreads from the axle due to coulombic repulsions of the dicationic TTF unit and the ammonium ion, which was shown by ^{1}H NMR spectroscopy. This effect is enhanced due to the $BArF_{24}^-$ counterion as the positive charges are poorly stabilised.

Likewise, the pseudorotaxane **A1**·PF_6@**NDIC8** can be disassembled by reduction (Figure 3.4 right and Section 6.6). However, in this case the driving force is the attractive noncovalent interaction between the reduced **NDIC8**$^{2-}$ and the cationic ammonium, seen in the high shifts of the reduction potentials towards less negative values in differential pulse voltammetry (DPV). A similar shift of the redox potentials of the NDI was observed in the presence of dimethylammonium PF_6^- instead of the axle. Hence, we hypothesised a strong ionic hydrogen bonding as the reason for these shifts in the redox potentials (Figure 3.4 right, green).[42]

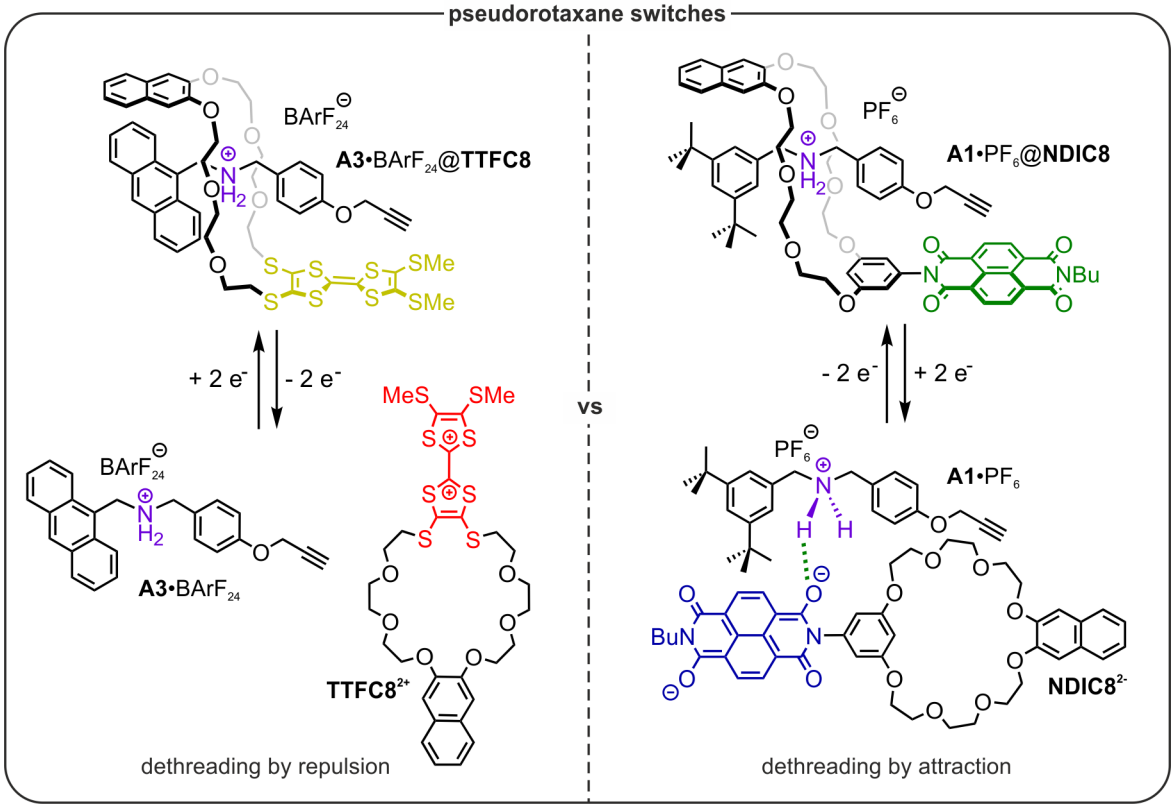

Figure 3.4. Overview on the redox switching of two pseudorotaxanes. The oxidative switch **A3**·$BArF_{24}$**@TTFC8** is described in detail in Section 6.2 and the reductive switch **A1**·PF_6**@NDIC8** in Section 6.6. The green dotted line indicates a possible attractive ionic hydrogen bonding.

The disassembly occurs in both pseudorotaxanes **A3**·$BArF_{24}$@**TTFC8** and **A1**·PF_6@**NDIC8** immediately due to a low kinetic barrier. We designed an axle with an increased steric demand to increase the kinetic barrier of threading and slow down the macrocycle exchange rate. After screening different sterically demanding groups, we picked the naphthalene unit in **A6**·$BArF_{24}$ as a 'speed bump' (Section 6.7). The formation of **A6**·$BArF_{24}$@**TTFC8** exhibited a half-life of $t_{1/2}$ = 120 min. **A6**·$BArF_{24}$@**TTFC8** showed properties of a *size-complementary* rotaxane. For example, it could be isolated with column chromatography (Figure 3.5 and Section 6.7). Interestingly, we observed with ^{1}H NMR spectroscopy that another complex is formed initially. With tandem MS this equilibrium could be studied further. The isolated pseudorotaxane **A6**·$BArF_{24}$@**TTFC8** was ionised, isolated, and then fragmented by CID, exhibiting a 50% survival yield voltage E_{50} = (39.2 ± 0.4) V (Figure 3.5b blue). A solution of **A6**·$BArF_{24}$ and **TTFC8** after 5 min of reaction time showed the formation of a complex with the same m/z but a lower gas-phase stability (Figure 3.5b red). Only 5% of the isolated ions fragment at similar voltages as in the isolated case and 95% of the ions fragment at lower voltages, which can be assigned to a non-threaded complex. After 135 min, a mixture of both complexes can be observed in the survival yield voltages (Figure 3.5b black). Consequently, these results evidence the conversion of the instantly formed but weaker non-threaded complex (with a lower K_{nt}, but higher rate constant k_{nt}) into the pseudorotaxane (with a higher K_{pt}, but lower k_{pt}) (Figure 3.5c).

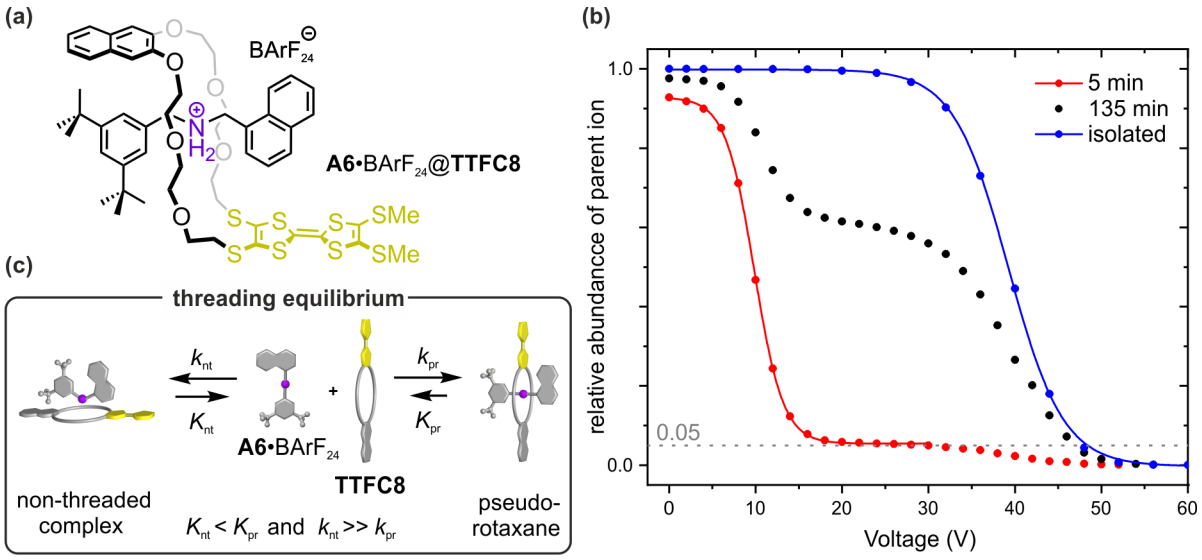

Figure 3.5. Size complementary rotaxane **A6**·$BArF_{24}$**@TTFC8**. (Details in Section 6.7). (a) Structure of the isolated pseudorotaxane. (b) Survival yield curves obtained for mass selected **A6**$^+$**@TTFC8** at increasing collision voltages. The red curve corresponds to the sample after 5 min, and the black curve to the sample at 135 min after mixing of wheel and axle. Blue curve: Isolated pseudorotaxane by column chromatography. Solid lines represent sigmoidal fitting to determine the 50% survival yield voltages E_{50}: red: E_{50} = (9.8 ± 0.2) V; blue: E_{50} = (39.2 ± 0.4) V. (c) Schematic representation of the equilibrium between non-threaded and pseudorotaxane complexes. Adapted from Gaedke *et al.*[130] with permission from the Chinese Chemical Society (CCS), Shanghai Institute of Organic Chemistry (SIOC), and the Royal Society of Chemistry (published under the CC BY-NC 3.0 licence).

The switching of **A6**·$BArF_{24}$**@TTFC8** with two different stimuli showed an interesting behaviour (Figure 3.6 and Section 6.7): deprotonation leads to immediate disassembly, before the first NMR spectrum could be recorded. In contrast, the dethreading after oxidation to TTF^{2+} occurred much slower with $t_{1/2}$ = 11 h and could be monitored with ^{1}H NMR spectroscopy.

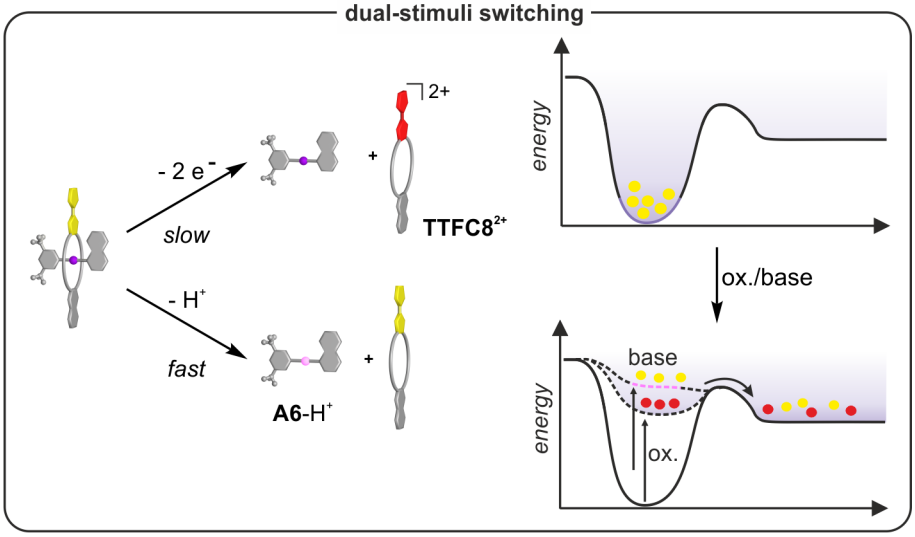

Figure 3.6. Schematic representation of the dethreading of **A6**·$BArF_{24}$**@TTFC8** induced by oxidation with $NOSbF_6$ and Schwesinger's P2 base immobilised on polystyrene. A schematic potential energy surface for both switching processes is shown with yellow circles representing the neutral **TTFC8** and red the oxidised **TTFC8**$^{2+}$ (Details in Section 6.7). Adapted from Gaedke *et al.*[130] with permission from the Chinese Chemical Society (CCS), Shanghai Institute of Organic Chemistry (SIOC), and the Royal Society of Chemistry (published under the CC BY-NC 3.0 licence).

Consequently, the kinetics of the switching processes do not depend only on the steric bulk of the speed bump, but also on the nature of the stimulus. We presume weak attractive forces between the oxidised **TTFC8**$^{2+}$ and the ammonium unit result in a local minimum in the potential energy surface and cause the slower dethreading (Figure 3.6).

3.3.2 Monovalent switchable [2]rotaxanes

The results discussed in this subchapter are part of five publications.[130,245-248]

To close the mechanical bond, pseudorotaxanes were reacted with an *N*-oxide stoper (2,6-dimethoxybenzonitrile oxide), which facilitates the 1,3-dipolar cycloaddition to a triple bond without the addition of any metal or base. This procedure is advantageous for avoiding the deprotonation of the axle, or the oxidation/reduction of the TTF, exTTF or NDI units. An overview of five constructed [2]rotaxanes with their respective switch function is depicted in Figure 3.7. Additional to NMR spectroscopy, the interlocked structure was confirmed by tandem MS, where no free axle was observed among the fragments, as it would be expected for pseudorotaxanes. Instead, only fragments of the axle were present. All rotaxanes were investigated through CV and UV/Vis absorption spectroscopy in their different switching states.

For the exTTF rotaxane **R4**·PF_6 no difference in the optoelectronic properties *versus* the free macrocycle was observed (Figure 3.7a and Section 6.3). Thereby, it remained an electrochromic switch which changes its colour in dependence of the redox state.

Likewise, the NDI rotaxane **R5**·$BArF_{24}$ showed very similar optoelectronic properties compared to the free macrocycle. The potential shifts observed in the pseudorotaxane **A1**·PF_6@**NDIC8** were absent in **R5**·$BArF_{24}$ because the mechanical bond prevents the dethreading of the macrocycle and no interaction between the anionic NDI and the ammonium of the axle was possible (Figure 3.7a and Section 6.6).

The three TTF-containing rotaxanes depicted in Figure 3.7 revealed emerging properties. For rotaxane **R6**·$BArF_{24}$, a shuttling motion of **TTFC8** upon oxidation to **TTFC8**$^{2+}$ was observed (Figure 3.7b and Section 6.2). The main analytical evidence for this translational motion was obtained by fluorescence spectroscopy, as the fluorescence emission of the anthracene increased after oxidation. The fluorescence is partially quenched in the pristine redox state due to the proximity of **TTFC8** to the anthracene unit. Additionally, the observed new peak at 1.08 V in the CV of **R6**·$BArF_{24}$ and signal shifts in the ^{1}H NMR spectrum of [**R6**·$BArF_{24}$]$^{2+}$ offered more indications for the shuttling of the macrocycle. For comparison, we also obtained a rotaxane from the pseudorotaxane **3**·$BArF_{24}$@**TTFC8**, which contained a shorter axle. Here, no clear evidence for a distinct shuttling motion could be gathered. From the strong shifts of the oxidation potentials ($\triangle E_{1/2}{}^1$ = 130 mV and $\triangle E_{1/2}{}^2$ = 360 mV) of this

rotaxane, we calculated a force of 35 kJ mol^{-1} for the Coulomb repulsion between the *sec*-ammonium ion and **TTFC8**$^{2+}$.

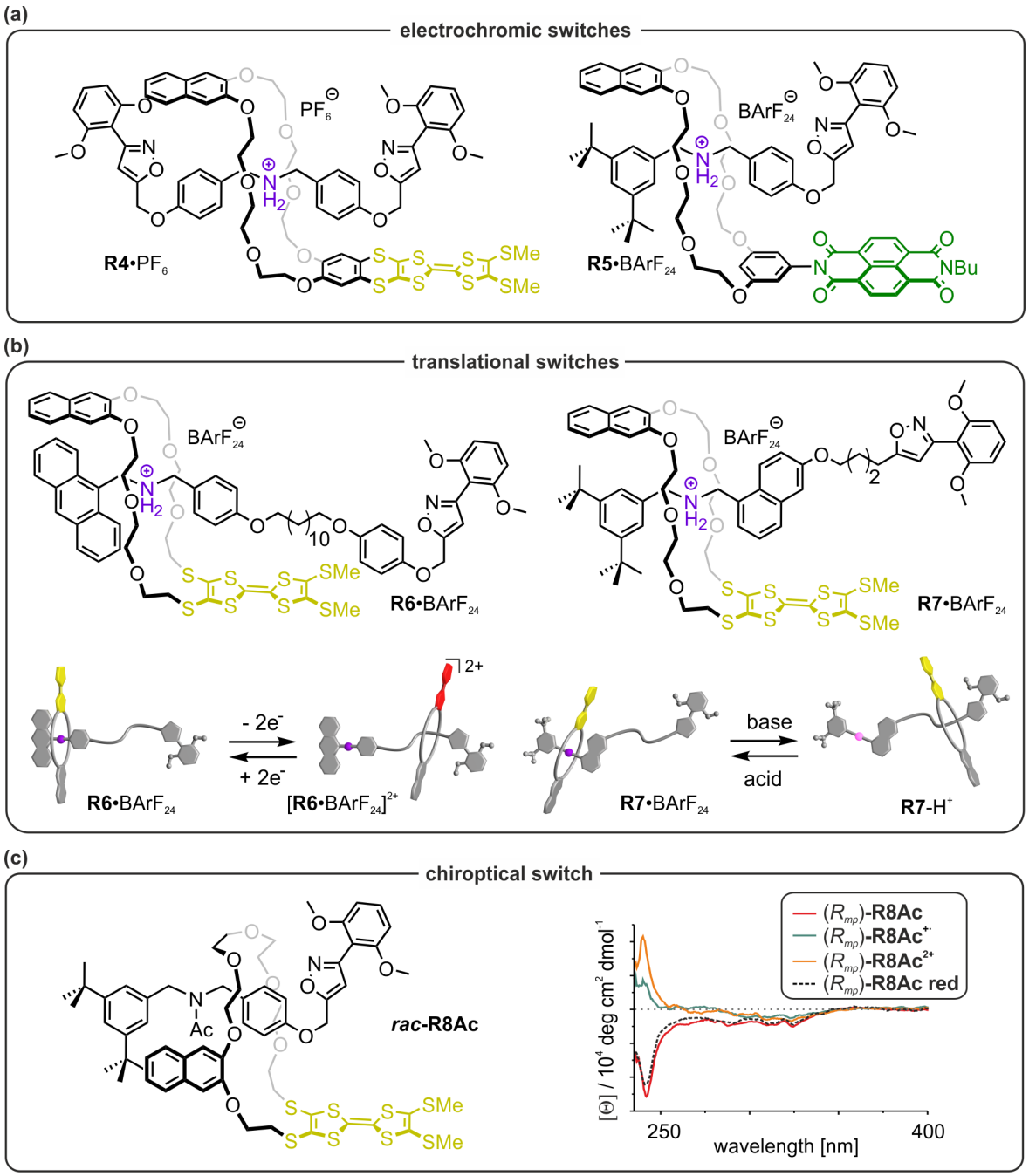

Figure 3.7. Overview on five [2]rotaxanes classified by their switch function. (a) Structures of electrochromic switches. Details for **R4**·PF_6 in Section 6.3 and for **R5**·$BArF_{24}$ in Section 6.6. (b) Structures of translational switches with a scheme of their operation mode. The pink circle represents the deprotonated *sec*-amine in the axle. Details for **R6**·$BArF_{24}$ in Section 6.2 and for **R7**·$BArF_{24}$ in Section 6.7. (c) Structure of chiroptical switch with electronic circular dichroism (ECD) spectra of one enantiomer (R_{mp})**-R8Ac** after oxidation and subsequent reduction. Details in Section 6.5. Adapted with permission from Gaedke *et al.*[245] (published by the Royal Society of Chemistry, under the CC BY-NC 3.0 licence).

We prepared rotaxane **R7**·$BArF_{24}$ containing the 'speed bump' introduced above to slow down the translational motion (Figure 3.7b and Section 6.7). However, ^{1}H NMR spectroscopy and DPV indicated that the oxidised macrocycle **TTFC8**$^{2+}$ resides still close to the ammonium

unit. In contrast, deprotonation of **R7**·$BArF_{24}$ leads to fast translocation of the macrocycle away from the *sec*-amine as was concluded from the ^{1}H NMR spectrum. These differences in the outcome of both stimuli are in parallel with the switching behaviour observed for the pseudorotaxane **A6**·$BArF_{24}$@**TTFC8** (Figure 3.6). Again, weak attractive forces of **TTFC8**$^{2+}$ to the ammonium ion may prevent the macrocycle to pass the 'speed bump'.

The construction of a rotaxane from the directional axle **A1**·$BArF_{24}$ and the directional macrocycle **dTTFC8** led to the formation of a mechanically planar chiral rotaxane. After the *N*-acetylation, the rotaxane ***rac*-R8Ac** was obtained and the two enantiomers could be separated by chiral HPLC (Figure 3.7c and Section 6.5). For the charged rotaxane the separation was not possible. In the acetylated rotaxane ***rac*-R8Ac** the strong hydrogen bonds of the ammonium ion to the crown ether are absent. Therefore, the macrocycle can move and fold more freely along the axle. Interestingly, the oxidation of the isolated enantiomers leads to a sign inversion of the main absorption at 242 nm in the ECD spectrum, as shown for (R_{mp})**-R8Ac** in Figure 3.7c. No clear analytical evidence for a reason for this observation could be obtained. However, time dependent DFT allowed to simulate the ECD spectra for different co-conformations in all switching states. We observed that different co-conformations have nearly no impact on the ECD spectra. Instead, the electron transition in the neutral state originates from an orbital located on the TTF to an orbital of the axle. In contrast, in the oxidised states the TTF is the target of the electron transitions. Consequently, the changes in the electronic structure caused by the oxidation are the reason of the chiroptical switching. Thereby, we described the first redox-controlled chiroptical switch based on a mechanically planar chiral rotaxane.

Based on the five examples here, we demonstrated how using the toolbox described in Section 3.2 different functions for the mechanically interlocked switches can be engineered. Moreover, secondary structural features as the axle length or the type of the stopper were observed to play an important role to achieve the desired function.

3.3.3 Rotational switchting in a homo[3]rotaxane

The results discussed in this subchapter are part of one publication.[247]

The special features of **exTTFC8**, *i.e.* that it does not experience strong Coulomb repulsion upon oxidation and instead favours noncovalent dimerisation, make the macrocycle an excellent candidate for studying homo[3]rotaxanes with two **exTTFC8** wheels. We used the divalent axle **A7**·$2PF_6$ to allow the binding of two crown ethers in close proximity (Figure 3.8a and Section 6.3). PF_6^- counterion were applied because the two charged binding stations in direct proximity are rather unstable and the strong binding of **exTTFC8** renders the use of $BArF_{24}^-$ not necessary.

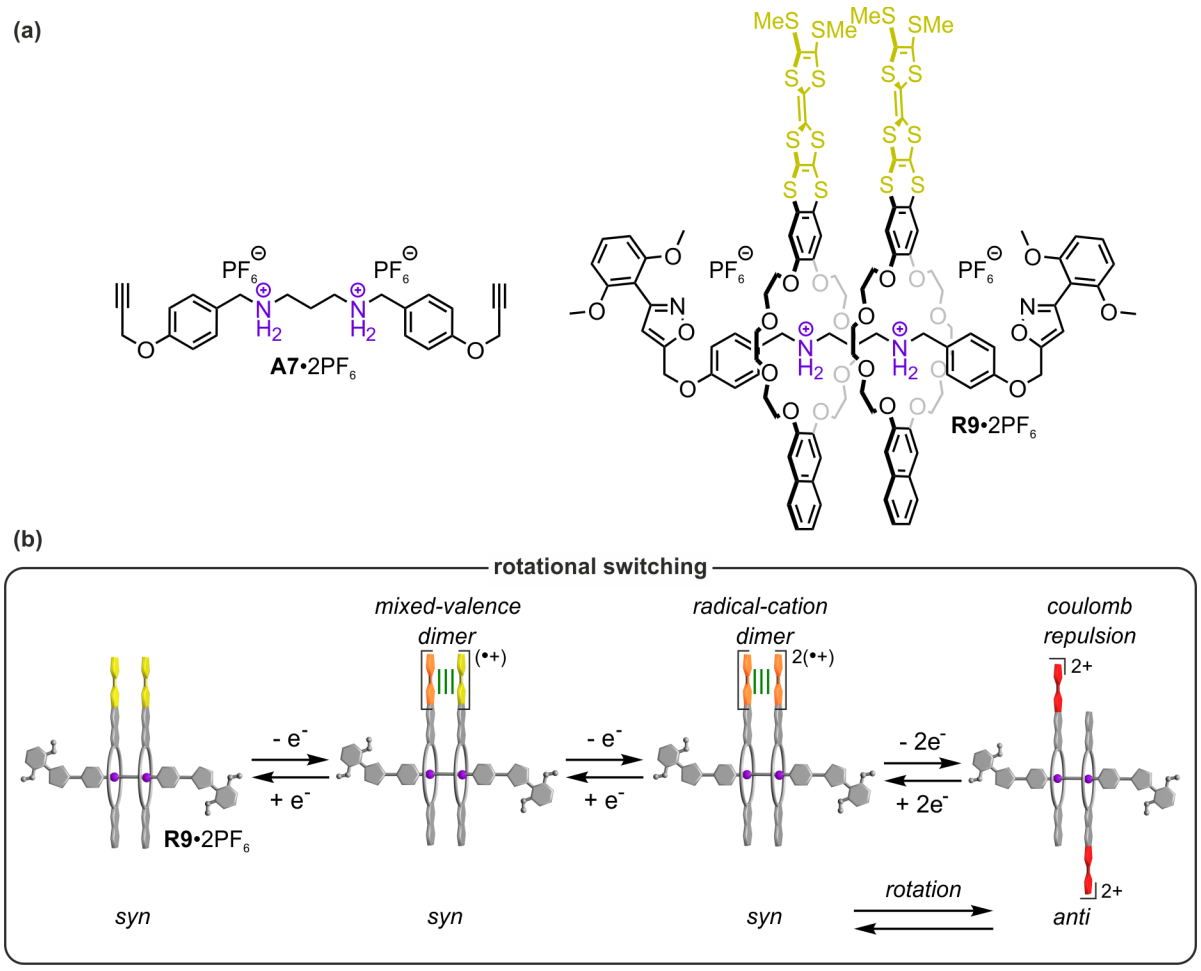

Figure 3.8. (a) Structures of the divalent axle and the homo[3]rotaxane constructed for studying rotational switching. (b) Scheme of the redox-switching mechanism. Attractive interactions are marked in green. Details in Section 6.3.

ITC titrations revealed negative allosteric cooperativity for the binding of the second macrocycle **exTTFC8** to **exTTFC8@A7**·2PF_6, as the first macrocycle can adopt a conformation where it binds to both *sec*-ammonium ions. Additionally, the second binding event leads to fixed conformations of macrocycles and axle, which results in a high entropic penalty of the second binding event. However, by comparing the ITC titration data of the axle **A7**·2PF_6 with **exTTFC8** and **DBC8**, an attractive interaction between the two **exTTFC8** could be identified, as the binding of the second **exTTFC8** to **exTTFC8@A7**·2PF_6 exhibits a higher binding enthalpy ΔH^0 compared to the second binding of **DBC8** to **DBC8@A7**·2PF_6.

After the successful formation of rotaxane **R9**·2PF_6, we were interested in how the oxidation of exTTF might influence the rotational co-conformations of the two rings. As crown ethers rotate very fast at room temperature in solution due to a low kinetic barrier, we were focussed on the rotational orientation of the two **exTTFC8** with respect to each other.

Alongside IMS results of the rotaxane **R9**·2PF_6, the ITC results indicate a *syn* co-conformation for the pristine redox state. CV experiments revealed four different oxidation states for

R9·2PF_6 (Figure 3.8b and Section 6.3). Based on the characteristic absorption bands in the UV/Vis-NIR and EPR spectra of the first two states of **R9**·2PF_6 *versus* the monovalent rotaxane **R4**·PF_6, an attractive mixed-valence and π-dimer interaction could be identified. These interactions are only possible for a face-centred arrangement of both exTTF units. Hence, we concluded a *syn* co-conformation also for these two states. The electrochemical data and digital simulations of the CV data for the fully oxidised state showed strong repulsive forces. We presume that the two $exTTF^{2+}$ units arrange at the highest distance between each other in an *anti* co-conformation. Consequently, the macrocycles undergo a 180° rotation with respect to each other. These thermodynamically stable co-confirmation for each switching state were supported by DFT calculations.

3.3.4 Self-sorting to construct hetero[3]rotaxanes

The results discussed in this subchapter are part of one publication.[244]

We intended to study the interactions of two different functional units in one rotaxane as well. Yet, with a symmetrical axle as **A7**·2PF_6 and two different crown ethers only inseparable mixtures of rotaxanes are expected. Therefore, we employed an integrative self-sorting approach to obtain hetero[3]rotaxanes.

Based on the thermodynamic binding data described in Section 3.2.1, we designed the divalent axle **A8**·2$BArF_{24}$ in analogy to a previously described integrative self-sorting system (Figure 3.9a).[158] The smaller crown-7 ethers cannot thread over the phenyl spacer. Therefore, they only bind at the alkylammonium binding station.

By mounting one functional unit on the crown-7 ether (here NDI) and one functional unit on the crown-8 ether (here TTF and NDI), these functional units can be combined in assembly (Figure 3.9a). From equimolar solutions containing the axle **A8**·2$BArF_{24}$, one crown-8 and one crown-7 ether, we obtained mixtures of different pseudorotaxens for all six macrocycle combinations (Figure 3.9a). The self-sorting equilibrium is schemed in Figure 3.9b for two generic crown ethers **C8** (pink) and **C7** (blue), showing the resulting pseudorotaxane species and including the two dead-end structures **PRC7** and **PRC8C8**. Through ^{1}H NMR correlation spectroscopy (COSY) we identified the signals for the desired hetero[3]pseudorotaxanes and calculated the amount of the hetero[3]pseudorotaxanes in the mixtures to be 56 – 74%, with the ones containing **NDIC7** showing a higher amount (Table 3.2).

The dominance of the smaller **C7** on the hetero[3]pseudorotaxane properties was also observed for the timeframe after the thermodynamic equilibrium was reached, as revealed by time dependant ESI-HRMS (Table 3.2): While for **NDIC7** containing mixtures the equilibrium was reached in hours, for **BC7** it took days instead. We identified the error-correction of **PRBC7** to be the reason for the differences in the equilibration timeframe. The high binding

constant of **BC7** to *sec*-ammonium $BArF_{24}^-$ salts caused a higher kinetic barrier for the dethreading of **BC7** as in previous examples.[102]

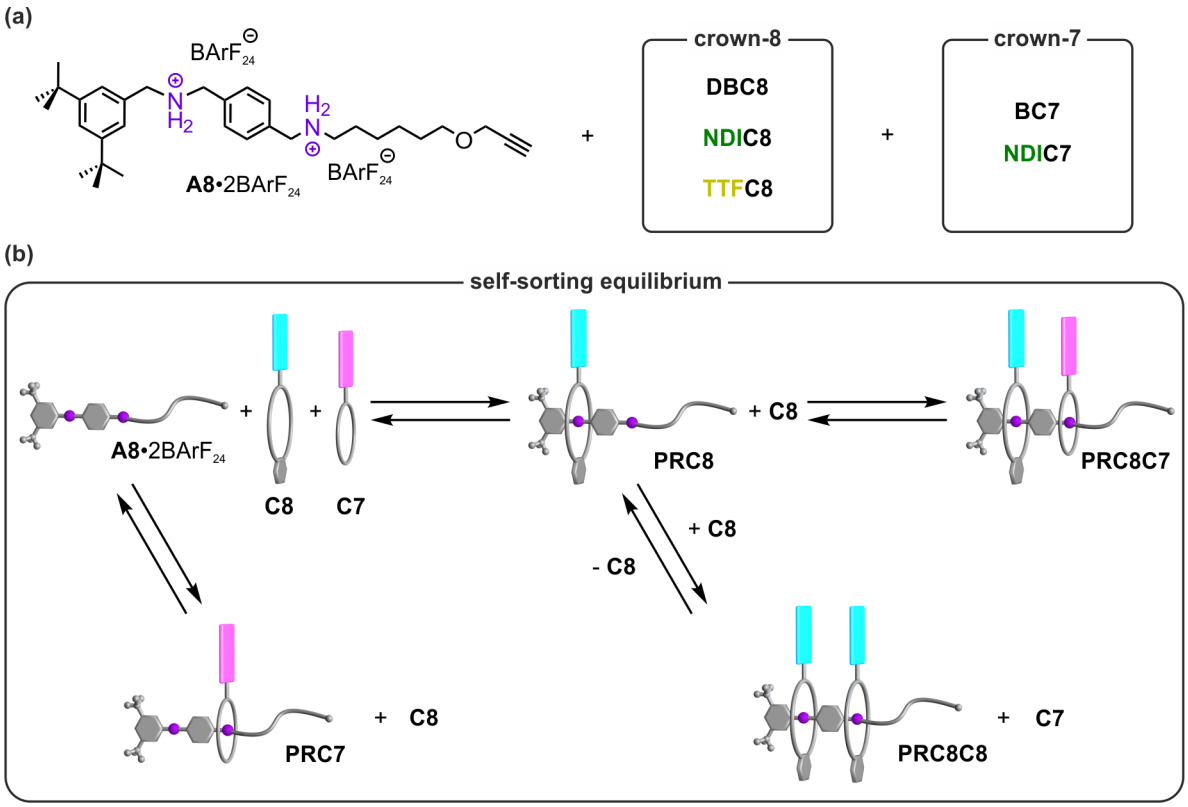

Figure 3.9. (a) Structure of the divalent axle and the crown ethers used for integrative self-sorting. (b) Schematic representation of the self-sorting equilibrium for two generic crown ethers. Details in Section 6.8.

The **BC7** containing hetero[3]pseudorotaxanes showed remarkable high gas-phase stabilities for a pseudorotaxane, as emphasised by the E_{50} value of isolated **PRC8BC7**$^{2+}$ ions (Table 3.2). CID fragmentations also occurred not by the dissociation of **BC7**, but by the breaking of a covalent bond on the axle (Section 6.8).

Table 3.2. Characterisation parameters for the self-sorting equilibrium of six macrocycle combinations with axle **A8**·2$BArF_{24}$ in equimolar solutions (Details in Section 6.8).

Macrocycle combination	DBC8 BC7	TTFC8 BC7	NDIC8 BC7	DBC8 NDIC7	TTFC8 NDIC7	NDIC8 NDIC7
Hetero[3]pseudorotaxane amount[a]	58%	56%	57%	72%	70%	74%
Threading timeframe[b]	Days	Days	Days	Hours	Hours	Hours
E_{50}	21.7 V	24.7 V	27.1 V	9.4 V	10.9 V	11.4 V

[a]Calculated from signal integration in ^{1}H NMR spectra (CD_2Cl_2, 298 K, 16 d). [b]Qualitative estimation from time dependent ESI-MS, when 90% of the maximum heteropseudo[3]rotaxane concentration is reached.

Remarkably, the **PRTTFC8BC7** pseudorotaxane could be isolated by column chromatography. In comparison, the **NDIC7** containing heteropseudo[3]rotaxanes were significantly less stable, but the benefit of faster threading kinetics for a self-sorting process

can be highlighted by the observation of a higher selectivity for the **NDIC7** containing heteropseudo[3]rotaxanes (Table 3.2). Overall, the conditions used in these studies were shown to be robust and facilitate the formation of heteropseudo[3]rotaxanes for all combinations.

We successfully synthesised four hetero[3]rotaxanes from these heteropseudo[3]rotaxanes by 1,3-dipolar cycloaddition (Figure 3.10), and their interlocked structures and sequence of macrocycles were confirmed by 2D NMR spectroscopy and tandem MS.

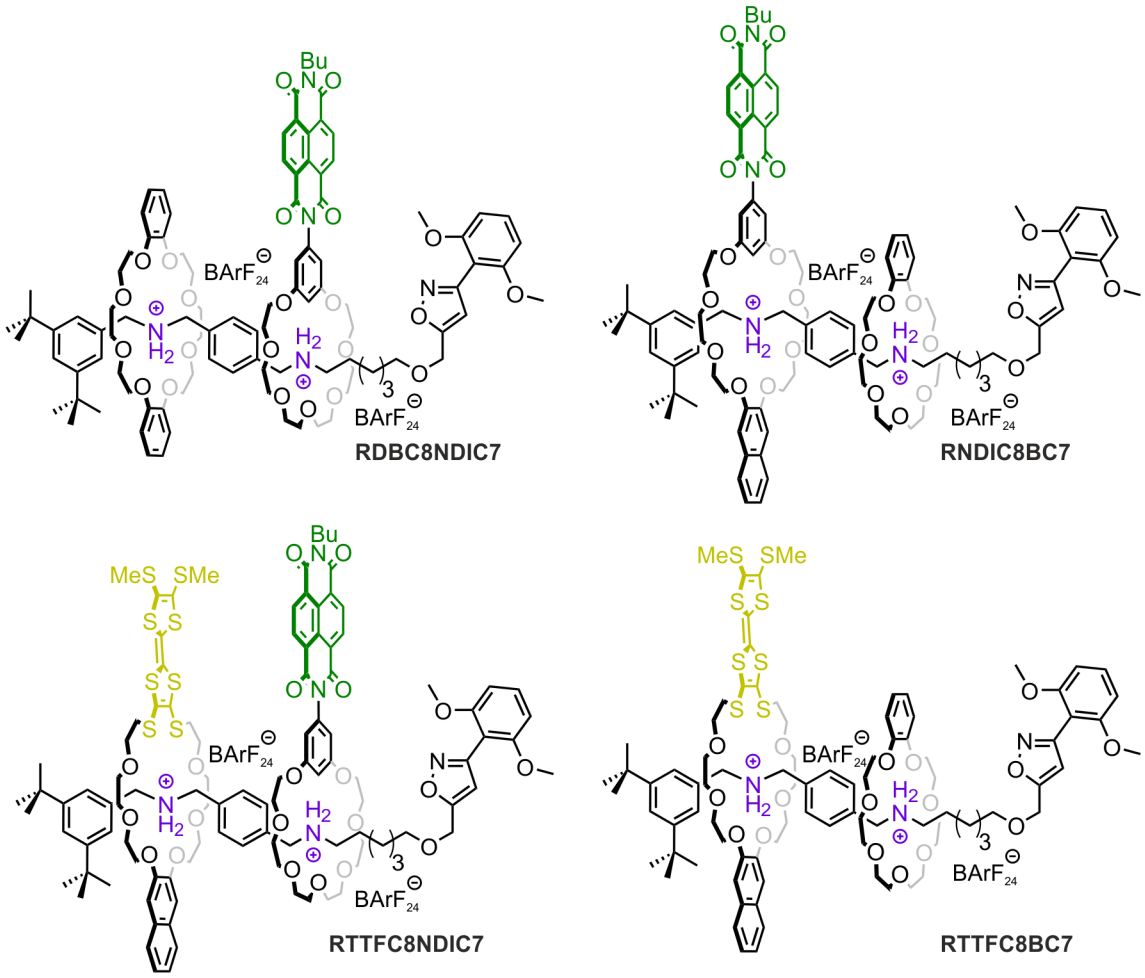

Figure 3.10. Structures of the hetero[3]rotaxanes synthesised with the integrative self-sorting approach. Details in Section 6.8.

The redox-switching of these rotaxanes was studied by CV and DPV, and compared to the free macrocycles and the **PRTTFC8BC7** pseudorotaxane (Figure 3.11). The oxidation processes at positive potentials can be attributed to the TTF, whilst the ones at negative potentials to NDI. In the donor-acceptor rotaxane **RTTFC8NDIC7**, five stable redox states were observed, without any indication for an interaction of the TTF and NDI units being found. Interestingly, the oxidation potentials of the pseudorotaxane **PRTTFC8BC7** were very similar to the ones of the two rotaxanes **RTTFC8NDIC7** and **RTTFC8BC7**. This emphasises that **PRTTFC8BC7** shows similar properties to a mechanically interlocked compound where the **BC7** acts as a 'stopper' for the **TTFC8** macrocycle.

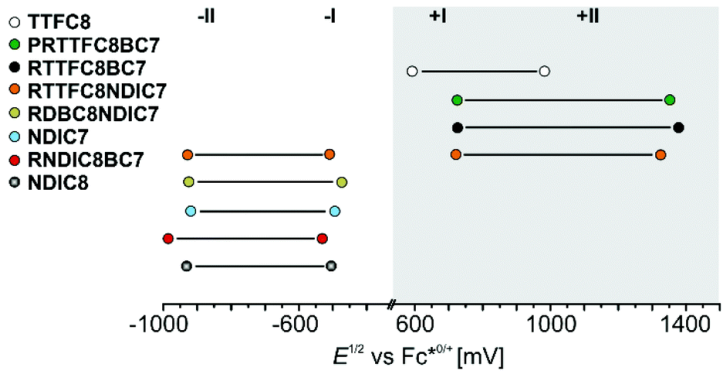

Figure 3.11. Correlation diagram of half wave potentials for hetero[3](pseudo)rotaxanes and free macrocycles determined by DPV in DCE with *n*-Bu_4NBArF_{24} as electrolyte. Referenced against $FeCp_2^{*0/+}$. Details in Section 6.8. Reprinted from Gaedke *et al.*[244] with permission from the Chinese Chemical Society (CCS), Shanghai Institute of Organic Chemistry (SIOC), and the Royal Society of Chemistry (published under the CC BY-NC 3.0 licence).

The reduction potentials of the NDI were shifted in **RNDIC8BC7** compared to the free macrocycles and to the other NDI containing rotaxanes **RDBC8NDIC7** and **RTTFC8NDIC7**. We attribute this difference to interactions of the NDI unit with one of the stoppers, which are only possible when the NDI is mounted on the left crown-8 ether as in **RNDIC8BC7**. Indeed, DFT calculations yielded a minimum structure for **RNDIC8BC7**, where the NDI is stacking with the dimethoxybenzene stopper. Consequently, the sequence of the functional units of the macrocycles on a directional axle can have an impact on their properties. Overall, for these four rotaxanes no mechanical motion could be identified and they can be considered as electrochromic switches.

3.3.5 Divalent pentastable donor-acceptor [2]rotaxane

The results discussed in this subchapter are part of one publication.[253]

While in the previous subchapter the donor TTF and acceptor NDI units in **RTTFC8NDIC7** possessed a high conformational flexibility, we aimed to fix the TTF and the NDI in a face-centred arrangement in a MIM by multivalent binding. Therefore, we synthesised an NDI-containing divalent axle **A9**·2$BArF_{24}$ and the divalent TTF crown ether **TTFdiC8** (Figure 3.12 and Section 6.1). We again used $BArF_{24}^-$ as the counter ion to facilitate a strongly bound complex.

NMR spectroscopy and MS confirmed a doubly threaded complex of **A9**·2$BArF_{24}$@**TTFdiC8**. The binding constant $K_a = (309 \pm 30)\ 10^3\ M^{-1}$ for **A9**·2$BArF_{24}$@**TTFdiC8** in 1,1,2,2-tetrachloroethane/CH_3CN (50:1) was determined through ITC. A DMC analysis with ITC data for monovalent mutations of the axle and the macrocycle allowed us to determine a strong chelate cooperativity, with $\beta = 61$ and $\beta' = 7$ for **A9**·2$BArF_{24}$@**TTFdiC8**. These data indicated attractive spacer-spacer interactions between TTF and NDI. The appearance of an intramolecular charge transfer (ICT) band in the UV/Vis absorption spectrum confirmed a donor-acceptor interaction of NDI and TTF. This ICT band disappeared after the addition of

sodium ions, which compete for binding inside the crown ether's cavity, further leading to the disassembly of **A9**·2BArF$_{24}$@**TTFdiC8.**

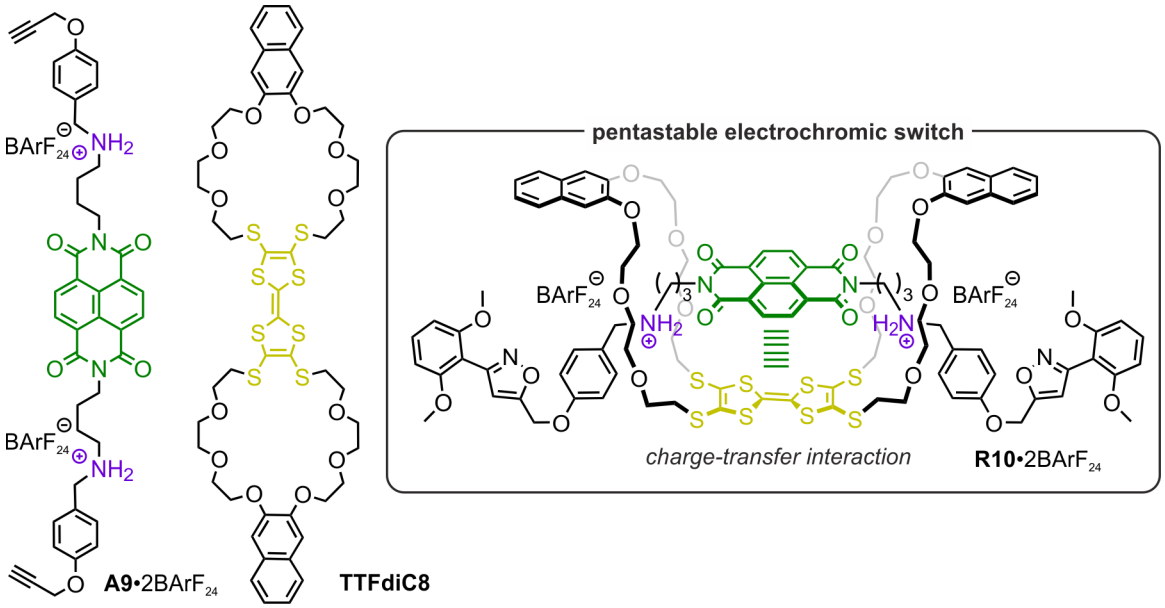

Figure 3.12. Structures of the divalent axle, macrocycle, and divalent rotaxane. Green lines indicate the attractive charge-transfer interactions. Details in Section 6.1.

The divalent [2]rotaxane **R10**·2BArF$_{24}$ was obtained from the pseudorotaxane by 1,3-dipolar cycloaddition with an *N*-oxide stopper (Figure 3.12). **R10**·2BArF$_{24}$ exhibited five stable redox states. The oxidation potentials of the TTF unit were shifted to higher potentials compared to the free macrocycle **TTFdiC8** influenced mainly by the Coulomb repulsion to the *sec*-ammonium ion. Also, the second reduction of the NDI was shifted to more negative potentials, which can be explained by the attractive interaction between donor TTF and acceptor NDI, which must be overcome by reduction. By combining the electrochemical measurements with DFT calculations of the involved frontier orbitals, the electronic communication of the NDI in the axle and the TTF in the macrocycle was studied. A HOMO-LUMO gap of 1.07 eV was obtained from the CV and corroborated with theoretical and optical HOMO-LUMO gaps of 1.34 eV and 1.24 eV, respectively. A comparably small HOMO-LUMO gap in donor-acceptor complexes is desired for optoelectronic applications.[254,255] Overall, this project emphasised the advantage of a multivalent binding approach that allows a higher positional control of the functional units due to less conformational flexibility.

4 Conclusion and Outlook

The redox-switchable units TTF, exTTF and NDI were incorporated into crown ethers and their thermodynamic binding properties with *sec*-ammonium axles were thoroughly investigated through ITC. The effects of the counterion, and of structural changes in the macrocycle and in the axle on the binding properties were identified. Additionally, a new flexible organic cage was developed, and its high affinities for cations were investigated. Based on this toolbox of molecular components different functions of molecular switches were engineered, and their operation was studied (Figure 4.1).

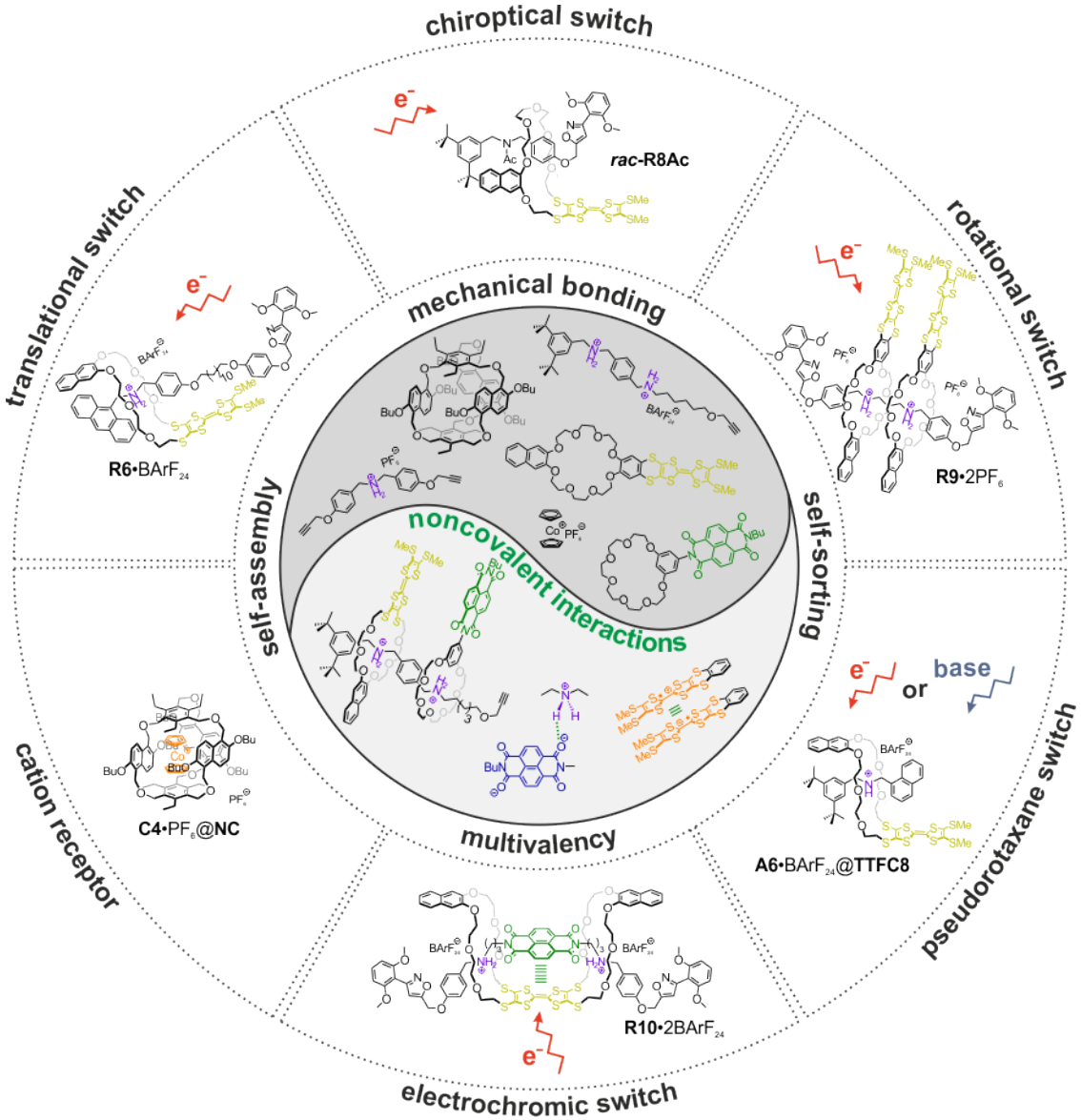

Figure 4.1. Schematic overview on some molecular switches which were studied in this thesis based on the noncovalent interactions between their components. Different functions of the molecular switches were achieved.

In this thesis, not only the free binding energy $\triangle G^0$, but also the binding enthalpy $\triangle H^0$ and entropy $\triangle S^0$ were studied for all complexes. The differentiation of enthalpic and entropic contributions to the binding events provided interesting insights: for example, the significantly high binding constants ($K_a > 10^9$ M^{-1}) of the organic cage **NC** were revealed to be mainly enthalpy driven, but the binding was revealed to be favoured entropically, as well. Studies with non-charged electron-poor guests, such as hexafluorobenzene or trifluoromethylbenzene, might offer insights if cation-π interactions are necessary to facilitate the complex formation.

Additionally, the stronger binding of *sec*-ammonium $BArF_{24}$ salts to crown ethers compared to *sec*-ammonium PF_6 salts is an entropic effect. This effect would be interesting to further investigate whether a trend can be observed in the binding of crown ethers to other *sec*-ammonium axles paired with other counterions such as hexafluoroborate, tosylate, trifluoroacetate, or aluminates.[256]

The results of this thesis emphasised also the necessity to combine many different analytical techniques and theoretical calculations to reveal the properties of the constructed molecular switches. By the combination of ^{1}H NMR spectroscopy, ITC, and tandem MS, we were able to evidence the formation of a non-threaded complex of *sec*-ammonium axle **A6**·$BArF_{24}$ and **TTFC8**. This possibly side-on bound structure has already been anticipated before, but not experimentally elucidated.[124]

Among the different crown ethers studied in this thesis, **TTFC8** showed certainly the most versatility, as it combined good binding properties with an interesting redox-switching behaviour. Its pseudorotaxane switch **A6**·$BArF_{24}$@**TTFC8** allowed us to reveal the differences in the disassembly kinetics triggered by either oxidation or the addition of a base. **A6**·$BArF_{24}$@**TTFC8** also represents a size-complementary rotaxane, which exhibits properties of a rotaxane and a pseudorotaxane at the same time.

From comparing the three monovalent rotaxanes incorporating TTF **R6**·$BArF_{24}$, **R7**·$BArF_{24}$ and ***rac*-R8Ac**, it became apparent that minor structural changes lead to significantly different outcomes upon redox-switching: while in **R6**·$BArF_{24}$ a translational motion was triggered, in **R7**·$BArF_{24}$ the macrocycle resided at the same position due to a higher kinetic barrier. However, the deprotonation of **R7**·$BArF_{24}$ could still trigger a translational motion. In the planar chiral rotaxane ***rac*-R8Ac**, the oxidation triggered a sign inversion in the ECD spectrum. This chiroptical property is quite unique among rotaxanes.

The strong binding of the **exTTFC8** macrocycle allowed us to construct the homo[3]rotaxane **R9**·$2PF_6$. The orientation of the two **exTTFC8** macrocycles with respect to each other in the four redox states was particularly difficult to elucidate. Only by a combination of ITC, ^{1}H NMR spectroscopy, CV, IMS, UV/Vis-NIR absorption spectroscopy, EPR spectroscopy, and theoretical calculations, the mixed-valence, and π-dimer interactions in the second and third

redox state could be identified, which evidence the *syn* co-conformation of both wheels. Oxidation of the two exTTF units to their dication was revealed to cause a 180° rotation of the two **exTTFC8**$^{2+}$ wheels with respect to each other to yield the *anti* co-conformation due to Coulomb repulsion. The interactions between both macrocycles are crucial to obtain this rotational switching.

The electronic communication between two different functional units TTF and NDI was achieved by applying a divalent approach fixing the two units in a face-centred arrangement in the divalent [2]rotaxane **R10**·2BArF$_{24}$. This divalent approach could be applied to different functional units, *i.e.*, in the crown ether an exTTF unit and in the axle a perylene diimide unit could be incorporated, and their interaction in a donor-acceptor complex could be studied.

Another method to combine the two functional units TTF and NDI was achieved in hetero[3](pseudo)rotaxanes. Here, a robust method for the assembly of differently functionalised crown ethers on a divalent axle was developed on the examples of **DBC8**, **TTFC8**, **NDIC8**, **NDIC7**, and **BC7**, based on integrative self-sorting. However, the drawback of high binding constants in a self-sorting process was observed. Due to the use of BArF$_{24}^-$ counterions, which were needed to allow pseudorotaxane formation with the weakly binding **NDIC7**, the binding constant of the **BC7** macrocycle was so high that error-correction was very slow. This resulted in a low selectivity for the desired hetero[3]pseudorotaxane and an impractical long equilibration time of two weeks. The switching properties of the obtained hetero[3]rotaxanes did not yield emerging properties of the assembly and exhibited similar optoelectronic properties to the individual functional units. It became clear, that the strength of this approach lies in the control over the sequence of the functional units on the axle and not in the interactions between the two. This could be exploited by the incorporation of 'non-passive' stoppers. For example, a stopper carrying a redox-switchable or light-switchable unit might pave the way to emerging functions of hetero[3]rotaxanes.

Generally, the herein developed redox-switchable MIMs based on TTF, and NDI crown ethers represent a versatile platform to develop new switching functions. Two different types of mechanical switches performing a translational, or a 180° rotational motion were constructed. Additionally, electrochromic and chiroptical properties of molecular switches were achieved from similar building blocks. These redox-switchable crown ether/*sec*-ammonium rotaxanes offer an alternative to the already existing redox-switchable MIMs that are mainly based on the 'bluebox' macrocycle.[44,178] For example, the possibility to have attractive interactions between two macrocycles, and the construction of planar chiral rotaxanes are not easily achievable with the 'bluebox' system.

A major progressing step towards molecular machines for the herein presented molecular redox-switches would certainly be mounting them on a surface or attaching them to an

interface to obtain coupled motions and possibly generate a macroscopic output. Preliminary studies showed the successful deposition of a terpyridine stoppered **TTFC8** containing rotaxane on a self-assembled monolayer on gold surfaces.

Another method to mount the molecular switches in an ordered manner would be incorporating them in metal-organic frameworks (MOFs). However, MOFs contain rigid and rather short organic ligands.[257] Therefore, translational motions might not be possible, as we observed that a certain linker length is needed to allow a translational motion of the wheel along the axle. Instead, a rotational switching, as observed in **R9**·2PF_6, might be a desired switching function in the organic ligand of a MOF.

5 Literature

[1] "device", in *Cambridge Dictionary Web Version*, Cambridge University Press 2021, 11.08.2021.

[2] R. P. Feynman, *Eng. Sci.* **1960**, *23*, 22-36.

[3] E. R. Kay, D. A. Leigh, *Angew. Chem. Int. Ed.* **2015**, *54*, 10080-10088.

[4] V. Balzani, A. Credi, M. Venturi, *Molecular Devices and Machines: Concepts and Perspectives for the Nanoworld*, 2 ed., Wiley-VCH, Weinheim, **2008**.

[5] D. Castelvecchi, *Nature* **2017**, *544*, 278-279.

[6] G. Rapenne, C. Joachim, *Nat. Rev. Mat.* **2017**, *2*, 17040.

[7] G. J. Simpson, V. Garcia-Lopez, P. Petermeier, L. Grill, J. M. Tour, *Nat. Nanotechnol.* **2017**, *12*, 604-606.

[8] V. Balzani, A. Credi, M. Venturi, *Nano Today* **2007**, *2*, 18-25.

[9] A. Perrot, E. Moulin, N. Giuseppone, *Trends in Chemistry* **2021**, *3*, 926-942.

[10] J. D. Harris, M. J. Moran, I. Aprahamian, *Proc. Natl. Acad. Sci. U. S. A.* **2018**, *115*, 9414-9422.

[11] C. C. Warford, V. Lemieux, N. R. Branda, *Molecular Switches*, Wiley-VCH, Weinheim, **2011**.

[12] S. Kassem, T. van Leeuwen, A. S. Lubbe, M. R. Wilson, B. L. Feringa, D. A. Leigh, *Chem. Soc. Rev.* **2017**, *46*, 2592-2621.

[13] X. Yin, Y. Zang, L. Zhu, J. Z. Low, Z. F. Liu, J. Cui, J. B. Neaton, L. Venkataraman, L. M. Campos, *Sci. Adv.* **2017**, *3*, eaao2615.

[14] Y. Chen, L. Huang, H. Chen, Z. Chen, H. Zhang, Z. Xiao, W. Hong, *Chin. J. Chem.* **2021**, *39*, 421-439.

[15] C. J. Bruns, J. F. Stoddart, *Acc. Chem. Res.* **2014**, *47*, 2186-2199.

[16] D. W. Steuerman, H. R. Tseng, A. J. Peters, A. H. Flood, J. O. Jeppesen, K. A. Nielsen, J. F. Stoddart, J. R. Heath, *Angew. Chem. Int. Ed.* **2004**, *43*, 6486-6491.

[17] S. Saha, J. F. Stoddart, *Chem. Soc. Rev.* **2007**, *36*, 77-92.

[18] S. Erbas-Cakmak, D. A. Leigh, C. T. McTernan, A. L. Nussbaumer, *Chem. Rev.* **2015**, *115*, 10081-10206.

[19] D. Dattler, G. Fuks, J. Heiser, E. Moulin, A. Perrot, X. Yao, N. Giuseppone, *Chem. Rev.* **2020**, *120*, 310-433.

[20] S. Shinkai, T. Nakaji, T. Ogawa, K. Shigematsu, O. Manabe, *J. Am. Chem. Soc.* **1981**, *103*, 111-115.

[21] E. R. Kay, D. A. Leigh, F. Zerbetto, *Angew. Chem. Int. Ed.* **2007**, *46*, 72-191.

[22] B. L. Feringa, *Angew. Chem. Int. Ed.* **2017**, *56*, 11060-11078.

[23] J. P. Sauvage, *Angew. Chem. Int. Ed.* **2017**, *56*, 11080-11093.

[24] J. F. Stoddart, *Angew. Chem. Int. Ed.* **2017**, *56*, 11094-11125.

[25] M. Baroncini, L. Casimiro, C. de Vet, J. Groppi, S. Silvi, A. Credi, *ChemistryOpen* **2018**, *7*, 169-179.

[26] I. Aprahamian, *ACS Cent. Sci.* **2020**, *6*, 347-358.

[27] M. A. Watson, S. L. Cockroft, *Chem. Soc. Rev.* **2016**, *45*, 6118-6129.
[28] O. Fitzmaurice, M. Bartkowski, S. Giordani, *Front. Chem.* **2022**, *10*, Article 859450.
[29] W. Szymanski, J. M. Beierle, H. A. Kistemaker, W. A. Velema, B. L. Feringa, *Chem. Rev.* **2013**, *113*, 6114-6178.
[30] W. A. Velema, W. Szymanski, B. L. Feringa, *J. Am. Chem. Soc.* **2014**, *136*, 2178-2191.
[31] J. Broichhagen, J. A. Frank, D. Trauner, *Acc. Chem. Res.* **2015**, *48*, 1947-1960.
[32] T. Takata, *Bull. Chem. Soc. Jpn.* **2019**, *92*, 409-426.
[33] H. Song, M. A. Reed, T. Lee, *Adv. Mater.* **2011**, *23*, 1583-1608.
[34] H. Chen, J. Fraser Stoddart, *Nat. Rev. Mater.* **2021**, *6*, 804-828.
[35] R. Gupta, P. Jash, P. Sachan, A. Bayat, V. Singh, P. C. Mondal, *Angew. Chem. Int. Ed.* **2021**.
[36] A. W. Heard, J. M. Suárez, S. M. Goldup, *Nat. Rev. Chem.* **2022**, *6*, 182-196.
[37] J. Andreasson, U. Pischel, *Chem. Soc. Rev.* **2015**, *44*, 1053-1069.
[38] S. Erbas-Cakmak, S. Kolemen, A. C. Sedgwick, T. Gunnlaugsson, T. D. James, J. Yoon, E. U. Akkaya, *Chem. Soc. Rev.* **2018**, *47*, 2228-2248.
[39] G. M. Whitesides, B. Grzybowski, *Science* **2002**, *295*, 2418-2421.
[40] P. R. Ashton, V. Balzani, J. Becher, A. Credi, M. C. T. Fyfe, G. Mattersteig, S. Menzer, M. B. Nielsen, F. M. Raymo, J. F. Stoddart, M. Venturi, D. J. Williams, *J. Am. Chem. Soc.* **1999**, *121*, 3951-3957.
[41] H. V. Schröder, C. A. Schalley, *Beilstein J. Org. Chem.* **2018**, *14*, 2163-2185.
[42] A. Altieri, F. G. Gatti, E. R. Kay, D. A. Leigh, D. Martel, F. Paolucci, A. M. Slawin, J. K. Wong, *J. Am. Chem. Soc.* **2003**, *125*, 8644-8654.
[43] C. J. Bruns, J. F. Stoddart, *The Nature of the Mechanical Bond: From Molecules to Machines*, Wiley, Hoboken, **2017**.
[44] H. V. Schröder, C. A. Schalley, *Chem. Sci.* **2019**, *10*, 9626-9639.
[45] J.-M. Lehn, *Angew. Chem. Int. Ed. Engl.* **1988**, *27*, 89-112.
[46] J.-M. Lehn, *Acc. Chem. Res.* **1978**, *11*, 49-57.
[47] C. J. Pedersen, *Angew. Chem. Int. Ed. Engl.* **1988**, *27*, 1021-1027.
[48] D. J. Cram, *Angew. Chem. Int. Ed. Engl.* **1988**, *27*, 1009-1020.
[49] J. E. Huheey, E. A. Keiter, R. L. Keiter, *Inorganic chemistry: principles of structure and reactivity*, 4. ed., New York, NY, HarperCollins College Publishers, **1993**.
[50] J. Chen, Q. Peng, X. Peng, H. Zhang, H. Zeng, *Chem. Rev.* **2022**, *122*, 14594-14678.
[51] F. Biedermann, H. J. Schneider, *Chem. Rev.* **2016**, *116*, 5216-52300.
[52] C. A. Schalley, *Analytical Methods in Supramolecular Chemistry*, 2. ed., Wiley-VCH, Weinheim, **2012**.
[53] J. W. Steed, J. L. Atwood, *Supramolecular Chemistry*, 2. ed., Wiley-VCH, Weinheim, **2009**.
[54] T. M. Beale, M. G. Chudzinski, M. G. Sarwar, M. S. Taylor, *Chem. Soc. Rev.* **2013**, *42*, 1667-1680.
[55] H. J. Schneider, *J. Phys. Org. Chem.* **2022**, *35*, e4340.
[56] Y. E. Alexeev, B. I. Kharisov, T. C. H. García, A. D. Garnovskii, *Coord. Chem Rev.* **2010**, *254*, 794-831.
[57] S. Datta, M. L. Saha, P. J. Stang, *Acc. Chem. Res.* **2018**, *51*, 2047-2063.

[58] M. Meot-Ner, *Chem. Rev.* **2005**, *105*, 213-284.
[59] C. R. Martinez, B. L. Iverson, *Chem. Sci.* **2012**, *3*, 2191-2201.
[60] C. A. Hunter, J. K. M. Sanders, *J. Am. Chem. Soc.* **1990**, *112*, 5525-5534.
[61] J. M. Spruell, *Pure Appl. Chem.* **2010**, *82*, 2281-2294.
[62] M. Giese, M. Albrecht, K. Rissanen, *Chem. Rev.* **2015**, *115*, 8867-8895.
[63] D. Quiñonero, C. Garau, C. Rotger, A. Frontera, P. Ballester, A. Costa, P. M. Deyà, *Angew. Chem. Int. Ed.* **2002**, *41*, 3389-3392.
[64] A. Das, S. Ghosh, *Angew. Chem. Int. Ed.* **2014**, *53*, 2038-2054.
[65] S. V. Rosokha, J. K. Kochi, *J. Am. Chem. Soc.* **2007**, *129*, 828-838.
[66] F. Biedermann, W. M. Nau, H. J. Schneider, *Angew. Chem. Int. Ed.* **2014**, *53*, 11158-11171.
[67] E. Persch, O. Dumele, F. Diederich, *Angew. Chem. Int. Ed.* **2015**, *54*, 3290-3327.
[68] D. J. Cram, *Angew. Chem. Int. Ed. Engl.* **1986**, *25*, 1039-1057.
[69] S. K. Chang, A. D. Hamilton, *J. Am. Chem. Soc.* **1988**, *110*, 1318-1319.
[70] J. M. McGrath, M. D. Pluth, *J. Org. Chem.* **2014**, *79*, 711-719.
[71] L. Kaufmann, E. V. Dzyuba, F. Malberg, N. L. Low, M. Groschke, B. Brusilowskij, J. Huuskonen, K. Rissanen, B. Kirchner, C. A. Schalley, *Org. Biomol. Chem.* **2012**, *10*, 5954-5964.
[72] E. Masson, X. Ling, R. Joseph, L. Kyeremeh-Mensah, X. Lu, *RSC Adv.* **2012**, *2*, 1213-1247.
[73] S. J. Barrow, S. Kasera, M. J. Rowland, J. Del Barrio, O. A. Scherman, *Chem. Rev.* **2015**, *115*, 12320-12406.
[74] Z. Lin, J. Sun, B. Efremovska, R. Warmuth, *Chem. Eur. J.* **2012**, *18*, 12864-12872.
[75] A. J. McConnell, *Chem. Soc. Rev.* **2022**, *51*, 2957-2971.
[76] E. Benchimol, B. T. Nguyen, T. K. Ronson, J. R. Nitschke, *Chem. Soc. Rev.* **2022**, *51*, 5101-5135.
[77] H. Takezawa, M. Fujita, *Bull. Chem. Soc. Jpn.* **2021**, *94*, 2351-2369.
[78] G. Zhang, M. Mastalerz, *Chem. Soc. Rev.* **2014**, *43*, 1934-1947.
[79] G. Monta-Gonzalez, F. Sancenon, R. Martinez-Manez, V. Marti-Centelles, *Chem. Rev.* **2022**, *122*, 13636-13708.
[80] F. Biedermann, V. D. Uzunova, O. A. Scherman, W. M. Nau, A. De Simone, *J. Am. Chem. Soc.* **2012**, *134*, 15318-15323.
[81] A. J. Metherell, W. Cullen, N. H. Williams, M. D. Ward, *Chem. Eur. J.* **2018**, *24*, 1554-1560.
[82] C. J. Pedersen, *J. Am. Chem. Soc.* **1967**, *89*, 2495-2496.
[83] C. J. Pedersen, *J. Am. Chem. Soc.* **1967**, *89*, 7017-7036.
[84] R. M. Izatt, K. Pawlak, J. S. Bradshaw, R. L. Bruening, *Chem. Rev.* **1995**, *95*, 2529-2586.
[85] P. R. Ashton, P. J. Campbell, P. T. Glink, D. Philp, N. Spencer, J. F. Stoddart, E. J. T. Chrystal, S. Menzer, D. J. Williams, P. A. Tasker, *Angew. Chem. Int. Ed. Engl.* **1995**, *34*, 1865-1869.
[86] J. A. A. De Boer, D. N. Reinhoudt, *J. Am. Chem. Soc.* **1985**, *107*, 5347-5351.

[87] P. R. Ashton, E. J. T. Chrystal, P. T. Glink, S. Menzer, C. Schiavo, N. Spencer, J. F. Stoddart, P. A. Tasker, A. J. P. White, D. J. Williams, *Chem. Eur. J.* **1996**, *2*, 709-728.
[88] C. Zhang, S. Li, J. Zhang, K. Zhu, N. Li, F. Huang, *Org. Lett.* **2007**, *9*, 5553-5556.
[89] F. Huang, J. W. Jones, C. Slebodnick, H. W. Gibson, *J. Am. Chem. Soc.* **2003**, *125*, 14458-14464.
[90] T. Clifford, A. Abushamleh, D. H. Busch, *Proc. Natl. Acad. Sci. U. S. A.* **2002**, *99*, 4830-4836.
[91] P. R. Ashton, R. Ballardini, V. Balzani, M. Gómez-López, S. E. Lawrence, M. V. Martínez-Díaz, M. Montalti, A. Piersanti, L. Prodi, J. F. Stoddart, D. J. Williams, *J. Am. Chem. Soc.* **1997**, *119*, 10641-10651.
[92] F. Nicoli, M. Baroncini, S. Silvi, J. Groppi, A. Credi, *Org. Chem. Front.* **2021**, *8*, 5531-5549.
[93] S. J. Cantrill, D. A. Fulton, A. M. Heiss, A. R. Pease, J. F. Stoddart, A. J. P. White, D. J. Williams, *Chem. Eur. J.* **2000**, *6*, 2274-2287.
[94] H. Nagai, Y. Suzaki, K. Osakada, *Eur. J. Inorg. Chem.* **2014**, *2014*, 4376-4384.
[95] J. W. Jones, H. W. Gibson, *J. Am. Chem. Soc.* **2003**, *125*, 7001-7004.
[96] H. W. Gibson, J. W. Jones, L. N. Zakharov, A. L. Rheingold, C. Slebodnick, *Chem. Eur. J.* **2011**, *17*, 3192-3206.
[97] D. Philp, J. F. Stoddart, *Angew. Chem. Int. Ed. Engl.* **1996**, *35*, 1154-1196.
[98] J. D. Halley, D. A. Winkler, *Complexity* **2008**, *14*, 10-17.
[99] C. Cheng, P. R. McGonigal, J. F. Stoddart, R. D. Astumian, *ACS Nano* **2015**, *9*, 8672-8688.
[100] J. M. Lehn, *Proc. Natl. Acad. Sci. U. S. A.* **2002**, *99*, 4763-4768.
[101] M. M. Safont-Sempere, G. Fernandez, F. Wurthner, *Chem. Rev.* **2011**, *111*, 5784-5814.
[102] Z. He, W. Jiang, C. A. Schalley, *Chem. Soc. Rev.* **2015**, *44*, 779-789.
[103] M. L. Saha, M. Schmittel, *Org. Biomol. Chem.* **2012**, *10*, 4651-4684.
[104] O. Miljanić, K. Osowska, *Synlett* **2011**, *2011*, 1643-1648.
[105] P. Mukhopadhyay, P. Y. Zavalij, L. Isaacs, *J. Am. Chem. Soc.* **2006**, *128*, 14093-14102.
[106] G. von Kiedrowski, S. Otto, P. Herdewijn, *J. Syst. Chem.* **2010**, *1*, 1-6.
[107] E. Mattia, S. Otto, *Nat. Nanotechnol.* **2015**, *10*, 111-119.
[108] C. Fasting, C. A. Schalley, M. Weber, O. Seitz, S. Hecht, B. Koksch, J. Dernedde, C. Graf, E. W. Knapp, R. Haag, *Angew. Chem. Int. Ed.* **2012**, *51*, 10472-10498.
[109] M. Mammen, S.-K. Choi, G. M. Whitesides, *Angew. Chem. Int. Ed.* **1998**, *37*, 2754-2794.
[110] J. D. Badjic, A. Nelson, S. J. Cantrill, W. B. Turnbull, J. F. Stoddart, *Acc. Chem. Res.* **2005**, *38*, 723-732.
[111] H. J. Hogben, J. K. Sprafke, M. Hoffmann, M. Pawlicki, H. L. Anderson, *J. Am. Chem. Soc.* **2011**, *133*, 20962-20699.
[112] C. A. Hunter, H. L. Anderson, *Angew. Chem. Int. Ed.* **2009**, *48*, 7488-7499.
[113] L. K. S. von Krbek, C. A. Schalley, P. Thordarson, *Chem. Soc. Rev.* **2017**, *46*, 2622-2637.

[114] G. Ercolani, L. Schiaffino, *Angew. Chem. Int. Ed.* **2011**, *50*, 1762-1768.
[115] L. K. von Krbek, A. J. Achazi, M. Solleder, M. Weber, B. Paulus, C. A. Schalley, *Chem. Eur. J.* **2016**, *22*, 15475-15484.
[116] W. Jiang, K. Nowosinski, N. L. Löw, E. V. Dzyuba, F. Klautzsch, A. Schäfer, J. Huuskonen, K. Rissanen, C. A. Schalley, *J. Am. Chem. Soc.* **2012**, *134*, 1860-1868.
[117] K. Nowosinski, L. K. von Krbek, N. L. Traulsen, C. A. Schalley, *Org. Lett.* **2015**, *17*, 5076-5079.
[118] L. K. von Krbek, A. J. Achazi, S. Schoder, M. Gaedke, T. Biberger, B. Paulus, C. A. Schalley, *Chem. Eur. J.* **2017**, *23*, 2877-2883.
[119] J. F. Stoddart, *Chem. Soc. Rev.* **2009**, *38*, 1802-1820.
[120] M. Xue, Y. Yang, X. Chi, X. Yan, F. Huang, *Chem. Rev.* **2015**, *115*, 7398-7501.
[121] E. A. Neal, S. M. Goldup, *Chem. Commun.* **2014**, *50*, 5128-5142.
[122] H. L. Frisch, E. Wasserman, *J. Am. Chem. Soc.* **1961**, *83*, 3789-3795.
[123] R. S. Forgan, J. P. Sauvage, J. F. Stoddart, *Chem. Rev.* **2011**, *111*, 5434-5464.
[124] P. R. Ashton, I. Baxter, M. C. T. Fyfe, F. M. Raymo, N. Spencer, J. F. Stoddart, A. J. P. White, D. J. Williams, *J. Am. Chem. Soc.* **1998**, *120*, 2297-2307.
[125] H. Sato, D. Aoki, T. Takata, *Chem. Asian J.* **2018**, *13*, 785-789.
[126] A. Affeld, Gosia M. Hübner, C. Seel, Christoph A. Schalley, *Eur. J. Org. Chem.* **2001**, *2001*.
[127] C. Heim, A. Affeld, M. Nieger, F. Vögtle, *Helv. Chim Acta* **1999**, *82*, 746-759.
[128] Y. Akae, Y. Koyama, S. Kuwata, T. Takata, *Chem. Eur. J.* **2014**, *20*, 17132-17136.
[129] K. Hirose, Y. Nakamura, Y. Tobe, *Org. Lett.* **2009**, *11*, 145-147.
[130] M. Gaedke, H. Hupatz, H. V. Schröder, S. Suhr, K. F. Hoffmann, A. Valkonen, B. Sarkar, S. Riedel, K. Rissanen, C. A. Schalley, *Org. Chem. Front.* **2021**, *8*, 3659-3667.
[131] P. R. Ashton, M. Bělohradský, D. Philp, J. F. Stoddart, *J. Chem. Soc., Chem. Commun.* **1993**, *0*, 1269-1274.
[132] M. A. Bolla, J. Tiburcio, S. J. Loeb, *Tetrahedron* **2008**, *64*, 8423-8427.
[133] J. D. Crowley, S. M. Goldup, A. L. Lee, D. A. Leigh, R. T. McBurney, *Chem. Soc. Rev.* **2009**, *38*, 1530-1541.
[134] V. Aucagne, J. Berna, J. D. Crowley, S. M. Goldup, K. D. Hanni, D. A. Leigh, P. J. Lusby, V. E. Ronaldson, A. M. Slawin, A. Viterisi, D. B. Walker, *J. Am. Chem. Soc.* **2007**, *129*, 11950-11963.
[135] D. Thibeault, J. F. Morin, *Molecules* **2010**, *15*, 3709-3730.
[136] T. Yuki, Y. Koyama, T. Matsumura, T. Takata, *Org. Lett.* **2013**, *15*, 4438-4441.
[137] F. Coutrot, E. Busseron, *Chem. Eur. J.* **2009**, *15*, 5186-5190.
[138] T. Matsumura, F. Ishiwari, Y. Koyama, T. Takata, *Org. Lett.* **2010**, *12*, 3828-3831.
[139] Y. Tachibana, H. Kawasaki, N. Kihara, T. Takata, *J. Org. Chem.* **2006**, *71*, 5093-5104.
[140] A. M. Albrecht-Gary, Z. Saad, C. O. Dietrich-Buchecker, J. P. Sauvage, *J. Am. Chem. Soc.* **1985**, *107*, 3205-3209.
[141] B. Baytekin, H. T. Baytekin, C. A. Schalley, *Org. Biomol. Chem.* **2006**, *4*, 2825-2841.
[142] G. De Bo, *Chem. Sci.* **2018**, *9*, 15-21.

[143] M. Zhang, G. De Bo, *J. Am. Chem. Soc.* **2019**, *141*, 15879-15883.
[144] H. Y. Zhou, Q. S. Zong, Y. Han, C. F. Chen, *Chem. Commun.* **2020**, *56*, 9916-9936.
[145] X. Q. Wang, W. J. Li, W. Wang, H. B. Yang, *Chem. Commun.* **2018**, *54*, 13303-13318.
[146] A. J. Avestro, D. M. Gardner, N. A. Vermeulen, E. A. Wilson, S. T. Schneebeli, A. C. Whalley, M. E. Belowich, R. Carmieli, M. R. Wasielewski, J. F. Stoddart, *Angew. Chem. Int. Ed.* **2014**, *53*, 4442-4449.
[147] D. Sluysmans, S. Hubert, C. J. Bruns, Z. Zhu, J. F. Stoddart, A.-S. Duwez, *Nat. Nanotech.* **2018**, *13*, 209-213.
[148] H. V. Schröder, F. Stein, J. M. Wollschläger, S. Sobottka, M. Gaedke, B. Sarkar, C. A. Schalley, *Angew. Chem. Int. Ed.* **2019**, *58*, 3496-3500.
[149] D. Whang, K.-M. Park, J. Heo, P. Ashton, K. Kim, *J. Am. Chem. Soc.* **1998**, *120*, 4899-4900.
[150] F. Huang, H. W. Gibson, *Prog. Polym. Sci.* **2005**, *30*, 982-1018.
[151] A. Harada, J. Li, M. Kamachi, *Nature* **1992**, *356*, 325-327.
[152] A. Harada, A. Hashidzume, H. Yamaguchi, Y. Takashima, *Chem. Rev.* **2009**, *109*, 5974-6023.
[153] A. M. Fuller, D. A. Leigh, P. J. Lusby, *J. Am. Chem. Soc.* **2010**, *132*, 4954-4959.
[154] H. Y. Au-Yeung, A. W. H. Ng, *Synlett* **2020**, *31*, 309-314.
[155] E. A. Wilson, N. A. Vermeulen, P. R. McGonigal, A. J. Avestro, A. A. Sarjeant, C. L. Stern, J. F. Stoddart, *Chem. Commun.* **2014**, *50*, 9665-9668.
[156] D. B. Amabilino, P. R. Ashton, M. Bělohradský, F. M. Raymo, J. F. Stoddart, *Chem. Commun.* **1995**, 747-750.
[157] K. Zhu, G. Baggi, S. J. Loeb, *Nat. Chem.* **2018**, *10*, 625-630.
[158] W. Jiang, H. D. Winkler, C. A. Schalley, *J. Am. Chem. Soc.* **2008**, *130*, 13852-13853.
[159] W. Jiang, A. Schafer, P. C. Mohr, C. A. Schalley, *J. Am. Chem. Soc.* **2010**, *132*, 2309-2320.
[160] W. Jiang, C. A. Schalley, *Proc. Natl. Acad. Sci. U. S. A.* **2009**, *106*, 10425-10429.
[161] X. Fu, Q. Zhang, S. J. Rao, D. H. Qu, H. Tian, *Chem. Sci.* **2016**, *7*, 1696-1701.
[162] S. J. Rao, Q. Zhang, J. Mei, X. H. Ye, C. Gao, Q. C. Wang, D. H. Qu, H. Tian, *Chem. Sci.* **2017**, *8*, 6777-6783.
[163] C. Ke, R. A. Smaldone, T. Kikuchi, H. Li, A. P. Davis, J. F. Stoddart, *Angew. Chem. Int. Ed.* **2013**, *52*, 381-387.
[164] E. A. Neal, S. M. Goldup, *Angew. Chem. Int. Ed.* **2016**, *55*, 12488-12493.
[165] L. Binks, C. Tian, S. D. P. Fielden, I. J. Vitorica-Yrezabal, D. A. Leigh, *J. Am. Chem. Soc.* **2022**.
[166] C. Cheng, P. R. McGonigal, S. T. Schneebeli, H. Li, N. A. Vermeulen, C. Ke, J. F. Stoddart, *Nat. Nanotechnol.* **2015**, *10*, 547-553.
[167] S. Amano, S. D. P. Fielden, D. A. Leigh, *Nature* **2021**, *594*, 529-534.
[168] H. M. Bandara, S. C. Burdette, *Chem. Soc. Rev.* **2012**, *41*, 1809-1825.
[169] R. Costil, M. Holzheimer, S. Crespi, N. A. Simeth, B. L. Feringa, *Chem. Rev.* **2021**, *121*, 13213-13237.
[170] R. Klajn, *Chem. Soc. Rev.* **2014**, *43*, 148-184.

[171] J. Ding, C. Zheng, L. Wang, C. Lu, B. Zhang, Y. Chen, M. Li, G. Zhai, X. Zhuang, *J. Mater. Chem. A* **2019**, *7*, 23337-23360.
[172] J. Shukla, P. Mukhopadhyay, *Eur. J. Org. Chem.* **2019**, *2019*, 7770-7786.
[173] G. Andric, J. F. Boas, A. M. Bond, G. D. Fallon, K. P. Ghiggino, C. F. Hogan, J. A. Hutchison, M. A. P. Lee, S. J. Langford, J. R. Pilbrow, G. J. Troup, C. P. Woodward, *Aust. J. Chem.* **2004**, *57*, 1011-1019.
[174] S. V. Bhosale, C. H. Jani, S. J. Langford, *Chem. Soc. Rev.* **2008**, *37*, 331-342.
[175] N. Martin, *Chem. Commun.* **2013**, *49*, 7025-7027.
[176] D. Canevet, M. Salle, G. Zhang, D. Zhang, D. Zhu, *Chem. Commun.* **2009**, 2245-2269.
[177] J. H. Tucker, S. R. Collinson, *Chem. Soc. Rev.* **2002**, *31*, 147-156.
[178] M. Baroncini, S. Silvi, A. Credi, *Chem. Rev.* **2020**, *120*, 200-268.
[179] P. R. Ashton, R. Ballardini, V. Balzani, M. T. Gandolfi, D. J. F. Marquis, L. Pérez-Garcia, L. Prodi, J. F. Stoddart, M. Venturi, *J. Chem. Soc., Chem. Commun.* **1994**, 177-180.
[180] X. Y. Chen, H. Chen, J. Fraser Stoddart, *Angew. Chem. Int. Ed.* **2023**, *62*, e202211387.
[181] C. L. Bird, A. T. Kuhn, *Chem. Soc. Rev.* **1981**, *10*.
[182] C. Wiberg, F. Owusu, E. Wang, E. Ahlberg, *Energy Technol.* **2019**, *7*.
[183] C. Wiberg, M. Busch, L. Evenäs, E. Ahlberg, *Electrochim. Acta* **2021**, *367*.
[184] A. Das, S. Ghosh, *Chem. Commun.* **2016**, *52*, 6860-6872.
[185] M. A. Kobaisi, R. S. Bhosale, M. E. El-Khouly, D. D. La, S. D. Padghan, S. V. Bhosale, L. A. Jones, F. Antolasic, S. Fukuzumi, S. V. Bhosale, *Sci. Rep.* **2017**, *7*, 16501.
[186] T. Ikeda, W. Nakanishi, *Mater. Today Chem.* **2022**, *24*.
[187] B. A. Scott, S. J. La Placa, J. B. Torrance, B. D. Silverman, B. Welber, *J. Am. Chem. Soc.* **2002**, *99*, 6631-6639.
[188] F. Gao, F. F. Zhu, X. Y. Wang, Y. Xu, X. P. Wang, J. L. Zuo, *Inorg. Chem.* **2014**, *53*, 5321-5327.
[189] W. Devonport, M. A. Blower, M. R. Bryce, L. M. Goldenberg, *J. Org. Chem.* **1997**, *62*, 885-887.
[190] S. M. Adeel, Q. Li, A. Nafady, C. Zhao, A. I. Siriwardana, A. M. Bond, L. L. Martin, *RSC Adv.* **2014**, *4*, 49789-49795.
[191] J. Sun, Y. Wu, Y. Wang, Z. Liu, C. Cheng, K. J. Hartlieb, M. R. Wasielewski, J. F. Stoddart, *J. Am. Chem. Soc.* **2015**, *137*, 13484-13487.
[192] P. M. Beaujuge, S. Ellinger, J. R. Reynolds, *Nat. Mater.* **2008**, *7*, 795-799.
[193] B. L. Feringa, R. A. van Delden, N. Koumura, E. M. Geertsema, *Chem. Rev.* **2000**, *100*, 1789-1816.
[194] B. L. Feringa, W. F. Jager, B. De Lange, E. W. Meijer, *J. Am. Chem. Soc.* **1991**, *113*, 5468-5470.
[195] W. F. Jager, J. C. de Jong, B. de Lange, N. P. M. Huck, A. Meetsma, B. L. Feringa, *Angew. Chem. Int. Ed. Engl.* **1995**, *34*, 348-350.
[196] D. Sahoo, R. Benny, N. K. Ks, S. De, *ChemPlusChem* **2021**, *87*, e202100322.
[197] M. Natali, S. Giordani, *Chem. Soc. Rev.* **2012**, *41*, 4010-4029.

[198] A. Jana, S. Bahring, M. Ishida, S. Goeb, D. Canevet, M. Salle, J. O. Jeppesen, J. L. Sessler, *Chem. Soc. Rev.* **2018**, *47*, 5614-5645.
[199] F. Le Derf, M. Mazari, N. Mercier, E. Levillain, P. Richomme, J. Becher, J. Garin, J. Orduna, A. Gorgues, M. Salle, *Inorg. Chem.* **1999**, *38*, 6096-6100.
[200] F. Le Derf, M. Mazari, N. Mercier, E. Levillain, G. Trippe, A. Riou, P. Richomme, J. Becher, J. Garin, J. Orduna, N. Gallego-Planas, A. Gorgues, M. Salle, *Chem. Eur. J.* **2001**, *7*, 447-455.
[201] F. L. Derf, M. Mazari, N. Mercier, E. Levillain, A. Gorgues, M. Sallé, P. Richomme, J. Becher, J. Garín, J. Orduna, *Chem. Commun.* **1999**, 1417-1418.
[202] S. G. Liu, H. Liu, K. Bandyopadhyay, Z. Gao, L. Echegoyen, *J. Org. Chem.* **2000**, *65*, 3292-3298.
[203] T. Bouwens, T. M. A. Bakker, K. Zhu, J. Hasenack, M. Dieperink, A. M. Brouwer, A. Huijser, S. Mathew, J. N. H. Reek, *Nat. Chem.* **2022**, DOI: 10.1038/s41557-41022-01068-y.
[204] C. I. Ratcliffe, J. A. Ripmeester, G. W. Buchanan, J. K. Denike, *J. Am. Chem. Soc.* **1992**, *114*, 3294-3299.
[205] V. N. Vukotic, K. J. Harris, K. Zhu, R. W. Schurko, S. J. Loeb, *Nat. Chem.* **2012**, *4*, 456-460.
[206] S. Silvi, M. Venturi, A. Credi, *J. Mater. Chem.* **2009**, *19*, 2279-2294.
[207] G. Gholami, K. Zhu, G. Baggi, E. Schott, X. Zarate, S. J. Loeb, *Chem. Sci.* **2017**, *8*, 7718-7723.
[208] P. G. Young, K. Hirose, Y. Tobe, *J. Am. Chem. Soc.* **2014**, *136*, 7899-7906.
[209] D. D. Gunbas, A. M. Brouwer, *J. Org. Chem.* **2012**, *77*, 5724-5735.
[210] M. V. Martínez-Díaz, N. Spencer, J. F. Stoddart, *Angew. Chem. Int. Ed.* **1997**, *36*, 1904-1907.
[211] G. Ragazzon, C. Schafer, P. Franchi, S. Silvi, B. Colasson, M. Lucarini, A. Credi, *Proc. Natl. Acad. Sci. U. S. A.* **2018**, *115*, 9385-9390.
[212] T. Heinrich, C. H. Traulsen, M. Holzweber, S. Richter, V. Kunz, S. K. Kastner, S. O. Krabbenborg, J. Huskens, W. E. Unger, C. A. Schalley, *J. Am. Chem. Soc.* **2015**, *137*, 4382-4390.
[213] K. Ariga, *Chem. Sci.* **2020**, *11*, 10594-10604.
[214] A. Goujon, T. Lang, G. Mariani, E. Moulin, G. Fuks, J. Raya, E. Buhler, N. Giuseppone, *J. Am. Chem. Soc.* **2017**, *139*, 14825-14828.
[215] Y. Feng, M. Ovalle, J. S. W. Seale, C. K. Lee, D. J. Kim, R. D. Astumian, J. F. Stoddart, *J. Am. Chem. Soc.* **2021**, *143*, 5569-5591.
[216] M. R. Wilson, J. Sola, A. Carlone, S. M. Goldup, N. Lebrasseur, D. A. Leigh, *Nature* **2016**, *534*, 235-240.
[217] S. Erbas-Cakmak, S. D. P. Fielden, U. Karaca, D. A. Leigh, C. T. McTernan, D. J. Tetlow, M. R. Wilson, *Science* **2017**, *358*, 340-343.
[218] M. Hänsel, C. Barta, C. Rietze, M. Utecht, K. Rück-Braun, P. Saalfrank, P. Tegeder, *J. Phys. Chem. C* **2018**, *122*, 25555-25564.
[219] P. Thordarson, *Chem. Soc. Rev.* **2011**, *40*, 1305-1323.
[220] H. Tian, Q. C. Wang, *Chem. Soc. Rev.* **2006**, *35*, 361-374.
[221] S. Grimme, *Chem. Eur. J.* **2012**, *18*, 9955-9964.

[222] J. J. Christensen, R. M. Izatt, L. D. Hansen, J. A. Partridge, *J. Phys. Chem.* **1966**, *70*, 2003-2010.
[223] F. P. Schmidtchen, in *Analytical Methods in Supramolecular Chemistry 2nd ed.* (Ed.: C. A. Schalley), Wiley-VCH, Weinheim, **2012**, 67-104.
[224] P. Duboc, I. Marison, U. von Stockar, in *Handbook of Thermal Analysis and Calorimetry, Vol. 4* (Ed.: R. B. Kemp), Elsevier Science B.V., Amsterdam, **1999**, 267-365.
[225] A. Thanassoulas, G. Nounesis, in *Thermodynamics and Biophysics of Biomedical Nanosystems: Applications and Practical Considerations* (Eds.: C. Demetzos, N. Pippa), Springer Singapore, Singapore, **2019**, 63-103.
[226] W. B. Turnbull, A. H. Daranas, *J. Am. Chem. Soc.* **2003**, *125*, 14859-14866.
[227] T. Wiseman, S. Williston, J. F. Brandts, L. N. Lin, *Anal. Biochem.* **1989**, *179*, 131-137.
[228] G. Krainer, S. Keller, *Methods* **2015**, *76*, 116-123.
[229] B. W. Sigurskjold, *Anal. Biochem.* **2000**, *277*, 260-266.
[230] L. Polewski, A. Springer, K. Pagel, C. A. Schalley, *Acc. Chem. Res.* **2021**, *54*, 2445-2456.
[231] J. B. Fenn, *Angew. Chem. Int. Ed.* **2003**, *42*, 3871-3894.
[232] L. Konermann, E. Ahadi, A. D. Rodriguez, S. Vahidi, *Anal. Chem.* **2013**, *85*, 2-9.
[233] L. Cera, C. A. Schalley, *Chem. Soc. Rev.* **2014**, *43*, 1800-1812.
[234] Z. Qi, T. Heinrich, S. Moorthy, C. A. Schalley, *Chem. Soc. Rev.* **2015**, *44*, 515-531.
[235] C. A. Schalley, P. Ghosh, M. Engeser, *Int. J. Mass Spec.* **2004**, *232*, 249-258.
[236] A. Kruve, K. Caprice, R. Lavendomme, J. M. Wollschläger, S. Schoder, H. V. Schröder, J. R. Nitschke, F. B. L. Cougnon, C. A. Schalley, *Angew. Chem. Int. Ed.* **2019**, *58*, 11324-11328.
[237] A. Memboeuf, A. Nasioudis, S. Indelicato, F. Pollreisz, A. Kuki, S. Keki, O. F. van den Brink, K. Vekey, L. Drahos, *Anal. Chem.* **2010**, *82*, 2294-2302.
[238] A. K. Shukla, J. H. Futrell, *J. Mass Spectrom.* **2000**, *35*, 1069-1090.
[239] M. W. Forbes, D. A. Volmer, G. J. Francis, D. K. Bohme, *J. Am. Soc. Mass Spectrom.* **2005**, *16*, 779-791.
[240] W. M. David, J. S. Brodbelt, *J. Am. Soc. Mass Spectrom.* **2003**, *14*, 383-392.
[241] V. Gabelica, A. A. Shvartsburg, C. Afonso, P. Barran, J. L. P. Benesch, C. Bleiholder, M. T. Bowers, A. Bilbao, M. F. Bush, J. L. Campbell, I. D. G. Campuzano, T. Causon, B. H. Clowers, C. S. Creaser, E. De Pauw, J. Far, F. Fernandez-Lima, J. C. Fjeldsted, K. Giles, M. Groessl, C. J. Hogan, Jr., S. Hann, H. I. Kim, R. T. Kurulugama, J. C. May, J. A. McLean, K. Pagel, K. Richardson, M. E. Ridgeway, F. Rosu, F. Sobott, K. Thalassinos, S. J. Valentine, T. Wyttenbach, *Mass Spectrom. Rev.* **2019**, *38*, 291-320.
[242] A. A. Shvartsburg, R. D. Smith, *Anal. Chem.* **2008**, *80*, 9689-9699.
[243] J. Ponthus, E. Riches, *Int. J. Ion Mobil. Spec.* **2013**, *16*, 95-103.
[244] M. Gaedke, H. Hupatz, F. Witte, S. M. Rupf, C. Douglas, H. V. Schröder, L. Fischer, M. Malischewski, B. Paulus, C. A. Schalley, *Org. Chem. Front.* **2022**, *9*, 64-74.

[245] M. Gaedke, F. Witte, J. Anhäuser, H. Hupatz, H. V. Schröder, A. Valkonen, K. Rissanen, A. Lützen, B. Paulus, C. A. Schalley, *Chem. Sci.* **2019**, *10*, 10003-10009.
[246] H. Hupatz, M. Gaedke, H. V. Schröder, J. Beerhues, A. Valkonen, F. Klautzsch, S. Müller, F. Witte, K. Rissanen, B. Sarkar, C. A. Schalley, *Beilstein J. Org. Chem.* **2020**, *16*, 2576-2588.
[247] H. V. Schröder, A. Mekic, H. Hupatz, S. Sobottka, F. Witte, L. H. Urner, M. Gaedke, K. Pagel, B. Sarkar, B. Paulus, C. A. Schalley, *Nanoscale* **2018**, *10*, 21425-21433.
[248] H. V. Schröder, S. Sobottka, M. Nößler, H. Hupatz, M. Gaedke, B. Sarkar, C. A. Schalley, *Chem. Sci.* **2017**, *8*, 6300-6306.
[249] P. R. Ashton, J. Becher, M. C. T. Fyfe, M. B. Nielsen, J. F. Stoddart, A. J. P. White, D. J. Williams, *Tetrahedron* **2001**, *57*, 947-956.
[250] H. V. Schröder, F. Witte, M. Gaedke, S. Sobottka, L. Suntrup, H. Hupatz, A. Valkonen, B. Paulus, K. Rissanen, B. Sarkar, C. A. Schalley, *Org. Biomol. Chem.* **2018**, *16*, 2741-2747.
[251] F. Jia, H. Hupatz, L. P. Yang, H. V. Schröder, D. H. Li, S. Xin, D. Lentz, F. Witte, X. Xie, B. Paulus, C. A. Schalley, W. Jiang, *J. Am. Chem. Soc.* **2019**, *141*, 4468-4473.
[252] F. Jia, H. V. Schröder, L. P. Yang, C. von Essen, S. Sobottka, B. Sarkar, K. Rissanen, W. Jiang, C. A. Schalley, *J. Am. Chem. Soc.* **2020**, *142*, 3306-3310.
[253] H. V. Schröder, H. Hupatz, A. J. Achazi, S. Sobottka, B. Sarkar, B. Paulus, C. A. Schalley, *Chem. Eur. J.* **2017**, *23*, 2960-2967.
[254] L. Dou, Y. Liu, Z. Hong, G. Li, Y. Yang, *Chem. Rev.* **2015**, *115*, 12633-12665.
[255] D. F. Perepichka, M. R. Bryce, *Angew. Chem. Int. Ed.* **2005**, *44*, 5370-5373.
[256] I. M. Riddlestone, A. Kraft, J. Schaefer, I. Krossing, *Angew. Chem. Int. Ed.* **2018**, *57*, 13982-14024.
[257] A. Saura-Sanmartin, A. Pastor, A. Martinez-Cuezva, G. Cutillas-Font, M. Alajarin, J. Berna, *Chem. Soc. Rev.* **2022**, *51*, 4949-4976.

6 Published Works

6.1 A Divalent Pentastable Redox-Switchable Donor-Acceptor Rotaxane

H.V. Schröder, H. Hupatz, A. J. Achazi, S. Sobottka, B. Paulus, B. Sarkar, C.A. Schalley

Chem. Eur J. **2017**, *23*, 2960-2967.

Submitted on December 7, 2016, first published on January 9, 2017 by Wiley-VCH Verlag GmbH & Co. KGaA, Weinheim.

An electronic version of the articles is available at: https://doi.org/10.1002/chem.201605710

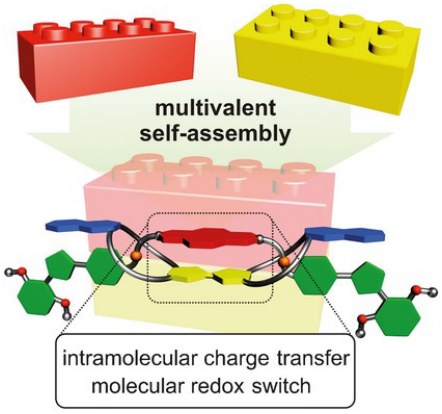

Figure 6.1. Graphical abstract. Reprinted with permission from Schröder *et al.*[253] (Copyright © 2017 Wiley-VCH Verlag GmbH & Co. KGaA, Weinheim).

Authors' contributions

Hendrik V. Schröder developed the general concept of this project and Hendrik V. Schröder, Christoph A. Schalley and I wrote the manuscript together with main contribution coming from Hendrik V. Schröder. Syntheses of the compounds and NMR, UV/Vis, IRMPD, and fluorescence experiments were done by Hendrik V. Schröder. I performed and evaluated the ITC measurements. Andreas J. Achazi and Beate Paulus did the DFT calculations. Sebastian Sobottka and Hendrik V. Schröder conducted the CV measurements and evaluated the results with Biprajit Sarkar. All authors contributed to the final version of the manuscript.

Molecular Devices

A Divalent Pentastable Redox-Switchable Donor–Acceptor Rotaxane

Hendrik V. Schröder,[a] Henrik Hupatz,[a] Andreas J. Achazi,[b] Sebastian Sobottka,[c] Biprajit Sarkar,[c] Beate Paulus,[b] and Christoph A. Schalley*[a]

Abstract: Donor–acceptor materials with small HOMO–LUMO gaps are important in molecular electronics, but are often difficult to synthesise. A simple and efficient way to position tetrathiafulvalene (TTF) as the donor and naphthalene diamide (NDI) as the acceptor in close proximity to each other in a divalent crown/ammonium pseudo[2]rotaxane is presented. The divalent design provides high chelate cooperativity and much stronger binding compared with a monovalent analogue. The pseudo[2]rotaxane was then doubly interlocked by stoppering it in a catalyst-free 1,3-dipolar cycloaddition. UV/Vis and cyclic voltammetry experiments with the resulting [2]rotaxane revealed the optoelectronic properties of an intramolecular charge transfer with a small HOMO–LUMO energy gap. Redox-switching experiments showed the rotaxane to be pentastable. DFT calculations provided insights into the electronic structures of the five redox states.

Introduction

The last decades have witnessed the rise of molecular electronics as a potential alternative to conventional silicon-based components in functional electronic devices.[1–3] Donor–acceptor (D-A) materials play a prominent role in this field and are crucial compounds in energy conversion,[4] organic (semi)conductors,[5] and organic nonlinear optics.[6] These species display partial π-electron sharing that results in emergent electronic properties, for example, intramolecular charge transfer (ICT). An important value is the energy gap (E_g) between the frontier molecular orbitals, which is often responsible for visible colours due to the charge-transfer absorption. In optoelectronic applications, a fine and purposeful tuning of the E_g value through structural optimisation is desirable.[7] Different strategies have been developed to address this task and to force the spatial proximity of donor and acceptor units. The group of Bryce and Perepichka published a series of covalently linked D-A dyads with very small E_g values (<0.5 eV).[8–10] The groups of Stoddart and Sanders studied template-directed supramolecular D-A complexes.[11–14] Recently, Stoddart and co-workers developed a strategy to enhance the co-crystallisation of D-A pairs through complementary hydrogen-bonding motifs.[15] However, D-A molecules with small E_g values are still challenging synthetic targets due to their electrochemical amphoterism, and new strategies that provide simple and efficient preparation are still required.

Multivalency is a key principle in nature that directs processes, such as virus docking or signal transduction, in biological systems.[16,17] Multiple interactions can create a strong, yet reversible, binding situation and thus allow error correction to occur in a supramolecular assembly. Researchers have made attempts to understand and analyse multivalency by determining characteristic cooperativity factors to quantify the effects of preorganisation and/or linker–linker interactions between the binding partners.[18,19] Multivalency is more and more frequently used to construct complex supramolecular architectures with precise control of the geometric arrangement of the binding partners.[20,21] Several multiply threaded non-covalent complexes and their applications as functional molecular devices have been reported recently. "Molecular elevators" are a salient example that can perform a stimuli-controlled shuttling motion.[22,23] Recently, we analysed a series of model systems to show how structural and electronic changes can influence multivalent binding and thus determine the structure and function of a supramolecular assembly.[24–28]

Herein, we employed divalent cooperative binding as an efficient tool to overcome the synthetic problems that arise in classical syntheses of D-A systems. A tetrathiafulvalene (TTF) donor unit was incorporated into a divalent crown ether macrocycle and a naphthalene diimide (NDI) acceptor unit was incorporated into a divalent bis-ammonium axle (Scheme 1). Simple mixing of the building blocks provided direct access to a doubly interpenetrated divalent crown/ammonium pseu-

[a] H. V. Schröder, H. Hupatz, Prof. Dr. C. A. Schalley
Institut für Chemie und Biochemie, Organische Chemie
Freie Universität Berlin, Takustraße 3, 14195 Berlin (Germany)
E-mail: c.schalley@fu-berlin.de
[b] A. J. Achazi, Prof. Dr. B. Paulus
Institut für Chemie und Biochemie, Theoretische Chemie
Freie Universität Berlin, Takustraße 3, 14195 Berlin (Germany)
[c] S. Sobottka, Prof. Dr. B. Sarkar
Institut für Chemie und Biochemie, Anorganische Chemie
Freie Universität Berlin, Fabeckstr. 34/36, 14195 Berlin (Germany)

Supporting information for this article can be found under http://dx.doi.org/10.1002/chem.201605710.

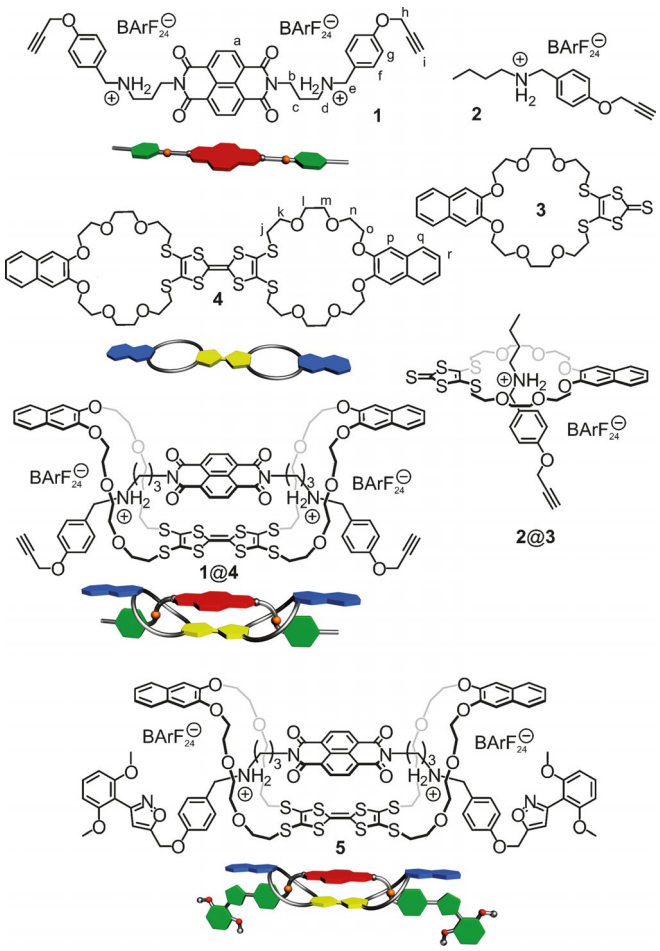

Scheme 1. The chemical structures of the axles, wheels and mono- and divalent complexes investigated in this report and the cartoons that represent them.

do[2]rotaxane. Isothermal titration calorimetry (ITC) and a double mutant cycle (DMC) analysis[29–33] revealed strong chelate cooperativity effects[34–39] to enhance the formation of the divalent complex. Furthermore, reversible control of the assembly and disassembly by chemical stimuli allowed the ICT to be switched on and off. To investigate the optoelectronic and ICT properties fully, the pseudo[2]rotaxane was mechanically locked by using a catalyst-free 1,3-dipolar cycloaddition stoppering reaction. The resulting doubly interlocked [2]rotaxane showed highly persistent ICT behaviour. Redox-switching experiments showed full reversibility and revealed that the [2]rotaxane is stable in five different redox states. Results from the DFT calculations agree nicely with the experimental data and provide insight into the electronic structures of the five different redox states.

Results and Discussion

Design considerations and building-block synthesis

To force the spatial proximity of the donor and acceptor units, a divalent supramolecular binding motif has been designed based on the well-established 24-crown-8/secondary ammonium pseudorotaxane motif.[40–43] An early study by Stoddart and co-workers showed that crown ether pseudorotaxanes and TTF are easily combined owing to their structures.[44] A TTF donor subunit can easily be integrated into the 24-crown-8 ether dimer as a spacer, as shown in compound **4** (Scheme 1). This, however, replaces two oxygen atoms in each crown ether by two sulfur atoms and leads to a significant weakening of the interaction with secondary ammonium ions compared with the oxygen analogue.[44,45] To overcome this drawback and ensure strong binding and an efficient pseudorotaxane formation, the tetrakis[(3,5-di-(trifluoromethyl)-phenyl]borate anion ($BArF_{24}^-$) was used as a weakly coordinating counterion. This not only waives the competition between the anion and the crown ether for the ammonium ions, but also ensures sufficient solubility of the axle in non-polar solvents, such as dichloromethane.

Similarly, the NDI acceptor subunit can be placed in the axle between the two ammonium ions (**1**). A crucial point in this divalent design is the spacer length, which significantly affects the positioning of the TTF and NDI units relative to each other. Based on an earlier work by Liu et al.,[46] propylammonium spacers attached to the NDI core promised a good fit.

The synthesis of the chloride salt of divalent axle **1** has been reported previously.[23] Subsequent ion exchange with $NaBArF_{24}$ in dichloromethane gave axle **1**. Monovalent axle **2** was synthesised by reductive amination of 4-(2-propyne-1-yloxy)benzaldehyde and n-butylamine, with sodium borohydride as the reducing agent. Protonation and a subsequent ion exchange gave axle **2** as the $BArF_{24}$ salt. Monovalent and divalent macrocycles **3** and **4** were synthesised by following a route for similar macrocyclic hosts reported by Becher and co-workers.[44,47–49] Detailed procedures and analytical data are provided in the Supporting Information.

Pseudo[2]rotaxane formation

^1H NMR spectroscopy confirmed the formation of a divalent pseudo[2]rotaxane from axle **1** and crown ether dimer **4** (Figure 1).[25,50] Axle protons H^d and H^e showed characteristic downfield shifts of $\Delta\delta = 0.08$ and 0.07 ppm and the crown ether methylene protons H^{j-o} became diastereotopic upon axle threading. As expected, two sets of methylene signals with more complex patterns are thus the most easily visible for protons H^j. Also, the axle was affected by the proximity of the crown ether dimer: The NDI protons H^a ($\Delta\delta = -0.10$ ppm) shifted upfield because of a shielding effect caused by the electron-rich TTF unit in wheel component **4**. These findings indicate a doubly interpenetrated complex in which the NDI is positioned in a face-to-face fashion above the TTF.

The UV/Vis spectrum of the pseudo[2]rotaxane is mainly dominated by the absorption bands of the single components (Figure 2). Minor band shifts and intensity variations are visible, such as a slight intensity decrease in the NDI π–π^* transition around $\lambda = 386$ nm. The greenish colour is expected for more highly concentrated pseudo[2]rotaxane solutions because of a broad band at $\lambda_{max}(\varepsilon) = 750$ nm (430 $L\,mol^{-1}\,cm^{-1}$), which we attributed to an intramolecular through-space charge transfer

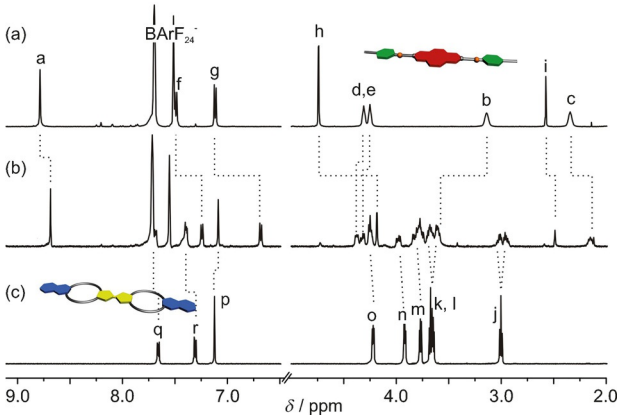

Figure 1. Partial ^{1}H NMR spectra (500 MHz, [D$_2$]DCM, 298 K) of: a) divalent axle **1**, b) an equimolar mixture of divalent axle **1** and macrocycle **4**, and c) macrocycle **4**.

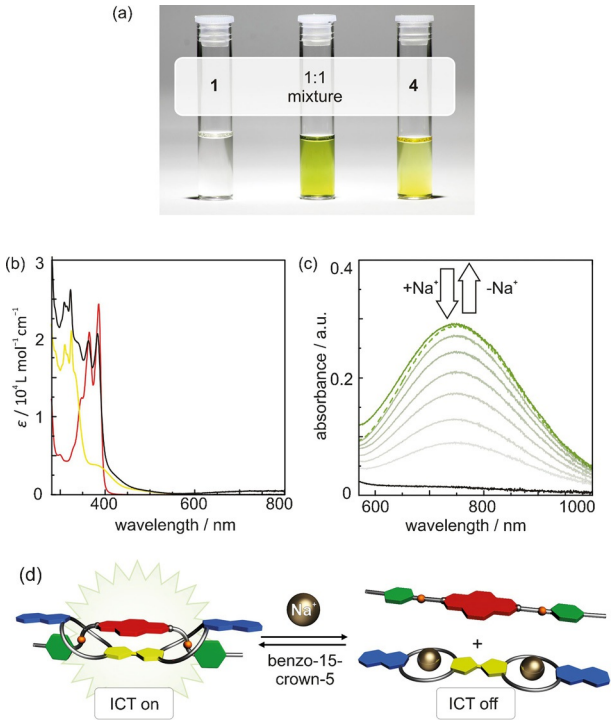

Figure 2. a) Photographs of 1.0×10^{-4} M solutions of axle **1**, macrocycle **4** and a 1:1 mixture of **1** and **4** in dichloromethane. b) Absorption spectra of axle **1** (red line), macrocycle **4** (yellow line) and pseudo[2]rotaxane **1@4** (black line) in dichloromethane (1.5×10^{-5} M) at 298 K. c) ICT band of **1@4** in dichloromethane (0.7×10^{-4} M) at 298 K. Addition of NaBArF$_{24}$ led to a decrease and subsequent stepwise addition of benzo-15-crown-5 to a full reappearance. d) Schematic representation of the chemical on–off switching process.

between the NDI and TTF units. The onset of the ICT band provides an optical HOMO–LUMO gap of $E_g^{opt} = (1.24 \pm 0.05)$ eV.

The reversible assembly and disassembly of pseudo[2]rotaxane **1@4** allows controlled on–off switching of the ICT properties by chemical stimuli. Addition of a competitive guest, such as NaBArF$_{24}$, to a solution of the rotaxane in dichloromethane led to the disassembly of the complex, as indicated by a complete disappearance of the observed ICT band (Figure 2c). Subsequently, the addition of benzo-15-crown-5, which is a better host for Na^+, restored the pseudo[2]rotaxane as indicated by the reappearance of the ICT band. This reversible switching thus provides control over the self-assembly process and makes the pseudo[2]rotaxane responsive to stimuli.

A Job plot constructed from the UV/Vis data at different molar fractions of axle and wheel showed a clear 1:1 stoichiometry for the pseudo[2]rotaxane and, thus, indicates selective divalent binding (Figure S5 in the Supporting Information). The 1:1 stoichiometry was also confirmed by ESI-MS experiments, which revealed the divalent 1:1 complex to be the base peak, whereas larger oligomers were not observed (see the Supporting Information). Isothermal titration calorimetry provided a full set of thermodynamic data for divalent complex **1@4**, monovalent reference **2@3**, and the mixed 1:2 and 2:1 complexes of axles and wheels (see the Supporting Information). The binding constant of divalent pseudo[2]rotaxane **1@4** is approximately 70 times higher than that of corresponding monovalent analogue **2@3** (Table 1). The complexation is clearly enthalpy driven. The divalent pseudo[2]rotaxane suffers from a higher entropic penalty than the monovalent analogue, likely due to a more severe conformational fixation of host and guest upon divalent binding.

No significant allosteric cooperativity ($\alpha_H = 1.1$) was observed for the divalent host when the divalent pseudo[2]rotaxane was compared with the 2:1 complex prepared from the divalent crown ether and the monovalent axle. However, a slightly negative allosteric cooperativity ($\alpha_G = 0.5$, related to a small negative cooperativity effect of the order of 2 kJ mol^{-1}) was found, as observed previously in similar cases[28] if the divalent axle was combined with two monovalent crown ethers and compared with the divalent pseudo[2]rotaxane.

A DMC analysis (see the Supporting Information), performed by following the procedure described earlier for similar systems,[25,28] results in clearly positive chelate cooperativity factors. Hunter's β value is 61 and Ercolani's β' value is 7. This positive chelate cooperativity can be traced back to spacer–

Table 1. Thermodynamic binding data obtained from ITC experiments in 1,1,2,2-tetrachloroethane (TCE)/acetonitrile (50:1)[a] at 298 K (for full data sets and details on the determination of effective molarity and cooperativity factors, see the Supporting Information).

	$K_a\times10^3$ [M^{-1}]	ΔG [kJ mol^{-1}]	ΔH [kJ mol^{-1}]	$T\Delta S$ [kJ mol^{-1}]	α_G[b]	α_H[b]	EM [mM]	β[b]	β'[b]
1@4	309 ± 30	−31.4 ± 0.2	−45.5 ± 0.7	−14.1 ± 0.9	0.5	1.1	27 ± 6	61	7
2@3	4.5 ± 0.5	−20.8 ± 0.2	−29.5 ± 0.6	−8.6 ± 0.8	–	–	–	–	–

[a] For reliable ITC measurements, the volatile dichloromethane was replaced by TCE/acetonitrile (50:1). For experimental details, see the Supporting Information. [b] Average errors of cooperativity factors: ±20%.

spacer interactions in the divalent pseudo[2]rotaxane between the electron-poor NDI and the electron-rich TTF moiety. These cooperativity factors are lower than those observed earlier for other crown/ammonium pseudo[2]rotaxanes.[28] This is likely due to the formation of competing intramolecular hydrogen bonds between the ammonium ions and the imide carbonyl oxygen atoms of the NDI in the free divalent axle. Similar interactions cannot occur in the monovalent analogue. These experiments clearly demonstrate the efficient self-assembly of the divalent pseudo[2]rotaxane. Positive chelate cooperativity ensures the formation of a doubly intertwined structure and thus brings the two redox-active components, that is, the TTF and the NDI spacers, into the desired face-to-face arrangement.

[2]Rotaxane synthesis

The oxidation of TTF to its radical cation or its dication is expected to result in charge repulsion between the crown ether dimer and the two positive charges of the axle and, presumably, to the dissociation of the pseudo[2]rotaxane. Therefore, it is useful to doubly interlock the divalent pseudo[2]rotaxane before investigating the redox properties. Because all tested copper(I)-catalysed alkyne–azide cycloadditions (CuAAC)[51] led to fast degradation, presumably due to redox reactions with the copper salt, a catalyst-free stoppering reaction described by Takata et al.[52] was applied. Divalent species **1**@**4** was treated with two equivalents of 2,6-dimethoxybenzonitrile oxide in dichloromethane (Figure 3) and the 1,3-dipolar cycloaddition of the nitrile oxide to the terminal alkynes of the pseudo[2]rotaxane axle led to the formation of [2]rotaxane **5** in 89% yield. The [2]rotaxane is stable for weeks (at least) in the pure form and in a variety of different solvents, such as dichloromethane, toluene, tetrahydrofuran, ethyl acetate, acetonitrile or acetone.

The doubly threaded structure was confirmed by using complementary NMR spectroscopy and tandem MS experiments. The 1D and 2D ^{1}H NMR spectra showed typical shifts that were also observed for the pseudo[2]rotaxane precursor. However,

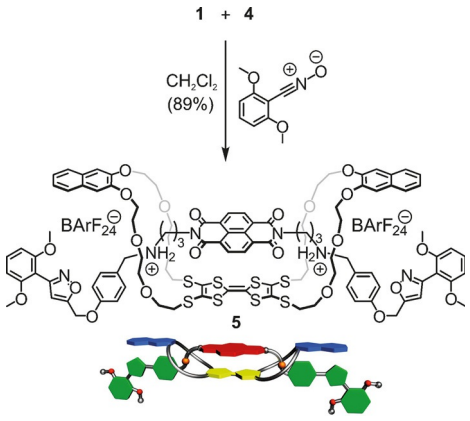

Figure 3. Stoppering reaction as the final step in the synthesis of [2]rotaxane **5**. The divalent pseudo[2]rotaxane, which is formed by an equimolar mixture of axle **1** and macrocycle **4**, has been mechanically interlocked in a catalyst-free 1,3-dipolar cycloaddition reaction.

the signal for alkyne protons H^i ($\Delta\delta$ = 3.88 ppm) showed a strong downfield shift caused by the transformation of the alkyne into the isoxazole during the 1,3-dipolar cycloaddition (see the Supporting Information). The absence of a second signal for H^i clearly reveals the doubly interlocked structure. To confirm the absence of singly threaded species, we performed infrared multiphoton dissociation (IRMPD) experiments to fragment the [2]rotaxane (Figure 4 and the Supporting Information). The ESI mass spectrum of [2]rotaxane **5** showed a prominent signal at *m/z* 1068, which corresponds to the dication [**5**−2 $BArF_{24}$]$^{2+}$. Following the mass selection of these ions, IRMPD led to a loss of part of the axle, which included one stopper, through cleavage of one of the benzylic C–N bonds. The fragment at *m/z* 1812 corresponds to the remaining singly charged complex and neither a free macrocycle nor an intact axle was observed. The absence of the free macrocycle in this spectrum clearly indicates the absence of singly threaded structures because cleavage of the interlocked side of the axle would lead to the liberation of the free macrocycle. Free macrocycles were only formed at higher laser intensities as a secondary fragment that originated from the primary fragment ion at *m/z* 1812, as also demonstrated in an MS^3 experiment. This process probably proceeds through a more energy-demanding pathway that involves a TTF-to-NDI electron transfer with subsequent radical-induced cleavage of the crown ether, which thus liberates the second part of the axle.[25,53,54]

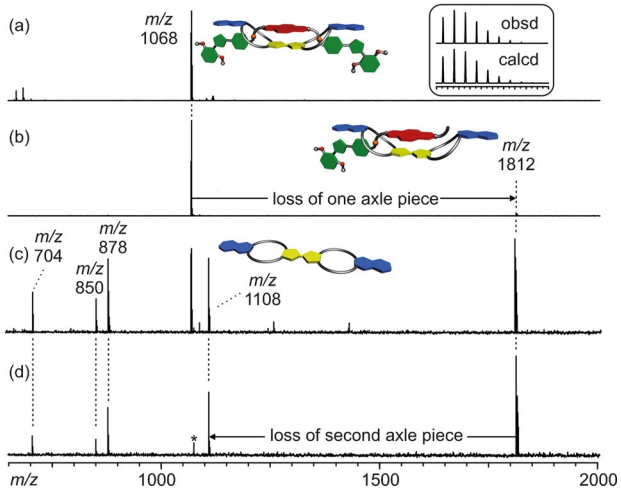

Figure 4. ESI-FTICR spectra for a solution of [2]rotaxane **5** (50 μM) in dichloromethane/methanol (1:1): a) mass spectrum; b) mass selection of *m/z* 1068 and IRMPD experiment (25% laser intensity); c) IRMPD experiment with 50% laser intensity; d) MS^3 experiment, in which the fragment ions at *m/z* 1812 were re-selected and subjected to an IRMPD experiment. Interference frequencies are marked with an asterisk.

Optoelectronic properties of [2]rotaxane 5

The interlocked nature of [2]rotaxane **5** allowed us to perform UV/Vis measurements in different solvents, even those in which a pseudo[2]rotaxane would not be stable (Table 2). [2]Rotaxane **5** has good solubility in a wide range of solvents,

Table 2. ICT band absorption maxima λ_{max}, molar absorption coefficient ε, FWHM $\Delta\nu_{1/2}$ and electronic coupling element H_{DA} of [2]rotaxane **5** in different solvents.

Solvent	λ^{max} [nm]	ε [L mol^{-1} cm^{-1}]	$\Delta\nu_{1/2}$ [cm^{-1}]	H_{DA} [cm^{-1}]
TCE	764	500	4040 ± 200	970 ± 40
TCE/acetonitrile (50:1)	764	510	4050 ± 200	980 ± 40
dichloromethane	750	430	4340 ± 200	940 ± 30
isopropanol	742	440	4880 ± 200	1010 ± 30
toluene	732	390	4980 ± 200	970 ± 30
tetrahydrofuran	718	440	5710 ± 200	1120 ± 30
ethyl acetate	716	420	6080 ± 200	1130 ± 30
acetonitrile	706	320	6350 ± 200	1010 ± 30
DMSO	697	330	6120 ± 200	1020 ± 30
acetone	696	450	6810 ± 200	1250 ± 30

but is insoluble in methanol or water. Following the absorption maxima of the ICT band from non-polar solvents, such as dichloromethane, to aprotic polar solvents, such as acetone, a distinct hypsochromic shift can be observed. This negative solvatochromic effect is a known feature of compounds with ICT character.[55] However, the shift does not strictly follow the solvent permittivities, which indicates that other effects between the solute and solvent also play a role.[56] A deeper understanding of the ICT can be achieved by application of the Marcus–Hush model for electron transfer. It allows a quantitative evaluation of the ICT from spectral features if the observed ICT band can be approximated by a Gaussian-shaped curve.[57] A characteristic value is the electronic coupling element (H_{DA}), which quantifies the coupling between the orbitals of donor and acceptor units and can be calculated from Equation (1), in which r_{DA} [Å] is the distance between the donor and acceptor, ν^{max} [cm^{-1}] is the absorption maximum of the ICT band, $\Delta\nu_{1/2}$ [cm^{-1}] is the full width at half maximum (FWHM) and ε is the molar absorption coefficient.[58–61]

$$H_{DA} = \frac{0.026}{r_{DA}}\sqrt{\nu^{max}\Delta\nu_{1/2}\varepsilon} \quad (1)$$

Fitting of the ICT bands with a Gaussian function gave $\Delta\nu_{1/2}$ values and corresponding H_{DA} values for the different solvents (Table 2). An r_{DA} value of 3.45 Å was taken from the DFT calculations, discussed below. The FWHM increased in more polar solvents. However, only a rather small change was found for the H_{DA} values, as a result of the highly preorganised and mechanically fixed structure of [2]rotaxane **5**.

Figure 5 reports the redox properties of axle **1**, macrocycle **4** and [2]rotaxane **5**, as determined by using cyclic voltammetry (CV). [2]Rotaxane **5** shows four reversible redox processes in which the two oxidations are TTF-centred and the two reduction processes are NDI-centred. However, the half-wave potentials of [2]rotaxane **5** differ from those of the free components. The potentials for the first and second oxidation are higher than for macrocycle **4**. The first reduction wave is similar to the potential of free axle **1**. Comparison of the second reduction potential of the [2]rotaxane to the free axle is difficult because the free axle undergoes adsorption at the electrode surface,

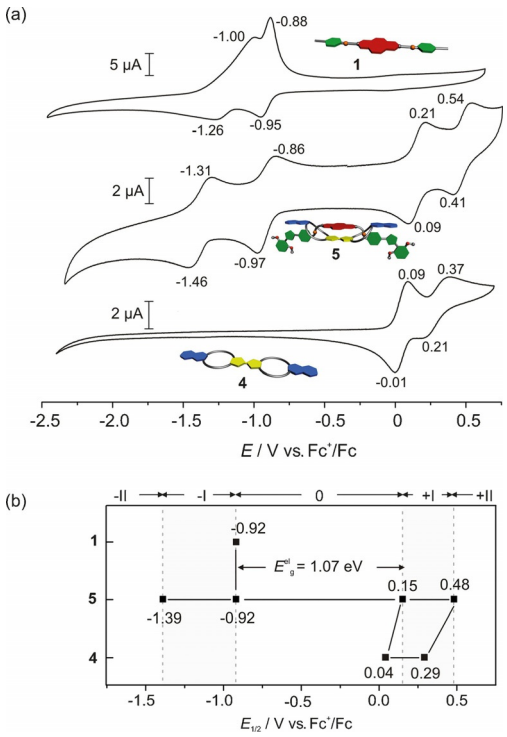

Figure 5. a) Cyclic voltammograms for **1**, **5** and **4** recorded at a scan rate of 100 mV s^{-1} versus Fc$^+$/Fc at 298 K in dichloromethane that contained $TBAPF_6$ (0.1 M). b) Comparison of the half-wave potentials between **1**, **5** and **4**.

which makes an exact determination of the second reduction potential for that case complicated (Figure 5a). However, the peak potentials indicate that the second reduction of **5** is unfavoured compared with axle **1**. It is clearly seen in Figure 5a that the redox stability of the D-A pair in [2]rotaxane **5** is drastically improved compared with both free axle **1** and free macrocycle **4**. This observation is likely important for applications of such D-A systems.

The potential differences between the [2]rotaxane and the free components can be mainly explained by two effects. First, oxidation generates additional positive charges in close spatial proximity to the two secondary ammonium ions and creates a strained species, which cannot dissociate,[47,62] despite the charge repulsion, due to its interlocked nature. Second, the ICT interaction between TTF and NDI leads to a stabilisation of their neutral forms because the electron density of TTF is decreased whereas that of NDI is increased. This makes the oxidation of TTF or reduction of NDI more difficult, which is, for example, reflected in the shift in the peak potential of the second reduction to a more negative potential. The potential difference between the first oxidation and first reduction waves reflects the electrochemical HOMO–LUMO gap, E_g^{el} = (1.07 ± 0.03) eV.

From a comparison of the UV/Vis data with the redox potentials, the Gibbs energy of photoinduced electron transfer ($\Delta_{ET}G^\circ$) can be obtained by using the Rehm–Weller equation [Eq. (2)], in which e is the elementary charge, ε_0 is the electric constant and ε_r is the relative static permittivity.[63] These values result in a $\Delta_{ET}G^\circ$ value of (−61.5 ± 6.8) kJ mol^{-1}

(−0.64 eV) in dichloromethane, which is in the upper range for similar supramolecular D-A systems.[64–67] Therefore, the charge separation between the excited D*-A complex and D^{+}-A^{-} is thermodynamically highly favoured.

$$\Delta_{ET}G^{\circ} = E_g^{el} - \frac{e}{4\pi\varepsilon_0\varepsilon_r r_{DA}} - E_g^{opt} \quad (2)$$

To show that [2]rotaxane **5** can also be switched in bulk, it was oxidised in dichloromethane by addition of $Fe(ClO_4)_3$ and reduced with Zn powder. The absorption spectra of the four accessible redox species, that is, charge states +1 to +4 (including the two charges of the axle ammonium ions), are shown in Figure 6. After the first oxidation to the +3 charge

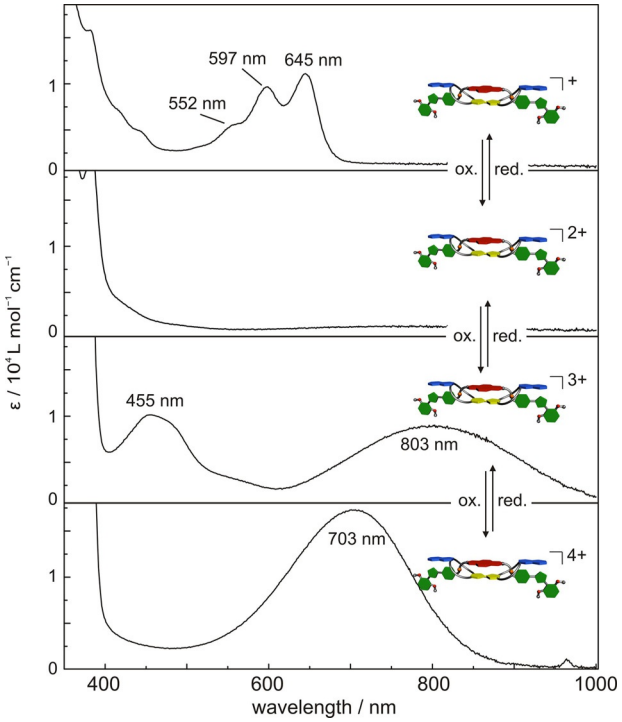

Figure 6. UV/Vis spectra of [2]rotaxane **5** (1.5×10^{-5} M) in dichloromethane (298 K) at charge states of +1, +2, +3 and +4, respectively.

state, the UV/Vis spectrum is dominated by a shouldered band at $\lambda^{max}(\varepsilon)=455$ nm (10000 L mol^{-1} cm^{-1}) and a broad band at $\lambda^{max}(\varepsilon)=803$ nm (8870 L mol^{-1} cm^{-1}), which can both be assigned to the thioalkyl-substituted $TTF^{+\bullet}$ cation radical.[68,69] Further oxidation to the +4 charge state initiated a colour change to deep blue, caused by a broad band at $\lambda^{max}(\varepsilon)=$ 703 nm (17200 L mol^{-1} cm^{-1}), which is a typical transition for substituted TTF^{2+} derivatives.[70,71] The radical-cation state showed only minor shifts compared with free host **4**, whereas the dication exhibited a bathochromic shift of $\lambda=35$ nm (Supporting Information). Suspended Zn powder was sufficient for a single-electron reduction of [2]rotaxane **5** to give a slight cyan solution. This was not possible for free axle **1**, which we explain by the low solubility of the singly reduced species. The typical $NDI^{-\bullet}$ anion-radical band pattern arose with maxima at $\lambda^{max}(\varepsilon)=552$ (4700), 597 (9000) and 645 nm (10300 L mol^{-1} cm^{-1}).[72]

Furthermore, the emission properties of [2]rotaxane **5** were investigated in different redox states (see the Supporting Information). An excitation–emission matrix showed that two different fluorophores are addressable in the non-switched state, namely, the two naphthalene subunits of the macrocycle with $\lambda^{max}{}_{em}=342$ nm and the axle NDI with $\lambda^{max}{}_{em}=400$ nm. The naphthalene emission band underwent only slight shifts after the first and the second oxidation; however, a broad low-energy transition arose for the radical cation. After reduction, both emission bands strongly increased in intensity compared with the +2, +3 and +4 charge states. The NDI-centred reduction process provides evidence that fluorescence quenching in [2]rotaxane **5** involves the LUMO orbital of the neutral NDI.

Theoretical calculations

To reduce computational cost, we used a mimic of [2]rotaxane **5**, in which we omitted the axle stoppers and the counterions and reduced the naphthalene units of the divalent macrocycle to benzenes. The geometries of all five redox states of the complex were optimised at the TPSS-D3(BJ)/def2-TZVP level of theory (Figure 7; see the Supporting Information for computational details and additional structures).

Each binding site has two NH–O hydrogen bonds, four CH–O hydrogen bonds (C–O bond lengths between 3.2 and 3.6 Å) and two CH–S hydrogen bonds (C–S bond lengths between 3.6 and 3.7 Å). In the +2 charge state, the TTF unit is not fully planar but is slightly bent away from the NDI plane along the central C=C axis, similar to previously reported findings.[44,73] The TTF–NDI plane-to-plane separation ranged between approximately 3.4 to 3.5 Å (3.43 Å between the central TTF C=C bond and the NDI plane). During the first and second oxidation, the separation slightly increased due to the loss of attrac-

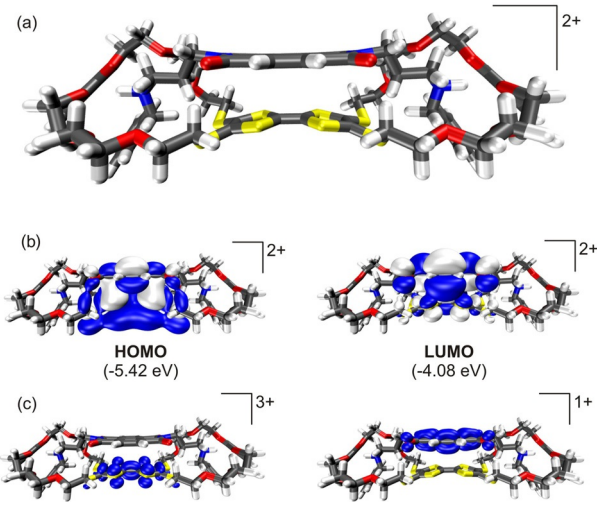

Figure 7. a) Lowest-energy structure of the mimic of [2]rotaxane **5** in the +2 charge state. b) Frontier molecular orbitals with energies for the +2 charge state. c) Spin densities of the oxidised (left) and reduced complex (right).

tive ICT interactions (see the Supporting Information). Furthermore, the TTF unit flattens during the oxidation steps. The NDI reduction also led to an increase in plane-to-plane separation, whereas this effect was smaller for the second reduction step, probably because of the overall neutral structure of the doubly reduced species.

The orbital energies of HOMO and LUMO (E_{HOMO} and E_{LUMO}) and the theoretical HOMO–LUMO gap (E_g^{calcd}) were calculated for the +2 charge state at the B3LYP/def2-TZVP level. The obtained E_g^{calcd} value of 1.34 eV matched the experimental results nicely (Table 3). The small deviations in the electrochemical and quantum chemical data are probably due to the solvent model (COSMO), which does not include electrode effects. Furthermore, we calculated the binding energies between axle and macrocycle in the complex for all five charge states and compared them with the difference in redox potentials (see the Supporting Information). In line with the increased oxidation potentials in the cyclic voltammogram of **5**, the binding is less favoured after the first oxidation and even less after the second oxidation. The first and second reductions show a similar decrease in binding affinity, which we attribute to the electroneutrality of the doubly reduced species.

Table 3. Electrochemical, theoretical and optical data for [2]rotaxane **5**, with the resulting orbital energies and HOMO–LUMO gaps (E_g) [eV].

	CV data[a]		DFT[b]		HOMO–LUMO gaps		
	E_{HOMO} [eV]	E_{LUMO} [eV]	E_{HOMO} [eV]	E_{LUMO} [eV]	E_g^{calcd} [eV]	E_g^{el} [eV]	$E_g^{opt[c]}$ [eV]
4	−4.84	–	−4.94	−1.24	3.70	–	–
1	–	−3.88	−7.66	−4.15	3.51	–	–
5	−4.95	−3.88	−5.42	−4.08	1.34	1.07 ± 0.03	1.24 ± 0.05

[a] Orbital energies were calculated from the first reduction or oxidation half-wave potentials and referenced to the Fc^+/Fc potential (−4.80 eV below vacuum level): $\varepsilon = (-(E_{1/2})/V - 4.80)$ eV. The error was estimated as ±15 meV. [b] DFT calculations (B3LYP/def2-TZVP) for a reduced structure of [2]rotaxane **5** with the COSMO ($\varepsilon_r = 9.08$) solvation model correction. [c] The optical HOMO–LUMO gap was determined from the onset of the ICT band observed in the UV/Vis measurements.

The spin densities (α density − β density) of the singly oxidised and reduced complexes are shown in Figure 7c. In the oxidised complex the spin density was mainly localised in the TTF unit, whereas reduction led to a spin density localised on the NDI. These calculations are in good agreement with the CV and UV/Vis data, in which the first oxidation process is mainly centred on the TTF moiety and the first reduction process is NDI-centred.

Conclusions

We used multivalent self-assembly as a tool to construct a D-A complex with a small HOMO–LUMO gap in a simple and efficient way. Chemical stimuli triggered the reversible on/off switching of the ICT complex. The self-assembly was evaluated by using detailed ITC studies and a DMC analysis showed much stronger binding compared with a monovalent model system. The strong cooperativity of multivalent binding in the divalent complex is in line with previously studied crown–ammonium complexes. After capping the pseudo[2]rotaxane, doubly interlocked [2]rotaxane **5** facilitated investigations of emergent ICT behaviour in a broad range of different solvents. The optoelectronic properties of [2]rotaxane **5** were investigated by using CV and UV/Vis spectroscopy and showed that the complex is redox-switchable and has good stability in five different redox states. DFT calculations support the experimental results and agree with the observed E_g values. In future, this multivalent approach can serve as a successful general construction strategy to obtain more complex D-A materials suitable for molecular electronics applications.

Acknowledgements

We thank Sebastian Müller, Amel Mekic and Marius Gaedke for synthetic help and Larissa von Krbek for support with the ITC measurements. This research was funded by the Deutsche Forschungsgemeinschaft (CRC 765) and the Fonds der Chemischen Industrie (FCI). H.S. thanks the FCI for a Chemiefonds Ph.D. fellowship. The ZEDAT (Freie Universität Berlin) is thanked for the use of their high-performance computing facilities.

Keywords: donor–acceptor systems · molecular devices · multivalency · redox chemistry · rotaxanes

[1] M. A. Ratner, *Mater. Today* **2002**, *5*, 20 – 27.
[2] R. M. Metzger, *Chem. Rev.* **2015**, *115*, 5056 – 5115.
[3] L. Sun, Y. A. Diaz-Fernandez, T. A. Gschneidtner, F. Westerlund, S. Lara-Avila, K. Moth-Poulsen, *Chem. Soc. Rev.* **2014**, *43*, 7378 – 7411.
[4] S. Günes, H. Neugebauer, N. S. Sariciftci, *Chem. Rev.* **2007**, *107*, 1324 – 1338.
[5] V. Coropceanu, H. Li, P. Winget, L. Zhu, J.-L. Brédas, *Annu. Rev. Mater. Res.* **2013**, *43*, 63 – 87.
[6] D. R. Kanis, M. A. Ratner, T. J. Marks, *Chem. Rev.* **1994**, *94*, 195 – 242.
[7] L. Dou, Y. Liu, Z. Hong, G. Li, Y. Yang, *Chem. Rev.* **2015**, *115*, 12633 – 12665.
[8] D. F. Perepichka, M. R. Bryce, C. Pearson, M. C. Petty, E. J. McInnes, J. P. Zhao, *Angew. Chem. Int. Ed.* **2003**, *42*, 4636 – 4639; *Angew. Chem.* **2003**, *115*, 4784 – 4787.
[9] D. F. Perepichka, M. R. Bryce, *Angew. Chem. Int. Ed.* **2005**, *44*, 5370 – 5373; *Angew. Chem.* **2005**, *117*, 5504 – 5507.
[10] D. F. Perepichka, M. R. Bryce, A. S. Batsanov, E. J. L. McInnes, J. P. Zhao, R. D. Farley, *Chem. Eur. J.* **2002**, *8*, 4656 – 4669.
[11] K. E. Griffiths, J. F. Stoddart, *Pure Appl. Chem.* **2008**, *80*, 485 – 506.
[12] B. Odell, M. V. Reddington, A. M. Z. Slawin, N. Spencer, J. F. Stoddart, D. J. Williams, *Angew. Chem. Int. Ed. Engl.* **1988**, *27*, 1547 – 1550; *Angew. Chem.* **1988**, *100*, 1605 – 1608.
[13] G. Barin, A. Coskun, M. M. G. Fouda, J. F. Stoddart, *ChemPlusChem* **2012**, *77*, 159 – 185.
[14] D. G. Hamilton, J. E. Davies, L. Prodi, J. K. M. Sanders, *Chem. Eur. J.* **1998**, *4*, 608 – 620.
[15] A. K. Blackburn, A. C. Sue, A. K. Shveyd, D. Cao, A. Tayi, A. Narayanan, B. S. Rolczynski, J. M. Szarko, O. A. Bozdemir, R. Wakabayashi, J. A. Lehrman, B. Kahr, L. X. Chen, M. S. Nassar, S. I. Stupp, J. F. Stoddart, *J. Am. Chem. Soc.* **2014**, *136*, 17224 – 17235.
[16] C. Fasting, C. A. Schalley, M. Weber, O. Seitz, S. Hecht, B. Koksch, J. Dernedde, C. Graf, E. W. Knapp, R. Haag, *Angew. Chem. Int. Ed.* **2012**, *51*, 10472 – 10498; *Angew. Chem.* **2012**, *124*, 10622 – 10650.
[17] M. Mammen, S.-K. Choi, G. M. Whitesides, *Angew. Chem. Int. Ed.* **1998**, *37*, 2754 – 2794; *Angew. Chem.* **1998**, *110*, 2908 – 2953.

[18] G. Ercolani, L. Schiaffino, *Angew. Chem. Int. Ed.* **2011**, *50*, 1762 – 1768; *Angew. Chem.* **2011**, *123*, 1800 – 1807.
[19] C. A. Hunter, H. L. Anderson, *Angew. Chem. Int. Ed.* **2009**, *48*, 7488 – 7499; *Angew. Chem.* **2009**, *121*, 7624 – 7636.
[20] A. Mulder, J. Huskens, D. N. Reinhoudt, *Org. Biomol. Chem.* **2004**, *2*, 3409 – 3424.
[21] J. D. Badjić, A. Nelson, S. J. Cantrill, W. B. Turnbull, J. F. Stoddart, *Acc. Chem. Res.* **2005**, *38*, 723 – 732.
[22] J. D. Badjic, V. Balzani, A. Credi, S. Silvi, J. F. Stoddart, *Science* **2004**, *303*, 1845 – 1849.
[23] Z. J. Zhang, M. Han, H. Y. Zhang, Y. Liu, *Org. Lett.* **2013**, *15*, 1698 – 1701.
[24] N. L. Löw, E. V. Dzyuba, B. Brusilowskij, L. Kaufmann, E. Franzmann, W. Maison, E. Brandt, D. Aicher, A. Wiehe, C. A. Schalley, *Beilstein J. Org. Chem.* **2012**, *8*, 234 – 245.
[25] W. Jiang, K. Nowosinski, N. L. Low, E. V. Dzyuba, F. Klautzsch, A. Schäfer, J. Huuskonen, K. Rissanen, C. A. Schalley, *J. Am. Chem. Soc.* **2012**, *134*, 1860 – 1868.
[26] L. Kaufmann, N. L. Traulsen, A. Springer, H. V. Schröder, T. Mäkelä, K. Rissanen, C. A. Schalley, *Org. Chem. Front.* **2014**, *1*, 521 – 531.
[27] A. J. Achazi, L. K. S. von Krbek, C. A. Schalley, B. Paulus, *J. Comput. Chem.* **2016**, *37*, 18 – 24.
[28] K. Nowosinski, L. K. S. von Krbek, N. L. Traulsen, C. A. Schalley, *Org. Lett.* **2015**, *17*, 5076 – 5079.
[29] P. J. Carter, G. Winter, A. J. Wilkinson, A. R. Fersht, *Cell* **1984**, *38*, 835 – 840.
[30] S. L. Cockroft, C. A. Hunter, *Chem. Soc. Rev.* **2007**, *36*, 172 – 188.
[31] H. Sun, C. A. Hunter, E. M. Llamas, *Chem. Sci.* **2015**, *6*, 1444 – 1453.
[32] H. Sun, C. A. Hunter, C. Navarro, S. Turega, *J. Am. Chem. Soc.* **2013**, *135*, 13129 – 13141.
[33] N. L. Traulsen, C. H. Traulsen, P. M. Deutinger, S. Muller, D. Schmidt, I. Linder, C. A. Schalley, *Org. Biomol. Chem.* **2015**, *13*, 10881 – 10887.
[34] E. L. Doyle, C. A. Hunter, H. C. Phillips, S. J. Webb, N. H. Williams, *J. Am. Chem. Soc.* **2003**, *125*, 4593 – 4599.
[35] G. Ercolani, *J. Am. Chem. Soc.* **2003**, *125*, 16097 – 16103.
[36] H. J. Hogben, J. K. Sprafke, M. Hoffmann, M. Pawlicki, H. L. Anderson, *J. Am. Chem. Soc.* **2011**, *133*, 20962 – 20969.
[37] E. T. Mack, P. W. Snyder, R. Perez-Castillejos, G. M. Whitesides, *J. Am. Chem. Soc.* **2011**, *133*, 11701 – 11715.
[38] J. K. Sprafke, B. Odell, T. D. Claridge, H. L. Anderson, *Angew. Chem. Int. Ed.* **2011**, *50*, 5572 – 5575; *Angew. Chem.* **2011**, *123*, 5687 – 5690.
[39] L. K. S. von Krbek, A. J. Achazi, M. Solleder, M. Weber, B. Paulus, C. A. Schalley, *Chem. Eur. J.* **2016**, *22*, 15475 – 15484.
[40] P. R. Ashton, P. J. Campbell, P. T. Glink, D. Philp, N. Spencer, J. F. Stoddart, E. J. T. Chrystal, S. Menzer, D. J. Williams, P. A. Tasker, *Angew. Chem. Int. Ed. Engl.* **1995**, *34*, 1865 – 1869; *Angew. Chem.* **1995**, *107*, 1997 – 2001.
[41] M. Xue, Y. Yang, X. Chi, X. Yan, F. Huang, *Chem. Rev.* **2015**, *115*, 7398 – 7501.
[42] N. Yamaguchi, H. W. Gibson, *Angew. Chem. Int. Ed.* **1999**, *38*, 143 – 147; *Angew. Chem.* **1999**, *111*, 195 – 199.
[43] T. J. Hubin, D. H. Busch, *Coord. Chem. Rev.* **2000**, *200 – 202*, 5 – 52.
[44] P. R. Ashton, J. Becher, M. C. T. Fyfe, M. B. Nielsen, J. F. Stoddart, A. J. P. White, D. J. Williams, *Tetrahedron* **2001**, *57*, 947 – 956.
[45] H. Nagai, Y. Suzaki, K. Osakada, *Eur. J. Inorg. Chem.* **2014**, 4376 – 4384.
[46] W. Jiang, M. Han, H. Y. Zhang, Z. J. Zhang, Y. Liu, *Chem. Eur. J.* **2009**, *15*, 9938 – 9945.
[47] T. K. Hansen, T. Jorgensen, P. C. Stein, J. Becher, *J. Org. Chem.* **1992**, *57*, 6403 – 6409.
[48] N. Svenstrup, K. M. Rasmussen, T. K. Hansen, J. Becher, *Synthesis* **1994**, *8*, 809 – 812.
[49] T. Jørgensen, T. K. Hansen, J. Becher, *Chem. Soc. Rev.* **1994**, *23*, 41 – 51.
[50] M. Lohse, K. Nowosinski, N. L. Traulsen, A. J. Achazi, L. K. S. von Krbek, B. Paulus, C. A. Schalley, S. Hecht, *Chem. Commun.* **2015**, *51*, 9777 – 9780.
[51] K. D. Hänni, D. A. Leigh, *Chem. Soc. Rev.* **2010**, *39*, 1240 – 1251.
[52] T. Matsumura, F. Ishiwari, Y. Koyama, T. Takata, *Org. Lett.* **2010**, *12*, 3828 – 3831.
[53] W. Jiang, C. A. Schalley, *J. Mass Spectrom.* **2010**, *45*, 788 – 798.
[54] W. Jiang, H. D. Winkler, C. A. Schalley, *J. Am. Chem. Soc.* **2008**, *130*, 13852 – 13853.
[55] C. Reichardt, *Chem. Rev.* **1994**, *94*, 2319 – 2358.
[56] A. V. Marenich, C. J. Cramer, D. G. Truhlar, *J. Phys. Chem. B* **2015**, *119*, 958 – 967.
[57] N. S. Hush, *Prog. Inorg. Chem.* **1967**, *8*, 391 – 444.
[58] A. C. Benniston, A. Harriman, *Angew. Chem. Int. Ed. Engl.* **1993**, *32*, 1459 – 1461; *Angew. Chem.* **1993**, *105*, 1553 – 1555.
[59] Q. Jiang, H. Y. Zhang, M. Han, Z. J. Ding, Y. Liu, *Org. Lett.* **2010**, *12*, 1728 – 1731.
[60] D. Cao, M. Amelia, L. M. Klivansky, G. Koshkakaryan, S. I. Khan, M. Semeraro, S. Silvi, M. Venturi, A. Credi, Y. Liu, *J. Am. Chem. Soc.* **2010**, *132*, 1110 – 1122.
[61] J. C. Barnes, A. C. Fahrenbach, S. M. Dyar, M. Frasconi, M. A. Giesener, Z. Zhu, Z. Liu, K. J. Hartlieb, R. Carmieli, M. R. Wasielewski, J. F. Stoddart, *Proc. Natl. Acad. Sci. USA* **2012**, *109*, 11546 – 11551.
[62] S. R. Miller, D. A. Gustowski, Z. H. Chen, G. W. Gokel, L. Echegoyen, A. E. Kaifer, *Anal. Chem.* **1988**, *60*, 2021 – 2024.
[63] D. Rehm, A. Weller, *Ber. Bunsen-Ges. Phys. Chem.* **1969**, *73*, 834 – 839.
[64] X. W. Xiao, W. Xu, D. Q. Zhang, H. Xu, H. Y. Lu, D. B. Zhu, *J. Mater. Chem.* **2005**, *15*, 2557 – 2561.
[65] Y. M. Zhang, Y. Chen, R. J. Zhuang, Y. Liu, *Photochem. Photobiol. Sci.* **2011**, *10*, 1393 – 1398.
[66] P. K. Poddutoori, L. P. Bregles, G. N. Lim, P. Boland, R. G. Kerr, F. D'Souza, *Inorg. Chem.* **2015**, *54*, 8482 – 8494.
[67] P. K. Poddutoori, N. Zarrabi, A. G. Moiseev, R. Gumbau-Brisa, S. Vassiliev, A. van der Est, *Chem. Eur. J.* **2013**, *19*, 3148 – 3161.
[68] V. Khodorkovsky, L. Shapiro, P. Krief, A. Shames, G. Mabon, A. Gorgues, M. Giffard, *Chem. Commun.* **2001**, 2736 – 2737.
[69] M. B. Kirketerp, L. A. Leal, D. Varsano, A. Rubio, T. J. Jorgensen, K. Kilsa, M. B. Nielsen, S. B. Nielsen, *Chem. Commun.* **2011**, *47*, 6900 – 6902.
[70] V. A. Azov, R. Gómez, J. Stelten, *Tetrahedron* **2008**, *64*, 1909 – 1917.
[71] M. Hasegawa, K. Daigoku, K. Hashimoto, H. Nishikawa, M. Iyoda, *Bull. Chem. Soc. Jpn.* **2012**, *85*, 51 – 60.
[72] G. Andric, J. F. Boas, A. M. Bond, G. D. Fallon, K. P. Ghiggino, C. F. Hogan, J. A. Hutchison, M. A. P. Lee, S. J. Langford, J. R. Pilbrow, G. J. Troup, C. P. Woodward, *Aust. J. Chem.* **2004**, *57*, 1011 – 1019.
[73] H. Kobayashi, A. Kobayashi, Y. Sasaki, G. Saito, H. Inokuchi, *Bull. Chem. Soc. Jpn.* **1986**, *59*, 301 – 302.

Manuscript received: December 7, 2016
Accepted Article published: January 9, 2017
Final Article published: February 1, 2017

CHEMISTRY
A European Journal

Supporting Information

A Divalent Pentastable Redox-Switchable Donor–Acceptor Rotaxane

Hendrik V. Schröder,[a] Henrik Hupatz,[a] Andreas J. Achazi,[b] Sebastian Sobottka,[c] Biprajit Sarkar,[c] Beate Paulus,[b] and Christoph A. Schalley*[a]

chem_201605710_sm_miscellaneous_information.pdf

A Divalent Pentastable Redox-Switchable Donor-Acceptor Rotaxane

Hendrik V. Schröder,[a] Henrik Hupatz,[a] Andreas J. Achazi,[b] Sebastian Sobottka,[c] Biprajit Sarkar,[c] Beate Paulus,[b] and Christoph A. Schalley*[a]

[a] Institut für Chemie und Biochemie, Organische Chemie, Freie Universität Berlin, Takustraße 3, 14195 Berlin, Germany, E-Mail: c.schalley@fu-berlin.de

[b] Institut für Chemie und Biochemie, Theoretische Chemie, Freie Universität Berlin, Takustraße 3, 14195 Berlin, Germany

[c] Institut für Chemie und Biochemie, Anorganische Chemie Freie Universität Berlin, Fabeckstr. 34/36, 14195 Berlin, Germany

Supporting Information

Index

General Information

All reagents and solvents were obtained from commercial sources and used without further purification. Dry solvents were purchased from Acros Organics. 4-(Prop-2-yn-1-yloxy)benzaldehyde was synthesized according to a literature procedure.[1] The synthesis for the chloride salt of divalent axle **1**[2], ditosylate **6**[4] and cyanoethyl-protected TTF precursor **8**[3] were reported elsewhere. The stopper, 2,6-dimethoxybenzonitrile oxide, was synthesized as previously reported.[5] For dialysis, pre-wetted RC tube dialysis membranes (MWCO 1 kD, Spectrumlabs) were used. Thin-layer chromatography was performed on silica gel coated plates with fluorescent indicator F254 (Merck). For column chromatography, silica gel (0.04-0.063 mm; Merck) was used.

^{1}H and ^{13}C NMR experiments were performed on JEOL ECP 500, Bruker AVANCE 500 or Bruker AVANCE 700 instruments. Solvent residue signals were used as internal standard. All shifts are reported in ppm and NMR multiplicities are abbreviated as s (singlet), d (doublet), t (triplet), m (multiplet) and br (broad). Coupling constants *J* are reported in Hertz. Compounds containing the tetrakis[3,5-bis(trifluoromethyl)phenyl]borate ($BArF_{24}^-$) anion show ^{19}F, ^{10}B and ^{11}B couplings in the ^{13}C NMR spectra which were denoted as one signal.

ITC titrations were carried out in dry TCE/ACN mixtures (1:0, 50:1 and 5:1) at 298 K on a TAM III microcalorimeter (Waters GmbH, TA Instruments, Eschborn, Germany). In a typical experiment, an 800 µL solution of crown ether was placed in the sample cell at a concentration of 1 mM, and 250 µL of a solution of the ammonium salt (8 mM) was put into the syringe. The titrations consisted of 32 consecutive injections of 8 µL each with a 20 min interval between injections. Heats of dilution were determined by titration of ammonium salt solutions into the sample cell containing blank solvent and were subtracted from each data set. The heat flow generated in the sample cell is measured as a differential signal between sample and reference cell. Hence, an exothermic event results in a positive and an endothermic in a negative heat flow. The data were analysed using the instrument's internal software package and fitted with a 1:1, 1:2 or 2:1 binding model. Each titration was conducted twice and the measured values for *K*, Δ*G* and Δ*H* were averaged.

High-resolution ESI mass spectra were measured on an Agilent 6210 ESI-TOF device (Agilent Technologies). HPLC grade solvents were used with a flow rate of 2-4 µL/min. Tandem MS and infrared multiphoton dissociation (IRMPD) experiments were performed on an Ionspec Q FT-7 (Varian Inc.) equipped with a 7 T superconducting magnet and a Micromass Z-spray ESI source.

Cyclic voltammetry was carried out in dry and degassed dichloromethane (DCM) solutions with tetrabutylammonium hexafluorophosphate (0.1 M) using a three-electrode configuration (glassy carbon or Pt working electrodes, Pt counter electrode, Ag wire as pseudoreference) and a PAR VersaSTAT 4 (Princeton Applied Research) potentiostat. The

decamethylferrocene/decamethylferrocenium ($[FeCp_2^*]^{+/0}$) was used as the internal reference and referred to the ferrocene/ferrocenium ($Fc^{+/0}$) couple.[6]

The UV/Vis measurements were performed on a Cary 50 Bio Photospectrometer (Varian) equipped with a xenon lamp. Solvents with HPLC grade or better and *Suprasil* glass cuvettes with a path-length of 1 cm were used. The Gaussian-shaped ICT bands were fitted with a non-linear Gauss fit in OriginPro 8 (OriginLab). The fluorescence spectra were obtained on a LS 50 B-luminescence spectrometer (PerkinElmer) using excitation and emission slits of 15 nm widths. *Suprasil* Fluorescence cuvettes (1 cm x 0.4 cm path-length) were used. DCM solutions of [2]rotaxane **5** were oxidized with $Fe(ClO_4)_3$ or reduced with Zn powder by stirring the suspension under argon atmosphere for several minutes. Both solids show very low solubility in DCM and were filtered off after oxidation or reduction.

Melting points were determined on a SMP 30 (Stuart) instrument.

Computational Details

The structure of the [2]rotaxane **5** mimic was optimized with DFT.[7] To minimize the calculation time, we reduced the structure of the benzo-derivative of the crown ether dimer, cut off the stoppers and omitted the counter ions. The optimization was done with the meta-GGA functional TPSS-D3(BJ)[8] which gives better structures for non-covalently bound systems compared to pure B3LYP, due to the dispersion correction D3(BJ).[9-10] Additionally, Multipole-Accelerated-Resolution-of-Identity-*J* (MARI-*J*)[11-12] was used to accelerate the TPSS calculation. For hybrid functionals, the speed up is much smaller due to the exchange part. Therefore, MARI-*J* was not used for the B3LYP calculation. A triple-ζ basis set, def2-TZVP[13-14], was used to avoid large basis set superposition errors which affect the geometry. The geometry optimization was done in vacuum.

The HOMO-LUMO gap was calculated with the hybrid functional B3LYP/def2-TZVP.[15-20] The B3LYP calculation was done in vacuum and in solvent. The solvent (DCM, ε_r = 9.08) is considered using the implicit solvent model COSMO.[21]

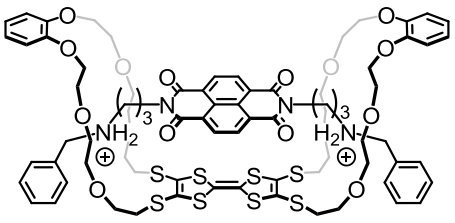

Figure S1. Structure of the mimic of rotaxane **5** in which the axle stoppers and counterions are omitted and the naphthalene units reduced to benzene rings, to minimize computational cost.

Table S1 shows the orbital energies of HOMO and LUMO and the HOMO-LUMO gap of the reagents. The difference of the HOMO-LUMO gap in vacuum and solvent calculation is small (less than 0.06 eV). On the contrary, the difference of the orbital energies in vacuum and solvent is large (partly greater than 2 eV). Counter-ions and effects of the electrodes are not considered. The calculated HOMO-LUMO gap (in vacuum and solvent) is close to the optical HOMO-LUMO gap. The vacuum result is a little bit closer, but the difference is small. The difference to the electrochemical HOMO-LUMO gap is much bigger. One reason for the bigger difference are electrode effects which are not considered in the calculation.

Table S1. Theoretical orbital energies and HOMO-LUMO gaps (E_g)

	Vacuum	Vacuum	Solvent (COSMO)	Solvent (COSMO)	Vacuum	Solvent (COSMO)
	ε_{HOMO} / eV	ε_{LUMO} / eV	ε_{HOMO} / eV	ε_{LUMO} / eV	E_g / eV	E_g / eV
4	-4.66	-1.02	-4.94	-1.24	3.64	3.70
1	-10.93	-7.41	-7.66	-4.15	3.52	3.51
5	-8.12	-6.81	-5.42	-4.08	1.31	1.34

Table S2 shows the binding energies of **5** and its oxidized and reduced species. The structures were optimised as before (with TPSS-D3(BJ)/def2-TZVP). In case of the +4 charge state of **5** and macrocycle $\mathbf{4}^{2+}$ the $\langle \hat{S}^2 \rangle$ expectation value deviates in the TPSS-D3(BJ) and the B3LYP-D3(BJ) vacuum calculation (all these calculations concern the binding energy of **5** in +4 charge state). For the axle **1** in 0 charge state (two times reduced **1**) the $\langle \hat{S}^2 \rangle$ expectation value deviates in the TPSS-D3(BJ) calculation (this concerns the binding energy of **5**). In the other TPSS-D3(BJ) and the B3LYP-D3(BJ) vacuum calculations and all B3LYP-D3(BJ) with COSMO the $\langle \hat{S}^2 \rangle$ expectation values are close to S(S+1). The structures with deviating $\langle \hat{S}^2 \rangle$ still look reasonable and the B3LYP-D3(BJ) calculations with COSMO have $\langle \hat{S}^2 \rangle$ expectation values close to S(S+1). Therefore, we assume that at least the binding energies in solvent are reasonable. The only doubtful binding energy is the vacuum binding energy of **5** in +4 charge state, but the vacuum binding energy has the same trend as the binding energy in solvent.

The basis set superposition error BSSE for **5** with B3LYP/def2-TZVP is 23.37 kJ mol^{-1}. The BSSE is small compared to the total binding energy and only the trend of the binding energy is compared to the experiment. Therefore, the BSSE correction of **5** was used for all oxidized and reduced species (the difference would probably be only a few kJ mol^{-1}). The binding energies of **5** show a similar trend as the electrochemical experiment: charge state +2 is the most stable component; charge state +1 and +2 are similar; and +3 and +4 are much weaker. The only difference to the experiment is charge state 0 which is in the experiment much weaker bound. The electroneutrality may lead to an overestimation of the binding

energy in the calculation. Solvent effects are taken in to account in the calculation with COSMO. But counter ion effects and effects of the electrodes are not taken into account.

Table S2. Calculated binding energies in vacuum and solvent and electrochemical data of **5** in different charge states

Charge state	Vacuum energy / kJ mol^{-1}	Solvent-corrected energy / kJ mol^{-1}	$\Delta E^{el[a]}$ / mV	$\Delta G^{el[b]}$ / kJ mol^{-1}
0	-535.86	-274.61	200	19.3
+1	-531.75	-272.22	20	1.9
+2	-557.96	-277.90	/	/
+3	-237.26	-217.78	120	11.6
+4	+148.56	-138.70	170	16.4

[a] Potential differences of oxidations or reductions were taken from shifts of peak potentials in the cyclic voltammogram between rotaxane **5** and free axle **1** and macrocycle **4**. [b] Energy difference calculated from $\Delta G = |-n\mathrm{F}\Delta E|$ where n is the number of electrons and F the Faraday constant.

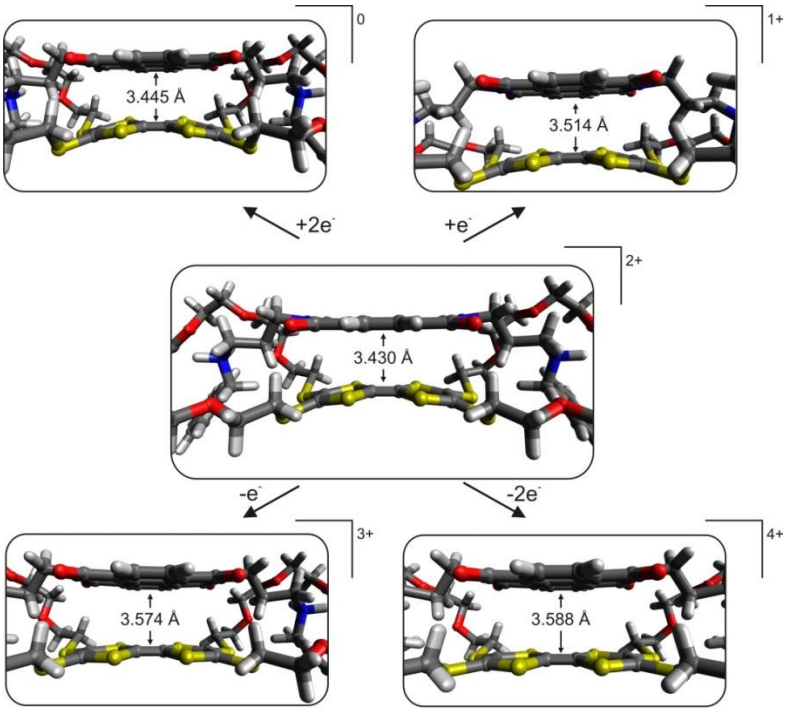

Figure S2. Structure and distance between the central C=C bond in the TTF and the NDI plane in rotaxane **5** with charge states 0, +1, +2, +3 and +4, respectively.

Synthesis

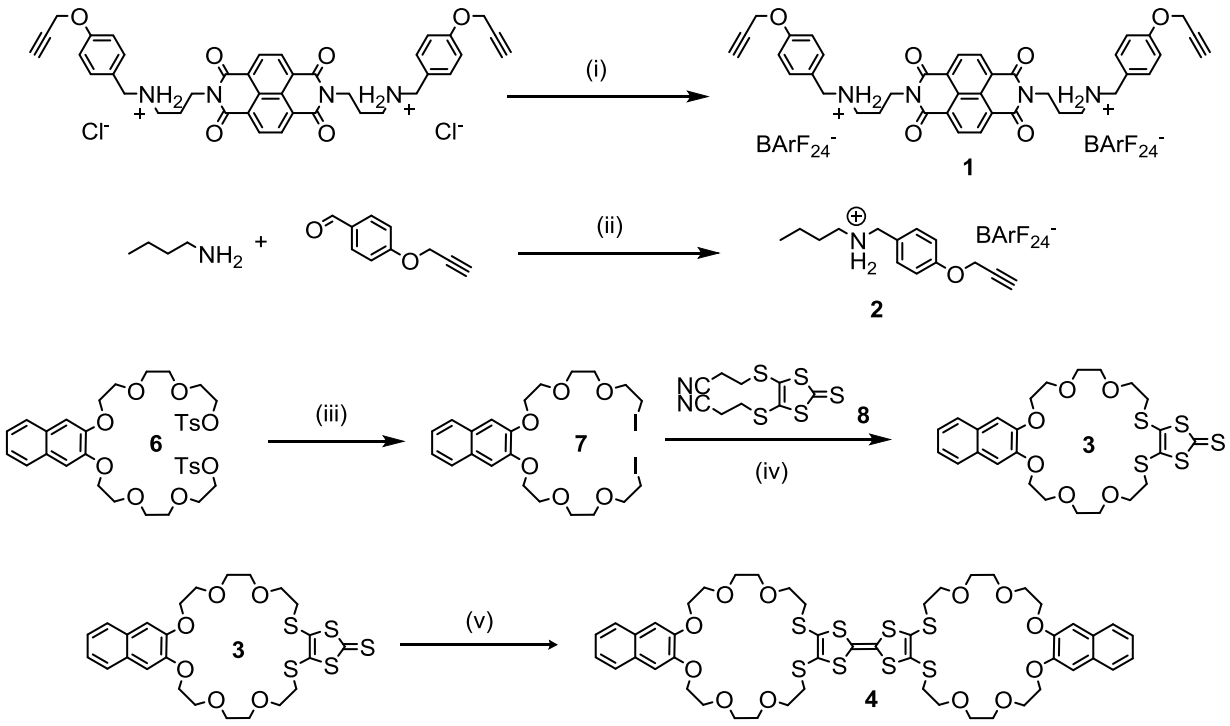

Figure S3. Synthetic procedures for divalent axle **1**, the monovalent axle **2**, the monovalent and divalent macrocycles **3** and **4**, respectively: (i) $NaBArF_{24}$, MeOH; (ii) EtOH reflux, $NaBH_4$, HCl, $NaBArF_{24}$; (iii) KI, acetone (iv) $CsOH{\cdot}H_2O$/MeOH, DMF, 0 °C; (v) $P(OEt)_3$, 130 °C.

Divalent Axle 1

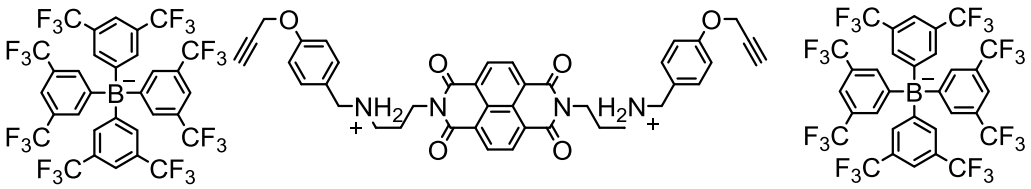

The dichloride of NDI axle (100 mg, 0.14 mmol) was dissolved with $NaBArF_{24}$ (240 mg, 0.27 mmol) in MeOH (30 mL). The mixture was stirred overnight. Afterwards, the solvent was removed under reduced pressure and the residue was dispersed in water (50 mL) through sonication. After stirring for 2 h, solvent was removed by filtration and the desired product (240 mg, 0.10 mmol, 74%) was obtained as a yellow powder.

m.p. 65 °C; ^{1}H NMR (700 MHz, [D$_2$]DCM, 298 K): δ = 8.79 (s, 4H, NDI), 7.75 (br, 4H, NH), 7.70 (br, 16H, BArF$_{24}$), 7.52 (br, 8H, BArF$_{24}$), 7.49 (AA'XX' spin system, $^{3}J_{AX}$ = 8.4 Hz, 4H, H$_{Ar}$), 7.12 (AA'XX' spin system, $^{3}J_{AX}$ = 8.4 Hz, 4H, H$_{Ar}$), 4.74 (d, ^{4}J = 2.4 Hz, 2H, C<u>H$_2$</u>CCH), 4.31 (br, 4H, CH$_2$), 4.25 (br, 4H, CH$_2$), 3.14 (br, 4H, CH$_2$), 2.57 (t, ^{3}J = 2.4 Hz, 2H, CC<u>H</u>), 2.34 (s, 4H, CH$_2$C<u>H$_2$</u>CH$_2$) ppm; ^{13}C-NMR (176 MHz, [D$_2$]DCM): δ = 164.78, 162.29, 160.11, 135.36, 132.73, 131.83, 129.28, 127.31, 126.70, 125.26, 121.87, 118.03, 116.86, 78.26, 76.50, 56.56, 53.58, 45.73, 37.46, 25.49 ppm; UV/vis (DCM): λ^{max} (ε) = 386 nm (23900 L·mol^{-1}·cm^{-1}); ESI-HRMS: *m/z*: calcd for [C$_{104}$H$_{62}$B$_2$F$_{48}$N$_4$O$_6$]: 335.1390 [M-2BArF$_{24}$]$^{2+}$, found: 335.1391.

Monovalent Axle 2

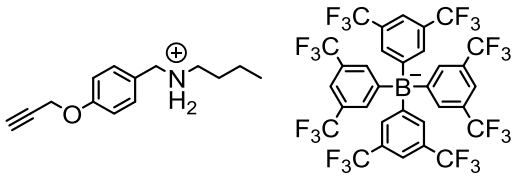

4-(Prop-2-yne-1-yloxy)benzaldehyde (320 mg, 2.0 mmol) and *n*-butylamine (200 µL, 2.0 mmol) were dissolved in dry EtOH (20 mL) and refluxed for 4 h. Afterwards, the solution was cooled to 0 °C and NaBH$_4$ (378 mg, 10 mmol) was slowly added. The mixture was warmed up to room temperature and stirred overnight. The reaction was quenched with a minimal amount of saturated sodium bicarbonate solution. The mixture was extracted with DCM (2·50 mL) and the combined organic layers were washed with brine (2 x 50 mL). After drying over MgSO$_4$, the solvent was removed under reduced pressure to give the crude product which was purified by column chromatography (SiO$_2$, DCM→DCM/MeOH = 20:1). The product was treated with a minimum of concentrated HCl and dispersed in Et$_2$O. Filtration gave the corresponding hydrochloride as white powder (216 mg, 0.85 mmol, 43%). The chloride (51 mg, 0.20 mmol) and NaBArF$_{24}$ (177 mg, 0.20 mmol) were dissolved in MeOH (1 mL) and stirred for 4 h. Afterwards, water (10 mL) was added and the aqueous phase was extracted with DCM(2·10 mL). The combined organic layers were dried over MgSO$_4$. Evaporation gave the desired product (205 mg, 0.19 mmol, 95%) as a sticky colorless oil.

^{1}H NMR (700 MHz, [D$_2$]DCM, 298 K): δ = 7.79 – 7.64 (br, 8H, BArF$_{24}$), 7.56 (br, 4H, BArF$_{24}$), 7.32 (AA'XX' spin system, $^{3}J_{AX}$ = 8.6 Hz, 2H, H$_{Ar}$), 7.10 (AA'XX' spin system, $^{3}J_{AX}$ = 8.6 Hz, 2H, H$_{Ar}$), 5.33 (br, 2H, NCH$_2$), 4.75 (d, ^{3}J = 2.5 Hz, 2H, OCH$_2$), 4.27 (s, 2H, CH$_2$), 3.21 (m, 2H, CH$_2$), 2.59 (t, ^{3}J = 2.5 Hz, 1H, CCH), 1.71 (tt, $^{3,3}J$ = 7.7, 7.7 Hz, 2H, CH$_2$), 1.40 (tq, $^{3,3}J$ = 7.5, 7.5 Hz, 2H, CH$_2$), 0.95 (t, ^{3}J = 7.5 Hz, 3H, CH$_3$) ppm; ^{13}C NMR (176 MHz, [D$_2$]DCM, 298

K): δ = 162.36, 160.33, 135.38, 131.65, 129.38, 125.16, 121.22, 118.07, 117.10, 78.12, 76.60, 56.59, 54.40, 49.47, 28.95, 20.01, 13.55 ppm; ESI-HRMS: *m/z*: calcd for $[C_{46}H_{32}BF_{24}NO]$: 218.1539 $[M- BArF_{24}]^+$, found: 218.1538.

Diiodide 7

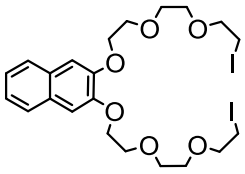

Potassium iodide (271 mg, 1.63 mmol) was dispersed in a solution of ditosylate **6** (300 mg, 0.41 mmol) in acetone (20 mL). After heating to reflux overnight, the solution was cooled to RT and the solvent was evaporated under reduced pressure. The residue was taken up in ethyl acetate (50 mL), washed with brine (3·50 mL) and the organic layer was dried over $MgSO_4$. After removing the solvent under reduced pressure, the desired product (230 mg, 0.36 mmol, 88%) was obtained as a pale yellow oil.

R_f = 0.60 in ethyl acetate; ^{1}H NMR (500 MHz, $CDCl_3$, 298 K): δ = 7.66 (AA'XX' spin system, $^3J_{AX}$ = 6.1 Hz, 4H, H_{Ar}), 7.33 (AA'XX' spin system, $^3J_{AX}$ = 6.1 Hz, 4H, H_{Ar}), 7.16 (s, 4H, H_{Ar}), 4.28 (t, ^3J = 5.6 Hz, 4H, CH_2), 3.95 (t, ^3J = 5.6 Hz, 4H, CH_2), 3.81 – 3.74 (m, 8H, CH_2), 3.71 – 3.67 (m, 4H, CH_2), 3.26 (m, 4H, CH_2) ppm.; ^{13}C NMR (126 MHz, $CDCl_3$): δ = 149.09, 129.43, 126.41, 124.34, 77.16, 72.08, 71.04, 70.42, 69.79, 68.56, 3.12 ppm. ESI-HRMS: *m/z*: calcd for $[C_{22}H_{30}I_2O_6]$: 682.9763 $[M+K]^+$, found: 682.9789.

Macrocycle 3

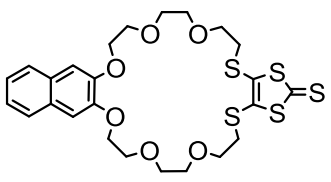

$CsOH·H_2O$ (662 mg, 3.94 mmol) was dissolved in dry MeOH (8 mL) under Ar atmosphere. This solution was added slowly over 30 min to thione **8** (600 mg, 1.97 mmol) in dry DMF (20 mL). After 1 h, the black solution was slowly added over 1 h to a solution of diiodide **7** (1270 mg, 1.97 mmol) in dry DMF (120 mL) at 0 °C. The mixture was allowed to warm to RT

and stirred overnight. Afterwards, solvent was removed under reduced pressure and the resulting residue was dissolved in DCM (100 mL). The organic layer was washed with brine (3 x 50 mL). After drying over $MgSO_4$, the solution was concentrated under reduced pressure and the residue was purified by column chromatography (SiO_2, DCM→EE = 100:1) to yield the desired product (705 mg, 1.20 mmol, 61%) as a yellow solid.

R_f = 0.30 in DCM; m.p. 138 °C; ^{1}H NMR (500 MHz, $CDCl_3$, 298 K): δ = 7.66 (AA'XX' spin system, $^3J_{AX}$ = 6.1, 2H, H_{Ar}), 7.32 (AA'XX' spin system, $^3J_{AX}$ = 6.1, 2H, H_{Ar}), 7.12 (s, 2H, H_{Ar}), 4.30 – 4.24 (m, 4H, OCH_2), 4.02 – 3.95 (m, 4H, OCH_2), 3.85 – 3.80 (m, 4H, OCH_2), 3.74 (t, ^3J = 5.9 Hz, 4H, $C\underline{H}_2CH_2S$), 3.70 – 3.66 (m, 4H, OCH_2), 3.06 (t, ^3J = 5.9 Hz, 4H, CH_2S) ppm; ^{13}C NMR (126 MHz, $CDCl_3$, 298 K): δ = 211.32, 149.03, 136.89, 129.39, 126.41, 124.36, 108.23, 71.18, 70.87, 69.84, 69.82, 69.01, 36.49 ppm; ESI-HRMS: *m/z*: calcd for $[C_{25}H_{30}O_6S_5]$: 609.0538 $[M+Na]^+$, found: 609.0568.

Divalent Macrocycle 4

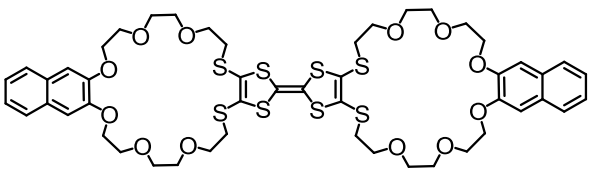

Macrocycle precursor **3** (100 mg, 170 µmol) was suspended in $P(OEt)_3$ (8 mL) and the mixture was heated to 130 °C in a sealed tube under Ar. After 40 min, the reaction was cooled to 0 °C. The formed precipitate was filtered off and washed with cold MeOH (3·2 mL). The crude product was purified by column chromatography (SiO_2, DCM→DCM/MeOH (50:1)) to obtain the desired product (67 mg, 60 µmol, 71%) as orange solid.

R_f = 0.75 in DCM/MeOH (50:1); m.p. 205 °C; ^{1}H NMR (500 MHz, $[D_2]$DCM, 298 K): δ = 7.66 (AA'XX' spin system, $^3J_{AX}$ = 6.2 Hz, 4H, H_{Ar}), 7.31 (AA'XX' spin system, $^3J_{AX}$ = 6.2 Hz, 4H, H_{Ar}), 7.13 (s, 4H, H_{Ar}), 4.30 – 4.17 (m, 8H, OCH_2), 3.92 (m, 8H, OCH_2), 3.77 (m, 8H, OCH_2), 3.77 (m, 8H, CH_2CH_2S), 3.66 (m, 8H, OCH_2), 3.00 (m, 8H, CH_2CH_2S) ppm; ^{13}C (176 MHz, $[D_2]$DCM, 298 K): δ = 149.59 , 129.88 , 128.85 , 126.78 , 124.72 , 111.06 , 108.48 , 71.41 , 71.14, 70.27, 70.12, 69.35, 36.30 ppm; UV/Vis (DCM): λ^{max} (ε) = 324 nm (20700 $L \cdot mol^{-1} \cdot cm^{-1}$); ESI-HRMS: *m/z*: calcd for $[C_{50}H_{60}O_{12}S_8]$: 1131.1748 $[M+Na]^+$, found: 1131.1715.

Divalent [2]Rotaxane 5

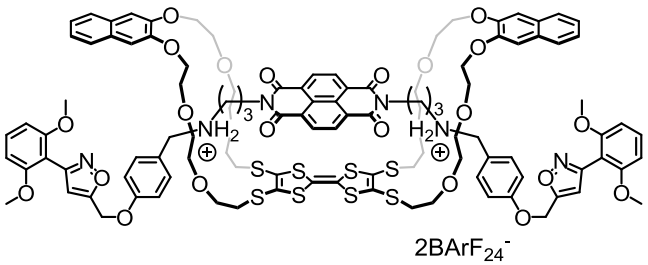

Axle **1** (12.0 mg, 5.00 µmol) and divalent macrocycle **4** (5.55 mg, 5.00 µmol) were dissolved in DCM (5 mL). Afterwards, 2,6-dimethoxybenzonitrile oxide (4.39 mg, 24.5 µmol) was added and the mixture was heated to 38 °C under Ar in a sealed tube for 8 days. Afterwards, the solution was dialyzed (MWCO 1 kD, against DCM) for 1 d. After removing the solvent under reduced pressure, the residue was purified by column chromatography (SiO_2, DCM→DCM/MeOH = 80:1). The desired rotaxane (17.1 mg, 4.42 µmol, 89%) was obtained as green oil.

R_f = 0.60 in DCM/MeOH (20:1); ^{1}H NMR (700 MHz, [D$_2$]DCM, 298 K): δ = 8.70 (s, 4H, NDI), 7.76 – 7.70 (br, 16H, $BArF_{24}$), 7.68 (m, 4H, H_{Ar}), 7.56 (br, 8H, $BArF_{24}$), 7.42 (br, 4H, NH_2^+), 7.37 (m, 6H, H_{Ar}), 7.25 (AA'XX' spin system $^3J_{AX}$ = 8.3 Hz, 4H, H_{Ar}), 7.08 (s, 4H, H_{Ar}), 6.71 (AA'XX' spin system $^3J_{AX}$ = 8.3 Hz, 4H, H_{Ar}), 6.67 (AXX' spin system $^3J_{AX}$ = 8.4 Hz, 4H, H_{ar}), 6.36 (s, 2H, H_{isox}), 4.63 (s, 4H, CH_2), 4.38 (m, 4H, CH_2), 4.28 (m, 16H, CH_2), 4.00 (s, 4H, CH_2), 3.77 (s, 12H, H_{Ar}), 3.93 – 3.56 (m, glycol signals), 3.03 (m, 4H, CH_2), 2.96 (m, 8H, CH_2), 2.18 (p, ^3J = 7.2 Hz, 4H, CH_2) ppm; ^{13}C NMR (176 MHz, [D$_2$]DCM, 298 K): δ = 166.15, 163.39, 162.34, 159.55, 159.20, 157.76, 147.21, 135.39, 131.96, 131.78, 131.65, 129.47, 127.21, 126.99, 126.87, 126.09, 125.90, 125.11, 118.06, 115.58, 108.87, 108.60, 107.32, 107.23, 104.70, 72.30, 71.36, 70.79, 70.39, 69.49, 61.17, 56.75, 56.51, 53.23, 47.45, 38.58, 36.60, 35.89, 25.87 ppm; UV/Vis (DCM): λ^{max} (ε) = 323 (25800), 382 (20300), 750 nm (430 L·mol^{-1}·cm^{-1}); ESI-HRMS: *m/z*: calcd for [$C_{108}H_{116}N_6O_{24}S_8^{2+}$]: 1068.7913 [M]$^{2+}$, found: 1068.7897.

Additional Analytical Data

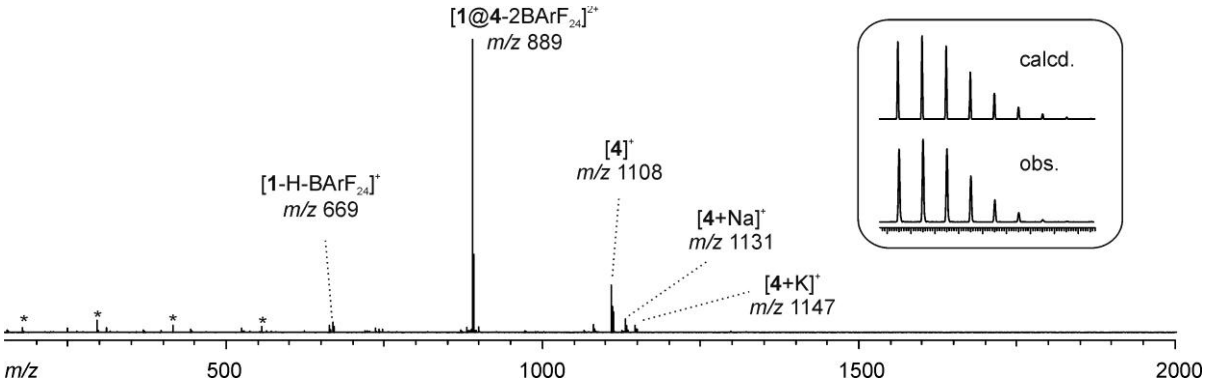

Figure S4. ESI-FTICR mass spectrum from a DCM solution of a 1:1 mixture of axle **1** and macrocycle **4** (50 μM). Clearly, only one prominent signal at *m/z* 889 is observed which corresponds to the divalent pseudorotaxane [**1**@**4**-2HBArF$_{24}$]$^{2+}$. No signal for oligomeric species was detected. The small signals at *m/z* 669, 1108, 1131 and 1147 correspond to the free axle **1** or to the macrocylce **4** and its sodium and potassium adducts. Interference frequencies are marked with an asterisk.

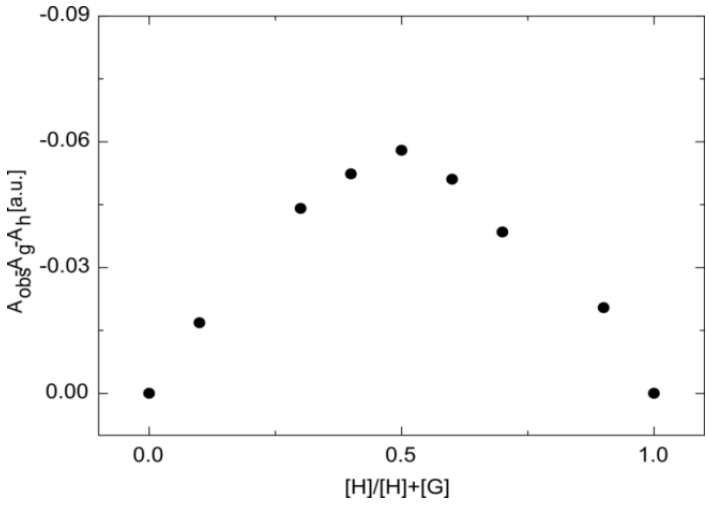

Figure S5. Job plot of pseudo[2]rotaxane **1**@**4** in DCM at 298 K. The sum of concentration was kept constant at 0.5 x 10^{-5} M. Absorbance intensity was recorded at 342 nm following π-π* transitions.

Isothermal Titration Calorimetry (ITC)

Solvent Dependence of Binding Constants

Due to its high volatility, dichloromethane makes ITC measurements at 25 °C difficult. Therefore, we used 1,1,2,2-tetrachloroethane (TCE) instead. We investigated different mixtures with acetonitrile (ACN) and observed a strong decrease of binding strength in a monovalent complex upon addition of ACN. This trend was previously observed[22] for crown/ammonium complexes with PF_6^- counter ions and attributed to the more polar solvent competing with host-guest complex formation. In our system, this effect is expressed even stronger due to the weaker coordinating $BArF_{24}^-$ ion. For reliable measurements, we choose TCE/ACN 50:1 as suitable solvent mixture.

Cooperativity

For the divalent complex under study, allosteric and chelate cooperativity were considered. Allosteric cooperativity describes for if the first binding event in a 1:2 complex facilitates or hampers the second binding event. It can be considered seperately for both the divalent host and the divalent guest. Allosteric cooperativity factors α_G and α_H can be expressed by the following equations:[23]

$$\alpha_G = \frac{K^{b1} \cdot K^{b2}}{(K^d)^2} \qquad \text{eq. S1}$$

$$\alpha_H = \frac{K^{c1} \cdot K^{c2}}{(K^d)^2} \qquad \text{eq. S2}$$

The binding constants K^{b1} and K^{b2} correspond to the two binding events of a monovalent host to a divalent guest and K^d is the binding constant of a monovalent model compound. A divalent compound exhibits positive allosteric cooperativity if $\alpha > 1$ and negative allosteric cooperativity if $\alpha < 1$.

In contrast, chelate cooperativity only operates in complexes of two di- or multivalent host/guest compounds. Hunter and Anderson[24] as well as Ercolani and Schiaffino[23] defined different chelate cooperativity factors *β and β*'.

$$\beta = K_{\text{mono}} \cdot EM \qquad \text{eq. S3}$$

$$\beta' = \frac{EM}{4[H]} \qquad \text{eq. S4}$$

Both cooperativity factors imply positive cooperativity if they are larger than 1 and are defined with the effective molarity *EM*, which describes the limit concentration where closed multivalent 1:1 complexes and open oligomers are present in a 50:50 ratio. At concentrations

lower than *EM* the closed complex dominates. *EM* is determined by a DMC analysis as described in detail before.[25, 26]

ITC Data and Titration Plots

Table 3. Thermodynamic binding data of the components of the double mutant cycle of complex **1@4** as obtained from ITC titrations (TCE/ACN (50:1), 298 K).

		K_a / 10^3 M^{-1}	ΔG / kJ mol^{-1}	ΔH / kJ mol^{-1}	$T\Delta S$ / kJ mol^{-1}	α	*EM* / mM	β	β^*
1@4	K^a	309 ± 31	-31.4 ± 0.2	-45.5 ± 0.7	-14.1 ± 0.9		27 ± 6	61 ± 15	7 ± 2
1@3	K^{b1}	10.1 ± 1.0	-22.9 ± 0.2	-27.9 ± 1.5	-5.1 ± 1.7	0.51 ± 0.09			
	K^{b2}	1.0 ± 0.1	-17.2 ± 0.3	-25.5 ± 0.2	-8.2 ± 0.5				
2@4	K^{c1}	9.0 ± 1.0	-22.6 ± 0.2	-31.6 ± 0.2	-8.9 ± 0.4	1.10 ± 0.19			
	K^{c2}	2.5 ± 0.3	-19.4 ± 0.3	-20.7 ± 1.7	-1.3 ± 1.9				
2@3	K^d	4.5 ± 0.5	-20.8 ± 0.3	-29.5 ± 0.6	-8.6 ± 0.9				

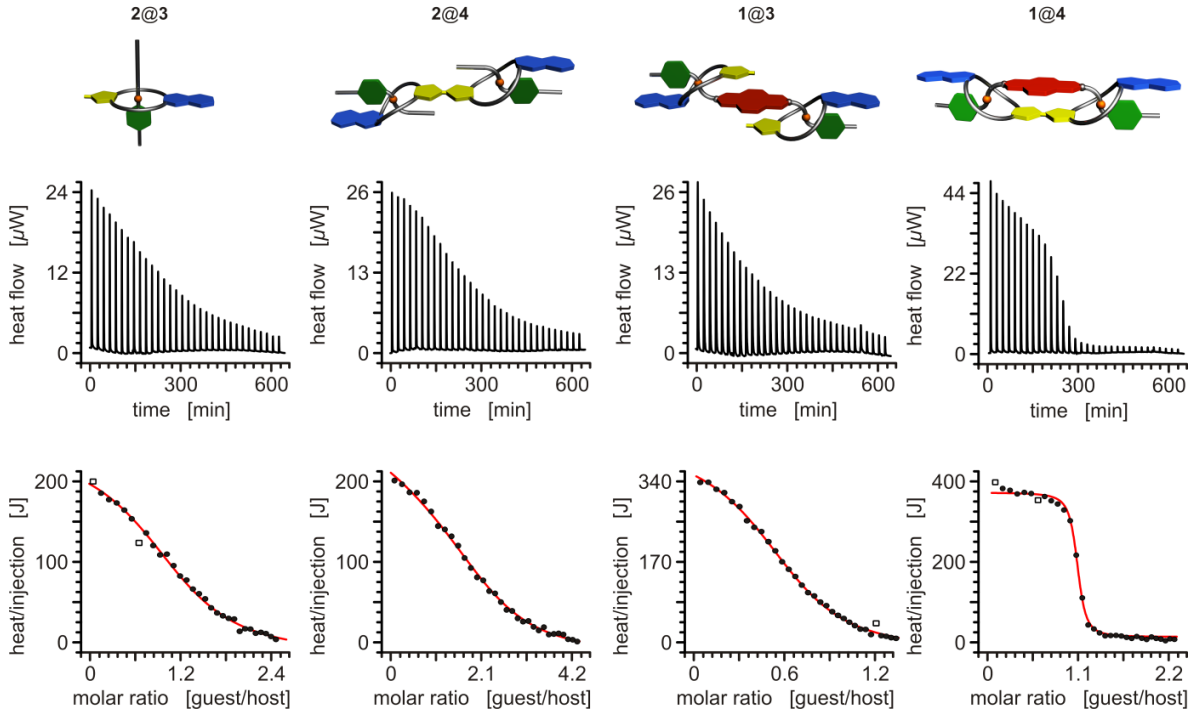

Figure S6. Titration Plots (heat flow versus time and heat/volume versus guest/host ratio) obtained from ITC experiments concerning the double mutant cycle of **1@4** in TCE/ACN 50:1 (v/v)**.** Points marked with a non-filled square were not considered in the fitting process.

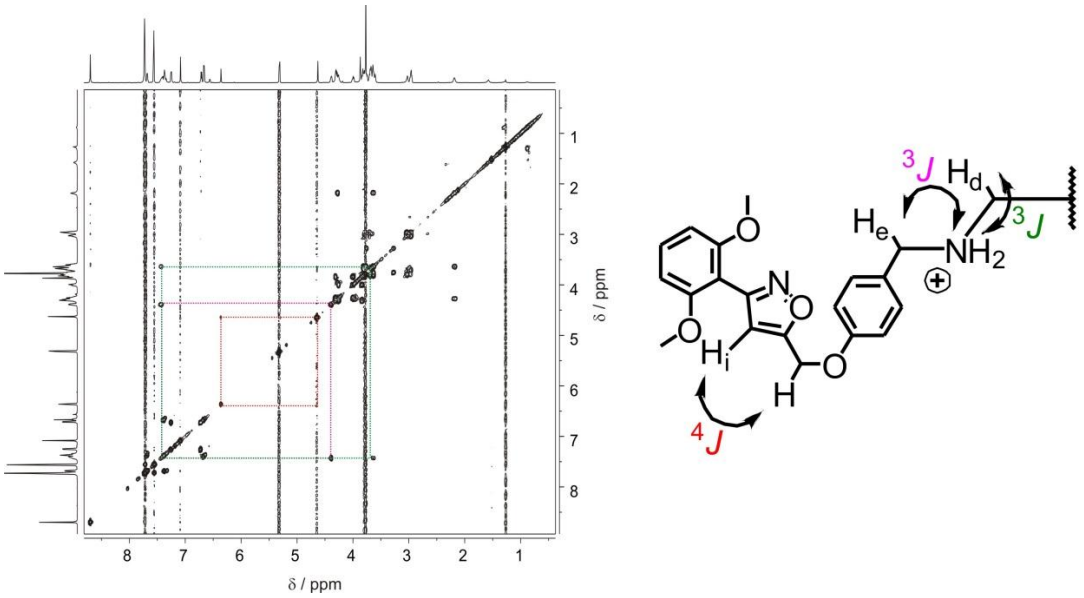

Figure S7. 700 MHz H,H-COSY spectrum of [2]rotaxane **5** in [D_2]DCM. The protons H_i, H_e and H_d can clearly be identified by cross peaks as indicated in the structure on the right.

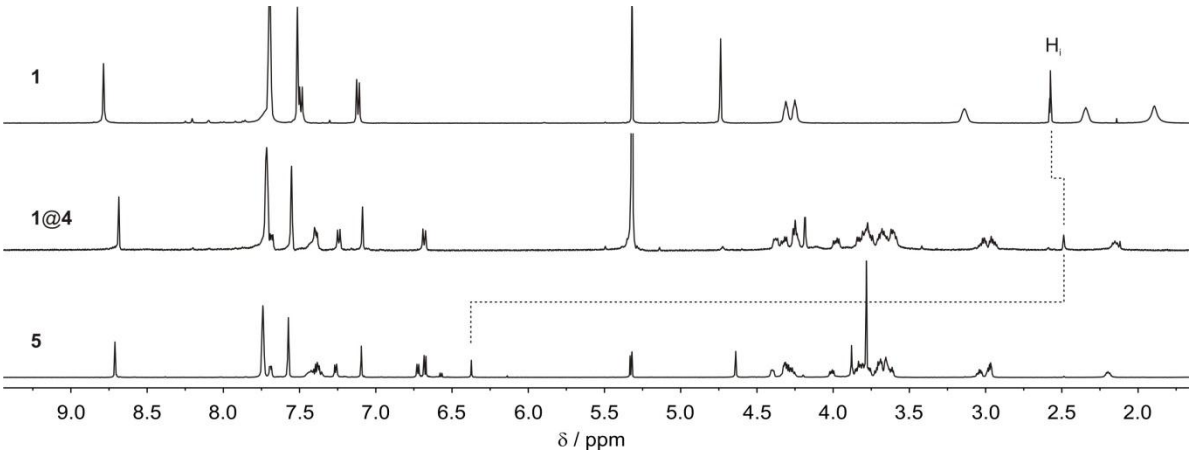

Figure S8. ^{1}H NMR spectra (500 MHz) of axle **1**, pseudo[2]rotaxane **1@4** and [2]rotaxane **5** in [D_2]DCM. The signal for protons H_i shift to lower field in [2]rotaxane **5** due to the incorporation in the isoxazole unit. The absence of other isoxazole signals indicates a C_2-symmetric doubly-threaded species.

Additional IRMPD Data, Fragmentation Pathways and Fragment Structures

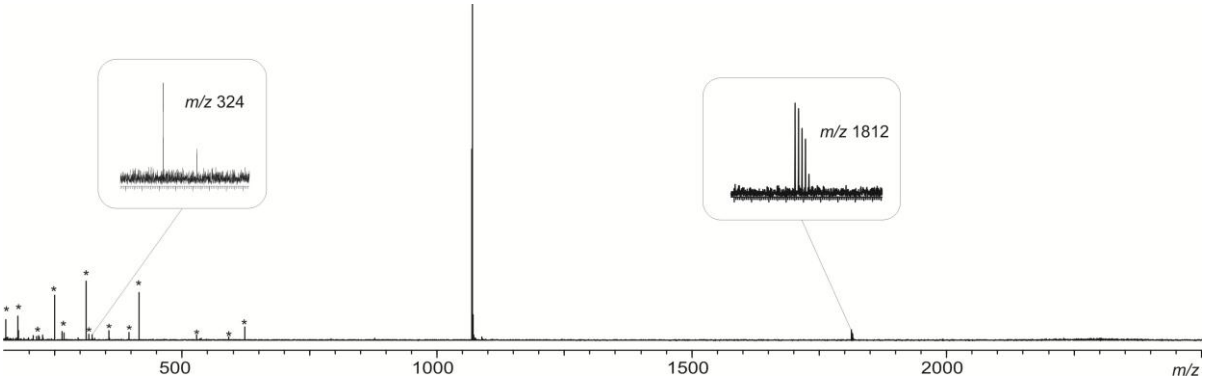

Figure S9. IRMPD experiment with mass-selected *m/z* 1068. At low laser intensity, the CN-bond breaks first and yields two singly charged fragments at *m/z* 324 and 1812. Interference frequencies are marked with an asterisk.

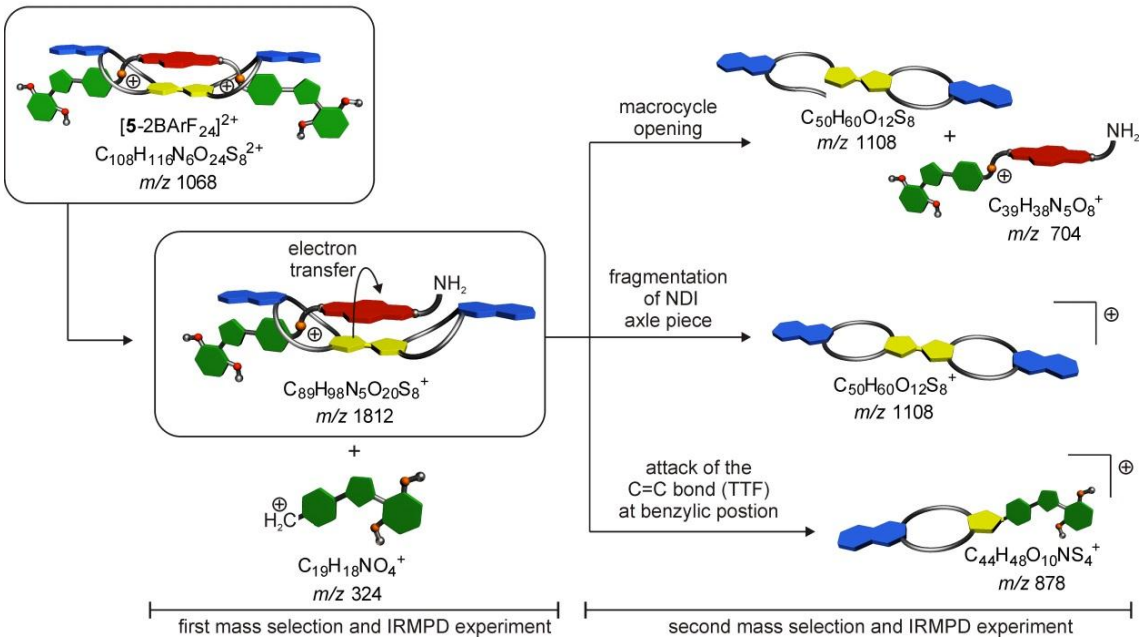

Figure S10. Fragmentation pathways and assignment of observed signals to fragments.

Additional UV/Vis and fluorescence data of [2]rotaxane 5

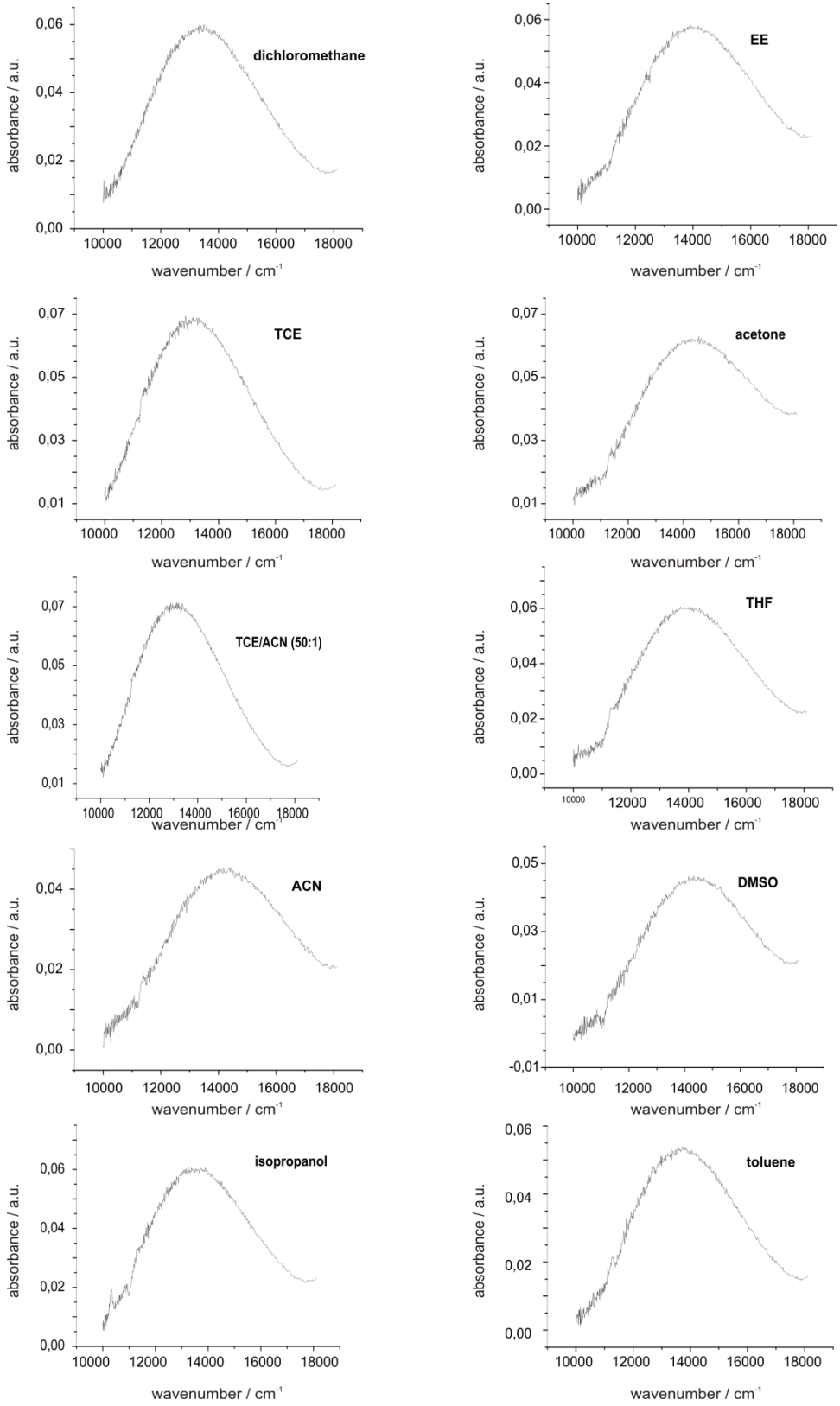

Figure S11. ICT bands of [2]rotaxane **5** ($1.4 \cdot 10^{-4}$ M) in different solvents.

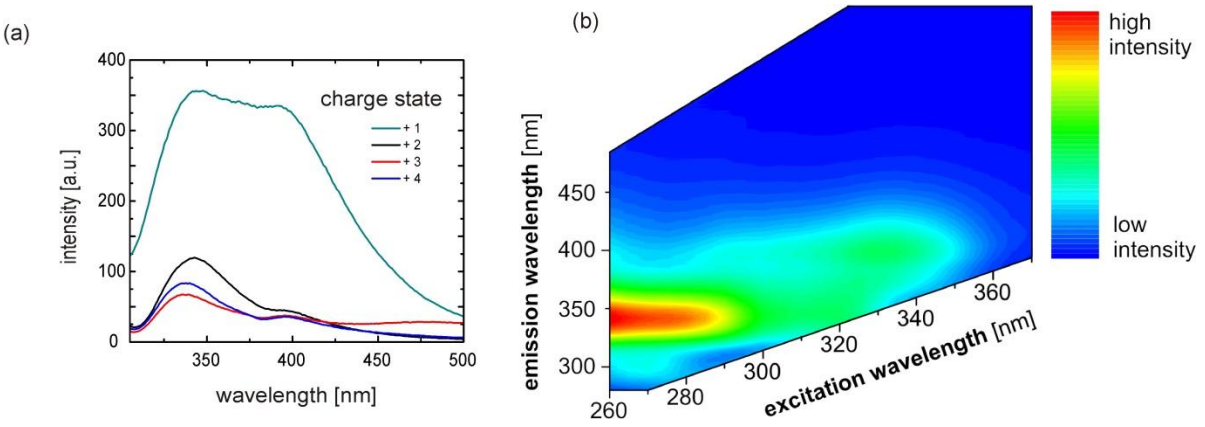

Figure S12. Fluorescence properties of rotaxane **5** ($1.5 \cdot 10^{-5}$ M) in DCM at 298 K: (a) Fluorescence spectra in different charge states after addition of oxidation or reducing agent with λ_{em} = 290 nm; (b) excitation-emission-matrix.

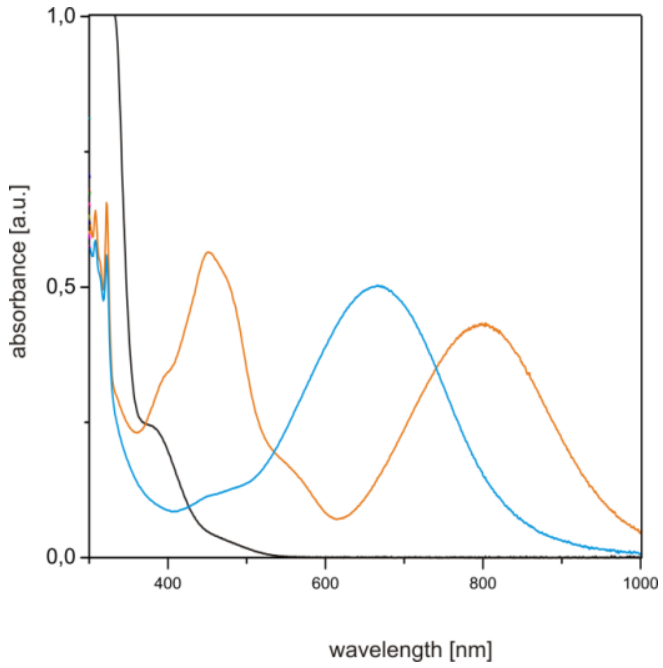

Figure S13. UV/vis spectra of divalent host **4** in neutral (black line) state, after first oxidation (orange line) and second oxidation (blue line). Spectra were recorded in DCM at 298 K.

^{1}H NMR and ^{13}C NMR Spectra of Reported Compounds

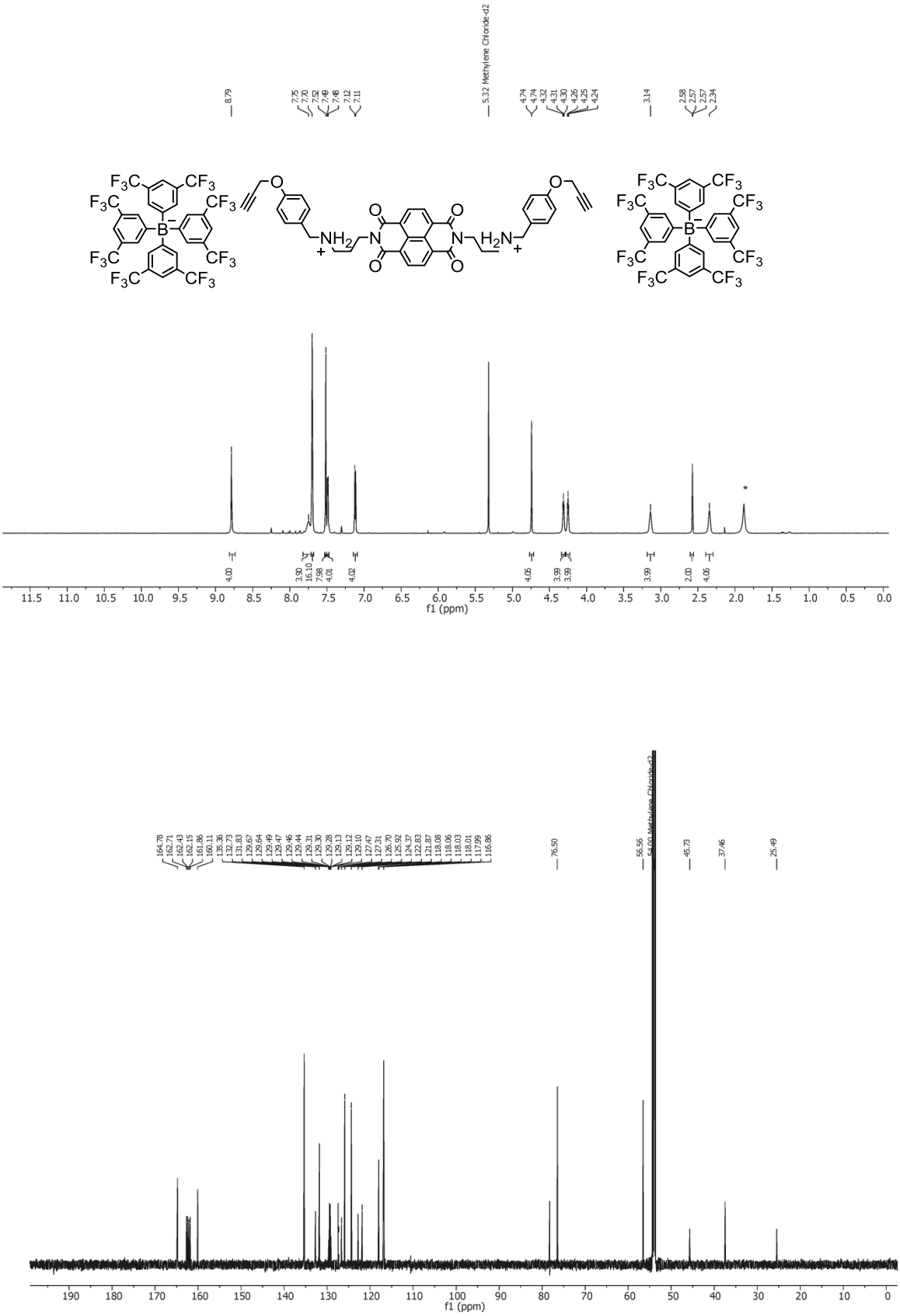

Figure S14. ^{1}H (top) and ^{13}C (bottom) NMR spectra of divalent axle **1** in [D_2]DCM at 298 K.

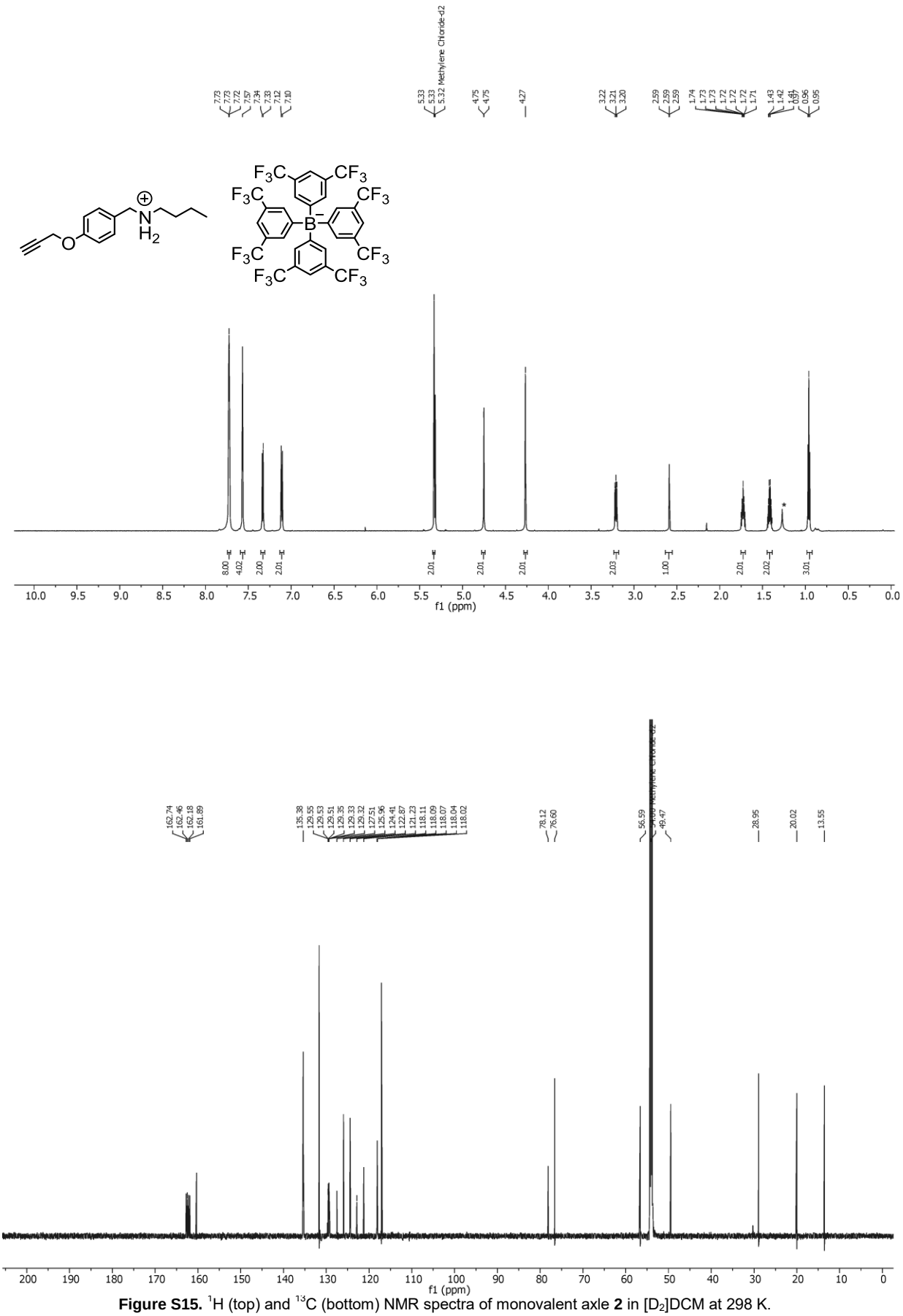

Figure S15. ^{1}H (top) and ^{13}C (bottom) NMR spectra of monovalent axle **2** in [D_2]DCM at 298 K.

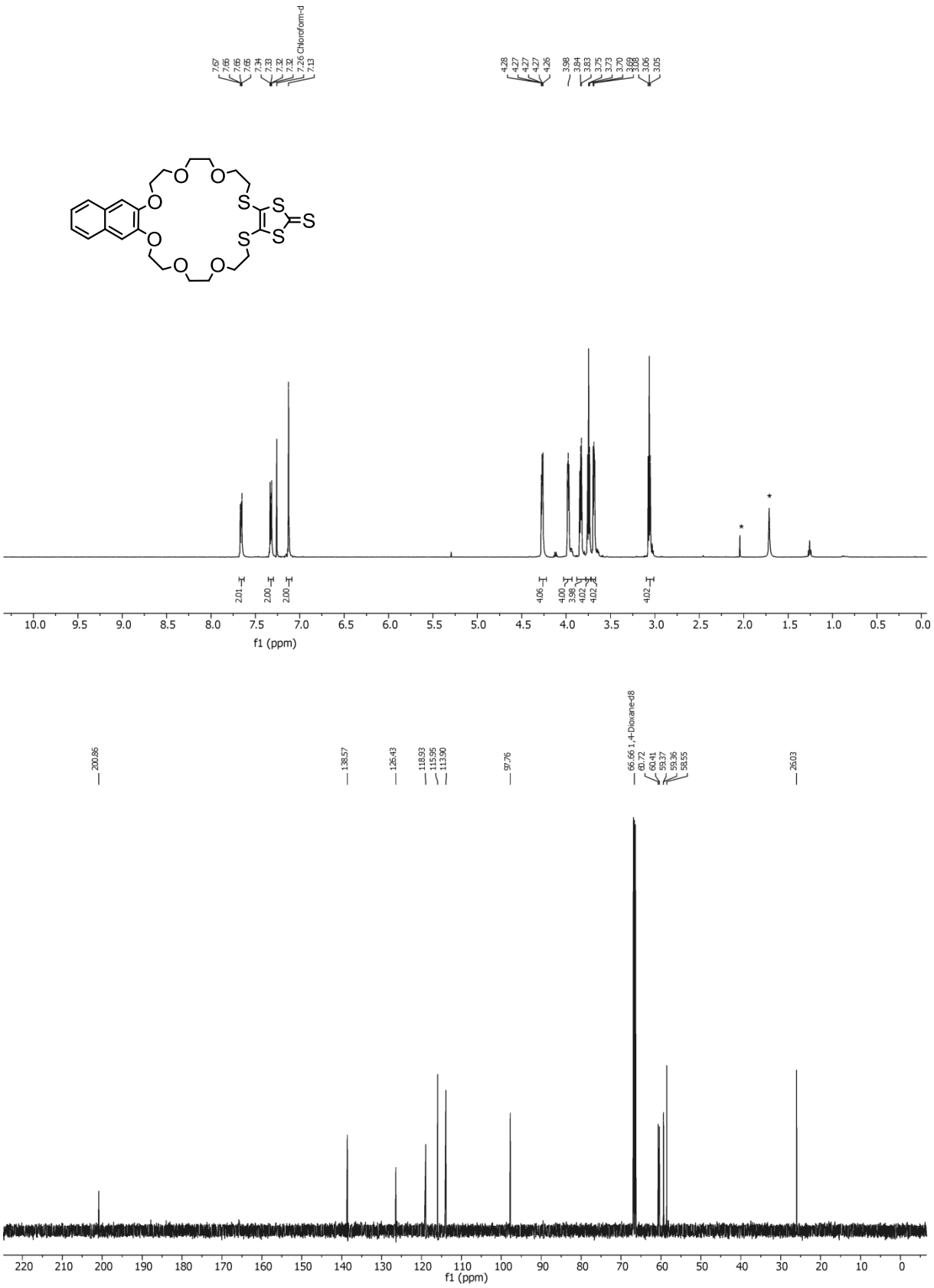

Figure S16. ^{1}H (top) and ^{13}C (bottom) NMR spectra of monovalent macrocycle **3** in $CDCl_3$ at 298 K.

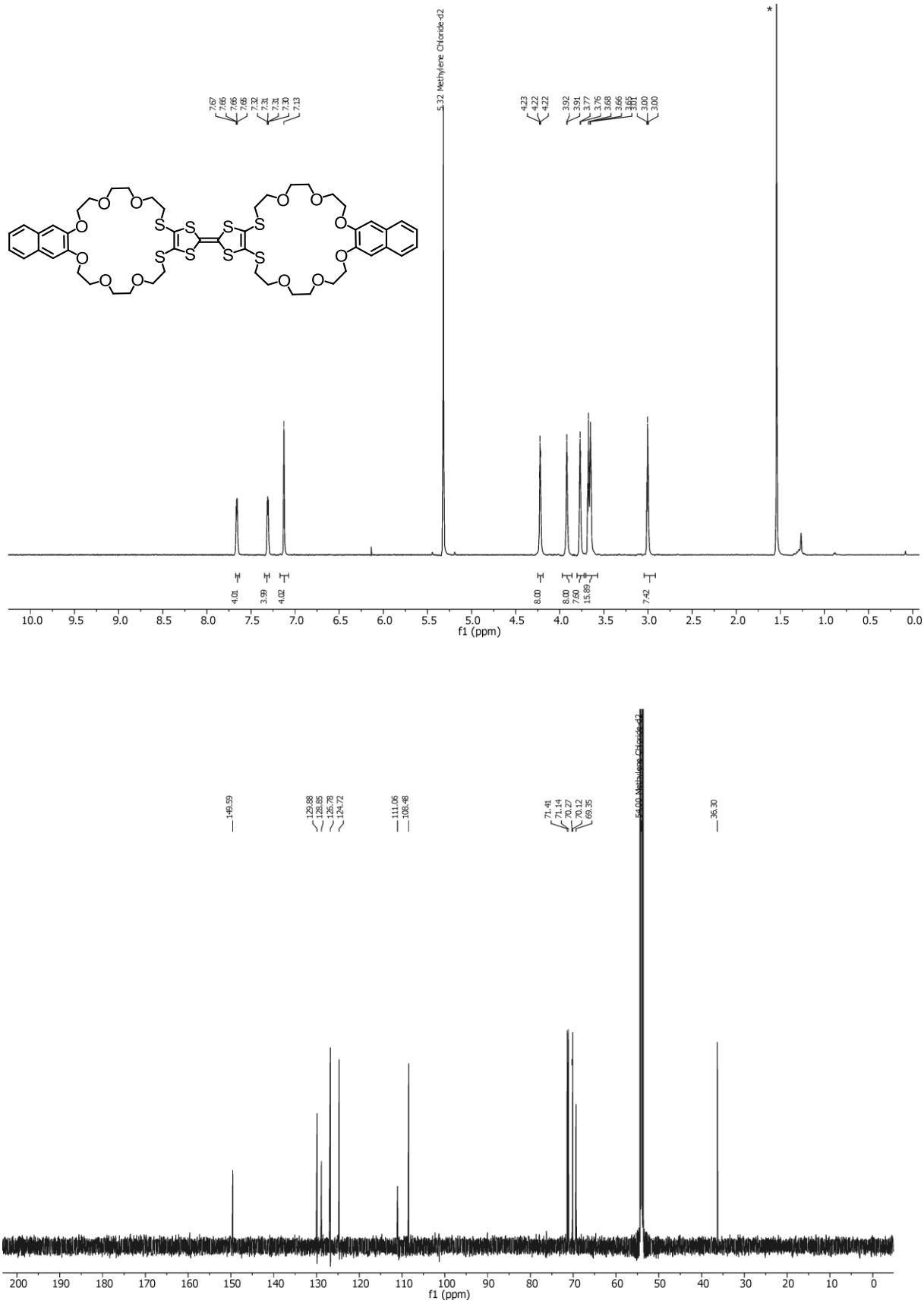

Figure S17. ^{1}H (top) and ^{13}C (bottom) NMR spectra of divalent macrocycle **4** in [D_2]DCM at 298 K.

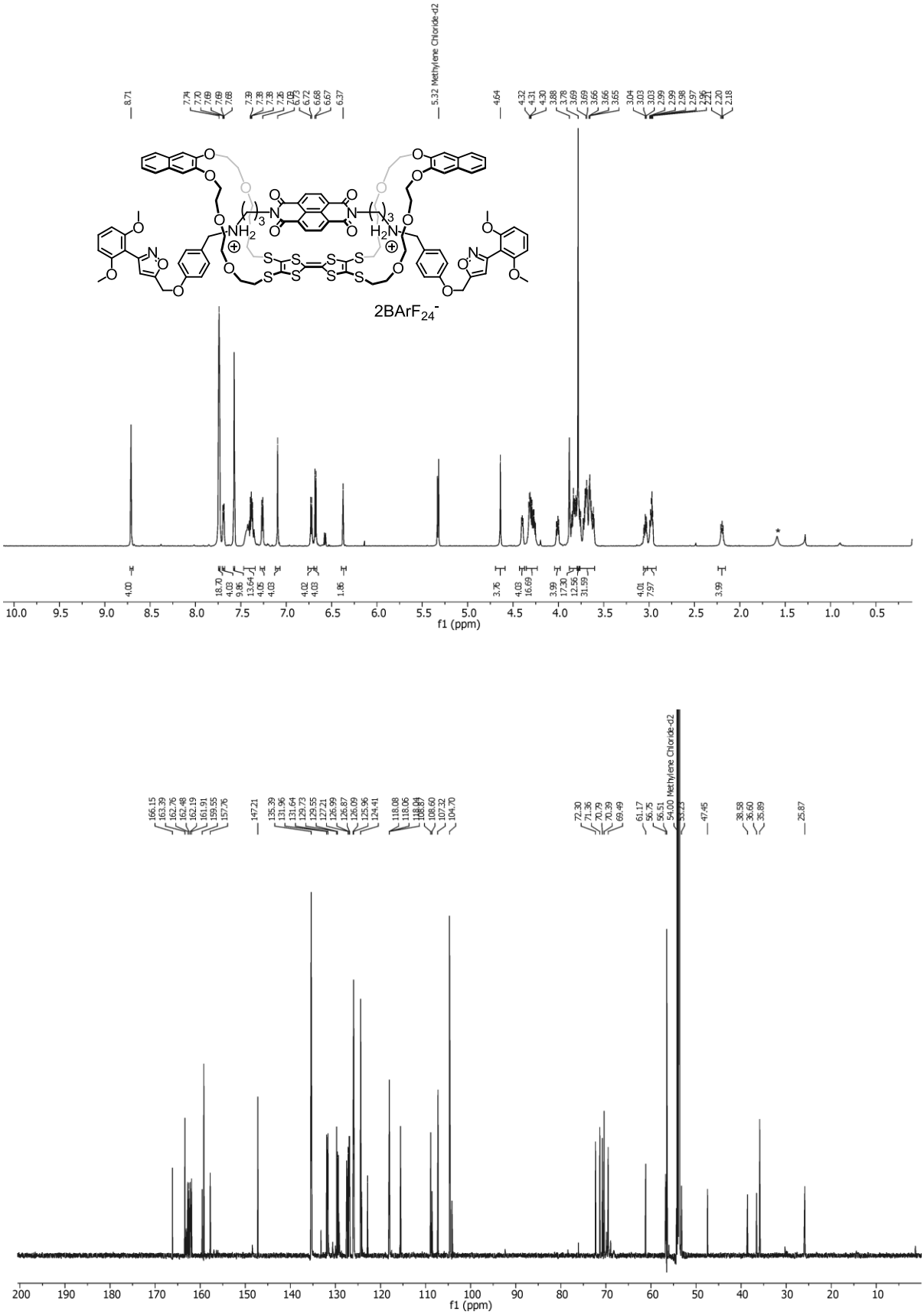

Figure S18. ^{1}H (top) and ^{13}C (bottom) NMR spectra of [2]rotaxane **5** in [D_2]DCM at 298 K.

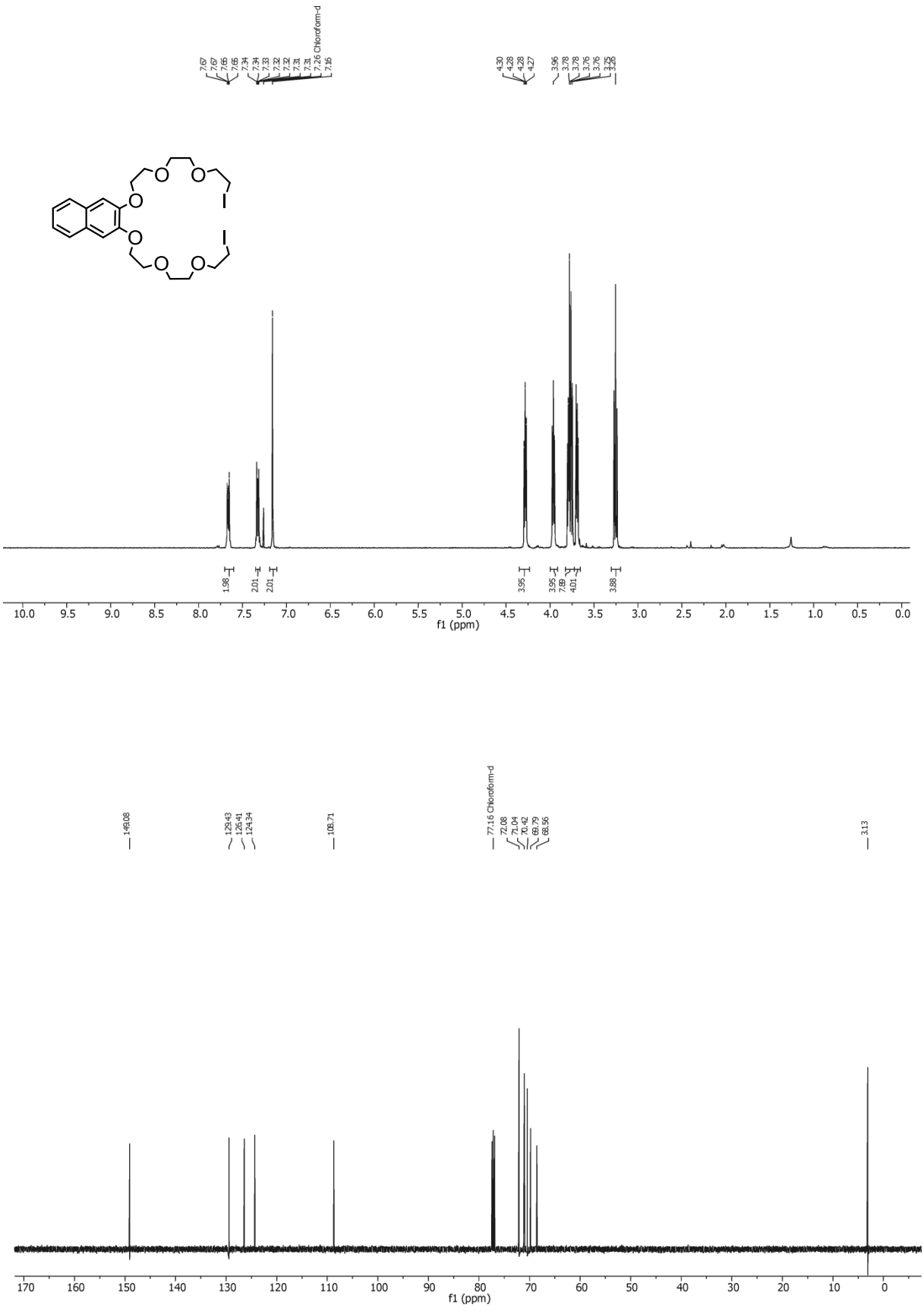

Figure S19. ^{1}H (top) and ^{13}C (bottom) NMR spectra of diiodide **7** in $CDCl_3$ at 298 K.

Supporting Information References

[1] D.-W. Hahn, D.-M. Byun, J. Tae, *Eur. J. Org. Chem.* **2005**, 63.

[2] W. Jiang, M. Han, H. Y. Zhang, Z. J. Zhang, Y. Liu, *Chem. Eur. J.* **2009**, *15*, 9938.

[3] N. Svenstrup, K. M. Rasmussen, T. K. Hansen, J. Becher, *Synthesis* **1994**, *1994*, 809.

[4] X.-Z. Zhu, C.-F. Chen, *J. Am. Chem. Soc.* **2005**, *127* , 13158.

[5] T. Matsumura, F. Ishiwari, Y. Koyama, T. Takata, *Org. Lett.* **2010**, *12*, 3828.

[6] J. R. Aranzaes, M.-C. Daniel, D. Astruc, *Can. J. Chem.* **2006**, *84*, 288.

[7] TURBOMOLE V7.0.1 2015, A development of University of Karlsruhe and Forschungszentrum Karlsruhe GmbH, 1989–2007, TURBOMOLE GmbH, since 2007. Available at: http://www.turbomole.com.

[8] J. Tao, J. P. Perdew, V. N. Staroverov, G. E. Scuseria, *Phys. Rev. Lett.* **2003**, *91*, 146401.

[9] S. Grimme, S. Ehrlich, L. Goerigk, *J. Comput. Chem.* **2011**, *32*, 1456.

[10] S. Grimme, J. Antony, S. Ehrlich, H. Krieg, *J. Chem. Phys.* **2010**, *132*, 154104.

[11] K. Eichkorn, O. Treutler, H. Öhm, M. Häser, R. Ahlrichs, *Chem. Phys. Lett.* **1995**, *240*, 283.

[12] M. Sierka, A. Hogekamp, R. Ahlrichs, *J. Chem. Phys.* **2003**, *118*, 9136.

[13] F. Weigend, M. Häser, H. Patzelt, R. Ahlrichs, *Chem. Phys. Lett*. **1998**, *294,* 143.

[14] F. Weigend, Phys. *Chem. Chem. Phys*. **2006**, *8*, 1057.

[15] P. A. M. Dirac, *Proc. Royal Soc. (London) A* **1929***, 123,* 714.

[16] J.C. Slater*, Phys. Rev.* **1951,** *81*, 385.

[17] S.H. Vosko, L. Wilk, M. Nusair, *Can. J. Phys*. **1980**, *58*, 1200.

[18] A.D. Becke, *Phys. Rev. A* **1988**, *38*, 3098.

[19] C. Lee, W. Yang, R. G. Parr, *Phys. Rev. B* **1988**, *37*, 785.

[20] A. D. Becke, *J. Chem. Phys.* **1993**, *98*, 5648.

[21] A. Klamt, G. Schüürmann, *J. Chem. Soc. Perkin Trans.* **1993**, *2*, 799.

[22] J. W. Jones, H. W. Gibson, *J. Am. Chem. Soc.* **2003**, *125*, 7001.

[23] G. Ercolani, L. Schiaffino, *Angew. Chem. Int. Ed.* **2011**, *50*, 1762.

[24] C. A. Hunter, H. L. Anderson, *Angew. Chem. Int. Ed.* **2009**, *48*, 7488.

[25] K. Nowosinski, L. K. S. von Krbek, N. L. Traulsen, C. A. Schalley, *Org. Lett.* **2015**, *17*, 5076.

[26] L. K. S. von Krbek, A. J. Achazi, M. Solleder, M. Weber, B. Paulus, C. A. Schalley, *Chem. Eur. J.* **2016**, 15475.

6.2 Impact of mechanical bonding on the redox-switching of tetrathiafulvalene in crown ether-ammonium [2]rotaxanes

H.V. Schröder, S. Sobottka, M. Nößler H. Hupatz, M. Gaedke B. Sarkar, C.A. Schalley

Chem. Sci. **2017**, *8*, 6300-6306.

Submitted on June 16, 2017, first published on July 10, 2017 by he Royal Society of Chemistry.

An electronic version of the articles is available at: https://doi.org/10.1039/C7SC02694C

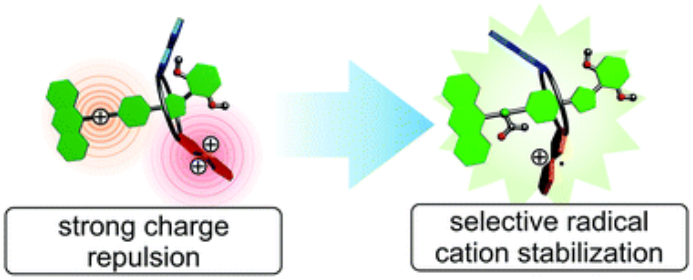

Figure 6.2. Graphical abstract. Reprinted with permission from Schröder *et al.*[248] (published by the Royal Society of Chemistry, under the CC BY-NC 3.0 licence).

Authors' contributions

Hendrik V. Schröder developed the general concept of this project. Christoph A. Schalley and Hendrik V. Schröder wrote the manuscript together with main contribution coming from Hendrik V. Schröder. Syntheses of the compounds were done by Maite Nößler and Hendrik V. Schröder. Hendrik V. Schröder further contributed with NMR, UV/Vis, CV, and fluorescence experiments. Sebastian Sobottka and Hendrik V. Schröder conducted the EPR measurements. Digital simulations were performed by Sebastian Sobottka and evaluated together with Biprajit Sarkar. I performed and evaluated the ITC measurements. Marius Gaedke did the IRMPD experiments. All authors contributed to the final version of the manuscript.

Chemical Science

EDGE ARTICLE

View Article Online
View Journal | View Issue

Cite this: *Chem. Sci.*, 2017, **8**, 6300

Impact of mechanical bonding on the redox-switching of tetrathiafulvalene in crown ether–ammonium [2]rotaxanes†

Hendrik V. Schröder,[a] Sebastian Sobottka,[b] Maite Nößler,[a] Henrik Hupatz,[a] Marius Gaedke,[a] Biprajit Sarkar[b] and Christoph A. Schalley *[a]

Received 16th June 2017
Accepted 7th July 2017

DOI: 10.1039/c7sc02694c

rsc.li/chemical-science

Switchable crown ether–ammonium [2]rotaxanes with a redox-active tetrathiafulvalene (TTF) unit implemented in their wheels were synthesised and fully characterised. Reversible operation in two modes is possible, in which the [2]rotaxane's axle is either charged or neutral. Cyclic voltammetry experiments reveal the effects of mechanical bonding on the electrochemical properties of TTF and show the [2]rotaxanes to perform a distinct function in both modes. In the charged mode, redox-switching is dominated by strong electrostatic repulsion in the [2]rotaxane which subsequently leads to a macrocycle translation along the axle. In the non-charged mode, a selective energetic stabilisation of TTF radical cations is observed, which can be attributed to an interplay of weak electrostatic interactions between wheel and axle.

Introduction

Mechanically interlocked molecules (MIMs) such as rotaxanes and catenanes have attracted increasing attention during the last decades not only because of their fascinating structure, but also because of unique properties caused by the mechanical bond.[1] Even very weak interactions, which would be negligible for non-interlocked complexes, can become significant, when the mechanical bond prevents dissociation.[2] As an early example, Sauvage and co-workers reported the "catenand effect" which describes the kinetic stabilisation of interlocked copper(I) complexes in comparison to their non-interlocked analogues.[3] Similar effects were observed for the neutralisation of crown ether–ammonium rotaxanes:[4] while a pseudorotaxane of this type is easily deprotonated, this is very challenging for the interlocked rotaxane without the aid of a second cationic station.[5] Until today, many researchers have tried to fathom these not yet fully understood phenomena and use them to create different emergent properties in MIMs.

A major aim in the field of MIMs is the design of switchable artificial molecular machines which can undergo dynamic conformational changes by applying external stimuli.[6] Archetypical examples for molecular machines are switchable rotaxane shuttles in which the macrocycle can undergo a translational movement relative to its axle counterpart.[7] Recently, molecular machinery based on shuttles was extended through more sophisticated architectures such as molecular elevators,[8] muscles,[9] pumps,[10] or even molecular motors.[11] However, the reported systems are often bistable and therefore limited for multi-purpose applications. The design and preparation of multistable molecular machines is therefore an appealing synthetic target for supramolecular chemists.[12] Furthermore, possible applications of MIMs such as information processing require fast and clean switching as well as easily readable output signals. This renders electrochemical and optical inputs and output most promising.[13]

Here, we report a novel tri-stable rotaxane based on the widely used 24-crown-8/secondary ammonium motif.[14] It incorporates a redox-switchable tetrathiafulvalene (TTF) unit in its wheel. TTF is a versatile organosulfur compound which can undergo two clean and reversible successive one-electron oxidations to generate the stable radical cation $TTF^{+\bullet}$ and the dication TTF^{2+}.[15] TTF-crown ether macrocycles have been described as redox-responsive and switchable supramolecular receptors for different metal cations.[16] Furthermore, Stoddart and co-workers reported pseudo[2]rotaxanes assembled from TTF-substituted crown ethers and dibenzylammonium hexafluorophosphate and concluded that the ammonium thread is not affecting the electronic properties of the TTF moiety.[17] In contrast, we recently showed the redox properties of a TTF-substituted crown ether in a divalent charge-transfer rotaxane to be strongly affected by the axle, when using media of low dielectric constant and weakly coordinating anions (WCAs) such as tetrakis(3,5-bis(trifluoromethyl)phenyl)borate ($BArF_{24}^-$).[18]

[a]*Institut für Chemie und Biochemie, Freie Universität Berlin, Takustr. 3, 14195 Berlin, Germany. E-mail: christoph@schalley-lab.de*

[b]*Institut für Chemie und Biochemie, Freie Universität Berlin, Fabeckstr. 34/36, 14195 Berlin, Germany*

† Electronic supplementary information (ESI) available: Synthetic procedures and full characterisation of new compounds, tandem MS experiments, ITC data, full electrochemical experiments and additional NMR data. See DOI: 10.1039/c7sc02694c

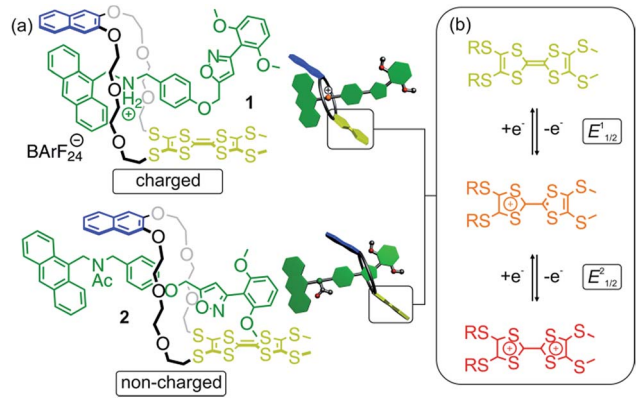

Fig. 1 (a) Structures of [2]rotaxanes **1** and **2** and cartoons representing them. (b) Schematic representation of the stepwise and reversible oxidations of the thioalkyl-substituted tetrathiafulvalene moiety.

Consequently, this observation opens the pathway for the construction of a novel class of redox-active MIMs which exhibit a strong effect on the electronic properties of TTF by the mechanical bond.

The rotaxanes reported here can be operated in two different modes in which the threaded axle is either charged or non-charged. In charged [2]rotaxane **1** (Fig. 1), redox-switching of the rotaxane can create strong charge repulsion effects between axle and oxidised macrocycle that subsequently lead to a translational motion of the macrocycle. The expulsive force and, thus, the conformational change can be adjusted by the stepwise oxidation of the TTF unit. In non-charged [2]rotaxane **2**, a selective stabilisation of the tetrathiafulvalene radical cation state ($TTF^{+\bullet}$) is observed, whereas the dicationic state (TTF^{2+}) is energetically disfavoured in comparison to the free wheel.

Results and discussion

Pseudo[2]rotaxane formation and redox-induced axle expulsion

An equimolar mixture of ammonium axle **3** and TTF crown ether **TTFC8** (Fig. 2, see Section 1.2 and 1.3 in the ESI† for synthetic procedures and characterisation data) in CH_2Cl_2 led to the quantitative formation of the 1 : 1 pseudo[2]rotaxane **3@TTFC8** as demonstrated by ^{1}H NMR. Typical downfield shifts for methylene protons H_f and H_g and a diastereotopic splitting of the macrocycle methylene protons confirm the interpenetrated structure as previously reported for similar intertwined structures (Fig. S4, ESI†).[18,19] Proton H_a experiences a significant upfield shift ($\Delta\delta = -1.43$ ppm) caused by π stacking of the anthracene stopper and the wheel's naphthalene unit (Fig. 2d).

The threading of **TTFC8** onto axle **3** can also be monitored by fluorescence spectroscopy using the anthracene as a probe:[20] if the macrocycle is in close proximity to the anthracene, its fluorescence (excitation wavelength $\lambda_{ex} = 370$ nm) is strongly quenched by a distance-dependent electron transfer consistent with the strong emission decrease upon pseudo[2]rotaxane formation (Fig. S11, ESI†).

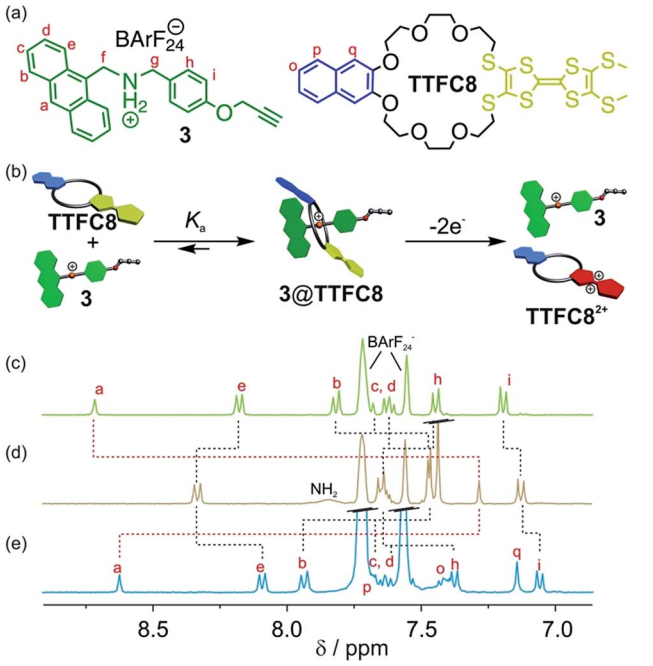

Fig. 2 (a) Structures of macrocycle **TTFC8** and ammonium axle **3**. (b) Schematic representation of the association between ammonium axle **3** and macrocycle **TTFC8** and the axle expulsion induced by double oxidation of the macrocycle. Stacked partial ^{1}H NMR spectra (400 MHz, 2 mM, CD_2Cl_2, 298 K) of (c) ammonium axle **3**, (d) pseudo[2]rotaxane **3@TTFC8** and (e) after oxidation by two equiv. of $Fe(ClO_4)_3$ and addition of 5 equiv. tetrabutylammonium $BArF_{24}$ as stabilising electrolyte.

Isothermal titration calorimetry (ITC) experiments in 1,2-dichloroethane confirmed the 1 : 1 complex stoichiometry and provide quantitative data on the axle–wheel interaction in pseudo[2]rotaxane **3@TTFC8** (Fig. S12, ESI†). The thermodynamic parameters ($\Delta G = (-32.9 \pm 0.3)$, $\Delta H = (-56.3 \pm 1.0)$, and $T\Delta S = (-23.4 \pm 1.3)$ kJ mol^{-1}) reveal a strong, enthalpy-driven complexation of axle and wheel. The binding constant $K_a = (5.9 \pm 0.6)\ 10^5$ M^{-1} at 298 K is remarkably high in comparison to similar systems.[14a] We attribute this to a combination of π-stacking and strong hydrogen bonding between the ammonium axle and the wheel which is enhanced by the poor coordination of the weakly coordinating $BArF_{24}^-$ counterion.[21]

As previously reported, the oxidation of TTF crown ether macrocycles in host–guest complexes can be used to trigger the expulsion of metal cations driven by charge repulsion.[16a,16d,22] Chemical oxidation of **3@TTFC8** in CH_2Cl_2 with two equivalents of the one-electron oxidant $Fe(ClO_4)_3$ leads to a virtually complete disassembly of the system as nicely shown by a back-shifting of the signal for proton H_a (Fig. 2e). To the best of our knowledge, this is the first example of TTF-crown pseudorotaxane with a controlled assembly/disassembly by redox-switching. Unfortunately, the non-interlocked character of the pseudo[2]rotaxane thus prevents a detailed investigation of the interactions between axle and macrocycle in all three switching states (TTF, $TTF^{+\bullet}$ and TTF^{2+}). To gain more insight, we therefore investigated the redox-properties in a mechanically interlocked [2]rotaxane.

Synthesis and characterisation of switchable [2]rotaxanes

The synthesis of [2]rotaxanes **1** and **2** is shown in Scheme 1. Following the catalyst-free stoppering strategy of Takata *et al.*,[23] a mixture of secondary ammonium axle **3** and **TTFC8** in CH_2Cl_2 was treated with nitrile oxide **4** to obtain the [2]rotaxane **1** (79% yield). Its ^{1}H NMR spectrum (Fig. 3b; for details of signal assignments, see Fig. S5–S7, ESI†) reveals similar characteristic chemical shifts: for methylene protons H_f and H_g and aromatic protons H_a and H_q as observed for the pseudorotaxane. In addition, a strong downfield shift of proton H_k ($\Delta\delta$ = +3.90 ppm) is observed due to isoxazole formation. Diastereotopic splitting of the macrocycle methylene proton signals confirms the threading of the unsymmetric axle. Comparison of [2]rotaxane **1** with a mixture of **TTFC8** and free stoppered axle **5** (see ESI, Section 1.2 for details†) clearly shows the ^{1}H NMR spectra not to be superimposable (Fig. S8, ESI†). The interlocked structure of rotaxane **1** was also confirmed by a HR-ESI mass spectrum and tandem MS experiments (Fig. S9 and S10, ESI†). The most prominent peak at *m*/*z* 1279, which corresponds to [2]rotaxane **1** after stripping off its counterion, was not observed for a 1 : 1 mixture of free stoppered axle **5** and macrocycle **TTFC8**. Therefore, we can safely conclude the interlocked structure of the rotaxanes to be intact.

N-Acetylation[24] of the ammonium station was achieved through the addition of acetic anhydride and triethylamine to obtain the non-charged rotaxane **2** in almost quantitative yield. As indicated by back-shifting of aromatic protons H_a and H_q, the ^{1}H NMR of [2]rotaxane **2** suggests that the wheel has moved away from the former ammonium station (Fig. 3d). The high-field shifts of phenyl ether protons H_h and H_i ($\Delta\delta$ = −0.42 and −0.46 ppm, respectively) and axle protons H_j ($\Delta\delta$ = −0.83 ppm) point to a shielding effect by the macrocycle. The downfield shift of the isoxazole signal H_k ($\Delta\delta$ = +0.16 ppm) is probably caused by the anisotropic effect of the oxygen atoms in the crown ether.[4a,24] Therefore, the chemical shifts are in good agreement with the wheel being located close to the isoxazole moiety. No *cis*–*trans* isomers were observed for the amide incorporated in the axle of **2** at 298 K.

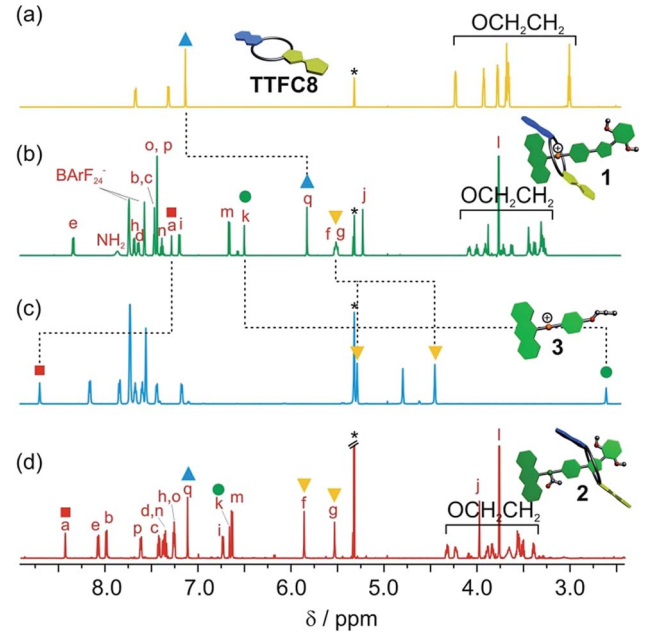

Fig. 3 Stacked partial ^{1}H NMR spectra (700 MHz, 2 mM, CD_2Cl_2, 298 K) of (a) macrocycle **TTFC8**, (b) charged [2]rotaxane **1**, (c) axle **3**, (d) neutral, acetylated [2]rotaxane **2**. Selected signals are marked with coloured symbols. The solvent residue signal is marked with an asterisk.

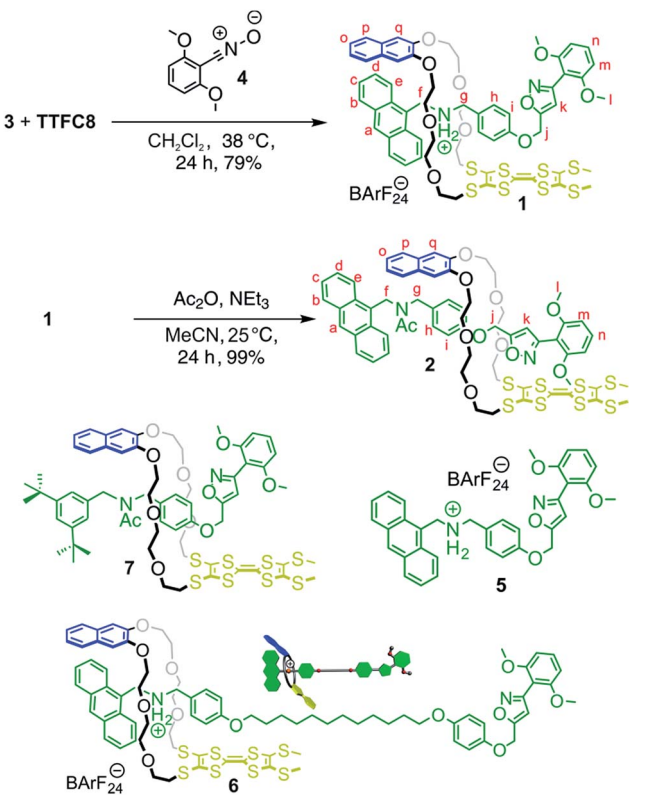

Scheme 1 Preparation of charged and non-charged [2]rotaxanes **1** and **2**; structures of free stoppered axle **5**, [2]rotaxanes **6** and **7**.

Electrochemical properties of rotaxanes 1 and 2

Photometric titrations of **1** and **2** (Fig. 4a) with $Fe(ClO_4)_3$ reveal optoelectronic properties consistent with a switching between three redox states (TTF, $TTF^{+\bullet}$, TTF^{2+}).[25] For each state, characteristic bands and clear-cut isosbestic points indicate clean and well-separated successive transitions. Furthermore, the characteristic absorptions are a straightforward optical output signal and make the switching states of the [2]rotaxanes easily identifiable by UV/Vis or even by the naked eye (Fig. 4b).

The singly oxidised radical cations $\mathbf{1}^{+\bullet}$ and $\mathbf{2}^{+\bullet}$ show a symmetric signal in their EPR spectra (Fig. 4c) with small ^{33}S couplings (0.35 mT) as expected for tetrathioalkyl-substituted $TTF^{+\bullet}$ radical cations.[25c] This speaks in favour of a clearly TTF-centred oxidation for the first redox step. The *g*-factors for [2]rotaxane $\mathbf{1}^{+\bullet}$ and $\mathbf{2}^{+\bullet}$ of 2.008 are close to values reported for similar TTF compounds.[25c,26]

Cyclovoltammetric (CV) experiments with [2]rotaxanes **1** and **2** and, for comparison, with free macrocycle **TTFC8** in CH_2Cl_2 reveal

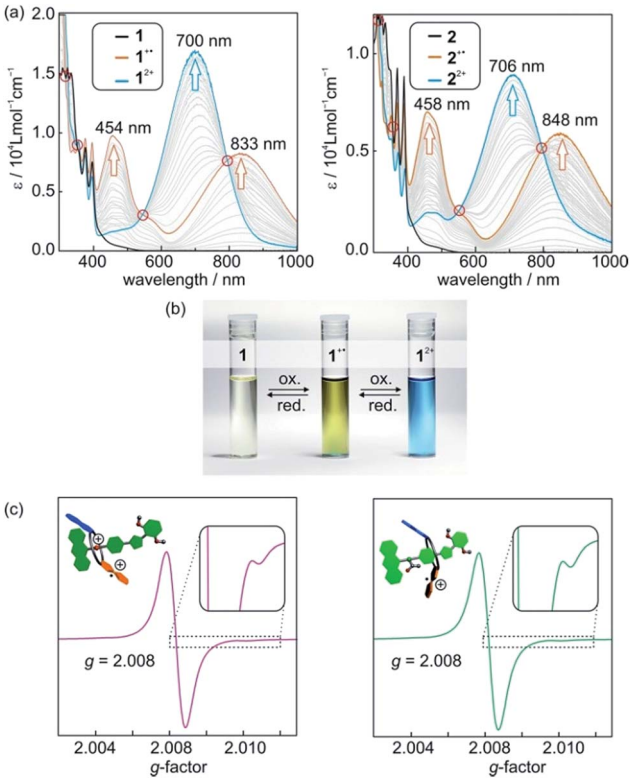

Fig. 4 (a) Photometric titrations of [2]rotaxanes **1** (left) and **2** (right) with $Fe(ClO_4)_3$ as the oxidant (50 μM rotaxane solutions in CH_2Cl_2). The isosbestic points indicate two clean one-electron oxidations and are marked with red circles. (b) Photographs of 1 mM CH_2Cl_2 solutions of [2]rotaxane **1** before oxidation and after the addition of one or two equivalents of oxidant $Fe(ClO_4)_3$. (c) X-band EPR spectra of CH_2Cl_2 solutions (0.1 mM) of [2]rotaxanes $\mathbf{1}^{+\bullet}$ (left) and $\mathbf{2}^{+\bullet}$ (right) after addition of one equivalent of $Fe(ClO_4)_3$.

the influence of mechanical bonding on their electrochemical properties (Fig. 5 and S13 ESI†). In accordance with the UV/vis and EPR results, both [2]rotaxanes show two fully reversible redox processes which are clearly centred on the TTF moiety. Thus, the mechanically interlocked structures remain intact during the redox switching. The potentials for [2]rotaxane **1** (0.74 V and 1.42 V) and [2]rotaxane **2** (0.56 V and 1.14 V) are distinctly shifted as compared to those of free **TTFC8** (0.61 V and 1.06 V), while such shifts are not observed for an equimolar mixture of free stoppered axle **5** and free **TTFC8** (Table S1, ESI†). Therefore, these effects are clearly a consequence of the mechanically interlocked structure. The strong potential difference for the first ($\Delta E^1_{1/2}$ = +0.13 V) and second oxidation ($\Delta E^2_{1/2}$ = +0.36 V) of [2]rotaxane **1** compared to free **TTFC8** demonstrates that the two TTF oxidations are both energetically disfavoured, likely because of charge repulsion between the TTF mono- and dications and the ammonium station. $\Delta E^1_{1/2}$ is remarkably high for TTF-crown ether macrocycles.[22c,22d] For [2]rotaxane **2**, a more complex redox behaviour is observed in that $E^1_{1/2}$ is decreased and $E^2_{1/2}$ increased as compared to free **TTFC8** (see below for the rationalisation of this observation).

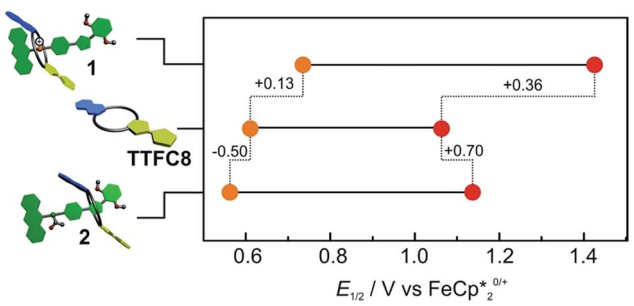

Fig. 5 Correlation diagram of half-wave potentials for charged [2]rotaxane **1**, macrocycle **TTFC8** and neutral, acetylated [2]rotaxane **2**. Half-wave potentials were determined by cyclic voltammetry measurements in CH_2Cl_2 against $Fe(Cp^*)_2^{0/+}$ with a 1 mM analyte concentration at a scan rate of 100 mV s^{-1} with tetrabutylammonium $BArF_{24}$ (0.1 M) as the electrolyte.

Oxidation-induced shuttling in charged [2]rotaxanes 1 and 6

Potentially, the repulsion in charged [2]rotaxane **1** between the ammonium station and the oxidised macrocycle $\mathbf{TTFC8}^{+\bullet}$ or $\mathbf{TTFC8}^{2+}$ can be used to trigger a shuttling of the macrocycle towards the isoxazole moiety. In most of the reported non-interlocked host–guest systems, a guest expulsion can be detected by a largely unaffected second redox potential.[16a,16d,22c] For [2]rotaxane **1**, however, the second oxidation is strongly affected which indicates that the repulsion between the ammonium station and $\mathbf{TTFC8}^{+\bullet}$ is not strong enough to trigger a translational movement. This is reasonable, as the potential difference (≙ repulsive force) for the first oxidation $\Delta E^1_{1/2}$ = +0.13 V (13 kJ mol^{-1}) is obviously smaller than the crown/ammonium binding energy of −32.9 kJ mol^{-1} determined by ITC. Therefore, we focused on the doubly oxidised species which displayed a much higher potential difference of $\Delta E^2_{1/2}$ = +0.36 V (35 kJ mol^{-1}) sufficient to overcome the binding energy.

To obtain evidence for the shuttling in [2]rotaxane **1**, fluorescence spectra of **1** and $\mathbf{1}^{2+}$ were recorded expecting that the anthracene fluorescence would become visible, when the wheel moves away from the ammonium station. However, fully oxidised [2]rotaxane $\mathbf{1}^{2+}$ showed no increase in fluorescence emission (Fig. 6a, left). This leads to the assumption that either no conformational change occurred or that the macrocycle is still close enough for an efficient quenching.

To clarify this question and to obtain a larger-amplitude shuttling, we synthesised [2]rotaxane **6** (Scheme 1, see Section 1.4 in the ESI for details†) that bears a longer alkyl spacer. Besides the increased spacer length allowing the wheel to undergo a larger translational motion, the binding motifs remain unchanged as compared to [2]rotaxane **1**. After double oxidation, the fluorescence spectrum of rotaxane $\mathbf{6}^{2+}$ clearly shows a significant increase in fluorescence indicative of the wheel's motion to a position sufficiently distant from the anthracene stopper to at least partly restore its emission (Fig. 6a). It is expected that the shuttling also occurs in [2]rotaxane **1**. Due to the smaller shuttling distance, however, this process cannot be detected by fluorescence spectroscopy.

The wheel shuttling in rotaxane $\mathbf{6}^{2+}$ was also evaluated by scan rate-dependent CV measurements (Fig. 6b). $E^1_{1/2}$ of [2]rotaxane **6** is

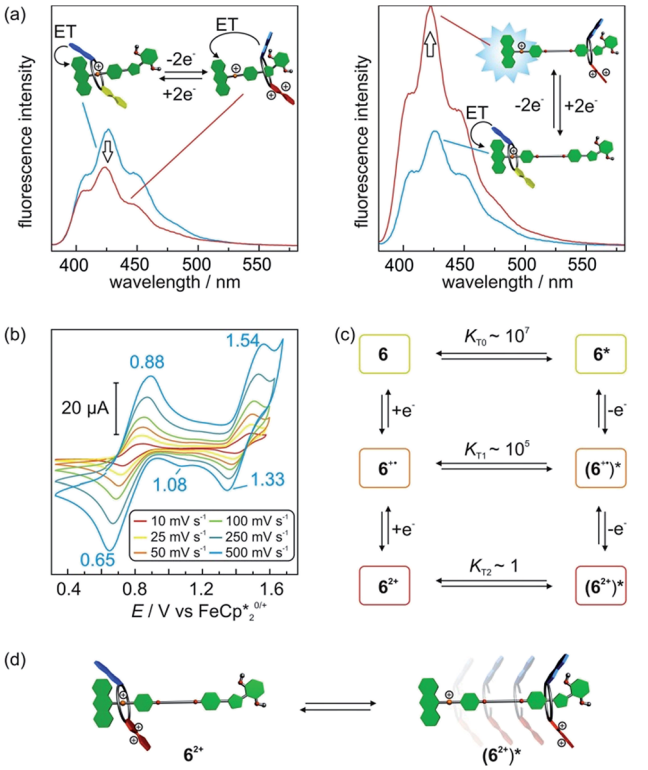

Fig. 6 (a) Fluorescence spectra (CH_2Cl_2, 50 μM, λ_{ex} = 370 nm) of [2]rotaxane **1** (left) and **6** (right) before and after double oxidation by addition of the oxidant $Fe(ClO_4)_3$. (b) Scan rate dependent cyclic voltammograms of [2]rotaxane **6** (5 mM) in CH_2Cl_2 against $Fe(Cp^*)_2^{0/+}$ with tetrabutylammonium $BArF_{24}^-$ (0.1 M) as electrolyte. (c) Six-member square scheme with thermodynamic parameters obtained by digital simulations for translation equilibria of **6**. (d) Schematic representation for the electrochemically triggered expulsion process in [2]rotaxane $\mathbf{6}^{2+}$.

similar to [2]rotaxane **1** whereas $E^2_{1/2}$ is slightly decreased by 0.03 V (Table S1, ESI†). A plot of the peak currents against the square root of the scan rates shows the first oxidation to be reversible whereas the second oxidation has a quasi-reversible character (Fig. S14, ESI†). Furthermore, a shoulder at 1.08 V is observed during the cathodic scan at high scan rates, which exhibits a peak potential similar to the reduction of acetylated [2]rotaxane $\mathbf{2}^{2+}$. These data point to a reaction mechanism in which the [2]rotaxane **6** undergoes two successive oxidations followed by a subsequent chemical reaction step. We identify this chemical reaction step with the translation of the wheel. The observed shoulder can then be attributed to the wheel residing in a position remote from the ammonium station and, thus, the TTF^{2+} moiety in $\mathbf{6}^{2+}$ shows a lower reduction potential.

We applied digital simulations to test the proposed mechanism and estimate the thermodynamic parameters of the translational motion. If equilibria between two distinguishable translational isomers $\mathbf{6}^{n+}$ and $(\mathbf{6}^{n+})^*$ (non-shuttled or shuttled) in all three oxidation states are considered, the system can be described by a six-member square scheme (Fig. 6c). The simulations based on this mechanism are in good agreement with the observed cyclic voltammograms (Fig. S15, ESI†). Fitting to the experimental data gives the intramolecular equilibrium constants K_{Tn} ($K_{Tn} = [\mathbf{6}^{n+}]/[(\mathbf{6}^{n+})^*]$) between the isomers in all oxidation states.[27] **6** and $\mathbf{6}^{+\bullet}$ display high values of $K_{T0} \sim 10^7$ and $K_{T1} \sim 10^5$, respectively. In these oxidation states, the wheel is indeed almost completely located on the ammonium station. For $\mathbf{6}^{2+}$, the simulations point to a much lower equilibrium constant of $K_{T3} \sim 1$. Hence, both translational isomers $\mathbf{6}^{2+}$ and $(\mathbf{6}^{2+})^*$ exist in significant amounts in equilibrium with each other at 298 K (Fig. 6d). Although a more exact determination of the equilibrium distribution is difficult to determine by digital simulations since the derived quantitative values of K_{Tn} are based on several assumptions and should be considered as estimates (see Section 6 in the ESI for details†), this is in good agreement with the energy values discussed above (32.9 kJ mol^{-1} for the axle binding in the pseudorotaxane and 35 kJ mol^{-1} for the potential shift in the doubly oxidised state). It may be worth mentioning that the present system allows an estimation of K_T values across a range of 1–10^7 which is extremely wide for an intramolecular quantity.[27,28]

In the ^{1}H NMR spectrum of [2]rotaxane $\mathbf{6}^{2+}$, only small shifts for the aromatic protons of axle and macrocycle are observed indicating π–stacking interactions to still play a significant role. This is reasonable, as ^{1}H NMR spectroscopy is often not sensitive enough to determine intramolecular K_T values.[27] Shifts of the isoxazole and methoxy stopper signals are observed which can be explained by major conformational changes in the [2]rotaxane structure (Fig. S16, ESI†). Inferences about the macrocycle positioning in the second translational isomer $(\mathbf{6}^{2+})^*$ could potentially be drawn from a ^{1}H NMR spectrum of non-charged acetylated [2]rotaxane $\mathbf{2}^{2+}$. However, the low solubility of this doubly oxidised species prevented an exact signal assignment.

The combination of all data obtained by fluorescence spectroscopy, CV and NMR spectroscopy confirms a translational motion in oxidised [2]rotaxane $\mathbf{6}^{2+}$. Therefore, the system can be operated as a novel type of switchable molecular shuttle reversibly driven by redox stimuli. However, only a partial expulsion is observed for $\mathbf{6}^{2+}$ due to a fine balance between charge repulsion and crown/ammonium binding. We assume that entropy effects and the lack of an alternative binding station energetically disfavours the translational isomer $(\mathbf{6}^{2+})^*$. The sharp contrast to the efficient expulsion in the non-interlocked pseudo[2]rotaxane **3@TTFC8** underlines the impact of mechanical bonding on the interplay between axle and macrocycle.

Wheel/axle interactions in non-charged, acetylated [2]rotaxane 2

The cyclic voltammogram of non-charged [2]rotaxane **2** draws a contrasting picture of the TTF redox potentials (Fig. 5). A behaviour similar to the free macrocycle is expected, since strong [N–H···O] hydrogen-bonds are eliminated and, in addition, effects of Coulomb repulsion are avoided. The potential decrease of the first oxidation ($\Delta E^1_{1/2} = -0.05$ V) indicates a $TTF^{+\bullet}$ radical cation stabilisation by −5 kJ mol^{-1}, whereas the second potential exhibits an increase of $\Delta E^2_{1/2} = +0.07$ V and thus a destabilisation of 7 kJ mol^{-1} as compared to the free macrocycle.

These findings imply a more complex interplay of different intermolecular forces between axle and wheel. Therefore, additional CV measurements were performed with both rotaxanes **1** and **2** using a series of tetrabutylammonium (TBA) salts with different WCAs (ClO_4^-, PF_6^-, $BArF_{24}^-$) as the electrolytes and two different solvents (dichloromethane and acetonitrile) to identify possible ion-pairing or solvent effects (Fig. 7).

In CH_2Cl_2, the choice of electrolyte has a strong impact on both redox potentials of charged [2]rotaxane **1** which identifies, as expected, charge repulsion as the most dominant interaction between axle and macrocycle. The order of potential increase (ClO_4^- < PF_6^- ≪ $BArF_{24}^-$) nicely reflects the coordination abilities of these WCAs[29] and, thus, the $\Delta E^1_{1/2}$ values provide an excellent means to easily quantify them. Non-charged [2]rotaxane **2** shows no clear response of $\Delta E^1_{1/2}$ to the electrolyte which excludes strong contribution of ion-pairing effects. However, the $\Delta E^2_{1/2}$ value for [2]rotaxane **2** increases slightly when going from ClO_4^- to $BArF_{24}^-$. This means that the TTF^{2+} species enjoys poorer stabilisation as compared to free **TTFC8**. We assume that the steric demand of the axle diminishes the accessibility for counterions. As a consequence, the doubly charged species lacks charge stabilisation by the counterion. This effect is most pronounced when using $TBABArF_{24}$ as the electrolyte.

The use of acetonitrile as a more polar solvent leads to a dampening effect on the charge repulsion effects for both oxidations in [2]rotaxane **1**. In non-charged [2]rotaxane **2**, $\Delta E^1_{1/2}$ is slightly decreased for all electrolytes in comparison to CH_2Cl_2 indicating that a more polar solvent weakens the $TTF^{+\bullet}$ stabilising interaction. The $\Delta E^2_{1/2}$ values are in the similar range as in CH_2Cl_2, but the electrolyte effects are no longer present.

Besides solvent and counterion effects, the contribution of structural modifications on the $TTF^{+\bullet}$ stabilising interaction was evaluated. We synthesised an acetylated [2]rotaxane **7** in which we replaced the anthracene stopper by a 3,5-di-*tert*-butyl benzyl stopper (Scheme 1, see Section 1.5 in the ESI for full synthesis†). We determined almost identical $E^1_{1/2}$ and $E^2_{1/2}$ values as for acetylated [2]rotaxane **2** (Table S1, ESI†) which indicates that the anthracene stopper has a minor effect for the observed stabilisation.

Overall, the electrochemical data reveals an interplay of different interactions during redox-switching for both [2]rotaxanes **1** and **2** as illustrated in Fig. 7c for the CH_2Cl_2/$TBABArF_{24}$ measurement. Whereas charge repulsion hampers the oxidations in charged [2]rotaxane **1**, the first oxidation in [2]rotaxane **2** is energetically favoured. An intramolecular interaction between the phenyl-ether/isoxazole/dimethoxybenzene axle part and radical cationic $TTF^{+\bullet}$ moiety of the macrocycle is likely. Regarding solvent dependence, electrostatic forces such as cation–dipole interactions are a reasonable assumption.

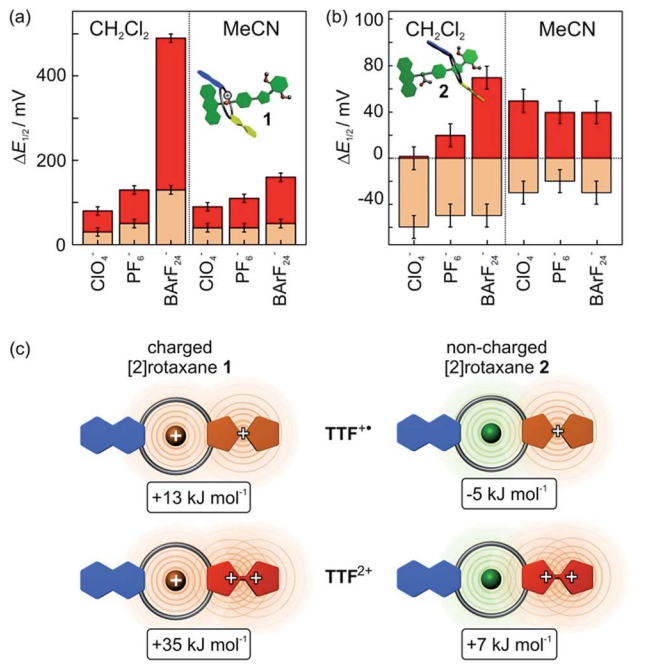

Fig. 7 Difference in the first and second oxidation potential $\Delta E^1_{1/2}$ (orange) and $\Delta E^2_{1/2}$ (red) for (a) charged [2]rotaxane **1** and (b) non-charged [2]rotaxane **2** in comparison to the free macrocycle **TTFC8**. Half-wave potentials were obtained by CV measurements with a 1 mM analyte concentration, 0.1 M $TBAX^-$ electrolyte concentration and 100 mV s^{-1} scan rate referenced against $Fe(Cp^*)_2^{0/+}$. (c) Top view scheme to illustrate electrostatic forces in different redox states (CH_2Cl_2, $TBABArF_{24}$) and resulting stabilisation and destabilisation energies between axle and macrocycle in [2]rotaxanes **1** (left) and **2** (right).

Conclusions

In summary, we have synthesised and fully characterised the structural and optoelectronic properties of novel redox-switchable [2]rotaxanes which incorporate a redox-active tetrathiafulvalene unit in the wheel. The [2]rotaxanes can be electrochemically operated in two modes in which the threaded axle is either charged or neutral. We found by cyclic voltammetry, that this difference has a dramatic effect on the redox potentials of these [2]rotaxanes. In the charged mode, electrostatic repulsion is identified as the dominant interaction. It can be used to trigger a charge expulsion and subsequently a stimuli-responsive translation motion of the macrocycle which has been analysed by fluorescence, scan rate depended CV, and ^1H NMR. In the non-charged mode, detailed CV investigations show a complex interplay of different stabilising and destabilising intramolecular effects in the interlocked system. This study nicely demonstrates that mechanical bonding is an outstanding strategy to create unpredictable emergent properties in MIMs. This novel type of redox-active rotaxane provides an excellent platform for the construction of switchable artificial molecular machines.

Acknowledgements

The authors thank the Deutsche Forschungsgemeinschaft (CRC 765) and the Fonds der Chemischen Industrie (FCI) for funding. H. V. S. thanks the FCI for a Chemiefonds Ph.D. fellowship. We thank Constantin Stuckhardt and Sebastian Müller for help with measurements and synthesis.

Notes and references

1 (*a*) J. F. Stoddart, *Chem. Soc. Rev.*, 2009, **38**, 1802; (*b*) E. A. Neal and S. M. Goldup, *Chem. Commun.*, 2014, **50**, 5128; (*c*) J. E. Lewis, M. Galli and S. M. Goldup, *Chem. Commun.*, 2016, **53**, 298.

2 (*a*) N. Kihara, M. Hashimoto and T. Takata, *Org. Lett.*, 2004, **6**, 1693; (*b*) F. Coutrot, *ChemistryOpen*, 2015, **4**, 556.

3 A. M. Albrecht-Gary, Z. Saad, C. O. Dietrich-Buchecker and J. P. Sauvage, *J. Am. Chem. Soc.*, 1985, **107**, 3205.

4 (*a*) K. Nakazono and T. Takata, *Chem.–Eur. J.*, 2010, **16**, 13783; (*b*) N. Kihara, Y. Tachibana, H. Kawasaki and T. Takata, *Chem. Lett.*, 2000, **29**, 506.

5 P. R. Ashton, R. Ballardini, V. Balzani, I. Baxter, A. Credi, M. C. T. Fyfe, M. T. Gandolfi, M. Gómez-López, M. V. Martínez-Díaz, A. Piersanti, N. Spencer, J. F. Stoddart, M. Venturi, A. J. P. White and D. J. Williams, *J. Am. Chem. Soc.*, 1998, **120**, 11932.

6 (*a*) S. Erbas-Cakmak, D. A. Leigh, C. T. McTernan and A. L. Nussbaumer, *Chem. Rev.*, 2015, **115**, 10081; (*b*) V. Balzani, A. Credi, F. M. Raymo and J. F. Stoddart, *Angew. Chem., Int. Ed.*, 2000, **39**, 3348.

7 (*a*) P. L. Anelli, N. Spencer and J. F. Stoddart, *J. Am. Chem. Soc.*, 1991, **113**, 5131; (*b*) J.-P. Collin, C. Dietrich-Buchecker, P. Gaviña, M. C. Jimenez-Molero and J.-P. Sauvage, *Acc. Chem. Res.*, 2001, **34**, 477.

8 (*a*) J. D. Badjic, V. Balzani, A. Credi, S. Silvi and J. F. Stoddart, *Science*, 2004, **303**, 1845; (*b*) Z. J. Zhang, M. Han, H. Y. Zhang and Y. Liu, *Org. Lett.*, 2013, **15**, 1698.

9 (*a*) C. J. Bruns and J. F. Stoddart, *Acc. Chem. Res.*, 2014, **47**, 2186; (*b*) B. K. Juluri, A. S. Kumar, Y. Liu, T. Ye, Y. W. Yang, A. H. Flood, L. Fang, J. F. Stoddart, P. S. Weiss and T. J. Huang, *ACS Nano*, 2009, **3**, 291.

10 (*a*) C. Cheng, P. R. McGonigal, S. T. Schneebeli, H. Li, N. A. Vermeulen, C. Ke and J. F. Stoddart, *Nat. Nanotechnol.*, 2015, **10**, 547; (*b*) G. Ragazzon, M. Baroncini, S. Silvi, M. Venturi and A. Credi, *Nat. Nanotechnol.*, 2015, **10**, 70.

11 (*a*) M. R. Wilson, J. Sola, A. Carlone, S. M. Goldup, N. Lebrasseur and D. A. Leigh, *Nature*, 2016, **534**, 235; (*b*) J. V. Hernandez, E. R. Kay and D. A. Leigh, *Science*, 2004, **306**, 1532.

12 W. Yang, Y. Li, H. Liu, L. Chi and Y. Li, *Small*, 2012, **8**, 504.

13 K. Szacilowski, *Chem. Rev.*, 2008, **108**, 3481.

14 (*a*) P. R. Ashton, P. J. Campbell, P. T. Glink, D. Philp, N. Spencer, J. F. Stoddart, E. J. T. Chrystal, S. Menzer, D. J. Williams and P. A. Tasker, *Angew. Chem., Int. Ed. Engl.*, 1995, **34**, 1865; (*b*) N. Yamaguchi and H. W. Gibson, *Angew. Chem., Int. Ed.*, 1999, **38**, 143; (*c*) A. G. Kolchinski, D. H. Busch and N. W. Alcock, *J. Chem. Soc., Chem. Commun.*, 1995, 1289.

15 (*a*) D. Canevet, M. Salle, G. Zhang, D. Zhang and D. Zhu, *Chem. Commun.*, 2009, 2245; (*b*) M. R. Bryce, *J. Mater. Chem.*, 2000, **10**, 589; (*c*) J. L. Segura and N. Martín, *Angew. Chem., Int. Ed.*, 2001, **40**, 1372; (*d*) F. Wudl, G. M. Smith and E. J. Hufnagel, *J. Chem. Soc., Chem. Commun.*, 1970, 1453.

16 (*a*) F. Le Derf, M. Mazari, N. Mercier, E. Levillain, G. Trippé, A. Riou, P. Richomme, J. Becher, J. Garín, J. Orduna, N. Gallego-Planas, A. Gorgues and M. Sallé, *Chem.–Eur. J.*, 2001, **7**, 447; (*b*) M. B. Nielsen and J. Becher, *Liebigs Ann.*, 1997, **1997**, 2177; (*c*) T. Jørgensen, T. K. Hansen and J. Becher, *Chem. Soc. Rev.*, 1994, **23**, 41; (*d*) T. K. Hansen, T. Joergensen, P. C. Stein and J. Becher, *J. Org. Chem.*, 1992, **57**, 6403.

17 P. R. Ashton, J. Becher, M. C. T. Fyfe, M. B. Nielsen, J. F. Stoddart, A. J. P. White and D. J. Williams, *Tetrahedron*, 2001, **57**, 947.

18 H. V. Schröder, H. Hupatz, A. J. Achazi, S. Sobottka, B. Sarkar, B. Paulus and C. A. Schalley, *Chem.–Eur. J.*, 2017, **23**, 2960.

19 W. Jiang, H. D. Winkler and C. A. Schalley, *J. Am. Chem. Soc.*, 2008, **130**, 13852.

20 (*a*) P. R. Ashton, R. Ballardini, V. Balzani, M. Gómez-López, S. E. Lawrence, M. V. Martínez-Díaz, M. Montalti, A. Piersanti, L. Prodi, J. F. Stoddart and D. J. Williams, *J. Am. Chem. Soc.*, 1997, **119**, 10641; (*b*) S. Garaudee, S. Silvi, M. Venturi, A. Credi, A. H. Flood and J. F. Stoddart, *ChemPhysChem*, 2005, **6**, 2145.

21 J. W. Jones and H. W. Gibson, *J. Am. Chem. Soc.*, 2003, **125**, 7001.

22 (*a*) C. Wartelle, P. M. Viruela, R. Viruela, E. Orti, F. X. Sauvage, E. Levillain, F. Le Derf and M. Salle, *J. Phys. Chem. A*, 2005, **109**, 1188; (*b*) M. R. Bryce, A. S. Batsanov, T. Finn, T. K. Hansen, J. A. K. Howard, M. Kamenjicki, I. K. Lednev and S. A. Asher, *Chem. Commun.*, 2000, 295; (*c*) J. Lyskawa, F. Le Derf, E. Levillain, M. Mazari, M. Salle, L. Dubois, P. Viel, C. Bureau and S. Palacin, *J. Am. Chem. Soc.*, 2004, **126**, 12194; (*d*) G. Trippé, E. Levillain, F. Le Derf, A. Gorgues, M. Sallé, J. O. Jeppesen, K. Nielsen and J. Becher, *Org. Lett.*, 2002, **4**, 2461.

23 T. Matsumura, F. Ishiwari, Y. Koyama and T. Takata, *Org. Lett.*, 2010, **12**, 3828.

24 Y. Tachibana, H. Kawasaki, N. Kihara and T. Takata, *J. Org. Chem.*, 2006, **71**, 5093.

25 (*a*) S. V. Rosokha and J. K. Kochi, *J. Am. Chem. Soc.*, 2007, **129**, 828; (*b*) M. B. Kirketerp, L. A. Leal, D. Varsano, A. Rubio, T. J. Jorgensen, K. Kilsa, M. B. Nielsen and S. B. Nielsen, *Chem. Commun.*, 2011, **47**, 6900; (*c*) V. Khodorkovsky, L. Shapiro, P. Krief, A. Shames, G. Mabon, A. Gorgues and M. Giffard, *Chem. Commun.*, 2001, 2736.

26 L. Avara, F. Gerson, D. O. Cowan and K. Lerstrup, *Helv. Chim. Acta*, 1986, **69**, 141.

27 G. Ragazzon, A. Credi and B. Colasson, *Chem.–Eur. J.*, 2017, **23**, 2149.

28 (*a*) A. C. Fahrenbach, J. C. Barnes, H. Li, D. Benitez, A. N. Basuray, L. Fang, C. H. Sue, G. Barin, S. K. Dey, W. A. Goddard III and J. F. Stoddart, *Proc. Natl. Acad. Sci. U. S. A.*, 2011, **108**, 20416; (*b*) A. C. Fahrenbach, C. J. Bruns, D. Cao and J. F. Stoddart, *Acc. Chem. Res.*, 2012, **45**, 1581.

29 (*a*) M. G. Hill, W. M. Lamanna and K. R. Mann, *Inorg. Chem.*, 1991, **30**, 4687; (*b*) R. J. LeSuer, C. Buttolph and W. E. Geiger, *Anal. Chem.*, 2004, **76**, 6395; (*c*) W. E. Geiger and F. Barriere, *Acc. Chem. Res.*, 2010, **43**, 1030.

Supporting Information

Impact of mechanical bonding on the redox-switching of tetrathiafulvalene in crown ether-ammonium [2]rotaxanes

Hendrik V. Schröder,[a] Sebastian Sobottka,[b] Maite Nößler,[a] Henrik Hupatz,[a] Marius Gaedke,[a] Biprajit Sarkar[b] and Christoph A. Schalley*[a]

[a]*Institut für Chemie und Biochemie, Freie Universität Berlin, Takustr. 3, 14195 Berlin, Germany. E-mail: christoph@schalley-lab.de*

[b]*Institut für Chemie und Biochemie, Freie Universität Berlin, Fabeckstr. 34/36, 14195 Berlin, Germany*

Table of contents

1. Experimental Details

1.1. General methods

All reagents and solvents were obtained from commercial sources and used without further purification. Dry solvents were purchased from Acros Organics. 4-(Prop-2-yn-1-yloxy)phenol,[1] 2,3-bis(2-cyanoethylthio)-6,7-bis(methylthio)tetrathiafulvalene,[2] 2,3-bis(2-(2-(2-iodoethoxy)ethoxy)ethoxy)naphthalene,[3] (4-(prop-2-yn-1-yloxy)phenyl)methanaminium chloride[4] and 2,6-dimethoxybenzonitrile oxide[5] were synthesised according to literature procedures. Thin-layer chromatography was performed on silica gel-coated plates with fluorescent indicator F254 (Merck). For column chromatography, silica gel (0.04-0.063 mm; Merck) was used.

^{1}H and ^{13}C NMR experiments were performed on JEOL ECX 400, JEOL ECP 500, Bruker AVANCE 500 or Bruker AVANCE 700 instruments. Solvent residue signals are abbreviated with an asterisk and were used as internal standard. All shifts are reported in ppm and NMR multiplicities are abbreviated as s (singlet), d (doublet), t (triplet), m (multiplet) and br (broad). Coupling constants *J* are reported in Hertz. Compounds containing the tetrakis[3,5-bis(trifluoromethyl)phenyl]borate ($BArF_{24}^-$) anion show ^{13}C NMR spectra with ^{19}F, ^{10}B and ^{11}B couplings. These signals were denoted as one signal.

High-resolution ESI mass spectra were measured on an Agilent 6210 ESI-TOF device (Agilent Technologies). HPLC grade solvents were used with a flow rate of 2-4 µL/min. Tandem MS and infrared multiphoton dissociation (IRMPD) experiments were performed on an Ionspec Q FT-7 (Varian Inc.) equipped with a 7 T superconducting magnet and a Micromass Z-spray ESI source.

Fluorescence spectra were obtained on a LS 50 B luminescence spectrometer (PerkinElmer) using excitation and emission slits of 10 nm widths. *Suprasil* fluorescence cuvettes (1 cm x 0.4 cm path-length) were used.

The UV/Vis measurements were performed on a Cary 50 Bio photospectrometer (Varian) equipped with a xenon lamp. Solvents with HPLC grade or better and *Suprasil* glass cuvettes with a path-length of 1 cm were used.

EPR spectra at X-band frequency (ca. 9.5 GHz) were obtained with a Magnettech MS-5000 benchtop EPR spectrometer equipped with a rectangular TE 102 cavity and TC HO4 temperature controller. The measurements were carried out in synthetic quarz glass tubes. Spectra were processed with ESRStudio.

Melting points were determined on a SMP 30 (Stuart) instrument. Melting points are uncorrected.

Electroactive macrocycles and rotaxanes in CH_2Cl_2 solutions were oxidised with $Fe(ClO_4)_3$ by stirring the suspension under argon atmosphere for several minutes. $Fe(ClO_4)_3$ shows very low solubility in CH_2Cl_2 and can be filtered off after oxidation.

1.2. Synthesis of axle 3 and free stoppered axle 5

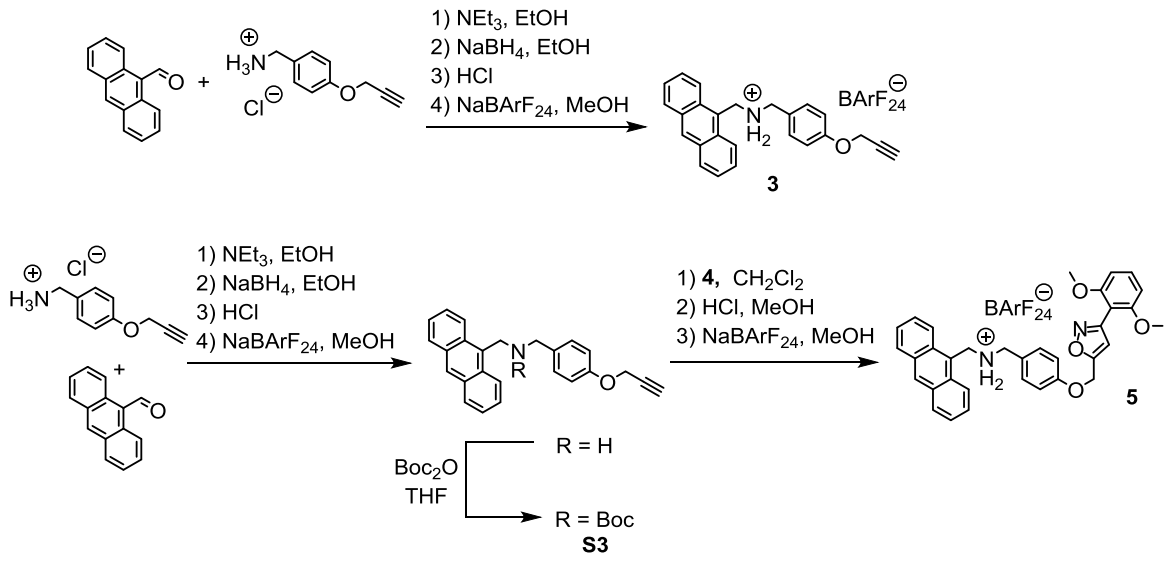

Fig. S1 Synthesis of axle **3** and free stoppered axle **5**

1-(Anthracen-9-yl)-*N*-(4-(prop-2-yn-1-yloxy)benzyl)methanaminium tetrakis[3,5-bis(trifluoromethyl)phenyl]borate

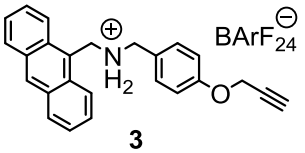

9-Anthracenecarboxaldehyde (413 mg, 2.0 mmol) and (4-(prop-2-yn-1-yloxy)phenyl)-methanaminium chloride (395 mg, 2.0 mmol) were dissolved in dry ethanol (40 mL), treated with NEt_4 (0.2 mL, 1.5 mmol) and the mixture was heated to reflux for 4 h under Ar. After cooling to room temperature, $NaBH_4$ (189 mg, 5.0 mmol) was added at 0 °C and the mixture was stirred overnight under Ar. Afterwards, saturated $NaHCO_3$ solution was added to quench the reaction, the solvent was removed under reduced pressure and CH_2Cl_2 (30 mL) was added. The organic layer was washed with brine (3x30 mL), dried over $MgSO_4$ and the solvent was removed under reduced pressure. The resulting yellow oil was purified by column chromatography (SiO_2, CH_2Cl_2 → CH_2Cl_2/MeOH = 20:1). The amine was obtained as a yellow oil, which was dissolved in Et_2O and precipitated with concentrated aqueous HCl to yield the corresponding hydrochloride (231mg, 0.60 mmol). The hydrochloride (77.6 mg, 0.20 mmol) and $NaBArF_{24}$ (177.2 mg, 0.20 mmol) were dissolved in MeOH (8 mL) and stirred at room temperature for 2 h. The solution was concentrated under reduced pressure and the residue was suspended in water (30 mL) and stirred for another 2 h. The desired product

was obtained through filtration as colourless powder (172.1 mg, 0.14 mmol, 21% over all steps). R_f = 0.50 in CH_2Cl_2/MeOH = 20:1; m.p. 93-95 °C; ^{1}H NMR (700 MHz, CD_2Cl_2): δ = 8.70 (s, 1H, H_{Ar}), 8.16 (d, ^3J = 9.3 Hz, 2H, H_{Ar}), 7.84 (d, ^3J = 9.8 Hz, 2H, H_{Ar}), 7.73 (s, 8H, H_{BArF24}), 7.70-7.65 (m, 2H, H_{Ar}), 7.61-7.58 (m, 2H, H_{Ar}), 7.56 (s, 4H, H_{BArF24}), 7.44 (d, ^3J = 9.3 Hz, 2H, $H_{Ar,}$), 7.17 (d, ^3J = 8.7 Hz, 2H, H_{Ar}), 5.29 (s, 2H, NCH_2), 4.80 (s, 2H, CH_2CCH), 4.45 (s, 2H, NCH_2), 2.61 (s, 1H, CH_2CH) ppm. ^{13}C NMR (176 MHz, CD_2Cl_2): δ = 162.31, 160.24, 135.38, 132.64, 131.93, 131.08, 130.86, 129.60, 129.41, 126.49, 125.20, 121.77, 121.21, 119.24, 118.06, 117.10, 78.21, 76.61, 56.63, 54.00, 53.44, 44.40 ppm; HRMS: *m/z* calcd for $[C_{57}H_{34}BF_{24}NO]$: 352.1696 $[M\text{-}BArF_{24}]^+$, found: 352.1676.

Tert-butyl (anthracen-9-ylmethyl)(4-(prop-2-yn-1-yloxy)benzyl)carbamate

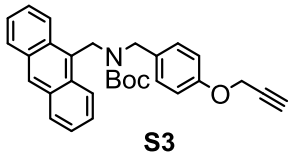

S3

Under argon, the hydrochloride of axle **3** (435 mg, 1.13 mmol), di-*tert*-butyl dicarbonate (296 mg, 1.36 mmol) and NEt_4 (0.24 mL, 1.70 mmol) were dissolved in dry tetrahydrofuran (10 mL) at 0 °C and the mixture was allowed to warm to room temperature while stirring overnight. After removing the volatiles *in vacuo*, the residue was dissolved in CH_2Cl_2 (50 mL) and washed with water (50 mL) and brine (50 mL). The organic phase was dried ($MgSO_4$) and the residue was purified by column chromatography (SiO_2, pentanes/CH_2Cl_2 = 2:1) to give the pure product as a colourless solid (509 mg, 99%). R_f = 0.40 in pentane/CH_2Cl_2 = 2:1; m.p. 66-68 °C; ^{1}H NMR (500 MHz, $CDCl_3$): δ = 8.43 (s, 1H, H_{Ar}), 8.19 (s, 2H, H_{Ar}), 8.00 (br, 2 H, H_{Ar}), 7.48 – 7.39 (m, 4H, H_{Ar}), 6.81 (br, 4H, H_{Ar}), 5.54 (br, 2H, CH_2), 4.68 (br, 2H, CH_2), 3.98 (br, 2H, CH_2), 2.55 (t, ^3J = 2.4 Hz, 1H, CCH), 1.44 – 1.96 (br, 9H, H_{Boc}) ppm. ^{13}C NMR (126 MHz, $CDCl_3$): δ = 156.53, 131.42, 129.16, 128.46, 128.30, 128.20, 126.15, 125.05, 124.60, 114.71, 80.26, 78.78, 75.56, 55.97, 47.19, 40.79, 28.59 ppm (only 17 of 20 signals for magnetic inequivalent carbons were observed due to strong signal broadening); ESI-HRMS: m/z calcd for $[C_{30}H_{29}NO_3]$: 474.2040 $[M+Na]^+$, found: 474.2050.

1-(Anthracen-9-yl)-N-(4-((3-(2,6-dimethoxyphenyl)isoxazol-5-yl)methoxy)benzyl)-methanaminium tetrakis[3,5-bis(trifluoromethyl)phenyl]borate

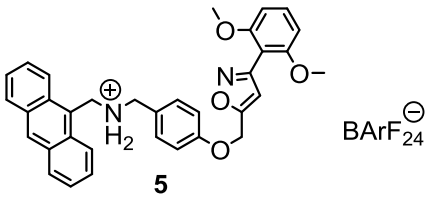

5

Axle **S3** (88 mg, 0.19 mmol), nitrile oxide **4** (36 mg, 0.20 mmol) were dissolved in CH_2Cl_2 (1 mL) and placed into a pressure tube. The mixture was stirred at 38 °C overnight. Purification using column chromatography (SiO_2, CH_2Cl_2) yielded the stoppered axle as a colourless solid (120 mg). Part of the Boc-protected axle (60 mg, 95 µmol) was dissolved in MeOH (10 mL) and concentrated aqueous HCl (1 mL) was added. The mixture was stirred at room temperature overnight. The solvent was removed *in vacuo*, Et_2O (10 mL) was added and the mixture was suspended by sonication. The mixture was filtered to quantitatively give the hydrochloride as a white solid. Part of the hydrochloride (31 mg, 55 µmol) and $NaBArF_{24}$ (49 mg, 55 µmol) were dissolved in MeOH (3 mL) and the mixture was stirred at room temperature for 5 h. After concentration under reduced pressure, water (5 mL) was added and the mixture was suspended by sonication. Filtration gave the desired product as an off-white solid (57 mg, 41 µmol, 72% over all steps). m.p. 88 °C (decompostion); H NMR (700 MHz, $CDCl_3$) δ = 8.40 (s, 1H, H_{Ar}), 8.16 (br, 2H), 7.95 (m, 2H, H_{Ar}), 7.83 – 7.72 (m, 2H, H_{Ar}), 7.69 – 7.71 (m, 8H, H_{BArF24}), 7.46 (s, 4H, H_{BArF24}), 7.44 – 7.40 (m, 2H, H_{Ar}), 7.23 – 7.18 (m, 2H, H_{Ar}), 7.13 (t, ^3J = 8.3 Hz, 1H), 6.80 (s, 2H, H_{Ar}), 6.44 (s, 1H, H_{isox}), 6.21 (d, ^3J = 8.3 Hz, 2H, H_{Ar}), 5.17 (br, 2H, CH_2), 4.97 (br, 2H, CH_2), 4.31 (br, 2H, CH_2), 3.32 (s, 6H, OCH_3) ppm. ^{13}C NMR (176 MHz, $CDCl_3$): δ = 165.94, 161.76, 159.36, 157.68, 157.23, 134.92, 132.64, 131.86, 131.51, 131.15, 130.37, 129.05, 128.77, 126.98, 124.69, 122.56, 122.34, 120.97, 118.64, 117.63, 115.95, 107.58, 105.14, 104.87, 77.16, 60.84, 56.26, 52.60, 44.37 ppm. ESI-HRMS: *m/z* calcd for $[C_{66}H_{43}BF_{24}N_2O_4]$ 531.2278 $[M\text{-}BArF_{24}]^+$, found: 531.2282.

1.3. Synthesis of macrocycle TTFC8 and [2]rotaxanes 1 and 2

Macrocycle TTFC8

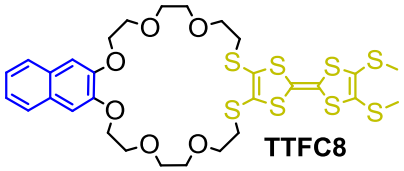

A solution of $CsOHxH_2O$ (302 mg, 1.80 mmol) in dry MeOH (5 mL) was added to a solution of 3,3'-((4',5'-bis(methylthio)-[2,2'-bi(1,3-dithiolylidene)]-4,5-diyl)bis(sulfanediyl))di-propane-nitrile (419 mg, 0.90 mmol) in dry dimethylformamide (15 mL) over 30 min. After the colour changed to deep red, this solution was added over 1 h to a solution of 2,3-bis(2-(2-(2-iodoethoxy)ethoxy)ethoxy)naphthalene (582 mg 0.90 mmol) in dry dimethylformamide (75 mL) at 0°C. The solution was stirred over night at room temperature. Afterwards, the solution was concentrated under reduced pressure and the residue was dissolved in CH_2Cl_2 (40 mL). The organic layer was washed with brine (3x30 mL) and dried over $MgSO_4$. The crude product was purified by column chromatography (SiO_2, CH_2Cl_2 → CH_2Cl_2/MeOH = 200:1). The crude product was recrystallized in acetonitrile to yield the desired product (432 mg, 57.7 mmol, 64 %) as an orange solid. R_f = 0.50 in CH_2Cl_2/MeOH = 150:1; m.p. 111-118 °C ; ^{1}H NMR (700 MHz, CD_2Cl_2): δ = 7.67 (AA'XX' spin system, $^3J_{AX}$ = 6.1, 2H, H_{Ar}); 7.32 (AA'XX' spin system, $^3J_{XA}$ = 6.1, 2H, H_{Ar}); 7.14 (s, 2H, H_{Ar}); 4.24 (m, 4H, OCH_2), 3.93-3.92 (m, 4H, OCH_2); 3.79-3.77 (m, 4H, OCH_2); 3.69-3.66 (m, 8 H OCH_2); 3.01 (t, ^3J = 6.3, 4H, SCH_2); 2.41 (s, 6H, SCH_3) ppm. ^{13}C NMR (176 MHz, CD_2Cl_2): δ = 149.63, 129.87, 128.86, 126.79, 124.68, 114.41, 108.44, 71.44, 71.11, 70.35, 70.13, 69.38, 36.34, 30.90 ppm. ESI-HRMS: *m/z* calcd for $[C_{30}H_{36}O_6S_8]$: 771.0169 $[M+Na]^+$, found: 771.0165.

[2]Rotaxane 1

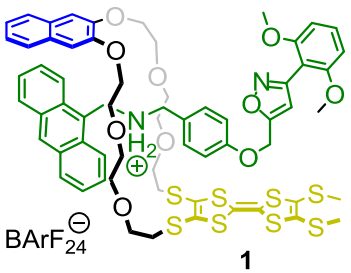

Axle **3** (48.6 mg, 40.0 µmol), macrocycle **TTFC8** (29.9 mg, 40.0 µmol) and nitrile oxide stopper **4** (9.3 mg, 52.0 mmol) were dissolved in CH_2Cl_2 (1 mL). The mixture was heated under argon atmosphere in a pressure tube for 1 d at 38 °C. Afterwards, the solution was directly purified by preparative thin layer chromatography (SiO_2, 2000 microns, CH_2Cl_2) to

yield the desired product as sticky orange oil (67.5 mg, 31.5 µmol, 79%). R_f = 0.80 in CH_2Cl_2; ^{1}H NMR (700 MHz, CD_2Cl_2): δ = 8.34 (d, ^3J = 8.8 Hz, 2H, H_{Ar}), 7.87 (br, 2H, NH_2), 7.74 (s, 8H, H_{BArF24}), 7.69 (d, ^3J = 8.6 Hz, 2H, H_{Ar}), 7.64 (m, 2H, H_{Ar}), 7.58 (s, 4H, H_{Ar}), 7.47 (m, 4H, H_{Ar}), 7.44 (br, 4H, H_{Ar}), 7.39 (t, ^3J = 8.4 Hz, 1H, H_{Ar}), 7.28 (s, 1H, H_{Ar}), 7.20 (d, ^3J = 8.9 Hz, 2H, H_{Ar}), 6.67 (d, ^3J = 8.4 Hz, 2H, H_{Ar}), 6.50 (s, 1H, H_{isox}), 5.83 (s, 2H, H_{Ar}), 5.52 (m, 4H, CH_2), 5.23 (s, 2H, $C\underline{H_2}CCH$), 4.00 (m, 8H, OCH_2), 3.77 (s, 6H, OCH_3), 3.39 (m, 16 H, OCH_2 2.35 (s, 6H, SCH_3) ppm. ^{13}C NMR (700 MHz, CD_2Cl_2): δ = 166.25, 163.06, 162.33, 159.18, 158.93, 157.82, 135.37, 131.95, 131.65, 131.27, 131.02, 130.16, 129.44, 129.38, 128.54, 128.50, 128.12, 128.06, 126.72, 126.04, 125.94, 125.35, 125.01, 123.71, 120.22, 118.04, 115.97, 114.12, 109.15, 107.45, 107.28, 104.67, 104.16, 71.93, 71.76, 71.10, 70.69, 68.67, 61.78, 56.51, 54.00, 53.36, 46.84, 37.49, 19.50 ppm. ESI-HRMS: *m/z* calcd for $[C_{96}H_{79}BF_{24}N_2O_{10}S_8]$: 1279.2556 $[M\text{-}BArF_{24}]^+$, found: 1279.2560.

[2]Rotaxane 2

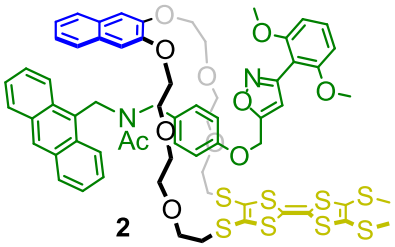

2

[2]Rotaxane **1** (21.4 mg, 10 µmol) was dissolved in acetonitrile (5 mL) and Ac_2O (200 µmol, 19 µL) and NEt_4 (14 µL, 100 µmol) were added. The mixture was stirred for 1 d at room temperature. Afterwards, the solvent was removed *in vacuo* and the residue was purified by a column chromatography (SiO_2, CH_2Cl_2) to yield the desired product as a sticky orange oil (13.2 mg, 9.9 µmol, 99%). R_f = 0.40 in CH_2Cl_2; ^{1}H NMR (700 MHz, CD_2Cl_2): δ = 8.43 (s, 1H, H_{Ar}), 8.08 (d, ^3J = 8.9 Hz, 2H, H_{Ar}), 7.99 (d, ^3J = 8.3 Hz, 2H, H_{Ar}), 7.62 (m, 2H, H_{Ar}), 7.39 (m, 5H, H_{Ar}), 7.26 (m, 4H, H_{Ar}), 7.12 (s, 2H, H_{Ar}), 6.73 (d, ^3J = 8.2 Hz, 2H, H_{Ar}), 6.66 (s, 1H, H_{isox}), 6.64 (d, ^3J = 8.4 Hz, 2H, H_{Ar}), 5.86 (s, 2H, CH_2), 5.53 (s, 2H, CH_2), 4.32 (m, 2H, OCH_2), 4.22 (m, 2H, OCH_2), 3.97 (m, 2H, CH_2), 3.88 (m, 2H, OCH_2), 3.83 (m, 2H, OCH_2), 3.75 (s, 6H, OCH_3), 3.65 (m, 4H, OCH_2), 3.59 – 3.47 (m, 8H, OCH_2), 3.38 (m, 2H, OCH_2), 3.06 (m, 2H, OCH_2), 2.21 (s, 6H, SCH_3), 2.01 (s, 3H, $OCCH_3$) ppm. ^{3}C NMR (176 MHz, CD_2Cl_2): δ = 171.30, 169.07, 159.26, 158.45, 157.40, 149.32, 132.06, 131.93, 131.46, 129.67, 129.53, 129.10, 128.84, 128.64, 128.23, 127.81, 127.13, 126.82, 126.71, 125.62, 125.08, 124.67, 116.23, 110.99, 110.58, 110.30, 108.29, 107.59, 104.53, 70.41, 70.32, 70.29, 69.84, 68.94, 61.62, 56.47, 54.00, 49.16, 39.47, 35.93, 22.16, 19.30 ppm. ESI-HRMS: *m/z* calcd for $[C_{66}H_{68}N_2O_{11}S_8]$: 1343.2481 $[M+Na]^+$, found: 1343.2502.

4. Synthesis of [2]rotaxane 6

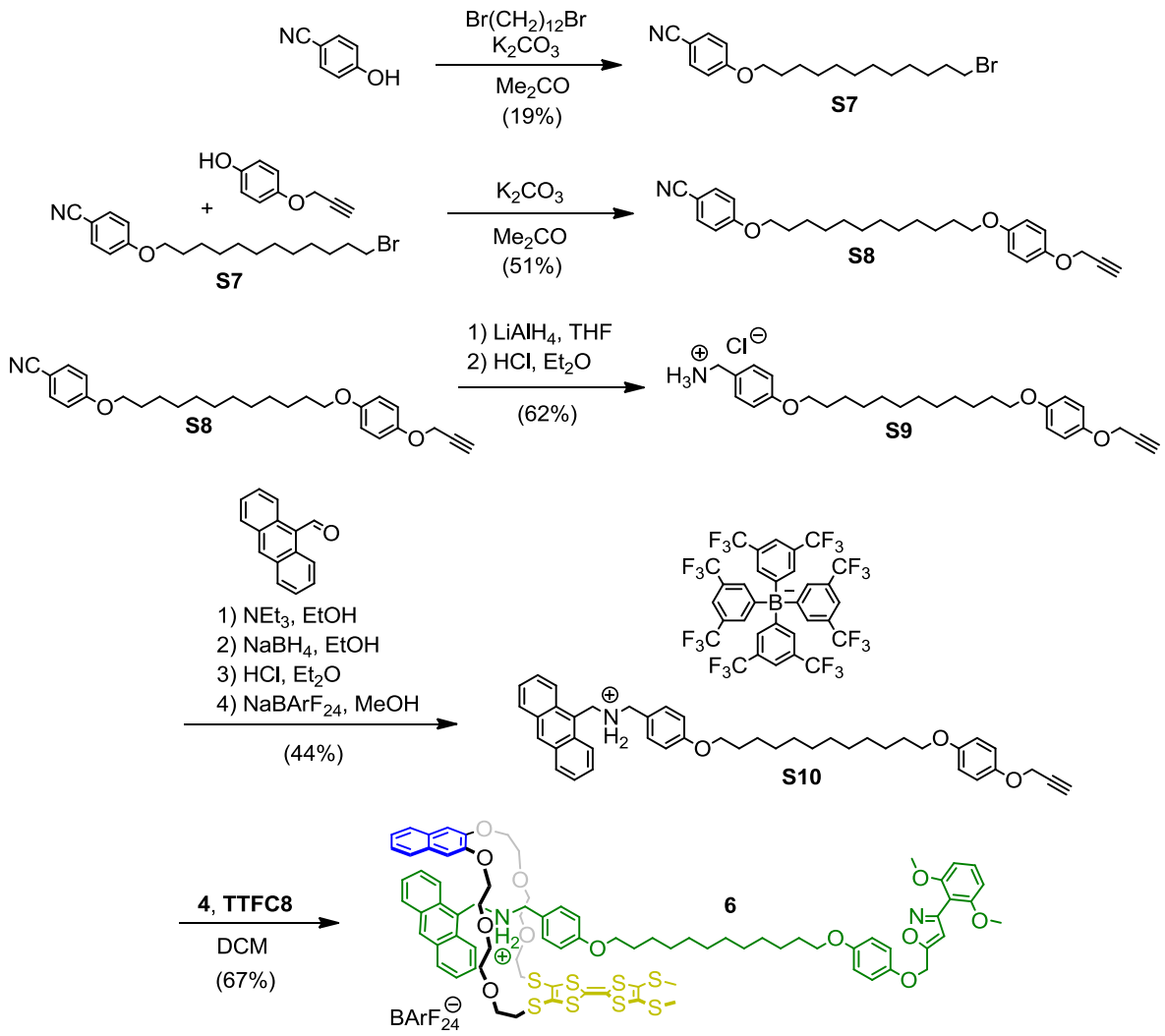

Fig. S2 Synthesis of [2]rotaxane **6**

4-((12-Bromododecyl)oxy)benzonitrile (S7)

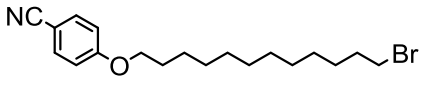

S7

4-Hydroxybenzonitrile (1.58 g, 13.3 mmol), 1,12-dibromododecane (4.35 g, 13.3 mmol) and K_2CO_3 (3.66 g, 26.6 mmol) were refluxed in acetone (100 mL) for 6 h. Afterwards, the mixtures was filtered and concentrated under reduced pressure. The residue was suspended in CH_2Cl_2 (50 mL) and washed with brine (3x50 mL). After the organic layer was dried over $MgSO_4$, the solvent was removed *in vacuo* and the residue was purified by column

chromatography (SiO_2, hexanes/CH_2Cl_2 = 2:1 → 1:1) followed by a recrystallization from MeOH to obtain the desired product as colourless crystals (930 mg, 2.53 mmol, 19%). R_f = 0.30 in hexanes/CH_2Cl_2 = 2:1; m.p. 57-59 °C; ^{1}H NMR (500 MHz, $CDCl_3$) δ = 7.57 (AA'XX' spin system, $^3J_{AX}$ = 8.9, 2H, H_{Ar}), 6.93 (AA'XX' spin system, $^3J_{XA}$ = 8.9, 2H, H_{Ar}), 3.99 (t, ^3J = 6.5 Hz, 2H, CH_2), 3.41 (t, ^3J = 6.9 Hz, 2H, CH_2), 1.82 (m, 4H, CH_2), 1.56 – 1.12 (m, 18H, CH_2) ppm. ^{13}C NMR (126 MHz, $CDCl_3$): δ = 162.59, 134.09, 119.47, 103.76, 77.16, 68.54, 34.21, 32.95, 29.63, 29.63, 29.62, 29.54, 29.43, 29.11, 28.88, 28.29, 26.06 ppm. ESI-HRMS: *m/z* calcd for $[C_{19}H_{28}BrNO]$: 404.0986 $[M+K]^+$; found: 404.0967.

4-((12-(4-(Prop-2-yn-1-yloxy)phenoxy)dodecyl)oxy)benzonitrile (S8)

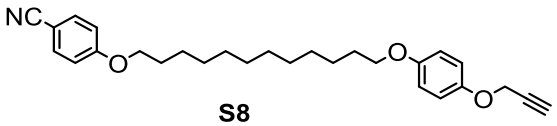

S8

Bromide **S7** (733 mg, 2.00 mmol), 4-(prop-2-yn-1-yloxy)phenol (593 mg, 4.00 mmol) and K_2CO_3 (553 mg, 4.00 mmol) were refluxed in acetone for 12 h. After cooling to room temperature, the mixture was filtered and concentrated under reduced pressure. The residue was suspended in CH_2Cl_2 (100 mL) and washed with brine (3x100 mL). The organic phase was dried over $MgSO_4$ and solvent was removed *in vacuo*. The residue was purified by column chromatography (SiO_2, pentanes → CH_2Cl_2) to obtain the desired product as a colourless solid (442 mg, 1.02 mmol, 51%). R_f = 0.40 in pentanes/CH_2Cl_2 = 1:1; m.p. 113-114 °C; ^{1}H NMR (500 MHz, $CDCl_3$): δ = 7.57 (AA'XX' spin system, $^3J_{XA}$ = 8.9, 2H, H_{Ar}), 6.94 – 6.89 (m, 4H, H_{Ar}), 6.83 (AA'XX' spin system, $^3J_{XA}$ = 9.1, 2H, H_{Ar}), 4.64 (d, ^4J = 2.4 Hz, 2H, C$\underline{H_2}$CCH), 3.99 (t, ^3J = 6.5 Hz, 2H, OCH_2), 3.90 (t, ^3J = 6.5 Hz, 2H, OCH_2), 2.50 (t, ^4J = 2.4 Hz, 1H, CCH), 1.83 – 1.71 (m, 4H, CH_2), 1.49 – 1.26 (m, 18H, CH_2) ppm. ^{13}C NMR (126 MHz, $CDCl_3$): δ = 162.60, 154.18, 151.71, 134.10, 119.48, 116.24, 115.44, 115.31, 103.77, 79.07, 77.16, 75.39, 68.68, 68.55, 56.75, 29.69, 29.68, 29.68, 29.65, 29.53, 29.50, 29.45, 29.11, 26.19, 26.07 ppm. ESI-HRMS: *m/z* calcd for $[C_{28}H_{35}NO_3]$: 456.2509; found: 456.2501.

(4-((12-(4-(Prop-2-yn-1-yloxy)phenoxy)dodecyl)oxy)phenyl)methanaminium chloride (S9)

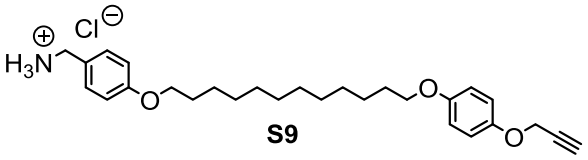

S9

Nitrile **S8** (240 mg, 0.56 mmol) was dissolved in dry THF (8 mL) and slowly dropped into an ice-cooled schlenk flask with dispersed $LiAlH_4$ (105 mg, 2.76 mmol) in dry THF under argon atmosphere. After warming up to room temperature, the mixture was stirred for 1 d. Unreacted $LiAlH_4$ was quenched with dropwise addition of saturated Na_2SO_4 solution. Afterwards, CH_2Cl_2 (50 mL) was added and the mixture was filtered. The filtrate was concentrated under reduced pressure and redissolved in CH_2Cl_2 (50 mL). The clear solution was washed with brine (2x50 mL) and dried over $MgSO_4$. The solvent was removed *in vacuo* and a minimum volume of Et_2O/CH_2Cl_2 (1:1) and concentrated aqueous HCl was added to precipitate the desired product as the hydrochloride. Drying *in vacuo* yielded the product as a colourless solid (163 mg, 0.34 mmol, 62%). m.p. 190 °C (decomposition); ^{1}H NMR (500 MHz, DMSO-d6): δ = 8.28 (br, 3H, NH_3), 7.36 (AA'XX' spin system, $^3J_{XA}$ = 8.7, 2H, H_{Ar}), 6.92 (AA'XX' spin system, $^3J_{AX}$ = 8.7, 2H, H_{Ar}), 6.89 – 6.79 (m, 4H, H_{Ar}), 4.68 (d, ^4J = 2.4 Hz, 2H, C$\underline{H}_2$CCH), 3.97 – 3.73 (m, 6H, CH_2), 3.51 (t, ^3J = 2.4 Hz, 1H, CCH), 1.72 – 1.57 (m, 4H, CH_2), 1.30 (m, 16H, CH_2) ppm. ^{13}C NMR (126 MHz, DMSO-d6): δ = 158.80, 153.27, 151.09, 130.50, 125.78, 115.90, 115.16, 114.43, 79.57, 77.97, 67.79, 67.51, 55.89, 41.69, 39.52, 29.02, 29.01, 28.99, 28.97, 28.79, 28.77, 28.63, 25.54, 25.53, 25.50 ppm. ESI-HRMS: *m/z* calcd for $[C_{28}H_{40}ClNO_3]$: 438.3003 $[M\text{-}Cl]^+$, found: 438.3000.

1-(Anthracen-9-yl)-N-(4-((12-(4-(prop-2-yn-1-yloxy)phenoxy)dodecyl)oxy)-benzyl)methanaminium tetrakis[3,5-bis(trifluoromethyl)phenyl]borate (S10)

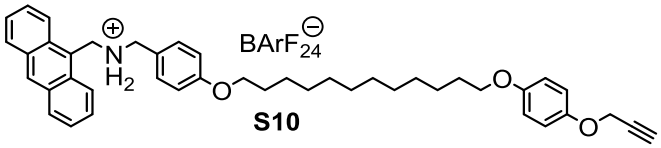

S10

Hydrochloride **S9** (130 mg, 274 µmol), 9-anthracenecarboxaldehyde (56.6 mg, 274 µmol) and NEt_4 (29 µL) were dissolved in dry EtOH (10 mL) and heated at reflux for 6 h under Ar atmosphere. After cooling to room temperature, additional EtOH (15 mL) and $NaBH_4$ (31.1 mg, 822 µmol) was added. The mixture was stirred overnight and quenched with a small volume of saturated $NaHCO_3$ solution. The mixture was concentrated under reduced pressure and redissolved in CH_2Cl_2 (50 mL). The organic phase was washed with saturated $NaHCO_3$ solution (50 mL), brine (50 mL) and dried afterwards over $MgSO_4$. Removing the solvent *in vacuo* yielded the crude amine which was purified by column chromatography (SiO_2, CH_2Cl_2, R_f = 0.15 in CH_2Cl_2). The amine was dissolved in a minimal volume of MeOH/ethyl acetate/concentrated aqueous HCl (10:10:1). Removal of the solvent and drying *in vacuo* yielded the hydrochloride as a colourless solid (115 mg, 173 µmol). The

hydrochloride (50 mg, 75 µmol) and $NaBArF_{24}$ (67 mg, 75 µmol) were dissolved in MeOH and the mixture was stirred for 3 h. After removal of the solvent *in vacuo*, the residue was dissolved in CH_2Cl_2 (5 mL) and washed with water (5 mL). The desired product was obtained as colourless oil (78 mg, 54 µmol, 44% over all steps) after evaporating the solvent. ^{1}H NMR (500 MHz, $CDCl_3$): δ = 8.66 (s, 1H, H_{Ar}), 8.14 – 8.09 (m, 2H, H_{Ar}), 7.72 (m, 8H, H_{BArF24}), 7.70 – 7.64 (m, 2H, H_{Ar}), 7.60 – 7.52 (m, 4H, H_{Ar}), 7.50 (m, 4H, H_{BArF24}), 7.23 (AA'XX' spin system, $^3J_{XA}$ = 8.7, 2H, H_{Ar}), 7.00 (m, 4 H, H_{Ar} and NH_2), 6.77 – 6.69 (m, 4H, H_{Ar}), 5.22 (m, 2H, CH_2), 4.50 (d, ^4J = 2.4 Hz, 2H, C$\underline{H_2}$CCH), 4.29 (m, 2H, CH_2), 3.99 (t, ^3J = 6.5 Hz, 2H, OCH_2), 3.82 (t, ^3J = 6.5 Hz, 2H, OCH_2), 2.44 (t, ^4J = 2.4, 1H, CCH), 1.82 (m, 4H, CH_2), 1.73 – 1.66 (m, 2H, CH_2), 1.47 (m, 2H, CH_2), 1.30 (m, 16H, CH_2) ppm. ^{13}C NMR (176 MHz, $CDCl_3$): δ = 161.82, 161.80, 154.30, 151.46, 134.95, 132.49, 131.42, 131.14, 130.83, 130.26, 129.48, 128.98, 126.15, 124.66, 120.09, 119.18, 117.90, 117.66, 116.62, 116.34, 115.76, 78.86, 77.16, 75.73, 69.01, 68.63, 57.33, 53.32, 44.01, 29.57, 29.52, 29.52, 29.51, 29.40, 29.37, 29.31, 29.08, 26.06, 25.99 ppm. ESI-HRMS: *m/z* calcd for $[C_{75}H_{62}BF_{24}NO_3]$: 628.3785 $[M\text{-}BArF_{24}]^+$, found: 628.3785.

[2]Rotaxane 6

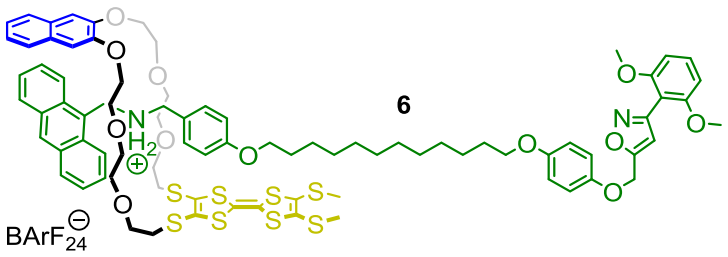

Ammonium axle **S10** (51.0 mg, 34.1 µmol), macrocycle **TTFC8** (25.5 mg, 34.1 µmol) and nitrile oxide stopper **4** (7.9 mg, 44.3 µmol) were dissolved in CH_2Cl_2 (1 mL) under Ar atmosphere. The solution was heated to 35 °C for 1 d in a pressure tube. Afterwards, the solution was directly purified by column chromatography (SiO_2, pentanes/CH_2Cl_2 = 1:1 → 1:2) to obtain the desired product as an orange oil (55.0 mg, 22.7 µmol, 67%). R_f = 0.50 in CH_2Cl_2; ^{1}H NMR (400 MHz, CD_2Cl_2): δ = 8.34 (d, ^3J = 9.0 Hz, 2H, H_{Ar}), 7.83 (br, 2H, NH_2), 7.73 (m, 12H, H_{Ar} and H_{BArF24}), 7.66 – 7.58 (m, 4H, H_{Ar}), 7.56 (s, 4H, H_{BArF24}), 7.46 (m, 4H, H_{Ar}), 7.43 (m, 4H, H_{Ar}), 7.38 (t, ^3J = 8.4 Hz, 1H, H_{Ar}), 7.28 (s, 1H, H_{Ar}), 7.03 (d, ^3J = 8.8 Hz, 2H, H_{Ar}), 6.93 (AA'XX' spin system, $^3J_{AX}$ = 9.1, 2H, H_{Ar}), 6.83 (AA'XX' spin system, $^3J_{XA}$ = 9.1, 2H, H_{Ar}), 6.66 (d, ^3J = 8.4 Hz, 2H, H_{Ar}), 6.41 (s, 1H, H_{isox}), 5.82 (s, 2H, H_{Ar}), 5.49 (m, 4H, CH_2), 5.11 (s, 2H, CH_2), 4.36 (m, 2H, OCH_2), 4.08 (m, 4H, OCH_2), 3.97 (m, 4H, OCH_2), 3.89 (m, 4H, OCH_2), 3.77 (s, 6H, OCH_3), 3.70 (m, 4H, OCH_2), 3.63 (m, 4H, OCH_2), 3.44 (m, 4H,

OCH_2), 3.29 (m, 4H, OCH_2), 2.98 (m, 2H, OCH_2), 2.35 (m, 6H, SCH_3), 1.76 (m, 4H, CH_2), 1.30 (m, 16H, CH_2) ppm. ^{13}C NMR (176 MHz, CD_2Cl_2): δ = 167.24, 163.08, 162.32, 160.15, 159.23, 157.71, 154.78, 152.61, 145.37, 135.37, 133.14, 131.77, 131.60, 131.27, 131.03, 130.14, 129.46, 129.38, 128.54, 128.08, 127.36, 126.72, 125.50, 125.35, 125.09, 124.51, 123.79, 120.33, 118.04, 116.56, 115.90, 115.44, 107.57, 107.44, 106.90, 104.63, 104.17, 71.95, 71.72, 71.08, 70.70, 69.13, 68.86, 68.67, 62.69, 56.76, 56.52, 54.00, 53.45, 46.79, 37.49, 36.76, 30.13, 30.12, 29.97, 29.95, 29.92, 29.80, 26.59, 19.53, 19.50 ppm. ESI-HRMS: *m/z* calcd for $[C_{114}H_{107}BF_{24}N_2O_{12}S_8]$: 1555.4645 $[M\text{-}BArF_{24}]^+$, found: 1555.4581.

1.5. Synthesis of acetylated [2]rotaxane 7

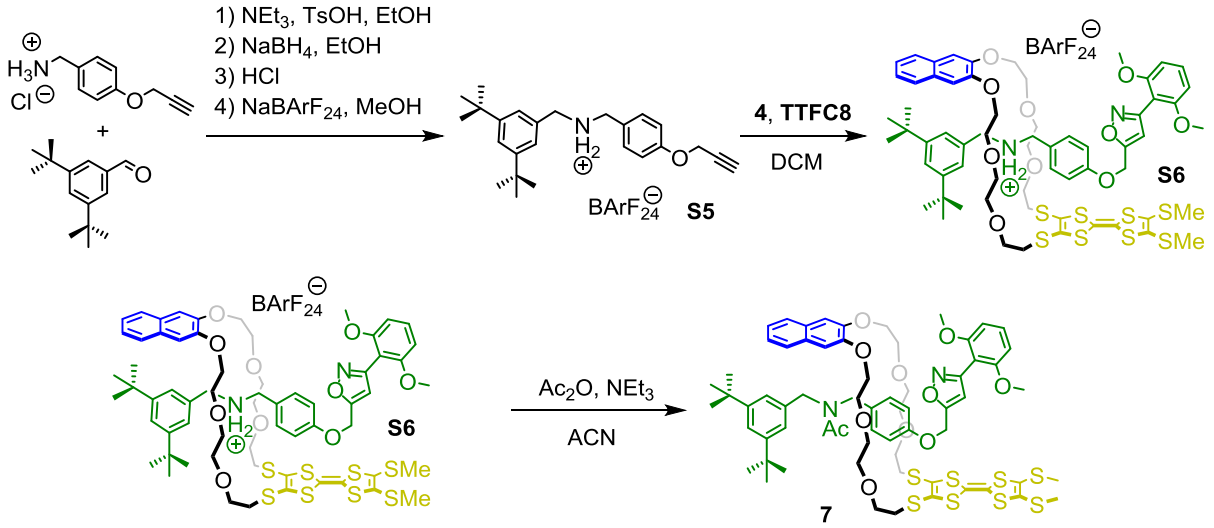

Fig. S3 Synthesis of reference [2]rotaxane **7** and the corresponding axle molecule

N-(3,5-Di-tert-butylbenzyl)-1-(4-(prop-2-yn-1-yloxy)phenyl)methanaminium tetrakis[3,5-bis(trifluoromethyl)phenyl]borate

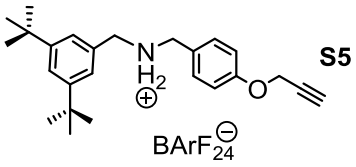

(4-(prop-2-yn-1-yloxy)phenyl)methanaminium chloride (594 mg, 3.00 mmol) was dispersed in dry ethanol (100 mL) under Ar atmosphere and NEt_4 was added untill the solution cleared up. Afterwards, $TsOHxH_2O$ (5.7 mg, 0.03 mmol) and 3,5-di-tert-butylbenzaldehyde (688 mg, 3.15 mmol) were added. The mixture was refluxed under Ar for 4 h. After cooling to room

temperature, $NaBH_4$ (567 mg, 15 mmol) was added in portions over 10 min. The solution was stirred over night at RT and quenched with sat. $NaHCO_3$ solution. The solvent was removed under reduced pressure and the remaining aqueous phase was extracted with CH_2Cl_2 (3x100 mL). The combined organic phases were dried over $MgSO_4$ and solvent was removed afterwards. The crude solid was purified by column chromatography (SiO_2, CH_2Cl_2 → CH_2Cl_2/MeOH/ NEt_4 = 200:10:1) and the amine (615 mg, 1.69 mmol) was obtained as a colourless oil. The amine (90.9 mg, 0.25 mmol) was dissolved in ethyl acetate (5 mL) and conc. aqueous HCl (0.3 mL) was added. The mixture was stirred overnight at room temperature. The solvent was removed under reduced pressure and the hydrochloride was quantitatively obtained as a colourless solid. $NaBArF_{24}$ (221.5 mg, 0.25 mmol, 1 eq.) was added and the solids were dissolved in MeOH (2 mL). The solution was stirred overnight and solvent was evaporated under reduced pressure. The remaining solid was dissolved in CH_2Cl_2 (10 mL) and washed with H_2O (2x5 mL). Drying over $MgSO_4$ and removal of the solvent yielded the desired product (258 mg, 0.21 mmol, 47 % over all steps) as a colourless powder. R_f = 0.40 in CH_2Cl_2/MeOH/NEt_4 = 100:10:1; m.p. 91-93 °C ; ^{1}HNMR (500 MHz, $CDCl_3$): δ = 7.76 – 7.68 (br, 8H, H_{BArF24}), 7.59 (t, ^4J = 1.8 Hz, 1H, H_{Ar}), 7.54 (br, 4H, H_{BArF24}), 7.17 (AA'XX' spin system, $^3J_{AX}$ = 8.7 Hz, 2H, H_{Ar}), 7.11 (d, ^4J = 1.8 Hz, 2H, H_{Ar}), 7.01 (AA'XX' spin system, $^3J_{AX}$ = 8.7 Hz, 2H, H_{Ar}), 4.68 (d, ^4J = 2.4 Hz, 2H, CH2CCH), 4.17 (s, 2H, NCH2), 4.12 (s, 2H, NCH2), 2.49 (t, ^4J = 2.4 Hz, 1H, CCH), 1.29 (s, 18H, H_{tBu}) ppm. ^{13}C NMR (126 MHz, $CDCl_3$): δ = 161.85, 159.76, 153.81, 134.98, 130.91, 129.04, 128.00, 125.71, 124.52, 123.28, 121.50, 117.70, 116.66, 77.54, 77.16, 76.40, 55.99, 53.36, 52.35, 35.14, 31.21 ppm. ESI-HRMS: *m/z* calcd for $[C_{57}H_{46}BF_{24}NO]$: 364.2640 $[M\text{-}BArF_{24}]^+$, found: 364.2647.

[2]Rotaxane S6

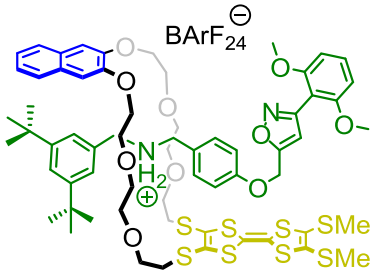

S6

Axle **S5** (45.0 mg, 36.6 µmol) and macrocycle **TTFC8** (27.4 mg, 36.6 µmol) were dissolved in CH_2Cl_2 (0.5 mL) and stirred for 1 h at room temperature. Afterwards, nitrile oxide **4** (7.9 mg, 43.9 µmol) was added and the mixture was heated to 38 °C in a pressure tube for 4 h. The mixture was directly purified by column chromatography (SiO_2, CH_2Cl_2). The desired product (48 mg, 22.3 µmol, 61%) was obtained as an orange sticky solid. R_f = 0.60 in CH_2Cl_2; ^{1}H NMR (500 MHz, $CDCl_3$): δ = 7.71 = (m, 8H, H_{BArF24}), 7.63 (AA'XX' spin system, $^3J_{AX}$ = 6.1 Hz,

2H, H_{Ar}), 7.53 (m, 4H, H_{BArF24}), 7.48 (t, ^4J = 1.7 Hz, 1H, HAr), 7.45 (d, ^4J = 1.7 Hz, 2H, H_{Ar}), 7.41 – 7.34 (m, 3H, H_{Ar}), 7.10 (AA'XX' spin system, $^3J_{AX}$ = 8.5 Hz, 2H, H_{Ar}), 6.91 (s, 2H, H_{Ar}), 6.65 (d, ^3J = 8.5 Hz, 2H, H_{Ar}), 6.44 (AA'XX' spin system, $^3J_{AX}$ = 8.5 Hz, 2H, H_{Ar}), 6.34 (s, 1H, H_{isox}), 4.82 – 4.74 (m, 2H, NCH_2), 4.58 (m, 2H, NCH_2), 4.28 (s, 2H, CH_2CC), 4.21 (m, 2H, OCH_2), 4.03 (m, 2H, OCH_2), 3.90 (m, 2H, OCH_2), 3.79 (s, 6H, OCH_3), 3.73 – 3.65 (m, 4H, OCH_2), 3.63 – 3.52 (m, 8H, OCH_2), 3.49 – 3.34 (m, 6H, OCH_2), 1.26 (s, 18H, H_{tBu}) ppm. ^{13}C-NMR (126 MHz, $CDCl_3$): δ = 165.66, 161.80, 158.89, 158.76, 157.28, 152.43, 134.96, 131.51, 130.84, 130.74, 129.09, 129.03, 127.95, 126.50, 125.79, 125.67, 124.11, 123.62, 123.31, 123.19, 121.45, 117.63, 114.74, 108.03, 106.60, 104.29, 77.16, 71.36, 70.51, 69.91, 68.39, 60.48, 56.16, 53.42, 53.04, 35.15, 31.40 ppm. ESI-HRMS: *m/z* calcd for $[C_{96}H_{91}BF_{24}N_2O_{10}S_8]$: 1291.3495 $[M\text{-}BArF_{24}]^+$, found: 1291.3442.

[2]Rotaxane 7

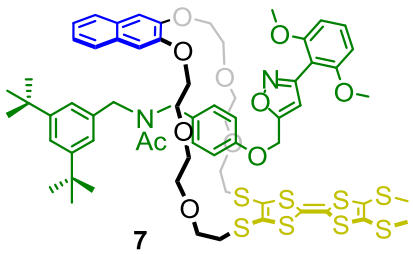

7

[2]Rotaxane **S6** (10.8 mg, 5.0 µmol) was dissolved in acetonitrile (2 mL) and trimethylamine (6.9 µL, 50 µmol) and Ac_2O (9.5 µL, 100 µmol) were added. The mixture was stirred at room temperature overnight and concentrated under reduced pressure. The residue was purified by column chromatography (SiO_2, CH_2Cl_2) to obtain the desired product as a yellow oil (5.2 mg, 3.9 µmol, 78%). R_f = 0.15 in CH_2Cl_2; (Because of the *cis-trans* isomerism of the amide bond, two sets of NMR signals are observed.) ^{1}H NMR (700 MHz, CD_2Cl_2): δ = 7.65 (m, 2H, H_{Ar}), 7.39 – 7.27 (m, 5H, H_{Ar}), 7.20 (m, 1H, H_{Ar}), 7.11 (m, 2H, H_{Ar}), 6.99-6.90 (m, 4H, H_{Ar}), 6.67 (m, 1H, H_{isox}), 6.63 (m, 2H, H_{Ar}), 5.84 (s, 2H, CH_2), 4.38 (m, 2H, CH_2), 4.29 (m, 2H, OCH_2), 4.21 (m, 2H, OCH_2), 4.19 (m, 2H, CH_2), 3.83 (m, 4H, OCH_2), 3.74 (m, 6H, OCH_3), 3.65 – 3.59 (m, 4H, OCH_2), 3.54 – 3.45 (m, 6H, OCH_2), 3.42 – 3.32 (m, 2H, OCH_2), 3.03 (m, 2H, OCH_2), 2.03 (m, 3H, $OCCH_3$), 1.30 (m, 18H, H_{tBu}) ppm. ^{13}C NMR (176 MHz, CD_2Cl_2): δ = 171.20, 169.21, 159.28, 158.64, 158.38, 157.41, 151.97, 149.38, 137.39, 131.45, 129.84, 129.69, 129.11, 127.87, 126.72, 124.68, 122.75, 121.93, 121.16, 116.26, 108.36, 107.58, 107.50, 104.56, 104.47, 70.40, 70.29, 69.86, 69.82, 68.96, 61.75, 56.53, 56.49, 54.00, 51.35, 48.76, 47.68, 35.29, 31.79, 21.96 ppm. ESI-HRMS: *m/z* calcd for $[C_{66}H_{80}N_2O_{11}S_8]$: 1333.3601 $[M+H]^+$, found: 1333.3542.

2. Additional NMR Data

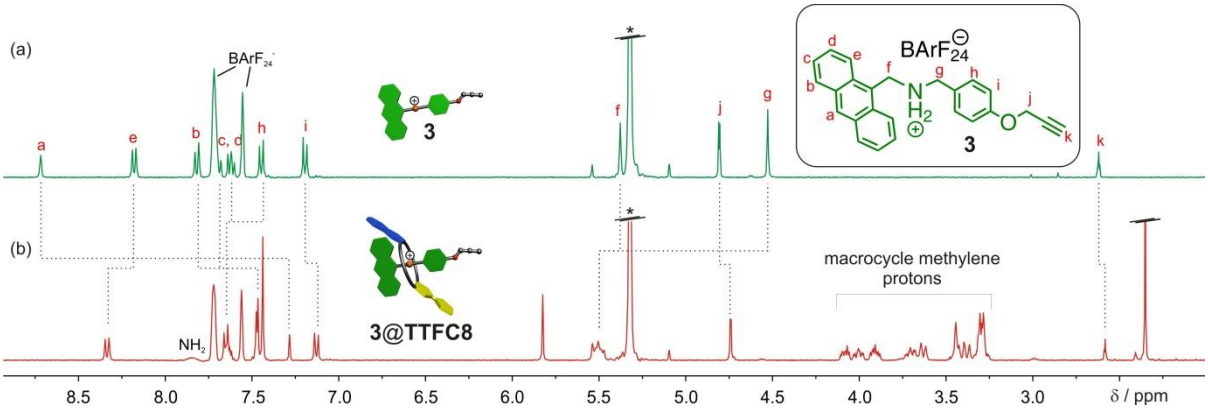

Fig. S4 Stacked ^{1}H NMR spectra (400 MHz, 2.0 mM, CD_2Cl_2, 298 K) of (a) axle **3** and (b) a 1:1 mixture of macrocycle **TTFC8** and axle **3**. Solvent residual signal is marked with an asterisk.

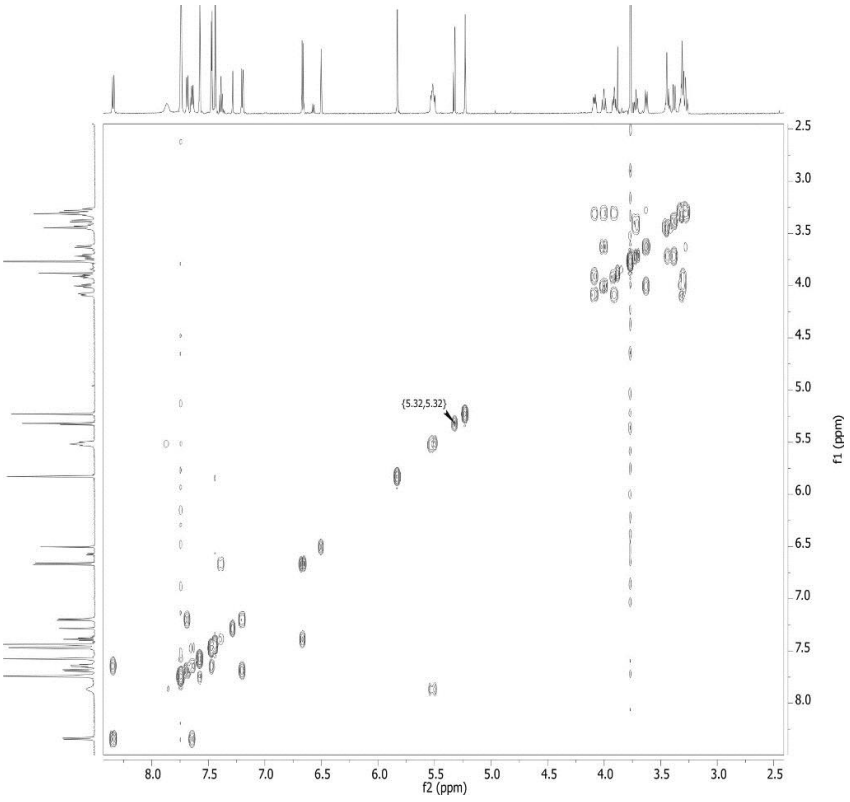

Fig. S5 ^{1}H,^{1}H COSY NMR spectrum (700 MHz, CD_2Cl_2, 298 K) of [2]rotaxane **1**

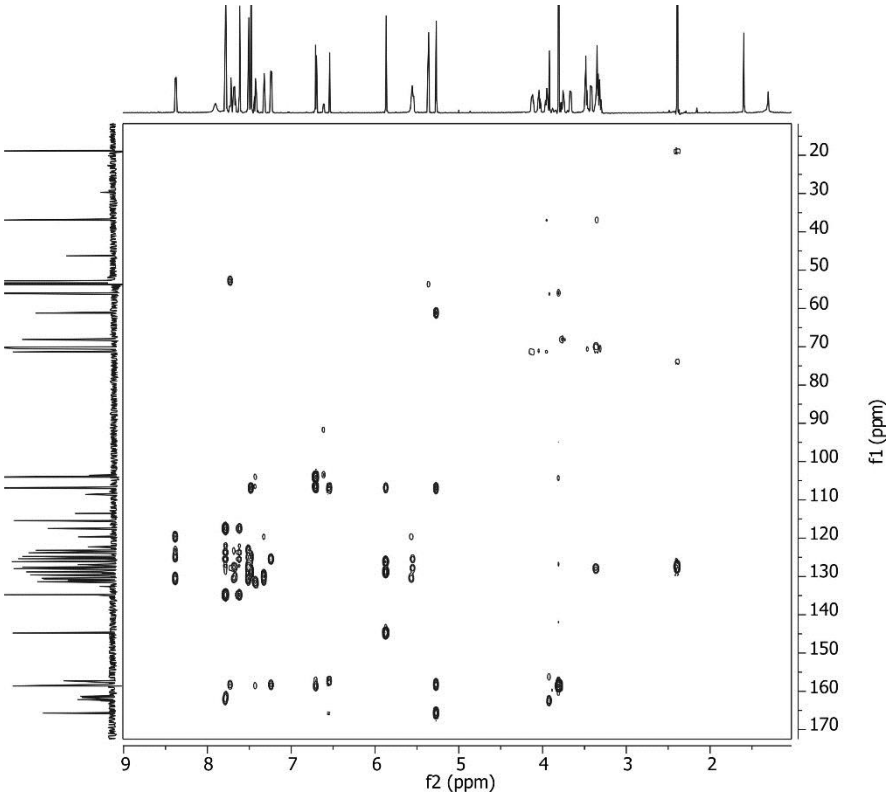

Fig. S6 HMBC spectrum (700 MHz, CD_2Cl_2, 298 K) of [2]rotaxane **1**

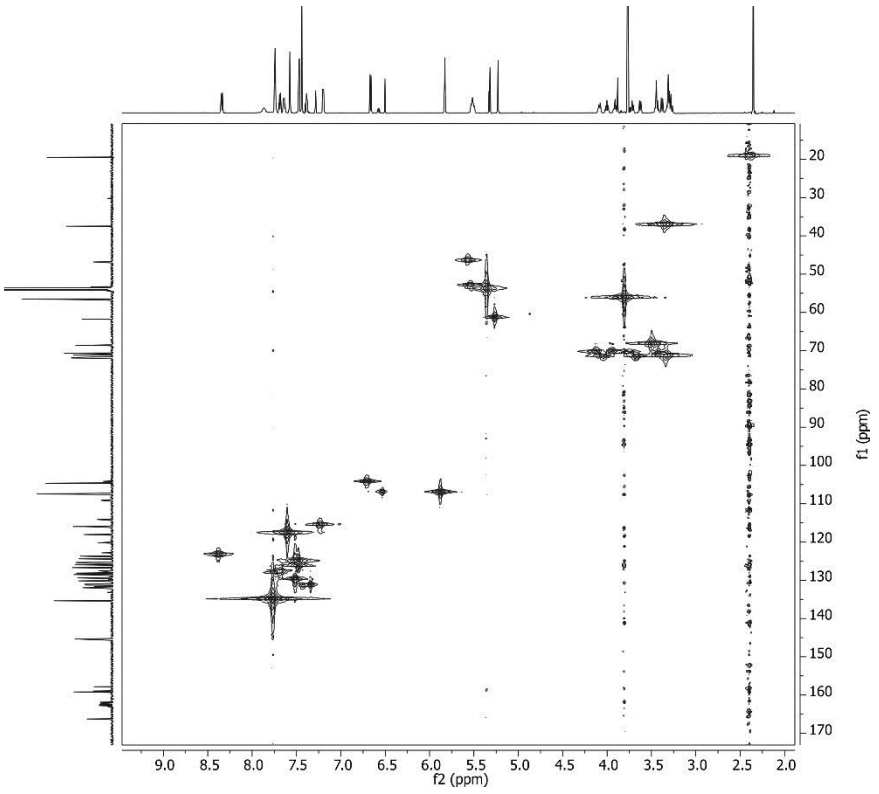

Fig. S7 HMQC spectrum (700 MHz, CD_2Cl_2, 298 K) of [2]rotaxane **1**

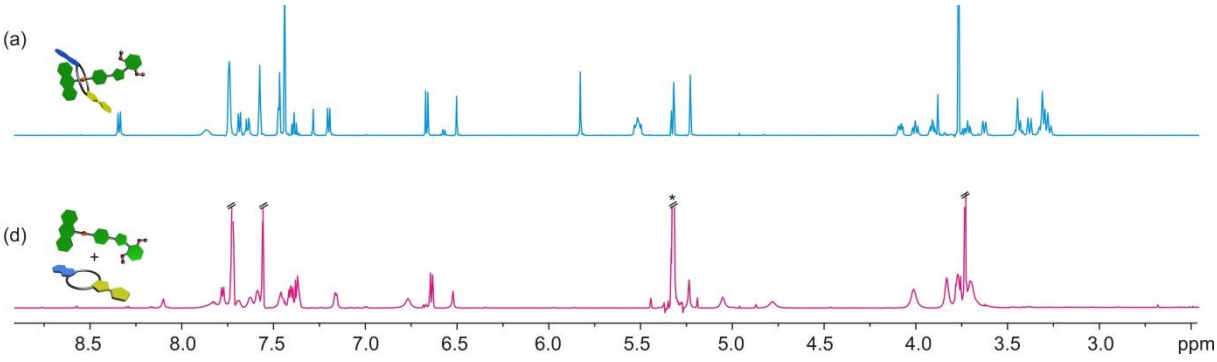

Fig. S8 Stacked ^{1}H NMR spectra (700 MHz, 2.0 mM, CD_2Cl_2, 298 K) of (a) [2]rotaxane **1** and (b) a 1:1 mixture of macrocycle **TTFC8** and free stoppered axle **5**. Clearly, the spectra are not superimposable which confirms the interlocked structure of [2]rotaxane **1**.

3. Mass spectrometric data

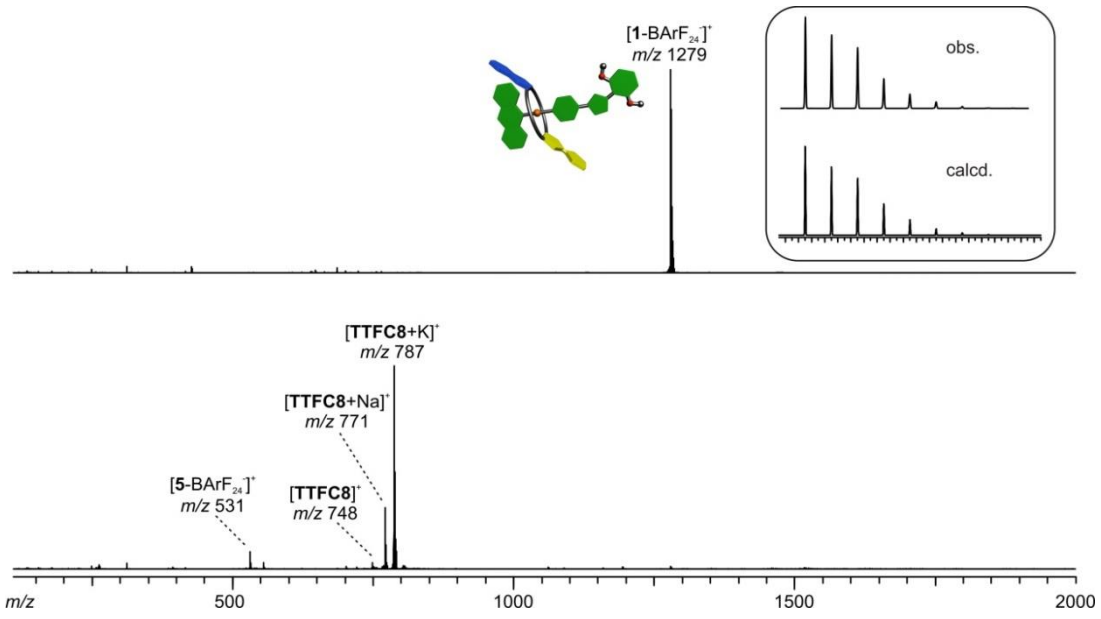

Fig. S9 ESI-FTICR mass spectrum obtained from a MeOH solution (10 μM) of [2]rotaxane **1** (top) and a 1:1 mixture of free stoppered axle **5** and TTF-macrocycle **TTFC8** (bottom). Comparison of both spectra clearly shows [2]rotaxane **1** to be mechanically interlocked and not to dissociate into the two components.

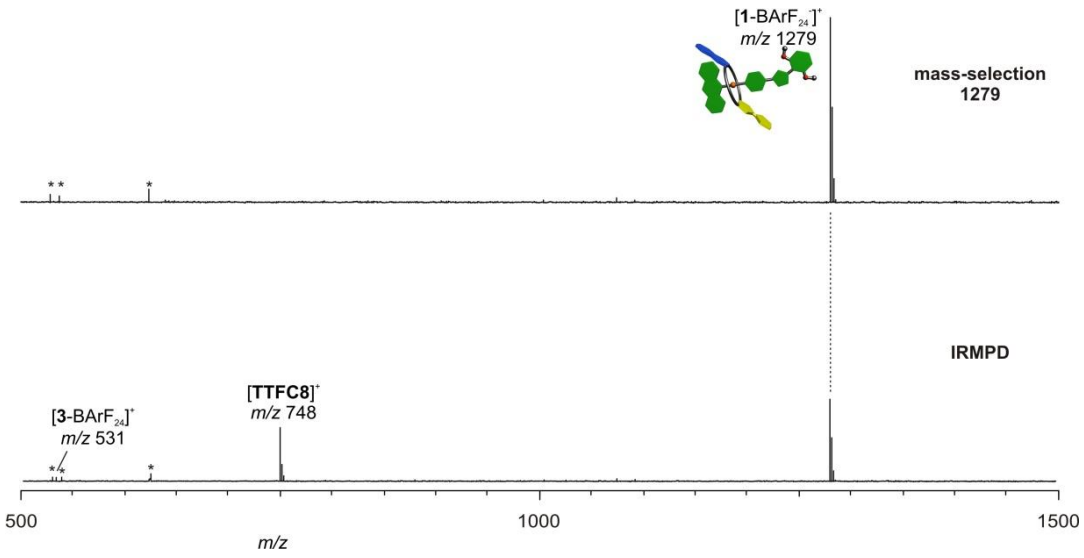

Fig. S10 Infrared multiphoton dissociation (IRMPD) experiment with mass-selected rotaxane ions at m/z 1279 generated from a MeOH solution (10 µM) of [2]rotaxane **1**: (top) after mass-selection; (bottom) after IRMPD experiment. As reported for a similar system, an electron transfer from the macrocycle to the axle occurs and releases the macrocycle cation-radical (*m/z* 748).[3] This fragmentation pathway speaks in favour of a mechanically interlocked structure of [2]rotaxane **1**.

4. Additional fluorescence spectra

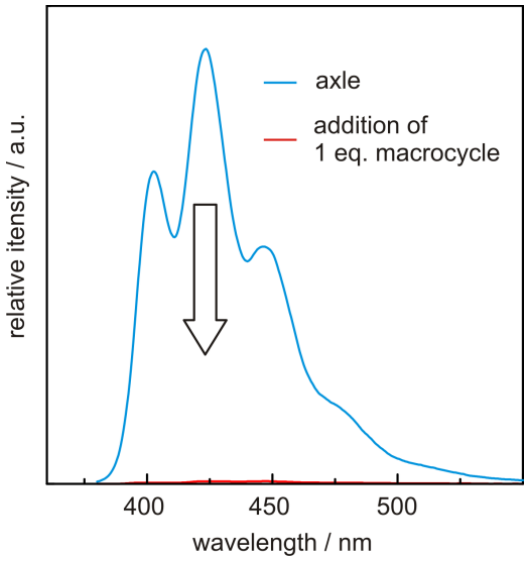

Fig. S11 Fluorescence spectra of axle **3** (blue) and pseudo[2]rotaxane **3@TTFC8** (red) in CH_2Cl_2 (50 µM) at 298 K (λ_{ex} = 370 nm). The fluorescence of axle **3** is strongly quenched due to an electron transfer from the macrocycle to the axle in the pseudo[2]rotaxane **3@TTFC8.**

5. Isothermal titration calorimetry

ITC titrations were carried out in dry 1,2-dichloroethane (DCE) at 298 K on a TAM III microcalorimeter (Waters GmbH, TA Instruments, Eschborn, Germany). A volume of 800 µL of a 1 mM solution of macrocycle **TTFC8** was placed in the sample cell and 250 µL of a solution of the axle **3** (8 mM) in the syringe. The titrations consisted of 32 consecutive injections of 8 µL each with a 20 min interval between injections. Heats of dilution were determined by titration of axle solutions into the sample cell containing blank solvent and were subtracted from each data set. The heat flow generated in the sample cell is measured as a differential signal between sample and reference cells. Hence, an exothermic event results in a positive and an endothermic in a negative heat flow. The data were analysed using the instrument's internal software package and fitted with a 1:1 binding model. Each titration was conducted twice and the measured values for K, ΔG, and ΔH were averaged.

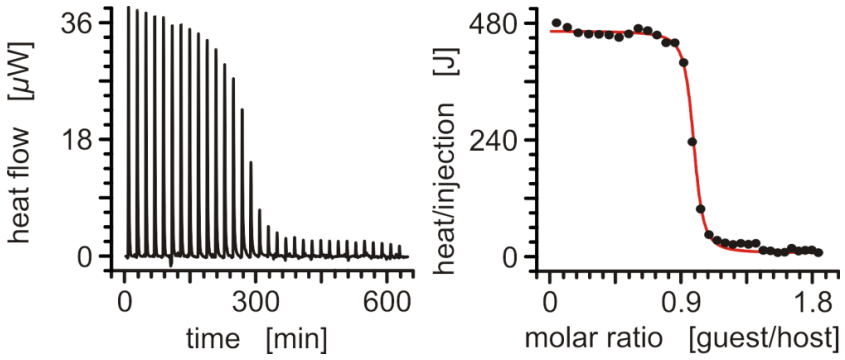

Fig. S12 Titration plots (heat flow over time (left) and heat/volume over guest/host ratio) obtained from ITC experiments conducted with axle **3** and wheel **TTFC8**.

6. Cyclic voltammetry and digital simulations

Redox-potentials reported in this study were obtained by cyclic voltammetry. All measurements were at least conducted twice. Measurements were carried out in dry and degassed CH_2Cl_2 or acetonitrile solutions with 0.1 M electrolyte and 1 mM analyte concentration using a three-electrode configuration (glassy carbon working electrodes, Pt counter electrode, Ag wire as pseudoreference) and an Autolab PGSTAT302N potentiostat. The decamethylferrocene/decamethylferrocenium ($[FeCp_2^*]^{+/0}$) couple was used as the internal reference for all measurements to ensure maximum comparability. Energy differences were calculated according to the equation $\Delta G = n F \Delta E$.

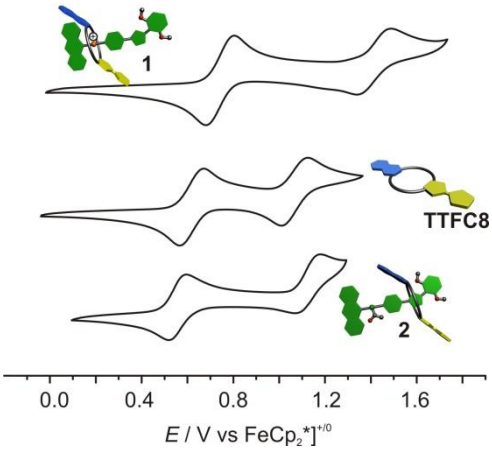

Fig. S13 Stacked cyclic voltammograms (CH_2Cl_2, $TBArF_{24}$ (0.1 M), 298 K) of electro-active species **1**, **TTFC8** and **2** (1 mM) at a scan rate of 100 mV s^{-1} corresponding to the correlation diagram in Fig. 5 in the main text.

Table 1 Electrochemical data obtained by cyclic voltammetry

entry	species	solvent	electrolyte[a]	$E^1_{1/2}$[b] / mV	$E^2_{1/2}$[b] / mV	$\Delta E^1_{1/2}$[c] / mV	$\Delta E^1_{1/2}$[c] / mV
1	**TTFC8**	CH_2Cl_2	$TBABArF_{24}$	610	1060	/	/
2	**TTFC8**	CH_2Cl_2	$TBAClO_4$	600	820	/	/
3	**TTFC8**	CH_2Cl_2	$TBAPF_6$	600	870	/	/
4	**TTFC8**	ACN	$TBABArF_{24}$	600	820	/	/
5	**TTFC8**	ACN	$TBAClO_4$	600	780	/	/
6	**TTFC8**	ACN	$TBAPF_6$	590	810	/	/
7	**1**	CH_2Cl_2	$TBABArF_{24}$	740	1420	130	360
8	**1**	CH_2Cl_2	$TBAClO_4$	640	870	30	50
9	**1**	CH_2Cl_2	$TBAPF_6$	660	960	50	80
10	**1**	ACN	$TBABArF_{24}$	650	930	50	110
11	**1**	ACN	$TBAClO_4$	630	830	40	50
12	**1**	ACN	$TBAPF_6$	640	870	40	70
13	**2**	CH_2Cl_2	$TBABArF_{24}$	560	1140	-50	70
14	**2**	CH_2Cl_2	$TBAClO_4$	540	820	-60	0
15	**2**	CH_2Cl_2	$TBAPF_6$	550	890	-50	20
16	**2**	ACN	$TBABArF_{24}$	570	870	-30	40
17	**2**	ACN	$TBAClO_4$	560	820	-30	50
18	**2**	ACN	$TBAPF_6$	570	840	-20	40
19	**7**	CH_2Cl_2	$TBAPF_6$	540	890	-60	20
20	**6**	CH_2Cl_2	$TBABArF_{24}$	740	1390	130	330
21	**6**	CH_2Cl_2	$TBAPF_6$	650	960	50	80
22	**5 + TTFC8**	CH_2Cl_2	$TBAPF_6$	610	880	10	0

[a] Electrolyte concentration of 0.1 M

[b] Half-wave potential against $[FeCp_2^*]^{+/0}$ at a scan rate of 100 mV s^{-1}. The error is estimated to be ± 5 mV.

[c] Difference of half-wave potentials between measured species and macrocycle **TTFC8**

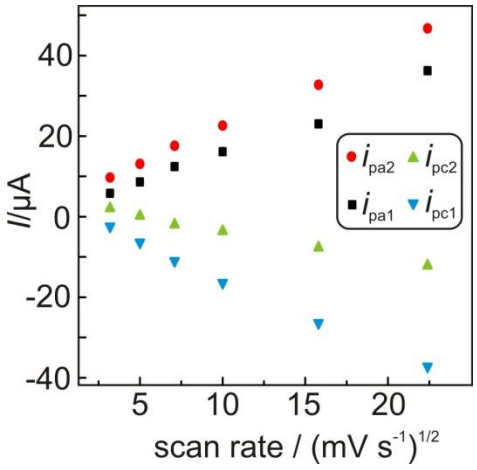

Fig. S14 Peak currents plotted against the square root of scan speed based on cyclic voltammograms of [2]rotaxane **6** (5 mM) in CH_2Cl_2 against $Fe(Cp^*)_2^{0/+}$ with tetrabutylammonium $BArF_{24}^-$ (0.1 M) as electrolyte.

The cyclic voltammogram of **6** was simulated in two segments from 0.30 V to 1.75 V and from 1.75 V to 0.30 V with the software DigiElch Professional[6] by using the Butler-Volmer equation. The surface area of the working electrode was set to 0.02 cm^2 and the starting concentration of **6** was set to 5 mM. The charge transfer coefficients α were left at their initial value of 0.5 and the heterogeneous rate constants k_s were calculated from the peak-to-peak separation[7] and consequently set to $4x10^{-3}$ cm^2 s^{-1}. The diffusion coefficients were left at their initial values of $1x10^{-5}$ cm^2 s^{-1}. The simulated charge-transfer reactions are described by the following equations (E1)-(E4), the E_0 values are given in brackets:

$\mathbf{6}^{2+}$	+	e^-	⇄	$\mathbf{6}^{+\bullet}$	(1.44 V)	(E1)
$\mathbf{6}^{+\bullet}$	+	e^-	⇄	**6**	(0.76 V)	(E2)
$(\mathbf{6}^{2+})^*$	+	e^-	⇄	$(\mathbf{6}^{+\bullet})^*$	(1.14 V)	(E3)
$(\mathbf{6}^{+\bullet})^*$	+	e^-	⇄	**(6)***	(0.61 V)	(E4)

The simulated shuttling mechanism is described by the following equations (C1)-(C3):

(6)*	⇄	**6**	(C1)
$(\mathbf{6}^{+\bullet})^*$	⇄	$\mathbf{6}^{+\bullet}$	(C2)
$(\mathbf{6}^{2+})^*$	⇄	$\mathbf{6}^{2+}$	(C3)

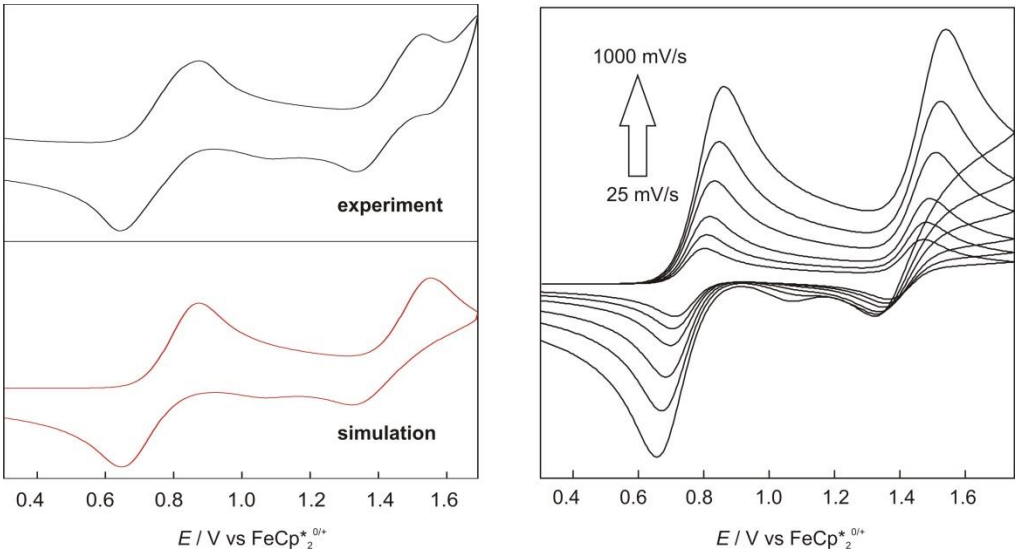

Fig. S15 (left) Comparison of the simulated (red) and experimental cyclic voltammogram (black) of [2]rotaxane **6** measured in CH_2Cl_2 at 298 K with $TBABArF_{24}$ (0.1 M) at 1000 mV s^{-1}. (right) Simulation with the derived parameters from fitting the experimental data for several scan speeds according to the experiment in Fig. 6b.

Table S2. Thermodynamic parameters for chemical reactions C1-C3 derived by fitting the experimental data and used for the simulation of cyclic voltammograms depicted in Fig. S15

reaction	K_{Tn}	k_f / s^{-1}	k_b / s^{-1}
C1	$2.7\ 10^7$	3500	0.00013
C2	$9.4\ 10^4$	80	0.00085
C3	1.0	6	6.2

7. NMR evidence for the switchability [2]rotaxane 6

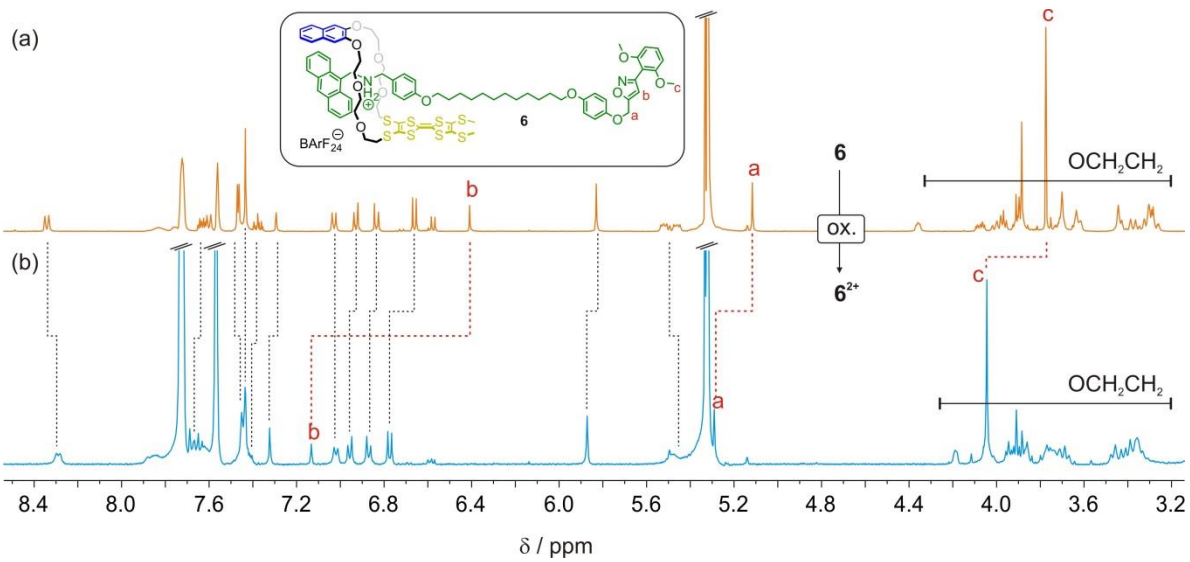

Fig. S16 ^{1}H NMR spectra (500 MHz, CD_2Cl_2, 298 K, 2.0 mM) of [2]rotaxane **6** (a) before and (b) after oxidation by $Fe(ClO_4)_3$ and addition of 5 equiv. $TBABArF_{24}$ as the stabilizing electrolyte. Only small shifts for the aromatic protons of axle and macrocycle are observed which indicates a similar binding situation as in the non-oxidised state. However, the significant downfield shifts of signals a, b and c which belong to the most distant part of the axle, namely the isoxazole/stopper moiety, suggests a major conformational change in the system.

8. ^{1}H and ^{13}C NMR spectra

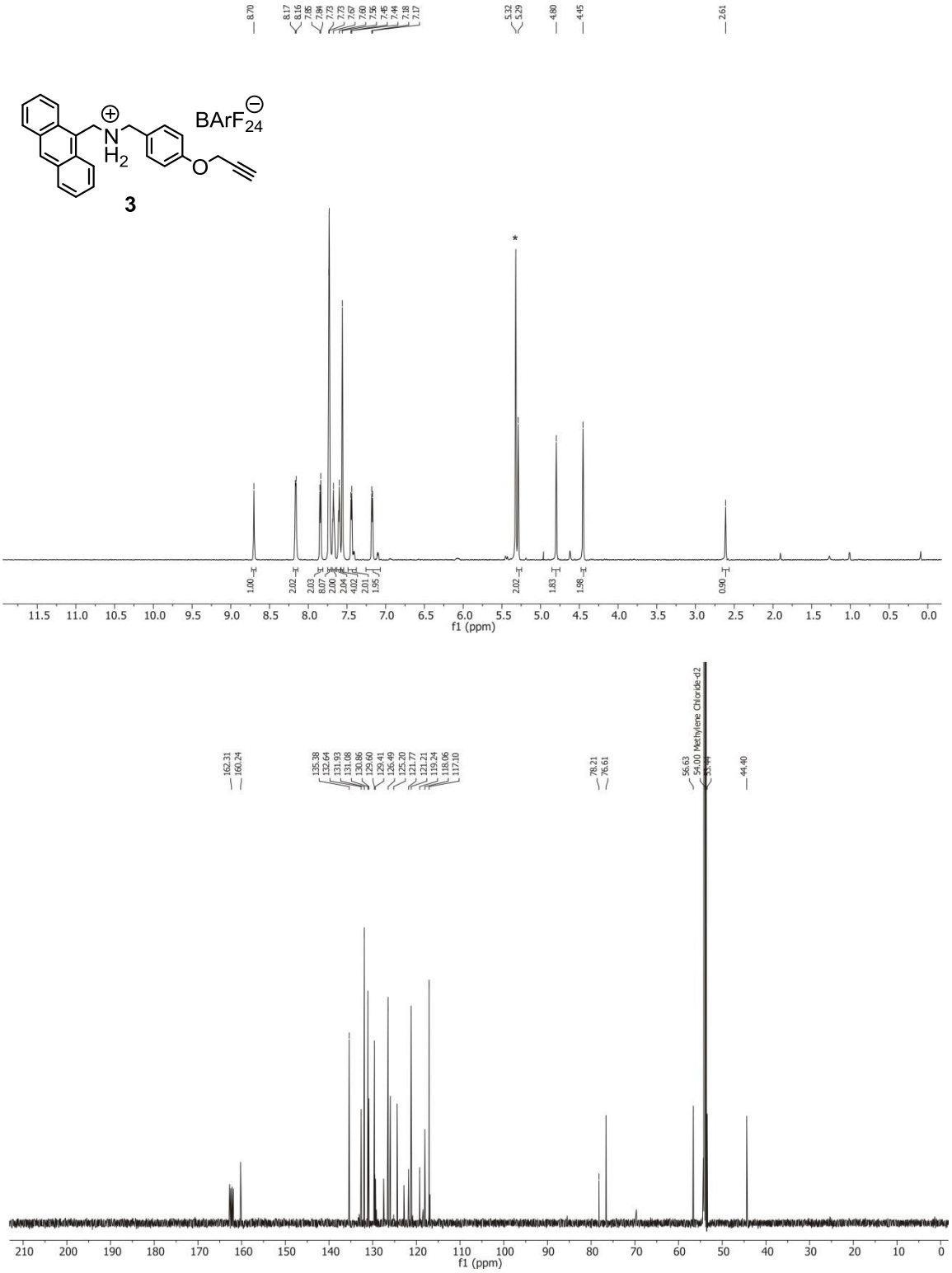

Fig. S17 (top) ^{1}H NMR (700 MHz, CD_2Cl_2, 298 K) spectrum of axle **3**; (bottom) ^{13}C NMR (176 MHz, CD_2Cl_2, 298 K) spectrum of axle **3**.

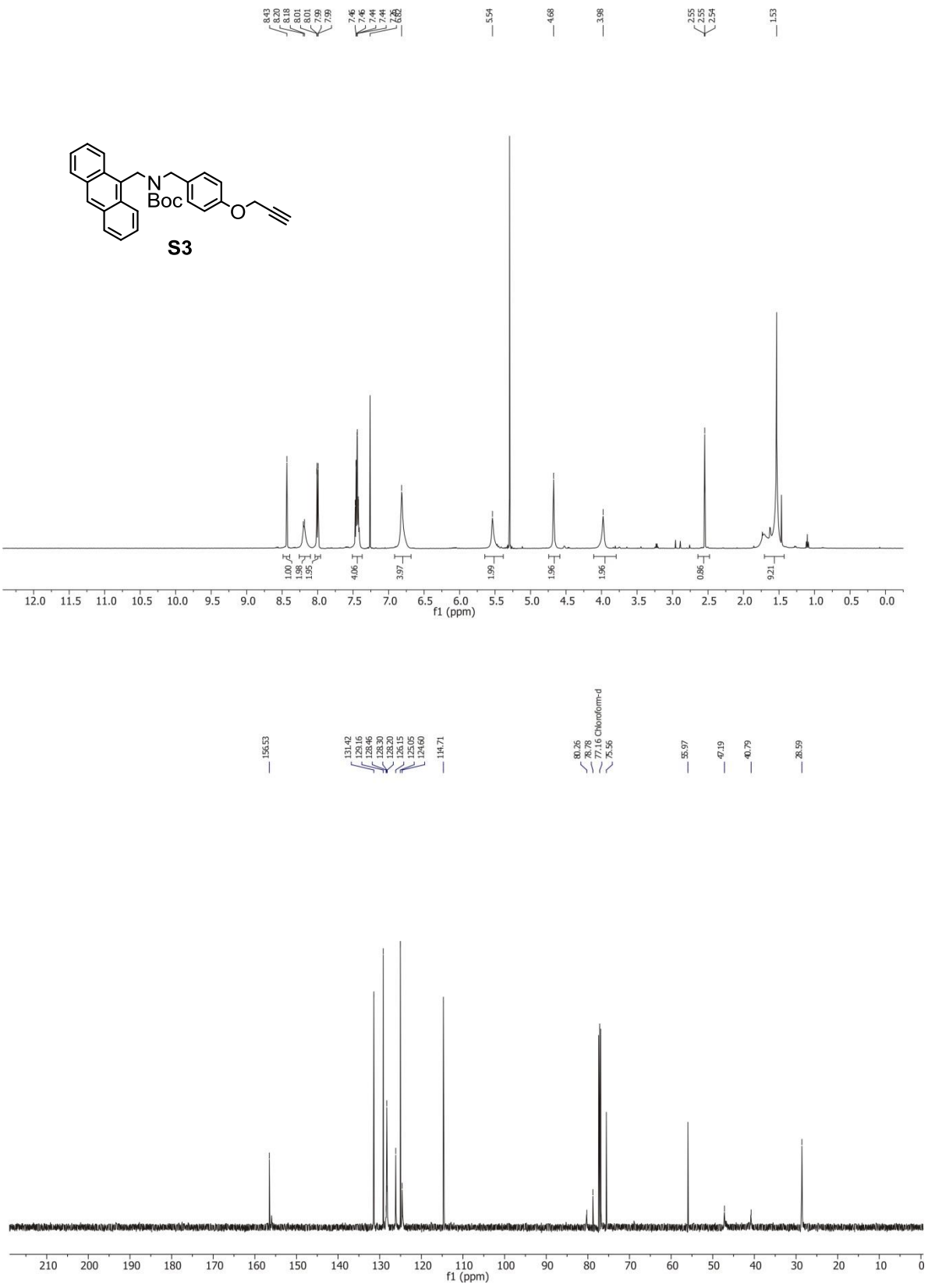

Fig. S18 (top) ^{1}H NMR (500 MHz, $CDCl_3$, 298 K) spectrum of axle **S3**; (bottom) ^{13}C NMR (126 MHz, $CDCl_3$, 298 K) spectrum of axle **S3**.

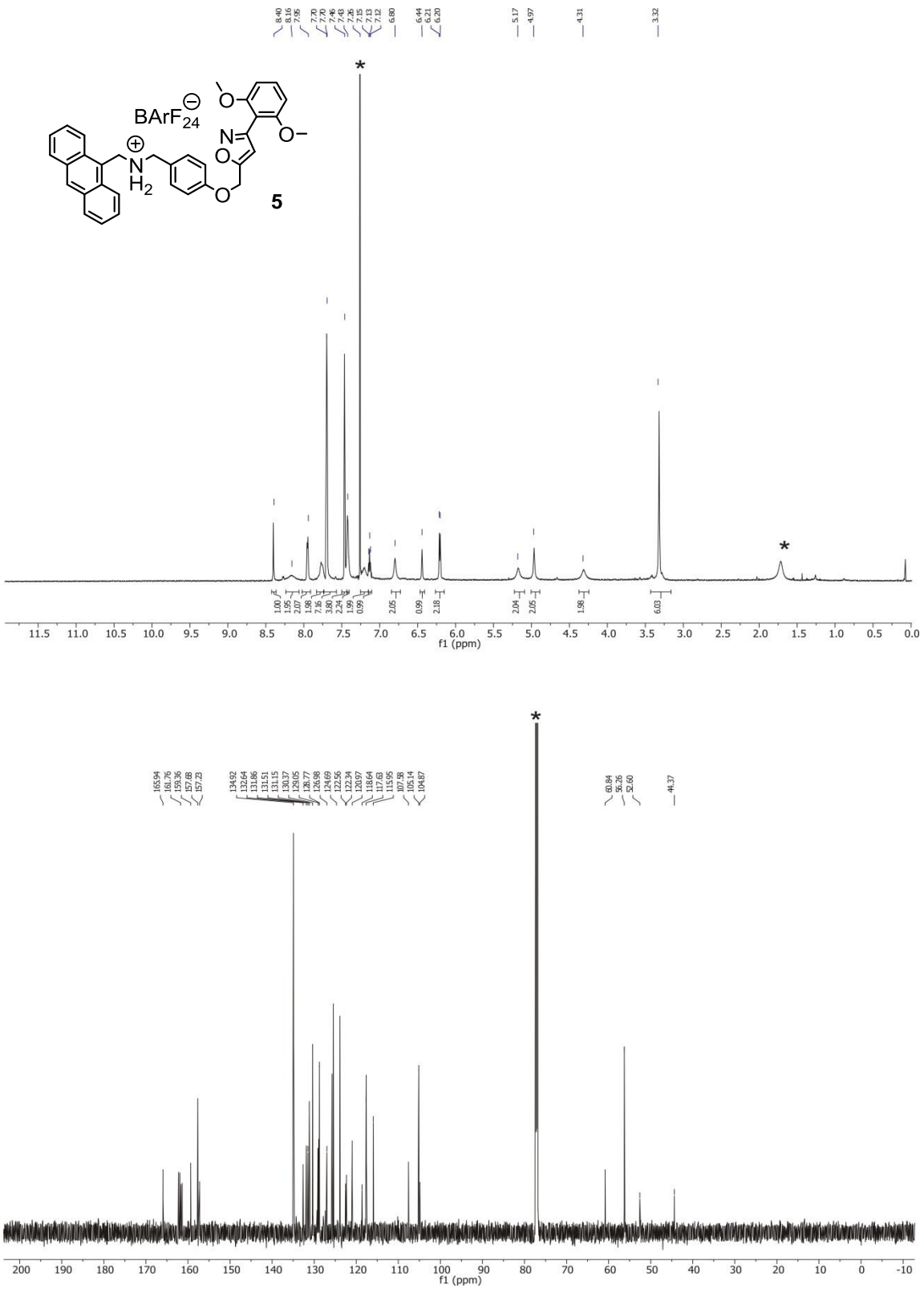

Fig. S19 (top) ^{1}H NMR (700 MHz, $CDCl_3$, 298 K) spectrum of free stoppered axle **5**; (bottom) ^{13}C NMR (176 MHz, $CDCl_3$, 298 K) spectrum free stoppered axle **5**.

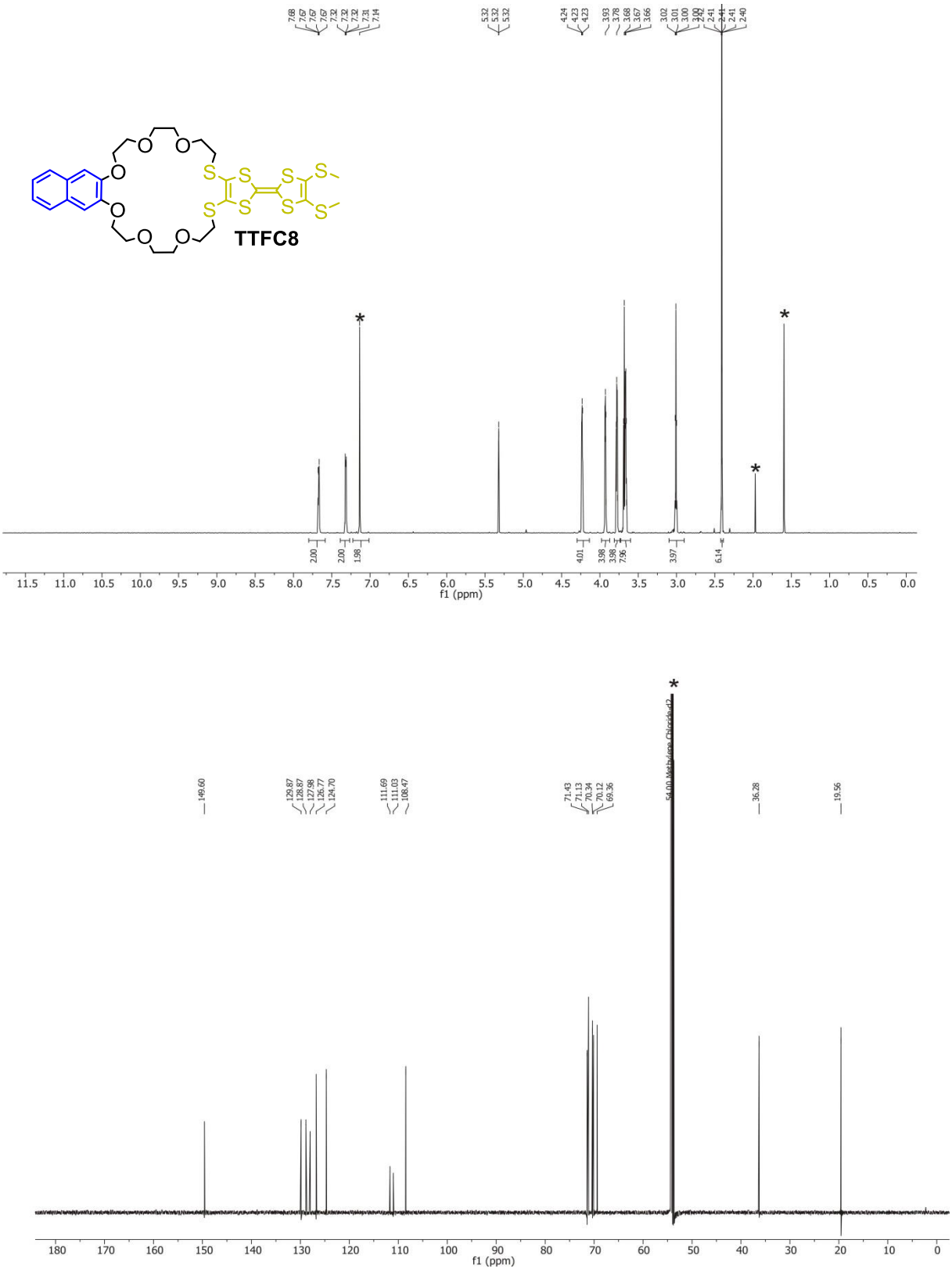

Fig. S20 (top) ^{1}H NMR (700 MHz, CD_2Cl_2, 298 K) spectrum of macrocycle **TTFC8**; (bottom) ^{13}C NMR (176 MHz CD_2Cl_2, 298 K) spectrum of macrocycle **TTFC8**.

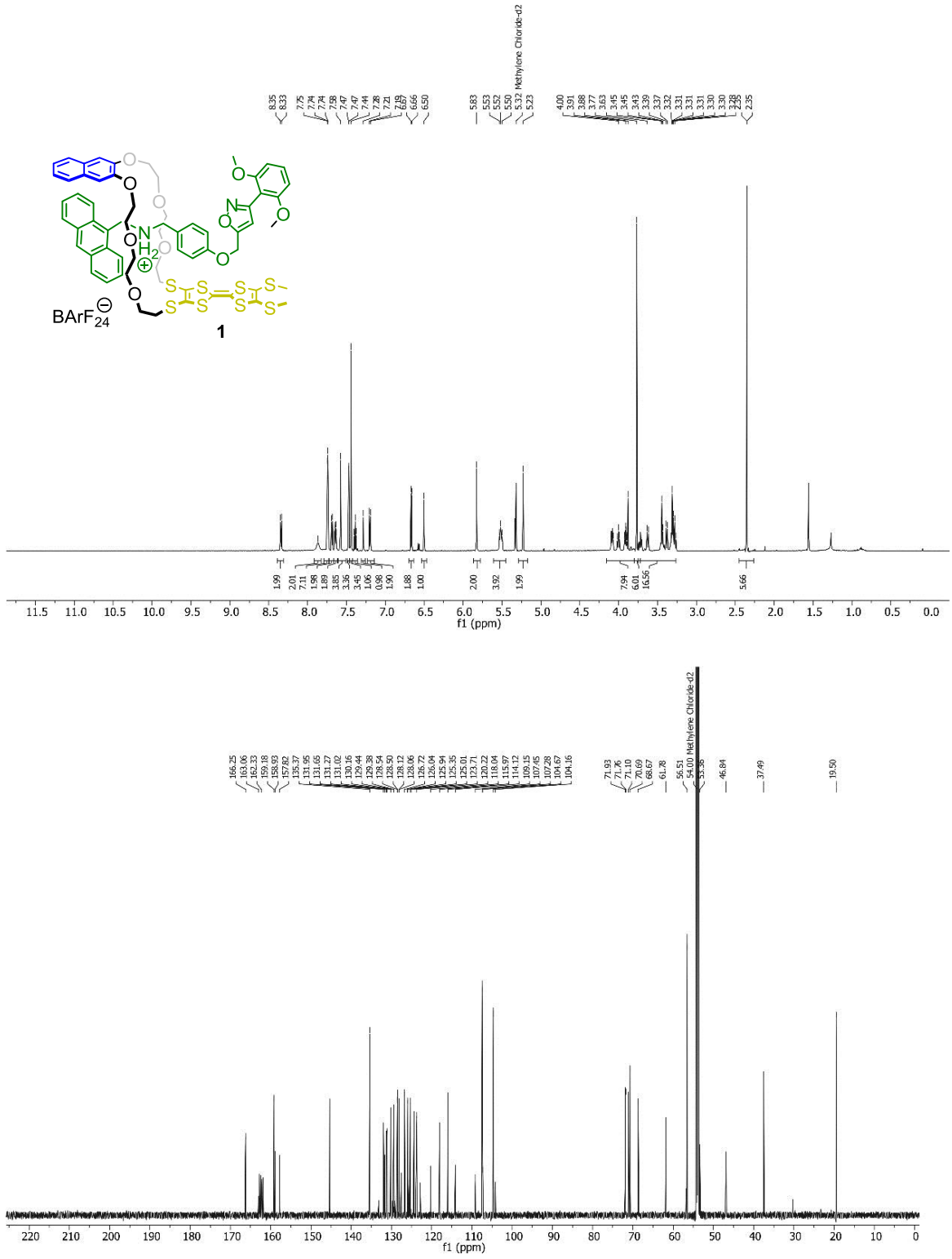

Fig. S21 (top) ^{1}H NMR (700 MHz, CD_2Cl_2, 298 K) spectrum of [2]rotaxane **1**; (bottom) ^{13}C NMR (176 MHz, CD_2Cl_2, 298 K) spectrum of [2]rotaxane **1**

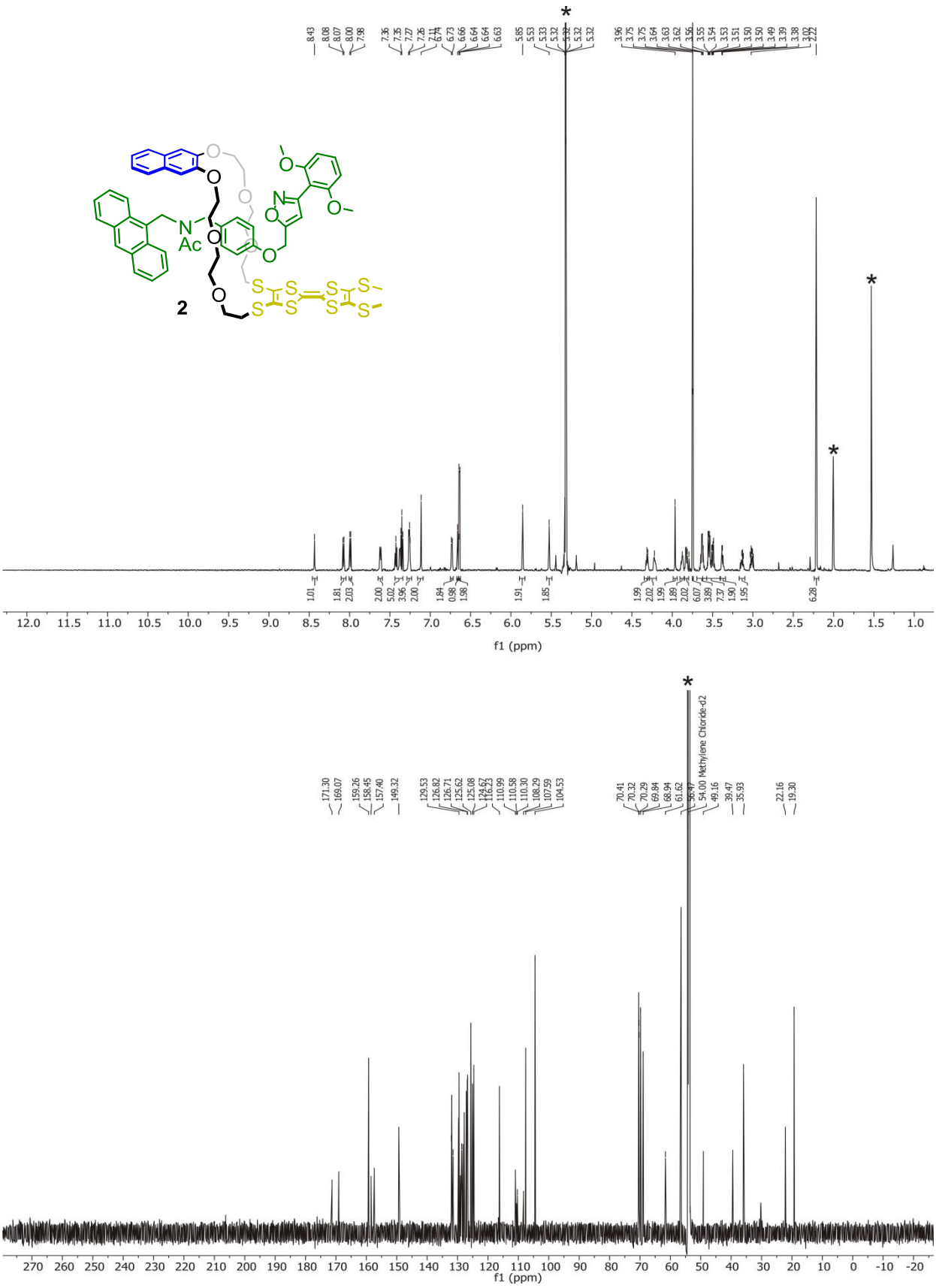

Fig. S22 (top) ^{1}H NMR (700 MHz, CD_2Cl_2, 298 K) spectrum of [2]rotaxane **2**; (bottom) ^{13}C NMR (176 MHz, CD_2Cl_2, 298 K) spectrum of [2]rotaxane 2**.**

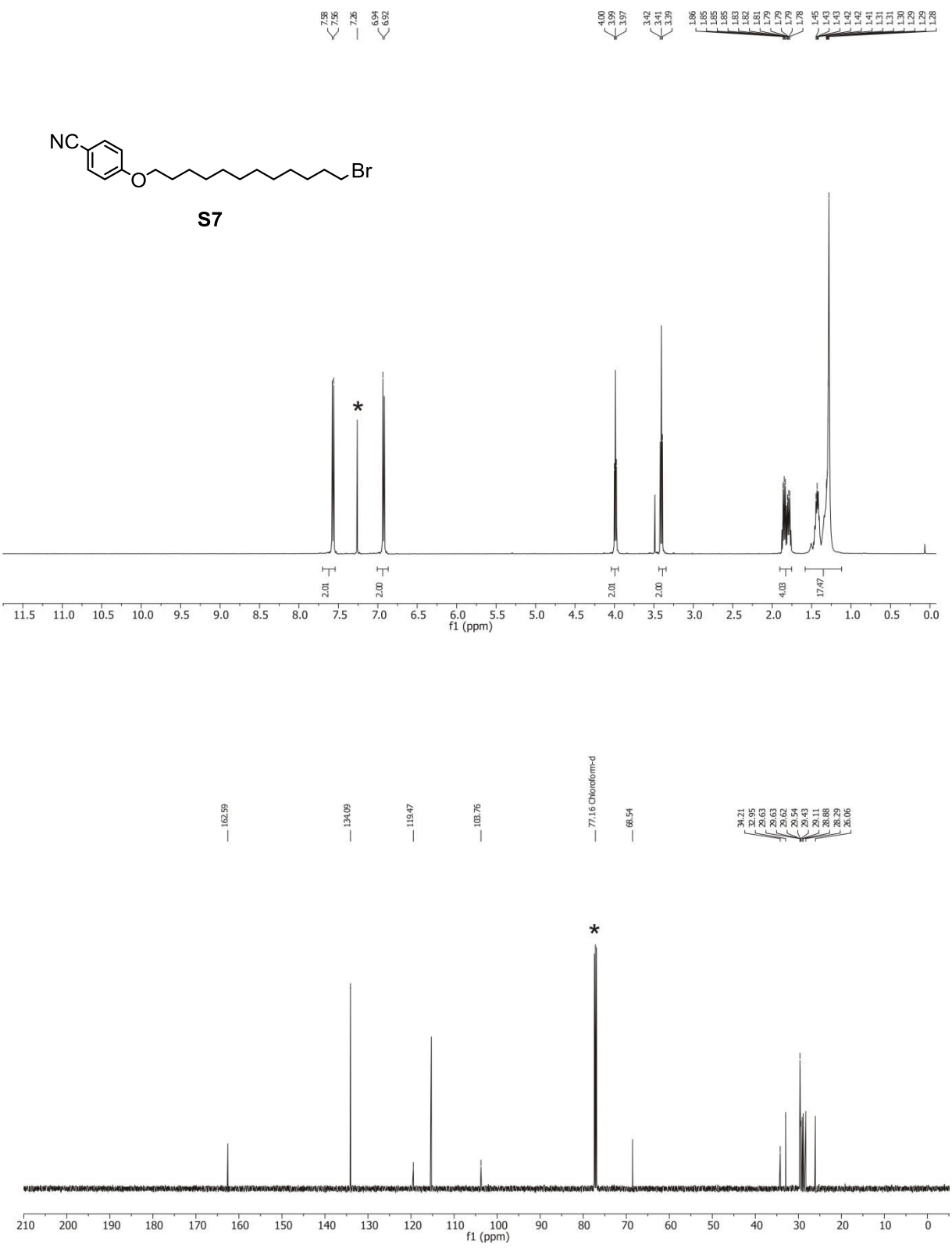

Fig. S23 (top) ^{1}H NMR (500 MHz, $CDCl_3$, 298 K) spectrum of nitrile **S7**; (bottom) ^{13}C NMR (126 MHz, $CDCl_3$, 298 K) spectrum of nitrile **S7**.

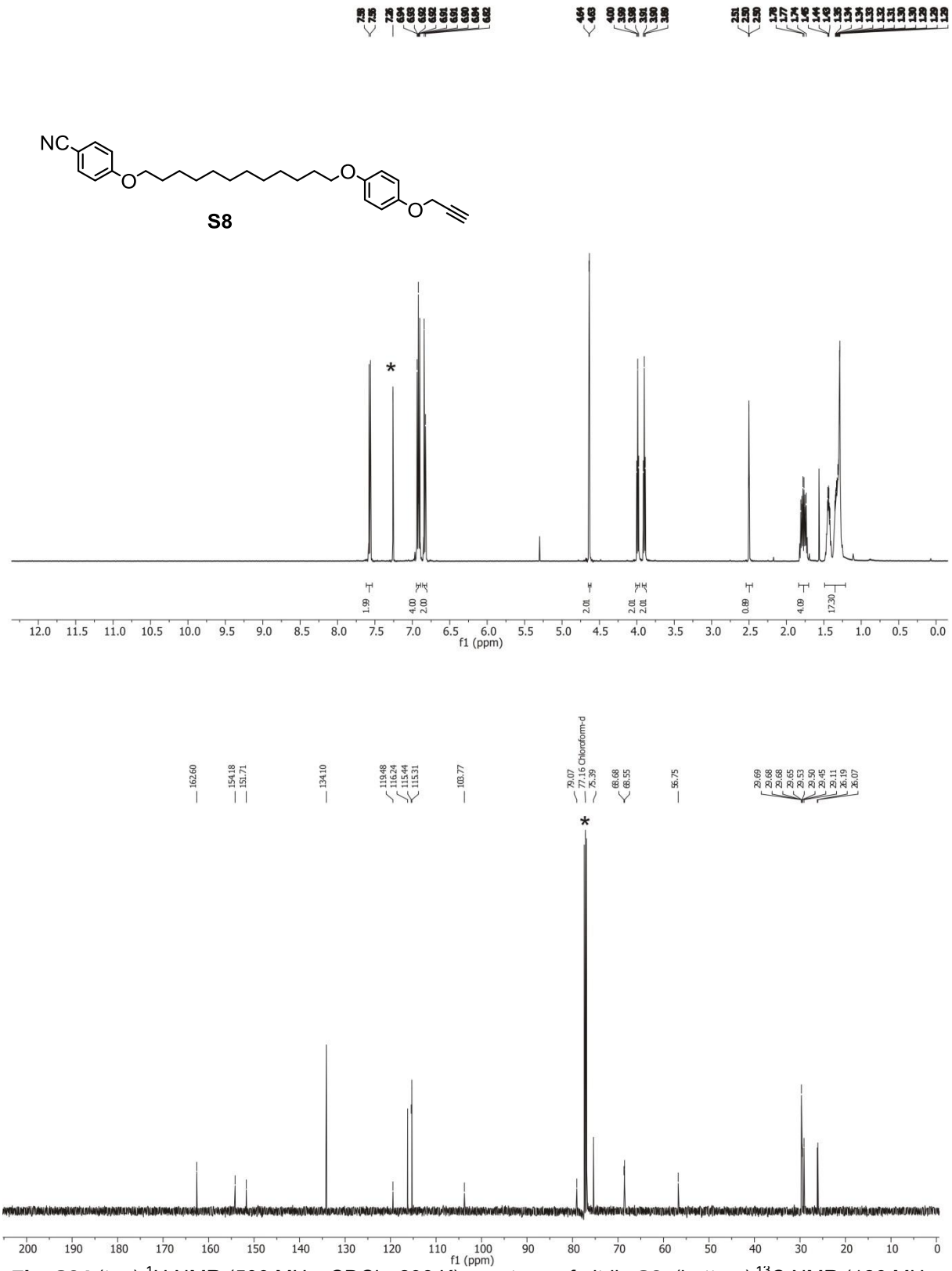

Fig. S24 (top) ^{1}H NMR (500 MHz, $CDCl_3$, 298 K) spectrum of nitrile **S8**; (bottom) ^{13}C NMR (126 MHz, $CDCl_3$, 298 K) spectrum of nitrile **S8**.

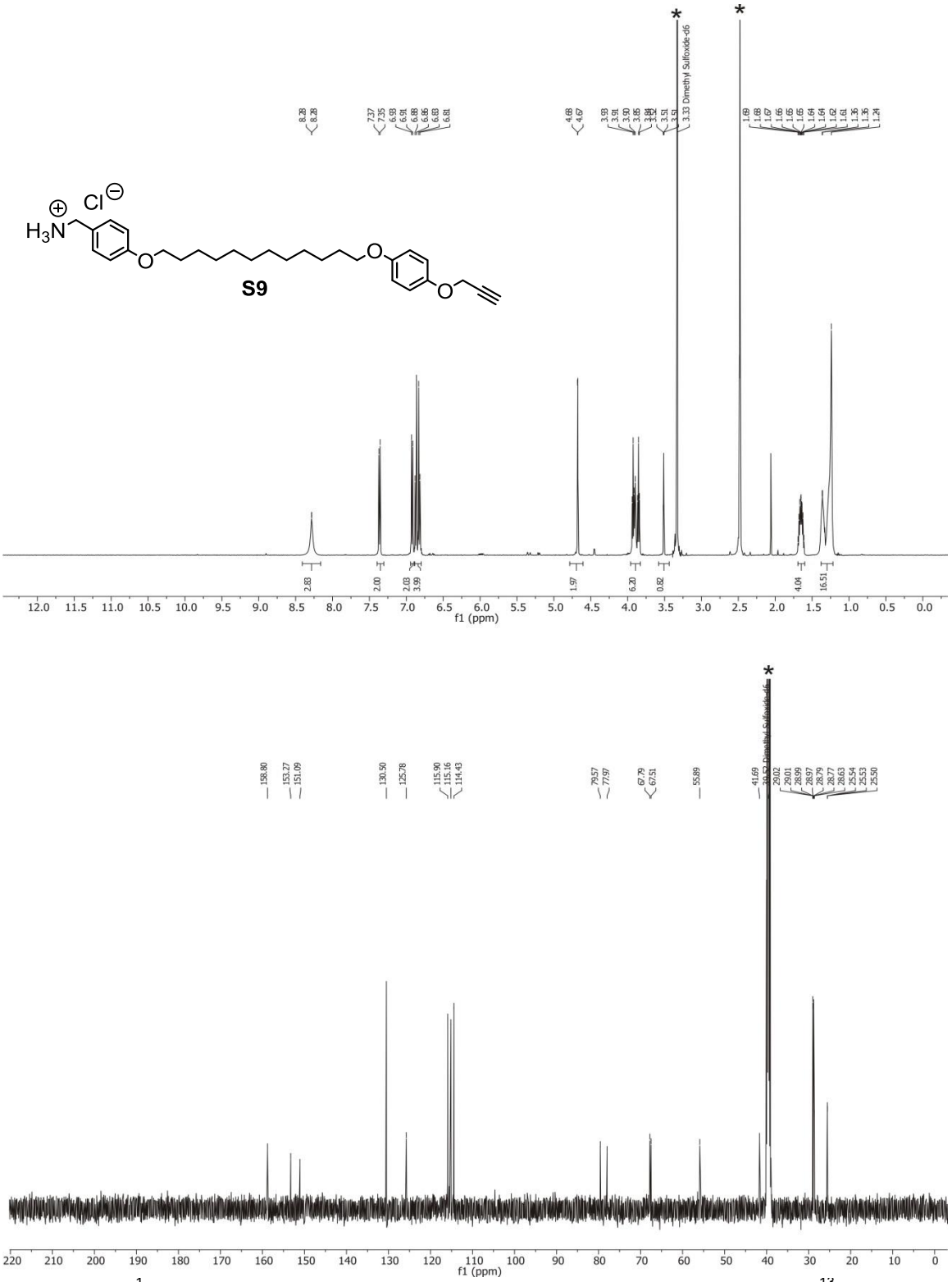

Fig. S25 (top) ^{1}H NMR (500 MHz, DMSO-d6, 298 K) spectrum of amine **S9**; (bottom) ^{13}C NMR (126 MHz, DMSO-d6, 298 K) spectrum of amine **S9**.

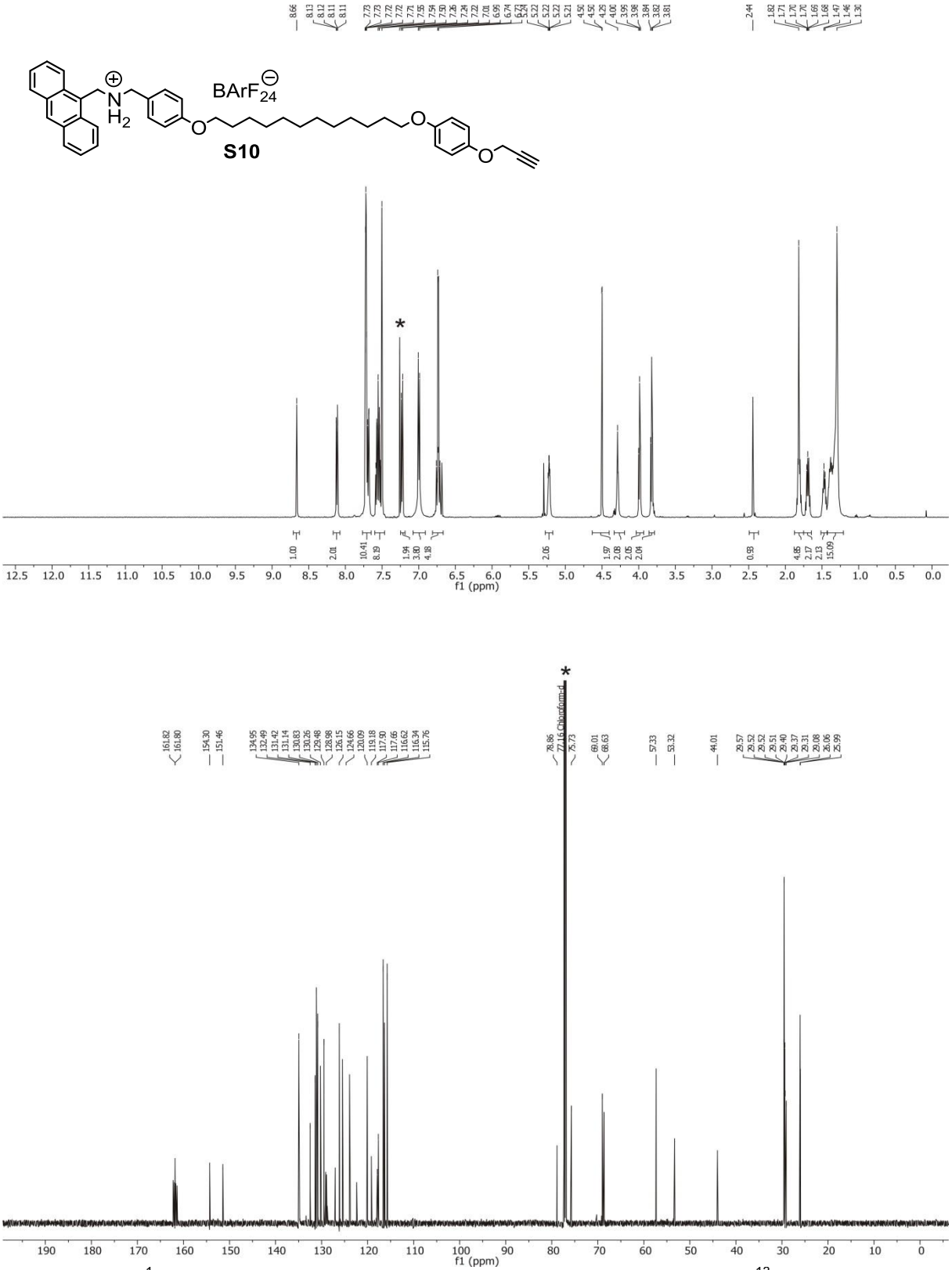

Fig. S26 (top) ^{1}H NMR (500 MHz, $CDCl_3$, 298 K) spectrum of axle **S10**; (bottom) ^{13}C NMR (176 MHz, $CDCl_3$, 298 K) spectrum of axle **S10**.

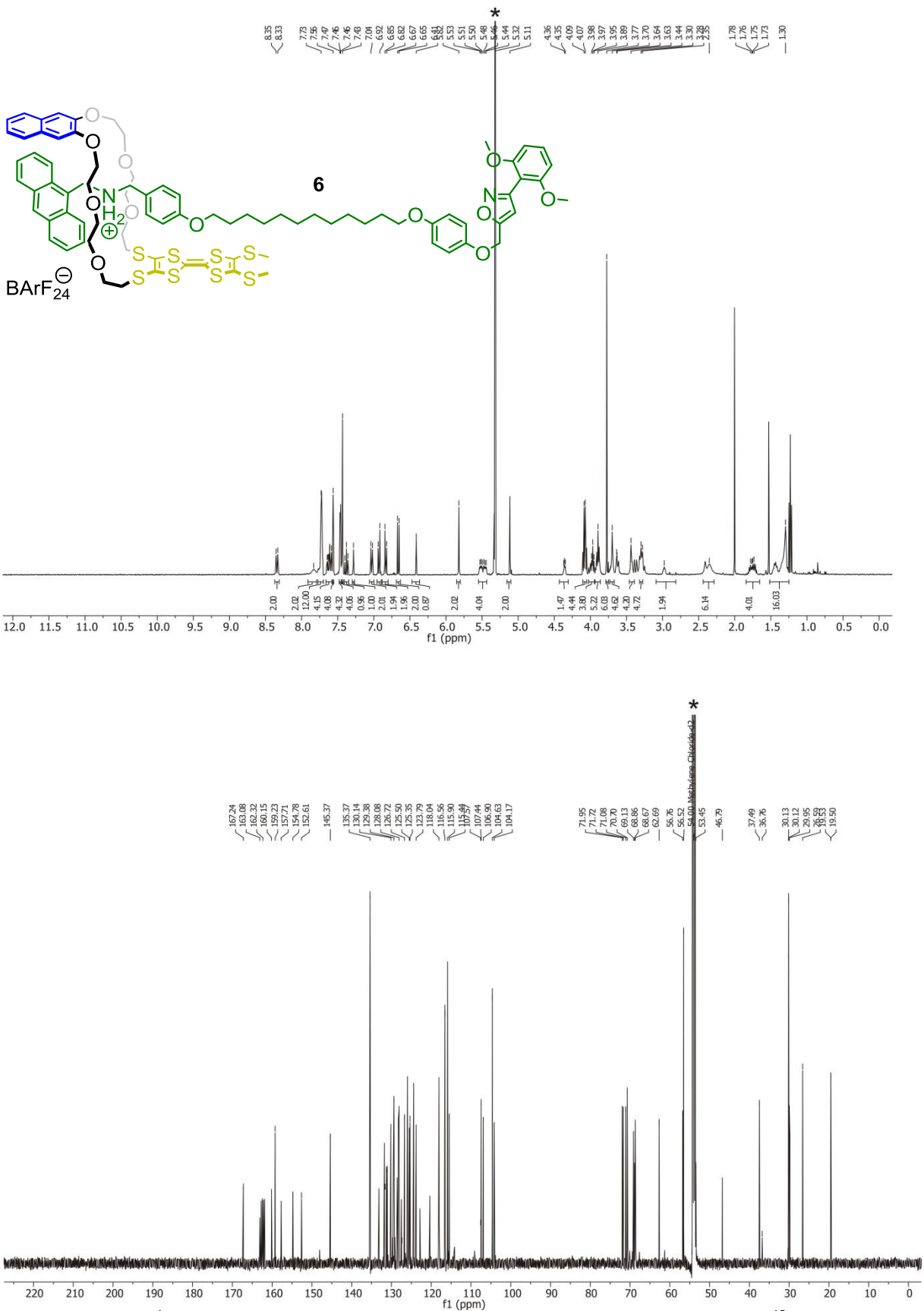

Fig. S27 (top) ^{1}H NMR (400 MHz, CD_2Cl_2, 298 K) spectrum of rotaxane **6**; (bottom) ^{13}C NMR (176 MHz, CD_2Cl_2, 298 K) spectrum of rotaxane **6**.

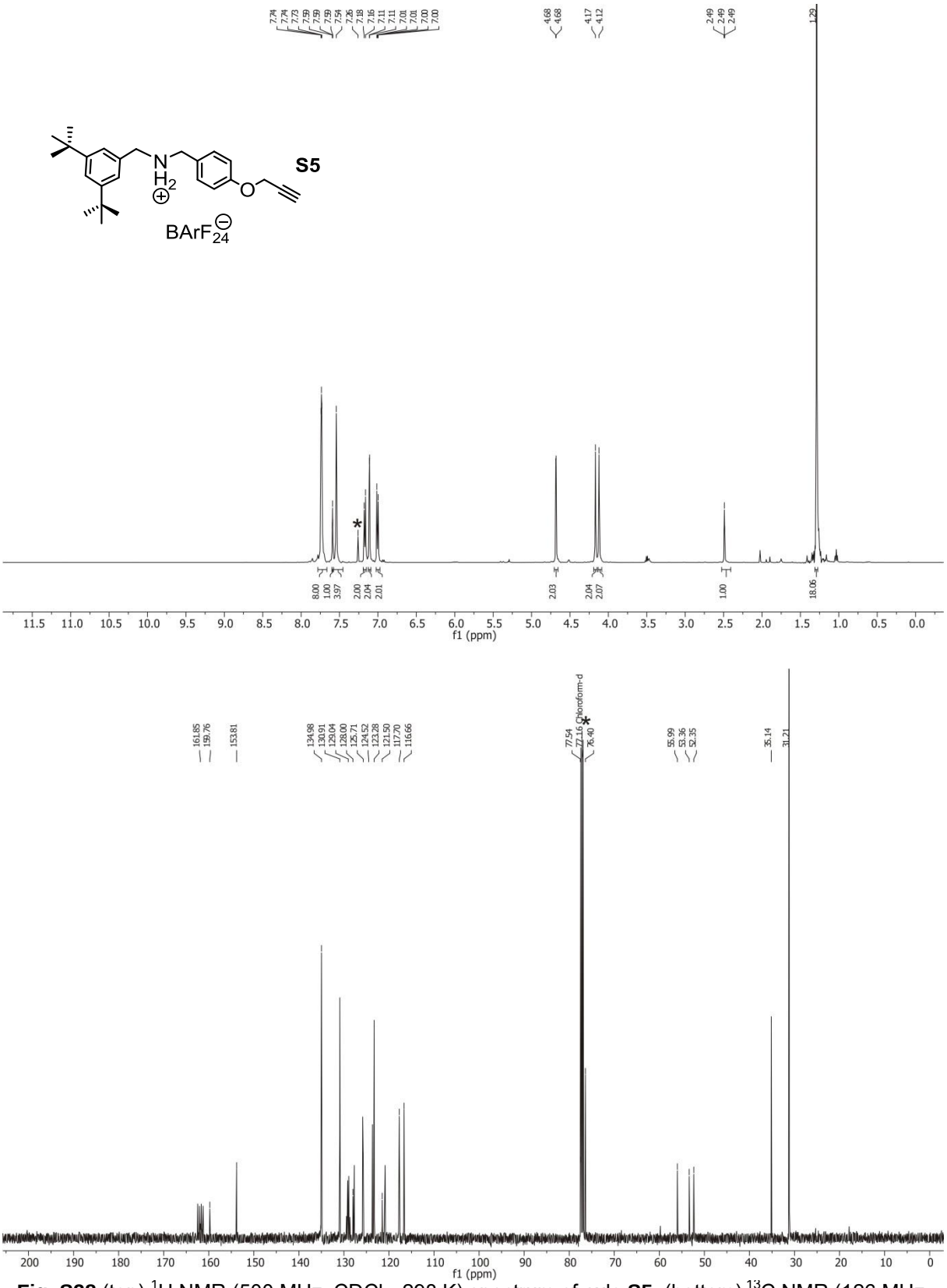

Fig. S28 (top) ^{1}H NMR (500 MHz, $CDCl_3$, 298 K) spectrum of axle **S5**; (bottom) ^{13}C NMR (126 MHz, $CDCl_3$, 298 K) spectrum of axle **S5**.

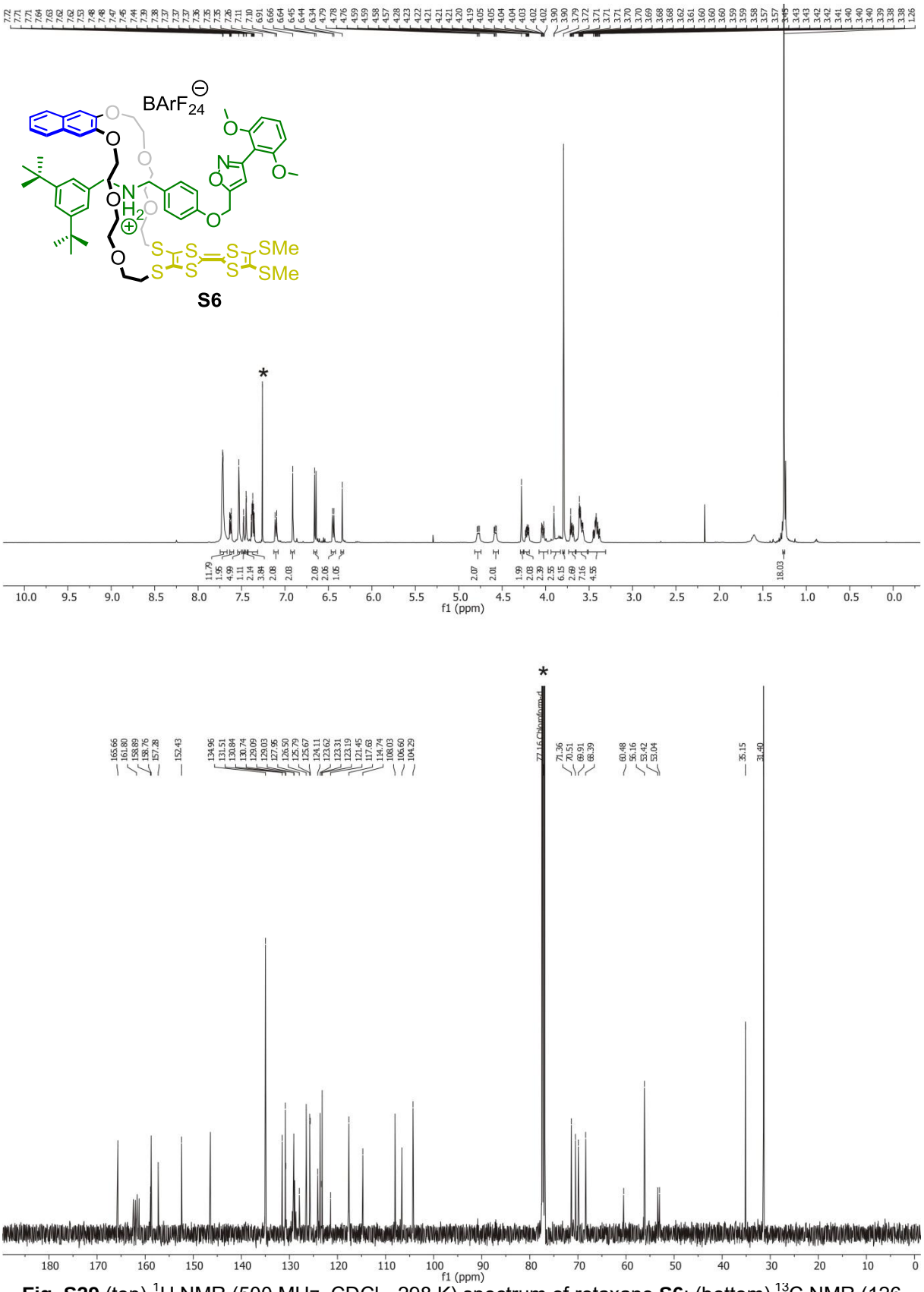

Fig. S29 (top) ^{1}H NMR (500 MHz, $CDCl_3$, 298 K) spectrum of rotaxane **S6**; (bottom) ^{13}C NMR (126 MHz, $CDCl_3$, 298 K) spectrum of rotaxane **S6**.

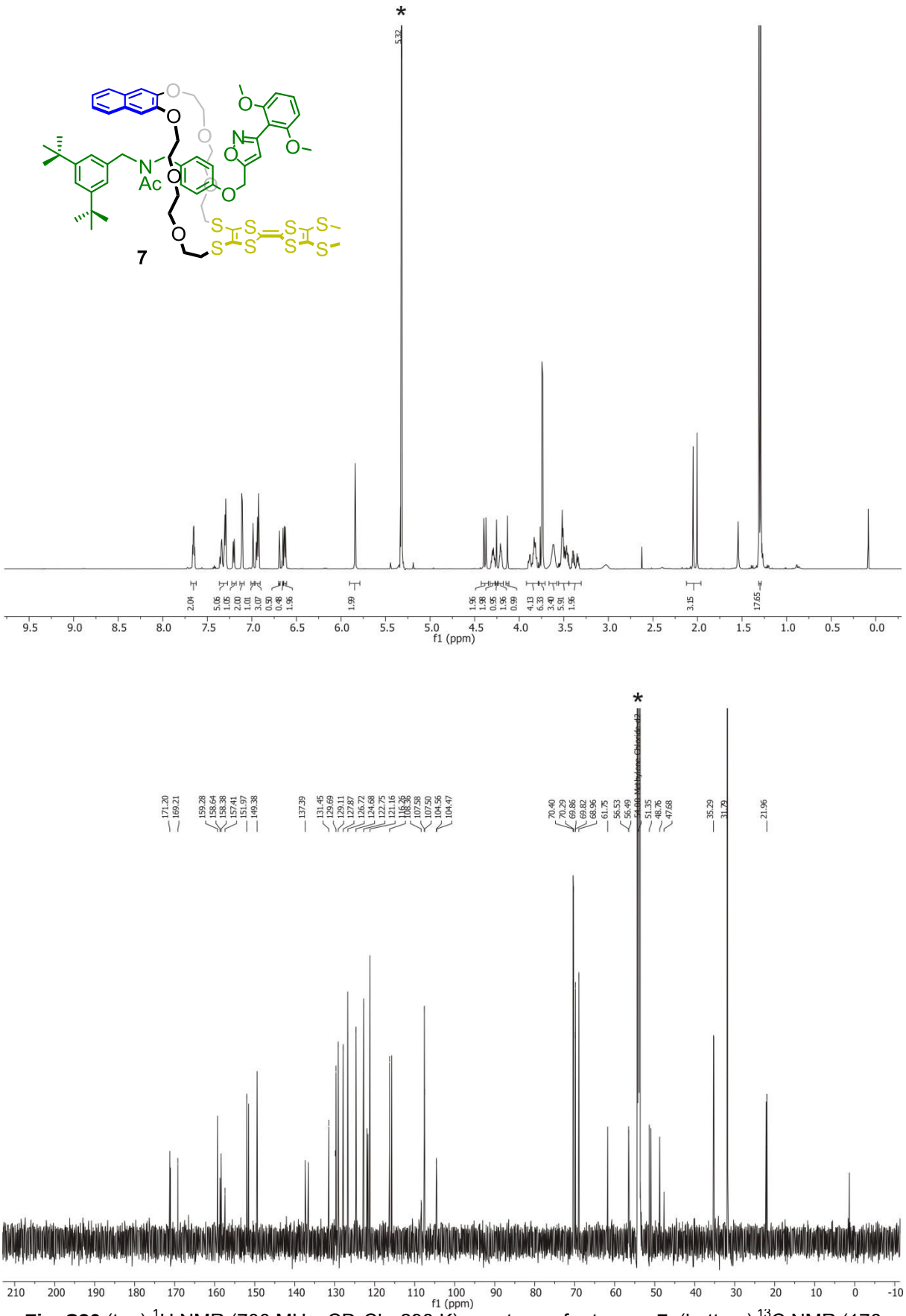

Fig. S30 (top) ^{1}H NMR (700 MHz, CD_2Cl_2, 298 K) spectrum of rotaxane **7**; (bottom) ^{13}C NMR (176 MHz, CD_2Cl_2, 298 K) spectrum of rotaxane **7**.

8. References

1 M. Srinivasan, S. Sankararaman , H. Hopf, I. Dix and P. G. Jones, *J. Org. Chem.*, 2001, **66**, 4299.

2 N. Svenstrup, K. M. Rasmussen, T. K. Hansen and J. Becher, *Synthesis*, 1994, **1994**, 809.

3 H. V. Schröder, H. Hupatz, A. J. Achazi, S. Sobottka, B. Sarkar, B. Paulus and C. A. Schalley, *Chem. Eur. J.*, 2017, **23**, 2960.

4 Z.-J. Zhang, H.-Y. Zhang, H. Wang and Y. Liu, *Angew. Chem. Int. Ed.*, 2011, **50**, 10834.

5 T. Matsumura, F. Ishiwari, Y. Koyama and T. Takata, *Org. Lett.*, 2010, **12**, 3828.

6 DigiElch Professional Version 7.FD 2006, ElchSoft GbR, Kleinromstedt, Germany.

7 (a) R. S. Nicholson, I. Shain, *Anal. Chem*., 1965, **37**, 1351; (b) A. S. N. Murthy, K. S. Reddy, *Electrochim. Acta*, 1983, **28**, 1677.

6.3 Switchable synchronization of pirouetting motions in a redox active [3]rotaxane

H.V. Schröder, A. Mekic, H. Hupatz, S. Sobottka, F. Witte, L.H. Urner, M. Gaedke, K. Pagel, B. Sarkar, B. Paulus, C.A. Schalley

Nanoscale. **2018**, *10*, 21425-21433.

Submitted on July 9, 2018, first published on October 24, 2018 by The Royal Society of Chemistry.

An electronic version of the articles is available at: https://doi.org/10.1039/C8NR05534C

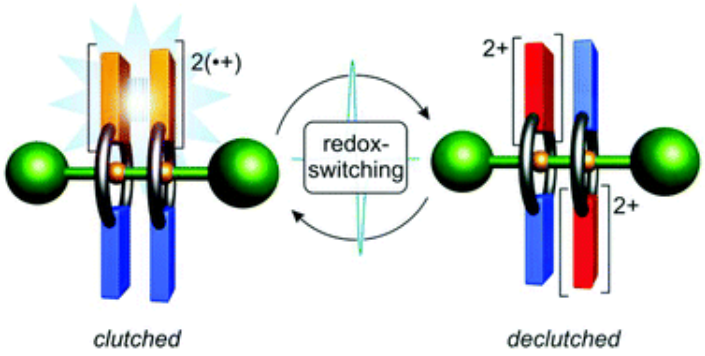

Figure 6.3. Graphical abstract. Reprinted from Schröder *et al.*[247] with permission from the Royal Society of Chemistry (Copyright © The Royal Society of Chemistry 2018).

Authors' contributions

Hendrik V. Schröder and I developed the general concept of this project with main contribution coming from Hendrik V. Schröder. Hendrik V. Schröder and Christoph A. Schalley wrote the manuscript with main contribution coming from Hendrik V. Schröder. The general synthesis route was elaborated by me, Amel Mekic, and Hendrik V. Schröder. Syntheses of the compounds and CV were measurements were done by Amel Mekic and Hendrik V. Schröder. Marius Gaedke additionally helped with the axle synthesis. Hendrik V. Schröder further contributed with NMR experiments, as well as with the digital simulations of the electrochemical data. I performed and evaluated the ITC measurements. Sebastian Sobottka and Hendrik V. Schröder conducted the EPR and UV/Vis-NIR measurements and evaluated the data together with Biprajit Sarkar. Felix Witte and Beate Paulus did the computational work. Leonhard H. Urner and Hendrik V. Schröder did the IM-MS experiments and CCS calculations. They evaluated the data together with Kevin Pagel. All authors contributed to the final version of the manuscript.

Nanoscale

PAPER

View Article Online
View Journal | View Issue

Cite this: *Nanoscale*, 2018, **10**, 21425

Switchable synchronisation of pirouetting motions in a redox-active [3]rotaxane†

Hendrik V. Schröder,[a] Amel Mekic,[a] Henrik Hupatz,[a] Sebastian Sobottka,[b] Felix Witte,[a] Leonhard H. Urner,[a] Marius Gaedke,[a] Kevin Pagel,[a,c] Biprajit Sarkar,[b] Beate Paulus[a] and Christoph A. Schalley*[a]

In this study, the crown/ammonium [3]rotaxane **R2** is reported which allows a switchable synchronisation of wheel pirouetting motions. The rotaxane is composed of a dumbbell-shaped axle molecule with two mechanically interlocked macrocycles which are decorated with a redox-active tetrathiafulvalene (TTF) unit. Electrochemical, spectroscopic, and electron paramagnetic resonance experiments reveal that rotaxane **R2** can be reversibly switched between four stable oxidation states (**R2**, $\mathbf{R2}^{\bullet+}$, $\mathbf{R2}^{2(\bullet+)}$, and $\mathbf{R2}^{4+}$). The oxidations enable non-covalent, cofacial interactions between the TTF units in each state—including a stabilised mixed-valence $(TTF_2)^{\bullet+}$ and a radical-cation $(TTF^{\bullet+})_2$ dimer interaction—which dictate a *syn* (**R2**, $\mathbf{R2}^{\bullet+}$, and $\mathbf{R2}^{2(\bullet+)}$) or *anti* ($\mathbf{R2}^{4+}$) ground state co-conformation of the wheels in the rotaxane. Furthermore, the strength of these wheel–wheel interactions varies with the oxidation state, and thus electrochemical switching allows a controllable synchronisation of the wheels' pirouetting motions. DFT calculations explore the potential energy surface of the counter-rotation of the two interacting wheels in all oxidation states. The controlled coupling of pirouetting motions in rotaxanes can lead to novel molecular gearing systems which transmit rotational motion by switchable non-covalent interactions.

Received 9th July 2018,
Accepted 23rd October 2018

DOI: 10.1039/c8nr05534c

rsc.li/nanoscale

Introduction

A great contemporary challenge in nanoscience is the construction of molecular machines and motors which can produce repetitive motion fuelled by external stimuli such as energy or concentration gradients.[1] Generation and control of rotational motion is one of the most worthwhile goals. Nature's biomachinery elegantly fulfils this task as seen for the unidirectional rotation in ATP synthase or the flagella-based motility of bacteria.[2] In the last two decades, directional rotation was also realised in artificial systems[3] including Feringa's light-driven rotary motors[4] based on overcrowded alkenes. However, a further step towards applicable artificial molecular machinery is a multi-component approach in which a molecular motor (active component) is coupled with a passive component to transmit rotational motion to the surrounding environment.[5]

Pioneering work on correlated rotational motion has been reported by Iwamura and Mislow who studied the dynamics of molecular bevel gears.[6] These gears consist of covalently linked and tightly intermeshed triptycene groups. Based on the idea of sterically correlated rotors, the coupling of rotation has been further investigated in more sophisticated gearing systems.[7] Moreover, it is desirable that molecular gears are also susceptible to external stimuli, and thus the transmission of rotational motion can be switched on and off or regulated in a controlled manner.[8] Examples of molecular gears have been reported in which the steric rotor correlation can be influenced by ions,[9] ligands,[10] or light and thermal stimuli.[11] Additionally, stimuli-controlled transmission of rotational motion has been achieved in gears based on organometallic carousel compounds such as metallocenes[12] or double-decker porphyrins.[13]

The operation of such controllable gearing systems is reminiscent of the working principle of macroscopic clutches, common mechanical devices which can be found, for example, in motor vehicles. Transmission of rotation is realised by a connection between two rotating shafts. A disengagement (declutching) of the shafts leads to desynchronisation of rotation rates, and thus to an interruption of power transmission. Although the technomimetic comparison of mole-

[a]*Institut für Chemie und Biochemie, Freie Universität Berlin, Takustraße 3, 14195 Berlin, Germany. E-mail: c.schalley@fu-berlin.de*
[b]*Institut für Chemie und Biochemie, Freie Universität Berlin, Fabeckstraße 34/36, 14195 Berlin, Germany*
[c]*Fritz Haber Institute of the Max Planck Society, Department of Molecular Physics, Faradayweg 4-6, 14195 Berlin, Germany*

†Electronic supplementary information (ESI) available: General experimental methods, synthetic procedures, rotaxane characterization, EPR, UV/VIS-NIR, ITC, CV and DS, IM-MS, VT-NMR, and computational details. See DOI: 10.1039/c8nr05534c

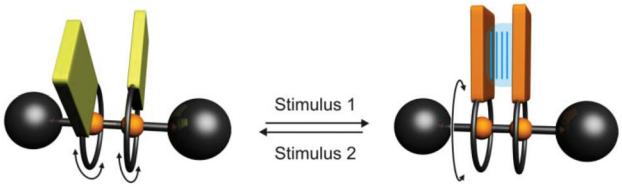

Fig. 1 Representation of a stimuli-responsive [3]rotaxane which allows a switchable synchronisation of macrocycle pirouetting motions.

cular machines at the nanoscale with macroscopic machines certainly has its limitations,[14] this approach has been frequently used by groups in the field as it provides an easy-to-understand description of the overall function of these molecular devices.

Here, we present a novel type of [3]rotaxane which allows the switchable synchronisation of pirouetting motions of two macrocycles (Fig. 1). Our molecular system is based on the symmetric [3]rotaxane **R2** (Fig. 2). Two macrocycles are threaded on a dumbbell-shaped axle molecule. A synchronisation or, in other words, a coupling of the wheel's pirouetting motions can be achieved by switchable non-covalent interactions between the wheels. In this study, we show by a combination of experimental and theoretical methods two major outcomes: (i) **R2** can be operated as a rotational switch in which the wheels adopt a *syn* or *anti* ground-state co-conformation. (ii) The wheel–wheel interactions, and thus the synchronisation of their pirouetting motions, can be adjusted by electrochemical switching.

Results and discussion

Design considerations and synthesis

In contrast to the well-studied wheel translation, for example in molecular shuttles,[15] the use of the pirouetting motion in rotaxanes to drive a molecular machine remains challenging.[1b,16] One reason is the high structural flexibility of most rotaxane architectures, which makes motion transmission by steric correlation difficult. However, a [3]rotaxane with two wheels is ideally suited to realise a coupling of wheel pirouetting motions. The wheels are spatially fixed in close contact by mechanical interlocking but can still freely rotate around the axle. The well-known crown/ammonium rotaxane motif was chosen due to its straightforward structural modifiability and high-yielding supramolecular synthesis.[17] Stoddart and co-workers showed that axles with a trismethylene group between two ammonium binding sites provide a suitable spacing (~3.4 Å) for π–π interactions between crown ether macrocycles.[18]

The key building block in rotaxane **R2** is the switching unit implemented in the wheels, which controls their non-covalent interactions. The organosulfur compound tetrathiafulvalene[19] (TTF) is suitable, because TTF can undergo two reversible one-electron oxidations to yield a stable radical-cation ($TTF^{\bullet+}$) and dication (TTF^{2+}).[20] Similar to viologen radical cations,[21] TTF radical cations have an outstanding ability to form long-bonded dimers with cofacial arrangements: the mixed-valence dimer $(TTF_2)^{\bullet+}$ and the radical-cation dimer $(TTF^{\bullet+})_2$.[22] These weakly-associated species are usually not stable in solution under ambient conditions.[23] However, TTF dimers have been lately observed in carefully designed supramolecular complexes with confined environments including capsules,[24] clips,[25] or mechanically interlocked architectures such as rotaxanes[26] or catenanes.[27]

In our previous work involving TTF-decorated crown/ammonium (pseudo)rotaxanes, we directly implemented the TTF unit in a [24]crown-8 wheel (**TTFC8**).[28] Coulomb repulsion between the oxidised wheel **TTFC8** and the charged ammonium axles was used as the basis for redox-switchable shuttles. However, this design leads to the major drawbacks for the concept of synchronised wheel pirouetting: (i) the sulfur atoms in the wheel drastically lower the binding constant to dialkyl ammonium axles due to weaker hydrogen bonding.[29] (ii) The spatial proximity of TTF and the axle causes charge repulsion between the oxidised TTF and the ammonium station.[28b] (iii) Unsubstituted TTF forms only weak dimers. To circumvent these difficulties, an extended

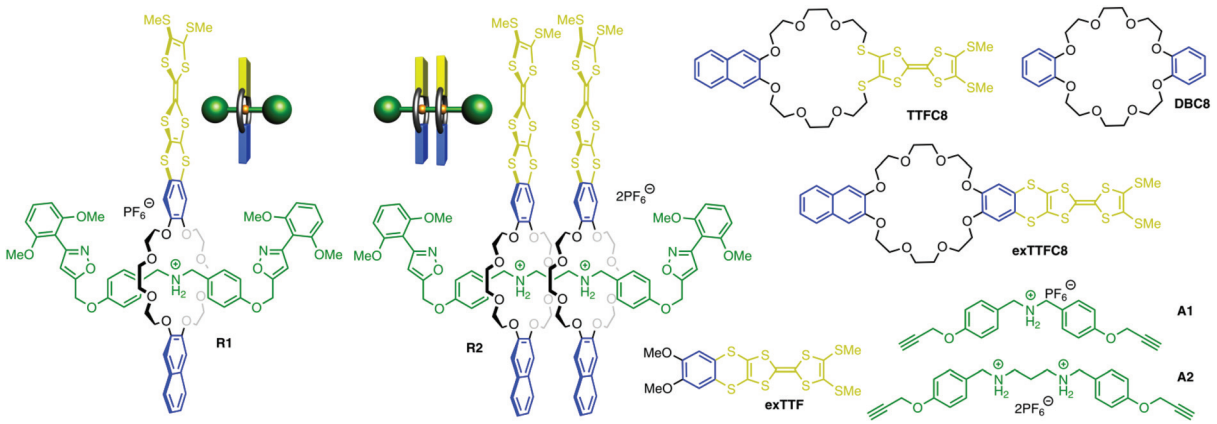

Fig. 2 Chemical structures of [3]rotaxane **R2** and other compounds investigated in this report.

macrocycle (**exTTFC8**) with a 1,2-dimercaptobenzene spacer between the TTF and the crown ether wheel was designed and synthesised (ESI, section 1.2†). In a very recent report, we showed that a TTF fused to a veratrole molecule (**exTTF**) features an enhanced dimer stability in comparison to unsubstituted TTF.[30]

A prerequisite for efficient rotaxane capping synthesis is a sufficiently strong template effect in the pseudorotaxane precursor complexes. Isothermal titration calorimetry (ITC) with monovalent axle **A1** and wheels **exTTFC8**, **TTFC8** and dibenzo-24-crown-8 (**DBC8**) showed mainly enthalpy-driven binding for all three pseudo[2]rotaxanes (ESI, section 4 and Table S1†). Compared to **TTFC8** (K_a = (3.8 ± 0.4) × 10^3 M^{-1} in $ClCH_2CH_2Cl$/CH_3CN = 10 : 1), a 13-fold increase of the binding constant is observed for **exTTFC8** (K_a = (50 ± 5) × 10^3 M^{-1}). Furthermore, similar ΔH and ΔS values of **exTTFC8** as compared to those of **DBC8** corroborate our previous assumption of a stronger binding due to the separation of the crown binding site and TTF unit.

A capping strategy introduced by Takata and co-workers using a catalyst-free click reaction with a nitrile oxide stopper[31] was employed for the synthesis of [3]rotaxane **R2** (see section 1.3 in the ESI† for details). Besides the target compound **R2**, the structurally similar [2]rotaxane **R1** bearing one wheel was synthesised. Since all intramolecular wheel–wheel interactions can be excluded, **R1** serves as an ideal control compound to identify the effects in **R2** that emerge from its divalent nature. Experimental evidence obtained by ^1H, ^{13}C, and 2D NMR, high-resolution mass spectrometry, and infrared multiphoton dissociation experiments is consistent with the mechanically interlocked structures of both rotaxanes **R1** and **R2** (Fig. S1–7, ESI†).

Electrochemical switching

Two major questions arise for the switching of [3]rotaxane **R2**: (i) what is the wheels' ground state co-conformation (GSCC) in each oxidation state (Fig. 3a)? (ii) How strong are the TTF-induced wheel–wheel interactions, and thus the coupling between the wheels in each state (Fig. 3b)?

Regarding the first question, both macrocycles can pirouette around the axle and many different rotamers are potentially accessible. Only in a *syn* or *anti* co-conformation of the wheels, however, favorable cofacial stacking between the TTF and/or the naphthalene units is possible.[32] Spectroscopic evidence for intramolecular TTF dimer interactions—for example mixed-valence or radical-cation interactions—would thus imply a *syn* GSCC of the wheels.

Initially, the electrochemical properties of rotaxanes **R1** and **R2** were probed by cyclic voltammetry (CV) experiments in CH_3CN (Fig. 4). [2]Rotaxane **R1** shows two reversible one-electron oxidations with half-wave potentials of $E^1_{1/2}$ = 0.16 V and

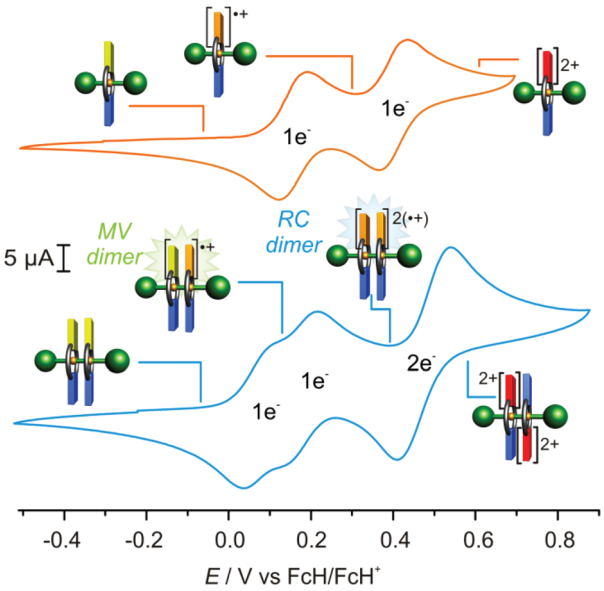

Fig. 4 Cyclic voltammograms (CH_3CN, 298 K, 1.0 mM, 100 mV s^{-1}) of rotaxanes **R1** (orange) and **R2** (blue) with *n*-Bu_4NPF_6 (0.1 M) as the electrolyte.

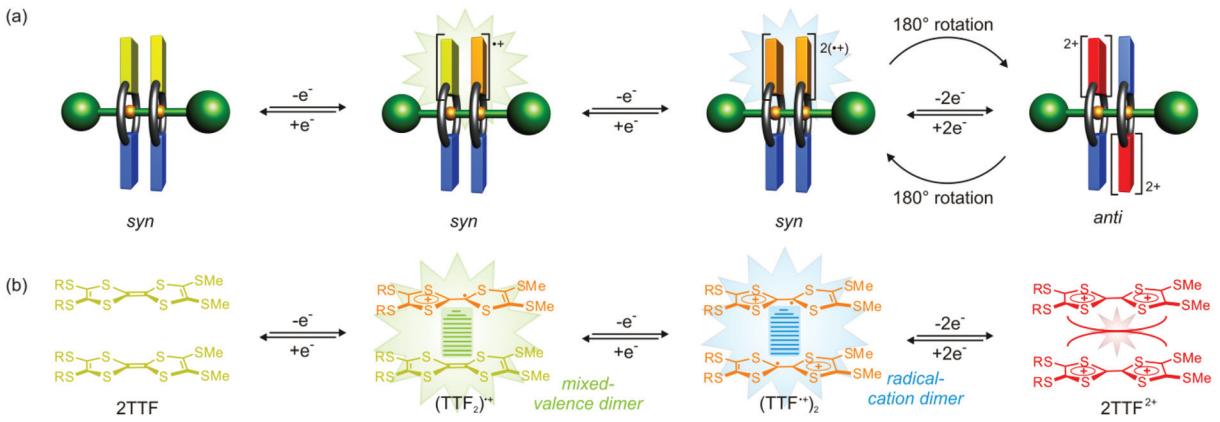

Fig. 3 (a) Graphical illustrations of [3]rotaxane **R2** in all oxidation states to illustrate the expected interconversion between the *syn* and *anti* ground state co-conformations of the wheels. (b) Cofacial TTF-TTF dimer interactions during successive oxidation of the two TTF molecules in **R2**.

$E^2_{1/2}$ = 0.40 V against the ferrocene/ferrocenium couple which we assign to the two oxidations of the TTF unit. The potentials are very similar to those of monomer **exTTF** (0.16 and 0.39 V).[30] This demonstrates that the positively charged ammonium axle has only a negligible effect on the TTF oxidation in **R1**. Additionally, no significant peak potential differences were observed for measurements of **R1** and **exTTFC8** in CH_2Cl_2 as a solvent of low dielectric constant (ESI, Fig. S12†). Thus, the charge–charge distance increase caused by the 1,2-dimercaptobenzene spacer sufficiently decreases the Coulomb repulsion between the oxidised TTF and charged axle.

[3]Rotaxane **R2** shows characteristic differences as compared to its monovalent analogue **R1**: three reversible oxidation processes are observed, two one-electron and a two-electron process with half-wave potentials of $E^1_{1/2}$ = 0.08 V, $E^2_{1/2}$ = 0.19 V, and $E^3_{1/2}$ = 0.48 V, respectively. The splitting of the first oxidation into two one-electron waves is indicative of an intramolecular mixed-valence interaction ($(TTF_2)^{\bullet+}$).[33] Based on the peak-to-peak separation, the comproportionation equilibrium of $\mathbf{R2}^{\bullet+}$ can be determined (K_c = 73) which clearly indicates a thermodynamically stable $\mathbf{R2}^{\bullet+}$ state.[33a,34] The third wave, corresponding to the $\mathbf{R2}^{2(\bullet+)} \rightarrow \mathbf{R2}^{4+}$ transition, is anodically shifted (+0.08 V) in contrast to the $\mathbf{R1}^{\bullet+} \rightarrow \mathbf{R1}^{2+}$ oxidation. This potential difference cannot merely be attributed to charge repulsion, as the system is flexible enough to elude the repulsion between the TTF^{2+} units by wheel pirouetting.[33c] Hence, the shift is assumed to be a consequence of an intramolecular stabilising interaction in the $\mathbf{R2}^{2(\bullet+)}$ state, most likely the radical-cation dimer $(TTF^{\bullet+})_2$, which has to be overcome by the additional potential.

In order to gain more detailed insight here, the CV data of **R2** were evaluated by electrochemical digital simulations (DS), a powerful tool to establish chemical–electrochemical mechanisms and to estimate the thermodynamic and kinetic parameters of equilibrium reactions (ESI, section 5†).[35] Our simulations indicate the states $\mathbf{R2}^{\bullet+}$ and $\mathbf{R2}^{2(\bullet+)}$ to be significantly stabilised by attractive wheel–wheel interactions. The estimated stabilisation energies in the four different states provide the following wheel–wheel interaction ranking: $\mathbf{R2}^{\bullet+}$ (mixed-valence dimer) > $\mathbf{R2}^{2(\bullet+)}$ (radical-cation dimer) > **R2** ≫ $\mathbf{R2}^{4+}$. This follows the order of the previously reported dimerisation energies of TTF monomers.[22,30] Notably, $\mathbf{R2}^{4+}$ displays a significantly smaller attractive interaction than neutral **R2** implying that the repulsive forces between the wheels affect the $\mathbf{R2}^{4+}$ state. Here, charge repulsion between the two TTF^{2+} units leads to an opening of the cofacial TTF dimer and subsequently to a change in the wheel's co-conformation.[27,33b] An *anti* GSCC is reasonable as it increases the charge–charge distance and simultaneously enables cofacial interactions between the electron-poor TTF^{2+} and the electron-rich naphthalene units.

The paramagnetic properties of **R1** and **R2** in their different oxidation states were investigated by continuous wave electron paramagnetic resonance (CW EPR) titration experiments (Fig. 5a). CH_3CN solutions of **R1** and **R2** were chemically oxidised by stepwise addition of $Fe(ClO_4)_3$ as a one-electron oxidant. A test reaction using Zn dust for back reduction

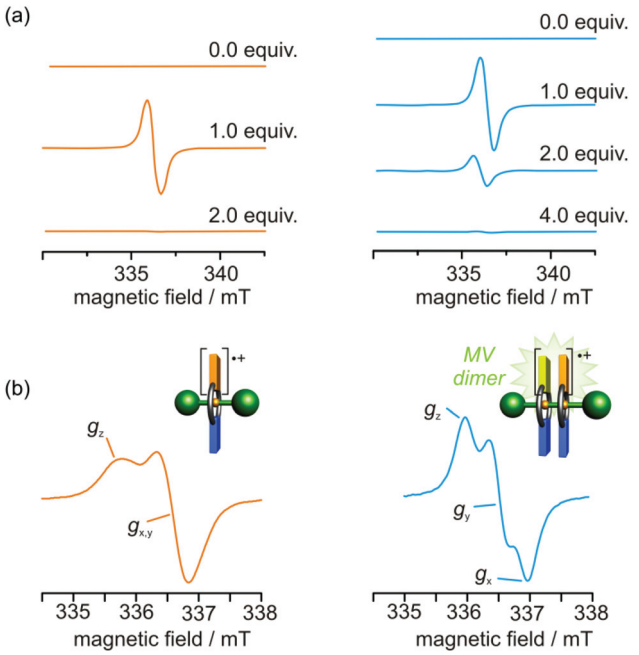

Fig. 5 (a) CW EPR spectra (CH_3CN, 298 K, 0.1 mM) of [2]rotaxane **R1** (orange) and [3]rotaxane **R2** (blue) upon titration with the oxidant Fe$(ClO_4)_3$. (b) EPR spectra (163 K, 0.1 mM) of frozen CH_2Cl_2 solutions of $\mathbf{R1}^{\bullet+}$ and $\mathbf{R2}^{\bullet+}$.

demonstrates the reversibility of this chemical oxidation (ESI, Fig. S9b†).[28a,30] After each addition of the oxidant, an EPR spectrum was recorded. For **R1**, addition of 1.0 equiv. of the oxidant leads to a signal with g = 2.010 which corresponds to the radical-cationic species $\mathbf{R1}^{\bullet+}$.[23] Further oxidation results in a decrease of intensity in accordance with an $\mathbf{R1}^{2+}$ singlet state. The same protocol was applied for [3]rotaxane **R2**. A maximum of intensity for the paramagnetic $\mathbf{R2}^{\bullet+}$ state (g = 2.010) is reached after the addition of 1.0 equiv. of the oxidant. The signal intensity decreases with further oxidation which indicates radical-paring and is thus indicative of the formation of a diamagnetic radical-cation dimer ($(TTF^{\bullet+})_2$) in rotaxane $\mathbf{R2}^{2(\bullet+)}$.[22,27,36] However, a weak signal is still present after adding 2.0 equiv. which may be explained by charge disproportionation or equilibria between the EPR-silent radical–cation dimer and alternative EPR-active co-conformations of $\mathbf{R2}^{2(\bullet+)}$.[27,37] Further oxidation leads to a virtual absence of any signal intensity which is, again, in accordance with the diamagnetic $\mathbf{R2}^{4+}$ state.

In solution, molecular tumbling of paramagnetic molecules often averages out the anisotropy of the g-factor which gives a more detailed view on the coupling to the electrostatic field of the spatial environment. In frozen solution, however, the g factor anisotropy can become visible.[38] Therefore, additional EPR experiments of $\mathbf{R1}^{\bullet+}$ and $\mathbf{R2}^{\bullet+}$ were performed in CH_2Cl_2 at room temperature and in frozen solutions (Fig. 5b). The radical species were prepared by prior chemical oxidation with $Fe(ClO_4)_3$. At room temperature, rotaxanes $\mathbf{R1}^{\bullet+}$ and $\mathbf{R2}^{\bullet+}$ show isotropic signals at g values of 2.009 and 2.008, respectively. In

frozen solution (163 K), however, $\mathbf{R1}^{\bullet+}$ exhibits *g*-anisotropy and shows an EPR spectrum of axial symmetry with *g*-values g_z = 2.012 and $g_{x,y}$ = 2.008. Going from $\mathbf{R1}^{\bullet+}$ to $\mathbf{R2}^{\bullet+}$, an EPR spectrum of rhombic symmetry with three *g*-values of 2.011, 2.008 and 2.005 is observed. This indicates that the radical in $\mathbf{R2}^{\bullet+}$ experiences environmental effects different from those in $\mathbf{R1}^{\bullet+}$ in agreement with the mixed-valence interaction in $\mathbf{R2}^{\bullet+}$.

The presence of a radical-cation dimer in $\mathbf{R2}^{2(\bullet+)}$ was further verified by UV/Vis-NIR spectroscopy in CH_3CN. Fig. 6a depicts the photometric titrations of rotaxanes **R1** and **R2** by the oxidant $Fe(ClO_4)_3$. After the addition of 1.0 equiv. of oxidant, $\mathbf{R2}^{\bullet+}$ displays characteristic $TTF^{\bullet+}$ bands (450, 870 nm) accompanied by a broad low intensity charge-resonance band (>1300 nm) of the mixed-valence dimer $(TTF_2)^{\bullet+}$.[30,37,39] The low-energy band disappears in the course of further oxidation. The addition of 2.0 equiv. results in the formation of the radical-cation dimer interaction $((TTF^{\bullet+})_2)$ as clearly seen from the emergent shoulder[33c] between 1000 and 1500 nm and the blue shift (ESI, Fig. S9a†) of the $TTF^{\bullet+}$ bands at 430 nm and 820 nm. This Davydov blue shift is diagnostic of cofacially stacked radical-cation dimers[40] and is not observed in the oxidation of **R1**. This is an additional strong piece of evidence for a *syn* GSCC in $\mathbf{R2}^{2(\bullet+)}$. A typical TTF^{2+} band at 660 nm is observed for the fully oxidised rotaxane $\mathbf{R2}^{4+}$. The differences in absorption for each state can also be easily identified with the naked eye (Fig. 6b). Including the sextuply (including the two ammonium ions of the axle) charged $\mathbf{R2}^{4+}$ state, all chemically generated oxidation states of **R2** showed remarkable stability in CH_3CN towards moisture and air for several months as indicated by the persistent colors of the solutions.

Co-conformation of non-switched R2

To reveal the co-conformation and wheel–wheel interactions of **R2** before electrochemical switching, further ITC investigations of the pseudo[3]rotaxane formation with divalent axle **A2** and **exTTFC8** were conducted and compared with the binding data obtained for the TTF-free control $\mathbf{A2}\subset(\mathbf{DBC8})_2$ (ESI, section 4 and Table S1†). Not unexpectedly, $\mathbf{A2}\subset(\mathbf{DBC8})_2$ displays similar binding enthalpies for both wheels (ΔH_1 = (−35.6 ± 1.3) kJ mol^{-1}; ΔH_2 = (−31.1 ± 4.9) kJ mol^{-1}). Consequently, non-cooperative binding occurs here. In marked contrast, the second crown ether in $\mathbf{A2}\subset(\mathbf{exTTFC8})_2$ binds significantly stronger than the first (ΔH_1 = (−32.6 ± 1.0) kJ mol^{-1}; ΔH_2 = (−45.4 ± 4.3) kJ mol^{-1}). This clearly points to positive cooperativity, which can easily be traced back to the attractive π-interactions between the two cofacial **exTTFC8** wheels. The TTF and naphthalene units are thus crucial for the wheel–wheel interactions in $\mathbf{A2}\subset(\mathbf{exTTFC8})_2$.[41] However, the more fixed conformation leads to a strong entropic penalty of the second binding event which decreases K_2 in comparison with K_1. In accordance with the ITC results, the ^{1}H NMR spectrum of **R2** shows significant high-field shifts of the wheels' naphthalene signals ($\Delta\delta$ = −0.24 ppm) in comparison with **R1** (Fig. S8, ESI†). We attribute these shifts to a shielding effect caused by the intramolecular π-interactions between the two wheels in **R2**.[18b]

Since no crystals suitable for X-ray diffraction could be obtained, ion mobility mass spectrometry (IM-MS) was applied to investigate the conformation and underpin the assumption of a *syn* GSCC of the wheels in the **R2** state (see section 6 and Table S2 in the ESI† for details). IM-MS has proven to be highly valuable to unravel the conformations of mechanically interlocked molecules.[18a,28c,42] The mass spectrum obtained from **R2** shows one signal (*m*/*z* = 1217) that corresponds to the $[\mathbf{R2} - 2PF_6]^{2+}$ ion (Fig. S15a, ESI†). IM-MS analysis revealed only one narrow and Gaussian-shaped arrival time distribution for the $[\mathbf{R2} - 2PF_6]^{2+}$ ion indicating the presence of one energetically preferred conformer (ESI, Fig. S15b†). The experimental collision cross section (CCS) of 410 Å^2 matches with the theoretical CCS calculated from a force-field-optimised structure in which the wheels adopt a *syn* GSCC (412 A^2). Theoretical CCS values calculated for other possible wheel co-conformations were instead not consistent with the experimental CCS, which underlines the assumption that the *syn* GSCC is the most relevant conformation (ESI, Table S2†). Although the structure of **R2** in the gas phase is not necessarily identical to that in solution, such a *syn* GSCC is in good agreement with the ITC data and NMR results.

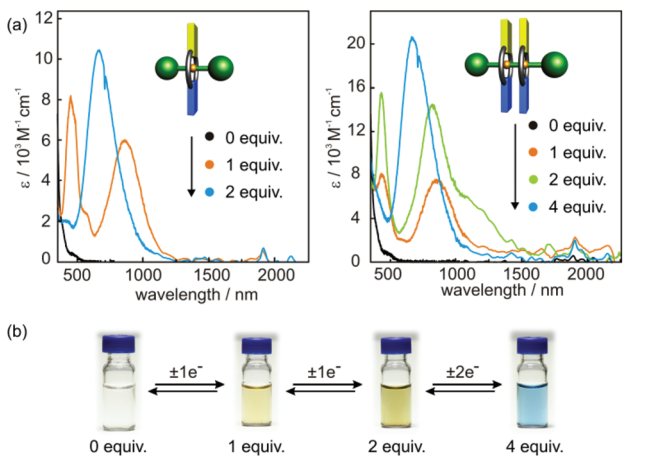

Fig. 6 (a) UV/Vis-NIR spectra (CH_3CN, 298 K, 2.5 × 10^{-5} M) of rotaxanes **R1** (left) and **R2** (right) upon titration with the oxidant $Fe(ClO_4)_3$. (b) Photographs of **R2** solutions (CH_3CN, 10^{-4} M) in all four stable oxidation states.

DFT calculations

Theoretical calculations were employed to gain further insight into the energetics and conformational aspects of **R2**. After structural relaxation of each co-conformation (*syn* and *anti*) in each of its four charge states, *i.e.* 8 structures in total, single point calculations at the PBE0-D3(BJ)/def2-TZVP level of DFT were performed to estimate co-conformational stabilities and oxidation potentials (for full computational details, see the ESI†). Additionally, the valence electronic structure of **R2** is investigated. We have shown previously that this level of theory sufficiently describes the conformational and electronic properties of our redox-active compounds.[30] Fig. 7 depicts the

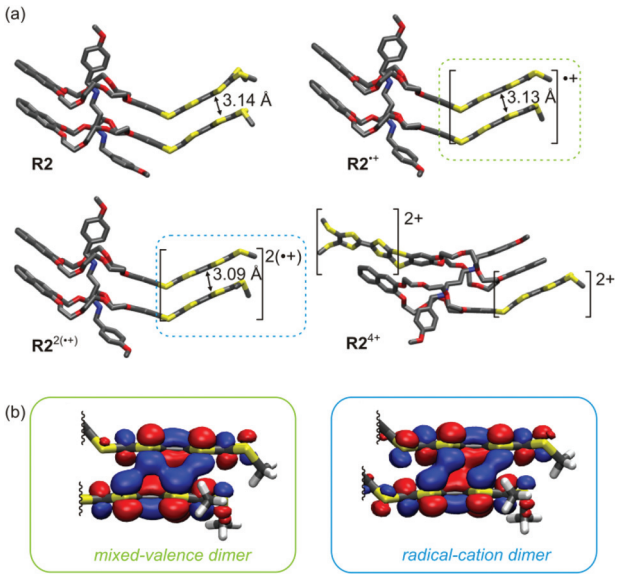

Fig. 7 (a) Calculated structures of the GSCC of a stopper-less pseudorotaxane analogue of **R2** in its four oxidation states. (b) Bonding orbitals of the TTF_2 complex in the mixed-valence and radical-cation dimer states.

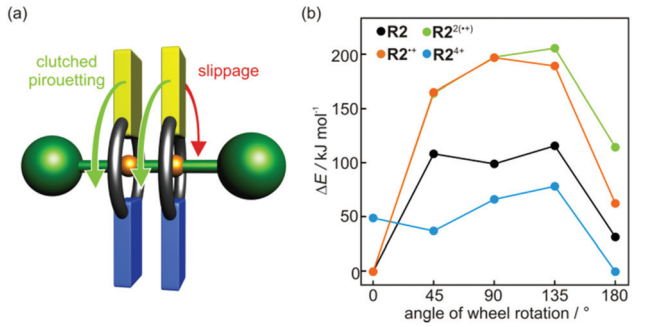

Fig. 8 (a) Schematic representation of the two rotational wheel motions in **R2** relative to the axle molecule. (b) DFT results of relaxed angular PES scans for counter-rotation of the wheels (slippage) in all stable oxidation states of **R2**.

most stable co-conformation of a computer-time-reducing, stopper-less pseudorotaxane analogue of **R2** in each state. In agreement with the experimental findings, the calculations suggest a *syn* GSCC for **R2**, $\mathbf{R2}^{\bullet+}$, and $\mathbf{R2}^{2(\bullet+)}$ whereas the *anti* co-conformation is lower in energy for $\mathbf{R2}^{4+}$. This is further supported by structural changes: during the first two oxidation processes in *syn*-**R2**, the interplanar distance between the TTF units decreases from 3.14 Å to 3.09 Å while the distance between the stacked naphthalene moieties remains rather constant around 3.32 Å. However, the last oxidation results in a significant increase of the TTF–TTF distance (from 3.09 Å to 3.17 Å) and a notable decrease of the naphthalene dimer separation (from 3.32 Å to 3.16 Å) due to the unfavourable electrostatic interaction of the two TTF^{2+} units. In contrast to *syn*-**R2**, the interplanar distances in *anti*-**R2** are only slightly altered upon oxidation (going from 3.31 Å in *anti*-**R2** to 3.27 Å in *anti*-$\mathbf{R2}^{4+}$).

Analysis of the molecular orbitals reveals that the valence electronic structure of $\mathbf{R2}^{\bullet+}$ and $\mathbf{R2}^{2(\bullet+)}$ is dominated by the mixed-valence and radical-cation dimer interactions, respectively, as visualised in Fig. 7b. The shape of the valence orbitals suggests multi-centered bonding[43] between the TTF units leading to attractive non-covalent interactions. Computed energies for the oxidative processes decently agree with experimental trends (Table S3, ESI†). Two contributions were considered: the pure electronic energy difference between two oxidation states and the difference arising from the rearrangement of a *syn* to an *anti* co-conformation or *vice versa*. For the second oxidative transition ($\mathbf{R2}^{\bullet+}/\mathbf{R2}^{2(\bullet+)}$) no rearrangement is expected and, hence, the mere electronic contribution reproduces the experiment very well.

Rotational motions

As illustrated in Fig. 8a, two rotational motions can be assumed for the wheels of **R2**: (i) a concerted pirouetting of the clutched macrocycles around the dialkyl ammonium thread (green arrow) or (ii) an independent counter-rotation of both wheels reminiscent of a slippage motion (red arrow).

The degree of concertedness of the wheel pirouetting increases with the strength of attractive wheel–wheel interactions in the different oxidation states as the most relevant parameter. However, in order to draw conclusions about the rotation from the interaction energies—that are thermodynamic values—it is necessary to know that there are no other barriers hampering the rotation of the wheels around the axle. In other words, only when the crown ethers are generally free to rotate, the TTF/TTF or TTF/naphthalene interactions will determine how much concerted, clutched motion occurs and how important gear slippage becomes.

Variable-temperature NMR (VT-NMR) experiments with **R2** result in only one set of signals for a C_{2v} symmetric species indicating a fast rotamer interconversion at room temperature. Upon gradual cooling to 203 K (400 MHz), the ^{1}H signals strongly broaden, but no decoalescence was observed. This is in accordance with other crown ether complexes, which show fast rotation with low barriers that is not detectable by standard VT-NMR techniques.[44] Consequently, the wheels in **R2** undergo a fast and random pirouetting motion even at temperatures significantly lower than room temperature. Unfortunately, the presence of paramagnetic species in the $\mathbf{R2}^{\bullet+}$, $\mathbf{R2}^{2(\bullet+)}$, and $\mathbf{R2}^{4+}$ states prevents reliable VT-NMR measurements for these states. Nevertheless, it is reasonable to assume that the rotation of the wheels is still fast in these states.

Quantum mechanical methods are a commonly-used tool[7] to approach the potential energy surface (PES) of molecular gears and rotors and to calculate energy barriers for different motions. Restricted optimisations and subsequent single-point calculations at the PBE0 level were performed for **R2** in steps of 45° for the dihedral angle between the two TTF units (Fig. S18, ESI†). Estimated barriers for counter-rotation of the wheels were obtained which are in the order of *ca.* 200 kJ mol^{-1} for $\mathbf{R2}^{\bullet+}$ and

$\mathbf{R2}^{2(\bullet+)}$ (Fig. 8b). These two oxidation states are thus much more strongly clutched in their *syn* co-conformation in comparison to **R2** and $\mathbf{R2}^{4+}$, for which these barriers are notably lower in energy. While non-switched **R2** shows a medium barrier height of approximately 100 kJ mol^{-1}, *syn*-$\mathbf{R2}^{4+}$ is not even predicted to be a local minimum structure. The latter readily falls into an intermediate structure at around 45° which in turn converts into the *anti* co-conformation with a barrier of ~40 kJ mol^{-1}. This can be attributed to the increasing Coulomb repulsion between the TTF^{2+} units. A clear differentiation between $\mathbf{R2}^{\bullet+}$ and $\mathbf{R2}^{2(\bullet+)}$ is rather difficult as their rotational motion is governed by a similar degree of non-covalent interactions. Although absolute values for rotational barriers may suffer from errors inherent in the applied DFT approach, their relative trends should be reliable. In spite of this, the calculations clearly indicate that a co-conformational change is accomplished in the last oxidative process when going from $\mathbf{R2}^{2(\bullet+)}$ to $\mathbf{R2}^{4+}$, which is in agreement with our experimental findings.

Overall, the experimental and computational results indicate stronger wheel–wheel interactions—and, thus, a higher barrier of wheel slippage—for the $\mathbf{R2}^{\bullet+}$ and $\mathbf{R2}^{2(\bullet+)}$ states than for the **R2** and $\mathbf{R2}^{4+}$ states. This clearly confirms the function as a switchable system with different motion coupling efficiencies in the four oxidation states. Although the wheels of the [3] rotaxane cannot be fully disengaged, the coupling can be adjusted by electrochemical switching.

Conclusions

In summary, the synthesis and electrochemical switching of a crown/ammonium [3]rotaxane **R2** consisting of a dumbbell-shaped axle with two tetrathiafulvalene-decorated wheels has been reported. The rotaxane can be switched between four stable oxidation states including two states featuring mixed-valence $(TTF_2)^{\bullet+}$ or radical-cation $(TTF^{\bullet+})_2$ dimer interactions. Each state shows a specific wheel ground state co-conformation and wheel–wheel interactions of different strengths. Quantum chemical calculations reveal that the barrier for gear slippage, which is identical to the counter-rotation of both wheels, can be adjusted by electrochemical switching. To the best of our knowledge, this is the first example of a gear-type system which operates with wheel pirouetting motions in a rotaxane. The switchable synchronisation of pirouetting motions equates with the working principle of a controllable gearing system. As a next step, ordered arrays of these rotaxanes on surfaces or in solid state materials could be investigated regarding their optoelectronic and conformational properties in external fields. A concerted behaviour of such multi-dimensional arrays may lead to macroscopic effects which are highly interesting for functional devices.

Conflicts of interest

There are no conflicts to declare.

Acknowledgements

This research was funded by the Deutsche Forschungsgemeinschaft (CRC 765). We thank Max Bartetzko and Mathias Ellwanger for NMR measurements, Fabian Klautzsch for help with the ITC, Jongcheol Seo for help with IM-MS, and Constantin Stuckhardt for help with synthesis.

Notes and references

1 (*a*) V. Balzani, A. Credi, F. M. Raymo and J. F. Stoddart, *Angew. Chem., Int. Ed.*, 2000, **39**, 3348; (*b*) S. Erbas-Cakmak, D. A. Leigh, C. T. McTernan and A. L. Nussbaumer, *Chem. Rev.*, 2015, **115**, 10081.
2 (*a*) D. Stock, *Science*, 1999, **286**, 1700; (*b*) H. Terashima, S. Kojima and M. Homma, *Int. Rev. Cell Mol. Biol.*, 2008, **270**, 39.
3 S. Kassem, T. van Leeuwen, A. S. Lubbe, M. R. Wilson, B. L. Feringa and D. A. Leigh, *Chem. Soc. Rev.*, 2017, **46**, 2592.
4 N. Koumura, R. W. Zijlstra, R. A. van Delden, N. Harada and B. L. Feringa, *Nature*, 1999, **401**, 152.
5 (*a*) P. Stacko, J. C. M. Kistemaker, T. van Leeuwen, M. C. Chang, E. Otten and B. L. Feringa, *Science*, 2017, **356**, 964; (*b*) M. Baroncini and A. Credi, *Science*, 2017, **356**, 906.
6 H. Iwamura and K. Mislow, *Acc. Chem. Res.*, 1988, **21**, 175.
7 G. S. Kottas, L. I. Clarke, D. Horinek and J. Michl, *Chem. Rev.*, 2005, **105**, 1281.
8 (*a*) W. R. Browne and B. L. Feringa, *Nat. Nanotechnol.*, 2006, **1**, 25; (*b*) B. L. Feringa, *Angew. Chem., Int. Ed.*, 2017, **56**, 11060.
9 W. Setaka, T. Nirengi, C. Kabuto and M. Kira, *J. Am. Chem. Soc.*, 2008, **130**, 15762.
10 K. Sanada, H. Ube and M. Shionoya, *J. Am. Chem. Soc.*, 2016, **138**, 2945.
11 H. Ube, Y. Yasuda, H. Sato and M. Shionoya, *Nat. Commun.*, 2017, **8**, 14296.
12 (*a*) J. D. Crowley, I. M. Steele and B. Bosnich, *Chem. – Eur. J.*, 2006, **12**, 8935; (*b*) A. Iordache, M. Oltean, A. Milet, F. Thomas, B. Baptiste, E. Saint-Aman and C. Bucher, *J. Am. Chem. Soc.*, 2012, **134**, 2653.
13 S. Ogi, T. Ikeda, R. Wakabayashi, S. Shinkai and M. Takeuchi, *Chem. – Eur. J.*, 2010, **16**, 8285.
14 J. Schummer, *Found. Chem.*, 2006, **8**, 53.
15 (*a*) P. L. Anelli, N. Spencer and J. F. Stoddart, *J. Am. Chem. Soc.*, 1991, **113**, 5131; (*b*) A. Altieri, F. G. Gatti, E. R. Kay, D. A. Leigh, D. Martel, F. Paolucci, A. M. Slawin and J. K. Wong, *J. Am. Chem. Soc.*, 2003, **125**, 8644; (*c*) F. Coutrot and E. Busseron, *Chem. – Eur. J.*, 2008, **14**, 4784.
16 (*a*) E. A. Neal and S. M. Goldup, *Chem. Commun.*, 2014, **50**, 5128; (*b*) C. A. Schalley, K. Beizai and F. Vögtle, *Acc. Chem. Res.*, 2001, **34**, 465.
17 (*a*) P. R. Ashton, P. J. Campbell, P. T. Glink, D. Philp, N. Spencer, J. F. Stoddart, E. J. T. Chrystal, S. Menzer, D. J. Williams and P. A. Tasker, *Angew. Chem., Int. Ed. Engl.*,

1995, **34**, 1865; (*b*) N. Yamaguchi and H. W. Gibson, *Angew. Chem., Int. Ed.*, 1999, **38**, 143; (*c*) T. J. Hubin and D. H. Busch, *Coord. Chem. Rev.*, 2000, **200–202**, 5; (*d*) X. Fu, Q. Zhang, S. J. Rao, D. H. Qu and H. Tian, *Chem. Sci.*, 2016, **7**, 1696; (*e*) S. J. Rao, Q. Zhang, J. Mei, X. H. Ye, C. Gao, Q. C. Wang, D. H. Qu and H. Tian, *Chem. Sci.*, 2017, **8**, 6777.

18 (*a*) M. E. Belowich, C. Valente, R. A. Smaldone, D. C. Friedman, J. Thiel, L. Cronin and J. F. Stoddart, *J. Am. Chem. Soc.*, 2012, **134**, 5243; (*b*) A. J. Avestro, D. M. Gardner, N. A. Vermeulen, E. A. Wilson, S. T. Schneebeli, A. C. Whalley, M. E. Belowich, R. Carmieli, M. R. Wasielewski and J. F. Stoddart, *Angew. Chem., Int. Ed.*, 2014, **53**, 4442.

19 (*a*) M. B. Nielsen, C. Lomholt and J. Becher, *Chem. Soc. Rev.*, 2000, **29**, 153; (*b*) C. P. Collier, G. Mattersteig, E. W. Wong, Y. Luo, K. Beverly, J. Sampaio, F. M. Raymo, J. F. Stoddart and J. R. Heath, *Science*, 2000, **289**, 1172; (*c*) J. L. Segura and N. Martín, *Angew. Chem., Int. Ed.*, 2001, **40**, 1372; (*d*) J. O. Jeppesen, M. B. Nielsen and J. Becher, *Chem. Rev.*, 2004, **104**, 5115; (*e*) D. Canevet, M. Sallé, G. Zhang, D. Zhang and D. Zhu, *Chem. Commun.*, 2009, 2245.

20 (*a*) D. L. Coffen and P. E. Garrett, *Tetrahedron Lett.*, 1969, **10**, 2043; (*b*) S. Hünig, G. Kießlich, H. Quast and D. Scheutzow, *Liebigs Ann. Chem.*, 1973, 310.

21 Q. Zhang, D. H. Qu, Q. C. Wang and H. Tian, *Angew. Chem., Int. Ed.*, 2015, **54**, 15789.

22 S. V. Rosokha and J. K. Kochi, *J. Am. Chem. Soc.*, 2007, **129**, 828.

23 V. Khodorkovsky, L. Shapiro, P. Krief, A. Shames, G. Mabon, A. Gorgues and M. Giffard, *Chem. Commun.*, 2001, 2736.

24 (*a*) A. Y. Ziganshina, Y. H. Ko, W. S. Jeon and K. Kim, *Chem. Commun.*, 2004, 806; (*b*) M. Yoshizawa, K. Kumazawa and M. Fujita, *J. Am. Chem. Soc.*, 2005, **127**, 13456.

25 P. T. Chiang, N. C. Chen, C. C. Lai and S. H. Chiu, *Chem. – Eur. J.*, 2008, **14**, 6546.

26 I. Aprahamian, J. C. Olsen, A. Trabolsi and J. F. Stoddart, *Chem. – Eur. J.*, 2008, **14**, 3889.

27 J. M. Spruell, A. Coskun, D. C. Friedman, R. S. Forgan, A. A. Sarjeant, A. Trabolsi, A. C. Fahrenbach, G. Barin, W. F. Paxton, S. K. Dey, M. A. Olson, D. Benitez, E. Tkatchouk, M. T. Colvin, R. Carmielli, S. T. Caldwell, G. M. Rosair, S. G. Hewage, F. Duclairoir, J. L. Seymour, A. M. Slawin, W. A. Goddard III, M. R. Wasielewski, G. Cooke and J. F. Stoddart, *Nat. Chem.*, 2010, **2**, 870.

28 (*a*) H. V. Schröder, H. Hupatz, A. J. Achazi, S. Sobottka, B. Sarkar, B. Paulus and C. A. Schalley, *Chem. – Eur. J.*, 2017, **23**, 2960; (*b*) H. V. Schröder, S. Sobottka, M. Nössler, H. Hupatz, M. Gaedke, B. Sarkar and C. A. Schalley, *Chem. Sci.*, 2017, **8**, 6300; (*c*) H. V. Schröder, J. M. Wollschläger and C. A. Schalley, *Chem. Commun.*, 2017, **53**, 9218.

29 H. Nagai, Y. Suzaki and K. Osakada, *Eur. J. Inorg. Chem.*, 2014, **2014**, 4376.

30 H. V. Schröder, F. Witte, M. Gaedke, S. Sobottka, L. Suntrup, H. Hupatz, A. Valkonen, B. Paulus, K. Rissanen, B. Sarkar and C. A. Schalley, *Org. Biomol. Chem.*, 2018, **16**, 2741.

31 T. Matsumura, F. Ishiwari, Y. Koyama and T. Takata, *Org. Lett.*, 2010, **12**, 3828.

32 (*a*) C. A. Hunter and J. K. M. Sanders, *J. Am. Chem. Soc.*, 1990, **112**, 5525; (*b*) C. R. Martinez and B. L. Iverson, *Chem. Sci.*, 2012, **3**, 2191.

33 (*a*) D. L. Sun, S. V. Rosokha, S. V. Lindeman and J. K. Kochi, *J. Am. Chem. Soc.*, 2003, **125**, 15950; (*b*) V. A. Azov, R. Gómez and J. Stelten, *Tetrahedron*, 2008, **64**, 1909; (*c*) M. Hasegawa, K. Daigoku, K. Hashimoto, H. Nishikawa and M. Iyoda, *Bull. Chem. Soc. Jpn.*, 2012, **85**, 51.

34 (*a*) K. D. Demadis, C. M. Hartshorn and T. J. Meyer, *Chem. Rev.*, 2001, **101**, 2655; (*b*) M. B. Robin and P. Day, *Adv. Inorg. Chem. Radiochem.*, 1968, **10**, 247.

35 (*a*) Y. Wang, S. Mendoza and A. E. Kaifer, *Inorg. Chem.*, 1998, **37**, 317; (*b*) W. S. Jeon, K. Moon, S. H. Park, H. Chun, Y. H. Ko, J. Y. Lee, E. S. Lee, S. Samal, N. Selvapalam, M. V. Rekharsky, V. Sindelar, D. Sobransingh, Y. Inoue, A. E. Kaifer and K. Kim, *J. Am. Chem. Soc.*, 2005, **127**, 12984.

36 J. M. Lu, S. V. Rosokha and J. K. Kochi, *J. Am. Chem. Soc.*, 2003, **125**, 12161.

37 A. Coskun, J. M. Spruell, G. Barin, A. C. Fahrenbach, R. S. Forgan, M. T. Colvin, R. Carmieli, D. Benitez, E. Tkatchouk, D. C. Friedman, A. A. Sarjeant, M. R. Wasielewski, W. A. Goddard III and J. F. Stoddart, *J. Am. Chem. Soc.*, 2011, **133**, 4538.

38 (*a*) F. A. Walker, H. Boi Hanh, W. R. Scheidt and S. R. Osvath, *J. Am. Chem. Soc.*, 1986, **108**, 5288; (*b*) C. Gouverd, F. Biaso, L. Cataldo, T. Berclaz, M. Geoffroy, E. Levillain, N. Avarvari, M. Fourmigué, F. X. Sauvage and C. Wartelle, *Phys. Chem. Chem. Phys.*, 2005, **7**, 85.

39 (*a*) G. Barin, A. Coskun, D. C. Friedman, M. A. Olson, M. T. Colvin, R. Carmielli, S. K. Dey, O. A. Bozdemir, M. R. Wasielewski and J. F. Stoddart, *Chem. – Eur. J.*, 2011, **17**, 213; (*b*) M. Hasegawa, J.-I. Takano, H. Enozawa, Y. Kuwatani and M. Iyoda, *Tetrahedron Lett.*, 2004, **45**, 4109.

40 (*a*) M. Iyoda, K. Hara, Y. Kuwatani and S. Nagase, *Org. Lett.*, 2000, **2**, 2217; (*b*) M. Iyoda, M. Hasegawa and Y. Miyake, *Chem. Rev.*, 2004, **104**, 5085; (*c*) M. Hasegawa, K. Nakamura, S. Tokunaga, Y. Baba, R. Shiba, T. Shirahata, Y. Mazaki and Y. Misaki, *Chem. – Eur. J.*, 2016, **22**, 10090.

41 (*a*) M. Lohse, K. Nowosinski, N. L. Traulsen, A. J. Achazi, L. K. S. von Krbek, B. Paulus, C. A. Schalley and S. Hecht, *Chem. Commun.*, 2015, **51**, 9777; (*b*) K. Nowosinski, L. K. S. von Krbek, N. L. Traulsen and C. A. Schalley, *Org. Lett.*, 2015, **17**, 5076; (*c*) L. K. S. von Krbek, A. J. Achazi, S. Schoder, M. Gaedke, T. Biberger, B. Paulus and C. A. Schalley, *Chem. – Eur. J.*, 2017, **23**, 2877.

42 E. Hanozin, B. Mignolet, D. Morsa, D. Sluysmans, A. S. Duwez, J. F. Stoddart, F. Remacle and E. De Pauw, *ACS Nano*, 2017, **11**, 10253.

43 (*a*) M. Capdevila-Cortada and J. J. Novoa, *Chem. – Eur. J.*, 2012, **18**, 5335; (*b*) M. Fumanal, M. Capdevila-Cortada and J. J. Novoa, *Phys. Chem. Chem. Phys.*, 2017, **19**, 3807.
44 (*a*) J. Dale and P. O. Kristiansen, *J. Chem. Soc. D*, 1971, 670; (*b*) D. K. Frantz, A. Linden, K. K. Baldridge and J. S. Siegel, *J. Am. Chem. Soc.*, 2012, **134**, 1528; (*c*) C. I. Ratcliffe, J. A. Ripmeester, G. W. Buchanan and J. K. Denike, *J. Am. Chem. Soc.*, 1992, **114**, 3294; (*d*) V. N. Vukotic, K. J. Harris, K. Zhu, R. W. Schurko and S. J. Loeb, *Nat. Chem.*, 2012, **4**, 456.

Electronic Supplementary Information (ESI†)

Switchable synchronisation of pirouetting motions in a redox active [3]rotaxane

Hendrik V. Schröder,[a] Amel Mekic,[a] Henrik Hupatz,[a] Sebastian Sobottka,[b] Felix Witte,[a] Leonhard H. Urner,[a] Marius Gaedke,[a] Kevin Pagel,[ac] Biprajit Sarkar,[b] Beate Paulus[a] and Christoph A. Schalley[a]*

[a] Institut für Chemie und Biochemie, Freie Universität Berlin
Takustraße 3, 14195 Berlin, Germany.
[b] Institut für Chemie und Biochemie, Freie Universität Berlin
Fabeckstraße 34/36, 14195 Berlin, Germany.
[c] Fritz Haber Institute of the Max Planck Society, Department of Molecular Physics,
Faradayweg 4-6, Berlin, 14195 Berlin, Germany.
*Corresponding author e-mail: c.schalley@fu-berlin.de

Table of contents

1. Experimental and synthetic details

1.1. General methods

All reagents and solvents were obtained from commercial sources and used without further purification. Dry solvents were purchased from Acros Organics. Monomer **exTTF**,[S1] ditosylate **A**,[S2] bis(4-(prop-2-yn-1-yloxy)benzyl)-ammonium hexafluorophosphate,[S3] 4-(prop-2-yn-1-yloxy)benzaldehyde[S4] and 2,6-dimethoxybenzonitrile oxide (**S1**)[S5] were synthesised according to literature procedures. Thin-layer chromatography was performed on silica gel-coated plates with fluorescent indicator F254 (Merck). For column chromatography, silica gel (0.04–0.063 mm, Merck) was used. ^{1}H and ^{13}C NMR experiments were performed on a JEOL ECX 400, JEOL ECP 500 or a Bruker AVANCE 700 MHz instrument. VT NMR experiments were performed on a JEOL ECS 400 MHz spectrometer. Solvent residue signals were used as the internal standard. All shifts are reported in ppm and NMR multiplicities are abbreviated as s (singlet), d (doublet), t (triplet), m (multiplet) and br (broad). Coupling constants *J* are reported in Hertz. Solvents and impurities are marked with an asterisk. High-resolution ESI mass spectra were measured on an Agilent 6210 ESI-TOF instrument (Agilent Technologies). Infrared multiphoton dissociation (IRMPD) experiments were performed on an Ionspec QFT-7 ESI-FTICR mass spectrometer from Varian Inc. equipped with a Micromass/Waters Z-spray electrospray ion source. IR laser pulses of 1000 ms width and 15–25 % laser intensity were applied to initiate fragmentation. HPLC grade solvents were used with a flow rate of 2–4 µL/min. Melting points were determined on a SMP 30 (Stuart) instrument. Melting points are uncorrected. EPR spectra at X-band frequency (ca. 9.5 GHz) were obtained with a Magnettech MS-5000 benchtop EPR spectrometer equipped with a rectangular TE 102 cavity and TC HO4 temperature controller. The measurements were carried out in synthetic quarz glass tubes. Dry and freshly distilled solvents (CH_2Cl_2 and CH_3CN) were used. Sample preparation and measurements were performed under nitrogen. UV/Vis spectra were recorded on a Varian Cary 50 Bio Photospectrometer equipped with a xenon lamp or on an Avantes spectrometer with a light source (AvaLight-DH-S-Bal), a UV/Vis detector (AvaSpec-ULS2048), and a NIR detector (AvaSpec-NIR256-TEC). Solvents with HPLC grade and Suprasil glass cuvettes with a path-length of 1 cm were used. Cyclic voltammetry was performed on an Autolab PGSTAT302N potentiostat using a three-electrode configuration: a freshly polished glassy carbon working electrode, a platinum wire counter electrode and a silver wire pseudoreference electrode. All measurements were conducted twice and with a broad range of different scan rates (25–1000 mV s^{-1}) to ensure electrochemical reversibility of the processes. The decamethylferrocene/ decamethylferrocenium couple was used as internal reference and the determined potentials are given against the ferrocene/ferrocenium (Fc/Fc^{+}) couple. Dry and argon purged solvents were used.

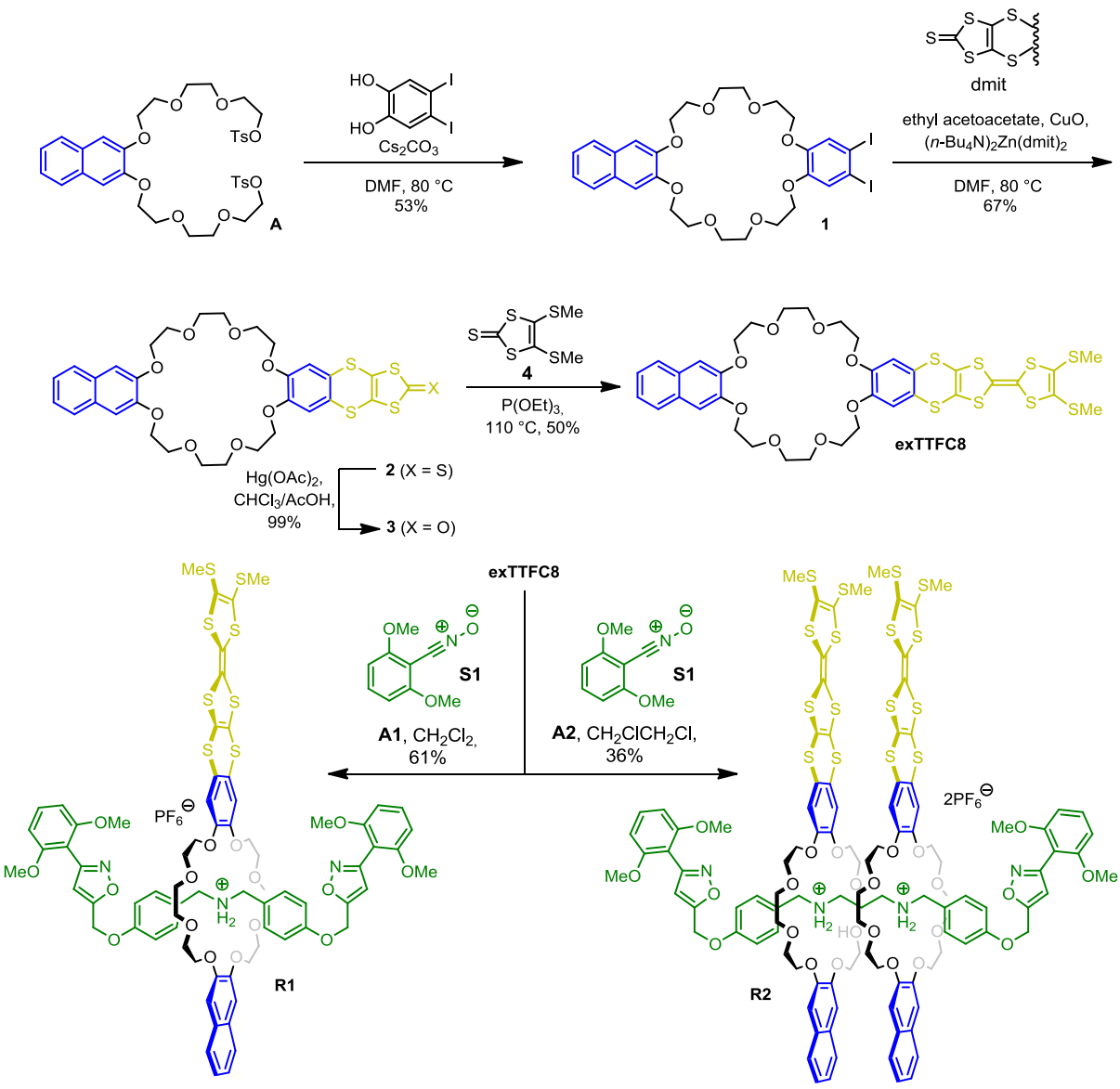

Scheme S1 General synthesis route to macrocycle **exTTFC8** and rotaxanes **R2** and **R3**.

1.2. Synthesis of macrocycle exTTFC8

Diiodide 1

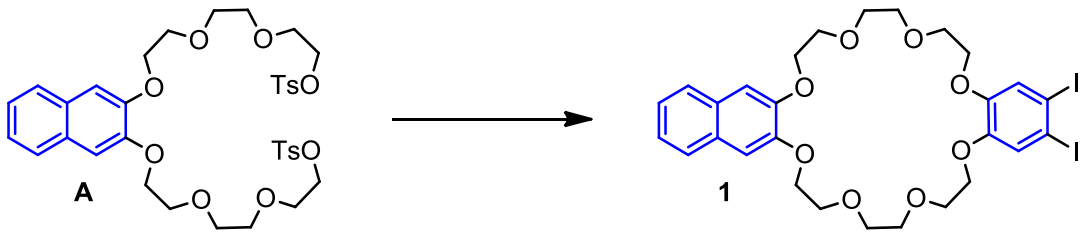

A solution of 4,5-diiodobenzene-1,2-diol (494 mg, 1.36 mmol) in dimethylformamide (DMF, 20 mL) was slowly added to a dispersion of Cs_2CO_3 (1.77 g, 5.44 mmol) in DMF (100 mL)

under argon atmosphere. Afterwards, the mixture was heated to 80 °C and a solution of ditosylate **A** (1.000 g, 1.36 mmol) in DMF (150 mL) was added dropwise over 2 h. The reaction was kept at 80 °C for another 2 d, before it was cooled down to room temperature. The solvent was removed *in vacuo* and the residue was dissolved in CH_2Cl_2. After filtering, the filtrate was concentrated *in vacuo* and purified by column chromatography (SiO_2, ethyl acetate/pentane = 3:1). The desired product (540 mg, 0.72 mmol, 53%) was obtained as a white solid. R_f ~ 0.4 in ethyl acetate/pentane = 3:1; m.p. 142 °C; ^{1}H NMR (500 MHz, $CDCl_3$, 298 K): δ = 7.64 (AA'XX' spin system , $^3J_{AA'XX'}$ = 6.1 Hz , 2H, H_{Ar}), 7.32 (AA'XX' spin system, $^3J_{AA'XX'}$ = 6.1 Hz , 2H, H_{Ar}), 7.22 (s, 2H, H_{Ar}), 7.09 (s, 2H, H_{Ar}), 4.27–4.22 (m, 4H, OCH_2), 4.09 – 4.06 (m, 4H, OCH_2), 4.00–3.97 (m, 4H, OCH_2), 3.91–3.85 (m, 8H, OCH_2), 3.83–3.81 (m, 2H, OCH_2) ppm; ^{13}C NMR (126 MHz, $CDCl_3$, 298 K): δ = 149.6, 149.1, 129.4, 126.5, 124.4, 124.1, 108.1, 96.6, 71.6, 71.6, 69.9, 69.8, 69.8, 69.3 ppm; ESI-HRMS: *m/z* calcd for $C_{28}H_{32}O_8I_2$: 788.9818 $[M+K]^+$, found: 788.9850.

Thioketone 2

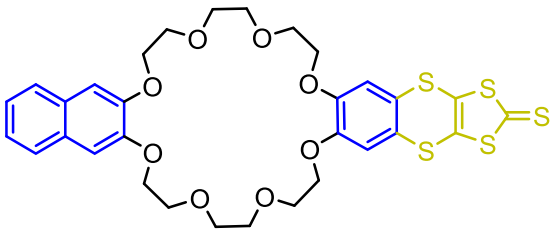

Diiodide **1** (360 mg, 0.48 mmol), $(NEt_4)_2[Zn(dmit)_2]$ (dmit = 1,3-dithiole-2-thione-4,5-dithiolate, 226 mg, 0.24 mmol), Cu_2O (7.2 mg, 0.01 mmol) and ethyl acetoacetate (13 µL, 0.10 mmol) were suspended in DMF (5 mL) and heated to 80 °C overnight. Afterwards, the reaction mixture was cooled down to room temperature and CH_2Cl_2 (20 mL) was added. The resulting mixture was washed with water (4x10 mL) and brine (10 mL) and dried over $MgSO_4$. The crude product was purified by column chromatography (SiO_2, CH_2Cl_2 → CH_2Cl_2/MeOH = 50:1) and the desired product (223 mg, 0.32 mmol, 67%) was obtained as a yellow solid. R_f = 0.4 in CH_2Cl_2/MeOH = 50:1; m.p. >189°C decomposition; ^{1}H NMR (700 MHz, $CDCl_3$. 298 K): δ = 7.64 (AA'XX' spin system, $^3J_{AA'XX'}$ = 6.2 Hz, 2H, HAr), 7.32 (AA'XX' spin system, $^3J_{AA'XX'}$ = 6.2 Hz, 2H, H_{Ar}), 7.09 (s, 2H, H_{Ar}), 6.91 (s, 2H, H_{Ar}), 4.27–4.24 (m, 4H, OCH_2), 4.13–4.10 (m, 4H, OCH_2), 4.01–3.97 (m, 4H, OCH_2), 3.93–3.90 (m, 4H, OCH_2), 3.89–3.86 (m, 4H, OCH_2), 3.84–3.81 (m, 4H, OCH_2) ppm; ^{13}C-NMR (176 MHz, $CDCl_3$, 298 K): δ = 212.8, 149.5, 149.0, 131.9, 129.4, 126.4, 125.7, 124.4, 114.0, 107.9, 71.6, 71.5, 69.9, 69.9, 69.7, 69.3 ppm; ESI-HRMS: *m/z* calcd for $C_{31}H_{32}O_8S_5$: 715.0593 $[M+K]^+$, found: 715.0598.

Ketone 3

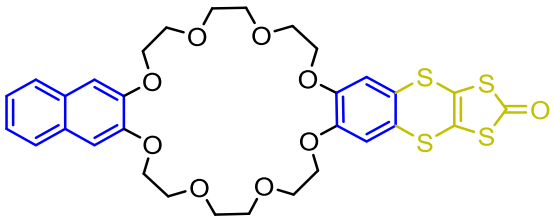

Thione **2** (150 mg, 0.22 mmol) and mercury(II) acetate (210 mg, 0.66 mmol) were dispersed in a mixture of $CHCl_3$ (7 mL) and acetic acid (2 mL) and stirred for 2 days at room temperature. Afterwards, the mixture was filtered through a celite pad, diluted with $CHCl_3$ and washed with saturated aqueous $NaHCO_3$ solution (50 mL) and brine (50 mL). The organic phase was dried over $MgSO_4$ and purified by column chromatography (SiO_2, CH_2Cl_2/Me_2CO = 1:1) to give the desired product (146 mg, 0.22 mmol, 99%) as an off-white solid. R_f = 0.30 in CH_2Cl_2/Me_2CO = 1:1; m. p. 174 °C; ^{1}H NMR (700 MHz, $CDCl_3$, 298 K): δ = 7.64 (m, 2H, H_{Ar}), 7.31 (m, 2H, H_{Ar}), 7.09 (s, 2H, H_{Ar}), 6.92 (s, 2H, H_{Ar}), 4.27–4.24 (m, 4H, OCH_2), 4.13–4.10 (m, 4H, OCH_2), 4.00–3.97 (m, 4H, OCH_2), 3.92–3.90 (m, 4H, OCH_2), 3.88–3.86 (m, 4H, OCH_2), 3.82 (m, 4H, OCH_2) ppm; ^{13}C NMR (176 MHz, $CDCl_3$, 298 K): δ = 191.82, 150.16, 149.62, 129.87, 126.77, 126.34, 124.69, 122.51, 114.48, 108.42, 71.83, 71.80, 70.26, 70.22, 70.11, 69.51 ppm; ESI-HRMS: *m/z* calcd for $C_{31}H_{32}O_9S_4$: 699.0821 $[M+Na]^+$, found: 699.0822.

Macrocycle exTTFC8

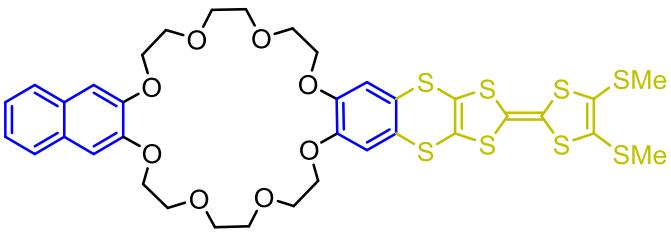

Ketone **3** (105 mg, 155 µmol) and 4,5-bis(methylthio)-1,3-dithiol-2-thione (35.1 mg, 155 µmol) were dissolved in $P(OEt)_3$ (40 mL) and the mixture was heated to 110 °C under argon atmosphere for 3 h. After cooling to room temperature, all volatiles were removed *in vacuo* and the residue was purified by column chromatography (SiO_2, CH_2Cl_2 → CH_2Cl_2/Me_2CO = 20:1). The desired product was obtained as a yellow solid (66.0 mg, 77.2 µmol, 50%). R_f = 0.30 in CH_2Cl_2/MeOH = 100:1; m.p. >189 °C decomposition;^{1}H NMR (700 MHz, CD_2Cl_2): δ = 7.65 (m, 2 H, H_{Ar}), 7.31 (m, 2H, H_{Ar}), 7.12 (s, 2H, H_{Ar}), 6.91 (s, 2H, H_{Ar}), 4.21 (m, 4H, OCH_2), 4.11 (m, 4H, OCH_2), 3.94 (m, 4H, OCH_2), 3.84 (m, 4H, OCH_2), 3.80 (m, 4H, OCH_2), 3.77 (m,

4H, OCH_2), 2.42 (s, 6H, SCH_3) ppm; ^{13}C NMR (176 MHz, CD_2Cl_2): δ = 149.76, 149.63, 129.88, 128.07, 126.97, 126.77, 124.68, 123.96, 116.72, 114.61, 113.33, 108.43, 71.81, 71.76, 70.22, 70.22, 70.13, 69.50, 54.00, 19.64 ppm; ESI-HRMS: *m/z* calcd for $C_{36}H_{38}O_8S_8$: 892.9969 $[M+K]^+$, found: 892.9995.

1.3. Synthesis of rotaxanes R1 and R2

***N*^{1},*N*^{3}-bis(4-(prop-2-yn-1-yloxy)benzyl)propane-1,3-diaminium dihexafluorophosphate (A2)**

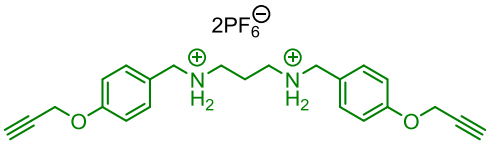

1,3-Diaminopropane (340 µL, 4.0 mmol) and 4-(prop-2-yn-1-yloxy)benzaldehyde (1.28 g, 8.0 mmol) were dissolved in dry EtOH (80 mL) under argon atmosphere and heated to reflux for 6 hours. Afterwards, the mixture was cooled to room temperature and $NaBH_4$ (1.51 g, 40 mmol) was carefully added. The reaction was stirred overnight. Superfluous $NaBH_4$ was quenched by slow addition of a small volume of saturated aqueous $NaHCO_3$ solution. After no gas evolution was observed anymore, all volatiles were removed *in vacuo*. The residue was dissolved in CH_2Cl_2 (50 mL), washed with saturated aqueous $NaHCO_3$ solution (50 mL) and brine (3x50 mL) and dried over $MgSO_4$. After solvent evaporation, the crude product was purified by column chromatograph (SiO_2, CH_2Cl_2 → CH_2Cl_2/MeOH/NEt_3 = 100:10:1). The resulting diamine was transferred to the corresponding hydrochloride by addition of conc. HCl in MeOH (5 mL, 1:1). After drying *in vacuo*, the desired hydrochloride (820 mg, 1.88 mmol) was obtained as a white solid. For the synthesis of the hexafluorophophate salt, part of the hydrochloride (200 mg, 0.46 mmol) and NH_4PF_6 (1.50 g, 9.2 mmol) were dissolved in CH_3CN/water (50 mL, 5:1) and the mixture was stirred for four hours at room temperature. After removing all solvents under reduced pressure, the residue was dissolved in ethyl acetate (100 mL) and washed with water (3x100 mL). Drying over $MgSO_4$ and concentration *in vacuo* yielded the desired product (180 mg, 0.28 mmol, 28% overall yield) as white powder. m.p. 198 °C (decomposition); ^1H NMR (400 MHz, CD_3CN, 298 K): δ = 7.48–7.34 (m, 4H, H_{Ar}), 7.05 (m, 4H, H_{Ar}), 4.77 (d, ^3J = 2.4 Hz, 4H, CH_2), 4.13 (s, 4H, CH_2), 3.15–3.00 (m, 4H, CH_2), 2.84 (t, ^3J = 2.4, 2H, CCH), 2.02 (t, ^3J = 7.8 Hz, 2H, CH_2) ppm; ^{13}C NMR (101 MHz, CD_3CN, 298 K): δ = 159.5, 132.8, 124.0, 116.3, 79.4, 77.2, 56.6, 52.3, 45.5, 23.3 ppm; ESI-HRMS: *m/z* calcd for $C_{23}H_{28}N_2O_2$: 363.2067 $[M-H-2PF_6]^+$, found: 363.2084.

[2]Rotaxane R1

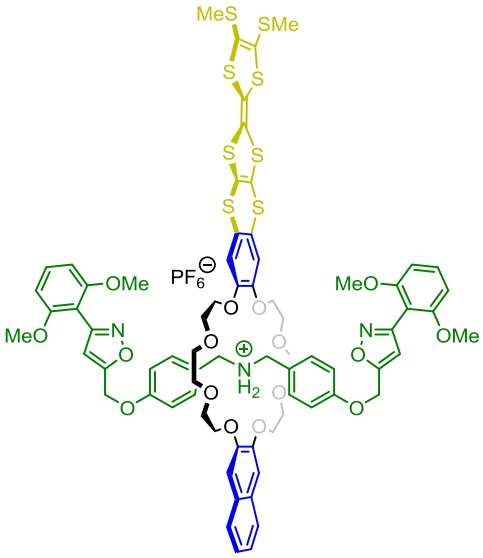

Bis(4-(prop-2-yn-1-yloxy)benzyl)ammonium hexafluorophosphate (4.4 mg, 9.8 µmol) and macrocycle **exTTFC8** (10 mg, 11.7 µmol) were suspended in CH_2Cl_2 (0.5 mL). The mixture was sonicated until the solids were fully dissolved. Afterwards, 2,6-dimethoxybenzonitrile oxide (4.2 mg, 23.4 µmol) was added and the reaction was stirred overnight at 30 °C. The mixture was directly subjected to column chromatography (SiO_2, CH_2Cl_2/MeOH = 250:1). The desired rotaxane **R1** was obtained as an orange solid (10 mg, 6.0 µmol, 61%). R_f = 0.20 in CH_2Cl_2/MeOH = 100:1; ^{1}H NMR (700 MHz, CD_2Cl_2, 298 K): δ = 7.66 (m, 2H, H_{Ar}), 7.44 (s, 2H, NH2), 7.39 (t, ^3J = 8.4 Hz, 2H, H_{Ar}), 7.35 (m, 2H, H_{Ar}), 7.27–7.25 (m, 4H, H_{Ar}), 6.99 (s, 2H, H_{Ar}), 6.83 (s, 2H, H_{Ar}), 6.76– 6.73 (m, 4H, H_{Ar}), 6.67 (d, ^3J = 8.4 Hz, 4H, H_{Ar}), 6.40 (s, 2H, H_{isox}), 4.86–4.81 (m, 4H, OCH_2), 4.62–4.58 (m, 4H, CH_2), 4.18–4.15 (m, 4H, OCH_2), 4.11–4.09 (m, 4H, OCH_2), 3.88–3.86 (m, 4H, OCH_2), 3.82–3.80 (m, 4H, OCH_2), 3.77 (s, 12H, OMe), 3.67–3.64 (m, 4H, OCH_2), 3.60–3.58 (m, 4H, OCH_2), 2.41 (s, 6H, SMe) ppm; ^{13}C NMR (176 MHz, CD_2Cl_2): δ = 166.3, 159.2, 159.1, 157.7, 148.4, 147.8, 131.9, 131.2, 129.7, 128.1, 127.5, 126.9, 125.4, 125.2, 123.8, 117.4, 115.3, 113.2, 112.8, 108.4, 107.4, 107.3, 104.7, 71.6, 71.3, 70.8, 70.7, 69.0, 68.8, 61.3, 56.5, 52.5, 19.6 ppm; ESI-HRMS: *m/z* calcd for $[C_{74}H_{76}N_3O_{16}S_8]^+$: 1518.2991 $[M\text{-}PF_6]^+$, found: 1518.3005.

[3]Rotaxane R2

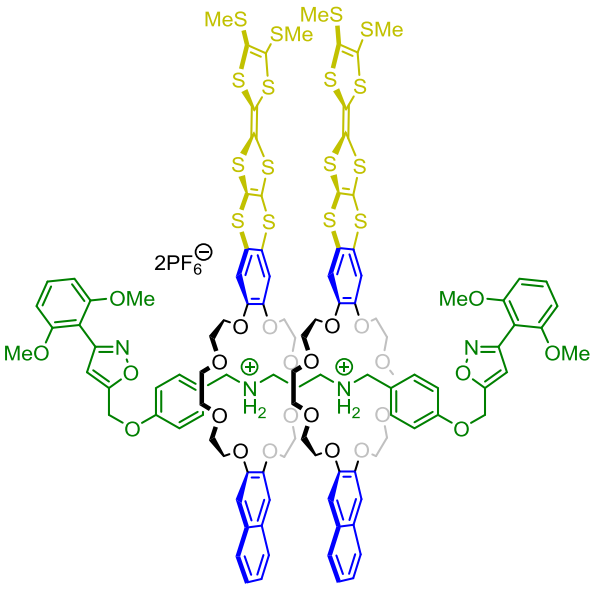

N^1,N^3-Bis(4-(prop-2-yn-1-yloxy)benzyl)propane-1,3-diaminium dihexafluorophosphate (3.3 mg, 5.0 µmol) and macrocycle **exTTFC8** (10 mg, 12.0 µmol) were suspended in 1,2-dichloroethane (1.8 mL). The mixture was sonicated until all solids were completely dissolved. Afterwards, stopper **S1** (2.7 mg, 15.0 µmol) was added and the reaction was stirred for 2 days at room temperature. The mixture was directly subjected to column chromatography (SiO_2, CH_2Cl_2/MeOH = 50:1). The desired product was obtained as an orange solid (5.0 mg, 1.8 µmol, 36%). R_f = 0.5 in SiO_2, CH_2Cl_2/MeOH = 25:1; m.p. >209°C decomposition; ^{1}H NMR (700 MHz, CD_2Cl_2/CD_3CN = 9:1, 298 K): δ = 7.36 (m, 6H, H_{Ar}), 7.11 (m, 8H, NH_2 and H_{Ar}), 7.05 (m, 4H, H_{Ar}), 6.87 (s, 4H, H_{Ar}), 6.72 (s, 4H, H_{Ar}), 6.65 (m, 4H, H_{Ar}), 6.58 (m, 4H, H_{Ar}), 6.32 (s, 2H, $H_{isox.}$), 4.66 (s, 4H, CH_2), 4.37 (m, 4H, $C\underline{H}_2NH_2$), 4.02 (m, 12H, OCH_2), 3.80 (m, 24H, OCH_2), 3.73 (s, 12H, OCH_3), 3.68 (m, 12H, OCH_2), 3.52 (m, 4H, $NH_2C\underline{H}_2CH_2$), 2.38 (s, 12H, SCH_3), 2.02 (m, 2H, $CH_2C\underline{H}_2CH_2$) ppm; ^{13}C NMR (176 MHz, CD_2Cl_2/CD_3CN = 9:1, 298 K): δ = 166.1, 159.1, 158.9, 157.5, 148.0, 147.4, 131.8, 131.2, 129.3, 127.7, 127.5, 126.5, 125.2, 124.1, 123.5, 116.9, 115.2, 113.3, 112.1, 108.8, 107.1, 107.1, 104.5, 71.2, 70.9, 70.6, 70.5, 68.7, 68.5, 61.0, 56.3, 54.0, 45.5, 30.0, 23.0, 19.3 ppm; ESI-HRMS: *m/z* calcd for $C_{113}H_{122}N_4O_{24}S_{16}P_2F_{12}$: 1215.1985 $[M\text{-}2PF_6]^{2+}$, found: 1215.1987.

2. Rotaxane characterisation

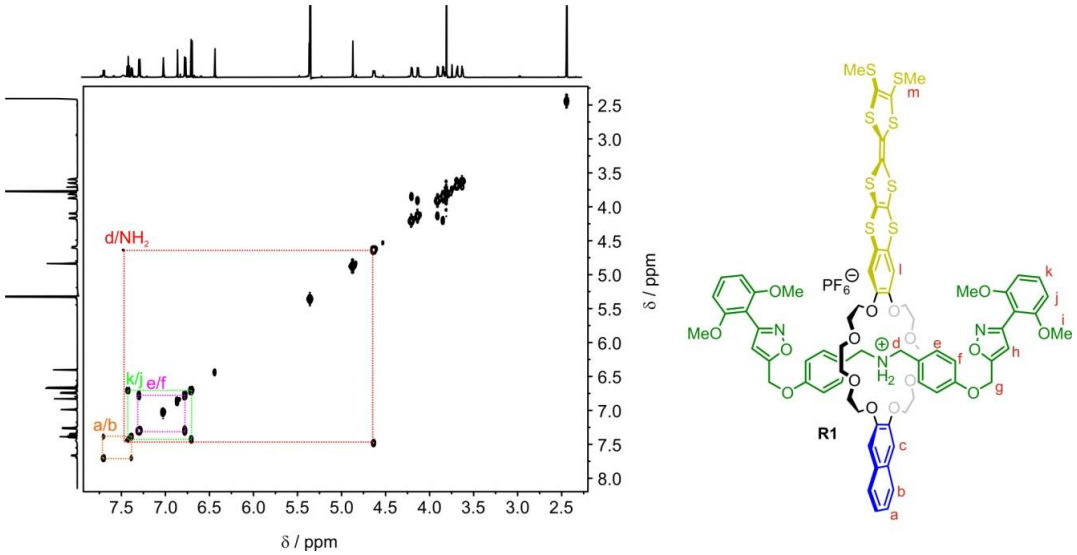

Fig. S1 ^{1}H,^{1}H COSY (700 MHz, CD_2Cl_2, 298 K) of [2]rotaxane **R1** with selected cross peaks confirming the depicted structure.

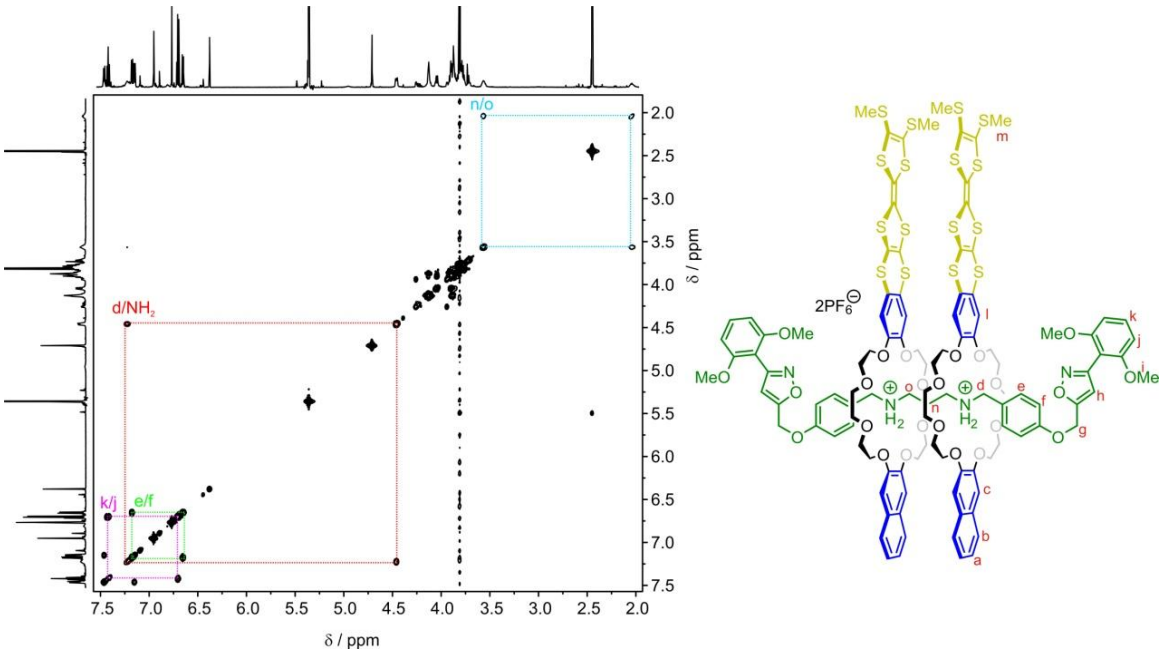

Fig. S2 ^{1}H,^{1}H COSY, (700 MHz, CD_2Cl_2, 298 K) of [3]rotaxane **R2** with selected cross peaks confirming the depicted structure.

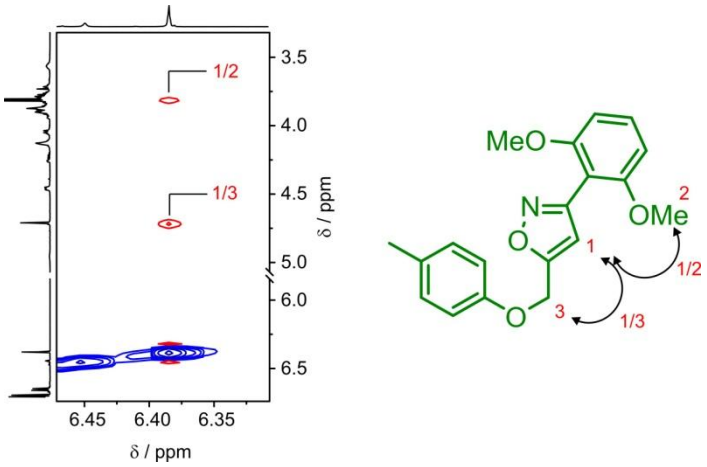

Fig. S3 Partial ^{1}H,^{1}H NOESY, (700 MHz, CD_2Cl_2, 298 K) of [3]rotaxane **R2** showing the cross peaks of the isoxazole signal arising by its spatial coupling with neighbouring protons.

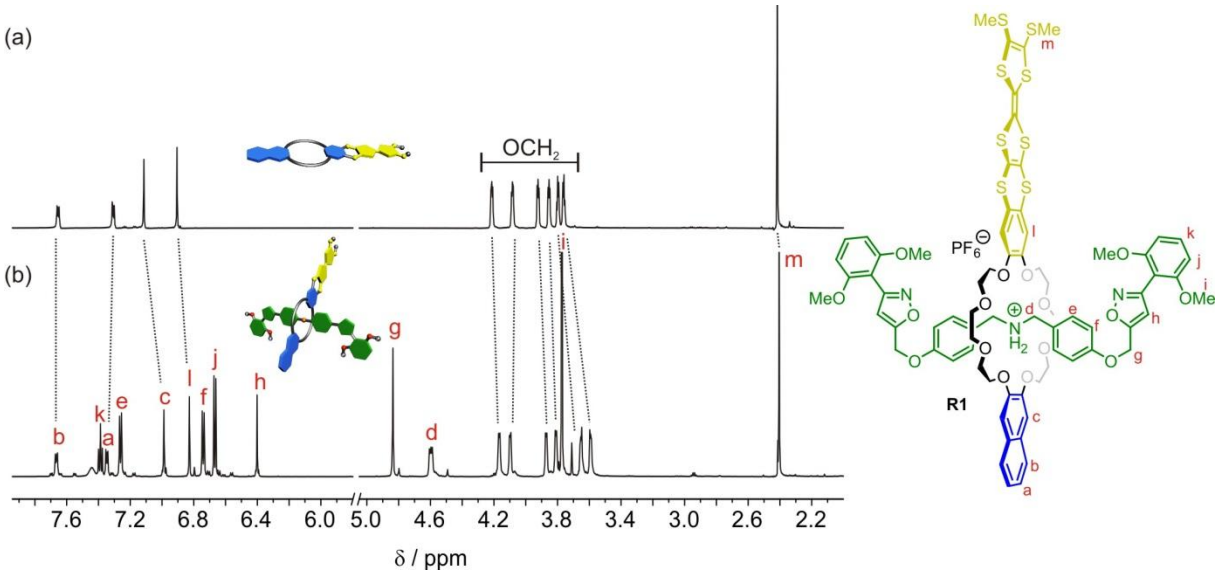

Fig. S4 Stacked ^{1}H NMR spectra (700 MHz, CD_2Cl_2, 298 K) of (a) macrocycle **exTTFC8** and (b) [2]rotaxane **R1** with characteristic signal shifts which can be addressed to a successful rotaxane formation.[S6]

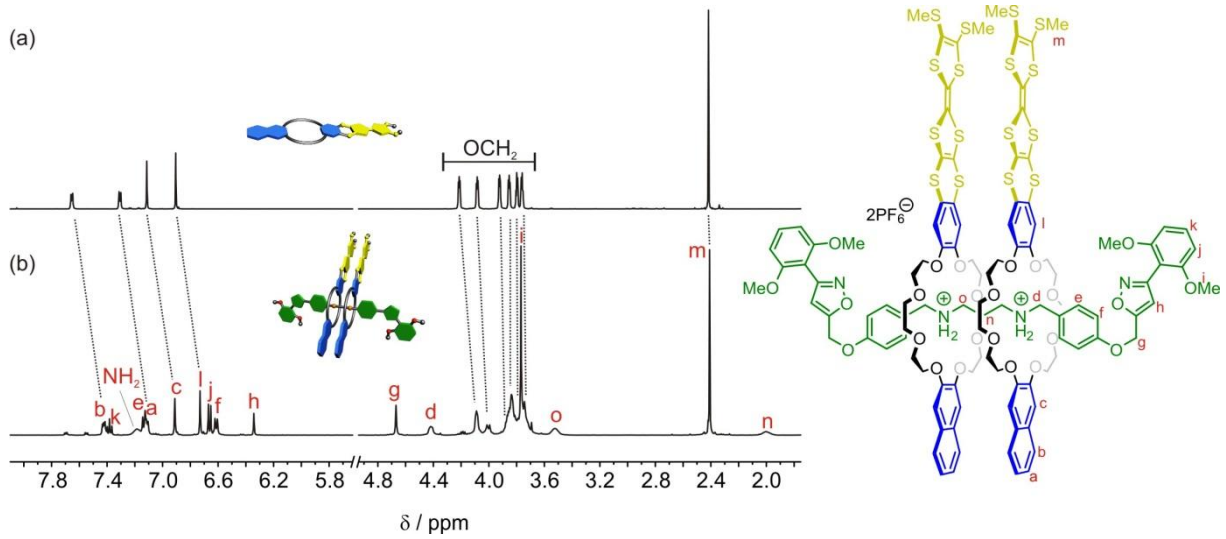

Fig. S5 Stacked ^{1}H NMR spectra (700 MHz, CD_2Cl_2, 298 K) of (a) macrocycle **exTTFC8**, (b) [2]rotaxane **R2** with characteristic signal shifts which can be addressed to a successful rotaxane formation.[S6]

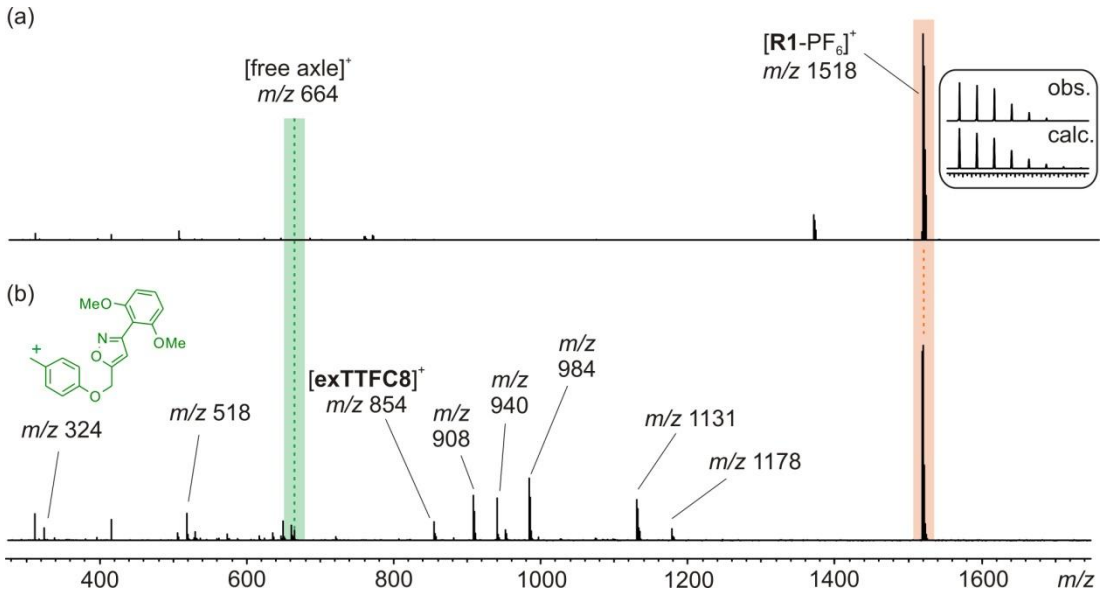

Fig. S6 ESI-FTICR spectra (MeOH, 50 µM, positive mode) of [2]rotaxane **R1**: (a) mass spectrum with base peak *m/z* 1518 (orange area) corresponding to [**R1**-PF_6]$^{+}$ and (b) mass spectrum after MS/MS IRMPD experiment with selected fragments. The signals *m/z* 854 and *m/z* 324 correspond to the oxidised macrocycle [**exTTFC8**]$^{+}$ and an axle fragment which results from CN bond breaking in the axle molecule, respectively. The green area indicates the channel for the *m/z* value for the axle without wheel, which is not observed in significant amounts. The fragments between *m/z* 908–1178 are also present in the fragmentation of **R2** and result from different fragmentation channels where an axle piece attacks the wheel. The signal *m/z* 1178, for example, can be addressed to a wheel (*m/z* 854) and the axle fragment (*m/z* 324). This fragmentation pathway speaks in favor of a mechanically interlocked structure as shown previously.[S6]

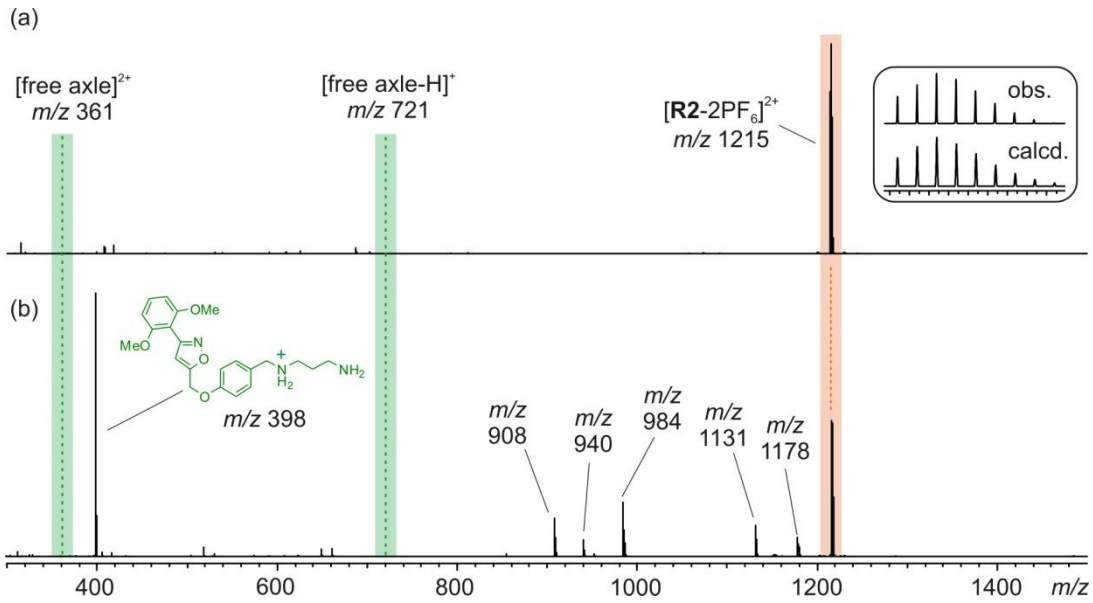

Fig. S7 ESI-FTICR spectra (MeOH, 50 µM, positive mode) of [2]rotaxane **R2**: (a) mass spectrum with base peak *m/z* 1215 (orange area) corresponding to [**R2**-2PF_6]$^{2+}$ and (b) mass spectrum after MS/MS IRMPD experiment with selected fragments. The signal *m/z* 398 corresponds to an axle fragment derived by CN bond breaking in the axle molecule. The green area indicates the channel for the *m/z* values for the axle without wheels, which is not observed. The fragments between *m/z* 908–1178 are also present in the fragmentation of **R1** and result from different fragmentation channels where an axle piece attacks the wheel. The signal *m/z* 1178, for example, can be addressed to a wheel (*m/z* 854) and the opposite axle fragment (*m/z* 324). This fragmentation pathway speaks in favor of a mechanically interlocked structure as shown previously.[S6]

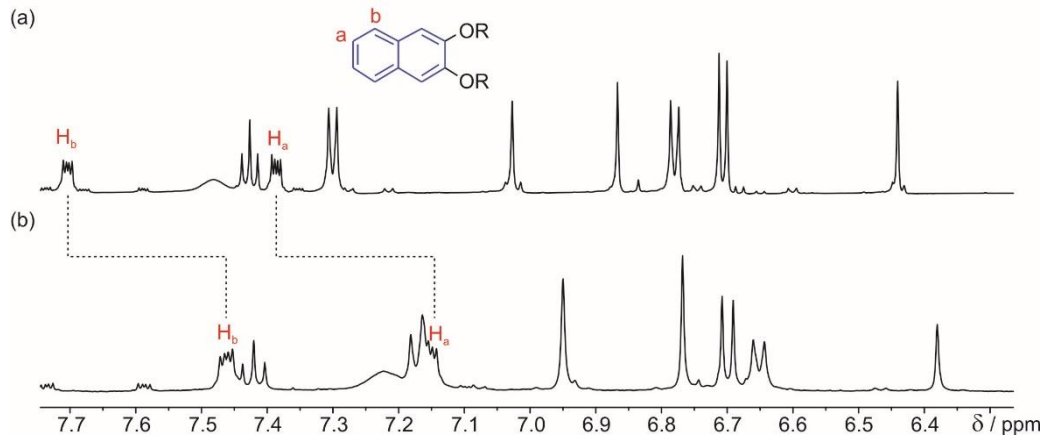

Fig. S8 Comparison of ^{1}H NMR spectra (700 MHz, CD_2Cl_2, 298 K) of (a) [2]rotaxane **R1** and (b) [3]rotaxane **R2** with characteristic signal shifts. For [3]rotaxane **R2**, both naphthalene signals $H_{a/b}$ are significantly shifted by $\Delta\delta$ = -0.24 ppm to higher field. As both rotaxanes are structurally similar, we attribute the quite pronounced upfield shifts of the naphthalene signals H_a and H_b to intramolecular π-stacking interactions between the two wheels in **R2**.

3. UV/Vis-NIR spectroscopy

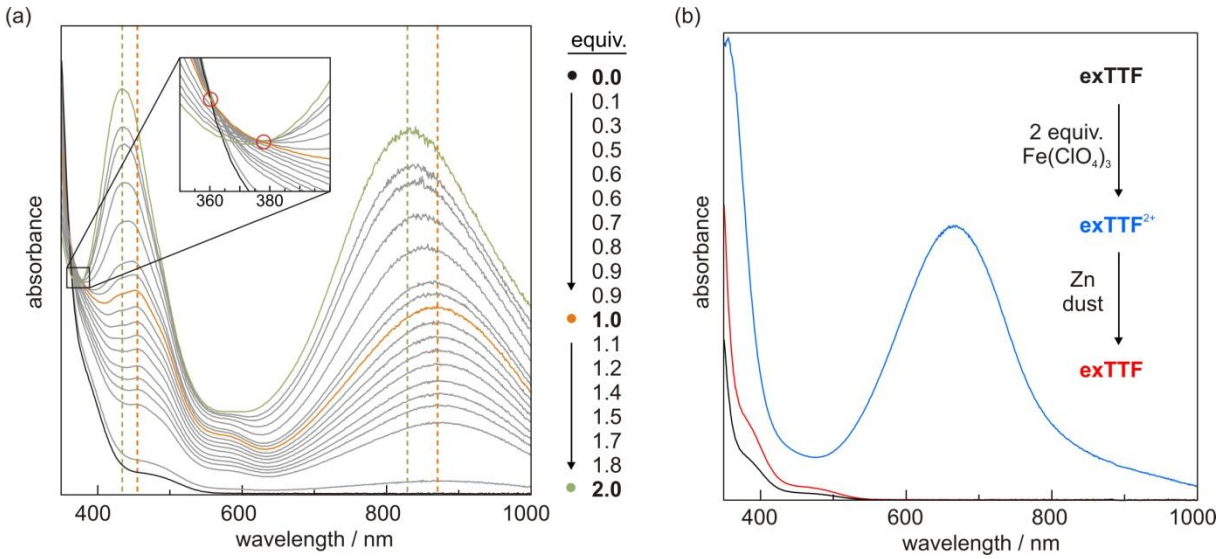

Fig. S9 (a) Photometric UV/Vis titration of **R2** (0.15 mM, CH_3CN, 298 K) by stepwise addition of two equivalents $Fe(ClO_4)_3$. The colored lines corresponds to the UV/Vis spectra of the **R2** (black), **R2**$^{\bullet+}$ (orange) and **R2**$^{2(\bullet+)}$ (green) oxidation state. The dotted lines mark the wavelength of maximum absorbance of the characteristic TTF$^{\bullet+}$ bands. The blue shift going from **R2**$^{\bullet+}$ to **R2**$^{2(\bullet+)}$ is known as "Davydov blue shift" which is characteristic for cofacial TTF radical-cation dimers.[S7] This is additionally supported by two isosbestic points (inset) which are in accordance to two separate transitions **R2**/**R2**$^{\bullet+}$ and **R2**$^{\bullet+}$/**R2**$^{2(\bullet+)}$. (b) UV/Vis spectra of redox-active building block **exTTF** (5 x 10^{-5} M, CH_3CN/CH_2Cl_2 (2:1), 298 K): before oxidation (black), after addition of two equivalents $Fe(ClO_4)_3$ (blue), and (iii) after back reduction by addition of excess Zn dust (red).

4. Isothermal titration calorimetry

ITC titrations were carried out in mixtures of dry 1,2-dichloroethane and acetonitrile (10:1) at 298 K on a TAM III microcalorimeter (Waters GmbH, TA Instruments, Eschborn, Germany). In a typical experiment, a solution of macrocycle (800 µL, 1 mM) was placed in the sample cell and a solution of the ammonium salt (250 µL, 8 mM) was put into a syringe. Titrations consisted of 32 consecutive injections of 8 µL, each with a 15 min interval between injections. Heats of dilution were determined by titration of ammonium salt solutions into the sample cell containing blank solvent and were subtracted from each data set. The heat flow generated in the sample cell is measured as a differential signal between sample and reference cell. Hence, an exothermic event results in a positive and an endothermic in a negative heat flow. The data were analysed using the instrument's internal software package

and fitted with a 1:1 or 1:2 binding model. Each titration was conducted three times and the measured values for K, ΔG and ΔH were averaged.

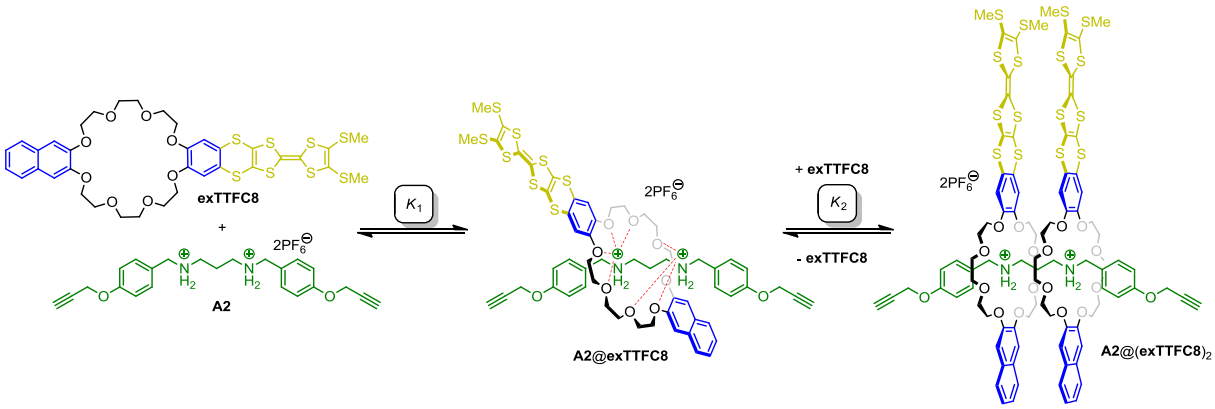

Fig. S10 Schematic representation of the two binding steps (with association constants K_1 and K_2) in the divalent pseudo[3]rotaxane **A2@(exTTFC8)**$_2$.

The trends in thermodynamic parameters in the pseudo[3]rotaxanes **A2@(exTTFC8)**$_2$ and **A2@(DBC8)**$_2$ can be explained by different effects. Considering statistics, a ratio between the binding constants of the monovalent (e.g. **A1@exTTFC8**) and divalent complex (e.g. **A2@(exTTFC8)**$_2$) of $K = K_1/2 = 2K_2$ is expected if no communication between the two binding sites occurs (non-cooperative binding). However, the ammonium binding station in the divalent axle **A2** is assumed to bind weaker to the wheel than the monovalent one due to the absence of a second polarisable benzylic methylene group. The observation that K_1 is roughly two times K is explained in Figure S10. We assume that the first wheel partially binds to both binding stations. Thus, the second ammonium station site is blocked for the second binding event and a lower K_2 value can thus easily be rationalised by the competition between the first and the second macrocycle for the second station. The high enthalpic gain of the second binding event, in case of **exTTFC8** macrocycle, can be attributed to rather strong attractive wheel-wheel interactions. On the other hand, this comes together with the high entropic penalty, as the conformation of the two crown ether macrocycles for additional wheel-wheel interactions is very rigid.

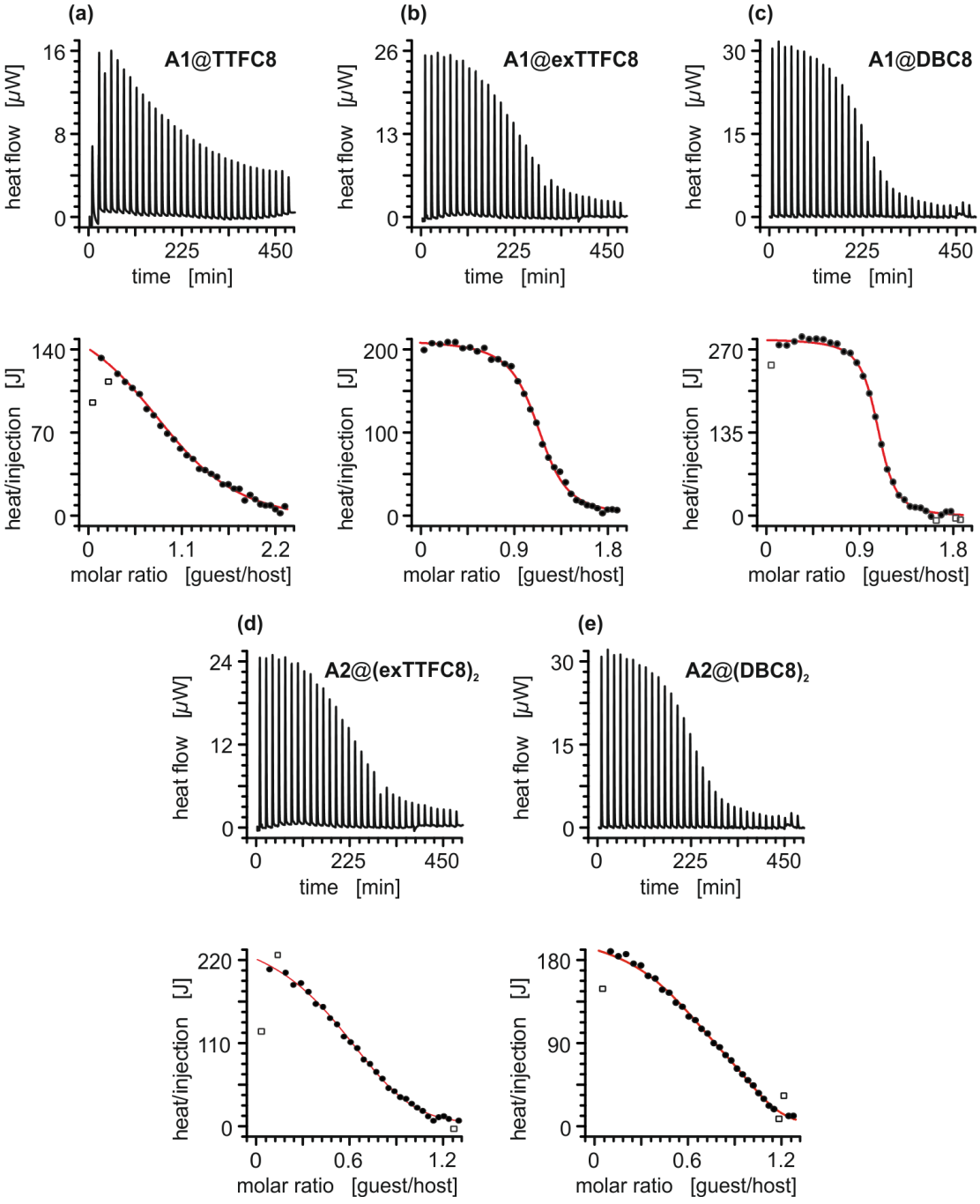

Fig. S11 Titration plots (heat flow versus time and heat/volume versus guest/host ratio) obtained from ITC experiments at 298 K in 1,2-dichloroethane/acetonitrile 10:1 (v/v). Concentrations: (a) host: 0.96 mM, guest: 7.7 mM; (b) host: 1.03 mM, guest: 6.0 mM; (c) host: 1.22 mM, guest: 7.6 mM; (d) host: 0.87 mM, guest: 3.2 mM; (e) host: 0.87 mM, guest: 3.3 mM; Points marked with a non-filled square were not included in the fitting process.

Table S1. Thermodynamic binding data of pseudo[2]- and [3]rotaxane formation between axles (**A1** and **A2**) and macrocycles (**exTTFC8**, **TTFC8**, and **DBC8**) obtained from ITC experiments in 1,2-dichloroethane/acetonitrile (10:1) at 298 K.

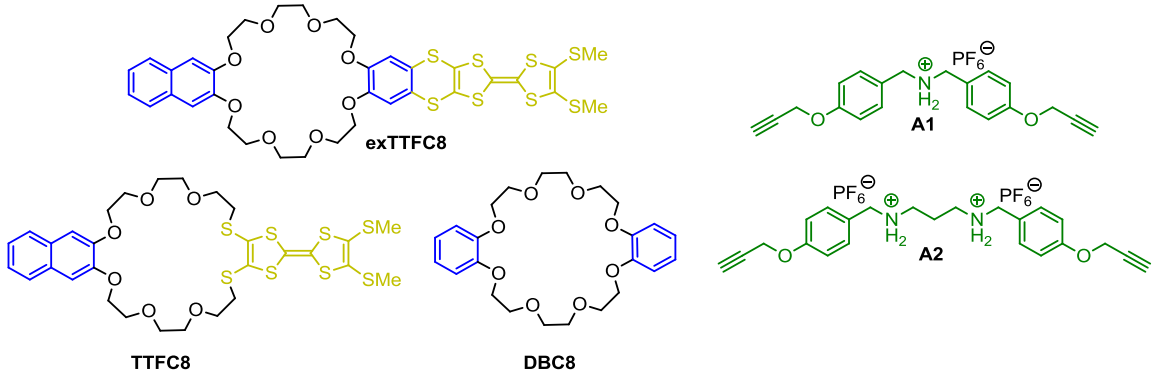

		K_n / 10^3 M^{-1}	ΔG / kJ mol^{-1}	ΔH / kJ mol^{-1}	$T\Delta S$ / kJ mol^{-1}
A1⊂exTTFC8	K_1	50 ± 5	-26.8 ± 0.2	-36.8 ± 1.2	-10.0 ± 1.4
A1⊂TTFC8	K_1	3.8 ± 0.4	-20.4 ± 0.3	-23.3 ± 0.4	-2.8 ± 0.7
A1⊂DBC8	K_1	90 ± 9	-28.3 ± 0.2	-35.7 ± 1.8	-8.0 ± 2.0
A2⊂(exTTFC8)$_2$	K_1	99 ± 30	-28.5 ± 0.7	-32.6 ± 1.0	-4.1 ± 1.7
	K_2	2.4 ± 0.6	-19.3 ± 0.5	-45.4 ± 4.3	-26.1 ± 4.8
A2⊂(DBC8)$_2$	K_1	180 ± 40	-30.0 ± 0.5	-35.6 ± 1.3	-5.6 ± 1.8
	K_2	2.7 ± 0.6	-19.5 ± 0.5	-31.1 ± 4.9	-11.7 ± 5.4

5. Cyclic voltammetry and digital simulations

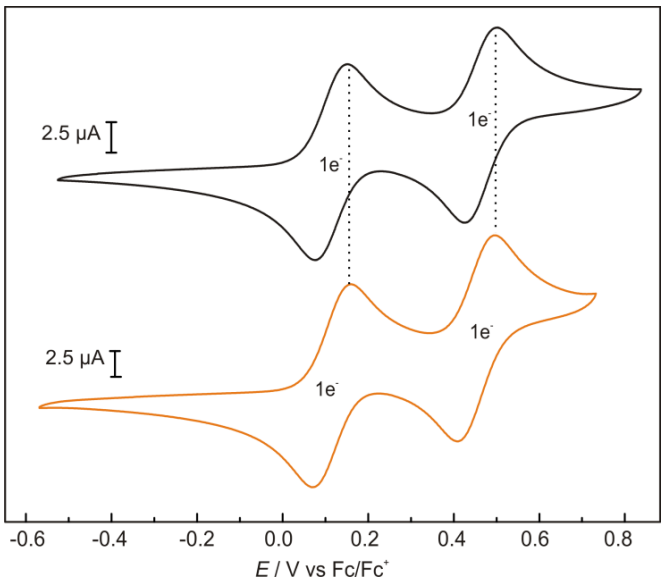

Fig. S12 Cyclic voltammograms (CH_2Cl_2, 298 K, 1 mM, 100 mV s^{-1}) of macrocycle **exTTFC8** (top) and [2]rotaxane **R1** (bottom). The potential were referenced against the ferrocene/ferrocenium (Fc/Fc^+) couple as described earlier.[S8] No significant difference in half-wave potentials is observed for the CH_2Cl_2 measurement which indicates that the charge repulsion between oxidised macrocycle and ammonium axle in **R1** does not play a significant role.

Digital simulations. The cyclic voltammogram of **R2** was simulated with the DigiElch Professional software (ElchSoft GbR) using the Butler-Volmer equation. The surface area of the working electrode was set to 0.14 cm^2 and the starting concentration of **R2** was set to 1 mM. The charge-transfer coefficients α were at the initial value of 0.5 and the heterogeneous rate constants k_s were estimated by the peak separation and set between 0.001 and 0.01 $cm^2\ s^{-1}$. The diffusion coefficient was roughly estimated by fitting the experimental electrochemical data and set to $1x10^{-10}\ m^2\ s^{-1}$.

The electrochemical reaction mechanism of **R2** can be described by an eight-member square scheme as depicted in Scheme 1. In each oxidation state, the electrochemical equilibrium is coupled with a reversible interaction (C1–C4) between the two wheels in **R2**. The wheel-wheel interactions (ΔG) result in an intramolecular binding constant K_{Cm} (m = 1–4). On the left side of the square scheme, the species marked with an asterisk ((**R2**$^{n+}$)*; n = 0, 1, 2, or 4) are representing an unbound situation in which wheel-wheel interaction are absent. The left side (**R2**$^{n+}$) displays the bound situation in which wheel-wheel interactions—such as attractive dispersion interactions or charge repulsion—are present. If all K_{Cm} values would be negligible ($\Delta G \approx 0$), the intramolecular equilibrium is mainly on the side of the non-

interacting species (**R2**$^{n+}$)*. This would be true, for example, if both wheels are widely separated by a long spacer and cannot form any type of interaction. Consequently, the potentials should be similar to those of monovalent [2]rotaxane **R1** (E1*–E3*) where all intramolecular wheel-wheel interaction can be fully excluded. If the K_{Cm} values are significant, however, the **R2**$^{n+}$ states are more populated which results in an altered voltammetric response (E1–E3).

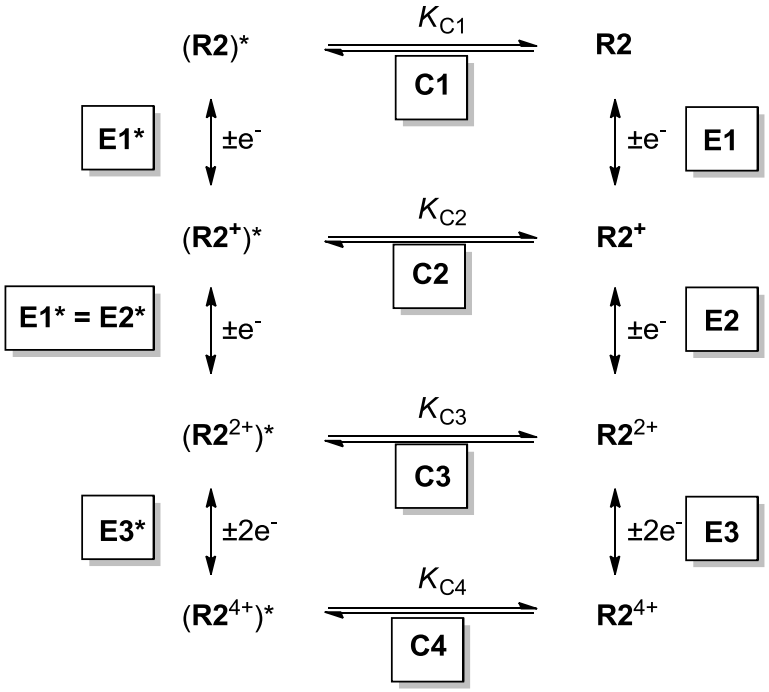

Scheme S2 Square scheme of the electrochemical reaction mechanism of **R2**

The experimental data were fitted according the following equilibria:

(**R2**)*		⇌	**R2**		(C1)
(**R2**$^{\bullet+}$)*		⇌	**R2**$^{\bullet+}$	MV Dimer	(C2)
(**R2**$^{2(\bullet+)}$)*		⇌	**R2**$^{2(\bullet+)}$	RC Dimer	(C3)
(**R2**$^{4+}$)*		⇌	**R2**$^{4+}$		(C4)
(**R2**$^{\bullet+}$)*	+e$^-$	⇌	(**R2**)*	(0.16 V)	(E1*)
(**R2**$^{2+}$)*	+e$^-$	⇌	(**R2**$^{\bullet+}$)*	(0.16 V)	(E2*)
(**R2**$^{4+}$)*	+2e$^-$	⇌	(**R2**$^{2(\bullet+)}$)*	(0.40 V)	(E3*)
R2$^{\bullet+}$	+e$^-$	⇌	**R2**	(0.08 V)	(E1)
R2$^{2(\bullet+)}$	+e$^-$	⇌	**R2**$^{\bullet+}$	(0.19 V)	(E1)
R2^{4+}	+2e$^-$	⇌	**R2**$^{2(\bullet+)}$	(0.48 V)	(E1)

The fitting and simulation process is based on several assumptions (see above) and involves a large number of fitting parameters. It is therefore important to emphasise that the computational model only gives a qualitative picture of the K_{Cm} values (wheel-wheel interactions) in the present situation.[S9] The applied model results in the following qualitative order of binding constants:

$$K_{C2}\ (\mathbf{R2}^{\bullet+}) > K_{C3}\ (\mathbf{R2}^{2(\bullet+)}) > K_{C1}\ (\mathbf{R2}) >> K_{C4}\ (\mathbf{R2}^{4+})$$

Furthermore, the model provides a rough estimate of the constant's relations:

$$K_{C1} \approx K_{C2}/18 \approx K_{C3}/4 \approx K_{C4}/0.01$$

In Figure S12, the effect of varying the absolute value of a binding constant on the simulated cyclic voltammogram is demonstrated using K_{C2} as example. A value of K_{C2} = 10 leads to a voltammetric response obviously different from the experimental one. By going to higher K_{C2} values, the model provides a good simulation at K_{C2} ≈ 1000. However, a further increase does not significantly influence the simulated cyclic voltammogram. This demonstrates that the present computational model, based on the proposed mechanism, can reproduce the experimental data, but is insufficient to determine reliable quantitative thermodynamic and kinetic values.

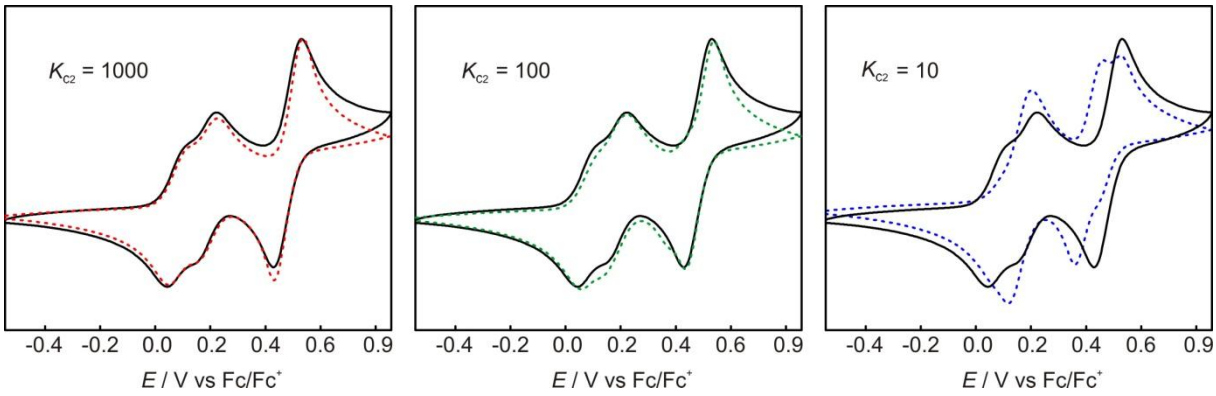

Fig. S13 Experimental cyclic voltammogram of **R2** (black trace, 100 mV s^{-1}, CH_3CN, 1 mM, 298 K) with *n*-Bu_4NPF_6 (0.1 M) as the electrolyte and simulated cyclic voltammograms with different values of the intramolecular binding constant K_{C2}.

6. IM-MS

Instrumentation and CCS determination. Ion mobility analysis was carried out by means of a home-built drift tube ion mobility-mass spectrometry (IM-MS) instrument (Fig. S14).[S10] Briefly, ions are generated by a nanoelectrospray ionisation (nESI) source (positive ion mode) and transferred into an ion funnel from which the ions are pulsed into the drift tube region (length = 80.55 cm). Guided by a weak electric field the ions traverse the drift tubes, which are filled with a neutral buffer gas (helium, 4.18 mbar, 23.4 °C). The time required for the ions to pass the drift tube region depends on their mobility, which in turn is dictated by the molecules' overall shape and charge. Compact molecules undergo fewer collisions with the buffer gas and traverse the drift tube region faster than more extended structures of same mass-to-charge ratio (*m/z*). The ions become subsequently guided by a second ion funnel into high vacuum where the ions are selected according to their *m/z* by means of a quadrupole mass analyser. The arrival time distributions (ATDs) of the ions are recorded by measuring the time that ions of a specific *m/z* need to traverse the drift region. The time which corresponds to the intensity maximum of the ATD was taken as the drift time (t_D). The t_D values were determined for different drift voltages (V_D) and plotted against $1/V_D$. The data were fitted to a linear function (Fig. S15b). As described previously, the slope of the linear fit was used to calculate the mobility of the ion from which finally the collision cross section (CCS) could be determined by using the Mason-Schamp equation.[S11,12]

Calculations. The calculated CCS values of model conformers of [3]rotaxane **R2** without PF_6^- counter ions (**A**–**H**) were obtained by the projection approximation (PA) method.[S13] For the conformer search, we structurally optimised different wheel coconformations (**C**–**H**) using the semi-empirical PM3 method as implemented in the ORCA 3.0.3 program package (Fig. S16).[S14,15] The conformers **A** and **B**—which were further optimised by the MMFF94 force field as implemented in the Avogadro[S15,16] 1.1.1 software—are representing a *syn* coconformation in which the stopper groups are either tightly wrapped around the stacked wheels (**A**) or off-standing (**B**).

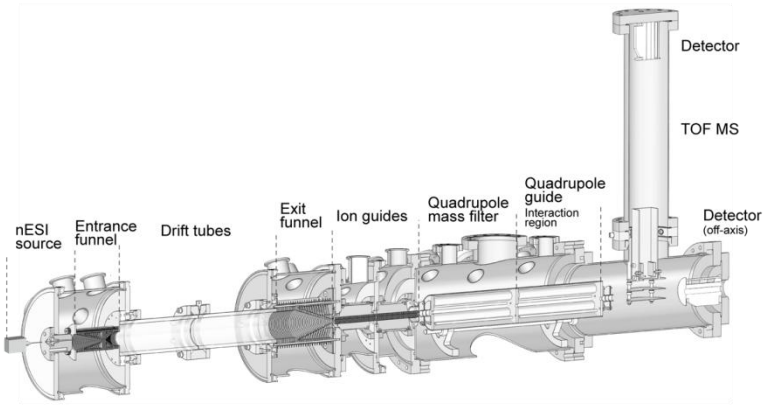

Fig. S14 Instrumental setup of the drift tube ion mobility mass spectrometer.[S10]

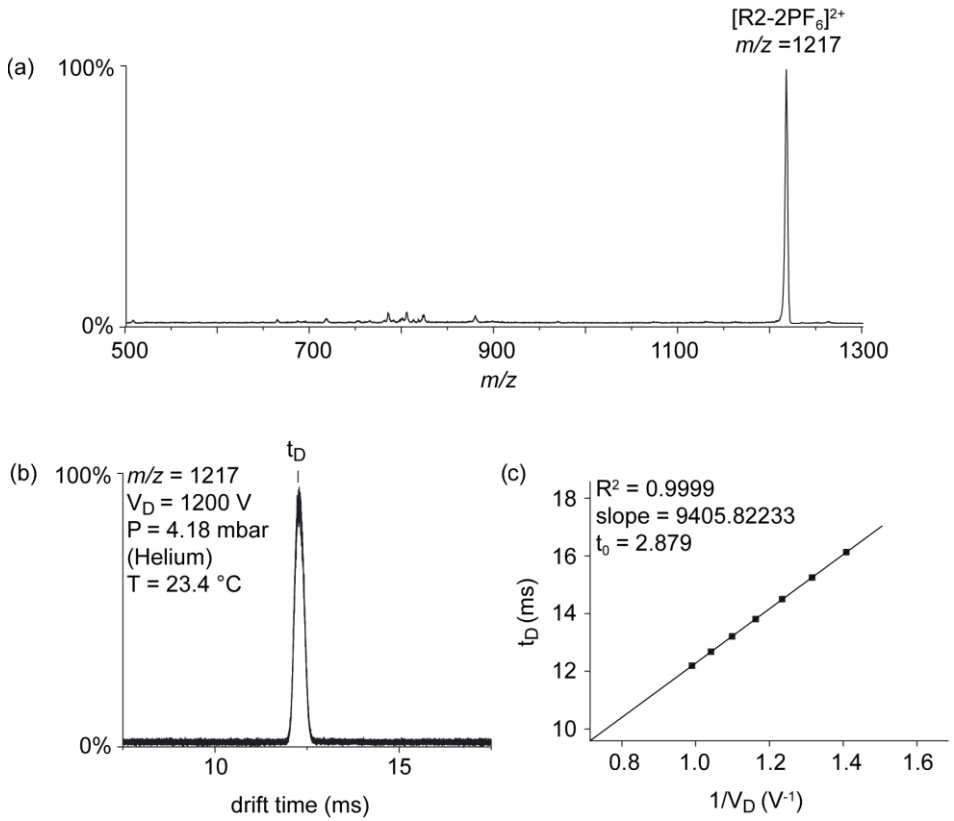

Fig. S15 Overview of IM-MS data: (a) nESI(+)-MS spectrum of **R2** sprayed from CH_2Cl_2, (b) Representative ATD obtained from the [**R2**-2PF_6]$^{2+}$ ion (*m/z* = 1217), (c) Drift time (t_D) values that were determined for the [**R2**-2PF_6]$^{2+}$ ion population at different drift voltages (V_D) and plotted against 1/V_D. The offset (t_0 - interception with the y-axis) is the time required for the ions to travel from the exit of the drift tubes to the detector.

Table S2 Comparison of experimental CCS of [**R2**-2PF_6]$^{2+}$ (*m/z* 1217) to theoretical CCS values of optimised conformer structures (**A**–**H**) depicted in Figure S15.

ion	**CCS_{exp}** / Å^2	**Conformer**	**CCS_{calcd}** / Å^2	**Deviation** / %
[**R2**-2PF_6]$^{2+}$	410	A	412.2	0.5
		B	464.2	13.2
		C	472.2	15.2
		D	472.4	15.2
		E	472.6	15.3
		F	477.7	16.5
		G	491.0	19.8
		H	498.2	21.5

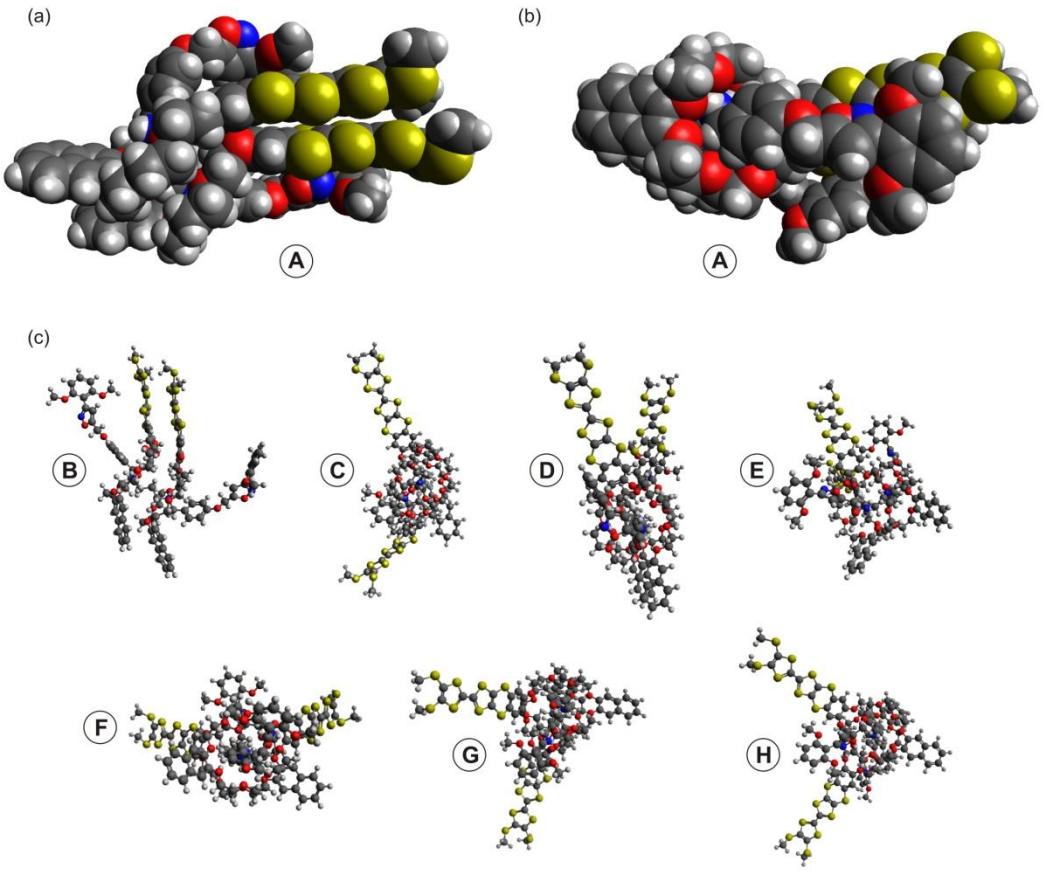

Fig. S16 PM3 (**C**–**H**) or force-field-optimised (**A** and **B**) conformers of [3]rotaxane **R2** without PF_6^- counter ions. (a) Side-view and (b) top-view of conformer **A** with *syn* coconformation of the wheels. The molecules are depicted as Van der Waals sphere models. (c) Ball and stick models of conformers **B**–**H**.

7. VT-NMR

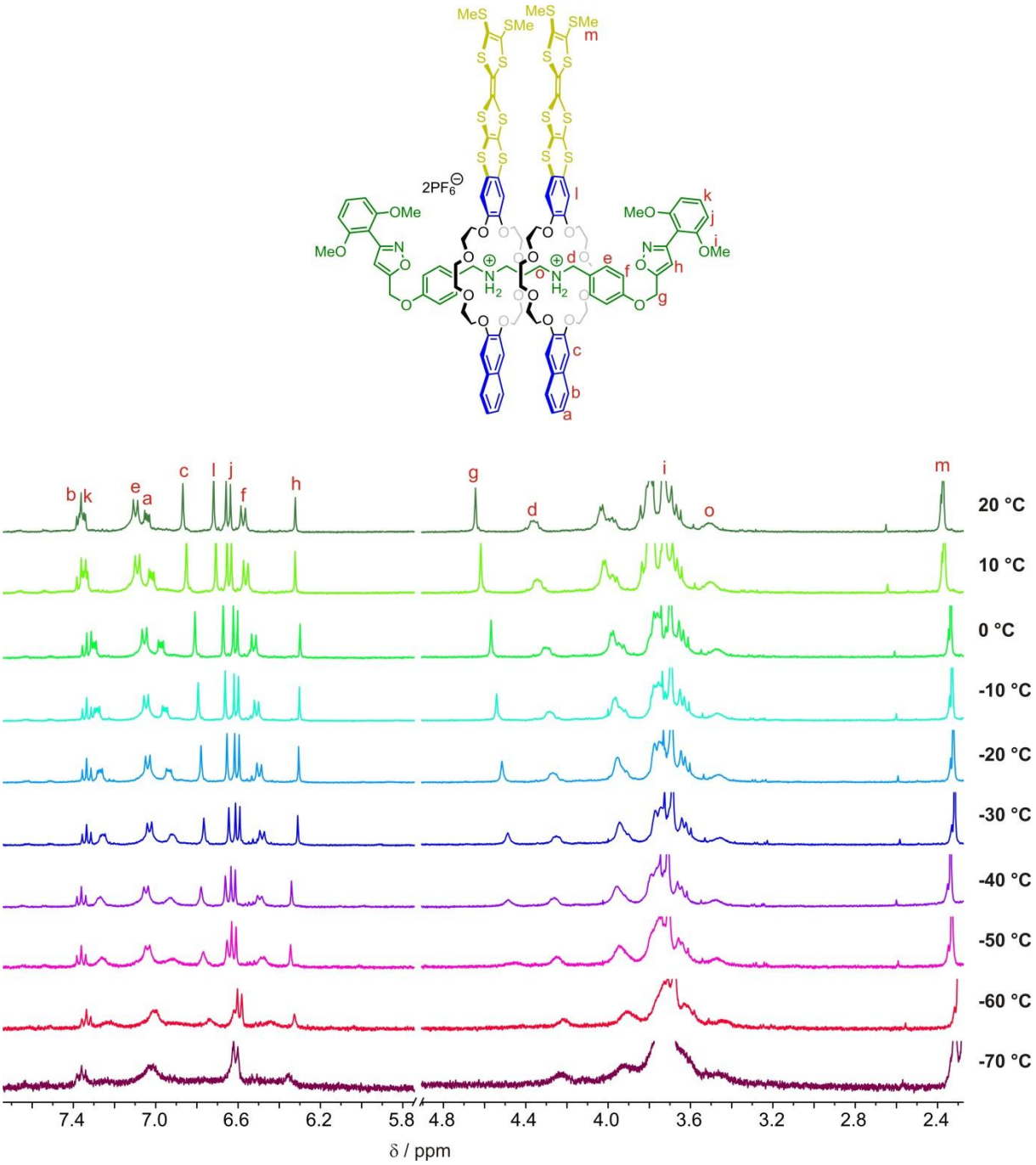

Fig. S17 ^{1}H NMR spectra (400 MHz, CD_2Cl_2/CD_3CN = 9:1, 1.0 mM) of **R2** with gradual cooling from 20 to -70 °C. No signal decoalescence was observed which indicates a fast rotamer interconversion and, thus, a low barrier for the pirouetting motion of the clutched wheels of **R2**.

8. Computational details

Structural ground-state aspects of *syn* and *anti* R2. All calculations were performed using the program package Turbomole (Version 7.0.1).[S18] Structure optimisations were carried out at the TPSS-D3(BJ)/def2-SVP[S19-22] level of DFT employing the RI*J*-approximation[S23,24] together with its multipole acceleration extension (MARIJ)[S25] and regarding implicit solvent effects with COSMO[S26] (ε = 36.64 for MeCN). We used a computer-time-reducing, stopper-less pseudorotaxane analogue. During the first two oxidation processes in *syn* **R2**, the interplanar distance between the TTF units decreases from 3.14 Å to 3.09 Å while the distance between the stacked naphthalene moieties remains rather constant around 3.32 Å. However, the last oxidation in *syn* **R2** results in a significant increase of the TTF-TTF distance (from 3.09 Å to 3.17 Å) and a notable decrease of the naphthalene dimer separation (from 3.32 Å to 3.16 Å). This corresponds to an influence being exerted by the naphthalene moieties on the electronic structure of *syn* **R2** upon the last oxidation process and relates to the unfavorable molecular structure of *syn* $\mathbf{R2}^{4+}$ in comparison to *anti* $\mathbf{R2}^{4+}$. In contrast to *syn* **R2**, the interplanar distances in *anti* **R2** are only slightly altered upon oxidation (going from 3.31 Å in *anti* **R2** to 3.27 Å in *anti* $\mathbf{R2}^{4+}$). Furthermore, *anti* **R2** displays a triply π-stacked system at one side, while the other is a somewhat distorted TTF-naphthalene dimer (see Fig. 7).

Electronic structure and energetic aspects. Single point calculations at the relaxed geometries were performed at the PBE0-D3(BJ)/def2-TZVP[S27] level using COSMO (ε = 36.64 for MeCN). The molecular orbitals obtained at this level of theory suggest that in each oxidation state the valence electronic structure of *syn* **R2** is dominated by the TTF dimer (see Fig. 6 for *syn* $\mathbf{R2}^{\bullet+}$ and *syn* $\mathbf{R2}^{2(\bullet+)}$). In *anti* **R2** on the other hand, the single TTF units both participate in the valence electronic structure, albeit without the non-covalent interactions between the moieties. Table S3 compares the calculated ionisation potentials to the experimentally determined values by CV. Since the CV measurement is considerably slower than the intramolecular rearrangements that constitute the switching from *syn* **R2** to *anti* **R2**, the energy of the rearrangement process between the two conformers is taken into account for the first (**R2/R2**$^{\bullet+}$) and third ($\mathbf{R2}^{2(\bullet+)}$**/R2**$^{4+}$) oxidation process. As seen in Table S3, no rearrangement needs to be considered for the second oxidation process ($\mathbf{R2}^{\bullet+}$/ $\mathbf{R2}^{2(\bullet+)}$). An overall decent agreement between experiment and theory is observed, especially in the case of the second oxidative process, which does not require any consideration about intramolecular rearrangements. The other processes do display small deviations from experimental values. This might be in parts due to the somewhat superficial treatment of the rearrangement energy and, moreover, due to inherent inaccuracies of the method.

Table S3 Calculated and experimental ionisation potentials (in eV) of **R2**. $\mathbf{IP_0}$ denotes the ionisation potential computed via $\mathbf{IP_0} = E(N) - E(N\text{-}1)$, where E is the ground state energy of the structurally relaxed compound. $\mathbf{IP_{rearr}}$ regards the rearrangement between *syn* **R2** and *anti* **R2** via $\mathbf{IP_{rearr}} = \mathbf{IP_0} + \Delta E_{syn/anti}$, where $\Delta E_{syn/anti}$ denotes the ground state energetic difference between the relaxed *syn* and *anti* structure. Experimental values are obtained by referencing the CV data to the Fc/Fc^+ couple according to $\mathbf{IP_{exp}} = (-(E_{1/2})/V\ -4.80)$ eV, where $E_{1/2}$ is the half-wave potential of the oxidation peak.

Oxidation	$\mathbf{IP_0}$	$\mathbf{IP_{rearr}}$	$\mathbf{IP_{exp}}$
$\mathbf{R2/R2^{\bullet+}}$	4.43	4.76	4.88
$\mathbf{R2^{\bullet+}/R2^{2(\bullet+)}}$	4.98	4.98*	4.99
$\mathbf{R2^{2(\bullet+)}/R2^{4+}}$	6.13	5.62	5.29

[a] No rotation occurs.

Rotational motion. In order to mimic the gear slippage motion of **R2** in its four oxidation states, one of the macrocycles was displaced against the other in steps of 45° (Fig. S18). At every position a restricted optimisation was performed by fixing the coordinates of the central C-C bond in each TTF unit to obtain an intermediate structure on the way between *syn* **R2** and *anti* **R2**. The method employed for the optimisation was the semi-empirical HF-3c approach recently proposed by Grimme,[S28] as conventional methods (e.g., TPSS-D3(BJ)) failed to converge the structures. The potential energy curves depicted in Fig. 7b were received at the PBE0-D3(BJ)/def2-TZVP level using COSMO[S26] (ε = 36.64 for MeCN).

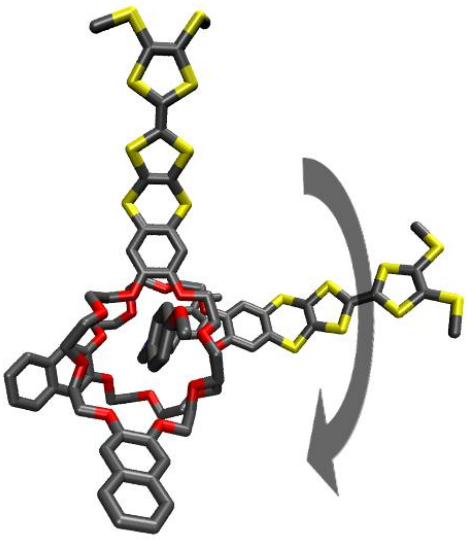

Fig. S18 Example for an intermediate structure between syn and *anti* **R2** (90°). The arrow indicates the rotational motion accomplished by displacing one macrocycle against the other. A computer-time-reducing, stopper-less pseudorotaxane analogue is used.

9. ^{1}H and ^{13}C NMR spectra

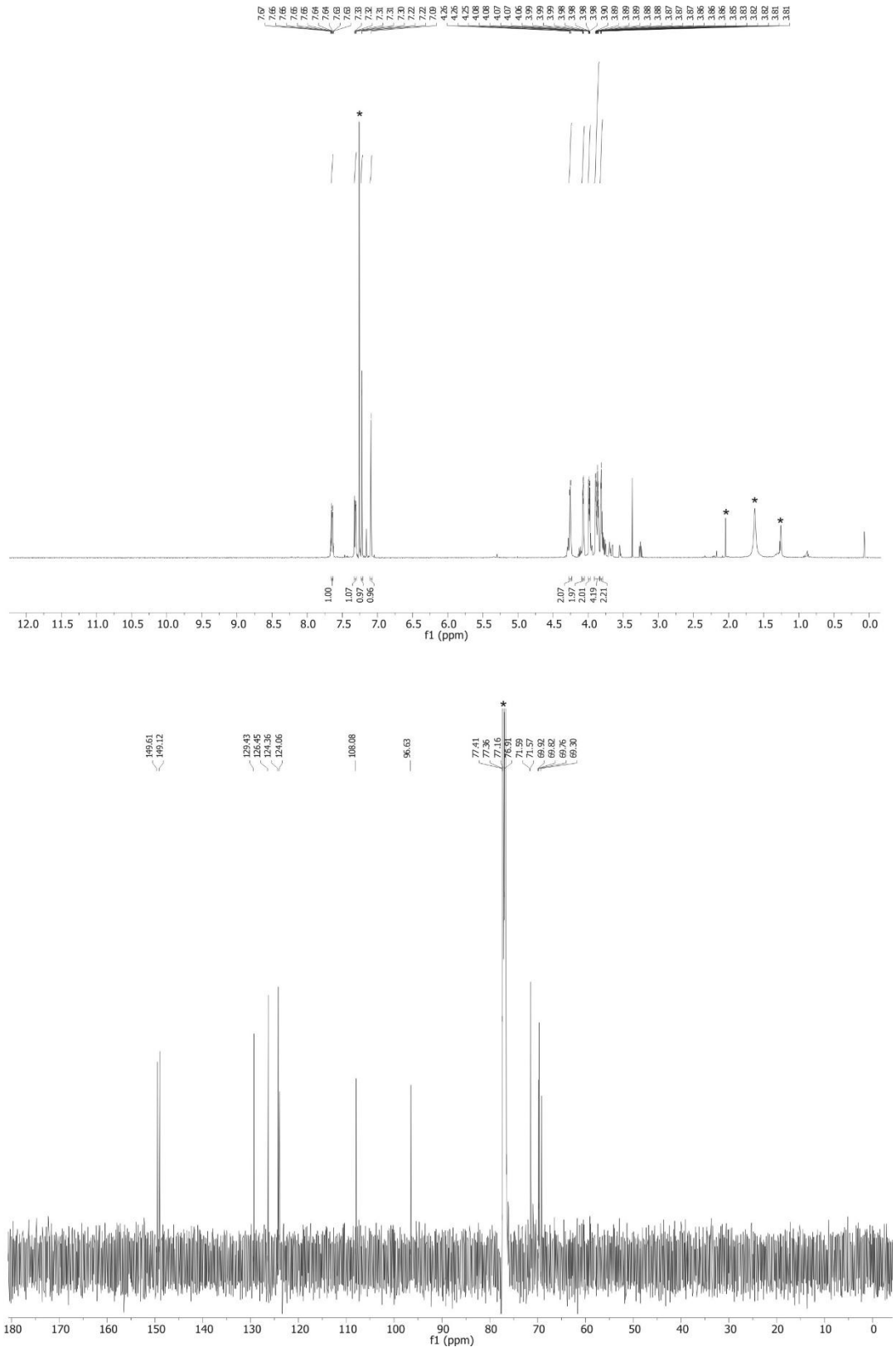

Fig. S19 ^{1}H and ^{13}C NMR spectrum (500/126 MHz, $CDCl_3$, 298 K) of diodide **1**.

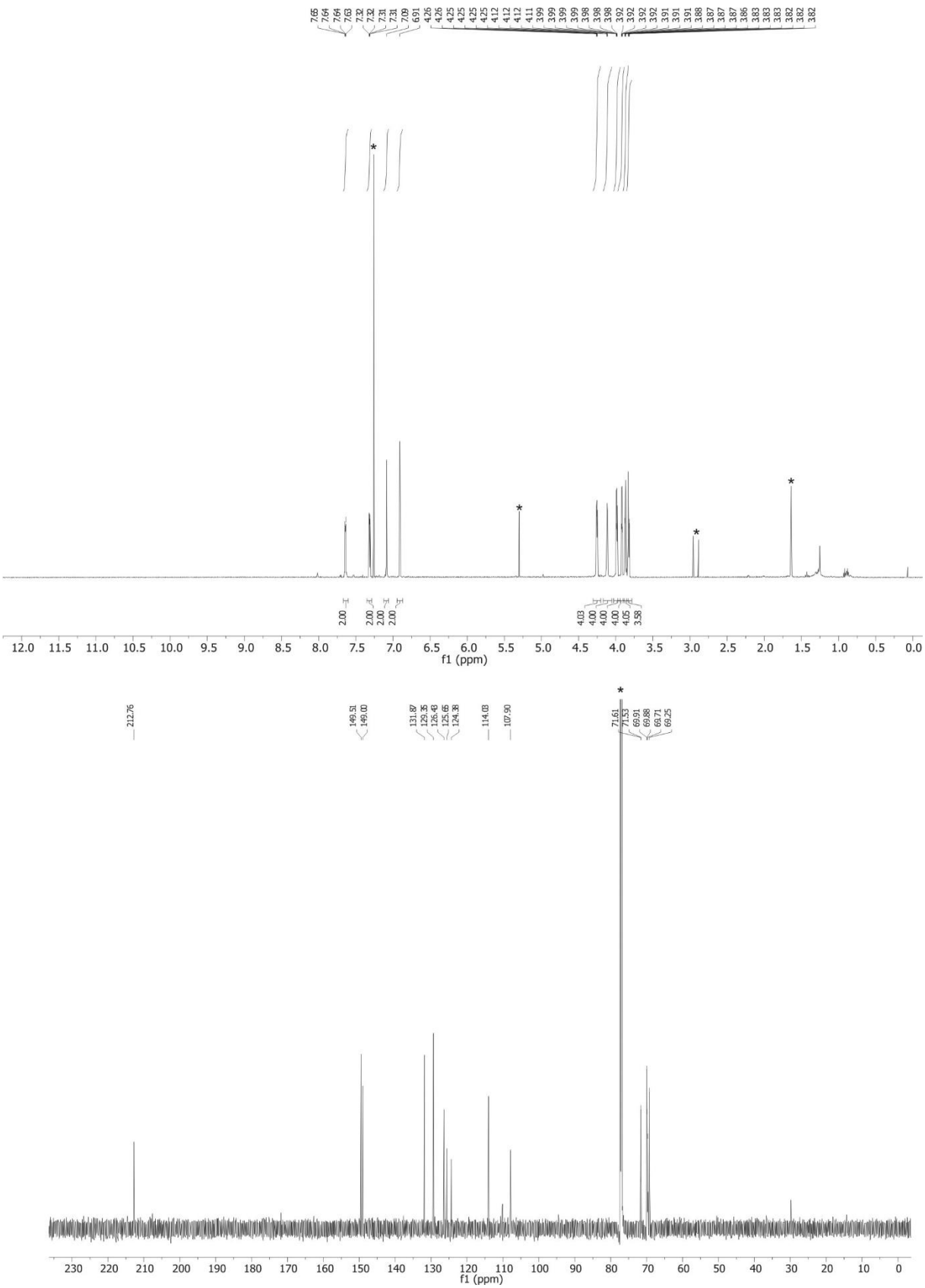

Fig. S20 ^{1}H and ^{13}C NMR spectrum (700/176 MHz, $CDCl_3$ 298 K) of thione **2**.

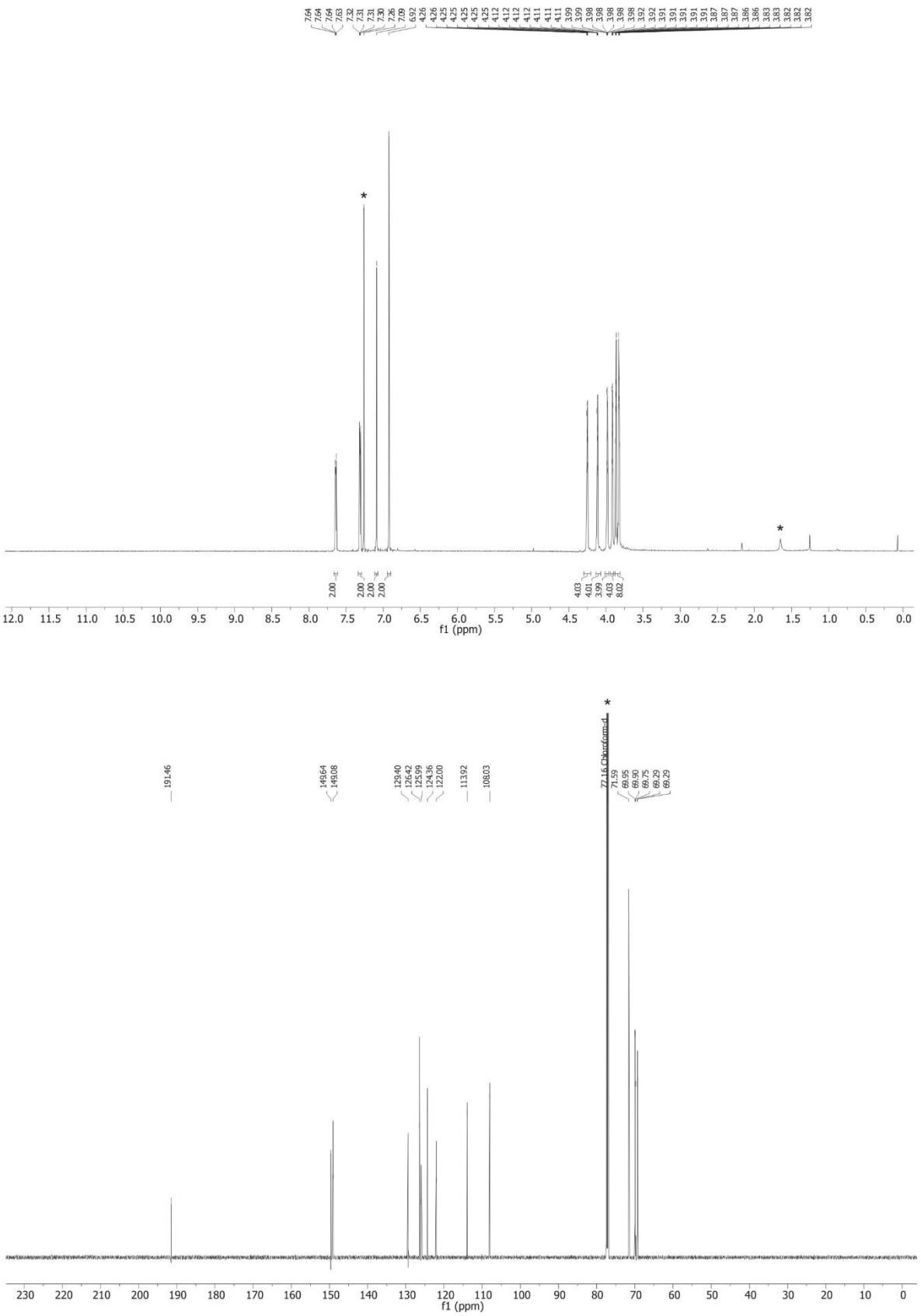

Fig. S21 ^{1}H and ^{13}C NMR spectrum (700/176 MHz, $CDCl_3$ 298 K) of ketone **3**.

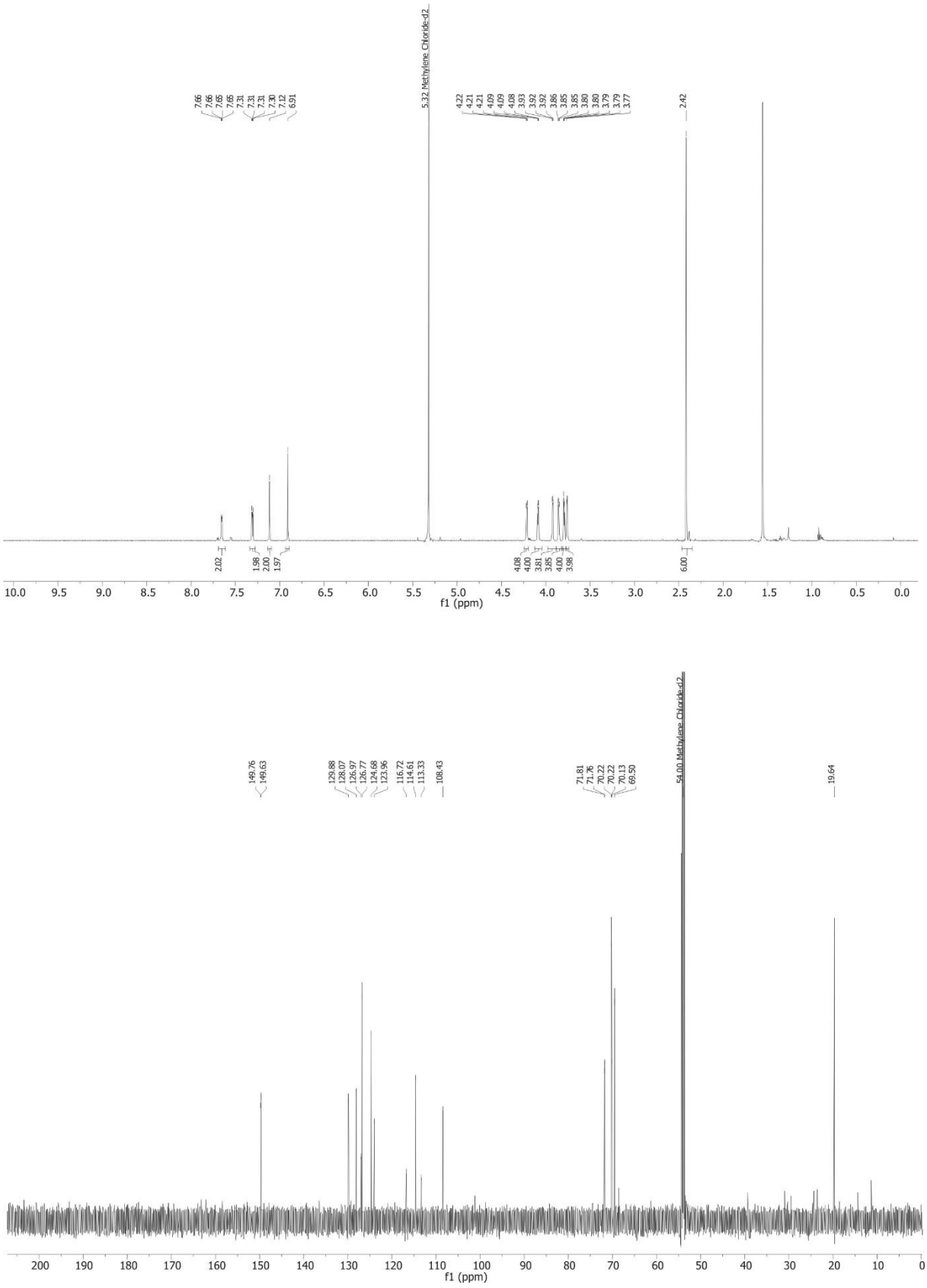

Fig. S22 ^{1}H and ^{13}C NMR spectrum (700/176 MHz, CD_2Cl_2, 298 K) of **exTTFC8**.

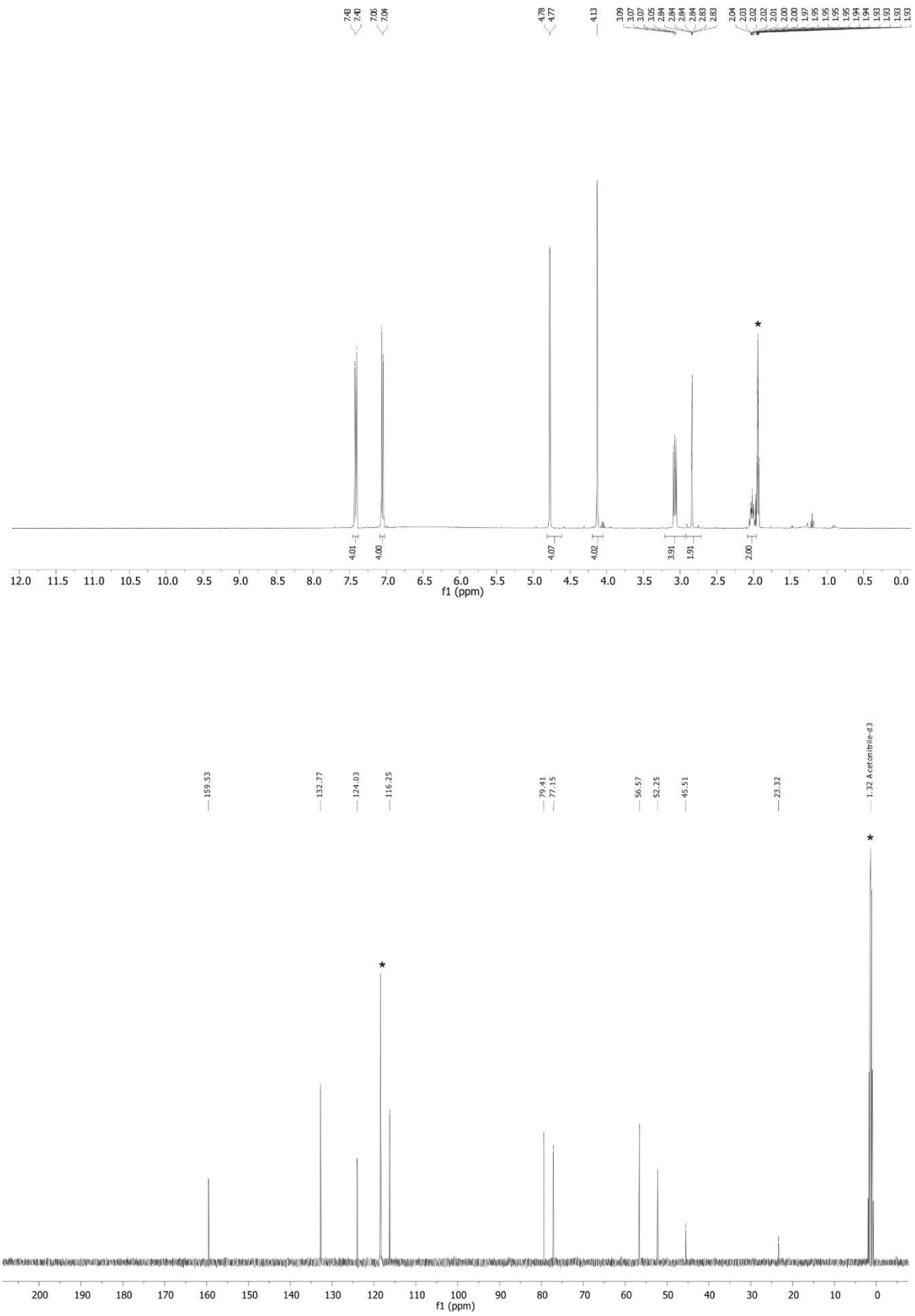

Fig. S23 ^{1}H and ^{13}C NMR spectrum (400/101 MHz, CD_2Cl_2, 298 K) of axle **A2**.

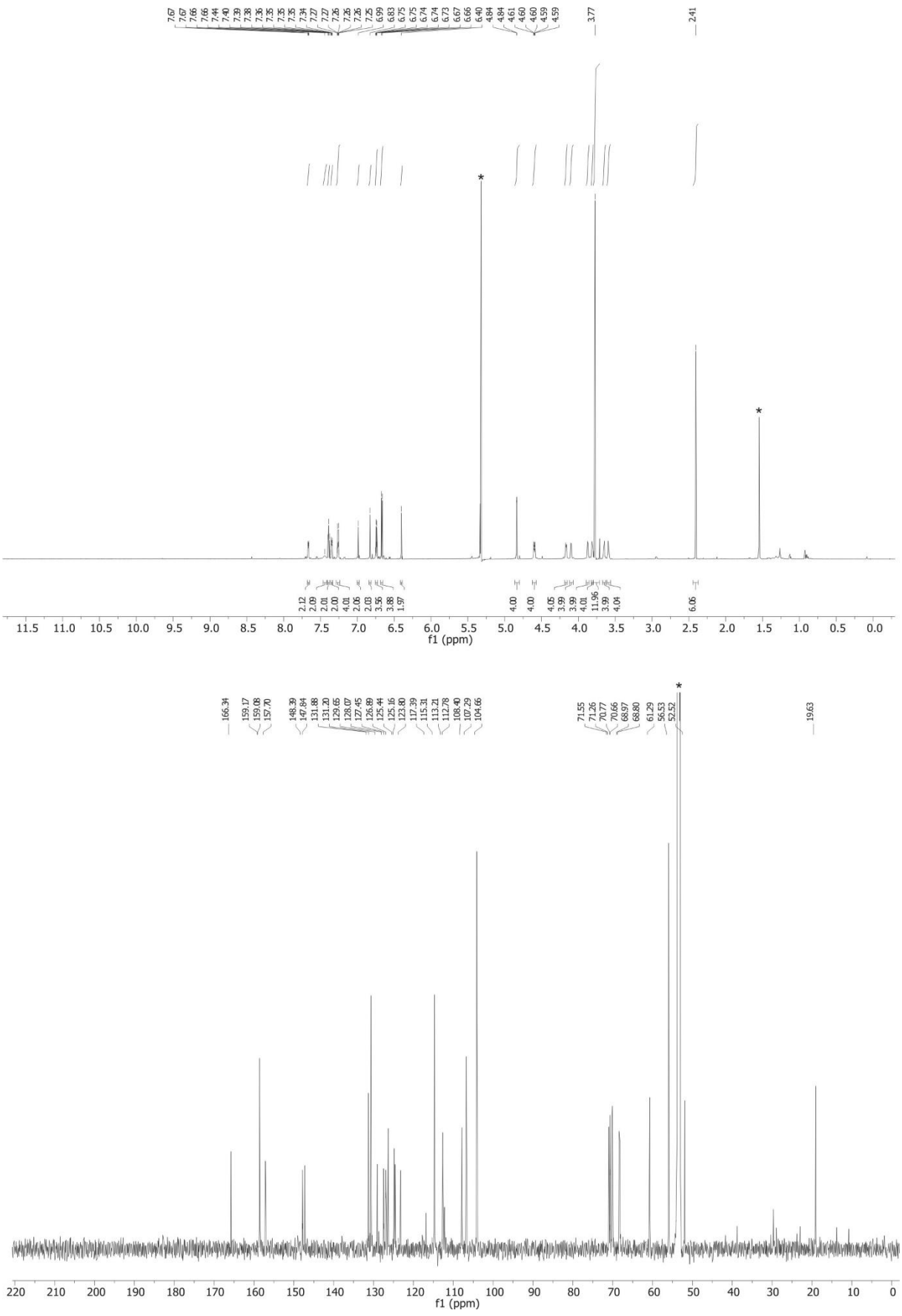

Fig. S24 ^{1}H and ^{13}C NMR spectrum (700/176 MHz, CD_2Cl_2, 298 K) of [2]rotaxane **R1**.

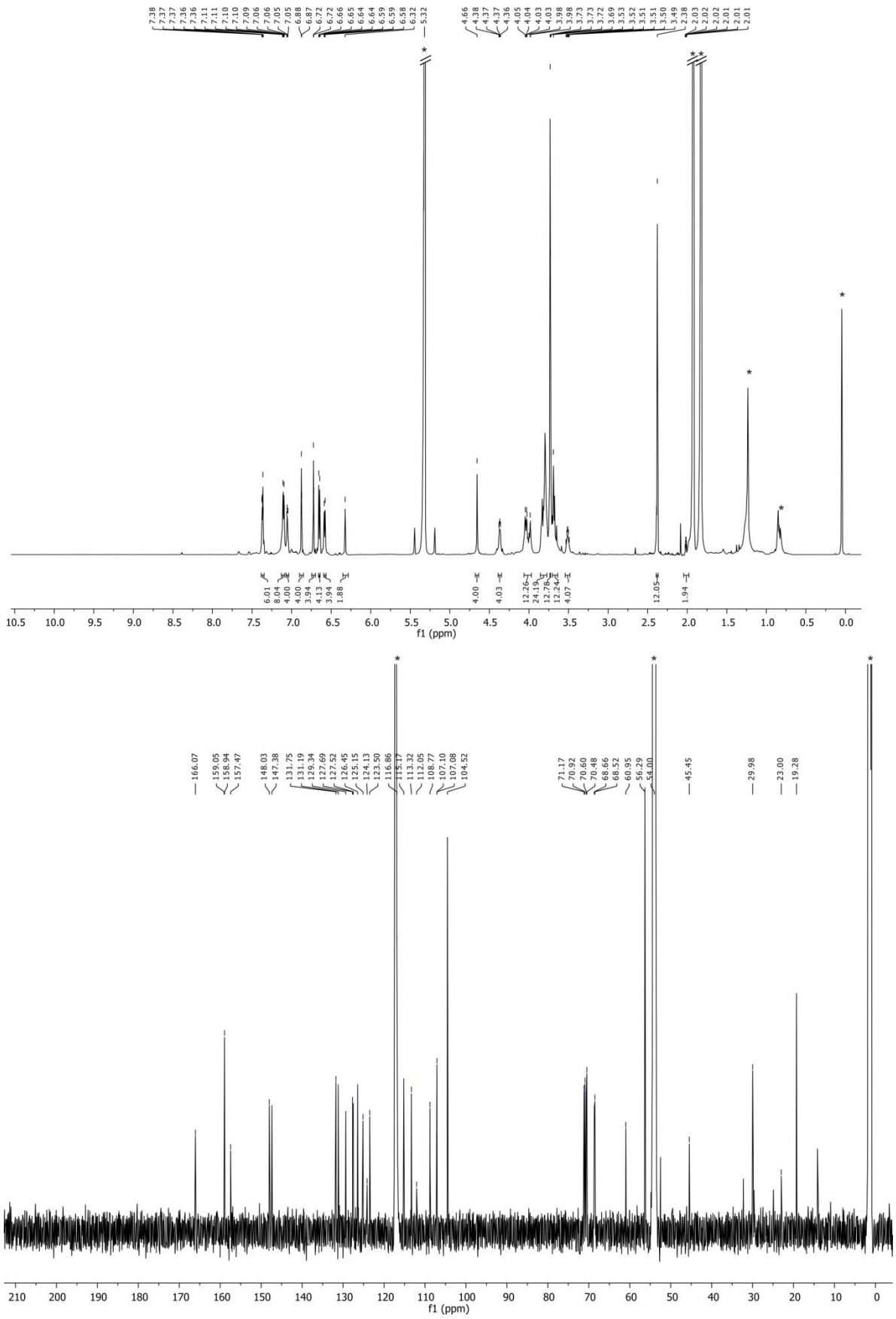

Fig. S25 ^{1}H and ^{13}C NMR spectrum (700/176 MHz, CD_2Cl_2/CD_3CN = 9:1, 298 K) of [3]rotaxane **R2**.

10. Supporting information references

S1 H. V. Schröder, F. Witte, M. Gaedke, S. Sobottka, L. Suntrup, H. Hupatz, A. Valkonen, B. Paulus, K. Rissanen, B. Sarkar and C. A. Schalley, *Org. Biomol. Chem.,* 2018*,* **16***,* 2741.

S2 J. D. Badjic, C. M. Ronconi, J. F. Stoddart, V. Balzani, S. Silvi and A. Credi, *J. Am. Chem. Soc.*, 2006, **128**, 1489.

S3 Z.-J. Zhang, H.-Y. Zhang, H. Wang and Y. Liu, *Angew. Chem. Int. Ed.*, 2011, **50**, 10834.

S4 M. Pal, K. Parasuraman and K. R. Yeleswarapu, *Org. Lett.*, 2003, **5**, 349.

S5 T. Matsumura, F. Ishiwari, Y. Koyama and T. Takata, *Org. Lett.*, 2010, **12**, 3828.

S6 H. V. Schröder, S. Sobottka, M. Nößler, H. Hupatz, M. Gaedke, B. Sarkar and C. A. Schalley, *Chem. Sci.*, 2017, **8**, 6300.

S7 J.-M. Lü, S. V. Rosokha and J. K. Kochi, *J. Am. Chem. Soc.*, 2003, **125**, 12161.

S8 J. R. Aranzaes, M.-C. Daniel, D. Astruc, *Can. J. Chem.*, 2006, **84**, 288.

S9 A. E. Kaifer and M. Gómez-Kaifer, *Supramolecular Electrochemistry*; Wiley, Weinheim, Germany, 1999.

S10 S. Warnke, C. Baldauf, M. T. Bowers, K. Pagel and G. von Helden, *J. Am. Chem. Soc.*, 2014, **136**, 10308.

S11 H. E. Revercomb and E. A. Mason, *Anal. Chem.*, 1975, **47**, 970.

S12 E. A. Mason and E. W. McDaniel, *Transport properties of ions in gases*, Wiley, New York, 1988, 145–159.

S13 G. von Helden, M. T. Hsu, N. Gotts and M. T. Bowers, *J. Phys. Chem.*, 1993, **97**, 8182.

S14 F. Neese, *WIREs Comput. Mol. Sci.*, 2012, **2**, 73.

S15 J. J. P. Stewart, *J. Comput. Chem.*, 1989, **10**, 209.

S16 M. D. Hanwell, D. E. Curtis, D. C. Lonie, T. Vandermeersch, E. Zurek and G. R. Hutchison, *J. Cheminform.*, 2012, **4**, 17.

S17 T. A. Halgren, *J. Comput. Chem.*, 1996, **17**, 490.

S18 TURBOMOLE V7.0 2015, a development of University of Karlsruhe and Forschungszentrum Karlsruhe GmbH, 1989-2007, TURBOMOLE GmbH, since 2007; available from http://www.turbomole.com.

S19 J. Tao, J. P. Perdew, V. N. Staroverov and G. E. Scuseria, *Phys. Rev. Lett.*, 2003, 91.

S20 S. Grimme, J. Antony, S. Ehrlich and H. Krieg, *J. Chem. Phys.*, 2010, **132**, 154104.

S21 S. Grimme, S. Ehrlich and L. Goerigk, *J. Comput. Chem.*, 2011, **32**, 1456.

S22 F. Weigend and R. Ahlrichs, *Phys. Chem. Chem. Phys.*, 2005, **7**, 3297.

S23 K. Eichkorn, O. Treutler, H. Ohm, M. Häser and R. Ahlrichs, *Chem. Phys. Lett.*, 1995, **240**, 283.

S24 F. Weigend, *Phys. Chem. Chem. Phys.*, 2006, **8**, 1057.

S25 M.Sierka, A. Hogekamp and R. Ahlrichs*, J. Chem. Phys.*, 2003, **118**, 9136.

S26 A. Klamt and G. Schüürmann, *J. Chem. Soc. Perkin Trans. 2*, 1993, 799.

S27 J. P. Perdew, M. Ernzerhof and K. Burke, *J. Chem. Phys.*, 1996, **105**, 9982.

S28 R. Sure and S. Grimme, *J. Comput. Chem.*, 2013, **34**, 1672.

6.4 Naphtocage: A Flexible yet Extremely Strong Binder for Singly Charged Organic Cations

F. Jia, H. Hupatz, L.-P. Yang, H.V. Schröder, D.-H. Li, S. Xin, D. Lentz, F. Witte, X. Xie, B. Paulus, C.A. Schalley, W. Jiang

J. Am. Chem. Soc. **2019**, *141*, 4468-4473.

Submitted on January 23, 2019, first published on February 20, 2019 by American Chemical Society.

An electronic version of the articles is available at: https://doi.org/10.1021/jacs.9b00445

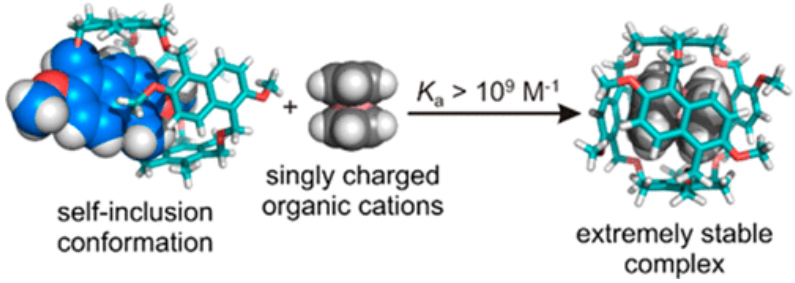

Figure 6.4. Graphical abstract. Reprinted with permission from Jia *et al.*[251]. Copyright © 2019 American Chemical Society.

Authors' contributions

Fei Jia designed, synthesised and characterised the naphtocage and its complexes by NMR spectroscopy and MS. Fei Jia the redox-switching experiments. Fei Jia grew crystals of the naphtocage. Dong-Hao Li and Liu-Pan Yang repeated the synthesis of naphtocage. Liu-Pan Yang and me performed the ITC and competition experiments. Liu-Pan Yang and I evaluated the ITC data with main contributions coming from my side. Hendrik V. Schröder performed and evaluated the CV measurements. Shan Xin and Xiaojiang Xie performed the ion-selective electrode experiments. Dieter Lentz measured and refined the crystal structure. Felix Witte performed the DFT calculations. Fei Jia, Wei Jiang, Hendrik V. Schröder, Christoph A. Schalley, and I wrote the manuscript together with main contributions coming from Fei Jia. All authors contributed to the final version of the manuscript.

JACS
JOURNAL OF THE AMERICAN CHEMICAL SOCIETY
Article
Cite This: J. Am. Chem. Soc. 2019, 141, 4468−4473
pubs.acs.org/JACS

Naphthocage: A Flexible yet Extremely Strong Binder for Singly Charged Organic Cations

Fei Jia,[†,‡] Henrik Hupatz,[†] Liu-Pan Yang,[‡] Hendrik V. Schröder,[†] Dong-Hao Li,[‡] Shan Xin,[‡] Dieter Lentz,[§] Felix Witte,[†] Xiaojiang Xie,[‡] Beate Paulus,[†] Christoph A. Schalley,*[,†] and Wei Jiang*[,‡]

[†]Institut für Chemie und Biochemie, Freie Universität Berlin, Takustrasse 3, 14195 Berlin, Germany

[‡]Department of Chemistry and Shenzhen Grubbs Institute, Southern University of Science and Technology, Xueyuan Boulevard 1088, Shenzhen 518055, China

[§]Institut für Chemie und Biochemie, Freie Universtät Berlin, Fabeckstrasse 34-36, 14195 Berlin, Germany

Supporting Information

ABSTRACT: We report a quite flexible naphthol-based cage (so-called "naphthocage") which adopts a self-inclusion conformation in its free state and is able to bind singly charged organic cations extremely strongly (K_a > 10^7 M^{-1}). Ion-selective electrodes prepared with this naphthocage show a super-Nernstian response to acetylcholine. In addition, the highly stable complex (10^{10} M^{-1}) between ferrocenium and the naphthocage can be switched electrochemically, which lays a basis for its application in stimuli-responsive materials.

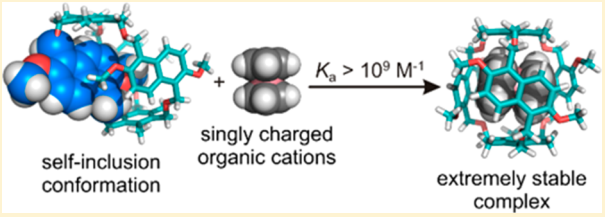

INTRODUCTION

Preorganization[1] is a key principle in supramolecular chemistry that has helped to explain many supramolecular phenomena and still guides the design of effective and selective molecular receptors. Highly preorganized molecular receptors are typically structurally rigid and, therefore, conformationally not responsive to environmental stimuli and often unable to accommodate even minor structural changes induced by a guest.[2] This is expressed in a relatively narrow binding scope and poor recognition ability of many rigid cage molecules in solutions.[3] Sanders[4] pointed out two decades ago that "the fear of entropy has taken supramolecular chemists too far in the direction of rigidity and preorganization, and...the future may lie in more flexible systems that rely on noncovalent interactions to impose order on three-dimensional structure." Flexible hosts are conformationally adaptive and can tolerate structural changes induced by the guests. Therefore, high selectivity may not be expected. However, by harnessing multiple noncovalent interactions cooperatively, high binding affinities would still be achieved despite the high entropic penalty caused by large amplitude conformational changes upon binding.[5] Compared to many biological, protein-based receptors,[6] however, flexible synthetic hosts have only achieved low to moderate binding affinities.

Recently, we reported a new class of conformationally flexible macrocycles, the oxatub[*n*]arenes.[7] In particular, oxatub[4]arene shows decent binding affinities to many organic cations (10^2−10^5 M^{-1} in CD_2Cl_2/CD_3CN (1:1)).[7b] Here, we report a new flexible naphthol-based cage (Figure 1a) which we—following the tradition of the naphthotubes[8]—coin "naphthocage". This cage is highly flexible and even adopts a self-inclusion conformation in solution when no cationic guest is present, in marked contrast to many other rigid cage structures.[3a,b] Despite the flexibility of the naphthocage, it shows remarkably high binding affinities to many singly charged organic cations (K_a > 10^7 M^{-1}) in CD_2Cl_2/CD_3CN (1:1). This naphthocage shows a super-Nernstian electrochemical response to acetylcholine in water when incorporated in ion-selective electrodes. The binding between ferrocenium and the naphthocage can be electrochemically switched as the naphthocage exhibits an extremely high binding selectivity for ferrocenium over ferrocene.

RESULTS AND DISCUSSION

Synthesis and Characterization of NC. *per*-Butyl-substituted naphthocage (**NC**, Figure 1a) was synthesized by reacting (2,6-dibutoxynaphthalene-1,5-diyl)dimethanol with 1,3,5-tris(bromomethyl)-2,4,6-triethylbenzene[9] in the presence of NaH in dry THF under pseudo-high-dilution conditions. Pure **NC** was then isolated through column chromatography as a white solid with a yield of 14%.

The structure of **NC** was characterized by NMR spectroscopy, mass spectrometry, and X-ray single crystallography (Figures S1−S13). Single crystals of **NC** were obtained by slow diffusion of diethyl ether into a saturated CH_3CN/CH_2Cl_2 (1:1) solution of **NC**. As shown in Figure 1b, a self-inclusion conformation is present in the crystal. This is in good

Received: January 23, 2019
Published: February 20, 2019

DOI: 10.1021/jacs.9b00445
J. Am. Chem. Soc. 2019, 141, 4468−4473

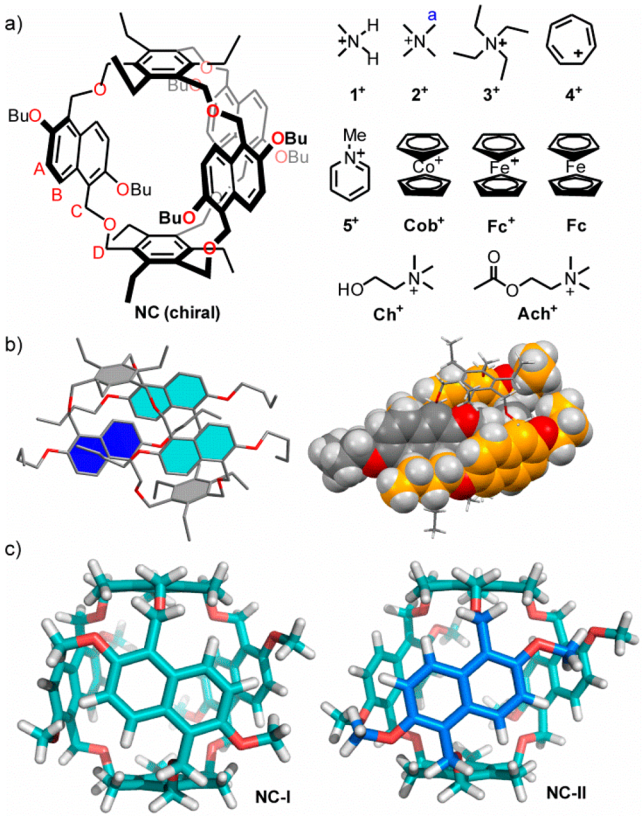

Figure 1. (a) Chemical structures of *per*-butyl naphthocage (**NC**) and the organic cations used as guests (used as PF_6^- salts). **NC** is chiral (only one enantiomer is shown). (b) X-ray single crystal structure of **NC** showing its self-inclusion conformation. CCDC nos. for **NC**: 1883700−1883701. (c) Conformers of **NC-I** and **NC-II** optimized at the TPSS-D_3(BJ) level of DFT are the structures of the **Cob**$^+$**@NC** complex in which **Cob**$^+$ has been omitted for viewing clarity (ethyl and butyl groups of **NC** are reduced to methyl groups for viewing clarity).

agreement with (variable-temperature) ^{1}H NMR data (Figures S12 and S13). The three signals for the $CH_2CH_2CH_3$ terminus of the butyl side chain included between the two outer naphthalenes appears in the spectra below 0 ppm as these protons experience the anisotropy of the surrounding aromatic rings. In the crystal, this conformation has C_1 symmetry. In solution, however, **NC** is highly flexible, and relatively slow conformational changes lead to broad signals in the ^{1}H NMR spectra of unbound **NC** in different solvents (Figure S12). Upon cooling to 218 K, the averaged signals split into the number of signals expected for a non-interconverting self-inclusion complex (Figure S13).

Guest-Binding Properties. Guests **1**$^+$−**5**$^+$, **Cob**$^+$, **Ch**$^+$, and **Ach**$^+$ (Figure 1a) are encapsulated by **NC** in the mixture of CD_2Cl_2 and CD_3CN (1:1) with surprisingly high binding constants. Significant shifts of the signals for both host and guest in 1:1 binding are observed in their ^{1}H NMR spectra (Figures 2 and S14−S21). In particular, all guest signals undergo drastic upfield shifts of about $\Delta\delta$ = 3.0−3.7 ppm due to the anisotropy of the surrounding aromatic rings thus supporting the cations to be encapsulated in the cavity of the cage. The 1:1 stoichiometry is further confirmed by predominant peaks for 1:1 host−guest complexes in the corresponding ESI mass spectra (Figures S25−S32).

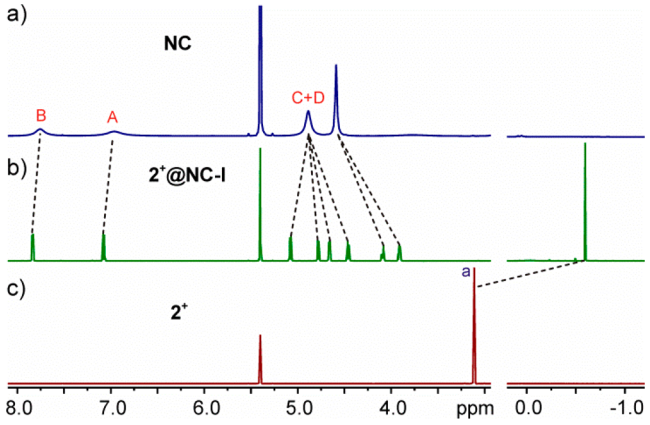

Figure 2. Partial ^{1}H NMR spectra (700 MHz, 2.0 mM, CD_2Cl_2:CD_3CN = 1:1, 298 K) of (a) **NC**, (b) **2**$^+$**@NC-I**, and (c) **2**$^+$.

Additional evidence confirms these guests to be encapsulated inside the cavity of **NC** and not merely attached to the exterior of the cage. Methylene protons *C* and *D* on the CH_2−O−CH_2 linkers (Figure 1a) are diastereotopic protons, but they constantly exchange positions through the conformational interconversion of free **NC**. When a guest is encapsulated inside the cavity of **NC**, this conformational interconversion is slowed down and its rate-determining step is guest exchange—a behavior similarly observed for oxatub[4]arenes.[7] This makes protons *C* and *D* split to four doublets (this analysis is only for conformer **NC-I**; 12 doublets would be expected for **NC-II**; see below for conformational analysis). This is observed for all of the guests discussed above (Figures 2 and S14−S21). However, when a guest only binds to the exterior of **NC**, it would not cause the similar splitting of protons *C* and *D*. By using this characteristic feature, we can determine whether a guest is encapsulated inside the cavity of **NC** or not. Tetramethylammonium **2**$^+$ and tetraethylammonium **3**$^+$ are guests for the cavity of **NC**, but tetrapropylammonium and tetrabutylammonium are not (Figure S22). This indicates the size limit in the cavity of **NC**, which would not be expected for exterior binding. Furthermore, NOE signals between the guests and the host in 2D NMR spectra (Figures S42−S57) confirm the encapsulation of these guests inside the cavity. These pieces of evidence taken together clearly speak in favor of guest encapsulation.

Host−guest binding is remarkably strong, and the binding constants exceed the limits of common spectroscopic titration experiments. Therefore, the binding constants in Table 1 were determined with isothermal titration calorimetry (ITC; Figures S34−S41). Except for those of **1**$^+$ and **4**$^+$, all association constants are larger than 10^7 M^{-1} and thus significantly larger than those of the same guest cations to oxatub[4]arene (10^2−10^5 M^{-1}).[7b] Even with guest **1**$^+$, which is not a guest for oxatub[4]arene in the same solvent, 10^5 M^{-1} was obtained in this study. Guests **5**$^+$, **Ach**$^+$, and **Cob**$^+$ exhibit binding constants even exceeding the limit of direct ITC titrations.[10] Therefore, we applied competition experiments[11] with **1**$^+$ as the reference guest to determine the binding constants of these three cations (for details, see Table S2). The quite extreme binding constants are even more remarkable when one considers (i) that **NC** is a highly flexible cage as expressed in the conformational dynamics discussed above and (ii) that it adopts a self-inclusion conformation in its free state so that guest binding does not benefit entropically from the liberation

DOI: 10.1021/jacs.9b00445
J. Am. Chem. Soc. 2019, 141, 4468−4473

Table 1. Association Constants and Thermodynamic Parameters of NC Binding to Different Organic Cations (in the Form of the Hexafluorophosphates) at 298 K As Determined by ITC Titrations

	K_a (M^{-1})	$\Delta G°$ (kJ/mol)	$\Delta H°$ (kJ/mol)	$-T\Delta S°$ (kJ/mol)
$\mathbf{1}^{+a}$	$(4.1 \pm 0.4) \times 10^5$	-32.0 ± 0.3	-37.1 ± 1.4	5.1 ± 1.7
$\mathbf{2}^{+a}$	$(1.6 \pm 0.3) \times 10^7$	-41.2 ± 0.3	-23.8 ± 0.5	-17.4 ± 0.8
$\mathbf{3}^{+a}$	$(3.7 \pm 0.4) \times 10^7$	-43.2 ± 0.3	-52.8 ± 1.2	9.6 ± 1.5
$\mathbf{4}^{+a}$	$(8.9 \pm 0.8) \times 10^6$	-39.7 ± 0.2	-34.6 ± 0.9	-5.1 ± 1.1
$\mathbf{5}^{+b}$	$(7.6 \pm 2.4) \times 10^8$	-50.7 ± 0.7	$-30.4^c \pm 0.2$	-20.3 ± 0.9
$\mathbf{Ch}^{+a}$	$(2.8 \pm 0.2) \times 10^7$	-42.5 ± 0.2	-35.9 ± 0.8	-6.6 ± 1.0
$\mathbf{Ach}^{+b}$	$(6.7 \pm 2.1) \times 10^9$	-56.1 ± 0.7	$-45.5^c \pm 0.3$	-10.6 ± 1.0
$\mathbf{Cob}^{+b}$	$(6.1 \pm 1.9) \times 10^9$	-55.8 ± 0.7	$-45.7^c \pm 0.3$	-10.1 ± 1.0

[a]Determined by direct ITC titrations. [b]Determined by ITC competition experiments with $\mathbf{1}^+$ as a reference. [c]$\Delta H°$ is taken from direct ITC titrations.

of solvent molecules from the cavity. In line with this argument, binding is dominated by enthalpy; presumably, cation–π interactions are the most important noncovalent forces involved.

Conformational Analysis. Two different orientations of the naphthalene moieties are possible when a guest cation occupies the cavity: in conformer **NC-I** (Figure 1c) and its enantiomer, all three naphthalenes have the same helical sense, while in conformer **NC-II** and its enantiomer, one naphthalene has flipped into the opposite sense. They differ in symmetry[12] (**NC-I**: D_3 symmetry; **NC-II**: C_2 symmetry) and thus are expected to show different aromatic signals patterns in the ^{1}H NMR spectra.[7a] As shown in Figure 2, the broadened signals of free **NC** sharpen drastically when adding one equivalent of $\mathbf{2}^+$ into the solution of **NC**. Titration experiments (Figure S14) confirm this to be caused by slow guest exchange. Only two doublets for the aromatic peak signals are observed. Protons *C* and *D* are diastereotopic and split into four doublets. This is only consistent with the symmetry of conformer **NC-I** (Figures 1c).

Similar peak patterns are observed for the **NC** complexes of guests $\mathbf{1}^+$, $\mathbf{3}^+$–$\mathbf{5}^+$, and $\mathbf{Ch}^+$, suggesting that **NC-I** is again the predominant conformer for these guests (Figures S42–S53, S56, and S57). As the symmetries of these guests differ from the D_3 symmetry of **NC-I**, a larger number of ^{1}H NMR signals would actually be expected. As this is not observed and as the guest exchange is slow on the NMR time scale, the guests must be small enough to tumble and rotate inside the **NC** cavity.[13]

For guests $\mathbf{1}^+$, $\mathbf{4}^+$, and $\mathbf{5}^+$, an additional set of six small doublets is observed in the aromatic region consistent with the C_2 symmetry of host conformer **NC-II**. The **NC-II** complexes represent a fraction of 18–22% of all **NC** complexes, while the **NC-I** complexes are still dominant. In contrast, **NC-II** is the predominant conformation for complexes of **NC** with $\mathbf{Ach}^+$ (Figures S54 and S55). Clearly, **NC** is conformationally flexible and can adapt to the size and shape requirements of its guests to maximize the noncovalent interactions.[7]

Ion-Selective Electrodes for Acetylcholine Chloride. Based on the strong binding of **NC** to $\mathbf{Ach}^+$, ion-selective electrodes (ISEs) for acetylcholine chloride in water were developed. ISEs normally require highly lipophilic receptors as the ionophore. This criterion is fully satisfied here, as **NC** exhibits very poor water solubility. The electrode membrane was prepared with plasticized poly(vinyl chloride) (PVC-DOS), cation-exchanger, and **NC** according to established procedures (see the Supporting Information for details).[14] As shown in Figure 3, a super-Nernstian response was observed with a slope of ca. 85 mV. Compared to conventional ISEs

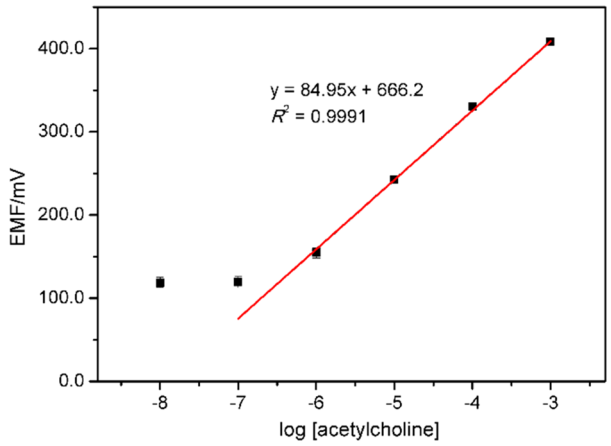

Figure 3. Super-Nernstian response curve of ISEs containing **NC** as the receptor for acetylcholine in water.

with Nernstian response, super-Nernstian electrodes can improve analytical sensitivity which is critical in real applications.[15] However, super-Nernstian ISEs are very rare and were so far only obtained for ionophores with extremely high binding affinities for metal ions (such as Ca^{2+}).[16] Therefore, this observation is fully in line with the above-mentioned high association constant (10^9 M^{-1}) between $\mathbf{Ach}^+$ and **NC**. While further optimization is certainly possible, the lower detection limit for acetylcholine with the **NC**-based ISEs is currently in the micromolar concentration range. This is among the best detection limits known so far for ISEs developed for different analytes.[17]

Redox-Responsive Complex. Redox-switchable organic cations are expected to provide access to redox-responsive supramolecular complexes with **NC**. For example, **NC** shows no obvious binding to neutral ferrocene (**Fc**), but ferrocenium ($\mathbf{Fc}^+$) is a strong binder to **NC** (Figures S23 and S24). The association constant between **NC** and $\mathbf{Fc}^+$ cannot be directly measured by ITC titration because of the intrinsic instability of $\mathbf{Fc}^+$ in air.[18] However, the binding constant of the structurally very similar and more stable cobaltocenium analogue $\mathbf{Cob}^+$ could be determined to amount to 10^9 M^{-1} (Table 1). The conversion between **Fc** and $\mathbf{Fc}^+$ can be easily manipulated through redox chemistry.[18] Therefore, the binding events between $\mathbf{Fc}^+$ and **NC** can be studied using cyclic voltammetry (CV). Addition of 1 equiv of **NC** significantly alters the CV peaks of **Fc** (Figures 4a,b). The anodic peak potential is cathodically shifted by ca. 80 mV, and the cathodic peak potential undergoes an enormous cathodic shift of 810 mV. The cathodic current associated with the reduction process of

DOI: 10.1021/jacs.9b00445
J. Am. Chem. Soc. 2019, 141, 4468–4473

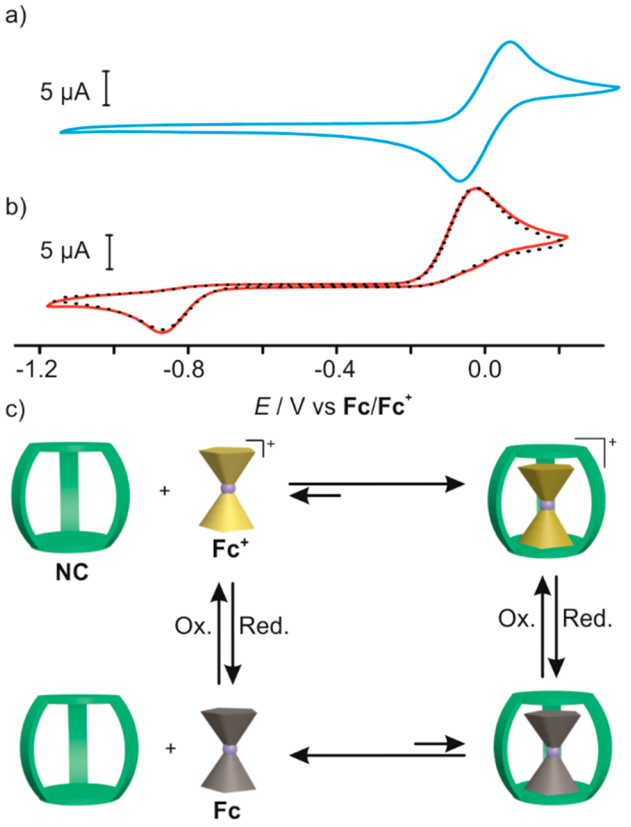

Figure 4. (a) Cyclic voltammogram of **Fc** (CH_2Cl_2, 1.0 mM, 298 K, 100 mV·s^{-1}) with *n*-Bu_4NPF_6 (0.1 M) as the electrolyte. (b) Cyclic voltammogram (solid red line) of **Fc** after addition of 1 equiv of **NC** and simulated cyclic voltammogram (dotted black line) by using thermodynamic and kinetic parameters in Table S3. (c) Cartoon representation of the redox-responsiveness of **Fc** and **Fc**$^+$**@NC**.

Fc$^+$ is slightly decreased owing to complexation with **NC**. The CV experiments are thus in excellent agreement with **Fc**$^+$ being highly stabilized in the presence of **NC**, whereas **Fc** displays no obvious affinity to the cage. Furthermore, the potential difference reveals an extremely large binding *selectivity* (ca. 10^{15} M^{-1}) of **Fc**$^+$ over **Fc** (Table S3). The CV experiments were repeated for a wide range of different scan rates (Figures S58–S60), and no significant change of the voltammograms was observed. This suggests that the chemical reversibility of the redox processes is stable.

To understand the binding behavior between **Fc**$^+$ and the **NC** complex, CV titration experiments were performed (Figure S61). Due to the strong binding, both voltammetric traces of free and complexed **Fc**$^+$ are observed when less than 1 equiv of **NC** is added. Addition of more than 1 equiv of **NC** has no further effect on the cyclic voltammograms.

Digital simulations were employed to evaluate host–guest binding between **Fc**/**Fc**$^+$ and **NC**. In accordance with the square scheme depicted in Figure 4c, we simulated the cyclic voltammogram of complex **Fc**$^+$**@NC** at different scan rates and concentrations of **NC**. The computational model provides a set of self-consistent values which are a reasonable estimation of thermodynamic and kinetic parameters (Tables S3 and S4). As expected, **Fc**$^+$ is strongly complexed to **NC** with an association constant of $K = 1.4 \times 10^{10}$ M^{-1} (in dichloromethane), whereas **Fc** shows no obvious binding affinity with **NC**. The fitted rate constant of dissociation $k_b = 5.6 \times 10^{-4}$ s^{-1} is quite low, in good agreement with a slow guest exchange as observed for the other guests as well in NMR experiments.

DFT calculations at the COSMO/B3LYP-D3(BJ) level were employed to evaluate binding energies and identify electronic interactions within **Cob**$^+$**@NC** (Figure 5). A free association

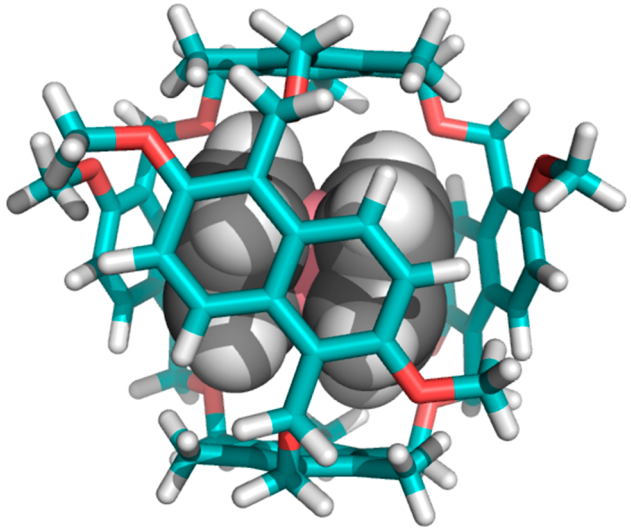

Figure 5. Conformer of complex **Cob**$^+$**@NC-I** optimized at the TPSS-D3(BJ) level of DFT. Butyl and ethyl groups of **NC** are shortened to methyl groups for viewing clarity.

enthalpy of −63.8 kJ/mol (Table S5) was computed, which is in good agreement with the ITC data, when one takes into account that dichloromethane was assumed as the solvent in the calculations, while a more polar solvent mixture was used in the ITC experiments (due to its low polarity dichloromethane can be described more accurately in the calculations than, e.g., acetonitrile, see SI for detailed explanation). Analysis of the valence orbital structure and surface charge properties of **Cob**$^+$**@NC** illustrates the noncovalent interactions, mainly of electrostatic nature, responsible for the large gain in electronic energy (Figures S64 and S65).

Redox-switchable supramolecular complexes have been widely used to prepare stimuli-responsive materials.[19] Complex **Fc**$^+$**@NC** can also be switched reversibly by redox chemistry. I_2 and $NaBH_4$/hydrazine are used as oxidant and reductant, respectively. KPF_6 was also added to provide counterions for oxidized **Fc**$^+$. At the initial state, K^+ is bound in the cavity of **NC** (Figure S4) and K^+**@NC** predominates in the presence of neutral **Fc**. When 1 equiva of I_2 is added, **Fc** is fully oxidized to **Fc**$^+$, which replaces the potassium cation in the cavity of **NC** giving rise to **Fc**$^+$**@NC**. Addition of $NaBH_4$ to the solution of **Fc**$^+$**@NC** reduces **Fc**$^+$ back to **Fc**, which leaves the cavity of **NC**. Now, one of the alkali metal ions binds to **NC** again. These processes can be monitored by ^{1}H NMR (Figures S66 and S67), UV–vis spectroscopy (Figures S68 and S69), and ESI mass spectrometry (Figure S70). The redox switching cycle can be repeated by adding I_2 and hydrazine alternately (Figure S71). The ability to induce guest exchanges by electrochemical stimuli lays the basis for the application of **NC** in stimuli-responsive materials.[19]

■ CONCLUSION

In summary, we have reported the synthesis and recognition behavior of "naphthocage" **NC**, a very flexible naphthol-based

DOI: 10.1021/jacs.9b00445
J. Am. Chem. Soc. 2019, 141, 4468–4473

cage receptor. In the free state, it adopts a self-inclusion conformation. Organic cations bind with surprisingly high affinities ($>10^7$ M^{-1}), even though quite substantial conformational changes are required to open the binding cavity for the guest. The cage can be used to prepare an ion-selective electrode with a super-Nernstian response to acetylcholine chloride in water. In addition, redox-switchable complexes were obtained from the naphthocage and ferrocenium, which paves the way for their application in stimuli-responsive materials. The present research also showcases flexibility is not necessarily the enemy of high-affinity binding. Harnessing multiple noncovalent interactions cooperatively would compensate the entropic penalty caused by large amplitude conformational changes upon binding.

■ ASSOCIATED CONTENT

Supporting Information

The Supporting Information is available free of charge on the ACS Publications website at DOI: 10.1021/jacs.9b00445.

Experimental and theoretical details, ^{1}H NMR spectra of the complexes, ITC titration data, control experiments, and single-crystal X-ray data (PDF)

Crystallographic data for **NC** (CIF)

■ AUTHOR INFORMATION

Corresponding Authors

*c.schalley@fu-berlin.de

*jiangw@sustc.edu.cn

ORCID

Hendrik V. Schröder: 0000-0002-6126-0055

Dong-Hao Li: 0000-0003-2556-1624

Dieter Lentz: 0000-0002-0583-7024

Xiaojiang Xie: 0000-0003-2629-8362

Wei Jiang: 0000-0001-7683-5811

Notes

The authors declare no competing financial interest.

■ ACKNOWLEDGMENTS

This paper is dedicated to Prof. Julius Rebek Jr. and Prof. Yu Liu on the occasion of their 75th and 65th birthdays, respectively. This research was financially supported by the National Natural Science Foundation of China (Grant Nos. 21572097, 21822104, and 21801125), the Shenzhen Special Funds (KQJSCX20170728162528382 and JCYJ20170307105848463), and the Shenzhen Nobel Prize Scientists Laboratory Project (C17213101). F.J. thanks the China Scholarship Council (CSC) for a PhD fellowship. We thank SUSTech-MCPC for support of the instruments. We thank Fabian Klautzsch for help with ITC. This work was made possible using the High-Performance Computing resources of the Zentraleinrich-tung für Datenverarbeitung (ZEDAT) of Freie Universität Berlin. Funding from the Deutsche Forschungsgemeinschaft (CRC 765) is gratefully acknowledged.

■ REFERENCES

(1) Cram, D. J. Preorganization—from Solvents to Spherands. *Angew. Chem., Int. Ed. Engl.* **1986**, *25*, 1039.

(2) Wittenberg, J. B.; Isaacs, L. Complementarity and Preorganization. In *Supramolecular Chemistry: From Molecules to Nanomaterials*; John Wiley & Sons, Ltd, 2012.

(3) (a) Zhang, G.; Mastalerz, M. Organic Cage Compounds – from Shape-Persistency to Function. *Chem. Soc. Rev.* **2014**, *43*, 1934. (b) Hasell, T.; Cooper, A. I. Porous Organic Cages: Soluble, Modular and Molecular Pores. *Nat. Rev. Mater.* **2016**, *1*, 16053. (c) Bisson, A. P.; Lynch, V. M.; Monahan, M. K. C.; Anslyn, E. V. Recognition of Anions through NH-π Hydrogen Bonds in a Bicyclic Cyclophane—Selectivity for Nitrate. *Angew. Chem., Int. Ed. Engl.* **1997**, *36*, 2340. (d) Tromans, R. A.; Carter, T. S.; Chabanne, L.; Crump, M. P.; Li, H. Y.; Matlock, J. V.; Orchard, M. M.; Davis, A. P. A Biomimetic Receptor for Glucose. *Nat. Chem.* **2019**, *11*, 52.

(4) Sanders, J. K. M. Supramolecular Catalysis in Transition. *Chem. - Eur. J.* **1998**, *4*, 1378.

(5) Borgia, A.; Borgia, M. B.; Bugge, K.; Kissling, V. M.; Heidarsson, P. O.; Fernandes, C. B.; Sottini, A.; Soranno, A.; Buholzer, K. J.; Nettels, D.; Kragelund, B. B.; Best, R. B.; Schuler, B. Extreme Disorder in an Ultrahigh-Affinity Protein Complex. *Nature* **2018**, *555*, 61.

(6) Houk, K. N.; Leach, A. G.; Kim, S. P.; Zhang, X. Binding Affinities of Host-Guest, Protein-Ligand, and Protein-Transition-State Complexes. *Angew. Chem., Int. Ed.* **2003**, *42*, 4872.

(7) (a) Jia, F.; He, Z.; Yang, L.-P.; Pan, Z.-S.; Yi, M.; Jiang, R.-W.; Jiang, W. Oxatub[4]arene: a Smart Macrocyclic Receptor with Multiple Interconvertible Cavities. *Chem. Sci.* **2015**, *6*, 6731. (b) Jia, F.; Wang, H.-Y.; Li, D.-H.; Yang, L.-P.; Jiang, W. Oxatub[4]arene: a Molecular "Transformer" Capable of Hosting a Wide Range of Organic Cations. *Chem. Commun.* **2016**, *52*, 5666. (c) Jia, F.; Li, D.-H.; Yang, T.-L.; Yang, L.-P.; Dang, L.; Jiang, W. Oxatub[5,6]arene: Synthesis, Conformational Analysis, and the Recognition of C60 and C70. *Chem. Commun.* **2017**, *53*, 336. (d) Jia, F.; Yang, L.-P.; Li, D.-H.; Jiang, W. Electronic Substituent Effects of Guests on the Conformational Network and Binding Behavior of Oxatub[4]arene. *J. Org. Chem.* **2017**, *82*, 10444.

(8) (a) Yang, L.-P.; Liu, W.-E.; Jiang, W. Naphthol-Based Macrocyclic Receptors. *Tetrahedron Lett.* **2016**, *57*, 3978. (b) Cui, J.-S.; Ba, Q.-K.; Ke, H.; Valkonen, A.; Rissanen, K.; Jiang, W. Directional Shuttling of a Stimuli-Responsive Cone-Like Macrocycle on a Single-State Symmetric Dumbbell Axle. *Angew. Chem., Int. Ed.* **2018**, *57*, 7809. (c) Chai, H.; Yang, L.-P.; Ke, H.; Pang, X.-Y.; Jiang, W. Allosteric Cooperativity in Ternary Complexes with Low Symmetry. *Chem. Commun.* **2018**, *54*, 7677. (d) Yao, H.; Ke, H.; Zhang, X.; Pan, S.-J.; Li, M.-S.; Yang, L.-P.; Schreckenbach, G.; Jiang, W. Molecular Recognition of Hydrophilic Molecules in Water by Combining the Hydrophobic Effect with Hydrogen Bonding. *J. Am. Chem. Soc.* **2018**, *140*, 13466.

(9) Wang, X.; Hof, F. How does 1,3,5-Triethylbenzene Scaffolding Work? Analyzing the Abilities of 1,3,5-Triethylbenzene- and 1,3,5-Trimethylbenzene-Based Scaffolds to Preorganize the Binding Elements of Supramolecular Hosts and to Improve Binding of Targets. *Beilstein J. Org. Chem.* **2012**, *8*, 1.

(10) Turnbull, W. B.; Daranas, A. H. On the Value of *c*: Can Low Affinity Systems Be Studied by Isothermal Titration Calorimetry? *J. Am. Chem. Soc.* **2003**, *125*, 14859.

(11) Sigurskjold, B. W. Exact Analysis of Competition Ligand Binding by Displacement Isothermal Titration Calorimetry. *Anal. Biochem.* **2000**, *277*, 260.

(12) (a) Müller, A.; Beugholt, C. The Medium is the Message. *Nature* **1996**, *383*, 296. (b) Beissel, T.; Powers, R. E.; Raymond, K. N. Symmetry-Based Metal Complex Cluster Formation. *Angew. Chem., Int. Ed. Engl.* **1996**, *35*, 1084.

(13) Rebek, J., Jr. Molecular Behavior in Small Spaces. *Acc. Chem. Res.* **2009**, *42*, 1660.

(14) Zhai, J.; Xie, X.; Bakker, E. Ionophore-Based Ion-Exchange Emulsions as Novel Class of Complexometric Titration Reagents. *Chem. Commun.* **2014**, *50*, 12659.

(15) Makarychev-Mikhailov, S.; Shvarev, A.; Bakker, E. Calcium Pulstrodes with 10-Fold Enhanced Sensitivity for Measurements in the Physiological Concentration Range. *Anal. Chem.* **2006**, *78*, 2744.

(16) Bakker, E.; Buhlmann, P.; Pretsch, E. Carrier-Based Ion-Selective Electrodes and Bulk Optodes. 1. General Characteristics. *Chem. Rev.* **1997**, *97*, 3083.
(17) For one recent ISE with micromolar sensitivity, see: He, C.; Wang, Z.; Wang, Y.; Hu, R. F.; Li, G. Nonenzymatic All-Solid-State Coated Wire Electrode for Acetylcholine Determination in vitro. *Biosens. Bioelectron.* **2016**, *85*, 679.
(18) (a) Connelly, N. G.; Geiger, W. E. Chemical Redox Agents for Organometallic Chemistry. *Chem. Rev.* **1996**, *96*, 877. (b) Astruc, D. Why is Ferrocene So Exceptional? *Eur. J. Inorg. Chem.* **2017**, *2017*, 6. (c) Ochi, Y.; Suzuki, M.; Imaoka, T.; Murata, M.; Nishihara, H.; Einaga, Y.; Yamamoto, K. Controlled Storage of Ferrocene Derivatives as Redox-Active Molecules in Dendrimers. *J. Am. Chem. Soc.* **2010**, *132*, 5061. (d) White, N. G.; Beer, P. D. A Ferrocene Redox-Active Triazolium Macrocycle That Binds and Senses Chloride. *Beilstein J. Org. Chem.* **2012**, *8*, 246.
(19) (a) Nakahata, M.; Takashima, Y.; Yamaguchi, H.; Harada, A. Redox-Responsive Self-Healing Materials Formed from Host−Guest Polymers. *Nat. Commun.* **2011**, *2*, 511. (b) Ahn, Y.; Jang, Y.; Selvapalam, N.; Yun, G.; Kim, K. Supramolecular Velcro for Reversible Underwater Adhesion. *Angew. Chem., Int. Ed.* **2013**, *52*, 3140. (c) Ni, M.; Zhang, N.; Xia, W.; Wu, X.; Yao, C.; Liu, X.; Hu, X.-Y.; Lin, C.; Wang, L. Dramatically Promoted Swelling of a Hydrogel by Pillar[6]arene−Ferrocene Complexation with Multistimuli Responsiveness. *J. Am. Chem. Soc.* **2016**, *138*, 6643.

DOI: 10.1021/jacs.9b00445
J. Am. Chem. Soc. 2019, 141, 4468−4473

Supporting Information

Naphthocage: A Flexible yet Extremely Strong Binder for Singly Charged Organic Cations

Fei Jia,[†,‡] Henrik Hupatz,[†] Liu-Pan Yang,[‡] Hendrik V. Schröder,[†] Dong-Hao Li,[‡] Shan Xin,[‡] Dieter Lentz,[§] Felix Witte,[†] Xiaojiang Xie,[‡] Beate Paulus,[†] Christoph A. Schalley,[†]* and Wei Jiang[‡]*

[†] *Institut für Chemie und Biochemie, Freie Universität Berlin, Takustrasse 3, 14195 Berlin, Germany*

[‡] *Department of Chemistry and Shenzhen Grubbs Institute, Southern University of Science and Technology, Xueyuan Blvd 1088, Shenzhen, 518055, China*

[§] *Institut für Chemie und Biochemie, Freie Universtät Berlin, Fabeckstr. 34–36, 14195 Berlin, Germany*

**E-mail: jiangw@sustc.edu.cn* and *c.schalley@fu-berlin.de*

Table of Contents

1. Experimental Section

1.1 General Methods

All reagents involved in this research were commercially available and used without further purification unless noted otherwise. Solvents were either employed as purchased or dried prior to use by standard laboratory procedures. Ferrocene and bis(cyclopentadienyl)cobalt(III) hexafluorophosphate were purchased from Sigma Aldrich. The electrolyte NBu_4PF_6 (TCI Chemicals) was dried *in vacuo* prior to usage. Host-guest complexes were prepared by simply mixing the guest cation salt and naphthocage (**NC**) in 1:1 stoichiometry in the corresponding solvent. The counterions of all guests are PF_6^-. Thin-layer chromatography was performed on silica gel-coated plates with fluorescent indicator F254 (Merck). For column chromatography, silica gel (0.04-0.063 mm; Merck) was used.

^1H and ^{13}C NMR experiments were performed on Bruker Avance 500 or 700 spectrometers. All chemical shifts are reported in ppm with residual solvents or TMS (tetramethylsilane) as the internal standards. The following abbreviations were used for signal multiplicities: s, singlet; d, doublet; t triplet; m, multiplet. Melting points were determined on a SMP 30 (Stuart) instrument and are uncorrected. Electrospray-ionization high-resolution mass spectrometry (ESI-HRMS) experiments were conducted on an Applied Q EXACTIVE mass spectrometer. ESI-FTICR mass spectrometric experiments were performed on a Varian/Ionspec QFT-7 FTICT mass spectrometer equipped with a superconducting 7-Tesla magnet and a micromass Z-spray ESI ion source. UV-Vis experiments were performed on a Cary 50 Bio spectrophotometer (Varian) equipped with a xenon lamp. HPLC grade solvents and Suprasil glass cuvettes with a path-length of 1 cm were used.

1.2 Synthetic Procedures

Naphthocage (NC)

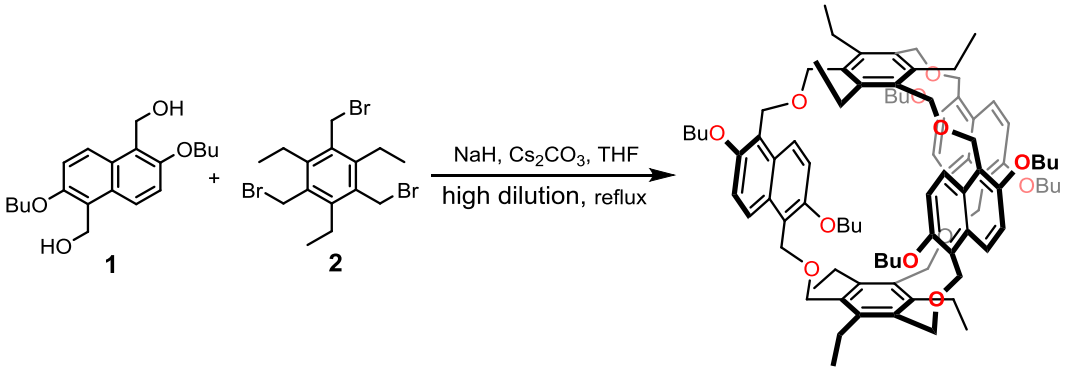

A solution of compound **1**[S1] (0.7 g, 2.1 mmol) and compound **2** (0.62 g, 1.4 mmol) in dry THF (50 mL) was added dropwise through a syringe pump over 4 h to a refluxed mixture of NaH (0.17 g, 4.2 mmol) and Cs_2CO_3 (1.4 g, 4.2 mmol) in dry THF (200 mL). The resulting mixture was refluxed for another 60 h. The solvent was removed under reduced pressure. The residue was suspended in H_2O (30 mL), and then extracted with CH_2Cl_2 (3 × 30 mL). The combined organic phases were washed with saturated NaCl and dried over anhydrous Na_2SO_4. The solvent was removed *in vacuo* to yield the crude product which was purified by column chromatography (SiO_2, *n*-hexane : ethylacetate = 20 : 1) to give naphthocage **NC** as a colorless solid (138 mg, yield 14%). m.p. > 320 ^oC (decomp.).

NC: ^1H NMR (500 MHz, CD_2Cl_2, 298 K) δ 7.82 (s, 6H), 7.089, 6.86 (d, 6H), 4.73 (d, 24H), 3.99 (s, 5H), 2.90 (s, 16H), 2.09 – 1.32 (m, 15H), 0.88 (d, 24H), -0.25 (s, 3H), -0.88 (d, 4H). ^{13}C NMR (125 MHz, $CDCl_3$, 298 K) δ [ppm] = 153.97, 152.32, 144.48, 132.23, 128.92, 126.10, 124.44, 120.56, 115.50, 69.93, 66.05, 62.76, 31.67, 22.32, 19.40, 16.74, 13.69. ESI-HRMS: m/z calcd for $[M+K]^+$ $C_{90}H_{120}O_{12}K^+$ 1431.8411; found 1431.8425 (Δm/z = 0.97 ppm). The ^1H and ^{13}C NMR signals of **NC** are broadened indicating dynamic processes with rates in the range of the NMR time scale. Three signals are shifted upfield into the 0 to -1 ppm range. This is clearly in line with self-inclusion as found in the crystal structure (for details, see below).

When NMR spectra of the cage are recorded in the presence of one equivalent of KPF_6 or Me_4NPF_6 as guests, the signals sharpen significantly, because the cage's conformational changes are suppressed:

K^+@NC: ^{1}H NMR (700 MHz, CD_2Cl_2:CD_3CN = 1:1, 298 K) δ 7.83 (s, 6H), 7.13 (s, 6H), 4.97 (d, *J* = 121.5 Hz, 12H), 4.60 (d, *J* = 109.8 Hz, 12H), 4.09 (s, 12H), 2.73 (s, 12H), 1.90 (s, 12H), 1.67 (s, 12H), 1.24 (s, 18H), 1.11 (s, 18H).

Me_4N^+@NC: ^{1}H NMR (700 MHz, CD_2Cl_2:CD_3CN = 1:1, 298 K) δ 7.84 (d, *J* = 9.3 Hz, 6H, CH), 7.08 (d, *J* = 9.4 Hz, 6H, CH), 5.08 (d, *J* = 9.0 Hz, 6H, CH_2OCH_2), 4.78 (d, *J* = 9.0 Hz, 6H, CH_2OCH_2), 4.66 (d, *J* = 9.5 Hz, 6H, CH_2OCH_2), 4.46 (d, *J* = 9.4 Hz, 6H, CH_2OCH_2), 4.09 (dt, *J* = 8.8, 6.2 Hz, 6H, OCH_2), 3.91 (dt, *J* = 8.8, 6.3 Hz, 6H, OCH_2), 2.70 (m, 12H, CH_2), 1.94 – 1.90 (m, 12H, CH_2), 1.74 – 1.67 (m, 12H, CH_2), 1.23 (t, *J* = 7.5 Hz, 18H, CH_3), 1.15 (t, *J* = 7.4 Hz, 18H, CH_3), -0.60 (s, 12H, Me_4N^+, interior). ^{13}C NMR (125 MHz, CD_2Cl_2:CD_3CN = 1:1, 298 K) δ [ppm] = 152.82, 143.90, 132.27, 128.51, 125.63, 120.51, 115.56, 70.06, 66.33, 62.34, 31.88, 21.65, 19.56, 16.34, 13.68. m/z calcd for [M + Me_4N]$^+$ $C_{94}H_{133}NO_{12}^+$ 1467.9822; found 1467.9781 (Δm/z = -2.8 ppm).

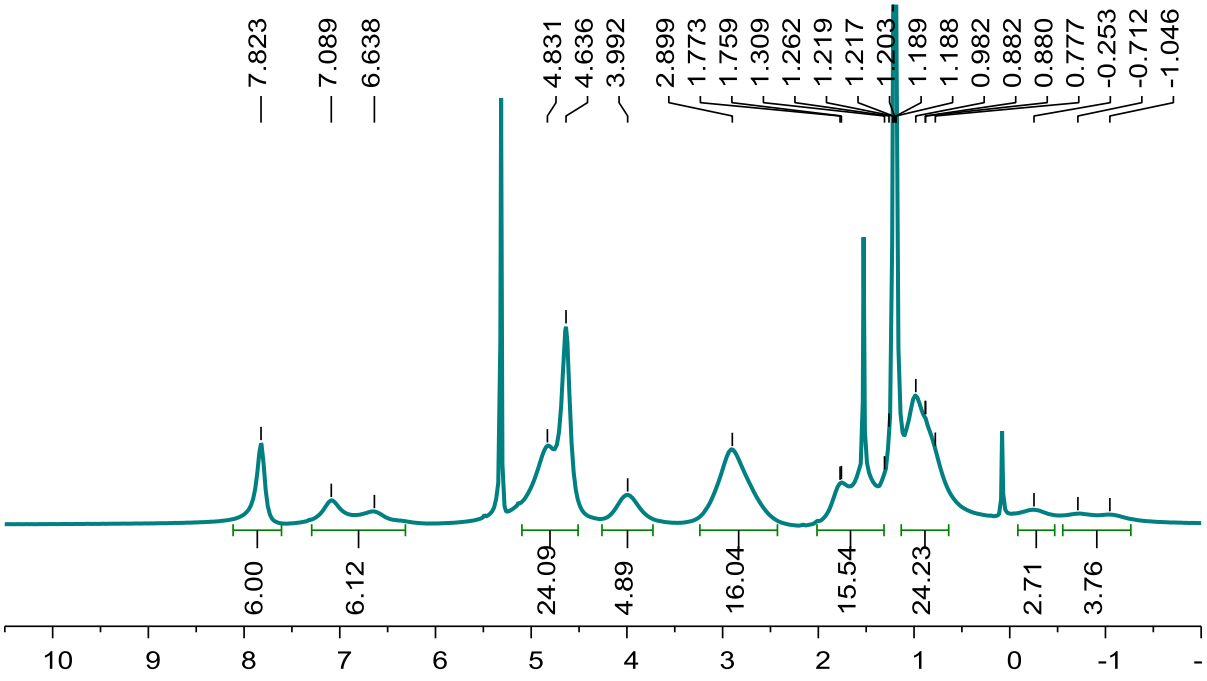

Figure S1. *^{1}H NMR spectrum (500 MHz, CD_2Cl_2, 15 mM, 298 K) of* ***NC***.

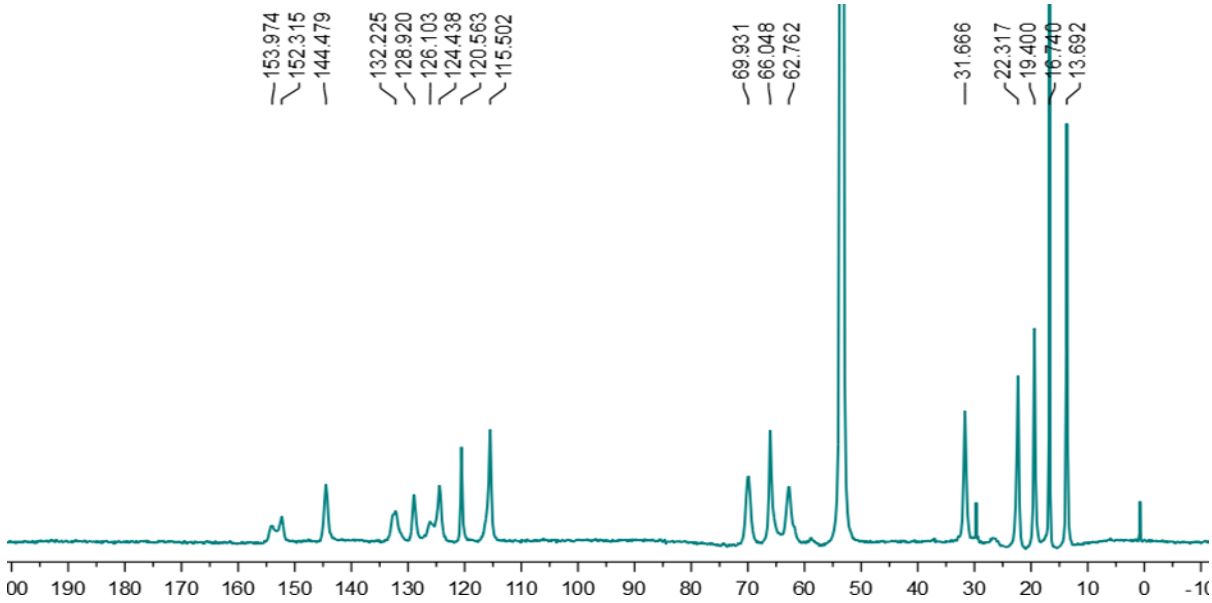

Figure S2. *^{13}C NMR spectrum (125 MHz, CD_2Cl_2, 15 mM, 298 K) of* ***NC****.*

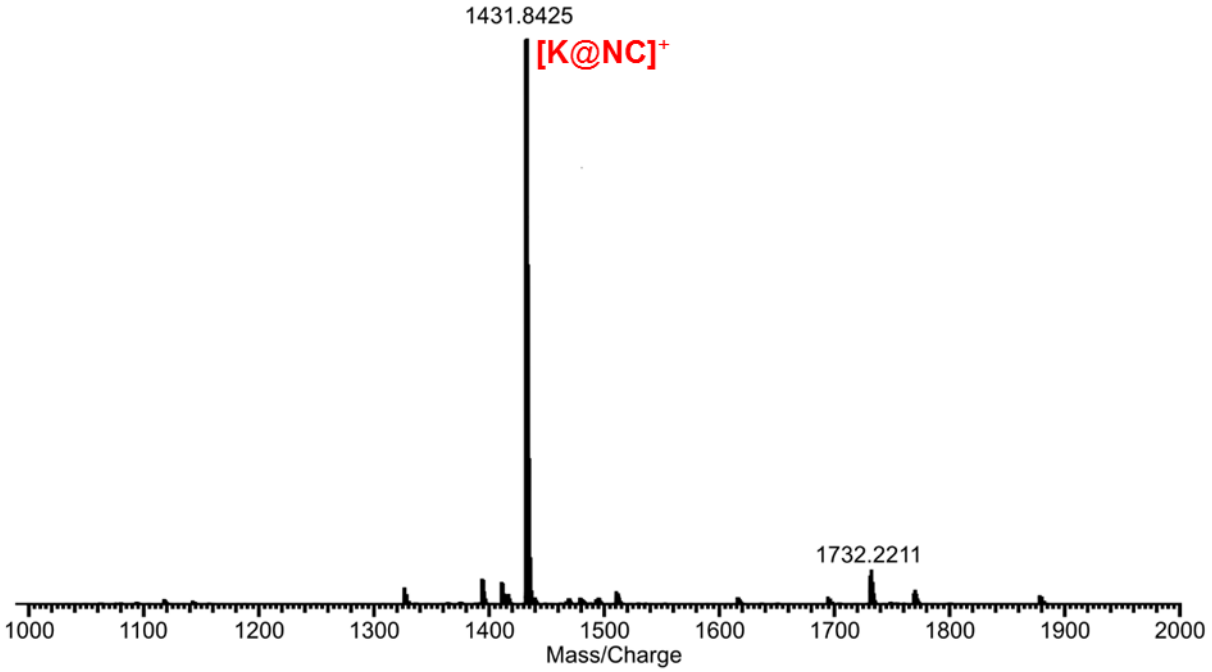

Figure S3. *ESI-HRMS of* ***NC****.*

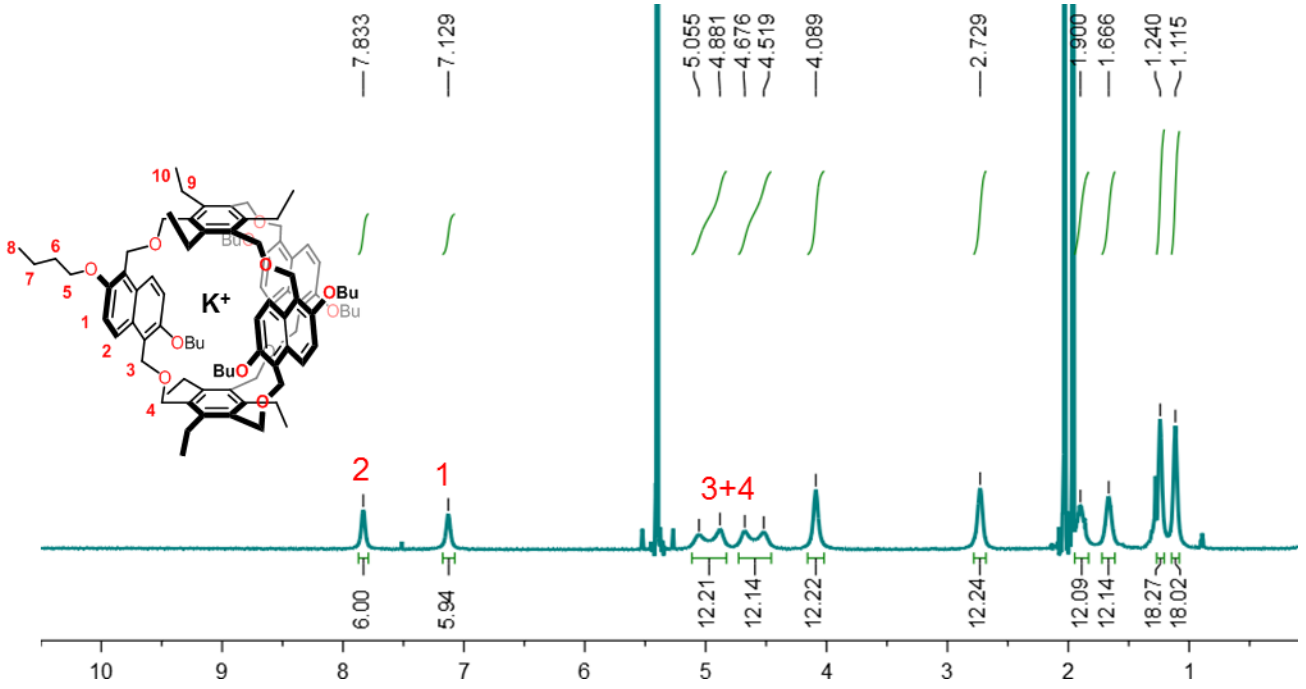

Figure S4. *^{1}H NMR spectrum (700MHz, CD_2Cl_2:CD_3CN = 1:1, 2 mM, 298 K) of* ***K^+@NC***.

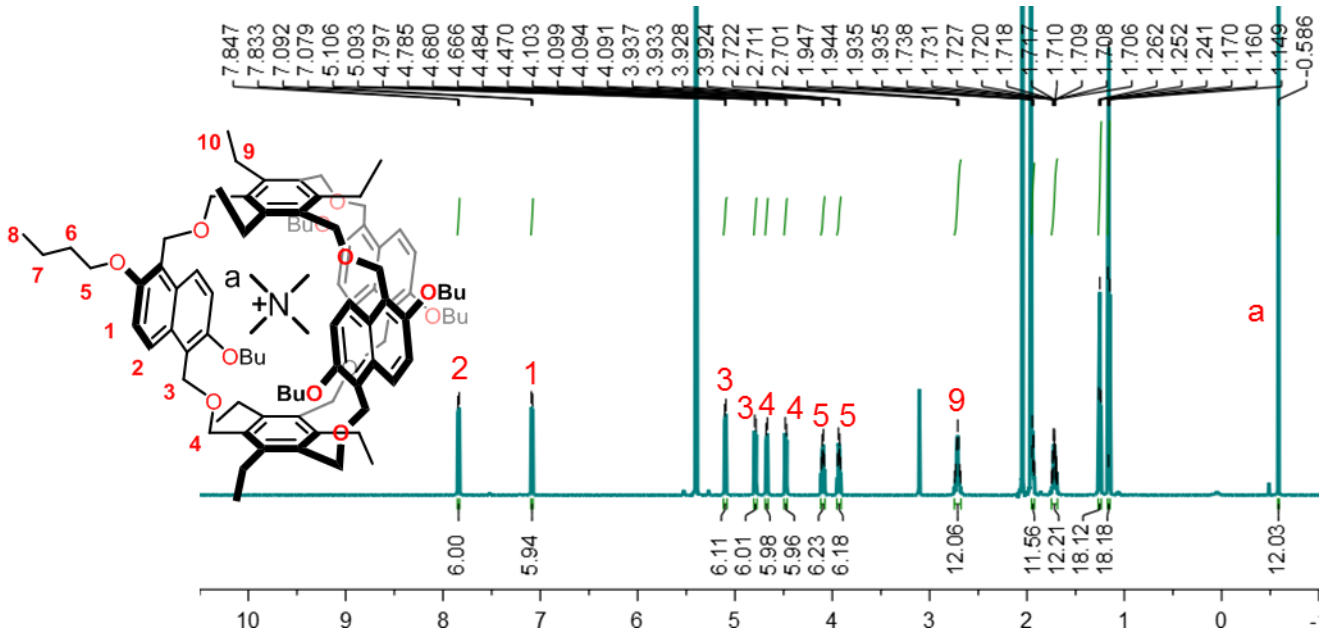

Figure S5. *^{1}H NMR spectrum (700 MHz, CD_2Cl_2:CD_3CN = 1:1, 2 mM, 298 K) of* ***Me_4N^+@NC***.

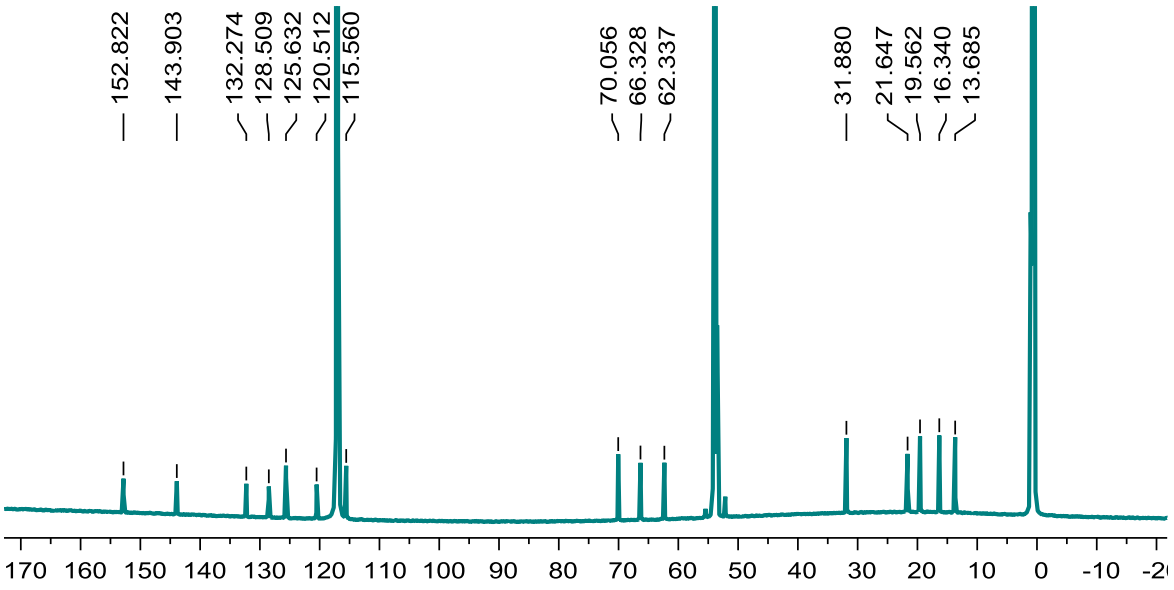

Figure S6. *^{13}C NMR spectrum (700 MHz, CD_2Cl_2:CD_3CN = 1:1, 2 mM, 298 K) of* ***Me_4N^+@NC***.

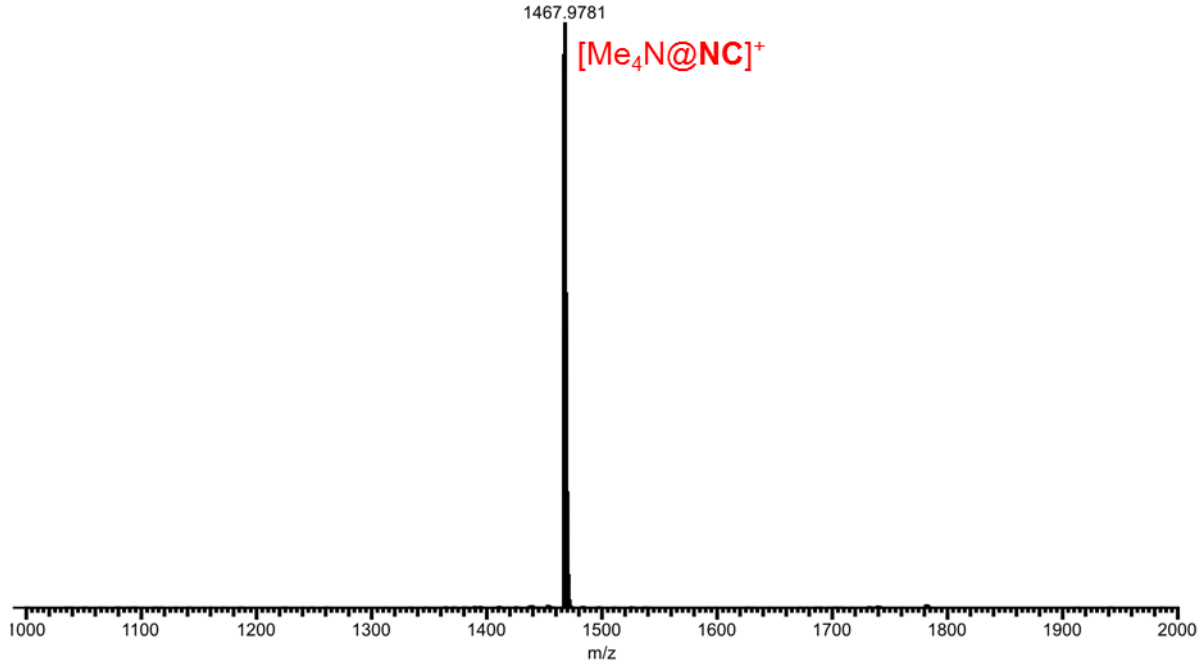

Figure S7. *ESI-HRMS of* ***Me_4N^+@NC***.

2. Single Crystal Structures

Crystals of **NC** were obtained by slow vapor diffusion of diethyl ether into a solution in CH_3CN and CH_2Cl_2 (1:1) or slow evaporation of THF through the cap of an NMR sample. Crystal data of **NC** was collected on a Bruker-AXS Venture instrument with Incoatec Microfocus sources for MoKα and CuKα radiation and a photon detector. The single crystal was mounted on a MiTeGen® kapton loop and placed in a 100(2) K nitrogen cold stream from Cryostream system. The raw data were processed with the Bruker APEX3 software package.[S2] The data were integrated using the SAINT[S3] and then corrected for absorption with SADABS[S4] routines. The structures were solved by intrinsic phasing (SHELXT-2016) and the refined by full-matrix least squares on F^2 (SHELXL-2016).[S5] Refinement details of each structure can be found in "refine_special_details" in the corresponding cif file. The Oakridge National Laboratories Thermal Ellipsoids Program ORTEP was used to create the plots.[S6]

Table S1. Crystal data and structure refinement for **NC** and **NC***THF

	NC	**NC***THF
Empirical formula	C_{90} H_{120} O_{12}	C_{94} H_{128} O_{13}
Formula weight	1393.85	1465.96
Temperature	100(2) K	100(2) K
Wavelength	1.54178 Å	0.71073 Å
Crystal system	Orthorhombic	Monoclinic
Space group	P 2_1 2_1 2_1	P 2_1/c
Unit cell dimensions	a = 13.7326(4) Å	a = 13.3946(10) Å
	b = 21.0505(5) Å	b = 21.1810(16) Å
	c = 27.1510(7) Å	c = 29.286(2) Å
	□ = 90°	□ = 90°
	□ = 90°	□ = 93.341(2)°
	□ = 90°	□ = 90°
Volume	7848.8(4) Å^3	8294.6(11) Å^3
Z	4	4
Density (calculated)	1.180 Mg/m^3	1.174 Mg/m^3
Absorption coefficient	0.602 mm^{-1}	0.076 mm^{-1}
F(000)	3024	3184
Crystal size	0.35 x 0.25 x 0.1 mm^3	0.300 x 0.210 x 0.190 mm^3
Theta range for data collection	2.656 to 73.279°	2.222 to 28.669°
Index ranges	-16<=h<=15	-17<=h<=17
	-26<=k<=23	-28<=k<=28
	-33<=l<=33	-39<=l<=39
Reflections collected	49590	176814
Independent reflections	15109 [R(int) = 0.0432]	21062 [R(int) = 0.0416]
Completeness to theta = 67.679°, 25.242°	99.7 %	99.9 %
Absorption correction	Semi-empirical from equivalents	
Max. and min. transmission	0.806 and 0.699	0.746 and 0.716
Refinement method	Full-matrix least-squares on F^2	
Data / restraints / parameters	15109 / 0 / 931	21062 / 0 / 1011
Goodness-of-fit on F^2	1.036	1.040
Final R indices [I>2sigma(I)]	R_1 = 0.0548, wR_2 = 0.1378	R_1 = 0.0650, wR_2 = 0.1566
R indices (all data)	R_1 = 0.0666, wR_2 = 0.1468	R_1 = 0.0850, wR_2 = 0.1689
Absolute structure parameter	0.05(6)	
Largest diff. peak and hole	0.895 and -0.334 e*Å^{-3}	1.085 and -0.891 e*Å^{-3}

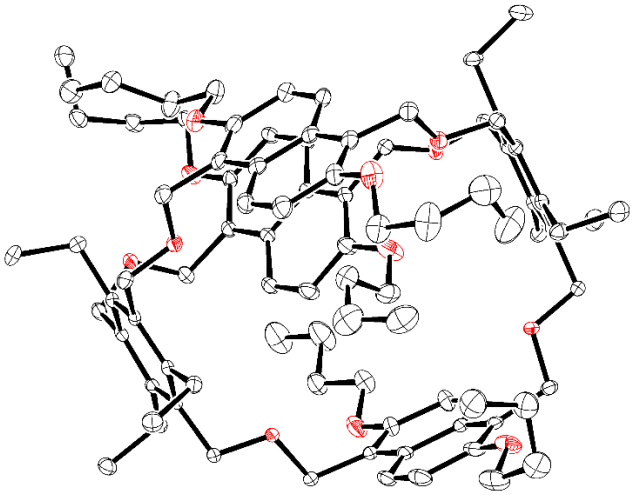

Figure S8. *ORTEP plot of the single crystal structure of* ***NC****. The C, N and O atoms are drawn as 30% thermal ellipsoids. Hydrogen atoms omitted for clarity.*

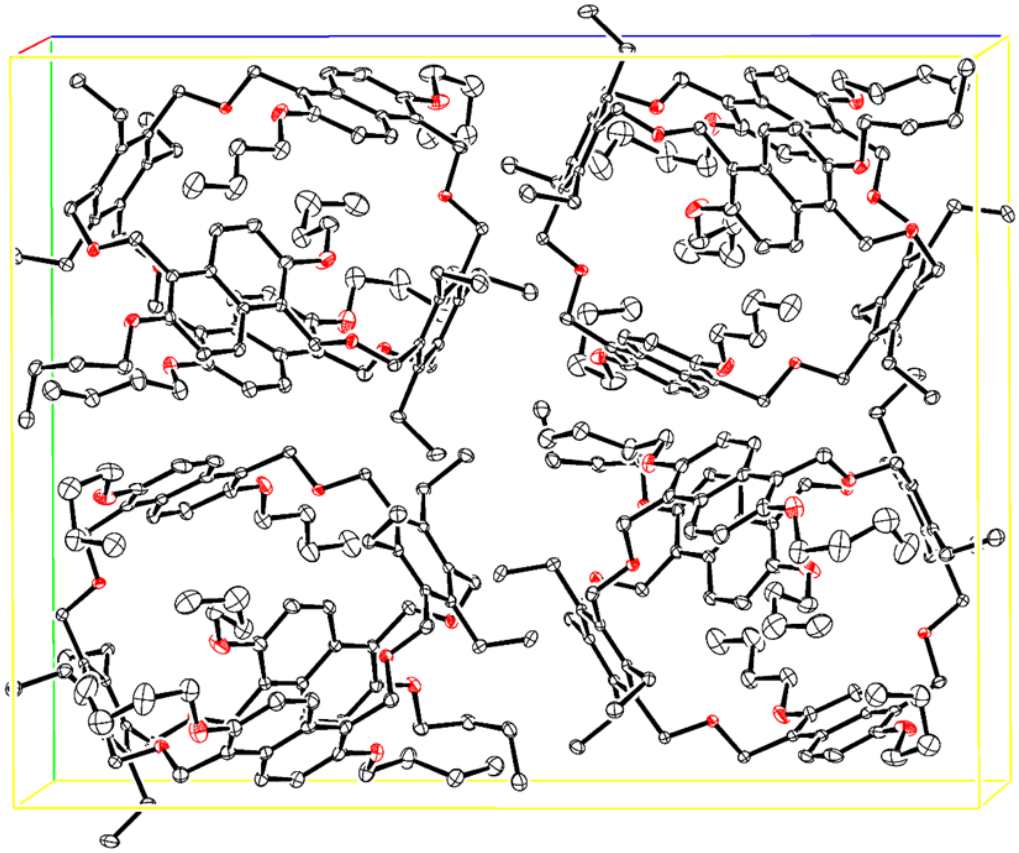

Figure S9. *Cell plot (ORTEP) of* ***NC****. The C, N and O atoms are drawn as 30% thermal ellipsoids. Hydrogen atoms omitted for clarity.*

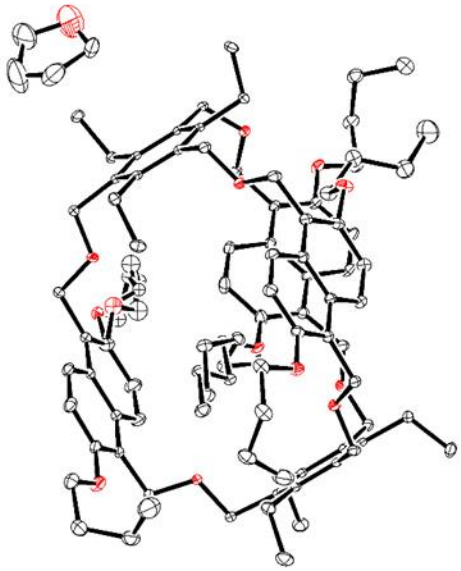

Figure S10. *ORTEP plot of the single crystal structure of* ***NC*****THF. The C, N and O atoms are drawn as 30% thermal ellipsoids. Hydrogen atoms omitted for clarity.*

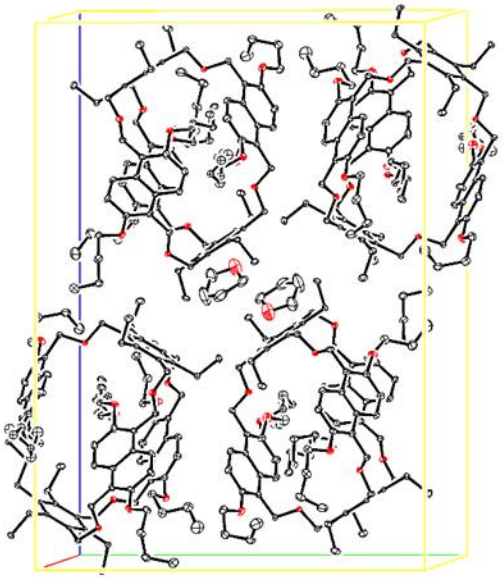

Figure S11*. Cell plot (ORTEP) of* ***NC*****THF. The C, N and O atoms are drawn as 30% thermal ellipsoids. Hydrogen atoms omitted for clarity.*

3. Variable-Temp ^{1}H NMR Experiments of Host

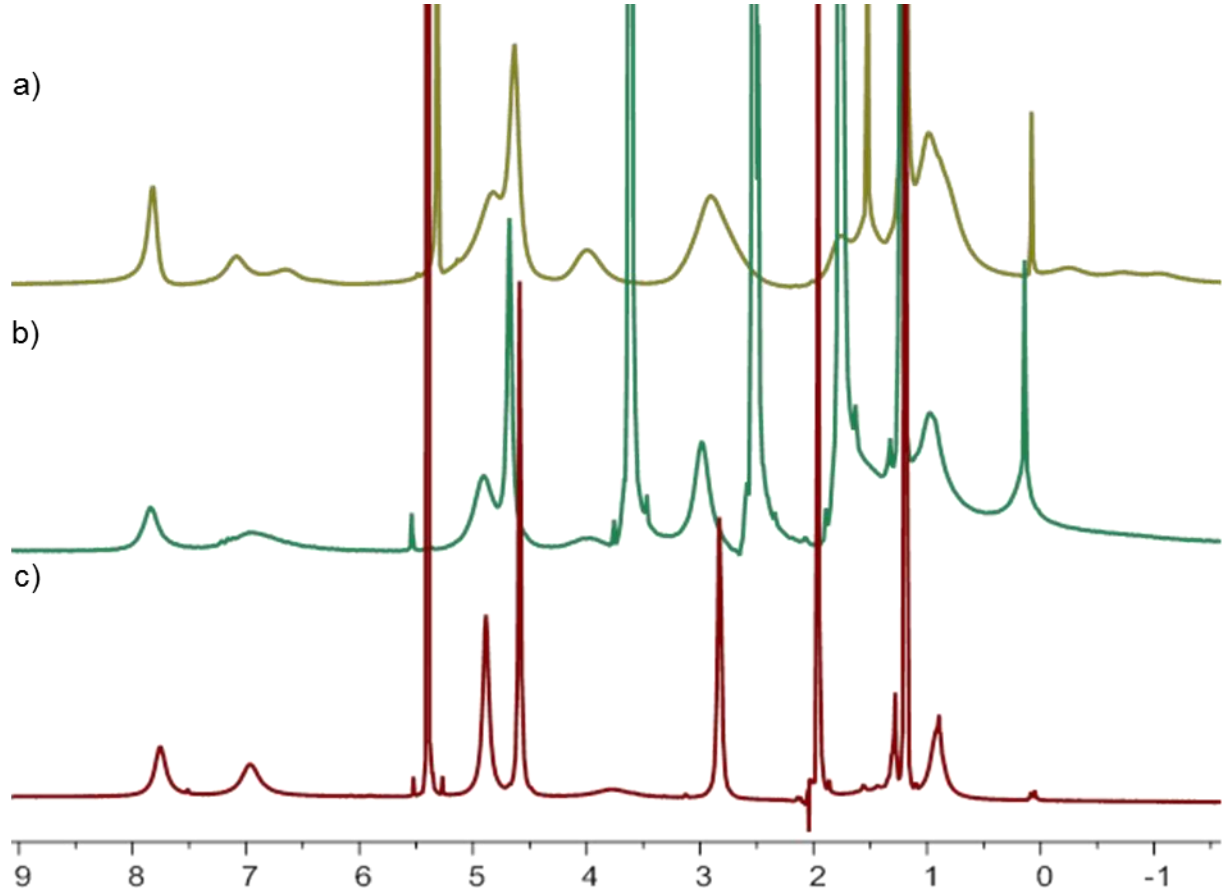

Figure S12. *^{1}H NMR spectra (500 MHz, 2.0 mM, 298 K) of **NC** in different deuterated solvents (a) CD_2Cl_2, (b) THF-d_8, and (c) CD_2Cl_2:CD_3CN = 1:1.*

Figure S12 depicts ^{1}H NMR spectra of **NC** in different organic solvents. Peak broadening is most prominently observed in dichloromethane. In this solvent, three peaks are observed in the 0 to -1 ppm range which correspond to the $CH_3CH_2CH_2$ end of one of the butyl side chain that is located inside the cage and thus experiences the anisotropy of the surrounding aromatic walls. This clearly indicates the presence of a self-inclusion structure also in solution. The signals sharpen significantly in THF-d_8 and in a CD_2Cl_2:CD_3CN 1:1 mixture. Here, the conformational dynamics of the cage are clearly faster than the NMR timescale. This also leads to the disappearance of the signals below 0 ppm, as they are averaged with the corresponding signals of the five remaining non-included butyl side chains.

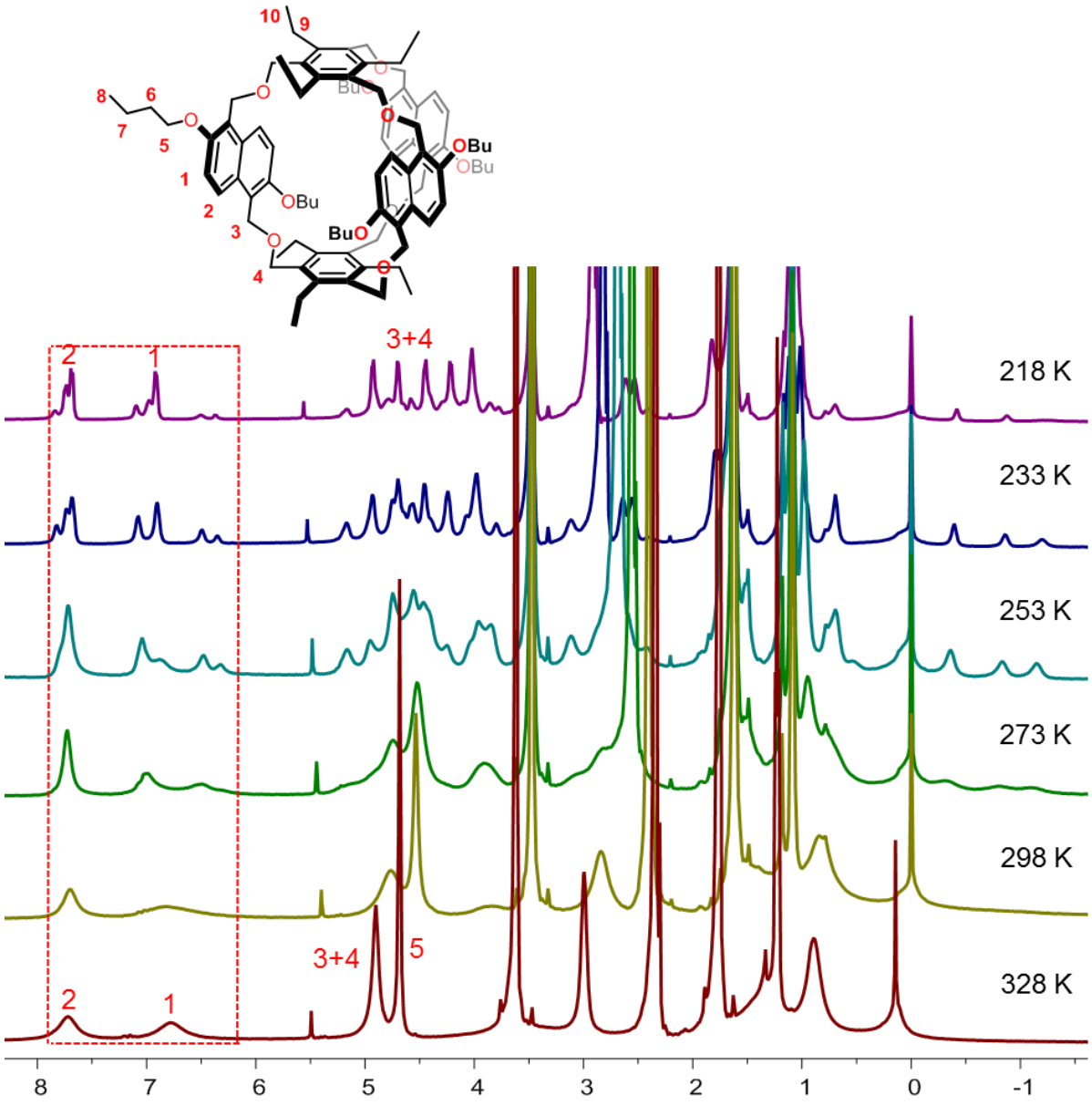

Figure S13**. Variable-temperature ^{1}H NMR spectra (500 MHz, THF-d_8) of **NC

Variable temperature NMR spectroscopy supports this: At 328 K, the naphthalene signals *1* and *2* (Figure S13; red dashed box) in the aromatic region of the spectrum are still broadened, but only one set of signals is observed. Below 273 K, again three signals appear below 0 ppm and indicate the presence of a self-inclusion structure of the cage. Also, other signals of the cage (e.g. between 4.0 and 5.5 ppm and in the aromatic region) split into several sets of signals in line with slow exchange processes between different conformations.

4. Host-Guest Chemistry

Upon addition of tetramethylammonium hexafluorophosphate **2**-PF_6, the aromatic protons of **NC** turn into sharp doublets and undergo a small downfield shift, while the protons of the encapsulated guest shift upfield drastically by 3.7 ppm because of the anisotropy of the surrounding aromatic rings. Also, the signals for free and encapsulated guests appear separately. These experiments thus demonstrate that the guest exchange is slow on the NMR timescale. The conformational dynamics of **NC** are decelerated significantly by encapsulation of $\mathbf{2}^+$ and occur on the same slow timescale.

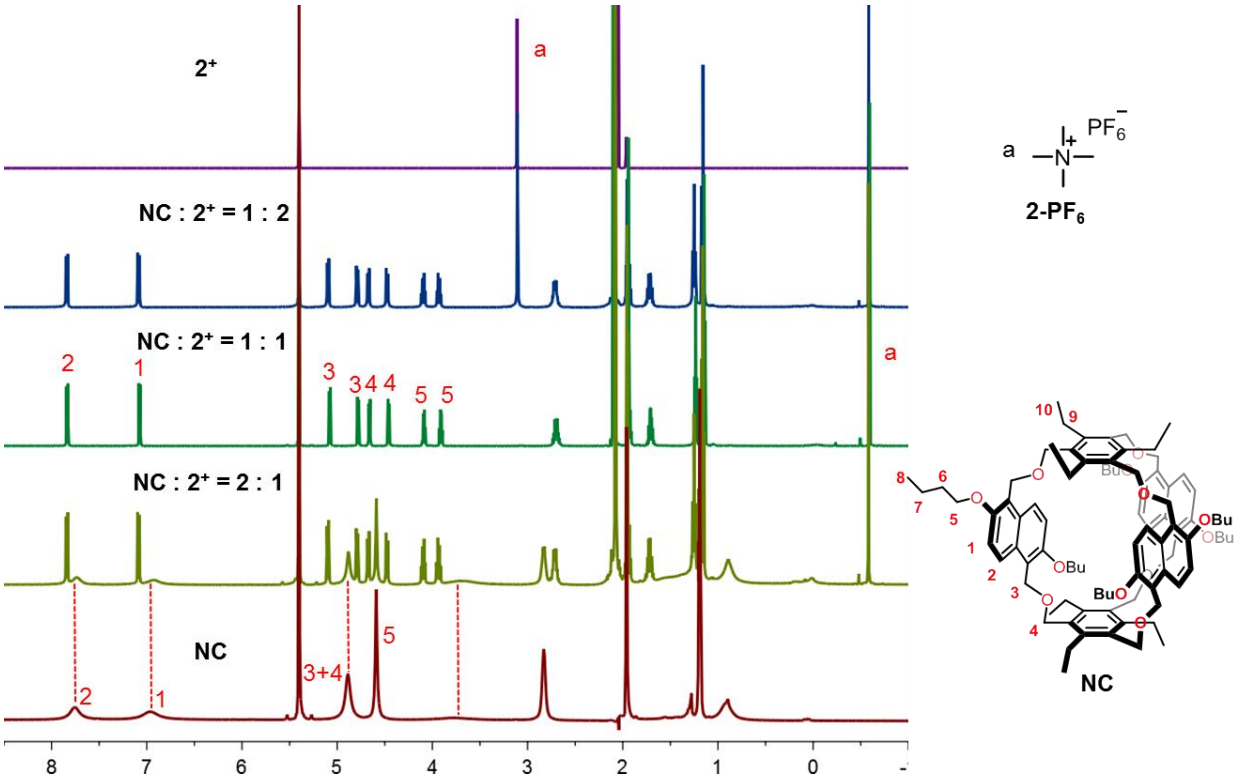

***Figure S14**. Full ^{1}H NMR spectra (700 MHz, CD_2Cl_2:CD_3CN = 1:1, 2.0 mM, 298 K) of **NC**, **2**-PF_6, and their mixture in 2:1, 1:1, and 1:2 ratio (from bottom to top).*

As the symmetries of guest and host do not match each other, one would expect to observe several sets of signals for both the guest and the host. This is however not the case and thus, we can conclude that the tumbling and rotation of the guest inside the host is (a) significantly faster than the NMR timescale and is (b) thus also significantly faster than guest exchange. Therefore, the guest exchange is (c) dominated kinetically by the size of the cage's holes through which it

must pass. The fact that the aromatic naphthalene signals are two sharp doublets clearly indicates that all three naphthalenes are equivalent. Consequently, conformer **NC-I** dominates by > 98%. The complete disappearance of free host and free guest in the 1:1 mixture of **NC** and $\mathbf{2}^{+}$ indicates strong binding between them. From the integrations, we estimate a lower limit for the binding constant of $8 \times 10^{4}\ M^{-1}$.

Similar results are obtained for the other host-guest complexes:

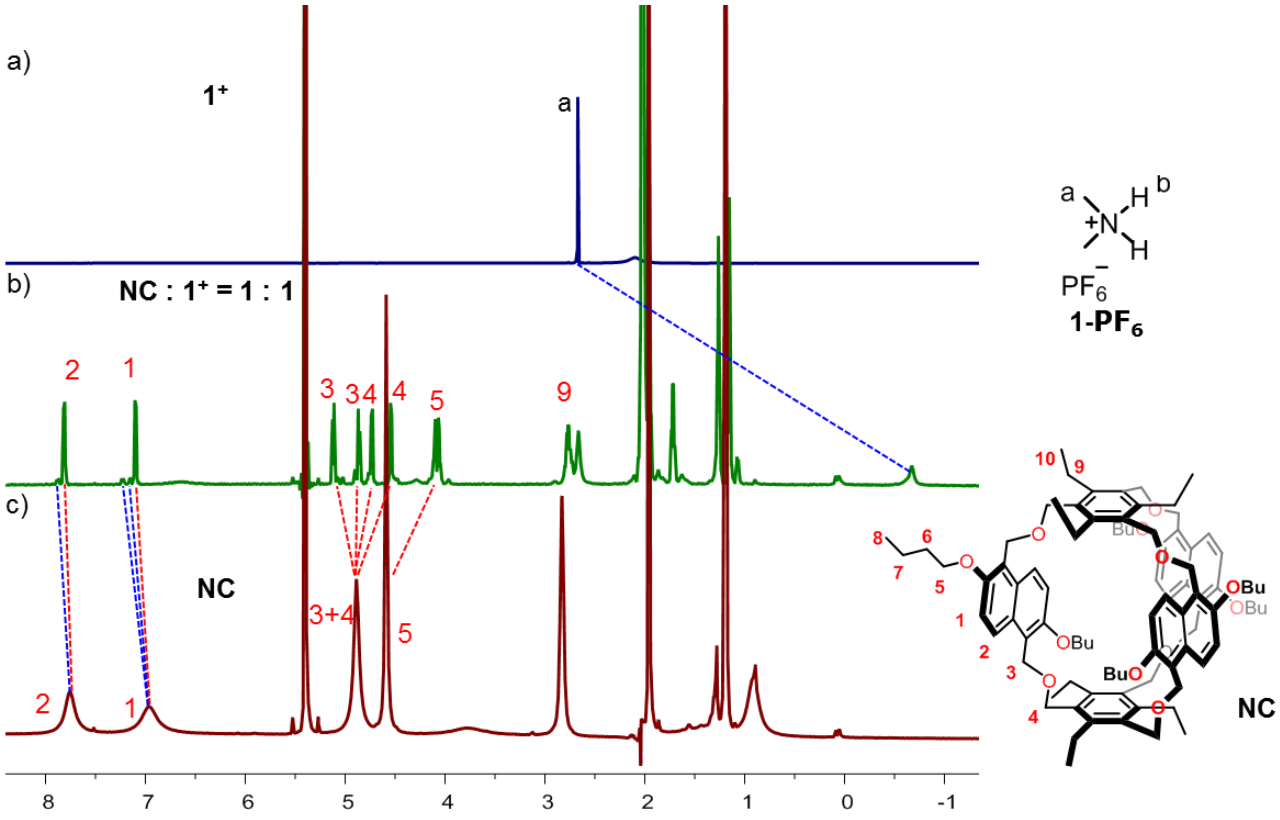

Figure S15. *Full ^{1}H NMR spectra (700 MHz, CD_2Cl_2:CD_3CN = 1:1, 2.0 mM, 298 K) of (a)* ***1***-PF_6^{+}*, (c)* ***NC****, and (b) their equimolar mixture. In the host-guest mixture, the aromatic protons of host* ***NC*** *become from two broadened peaks to two big doublets and six small doublets, and shift downfield, while the protons of the guest shift to upfield (-3.2 ppm) with a broadened peak. These experiments suggest that guest* $\mathbf{1}^{+}$ *and* ***NC*** *experience a slow guest exchange. The aromatic NMR peak pattern indicates that two conformers of* ***NC-I*** *and* ***NC-II*** *coexist in the complex, and conformer* ***NC-I*** *(80%) exists as the dominating conformer.*

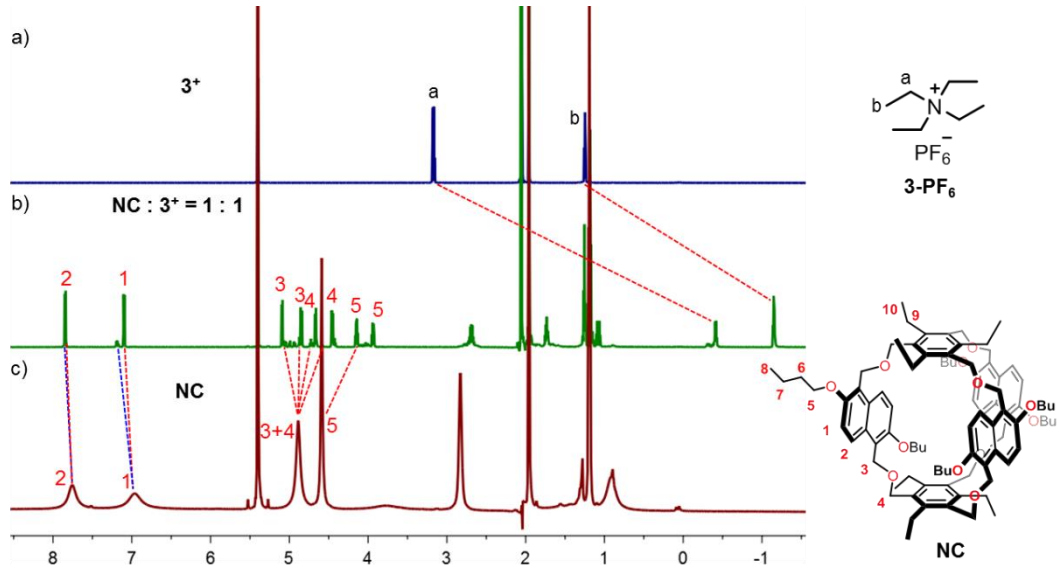

Figure S16. *Full ^{1}H NMR spectra (700 MHz, CD_2Cl_2:CD_3CN = 1:1, 2.0 mM, 298 K) of (a)* ***3***-PF_6*, (c)* ***NC****, and (b) their equimolar mixture. In the host-guest mixture, the aromatic protons of host* ***NC*** *appear as two large and four small doublets indicating host conformers* ***NC-I*** *(72%) and* ***NC-II*** *(28%) to coexist in the complex.*

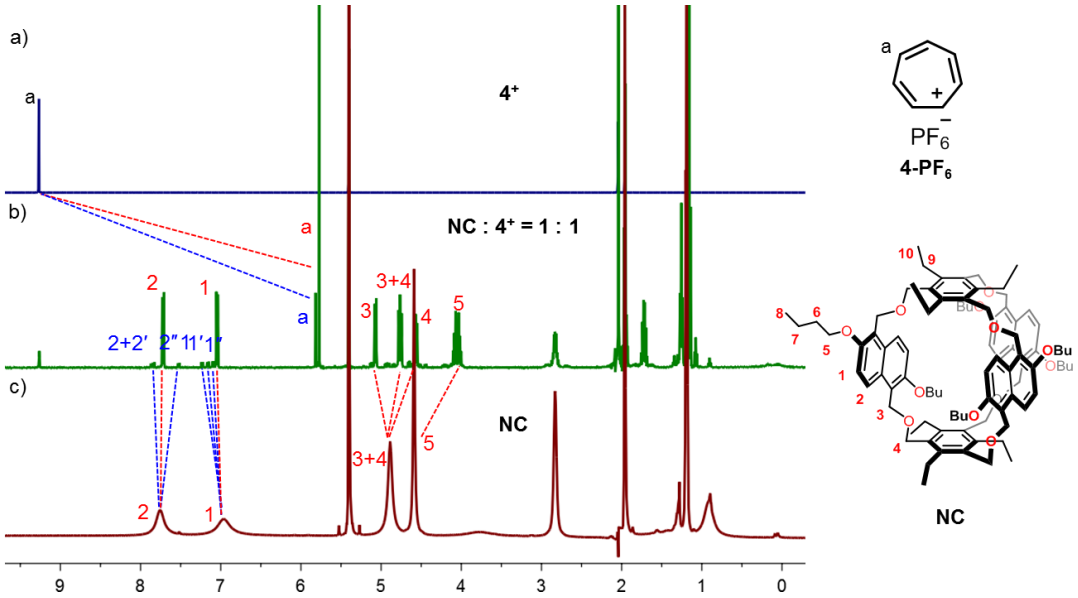

Figure S17. *Full ^{1}H NMR spectra (700 MHz, CD_2Cl_2:CD_3CN = 1:1, 2.0 mM, 298 K) of (a)* ***4***-PF_6*, (c)* ***NC****, and (b) their equimolar mixture. Host conformers* ***NC-I*** *(81%) and* ***NC-II*** *(19%) coexist.*

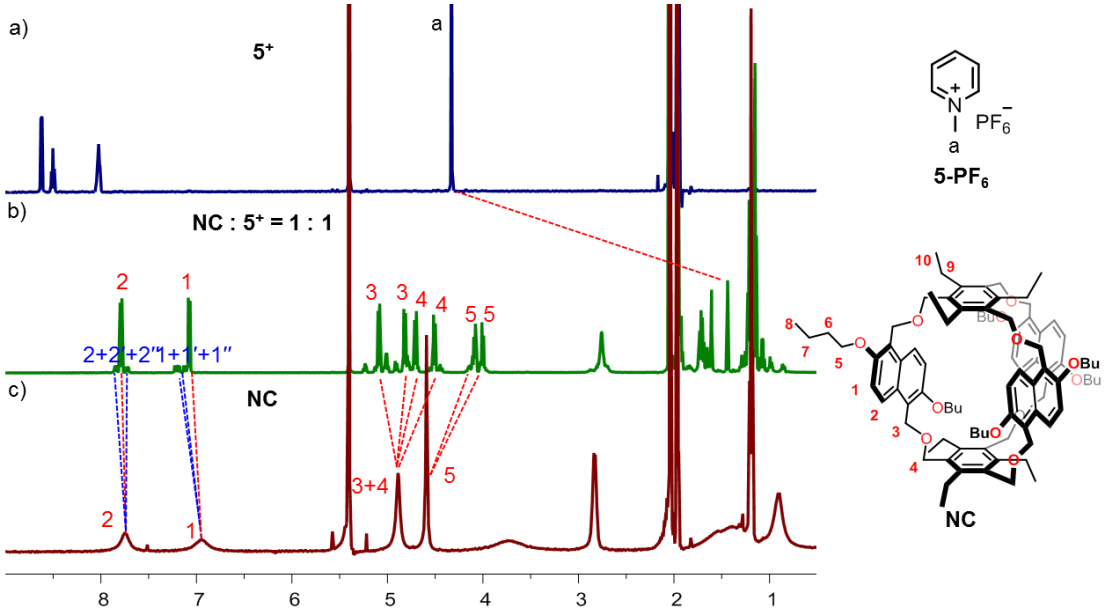

Figure S18. *Full ^{1}H NMR spectra (500 MHz, CD_2Cl_2:CD_3CN = 1:1, 2.0 mM, 298 K) of (a)* ***5-PF$_6$****, (c)* ***NC****, and (b) their equimolar mixture. Host conformers* ***NC-I*** *(78%) and* ***NC-II*** *(22%) coexist.*

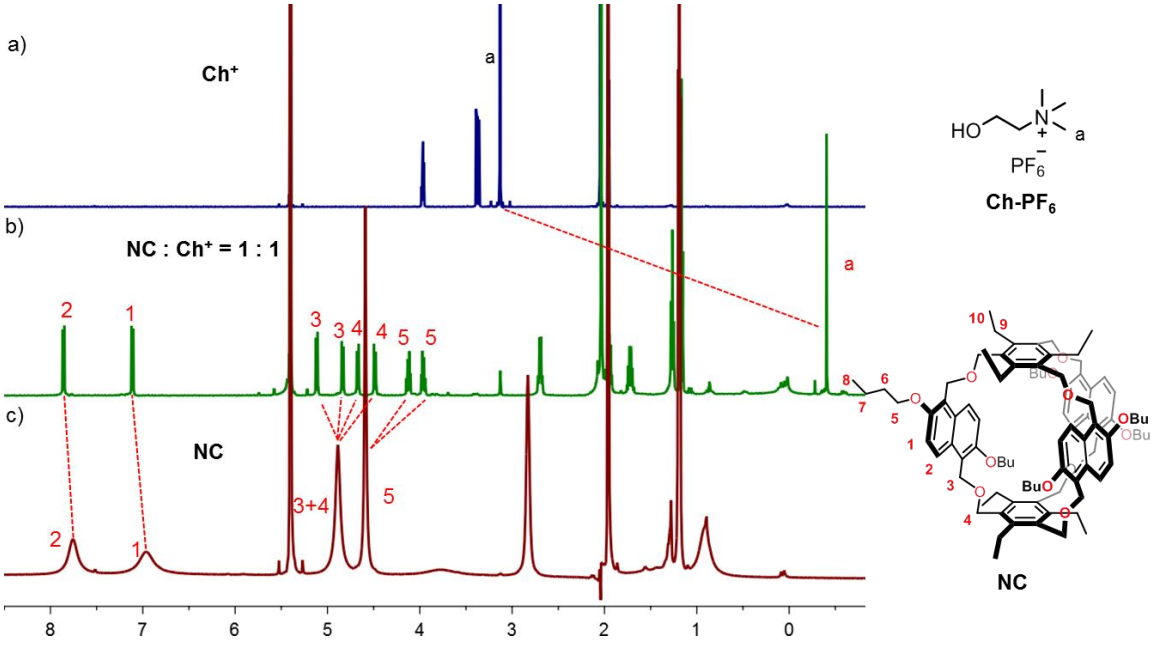

Figure S19. *Full ^{1}H NMR spectra (700 MHz, CD_2Cl_2:CD_3CN = 1:1, 2.0 mM, 298 K) of (a)* ***Ch-PF$_6$****, (c)* ***NC****, and (b) their equimolar mixture. Host conformer* ***NC-I*** *exists as the dominating conformer (> 95%).*

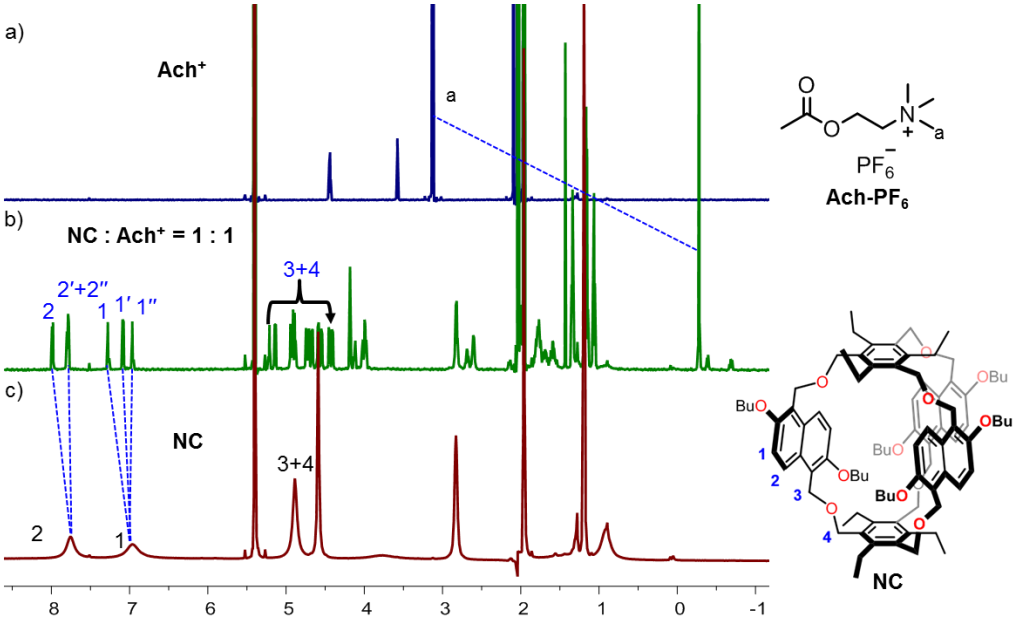

Figure S20. *Full* ^{1}*H NMR spectra (700 MHz,* CD_2Cl_2*:*CD_3CN *= 1:1, 2.0 mM, 298 K) of (a)* ***Ach****-*PF_6*, (c)* ***NC****, and (b) their equimolar mixture. The aromatic protons of* ***NC*** *appear as six doublets in agreement with an almost exclusive formation of complexes in which the host adopts the* ***NC-II*** *conformation. It is quite remarkable that two related compounds such as choline and acetylcholine exhibit such a pronouncedly different preference for the two host conformations.*

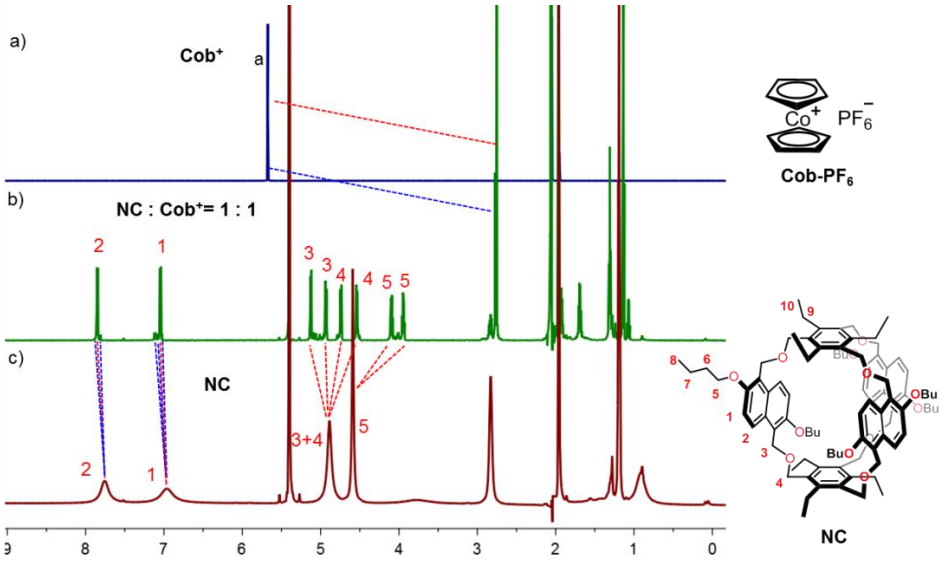

Figure S21. *Full* ^{1}*H NMR spectra (700 MHz,* CD_2Cl_2*:*CD_3CN *= 1:1, 2.0 mM, 298 K) of (a)* ***Cob****-*PF_6*, (c)* ***NC****, and (b) their equimolar mixture. Host conformers* ***NC-I*** *(72%) and* ***NC-II*** *(28%) coexist.*

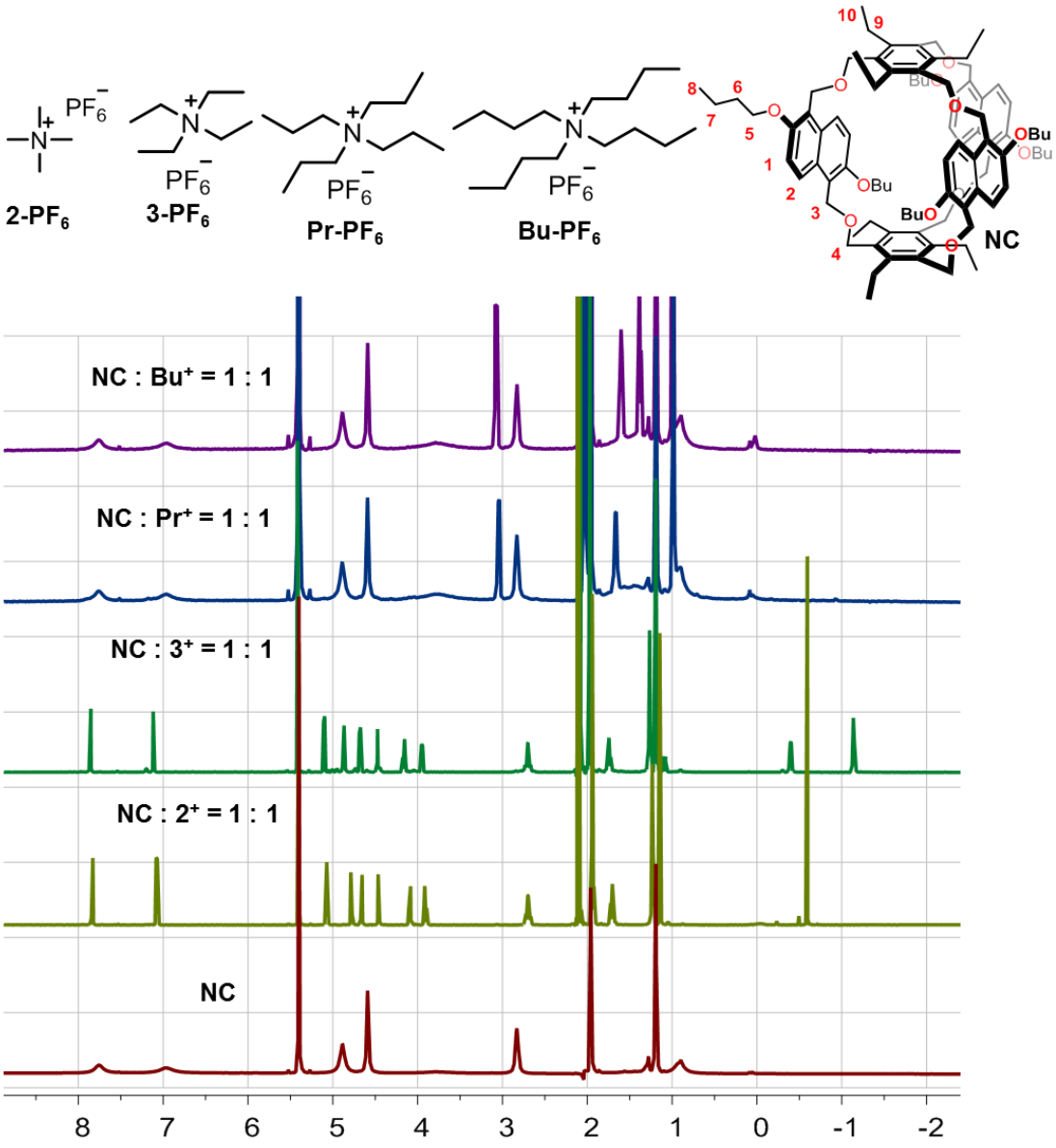

Figure S22 ^{1}H NMR spectra (700 MHz, CD_2Cl_2:CD_3CN=1:1, 2.0 mM, 298 K) of **NC** in the absence and the presence of one equivalent of individual guest **2-PF$_6$**, **3-PF$_6$**, **Pr$_4$N-PF$_6$**, or **Bu$_4$N-PF$_6$**. Methylene protons on the CH_2-O-CH_2 linkers are split into four doublets for **2-PF$_6$** and **3-PF$_6$**, indicating they are encapsulated inside the cavity of NC. No obvious splitting was observed for **Pr$_4$N-PF$_6$** and **Bu$_4$N-PF$_6$**, suggesting that they are too large to fit into the cavity of **NC**.

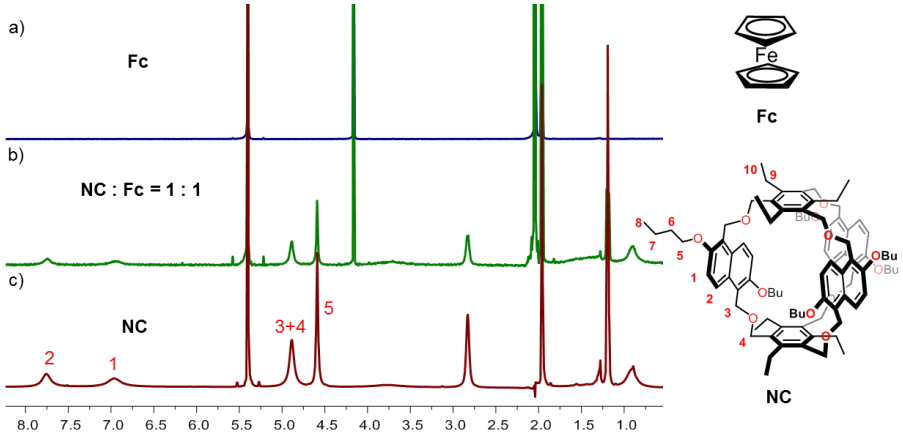

Figure S23. *^{1}H NMR spectra (500 MHz, CD_2Cl_2:CD_3CN = 1:1, 2.0 mM, 298 K) of a)* ***Fc****, b)* ***NC*** *with one equivalent of* ***Fc****, c)* ***NC****. The spectrum obtained for the host-guest mixture is clearly a superposition of the two spectra of free host and free guest. Consequently, neutral* ***Fc*** *is not encapsulated in the* ***NC*** *cavity.*

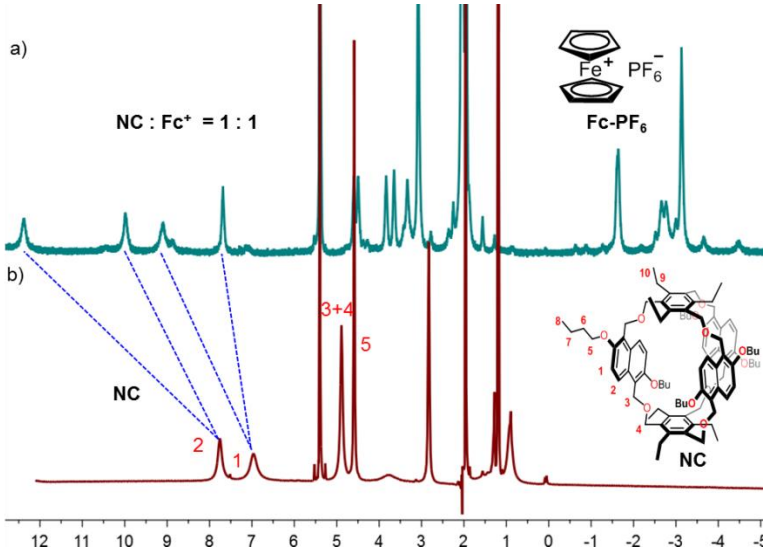

Figure S24. *Full ^{1}H NMR spectra (700 MHz, CD_2Cl_2:CD_3CN = 1:1, 2.0 mM, 298 K) of (a)* ***NC*** *with one equivalent of* ***Fc****-PF_6, and (b) free* ***NC****. Peak broadening, the strong downfield shifts of the aromatic cage signals and upfield shifts of cage signals into the 0 to -5ppm range are not only due host-guest complex formation, but also to the paramagnetic nature of ferrocenium. The ferrocenium paramagnetism also made it impossible to obtain an NMR spectrum of free ferrocenium for comparison.*

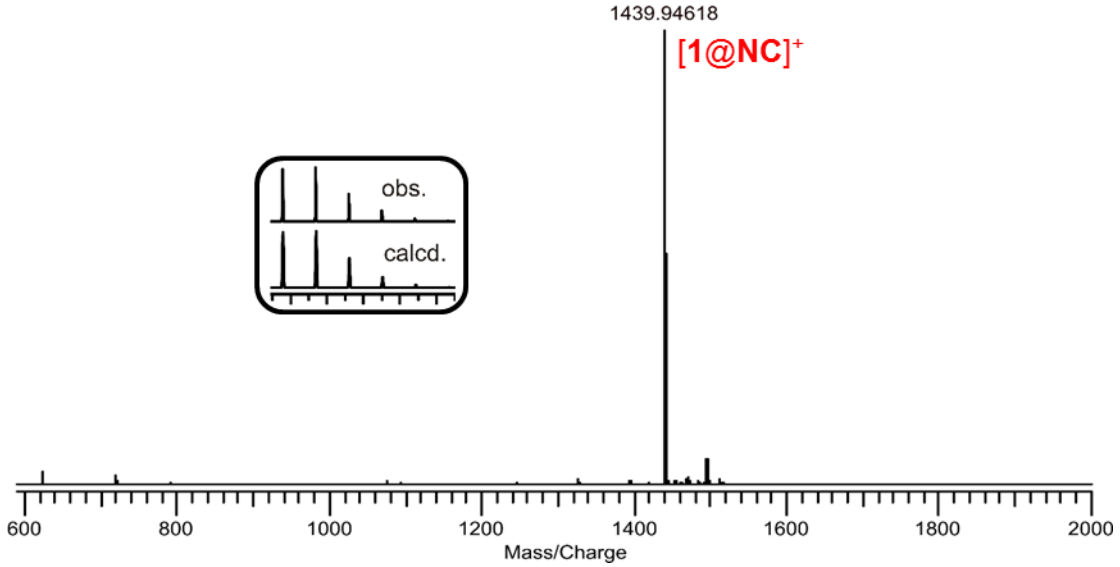

***Figure S25**. ESI-FTICR mass spectrum of a 1:1 mixture of **1**-PF_6 and **NC** (20 μM each) in dichloromethane/acetonitrile (1:1). The mass spectrum indicates **1**$^+$ and **NC** to form a 1:1 complex.*

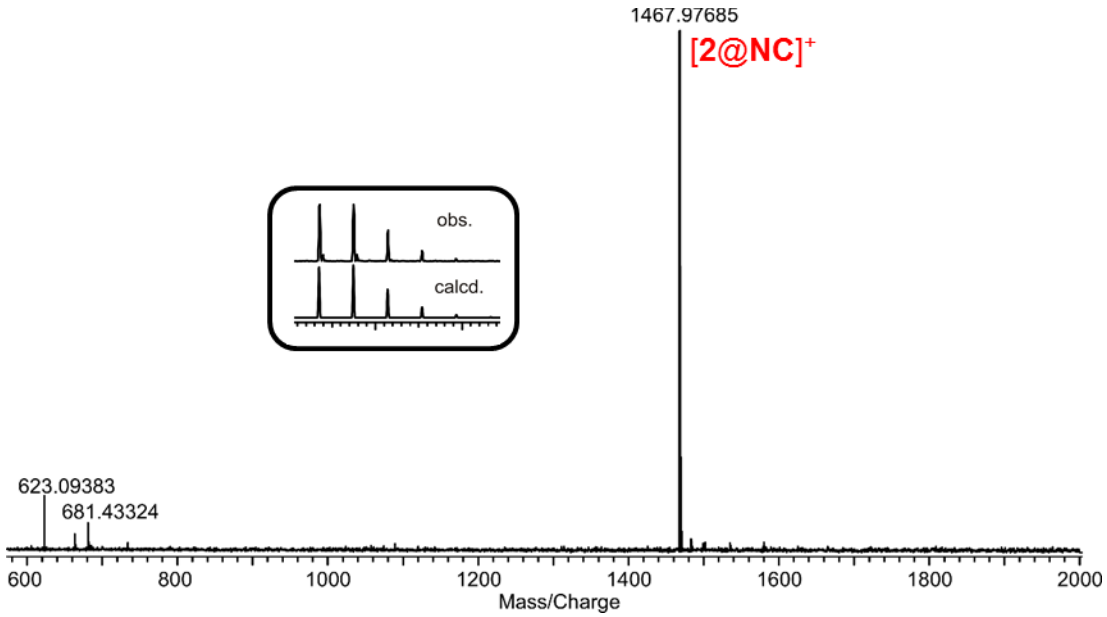

***Figure S26**. ESI-FTICR mass spectrum of a 1:1 mixture of **2**-PF_6 and **NC** (20 μM each) in dichloromethane/acetonitrile (1:1). The mass spectrum indicates **2**$^+$ and **NC** to form a 1:1 complex.*

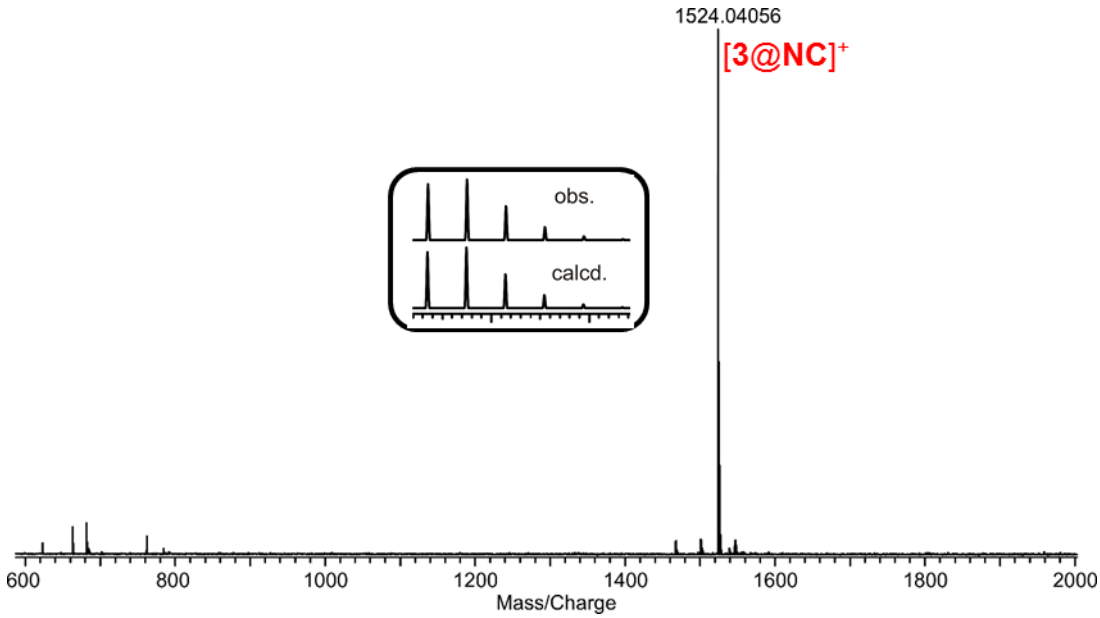

***Figure S27**. ESI-FTICR mass spectrum of a 1:1 mixture of **3**-PF_6 and **NC** (20 μM each) in dichloromethane/acetonitrile (1:1). The mass spectrum indicates **3**$^+$ and **NC** to form a 1:1 complex.*

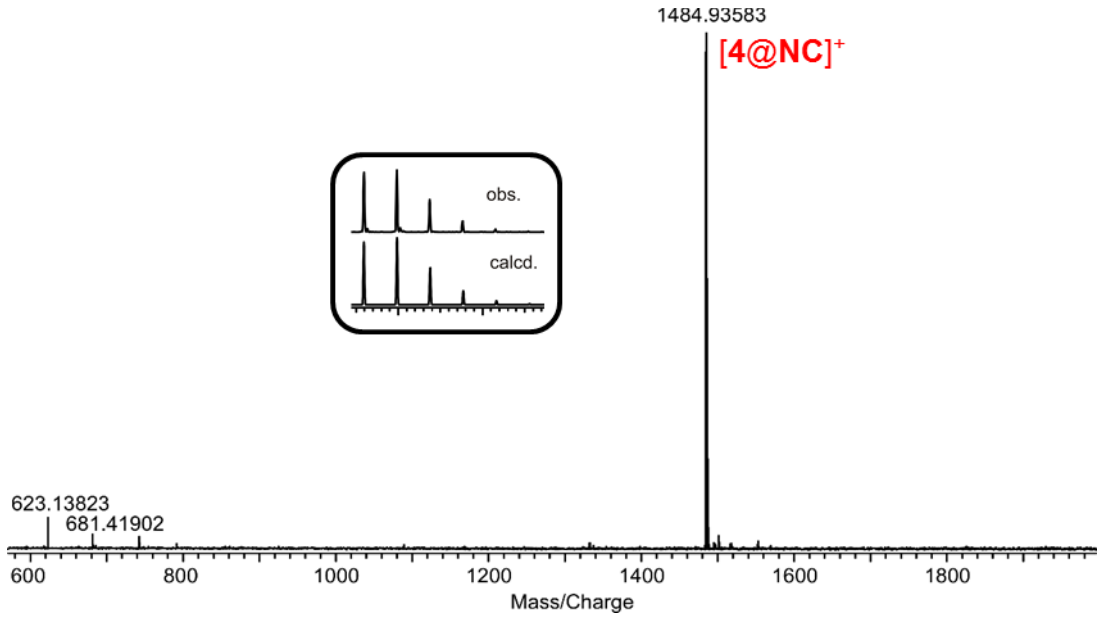

***Figure S28**. ESI-FTICR mass spectrum of a 1:1 mixture of **4**-PF_6 and **NC** (20 μM each) in dichloromethane/acetonitrile (1:1). The mass spectrum indicates **4**$^+$ and **NC** to form a 1:1 complex.*

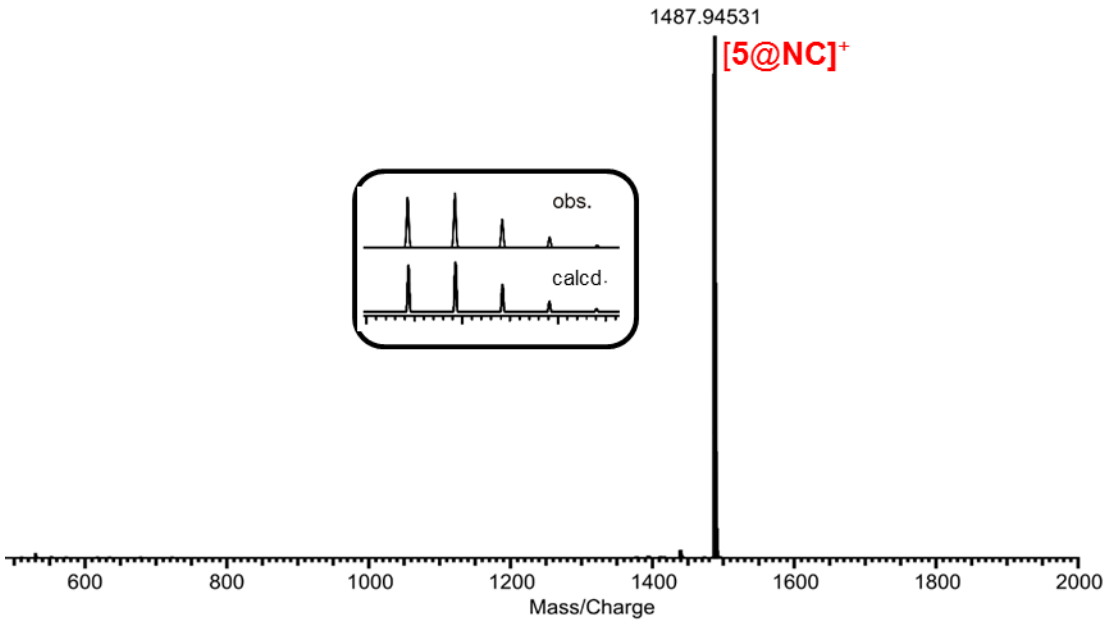

Figure S29. *ESI-FTICR mass spectrum of a 1:1 mixture of* ***5***-PF_6 *and* ***NC*** *(20 μM each) in dichloromethane/acetonitrile (1:1). The mass spectrum indicates* $\mathbf{5}^+$ *and* ***NC*** *to form a 1:1 complex.*

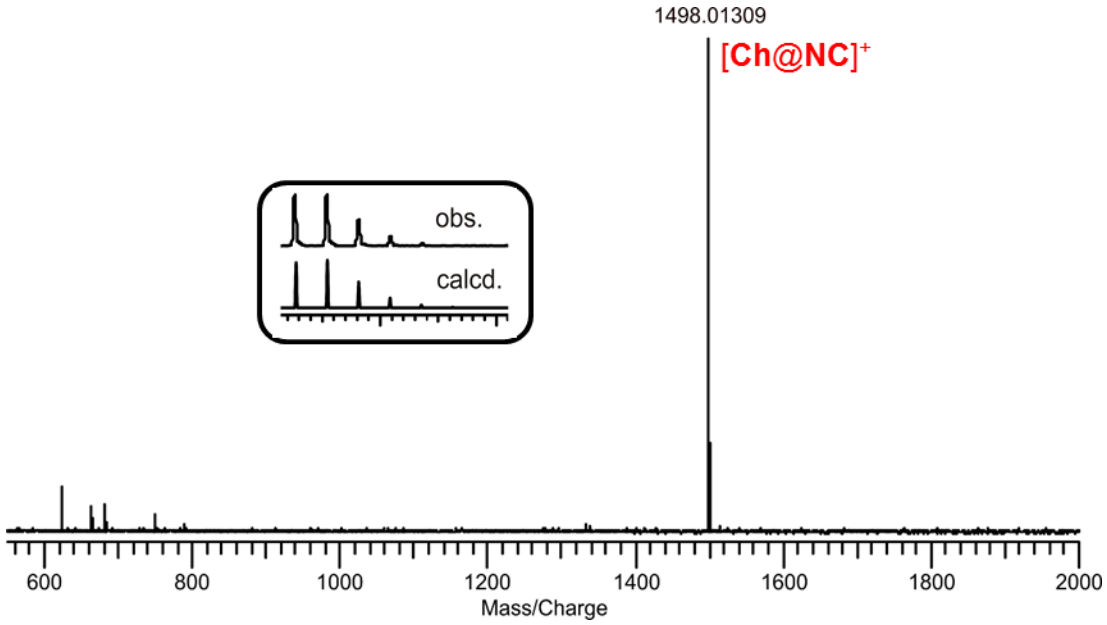

Figure S30. *ESI-FTICR mass spectrum of a 1:1 mixture of* ***Ch***-PF_6 *and* ***NC*** *(20 μM each) in dichloromethane/acetonitrile (1:1). The mass spectrum indicates* $\mathbf{Ch}^+$ *and* ***NC*** *to form a 1:1 complex.*

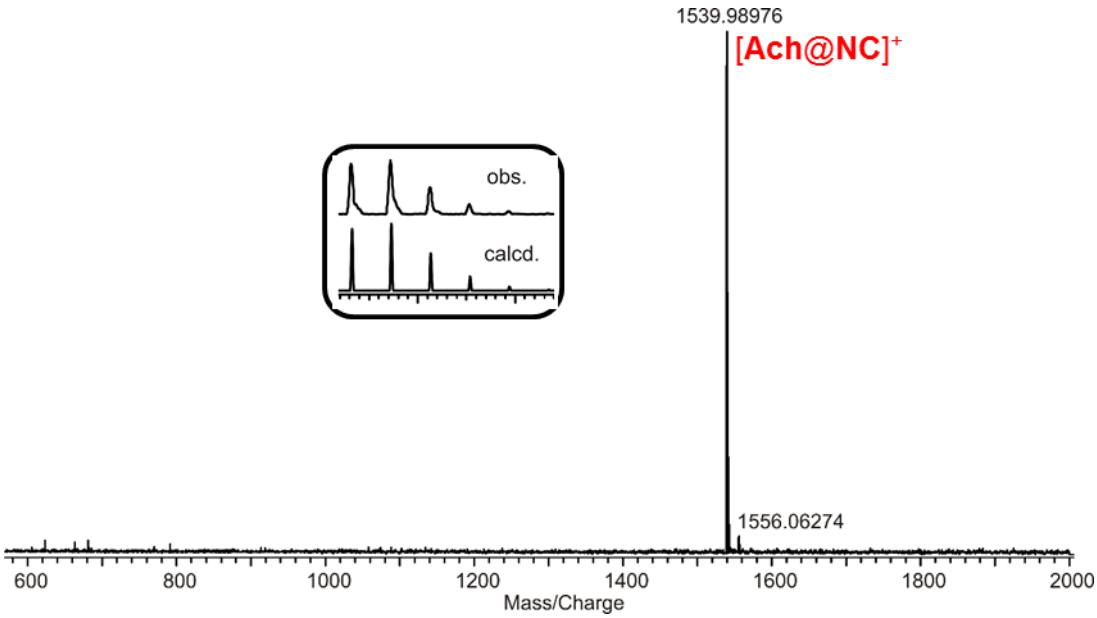

Figure S31. *ESI-FTICR mass spectrum of a 1:1 mixture of* ***Ach***-PF_6 *and* ***NC*** *(20 μM each) in dichloromethane/acetonitrile (1:1). The mass spectrum indicates* $\mathbf{Ach}^+$ *and* ***NC*** *to form a 1:1 complex.*

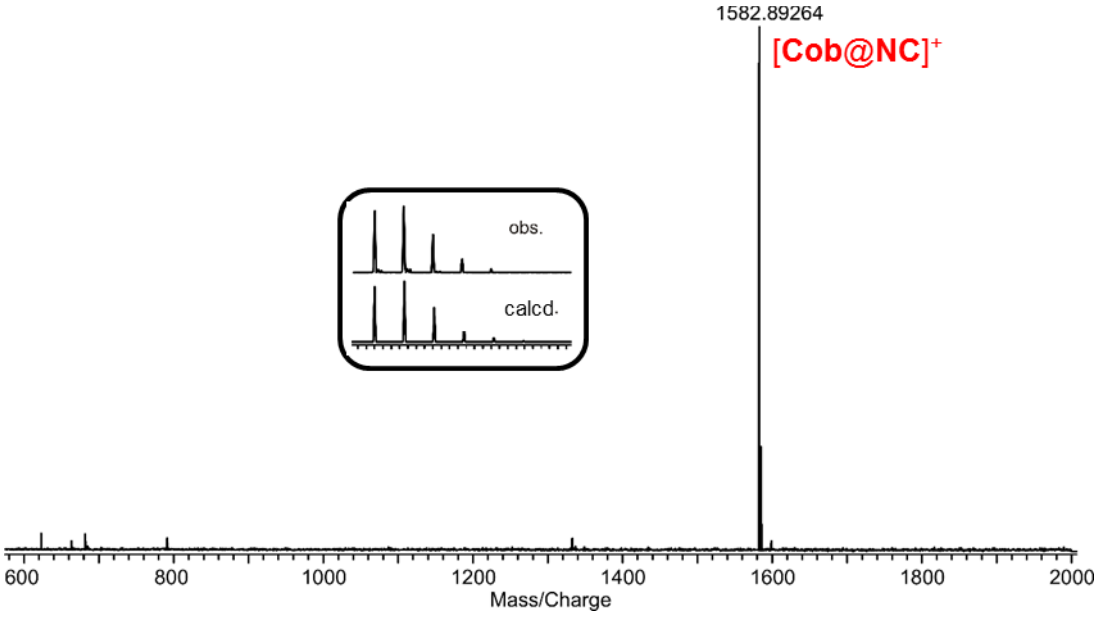

Figure S32. *ESI-FTICR mass spectrum of a 1:1 mixture of* ***Cob***-PF_6 *and* ***NC*** *(20 μM each) in dichloromethane/acetonitrile (1:1). The mass spectrum indicates* $\mathbf{Cob}^+$ *and* ***NC*** *to form a 1:1 complex.*

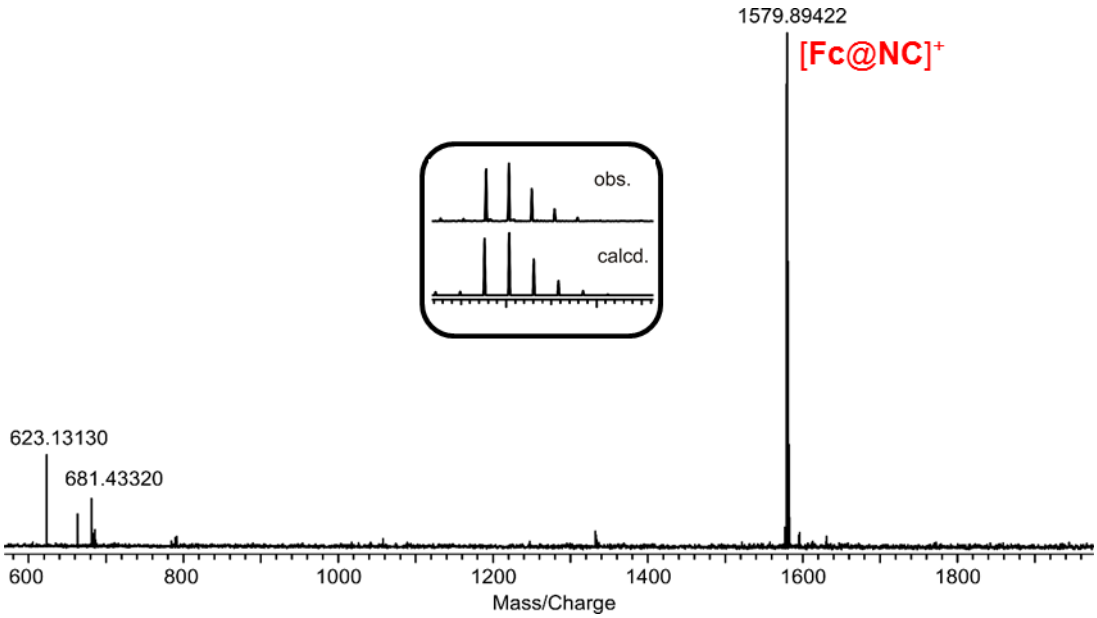

Figure S33*. ESI-FTICR mass spectrum of a 1:1 mixture of* ***Fc****-PF_6 and* ***NC*** *(20 μM each) in dichloromethane/acetonitrile (1:1). The mass spectrum indicates* $\boldsymbol{Fc}^+$ *and* ***NC*** *to form a 1:1 complex.*

5. Isothermal Titration Calorimetry

ITC experiments were carried out by using two ITC instruments. In both cases, the dry solvent mixture of 1,2-dichloroethane (DCE) and acetonitrile (ACN) (1:1, v/v) was degassed at 298 K before use. 1,2-Dichloroethane was used instead of dichloromethane, because the high volatility of dichloromethane leads to solvent evaporation during the course of the experiment and thus would lead to a change in solvent composition over time and another unwanted heat contribution.

The first instrument is a Nano ITC LV – 190 μL (Waters GmbH, TA Instruments, Eschborn, Germany). In a typical experiment, a 190 μL solution of **NC** was placed in the sample cell at a concentration of 0.16 mM, and 50 μL of a solution of the hexafluorophosphate salt (1.0 mM in the same solvent) was placed in the injection syringe. The titrations consisted of 25 consecutive injections of 1.96 μL with 5 min intervals between injections. Heats of dilution, measured by titration of the salt into the sample cell with blank solvent, were subtracted from each data set. The data were analyzed using the instrument's internal software package and fitted with a 1:1 binding model. Each titration was conducted three times and the measured values for K and ΔH were averaged.

The second instrument is a TAM III microcalorimeter (Waters GmbH, TA Instruments, Eschborn, Germany). On this instrument, higher measuring concentrations are needed. This allows direct titrations only up to a binding constant limit of ca. 10^6. Hence, we conducted direct titrations only for guest $\mathbf{1}^+$. The binding constants of all other guests were determined by competition experiments between $\mathbf{1}^+$ and the guest on this instrument. In the direct titration experiment, an 800 μL solution of **NC** (1.1 mM) was placed in the sample cell and 250 μL of a solution of guest $\mathbf{1}^+$ (8.0 mM) were put into the syringe. In a competition experiment, an 800 μL solution of **NC** (1.1 mM) and $\mathbf{1}^+$ (32.0 mM) was placed in the sample cell and 250 μL of a solution of a guest (8.0 mM) were put into the syringe. The titrations consisted of 32 consecutive injections of 8 μL each with a 10 min interval between injections. The heat flow generated in the sample cell is measured as a differential signal between sample and reference cell. Hence, an exothermic event results in a positive and an endothermic in a negative heat flow. The data were analysed using the instrument's internal software package and fitted with a 1:1 binding model. Each titration was conducted three times and the measured values for K and ΔH were averaged.

The measured competition constants K_{comp} for the equilibrium in eq. (1) and the corresponding enthalpies ΔH_{comp} were converted into K_a and ΔH according to equations (2) and (3):

(1) **G1@NC** + **G2** ⇌ **G2@NC** + **G1**

(2) $K_{comp} = \frac{K_2}{K_1 \cdot [G1]+1}$

(3) $\Delta H_{comp} = \Delta H_2 - \Delta H_1 \cdot \frac{K1 \cdot [G1]}{K_1 \cdot [G1]+1}$

Table S2*. Thermodynamic association data as obtained from ITC titrations (1,2-dichloroethane/ acetonitrile = 1:1, 298 K, the counterion is PF_6^-).*

Guest	K_{comp} [c]	K_a (M^{-1})	n	ΔG (kJ/mol)	ΔH_{comp} [c] (kJ/mol)	ΔH (kJ/mol)	$T\Delta S$ (kJ/mol)
1^{+} [b]		(4.1 ± 0.4) ×10^5	1	-32.0 ± 0.3		-37.1 ± 1.4	-5.1 ± 1.7
2^{+} [a]		(1.6 ± 0.3) ×10^7	1	-41.2 ± 0.3		-23.8 ± 0.5	17.4 ± 0.8
3^{+} [a]		(3.7 ± 0.4) ×10^7	1	-43.2 ± 0.3		-52.8 ± 1.2	-9.6 ± 1.5
4^{+} [a]		(8.9 ± 0.8) ×10^6	1	-39.7 ± 0.2		-34.6 ± 0.9	5.1 ± 1.1
5^{+} [a]		>10^8		-[d]		-30.4 ± 0.2	-[d]
5^{+} [b]	(6.1 ± 2.0) ×10^4	(7.6 ± 2.4) ×10^8	1	-50.7 ± 0.7	9.0 ± 0.5	-28.1 ± 2.0	22.6 ± 2.7
Ch^{+} [a]		(2.8 ± 0.2) ×10^7	1	-42.5 ± 0.2		-35.9 ± 0.8	6.6 ± 1.0
Ach^{+} [a]		>10^9	1	-[d]		-45.5 ± 0.3	-[d]
Ach^{+} [b]	(5.1 ± 0.5) ×10^5	(6.7 ± 2.1) ×10^9	1	-56.1 ± 0.7	-5.1 ± 0.7	-42.2 ± 2.0	13.9 ± 2.6
Cob^{+} [a]		>10^9	1	-[d]		-45.7 ± 0.3	-[d]
Cob^{+} [b]	(4.0 ± 0.4) ×10^5	(6.1 ± 1.9) ×10^9	1	-55.8 ± 0.7	-10.2 ± 3.0	-47.0 ± 3.0	8.8 ± 4.7

*[a] Determined directly by Nano ITC titrations; [b] direct titration of **1**$^{+}$ and competition experiments were conducted by TAM III microcalorimeter; [c] for the definition of K_{comp} and ΔH_{comp} see eq. 2 and 3 above; [d] not determined, as the binding constant is approaching the limits of direct ITC titrations and thus is only an estimate. Although the enthalpy can be obtained quite precisely, the uncertainty in binding constant and consequently □G and □S is high.*

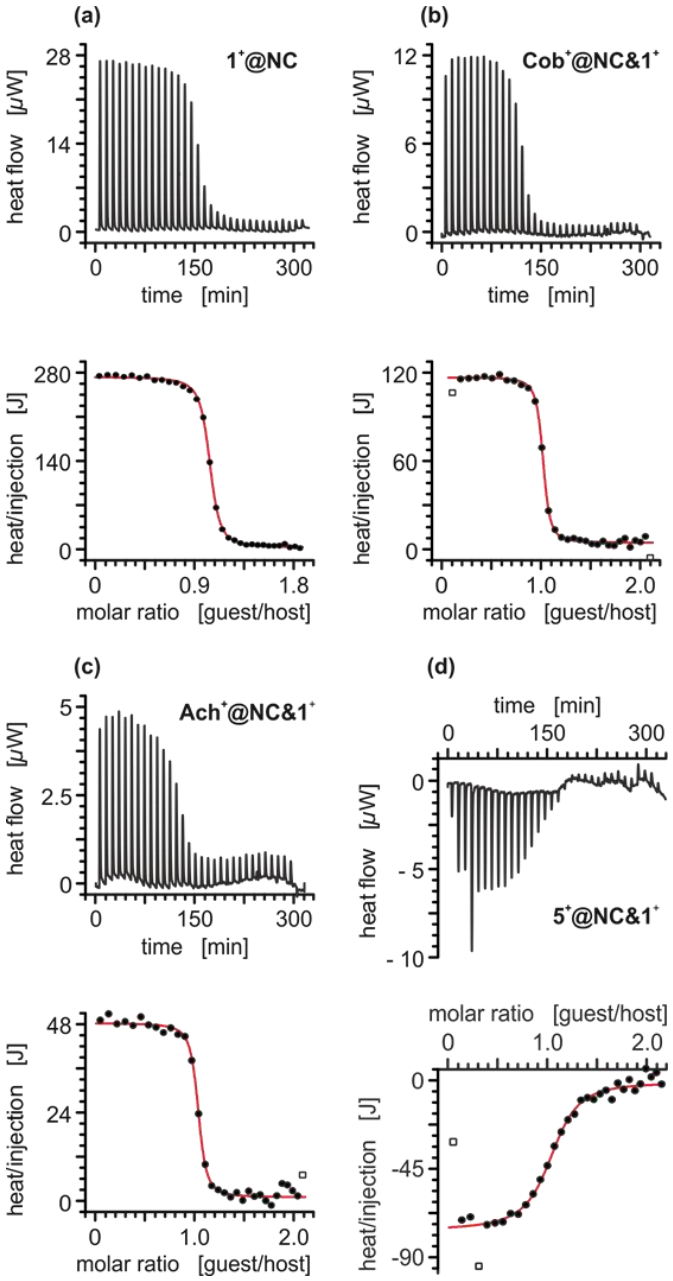

Figure S34*. Titration plots (top: heat flow versus time; bottom: heat/volume versus guest/host ratio) obtained from ITC experiments at 298 K in 1,2-dichloroethane/acetonitrile 1:1 (v/v). (a) direct titration with* ***NC*** *and* ***1****-PF_6; (b) competition experiment vessel:* ***NC*** *and* ***1****-PF_6; syringe:* ***Cob****-PF_6; (c) competition experiment vessel:* ***NC*** *and* ***1****-PF_6; syringe:* ***Ach****-PF_6; (d) competition experiment vessel:* ***NC and 1****-PF_6; syringe:* ***5****-PF_6 (data points marked with a non-filled square were not considered in the fitting process).*

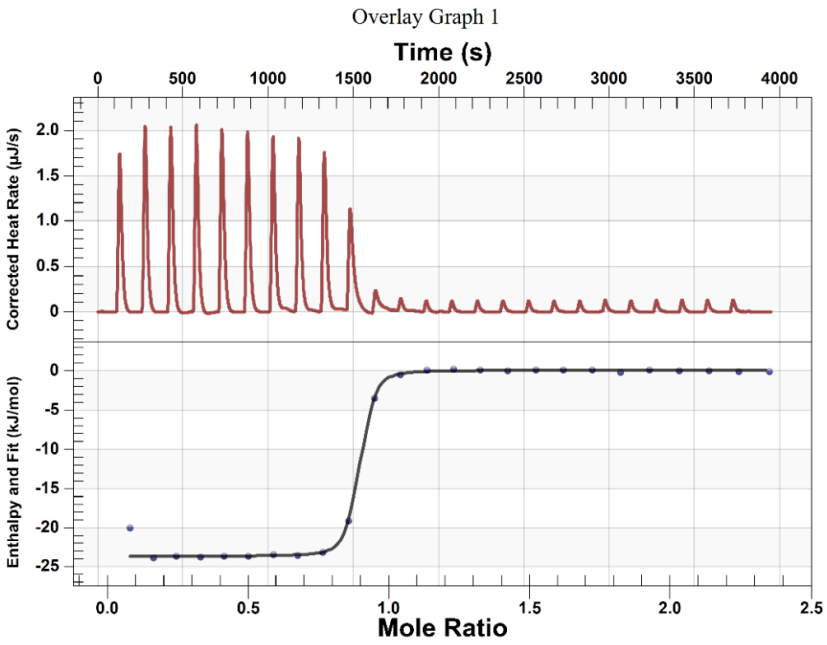

Figure S35. *Titration plots (heat flow versus time and heat versus guest/host ratio) obtained from ITC experiments of* ***NC*** *with* ***2***-PF_6 *in the 1:1 mixture of 1,2-dichloroethane and* CH_3CN.

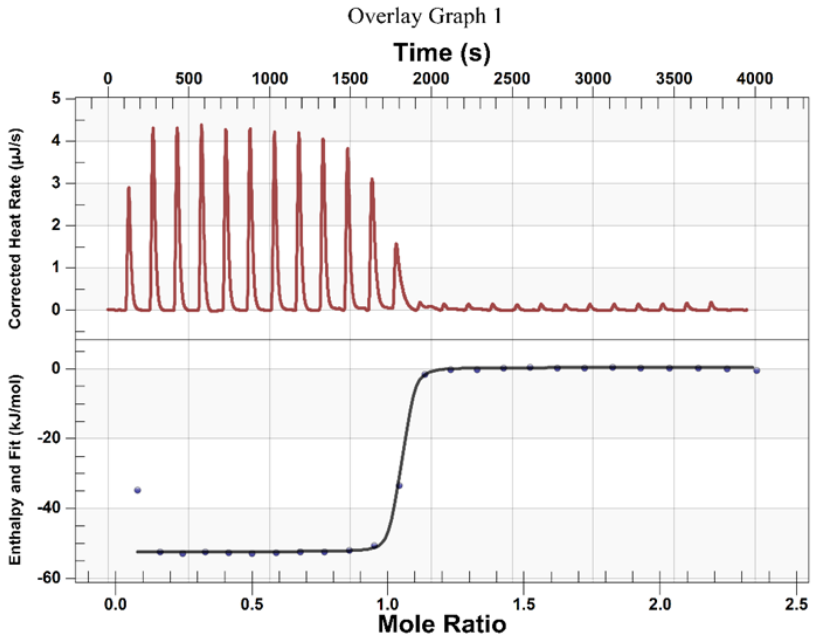

Figure S36. *Titration plots (heat flow versus time and heat versus guest/host ratio) obtained from ITC experiments of* ***NC*** *with* ***3***-PF_6 *in the 1:1 mixture of 1,2-dichloroethane and* CH_3CN.

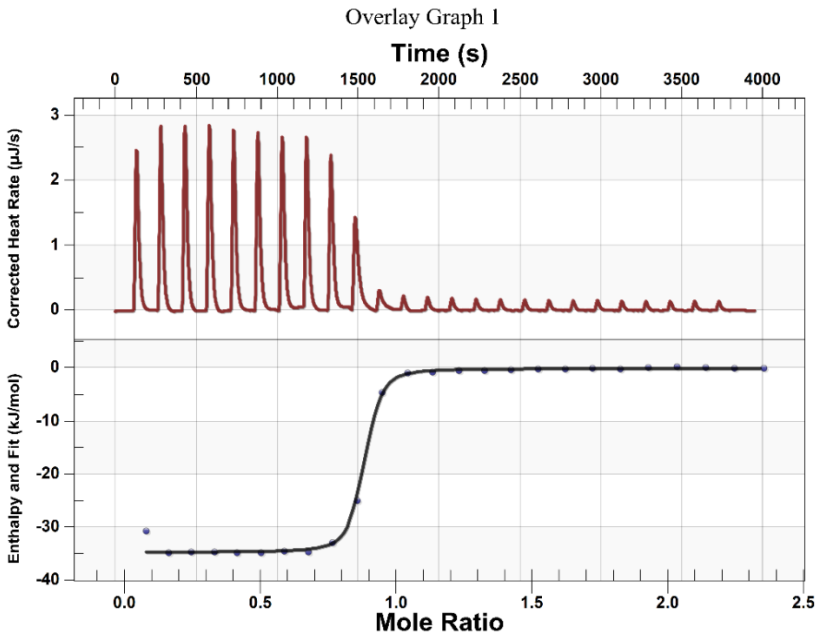

***Figure S37**. Titration plots (heat flow versus time and heat versus guest/host ratio) obtained from ITC experiments of **NC** with **4**-PF_6 in the 1:1 mixture of 1,2-dichloroethane and CH_3CN.*

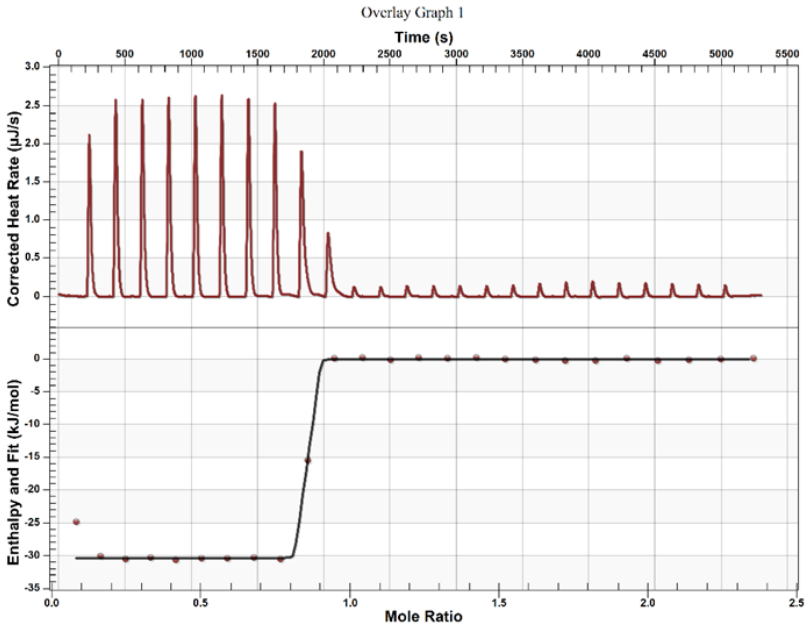

***Figure S38**. Titration plots (heat flow versus time and heat versus guest/host ratio) obtained from ITC experiments of **NC** with **5**-PF_6 in the 1:1 mixture of 1,2-dichloroethane and CH_3CN. The binding constant approaches the limits of direct Nano ITC titrations and can only be estimated.*

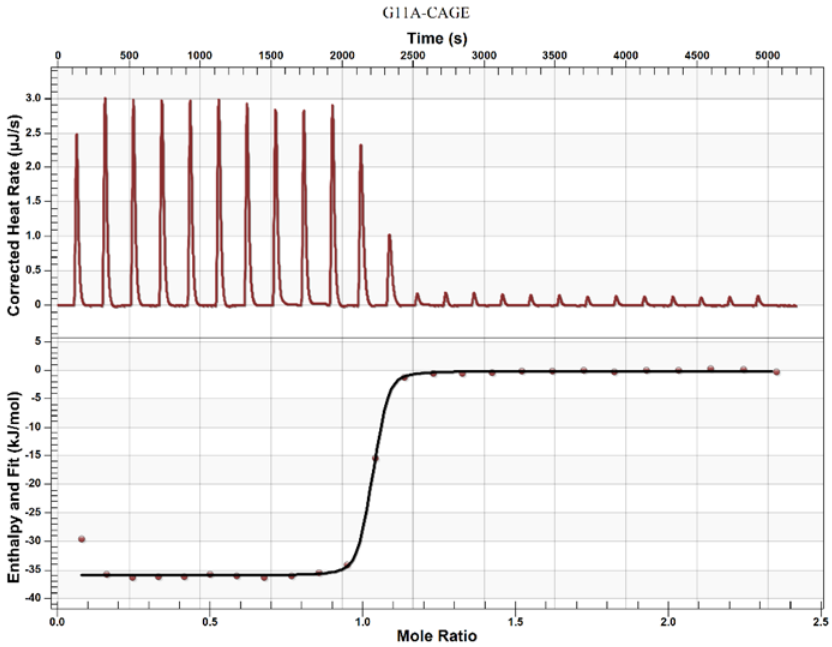

Figure S39. *Titration plots (heat flow versus time and heat versus guest/host ratio) obtained from ITC experiments of* ***NC*** *with* ***Ch****-PF_6 in the 1:1 mixture of 1,2-dichloroethane and CH_3CN.*

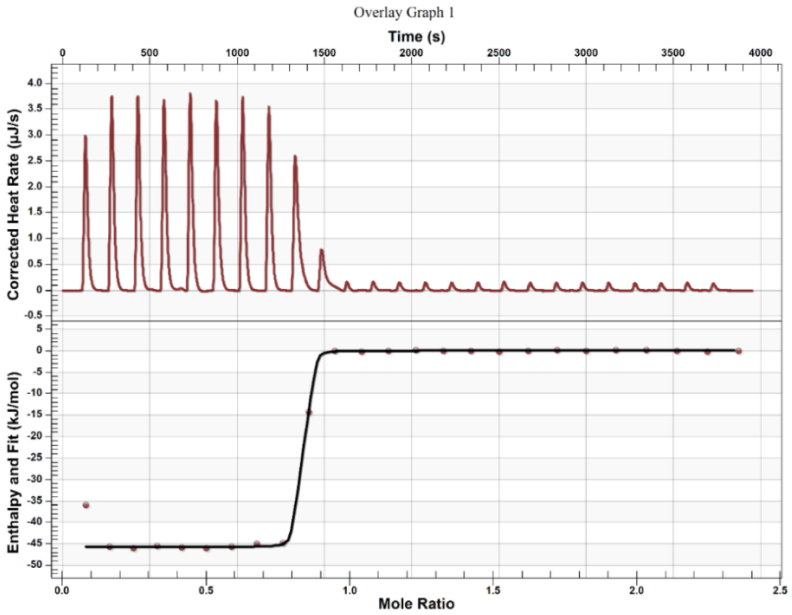

Figure S40. *Titration plots (heat flow versus time and heat versus guest/host ratio) obtained from ITC experiments of* ***NC*** *with* ***Ach****-PF_6 in the 1:1 mixture of 1,2-dichloroethane and CH_3CN. The binding constant approaches the limits of direct Nano ITC titrations and can only be estimated.*

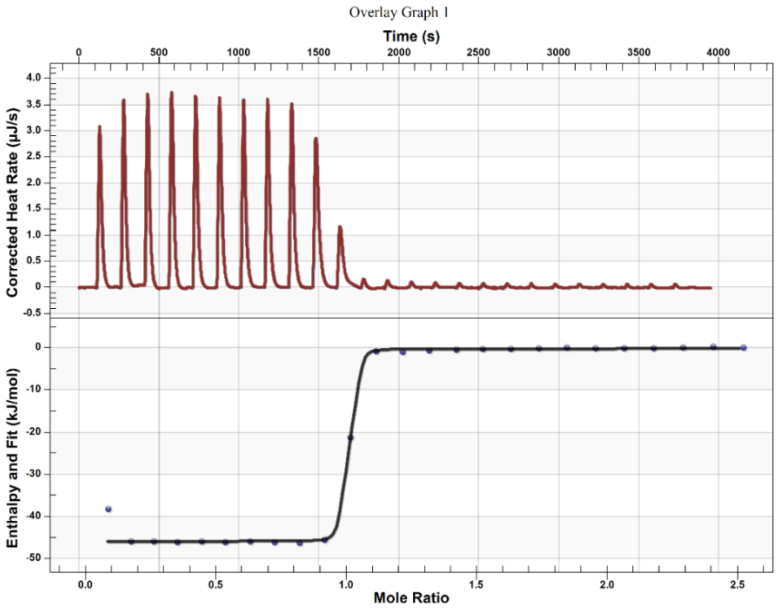

Figure S41. *Titration plots (heat flow versus time and heat versus guest/host ratio) obtained from ITC experiments of* ***NC*** *with* ***Cob****-PF_6 in the 1:1 mixture of 1,2-dichloroethane and CH_3CN. The binding constant approaches the limits of direct Nano ITC titrations and can only be estimated.*

6. 2D NMR Spectra of the Complexes

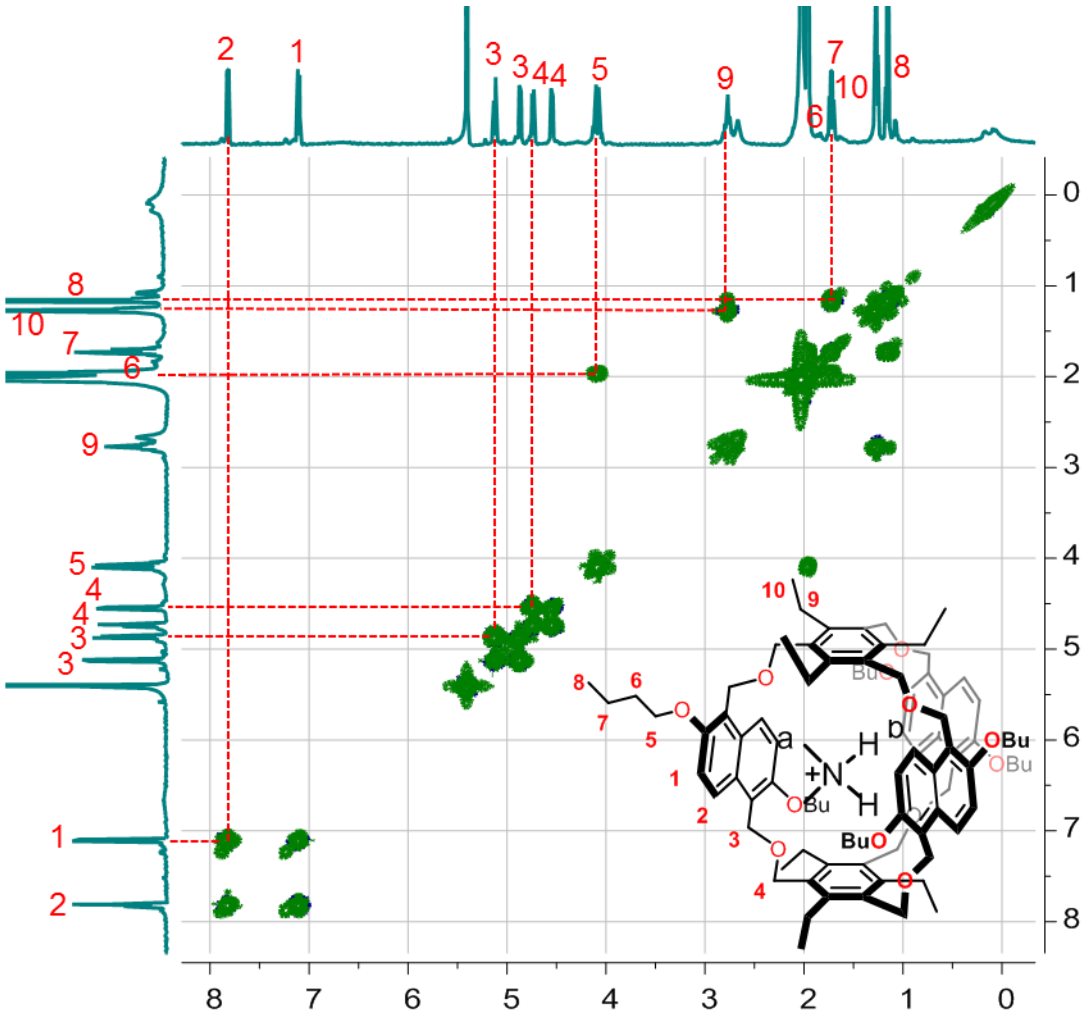

Figure S42. *Full ^{1}H, ^{1}H-COSY NMR spectrum (500 MHz, CD_2Cl_2:CD_3CN = 1:1, 2.0 mM, 298 K) of [**1**$^{+}$@**NC**]PF_6^{-}.*

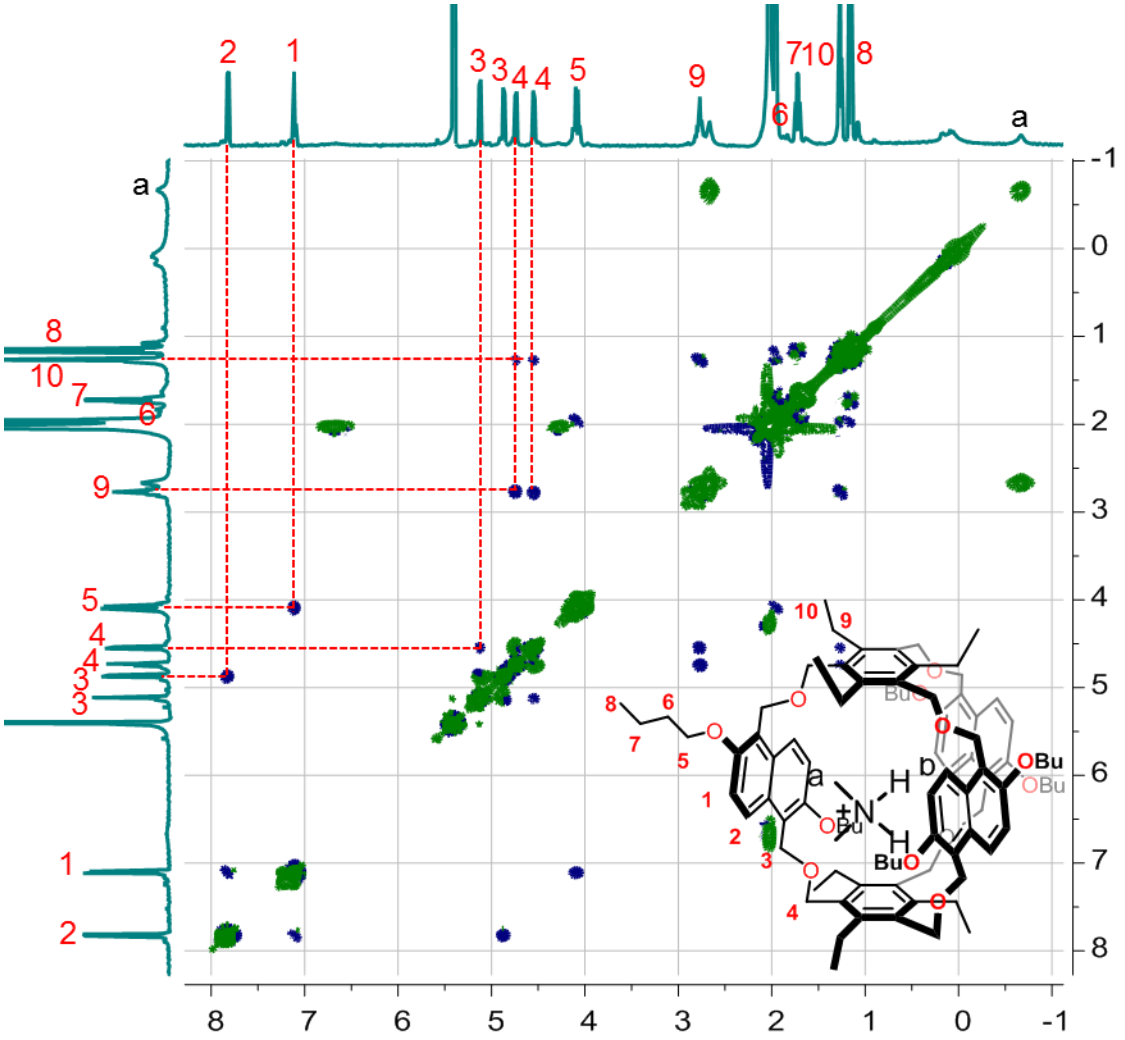

Figure S43. *Full ^{1}H, ^{1}H-ROESY NMR spectrum (500 MHz, CD_2Cl_2:CD_3CN = 1:1, 2.0 mM, 298 K) of [**1**$^{+}$@**NC**]PF_6^{-}. No NOE cross peaks were detected between the host protons and the guest protons, presumably because the signals of the guest is broadened and it is difficult to give a sharp NOE peak for detection.*

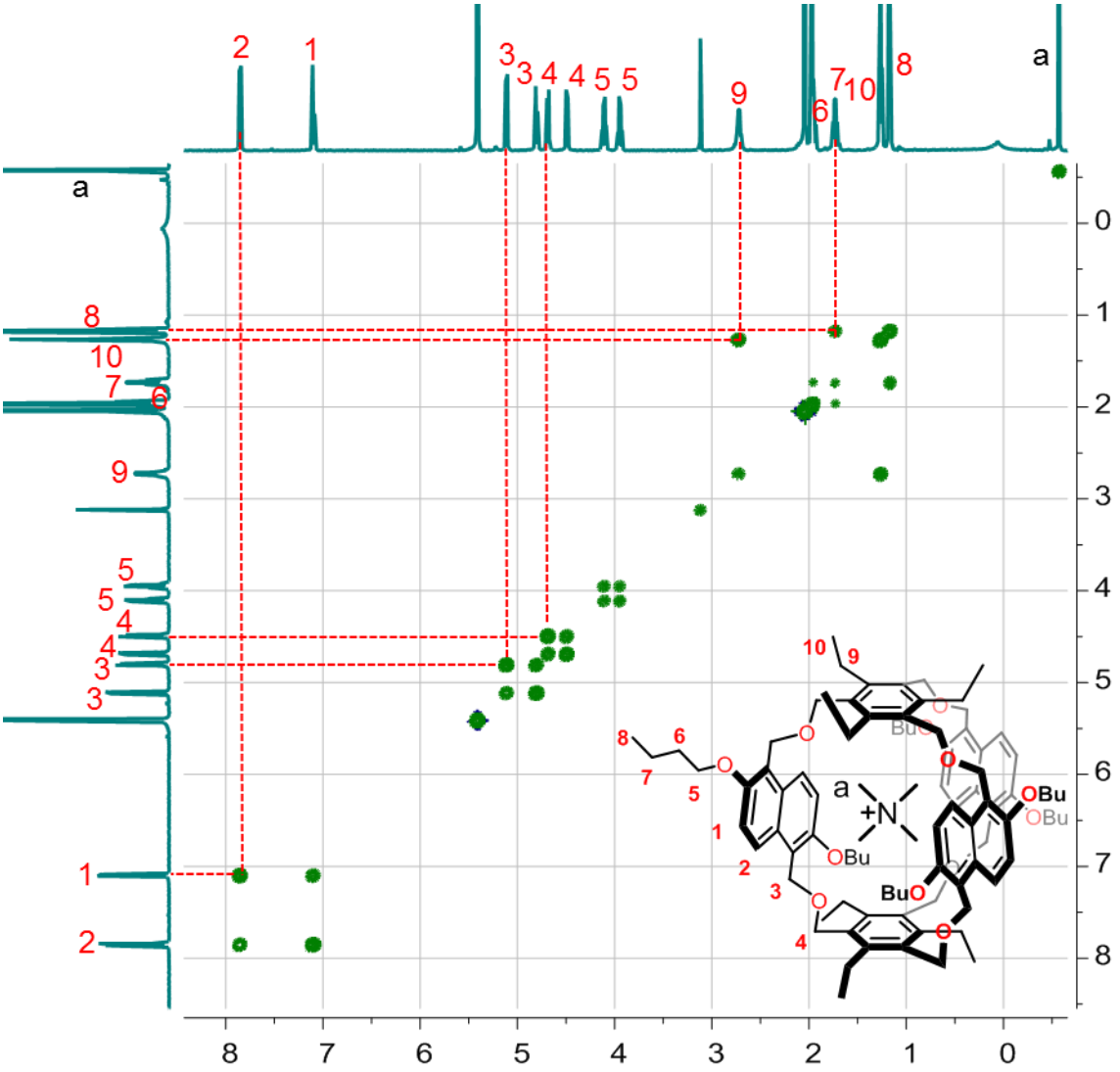

Figure S44. *Full ^{1}H, ^{1}H-COSY NMR spectrum (500 MHz, CD_2Cl_2:CD_3CN = 1:1, 2.0 mM, 298 K) of [**2**$^{+}$@**NC**]PF_6^{-}.*

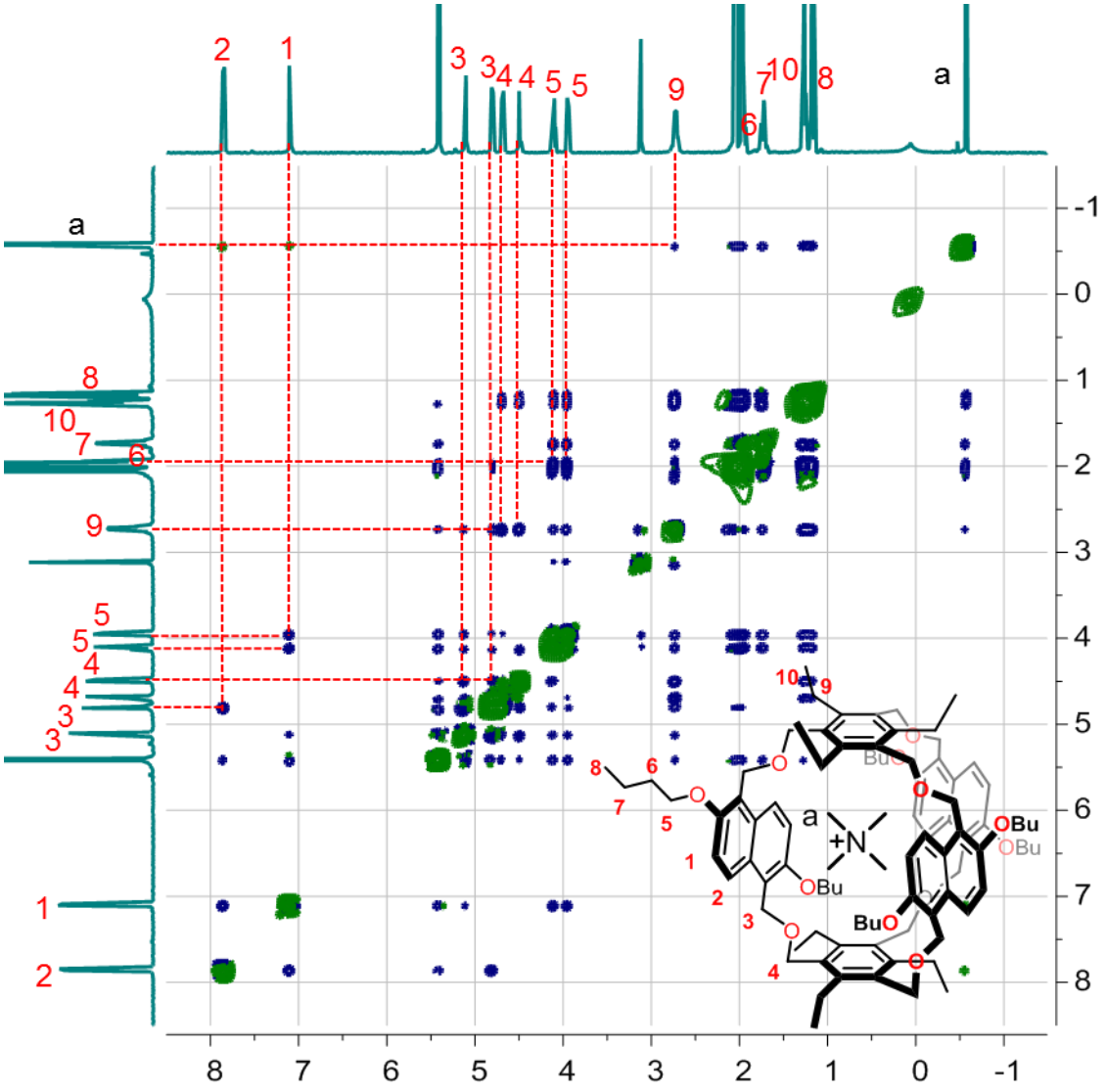

Figure S45. *Full ^{1}H, ^{1}H-ROESY NMR spectrum (500 MHz, CD_2Cl_2:CD_3CN = 1:1, 2.0 mM, 298 K) of [**2**$^{+}$@**NC**]PF_6^{-}. NOE cross peaks exist between protons 9 and the guest protons a, supporting the guest is encapsulated inside the cavity of **NC**. This is because that protons 9 point towards the cavity space.*

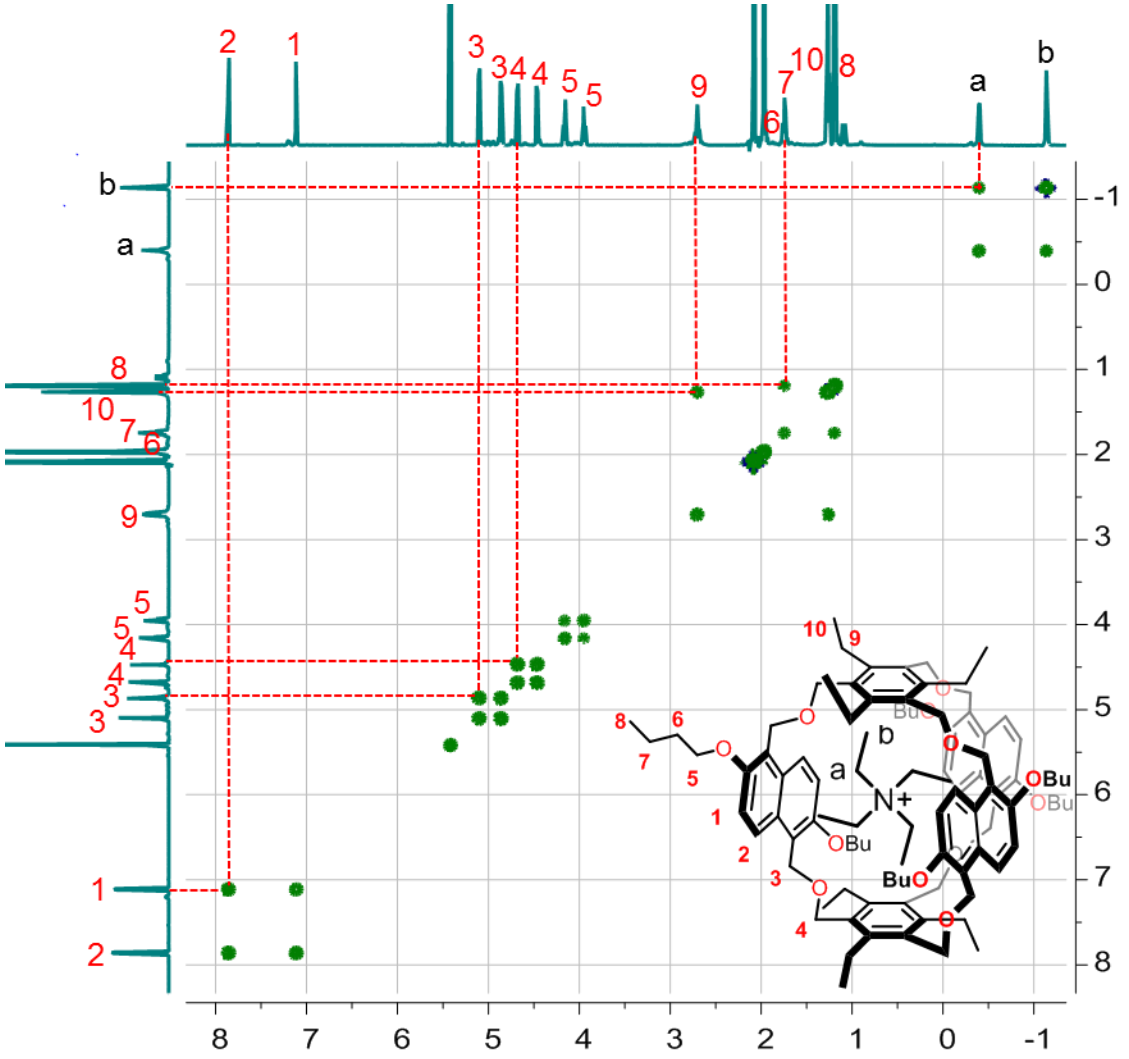

Figure S46. *Full ^{1}H, ^{1}H-COSY NMR spectrum (500 MHz, CD_2Cl_2:CD_3CN = 1:1, 2.0 mM, 298 K) of [**3**$^{+}$@**NC**]PF_6^{-}.*

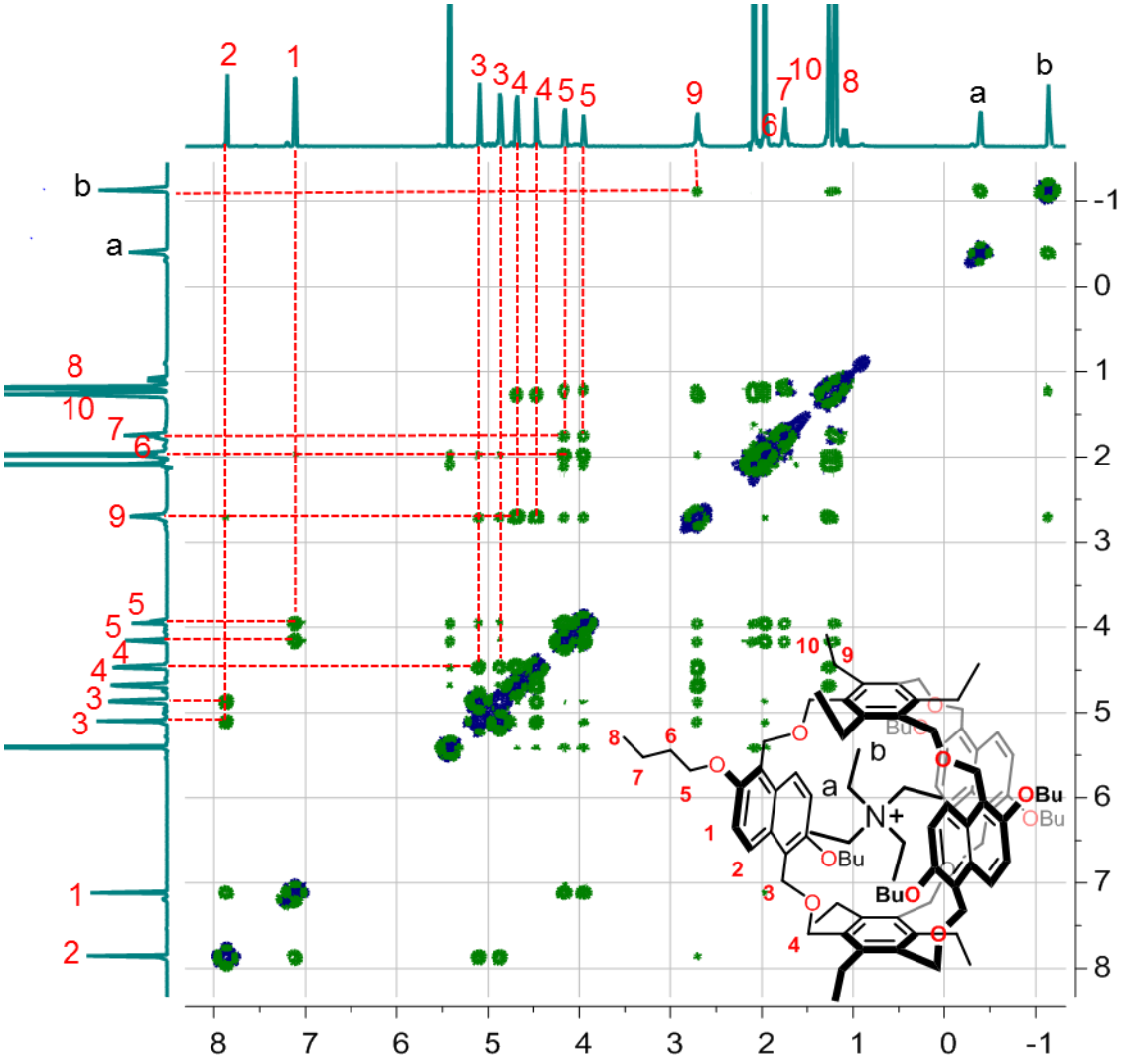

Figure S47. *Full ^{1}H, ^{1}H-ROESY NMR spectrum (500 MHz, CD_2Cl_2:CD_3CN = 1:1, 2.0 mM, 298 K) of [**3**$^{+}$@**NC**]PF_6^{-}. NOE cross peaks exist between protons 9 and the guest protons b, supporting the guest is encapsulated inside the cavity of **NC**. This is because that protons 9 point towards the cavity space.*

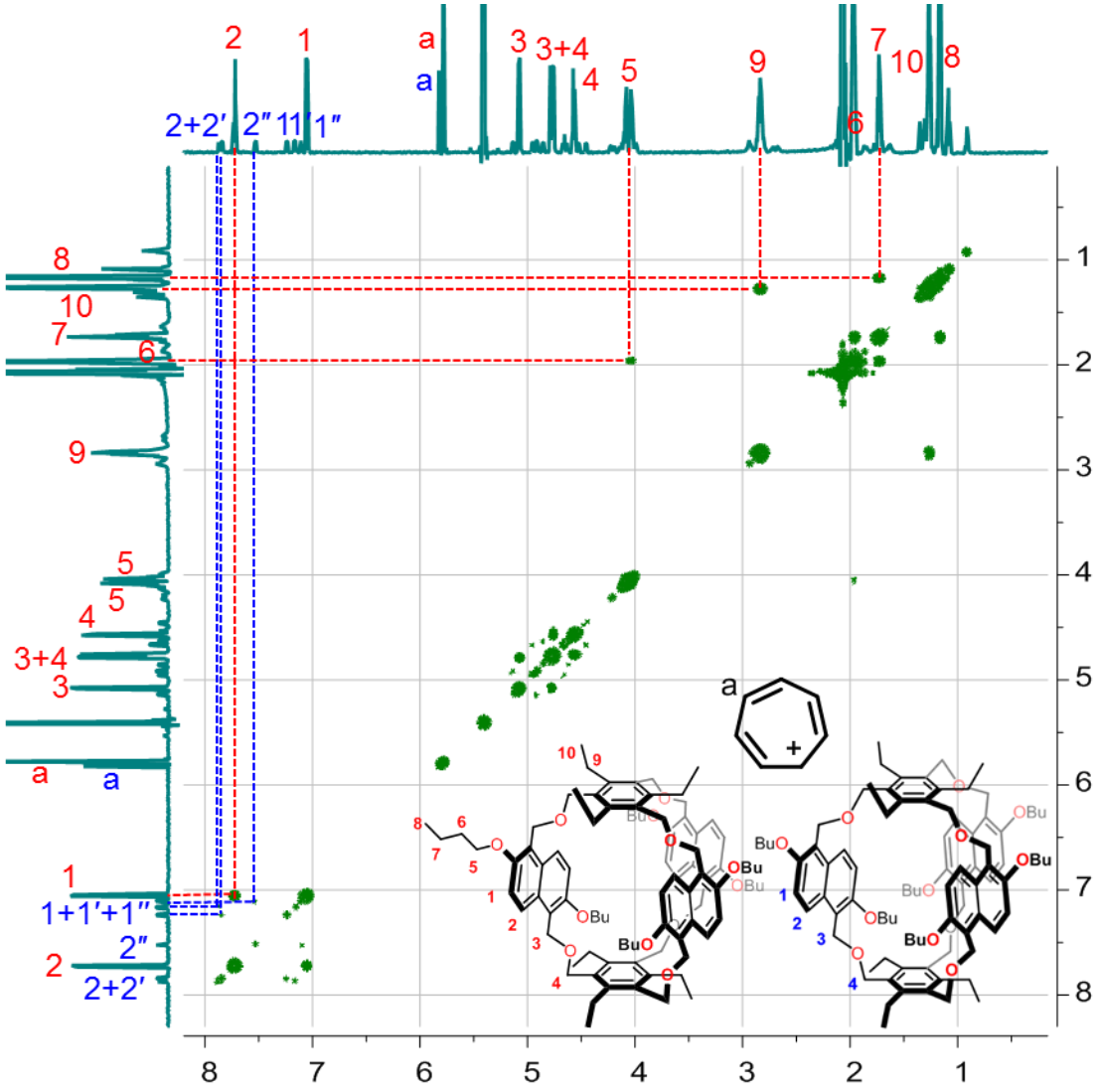

Figure S48. *Full ^{1}H, ^{1}H-COSY NMR spectrum (700 MHz, CD_2Cl_2:CD_3CN = 1:1, 2.0 mM, 298 K) of [**4**$^{+}$@**NC**]PF_6^{-}.*

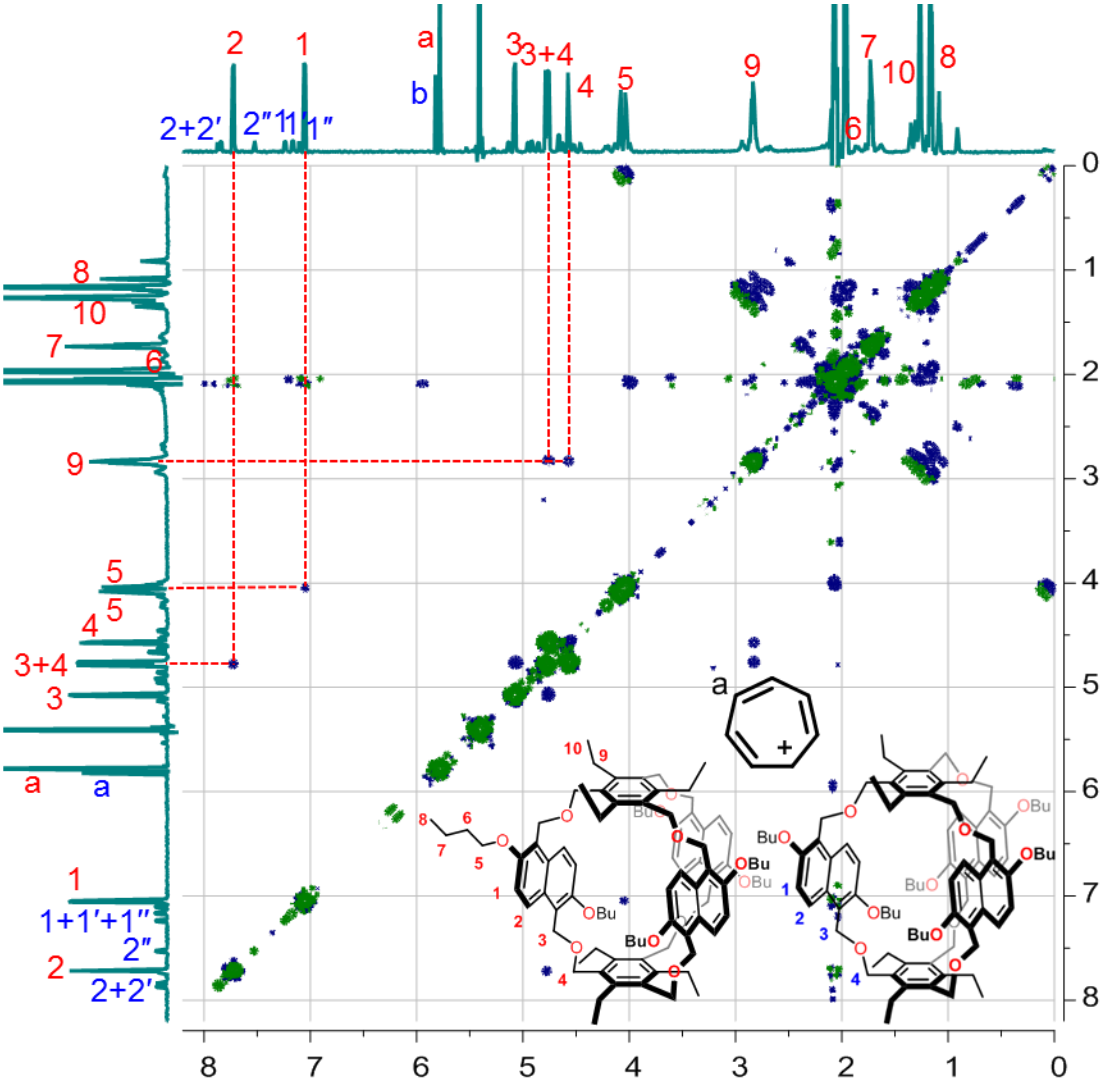

Figure S49. *Full ^{1}H, ^{1}H-ROESY NMR spectrum (700 MHz, CD_2Cl_2:CD_3CN = 1:1, 2.0 mM, 298 K) of [**4**$^{+}$@**NC**]PF_6^{-}. No NOE cross peaks were detected between the host protons and the guest protons, presumably because the guest structure is flat and undergoes constant tumbling the cavity of NC.*

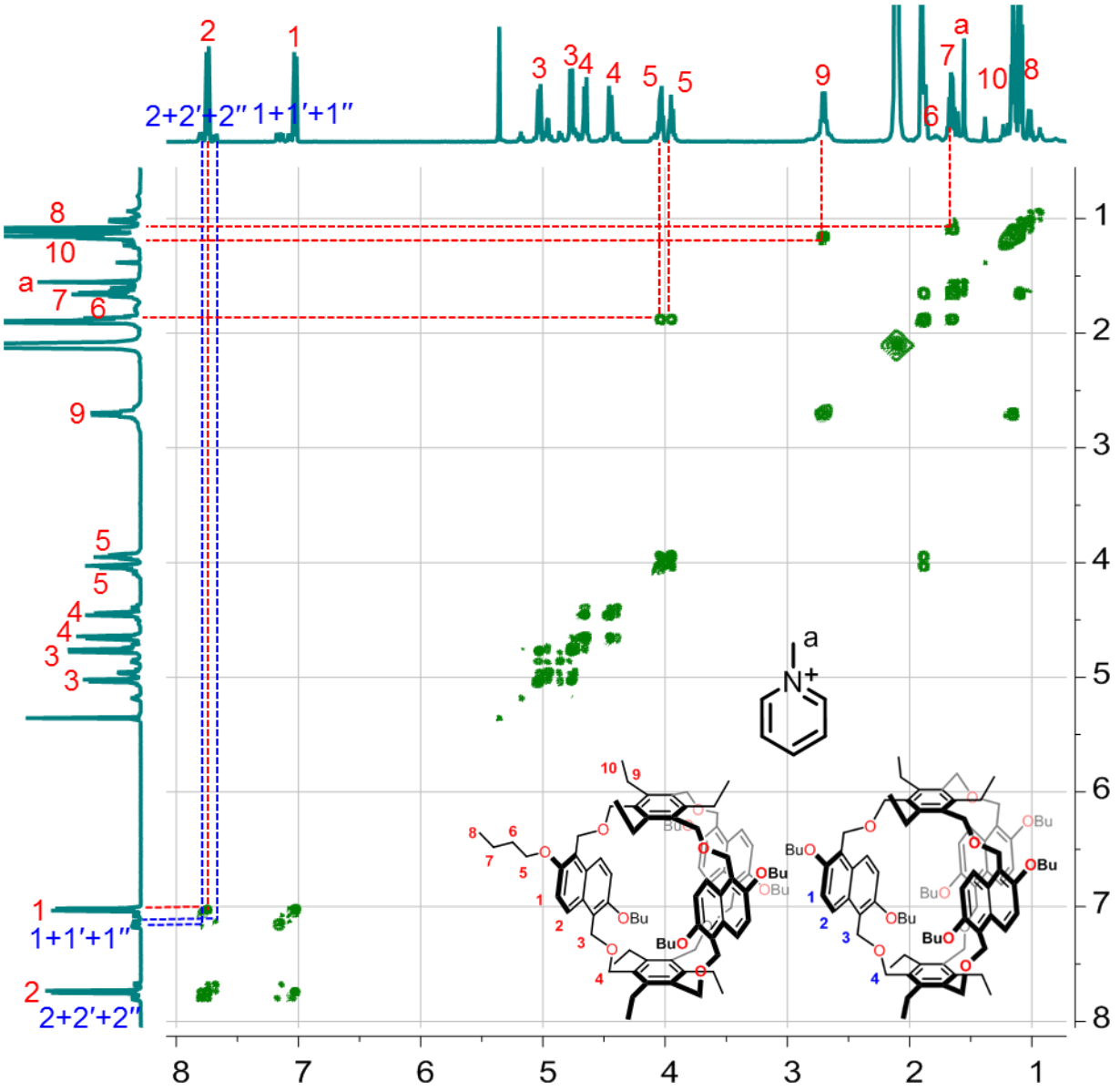

Figure S50. *Full ^{1}H, ^{1}H-COSY NMR spectrum (500 MHz, CD_2Cl_2:CD_3CN = 1:1, 2.0 mM, 298 K) of [**5**$^{+}$@**NC**]PF_6^{-}.*

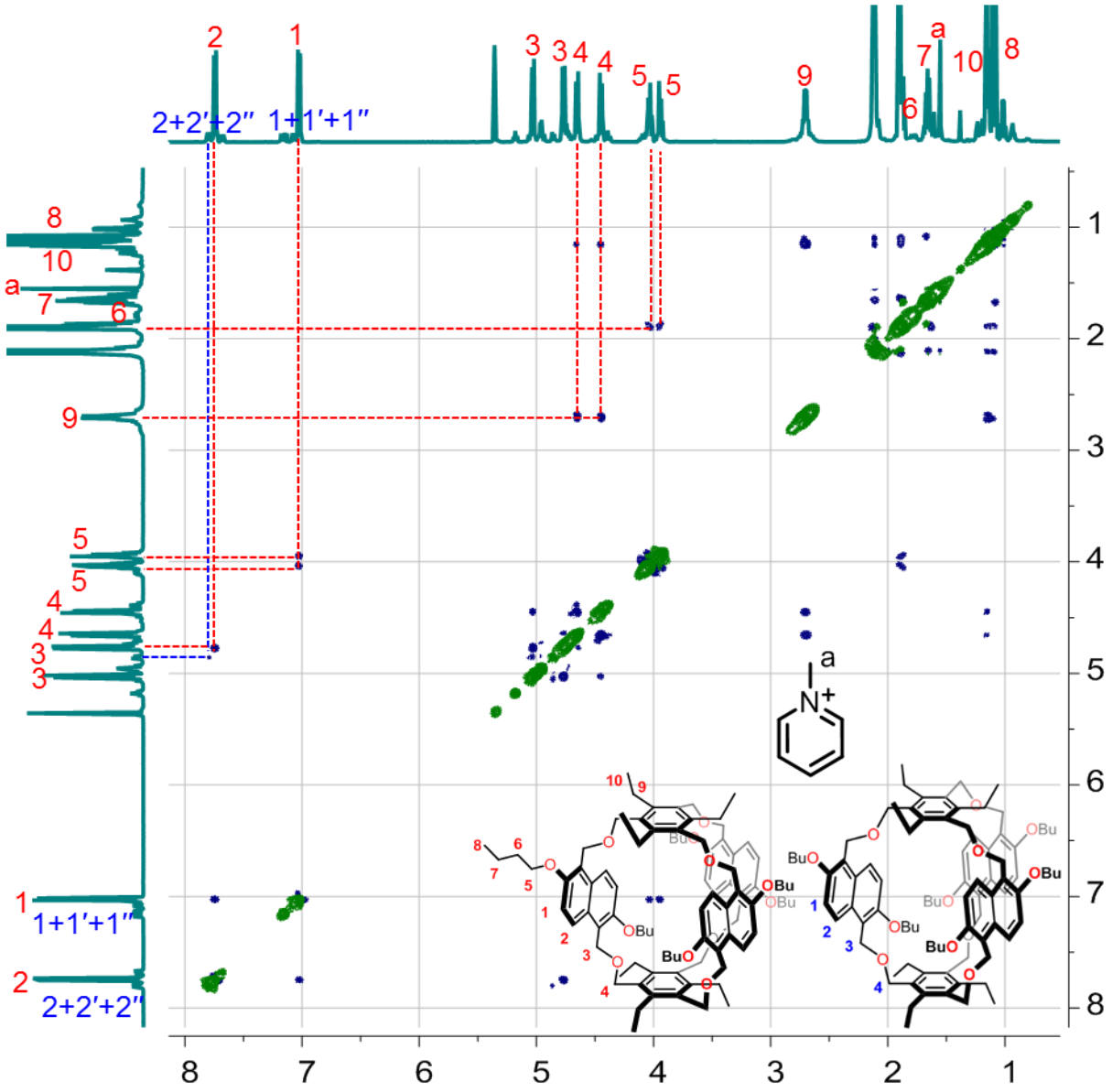

Figure S51. *Full ^{1}H, ^{1}H-ROESY NMR spectrum (500 MHz, CD_2Cl_2:CD_3CN = 1:1, 2.0 mM, 298 K) of [**5**$^{+}$@**NC**]PF_6^{-}. No NOE cross peaks were detected between the host protons and the guest protons, presumably because the guest structure is flat and undergoes constant tumbling the cavity of NC.*

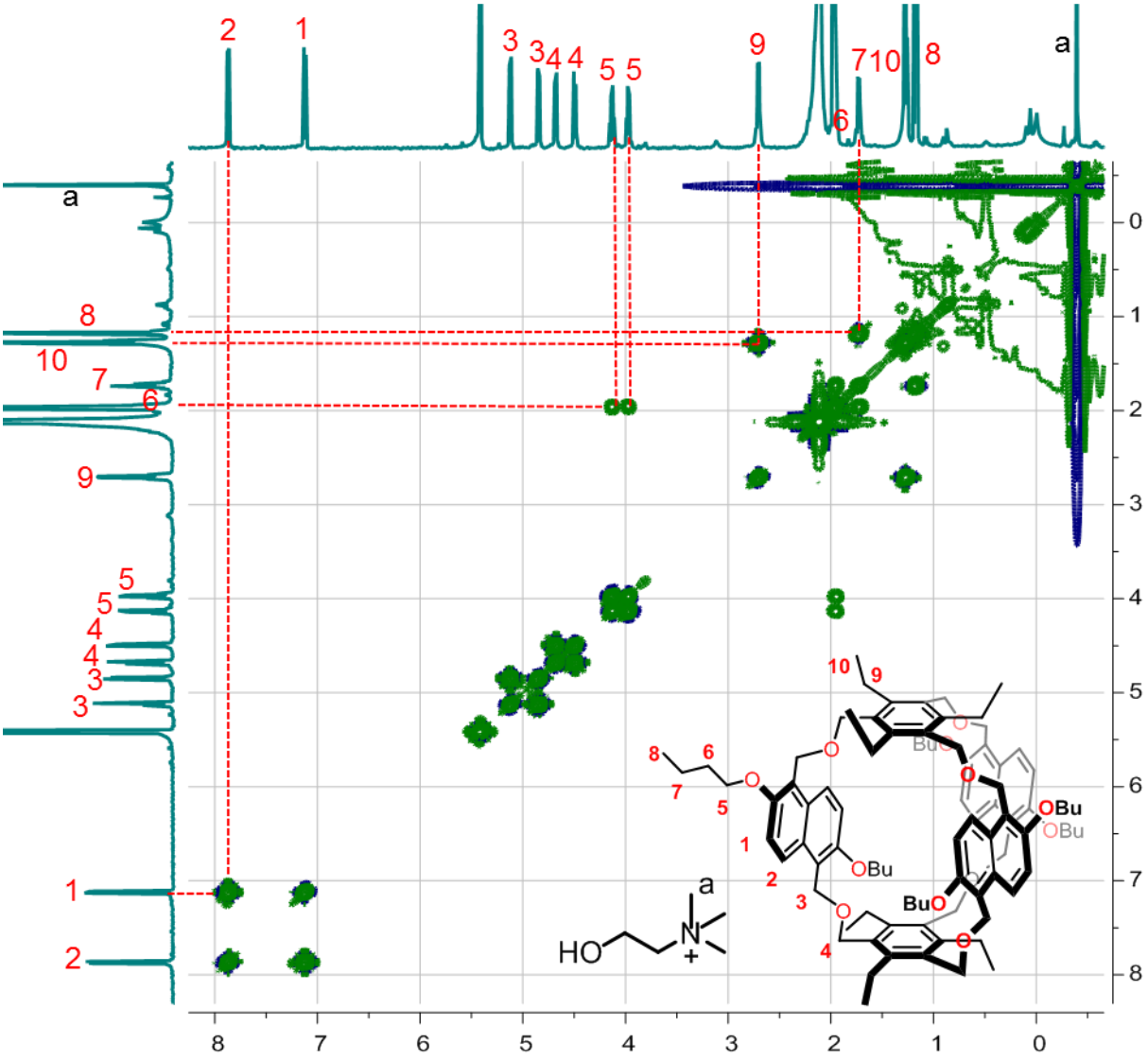

Figure S52. *Full ^{1}H, ^{1}H-COSY NMR spectrum (500 MHz, CD_2Cl_2:CD_3CN = 1:1, 2.0 mM, 298 K) of [**Ch**$^{+}$@**NC**]PF_6^{-}.*

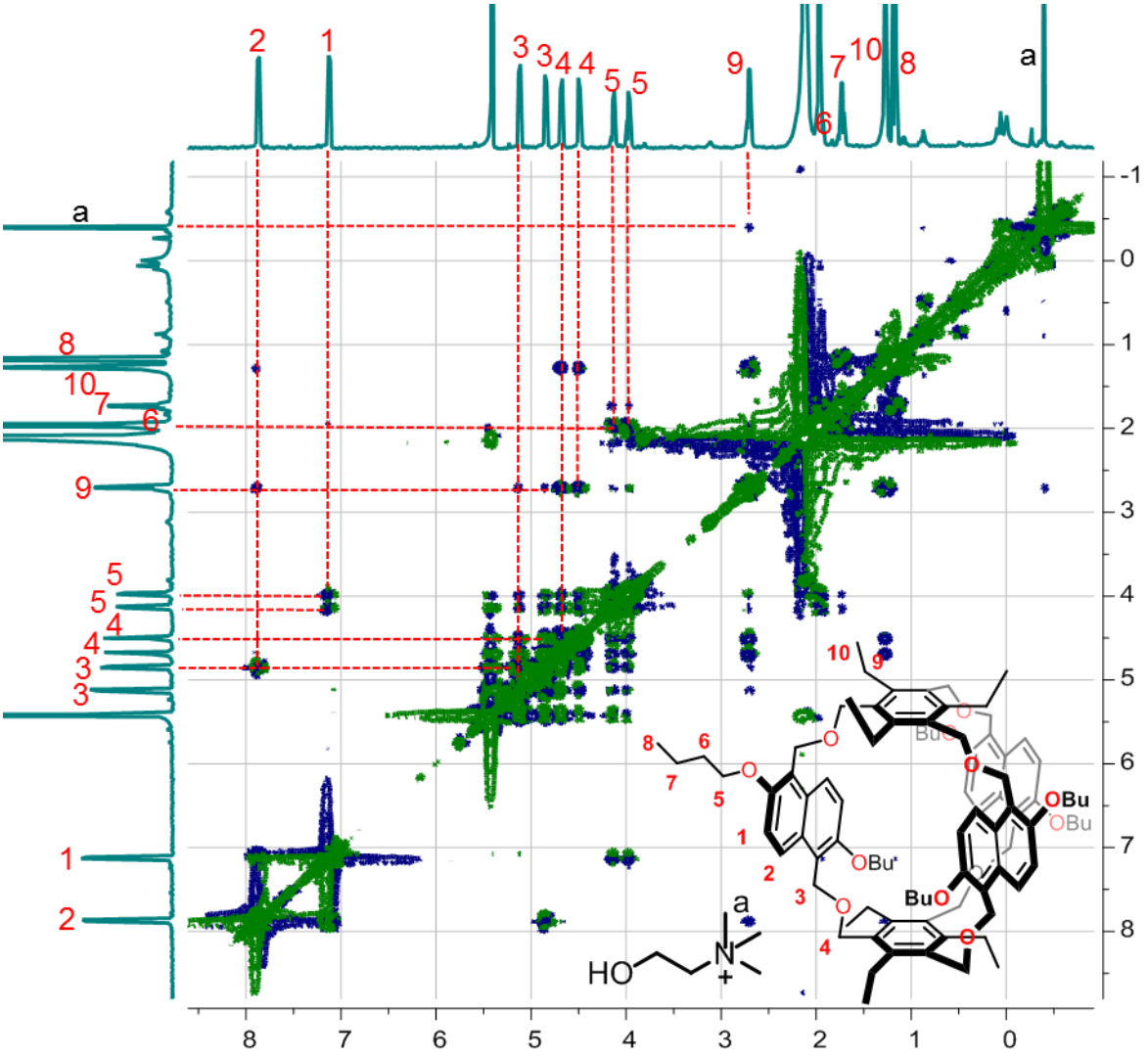

Figure S53. *Full ^{1}H, ^{1}H-ROESY NMR spectrum (500 MHz, CD_2Cl_2:CD_3CN = 1:1, 2.0 mM, 298 K) of [**Ch**$^{+}$@**NC**]PF_6^{-}. NOE cross peaks exist between protons 9 and the guest protons a, supporting the guest is encapsulated inside the cavity of **NC**. This is because that protons 9 point towards the cavity space.*

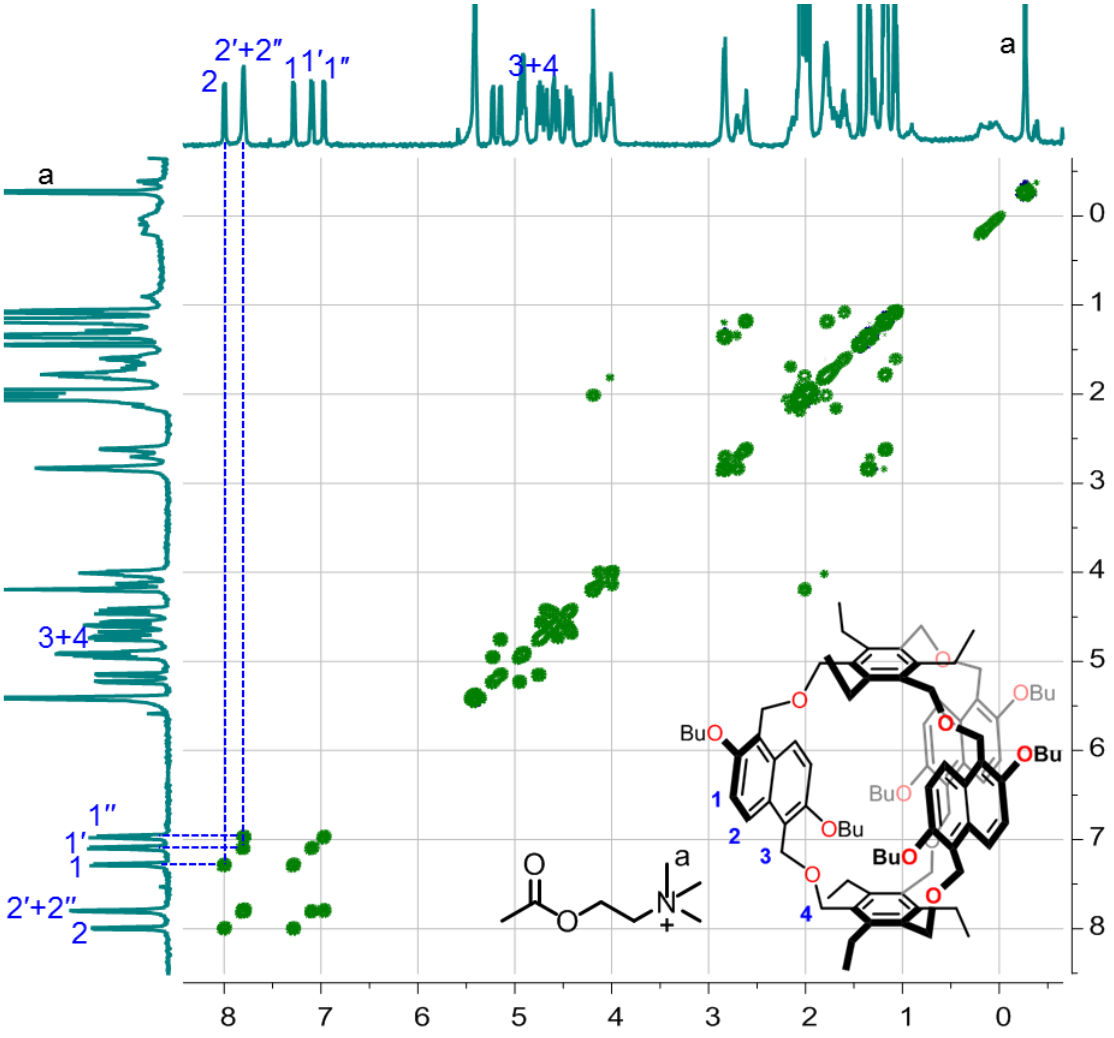

Figure S54. *Full ^{1}H, ^{1}H-COSY NMR spectrum (500 MHz, CD_2Cl_2:CD_3CN = 1:1, 2.0 mM, 298 K) of [**Ach**$^{+}$@**NC**]PF_6^{-}.*

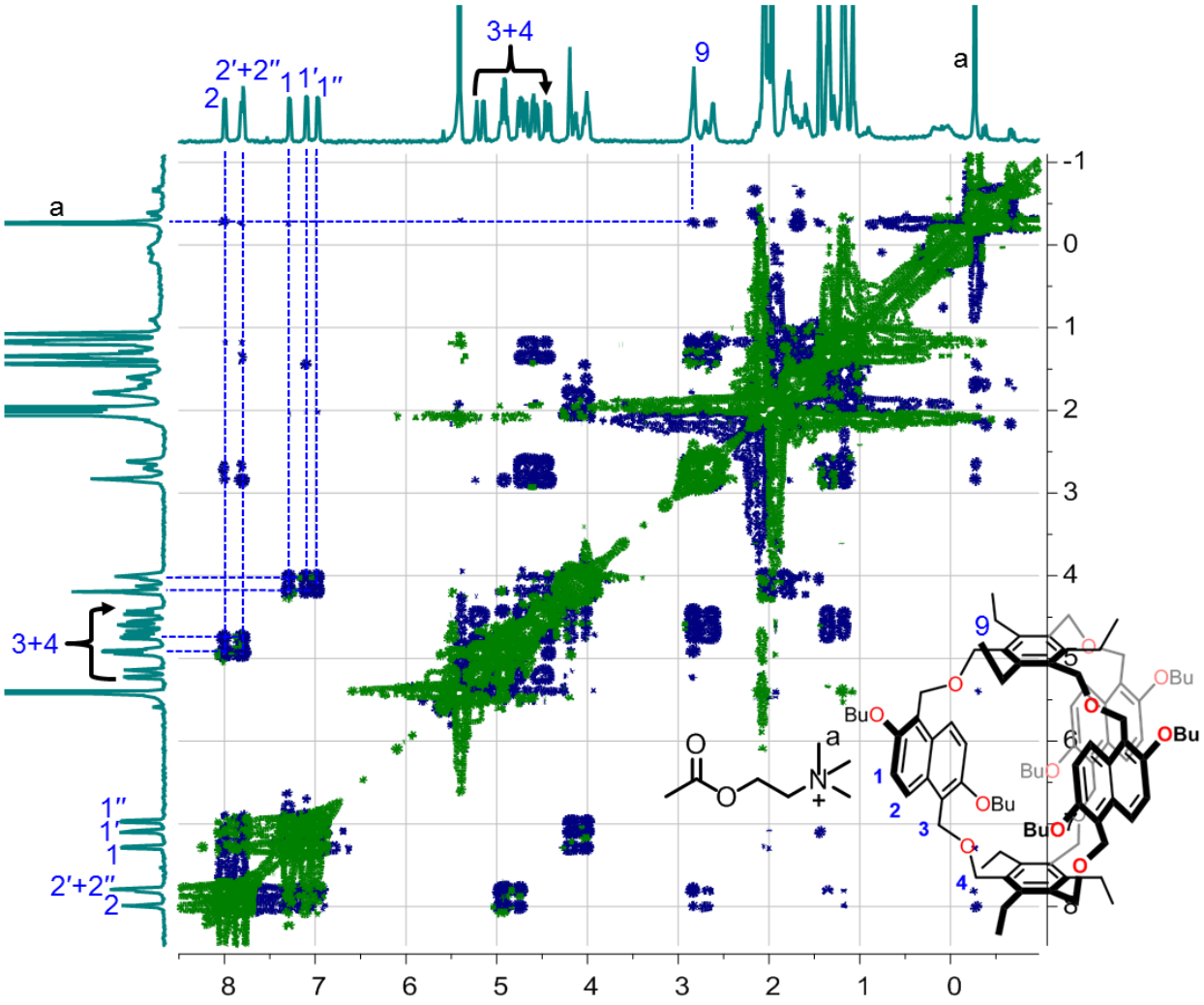

Figure S55. *Full ^{1}H, ^{1}H-ROESY NMR spectrum (500 MHz, CD_2Cl_2:CD_3CN = 1:1, 2.0 mM, 298 K) of [**Ach**$^{+}$@**NC**]PF_6^{-}. NOE cross peaks exist between protons 9 and the guest protons a, supporting the guest is encapsulated inside the cavity of **NC**. This is because that protons 9 point towards the cavity space.*

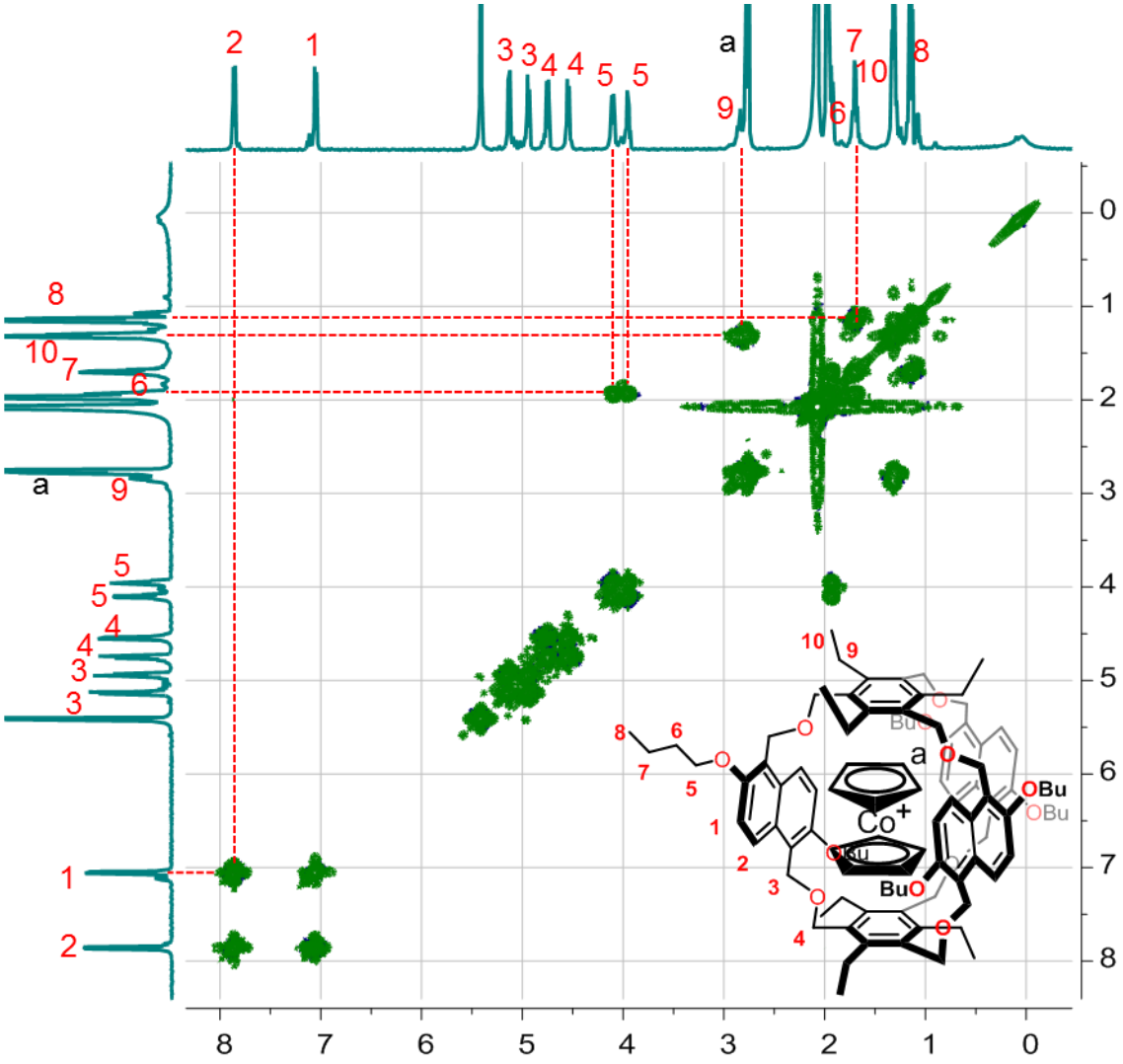

Figure S56. *Full ^{1}H, ^{1}H-COSY NMR spectrum (500 MHz, CD_2Cl_2:CD_3CN = 1:1, 2.0 mM, 298 K) of [**Cob**$^{+}$@**NC**]PF_6^{-}.*

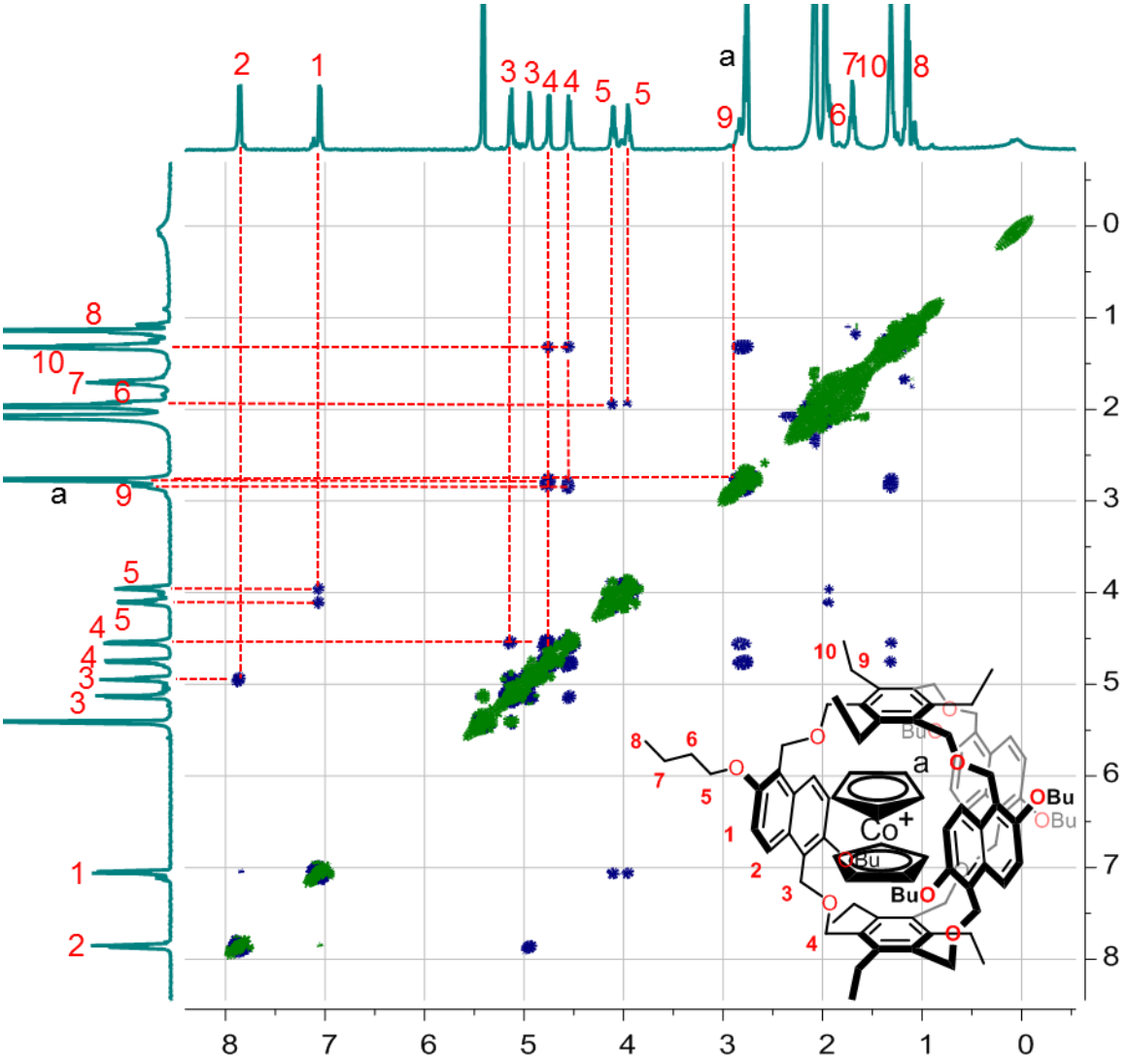

Figure S57. *Full* ^{1}H, ^{1}H*-ROESY NMR spectrum (500 MHz,* CD_2Cl_2*:*CD_3CN *= 1:1, 2.0 mM, 298 K) of [**Cob**$^{+}$**@NC**]*PF_6^-. *NOE cross peaks exist between protons 9 and the guest protons a, supporting the guest is encapsulated inside the cavity of* ***NC****. This is because that protons 9 point towards the cavity space.*

7. Electrode Preparation and Sensing Experiments

The electrode membrane was prepared by dissolving a mixture (total weight 144 mg) composed of 10 mmol/kg of **NC**, 1.6 mmol/kg of ion-exchanger sodium tetrakis[3,5-bis(trifluoromethyl)phenyl]borate (NaTFPB), 32.5 wt% of poly(vinyl chloride) (PVC) and 66.2 wt% bis(2-ethylhexyl)sebacate (DOS) in 1.5 mL THF (Selectophore grade). The THF solution was transferred into a glass ring with a diameter of 22 mm placed on a glass slide. THF was evaporated overnight at room temperature in a dust-free environment. Small disks were punched from the cast film and mounted into Ostec electrode bodies (Ostec, Sargans, Switzerland) using 1 mM NaCl inner solution. The electrode potential against a double junction Ag/AgCl reference electrode was measured with an EMF 16 high impedance electrochemical interface (Lawson Labs Inc., U.S.A.). Calibrations were performed and repeated in deionized water by stepwise addition of acetylcholine stock solutions.

8. Cyclic Voltammetry and Digital Simulations

Cyclic voltammetry was carried out on a PGSTAT302N potentiostat (Autolab). A three-electrode configuration in a single-compartment cell (5 mL) was used including a freshly polished glassy carbon working electrode, a platinum-wire counter-electrode and a silver-wire pseudoreference electrode. All solutions were argon-purged beforehand and kept under argon atmosphere during the measurements. All measurements were conducted at least twice over a wide range of different scan rates (25, 50, 100, 250, 500, 1000, 2000 and 2500 $mV \cdot s^{-1}$). The measurements were performed in dry and degassed dichloromethane (DCM), tetrahydrofuran (THF) and a 1:1 mixture solvent of 1,2-dichlorethane (DCE) and acetonitrile (ACN), respectively. The ferrocene/ferrocenium (**Fc**/**Fc**$^+$) and cobaltocene/cobaltocenium (**Cob**/**Cob**$^+$) couples were used as internal references. For the titration experiments, **NC** was dissolved in the respective solvent (0.2 mL) and titrated stepwise to the metallocene solution (2.0 mL). After each titration step, the mixture was stirred for several minutes under argon atmosphere. The host (**NC**) itself shows no redox activity in the potential window (~-1.7–0.5 V against **Fc**/**Fc**$^+$) used for the cyclovoltammetric experiments.

Cyclic voltammograms were simulated with the DigiElch Professional software (ElchSoft GbR, Kleinromstedt, Germany) using the Butler-Volmer equation. The simulations are based on a four-membered square scheme as depicted in Figure 4 (see main text). The charge-transfer coefficients α were at the initial value of 0.5 and the heterogeneous rate constants k_s were estimated by the peak-to-peak separation[S7] and set to 0.065 $cm^2 \cdot s^{-1}$. The diffusion coefficient was set to an initial value 1.0×10^{-5} $cm^2 \cdot s^{-1}$. The fitting and simulation process were repeated with cyclic voltammograms at different scan rates and at different host concentrations to ensure the reliability of thermodynamic and kinetic parameters.

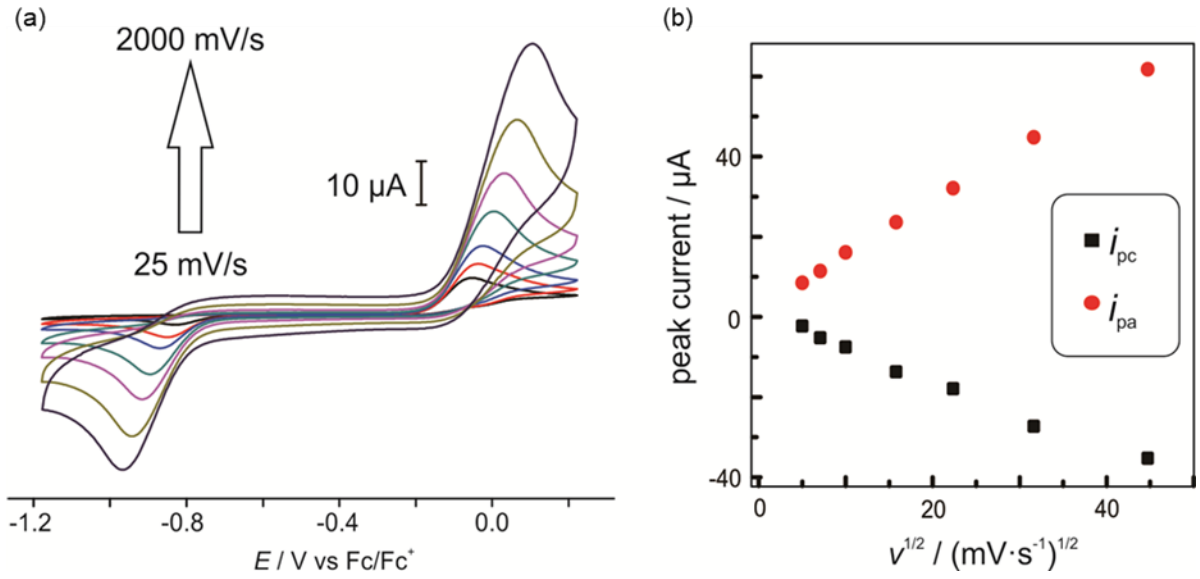

Figure S58. *(a) Cyclic voltammograms (CH_2Cl_2, 298K) of* ***Fc*** *(1.0 mM) with* ***NC*** *(1.0 mM), and with n-NBu_4PF_6 (0.1 M) as the electrolyte at different scan rates (25, 50, 100, 250, 500, 1000 and 2000) in mV·s^{-1}. (b) Peak currents plotted against the square root of the scan speed.*

Table S3. *Thermodynamic and kinetic parameters obtained by digital simulation of host-guest equilibria between* ***Fc***, ***Fc***$^+$ *and* ***NC*** *in dichloromethane.*

Guest	K_{eq} / M^{-1}	k_f / M^{-1}·s^{-1}	k_b /s^{-1}
Fc	<< 1	0.3	1×10^{5}
Fc$^+$	1.4×10^{10}	8.1×10^{6}	5.6×10^{-4}

K_{eq}, k_f and k_b are the equilibrium constant, and the forward and backward rate constants, respectively.

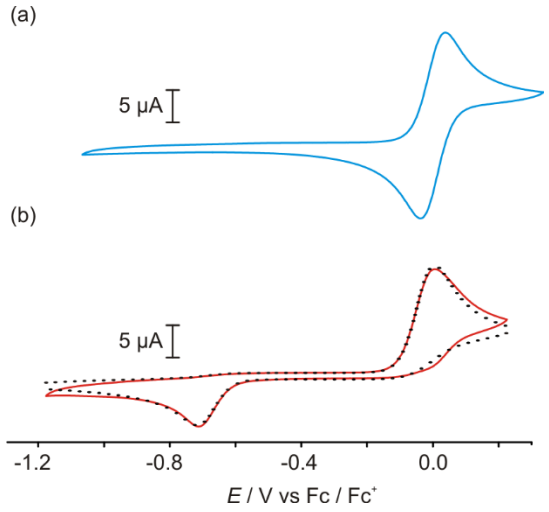

Figure S59. *(a) Cyclic voltammogram of* ***Fc*** *($CH_2ClCH_2Cl:CH_3CN$ = 1:1, 1.0 mM, 298 K, 100 $mV{\cdot}s^{-1}$) with n-NBu_4PF_6 (0.1 M) as the electrolyte; (b) cyclic voltammogram (solid red line) of* ***Fc*** *after the addition of 1 equivalent* ***NC*** *and simulated cyclic voltammogram (dotted black line) by using the thermodynamic and kinetic parameters in Table S3.*

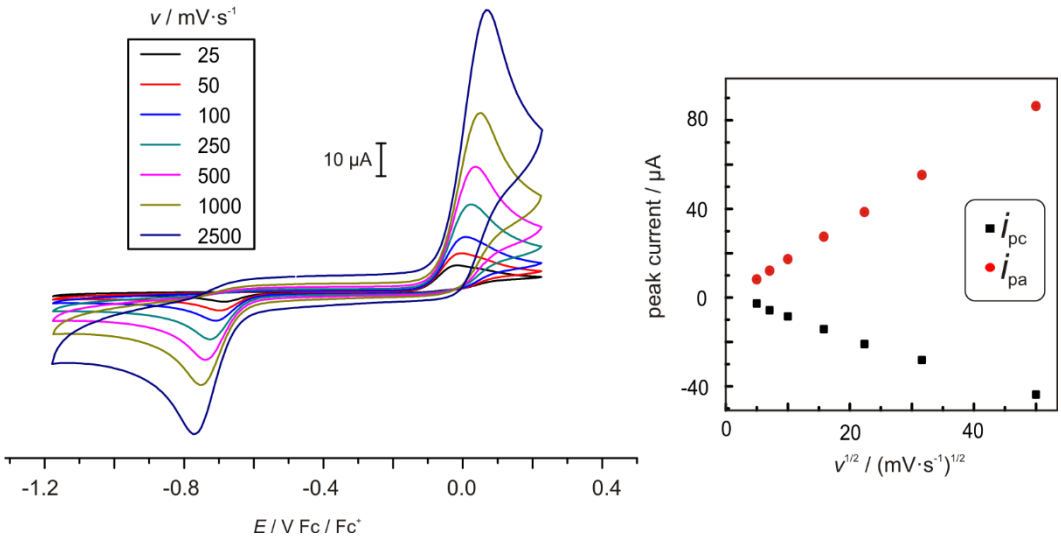

Figure S60. *(a) Cyclic voltammograms ($CH_2ClCH_2Cl:CH_3CN$ = 1:1, 1.0 mM, 298K) of* ***Fc*** *(1.0 mM) with* ***NC*** *(1.0 mM), and with n-NBu_4PF_6 (0.1 M) as the electrolyte at different scan rates (25, 50, 100, 250, 500, 1000 and 2500) in $mV{\cdot}s^{-1}$. (b) Peak currents plotted against the square root of scan speed (CH_2Cl_2, 298K) of* ***Fc*** *(1.0 mM) with* ***NC*** *(1.0 mM), and with NBu_4PF_6 (0.1 M) as the electrolyte.*

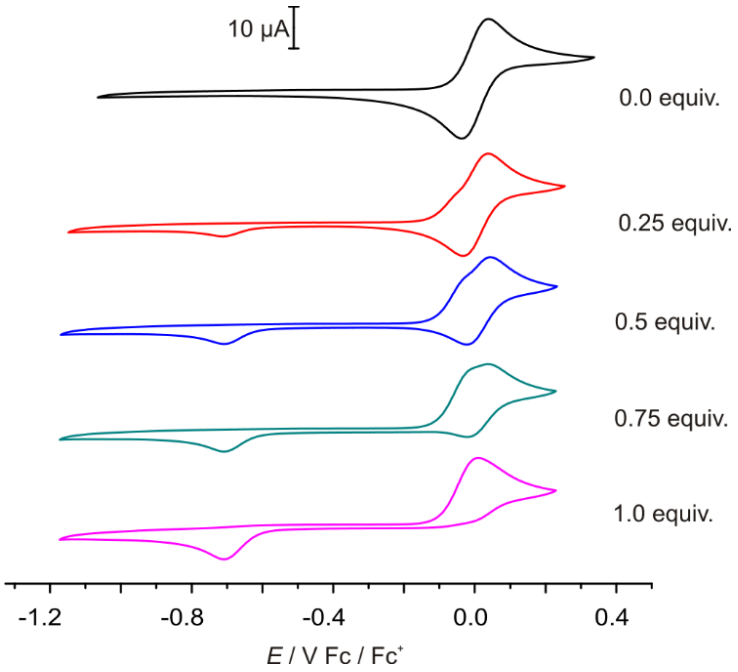

Figure S61. *Voltammetric titration ($CH_2Cl_2CH_2Cl_2$:CH_3CN = 1:1, 298 K, 100 mV·s^{-1}) obtained during a titration of* ***Fc*** *(1.0 mM) titrated with* ***NC****.*

Table S4*. Thermodynamic and kinetic parameters obtained by digital simulation of host-guest equilibria between* ***Fc*** *and* ***NC*** *in 1,2-dichloroethane and acetonitrile (1:1).*

Guest	K_{eq} / M^{-1}	k_f / M^{-1}·s^{-1}	k_b /s^{-1}
Fc	<< 1	0.1	2.4×10^{4}
Fc$^+$	1.3×10^{8}	8.1×10^{5}	6.4×10^{-3}

K_{eq}, k_f and k_b are the equilibrium constant, and the forward and backward rate constants, respectively.

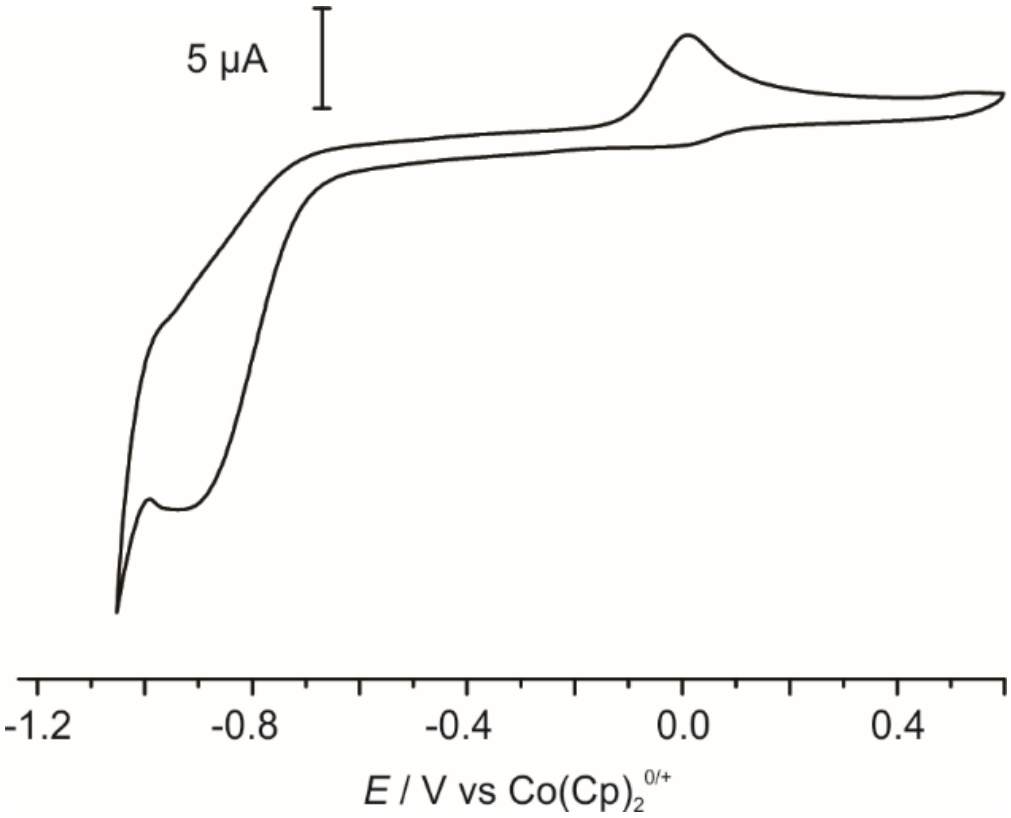

Figure S62. *Cyclic voltammograms (THF, 298 K, 100 mV·s^{-1}) of* ***Co(Cp)$_2^+$*** *(1.0 mM) with* ***NC*** *(1.0 mM), and with n-NBu$_4$PF$_6$ (0.1 M) as electrolyte. Similar electrochemical behavior for* ***Cob$^+$@NC*** *was observed with a shift of the cathodic peak potential of 900 mV in the presence of* ***NC*** *in tetrahydrofuran. However, due to the more negative electrochemical potential of* ***Cob/Cob$^+$****, and the strong cathodic shift of the cathodic peak potential, sufficiently experimental data for digital simulations could not be obtained.*

9. DFT Calculations

9.1. Computational Details

Quantum chemical calculations at the density functional theory (DFT) level were employed to examine different conformations of **NC** and identify the most important contributions to the large binding constants of the host-guest complexes. As a model guest, we chose the closed-shell compound cobaltocenium (**Cob**$^+$) and analyzed the thermodynamic properties of its complexation in the cavity of **NC**. To save computational resources, a shortened version of **NC** was used with ethoxy and methyl groups instead of butoxy and ethyl groups, respectively. The program package Turbomole (version 7.1)[S8] was used for structure optimizations and normal mode analyses at the TPSS-D3(BJ)/def2-SVP[S9] level of DFT together with COSMO[S10] as a solvent model (dielectric constant: 9.08[S 11] for unpolar dichloromethane) to account for bulk effects and the RI-*J* approximation[S12] to speed up calculations. Single point energy calculations were performed at the COSMO/B3LYP-D3(BJ)/def2-TZVP[S13] level.

As COSMO does not allow to model solvent mixtures, such as 1,2-dichloroethane/acetonitrile pair in the experiment, dichloromethane was used as the solvent in the calculations. Dichloromethane was chosen for two reasons. First, it is far more likely to yield smoothly converging molecular structures than 1,2-dichloroethane while the difference of the two in the implicit solvent model is negligible. Second, CH_2Cl_2 can be assumed to yield accurate results, which CH_3CN (or CH_2ClCH_2Cl/CH_3CN) will quite likely not do or at least not to the same extent. This is due to an inherent shortcoming of all continuum solvation models (CSMs), such as COSMO. All CSMs assume a linear response of the solvent reorganization energy with respect to the solute dipole moment. However, this assumption does not hold in the case of polar solvent molecules, where the reorganization energy is usually much larger than the thermal energy (k_BT). This renders any approach, which only uses the dielectric constant to represent the solvent, inaccurate with only little means to estimate the introduced error.[S14] Thus, with CH_2Cl_2 as the solvent, we can easily rationalize the error we make. But if CH_3CN was used as the solvent, it is unclear to what extent the linear response in CSMs is erratic. The only drawback of using dichloromethane is that the theoretical binding energies will likely be somewhat higher than those obtained in the ITC experiments (see below).

9.2 Structural Aspects

NC was considered in different conformations in solution (Figure S62) including the two possible conformers of the complexes, **NC-I** and **NC-II**, with three explicit dichloromethane molecules as guests.

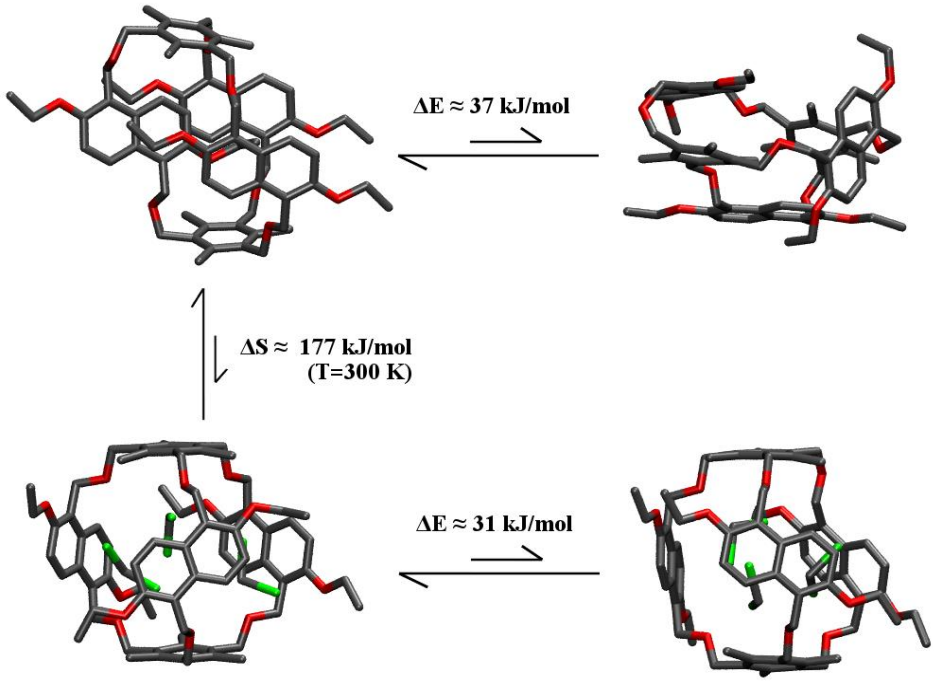

Figure S63 *Different possible conformations of* ***NC****:* ***NC$_{self}$*** *(top left), a collapsed open-form conformation (top right),* ***NC-I*** *with three dichloromethane molecules as guests (bottom left), and* ***NC-II*** *with three dichloromethane molecules as guests (bottom right). Hydrogen atoms are omitted for clarity. Indicated are the differences in electronic energy between conformations with the same number of atoms and the change in free enthalpy (which includes the entropic loss) that emerges when going from* ***NCself*** *to* ***NC-I****.*

The large amount of non-covalent π-π-stacking interactions renders the self-included structure **NC$_{self}$** (top left, most resembling the crystal structure) the most favorable in solution when no charged guest is present. A conformation that does not self-include its naphthalene units but also exhibits a large amount of intramolecular non-covalent interactions is the structure shown on the top right, which may be interpreted as a collapsed open-form geometry. It should be noted that

this structure ran into severe structure convergence problems and is likely to be a little more stable than what our calculation predicts. It is computed to be approximately 37.6 kJ/mol higher in energy than $\mathbf{NC_{self}}$, which suggests that **NC** will barely access this conformation. Another conceivable conformation in solution is the open form where solvent molecules function as guests. **NC-I** (bottom left) is computed to be roughly 30.9 kJ/mol more energetically stable than **NC-II** (bottom right). **NC-I** exceeds the energetic stability of $\mathbf{NC_{self}}$ by around 85.9 kJ/mol. However, incorporating three dichloromethane molecules comes at a significant loss in entropy (ca. 177 kJ/mol at 300 K), which results in a free enthalpy difference of over 91.3 kJ/mol in favor of $\mathbf{NC_{self}}$. The flexibility of **NC** in solution is, hence, mainly based on the constantly repeating self-inclusion of one of the naphthalene units.

9.3 Free Association Enthalpy

The free enthalpy of association ΔG_a of the complexation can be calculated by eq. 4:

$$\Delta G_a = \Delta E + \Delta H_{vib} + \Delta S_{RRHO} \quad (4)$$

where ΔE is the electronic energy difference of free $\mathbf{Cob^+}$ and $\mathbf{NC_{self}}$ and the complex $\mathbf{Cob^+}$**@NC-I**, ΔH_{vib} and ΔS_{RRHO} are the enthalpic and entropic contribution calculated from a vibrational normal mode analysis. The latter was corrected by Grimme's *rigid-rotor harmonic-oscillator* approach, which takes into account the anharmonicity of low-lying frequencies, that often lead to inaccuracies in the calculation of binding energies.[S15] Table S5 summarizes the computed values for the association processes.

Table S5*: Free association enthalpy of the complexation of* $\mathbf{Cob^+}$ *in the cavity of* ***NC-I*** *and its various contributions (values given in kJ/mol at T = 300K)*

ΔG_a	ΔE	ΔH_{vib}	ΔS_{RRHO}
-63.8	-130.6	5.4	61.4

The large binding strength can be described by a notable electronic interaction (ΔE) that is compensated to some extent by a loss in entropy (ΔS_{RRHO}). The absolute value of ΔG_a is comparable to its experimental counterpart (-55.8 kJ/mol versus -63.8 kJ/mol). Apart from the inherent error in the employed density functional method, deviations occur since the calculations

assume pure dichloromethane as a solvent, whereas in the experiment a mixture of 1,2-dichloroethane and acetonitrile was used. The more polar solvent mixture in the experiment can be expected to solvate the salt better outside the cage than unpolar dichloromethane, which leads to smaller experimentally determined binding constants. The corresponding complex with **NC-II** lies 9.2 kJ/mol higher in energy and is not assumed to exert a strong influence on the binding constant.

9.4 Electronic Interactions

Molecular orbital (MO) theory provides insight into the electronic properties of **Cob**$^{+}$**@NC**. Figure S63 displays the HOMO and LUMO orbitals of **Cob**$^{+}$**@NC**.

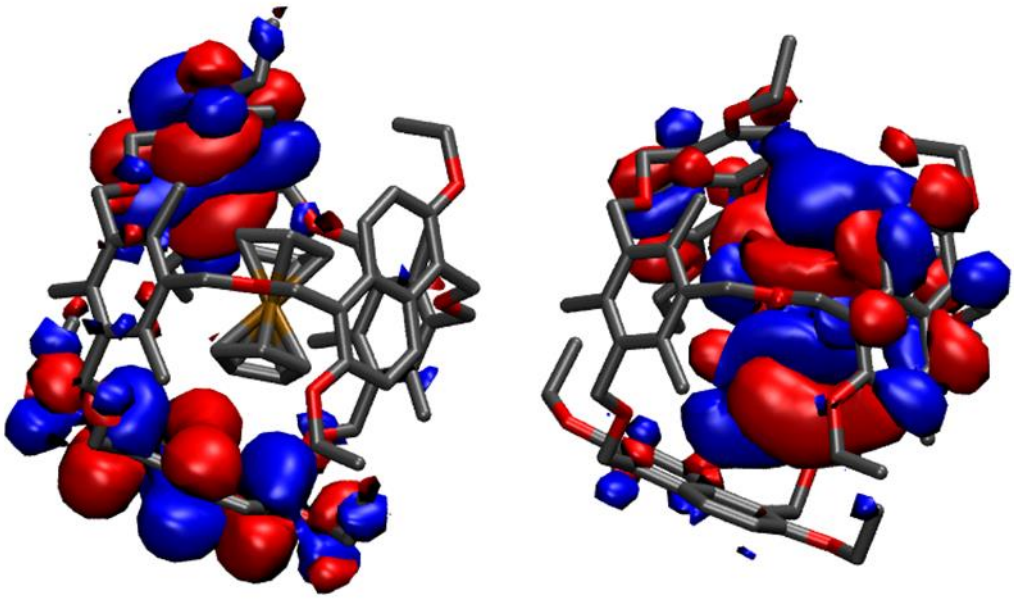

Figure S64*. HOMO (left) and LUMO (right) of the complex structure (isovalue: 0.01 Å*$^{-3}$*). Hydrogen atoms are omitted for clarity.*

Especially in the LUMO, a significant overlap of basis functions centered at the **NC** and the **Cob**$^{+}$ unit can be observed, while the HOMO shapes are dominated by basis functions centered at **NC** itself.

Furthermore, the COSMO methodology allows calculating so-called screening charges of the molecules that the implicit bulk is interacting with. Screening charges are defined by the charge density at a surface segment of the molecule.[S10] While surface charges generated from

electrostatic potentials refer to the partial charge of the surface segment itself, screening charges refer to the affinity of this segment towards charged species outside the so-called σ-surface. A large positive value, hence, indicates a large affinity towards positive charges and *vice versa*. Figure S64 shows the σ-surfaces of **NC**$_{self}$ and **Cob**$^{+}$**@NC-I** (as an example).

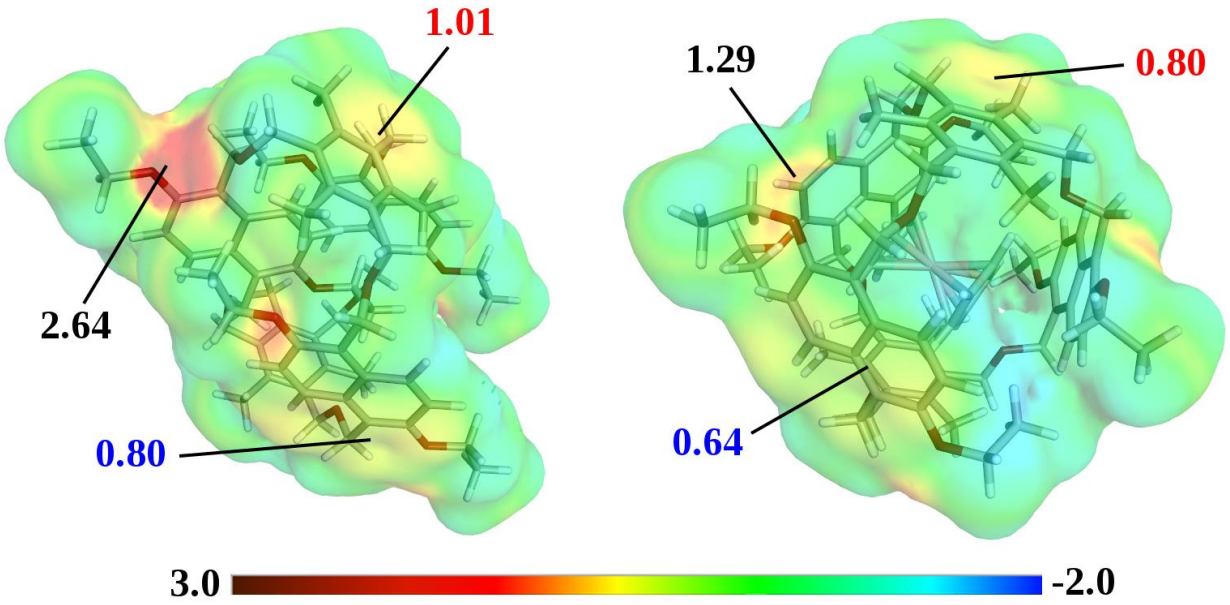

Figure S65. *Analysis of the screening charges (so-called σ-surface, unit in e^{-}/nm^{2}) of* ***NC****$_{self}$ (left) and* ***Cob***$^{+}$***@NC-I*** *(right) generated at the COSMO/B3LYP-D3(BJ)/def2-TZVP level of DFT with the program COSMOthermX16*[S 16]. *Indicated is the variation of the screening charges of representative surface segments. Blue numbers: naphthalene site, red numbers: phenyl site, black numbers: highest screening charges found on the surface.*

The effect of the encapsulated **Cob**$^{+}$ on **NC** can be described as decreasing screening charges when going from **NC**$_{self}$ to **Cob**$^{+}$**@NC-I** (on average 25 % less). This can be rationalized by the charged guest inside, which interacts in a predominantly electrostatic manner with the (induced) dipoles of the cage and possibly by cation-π interactions between the charged guest and the quadrupoles of the aromatic rings surrounding it.

10. Evidence for Redox Switching

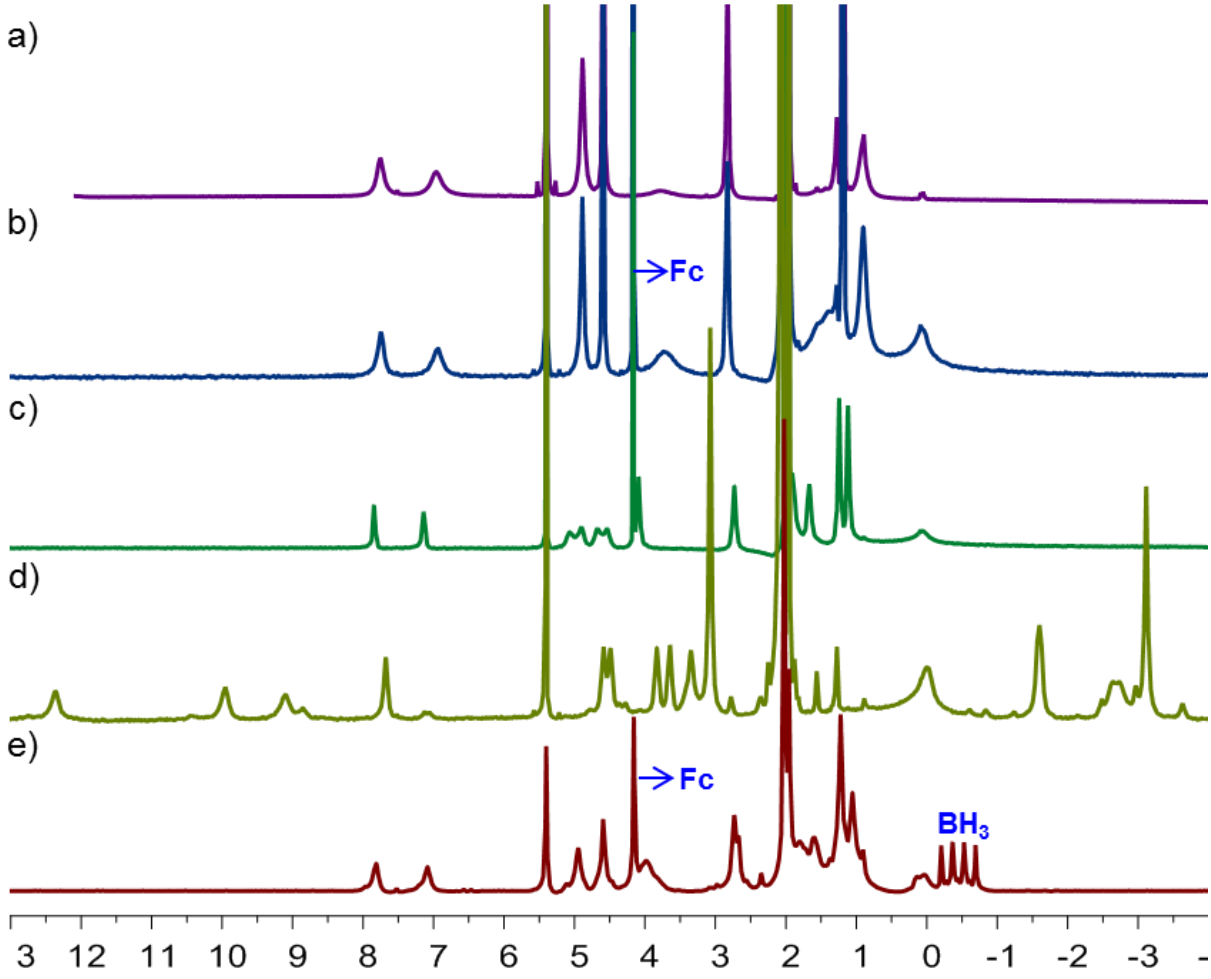

Figure S66. *^{1}H NMR spectra (500 MHz, CD_2Cl_2:CD_3CN = 1:1, 4.0 mM, 298 K) of a)* ***NC****, b)* ***NC*** *with one equivalent of neutral* ***Fc****, c) the mixture of* ***Fc*** *and* ***NC*** *with one equivalent of KPF_6, in which K^+@****NC*** *forms showing K^+ to be a better guest than* ***Fc****, d) the mixture of* ***Fc*** *and K^+@****NC*** *after addition of one equivalent I_2, e) the mixture of I_2 and* ***Fc*** *and K^+@****NC*** *after addition of one equivalent of tributylamine (n-NBu_3 as a reagent to neutralize Lewis-acidic boron compounds that may open the acid-labile benzyl ethers of the cage) and addition 0.25-0.5 equivalent $NaBH_4$, and sonication the mixture solution together for 1 h, and obtaining the complex of K^+ or Na^+****@NC*** *and free neutral* ***Fc****. These experiments suggest that the redox switching is achieved by oxidant and reductant in the presence of* ***NC*** *in solution.*

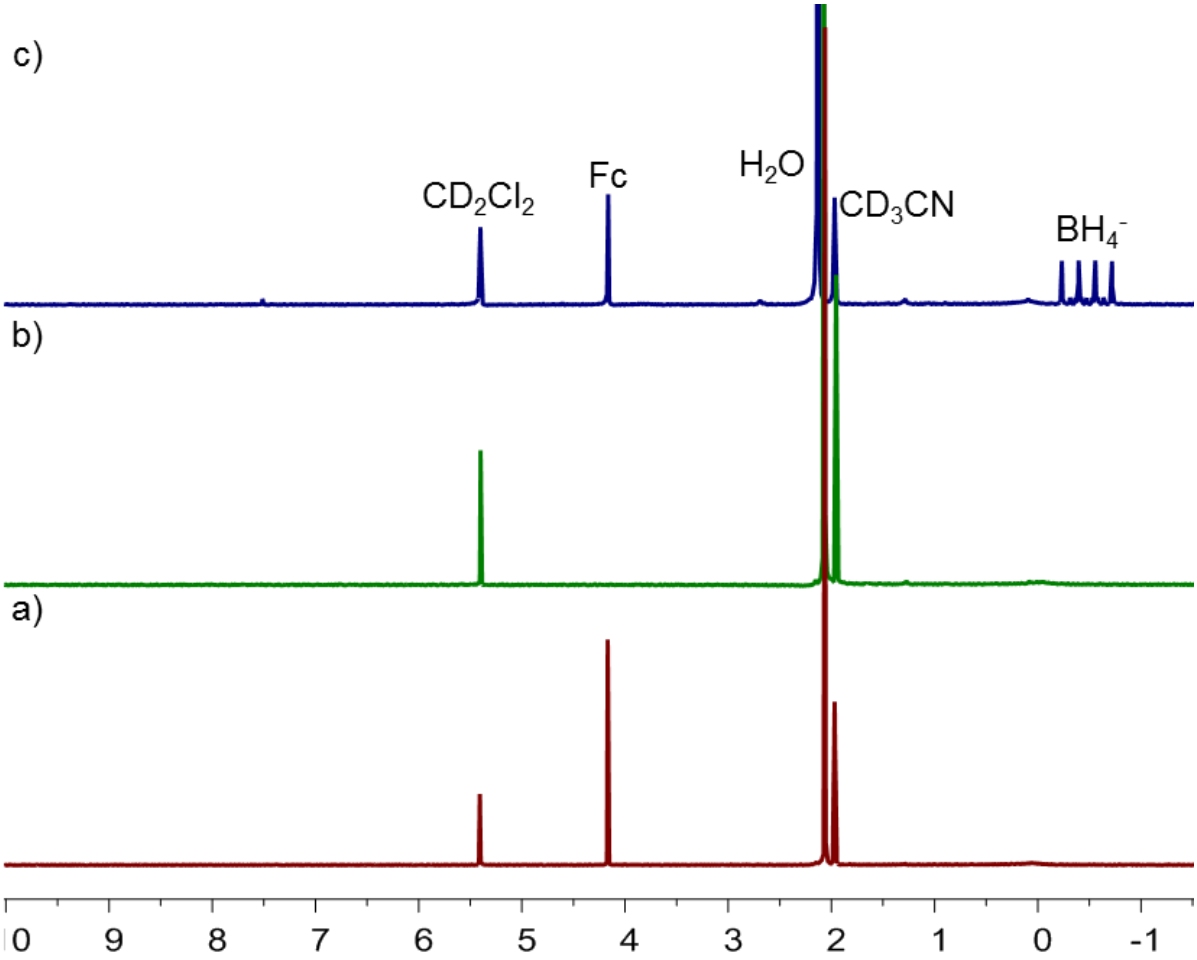

Figure S67. *^{1}H NMR spectra (500 MHz, CD_2Cl_2:CD_3CN=1:1, 2.0 mM, 298 K) of a) neutral **Fc** in the absence of **NC**, b) upon addition of one equivalent I_2 to **Fc**, the single peak of **Fc** disappears into the baseline because of the paramagnetic nature of **Fc**$^+$, and c) upon addition of 0.25 equivalent of $NaBH_4$ to the above solution. Neutral **Fc** emerges again. These experiments demonstrate that **Fc** and **Fc**$^+$ can be switched reversibly in solution by I_2 and $NaBH_4$, respectively.*

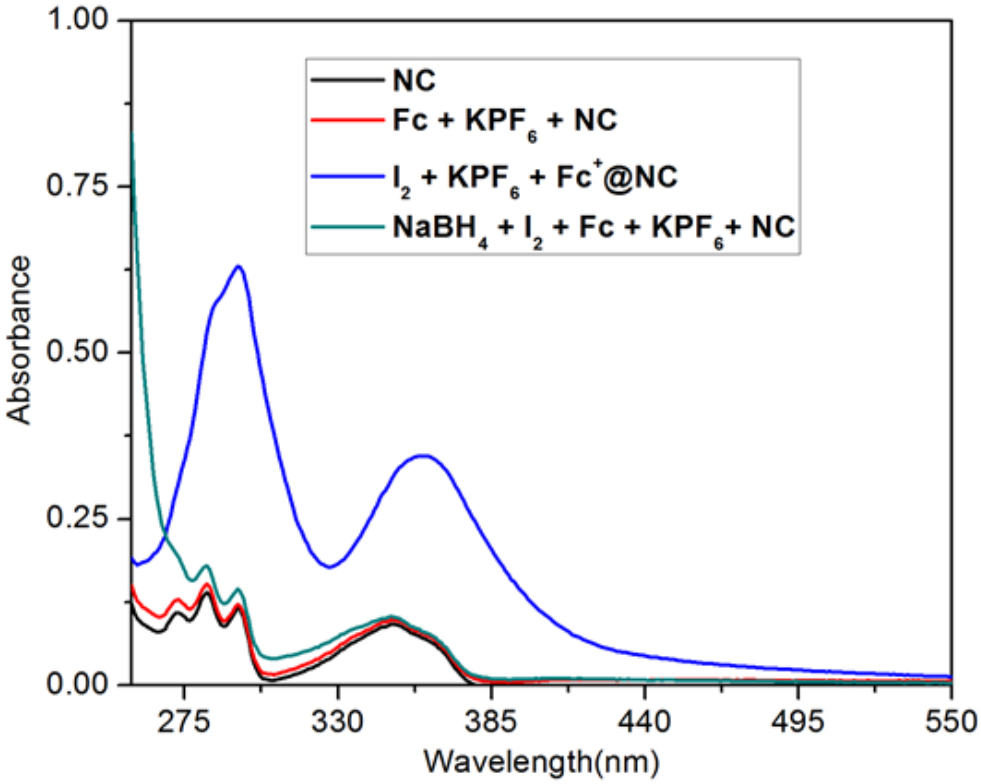

Figure S68. *UV-Vis absorption spectra of* ***NC*** *(0.01 mM) in a 1:1 solvent mixture of acetonitrile and dichloromethane, and addition of one equivalent of* ***Fc*** *and* KPF_6 *respectively, and then addition of one equivalent of* I_2 *to the above solution. After addition of* I_2*, the absorbance of* ***Fc*****$^+$****@NC** *is enhanced significantly at 290 nm and 350 nm, suggesting* ***Fc*** *is oxidized to* ***Fc*****$^+$** *by* I_2*, and bound to the cavity of* ***NC****. Binding inside the cavity is also confirmed by the broad charge-transfer band at 390nm. Upon addition of* $NaBH_4$ *with* NBu_3 *to the above mixture, and sonication for 30 min,* ***Fc*****$^+$** *is reduced to* ***Fc*** *and leaves the cage.*

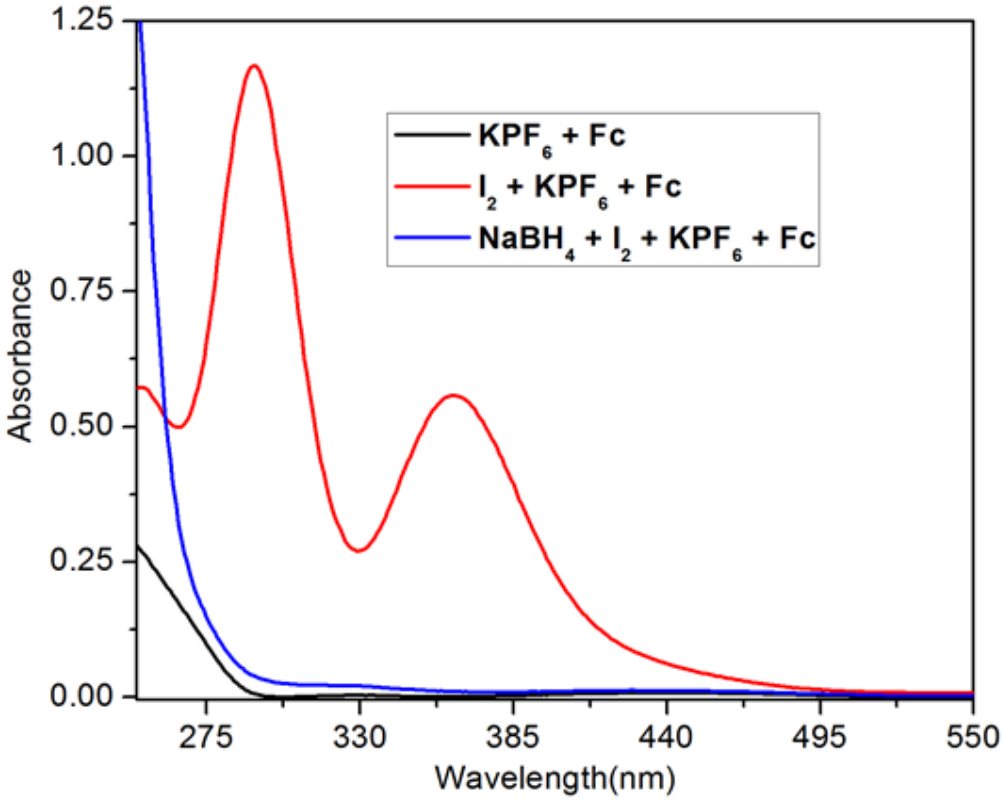

Figure S69. *UV-vis absorption spectra of* ***Fc*** *and* KPF_6 *(0.1 mM) in a 1:1 solvent mixture of acetonitrile and dichloromethane, with addition one equivalent of* I_2 *to the above mixture, suggesting neutral* ***Fc*** *is oxidized to* $\boldsymbol{Fc}^+$. *Clearly, the absorbance increases are caused by the oxidation of* ***Fc*** *to* $\boldsymbol{Fc}^+$. *After adding* $NaBH_4$ *to the mixture and sonicating for 5 min, the reduction of* $\boldsymbol{Fc}^+$ *leads almost back to the initial spectrum.*

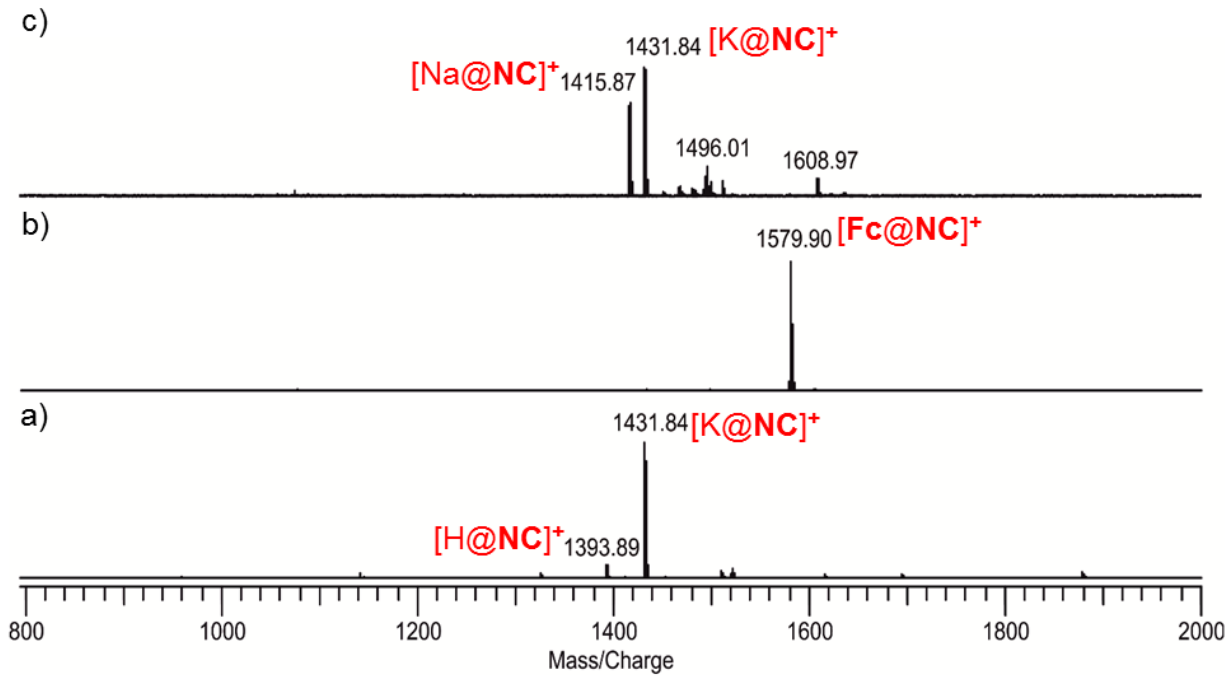

Figure S70. *ESI-FTICR mass spectrum of a)* ***Fc*** *and* K^+*@****NC*** *before oxidation, b) after oxidation with* I_2*, and c) after reduction with* $NaBH_4$*. Clearly, redox switching is achieved.*

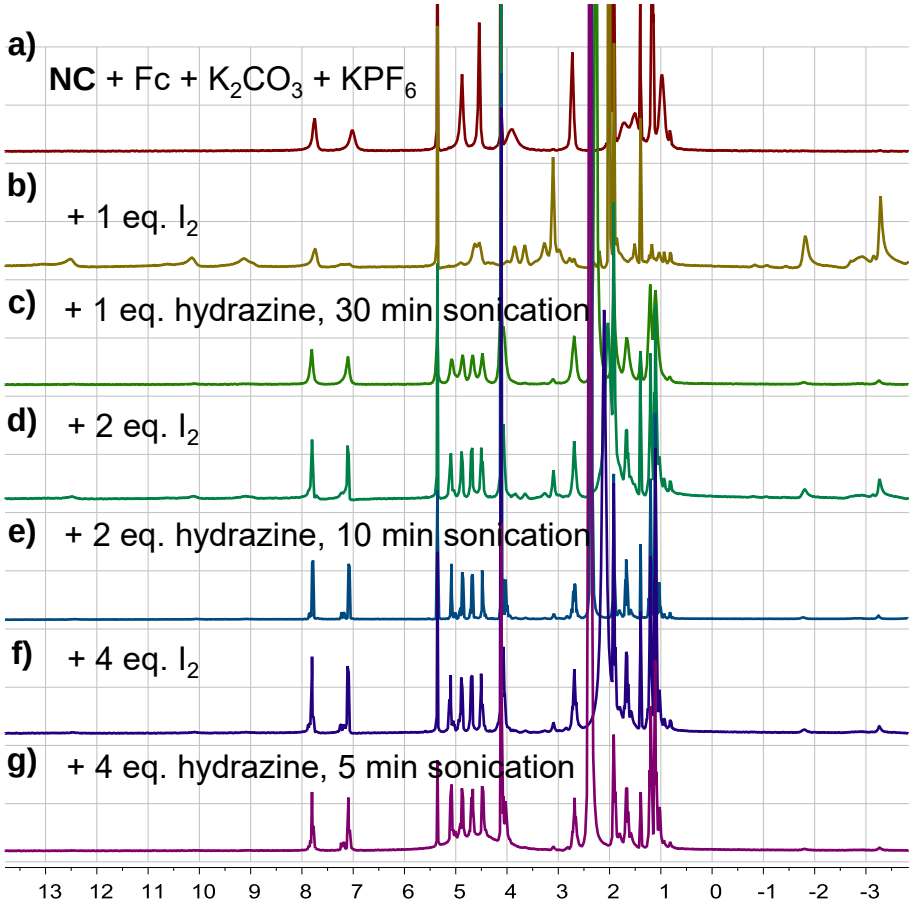

Figure S71. *^{1}H NMR spectra spectra (400 MHz, CD_2Cl_2:CD_3CN = 1:1, 298 K) of* ***NC*** *(4.0 mM) and* ***Fc*** *(4.0 mM) in the presence of KPF_6 (4.0 mM) and K_2CO_3 (80 mM; K_2CO_3 is used as a base to neutralize HI that may open the acid-labile benzyl ethers of the cage) when adding I_2 and hydrazine alternately. The reduction of Fc^+ encapsulated inside the cavity of* ***NC*** *by* $NaBH_4$ *is quite slow, and requires several (ca. 5) hours under sonication to finish. This may be due to that $NaBH_4$ is hardly soluble in the* solvent. Hydrazine is well soluble in this solvent and thus reduces *Fc^+@**NC** much more quickly. But it still costs 30 min under sonication for full reduction, presumably the "encapsulation effect" of* ***NC****. When performing the second cycle, only part of* ***NC*** *becomes occupied by Fc^+. We think there is some positively charged species generated during the redox reaction which occupied the cavity (this is indicated by the peak splitting at ca. 5 ppm), preventing the encapsulation of Fc^+. Consequently, the redox-switched binding cycle can be repeated chemically, but deteriorate quickly when adding more chemicals. However, the redox-switched binding cycle can be switched many times electrochemically. Please see Figures S58, S60 and S61.*

11. References

(S1) Jia, F.; He, Z.; Yang, L.-P.; Pan, Z.-S.; Yi, M.; Jiang, R.-W.; Jiang, W. Oxatub [4] arene: a smart macrocyclic receptor with multiple interconvertible cavities. *Chem. Sci.* **2015**, *6*, 6731-6738.

(S2) Bruker. *APEX3*. Bruker AXS Inc., Madison, Wisconsin, USA, **2012**.

(S3) Bruker. *SAINT*. Bruker AXS Inc., Madison, Wisconsin, USA, **2012**.

(S4) Bruker. *SADABS.* Bruker AXS Inc., Madison, Wisconsin, USA, **2012**.

(S5) (a) Sheldrick, G. M. SHELXT–Integrated space-group and crystal-structure determination. *Acta Crystallogr., Sect. A* **2015**, *71*, 3-8. (b) Sheldrick, G. M. Crystal structure refinement with SHELXL. *Acta Crystallogr. Sect. C* **2015**, *71*, 3-8.

(S6) (a) Burnett, M. N.; Johnson, C. K. ORTEP-III Report ORNL-6895. Oakridge National Laboratory, Tennessee, USA 1996; (b) Farrugia, L. J. *ORTEP*‐3 for Windows ‐ a version of *ORTEP*‐III with a Graphical User Interface (GUI). *J. Appl. Cryst.* **1997**, *30*, 565.

(S7) (a) Nicholson, R. S. Theory and application of cyclic voltammetry for measurement of electrode reaction kinetics. *Anal. Chem.* **1965**, *37*, 1351-1355; (b) Murthy, A. S. N.; Reddy, K. S. Cyclic voltammetric studies of methylene blue in presence of Fe^{3+}: catalytic currents. *Electrochim. Acta* **1983**, *28*, 1677-1680.

(S8) Ahlrichs, R.; Bär, M.; Häser, M.; Horn, M.; Kölmel, C. Electronic structure calculations on workstation computers: The program system turbomole. *Chem. Phys. Lett*. **1989**, 162, 165-169.

(S9) (a) Tao, J. M.; Perdew, J. P.; Staroverov, V. N.; Scuseria, G. E. Climbing the density functional ladder: Nonempirical meta–generalized gradient approximation designed for molecules and solids. *Phys. Rev. Lett.* **2003**, *91*, 146401-4. (b) Grimme, S.; Antony, J.; Ehrlich, S.; Krieg, H. A consistent and accurate ab initio parametrization of density functional dispersion correction (DFT-D) for the 94 elements H-Pu. *J. Chem. Phys.* **2010**, *132*, 154104-19. (c) Grimme, S.; Ehrlich, S.; Goerigk, L. Effect of the damping function in dispersion corrected density functional theory. *J. Comput. Chem.* **2011**, *32*, 1456-1465. (d) Weigend, F.; Ahlrichs, R. Balanced basis sets of split valence, triple zeta valence and

quadruple zeta valence quality for H to Rn: Design and assessment of accuracy. *Phys. Chem. Chem. Phys.* **2005**, *7*, 3297-3305.

(S10) Klamt, A.; Schüürmann, G. COSMO: a new approach to dielectric screening in solvents with explicit expressions for the screening energy and its gradient. *J. Chem. Soc., Perkin Trans. 2* **1993**, 799-805.

(S11) Lide, D. R. (ed.), *CRC Handbook of Chemistry and Physics*, CRC Press, Boca Raton, FL, **2005**.

(S12) Eichkorn, K; Treutler, O.; Öhm, H.; Häser, M.; Ahlrichs, R. Auxiliary basis sets to approximate Coulomb potentials. *Chem. Phys. Lett.* **1995**, *240*, 283-290.

(S13) Becke, A. D. Density‐functional thermochemistry. III. The role of exact exchange. *J. Chem. Phys.* **1993**, *98*, 5648-5652.

(S14) Klamt, A. *Wiley Interdiscip. Rev. Comp. Mol. Sci.* **2018**, *1*, 699-709.

(S15) Grimme, S. Supramolecular binding thermodynamics by dispersion‐corrected density functional theory. *Chem. Eur. J.* **2012**, *18*, 9955-9964.

(S16) Eckert, F.; Klamt, A. *COSMOtherm*, Version C3.0, Release 13.01; COSMOlogic GmbH & Co. KG, Leverkusen, Germany, **2013**.

6.5 Chiroptical inversion of a planar chiral redox-switchable rotaxane

M. Gaedke, F. Witte, J. Anhäuser, H. Hupatz, H.V. Schröder, A. Valkonen, K. Rissanen, A. Lützen, B. Paulus, B. Sarkar, C.A. Schalley

Chem. Sci. **2019**, *10*, 10003-10009.

Submitted on July 26, 2019, first published on September 4, 2019 by The Royal Society of Chemistry.

An electronic version of the articles is available at: https://doi.org/10.1039/C9SC03694F

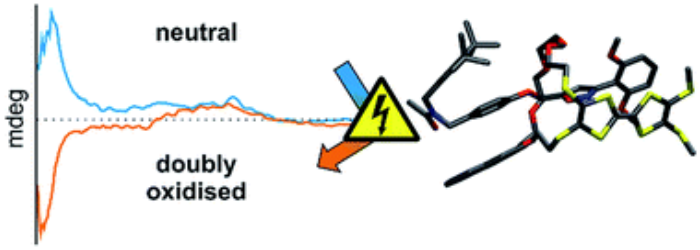

Figure 6.5. Graphical abstract. Reprinted with permission from Gaedke *et al.*[245] (published by the Royal Society of Chemistry, under the CC BY-NC 3.0 licence).

Authors' contributions

The project was conceived by Marius Gaekd with help from Hendrik V. Schröder and me. Felix Witte, Jana Anhäuser, Christoph A. Schalley, and Marius Gaedke wrote the manuscript with main contributions from Marius Gaedke. Marius Gaedke carried out the synthetic work including preparation of single crystals, NMR, UV/Vis, CV, MS and CD measurements. All computational work was done by Felix Witte and Beate Paulus. The chiral HPLC separations were performed and analysed by Jana Anhäuser and Arne Lützen. I measured and analysed the ITC data. Arto Valkonen and Kari Rissanen measured and solved the SCXRD data. Hendrik V. Schröder helped with synthetic work and data analysis. All Authors contributed to the final version of the manuscript.

Chemical Science

EDGE ARTICLE

View Article Online
View Journal | View Issue

Cite this: *Chem. Sci.*, 2019, **10**, 10003

All publication charges for this article have been paid for by the Royal Society of Chemistry

Received 26th July 2019
Accepted 4th September 2019

DOI: 10.1039/c9sc03694f

rsc.li/chemical-science

Chiroptical inversion of a planar chiral redox-switchable rotaxane†

Marius Gaedke,[a] Felix Witte,[a] Jana Anhäuser,[b] Henrik Hupatz,[a] Hendrik V. Schröder,[a] Arto Valkonen,[c] Kari Rissanen,[c] Arne Lützen,[b] Beate Paulus[a] and Christoph A. Schalley*[a]

A tetrathiafulvalene (TTF)-containing crown ether macrocycle with C_s symmetry was designed to implement planar chirality into a redox-active [2]rotaxane. The directionality of the macrocycle atom sequence together with the non-symmetric axle renders the corresponding [2]rotaxane mechanically planar chiral. Enantiomeric separation of the [2]rotaxane was achieved by chiral HPLC. The electrochemical properties – caused by the reversible oxidation of the TTF – are similar to a non-chiral control. Reversible inversion of the main band in the ECD spectra for the individual enantiomers was observed after oxidation. Experimental evidence, conformational analysis and DFT calculations of the neutral and doubly oxidised species indicate that mainly electronic effects of the oxidation are responsible for the chiroptical switching. This is the first electrochemically switchable rotaxane with a reversible inversion of the main ECD band.

Introduction

Evidenced by the homochirality in our biosphere,[1–3] chirality is a fundamental principle, which governs the molecular recognition and activity of virtually all biomolecules. Therefore, gaining control over the preferred isomer of a molecule or an assembly by carefully designing a molecular system is a worthwhile endeavour.

The term "chiroptical switch" has been used by Canary to refer to molecules, which are capable of "changes in their interaction with polarized light".[4] Potential applications are information processing, data storage and sensing. In this context, the ground breaking work of Feringa and co-workers[5–7] on overcrowded alkenes, which act as light triggered chiroptical switches was awarded with the Nobel Prize in chemistry 2016 "for the design and synthesis of molecular machines"[8] and underlines the general interest in this topic.

Mechanically interlocked molecules (MIMs)[9–12] consist of parts that can move relative to each other guided by intramolecular forces. Therefore, we envisioned them to be ideal candidates for chiroptical switches in which co-conformational or even configurational changes in the MIM occur.

An achiral wheel with directionality in its atom sequence forms a chiral [2]rotaxane, when threaded onto a directional

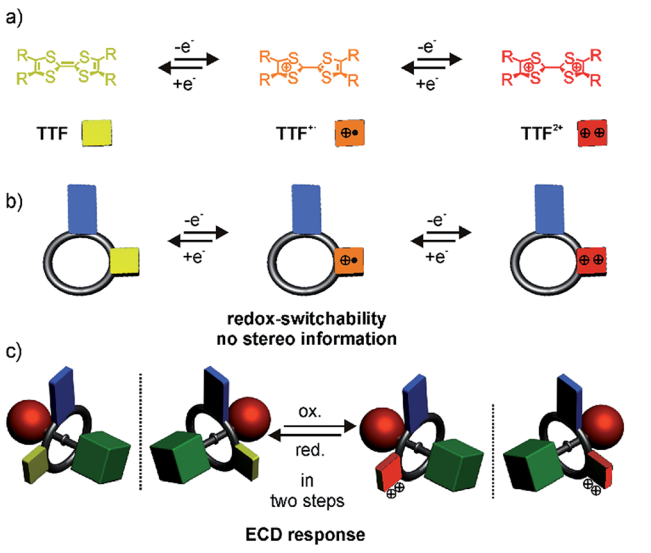

Scheme 1 (a) Reversible one-electron oxidations of the TTF moiety, (b) reversible oxidation of a directional crown ether wheel bearing a TTF unit, (c) chiroptical switching of the planar chiral [2]rotaxane enantiomers.

[a]Institut für Chemie und Biochemie, Freie Universität Berlin, Takustr. 3, 14195 Berlin, Germany. E-mail: c.schalley@schalley-lab.de

[b]Kekulé-Institut für Organische Chemie und Biochemie, Universität Bonn, Gerhard-Domagk-Str. 1, 53121 Bonn, Germany

[c]University of Jyvaskyla, Department of Chemistry, P.O. Box 35, 40014 Jyväskylä, Finland

† Electronic supplementary information (ESI) available: Synthetic procedures including full characterisation of new compounds, electrochemical data, crystallographic data and mass spectrometry data. CCDC 1910670. For ESI and crystallographic data in CIF or other electronic format see DOI: 10.1039/c9sc03694f

axle (Scheme 1). In 1997, Vögtle *et al.* reported on the first resolution of a racemate of such mechanically planar chiral rotaxanes.[13] Chiral rotaxanes may be chiral from inclusion of classical stereogenic elements or by virtue of being mechanically planar chiral. Since then, several examples followed,[14–25] in which the mechanically interlocked structure was used to induce directionality in polymers,[26–28] for sensing,[29–31] and to act as an enantioselective catalyst.[32] Today, sophisticated synthetic protocols allow an efficient enantioselective synthesis. For example, Goldup and co-workers[33,34] described elegant protocols to synthesise planar chiral enantiopure [2]rotaxanes using readily available chiral auxiliaries. However, switchable planar chiral rotaxanes remain rare. So far, the modulation of chirality relies on heat,[21] the choice of solvent, anion exchange,[35] or pH.[36]

Recently, we described redox-switchable rotaxanes, in which the wheels are decorated with tetrathiafulvalenes (TTF).[37–41] TTF can be reversibly oxidised to the $TTF^{\bullet+}$ and TTF^{2+} states (Scheme 1). Large-amplitude motion and co-conformational changes in (oligo)rotaxanes were triggered by redox chemistry.[38,42–50] Apart from rotaxanes, TTF derivatives with covalently bound chiral substituents exhibited a chiroptical response to a change of their redox-state.[51–57] Hence, our switchable rotaxanes display ideal optoelectronic properties since they are air stable in their neutral and oxidised form and show a clear-cut optical output,[37] which is even visible by the naked eye.

In this paper, we report the synthesis, characterisation and optical resolution of a new mechanically planar chiral tristable [2]rotaxane based on the 24-crown-8/secondary ammonium binding motif.[58] The rotaxane consists of the directional wheel **dTTFC8** (Scheme 2), which is derived from a C_{2v}-symmetric TTF-decorated crown ether **TTFC8** (Scheme 2) published by our group recently.[38] ECD measurements show reversible chiroptical switching, which can be explained mainly by electronic changes. The measurements are supported by quantum chemical calculations, which were also used to determine the absolute configuration. To the best of our knowledge, this is the first example of a chiroptical switch with a complete sign reversal of the main band in the ECD spectra based on electronic changes in a mechanically bound assembly.

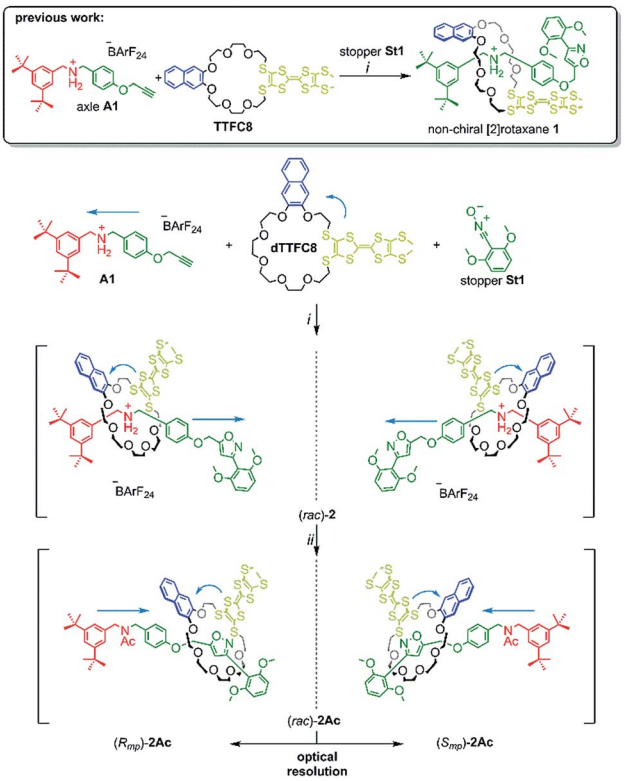

Scheme 2 Synthesis of rotaxanes (*rac*)-**2** and (*rac*)-**2Ac**. Conditions and reagents: (i) DCM, 35 °C, 12 h (73%); (ii) Ac_2O, NEt_3, ACN, 12 h, r.t. (95%).

Results and discussion

Synthesis and characterisation

The prerequisite for rotaxane formation is a sufficiently high binding constant between the crown ether and the ammonium axle. ITC experiments revealed an association constant of $K_a = (3.6 \pm 0.3)\ 10^5\ M^{-1}$ and a 1 : 1 stoichiometry for pseudorotaxane formation from **dTTFC8** and axle **A1** (Scheme 2). The binding constant is very similar to that of our previous non-directional TTF-decorated wheel **TTFC8** ($K_a = (4.4 \pm 0.4)\ 10^5\ M^{-1}$, for thermodynamic parameters see ESI,† Section 4),[38] which indicates the positional change of the TTF unit not to significantly affect the binding properties of the wheel.

As for the non-chiral [2]rotaxane **1**, rotaxane formation was achieved with nitrile-oxide stopper **St1** using a catalyst-free end-capping protocol established by Takata and co-workers[59] yielding a racemic mixture of rotaxane (*rac*)-**2** (73%). The non-ionic version (*rac*)-**2Ac** (95%) was obtained through *N*-acylation with Ac_2O[60] (Scheme 2). The ^1H NMR spectra of (*rac*)-**2** and (*rac*)-**2Ac** (Fig. 1) reveal a diastereotopic splitting of the macrocycle's methylene protons as well as of the axle methylene protons H_h.[37,38] The splitting of both macrocycle and axle protons is characteristic for the formation of a chiral, yet racemic [2]rotaxane. Isoxazole formation during stopper attachment leads to a strong downfield shift of 3.88 ppm for proton H_i.

In (*rac*)-**2**, the *S*-methyl protons on **dTTFC8** split into two singlets of the same intensity. Comparable rotaxanes also showed this behaviour on the same position.[27,28] HR-ESI mass and tandem MS experiments support the interlocked architecture (Fig. S1†).

For non-ionic (*rac*)-**2Ac**, the shift of H_i ($\Delta\delta = +0.28$ ppm) and H_h ($\Delta\delta = +0.76$ ppm) relative to (*rac*)-**2** suggests that the wheel translates towards the isoxazole moiety in the absence of attractive interactions with the ammonium ion. Two sets of signals are observed due to the *cis–trans* isomerism of the amide bond in (*rac*)-**2Ac**. Variable temperature NMR experiments (Fig. S3†) in DMSO-d_6 reveal the same barrier ($\Delta G^{\ddagger} = 74 \pm 2$ kJ mol^{-1}) for amide *cis–trans* isomerisation as observed for a similar acetylated rotaxane.[41]

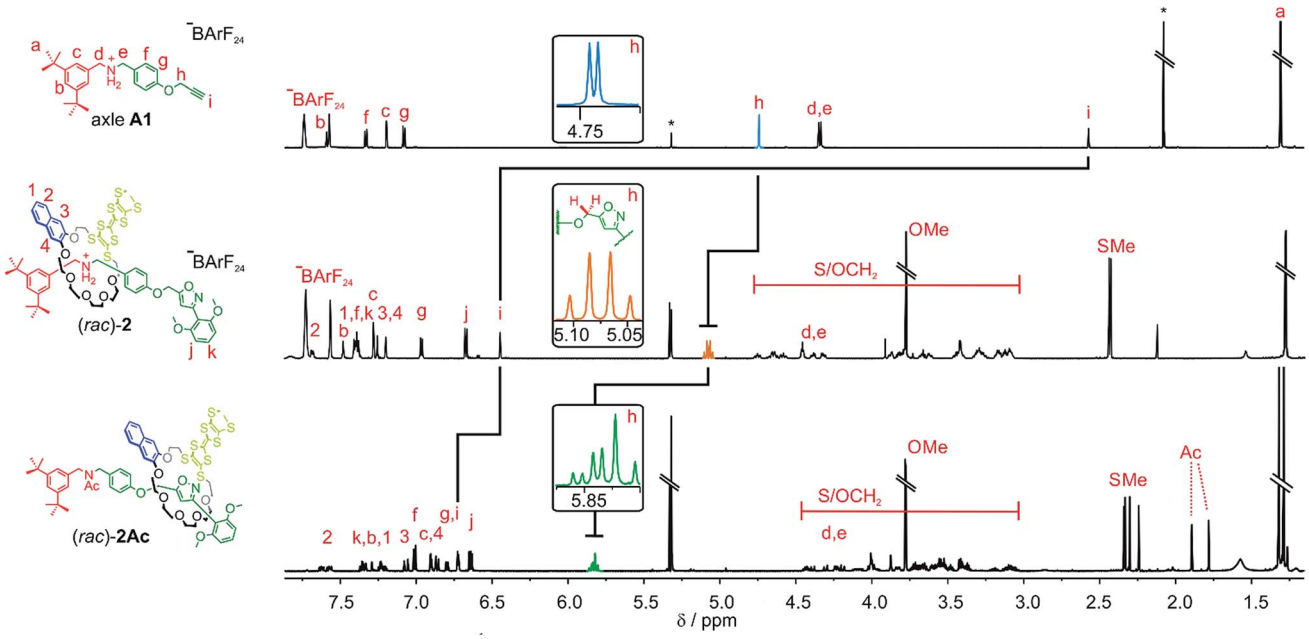

Fig. 1 Comparison of the shifts and splitting in the partial ^{1}H NMR spectra of the methylene groups on the axle **A1** (top), rotaxane (*rac*)-**2** (middle) and acetylated rotaxane (*rac*)-**2Ac** (bottom) (700 MHz, 298 K, CD_2Cl_2).

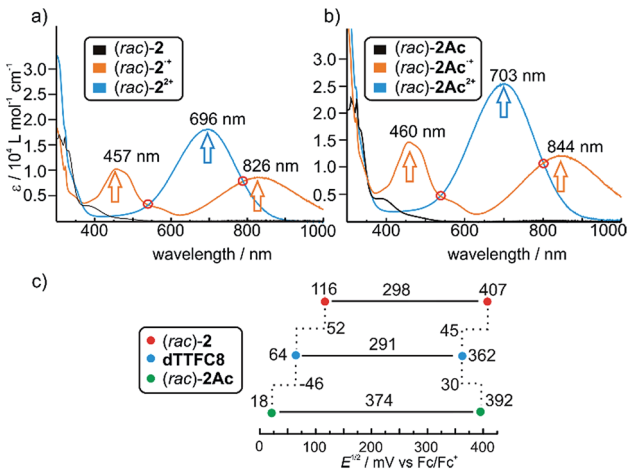

Fig. 2 UV/Vis spectra of (a) ionic (*rac*)-**2** and (b) non-ionic (*rac*)-**2Ac** in different oxidation states. Isosbestic points indicating a clean transition from $TTF^{\bullet+}$ to TTF^{2+} are highlighted with red circles. Spectra were obtained with 25 μM solutions in CH_2Cl_2 using bulk $Fe(ClO_4)_3$ as the oxidant; (c) correlation diagram of half-wave potentials obtained by cyclic voltammetry for the first and second redox process of (*rac*)-**2**, **dTTFC8** and (*rac*)-**2Ac** (each 1 mM) in CH_2Cl_2 referenced against $Fe(Cp)_2^{0/+}$ with NBu_4PF_6 (0.1 M) as the electrolyte.

Optoelectronic properties

Photometric titrations of (*rac*)-**2** and (*rac*)-**2Ac** with $Fe(ClO_4)_3$ (Fig. 2a and b) show similar bands for the three redox states (TTF, $TTF^{\bullet+}$ and TTF^{2+})[61–63] of both rotaxanes with distinct isosbestic points. These findings are consistent with structurally related rotaxanes featuring a non-directional TTF-decorated wheel.[38]

Cyclovoltammetric (CV) experiments were conducted with **dTTFC8**, (*rac*)-**2** and (*rac*)-**2Ac** in dichloromethane (Fig. 2c). The potentials for (*rac*)-**2** (116 mV and 407 mV) are considerably higher for both oxidation steps as compared to **dTTFC8** (64 mV and 362 mV). Both oxidations are thus energetically disfavoured because of the charge repulsion between the TTF cation radical as well as the TTF dication and the ammonium station. In case of (*rac*)-**2Ac** (18 mV and 392 mV) the first oxidation is more easily accomplished in comparison to the free macrocycle and the second oxidation is disfavoured. We attribute this behaviour to a stabilising interaction with the isoxazole moiety on the axle for the first oxidation.

For the second oxidation, the limited accessibility of the TTF^{2+} by counterions caused by the steric demand of the axle needs to be taken into account. Again these trends were already observed for the non-directional macrocycle and rotaxanes thereof.[38] The reversibility of the redox-waves of (*rac*)-**2** and (*rac*)-**2Ac** strongly indicated that the interlocked structures remain intact during the redox switching, however it is reasonable to assume conformational changes to occur due to charge repulsion and charge stabilisation. The data does not show any significant change in the electrochemical properties by introducing directionality into the TTF decorated wheel.

Enantiomer separation on chiral HPLC and CD spectroscopy

The two enantiomers of (*rac*)-**2Ac** could be separated using HPLC with a CHIRALPAK® IA stationary phase. The optical purity was determined (>99% ee; Fig. 3a) and mirror-image CD spectra were obtained for the neutral enantiomers with bands at 242 nm and 325 nm (Fig. 3b). We assigned the absolute configuration based on the computational results (see below).

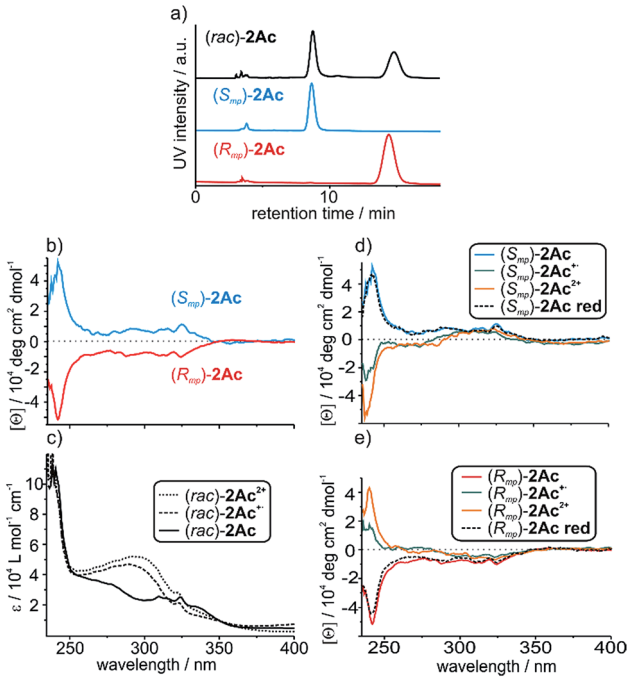

Fig. 3 (a) Traces of analytical chiral HPLC. The chromatographic resolution of (*rac*)-**2Ac** was realised by chiral phase HPLC on a CHIRALPAK® IA column using methyl *tert*-butylether/CH_2Cl_2 80 : 20 (v/v) as the eluent. (b) CD spectra of the individual neutral enantiomers and (c) partial UV/Vis spectra of the neutral, singly and doubly oxidized (*rac*)-**2Ac**. (d and e) CD spectra of the individual enantiomers in their three oxidation states and after reduction to the neutral state. Spectra were taken from 160 μM solutions in CH_2Cl_2 using bulk $Fe(ClO_4)_3$ as the oxidant and Zn dust as the reductant.

The oxidised species $\mathbf{2Ac}^{\bullet+}$ and $\mathbf{2Ac}^{2+}$ show bands at the same wavelengths. While no sign inversion occurs at 325 nm, the band at 242 nm exhibits a sign inversion during the first and a significant intensity increase during the second oxidation step. To exclude decomposition to be responsible for the switching, $\mathbf{2Ac}^{2+}$ was reduced back to the neutral state using Zn dust and then showed the initial CD spectrum again (Fig. 3d and e dashed lines). Surprisingly, no other CD signals are observed at a higher wavelength, although the change in UV/Vis absorption is most pronounced at 460 nm and 844 nm for the radical cation and at 703 nm for the dication (Fig. 2b). The reason for the sign change remains ambiguous. In fact, conformational changes were observed to induce transitions in CD spectra of non-interlocked TTF derivatives with centrochiral elements earlier.[53,64] Other examples show varying intensities[54] or shifts of the maxima[56] upon oxidation of the TTF attached.

Nevertheless, no TTF derivative is reported that shows a sign reversal in the maximum of an ECD spectrum without a shift in the wavelength. Apart from TTF derivatives, chiroptical switching *via* a redox process can be achieved with catechol,[65] viologen,[66] and tetraarylethylene[67] building blocks. Intense switching with a sign reversal was also observed for a viologen-type dicationic helquat.[68] Chiral inversion can also be achieved with metal ion complexation[69,70] acid–base-[71] and photoswitching.[6,68,72]

Computational results

To investigate whether the redox-induced sign inversion at 242 nm in the ECD spectra of (R_{mp})-**2Ac** is due to a change in its electronic properties or to a (co-)conformational change, density functional theory (DFT) calculations were performed at the TPSS-D3(BJ)[73–75] and ωB97X-D3 (ref. 76) levels. Conformational analyses reveal the structure depicted in Fig. 4 (left) to be the most stable one for (R_{mp})-**2Ac**. It is at least 18 kJ mol^{-1} more favourable than any other possible conformation found by theory (see Table S2†). For (R_{mp})-$\mathbf{2Ac}^{2+}$, there are two conformations relatively close in electronic energy: Conformer **A** (Fig. 4 middle) and **B** (Fig. 4 right) with a flipped naphthalene unit, *ca.* 9 kJ mol^{-1} more stable than **A**. This conformational change is explained by the oxidation of (R_{mp})-**2Ac** occuring fairly localised at the TTF unit.[77] The emerging charge of the oxidised TTF moiety is then stabilised by the naphthalene that moves into close proximity of the TTF^{2+}. Additionally, an atoms-in-molecules (AIM) analysis suggests that the electrostatic attraction between the naphthalene and TTF moieties outweighs all other non-covalent interactions for (R_{mp})-$\mathbf{2Ac}^{2+}$, while the maximisation of non-covalent interactions (C–H···π and π–π-stacking) is the most important factor in the neutral state (see ESI† for details).

The simulated CD spectra in Fig. 4 were obtained using simplified time-dependent DFT[78] at the ωB97X-D3 level. The spectrum of (R_{mp})-**2Ac** shows a deviation of around 40–50 nm, while that of (R_{mp})-$\mathbf{2Ac}^{2+}$ is off by less than 20 nm compared to experiment. The experimentally detected sign inversion at 242 nm is reproduced well by the calculations. The conformational change of (R_{mp})-**2Ac** upon oxidation, however, hardly influences the shape of the CD spectra as both conformations yield very similar CD spectra in the region between 230 and 400 nm. Therefore, we exclude the conformational change as the prime origin of the sign inversion.

To rationalise the optical behaviour of (R_{mp})-**2Ac** and (R_{mp})-$\mathbf{2Ac}^{2+}$, we examined its valence electronic structure, which is, as expected, dominated by orbitals localised at the TTF moiety (see Fig. S20†). Analysing the electronic transitions in the spectral region between 230 and 400 nm reveals that practically every excitation involves the TTF unit to some extent. While many transitions are of local nature, *i.e.*, between orbitals in close proximity, quite a few display a charge-transfer-like behaviour (insets Fig. 4 and S21†). For neutral (R_{mp})-**2Ac**, the vast majority of these transitions can be described by advancing an electron from an orbital centred at the TTF core, usually the HOMO, into an orbital located in another part of the rotaxane (*e.g.* the dimethoxy-phenyl moiety). For (R_{mp})-$\mathbf{2Ac}^{2+}$, the corresponding transitions progress from some orbital in the molecule into an orbital localised at the TTF moiety, usually the LUMO or LUMO+1. This induces differently oriented magnetic dipole transition moments leading to different signs in the CD spectrum. Hence, we conclude that the sign inversion in the CD spectra upon oxidation can be exclusively attributed to the change of the electronic structure.

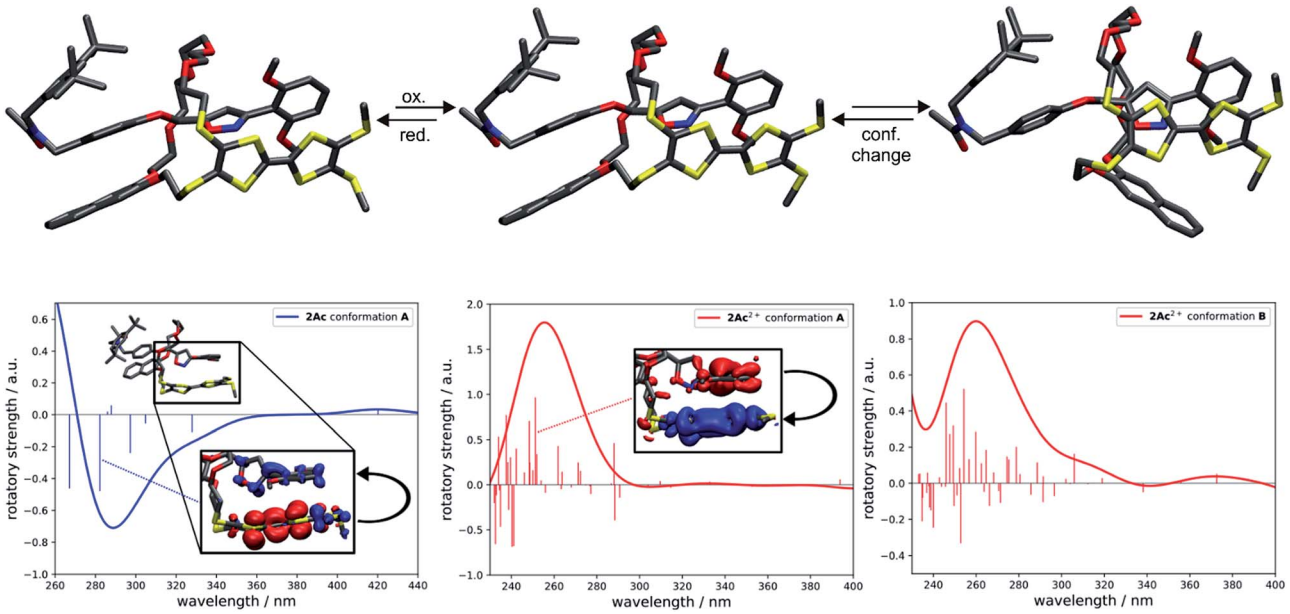

Fig. 4 Structural and spectral comparison of the most stable conformation of (R_{mp})-**2Ac** and the two most stable conformations, **A** and **B**, of (R_{mp})-**2Ac**$^{2+}$. Oxidation induces a flip of the naphthalene moiety in **A** towards the TTF unit yielding conformation **B**. The difference in electronic energy between **A** and **B** is around 9 kJ mol^{-1}. All structures were obtained at the TPSS-D3(BJ) level. Corresponding simulated CD spectra with excited state difference densities of selected transitions (insets) visualising the change in electronic structure upon photoexcitation of (R_{mp})-**2Ac** (left) and (R_{mp})-**2Ac**$^{2+}$ (middle). The difference in the CD spectra due to the conformational change of (R_{mp})-**2Ac**$^{2+}$ is negligible in the region of interest. The spectra were obtained at the ωB97X-D3 level using sTD-DFT. Gaussian line broadening with $\sigma = 20$ nm was applied. Insets: blue and red zones correspond to areas of electron enhancement and electron depletion, respectively. Isovalue = 0.001 a_0^{-3}.

Conclusions

In conclusion, electrochemically switchable crown ether/ammonium [2]rotaxanes bearing a directional wheel are reported. The wheel features a redox-switchable TTF unit. The directionality had no observable impact on the electrochemical and optical properties of the racemic mixtures determined by UV/Vis spectroscopy and CV measurements. Instead, the pure enantiomers of the acetylated non-ionic derivatives display a redox-induced reversible inversion of the sign in the ECD spectrum without a change of absolute configuration. The mechanism and the absolute configuration of this chiroptical switch has been examined by computational methods. While co-conformational changes have hardly any impact on the ECD spectra, the changes in electronic structure induced by oxidation play a pivotal role. These results underline the impact of the mechanical bond, which allows the construction of intriguing switchable chemical assemblies with unexpected properties. This is the first in class example of a redox-controlled chiroptical switch with a complete sign reversal based on a mechanically planar chiral rotaxane. In the future, these properties could be employed in materials science to construct novel optoelectronic building blocks.

Conflicts of interest

There are no conflicts to declare.

Acknowledgements

We thank the Deutsche Forschungsgemeinschaft (CRC 765) and Academy of Finland (KR proj. no. 309399, AV proj. no. 314343) for funding. We are grateful to the Alexander von Humboldt-Foundation for support of KR (AvH research award). JA thanks the Studienstiftung des deutschen Volkes for a doctoral scholarship. Furthermore, we thank Dr Lucia Volbach for help with the chiral separation and Dr Rakesh Puttreddy for help with the crystallisation.

Notes and references

1 R. Breslow and Z. L. Cheng, *Proc. Natl. Acad. Sci. U. S. A.*, 2009, **106**, 9144–9146.
2 F. Jafarpour, T. Biancalani and N. Goldenfeld, *Phys. Rev. E*, 2017, **95**, 032407.
3 D. G. Blackmond, *Cold Spring Harbor Perspect. Biol.*, 2010, **2**, a002147.
4 J. W. Canary, *Chem. Soc. Rev.*, 2009, **38**, 747–756.
5 N. Koumura, R. W. Zijlstra, R. A. van Delden, N. Harada and B. L. Feringa, *Nature*, 1999, **401**, 152–155.
6 B. L. Feringa, R. A. van Delden, N. Koumura and E. M. Geertsema, *Chem. Rev.*, 2000, **100**, 1789–1816.
7 B. L. Feringa, R. A. van Delden and M. K. J. ter Wiel, *Pure Appl. Chem.*, 2003, **75**, 563–575.
8 B. L. Feringa, *Angew. Chem., Int. Ed.*, 2017, **56**, 11060–11078.
9 J. F. Stoddart, *Angew. Chem., Int. Ed.*, 2017, **56**, 11094–11125.

10 E. A. Neal and S. M. Goldup, *Chem. Commun.*, 2014, **50**, 5128–5142.
11 J. F. Stoddart, *Chem. Soc. Rev.*, 2009, **38**, 1802–1820.
12 J. E. Lewis, M. Galli and S. M. Goldup, *Chem. Commun.*, 2016, **53**, 298–312.
13 C. Yamamoto, Y. Okamoto, T. Schmidt, R. Jäger and F. Vögtle, *J. Am. Chem. Soc.*, 1997, **119**, 10547–10548.
14 E. M. G. Jamieson, F. Modicom and S. M. Goldup, *Chem. Soc. Rev.*, 2018, **47**, 5266–5311.
15 N. H. Evans, *Chem.–Eur. J.*, 2018, **24**, 3101–3112.
16 P. E. Glen, J. A. T. O'Neill and A.-L. Lee, *Tetrahedron*, 2013, **69**, 57–68.
17 N. Kameta, K. Hiratani and Y. Nagawa, *Chem. Commun.*, 2004, 466–467.
18 J. Niemeyer and N. Pairault, *Synlett*, 2018, **29**, 689–698.
19 Y. Makita, N. Kihara, N. Nakakoji, T. Takata, S. Inagaki, C. Yamamoto and Y. Okamoto, *Chem. Lett.*, 2007, **36**, 162–163.
20 Y. Tachibana, N. Kihara, Y. Ohga and T. Takata, *Chem. Lett.*, 2000, **29**, 806–807.
21 Y. Mochizuki, K. Ikeyatsu, Y. Mutoh, S. Hosoya and S. Saito, *Org. Lett.*, 2017, **19**, 4347–4350.
22 M. Asakawa, G. Brancato, M. Fanti, D. A. Leigh, T. Shimizu, A. M. Z. Slawin, J. K. Y. Wong, F. Zerbetto and S. Zhang, *J. Am. Chem. Soc.*, 2002, **124**, 2939–2950.
23 T. Ogoshi, D. Yamafuji, T. Aoki, K. Kitajima, T. A. Yamagishi, Y. Hayashi and S. Kawauchi, *Chem.–Eur. J.*, 2012, **18**, 7493–7500.
24 G. Bottari, D. A. Leigh and E. M. Pérez, *J. Am. Chem. Soc.*, 2003, **125**, 13360–13361.
25 P. R. Ashton, J. A. Bravo, F. M. Raymo, J. F. Stoddart, A. J. P. White and D. J. Williams, *Eur. J. Org. Chem.*, 1999, 899–908.
26 Y.-G. Lee, Y. Koyama, M. Yonekawa and T. Takata, *Macromolecules*, 2010, **43**, 4070–4080.
27 S. Suzuki, F. Ishiwari, K. Nakazono and T. Takata, *Chem. Commun.*, 2012, **48**, 6478–6480.
28 F. Ishiwari, K. Nakazono, Y. Koyama and T. Takata, *Angew. Chem., Int. Ed.*, 2017, **56**, 14858–14862.
29 N. Kameta, Y. Nagawa, M. Karikomi and K. Hiratani, *Chem. Commun.*, 2006, 3714–3716.
30 J. Y. C. Lim, I. Marques, V. Felix and P. D. Beer, *Angew. Chem., Int. Ed.*, 2018, **57**, 584–588.
31 K. Hirose, M. Ukimi, S. Ueda, C. Onoda, R. Kano, K. Tsuda, Y. Hinohara and Y. Tobe, *Symmetry*, 2018, **10**, 20.
32 Y. Tachibana, N. Kihara and T. Takata, *J. Am. Chem. Soc.*, 2004, **126**, 3438–3439.
33 R. J. Bordoli and S. M. Goldup, *J. Am. Chem. Soc.*, 2014, **136**, 4817–4820.
34 M. A. Jinks, A. de Juan, M. Denis, C. J. Fletcher, M. Galli, E. M. G. Jamieson, F. Modicom, Z. Zhang and S. M. Goldup, *Angew. Chem., Int. Ed.*, 2018, **57**, 14806–14810.
35 S. Corra, C. de Vet, J. Groppi, M. La Rosa, S. Silvi, M. Baroncini and A. Credi, *J. Am. Chem. Soc.*, 2019, **141**, 9129–9133.
36 C. E. Gell, T. A. McArdle-Ismaguilov and N. H. Evans, *Chem. Commun.*, 2019, **55**, 1576–1579.
37 H. V. Schröder, H. Hupatz, A. J. Achazi, S. Sobottka, B. Sarkar, B. Paulus and C. A. Schalley, *Chem.–Eur. J.*, 2017, **23**, 2960–2967.
38 H. V. Schröder, S. Sobottka, M. Nößler, H. Hupatz, M. Gaedke, B. Sarkar and C. A. Schalley, *Chem. Sci.*, 2017, **8**, 6300–6306.
39 H. V. Schröder, J. M. Wollschläger and C. A. Schalley, *Chem. Commun.*, 2017, **53**, 9218–9221.
40 H. V. Schröder, A. Mekic, H. Hupatz, S. Sobottka, F. Witte, L. H. Urner, M. Gaedke, K. Pagel, B. Sarkar, B. Paulus and C. A. Schalley, *Nanoscale*, 2018, **10**, 21425–21433.
41 H. V. Schröder, F. Stein, J. M. Wollschläger, S. Sobottka, M. Gaedke, B. Sarkar and C. A. Schalley, *Angew. Chem., Int. Ed.*, 2019, **58**, 3496–3500.
42 H. V. Schröder and C. A. Schalley, *Beilstein J. Org. Chem.*, 2018, **14**, 2163–2185.
43 A. Coskun, M. Banaszak, R. D. Astumian, J. F. Stoddart and B. A. Grzybowski, *Chem. Soc. Rev.*, 2012, **41**, 19–30.
44 S. Erbas-Cakmak, D. A. Leigh, C. T. McTernan and A. L. Nussbaumer, *Chem. Rev.*, 2015, **115**, 10081–10206.
45 A. Jana, M. Ishida, J. S. Park, S. Bahring, J. O. Jeppesen and J. L. Sessler, *Chem. Rev.*, 2017, **117**, 2641–2710.
46 M. Fumanal, M. Capdevila-Cortada, J. S. Miller and J. J. Novoa, *J. Am. Chem. Soc.*, 2013, **135**, 13814–13826.
47 M. Yoshizawa, K. Kumazawa and M. Fujita, *J. Am. Chem. Soc.*, 2005, **127**, 13456–13457.
48 M. R. Bryce, *J. Mater. Chem.*, 2000, **10**, 589–598.
49 D. Canevet, M. Salle, G. Zhang, D. Zhang and D. Zhu, *Chem. Commun.*, 2009, 2245–2269.
50 J. L. Segura and N. Martín, *Angew. Chem., Int. Ed.*, 2001, **40**, 1372–1409.
51 A. Saad, F. Barriere, E. Levillain, N. Vanthuyne, O. Jeannin and M. Fourmigue, *Chem.–Eur. J.*, 2010, **16**, 8020–8028.
52 M. Hasegawa, J. Endo, S. Iwata, T. Shimasaki and Y. Mazaki, *Beilstein J. Org. Chem.*, 2015, **11**, 972–979.
53 F. Pop, S. Laroussi, T. Cauchy, C. J. Gomez-Garcia, J. D. Wallis and N. Avarvari, *Chirality*, 2013, **25**, 466–474.
54 E. Gomar-Nadal, J. Veciana, C. Rovira and D. B. Amabilino, *Adv. Mater.*, 2005, **17**, 2095–2098.
55 Y. Zhou, D. Zhang, L. Zhu, Z. Shuai and D. Zhu, *J. Org. Chem.*, 2006, **71**, 2123–2130.
56 T. Biet, A. Fihey, T. Cauchy, N. Vanthuyne, C. Roussel, J. Crassous and N. Avarvari, *Chem.–Eur. J.*, 2013, **19**, 13160–13167.
57 F. Riobe and N. Avarvari, *Chem. Commun.*, 2009, 3753–3755.
58 P. R. Ashton, P. J. Campbell, P. T. Glink, D. Philp, N. Spencer, J. F. Stoddart, E. J. T. Chrystal, S. Menzer, D. J. Williams and P. A. Tasker, *Angew. Chem., Int. Ed.*, 1995, **34**, 1865–1869.
59 T. Matsumura, F. Ishiwari, Y. Koyama and T. Takata, *Org. Lett.*, 2010, **12**, 3828–3831.
60 Y. Tachibana, H. Kawasaki, N. Kihara and T. Takata, *J. Org. Chem.*, 2006, **71**, 5093–5104.
61 S. V. Rosokha and J. K. Kochi, *J. Am. Chem. Soc.*, 2007, **129**, 828–838.
62 M. B. Kirketerp, L. A. Leal, D. Varsano, A. Rubio, T. J. Jorgensen, K. Kilsa, M. B. Nielsen and S. B. Nielsen, *Chem. Commun.*, 2011, **47**, 6900–6902.

63 V. Khodorkovsky, L. Shapiro, P. Krief, A. Shames, G. Mabon, A. Gorgues and M. Giffard, *Chem. Commun.*, 2001, 2736–2737.
64 T. Cauchy, F. Pop, J. Cuny and N. Avarvari, *Chimia*, 2018, **72**, 389–393.
65 M. Fukui, T. Mori, Y. Inoue and R. Rathore, *Org. Lett.*, 2007, **9**, 3977–3980.
66 J. Deng, N. Song, Q. Zhou and Z. Su, *Org. Lett.*, 2007, **9**, 5393–5396.
67 T. Mori and Y. Inoue, *J. Phys. Chem. A*, 2005, **109**, 2728–2740.
68 L. Pospisil, L. Bednarova, P. Stepanek, P. Slavicek, J. Vavra, M. Hromadova, H. Dlouha, J. Tarabek and F. Teply, *J. Am. Chem. Soc.*, 2014, **136**, 10826–10829.
69 E. Lee, H. Ju, I. H. Park, J. H. Jung, M. Ikeda, S. Kuwahara, Y. Habata and S. S. Lee, *J. Am. Chem. Soc.*, 2018, **140**, 9669–9677.
70 A. Homberg, E. Brun, F. Zinna, S. Pascal, M. Gorecki, L. Monnier, C. Besnard, G. Pescitelli, L. Di Bari and J. Lacour, *Chem. Sci.*, 2018, **9**, 7043–7052.
71 T.-Y. Tai, Y.-H. Liu, C.-C. Lai, S.-M. Peng and S.-H. Chiu, *Org. Lett.*, 2019, **21**, 5708–5712.
72 C. Petermayer and H. Dube, *J. Am. Chem. Soc.*, 2018, **140**, 13558–13561.
73 J. Tao, J. P. Perdew, V. N. Staroverov and G. E. Scuseria, *Phys. Rev. Lett.*, 2003, **91**, 146401.
74 S. Grimme, S. Ehrlich and L. Goerigk, *J. Comput. Chem.*, 2011, **32**, 1456–1465.
75 F. Weigend and R. Ahlrichs, *Phys. Chem. Chem. Phys.*, 2005, **7**, 3297–3305.
76 J. D. Chai and M. Head-Gordon, *J. Chem. Phys.*, 2008, **128**, 084106.
77 R. F. W. Bader, *Chem. Rev.*, 1991, **91**, 893–928.
78 H. J. C. Berendsen, J. P. M. Postma, W. F. van Gunsteren, A. DiNola and J. R. Haak, *J. Chem. Phys.*, 1984, **81**, 3684–3690.

Supporting Information

Chiroptical inversion of a planar chiral redox-switchable rotaxane

Marius Gaedke,[a] Felix Witte,[a] Jana Anhäuser,[b] Henrik Hupatz,[a] Hendrik V. Schröder,[a] Arto Valkonen,[c], Kari Rissanen,[c] Arne Lützen,[b] Beate Paulus[a] and Christoph A. Schalley*[a]

[a] Institut für Chemie und Biochemie, Organische Chemie, Freie Universität Berlin, Takustraße 3, 14195 Berlin, Germany.
[b] Kekulé-Institut für Organische Chemie und Biochemie, Universität Bonn, Gerhard-Domagk-Str. 1, 53121 Bonn, Germany.
[c] University of Jyvaskyla, Department of Chemistry, P.O. Box 35, 40014 Jyväskylä, Finland.
*Corresponding author e-mail: c.schalley@fu-berlin.de

Table of contents

1. Experimental details

1.1. General methods

All reagents and solvents were obtained from commercial sources and used without further purification. Dry solvents were purchased from Acros Organics or obtained from the M. BRAUN Solvent purification system SPS 800. 2-Hydroxyethyl 4-methylbenzenesulfonate **S4**,[1] 2-[(tetrahydropyran-2-yl)oxy]ethyl *p*-toluenesulfonate) **S5**,[2] 2,3-bis(2-cyanoethylthio)-6,7-bis(methylthio)tetrathiafulvalene **S12**,[3] axle **A1**,[4] and 2,6-dimethoxybenzonitrile oxide stopper **St1**[5] were synthesised according to literature procedures. Thin-layer chromatography was performed on silica gel-coated plates with fluorescent indicator F254 (Merck). For column chromatography, silica gel (0.04-0.063 mm, Merck) was used.

^{1}H and ^{13}C NMR experiments were performed on JEOL ECX 400, JEOL ECP 500, Bruker AVANCE 500 or Bruker AVANCE 700 instruments. Residual solvent signals were used as the internal standards. All shifts are reported in ppm and NMR multiplicities are abbreviated as s (singlet), d (doublet), t (triplet), m (multiplet) and br (broad). Coupling constants *J* are reported in Hertz. Compounds containing the tetrakis[3,5-bis(trifluoromethyl)phenyl]borate ($BArF_{24}^-$) anion show ^{13}C NMR spectra with ^{19}F, ^{10}B and ^{11}B couplings. These signals were denoted as one signal.

Melting points were determined on a SMP 30 (Stuart) instrument and are uncorrected.

High-resolution ESI mass spectra were measured on an Agilent 6210 ESI-TOF device. Tandem MS and infrared multiphoton dissociation (IRMPD) experiments were performed on a Varian Inc. Ionspec Q FT-7 equipped with a 7 T superconducting magnet and a Micromass Z-spray ESI source. HPLC grade solvents were used for sample preparation and the samples introduced into the ion source with a flow rate of 2-4 µL/min.

UV/Vis spectra were recorded with a Varian Cary 50 Bio spectrometer equipped with a xenon lamp. Solvents with HPLC grade and Suprasil glass cuvettes with a path-length of 1 cm were used.

ECD spectra were recorded on a JASCO-8-10 spectropolarimeter at 20°C. Solvents with HPLC grade and Suprasil glass cuvettes with a path-length of 2 mm were used. During the measurements, a constant flow of 3.2 L/min N_2 was provided. Each dataset is an average of three subsequent measurements.

CV measurements were carried out with an Autolab PGSTAT302N potentiostat in a 2 mL measuring cell in dichloromethane with 0.1 M n-Bu_4NPF_6 as the conducting salt. The working electrode was made of glassy carbon, the reference Ag electrode was etched with conc. aq. HCl. A Pt wire worked as a counter electrode. The cyclic voltammogram traces were recorded with 10, 25, 50, 100, 250, 500, 1000 and 2500 mV/s scan rates, to ensure that the observed

processes are reversible and diffusion-limited. For better comparability, only the 100 mV/s traces were plotted and compared in the discussion. In order to obtain the correct half-wave potentials, FeCp*/FeCp*$^{+}$ was used as the reference. These values were afterwards referenced to Fc/Fc^{+} as described in the literature.[6] The raw data was treated with Nova 1.5 by Metrohm and the plots were made with Origin *8* by OriginLab.

The chromatographic resolution was performed on a Shimadzu Prominence LC-20 HPLC system, equipped with two LC20-AT pumps, a DGU-20A3 solvent degasser, a diode array detector SPD-M20A (190-640 nm) and a fraction collector FRC-10A. For the analytical HPLC resolution, a Daicel CHIRALPAK® IA column (0.46 cm Ø, 25 cm) was used as the chiral stationary phase and *tert*-butyl methyl ether/CH_2Cl_2 (HPLC grade, 80:20 v/v) as the eluent with a flow rate of 1 mL/min. For the semi-preparative HPLC resolution, a CHIRALPAK® IA column (1 cm Ø, 25 cm) was used as the chiral stationary phase and *tert*-butyl methyl ether/dichloromethane (HPLC grade, 80:20 v/v) as the eluent with a flow rate of 4 mL/min.

1.2. Synthesis of dTTFC8

The directional wheel **dTTFC8** was synthesised starting from naphthalene-2,3-diol through consecutive substitution[7] with tetrahydropyranyl-protected mono- and pentaethylene glycol. After deprotection[8] to the diol and tosylation,[9] the corresponding diiodide was formed through a Finkelstein reaction.[4] In the last step, a CsOH•H_2O-mediated macrocyclisation[10] with the dicyanoethyl-protected TTF derivative[11] was carried out.

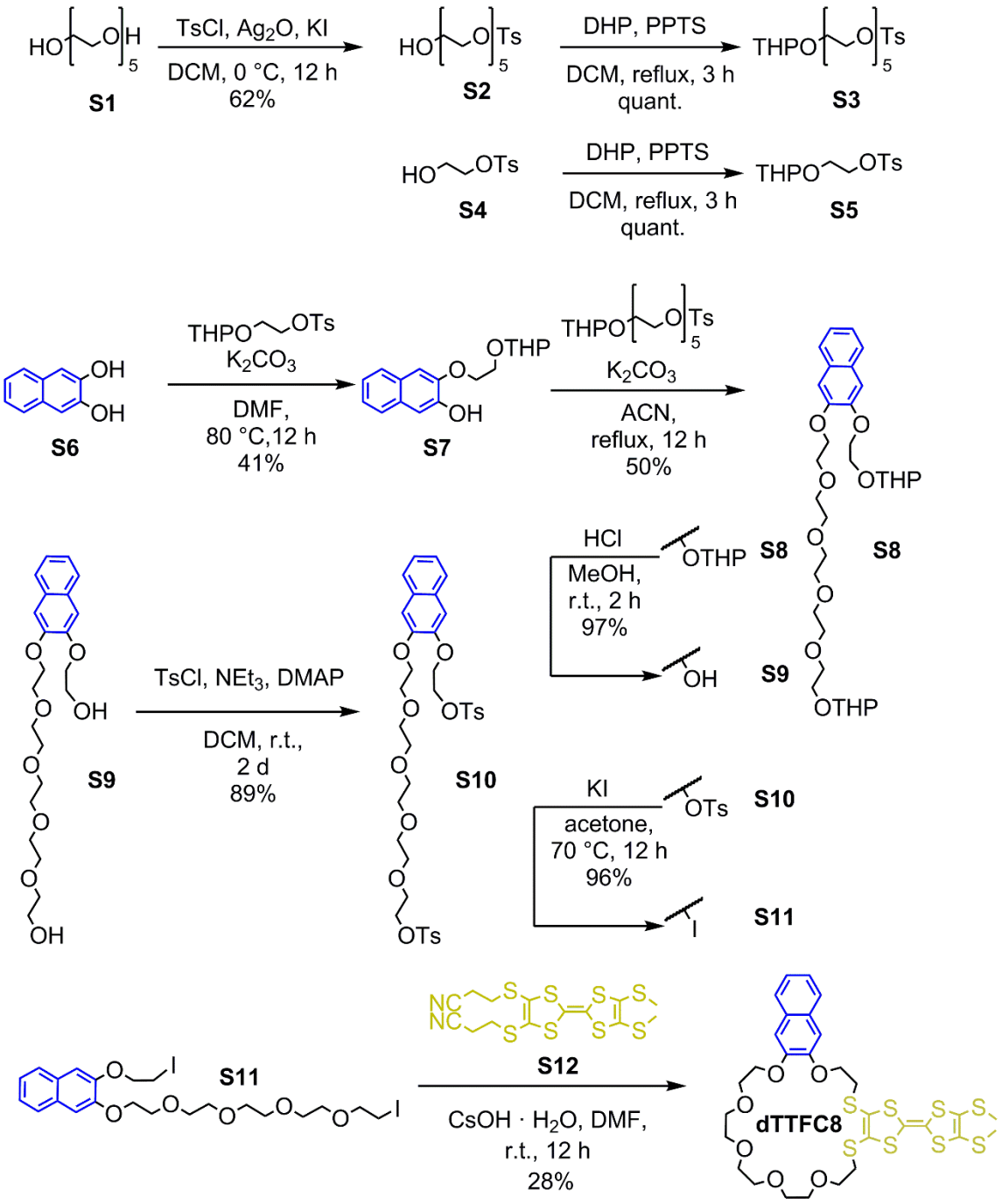

Scheme S1 Synthesis of wheel **dTTFC8** with a directional atom sequence.

14-Hydroxy-3,6,9,12-tetraoxatetradecyl 4-methylbenzenesulfonate[12]

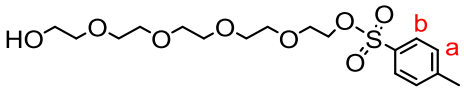

S2

4-Toluenesulfonyl chloride (444 mg, 2.3 mmol, 1.1 equiv.) was slowly added to a suspension of pentaethylene glycol **S1** (0.45 mL 1.9 mmol, 1.0 equiv.), KI (71.0 mg 0.42 mmol, 0.2 equiv.) and fresh Ag_2O (770 mg 3.3 mmol, 1.5 eq) in CH_2Cl_2 (21 mL) at 0 °C. The mixture was stirred overnight in a thawing ice bath. Afterwards, the mixture was filtered through a short celite pad and rinsed with EtOAc. After removal of the solvent, the crude product was purified by column chromatography (SiO_2, EtOAc/hexane = 2:1 → EtOAc, R_f ~ 0.3 in EtOAc) to isolate the desired product **S2** as a colourless oil in a 62% yield (466 mg, 1.2 mmol). **^{1}H NMR** (500 MHz, $CDCl_3$): δ = 2.42 (s, 3H, -C$\underline{H}_3$), 2.69 (s, 1H, -O$\underline{H}$), 3.47 – 3.70 (m, 18H, -OC$\underline{H}_2$), 4.08 – 4.17 (m, 2H, TsO-C$\underline{H}_2$-), 7.31 (d, J = 8.1 Hz, 2H, a), 7.76 (d, J = 8.1 Hz, 2H, b) ppm. **^{13}C NMR** (126 MHz, $CDCl_3$): δ = 21.7, 61.7, 68.7, 69.3, 70.3, 70.5, 70.6, 70.6, 70.6, 72.5, 128.0, 129.9, 133.0, 144.9 ppm. **ESI-HRMS**(ACN): *m/z* calcd. for $[C_{17}H_{28}O_8S]$: 415.1398 $[M+Na]^+$, found: 415.1394; calcd. for $[M+K]^+$:431.1137, found: 431.1130.

14-((Tetrahydro-2*H*-pyran-2-yl)oxy)-3,6,9,12-tetraoxatetradecyl 4-methylbenzenesulfonate[12]

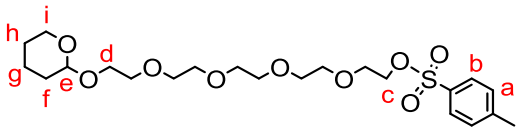

S3

A solution of monotosylate **S2** (1.00 g, 2.6 mmol, 1.0 equiv.), pyridinium tosylate (132 mg, 0.5 mmol, 0.2 equiv.) and 3,4-dihydro-*2H*-pyran (360 µL, 3.8 mmol, 97%, 1.5 equiv.) in CH_2Cl_2 (40 mL) was refluxed for 3 h. Afterwards, the mixture was poured into ice water, then extracted with CH_2Cl_2, washed with brine and dried with $MgSO_4$. After removal of the solvent, the crude product was purified by column chromatography (SiO_2, EtOAc, R_f ~ 0.6 in EtOAc) to isolate the desired product **S3** as a colourless oil in quantitative yield (1.26 g, 2.6 mmol). **^{1}H NMR** (500 MHz, $CDCl_3$): δ = 1.38 – 1.84 (m, 6H, f, g, h), 2.38 (s, 3H, -C$\underline{H}_3$), 3.38 – 3.49 (m, 2H, d), 3.49 – 3.65 (m, 16H, O-CH_2), 3.73 – 3.86 (m, 2H, i), 4.04 – 4.13 (m, 2H, c), 4.56 (dd, J = 4.3, 2.9 Hz, 1H, e), 7.29 (d, J = 8.1 Hz, 2H, a), 7.73 (d, J = 8.1 Hz, 2H, b) ppm. **^{13}C NMR:** (126 MHz, $CDCl_3$) δ = 19.4, 19.7, 21.6, 25.4, 30.5, 30.6, 43.6, 62.1, 62.8, 66.6, 68.6, 69.2, 70.4, 70.5, 70.6, 94.5, 94.5, 98.8, 98.9, 127.9, 129.8, 132.9 ppm. **ESI-HRMS**(ACN): *m/z* calcd. for $[C_{22}H_{36}O_9S]$: 499.1972 $[M+Na]^+$, found: 499.1955; calcd. for $[M+K]^+$: 515.1712, found: 515.1694.

3-(2-((Tetrahydro-2*H*-pyran-2-yl)oxy)ethoxy)-2-naphthol[7]

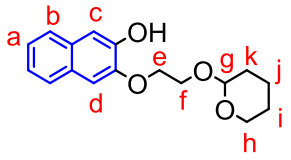

S7

A solution of protected monotosylate **S5** (96.0 mg, 0.32 mmol, 1.0 equiv.), naphthol **S6** (51.0 mg, 0.32 mmol, 1.0 equiv.) and K_2CO_3 (190 mg, 1.4 mmol, 4.3 eq) in dry DMF (20 mL) was stirred at 80 °C in an argon atmosphere for 12 h. Afterwards, residual K_2CO_3 was filtered off and the solvent was removed under reduced pressure. The crude product was then purified by column chromatography (SiO_2, CH_2Cl_2/MeOH = 100:1, R_f ~ 0.8 in CH_2Cl_2/MeOH = 50:1) to isolate the desired product **S7** as a colourless oil in a 41% yield (37.5 mg, 0.13 mmol). **^{1}H NMR** (500 MHz, $CDCl_3$): δ = 1.50 – 1.91 (m, 6H, j, k, l), 3.53 – 3.60 (m, 1H, h'), 3.89 – 3.97 (m, 2H, h'', f'), 4.07 – 4.16 (m, 1H,f''), 4.31 – 4.35 (m, 2H, e), 4.73 (dd, J = 4.6, 2.9 Hz, 1H, g), 7.20 (s, 1H, c), 7.27 (s, 1H, d), 7.28 – 7.34 (m, 2H, a, a'), 7.63 – 7.67 (m, 2H, b, b') ppm. **^{13}C NMR** (126 MHz, $CDCl_3$): δ = 19.7, 25.4, 30.7, 30.8, 62.8, 66.4, 69.5, 99.7, 109.0, 110.0, 123.5, 123.9, 124.6, 126.5, 126.7, 128.9, 130.4, 146.7, 147.0 ppm. **ESI-HRMS**(MeOH): *m/z* calcd. for $[C_{17}H_{20}O_4]$: 311.1254 $[M+Na]^+$, found: 311.1279; calcd for $[M+K]^+$ 327.0993, found: 327.1018.

2-(2-((3-((14-((Tetrahydro-2*H*-pyran-2-yl)oxy)-3,6,9,12-tetraoxatetradecyl)oxy)naphthalen-2-yl)oxy)ethoxy)tetrahydro-2*H*-pyran[7]

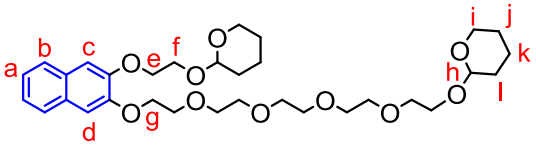

S8

A suspension of protected monotosylate **S3** (3.10 g, 6.44 mmol, 1 equiv.), monosubstituted naphthol **S7** (1.86 g, 6.44 mmol, 1 equiv.) and K_2CO_3 (3.80 g, 27.7 mmol, 4.3 equiv.) in dry ACN (100 mL) was refluxed under an argon atmosphere overnight. Afterwards K_2CO_3 was filtered off and the solvent was removed under reduced pressure. The crude product was then purified by column chromatography (SiO_2, EtOAc, R_f ~ 0.5 in EtOAc) to isolate the desired product **S8** as a colourless oil in a 50% yield (1.90 g, 3.21 mmol). **^{1}H NMR** (500 MHz, $CDCl_3$): δ = 1.44 – 1.90 (m, 12H, j, k, l), 3.45 – 3.61 (m, 4H, i), 3.61 – 3.91 (m, 15H, O-C$\underline{H}_2$), 3.91 – 3.96 (m, 2H, f), 3.96 – 4.02 (m, H, O-C$\underline{H}_2$), 4.11 – 4.16 (m, 1H, O-C$\underline{H}_2$), 4.17 – 4.23 (m, 1H, O-C$\underline{H}_2$), 4.25 – 4.33 (m, 4H, e, g), 4.59 – 4.63 (m, 1H, h), 4.73 – 4.78 (m, 1H, h'), 7.16 (s, 1H, d), 7.18 (s, 1H, c), 7.29 – 7.35 (m, 2H, a, a'), 7.63 – 7.67 (m, 2H, b, b') ppm. **^{13}C NMR** (126 MHz,

$CDCl_3$): δ = 19.4, 19.6, 19.9, 25.5, 25.6, 30.6, 30.7, 30.8, 62.2, 62.3, 65.7, 66.7, 68.3, 68. 6, 69.7, 70.6, 70.7, 70.7, 70.8, 71.1, 99.0, 108.7, 108.8, 124.3, 124.3, 124.5, 124.5, 126.4, 126.4, 126.5, 126.5, 129.4, 129.5, 129.6, 149.2, 149.3 ppm. **ESI-HRMS**(MeOH): *m/z* calcd. for [$C_{32}H_{48}O_{10}$]: 615.3140 [M+Na]$^+$, found: 615.3136; calcd for [M+K]$^+$: 631.2879, found: 631.2876.

14-((3-(2-Hydroxyethoxy)naphthalen-2-yl)oxy)-3,6,9,12-tetraoxatetradecan-1-ol[8]

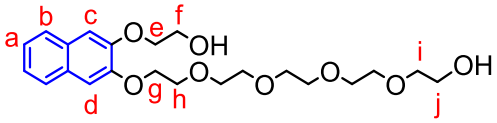

S9

A solution of diprotected glycol ether **S8** (1.90 g, 3.21 mmol) in MeOH (50 mL) was acidified with conc. HCl, until the solution reached pH = 1. After 2 h stirring at r.t. the solvent was removed under reduced pressure and the oily residue was stirred at 40 °C in oil pump vacuum for 5 h to obtain the desired product **S9** as a colourless oil in a 96% yield (1.31 g, 3.08 mmol). **^{1}H NMR** (500 MHz, $CDCl_3$): δ = 3.53 – 3.58 (m, 2H, j), 3.61 – 3.73 (m, 12H, O-C$\underline{H}_2$), 3.73 – 3.77 (m, 2H, i), 3.91 – 3.95 (m, 2H, h), 3.97 – 4.02 (m, 2H, f), 4.14 – 4.19 (m, 2H, e), 4.25 – 4.29 (m, 2H, g), 7.09 (s, 2H, d), 7.15 (s, 2H, c), 7.28 – 7.34 (m, 2H ,a, a'), 7.61 – 7.68 (m, 2H, b, b') ppm. **^{13}C NMR** (126 MHz, $CDCl_3$): δ = 60.9, 61.7, 68.2, 69.5, 70.3, 70.4, 70.6, 70.6, 70.7, 71.1, 72.7, 108.0, 108.1, 124.3, 124.5, 124.5, 126.4, 126.4, 129.2, 129.5, 148.7, 148.9 ppm. **ESI-HRMS**(ACN): *m/z* calcd. for [$C_{22}H_{32}O_8$]: 447.1989 [M+Na]$^+$, found: 447.1968; calcd for [M+K]$^+$: 463.1729, found: 463.1706.

2-((3-((14-(Tosyloxy)-3,6,9,12-tetraoxatetradecyl)oxy)naphthalen-2-yl)oxy)ethyl 4-methylbenzenesulfonate[9]

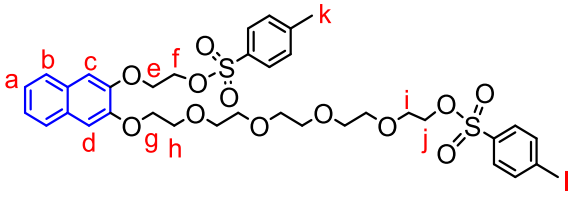

S10

A solution of 50 mg (0.12 mmol, 1.0 equiv.) diol **S9**, 100 µL (0.71 mmol, 6.0 eq) NEt_3, 0.1 mg (0.6 µmol, 0.5 mol%) DMAP and 135 mg (0.71 mmol, 6 eq) 4-toluenesulfonyl chloride in dry methylene chloride (25 mL) was left stirring at r.t. for 2 days. The reaction mixture was washed with saturated NH_4Cl aq. solution and dried with $MgSO_4$. The crude product was then purified by column chromatography (SiO_2, CH_2Cl_2 → EtOAc, R_f ~ 0.8 in EtOAc) to obtain the desired product **S10** as a colourless oil in 89% yield (77 mg, 0.11 mmol). **^{1}H NMR** (500 MHz, $CDCl_3$):

δ = 2.38 (s, 3H, l), 2.41 (s, 3H, k), 3.52 – 3.69 (m, 12H, O-CH_2), 3.75 – 3.78 (m, 2H, i), 3.91 – 3.95 (m, 2H, h), 4.11 – 4.15 (m, 2H, j), 4.22 – 4.26 (m, 2H, g), 4.27 – 4.32 (m, 2H, e), 4.41 – 4.47 (m, 2H, f), 7.04 (s, 1H, d), 7.14 (s, 1H, c), 7.27 – 7.36 (m, 6H, a, a', H-Ar-CCH_3), 7.58 – 7.67 (m, 2H, b, b'), 7.76 – 7.83 (m, 4H, H-Ar-CSO_3R) ppm. **^{13}C NMR** (126 MHz, $CDCl_3$): δ = 21.7, 21.7, 66.7, 68.2, 68.6, 68.7, 69.4, 69.6, 70.6, 70.6, 70.7, 70.8, 70.8, 71.0, 100.1, 108.9, 110.0, 110.0, 124.4, 124.7, 126.4, 126.5, 128.0, 128.1, 129.2, 129.9, 129.9, 129.9, 130.0, 133.0, 133.1, 144.9, 144.9, 145.0, 148.2, 149.1 ppm. **ESI-HRMS**(ACN): *m/z* calcd. for [$C_{36}H_{44}O_{12}S_2$]: 755.2166 [M+Na]$^+$, found: 755.2168; calcd for [M+K]$^+$: 771.1906, found: 771.1905.

1-Iodo-14-((3-(2-iodoethoxy)naphthalen-2-yl)oxy)-3,6,9,12-tetraoxatetradecane[4]

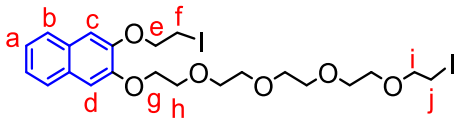

S11

A solution of 61.4 mg (83.8 µmol, 1.0 eq) ditosylate **S10** and 55.6 mg (335 mmol, 4.0 eq) KI in acetone (5 mL) was stirred at 70 °C overnight. When the reaction mixture turned yellow and a white precipitate formed, the solvent was removed under reduced pressure. The residue was dissolved in EtOAc and washed with brine. After drying with $MgSO_4$, the solvent was removed to isolate the desired product **S11** as a yellowish oil in a 96% yield (52 mg, 80.9 µmol). **^{1}H NMR** (500 MHz, $CDCl_3$): δ = 3.21 – 3.25 (m, 2H, j), 3.49 – 3.53 (m, 2H, f), 3.61 – 3.71 (m, 10H, O-CH_2), 3.71 – 3.74 (m, 2H, i), 3.78 – 3.82 (m, 2H, O-CH_2), 3.94 – 3.97 (m, 2H, h), 4.26 – 4.30 (m, 2H, g), 4.35 – 4.40 (m, 2H, e), 7.15 (s, 1H, d), 7.18 (s, 1H, c), 7.31 – 7.34 (m, 2H, a, a'), 7.64 – 7.67 (m, 2H, b, b') ppm. **^{13}C NMR** (126 MHz, $CDCl_3$): δ = 68.8, 69.7, 69.9, 70.3, 70.3, 70.7, 70.7, 70.8, 70.8, 71.1, 72.1, 72.1, 109.0, 109.9, 124.5, 124.7, 126.5, 126.5, 129.3, 129.8, 148.1, 149.1 ppm. **ESI-HRMS**(ACN): *m/z* calcd. for [$C_{22}H_{30}I_2O_6$]: 667.0024 [M+Na]$^+$, found: 666.9996; calcd. for [M+K]$^+$: 682.9763, found: 682.9730.

2-(4,5-Bis(methylthio)-1,3-dithiol-2-ylidene)-5,6,8,9,11,12,14,15,17,18,27,28-dodeca-hydro-[1,3]dithiolo[4,5-t]naphtho[2,3-b][1,4,7,10,13,16]hexaoxa[19,22]dithiacyclo-tetracosane[10]

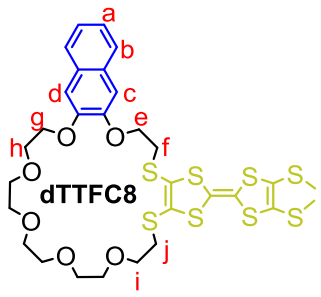

A solution of 74 mg (0.44 mmol, 2.0 equiv.) CsOH · H_2O in dry MeOH (2 mL) was added over 30 min to 104 mg (0.22 mmol, 1.0 equiv.) TTF precursor **S12** in dry DMF (5 mL). After the mixture turned dark red, it was added over 1 h to 143 mg (0.22 mmol, 1.0 equiv.) to diiodide **S11** in dry DMF (25 mL) and stirred at r.t. under argon overnight. Afterwards, the solvent was removed under reduced pressure and the residue was dissolved in CH_2Cl_2. The solution was washed with water and brine. After drying with $MgSO_4$, the crude product was purified by column chromatography (SiO_2, CH_2Cl_2, R_f ~ 0.5 in CH_2Cl_2/MeOH = 100:1) to isolate the desired product **dTTFC8** as an orange powder in a 28% yield (45.7 mg, 61 µmol). **M.p.** 79.3°C; **^{1}H NMR** (700 MHz, CD_2Cl_2): δ = 2.43 (s_{br}, 6H, S-CH_3), 3.02 (s_{br}, 4H, j), 3.30 (t, J = 6.5 Hz, 2H, f), 3.49 – 3.52 (m, 2H, O-C$\underline{H}_2$), 3.53 – 3.56 (m, 2H, O-C$\underline{H}_2$), 3.56 – 3.59 (m, 2H, O-C$\underline{H}_2$), 3.59 – 3.65 (m, 4H, i, O-C$\underline{H}_2$), 3.65 – 3.68 (m, 2H, O-C$\underline{H}_2$), 3.76 – 3.79 (m, 2H, O-C$\underline{H}_2$), 3.89 – 3.97 (m, 2H, h), 4.25 (m, 2H, O-C$\underline{H}_2$), 4.38 (s_{br}, 2H, e), 7.17 (s, 1H, c), 7.20 (s, 1H, d), 7.30 – 7.35 (m, 2H, a), 7.66 – 7.70 (m, 2H, b).ppm. **^{13}C NMR** (176 MHz, CD_2Cl_2): δ = 23.3, 29.9, 30.3, 32.5, 68.4, 69.5, 70.0, 71.0, 71.1, 71.2, 71.3, 71.7, 109.1, 109.8, 124.8, 124.9, 126.8, 126.9, 129.8, 130.2, 149.1, 149.7 ppm. **ESI-HRMS**(ACN): *m/z* calcd. for [$C_{30}H_{36}O_6S_8$]: 771.0170 [M+Na]$^+$, found: 771.0182; calcd. for [M+K]$^+$: 786.9909, found: 786.9916.

1.3. Synthesis of [2]rotaxane (*rac*)-2 and (*rac*)-2Ac

[2]Rotaxane (*rac*)-2

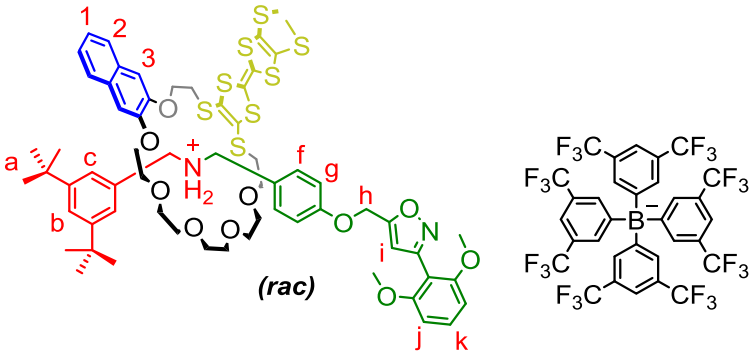

(*rac*)-**2**

Axle **A1** (74 mg, 60 µmol, 1.0 equiv.) and macrocycle **dTTFC8** (50 mg, 67 µmol, 1.1 equiv.) were dissolved in dry CH_2Cl_2 (200 µL) and stirred at r.t. for 10 min. Afterwards 2,6-dimethoxybenzonitrile oxide **St1** (14 mg, 78 µmol, 1.3 equiv.) was added and the mixture was stirred in a sealed tube under argon at 35 °C overnight. Then, the mixture was applied directly onto a preparative thin layer chromatography plate (SiO_2 2000 µm, CH_2Cl_2, R_f ~ 0.6 in CH_2Cl_2) to obtain the desired racemic product (*rac*)-**2** (129 mg, 60 µmol, 73 %) as a yellowish oil. **^{1}H NMR** (700 MHz, CD_2Cl_2): δ = 1.25 (s, 18H, a), 2.42 (s, 3H, -SMe), 2.43 (s, 3H, -SMe), 3.05 – 3.18 (m, 6H, O-C$\underline{H}_2$), 3.23 – 3.33 (m, 4H, O-C$\underline{H}_2$), 3.37 – 3.46 (m, 4H, O-C$\underline{H}_2$), 3.58 – 3.68 (m, 2H, O-C$\underline{H}_2$), 3.75 – 3.91 (m, 10H, O-C$\underline{H}_2$, -OMe), 4.28 – 4.40 (m, 2H, O-C$\underline{H}_2$), 4.43 – 4.46 (m, 2H, O-C$\underline{H}_2$), 4.53 – 4.77 (m, 4H, C$\underline{H}_2$-NH_2), 5.04 (d, *J* = 12.8 Hz, 1H, h), 5.08 (d, *J* = 13.0 Hz, 1H, h), 6.44 (s, 1H, i), 6.66 (d, *J* = 8.5 Hz, 2H, j), 6.95 (d, *J* = 8.7 Hz, 2H, g), 7.19 (s, 1H, 3), 7.24 (s, 1H, 3), 7.27 (d, *J* = 1.6 Hz, 2H, c), 7.35 – 7.41 (m, 5H, f, k, 1), 7.47 (t, *J* = 1.8 Hz, 1H, b), 7.55 (s_{br}, 4H, $BArF_{24}$), 7.66 – 7.69 (m, 2H, 2), 7.69 (s_{br}, 8H, $BArF_{24}$) 7.77 – 7.86 (m, 2H, NH_2) ppm. **^{13}C NMR** (176 MHz, CD_2Cl_2): δ = 19.6, 31.7, 35.4, 36.3, 37.3, 53.3, 56.5, 61.6, 68.7, 69.4, 70.5, 70.6, 71.0, 71.2, 71.2, 71.3, 71.5, 104.7, 107.3, 107.4, 109.1, 109.3, 109.6, 113.8, 115.6, 118.0, 118.1, 124.4, 124.7, 124.8, 125.0, 125.7, 126.0, 126.9 127.5, 127.8, 128.2, 128.2, 128.8, 129.4, 129.8, 129.9, 130.9, 132.0, 132.0, 135.4, 148.3, 148.4, 152.4, 157.8, 159.5, 162.3, 166.2 ppm. **ESI-HRMS**(MeOH): *m/z* calcd. for $[C_{64}H_{79}N_2O_{10}S_8]^+$: 1291.3495 $[M]^+$, found: 1291.3479.

[2]Rotaxane (*rac*)-2Ac

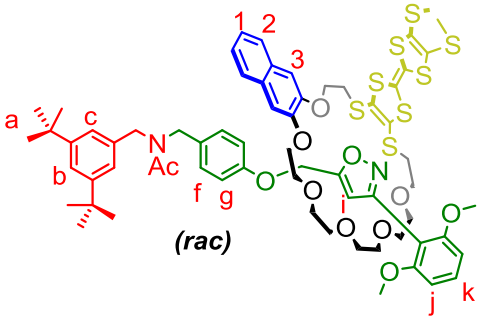

(*rac*)-**2Ac**

Rotaxane (*rac*)-**2** (14 mg, 6.5 µmol, 1.0 equiv.), NEt_3 (27 µL, 190 µmol, 30.0 equiv.) and Ac_2O (18 µL, 190 µmol, 30.0 equiv.) were dissolved in ACN (5 mL) and stirred at r.t. overnight. Then, the crude mixture was purified by preparative TLC (SiO_2 2000 µm, CH_2Cl_2/MeOH 50:1, R_f ~ 0.3 in CH_2Cl_2/MeOH = 50:1) to isolate the desired racemic product (*rac*)-**2Ac** as a yellowish oil in 95% yield (8.2 mg, 3.5 µmol). **^{1}H NMR** (700 MHz, CD_2Cl_2): δ = 1.29 (s, 9H, a), 1.32 (s, 9H, a), 1.78 (s, 1.5H, Ac), 1.90 (s, 1.5H, Ac), 2.24 (s, 1.5H, SMe), 2.30 (s, 1.5H, SMe), 2.33 (s, 1.5H, SMe), 2.34 (s, 1.5H, SMe), 3.02 – 3.15 (m, 3.6H, O-CH_2), 3.16 – 3.22 (m, 1.4H, O-CH_2), 3.34 – 3.44 (m, 4.5H, O-CH_2), 3.45 – 3.62 (m, 8H, O-CH_2), 3.64 – 3.74 (m, 5H, O-CH_2), 3.78 (d, *J* = 3.9 Hz, 6H, OMe), 3.81 – 3.83 (m, 0.7H, O-CH_2), 3.83 – 3.85 (m, 0.7H, O-CH_2), 3.95 – 4.04 (m, 4H, CH_2-N, O-CH_2), 4.05 – 4.13 (m, 2H, O-CH_2), 4.18 – 4.21 (m, 1H, CH_2-N), 4.22 – 4.26 (m, 1H, O-CH_2), 4.29 – 4.32 (m, 1H, CH_2-N), 4.37 – 4.40 (m, 1H, CH_2-N), 4.41 – 4.46 (m, 1H, CH_2-N), 5.80 – 5.87 (m, 2H, h), 6.64 (dd, *J* = 8.4, 5.6 Hz, 2H, j), 6.71 – 6.73 (m, 2H, g, i), 6.78 – 6.81 (m, 1H, g), 6.85 (s, 0.5H, 3), 6.87 (d, *J* = 1.8 Hz, 1H, c), 6.90 (s, 0.5H, 3), 6.91 (d, *J* = 1.8 Hz, 1H, c), 7.00 – 7.02 (m, 2H, f), 7.05 (*s*, 0.5H, 3), 7.07 (*s*, 0.5H, 3), 7.19 – 7.25 (m, 2H, 1), 7.29 (t, *J* = 1.9 Hz, 0.5H, b), 7.33 (t, *J* = 1.8 Hz, 0.5H, b), 7.35 (td, *J* = 8.4, 4.6 Hz, 1H, k), 7.55 – 7.59 (m, 1H, 2), 7.60 – 7.64 (m, 1H, 2) ppm. **^{13}C NMR** (176 MHz, CD_2Cl_2): δ = 19.2, 19.3, 19.3, 19.4, 21.8, 21.8, 30.3, 31.8, 32.5, 34.6, 35.2, 35.3, 35.5, 35.6, 46.59, 47.9, 48.8, 50.9, 51.3, 56.5, 56.5, 61.4, 61.4, 67.5, 67.5, 69.1, 69.2, 70.1, 70.2, 70.2, 70.5, 70.5, 71.2, 71.3, 71.3, 71.5, 71.5, 71.7, 71.7, 71.9, 104.5, 104.6, 107.1, 107.4, 107.5, 108.0, 108.1, 108.4, 108.4, 110.0, 110.1, 110.8, 115.2, 115.4, 121.0, 121.6, 121.8, 122.4, 123.9, 124.3, 124.6, 124.6, 124.6, 126.6, 126.7, 126.7, 126.7, 127.6, 127.7, 128.8, 129.0, 129.5, 129.6, 129.6, 129.9, 131.5, 131.5, 134.2, 134.5, 136.7, 137.3, 148.8, 148.9, 149.0, 149.1, 151.9, 157.4, 158.2, 158.3, 159.3, 168.9, 169.1, 171.1, 171.2 ppm. **ESI-HRMS**(MeOH): *m/z* calcd. for $[C_{66}H_{80}N_2O_{11}S_8]$: 1333.3606 $[M+H]^+$, found: 1333.3505; calcd. for $[M+Na]^+$: 1355.3425, found: 1355.3442; calcd. for $[M+K]^+$: 1371.3165, found: 1371.3185.

2. FTICR mass spectroscopy

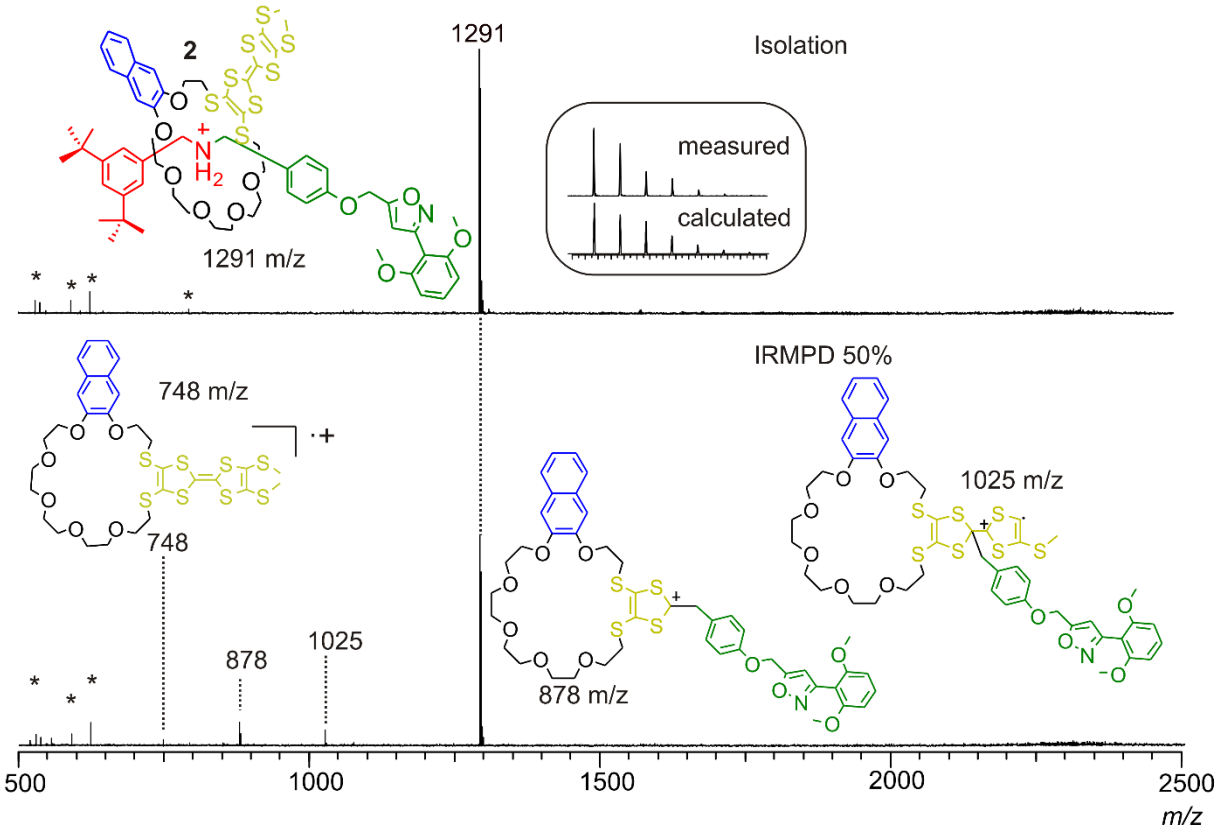

Fig. S1 ESI-FTICR infrared multiphoton dissociation (IRMPD) experiment with mass-selected rotaxane ions at *m/z* 1291 obtained from a MeOH solution (10 µM) of [2]rotaxane (*rac*)-**2**: (top) after mass-selection; (bottom) after fragmentation. The fragment peaks could be assigned to the free macrocycle as a radical cation (748 *m/z*) and two adducts, which arise from an attack of the TTF moiety on the benzylic position next to the nitrogen of the axle. These fragments are in line with the fragments obtained from rotaxanes of the non-directional **TTFC8** macrocycle.[4] As no free axle is observed as the fragmentation product, it can be concluded that the ionised and mass selected species are in fact mechanically interlocked. Electromagnetic stray radiation is marked with asterisks.

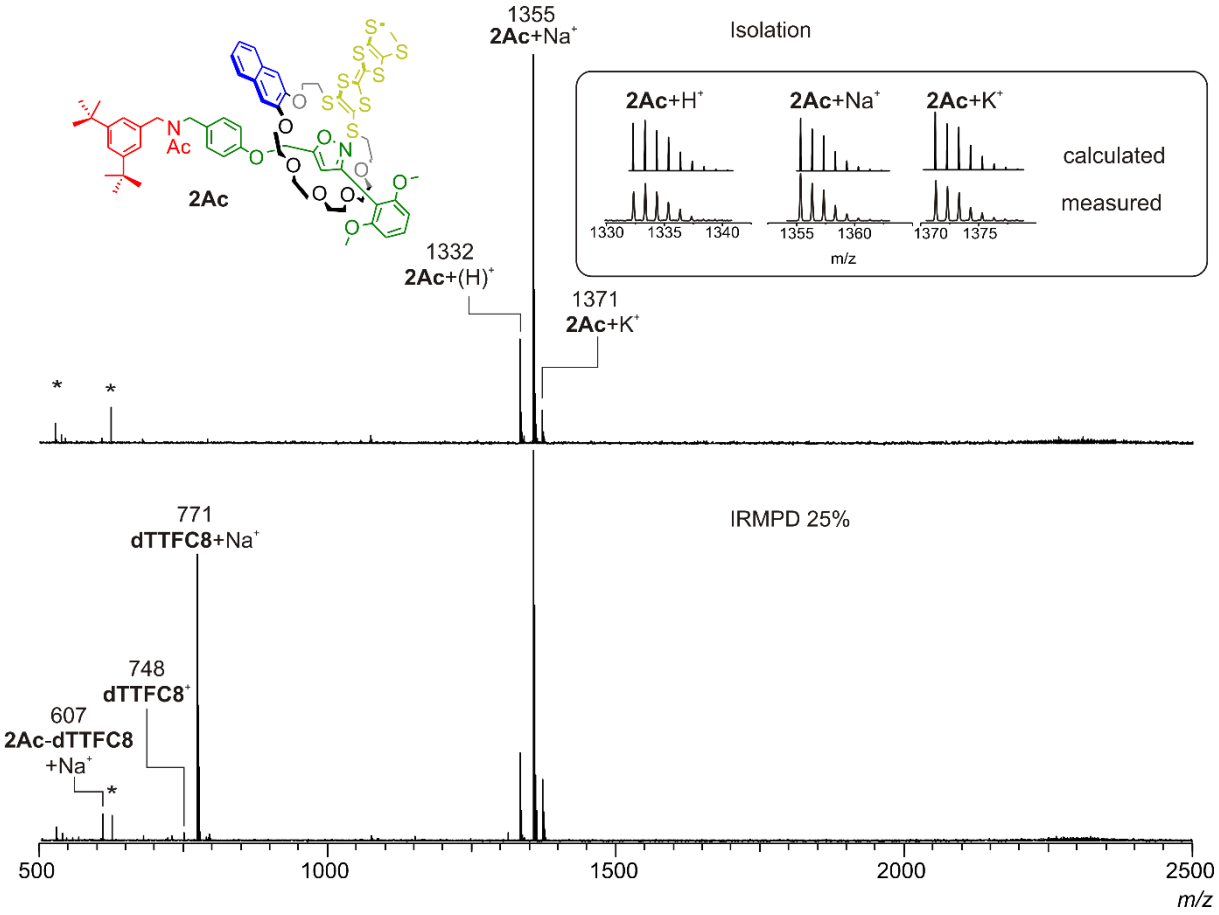

Fig. S2 ESI-FTICR infrared multiphoton dissociation (IRMPD) experiment with mass range-selected rotaxane ions obtained from a MeOH solution (10 µM) of [2]rotaxane (*rac*)-**2Ac**. The acetylated [2]rotaxane **2Ac** ions do not show the same fragmentation pattern as **2,** as no fragments from an intramolecular attack could be observed. Fragmentation proceeds by either losing the macrocycle (607 m/z) or fragmenting the axle leaving the charge on the macrocycle (748 and 771 m/z)

3. Variable Temperature NMR Spectroscopy

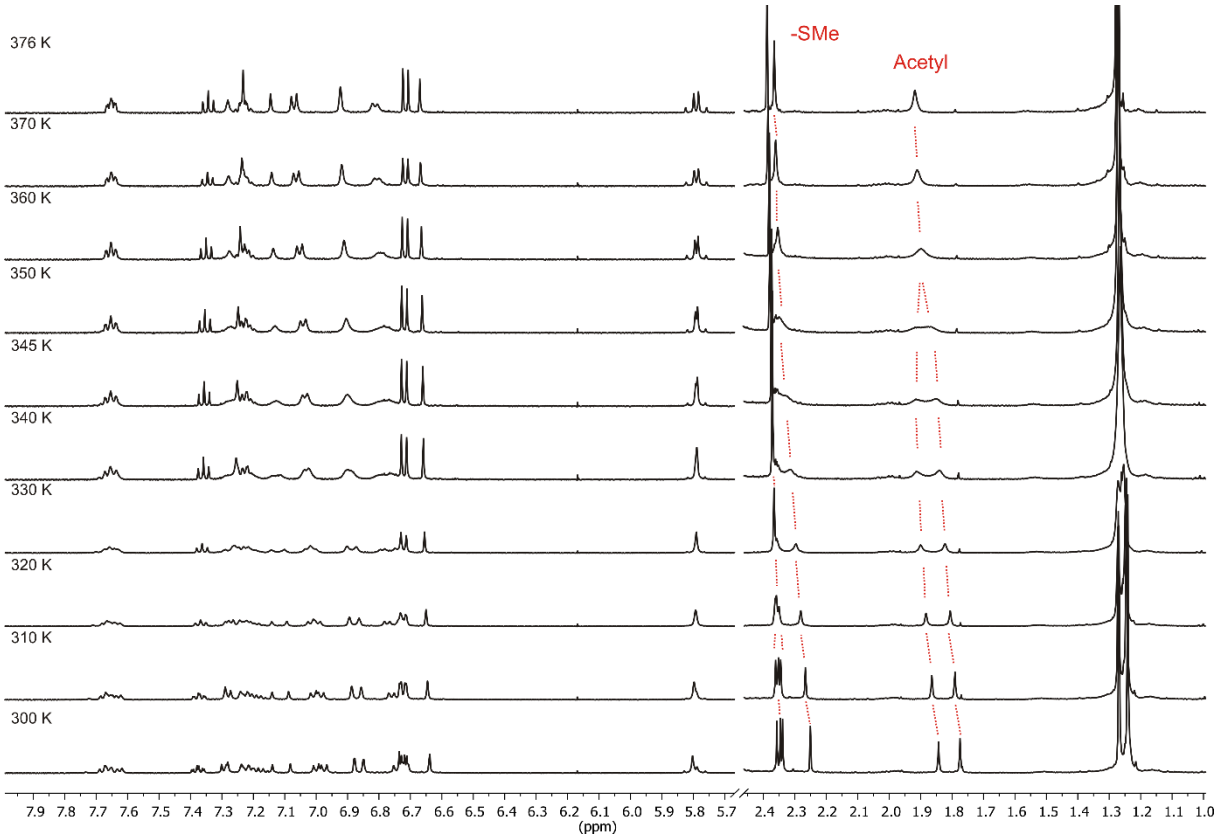

Fig. S3 Partial spectra of [2]rotaxane (*rac*)-**2Ac** in a VT ^{1}H NMR (500 MHz, DMSO-d6) experiment (gradual heating from 300 to 375 K), showing the coalescence of the acetyl groups and merging of the four singlets corresponding to SMe on the TTF into two singlets upon heating.

The free energy of activation ($\Delta G^{\ddagger}$) was calculated using the modified Eyring equation (eq. 1), where R is the ideal gas constant, T_c the coalescence temperature and $\Delta\nu$ the peak to peak separation between the signals for the two interconverting isomers in Hz.

$$\Delta G^{\ddagger} = R\,T_c\,(22.96 + \ln(T_c/\Delta\nu))\ \text{kJ mol}^{-1} \qquad \text{(eq. 1)}$$

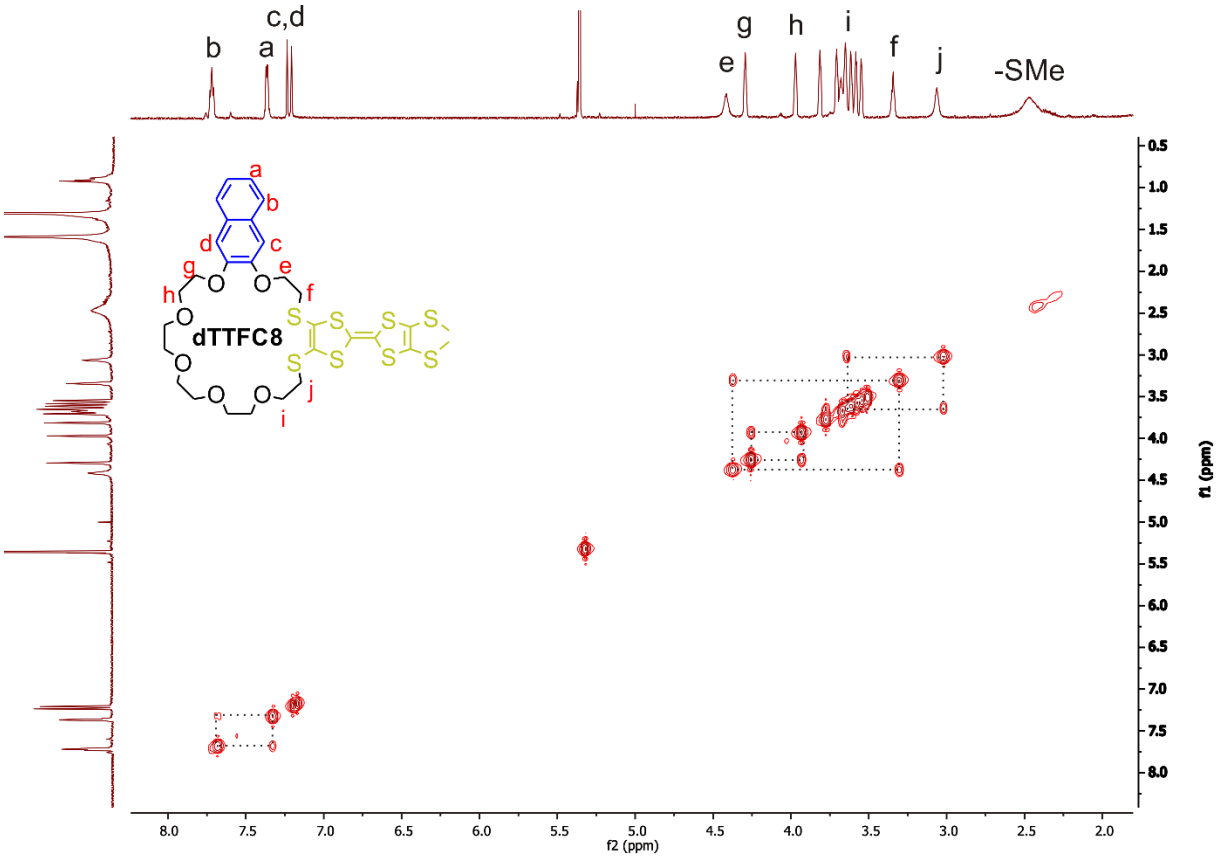

Fig. S4 COSY spectrum of **dTTFC8** in a (700 MHz, CD_2Cl_2).

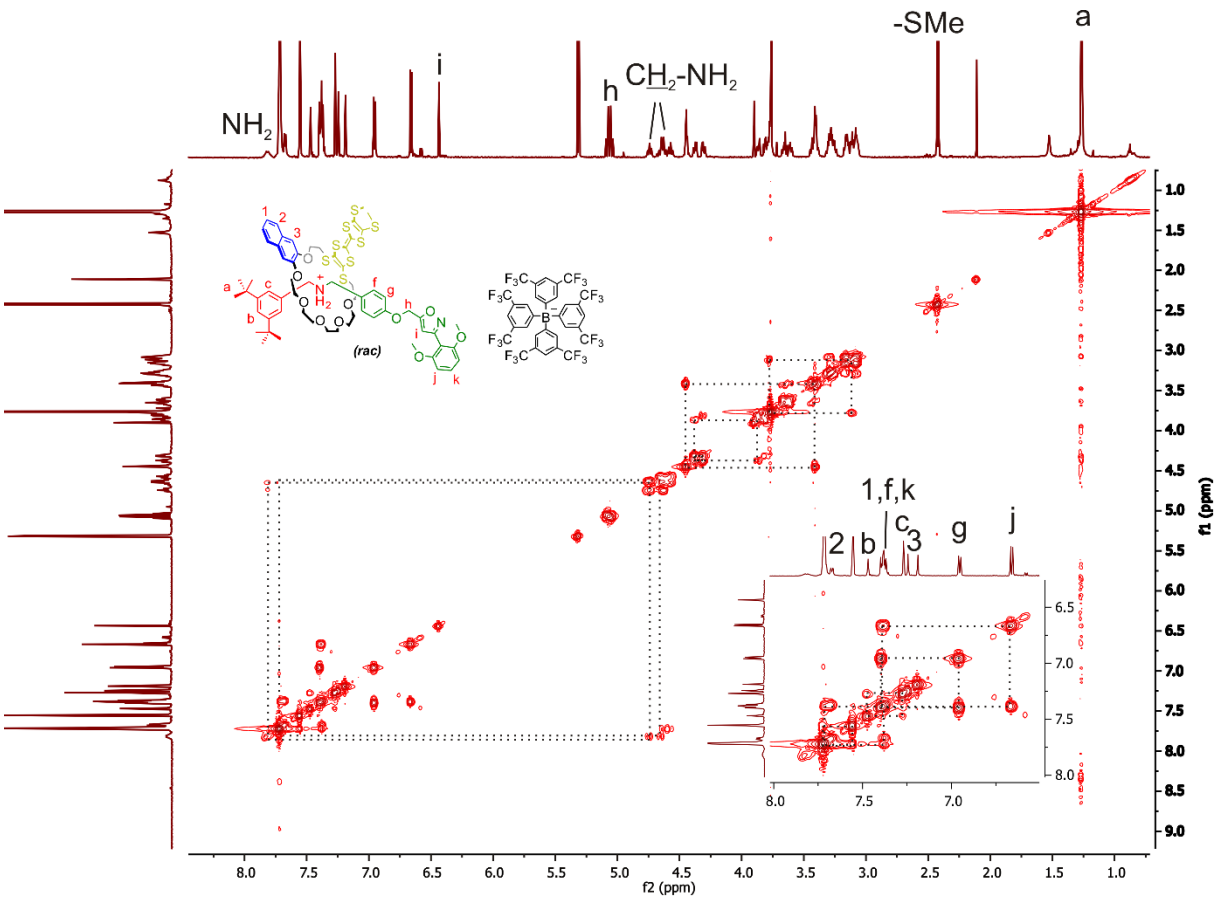

Fig. S5 COSY spectrum of (*rac*)-**2** in a (700 MHz, CD_2Cl_2).

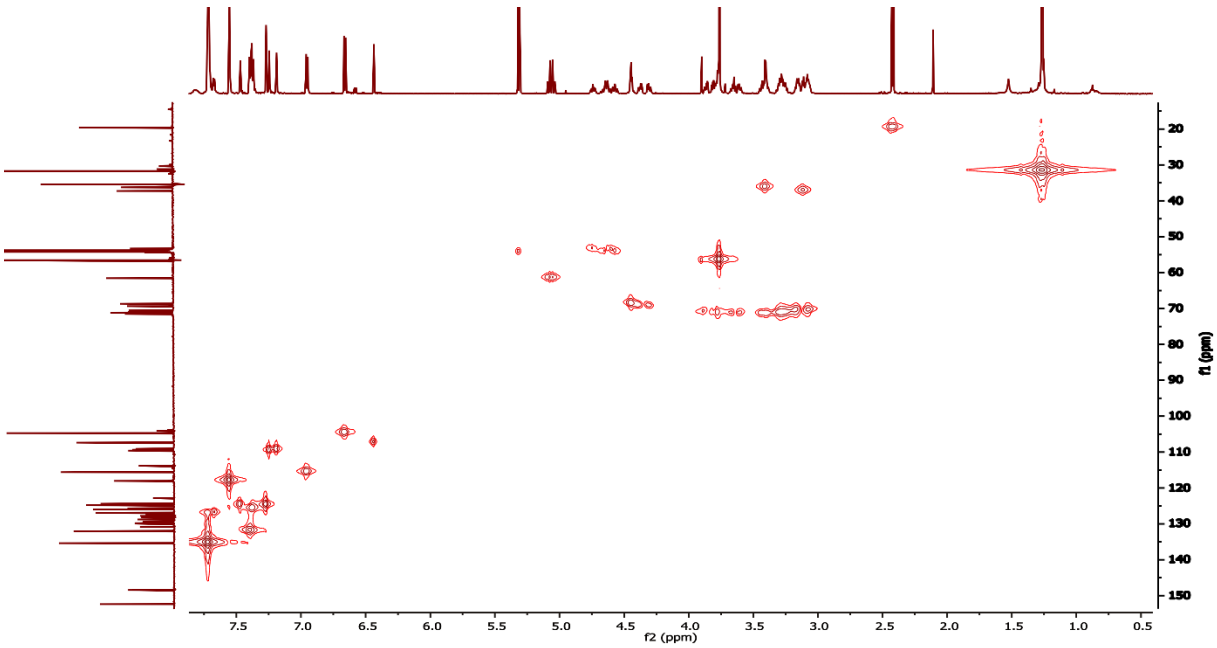

Fig. S6 HMQC spectrum of (*rac*)-**2** in a (700 MHz, CD_2Cl_2).

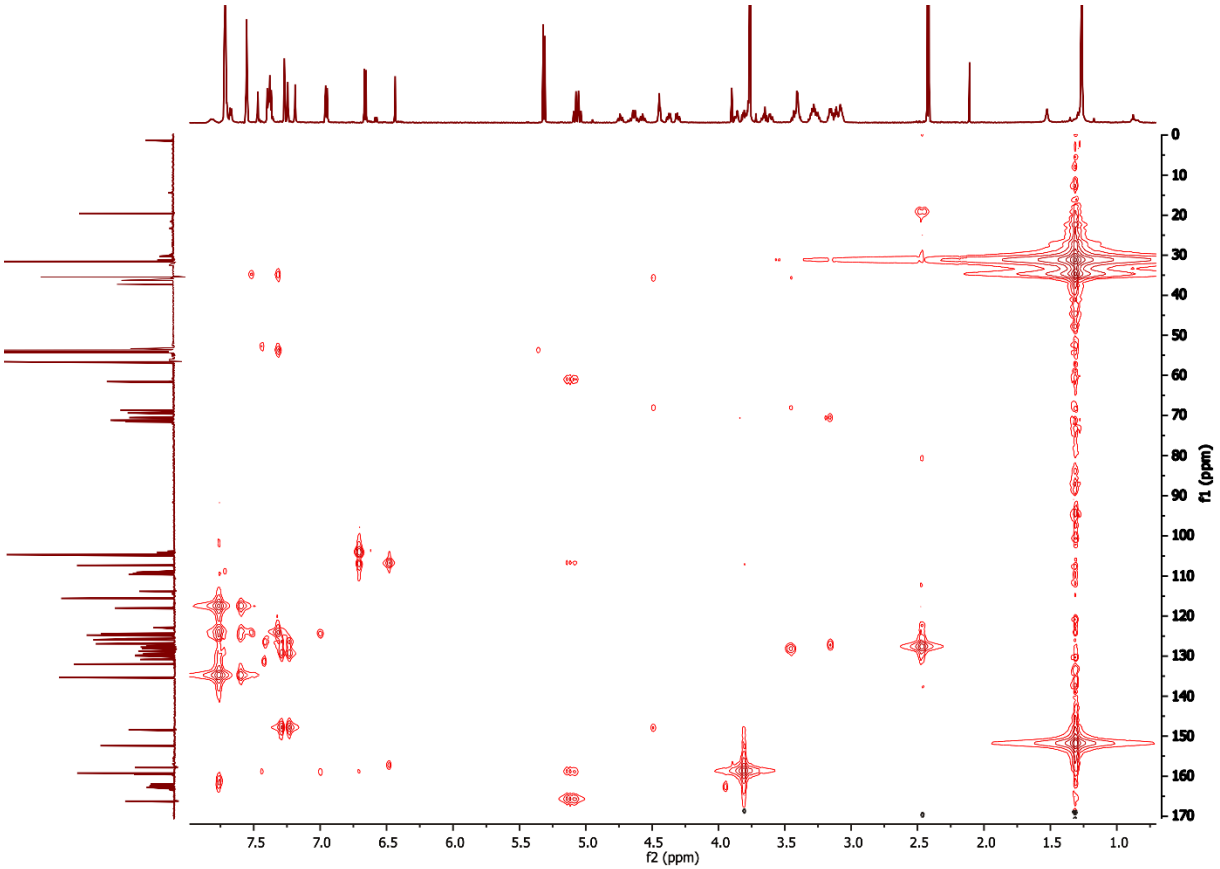

Fig. S7 HMBC spectrum of (*rac*)-**2** in a (700 MHz, CD_2Cl_2).

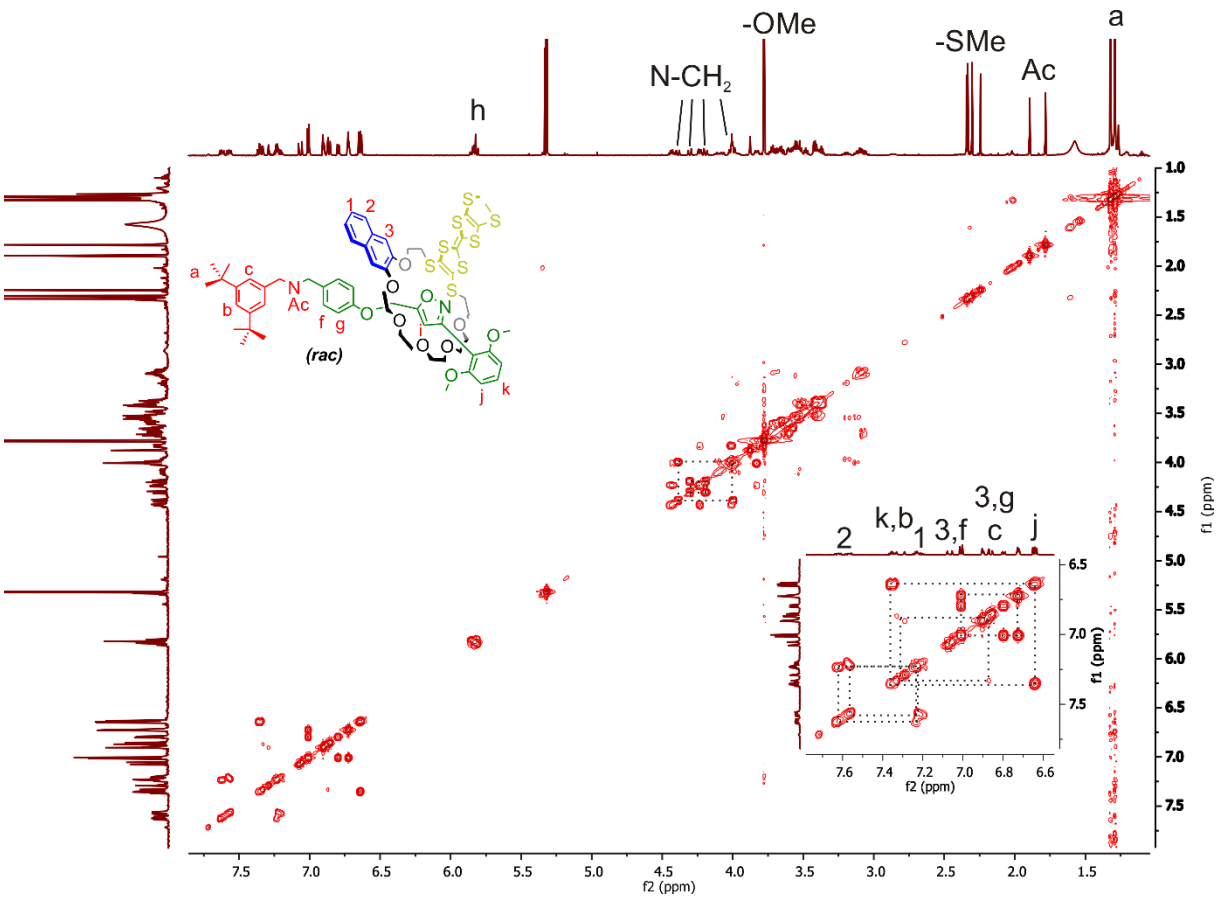

Fig. S8 COSY spectrum of (*rac*)-**2Ac** in a (700 MHz, CD_2Cl_2).

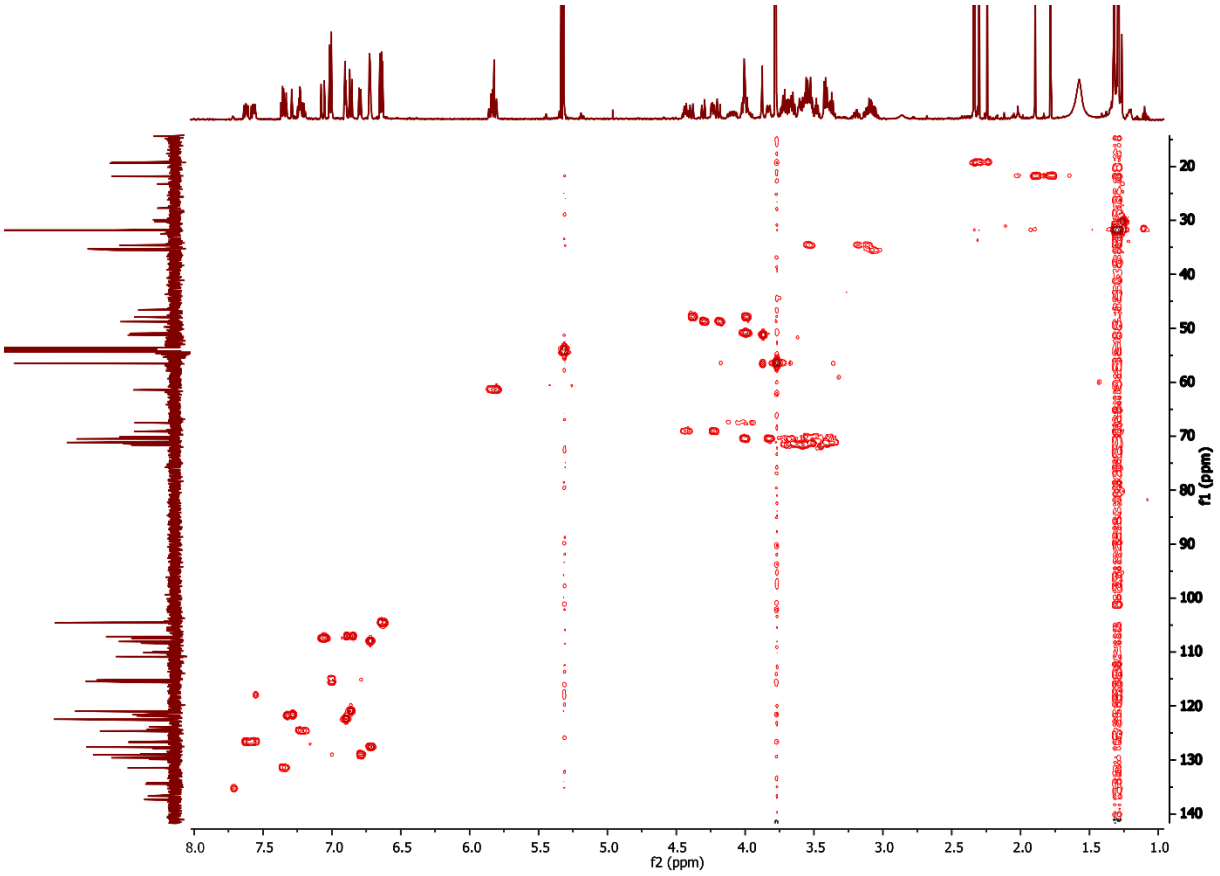

Fig. S9 HMQC spectrum of (*rac*)-**2Ac** in a (700 MHz, CD_2Cl_2).

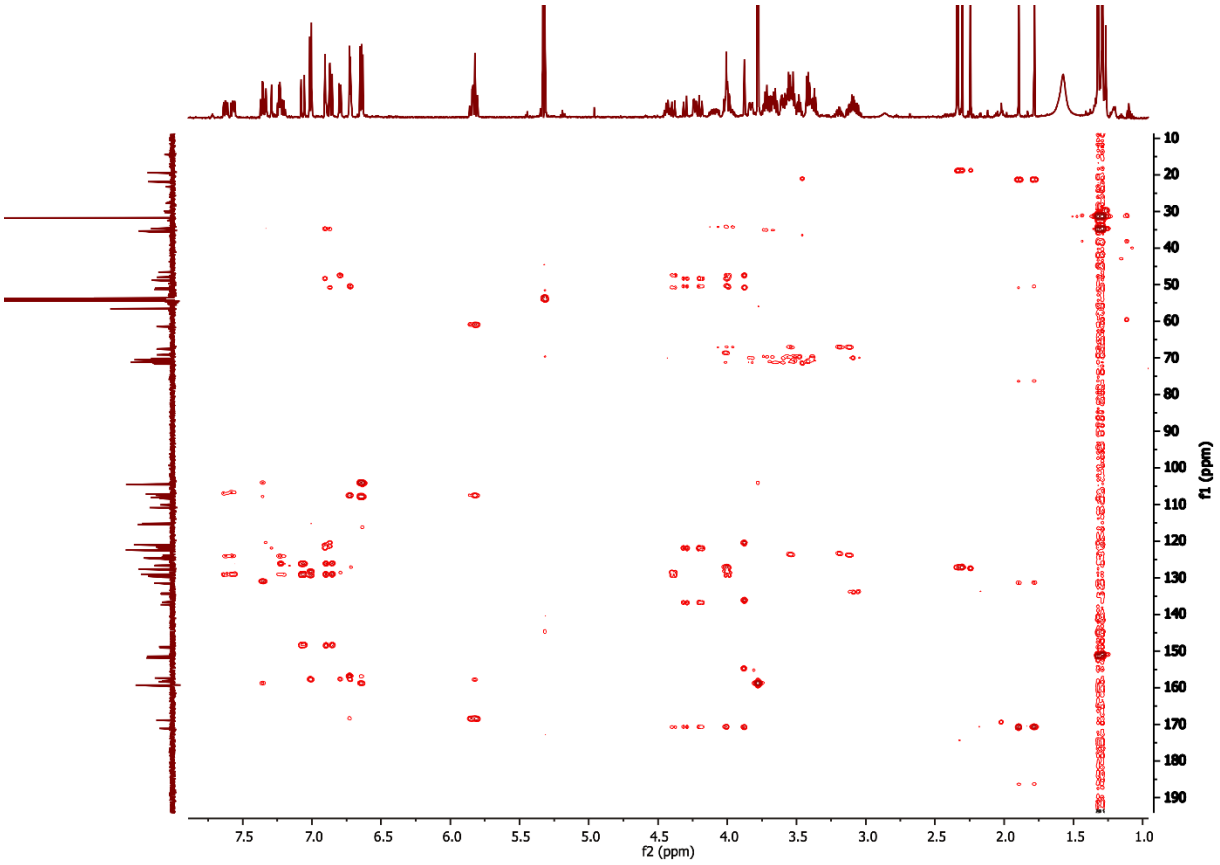

Fig. S10 HMBC spectrum of (*rac*)-**2Ac** in a (700 MHz, CD_2Cl_2).

4. Isothermal titration calorimetry

ITC experiments were carried out in dry 1,2-dichloroethane at 298 K on a TAM III microcalorimeter (Waters GmbH, TA Instruments, Eschborn, Germany). In a typical experiment, an 800 µL solution of crown ether was placed in the sample cell at a concentration of 1.1 mM, and 250 µL of a solution of the ammonium salt (8.0 mM) were put into the syringe. The titrations consisted of 32 consecutive injections of 8 µL each with a 15 min interval between injections. Heats of dilution were determined by titration of ammonium salt solutions into the sample cell containing blank solvent and were subtracted from each data set. The heat flow generated in the sample cell is measured as a differential signal between sample and reference cell. Hence, an exothermic event results in a positive and an endothermic in a negative heat flow. The data were analysed using the instrument's internal software package and fitted with a 1:1 binding model. Each titration was conducted three times and the measured values for *K* and Δ*H* were averaged.

Tab. S1: Thermodynamic data obtained from the ITC experiments.

	K_a /10^5 M^{-1}	ΔG / kJ mol^{-1}	ΔH / kJ mol^{-1}	$T\Delta S$ / kJ mol^{-1}
axle **A1⊂TTFC8**	4.4 ± 0,4	-32.2 ± 0.3	-46.2 ± 0.7	-14.0 ± 1.0
axle **A1⊂dTTFC8**	3.6 ± 0.3	-31.7 ± 0.2	-41.1 ± 1.1	-11.0 ± 1.3

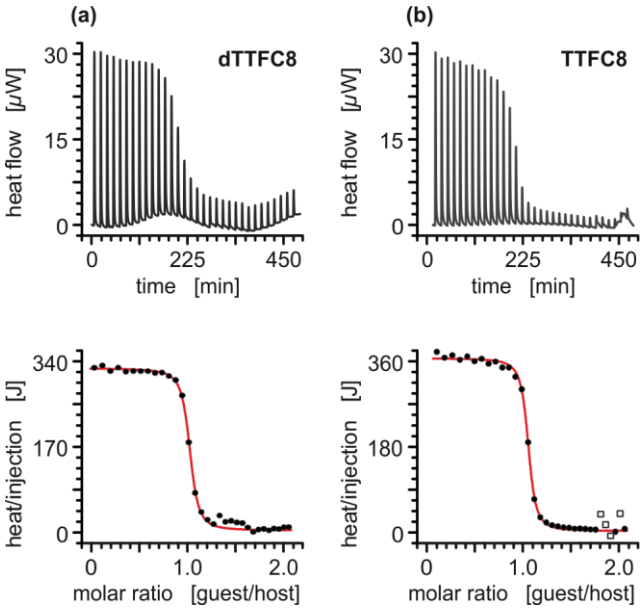

Figure S11. Titration plots (heat flow versus time and heat/volume versus guest/host ratio) obtained from ITC experiments at 298 K in 1,2-dichloroethane**: (a)** vial: **dTTFC8**, syringe: axle **A1**; **(b)** vial: **TTFC8**, syringe: axle **A1**; Points marked with non-filled squares were not considered in the fitting process.

5. Electrochemical measurements

Redox-potentials reported in this study were obtained by cyclic voltammetry. All measurements were at least conducted twice. Measurements were conducted in CH_2Cl_2 with 0.1 M electrolyte and 1 mM analyte concentration.

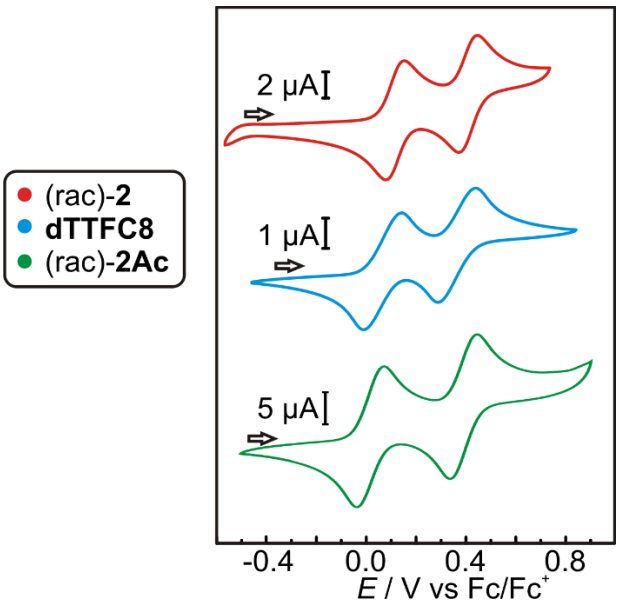

Fig. S12 Stacked cyclic voltammograms (CH_2Cl_2, n-Bu_4NPF_6, 298 K) of (*rac*)-**2**, **dTTFC8** and (*rac*)-**2Ac**

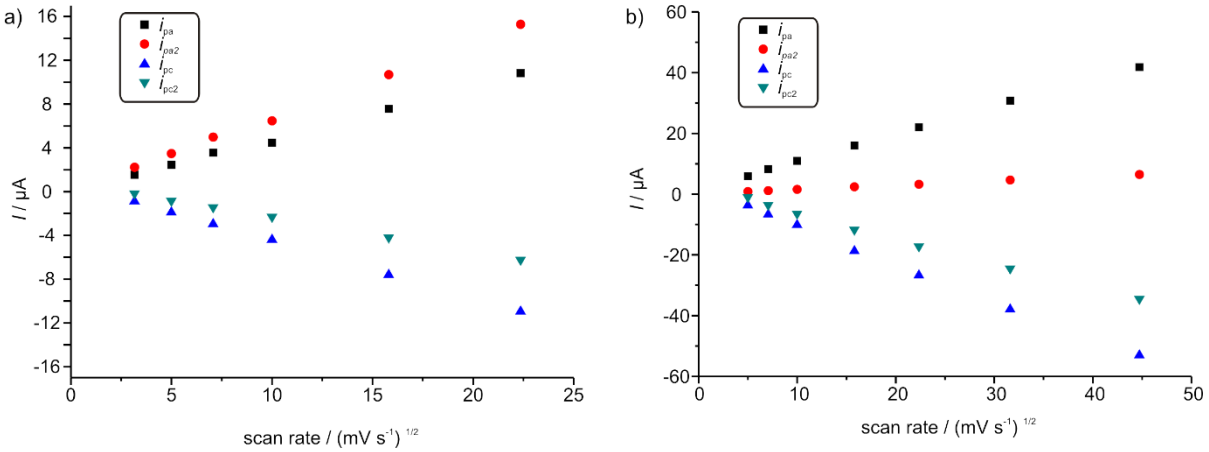

Fig. S13 Peak currents plotted against the square root of scan speed based on cyclic voltammograms of a) (*rac*)-**2** and b) (*rac*)-**2Ac** (CH_2Cl_2, with n-Bu_4NPF_6 as the electrolyte, 298 K). The peak currents can be approximated by linear functions, showing the reversibility of the redox process.

6. CD spectra

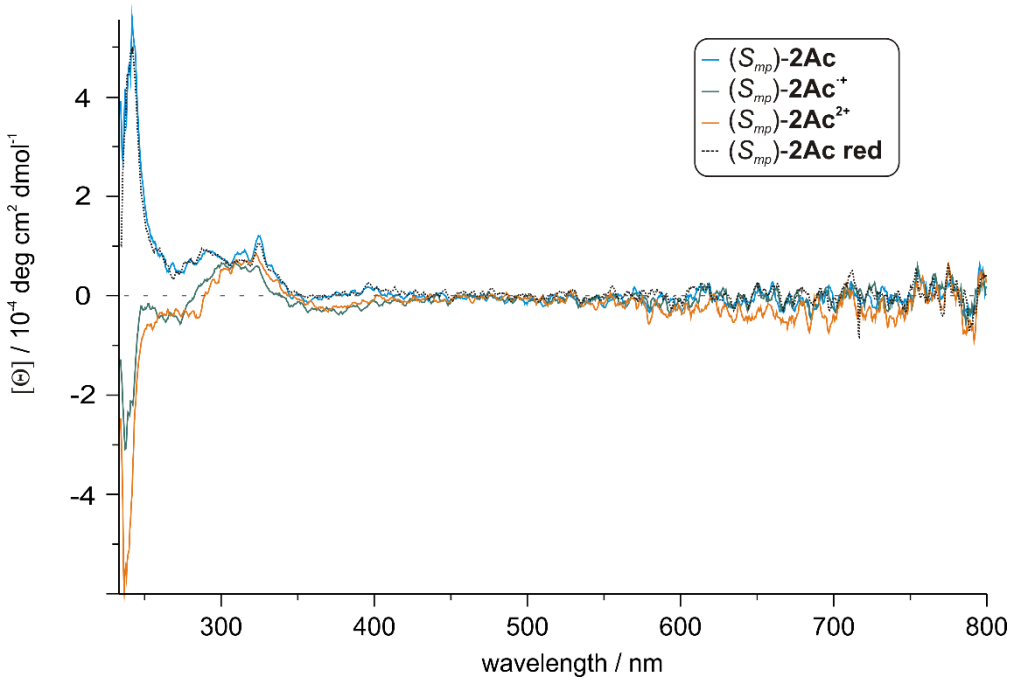

Fig. S14 CD spectra of (S_{mp})-**2Ac** (160 µM in CH_2Cl_2, 298 K, bulk $Fe(ClO_4)_3$ as the oxidant) in the TTF^0, $TTF^{\bullet+}$ and TTF^{2+} state and after reduction to the neutral form with Zn dust.

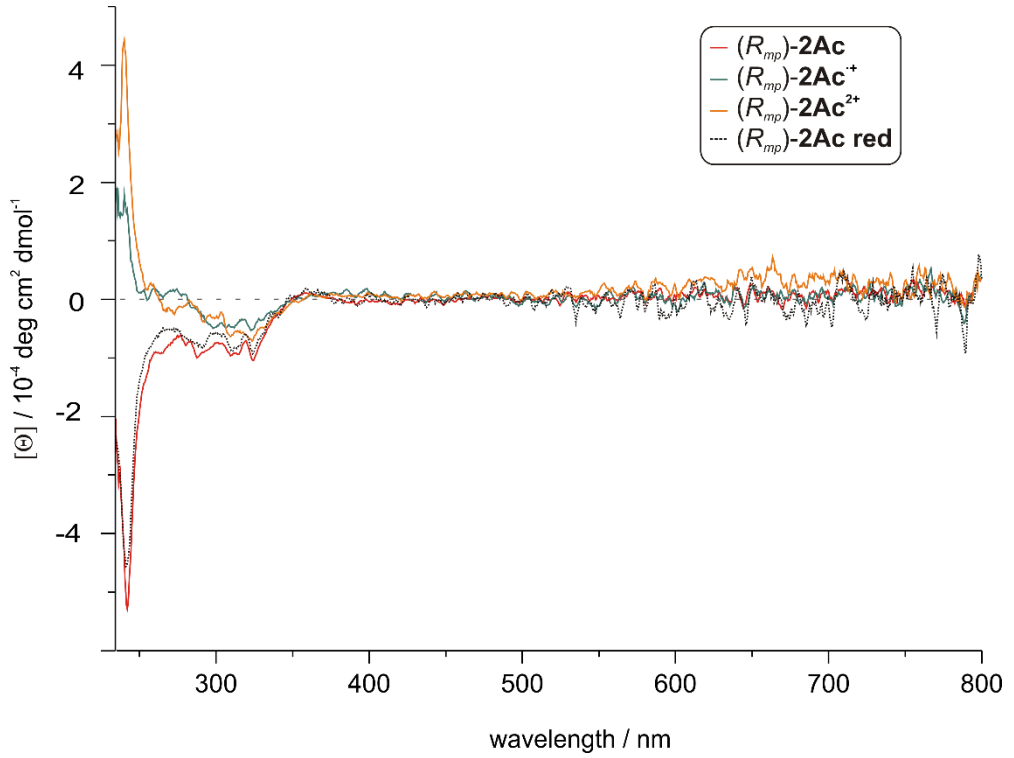

Fig. S15 CD spectra of (R_{mp})-**2Ac** (160 µM in CH_2Cl_2, 298 K, bulk $Fe(ClO_4)_3$ as oxidant) in the TTF^0, $TTF^{\bullet+}$ and TTF^{2+} state and after reduction to the neutral form with Zn dust.

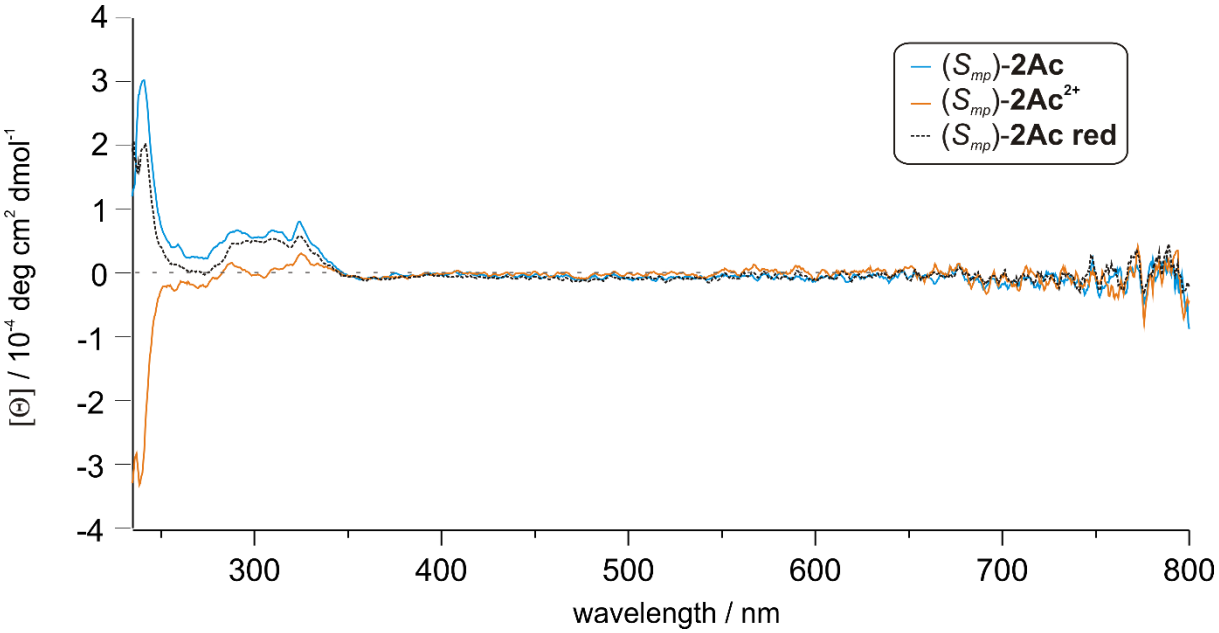

Fig. S16 CD spectra of (S_{mp})-**2Ac** (220 µM in ACN, 298 K, bulk $Fe(ClO_4)_3$ as the oxidant) in the TTF^0 and TTF^{2+} state and after reduction to the neutral form with Zn dust.

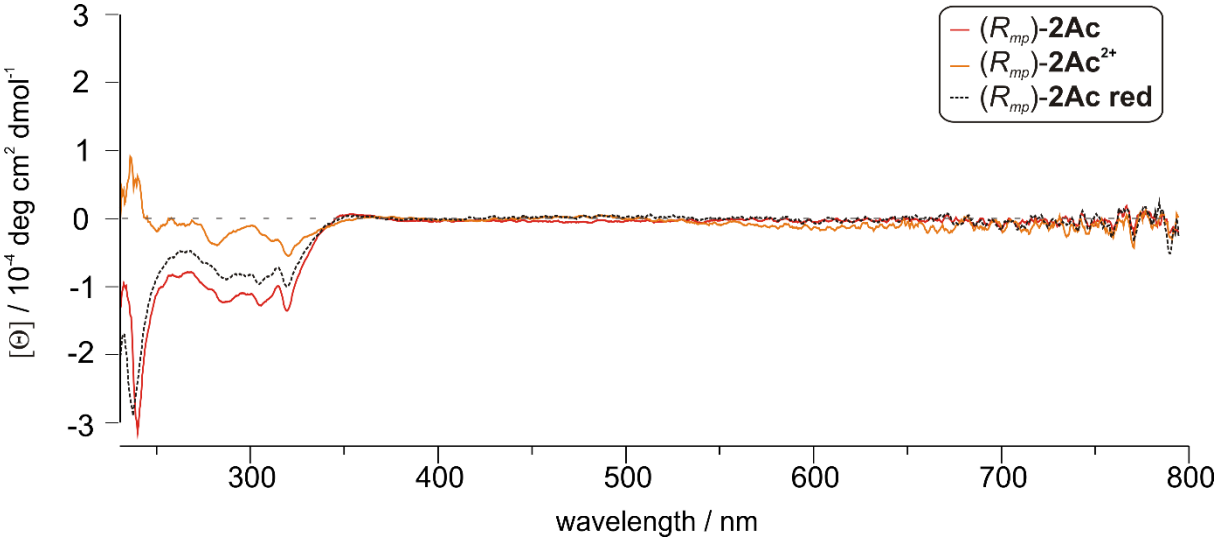

Fig. S17 CD spectra of (R_{mp})-**2Ac** (220 µM in ACN, 298 K, bulk $Fe(ClO_4)_3$ as oxidant) in the TTF^0 and TTF^{2+} state and after reduction to the neutral form with Zn dust.

7. Computational details

Conformational search. To study the influence of different conformations on the optical activity of *(*R_{mp}*)*-**2Ac**, we performed simulated annealing with the xTB (extended tight-binding) programme by Stefan Grimme.[13] This approach is based on DFTB (density functional tight binding)[14] and has been optimised for non-covalent interactions. GBSA (generalised Born accessible surface area)[15] was included as an implicit solvent model in the calculation. Using the Berendsen thermostat,[16] a maximum and minimum temperature of 1000 K and 300 K were chosen for annealing, respectively. The run time for each annealing step was 50 ps, the time step was 2 fs, and structures were dumped every 50 fs. Furthermore, the SHAKE algorithm[17] was applied to restrain hydrogen atoms from dissociating.

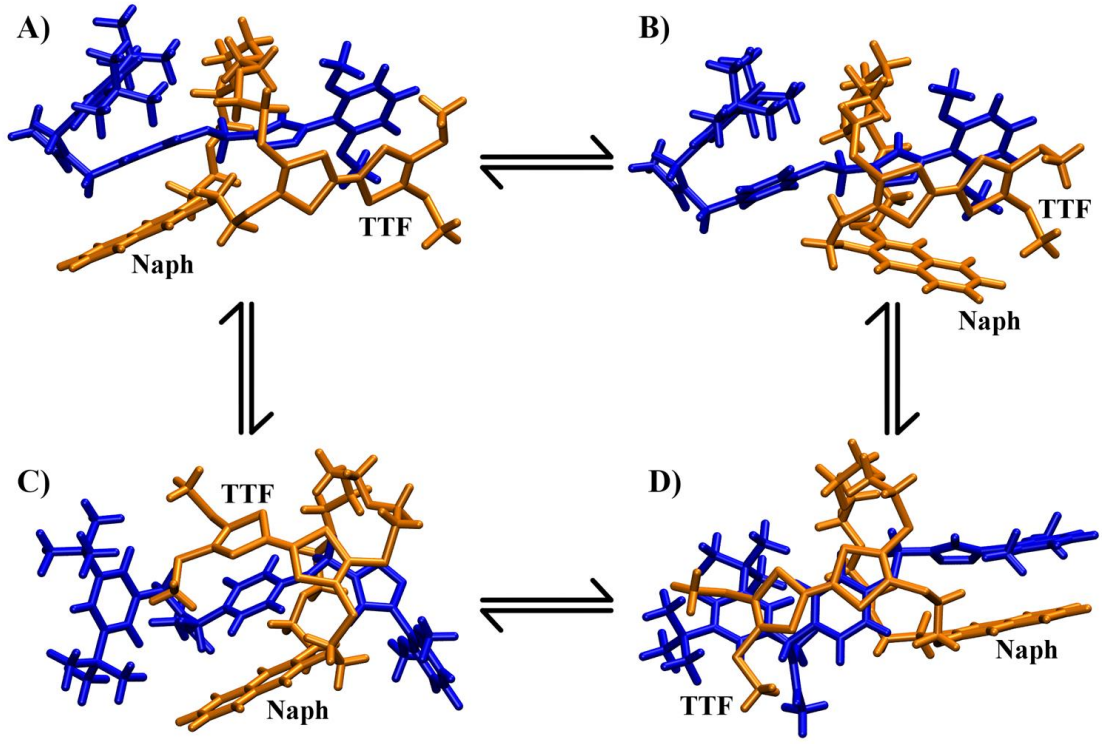

Fig. S18: The four most favourable conformations of (*R*$_{mp}$)-**2Ac**: **A**, **B**, **C**, and **D**. The conformations differ in the way the TTF core, the naphthalene unit, and the axle are positioned with respect to each other. Every conformation can be interconverted into another by flipping the TTF or the naphthalene unit or both.

Fig. S18 displays the four most stable conformations re-optimised at the RI*J*-TPSS-D3(BJ)/def2-SVP[18-22] level of density functional theory (DFT) with the programme package Turbomole (version 7.1)[23]. COSMO (ε = 8.9 for CH_2Cl_2)[24] was employed as the solvent model. Subsequent single-point calculations to assess the relative stabilities of the four conformations (see Table S2) were performed at the RI*J*COSX-ωB97X-D3/def2-TZVP[25, 26] level with CPCM[27]

as solvent model using ORCA (version 4.0.1)[28]. Finally, Grimme's sTD-DFT (simplified time-dependent DFT)[29] approach was used at the same level to connect electronic properties and optical activity, i.e. the ECD spectra (Fig. 4 in main text) of (R_{mp})-**2Ac**. The entire procedure was conducted for both (R_{mp})-**2Ac** and (R_{mp})-**2Ac^{2+}**.

Tab. S2: Relative electronic energies of all conformations in charge states 0 and 2+ calculated at the ωB97X-D3 level of DFT (values in kJ/mol)

charge state	conformer A	conformer B	conformer C	conformer D
0	0.0	30.4	43.9	17.9
2+	8.5	0.0	54.6	58.6

Calculations at other levels of theory (PBE0[30], CAM-B3LYP[31], and M06-2X[32]) confirm the relative stabilities of the four conformers. Moreover, the shapes of the simulated ECD spectra are considered reliable as they agree with each other regarding the signs of the CD bands. Nevertheless, a systematic red-shift in wavelengths of sometimes up to 50 nm compared to experiment is observed, which is however expected for different density functionals (see Fig. S19 for an illustrative example).

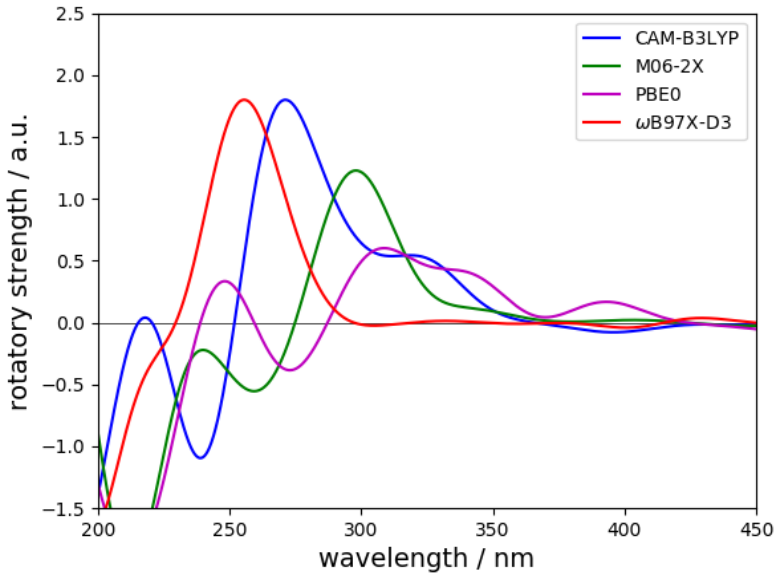

Fig. S19: ECD spectra of (R_{mp})-**2Ac**$^{2+}$ in conformation **A** computed at the sTD-DFT level with various functionals. Gaussian line broadening with σ = 20 nm was applied. Vertical transition lines are omitted for clarity. It can be observed that the general shapes of the spectra agree while the absolute positions of the signals vary in wavelengths to some extent.

Furthermore, it should be noted that (R_{mp})-**2Ac**$^{2+}$ in all four conformations displays non-negligible rotarory strengths for the TTF-centered transition at around 650-700 nm (not shown in Fig. S19) which is caused by an overestimation of the magnetic dipole transition moment

owing to a seemingly poor description of the TTF-TTF transition within the sTD-DFT framework.

Electronic structure and transitions.

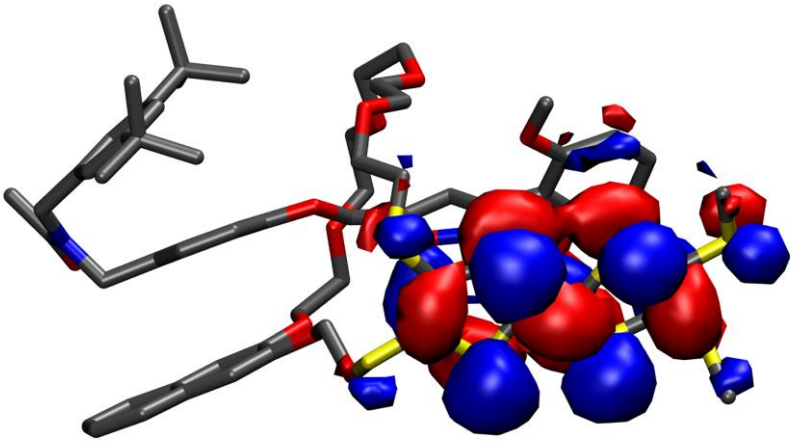

Fig. S20: HOMO of **2Ac** in conformation **A** (the same nodal shape can be observed for the LUMO of **2Ac**$^{2+}$), isovalue = 0.01 a_0^{-3}.

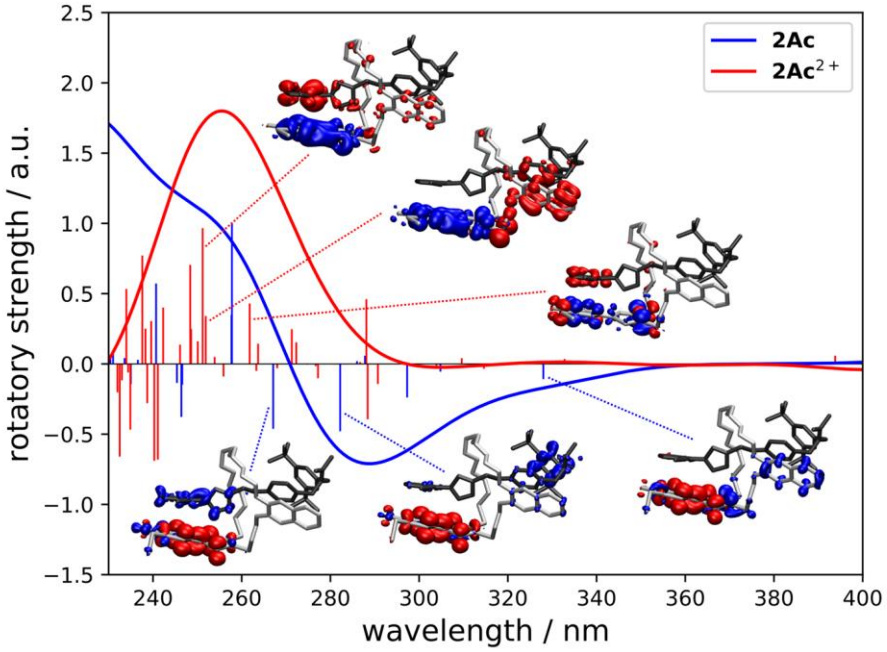

Fig. S21: Simulated ECD spectra of (R_{mp})-**2Ac** and (R_{mp})-**2Ac^{2+}** both in conformation **A** obtained at the ωB97X-D3/def2-TZVP level of sTD-DFT. Gaussian line broadening with σ = 20 nm was applied. Insets: Excited state difference densities of selected transitions to visualise the electron flow during these excitations. Blue and red zones correspond to areas of electron-enhancement and electron-depletion, respectively. Isovalue: 0.001 a_0^{-3}.

Intramolecular interactions. An atoms-in-molecules (AIM)[33] bonding analysis was performed for *(R_{mp})*-**2Ac** in all *four* conformations and charge state 0 and 2+. Fig. S22 shows *(R_{mp})*-**2Ac** in conformation **A** with its bond critical points as a representative example. An AIM analysis is useful for studying non-covalent interactions. C-H···π and π-π-stacking interactions can thus be easily identified within *(R_{mp})*-**2Ac**. Together with the results from our DFT calculations at the RI*J*COSX-ωB97X-D3/def2-TZVP level, we can deduce what is likely responsible for the conformational behaviour of *(R_{mp})*-**2Ac** and *(R_{mp})*-**2Ac**$^{2+}$. Important aspects are the energetic gain through π-π-stacking between the various (aromatic) units and the delocalisation of electron density near the TTF unit.

First, we will discuss the neutral molecule *(R_{mp})*-**2Ac**. Conformation **A** exhibits a large amount of intramolecular interactions especially through π-π-stacking of aromatic units. Furthermore, the TTF unit's proximity to the isoxazole core and the dimethoxy-phenyl moiety yield non-covalent interactions. In conformation **B**, many of the π-π-stacking interactions are lost as the naphthalene moiety attaches itself to the TTF unit, which makes this conformation around 30 kJ/mol less stable. The energetic gain in conformation **D** is based on the interaction

between the naphthalene, the isoxazole core, and the dimethoxy-phenyl unit and the stacking of the TTF unit and the phenyl spacer. However, the di-*tert*butyl-phenyl unit is not able to stack with any of the other aromatic units anymore, which results in a net loss of almost 18 kJ/mol with respect to conformation **A**. Finally, conformation **C** is the least stable structure (ca. 44 kJ/mol with respect to **A**) since effective π-π-stacking is neither achieved by the isoxazole unit nor by the dimethoxy-phenyl ring nor by the di-*tert*butyl-phenyl moiety. The energetic gain through non-covalent interactions is solely based on the arguably inefficient stacking between TTF core, phenyl spacer and naphthalene unit.

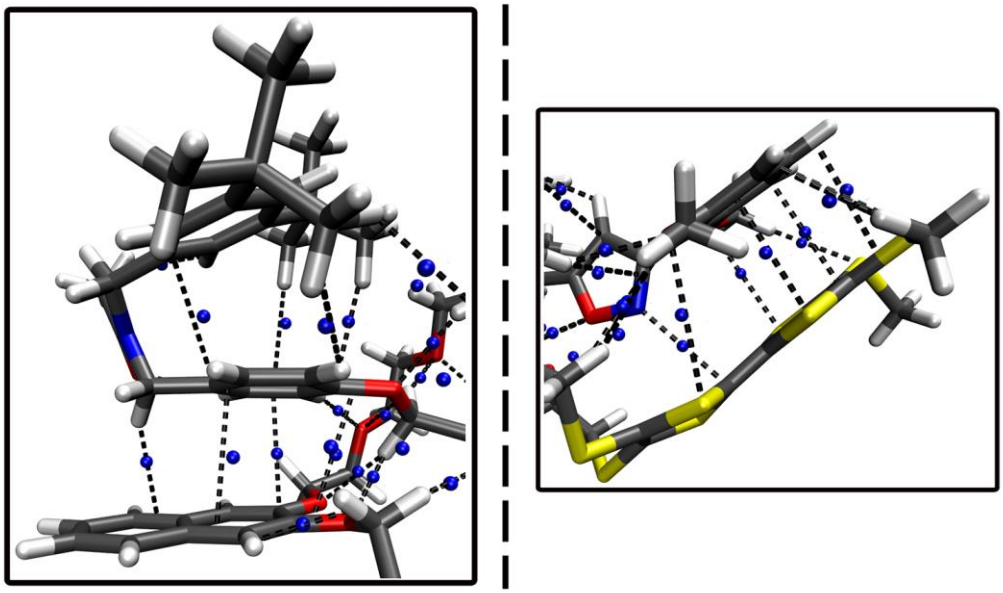

Fig. S22: Bond critical points (blue spheres) obtained at the ωB97X-D3/def2-TZVP level utilising the Multiwfn programme[34] near the naphthalene moiety (left) and the TTF unit (right) illustrating the non-covalent interactions within **2Ac** in conformation **A**.

For *(R_{mp})*-**2Ac**$^{2+}$ the picture is quite different. Now conformation **B** is the most stable structure since the charge, which is mostly localised on the TTF unit, can be delocalised over the TTF core, the naphthalene unit, the isoxazole ring, and the dimethoxy-phenyl moiety. Additionally, there is still the π-π-stacking interaction between the di-*tert*butyl-phenyl unit and the phenyl spacer contributing to its energetic stability. The charge delocalisation over four different units in the molecule is missing in conformation **A**, which makes it somewhat less stable than **B** (~ 9 kJ/mol). Similar arguments account for conformation **D**, which is – maybe somewhat surprisingly - by far the least stable structure now (over 58 kJ/mol), as the charge is not efficiently delocalised which seems to massively overcompensate any π-π-stacking interactions. In conformation **C**, the charge can be somewhat better delocalised than in **D**,

however, due to its lack of more efficient π-π-stacking interactions it is also somewhat less stable than **B** (ca. 55 kJ/mol).

8. Crystallographic data

General details. Single crystal X-ray data in the present study were collected at 170 K on a Bruker-Nonius KappaCCD diffractometer with APEX-II detector and graphite monochromatized Mo-Kα (λ = 0.71073 Å) radiation. The *COLLECT*[35] software was used for data collection (θ and ω scans) and *DENZO-SMN*[36] for the processing. Lorentzian polarization correction was applied on all data and absorption effects were corrected with multi-scan method (*SADABS*[37]). The structures were solved by intrinsic phasing methods (*SHELXT*[38]) and refined by full-matrix least squares on F^2 using *SHELXL*-2018/3.[39] The *SQUEEZE* module of *PLATON*[40, 41] was utilized in the structure refinement to remove the residual electron densities, which could not be reliably assigned and refined. Anisotropic displacement parameters were assigned to non-H atoms. Positional disorder in the structures was treated by gently restraining geometric and anisotropic displacement parameters. All hydrogen atoms were refined using riding models with U_{eq}(H) of 1.5U_{eq}(C) for terminal methyl groups and of 1.2U_{eq}(C) for other groups. The main details of crystal data collection and refinement parameters are presented below. CCDC 1910670 contains the supplementary crystallographic data for this paper. These data can be obtained free of charge via http://www.ccdc.cam.ac.uk/conts/retrieving.html (or from the CCDC, 12 Union Road, Cambridge CB2 1EZ, UK; Fax: +44 1223 336033; E-mail: deposit@ccdc.cam.ac.uk).

Structure of dTTFC8: Compound **dTTFC8** was crystallised as orange needles with vapour diffusion of Et_2O into CH_2Cl_2 solution of the compound. Crystal data and refinement parameters of **dTTFC8**: $C_{30}H_{36}O_6S_8$, M = 749.07, monoclinic, space group $P2_1/n$ (no. 14), a = 25.1361(6), b = 5.09490(10), c = 30.6018(9) Å, β = 109.649(2)°, V = 3690.8(2) Å^3, Z = 4, ρ_{calc} = 1.348 Mgm^{-3}, μ = 0.522 mm^{-1}, F_{000} = 1568, θ range = 1.82-26.37°, 14025 reflections collected of which 7554 unique (R_{int} = 0.1129), No. of reflections with $I>2\sigma(I)$ = 3856, which were used in all calculations, 409 parameters and 32 restraints, Goodness-of-fit (F^2) = 1.018. The final R indices [$I>2\sigma(I)$]: R1 = 0.0734 and wR2 = 0.1436. R indices (all data): R1 = 0.1606 and wR2 = 0.1770. Largest residual electron densities: 0.598 and -0.408 e.Å^{-3}.

Structure description for dTTFC8: Crystal structure solution of **dTTFC8** shows nicely that the substituted TTF is attached to the naphthalene crown ether macrocycle. There is a slight disorder in one oxygen atom of crown ether, which is divided over two spatial positions. The substituted TTF moiety exhibits typical bond distances for neutral TTF derivatives,[42-44] like

characteristically short C=C distance of 1.345(7) Å between the 1,3-dithiole rings and a distance range of 1.749(6) to 1.764(5) Å for C-S bonds. An Interesting geometric feature is the planarity of substituted TTF moiety with both 1,3-dithiole rings and all S atoms, as well lying in the same plane. The notably acute angle between the naphthalene and TTF planes (74.8°) can be attributed to the connecting ethylene bridge which avoids ecliptic and gauche conformations by maintaining an OCCS dihedral angle of 159.4°. In the crystal packing, the molecules are arranged in columnar stacks. Naphthalenes stack with naphthalenes with a plane-to-plane distance of 3.29 Å shifted sideways by 3.88 Å and TTFs on top of each other. Instead, TTFs stack with plane-to-plane distances of 3.47 Å, and a sideways slip of 3.73 Å, respectively.

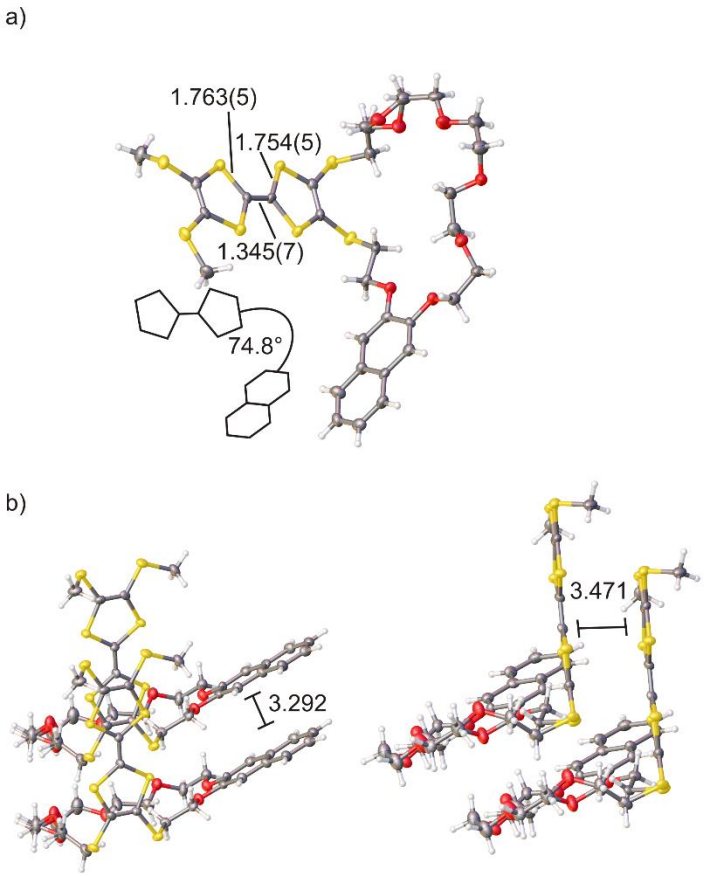

Figure S23: Solid-state structure of **dTTFC8**. (a) Top view with selected bond lengths (Å) and the angle between the naphthalene and the TTF plane. (b) Side view of two stacked **dTTFC8** molecules in the crystal with distances (Å) between molecule planes. Colour codes: S = yellow; O = red; C = grey; H = black (spheres).

9. ^{1}H, ^{13}C NMR

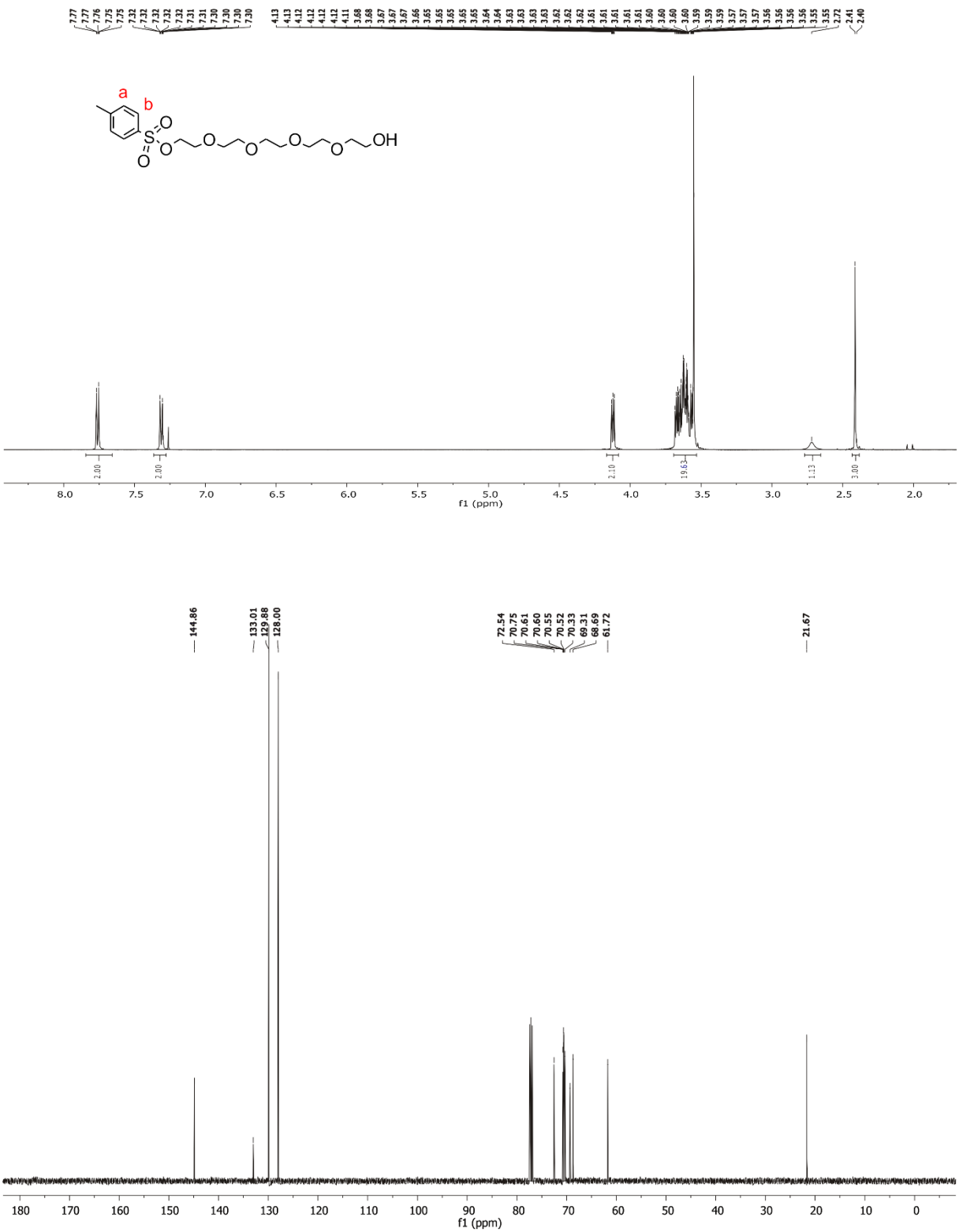

Fig. S24 ^{1}H (top) and ^{13}C (bottom) NMR spectrum (500/126 MHz, $CDCl_3$, 298 K) of **S2**.

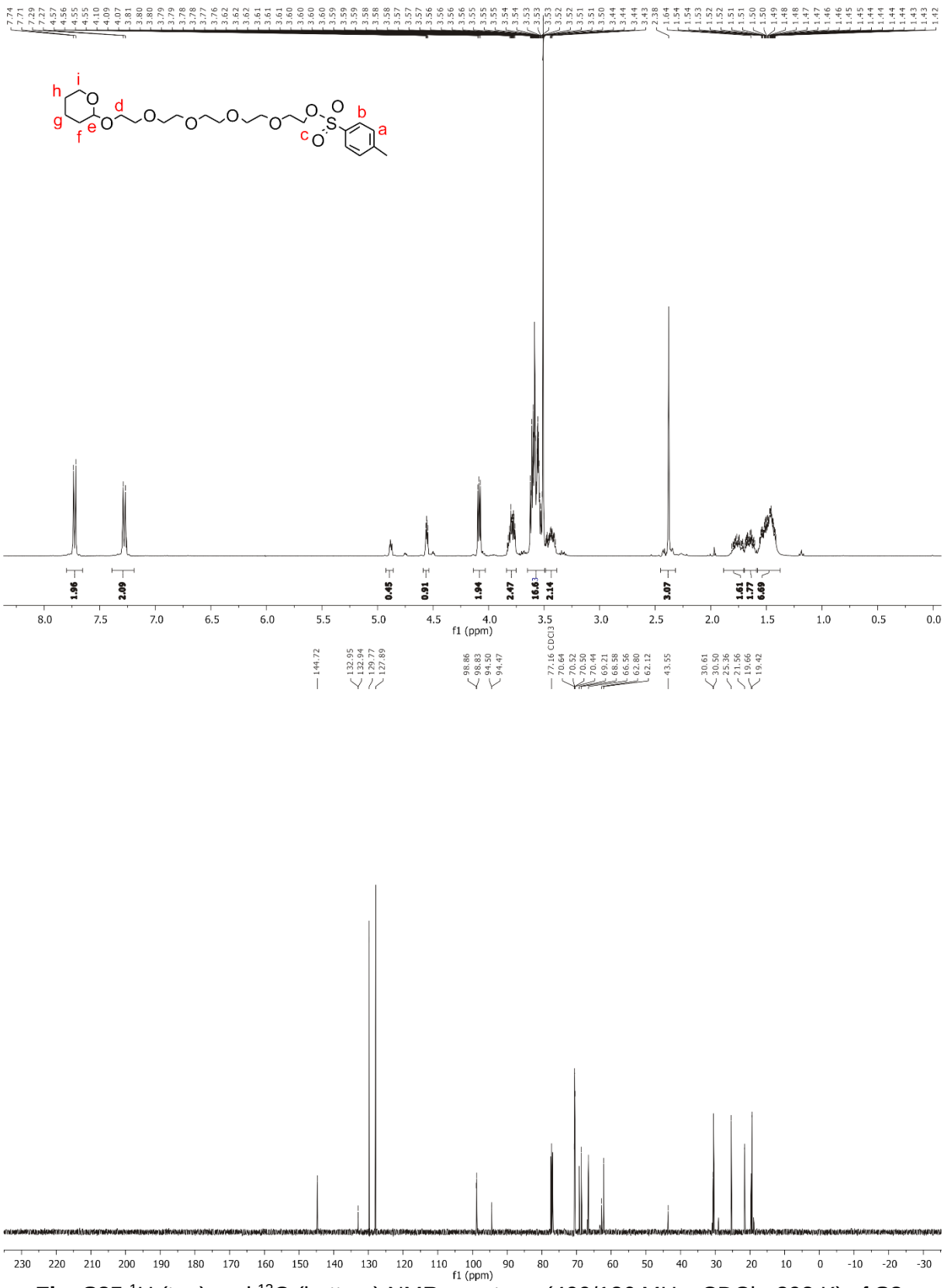

Fig. S25 ^{1}H (top) and ^{13}C (bottom) NMR spectrum (400/126 MHz, $CDCl_3$, 298 K) of **S3**.

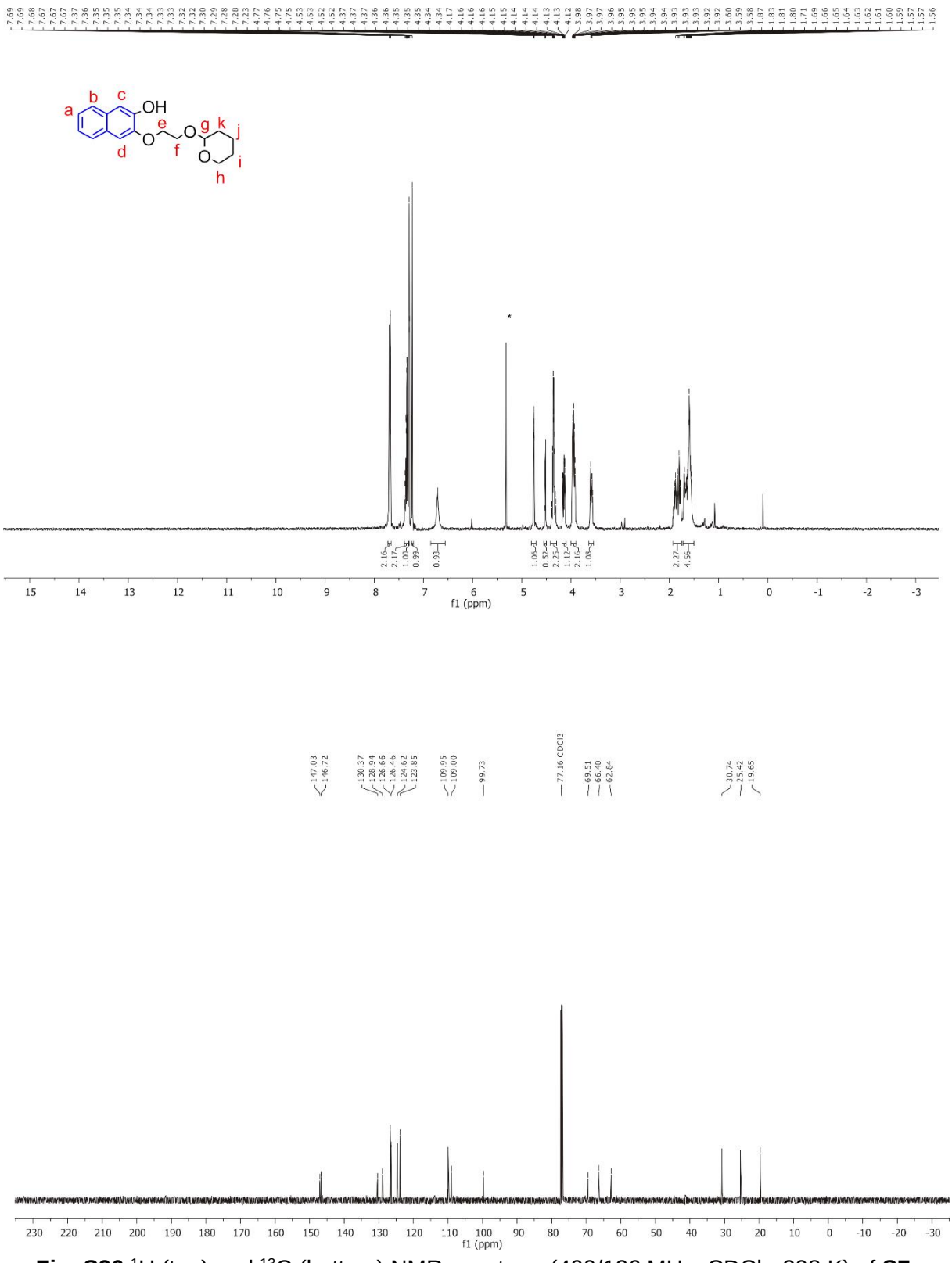

Fig. S26 ^{1}H (top) and ^{13}C (bottom) NMR spectrum (400/126 MHz, $CDCl_3$, 298 K) of **S7**.

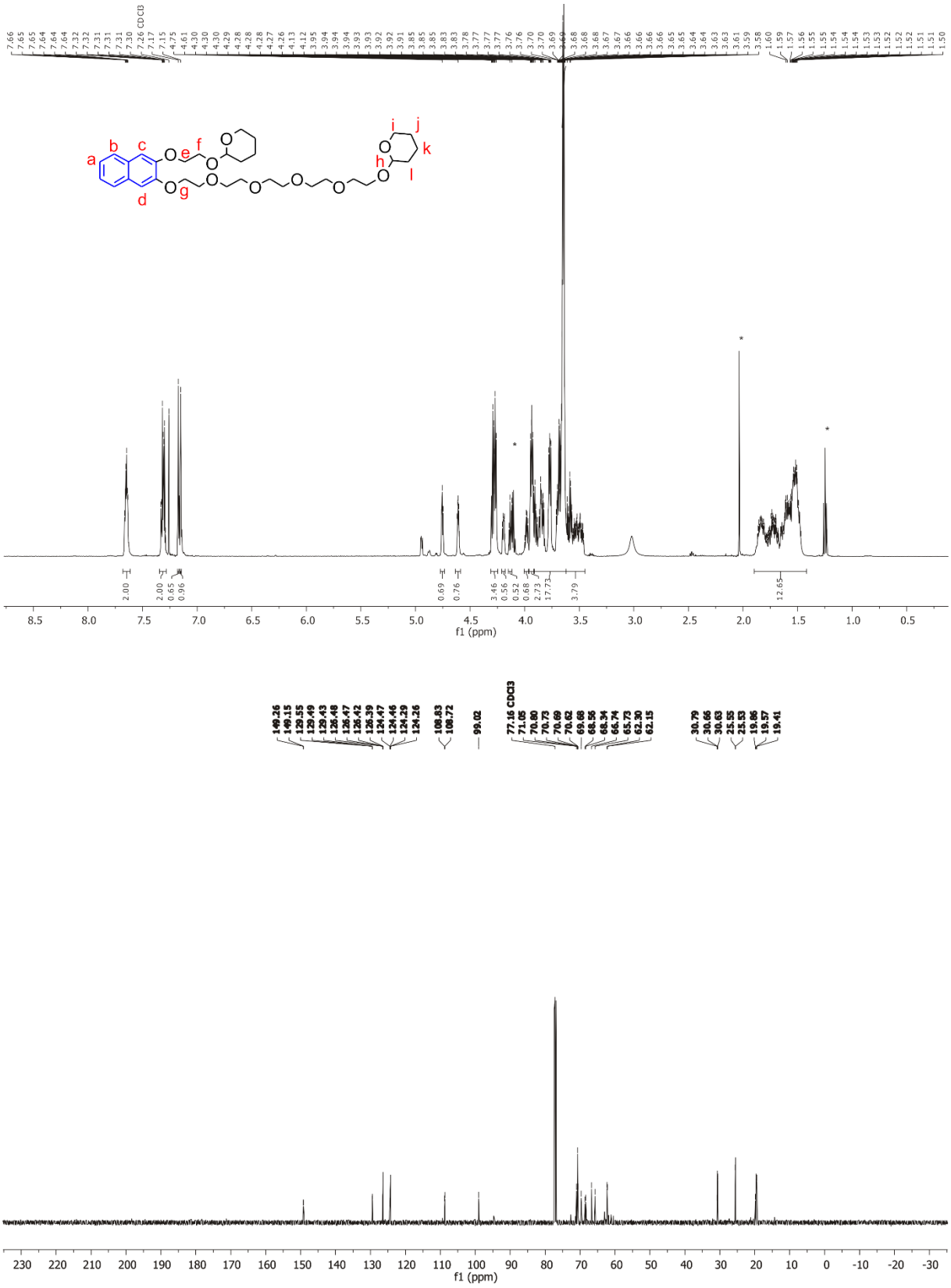

Fig. S27 ^{1}H (top) and ^{13}C (bottom) NMR spectrum (500/126 MHz, $CDCl_3$, 298 K) of **S8**.

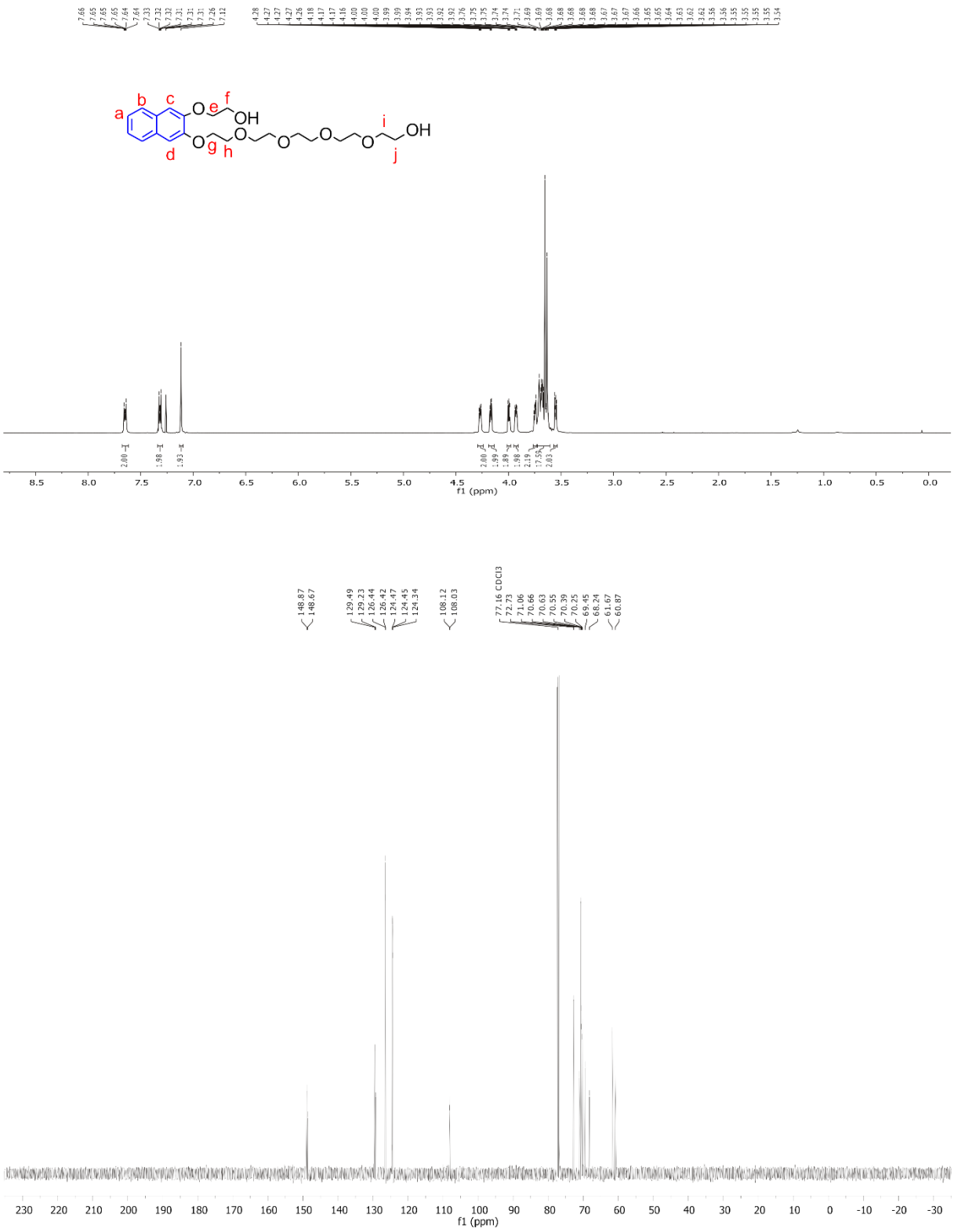

Fig. S28 ^{1}H (top) and ^{13}C (bottom) NMR spectrum (500/126 MHz, $CDCl_3$, 298 K) of **S9**.

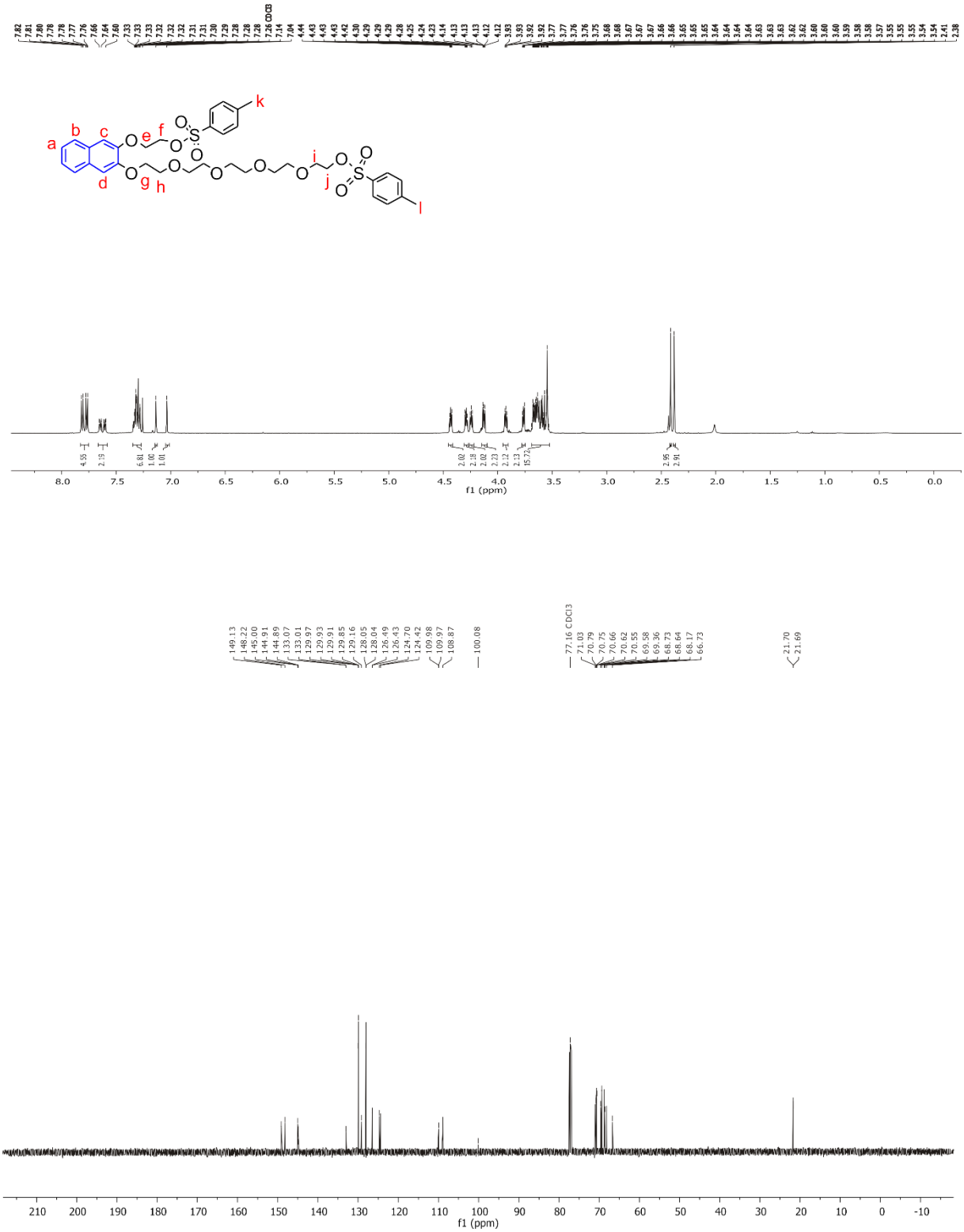

Fig. S29 ^{1}H (top) and ^{13}C (bottom) NMR spectrum (500/126 MHz, $CDCl_3$, 298 K) of **S10**.

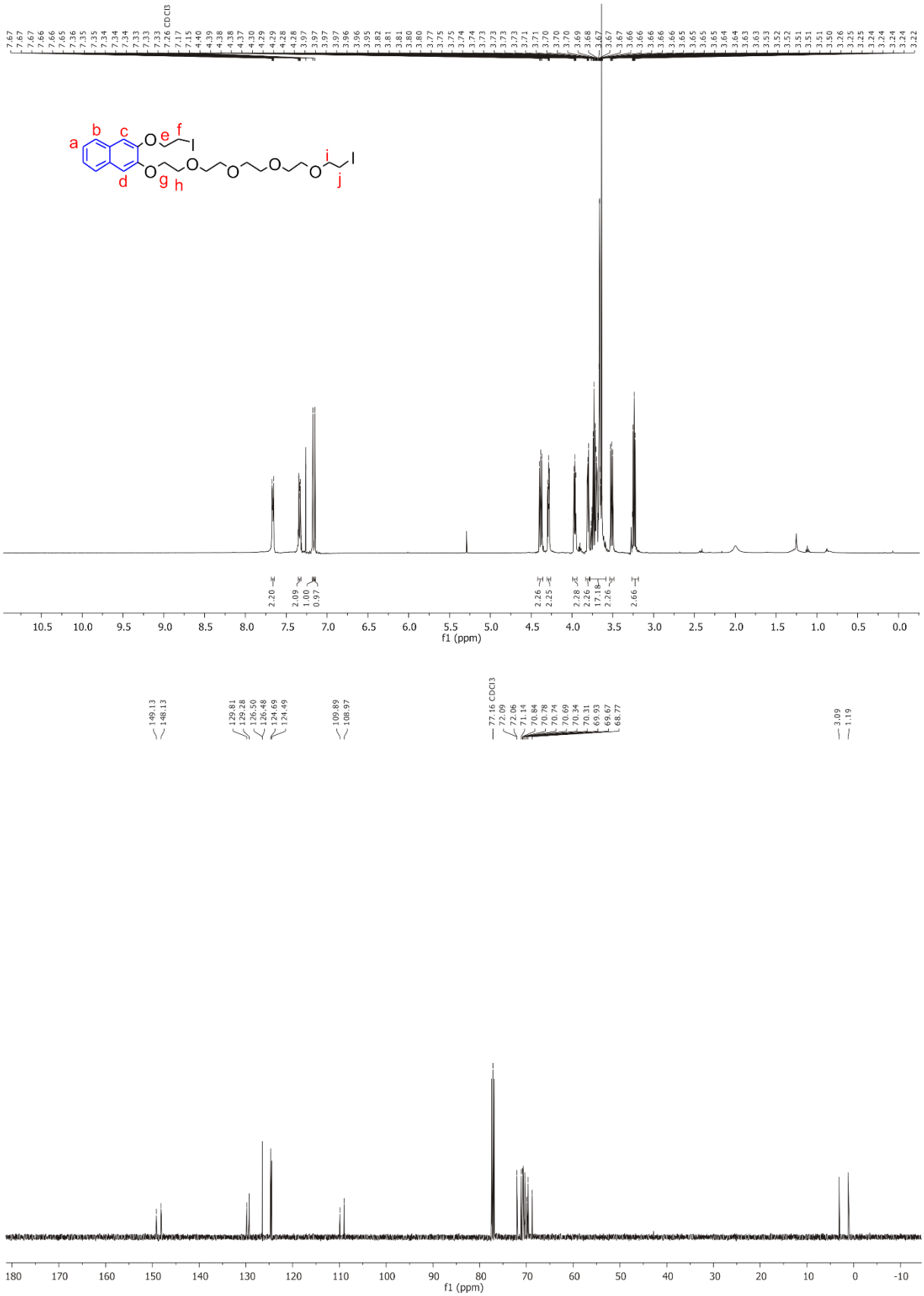

Fig. S30 ^{1}H (top) and ^{13}C (bottom) NMR spectrum (500/126 MHz, $CDCl_3$, 298 K) of **S11**.

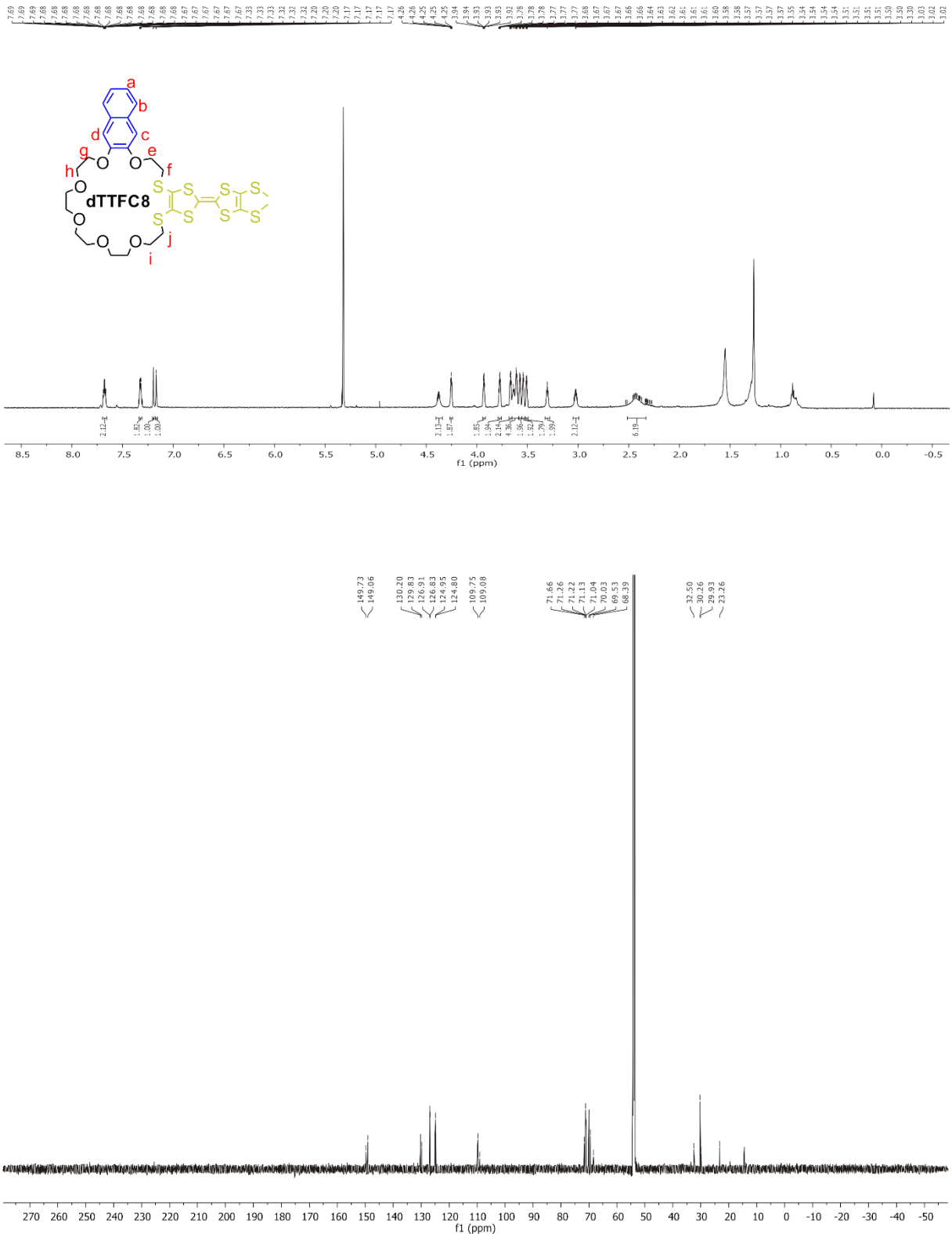

Fig. S31 ^{1}H (top) and ^{13}C (bottom) NMR spectrum (700/176 MHz, $CDCl_3$, 298 K) of **dTTFC8**.

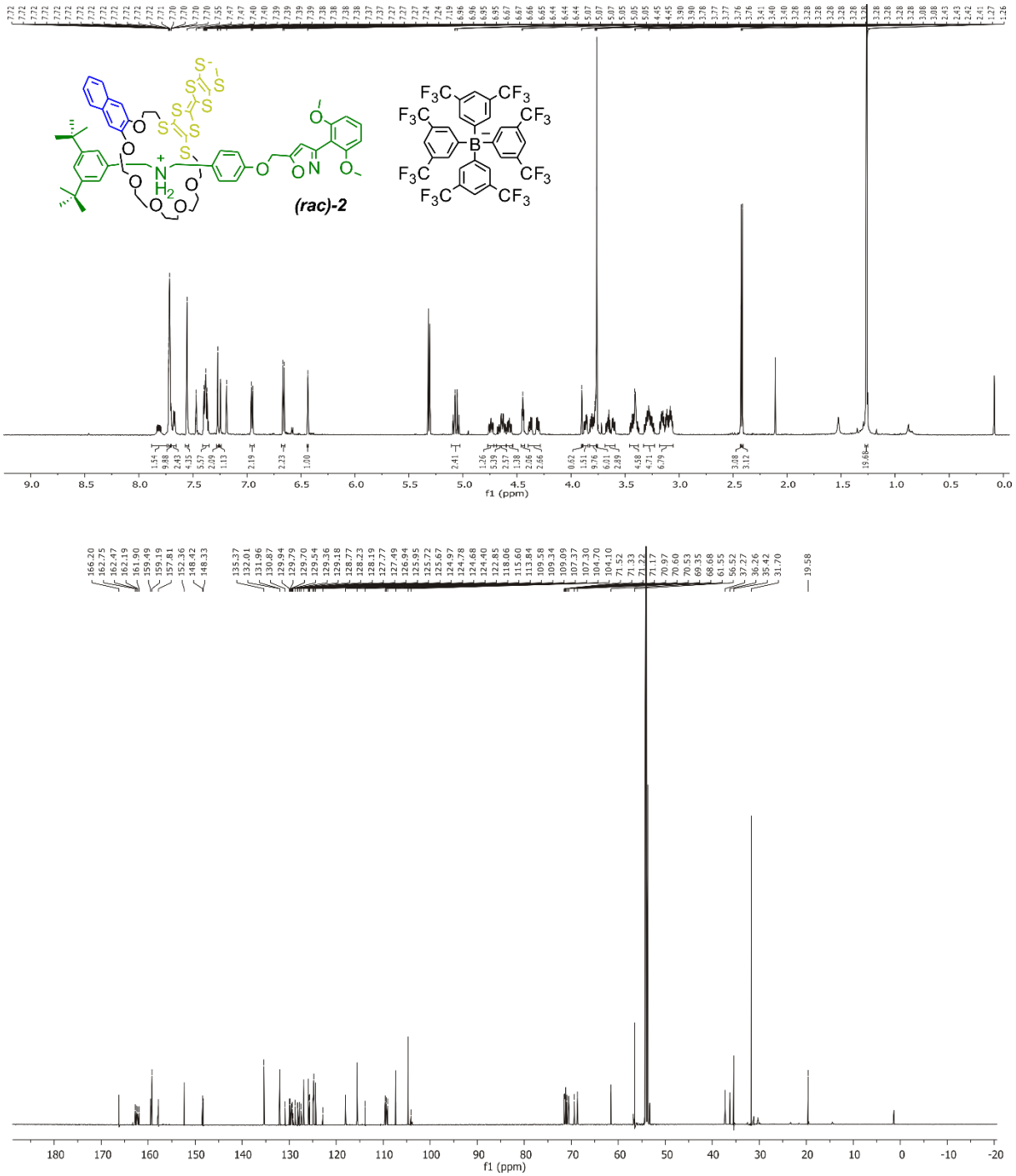

Fig. S32 ^{1}H (top) and ^{13}C (bottom) NMR spectrum (700/176 MHz, CD_2Cl_2, 298 K) of the racemic mixture of **2**.

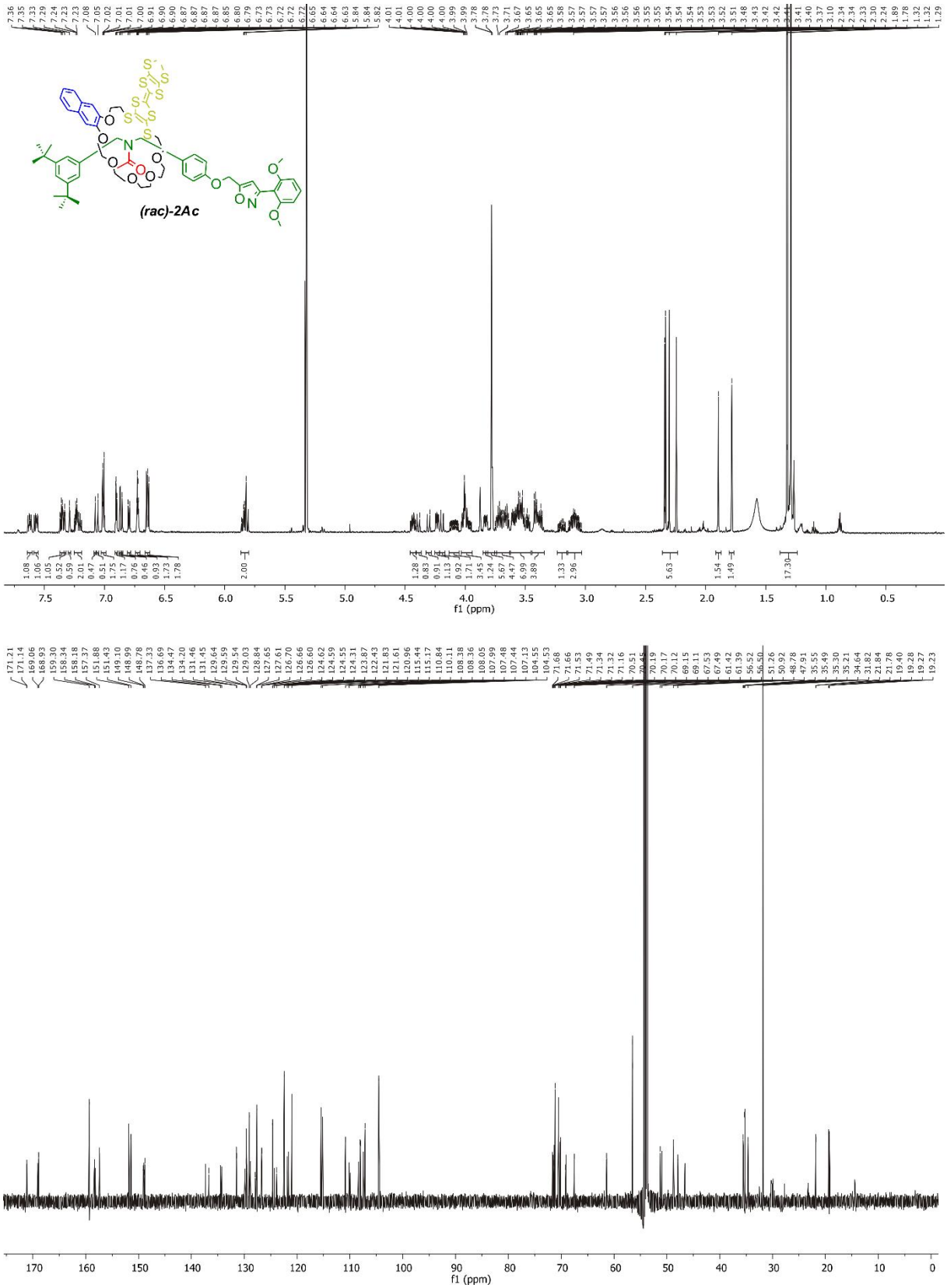

Fig. S33 ^{1}H (top) and ^{13}C (bottom) NMR spectrum (700/176 MHz, CD_2Cl_2, 298 K) of the racemic mixture of **2Ac**.

9. HR-MS

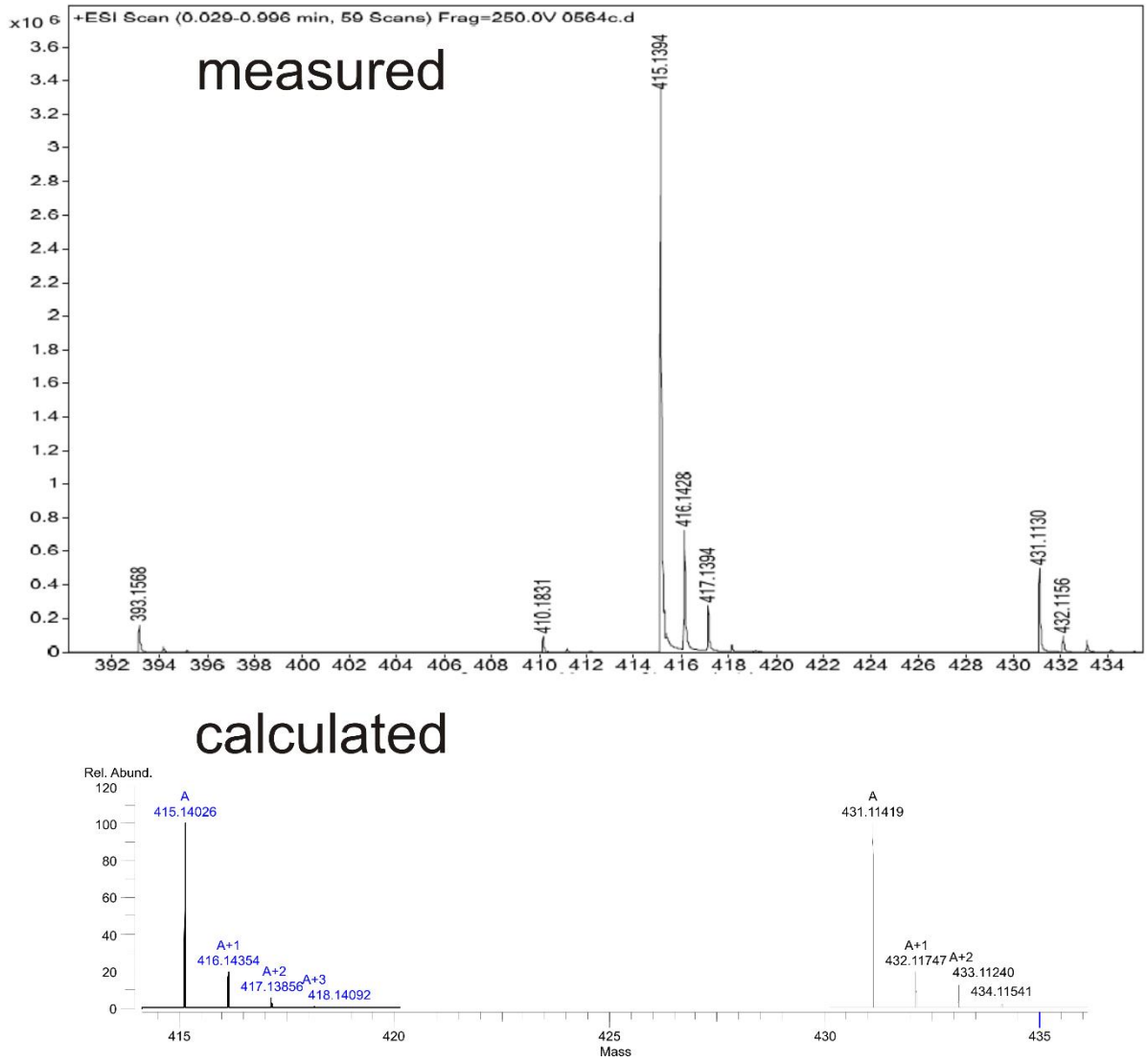

Fig. S34 HRMS ESI$^+$ (top) and calculated (bottom) of **S2**.

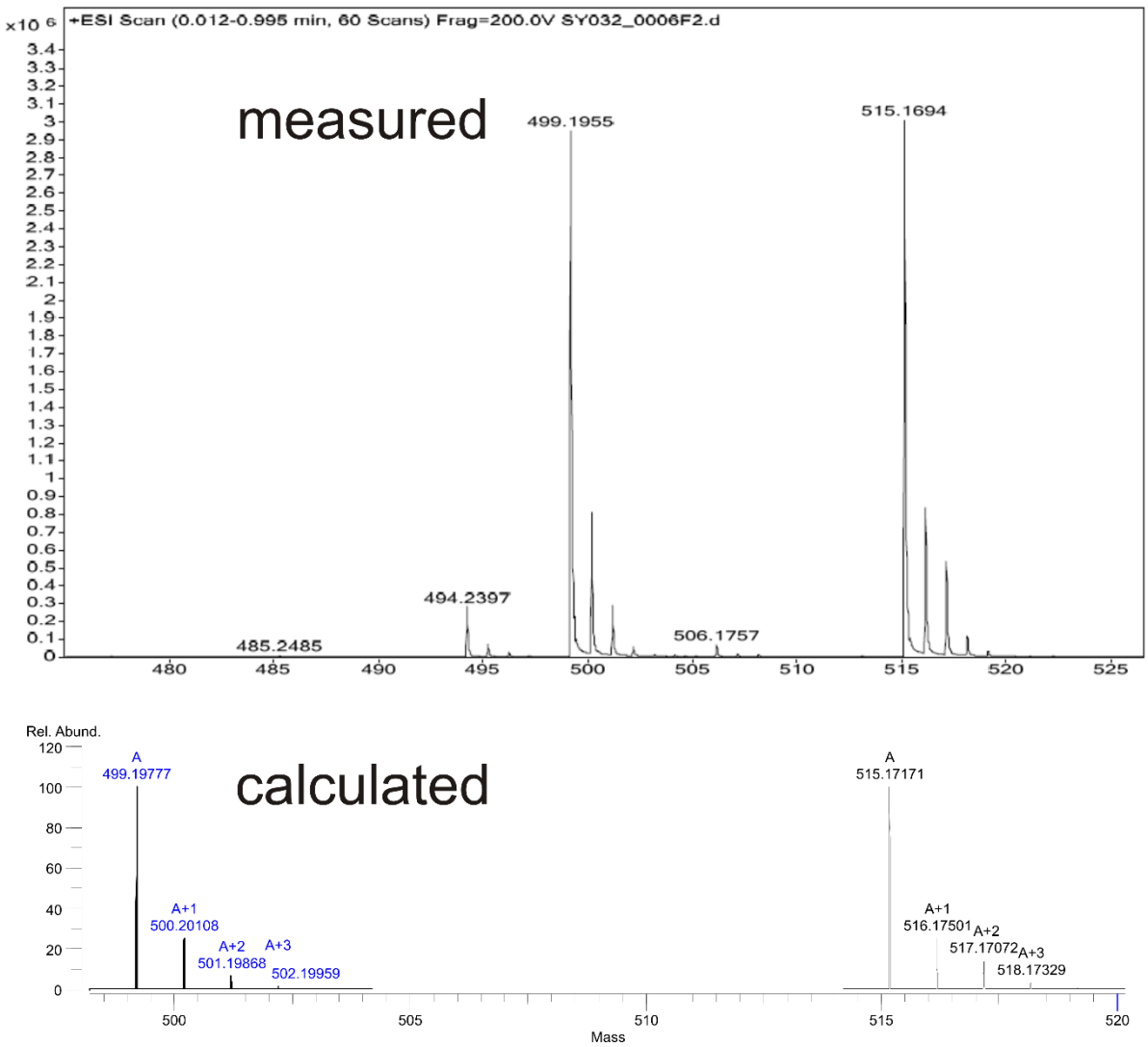

Fig. S35 HRMS ESI$^+$ (top) and calculated (bottom) of **S3**.

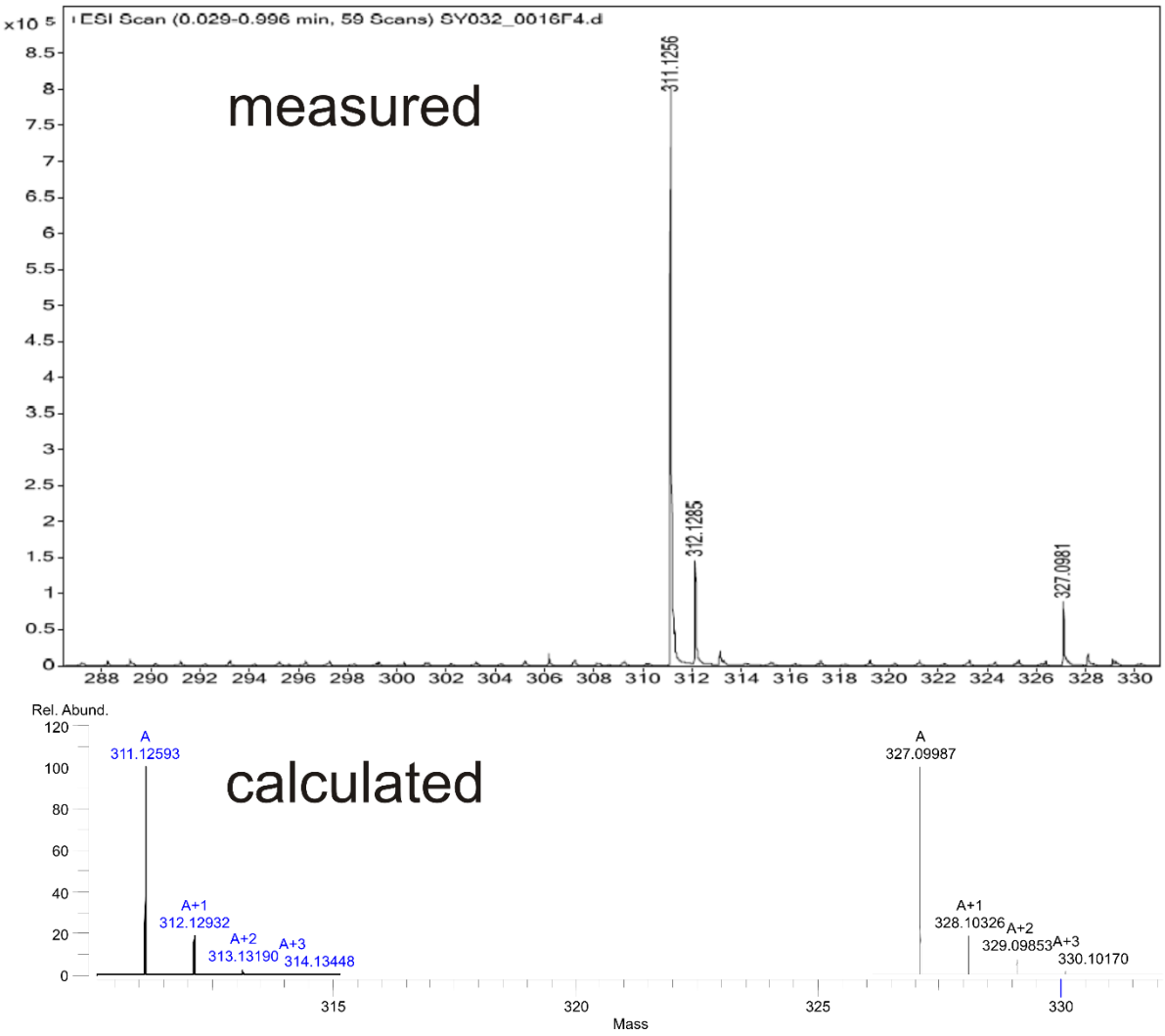

Fig. S36 HRMS ESI$^+$ (top) and calculated (bottom) of **S7**.

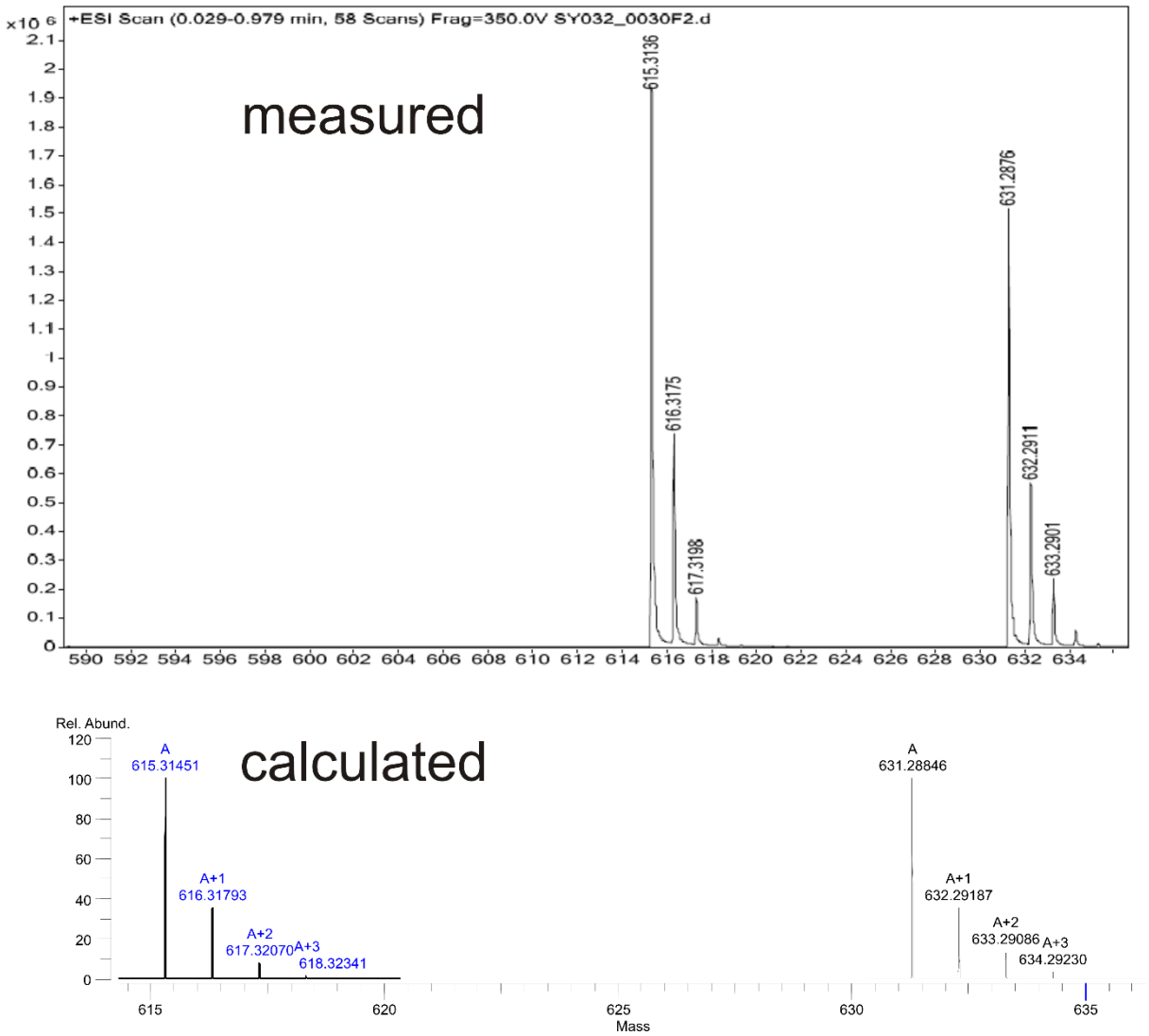

Fig. S37 HRMS ESI$^+$ (top) and calculated (bottom) of **S8**.

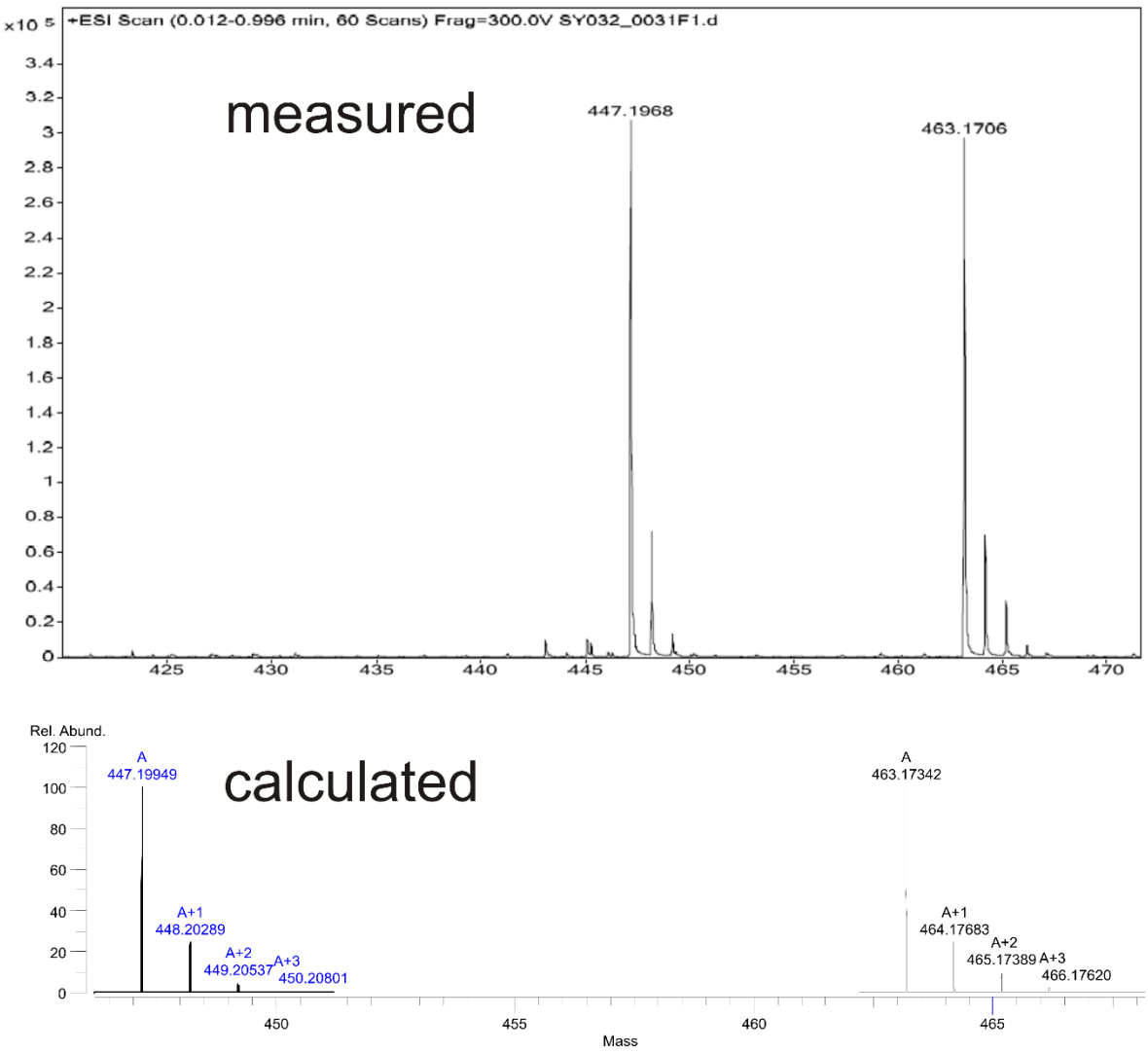

Fig. S38 HRMS ESI$^+$ (top) and calculated (bottom) of **S9**.

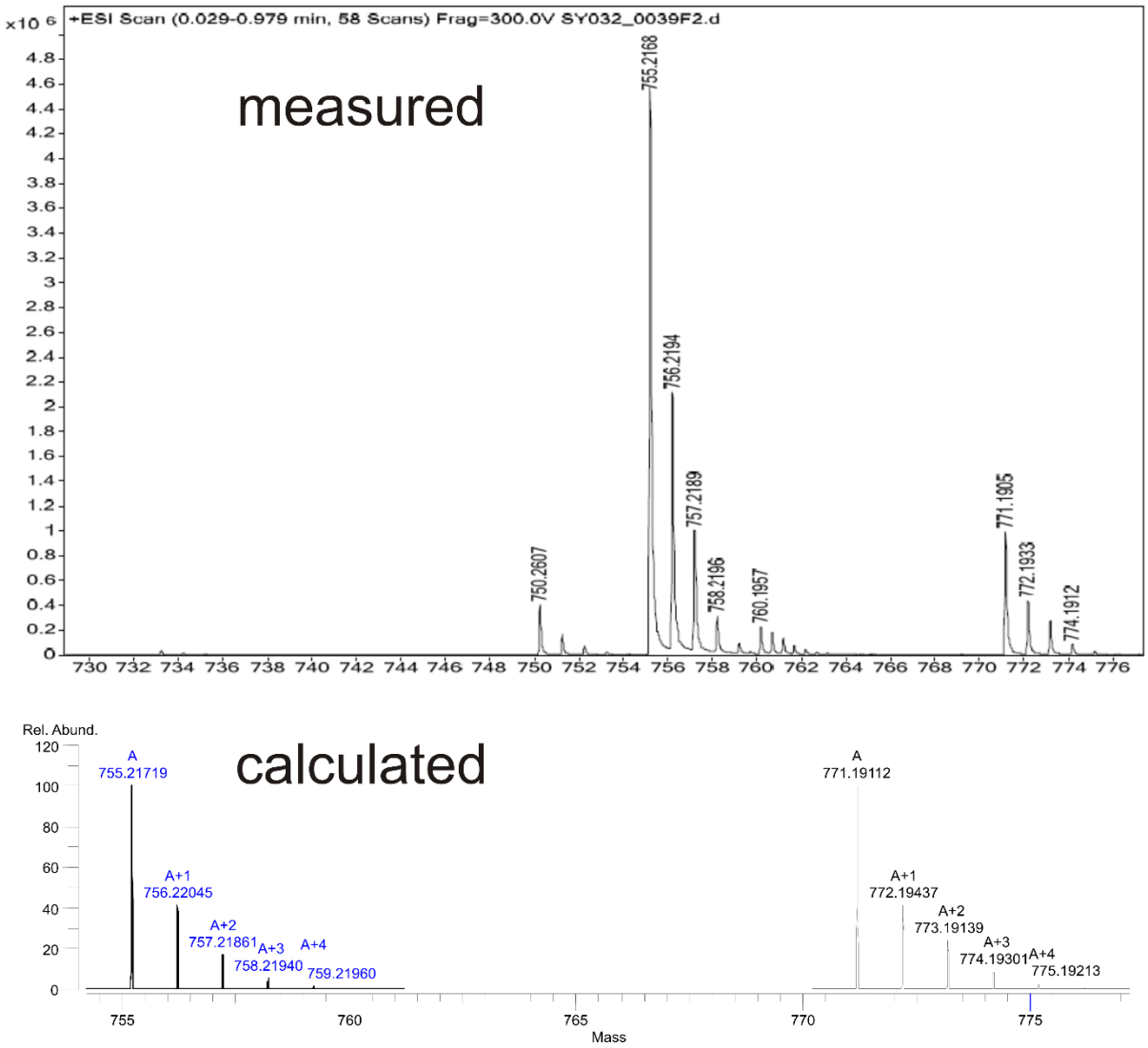

Fig. S39 HRMS ESI$^+$ (top) and calculated (bottom) of **S10**.

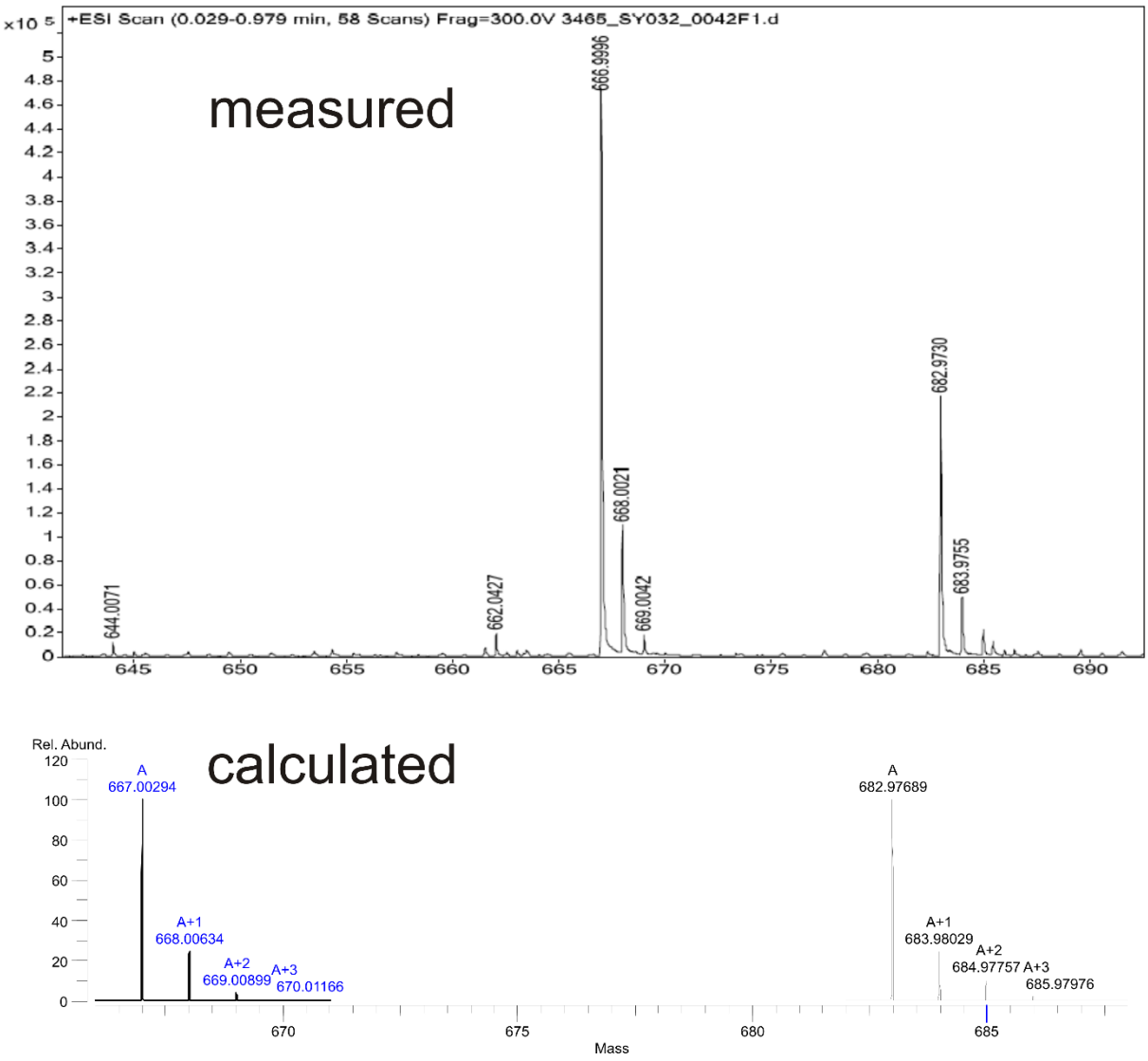

Fig. S40 HRMS ESI$^+$ (top) and calculated (bottom) of **S11**.

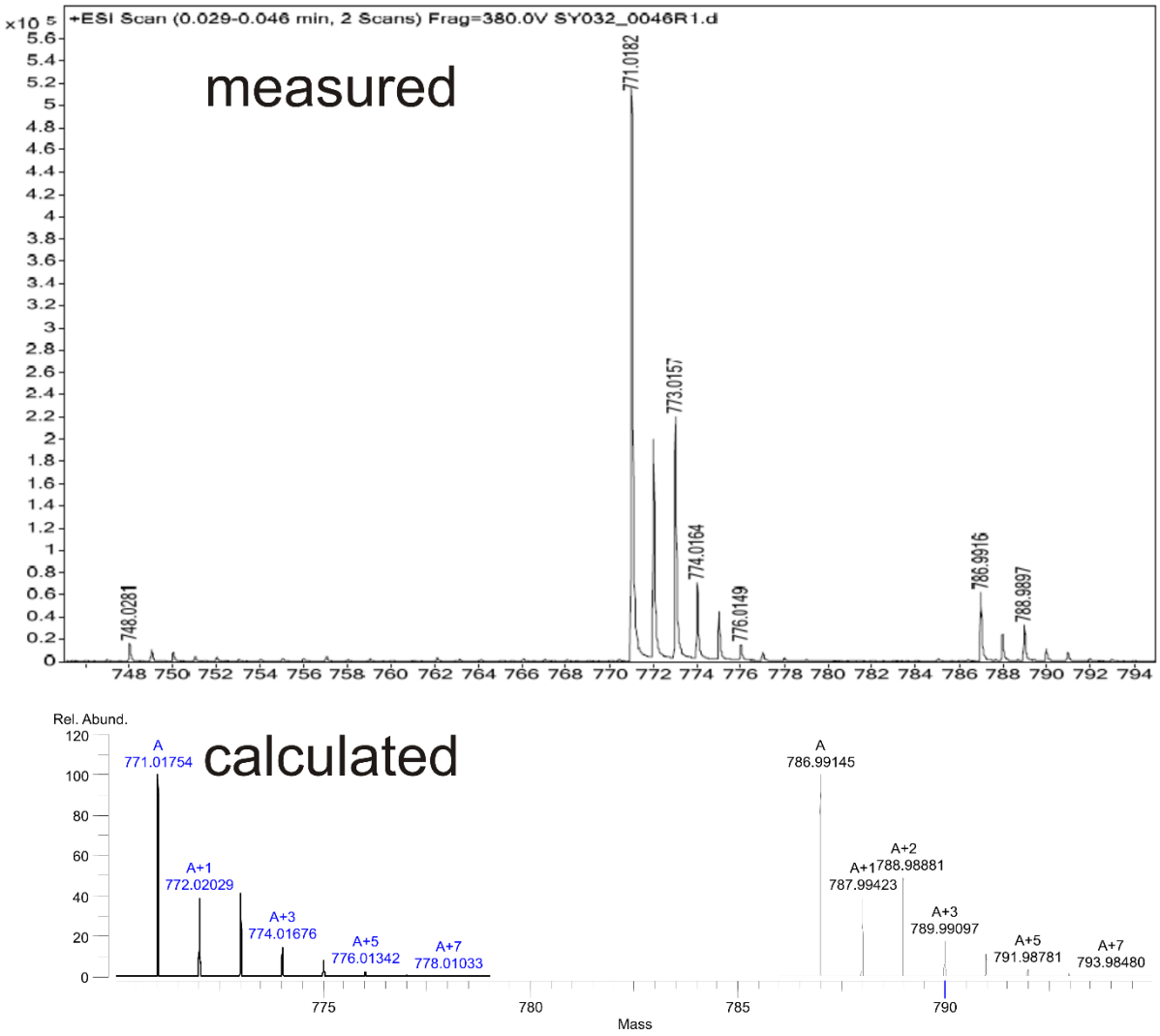

Fig. S41 HRMS ESI$^+$ (top) and calculated (bottom) of **dTTFC8**.

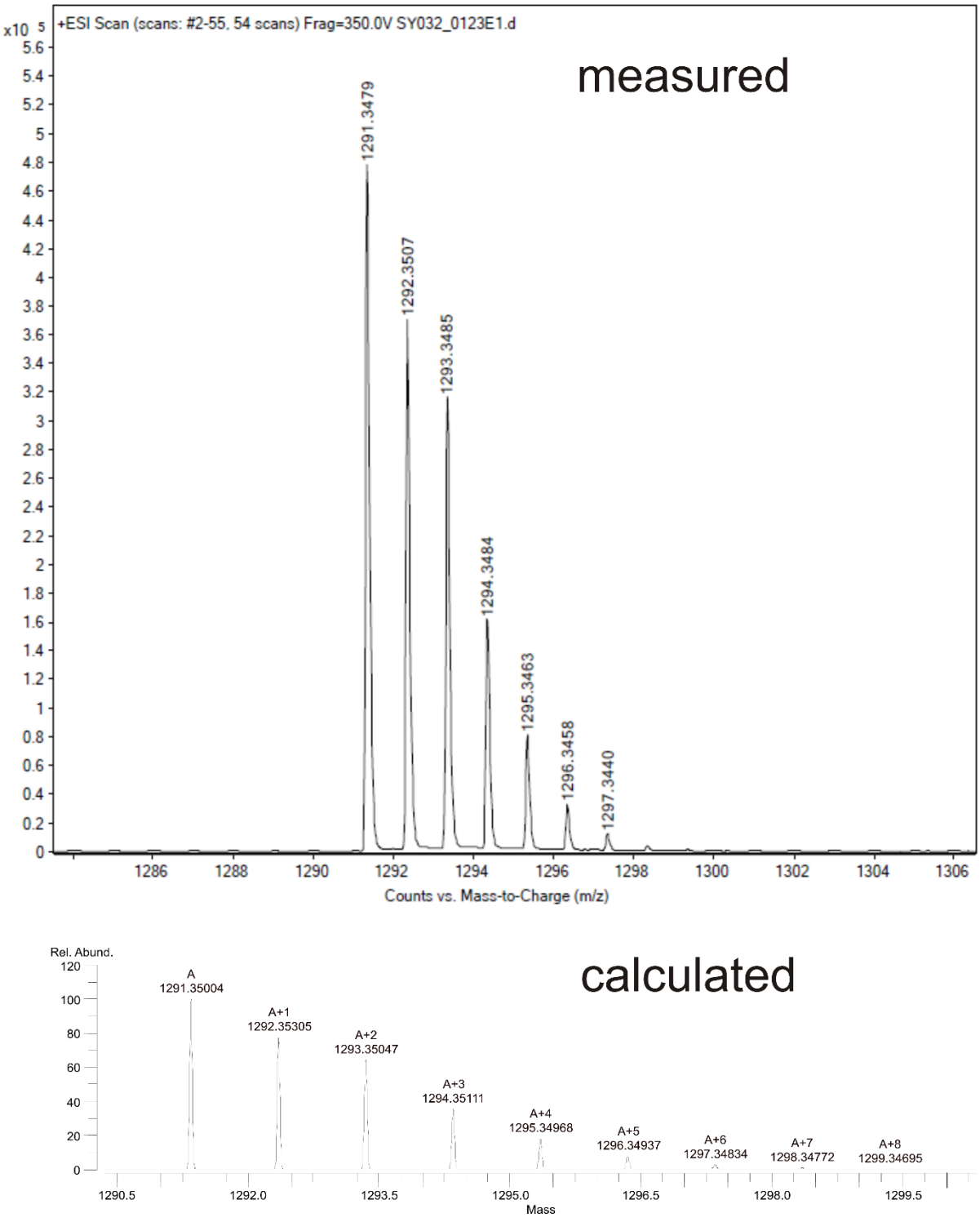

Fig. S42 HRMS ESI$^+$ (top) and calculated (bottom) of (*rac*)-**2**.

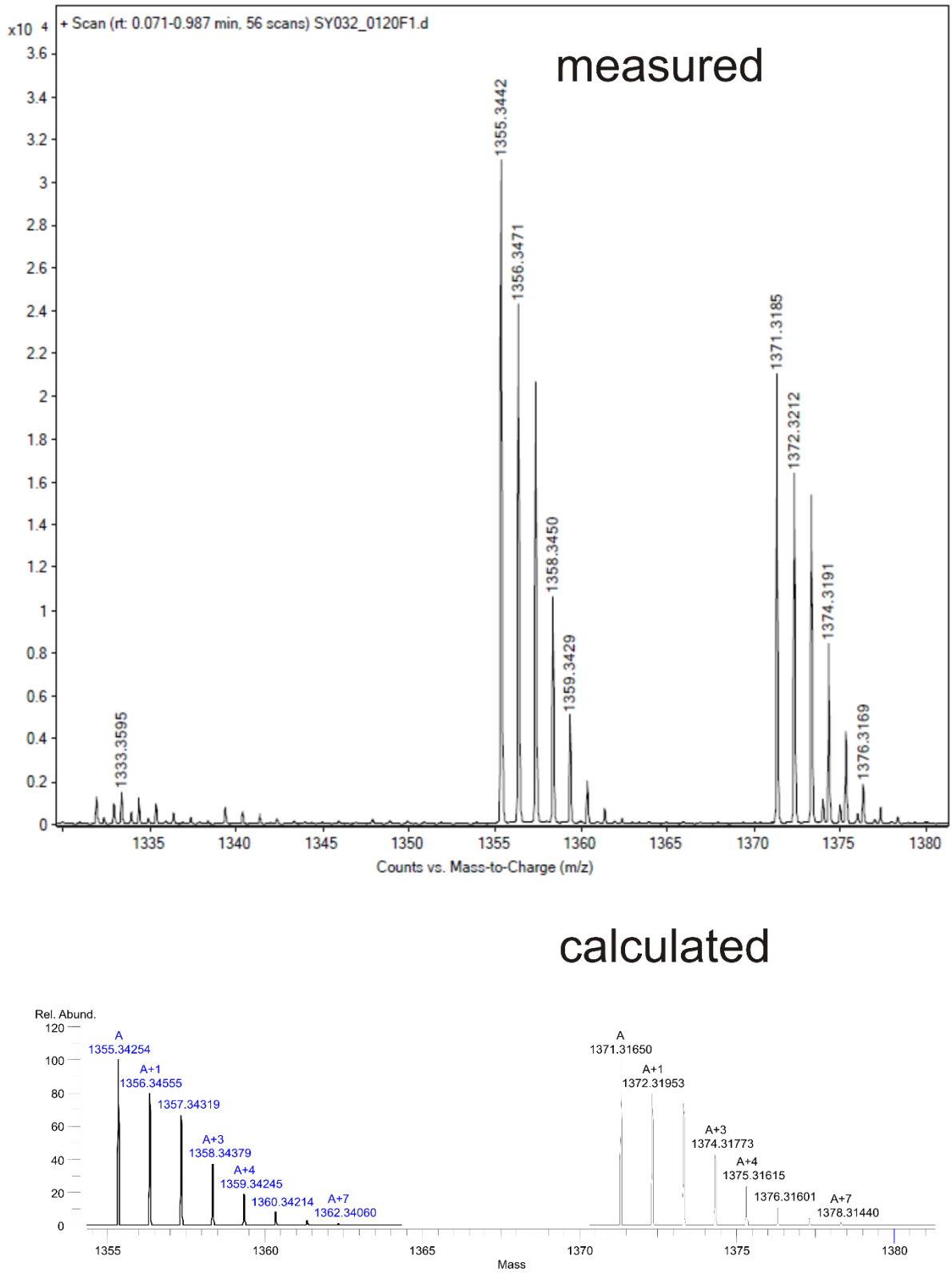

Fig. S43 HRMS ESI$^+$ (top) and calculated (bottom) of (*rac*)-**2Ac**.

11. References

1. M. Popr, S. Hybelbauerova and J. Jindrich, *Beilstein J. Org. Chem.*, 2014, **10**, 1390-1396.
2. W. Mamdouh, I. H. Uji, A. E. Dulcey, V. Percec, S. De Feyter and F. C. De Schryver, *Langmuir*, 2004, **20**, 7678-7685.
3. N. Svenstrup, K. M. Rasmussen, T. K. Hansen and J. Becher, *Synthesis*, 1994, **1994**, 809-812.
4. H. V. Schröder, S. Sobottka, M. Nößler, H. Hupatz, M. Gaedke, B. Sarkar and C. A. Schalley, *Chem. Sci.*, 2017, **8**, 6300-6306.
5. T. Matsumura, F. Ishiwari, Y. Koyama and T. Takata, *Org. Lett.*, 2010, **12**, 3828-3831.
6. J. R. Aranzaes, M.-C. Daniel and D. Astruc, *Can. J. Chem.*, 2006, **84**, 288-299.
7. X. Z. Zhu and C. F. Chen, *J. Am. Chem. Soc.*, 2005, **127**, 13158-13159.
8. K. Zimmermann, *Synth. Commun.*, 1995, **25**, 2959-2962.
9. S. Passemard, D. Staedler, L. Ucnova, G. S. Schneiter, P. Kong, L. Bonacina, L. Juillerat-Jeanneret and S. Gerber-Lemaire, *Bioorg. Med. Chem. Lett.*, 2013, **23**, 5006-5010.
10. J. Sly, P. Kasak, E. Gomar-Nadal, C. Rovira, L. Gorriz, P. Thordarson, D. B. Amabilino, A. E. Rowan and R. J. Nolte, *Chem. Commun.*, 2005, **10**, 1255-1257.
11. K. B. Simonsen, N. Svenstrup, J. Lau, O. Simonsen, P. Mørk, G. J. Kristensen and J. Becher, *Synthesis*, 1996, **1996**, 407-418.
12. F. A. Loiseau, K. K. Hii and A. M. Hill, *J. Org. Chem.*, 2004, **69**, 639-647.
13. S. Grimme, C. Bannwarth and P. Shushkov, *J. Chem. Theory. Comput.*, 2017, **13**, 1989-2009.
14. D. Porezag, T. Frauenheim, T. Köhler, G. Seifert and R. Kaschner, *Phys. Rev. B*, 1995, **51**, 12947-12957.
15. *Grimme et. al.*
16. H. J. C. Berendsen, J. P. M. Postma, W. F. van Gunsteren, A. DiNola and J. R. Haak, *J. Chem. Phys.*, 1984, **81**, 3684-3690.
17. J.-P. Ryckaert, G. Ciccotti and H. J. C. Berendsen, *J. Comput. Phys.*, 1977, **23**, 327-341.
18. K. Eichkorn, O. Treutler, H. Öhm, M. Häser and R. Ahlrichs, *Chem. Phys. Lett.*, 1995, **240**, 283-290.
19. J. Tao, J. P. Perdew, V. N. Staroverov and G. E. Scuseria, *Phys. Rev. Lett.*, 2003, **91**, 146401.
20. S. Grimme, J. Antony, S. Ehrlich and H. Krieg, *J. Chem. Phys.*, 2010, **132**, 154104.
21. S. Grimme, S. Ehrlich and L. Goerigk, *J. Comput. Chem.*, 2011, **32**, 1456-1465.
22. F. Weigend and R. Ahlrichs, *Phys. Chem. Chem. Phys.*, 2005, **7**, 3297-3305.
23. R. Ahlrichs, M. Bär, M. Häser, H. Horn and C. Kölmel, *Chem. Phys. Lett.*, 1989, **162**, 165-169.
24. A. Klamt and G. Schüürmann, *Perkin Trans. 2*, 1993, **5**, 799-805.
25. F. Neese, F. Wennmohs, A. Hansen and U. Becker, *Chem. Phys.*, 2009, **356**, 98-109.
26. J. D. Chai and M. Head-Gordon, *J. Chem. Phys.*, 2008, **128**, 084106.
27. V. Barone and M. Cossi, *J. Phys. Chem. A*, 1998, **102**, 1995-2001.
28. F. Neese, *Wiley Interdiscip. Rev.-Comput. Mol. Sci.*, 2012, **2**, 73-78.
29. C. Bannwarth and S. Grimme, *Comput. Theor. Chem.*, 2014, **1040-1041**, 45-53.
30. J. P. Perdew, M. Ernzerhof and K. Burke, *J. Chem. Phys.*, 1996, **105**, 9982-9985.
31. T. Yanai, D. P. Tew and N. C. Handy, *Chem. Phys. Lett.*, 2004, **393**, 51-57.
32. Y. Zhao and D. G. Truhlar, *Theor. Chem. Acc.*, 2007, **120**, 215-241.
33. R. F. W. Bader, *Chem. Rev.*, 1991, **91**, 893-928.
34. T. Lu and F. Chen, *J. Comput. Chem.*, 2012, **33**, 580-592.
35. COLLECT, Bruker AXS, Inc., Madison, Wisconsin, USA, 2008.
36. Z. O. a. W. Minor, *Methods Enzymol., vol. 276, Macromolecular Crystallography, Part A,* , Academic Press, New York, 1997.
37. G. M. Sheldrick, *SADABS*. University of Göttingen, Germany, **1996**.
38. G. M. Sheldrick, *Acta Crystallogr., Sect. A: Found. Adv.*, 2015, **71**, 3-8.
39. G. M. Sheldrick, *Acta Crystallogr., Sect. C: Struct. Chem.*, 2015, **71**, 3-8.
40. A. L. Spek, *Acta Crystallogr., Sect. C: Struct. Chem.*, 2015, **71**, 9-18.

41. A. L. Spek, *Acta Crystallogr., Sect. D: Biol. Crystallogr.*, 2009, **65**, 148-155.
42. J. Sun, X. Lu, J. Shao, X. Li, S. Zhang, B. Wang, J. Zhao, Y. Shao, R. Fang, Z. Wang, W. Yu and X. Shao, *Chem. Eur. J.*, 2013, **19**, 12517-12525.
43. H. Kobayashi, R. Kato, T. Mori, A. Kobayashi, Y. Sasaki, G. Saito, T. Enoki and H. Inokuchi, *Mol. Cryst. Liq. Cryst.*, 2011, **107**, 33-43.
44. P. R. Ashton, J. Becher, M. C. T. Fyfe, M. B. Nielsen, J. F. Stoddart, A. J. P. White and D. J. Williams, *Tetrahedron*, 2001, **57**, 947-956.

6.6 Thermodynamic and electrochemical study of tailor-made crown ethers for redox-switchable (pseudo)rotaxanes

H. Hupatz, M. Gaedke, H.V. Schröder, J. Beerhues, A. Valkonen, F. Klautzsch, S. Müller, F. Witte, K. Rissanen, B. Sarkar, C.A. Schalley

Beilstein J. Org. Chem. **2020**, *16*, 2576-2588.

Submitted on August 7, 2020, first published on October 20, 2020 by the Beilstein-Institut.

An electronic version of the articles is available at: https://doi.org/10.3762/bjoc.16.209

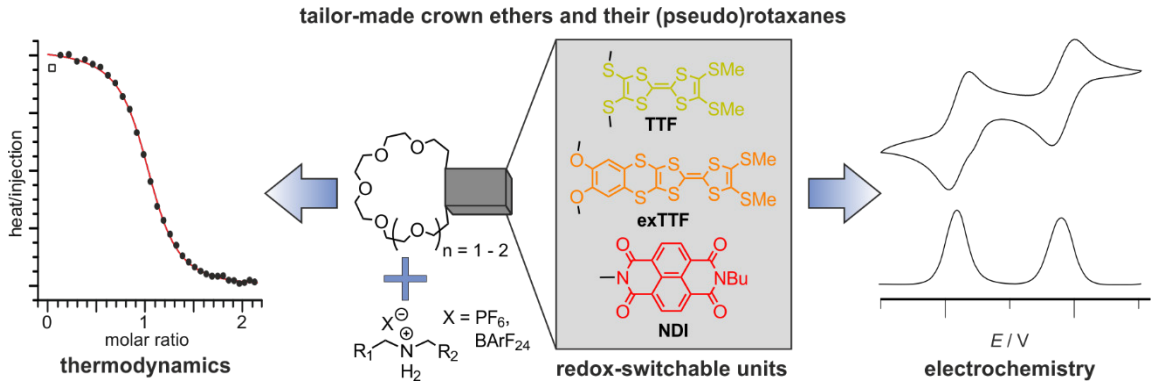

Figure 6.6. Graphical abstract. Reprinted with permission from Hupatz *et al.*[246] (published by the Beilstein-Institut, under the CC BY-NC 4.0 licence).

Authors' contributions

The project was conceived by me with ideas coming from Marius Gaedke and Hendrik V. Schröder. Marius Gaedke, Hendrik V. Schröder, Christoph A. Schalley and me wrote the manuscript with main contributions from my side. The synthetic work was carried out by Marius Gaedke, Felix Witte, Sebastian Müller, Hendrik V. Schröder, and me including NMR, UV/Vis, CV and MS measurements. Marius Gaedke prepared the single crystals. Fabian Klautzsch and I measured ITC data and I analysed the data. Julia Beerhues, Arto Valkonen, Biprajit Sarkar and Kari Rissanen measured and solved the SCXRD data. All Authors contributed to the final version of the manuscript.

BEILSTEIN JOURNAL OF ORGANIC CHEMISTRY

Thermodynamic and electrochemical study of tailor-made crown ethers for redox-switchable (pseudo)rotaxanes

Henrik Hupatz[1], Marius Gaedke[1], Hendrik V. Schröder[1,2], Julia Beerhues[3,4], Arto Valkonen[5], Fabian Klautzsch[1], Sebastian Müller[1], Felix Witte[1], Kari Rissanen[5], Biprajit Sarkar[3,4] and Christoph A. Schalley[*1]

Full Research Paper

Open Access

Address:
[1]Institut für Chemie und Biochemie, Freie Universität Berlin, Arnimallee 20, 14195 Berlin, Germany, [2]present address: Department of Chemical and Biological Engineering, Princeton University, Princeton, NJ08544, USA, [3]Institut für Chemie und Biochemie, Freie Universität Berlin, Fabeckstr. 34/36, 14195 Berlin, Germany, [4]present address: Lehrstuhl für Anorganische Koordinationschemie, Institut für Anorganische Chemie, Universität Stuttgart, Pfaffenwaldring 55, 70569 Stuttgart, Germany and [5]Department of Chemistry, University of Jyvaskyla P. O. Box 35, 40014 Jyväskylä, Finland

Email:
Christoph A. Schalley[*] - c.schalley@schalley-lab.de

* Corresponding author

Keywords:
crown ether; isothermal titration calorimetry; redox chemistry; rotaxanes; supramolecular chemistry

Beilstein J. Org. Chem. **2020,** *16,* 2576–2588.
https://doi.org/10.3762/bjoc.16.209

Received: 07 August 2020
Accepted: 02 October 2020
Published: 20 October 2020

This article is part of the thematic issue "Molecular recognition" and is dedicated to the memory of Carsten Schmuck.

Guest Editor: T. Schrader

Abstract

Crown ethers are common building blocks in supramolecular chemistry and are frequently applied as cation sensors or as subunits in synthetic molecular machines. Developing switchable and specifically designed crown ethers enables the implementation of function into molecular assemblies. Seven tailor-made redox-active crown ethers incorporating tetrathiafulvalene (TTF) or naphthalene diimide (NDI) as redox-switchable building blocks are described with regard to their potential to form redox-switchable rotaxanes. A combination of isothermal titration calorimetry and voltammetric techniques reveals correlations between the binding energies and redox-switching properties of the corresponding pseudorotaxanes with secondary ammonium ions. For two different weakly coordinating anions, a surprising relation between the enthalpic and entropic binding contributions of the pseudorotaxanes was discovered. These findings were applied to the synthesis of an NDI-[2]rotaxane, which retains similar spectroelectrochemical properties compared to the corresponding free macrocycle. The detailed understanding of the thermodynamic and electrochemical properties of the tailor-made crown ethers lays the foundation for the construction of new types of molecular redox switches with emergent properties.

Introduction

Pedersen discovered crown ethers in 1967 while searching for multidentate ligands for the vanadyl group [1-3]. He was later awarded the Nobel Prize in Chemistry for his studies on the crown ether selective binding properties towards alkali metal ions [2]. Crown ethers and their binding properties nowadays find frequent application, e.g., as cation sensors [4-7], as phase-transfer catalysts [8-10], or as drug delivery systems [11-13].

Already at the early stages of crown ether research, considerable effort has been made towards switchable macrocyclic receptors, in which crown ethers are functionalized with a stimuli-responsive unit [14,15]. These studies were mainly motivated by a biomimetic approach and included examples such as crown ethers incorporating photo-responsive azobenzene [15,16] or redox-active ferrocene [14,17]. Yet, switchable crown ethers are also widely applied as cation sensors, where the sensor activity can be controlled by external stimuli, e.g., light, the redox potential or chemical reagents [14,17]. Redox-switchable crown ethers have been shown to sense cations by the generation of an electrochemical output. For example, crown ethers containing tetrathiafulvalene (TTF) derivatives, which enable two reversible oxidation processes from the neutral to the dicationic state, were applied to sense various cations, e.g., alkali metal ions, Pb^{2+}, and Ba^{2+} [18-21].

Furthermore, with the first synthesis of crown ether-based rotaxanes in 1995, crown ethers played a crucial role in the development of mechanically interlocked molecules (MIMs) [22,23]. This rotaxane synthesis was facilitated by the formation of a threaded complex (pseudorotaxane) between a secondary ammonium ion and dibenzo-24-crown-8 (**DBC8**, Figure 1), which bind through noncovalent interactions. In detail, these interactions are strong hydrogen bonds between ether oxygen atoms and ammonium protons. In addition, weaker C–H···O hydrogen bonds with the CH_2 groups adjacent to the ammonium nitrogen as well as π–π-interactions between the catechol ring of the crown ether and aromatic moieties of the secondary ammonium ion contribute to the complex formation [22-25].

Over the last 25 years, a detailed understanding of the thermodynamic and kinetic properties of crown ether/ammonium complexes has developed enabling the construction of more complex molecular structures [24,26,27]. With the introduction of stimuli-responsive units, crown ether/ammonium-based MIMs have evolved into molecular switches and motors [24,28]. Intriguing examples among them are a light-powered molecular pump [29], a chemical-fuel-driven molecular rotary motor [30], and an acid/base-switchable asymmetric organocatalyst [31].

In addition to MIMs switchable by light or chemical reagents, redox-switchable molecular assemblies are of particular interest, since redox switching at electrodes is considered to operate without chemical waste and electrochemical analytical tools, e.g., cyclic voltammetry (CV), exhibit great potential to investigate the kinetic and thermodynamic parameters of the switching processes [32,33]. Although various redox-active crown ethers have been described [14,21,34], they are not commonly implemented into crown ether/ammonium (pseudo)rotaxanes. One reason is that functionalized crown ethers can cause major obstacles in the synthesis of (pseudo)rotaxanes, as their functionalization can strongly interfere with the binding properties of the crown ether [24,25]. Recently, we have investigated examples for redox-switchable MIMs based on two 24-crown-8 ethers functionalized with TTF **TTFC8** [35,36] and **exTTFC8** [37] (Figure 1). Several **TTFC8**-derived molecular assemblies have been studied and provided access to new switching modes [35,36,38] and emergent optoelectronic properties [35,36,39,40], demonstrating the great potential of tailor-made redox-active crown ethers for the development of new molecular switches.

Yet, a careful design of tailor-made redox-active crown ethers is of great importance for tuning the crown ether binding and redox properties to achieve the desired molecular structure and switching mode, which motivated us to conduct the present study on the thermodynamic and electrochemical properties of seven redox-active crown ethers of different ring sizes in comparison to the unfunctionalized analogs **DBC8** and **BC7** (Figure 1). Crown ethers incorporating TTF, an extended TTF, and naphthalene diimide (NDI) as redox-active units were investigated with respect to the impact of the functionalization on the thermodynamic binding properties towards secondary ammonium axles using isothermal titration calorimetry (ITC). The electrochemical switching properties of the redox-active crown ethers were examined using differential pulse voltammetry (DPV) and compared to those of their corresponding pseudo[2]rotaxanes. Additionally, we report the synthesis of a novel NDI-[2]rotaxane and study the impact of the mechanical bond on the optoelectronic properties of the NDI unit by CV and spectroelectrochemical measurements.

Results and Discussion

Design considerations

The nine crown ether wheels and two ammonium axles used in this study are depicted in Figure 1. Previously, we investigated the thermodynamic and electrochemical properties of pseudorotaxanes made from **TTFC8** and **exTTFC8** in two separate studies [35,37]. Herein, we compare these two crown ethers, their smaller analogs and add a two TTF-units containing crown

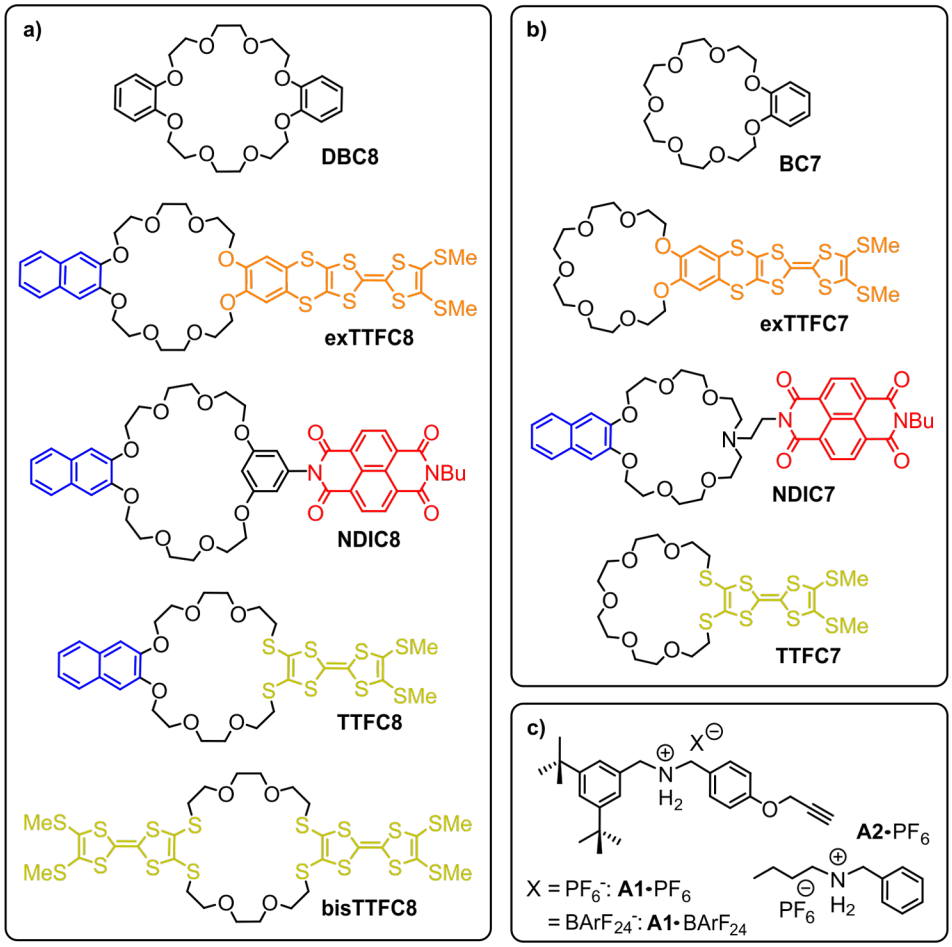

Figure 1: Structures of the compounds used in this study: a) crown-8 analogs; b) crown-7 analogs; c) secondary ammonium axles. $BArF_{24}^-$ represents tetrakis(3,5-bis(trifluoromethyl)phenyl)borate.

ether **bisTTFC8**, which was previously synthesized by Becher and co-workers [41]. These TTF-containing crown ethers become positively charged upon electrochemical oxidation, resulting in Coulomb repulsion with the ammonium axle [35,36,38].

A second goal was to add crown ethers, that can be reversibly reduced from the neutral to the dianionic state, as these crown ethers become negatively charged upon electrochemical switching and thus are expected to cause a Coulomb attraction between the ammonium axle and the crown ether. The NDI moiety, which is readily applied in various redox-active MIMs, was selected because of its high stability and synthetic accessibility [42].

An NDI-containing crown ether was reported by Sanders and co-workers, where the NDI unit is directly connected into the oligoglycol ring framework of the crown ether by the two nitrogen atoms [43]. However, the increased ring size and altered binding properties, which are dominated by the large π-systems of the NDI units, rendered this design unsuitable for our study. Therefore, we chose a similar design for the targeted NDI-functionalized crown ether as for the TTF crown ethers, where the NDI unit is in a position more remote from the crown ether binding site. Yet, keeping the formal C_2-symmetry of the macrocycle is important to avoid mixtures of isomers upon the threading of directional axles, such as **A1**·PF_6 (Figure 1c) [40]. Consequently, we chose to use a resorcinol-connected crown ether motif introduced by Stoddart and co-workers [44] for the NDI-crown-8 **NDIC8** (Figure 1).

To compare the larger crown ethers with smaller analogs, benzo-21-crown-7 (**BC7**) and the derivatives were also included, as at least the parent compound forms stronger complexes with secondary ammonium ions than the larger analog. But since phenyl groups already act as a stopper for **BC7**, one

side of the ammonium axle must be an alkyl chain, as in **A2**·PF_6 to enable pseudo[2]rotaxane formation (Figure 1c) [45,46].

The smaller TTF-containing crown ethers **TTFC7** and **exTTFC7** were designed in analogy to their crown-8 analogs (Figure 1). To access the NDI-functionalized crown-7 analog **NDIC7**, we chose an aza-crown-7 core, similar to the divalent crown ether described by Das and co-workers [47]. Comparing both NDI-containing crown ethers, **NDIC8** exhibits a rather rigid connection to the crown ether core, and in **NDIC7**, a more flexible ethylenediamine linker is used.

Crown ether synthesis and crystal structures

With respect to the synthesis of previously reported **TTFC8** and **exTTFC8** [35,37], we synthesized the novel 21-crown-7 analogs following a similar synthetic route, yielding **TTFC7** in one step and with good yield of 69% from the diiodide **1**, and **exTTFC7** with a good yield (31% over 4 steps) from **BC7** (Scheme 1, for the detailed synthetic procedure and characterization data, see Supporting Information File 1, section 1). Both NDI macrocycles **NDIC8** and **NDIC7** were synthesized in moderate yields of 24% and 26%, respectively, over three steps from the same two building blocks, the ditosylate **5** and the monobutyl-protected NDI precursor **7** (Scheme 1).

The connectivity and conformation of **exTTFC7** was observed in the crystal structure obtained from crystals generated through slow evaporation of a CH_2Cl_2/CH_3CN solution. The structure of the exTTF unit does not exhibit any significant changes upon incorporation into the crown ether [48]. No intermolecular stacking between the exTTF units was observed in the crystal structure of **exTTFC7** (Figure 2a and section 2 in Supporting Information File 1). Slow diffusion of CH_3CN into a concentrated solution of **NDIC7** in CH_2Cl_2 yielded single crystals suitable for X-ray diffraction (Figure 2b). The macrocycle displays a folded conformation in the solid state due to the flexible linker, featuring an intramolecular NDI/naphthalene stacking with a typical π-stacking distance of 3.58 Å and a tilt angle of 5.8°. The free electron pair of the tertiary amine points towards the inside of the crown ether. In contrast, single crystals of **NDIC8** (Figure 2c), obtained by slow evaporation of a concentrated dimethylformamide (DMF) solution, exhibit a non-folded conformation. The torsional angle between the central phenyl ring and the NDI is 84.2° in order to avoid strain between the protons of the resorcinol and the carbonyl groups of the NDI. Consequently, an intramolecular π–π-interaction with the naphthalene on the other side of the macrocycle is impeded. **NDIC8** therefore does not fold but stacks with the naphthalene and NDI moieties of the neighbors alternatingly in the solid state and with a typical plane/plane distance of 3.57 Å [49].

Thermodynamic analysis of crown ether/ammonium complexes

For the investigation of the thermodynamic binding properties, isothermal titration calorimetry is an advantageous method as it yields the binding stoichiometry, the binding constant K_a and the binding enthalpy ΔH^0 in one measurement. From these data, the Gibbs free binding energy ΔG^0 and the binding entropy ΔS^0 can be calculated. Pseudo[2]rotaxanes formed from crown ethers and ammonium axles are generally more strongly bound in solvents with low dielectric constants and in combination with weakly coordinating anions (WCAs) [24,50,51]. Therefore, we chose 1,2-dichloroethane (DCE) as the solvent and hexafluorophosphate (PF_6^-) as the counter ion, which resulted in binding constants in the optimal range for ITC titrations [52,53]. The even more weakly coordinating tetrakis(3,5-bis(trifluoromethyl)phenyl)borate ($BArF_{24}^-$) anion exemplarily served for comparison to study the influence of the anion on the binding constant.

Two different ammonium axles were employed: On the one hand, **A1**·PF_6 can only form a threaded complex with crown-8 ether derivatives due to the two bulky benzyl substituents on the ammonium ion. On the other hand, **A2**·PF_6 possesses one narrow alkyl substituent allowing both crown-8 and crown-7 ethers to form threaded complexes.

All possible pseudo[2]rotaxanes show strongly enthalpy-driven binding – with the notable exception of **NDIC7** (Table 1). The unfunctionalized crown ethers **BC7** and **DBC8** are the strongest binders among the corresponding derivatives with ΔG^0 of −34.6 kJ/mol and −34.8 kJ/mol, respectively (Table 1, entries 1 and 9).

Focusing on the combinations of crown-8 ethers and **A1**·PF_6, **exTTFC8** also forms a strong complex, with ΔG^0 being only ≈1 kJ/mol (Table 1, entry 10) lower than that of the **A1**·PF_6@**DBC8** complex. In contrast, the binding of **TTFC8** is more than 9 kJ/mol weaker (Table 1, entry 12), caused by the weaker hydrogen-bond-acceptor ability of the sulfur atoms incorporated in the **TTFC8** crown ether ring [34,54]. **NDIC8** also exhibits a comparably low binding energy, likely due to the increased ring size and the consequently weakened hydrogen-bonding pattern (Table 1, entry 11) [44].

However, **NDIC8** and **TTFC8** differ significantly in the entropic and enthalpic contributions to the binding energy (Table 1, entries 11 and 12). The comparably rigid structure of **NDIC8** is unable to adjust the conformation in the complex to achieve an optimal hydrogen-bonding pattern with the ammonium axle, and simultaneously, maximized π–π-interactions with the axle because of the 84° torsional angle between the resorcinol and

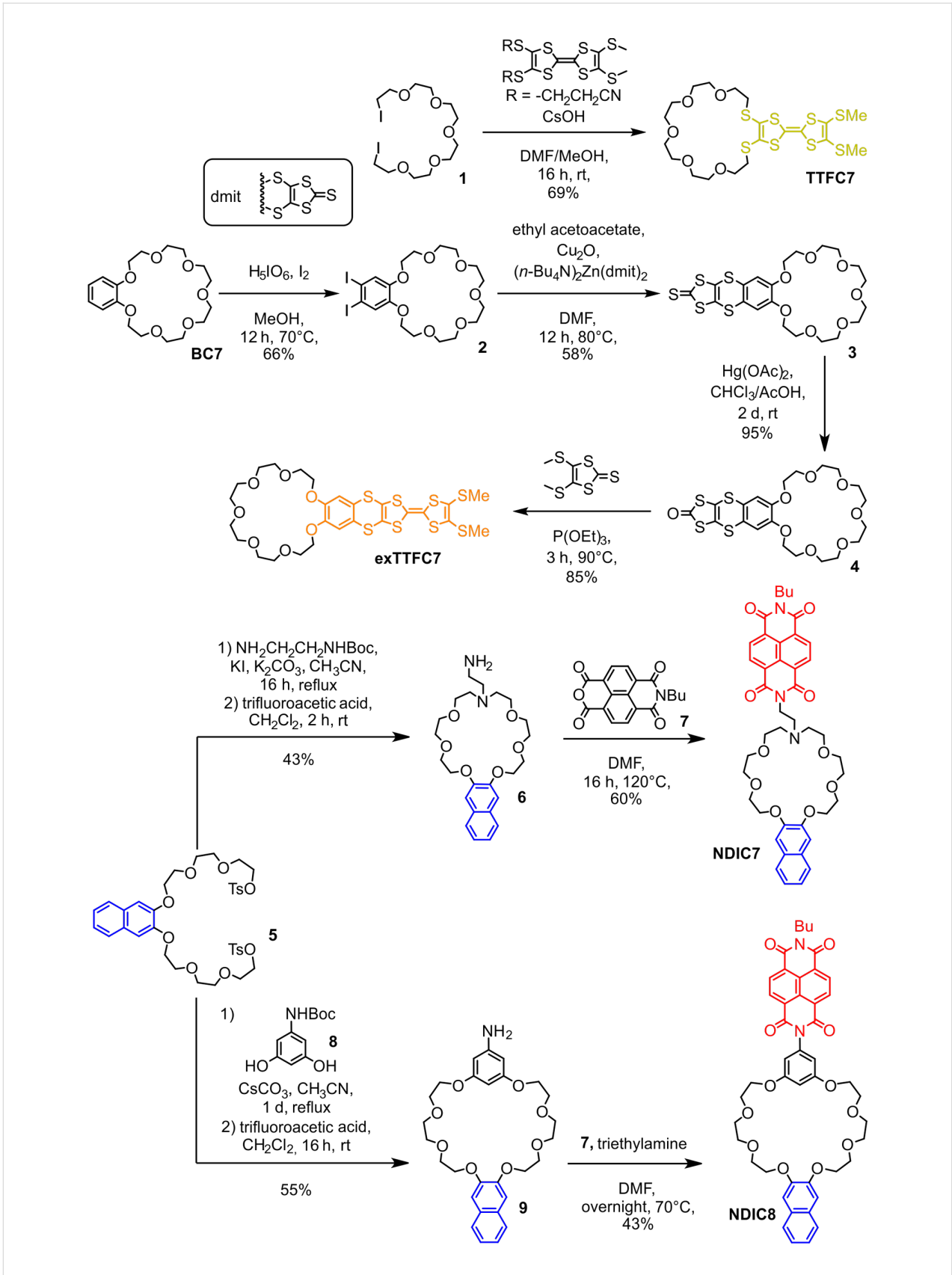

Scheme 1: Schematic representation of synthetic routes towards **TTFC7**, **exTTFC7**, **NDIC7**, and **NDIC8**.

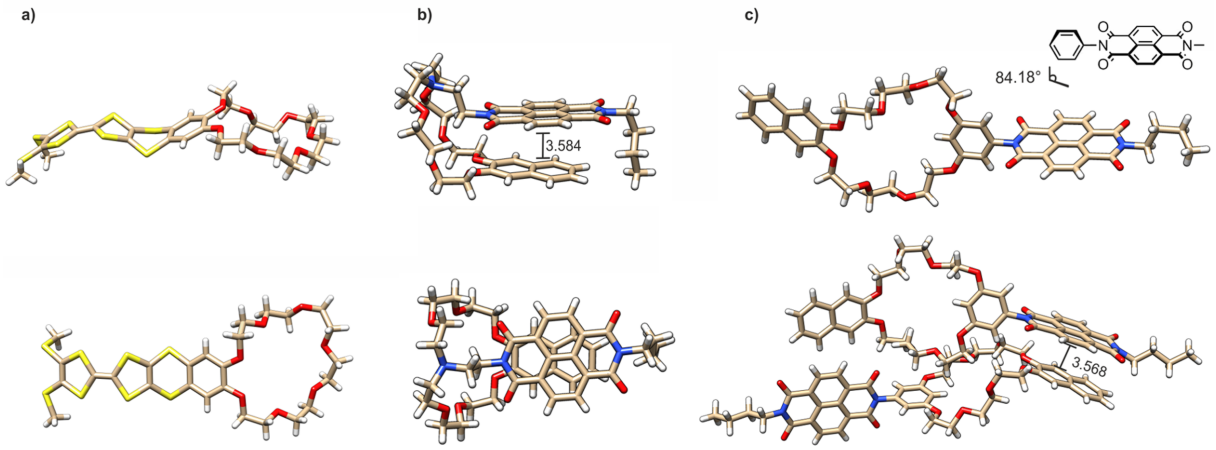

Figure 2: Solid-state structures of a) **exTTFC7** (CH_3CN molecule omitted for clarity), b) **NDIC7** (CH_3CN molecule omitted for clarity) and c) **NDIC8**.

Table 1: Thermodynamic binding data of different crown ether/secondary ammonium axle complexes obtained by ITC titrations in DCE at 298 K (for full data set and titration curves, see Supporting Information File 1, section 3).

entry	macrocycle	axle	K_a [10^3 M^{-1}]	ΔG^0 [kJ/mol]	ΔH^0 [kJ/mol]	$T\Delta S^0$ [kJ/mol]
1	**BC7**	**A2**·PF_6	1200 ± 100	−34.6 ± 0.2	−63.0 ± 0.5	−28.3 ± 0.7
2	**exTTFC7**		260 ± 30	−30.9 ± 0.3	−63.6 ± 1.0	−32.7 ± 1.3
3	**NDIC7**[a]		n. d.	n. d.	n. d.	n. d.
4	**TTFC7**		8.0 ± 1.0	−22.3 ± 0.2	−55.8 ± 1.5	−33.4 ± 1.7
5	**DBC8**	**A2**·PF_6	480 ± 70	−32.4 ± 0.3	−60.4 ± 1.5	−28.0 ± 1.8
6	**exTTFC8**		160 ± 20	−29.7 ± 0.3	−57.2 ± 2.0	−27.5 ± 2.3
7	**NDIC8**		13 ± 1	−23.4 ± 0.2	−48.1 ± 1.0	−24.7 ± 1.2
8	**TTFC8**		7.0 ± 1.0	−22.1 ± 0.2	−50.3 ± 1.0	−28.3 ± 1.2
9	**DBC8**	**A1**·PF_6	1300 ± 100	−34.8 ± 0.3	−60.9 ± 2.0	−26.1 ± 2.3
10	**exTTFC8**		780 ± 70	−33.6 ± 0.2	−58.6 ± 0.9	−25.0 ± 1.1
11	**NDIC8**		49 ± 6	−26.7 ± 0.3	−46.6 ± 2.0	−19.9 ± 2.3
12	**TTFC8**		33 ± 3	−25.7 ± 0.2	−51.5 ± 0.9	−25.9 ± 1.1
13	**NDIC8**	**A1**·$BArF_{24}$	1000 ± 100	−34.2 ± 0.2	−42.9 ± 1.2	−8.7 ± 1.4
14	**TTFC8**[b]		440 ± 100	−32.2 ± 0.3	−46.2 ± 0.7	−14.0 ± 1.0
15	**bisTTFC8**		2.0 ± 0.5	−18.7 ± 0.6	−21.0 ± 2.0	−2.2 ± 2.6

[a]ITC titrations cannot be fitted to a 1:1 pseudo[2]rotaxane binding model (for details, see text below and Supporting Information File 1, Figure S5).
[b]Taken from a previous report [40].

the NDI unit. Consequently, the complexation of **NDIC8** is less enthalpically favored than that of **TTFC8**. However, the more rigid structure of **NDIC8** also leads to a lower degree of conformational fixation in the pseudorotaxane of **NDIC8**, and thus to a more favorable binding entropy compared to the pseudorotaxane of **TTFC8**. For **TTFC8**, the increased binding enthalpy can be explained by additional π–π-interactions between the naphthalene and TTF unit of the crown ether and the ammonium axle, resulting in a rather rigid crown ether conformation in the complex as compared to the free macrocycle. This loss of conformational flexibility rationalizes the increased entropic penalty. A similar trend is observed for the binding enthalpy and entropy of **NDIC8** and **TTFC8** with the axles **A2**·PF_6 (Table 1, entries 7 and 8) and **A1**·$BArF_{24}$ (Table 1, entries 13 and 14), showing that this effect is caused by the macrocycle and not the ammonium axle.

The Gibbs free binding energy ΔG^0 of all four crown-8 ethers to axle **A2**·PF_6 is collectively 2–4 kJ/mol lower (Table 1, entries 5–8) in comparison to that of **A1**·PF_6. On the one hand, additional π–π-interactions of the phenyl ring in **A1**·PF_6 to the crown ether aromatic rings favor the complex formation. On the other hand, the flexibility of the alkyl substituent in **A2**·PF_6 is diminished upon complexation, inducing a larger entropic penalty visible in the overall more negative binding entropies in pseudo[2]rotaxanes of **A2**·PF_6 as compared to those formed from **A1**·PF_6.

Furthermore, the three crown-7 macrocycles **BC7**, **exTTFC7**, and **TTFC7** bind **A2**·PF_6 with a binding energy (entries 1, 2, and 4 in Table 1) slightly higher than the crown-8 analogs (entries 5, 6, and 8 in Table 1). Moreover, ΔG^0 follows the same trend as observed for crown-8 analogs with **A1**·PF_6 (entries 9, 10, and 12 in Table 1) and discussed above: the binding energy decreases from **BC7** over **exTTFC7** to **TTFC7**.

The azacrown-7 **NDIC7** is an exception: The ITC titration with the ammonium axle **A2**·PF_6 does not exhibit the anticipated sigmoidal shape of a 1:1 bonded complex (see Figure S5a in Supporting Information File 1). The curve shape suggests a more complex chemical equilibrium that involves more than one chemical process generating heat, taking place in the titration experiment. One process is likely a proton transfer from the secondary ammonium group of the axle to the tertiary amine in the crown ether wheel. An ITC titration with **A1**·PF_6 gave a similar curve shape (see Figure S5b in Supporting Information File 1), though crown-7 ethers are too small to thread over the phenyl ring of **A1**·PF_6 under the conditions of the experiment. The folded structure observed in the crystal structure hints towards a possible "side-on" complex, where the ammonium axle is not threading through the ring of the macrocycle, yet still forms hydrogen bonds to the crown ether [24,25] (see spectroelectrochemical measurements below). These results suggest that both ammonium axles form a similar type of equilibrium with **NDIC7**, where the protonation of the tertiary amine and the complexation in a nonthreaded complex might contribute.

When using $BArF_{24}^-$ as the counterion for **A1**, the binding energies increase by 6–8 kJ/mol, which results in a 10–20-fold increase of the binding constants as observed for the weaker binding macrocycles **TTFC8** and **NDIC8** (Table 1, entries 13 and 14). **A1**·$BArF_{24}$ even allows the formation of a pseudo[2]rotaxane with the **bisTTFC8** macrocycle (Table 1, entry 15), to which **A1**·PF_6 binds too weakly to determine the binding data by ITC. The observed decrease of the binding energy with more sulfur atoms in the crown ether ring from **DBC8** over **TTFC8** to **bisTTFC8** is consistent with a systematic study on thiacrown ethers [54].

Surprisingly, the increased Gibbs free binding energy ΔG^0 for **A1**·$BArF_{24}$ compared to **A1**·PF_6, is not caused by the binding enthalpy ΔH^0 (entries 11–14 in Table 1), as one might have expected, assuming the ion pairing to compete with the pseudorotaxane formation. In contrast, the enthalpic contribution is 4–6 kJ/mol less negative with **A1**·PF_6 than in **A1**·$BArF_{24}$ complexes, but the formation of the **A1**·$BArF_{24}$ pseudo[2]rotaxanes is less entropically disfavored, reflected by 11–12 kJ/mol less negative $T\Delta S^0$ (Table 1, entries 13 and 14). To the best of our knowledge, the study of weakly coordinating anions in the formation of pseudorotaxane complexes has been limited to their impact on the binding constant, but enthalpic and entropic contributions have not yet been studied [50,51,55]. As PF_6^- is more strongly coordinating than $BArF_{24}^-$, a larger fraction of **A1**·PF_6 ion pairs is present in nonpolar solvents such as DCE. Upon complexation, the ion pair of **A1**·PF_6 must dissociate, releasing PF_6^- anions into the bulk solution where they are solvated by a number of solvent molecules. The charge-induced order of the solvent dipoles in the solvent shell is entropically unfavorable and more pronounced for PF_6^-. Consequently, the main reason for the observed effects is likely a change in the solvation entropy. However, to further elucidate the role of WCAs in crown/ammonium complexes, more detailed studies are certainly indicated.

Electrochemistry

The electrochemical properties of the TTF and NDI-bearing macrocycles and pseudorotaxanes are summarized in Table 2. To get some insight into the solvent dependence of the electrochemical data, the measurements were performed in 1:1 DCE/CH_3CN (increased solubility of the axle salts, weaker pseudo[2]rotaxane binding) and in pure DCE (stronger pseudo[2]rotaxane binding). Generally, the oxidation potentials are shifted to higher values, and the reduction potentials are shifted to lower values in pure DCE due to decreased charge stabilization.

As expected, all TTF macrocycles display two reversible oxidation processes ($E_{1/2}^{ox1}$, $TTF \rightarrow TTF^{\bullet+}$ and $E_{1/2}^{ox2}$, $TTF^{\bullet+} \rightarrow TTF^{2+}$). $E_{1/2}^{ox1}$ and $E_{1/2}^{ox2}$ of the free **exTTFC8** and **exTTFC7** crown ethers are anodically shifted compared to those of **TTFC8** and **TTFC7**, in which the TTF units are directly incorporated into the crown ethers. This behavior is known also for the two redox-active TTF building blocks **exTTF** and tetramethylene-TTF, which are not part of a macrocycle [48].

The addition of the axles **A1**·PF_6 or **A2**·PF_6 to **TTFC8** and **TTFC7**, respectively, in a DCE/CH_3CN 1:1 solution has no significant effect on $E_{1/2}^{ox1}$ and $E_{1/2}^{ox2}$ (see Supporting Information File 1). However, an increase in the oxidation potential

Table 2: Electrochemical data obtained by differential pulse voltammetry (for voltammograms and experimental details see Supporting Information File 1, section 4).

entry	compound	solvent[a]	$E_{1/2}^{red2}$ [V][b]	$E_{1/2}^{red1}$ [V][b]	$E_{1/2}^{ox1}$ [V][b]	$E_{1/2}^{ox2}$ [V][b]
			reversible reductions		reversible oxidations	
1	**exTTFC7**	DCE/CH_3CN 1:1	/	/	0.66	0.95
2	**exTTFC8**[c]		/	/	0.66	0.93
3	**TTFC7**		/	/	0.59	0.83
4	**TTFC8**		/	/	0.59	0.83
5	**bisTTFC8**[c]		/	/	0.57	0.93
6	**NDIC7**		–0.96	–0.54	/	/
7	**NDIC7** + **A2**·PF_6[d]		–0.70	–0.46	/	/
8	**NDIC8**[c]		–0.95	–0.49	/	/
9	**NDIC8**[c] + **A1**·PF_6[d]		–0.72	–0.49	/	/
10	**NDIC8**[c] + $(CH_3)_2NH_2PF_6$[d]		–0.78	–0.45		
11	**NDIC8Rot**		–0.95	–0.50		
12	**exTTFC7**	DCE	/	/	0.65	1.01
13	**exTTFC7** + **A2**·PF_6[d]		/	/	0.67	1.01
14	**TTFC7**		/	/	0.59	0.87
15	**TTFC7** + **A2**·PF_6[d]		/	/	0.63	0.87
16	**bisTTFC8**		/	/	0.56	0.95
17	**NDIC8**[c]		–0.97	–0.53	/	/
18	**NDIC8Rot**		–0.96	–0.51	/	/

[a]With *n*-Bu_4NPF_6 (0.1 M) as the electrolyte. [b]Half-wave potentials are given against the decamethylferrocene/decamethylferrocenium couple as the reference; error = ±0.01 V. [c]The compound showed only moderate solubility in the corresponding solvent. [d]Five equivalents of the ammonium guest were added.

($\Delta E_{1/2}^{ox1}$ = +0.04 V) was observed for the **A2**·PF_6@**TTFC7** complex in pure DCE, which can be attributed to the increased strength of the hydrogen bonds in the neutral complex and Coulomb repulsion in the oxidized complex [35]. This effect is less pronounced for the complex **A2**·PF_6@**exTTFC7** because the TTF unit is more distant to the ammonium unit [37].

The macrocycle **bisTTFC8**, bearing two TTF units, shows a broadening of the signal for the first oxidation (Figure S9 in Supporting Information File 1), presumably due to intramolecular TTF–TTF interactions [35,36,56]. In comparison to the wheel **TTFC8**, the second oxidation of **bisTTFC8** is anodically shifted by $\Delta E_{1/2}^{ox2}$ = +0.10 V, indicating intramolecular Coulomb repulsion between the two TTF^{2+} units. The addition of **A1**·PF_6 does not have any impact on the redox properties of **bisTTFC8**, as hardly any pseudo[2]rotaxane forms with this axle.

The NDI-decorated wheels **NDIC8** and **NDIC7** undergo two reversible reduction processes ($E_{1/2}^{red1}$, $NDI \rightarrow NDI^{\bullet -}$ and $E_{1/2}^{red2}$, $NDI^{\bullet -} \rightarrow NDI^{2-}$). Here, the addition of the corresponding ammonium axles **A1**·PF_6 and **A2**–PF_6 drastically shifts the reduction potentials in DCE/CH_3CN 1:1 (**NDIC7**: +0.08 V and +0.26 V; **NDIC8**: 0 V and +0.23 V, for $\Delta E_{1/2}^{red1}$ and $\Delta E_{1/2}^{red2}$, respectively). We assume that the negatively charged reduced forms $NDI^{\bullet -}$ and NDI^{2-} form strong electrostatic interactions to ammonium ions and act as strong, competitive hydrogen-bond acceptors [57]. The high anodic shifts indicate strong attractive interactions between the wheels and axles, which compete with the coordination of the crown ether moiety. Thus, the secondary ammonium axles form presumably a non-threaded complex with the reduced NDI crown ethers, where the charged ions are in closer proximity than in the pseudo[2]rotaxane. This assumption was further confirmed by the addition of the hydrogen bond donor $(CH_3)_2NH_2PF_6$ to a solution of the wheel **NDIC8**, which again leads to strong anodic shifts in the voltammogram ($\Delta E_{1/2}^{red1}$ = +0.04 V, $\Delta E_{1/2}^{red2}$ = +0.17 V, Table 2, entry 10) and will be further elucidated below.

Synthesis and spectroelectrochemical characterization of [2]rotaxane with NDI crown ether

For **TTFC8**, we have recently shown, that rotaxane formation influences the optoelectronic properties of the TTF unit [35],

yet for **exTTFC8** the [2]rotaxane shows very similar properties as compared to the free macrocycle [37]. As **NDIC8** and the **A1**·PF_6@**NDIC8** pseudo[2]rotaxane also reveal distinctly different electrochemical potentials, we investigated the impact of mechanical bonding on the optoelectronic properties of the NDI unit. The binding properties suggest that the combination of the **A1**·$BArF_{24}$ axle and **NDIC8** is optimal for the synthesis of an NDI-containing [2]rotaxane. We applied Takata's catalyst-free stoppering approach [58] using the nitrile oxide **St** for the preparation of the [2]rotaxane **NDIRot**, which was obtained in 43% yield (Figure 3a).

The formation of the isoxazole can be recognized by the strong downfield shift of the proton H^j in the ^{1}H NMR spectrum (Figure 3b, for 2D spectra and signal assignment, see Supporting Information File 1, section 5.1). Furthermore, a diastereotopic splitting of the crown ether methylene protons and downfield shifts of the axle methylene protons H^d and H^f clearly point at the rotaxane formation. Additionally, a strong upfield shift observed for the resonance of the phenylic proton H^h ($\Delta\delta$ = 0.5 ppm) is in line with rotaxane formation, even though it has not previously been observed for similar TTF-containing rotaxanes [35,40]. This finding indicates a different conformation of the macrocycles in the NDI and TTF [2]rotaxanes.

Even though the signals of the NDI protons H^6 and $H^{6'}$ do not shift significantly which would be expected for strong π–π-interactions, they split from one pseudo singlet into two doublets upon rotaxane formation, indicating a lower symmetry of the NDI unit. The resorcinol proton H^4 exhibits a significant upfield shift ($\Delta\delta$ = −0.2 ppm), which can be rationalized by the position in the crown ether cavity close to the positively charged ammonium ion.

The collision-induced dissociation of mass-selected rotaxane ions occurs only at comparably high collision energy. Only axle fragments are observed while the intact axle is not seen among

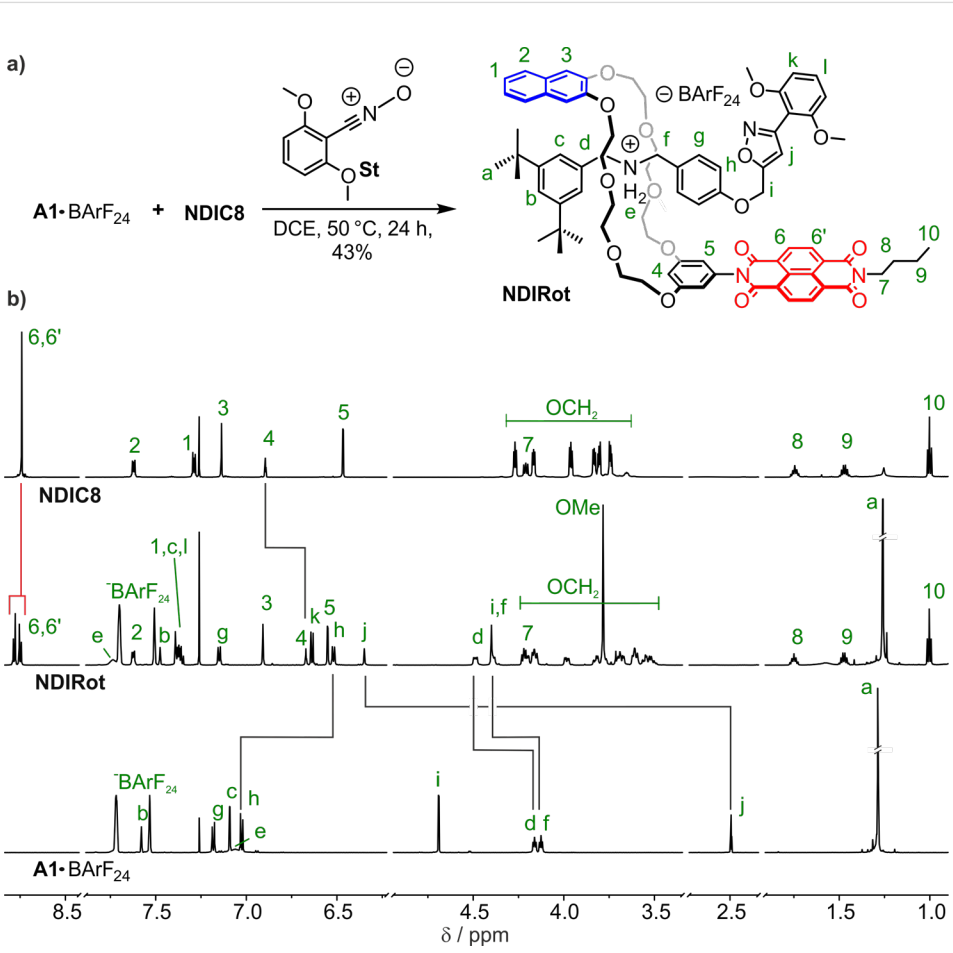

Figure 3: a) Synthesis of the [2]rotaxane **NDIRot**. b) Stacked ^{1}H NMR spectra (700 MHz, $CDCl_3$, 298 K) of **NDIC8** (top), **NDIRot** (middle), and **A1**·$BArF_{24}$ (bottom). The signal assignment was done by 2D NMR spectroscopy.

the fragments (Figures S15 and S16 in Supporting Information File 1). This clearly supports the mechanically interlocked structure for **NDIRot** in analogy to similar structures investigated by tandem mass spectrometry earlier [35,40].

Cyclic voltammograms of **NDIRot** show two reversible reductions $E_{1/2}^{red1}$ and $E_{1/2}^{red2}$ independent of the used solvent (pure DCE or DCE/CH_3CN 1:1, Figure S11 and Table S2 in Supporting Information File 1). Additionally, the two reduction potentials are very similar to those of free **NDIC8** and not the pseudo[2]rotaxane **A1**·PF_6@**NDIC8** (see Table 2, entries 8–11). This agrees well with the assumption that the reduction of the NDI leads to a complete rearrangement of the pseudo[2]rotaxane into a non-threaded complex as discussed above. As dethreading is impossible in **NDIRot**, the electrochemical data are significantly different from those of the non-threaded complexes formed from the pseudorotaxane and the $(CH_3)_2NH_2PF_6$ complex of **NDIC8**.

The optoelectronic properties of the rotaxane **NDIRot** were investigated by UV–vis–NIR spectroelectrochemistry in a CH_2Cl_2/CH_3CN 1:1 mixture and compared to **NDIC8** and **NDIC7** (Figure 4 and Table S3 in Supporting Information File 1). In the neutral state, the rotaxane displays the typical absorption pattern of an *N*,*N'*-disubstituted NDI monomer between 300 and 380 nm (Figure 4a–c, black) [59]. A weak charge-transfer band at ≈450 nm is observed for the free macrocycle **NDIC7** (Figure 4a, black), which is most likely caused by an intramolecularly folded naphthalene–NDI complex in solution, similar to the crystal structure. In contrast, no charge-transfer band is present, neither for **NDIRot** nor for **NDIC8**, ruling out the formation of similar charge-transfer complexes in **NDIC8** or in the corresponding rotaxane.

After one-electron reduction (NDI → $NDI^{\bullet-}$), a complex absorption band pattern emerges in the visible region of all three spectra. These bands are indicative of the radical anion $NDI^{\bullet-}$ (Figure 4a–c, red curves) [59]. The radical character of **NDIC8** was additionally confirmed by spectroelectrochemical EPR measurements, which showed an isotropic signal with a g-value of 2.004 (Figure S17 in Supporting Information File 1).

Upon further reduction, a new absorption pattern emerges for **NDIC7**, in accordance to a second electrochemical reduction ($NDI^{\bullet-}$ → NDI^{2-}) (Figure 4a, blue curve). However, only small shifts and intensity changes are observed for **NDIC8** and the rotaxane **NDIRot** when going to a more negative potential (−1.2 V), which can be explained by diffusion and comproportionation of the dianion, as it was observed earlier for other NDI^{2-} species [59]. Applying more positive potentials gradually converts the spectra back to the initial forms, which confirms the reversibility of the reduction processes. Overall, the comparison of all absorption spectra clearly demonstrates that the rotaxane formation does not significantly influence the optoelectronic properties of the NDI unit. This can be explained by the position of the NDI moiety being rather remote from the binding site of the crown ether.

Conclusion

In conclusion, the comparison of the thermodynamic properties of a series of functionalized crown ethers showed a small effect of redox-active units remotely attached to the crown ether on the binding of secondary ammonium ions. However, if the redox-active unit is incorporated directly into the crown ether core, as in **TTFC8** and **TTFC7**, the binding properties are altered significantly. The redox properties do not depend much on the crown ether core, irrespective of whether the redox-

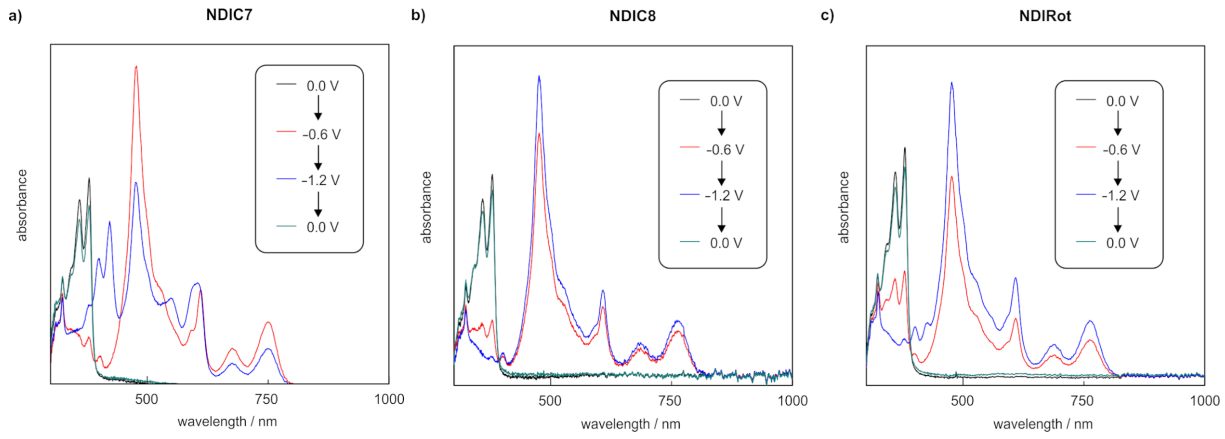

Figure 4: UV–vis–NIR spectra obtained by spectroelectrochemical measurements (0.1 M *n*-Bu_4PF_6, CH_2Cl_2/CH_3CN 1:1, 298 K) of a) **NDIC7** (0.5 mM), b) **NDIC8** (0.5 mM), and c) **NDIRot** (1 mM). Potentials are referenced against a silver wire pseudo-reference electrode.

active unit is attached in a remote position or incorporated in the crown ether.

Our findings provide some guidelines for how the binding and redox-switching properties can be fine-tuned for the construction of a desired crown ether-based switchable MIM: while **bisTTFC8** shows interesting redox properties but very low binding constants and **exTTFC8** displays a high binding constant, yet no strong interaction of the ammonium-binding site and the redox unit, **TTFC8** offers the best compromise of sufficiently high binding constants combined with sufficient Coulomb repulsion between the oxidized TTF and the ammonium ion to construct a molecular switch [35]. This trend can directly be translated to the smaller **exTTFC7** and **TTFC7**, which exhibit very similar thermodynamic and redox properties as compared to the corresponding crown-8 derivatives.

The important role that weakly coordinating counterions play in the binding of crown ether/ammonium pseudorotaxanes needs to be emphasized: a significant binding enhancement is achieved when $BArF_{24}$ anions are used compared to hexafluorophosphate. Surprisingly, this increased binding energy is not caused by a higher binding enthalpy, but can be attributed to a favorable change in the solvation entropy.

Two novel NDI-containing crown ethers have been successfully synthesized and characterized. Both compounds exhibit two reversible reduction processes. The lariat ether **NDIC7** is not suitable for rotaxane synthesis as it forms a complex equilibrium involving the deprotonation of the secondary ammonium axle and does not form 1:1 pseudorotaxanes. Additionally, the pseudorotaxane is hampered by intramolecular folding which was observed in the solid-state structure and is likely also present in solution, as indicated by a charge-transfer band. Nevertheless, it might be applicable for redox-controlled metal-sensing [60-62].

On the contrary, **NDIC8** forms pseudo[2]rotaxanes and facilitates the synthesis of a [2]rotaxane. Due to the remote position of the NDI unit and the rigid linker, rotaxane formation does not have a significant impact on the optoelectronic properties of the NDI moiety. The electrostatic interaction observed for NDI^{2-} and ammonium ions observed in the pseudo[2]rotaxane **A1**·PF_6@**NDIC8**, which even results in dethreading of the pseudorotaxane, may give rise to new switching modes in more complex molecular structures.

Overall, these findings demonstrate the benefit of detailed and systematic studies on the noncovalent interactions cohering the components of switchable MIMs for the construction of new architectures with emergent properties.

Supporting Information

Supporting Information File 1

Experimental section, including synthetic procedures, copies of NMR spectra, ITC, electrochemical, mass spectrometric and spectroelectrochemical data.
[https://www.beilstein-journals.org/bjoc/content/supplementary/1860-5397-16-209-S1.pdf]

Supporting Information File 2

Crystallographic data (cif) for **exTTFC7**, **NDIC7**, and **NDIC8**.
[https://www.beilstein-journals.org/bjoc/content/supplementary/1860-5397-16-209-S2.zip]

Acknowledgements

We thank Sebastian Sobottka for help with spectroelectrochemical measurements and Maite Nößler for help with synthesis.

Funding

This research was funded by the Deutsche Forschungsgemeinschaft and the Academy of Finland (decision no. 314343).

ORCID® iDs

Henrik Hupatz - https://orcid.org/0000-0002-2789-6279
Hendrik V. Schröder - https://orcid.org/0000-0002-6126-0055
Arto Valkonen - https://orcid.org/0000-0003-2806-3807
Felix Witte - https://orcid.org/0000-0002-6396-0178
Christoph A. Schalley - https://orcid.org/0000-0002-8634-3578

References

1. Pedersen, C. J. *J. Am. Chem. Soc.* **1967,** *89,* 2495–2496. doi:10.1021/ja00986a052
2. Pedersen, C. J. *Angew. Chem., Int. Ed. Engl.* **1988,** *27,* 1021–1027. doi:10.1002/anie.198810211
3. Pedersen, C. J. *J. Am. Chem. Soc.* **1967,** *89,* 7017–7036. doi:10.1021/ja01002a035
4. Cox, R. P.; Sandanayake, S.; Scarborough, D. L. A.; Izgorodina, E. I.; Langford, S. J.; Bell, T. D. M. *New J. Chem.* **2019,** *43,* 2011–2018. doi:10.1039/c8nj05666h
5. Li, J.; Yim, D.; Jang, W.-D.; Yoon, J. *Chem. Soc. Rev.* **2017,** *46,* 2437–2458. doi:10.1039/c6cs00619a
6. Pedersen, C. J.; Frensdorff, H. K. *Angew. Chem., Int. Ed. Engl.* **1972,** *11,* 16–25. doi:10.1002/anie.197200161
7. Gokel, G. W.; Leevy, W. M.; Weber, M. E. *Chem. Rev.* **2004,** *104,* 2723–2750. doi:10.1021/cr020080k
8. Landini, D.; Montanari, F.; Pirisi, F. M. *J. Chem. Soc., Chem. Commun.* **1974,** 879–880. doi:10.1039/c39740000879
9. Gokel, G. W.; Durst, H. D. *Synthesis* **1976,** 168–184. doi:10.1055/s-1976-23980

10. Stuart, A. M.; Vidal, J. A. *J. Org. Chem.* **2007,** *72,* 3735–3740. doi:10.1021/jo062606x
11. Morrison, P. W. J.; Porfiryeva, N. N.; Chahal, S.; Salakhov, I. A.; Lacourt, C.; Semina, I. I.; Moustafine, R. I.; Khutoryanskiy, V. V. *Mol. Pharmaceutics* **2017,** *14,* 3528–3538. doi:10.1021/acs.molpharmaceut.7b00556
12. You, X.-R.; Ju, X.-J.; He, F.; Wang, Y.; Liu, Z.; Wang, W.; Xie, R.; Chu, L.-Y. *ACS Appl. Mater. Interfaces* **2017,** *9,* 19258–19268. doi:10.1021/acsami.7b05701
13. Chehardoli, G.; Bahmani, A. *Supramol. Chem.* **2019,** *31,* 221–238. doi:10.1080/10610278.2019.1568432
14. Beer, P. D. *Chem. Soc. Rev.* **1989,** *18,* 409–450. doi:10.1039/cs9891800409
15. Shinkai, S.; Nakaji, T.; Nishida, Y.; Ogawa, T.; Manabe, O. *J. Am. Chem. Soc.* **1980,** *102,* 5860–5865. doi:10.1021/ja00538a026
16. Shinkai, S.; Nakaji, T.; Ogawa, T.; Shigematsu, K.; Manabe, O. *J. Am. Chem. Soc.* **1981,** *103,* 111–115. doi:10.1021/ja00391a021
17. Saji, T. *Chem. Lett.* **1986,** *15,* 275–276. doi:10.1246/cl.1986.275
18. Hansen, T. K.; Joergensen, T.; Stein, P. C.; Becher, J. *J. Org. Chem.* **1992,** *57,* 6403–6409. doi:10.1021/jo00050a010
19. Le Derf, F.; Mazari, M.; Mercier, N.; Levillain, E.; Trippé, G.; Riou, A.; Richomme, P.; Becher, J.; Garín, J.; Orduna, J.; Gallego-Planas, N.; Gorgues, A.; Sallé, M. *Chem. – Eur. J.* **2001,** *7,* 447–455. doi:10.1002/1521-3765(20010119)7:2<447::aid-chem447>3.0.co;2-a
20. Trippé, G.; Levillain, E.; Le Derf, F.; Gorgues, A.; Sallé, M.; Jeppesen, J. O.; Nielsen, K.; Becher, J. *Org. Lett.* **2002,** *4,* 2461–2464. doi:10.1021/ol0260829
21. Jana, A.; Bähring, S.; Ishida, M.; Goeb, S.; Canevet, D.; Sallé, M.; Jeppesen, J. O.; Sessler, J. L. *Chem. Soc. Rev.* **2018,** *47,* 5614–5645. doi:10.1039/c8cs00035b
22. Ashton, P. R.; Campbell, P. J.; Glink, P. T.; Philp, D.; Spencer, N.; Stoddart, J. F.; Chrystal, E. J. T.; Menzer, S.; Williams, D. J.; Tasker, P. A. *Angew. Chem., Int. Ed. Engl.* **1995,** *34,* 1865–1869. doi:10.1002/anie.199518651
23. Kolchinski, A. G.; Busch, D. H.; Alcock, N. W. *J. Chem. Soc., Chem. Commun.* **1995,** 1289–1291. doi:10.1039/c39950001289
24. Bruns, C. J.; Stoddart, J. F. *The Nature of the Mechanical Bond: From Molecules to Machines;* John Wiley & Sons, Inc.: Hoboken, NJ, USA, 2017. doi:10.1002/9781119044123
25. Ashton, P. R.; Chrystal, E. J. T.; Glink, P. T.; Menzer, S.; Schiavo, C.; Spencer, N.; Stoddart, J. F.; Tasker, P. A.; White, A. J. P.; Williams, D. J. *Chem. – Eur. J.* **1996,** *2,* 709–728. doi:10.1002/chem.19960020616
26. Zhang, M.; Yan, X.; Huang, F.; Niu, Z.; Gibson, H. W. *Acc. Chem. Res.* **2014,** *47,* 1995–2005. doi:10.1021/ar500046r
27. Clifford, T.; Abushamleh, A.; Busch, D. H. *Proc. Natl. Acad. Sci. U. S. A.* **2002,** *99,* 4830–4836. doi:10.1073/pnas.062639799
28. Balzani, V.; Gómez-López, M.; Stoddart, J. F. *Acc. Chem. Res.* **1998,** *31,* 405–414. doi:10.1021/ar970340y
29. Ragazzon, G.; Baroncini, M.; Silvi, S.; Venturi, M.; Credi, A. *Nat. Nanotechnol.* **2015,** *10,* 70–75. doi:10.1038/nnano.2014.260
30. Erbas-Cakmak, S.; Fielden, S. D. P.; Karaca, U.; Leigh, D. A.; McTernan, C. T.; Tetlow, D. J.; Wilson, M. R. *Science* **2017,** *358,* 340–343. doi:10.1126/science.aao1377
31. Blanco, V.; Leigh, D. A.; Marcos, V.; Morales-Serna, J. A.; Nussbaumer, A. L. *J. Am. Chem. Soc.* **2014,** *136,* 4905–4908. doi:10.1021/ja501561c
32. Schröder, H. V.; Schalley, C. A. *Chem. Sci.* **2019,** *10,* 9626–9639. doi:10.1039/c9sc04118d
33. Baroncini, M.; Silvi, S.; Credi, A. *Chem. Rev.* **2020,** *120,* 200–268. doi:10.1021/acs.chemrev.9b00291
34. Ashton, P. R.; Becher, J.; Fyfe, M. C. T.; Nielsen, M. B.; Stoddart, J. F.; White, A. J. P.; Williams, D. J. *Tetrahedron* **2001,** *57,* 947–956. doi:10.1016/s0040-4020(00)01062-0
35. Schröder, H. V.; Sobottka, S.; Nößler, M.; Hupatz, H.; Gaedke, M.; Sarkar, B.; Schalley, C. A. *Chem. Sci.* **2017,** *8,* 6300–6306. doi:10.1039/c7sc02694c
36. Schröder, H. V.; Stein, F.; Wollschläger, J. M.; Sobottka, S.; Gaedke, M.; Sarkar, B.; Schalley, C. A. *Angew. Chem., Int. Ed.* **2019,** *58,* 3496–3500. doi:10.1002/anie.201813265
37. Schröder, H. V.; Mekic, A.; Hupatz, H.; Sobottka, S.; Witte, F.; Urner, L. H.; Gaedke, M.; Pagel, K.; Sarkar, B.; Paulus, B.; Schalley, C. A. *Nanoscale* **2018,** *10,* 21425–21433. doi:10.1039/c8nr05534c
38. Schröder, H. V.; Wollschläger, J. M.; Schalley, C. A. *Chem. Commun.* **2017,** *53,* 9218–9221. doi:10.1039/c7cc05259f
39. Schröder, H. V.; Hupatz, H.; Achazi, A. J.; Sobottka, S.; Sarkar, B.; Paulus, B.; Schalley, C. A. *Chem. – Eur. J.* **2017,** *23,* 2960–2967. doi:10.1002/chem.201605710
40. Gaedke, M.; Witte, F.; Anhäuser, J.; Hupatz, H.; Schröder, H. V.; Valkonen, A.; Rissanen, K.; Lützen, A.; Paulus, B.; Schalley, C. A. *Chem. Sci.* **2019,** *10,* 10003–10009. doi:10.1039/c9sc03694f
41. Akutagawa, T.; Abe, Y.; Nezu, Y.-i.; Nakamura, T.; Kataoka, M.; Yamanaka, A.; Inoue, K.; Inabe, T.; Christensen, C. A.; Becher, J. *Inorg. Chem.* **1998,** *37,* 2330–2331. doi:10.1021/ic971623p
42. Diac, A.; Matache, M.; Grosu, I.; Hădade, N. D. *Adv. Synth. Catal.* **2018,** *360,* 817–845. doi:10.1002/adsc.201701362
43. Hansen, J. G.; Feeder, N.; Hamilton, D. G.; Gunter, M. J.; Becher, J.; Sanders, J. K. M. *Org. Lett.* **2000,** *2,* 449–452. doi:10.1021/ol991289w
44. Cantrill, S. J.; Fulton, D. A.; Heiss, A. M.; Pease, A. R.; Stoddart, J. F.; White, A. J. P.; Williams, D. J. *Chem. – Eur. J.* **2000,** *6,* 2274–2287. doi:10.1002/1521-3765(20000616)6:12<2274::aid-chem2274>3.0.co;2-2
45. Zhang, C.; Li, S.; Zhang, J.; Zhu, K.; Li, N.; Huang, F. *Org. Lett.* **2007,** *9,* 5553–5556. doi:10.1021/ol702510c
46. Jiang, W.; Schalley, C. A. *Beilstein J. Org. Chem.* **2010,** *6,* No. 14. doi:10.3762/bjoc.6.14
47. Mandal, A. K.; Suresh, M.; Das, A. *Org. Biomol. Chem.* **2011,** *9,* 4811–4817. doi:10.1039/c0ob01106a
48. Schröder, H. V.; Witte, F.; Gaedke, M.; Sobottka, S.; Suntrup, L.; Hupatz, H.; Valkonen, A.; Paulus, B.; Rissanen, K.; Sarkar, B.; Schalley, C. A. *Org. Biomol. Chem.* **2018,** *16,* 2741–2747. doi:10.1039/c8ob00415c
49. Blackburn, A. K.; Sue, A. C.-H.; Shveyd, A. K.; Cao, D.; Tayi, A.; Narayanan, A.; Rolczynski, B. S.; Szarko, J. M.; Bozdemir, O. A.; Wakabayashi, R.; Lehrman, J. A.; Kahr, B.; Chen, L. X.; Nassar, M. S.; Stupp, S. I.; Stoddart, J. F. *J. Am. Chem. Soc.* **2014,** *136,* 17224–17235. doi:10.1021/ja509442t
50. Gibson, H. W.; Jones, J. W.; Zakharov, L. N.; Rheingold, A. L.; Slebodnick, C. *Chem. – Eur. J.* **2011,** *17,* 3192–3206. doi:10.1002/chem.201002522
51. Jones, J. W.; Gibson, H. W. *J. Am. Chem. Soc.* **2003,** *125,* 7001–7004. doi:10.1021/ja034442x
52. Wiseman, T.; Williston, S.; Brandts, J. F.; Lin, L.-N. *Anal. Biochem.* **1989,** *179,* 131–137. doi:10.1016/0003-2697(89)90213-3
53. Turnbull, W. B.; Daranas, A. H. *J. Am. Chem. Soc.* **2003,** *125,* 14859–14866. doi:10.1021/ja036166s

54. Nagai, H.; Suzaki, Y.; Osakada, K. *Eur. J. Inorg. Chem.* **2014,** 4376–4384. doi:10.1002/ejic.201402465
55. Suzaki, Y.; Nagai, H.; Osakada, K. *Chem. Lett.* **2014,** *43,* 714–716. doi:10.1246/cl.131213
56. Rosokha, S. V.; Kochi, J. K. *J. Am. Chem. Soc.* **2007,** *129,* 828–838. doi:10.1021/ja064166x
57. Altieri, A.; Gatti, F. G.; Kay, E. R.; Leigh, D. A.; Martel, D.; Paolucci, F.; Slawin, A. M. Z.; Wong, J. K. Y. *J. Am. Chem. Soc.* **2003,** *125,* 8644–8654. doi:10.1021/ja0352552
58. Matsumura, T.; Ishiwari, F.; Koyama, Y.; Takata, T. *Org. Lett.* **2010,** *12,* 3828–3831. doi:10.1021/ol101543x
59. Andric, G.; Boas, J. F.; Bond, A. M.; Fallon, G. D.; Ghiggino, K. P.; Hogan, C. F.; Hutchison, J. A.; Lee, M. A.-P.; Langford, S. J.; Pilbrow, J. R.; Troup, G. J.; Woodward, C. P. *Aust. J. Chem.* **2004,** *57,* 1011–1019. doi:10.1071/ch04130
60. Hangarge, R. V.; La, D. D.; Boguslavsky, M.; Jones, L. A.; Kim, Y. S.; Bhosale, S. V. *ChemistrySelect* **2017,** *2,* 11487–11491. doi:10.1002/slct.201702085
61. Lin, H.; Cinar, M. E.; Schmittel, M. *Dalton Trans.* **2010,** *39,* 5130–5138. doi:10.1039/c000449a
62. Pond, S. J. K.; Tsutsumi, O.; Rumi, M.; Kwon, O.; Zojer, E.; Brédas, J.-L.; Marder, S. R.; Perry, J. W. *J. Am. Chem. Soc.* **2004,** *126,* 9291–9306. doi:10.1021/ja049013t

License and Terms

BEILSTEIN JOURNAL OF ORGANIC CHEMISTRY

Supporting Information

for

Thermodynamic and electrochemical study of tailor-made crown ethers for redox-switchable (pseudo)rotaxanes

Henrik Hupatz, Marius Gaedke, Hendrik V. Schröder, Julia Beerhues, Arto Valkonen, Fabian Klautzsch, Sebastian Müller, Felix Witte, Kari Rissanen, Biprajit Sarkar and Christoph A. Schalley

Beilstein J. Org. Chem. **2020,** *16,* 2576–2588. doi:10.3762/bjoc.16.209

Experimental section, including synthetic procedures, copies of NMR spectra, ITC, electrochemical, mass spectrometric and spectroelectrochemical data

Table of contents

1. Experimental details

1.1. General Methods

All reagents and solvents were obtained from commercial sources and used without further purification. Dry solvents were purchased from Acros Organics or obtained from the M. BRAUN Solvent purification system SPS 800. 2,3-bis(2-cyanoethylthio)-6,7-bis(methylthio)tetrathiafulvalene [1], diiodide **1** [2], **BC7** [3], ditosylate **5** [4], monoanhydride **7** [5], (4-(prop-2-yn-1-yloxy)phenyl)methanaminium chloride [6], **A2**·PF_6 [7], **A1**·$BArF_{24}$ [8], and 2,6-dimethoxybenzonitrile oxide stopper **St1** [9], were synthesized according to literature procedures. Thin-layer chromatography was performed on silica gel-coated plates with fluorescent indicator F254 (Merck). For column chromatography, silica gel (0.04–0.063 mm, Merck) was used.

^{1}H and ^{13}C NMR experiments were performed on JEOL ECX 400, JEOL ECP 500, Bruker AVANCE 500 or Bruker AVANCE 700 instruments. Residual solvent signals were used as the internal standards. All shifts are reported in ppm and NMR multiplicities are abbreviated as s (singlet), d (doublet), t (triplet), m (multiplet), and br (broad). Coupling constants *J* are reported in hertz. Compounds containing the tetrakis[3,5-bis(trifluoromethyl)phenyl]borate ($BArF_{24}^{-}$) anion show ^{13}C NMR spectra with ^{19}F, ^{10}B, and ^{11}B couplings. These signals were denoted as one signal.

Electrospray ionization high-resolution mass spectra (HRMS) were measured on an Agilent 6210 ESI-TOF device.

1.2. Synthetic procedures

TTFC7

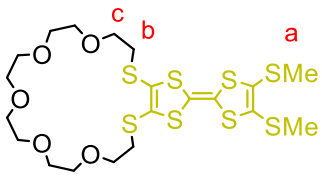

2,3-Bis(2-cyanoethylthio)-6,7-bis(methylthio)tetrathiafulvalene (50.0 mg, 0.11 mmol, 1 equiv) was dissolved in dry DMF (4 mL) and CsOH·H_2O (35.8 mg, 0.22 mmol, 2 equiv) dissolved in dry MeOH (1.5 mL) was added dropwise over 30 min under an Ar atmosphere. After stirring for 1 h, the resulting dark red solution was dropped to a solution of diiodide **1** (53.7 mg, 0.11 mmol, 1 equiv) in DMF (20 mL) in an ice bath over 1 h. The mixture was stirred in the thawing ice bath overnight. Afterwards, the solvent was removed under reduced pressure and the resulting residue was dissolved in CH_2Cl_2 (50 mL). The organic layer was washed with water (50 mL) and brine (50 mL). After drying over $MgSO_4$, the solution was concentrated under reduced pressure and the residue was purified by column chromatography (SiO_2, CH_2Cl_2

→ CH_2Cl_2/MeOH 100:1, R_f ≈ 0.6 in CH_2Cl_2/MeOH 50:1). The desired product (45 mg, 0.07 mmol, 69%) was obtained as dark red oil.

^{1}H NMR (700 MHz, CD_2Cl_2): δ = 2.42 (s, 6H, a), 3.03 (t, ^3J = 6.2 Hz, 4H, b), 3.62 – 3.61 (m, 16H, OCH_2), 3.69 (t, ^3J = 6.2 Hz, 4H, c) ppm. **^{13}C NMR** (176 MHz, CD_2Cl_2): δ = 19.6, 36.4, 70.2, 71.2, 71.2, 71.3, 71.3, 111.2, 128.1, 128.7 ppm. **ESI-HRMS** (CH_3CN): m/z calcd. for $[C_{20}H_{30}O_5S_8]$: $[M]^+$ 605.9853, found: 605.9843; calcd. for $[M+Na]^+$ 628.9751, found: 628.9734; calcd. for $[M+K]^+$ 644.9490, found: 644.9492.

21,22-Diiodo-2,3,5,6,8,9,11,12,14,15,17,18-dodecahydrobenzo[*b*][1,4,7,10,13,16,19]-heptaoxacyclohenicosine (**2**)

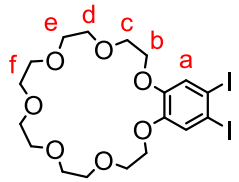

Periodic acid (231 mg, 1.01 mmol, 1.8 equiv) and iodine (114 mg, 0.45 mmol, 0.8 equiv) were dissolved in dry MeOH (5 mL) and stirred for 5 min under argon at rt. Afterwards, **BC7** (200 mg, 0.56 mmol, 1.0 equiv) dissolved in dry MeOH (7 mL) was added to the mixture and stirred for 12 h at 70 °C. The reaction mixture was quenched with a saturated aqueous $Na_2S_2O_3$ solution. The solvent was removed under reduced pressure and the residue dissolved in CH_2Cl_2 (50 mL). The organic phase was washed three times with water and brine. The organic phase was dried over $MgSO_4$ and the solvent was removed to isolate the desired product **2** (240 mg, 0.4 mmol, 66%) as light-yellow oil.

^{1}H NMR (500 MHz, $CDCl_3$): δ = 3.64 – 3.68 (m, 8H, f), 3.70 – 3.73 (m, 4H, e), 3.75 – 3.78 (m, 4H, d), 3.87 – 3.90 (m, 4H, c), 4.09 – 4.12 (m, 4H, b), 7.28 (s, 2H, a) ppm. **^{13}C NMR** (176 MHz, $CDCl_3$) *δ* = 69.6, 69.6, 70.7, 71.1, 71.1, 71.3, 96.7, 124.4, 149.6. ppm. **ESI-HRMS** (CH_3CN): m/z calcd. for $[C_{18}H_{26}I_2O_7]$: 626.0106 $[M+NH_4]^+$ found: 626.0094; calcd. for $[M+Na]^+$ 630.9660, found: 646.9644; calcd. for $[M+K]^+$ 646.9399, found: 646.9397.

7,8,10,11,13,14,16,17,19,20,22,23-Dodecahydro[1,3]dithiolo[4'',5'':5',6'][1,4]dithiino-[2',3':4,5]benzo[1,2-*b*][1,4,7,10,13,16,19]heptaoxacyclohenicosine-2-thione (**3**)

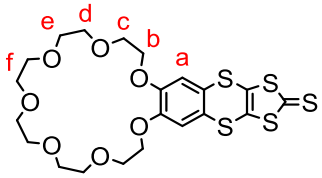

The diiodide **2** (235 mg, 0.38 mmol, 1.0 equiv), $(NEt_4)_2[Zn(dmit)_2]$ (dmit = 1,3 dithiole-2-thione-4,5-dithiolate (183 mg, 0.19 mmol, 0.5 equiv), Cu_2O (7 mg, 0.05 mmol, 0.1 equiv), and ethyl

acetoacetate (50 µL, 0.4 mmol, 1.0 equiv) were suspended in dry DMF (10 mL) and stirred for 12 h at 80 °C. Afterwards, the solvent was removed under reduced pressure and the residue was dissolved in CH_2Cl_2 (50 mL). The organic phase was washed three times with water and brine. The organic phase was dried over $MgSO_4$ and the solvent was removed. The crude product was purified via column chromatography (SiO_2, CH_2Cl_2 → CH_2Cl_2/EtOH 20:1, $R_f \approx 0.3$ in CH_2Cl_2/EtOH 20:1) to isolate the desired thione **3** as yellowish powder in 58% yield (121 mg, 0.22 mmol).

^{1}H NMR (500 MHz, $CDCl_3$): δ = 3.64 – 3.68 (m, 8H, f), 3.71 – 3.73 (m, 4H, e), 3.76 – 3.79 (m, 4H, d), 3.90 – 3.93 (m, 4H, c), 4.13 – 4.17 (m, 4H, b), 6.97 (s, 2H, a) ppm. **^{13}C NMR** (176 MHz, $CDCl_3$) *δ* = 69.7, 69.9, 70.7, 71.2, 71.2, 71.4, 114.6, 125.8, 131.9, 149.7, 212.7 ppm. **ESI-HRMS** (MeOH): m/z calcd. for $[C_{21}H_{26}O_7S_5]$: $[M+NH_4]^+$ 568.0620 found: 568.0631; calcd. for $[M+Na]^+$ 573.0174, found: 573.0185; calcd. for $[M+K]^+$ 588.9914, found: 588.9926.

7,8,10,11,13,14,16,17,19,20,22,23-Dodecahydro[1,3]dithiolo[4'',5'':5',6'][1,4]dithiino[2',3':4,5]-benzo[1,2-*b*][1,4,7,10,13,16,19]heptaoxacyclohenicosine-2-one (**4**)

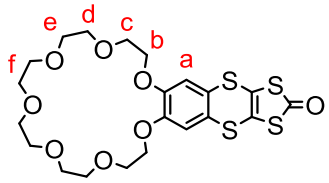

The thione **3** (58 mg, 0.11 mmol, 1 equiv) and mercury(II) acetate (101 mg, 0.33 mmol, 3 equiv) were dispersed in a mixture of $CHCl_3$ (5 mL) and acetic acid (2 mL). After stirring for 2 days at rt the reaction mixture was filtered through a celite pad, diluted with $CHCl_3$, and quenched with saturated aq. $NaHCO_3$ (20 mL). The organic phase was washed with brine, dried over $MgSO_4$, and the solvent was removed. The desired product **10** could be isolated as yellow powder in 95% yield (53 mg, 0.10 mmol).

^{1}H NMR (600 MHz, $CDCl_3$): δ = 3.63 – 3.67 (m, 8H, f), 3.69 – 3.72 (m, 4H, e), 3.75 – 3.78 (m, 4H, d), 3.89 – 3.92 (m, 4H, c), 4.13 – 4.17 (m, 4H, b), 6.97 (s, 2H, a) ppm. **^{13}C NMR** (126 MHz, $CDCl_3$) *δ* = 69.6, 69.8, 70.7, 71.1, 71.2, 71.3, 114.3, 122.0, 126.1, 149.7, 191.4 ppm. **ESI-HRMS** (MeOH): m/z calcd. for $[C_{21}H_{26}O_8S_4]$: $[M+K]^+$ 573.0142, found: 573.0126.

exTTFC7

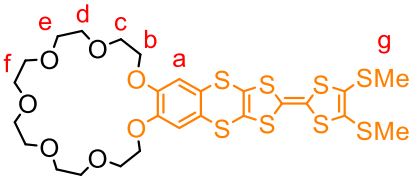

The one **4** (53 mg, 0.10 mmol, 1.0 equiv) and 4,5-bis(methylthio)-1,3-dithiole-2-thione (25 mg, 0.11 mmol, 1.1 equiv) were dissolved in $P(OEt)_3$ (20 mL). After stirring for 2 h at 80°C the solvent was removed in oil pump vacuum and the residue was dissolved in CH_2Cl_2 (50 mL). The crude product was purified by preparative thin layer chromatography plate (2000 µm, SiO_2, CH_2Cl_2/EtOH 30:1, $R_f \approx 0.4$ in CH_2Cl_2/EtOH 20:1) to isolate the desired product **exTTFC7** as yellow powder in 85% yield (61 mg, 0.09 mmol).

^{1}H NMR (700 MHz, CD_2Cl_2): δ = 2.42 (s, 6H, g), 3.59 – 3.61 (m, 8H, f), 3.63 – 3.65 (m, 4H, e), 3.68 – 3.71 (m, 4H, d), 3.83 – 3.86 (m, 4H, c), 4.10 – 4.12 (m, 4H, b), 6.94 (s, 2H, a) ppm. **^{13}C NMR** (176 MHz, $CDCl_3$) δ = 19.6, 70.0, 70.0, 71.1, 71.3, 71.4, 71.6, 113.3, 114.8, 116.7, 123.9, 127.0, 128.1, 149.7 ppm. **ESI-HRMS** (MeOH): m/z calcd. for $[C_{26}H_{32}O_7S_8]$: $[M+K]^+$ 750.9545, found: 750.9572.

2-(5,6,8,9,11,12,14,15,17,18-Decahydro-2H-naphtho[2,3-*h*][1,4,7,10,13,16,19]-hexaoxaazacyclohenicosin-10(3*H*)-yl)ethanamine (**6**)

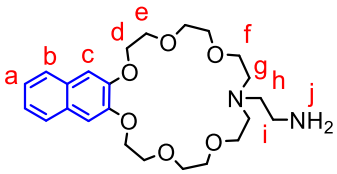

Ditosylate **5** (800 mg, 1.09 mmol, 1.0 equiv), EDABoc (174 mg, 1.09 mmol, 1.0 equiv), potassium iodide (262 mg, 1.58 mmol, 1.5 equiv), and K_2CO_3 (1506 mg, 10.9 mmol, 10 equiv) were dissolved in acetonitrile (25 mL) and heated to reflux overnight. After cooling to rt and filtration, the solvent was removed under reduced pressure and the residue was purified by column chromatography (SiO_2, CH_2Cl_2→ CH_2Cl_2/MeOH 10:1, $R_f \approx 0.1$ in CH_2Cl_2) to obtain pure protected amine (410 mg, 0.75 mmol, 69%) as pale yellow oil.

The protected amine was dissolved in CH_2Cl_2/trifluoroacetic acid (3:2, 2.5 mL) and stirred for 2 h at rt. The solution was concentrated under reduced pressure and the residue was solved in saturated $NaHCO_3$ solution (40 mL). The aqueous phase was extracted with CH_2Cl_2 (3 × 40 mL) and the combined organic phases were dried over $MgSO_4$. After removing the solvent, the crude product was purified by column chromatography (SiO_2, CH_2Cl_2 → CH_2Cl_2/MeOH 20:1, $R_f \approx 0.3$ in CH_2Cl_2/MeOH 20:1) to yield the desired product (204 mg, 0.46 mmol, 62%) as colorless oil. The product was obtained in an overall yield of 43%.

^{1}H NMR (500 MHz, $CDCl_3$): δ = 2.16 (s, 2H, j), 2.75 – 2.77 (m, 4H, g), 2.78 (br, 4H, h,i), 3.54 – 3.56 (m, 4H, f), 3.71 – 3.72 (m, 4H, OCH_2), 3.78 – 3.79 (m, 4H, OCH_2), 4.00 – 4.02 (m, 4H, e), 4.30 – 4.32 (m, 4H, d), 7.27 (s, 2H, c), 7.35 (AA'XX' spin system, $J_{AA'XX'}$ = 3.3, 6.2 Hz, 2H, a), 7.67 (AA'XX' spin system, $J_{AA'XX'}$ = 3.3, 6.2 Hz, 2H, b) ppm. **^{13}C NMR** (176 MHz, $CDCl_3$) δ

= 38.9, 51.8, 56.2, 68.6, 69.6, 69.9, 70.5, 70.6, 108.6, 124.9, 126.6, 129.5, 148.0 ppm. **ESI-HRMS** (CH_3CN): m/z calcd. for $[C_{24}H_{36}O_6N_2]$: $[M+H]^+$ 449.2646, found: 449.2661.

NDIC7

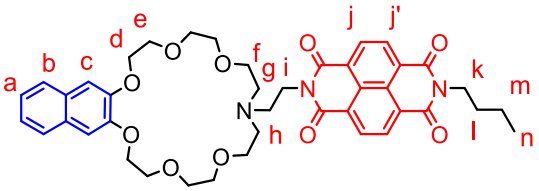

To a solution of amine **6** (170 mg, 0.38 mmol, 1.1 equiv) in DMF (2 mL) was added dropwise a solution of monoanhydride **7** (107 mg, 0.35 mmol, 1.0 equiv) in DMF (1 mL). The solution was stirred at 120 °C under Ar in a sealed tube overnight. After cooling to rt, the solvent was removed and the residue was purified by column chromatography (SiO_2, CH_2Cl_2/MeOH 20:1 → 10:1, $R_f \approx 0.4$ in CH_2Cl_2/MeOH 10:1) to yield the desired product **NDIC7** (158 mg, 0.21 mmol, 60%) as orange solid.

^{1}H NMR (500 MHz, $CDCl_3$): δ = 1.00 (t, ^3J = 7.4 Hz, 3H, n), 1.43 – 1.51 (m, 2H, m), 1.70 – 1.76 (m, 4H, l), 2.80 – 2.83 (m, 2H, h), 2.87 – 2.89 (m, 4H, g), 3.66 (br, 4H, f) 3.71 – 3.73 (m, 4H, OCH_2), 3.78 – 3.80 (m, 4H, OCH_2), 3.96 – 3.97 (m, 4H, e), 4.14 – 4.17 (m, 6H, d,k), 4.28 – 4.31 (m, 2H, i), 6.76 (s, 2H, c), 7.00 – 7.02 (m, 2H a), 7.24 – 7.26 (m, 2H, b), 8.56 – 8.60 (m, 4H, j, j') ppm. **^{13}C NMR** (176 MHz, $CDCl_3$) δ = 14.0, 20.5, 30.3, 39.4, 40.8, 52.3, 55.7, 68.8, 69.8, 70.2, 71.0, 71.2, 107.7, 123.8, 126.1, 126.5, 126.5, 126.5, 126.6, 128.9, 130.5, 130.7, 148.9, 162.8, 162.9 ppm. **ESI-HRMS** (CH_3CN): m/z calcd. for $[C_{42}H_{47}N_3O_{10}]$: $[M+H]^+$ 754.3334 found: 754.3361; calcd. for $[M+Na]^+$ 776.3154, found: 776.3180; calcd. for $[M+K]^+$ 792.2893, found: 792.2922.

tert-Butyl (3,5-dihydroxyphenyl)carbamate (**8**)

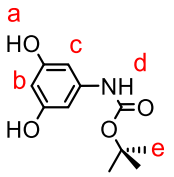

Aqueous NH_3 (28%, 100 mL) was purged with argon for 20 min. Benzene-1,3,5-triol (20.0 g, 0.16 mol, 2 equiv) was added and the mixture was stirred at rt for 2 h. The solvent was removed at reduced pressure, to the residue, toluene was added and removed at reduced pressure. The crude product was suspended in THF (150 mL) and Boc anhydride (17.5 g, 0.08 mol, 1 equiv) was added. The mixture was stirred under Ar overnight at rt and the solvent was

removed at reduced pressure. The crude product was purified by column chromatography (SiO_2, CH_2Cl_2/MeOH 15:1) and yielded a white solid (8.8 g, 0.04 mol, 25%).

^{1}H NMR (700 MHz, DMSO-d_6): δ = 1.43 (s, 9H, e), 5.80 (s, 1H, b), 6.40 (s, 2H, c), 9.01 (br, 1H, d), 9.02 (br, 2H, a) ppm. **^{13}C NMR** (176 MHz, DMSO-d_6) δ = 28.2, 78.7, 96.8, 96.6 140.9, 152.6, 158.3 ppm. **ESI-HRMS** (MeOH): m/z calcd. for $[C_{11}H_{15}NO_4]$: $[M+Na]^+$ 248.0893, found: 248.0884.

2,5,8,11,13,16,19,22-Octaoxa-1(2,3)-naphthalena-12(1,3)-benzenacyclodocosaphan-12^5-amine (**9**)

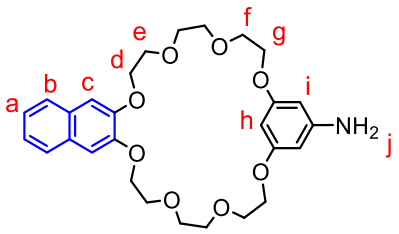

Cs_2CO_3 (5.0 g, 15.5 mmol, 5 equiv) was dissolved in acetonitrile (500 mL) and heated to reflux. A solution of ditosylate **5** (2.3 g, 3.1 mmol, 1 equiv) in acetonitrile (250 mL) and a solution of diol **8** (0.7 g, 3.1 mmol, 1 equiv) in acetonitrile (250 mL) were added dropwise and simultaneously. The mixture was stirred under reflux for 3 d. After cooling to rt and filtration, the solvent was removed under reduced pressure. The residue was dissolved in CH_2Cl_2 (300 mL) and washed three times with water and brine. After evaporation of the solvent, the crude product was purified by column chromatography (SiO_2, pentane/EtOAc/Et_3N 300:200:1 → 50:450:1, R_f ≈ 0.7 in 50:450:1) to obtain pure protected amine (1.1 g, 1.7 mmol, 55%) as yellow solid.

The protected amine and trifluoroacetic acid (2.6 mL, 34 mmol, 20 equiv) were dissolved in CH_2Cl_2 (100 mL) at 0 °C. The solution was warmed to rt and stirred for 16 h. The solvent was removed under reduced pressure and the residue was dissolved in saturated $NaHCO_3$ solution (200 mL). The aqueous phase was extracted with CH_2Cl_2 (3 × 200 mL). The combined organic phases were washed with water and dried over $MgSO_4$. After removing of the solvent, the crude product was purified by column chromatography (SiO_2, EtOAc/Et_3N 10:1, R_f ≈ 0.3) to yield the desired product (0.86 g, 1.7 mmol, quantitative) as pale yellow solid. The product was obtained in an overall yield of 55%.

^{1}H NMR (700 MHz, $CDCl_3$): δ = 3.61 (s, 2H, j), 3.72 – 3.73 (m, 4H, OCH_2), 3.77 – 3.78 (m, 4H, OCH_2), 3.79 – 3.80 (m, 4H, f), 3.93 – 3.95 (m, 4H, e), 4.07 – 4.09 (m, 4H, g), 4.24 – 4.26 (m, 4H, d), 5.85 (d, 2H, ^4J = 2.2 Hz, i), 6.12 (t, 1H, ^4J = 2.2 Hz, h), 7.15 (s, 2H, c), 7.31 (AA'XX' spin system, $J_{AA'XX'}$ = 3.3, 6.1 Hz, 2H, a), 7.65 (AA'XX' spin system, $J_{AA'XX'}$ = 3.3, 6.1 Hz, 2H, b) ppm. **^{13}C NMR** (176 MHz, $CDCl_3$) δ = 68.0, 68.9, 69.8, 70.0, 71.1, 71.3, 93.3, 95.5, 109.0, 123.3, 126.4, 129.5, 148.4, 149.2, 160.9 ppm. **ESI-HRMS** (CH_3CN): m/z calcd. for

[$C_{24}H_{36}O_8N_1$]: [M+Na]$^+$ 536.2255, found: 536.2276; calcd. for [M+K]$^+$ 552.1994, found: 552.2011.

NDIC8

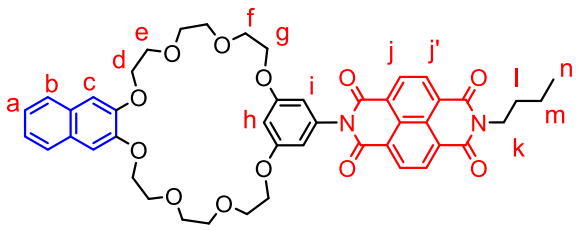

Monoanhydrate **7** (510 mg, 1.6 mmol, 1.1 equiv) was dissolved in dry DMF (55 mL) and stirred at 70 °C for 10 minutes in an Ar atmosphere. Et_3N (0.6 mL, 4.3 mmol, 3.0 equiv) and amine **9** (737 mg, 1.4 mmol, 1.0 equiv) were added and the solution was stirred at 70 °C for 24 h. The mixture was diluted in H_2O (200 mL) and extracted with EtOAc (2 × 200 mL). The solution was washed with brine and dried over MgSO4. The solvents were removed under reduced pressure and the crude product was purified by column chromatography (SiO_2, CH_2Cl_2/EtOAc 1:3, $R_f \approx$ 0.6 in EtOAc/Et_3N 40:1) to yield an orange solid (502 mg, 0.60 mmol, 43%)
^{1}H NMR (700 MHz, $CDCl_3$): δ = 1.00 (t, ^3J = 7.4 Hz, 3H, n), 1.47 (h, 2H, ^3J = 7.4 Hz, m), 1.72 – 1.77 (m, 2H, l), 3.74 – 3.75 (m, 4H, OCH_2), 3.80 – 3.81 (m, 4H, OCH_2), 3.83 – 3.84 (m, 4H, f) 3.95 – 3.97 (m, 4H, e), 4.16 – 4.17 (m, 4H, g), 4.20 – 4.21 (m, 2H, k), 4.26 – 4.28 (m, 4H, d), 6.47 (d, 2H, ^4J = 2.2 Hz, i), 6.89 (t, 1H, ^4J = 2.2 Hz, h), 7.14 (s, 2H, c), 7.29 (AA'XX' spin system, $J_{AA'XX'}$ = 3.3, 6.1 Hz, 2H, a), 7.62 (AA'XX' spin system, $J_{AA'XX'}$ = 3.3, 6.1 Hz, 2H, b), 8.74 (m, 4H, j, j') ppm. **^{13}C NMR** (176 MHz, $CDCl_3$) δ = 13.9, 20.5, 30.3, 40.9, 68.5, 68.8, 69.9, 70.1, 71.2, 71.3, 103.5, 108.6, 109.0, 124.3, 126.4, 126.8, 126.9, 127.0, 127.1, 129.5, 131.1, 131.4, 136.0, 149.3, 160.8, 162.8, 162.9 ppm. **ESI-HRMS** (CH_3CN): m/z calcd. for [$C_{46}H_{46}O_{12}N_2$]: [M+NH_4]$^+$ 836.3389 found: 836.3397; calcd. for [M+Na]$^+$ 841.2943, found: 841.2962; calcd. for [M+K]$^+$ 857.2682, found: 857.2701.

A1·PF_6

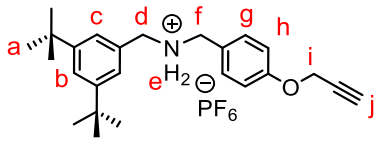

(4-(Prop-2-yn-1yloxy)phenyl)methanaminium chloride (473 mg, 2.4 mmol, 1 equiv) was dispersed in dry EtOH (40 mL) and Et_3N (242 mg, 2.4 mmol, 1 equiv) was added. Afterwards, 3,5-di-*tert*-butylbenzaldehyde (522 mg, 2.4 mmol, 1 equiv) was added and the mixture was stirred at reflux under Ar atmosphere for 3 h. The solution was cooled to 0 °C and $NaBH_4$ (454 mg, 12 mmol, 5 equiv) was added. After stirring at rt overnight, the suspension was

quenched with sat. $NaHCO_3$ solution. The mixture was filtered and the solid residue was washed with CH_2Cl_2 (150 mL). The combined filtrate was phase separated and the organic phase was washed with water (3 × 100 mL). It was dried with $MgSO_4$ and the solvent was removed at reduced pressure. The crude product was purified by column chromatography (SiO_2, CH_2Cl_2/MeOH 80:1 → 50:1) to yield a colorless oil.

The amine (745 mg, 2.0 mmol, 83 %) was dissolved in acetonitrile (10 mL), NH_4PF_6 (379 mg, 2.3 mmol) was added and argon was bubbled through the solution for 4 h. The solvent was removed at reduced pressure and the residue was suspended in water (100 mL). The suspension was extracted with Et_2O (3 × 100 mL) and the combined organic phases were washed with water (100 mL). After drying with $MgSO_4$, the solvent was removed at reduced pressure to yield the desired product **A1**•PF_6 (1010 mg, 2.0 mmol, quantitative) as white solid. **^{1}H NMR** (700 MHz, $CDCl_3$): δ = 1.32 (s, 18H, a), 2.50 (t, ^4J = 2.4 Hz, 1H, j), 4.09 (s, 2H, f), 4.13 (s, 2H, d), 4.63 (d, ^4J = 2.4 Hz, 2H, i), 6.10 (br, 2H, e), 6.97 – 6.98 (m, 2H, h), 7.18 (d, ^4J = 1.8 Hz, 2H, c), 7.27 – 7.28 (m, 2H, g), 7.47 (t, ^4J = 1.8 Hz, 1H, b) ppm. **^{13}C NMR** (176 MHz, $CDCl_3$) δ = 31.4, 35.1, 50.7, 52.0, 55.9, 76.1, 78.1, 115.9, 122.4, 124.0, 124.2, 128.7, 131.5, 152.7, 158.9. **ESI-HRMS** (CH_3CN): m/z calcd. for $[C_{25}H_{34}F_6NOP]$: $[M\text{-}PF_6]^+$ 364.2635, found: 364.2639.

NDIC8Rot

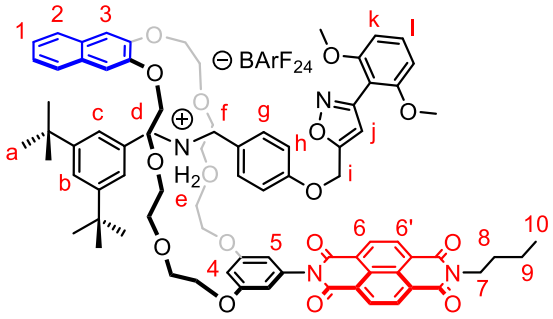

NDIC8 (28 mg, 34 µmol, 1.1 equiv) and **A1**•$BArF_{24}$ (38 mg, 31 µmol, 1.0 equiv) were dissolved in dry 1,2-dichloroethane (1.5 mL) and ultra-sonicated for 10 min. **St** (11 mg, 62 µmol, 2.0 equiv) was added and the solution was stirred at 50 °C for 3 days. The solvent was removed under reduced pressure and the crude product was purified by column chromatography (SiO_2, CH_2Cl_2/MeOH 100:1, R_f ≈ 0.4) and preparative thin layer chromatography plate (SiO_2, 500 µm, CH_2Cl_2/MeOH 100:1) to yield an orange solid (30 mg, 14 µmol, 45%).

^{1}H NMR (700 MHz, $CDCl_3$): δ = 1.00 (t, ^3J = 7.4 Hz, 3H, 10), 1.26 (s, 18H, a), 1.45 – 1.53 (m, 2H, 9), 1.73 – 1.77 (m, 2H, 8), 3.50 - 3.57 (m, 4H, OCH_2), 3.59 – 3.62 (m, 4H, OCH_2), 3.67 – 3.71 (m, 4H, OCH_2), 3.76 – 3.78 (m, 8H, OMe, OCH_2), 3.81 – 3.83 (m, 2H, OCH_2), 3.97 – 4.00 (m, 2H, OCH_2), 4.15 – 4.17 (m, 4H, OCH_2), 4.19 – 4.23 (m, 4H, 7, OCH_2), 4.38 – 4.40 (m, 4H,

i, f), 4.48 – 4.50 (m, 2H, d), 6.35 (s, 1H, j), 6.51 – 6.52 (m, 2H, h), 6.55 (d, ^{4}J = 2.2 Hz, 2H, 5), 6.64 (d, ^{3}J = 8.4 Hz, 2H, k), 6.67 (t, ^{4}J = 2.2 Hz, 1H, 4), 6.91 (s, 2H, 3), 7.14 – 7.15 (m, 2H, g), 7.35 – 7.39 (m, 5H, 1, c, l), 7.48 (t, ^{4}J = 1.8 Hz, 1H, b), 7.50 – 7.51 (m, 4H, $BArF_{24}$), 7.62 (AA'XX' spin system, $J_{AA'XX'}$ = 3.3, 6.1 Hz, 2H, 2), 8.56 – 8.60 (m, 4H, j), 7.69 – 7.70 (m, 8H, $BArF_{24}$), 7.73 (br, 2H, e), 8.75 (d, ^{3}J = 7.6 Hz, 2H, 6/6'), 8.78 (d, ^{3}J = 7.6 Hz, 2H, 6/6') ppm. **^{13}C NMR** (176 MHz, $CDCl_3$) δ = 13.9, 20.5, 30.3, 31.4, 35.1, 41.0, 52.4, 53.0, 56.2, 60.6, 68.0, 68.2, 69.4, 70.5, 70.9, 71.6, 104.3, 104.6, 106.6, 106.9, 108.0, 108.7, 114.8, 117.6, 123.2, 123.3, 124.1, 124.7, 125.7, 126.5, 127.0, 127.1, 127.3, 129.0, 130.5, 131.1, 131.1, 131.5, 131.5, 134.9, 137.1, 146.4, 152.3, 157.3, 158.7, 159.0, 160.5, 161.9, 162.8, 163.0, 165.7 ppm. **ESI-HRMS** (CH_3CN): m/z calcd. for $[C_{112}H_{101}BF_{24}N_4O_{16}]$: $[M\text{-}BArF_{24}]^+$ 1361.6274 found: 1361;6277.

.

2. Crystallographic data

General details. Single crystal X-ray data for **exTTFC7** were collected at 120 K on an Agilent Super-Nova dual wavelength diffractometer with a micro-focus X-ray source and multilayer optics monochromatized CuKα (λ = 1.54184 Å) radiation. Program *CrysAlisPro* [10] was used for collection and reduction of data. The diffraction intensities were corrected for absorption using analytical face index absorption correction method [11] for the data. The structures were solved with direct methods (*SHELXT*) [12] and refined by full-matrix least squares on F^2 using *SHELXL*-2018/3 [13]. Anisotropic displacement parameters were assigned to non-hydrogen atoms. All hydrogen atoms were constrained to their idealised positions and refined using riding models with U_{eq}(H) of 1.5U_{eq}(C) for terminal methyl groups, and of 1.2U_{eq}(C) for other groups. The summary details of crystal data, data collection, and the refinement results are documented below.

Single crystal X-ray data for **NDIC8** and **NDIC7** were collected on a Bruker D8 Venture system at 100(2) K using graphite-monochromated MoKα (λα = 0.71073 Å) and CuKα (λ = 1.54184 Å) radiation. The strategy for the data collection was evaluated using APEX3 software and the data were collected by the omega + phi scan techniques. The data were scaled and reduced using SAINT+ and SADABS software. The structure was solved by intrinsic phasing using SHELXT-2014/7. It was refined by full matrix least-squares using SHELXL-2014/7 and was refined on F^2. Non-hydrogen atoms were refined anisotropically [13-19].

Deposition numbers CCDC 1977518 (**exTTFC7**), 1902746 (**NDIC7**), and 1906086 (**NDIC8**) contains the supplementary crystallographic data for this paper. These data are provided free of charge by the joint Cambridge Crystallographic Data Centre and Fachinformationszentrum Karlsruhe Access Structures service www.ccdc.cam.ac.uk/structures.

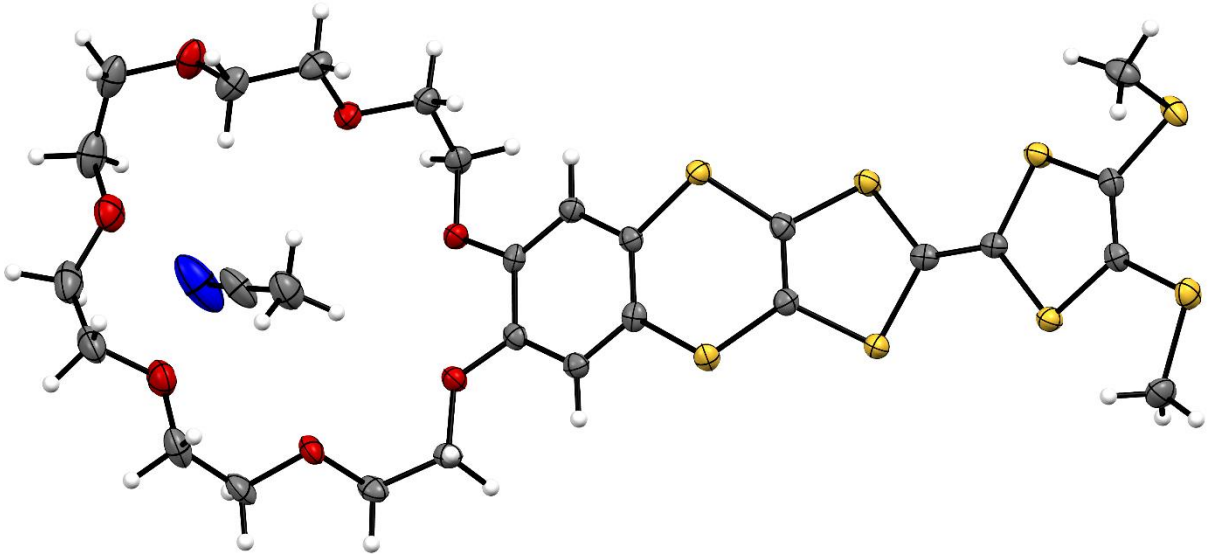

Figure S1: Thermal ellipsoid diagram of **exTTFC7** with 50% ellipsoid probability level. Colour codes: C (dark grey), H (white), N (blue), O (red) and S (yellow).

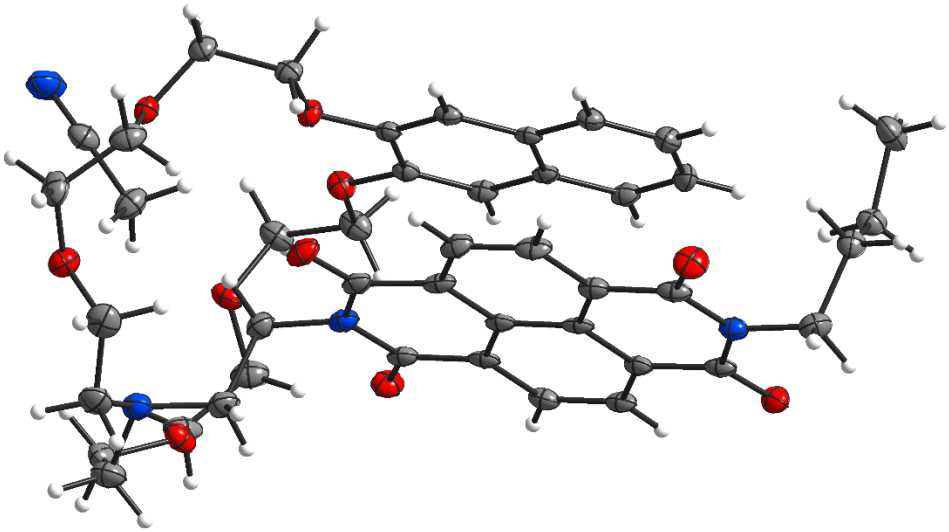

Figure S2: Thermal ellipsoid diagram of **NDIC7** with 50% ellipsoid probability level. Colour codes: C (dark grey), H (white), N (blue) and O (red).

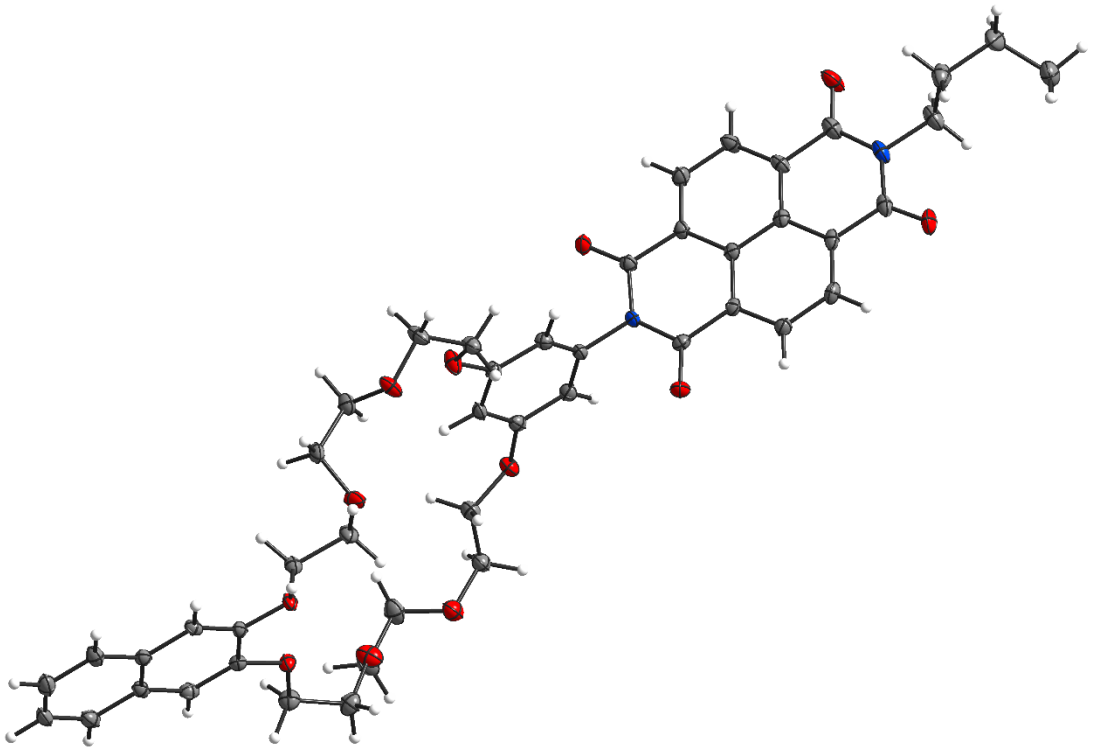

Figure S3: Thermal ellipsoid diagram of **NDIC8** with 50% ellipsoid probability level. Colour codes: C (dark grey), H (white), N (blue) and O (red).

Table S1: Crystallographic data.

compound	exTTFC7	NDIC7	NDIC8
chemical formula	$C_{28}H_{35}NO_7S_8$	$C_{44}H_{50}N_4O_{10}$	$C_{46}H_{46}N_2O_{12}$
*M*r / g mol^{-1}	754.05	794.88	818.85
crystal system	monoclinic	monoclinic	monoclinic
space group	*P2$_1$/c*	*P2$_1$/c*	*P2$_1$*
a / Å	31.5592(13)	13.6717(13)	19.695(4)
b / Å	12.8309(5)	9.8821(10)	9.1282(16)
c / Å	8.3107(3)	28.639(3)	21.618(4)
α / °	90	90	90
β / °	94.379(3)	90.657(4)	96.451(11)
γ / °	90	90	90
V / Å	3355.5(2)	3869.1(7)	3861.8(13)
Z	4	4	4
density / g cm^{-3}	1.493	1.365	1.408
F(000)	1576	1688	1728
radiation type	CuK_α	MoK_α	CuK_α
μ / mm^{-1}	5.317	0.097	0.845
crystal size / mm	0.12 x 0.09 x 0.05	0.42 x 0.22 x 0.10	0.31 x 0.09 x 0.07
meas refl.	13226	134093	125951
indep. refl.	6545	7104	16640
obsvd. [I > 2σ(I)] refl.	5274	5843	14307
max. and min. transmission	0.842, 0.629	0.745, 0.708	0.727, 0.654
R_{int}	0.0344	0.0678	0.0897
R [$F^2 > 2\sigma(F^2)$], wR(F^2), S	0.0487, 0.0860, 1.034	0.0522, 0.1254, 1.103	0.0449, 0.1064, 1.033
$\Delta\rho$max, $\Delta\rho$min (e Å^{-3})	0.487, -0.326	0.597, -0.285	0.663, -0.319

3. Isothermal titration calorimetry

ITC titrations were carried out in dry 1,2-dichloroethane (DCE) at 298 K on a TAM III microcalorimeter (Waters GmbH, TA Instruments, Eschborn, Germany). In a typical experiment, an 800 µL solution of the crown ether was placed in the sample cell at a concentration of 1.1 mM, and 250 µL of a solution of the ammonium salt (8.0 mM) were put into the syringe. The titrations consisted of 32 consecutive injections of 8 µL each with a 20 min interval between the injections. The heat of dilution was determined by titration of ammonium salt solutions into the sample cell containing blank solvent and were subtracted from each data set. The heat flow generated in the sample cell was measured as a differential signal between sample and reference cell. Hence, an exothermic event results in a positive and an endothermic in a negative heat flow. The data were analysed using the instrument's internal software package and fitted with a 1:1 binding model. Each titration was conducted at least three times and the measured values for K and ΔH were averaged.

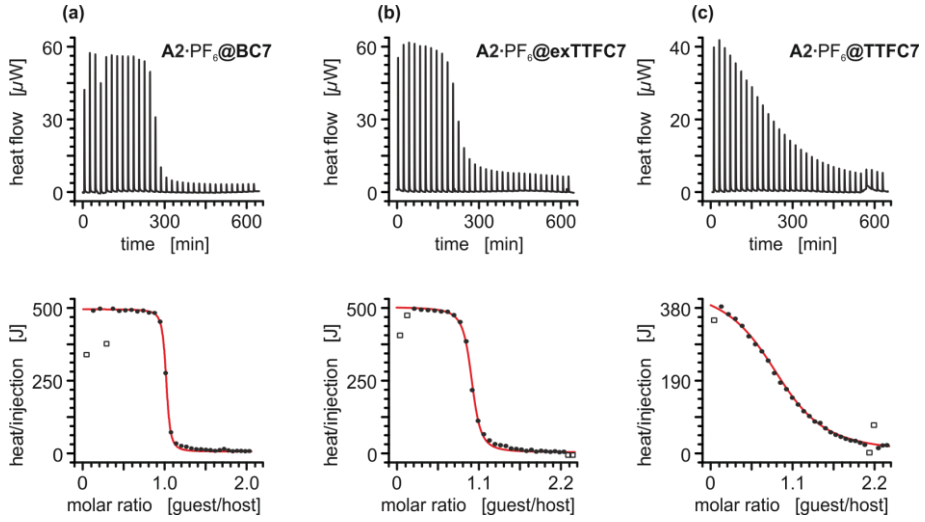

Figure S4: Titration plots (heat flow versus time and heat/volume versus guest/host ratio) obtained from ITC experiments at 298 K in 1,2-dichloroethane: (a) vial: **BC7**, syringe: axle **A2**•PF_6; (b) vial: **exTTFC7**, syringe: axle **A2**·PF_6; (c) vial: **TTFC7**, syringe: axle **A2**•PF_6. Points marked with non-filled squares were not considered in the fitting process.

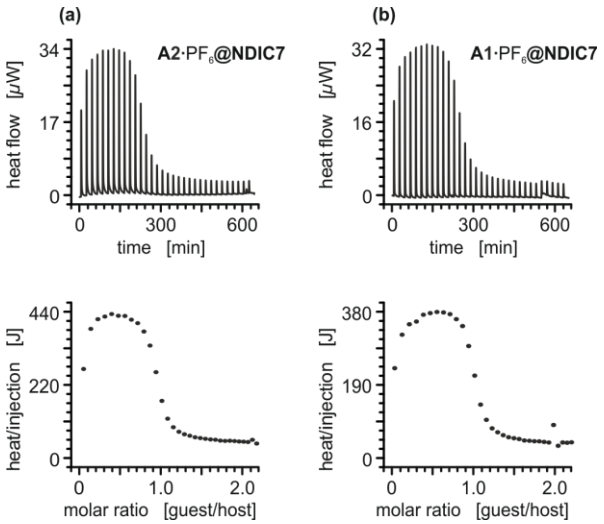

Figure S5: Titration plots (heat flow versus time and heat/volume versus guest/host ratio) obtained from ITC experiments at 298 K in 1,2-dichloroethane: (a) vial: **NDIC7**, syringe: axle **A2**•PF_6; (b) vial: **NDIC7**, syringe: axle **A1**•PF_6.The data points of the **A2**•PF_6**@NDIC7** do not agree with a 1:1 binding model. The increasing heat generated in the first 5 data points suggests a second process taking place in the mixture, which could be explained with the protonation of the tertiary amine of **NDIC7** by **A2**•PF_6. **A1**•PF_6 is sterically too big to thread **NDIC7** for a pseudo[2]rotaxane. Yet, the titration of **NDIC7** with the larger axle **A1**•PF_6 exhibits very similar results as with the smaller axle **A2**•PF_6. These results suggest that both ammonium axles undergo a similar type of reaction with **NDIC7**, which could be the protonation of the tertiary amine or the complexation in a non-threaded complex.

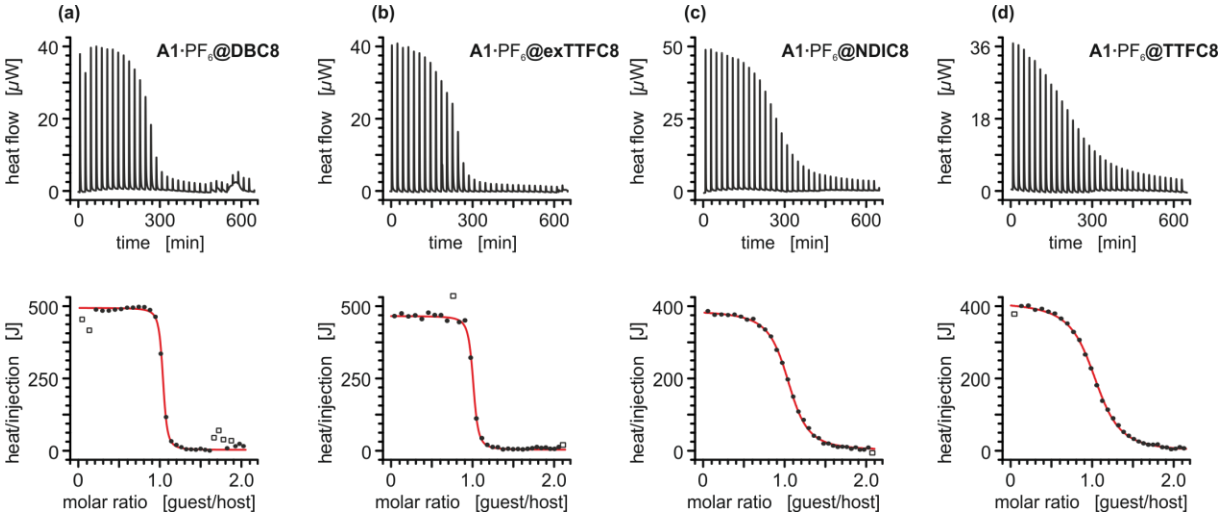

Figure S6: Titration plots (heat flow versus time and heat/volume versus guest/host ratio) obtained from ITC experiments at 298 K in 1,2-dichloroethane: (a) vial: **DBC8**, syringe: axle **A2**•PF_6; (b) vial: **exTTFC8**, syringe: axle **A2**•PF_6; (c) vial: **NDIC8**, syringe: axle **A2**•PF_6; (d) vial: **TTFC8**, syringe: axle **A2**•PF_6. Points marked with non-filled squares were not considered in the fitting process.

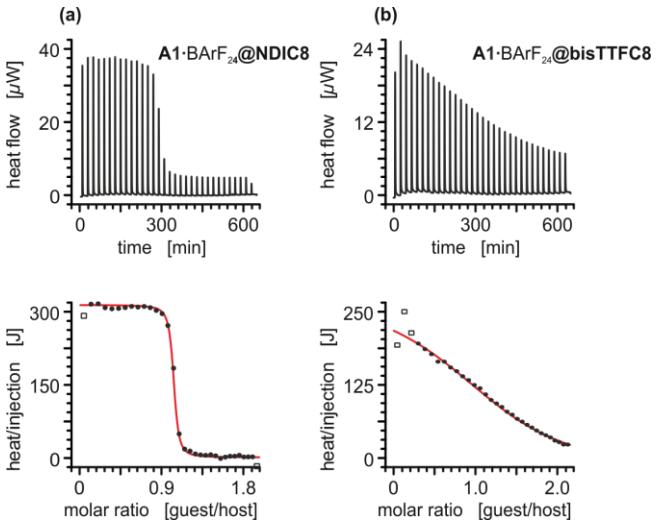

Figure S7: Titration plots (heat flow versus time and heat/volume versus guest/host ratio) obtained from ITC experiments at 298 K in 1,2-dichloroethane: (a) vial: **DBC8**, syringe: axle **A1**•PF_6; (b) vial: **exTTFC8**, syringe: axle **A1**•PF_6; (c) vial: **NDIC8**, syringe: axle **A1**•PF_6; (d) vial: **TTFC8**, syringe: axle **A1**•PF_6. Points marked with non-filled squares were not considered in the fitting process.

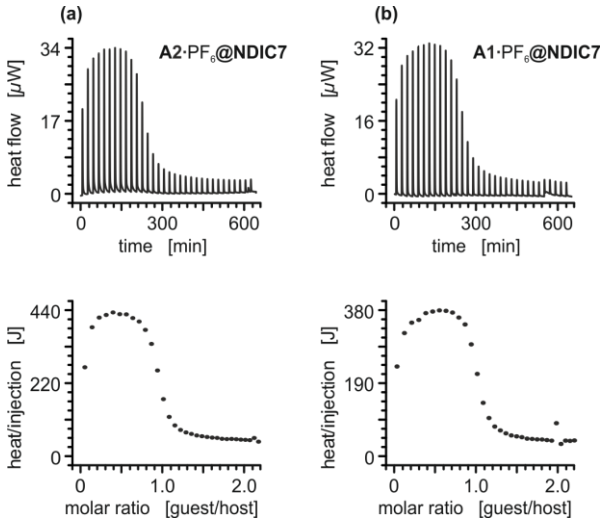

Figure S8: Titration plots (heat flow versus time and heat/volume versus guest/host ratio) obtained from ITC experiments at 298 K in 1,2-dichloroethane: (a) vial: **NDIC8**, syringe: axle **A1**•$BArF_{24}$; (b) vial: **bisTTFC8**, syringe: axle **A1**•$BArF_{24}$. Points marked with non-filled squares were not considered in the fitting process.

4. Electrochemical measurements

Cyclic voltammetry (CV) and differential pulse voltammetry (DPV) were performed on an Autolab PGSTAT302N potentiostat using a three-electrode configuration: a freshly polished glassy carbon working electrode, a platinum wire counterelectrode and a silver wire pseudoreference electrode. The decamethylferrocene/decamethylferrocenium ($FeCp^*_2{}^{(0/+)}$) couple was used as internal reference. Dry and argon purged solvents were used. Half-wave potentials were determined by DPV measurements and confirmed with CV (scan rate 100 mV s^{-1}), which also ensured reversibility of the reduction or oxidation processes. During experiments using axle **A1**•PF_6, an irreversible oxidation at ≈1.4 V vs. $FeCp^*_2{}^{(0/+)}$ was observed after addition of the axle. We address this signal to the oxidation of the axle phenol ether unit. The cyclic voltammogram traces of **NDIRot** were recorded with 10, 25, 50, 100, 250, 500, 1000, and 2500 mV/s scan rates, to ensure that the observed processes are reversible and diffusion limited. In order to obtain the correct half-wave potentials, $FeCp^{*0}$/$FeCp^{*+}$ was used as the reference. These values were later referenced to $FeCp/FeCp^+$ as described in the literature [20]. The raw data was treated with Nova 1.5 by Metrohm and the plots were made with Origin *8* by OriginLab.

Table S2: Electrochemical data obtained by differential pulse voltammetry.

entry	compound	solvent[a]	$E_{1/2}^{r2}$ / V[b]	$E_{1/2}^{r1}$ / V[b]	$E_{1/2}^{o1}$ / V[b]	$E_{1/2}^{o2}$ / V[b]
			reversible reductions		reversible oxidations	
1	**exTTFC7**	DCE/	/	/	0.67	0.95
2	**exTTFC7** + **A2**·PF_6[d]	CH_3CN	/	/	0.67	0.95
3	**exTTFC8**[c]	(1:1)	/	/	0.66	0.93
4	**exTTFC8** + **A1**·PF_6[d]		/	/	0.67	0.91
5	**TTFC7**		/	/	0.59	0.83
6	**TTFC7** + **A2**·PF_6[d]		/	/	0.60	0.84
7	**TTFC8**		/	/	0.59	0.83
8	**TTFC8** + **A1**·PF_6[d]		/	/	0.59	0.82
9	**bisTTFC8**[c]		/	/	0.57	0.93
10	**bisTTFC8** + **A1**·PF_6[d]		/	/	0.57	0.92
11	**NDIC7**		-0.96	-0.54	/	/
12	**NDIC7** + **A2**·PF_6[d]		-0.70	-0.46	/	/
13	**NDIC8**[c]		-0.95	-0.49	/	/
14	**NDIC8**[c] + **A1**·PF_6[d]		-0.72	-0.49	/	/
15	**NDIC8**[c] + $(CH_3)_2NH_2PF_6$[d]		-0.78	-0.45		
16	**NDIC8Rot**		-0.95	-0.50		
17	**exTTFC7**	DCE	/	/	0.65	1.01
18	**exTTFC7** + **A2**·PF_6[d]		/	/	0.67	1.01
19	**TTFC7**		/	/	0.59	0.87
20	**TTFC7** + **A2**·PF_6[d]		/	/	0.63	0.87
21	**bisTTFC8**		/	/	0.56	0.95
22	**NDIC8**[c]		-0.97	-0.53	/	/
23	**NDIC8Rot**		-0.96	-0.51	/	/

[a]With *n*-Bu_4NPF_6 (0.1 M) as the electrolyte. [b]Half-wave potentials are given against the decamethylferrocene/decamethylferrocenium couple as the reference; error = ± 0.01 V. [c]The compound showed only moderate solubility in the corresponding solvent. [d]Five equiv of the ammonium guest were added.

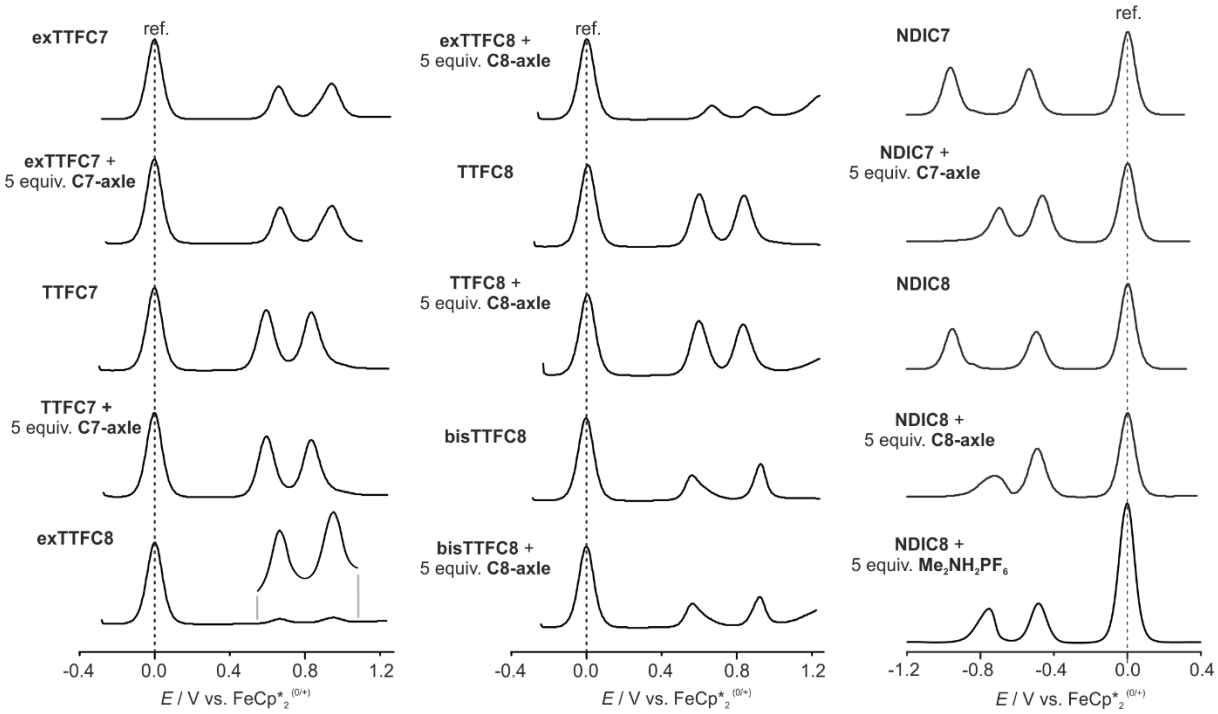

Figure S9: Differential pulse voltammograms (1 mM analyte, DCE/CH_3CN 1:1, 0.1 M *n*-Bu_4PF_6, 10 mV s^{-1} scan rate, 25 mV modulation amplitude, 50 ms modulation time, 5 mV step potential, 0.5 s interval time).

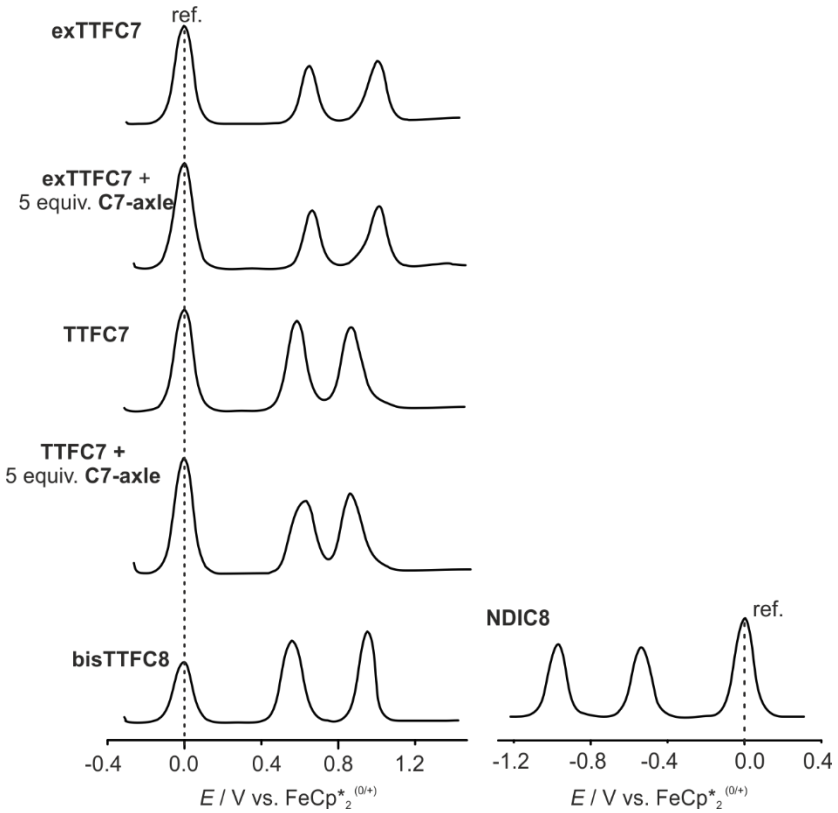

Figure S10: Differential pulse voltammograms (1 mM analyte, DCE, 0.1 M *n*-Bu_4PF_6, 10 mV s^{-1} scan rate, 25 mV modulation amplitude, 50 ms modulation time, 5 mV step potential, 0.5 s interval time).

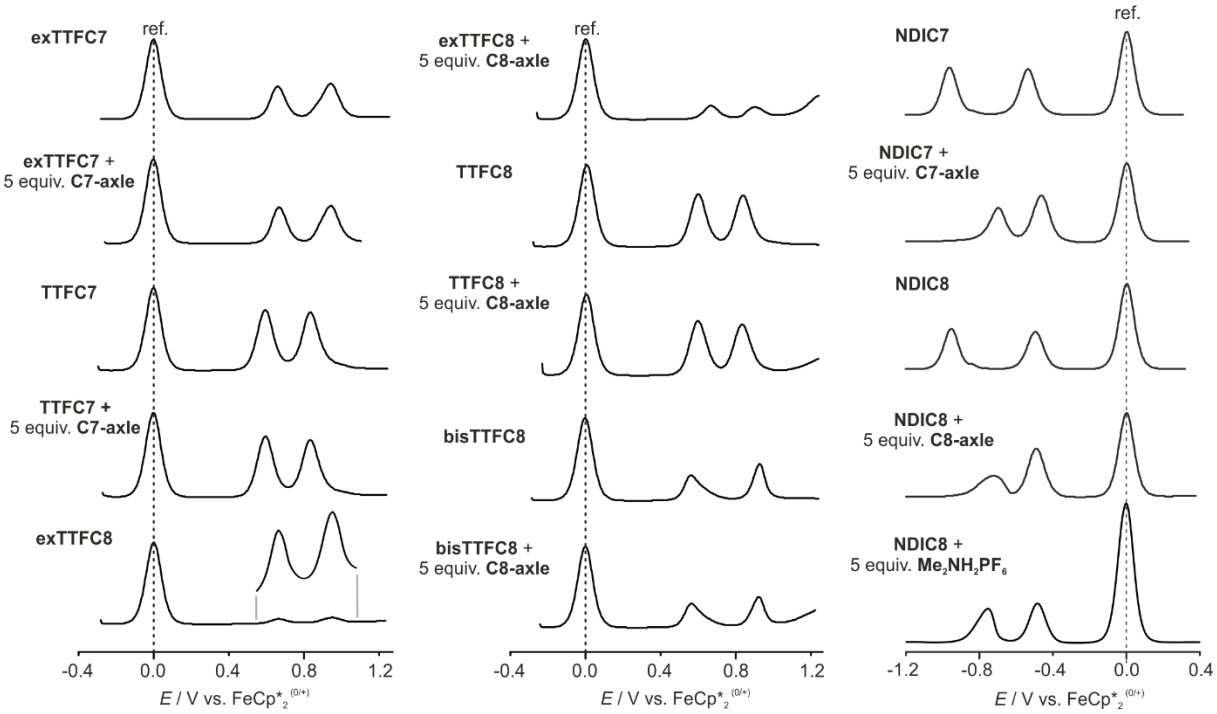

Figure S11: Differential pulse voltammogram (10 mV s^{-1} scan rate, 25 mV modulation amplitude, 50 ms modulation time, 5 mV step potential, 0.5 s interval time) and cyclic voltammogram (100 mV s^{-1}) of [2]rotaxane **NDIRot** (1.0 mM) in mixture of DCE/CH_3CN 1:1 and pure DCE (0.1 M *n*-Bu_4PF_6). The small signal at approximately −0.8 V was observed before adding the rotaxane and is addressed to an impurity. The decamethylferrocene/decamethylferrocenium couple was used as reference.

5. Rotaxane characterization

5.1. 2D NMR spectroscopy

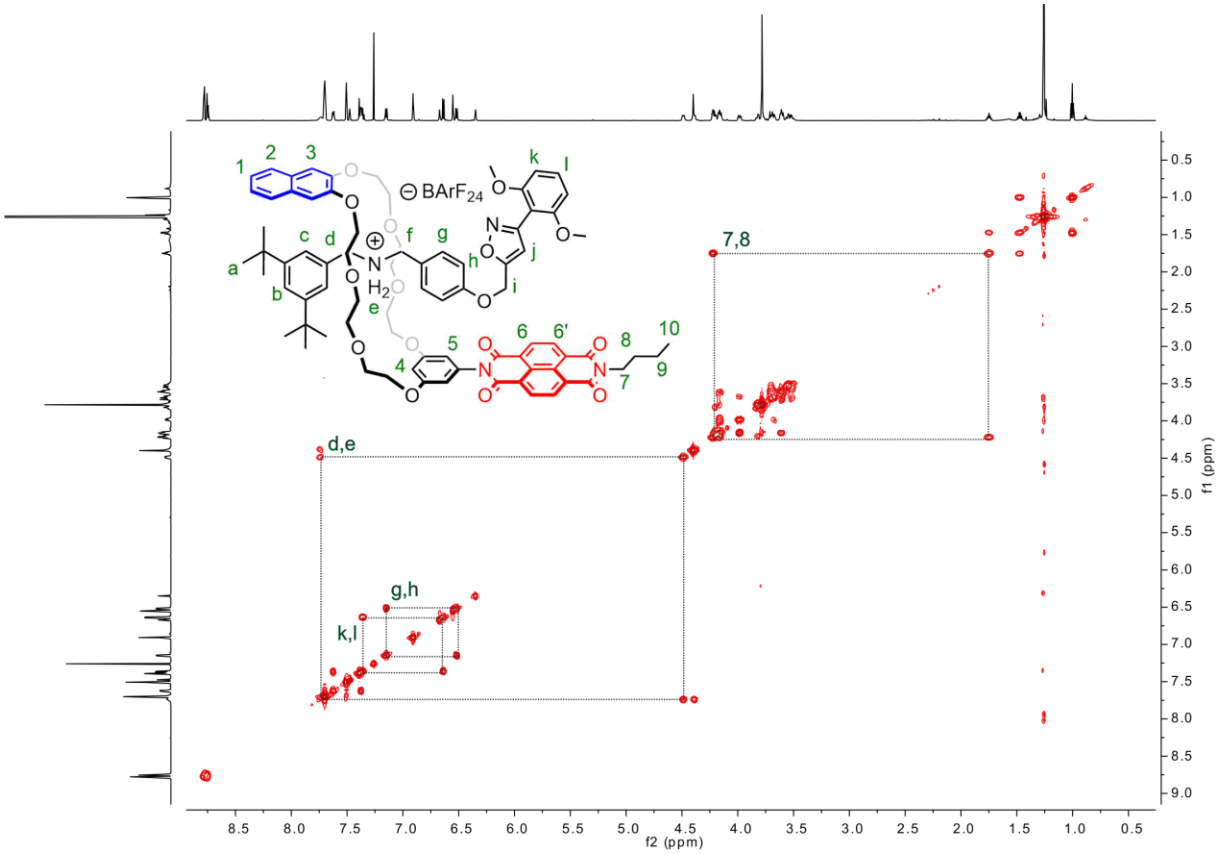

Figure S12: ^{1}H, ^{1}H COSY NMR spectrum (700 MHz, $CDCl_3$, 298 K) of rotaxane **NDIRot** with selected cross peaks for peak assignment.

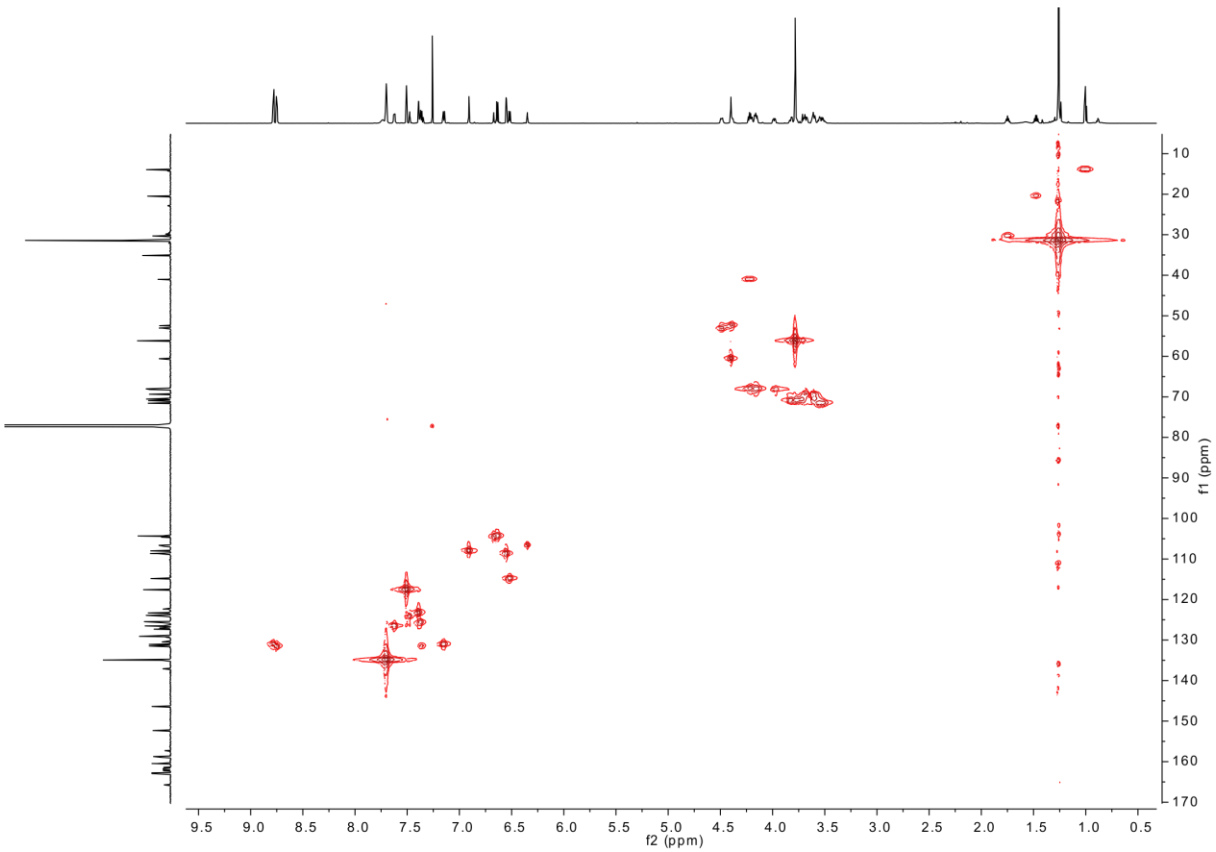

Figure S13: ^{1}H, ^{13}C HMQC NMR spectrum (700 MHz, $CDCl_3$, 298 K) of rotaxane **NDIRot**.

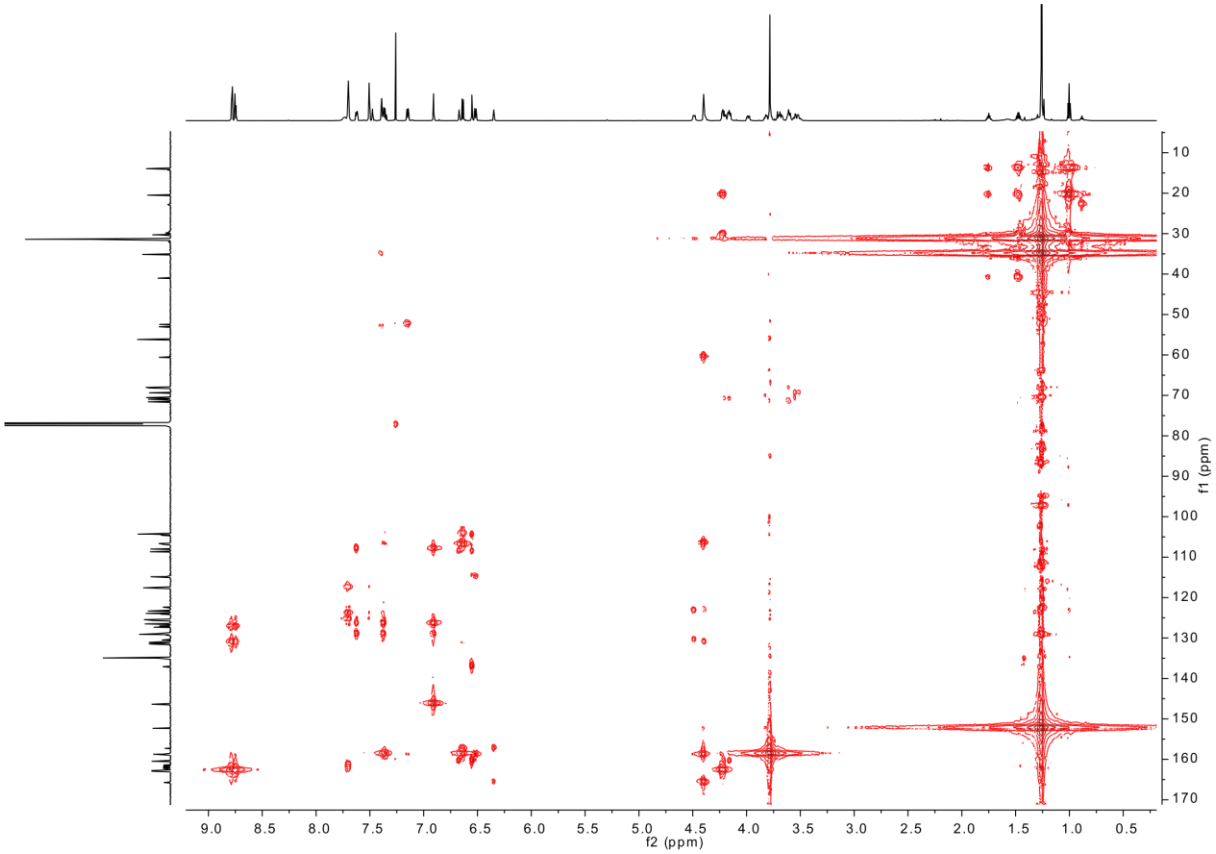

Figure S14: ^{1}H, ^{13}C HMBC NMR spectrum (700 MHz, $CDCl_3$, 298 K) of rotaxane **NDIRot**.

5.2. Tandem mass spectrometry

A Synapt G2-S HDMS (Waters Co., Milford, MA, USA) instrument with a quadrupole-time-of-flight high resolution mass detector was used to perform electrospray ionization tandem mass spectrometry. Employing collision-induced dissociation (CID) of mass-selected ions, using the following settings: flow rate 10 µL min^{-1}, capillary voltage 1.5 kV, sample cone voltage 34 V, source offset 54 V, source temperature 100 °C, desolvation temperature 20 °C, nebulizer gas 5 bar, desolvation gas flow 460 L h^{-1}. For CID, N_2 was used as the collision gas. Fragmentation experiments were conducted in the trap cell of the Synapt G2-S HDMS instrument with collision energies of 4–72 V. Data acquisition and processing was carried out using MassLynx™ (version 4.1).

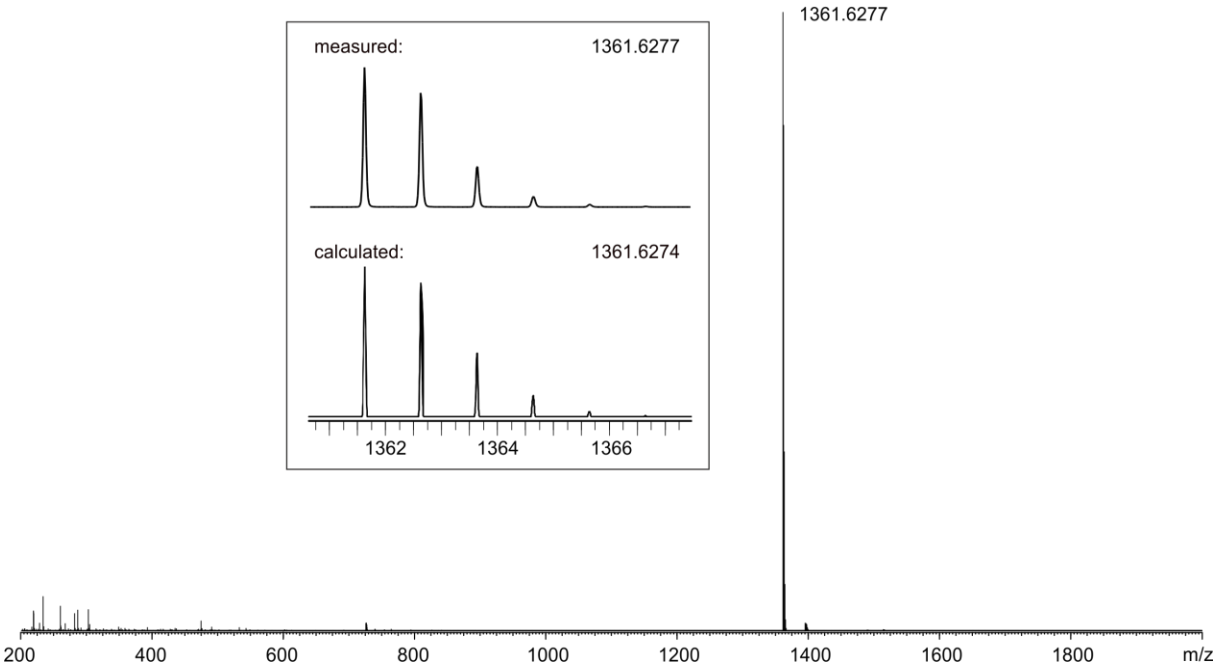

Figure S15: ESI-Q-TOF-HRMS spectrum of **NDIRot** (1 µM in CH_3CN); (inset) comparison of measured and calculated isotopic patterns.

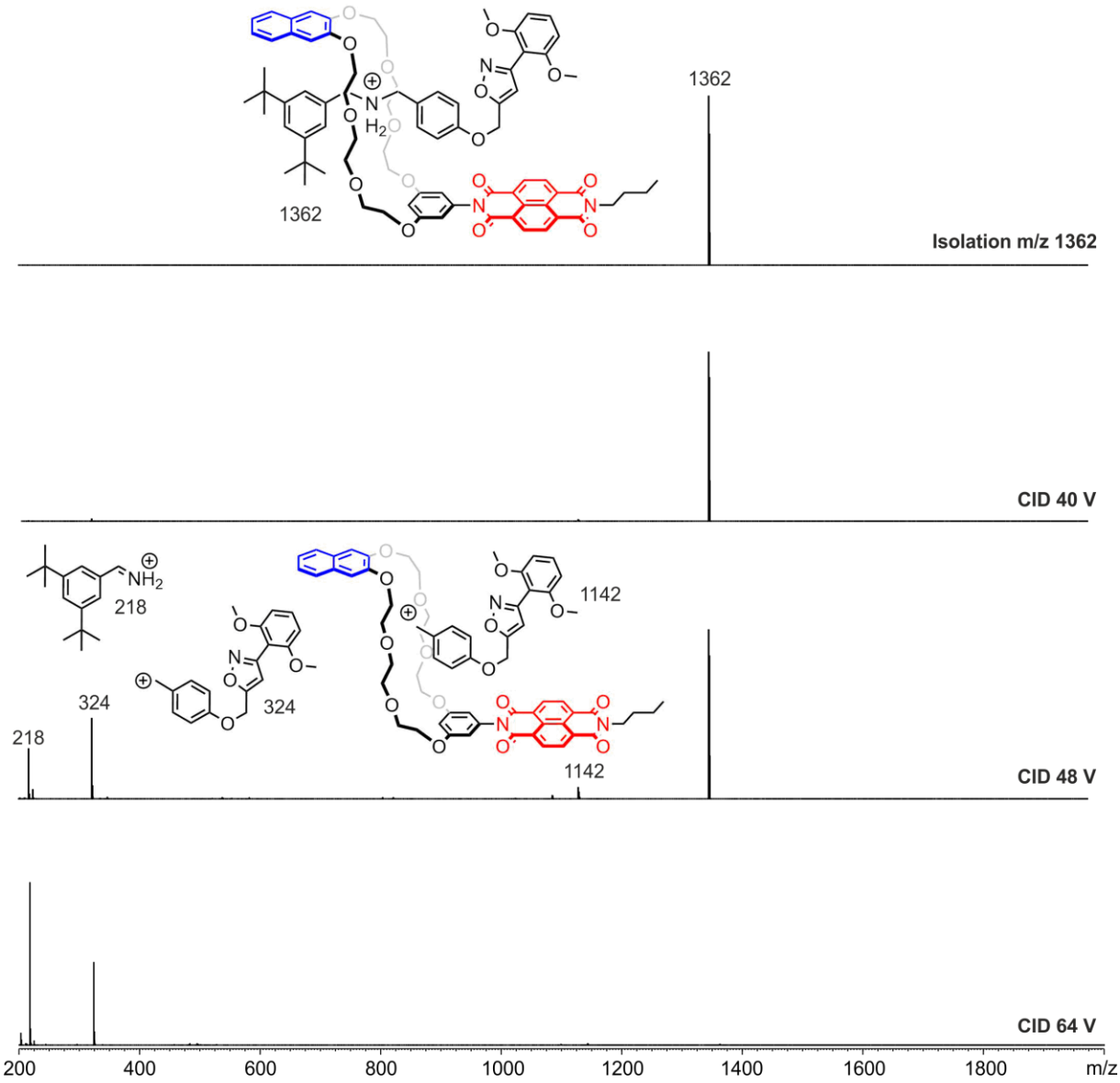

Figure S16: Collision-induced dissociation (CID) experiment with mass-selected rotaxane ions at *m/z* 1362 obtained from a CH_3CN solution (1 µM) of **NDIRot**: (top) after mass selection; (bottom) after fragmentation at different voltages. The fragment peaks could be assigned to ions formed by α-cleavage at the ammonium group of the axle. As no free axle (*m/z* 543) is observed in the fragmentation pattern, the interlocked structure of the selected rotaxane ion can be concluded.

6. Spectroelectrochemical measurements

UV–vis–NIR

The UV–vis–NIR spectroelectrochemistry measurements were performed on an Avantes spectrometer with an AvaLight-DH-S-Bal light source, an AvaSpec-ULS2048 UV/Vis detector, and an AvaSpec-NIR256-TEC NIR detector. Dry, freshly distilled and Argon purged solvents (CH_3CN and CH_2Cl_2) were used. The measurements were carried out in an optically transparent thin-layer electrochemical (OTTLE) cell (CaF_2 windows) with a platinum-mesh working electrode, a platinum-mesh counter electrode, and a silver-foil pseudoreference electrode. Voltammetric cycles between 0 and −1.2 V (vs. silver pseudoreference) were performed.

Table S3: Absorption maxima[a] (in nm) obtained by spectroelectrochemistry UV–vis–NIR measurements (0.1 M *n*-Bu_4PF_6, CH_2Cl_2/CH_3CN 1:1, 298 K).

oxidation state	NDIC7	NDIC8	NDIRot
NDI (0.0 V)	325, 342 (sh), 360, 380, 450 (sh)	324, 341 (sh), 359, 379	324, 341 (sh), 359, 379
$NDI^{\bullet-}$ (-0.6 V)	380, 402, 477, 528 (sh), 561 (sh), 592, 611, 674, 750	358, 380, 400, 476, 527 (sh), 589 (sh), 609, 685, 763	341, 359, 379, 399, 476, 527 (sh), 559 (sh), 589 (sh), 609, 689, 763
NDI^{2-} (-1.2 V)	379, 400, 422, 476, 549, 601, 675, 750	/[b]	/[b]

[a]sh = shoulder. [b]No significant band shifts and changes in absorbance were observed at more negative potential (−1.2 V vs silver wire), which can be explained by diffusion from the electrode and comproportionation of the doubly reduced species

Continuous-wave electron paramagnetic resonance spectroscopy

Continuous-wave electron paramagnetic resonance (CW-EPR) spectra at X-band frequency (ca. 9.5 GHz) were obtained with a Magnettech MS-5000 benchtop EPR spectrometer equipped with a rectangular TE 102 cavity and TC HO4 temperature controller. The measurements were carried out in synthetic quartz glass tubes. Dry, Argon purged and freshly distilled solvents were used. For the in situ preparation of the oxidized species, a three-electrode setup was employed using two Teflon-coated platinum wires (0.005″ bare, 0.008″ coated) as working and counter electrode and a Teflon-coated silver wire (0.005″ bare, 0.007″ coated) as pseudoreference electrode.

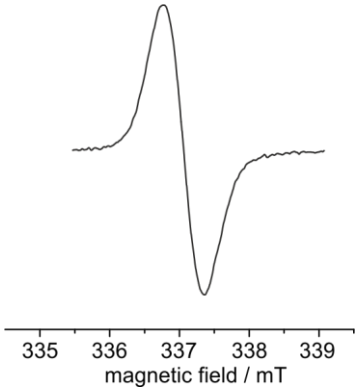

Figure S17: EPR spectroelectrochemistry measurements (0.1 M *n*-Bu_4PF_6, CH_2Cl_2/CH_3CN 1:1, 298 K) of radical species **NDIRot** (1 mM).

7. ^{1}H and ^{13}C NMR spectra

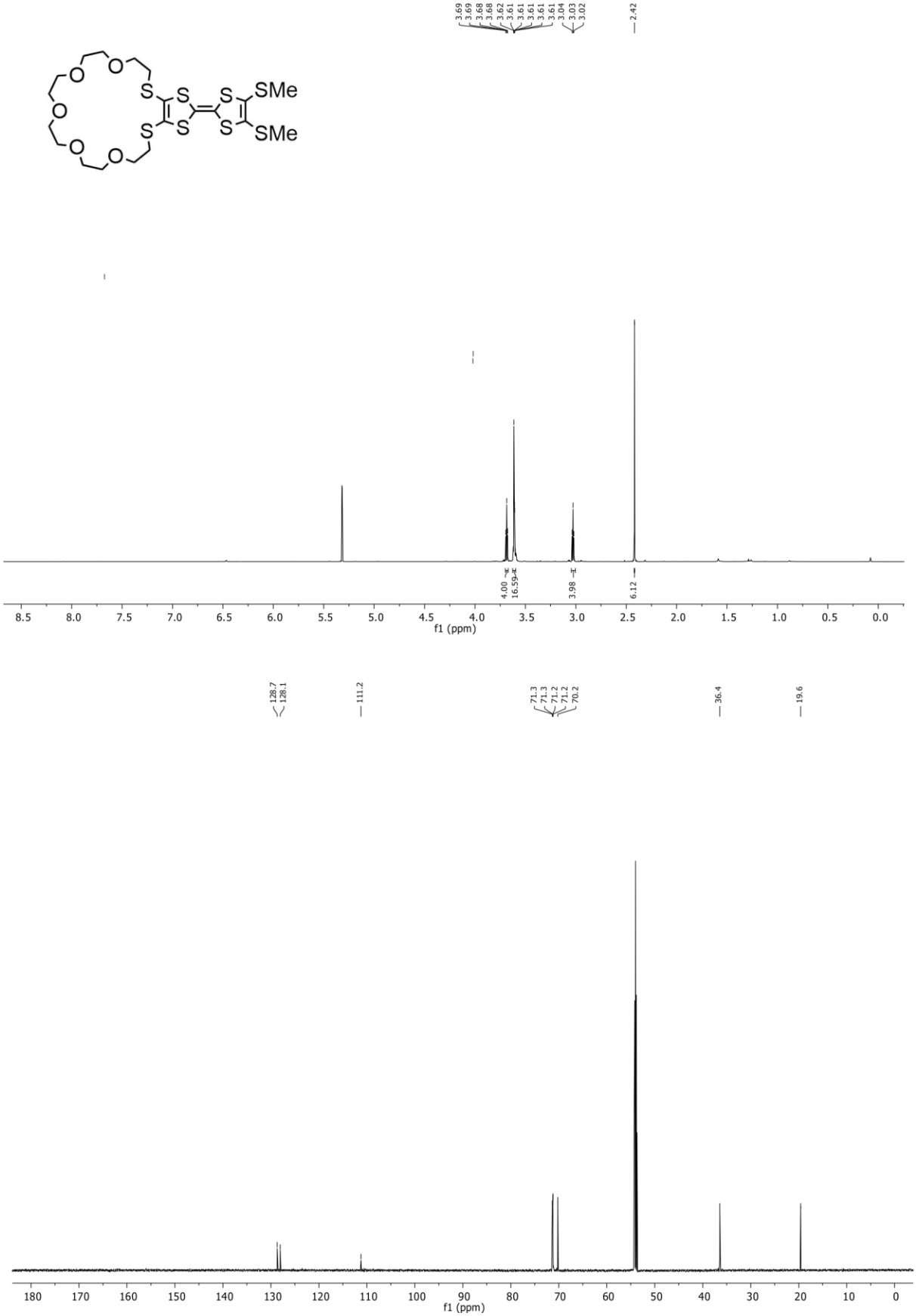

Figure S18: ^{1}H (top) and ^{13}C (bottom) NMR spectrum (700/176 MHz, CD_2Cl_2, 298 K) of **TTFC7**.

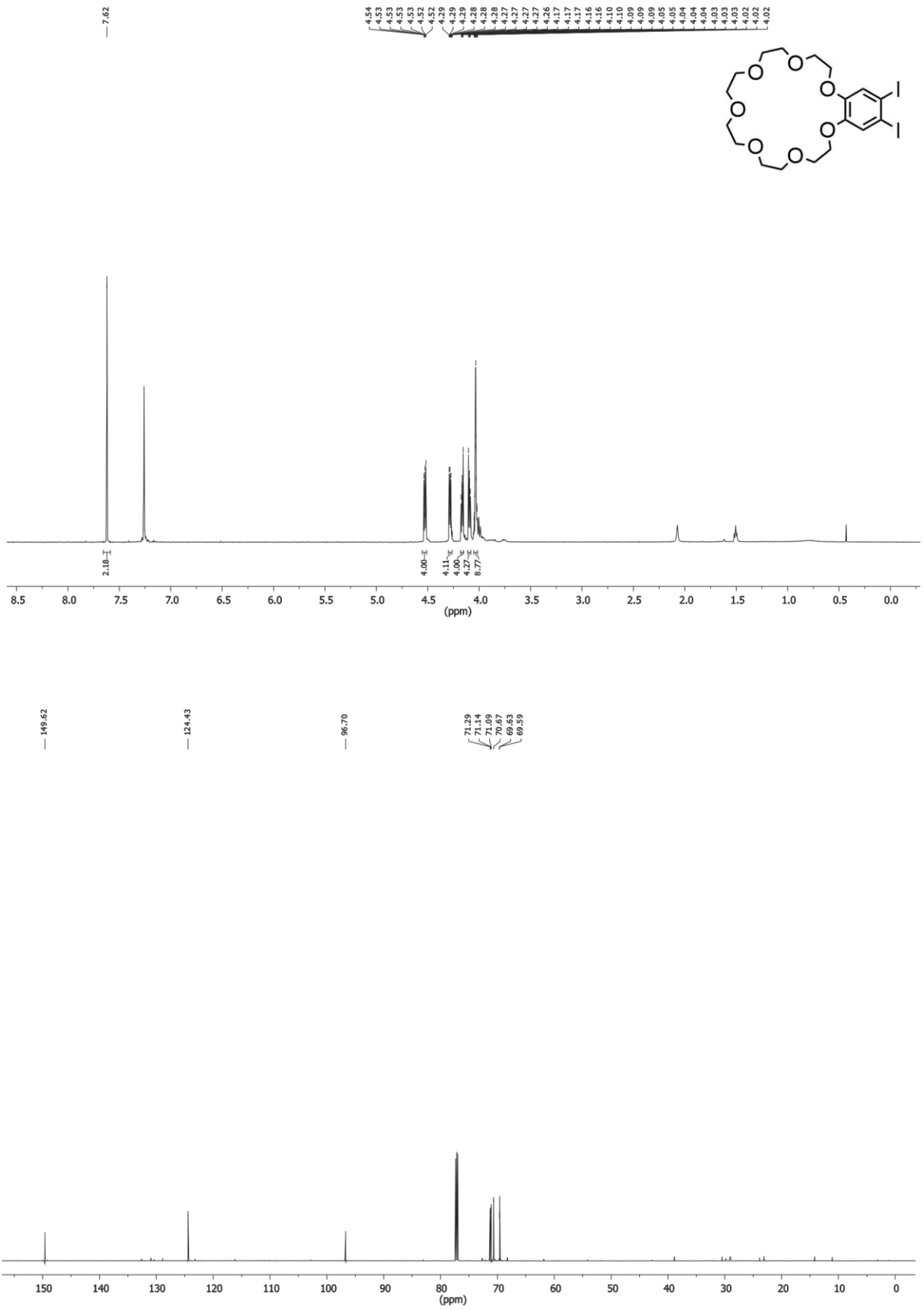

Figure S19: ^{1}H (top) and ^{13}C (bottom) NMR spectrum (500/176 MHz, $CDCl_3$, 298 K) of Diiodide **2**.

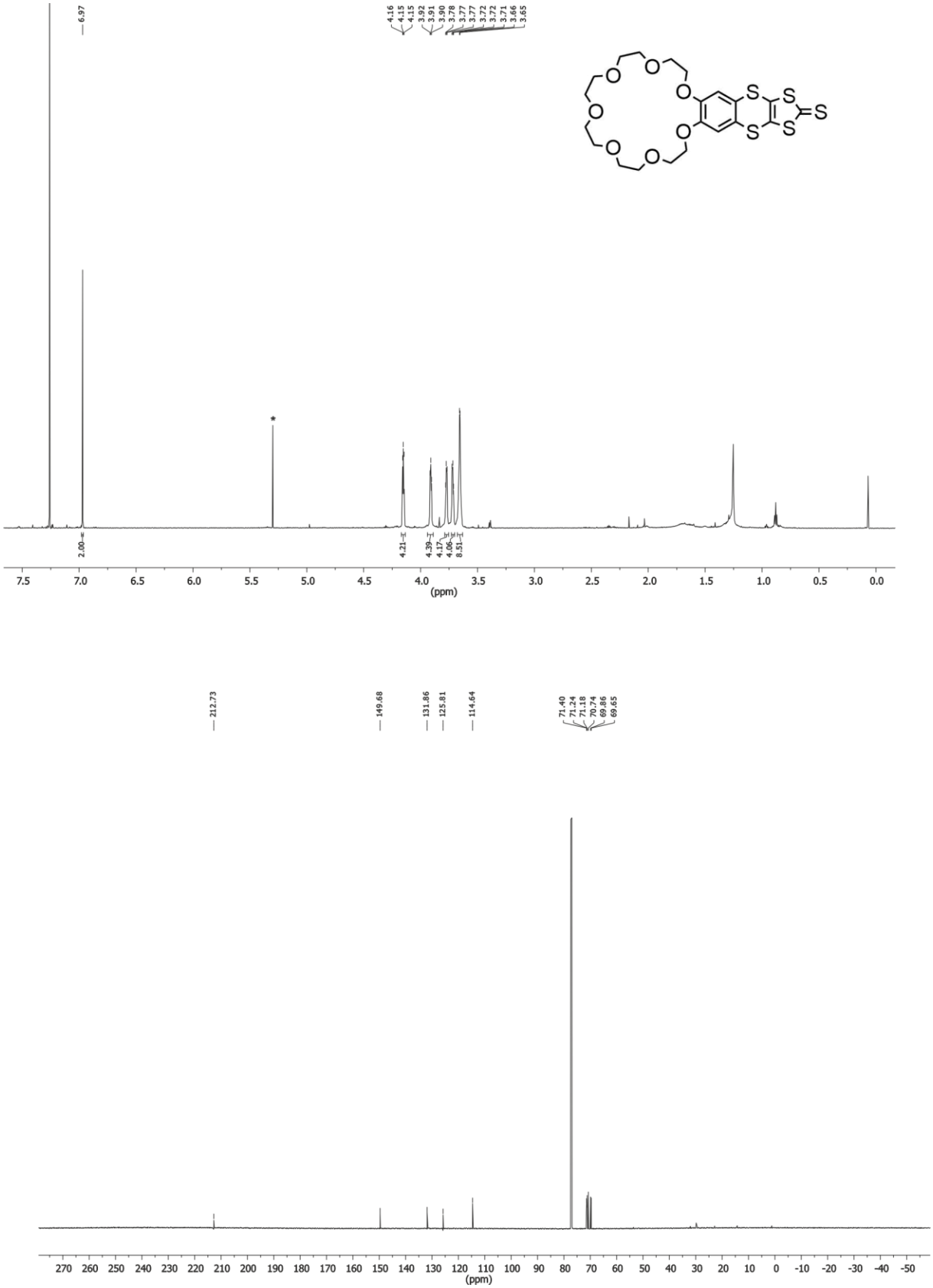

Figure S20: ^{1}H (top) and ^{13}C (bottom) NMR spectrum (500/176 MHz, $CDCl_3$, 298 K) of Thione **3**.

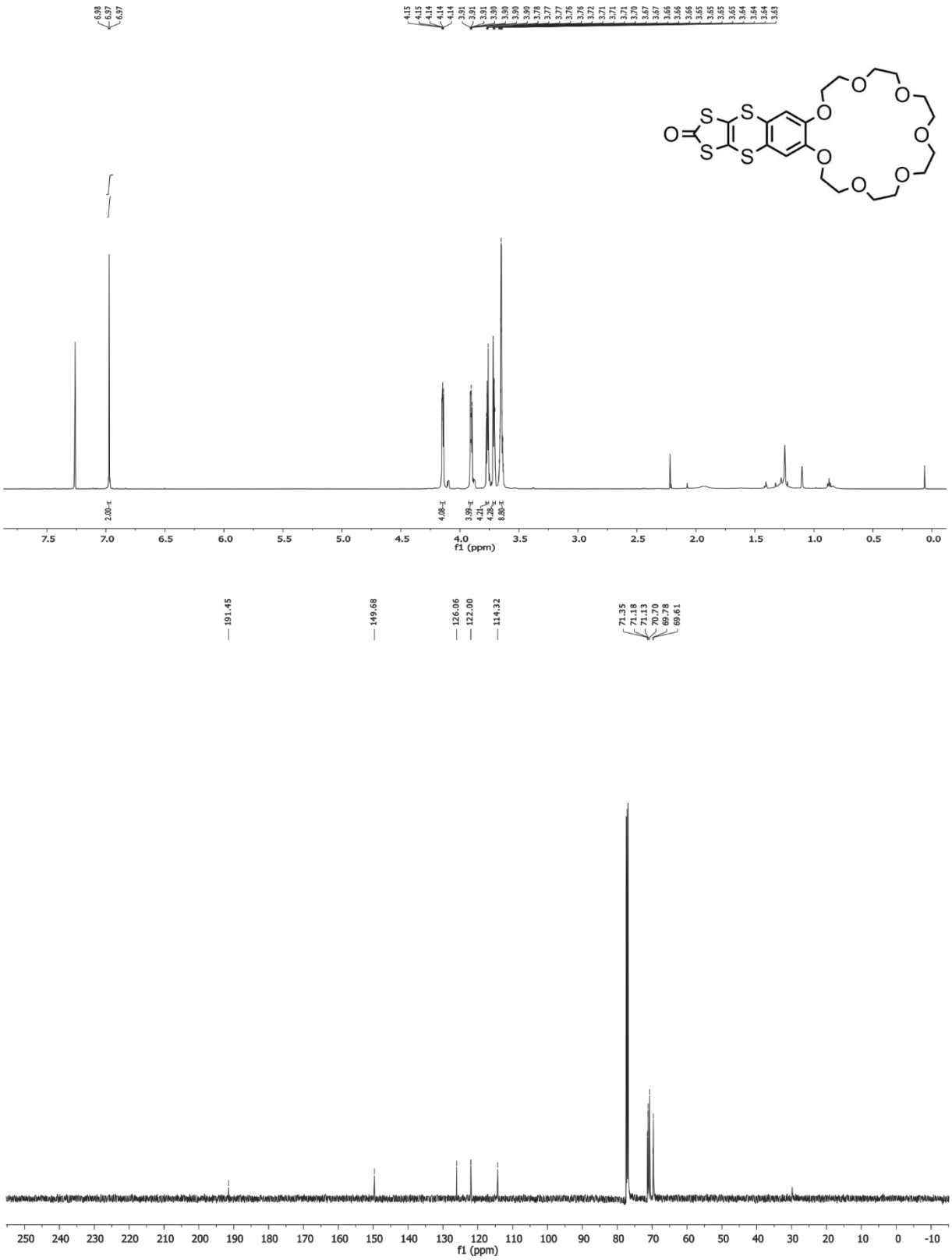

Figure S21: ^{1}H (top) and ^{13}C (bottom) NMR spectrum (500/176 MHz, $CDCl_3$, 298 K) of One **4**.

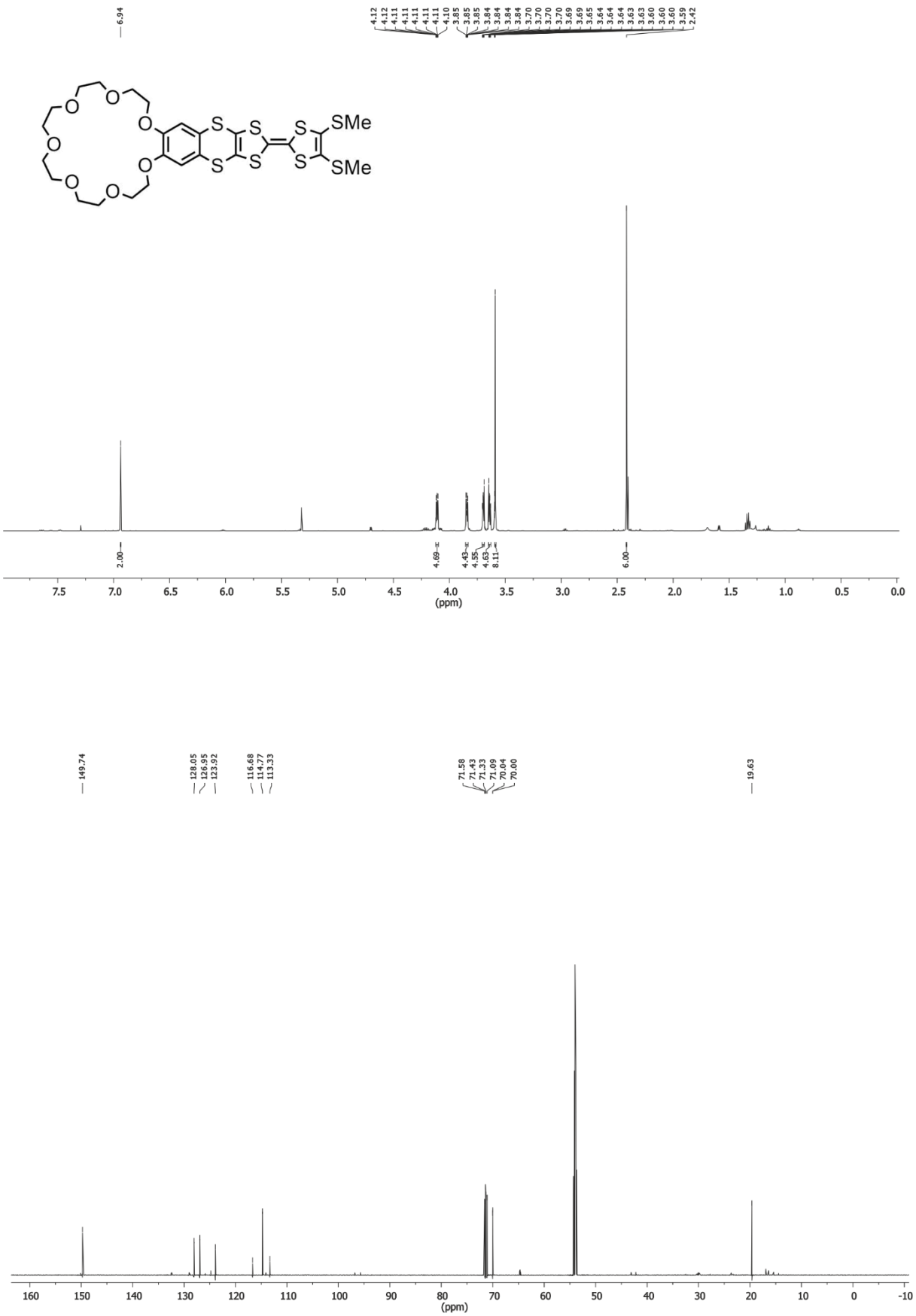

Figure S22: ^{1}H (top) and ^{13}C (bottom) NMR spectrum (700/176 MHz, CD_2Cl_2, 298 K) of **exTTFC7**.

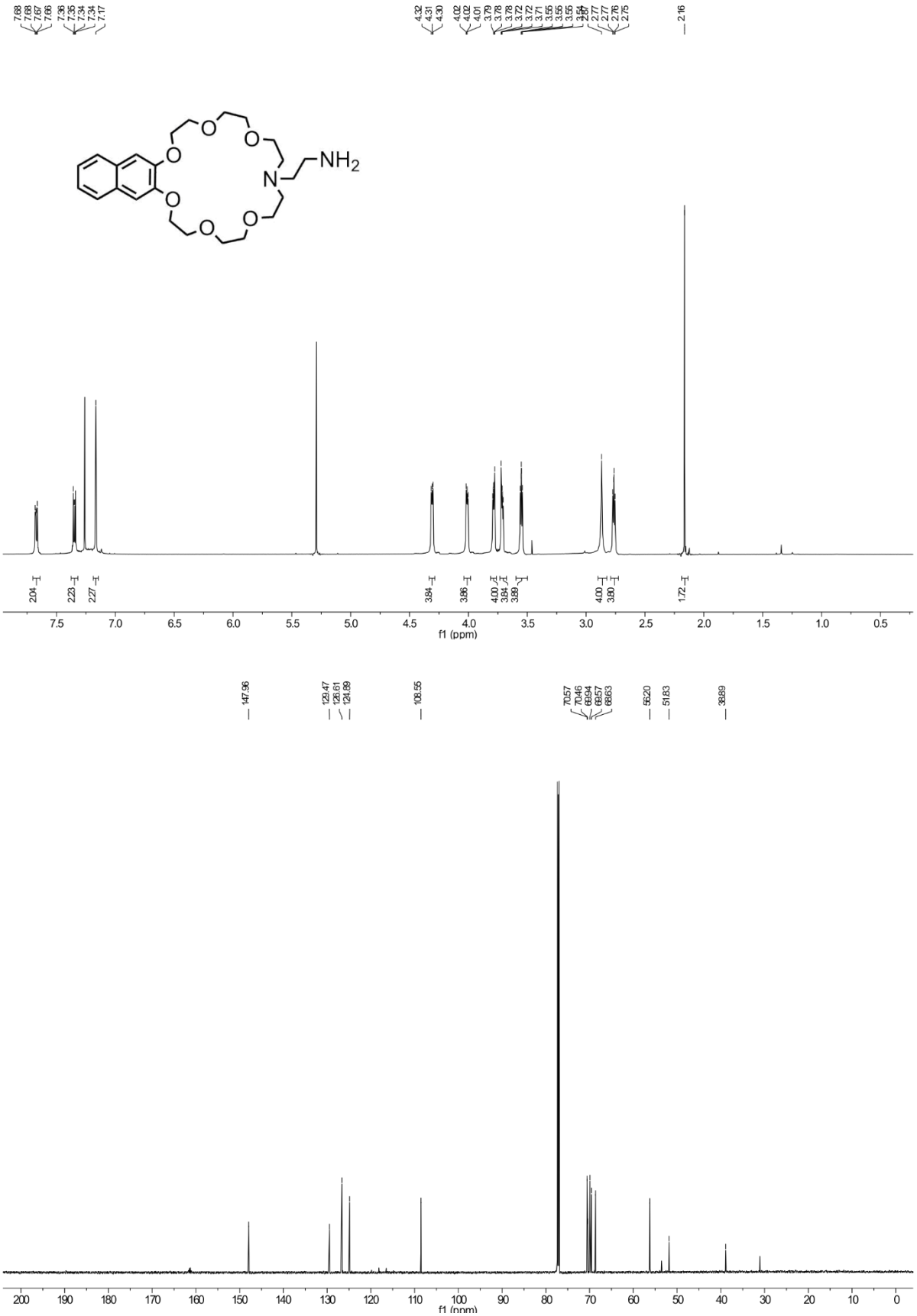

Figure S23: ^{1}H (top) and ^{13}C (bottom) NMR spectrum (500/176 MHz, $CDCl_3$ 298 K) of amine **6**.

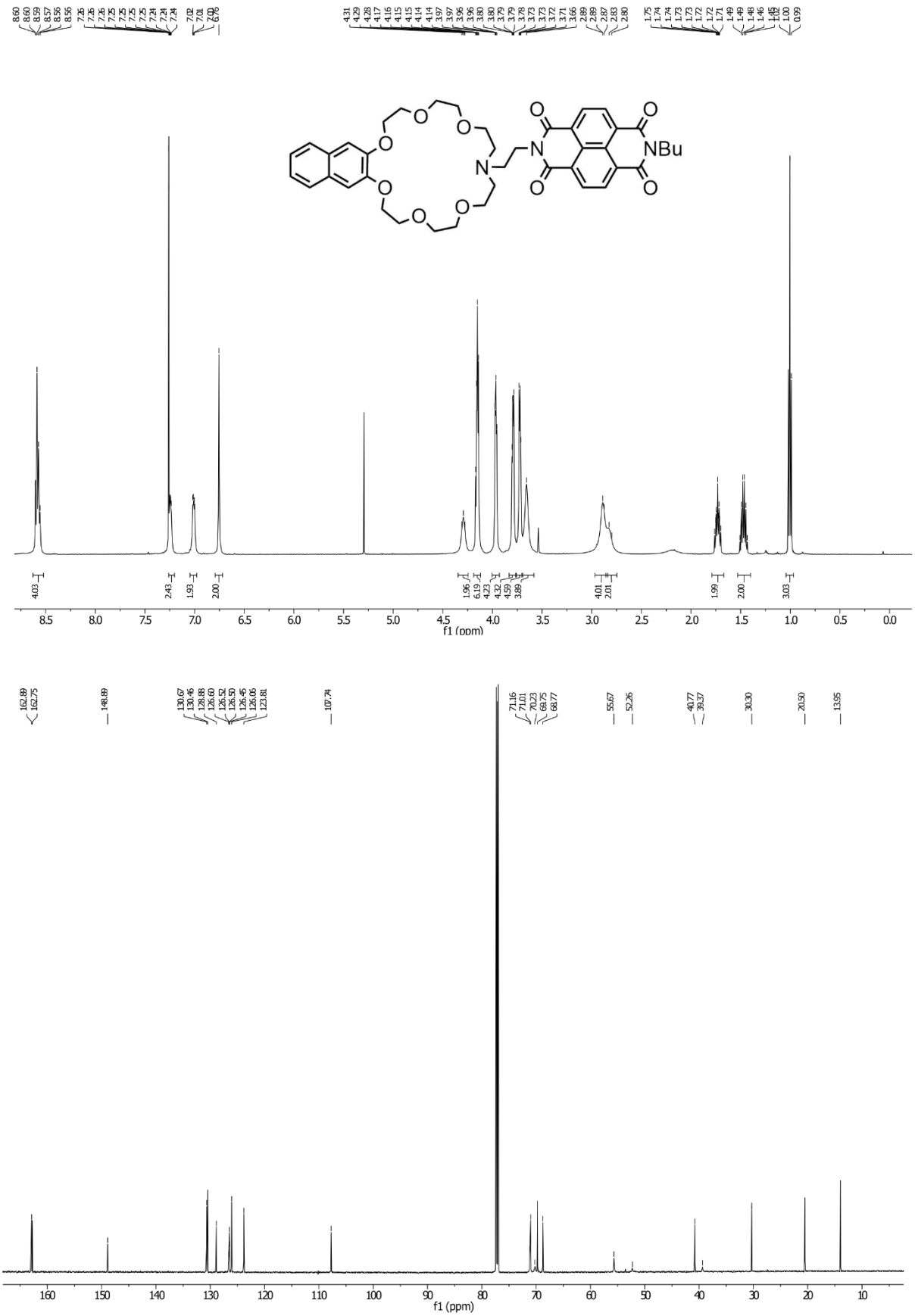

Figure S24: ^{1}H (top) and ^{13}C (bottom) NMR spectrum (500/176 MHz, $CDCl_3$, 298 K) of **NDIC7**.

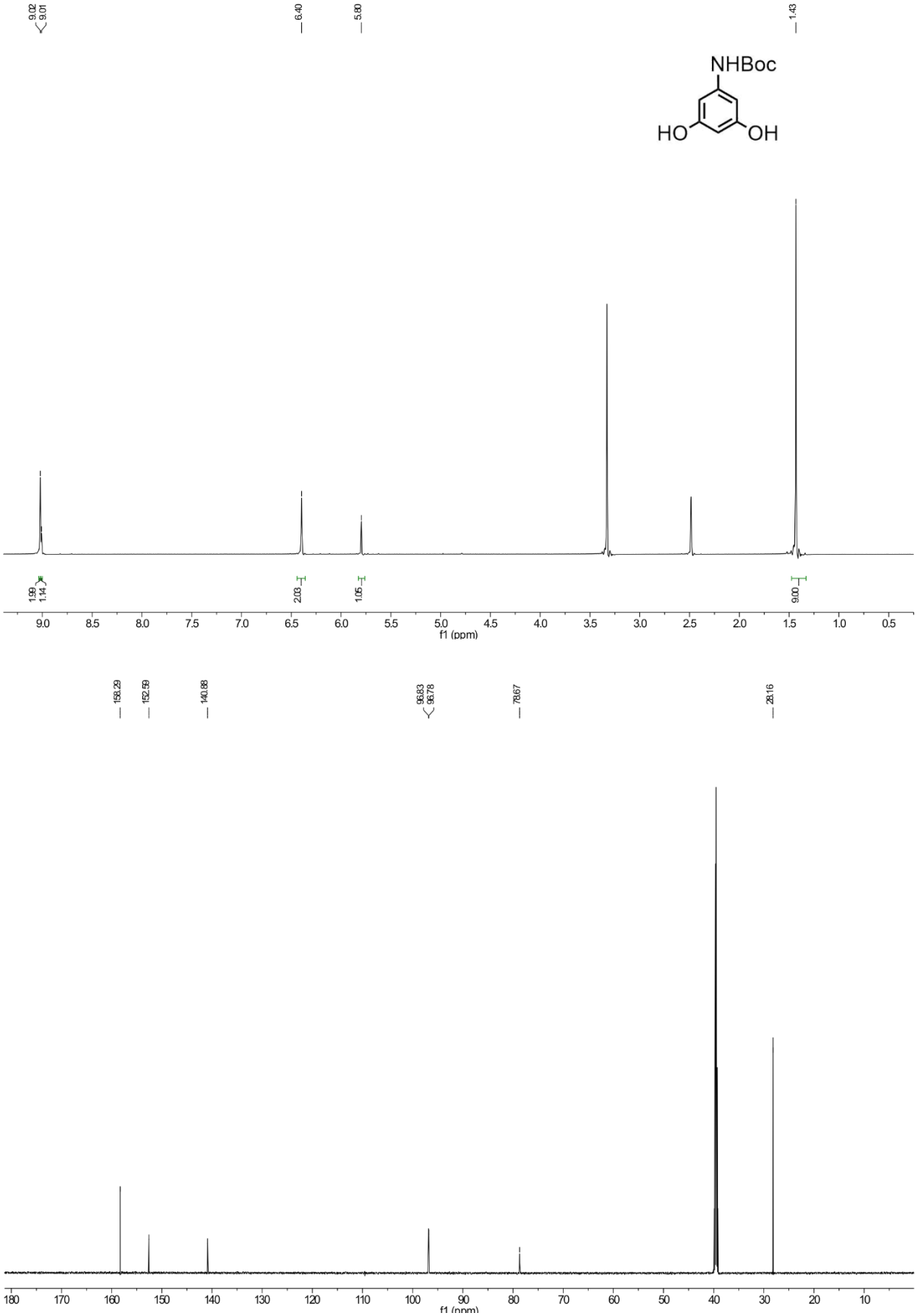

Figure S25: ^{1}H (top) and ^{13}C (bottom) NMR spectrum (700/176 MHz, $CDCl_3$, 298 K) of catechol **8**.

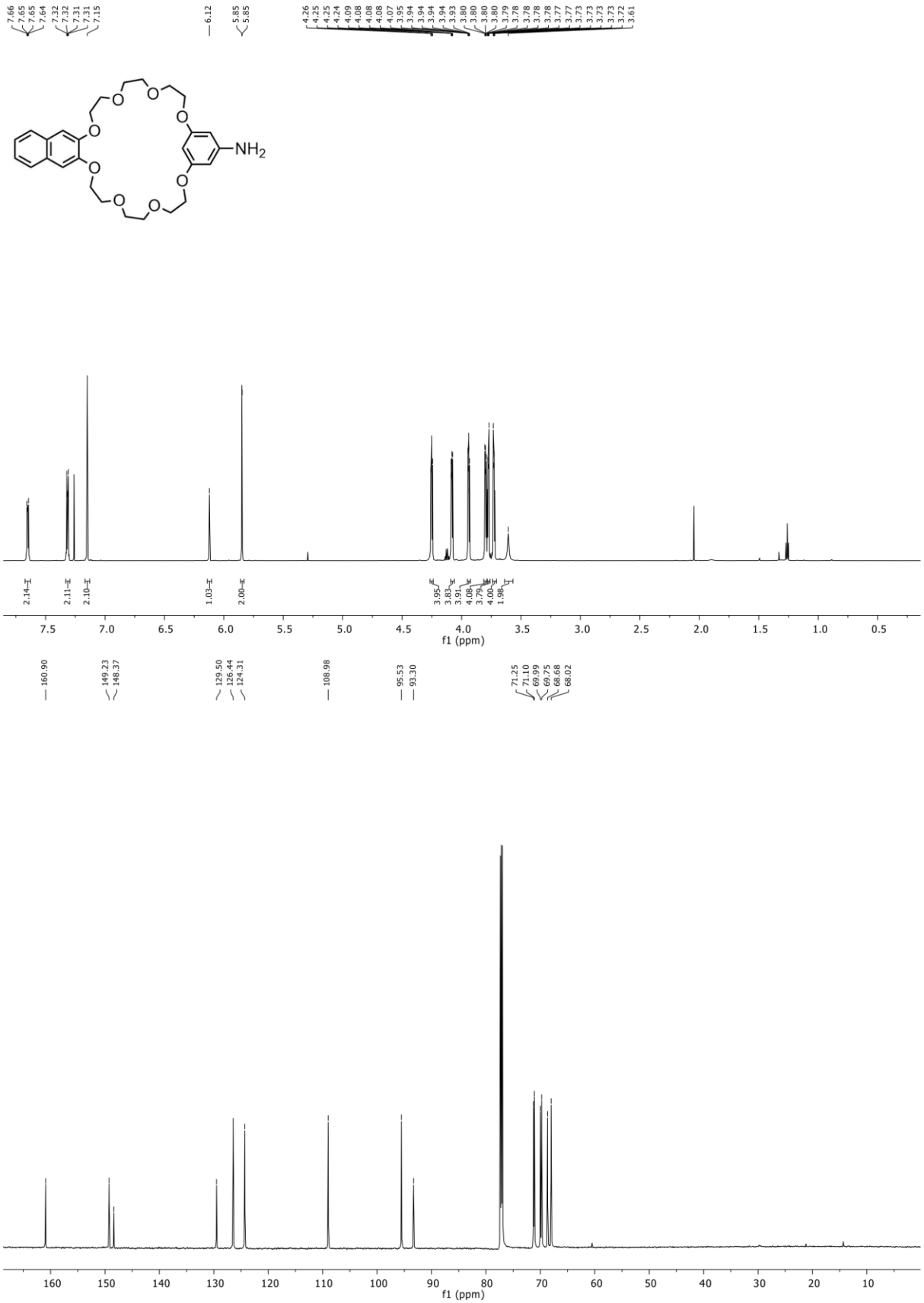

Figure S26: ^{1}H (top) and ^{13}C (bottom) NMR spectrum (700/176 MHz, $CDCl_3$, 298 K) of amine **9**.

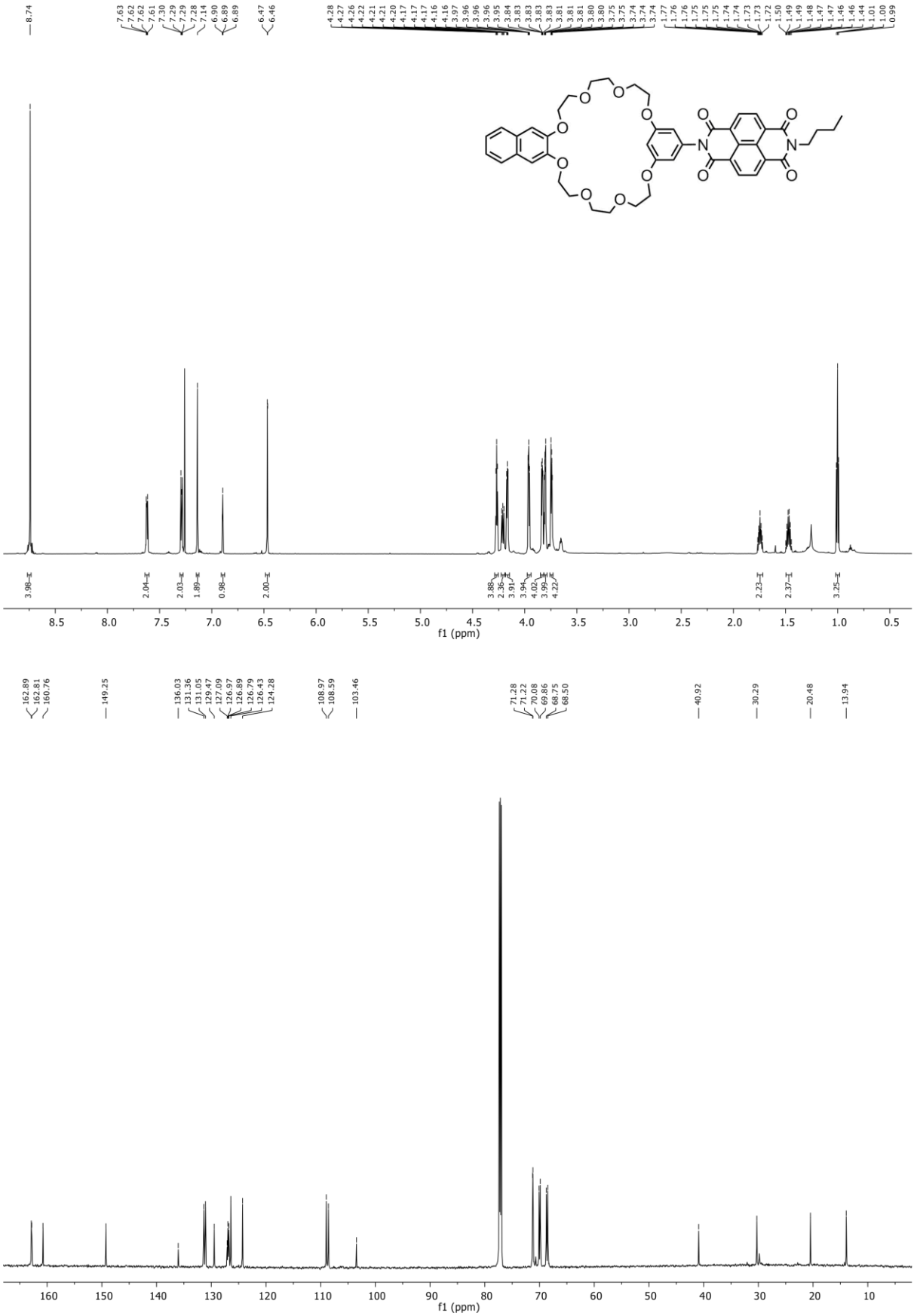

Figure S27: ^{1}H (top) and ^{13}C (bottom) NMR spectrum (700/176 MHz, $CDCl_3$, 298 K) of **NDIC8**.

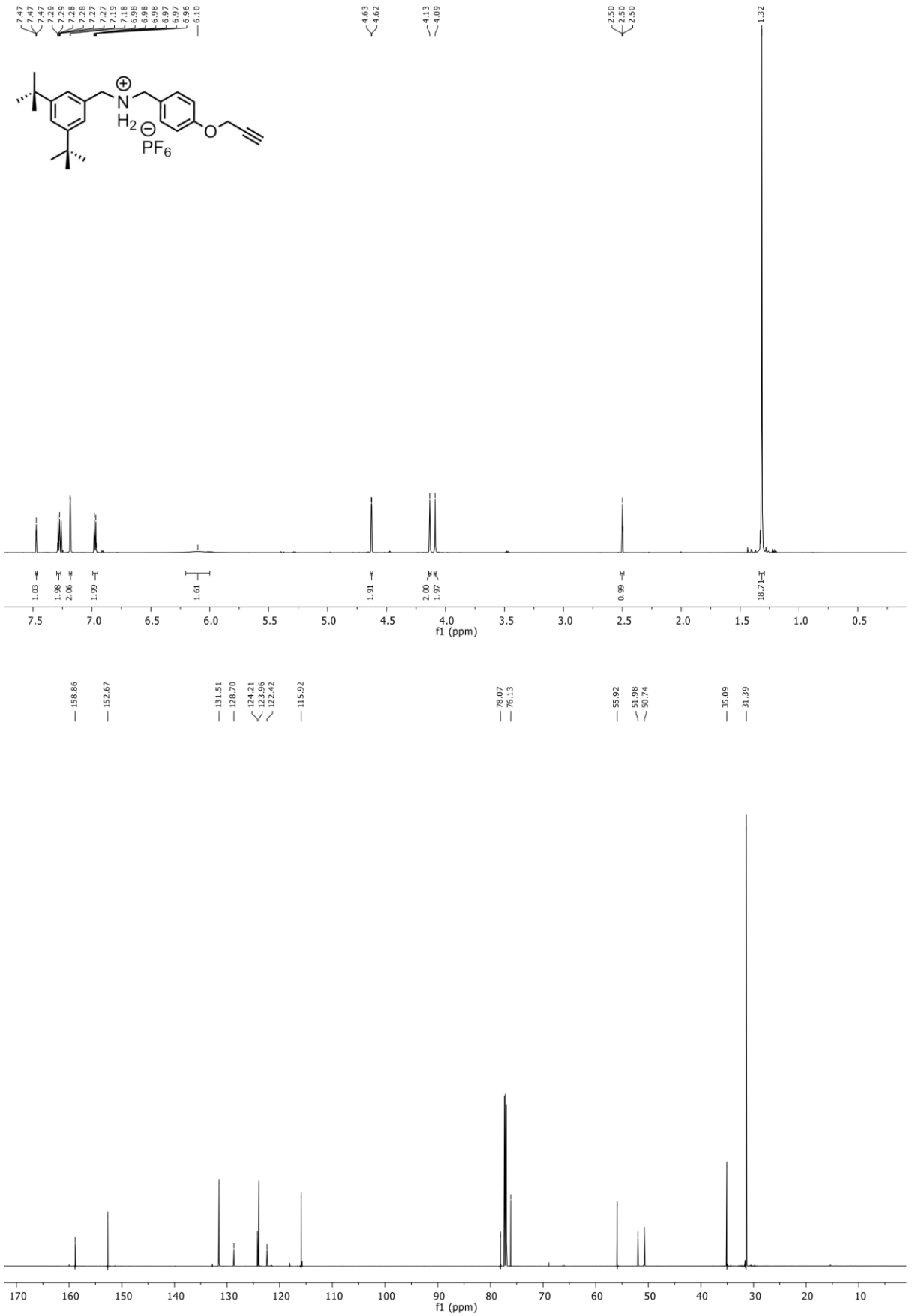

Figure S28: ^{1}H (top) and ^{13}C (bottom) NMR spectrum (700/176 MHz, $CDCl_3$, 298 K) of **A1**•PF_6.

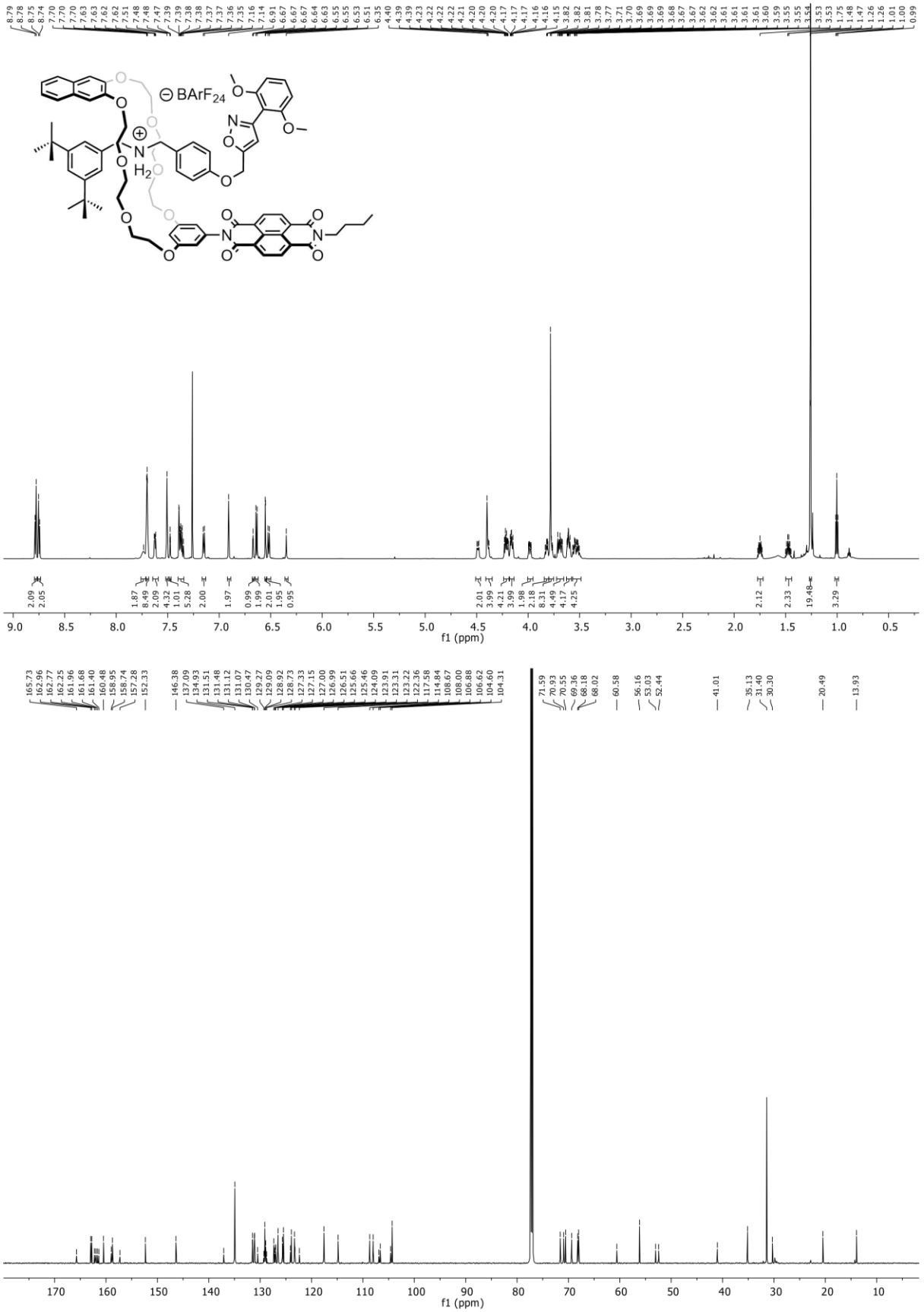

Figure S29: ^{1}H (top) and ^{13}C (bottom) NMR spectrum (700/176 MHz, $CDCl_3$, 298 K) of **NDIRot**.

8. References

1. N. Svenstrup, K. M. Rasmussen, T. K. Hansen, J. Becher, *Synthesis* **1994**, 809-812.

2. Y. Aoki, N. Umezawa, Y. Asano, K. Hatano, Y. Yano, N. Kato, T. Higuchi, *Bioorg. Med. Chem.* **2007**, *15*, 7108-7115.

3. W. Jiang, C. A. Schalley, *Beilstein J. Org. Chem.* **2010**, *6*, No. 14.

4. J. D. Badjic, C. M. Ronconi, J. F. Stoddart, V. Balzani, S. Silvi, A. Credi, *J. Am. Chem. Soc.* **2006**, *128*, 1489-1499.

5. H. Shao, T. Nguyen, N. C. Romano, D. A. Modarelli, J. R. Parquette, *J. Am. Chem. Soc.* **2009**, *131*, 16374-16376.

6. Z.-J. Zhang, H.-Y. Zhang, H. Wang, Y. Liu, *Angew. Chem. Int. Ed.* **2011**, *50*, 10834-10838.

7. C. Zhang, S. Li, J. Zhang, K. Zhu, N. Li, F. Huang, *Org. Lett.* **2007**, *9*, 5553-5556.

8. H. V. Schröder, S. Sobottka, M. Nößler, H. Hupatz, M. Gaedke, B. Sarkar, C. A. Schalley, *Chem. Sci.* **2017**, *8*, 6300-6306.

9. T. Matsumura, F. Ishiwari, Y. Koyama, T. Takata, *Org. Lett.* **2010**, *12*, 3828-3831.

10. *CrysAlisPro* (Version 1.171.39.43c.), Rigaku Oxford Diffraction, **2015**.

11. R. C. Clark, J. S. Reid, *Acta Crystallogr., Sect. A. Found. Crystallogr.* **1995**, *51*, 887-897.

12. G. M. Sheldrick, *Acta Crystallogr., Sect. A Found. Adv.* **2015**, *71*, 3-8.

13. G. M. Sheldrick, *Acta Crystallogr., Sect. C Struct Chem.* **2015**, *71*, 3-8.

14. G. M. Sheldrick, *Acta Crystallogr. , Sect. A Found. Crystallogr.* **2008**, *64*, 112-122.

15. C. B. Hübschle, G. M. Sheldrick, B. Dittrich, *J. Appl. Crystallogr.* **2011**, *44*, 1281-1284.

16. *in APEX3*, Bruker AXS Inc., Madison, Wisconsin, USA, **2015**.

17. G. M. Sheldrick, Version 2008/1, University of Göttingen, Germany, **2008**.

18. SAINT+, Version 8.27b © ed., Bruker AXS Inc., Madison, Wisconsin, USA, **1997-2012**.

19. G. M. Sheldrick, Version 2014/7 ed, University of Göttingen, Germany, **2014**.

20. J. R. Aranzaes, M.-C. Daniel, D. Astruc, *Can. J. Chem.* **2006**, *84*, 288-299.

6.7 Dual-stimuli pseudorotaxane switches under kinetic kontrol

M. Gaedke, H. Hupatz, H.V. Schröder, S. Suhr, K.F. Hoffmann, A. Valkonen, B. Sarkar, S. Riedel, K. Rissanen, C.A. Schalley

Org. Chem. Front. **2021**, *8*, 3659-3667.

Submitted on March 31, 2021, first published on April 29, 2021 by the Chinese Chemical Society (CCS), Shanghai Institute of Organic Chemistry (SIOC) and the Royal Society of Chemistry.

An electronic version of the articles is available at: https://doi.org/10.1039/D1QO00503K

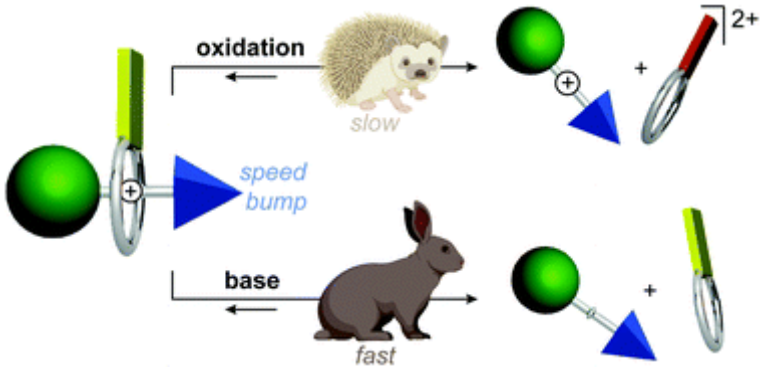

Figure 6.7. Graphical abstract. Reprinted from Gaedke *et al.*[130] with permission from the Chinese Chemical Society (CCS), Shanghai Institute of Organic Chemistry (SIOC), and the Royal Society of Chemistry (published under the CC BY-NC 3.0 licence).

Authors' contributions

Marius Gaedke developed the general concept of this project with help of Hendrik V. Schröder. Marius Gaedke, Hendrik V. Schröder, Christoph A. Schalley, and me wrote the manuscript with main contributions from Marius Gaedke. The synthetic work was carried out by Marius Gaedke, Kurt F. Hoffmann and Hendrik V. Schröder. Marius Gaedke carried out the time dependent NMR, as well as UV/Vis, CV and MS measurements. Kurt F. Hoffmann, Sebastian Riedel and Marius Gaedke conducted the low temperature, oxidation and deprotonation NMR experiments. I measured and analysed the ITC data. I performed tandem mass spectrometry and analysed the data. Marius Gaedke prepared the single crystals. Simon Suhr and Biprajit Sarkar conducted the bulk electrolysis. Arto Valkonen, and Kari Rissanen measured and solved the SCXRD data. All Authors contributed to the final version of the manuscript.

ORGANIC CHEMISTRY FRONTIERS

RESEARCH ARTICLE

View Article Online
View Journal | View Issue

Cite this: *Org. Chem. Front.*, 2021, **8**, 3659

Dual-stimuli pseudorotaxane switches under kinetic control†‡

Marius Gaedke, [a] Henrik Hupatz,[a] Hendrik V. Schröder, §[a] Simon Suhr,[b] Kurt F. Hoffmann, [c] Arto Valkonen, [d] Biprajit Sarkar, [b] Sebastian Riedel, [c] Kari Rissanen [d] and Christoph A. Schalley *[a]

A series of dumbbell-shaped *sec*-ammonium salts with bulky (pseudo)stoppers ('speed bumps') were tested for their ability to form pseudorotaxanes with a redox-switchable, tetrathiafulvalene (TTF)-decorated [24]crown-8 ether. Depending on the size of the pseudostoppers, fast (less than ten minutes), slow (hours to days) and very slow (no pseudorotaxanes observed) threading has been observed. NMR spectroscopy as well as tandem mass spectrometry indicate the formation of non-threaded face-to-face complexes prior to pseudorotaxanes formation. Both isomers can be distinguished by their substantially different stability in collision-induced dissociation (CID) experiments. Two external stimuli affect the stability of the pseudorotaxanes: Deprotonation of the ammonium ion results in fast dethreading, while dethreading is much slower when induced by the charge repulsion upon chemical oxidation of the TTF moiety. Remarkably, the same steric bulk of the pseudostopper thus leads to different dethreading rates depending on the stimulus applied. Based on these findings, two redox-switchable rotaxanes containing a 1-naphthyl and a phenyl moiety as sterically different 'speed bumps' in the axle centre were synthesised. Bulk electrolysis of the rotaxanes did not result in the expected macrocycle translocation on the axle independent of the 'speed bump' as a remarkable consequence of the mechanical bond.

Received 31st March 2021,
Accepted 28th April 2021

DOI: 10.1039/d1qo00503k

rsc.li/frontiers-organic

Introduction

Artificial molecular switches[1] are controlled by external chemical,[2,3] light,[4,5] or electrochemical[6] stimuli. In mechanically interlocked molecules (MIMs) such as rotaxanes and catenanes, stimuli-induced switching manipulates the interactions of the wheels with their binding sites on the other component in a controlled manner.[7,8] Pseudorotaxanes are non-interlocked, but threaded axle-wheel complexes able to dissociate without breaking a covalent bond. Depending on the bulkiness of the axle end groups, they encompass a broad range of dethreading rates with the rotaxane at the very end, where no wheel exchange takes place (Fig. 1a).[9] Thus, (pseudo)rotaxanes allow us to study stimuli-induced switching with and without wheel exchange. In rotaxanes, the wheel's translational freedom is limited to the track provided by the axle[10] and switching can be converted into directed co-conformational changes, which can propel artificial molecular motors and machines.[7,8,11] The impact of the wheel exchange rate on dual-stimuli-induced switching has not been studied for kinetically hindered pseudorotaxanes, but rather for pseudorotaxanes with fast exchange or for rotaxanes (no exchange). This raises an interesting question: Can different stimuli applied to a dual-stimuli-responsive *and* kinetically hindered pseudorotaxane result in different timescales for dethreading over a 'speed bump' pseudostopper, even when the steric size of the 'speed bump' remains unchanged?

The energy landscapes of switchable (pseudo)[2]rotaxanes change, when stimuli are applied. In Fig. 1, which exemplarily depicts an acid/base- *and* redox-switchable pseudorotaxane (Fig. 1b and c) and its 'speed bump' containing rotaxane analogue (Fig. 1d and e), the yellow dots represent the (pseudo) rotaxane populations. Initially, the wheels reside on the binding site. Upon applying one of the two stimuli, the former binding site becomes disfavoured and the macrocycles migrate over the blue 'speed bump'. For the pseudo[2]rotaxane, the wheel is released from the axle over the barrier caused by the

[a]*Institut für Chemie und Biochemie der Freien Universität Berlin, Arnimallee 20, 14195 Berlin, Germany. E-mail: c.schalley@fu-berlin.de*
[b]*Lehrstuhl für Anorganische Koordinationschemie, Institut für Anorganische Chemie, Universität Stuttgart, Pfaffenwaldring 55, 70569 Stuttgart, Germany*
[c]*Institut für Chemie und Biochemie der Freien Universität Berlin, Fabeckstr. 34/36 14195, Berlin, Germany*
[d]*Department of Chemistry P.O. Box 35, 40014 Jyväskylä, Finland*

† Dedicated to Prof. Placido Neri upon the occasion of his 60th birthday.

‡ Electronic supplementary information (ESI) available. CCDC 2073308. For ESI and crystallographic data in CIF or other electronic format see DOI: 10.1039/d1qo00503k

§ Present address: Dr H. V. Schröder Department of Chemical and Biological Engineering, Princeton University, Princeton, NJ08544, USA

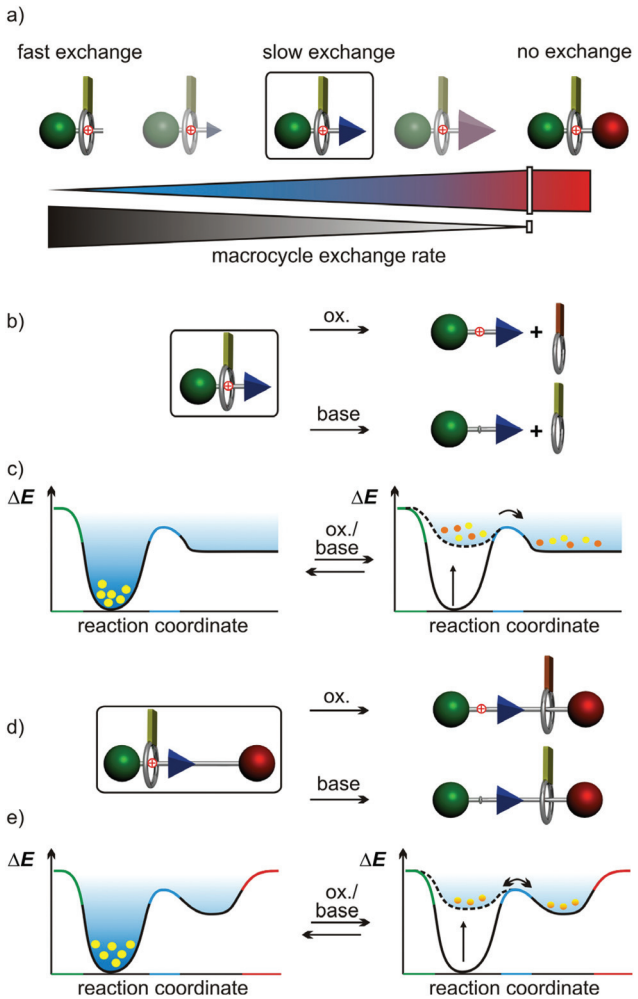

Fig. 1 (a) Range of macrocycle exchange rates from a quickly reversible pseudorotaxane formation (light blue, small 'speed bump') to a fully interlocked rotaxane (red stopper). (b) Stimuli-induced shuttling or unthreading and (c) the corresponding changes of the energy landscapes of a pseudorotaxane as well as (d and e) of a rotaxane (stoppers: green/red, steric 'speed bump' in the axle: blue, TTF oxidation states in yellow (reduced)/orange (oxidized to TTF^{2+}).

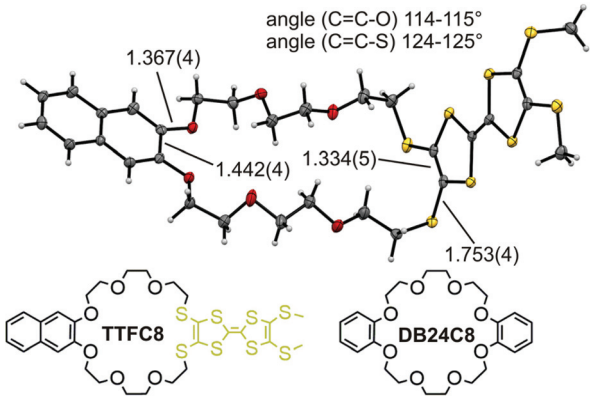

Fig. 2 Solid-state structure of **TTFC8** with selected bond lengths (Å) and angles.

pseudostopper, while the wheel cannot escape from the axle in the [2]rotaxane. It will nevertheless move across the 'speed bump' back and forth and a new equilibrium distribution of positional isomers is finally reached on a time scale depending on the 'speed bump' size.

From the broad variety of available binding motifs,[12,13] *sec*-ammonium/crown ether (pseudo)rotaxanes provide an easy access to dual-stimuli-responsive compounds that allow us to investigate the above question in detail. In this motif, a crown ether encircles the ammonium ion with binding constants typically in the range of 10^2 to 10^6 M^{-1} in non-protic organic solvents. In thermodynamic terms, ammonium ions form threaded complexes depending on the number of hydrogen bonds (including C–H···O hydrogen bonds involving the methylene groups next to the ammonium ion), charge distribution and ion pair separation energies of the ammonium salt.[14,15] Only face-to-face interactions are possible,[16] when the axle end groups are sterically too bulky. A large number of pseudo[2]rotaxanes with different crown ether sizes and different end groups have been reported to form in a broad variety of solvents.[17–19] In marked contrast, only few examples of rotaxanes with 'speed bumps' along their axles have been studied to unravel the influence of the mechanical bond.[20–25] The studies on shuttling in crown ether rotaxanes mostly focus on degenerate shuttles with two or more equivalent binding sites.[20,24] However, non-degenerate shuttles are more suitable for directional movement,[26] among which only very few are responsive to both acid/base and redox stimuli.[27]

Here, we make use of the *sec*-ammonium/crown ether binding motif and describe a series of pseudorotaxanes responsive to both stimuli with differently sized and differently shaped pseudostoppers. The ammonium/crown ether interaction can be disrupted by deprotonation of the ammonium group with a strong base.[28] Introducing a tetrathiafulvalene (TTF) into the crown ether (**TTFC8**, Fig. 2) implements also the second stimulus: Two-electron oxidation of the TTF unit to its dication induces coulombic repulsion between the wheel and the ammonium station and is expected to lead to dethreading as well.[29,30] Hence, these dual-stimuli-responsive pseudorotaxanes allow comparing the dethreading rates after deprotonation with those after oxidation, while maintaining the same steric bulk of the 'speed bump' pseudostopper. After identifying a suitable pseudostopper in pseudorotaxane dethreading experiments, this 'speed bump' can be integrated into a rotaxane axle to investigate co-conformational changes in the dual-stimuli-responsive [2]rotaxane, in which the mechanical bond prevents dethreading.

Results and discussion

The wheel: crystal structure of TTFC8

The redox-active wheel **TTFC8** used in this study was synthesized as reported earlier.[29] This macrocycle and the commercially available and widely used dibenzo[24]crown-8 ether (**DB24C8**) have the same number of 24 atoms along their cir-

cumference. Nevertheless, the substitution of two catechol oxygen by sulfur atoms affects both the structure and the conformational properties of the ring,[31] as becomes clear, when comparing the new solid state structure of **TTFC8** (Fig. 2, also see ESI section 8‡) with the known structure of **DB24C8**.[31]

The naphthalene-substituted side of **TTFC8** only shows a minor elongation in the central C=C bond (1.44 Å compared to 1.41 Å for **DB24C8**), the C–O bond lengths and C=C–O angles are virtually the same (1.37 Å and 115°). Although a shorter central C=C bond (1.33 Å) can be found on the TTF side, the C–S bond lengths (1.75 Å *vs.* 1.37 Å) and C=C–S bond angles (125° *vs.* 115°) notably enlarge the macrocycle cavity on the TTF-substituted side consistent with other published thiacrown derivatives.[32–34] The S atoms are *exo* to the ring rather than *endo*, like the oxygens on the other side. The effect of the structure on binding ammonium guests was investigated in our previous paper.[30]

Threading experiments

To test whether these differences in ring annulus lower the barrier to overcome bulky substituents, various *sec*-ammonium axles were synthesised as tetrakis(3,5-bis(trifluoromethyl) phenyl) borate ($BArF_{24}^-$) salts to compensate for the reduced binding constants of the thiacrown (see ESI section 5‡ for details).[29] Using $BArF_{24}^-$ with respect to PF_6^- results in a 10 to 20-fold increase of the binding constant.[30] The axles only differ in their terminal groups on one side (shown in blue in Fig. 3). As a guideline for the pseudostopper size and shape literature data available for **DB24C8**-based (pseudo–)rotaxanes with PF_6^- counterions was used.[16,19,35]

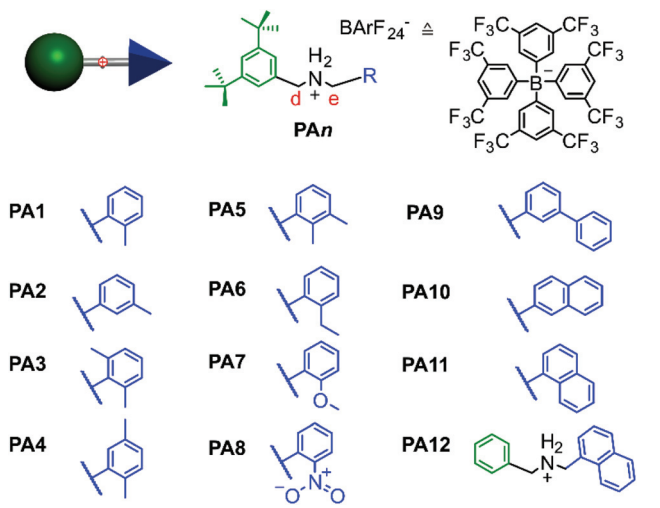

Fig. 3 The synthesised axles PA*n*.

The axles were mixed with either **DB24C8** or **TTFC8** in a 1 : 1 ratio in CD_2Cl_2. ^{1}H NMR spectra were taken at regular intervals to compare the half-lives ($t_{1/2}$) of the threading reactions for 4 mM solutions at room temperature by following the changing integrals of the $C\underline{H}_2$–NH_2–$C\underline{H}_2$ signals (see Table 1 and ESI section 2 Fig. S27–41‡ for the NMR spectra). Upon threading, the two methylene group signals shift downfield ($\Delta\delta \geq +0.2$ ppm). Furthermore, diastereotopic splitting of the crown ether methylene groups is observed for the pseudorotaxanes due to the directionality of the axle.[16,36]

An initial kinetic screening categorizes the axles into three groups. The first group (**PA1**, **PA2**, **PA4**, **PA8**, **PA9** and **PA10**) shows complete conversion into the threaded complex with **TTFC8** and **DB24C8** within less than 10 min. The second group (**PA5**, **PA6**, **PA7** and **PA11**) reveals half-lives in the range of hours to days. In addition, **PA5**, **PA6** and **PA7** form pseudorotaxanes with **TTFC8**, but not with **DB24C8** (even within 14 days). Both crown ethers can, however, pass the 1-naphthalene pseudostopper of **PA11** to form threaded complexes. Here, the slightly larger **TTFC8** threaded onto the axle approximately 120 times more quickly. Finally, no sign of threading is observed for **PA3** neither with **DB24C8** nor **TTFC8** within 14 days. These results are in good agreement with a recent study by Credi *et al.*[19] which also showed the 3,5-dimethyl phenyl moiety to be an efficient stopper in **DB24C8** containing rotaxanes[37–40] and identified the 2,6-dimethyl phenyl moiety as kinetically inert to threading of **DB24C8**.[19] Consequently, out of these candidates we chose **PA11** (1-naphthyl) as the most suitable pseudostopper for dual-stimuli-induced switching experiments, because threading occurs at time intervals that are conveniently observable by NMR spectroscopy.

In summary, the slight differences in size and shape apparent from the comparison of the crystal structures clearly affect the threading kinetics even though **TTFC8** and **DB24C8** share the same number of atoms in the wheel circumference.

Face-to-face complexes *vs.* pseudorotaxanes

In order to obtain some orienting insight into the thermodynamic binding properties of **PA11**, axle **PA12** has been synthesized, which allows fast threading of **TTFC8** over the phenyl group. The association constant obtained by isothermal titration calorimetry amounts to $K_a = (3.9 \pm 0.7)\ 10^5\ M^{-1}$ (ΔG° =

Table 1 Screening of threading timescales in model pseudo[2]rotaxanes PA*n*@MC and their corresponding half-lives $t_{1/2}$ for **DB24C8** and **TTFC8** threading monitored by ^{1}H NMR (4 mM in $CD_2Cl_2/CDCl_3$ 400/500 MHz at r.t.)

Entry[a]	PA1	PA2	PA3	PA4	PA5	PA6	PA7	PA8	PA9	PA10	PA11
DB24C8	<10 min	<10 min	≫14 days	<10 min	≫14 days	≫14 days	≫14 days	<10 min	<10 min	<10 min	10 days
TTFC8	<10 min	<10 min	≫14 days	<10 min	50 h	14 days	22 h	<10 min	<10 min	<10 min	2 h

[a] Axles denoted with "≫14 days" were considered to be not suitable for this study. It does not necessarily exclude a threaded complex to be achievable over time with suitable temperature and concentration.

(-31.9 ± 0.4) kJ mol^{-1}, ΔH° = (-44.1 ± 1.2) kJ mol^{-1}, $T\Delta S^{\circ}$ = (-12.2 ± 1.6) kJ mol^{-1}; also, see ESI section 5 and Table S2†). This binding data is very similar to that of the symmetrical dibenzylammonium axle (**DBA**) (K_a = (7.7 ± 1.0) 10^5 M^{-1} (ΔG° = (-33.6 ± 0.3) kJ mol^{-1}, ΔH° = (-39.8 ± 1.0) kJ mol^{-1}, $T\Delta S^{\circ}$ = (-6.2 ± 1.3) kJ mol^{-1}). We therefore assume the binding data for **PA11** to be in a similar range.

An ITC experiment with **PA11** was also attempted with titration intervals of 20 min to account for the slow threading. Remarkably, very sharp heat signals were observed. The quick heat evolution is not consistent with the slow pseudorotaxane formation as observed in ^{1}H NMR experiments. Obviously, the axle and the crown ether quickly form a non-threaded complex (Fig. 4a),[16] for which an upper limit for K_a of *ca.* 10^4 M^{-1} is estimated (see ESI section 5 and Fig. S53‡). ^{1}H NMR experiments confirm this face-to-face complex formation that is expressed in a minor shift for the methylene protons next to the ammonium moiety. These signals vanish slowly over time with the appearance of pseudorotaxane signals (Fig. S41‡).

Besides the evidence from ITC and NMR experiments, tandem mass spectrometry complements the picture. As one can expect the face-to-face complexes to easily dissociate in the gas phase upon collision-induced dissociation (CID), the dethreading of the pseudorotaxanes should require higher collision energies due to the steric barrier caused by the pseudostopper. Fig. 4b shows the survival yield curves for **PA11@TTFC8** separately prepared and isolated by column chromatography (blue) in comparison to a mixture of **PA11** and **TTFC8** subjected to the collision experiment 5 (red) and 135 minutes (black) after sample preparation. The red curve is indicative of a complex, which fragments at rather low collision voltages ($E_{1/2}$ = 9.8 ± 0.2 V). A small amount of 5% of the complex remains intact and half of it is fragmented at *ca.* 39 V. The blue curve shows only one, more stable complex ($E_{1/2}$ = 39.2 ± 0.4 V). For the sample taken after 135 min roughly 40% of the complex fragment at the lower collision voltage, while 60% fragment at the higher one. Clearly, two differently stable complexes form, *i.e.* the instantly forming face-to-face complex and the pseudorotaxane, which increases in abundance over time. This nicely shows the conversion of the instantly formed, but weaker non-threaded complex (lower equilibrium constant K_1, but higher rate constant k_1) into the pseudorotaxane (higher equilibrium constant K_2, but lower rate constant k_2).

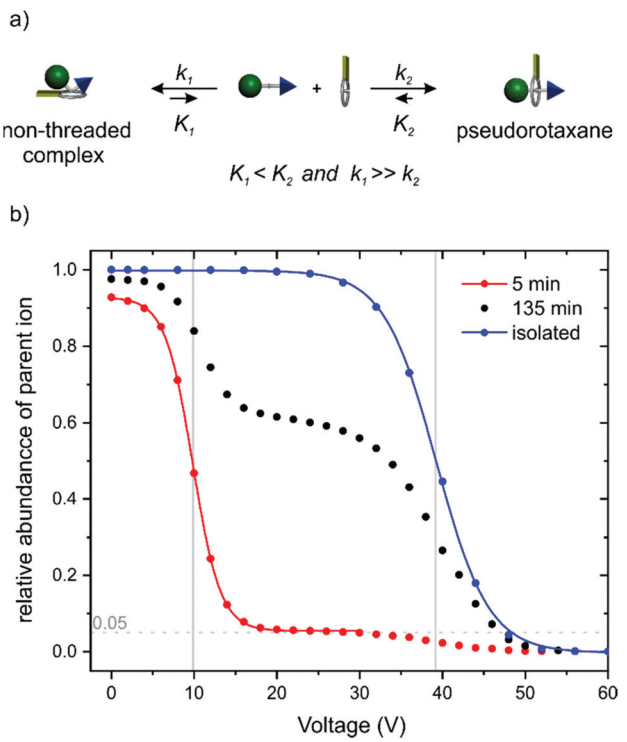

Fig. 4 (a) Schematic representation of the equilibrium for face-to-face complexation which competes with the formation of **PA11@TTFC8**. (b) Survival yield curves obtained for mass-selected [**PA11**·**TTFC8**]$^+$ ions (*m*/*z* 1108) at increasing collision voltages. Red curve: sample 5 min; black curve: sample 135 min after mixing of axle and wheel. Blue curve: pre-formed pseudorotaxane isolated by column chromatography before the experiment. The solid lines represent a sigmoidal fitting to determine 50% survival yield voltages $E_{1/2}$: red: $E_{1/2}$ = (9.8 ± 0.2) V; blue: $E_{1/2}$ = (39.2 ± 0.4) V (for experimental details, see ESI section 3‡).

Dual-stimuli responsiveness

When pseudo[2]rotaxane **PA11@TTFC8** is deprotonated with an excess of polystyrene-immobilized P2 base, quick dethreading is observed (Fig. 5b and ESI section 2 Fig. S32, S34, S36

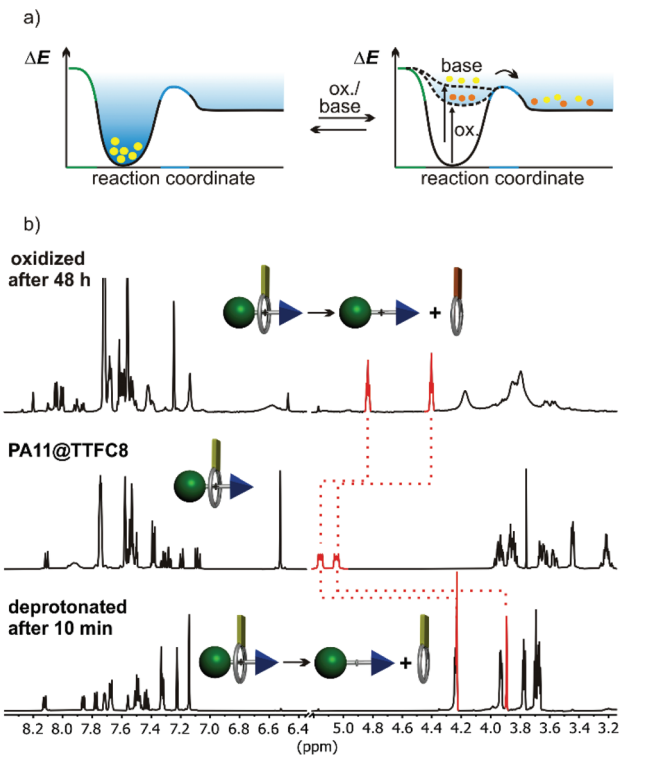

Fig. 5 (a) Dual-stimuli switching expressed in terms of the potential energy surface of the pseudorotaxane **PA11@TTFC8**. (b) ^{1}H NMR spectra (600 MHz, dry CD_2Cl_2, 298 K) of **PA11@TTFC8** (center), 48 hours after oxidation with excess $NOSbF_6$ (top), and 10 minutes after deprotonation with an excess of Schwesinger's P2 base immobilized on polystyrene (bottom).

and S42‡). No indication for hydrogen bonding of neutral **TTFC8** to the neutral axle was observed in the ^{1}H NMR spectra in contrast to earlier reports on complexes of neutral *primary* amines.[41] Dethreading is indicated by an emerging set of methylene proton signals (H_d, H_e), upfield shifted by $\Delta\delta \approx 0.8$ ppm upon deprotonation and dethreading. The pseudo[2]rotaxanes **PA5@TTFC8** (2,3-dimethylbenzyl end group), **PA6@TTFC8** (2-ethylbenzyl) and **PA7@TTFC8** (2-methoxybenzyl) were also subjected to deprotonation. Again, dethreading *via* deprotonation occurred immediately (see ESI Fig. S42 and Table S1‡).

The pseudorotaxane **PA11@TTFC8** can also successfully be oxidized with excess $NOSbF_6$ in dry CD_2Cl_2 under argon atmosphere. Two subsequent one-electron-oxidation steps lead to the TTF dication **PA11@TTFC8**$^{2+}$ easily recognizable from its instantaneously appearing deep blue colour. The oxidized macrocycle unthreads with a $t_{1/2}$ of 11 h (Fig. 5b, ESI section 2 Fig. S42‡). As the dication is again diamagnetic, unthreading can also be followed by integrating of a new set of methylene proton signals (H_d, H_e), upfield shifted by $\Delta\delta \approx 0.3$ and 0.6 ppm. This is confirmed by monitoring the dethreading of pseudo[2]rotaxanes **PA5@TTFC8**, **PA6@TTFC8** and **PA7@TTFC8** after oxidation. Complete dethreading occurred only for **PA7@TTFC8** and required a substantially longer time ($t_{1/2}$ = 22 h, see ESI section 2 Fig. S36‡).

These experiments clearly reveal that the dethreading rate does not only depend on the steric bulk of the axles' terminal groups, but also change significantly with the nature of the stimulus applied. Earlier, we reported attractive forces to still occur even between the doubly oxidized **TTFC8** and secondary ammonium axles.[29] Assuming that the ring circumference and conformational flexibility of **TTFC8** is not significantly altered upon oxidation[42] and taking into account that the oxidation itself occurs almost instantaneously, we therefore hypothesize that these residual interactions are the cause for the slower dethreading after oxidation. Fig. 5a qualitatively visualizes this in the framework of the energy landscapes after oxidation and after deprotonation: The oxidized pseudorotaxane resides in a somewhat lower local minimum on its potential energy surface as compared to the deprotonated pseudorotaxane.

Synthesis of 'speed bump' rotaxanes

Axle **6** (Fig. 6) features the bulky 1-naphthalene moiety and can easily be equipped with a stopper. After stirring **6** with **TTFC8** for three days at 40 °C (for **R1**, Fig. 6) or **S4** (axle of rotaxane **R2**) with **TTFC8** for 10 minutes at room temperature (for **R2**), nitrile-oxide stopper **St1**[43] was added and the mixtures were stirred at 35 °C overnight. Two rotaxanes (**R1** and **R2**) were isolated only differing by the size of the connecting blue 'speed bump'.

In the ^{1}H NMR spectra, successful rotaxane formation is evidenced by a downfield shift ($\Delta\delta$ = +0.5 ppm) of the methylene protons next to the ammonium, as well as the strong downfield shift ($\Delta\delta$ = +4.0 ppm) of the former alkyne proton that is incorporated in the newly formed isoxazole (H_p for **R1** and H_j for **R2**). Additionally, the methylene protons next to the

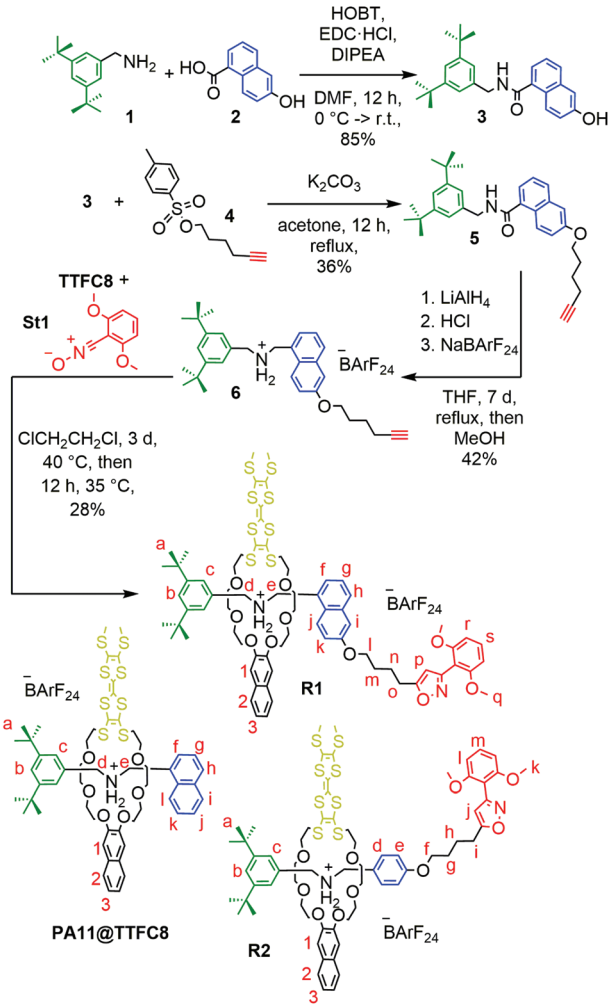

Fig. 6 Synthesis of rotaxane **R1**. Rotaxane **R2** and pseudo[2]rotaxane **PA11@TTFC8** are shown for comparison. For details of the synthesis of **R2**, see ESI, Scheme S3.‡

axle ether oxygen atom (H_l for **R1** and H_f for **R2**) shows an upfield shift ($\Delta\delta$ = 1.0 ppm) due to the close proximity to the naphthalene and/or TTF moiety of **TTFC8** (see ESI Fig. S19 and S26‡). The interlocked structure was further supported by tandem mass spectrometry. Collision-induced dissociation of mass-selected rotaxane parent ions occurred only at high collision energies. As the intact axle is not observed among the fragments, it is clear that dissociation of the two components is only possible after covalent bond cleavage within the axle, which excludes a non-threaded complex. Also, the collision energies required for dissociation as well as the observed fragment ions are comparable to other similar rotaxanes.[29]

Deprotonation of the rotaxanes

Deprotonation of **R1** with polystyrene-immobilized P2 base yields a neutral amine (Fig. 7d) which is indicated by a strong highfield shift of methylene protons $H_{d,e}$ ($\Delta\delta$ = 1 ppm solid line). The positions of these signals are similar to those of the deprotonated free axle (Fig. 7e). Other significant shifts

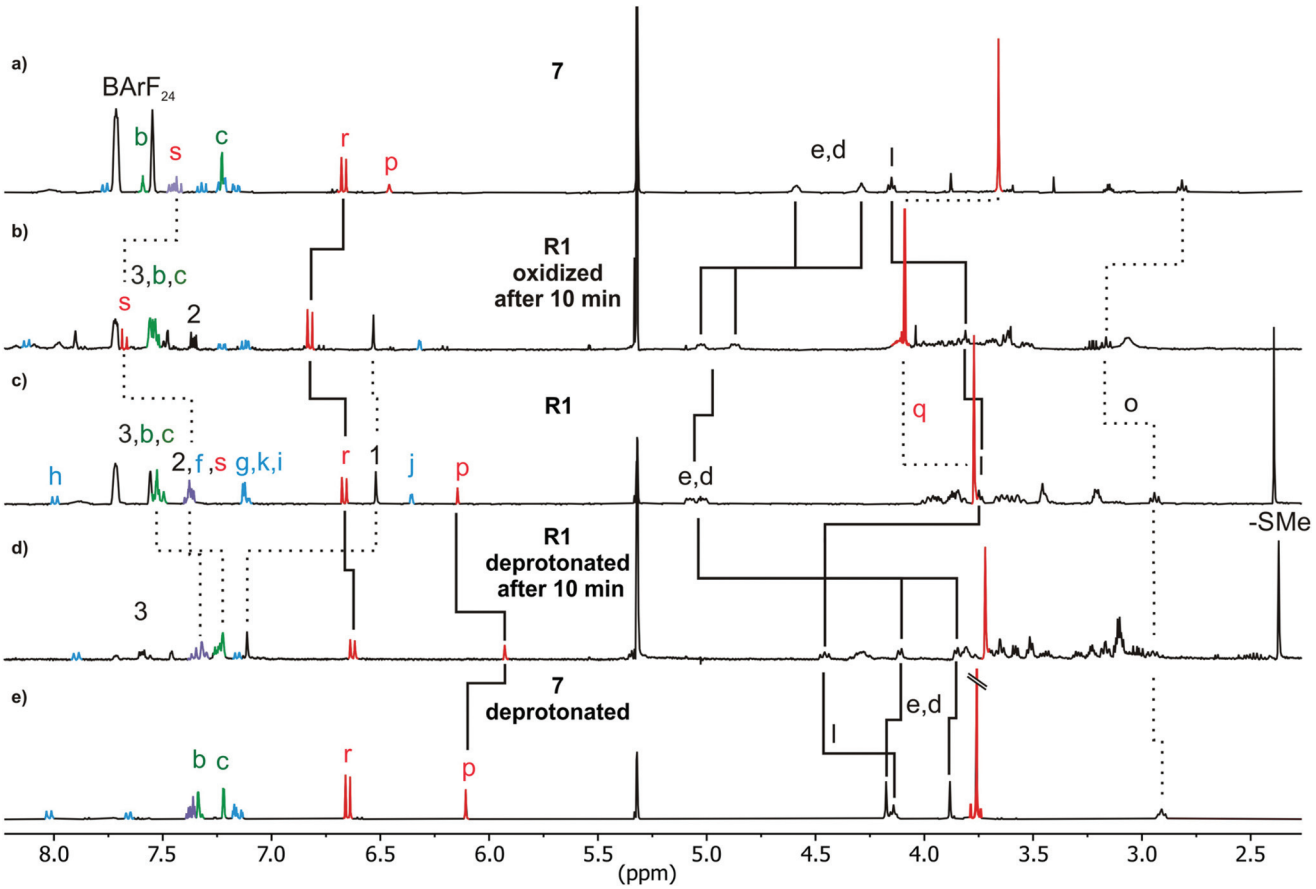

Fig. 7 ^{1}H NMR spectra (400 MHz, 298 K, CD_2Cl_2) of (a) stoppered axle **7** (b) **R1** 10 min after two-electron-oxidation (c) **R1** (d) **R1** 10 minutes after deprotonation and (e) deprotonated **7** with selected shifts highlighted.

include the isoxazole proton H_p ($\Delta\delta$ = −0.5 ppm), and alkyl chain methylene protons H_l ($\Delta\delta$ = +0.7 ppm solid line). Together with the downfield shift of H_l, this clearly indicates a deprotonation-induced shuttling away from the amine and towards the alkyl chain. No such shift of H_l is observed when free axle **7** (**6+St1**) is deprotonated (Fig. 7a/e). Rotaxane **R2** behaves similarly (Fig. S43 bottom‡). Variable temperature ^{1}H NMR experiments (see ESI, Fig. S51 and S52‡) performed with deprotonated **R1** and **R2** to test whether the two positional isomers of the wheel would be distinguishable unfortunately remained inconclusive.[24,44–50] Nevertheless, the NMR data is in agreement with a shift of the wheel across the 'speed bump' in the axle centre upon deprotonation.

Oxidation of the rotaxanes

The ^{1}H NMR spectrum of **R1** recorded 10 minutes after oxidation with $NOSbF_6$ to $\mathbf{R1}^{2+}$ is shown in Fig. 7b and did not change over the following 48 hours. The methylene protons $H_{d,e}$ next to the ammonium ion undergo only a small upfield shift ($\Delta\delta$ = −0.1 ppm). Also, proton H_l is shifted only by a small amount. As the small shifts can easily be rationalized by the additional charge induced through oxidation, these findings indicate that the wheel still occupies the ammonium station. However, protons H_r and H_s of the dimethoxyphenyl stopper at the opposite end of the axle shift downfield to some extent ($\Delta\delta$ = 0.2 to 0.25 ppm). Although this observation may at first glance seem inconsistent with the interpretation that the wheel remains on the ammonium side of the axle, these shift differences can be easily explained by invoking p-donor–p-acceptor complex formation between the strongly electron-deficient TTF^{2+} dication and the rather electron-rich dimethoxyphenyl stopper. The ^{1}H NMR spectrum of the oxidized rotaxane thus indicates that the macrocycle still encircles the ammonium ion, while refolding of the more remote axle half occurs.

More evidence can be obtained from cyclovoltammetric (CV) and differential pulse voltammetric (DPV) experiments with which the half-wave potentials of the two reversible TTF redox waves can be obtained. These potentials characteristically shift depending on the interactions between axle and wheel, as shown earlier for **TTFC8**-containing rotaxanes.[29,51,52] The correlation diagram in Fig. 8a contains the peak potentials obtained by DPV measurements in CH_2Cl_2 with n-Bu_4NBArF_{24} as the supporting electrolyte. Compared to the free wheel, the redox potentials $E^1_{1/2}(TTF^{0/+})$ and $E^2_{1/2}(TTF^{+/2+})$ are anodically shifted for all species bound to an axle. **PA12@TTFC8** is a diagnostic control compound, as two sets of TTF redox processes corresponding to the threaded ($E^1_{1/2}$, $E^2_{1/2}$) and unthreaded wheel ($E^1_{1/2}$, $E'_{1/2}$) are observed (see ESI Fig. S55‡). The low

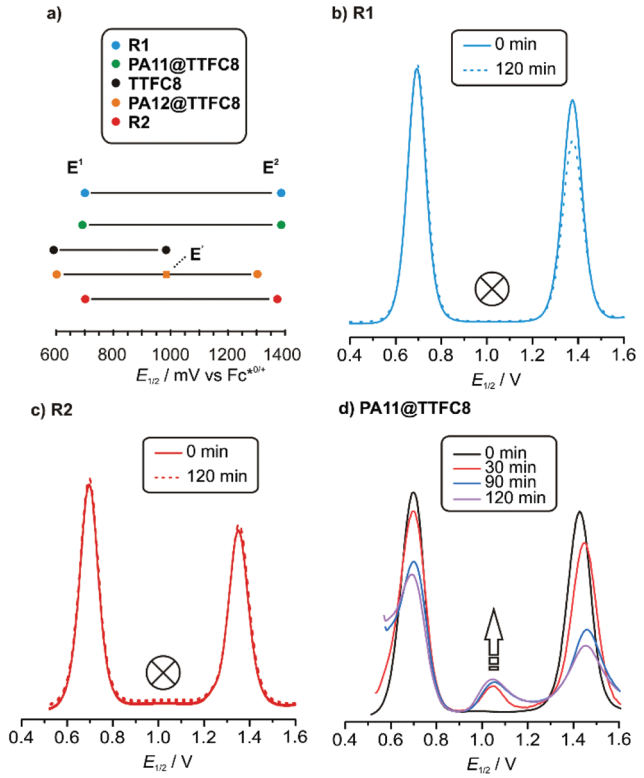

Fig. 8 Electrochemical data: (a) Correlation diagram of DPV peak potentials of all relevant (pseudo)rotaxane species, DPVs before and after electrolysis of (b) **R1**, (c) **R2**, (d) **PA11@TTFC8** (CH_2Cl_2, with *n*-Bu_4NBArF_{24} as the electrolyte (0.1 M), 298 K, 1 mM analyte, 25 mV modulation amplitude, 50 ms modulation time, 5 mV step potential, 0.5 s interval time).

steric bulk of the phenyl group allows fast interconversion between threaded and unthreaded on the CV timescale (in the DPV only one peak for $TTF^{0/+}$ redox couple is visible). In contrast, the isolated pseudorotaxane **PA11@TTFC8** only shows one redox couple for $TTF^{0/+}$ and $TTF^{+/2+}$ due to the sterically hindered unthreading. The mechanically interlocked structures **R1** and **R2** show no third feature ($E'_{1/2}$), meaning that the voltammograms indicate no significant wheel shuttling away from the ammonium station on the timescale of the experiment. Bulk electrolysis (Fig. 8b–d) of the (pseudo)rotaxanes for 2 h did not show a change in the DPV for **R1** and **R2**. However, for **PA11@TTFC8** signal broadening and lowered amperage in the course of electrolysis was observed. Bulk electrolysis gave rise to a new signal, which corresponds to the second oxidation of unbound **TTFC8**. The bulk electrolysis experiments suggest, that electrochemically–induced migration over the naphthalene moiety does take place for pseudorotaxane **PA11@TTFC8**. On the contrary, no such behavior was observed for the rotaxanes **R1** and **R2**. These results clearly support the ^{1}H NMR data, that no oxidation-induced shuttling occurs in the mechanically interlocked species.

Consequently, the behaviour of the rotaxanes parallels that of the pseudorotaxanes in that the two different stimuli cause significant differences in dethreading/shuttling rates despite of the steric barrier remaining unchanged. Also, the reason – a binding interaction of the crown ether wheel to the ammonium ion that is stronger than the effects of charge repulsion – is likely the same. Nevertheless, there are also differences: While the pseudorotaxane finally dethreads over 48 hours, no change is observed on a similar time scale for the rotaxane. This is an effect of the mechanical bond. While dethreading of the pseudorotaxane is entropically favoured by an increase in particle number, such wheel shuttling in the rotaxanes does not benefit from such entropic benefit.

Conclusions

A set of $BArF_{24}^-$ salts of *sec*-ammonium ions bearing different bulky end groups have been investigated with respect to their ability to form crown ether/ammonium pseudorotaxanes. The small differences in bond lengths between the two crown ethers **DB24C8** and **TTFC8** change the threading barrier significantly and threading occurs significantly faster for **TTFC8**. Three groups of quickly threading, kinetically hindered slowly threading, and non-threading axles can be distinguished. For the slowly and non-threading axle/wheel pairs, the formation of face-to-face crown ether/ammonium complexes occurs, which has been exemplarily studied in more detail for **PA11** by ^{1}H NMR, tandem MS and ITC experiments. To our knowledge this is the first time that an equilibrium of a threaded and non-threaded complex was quantitatively studied for the same axle macrocycle combination.

Deslipping of **TTFC8** from different axles could be achieved by deprotonation of the axle or by chemical oxidation of the macrocycle. Upon deprotonation, the pseudorotaxanes dissociate quickly. Chemical oxidation to the TTF dication lead to much slower dethreading. The difference in dethreading rates for the two stimuli can be explained by residual attractive interaction of the oxidized $TTFC8^{2+}$ and the axle. It is quite remarkable that two different stimuli lead to so clearly different dethreading rates, even though the steric barrier remains unchanged. Clearly, an interplay between the steric barrier and the changes in the interactions between wheel and its binding stations is observed here which complicates the analysis of such steric 'speed bumps' in molecular interlocked switches and machines.

The shuttling of the wheel in the rotaxanes on one hand behaves similarly in that the two stimuli cause different effects on the shuttling. But the behaviour is not fully analogous. The comparison of rotaxanes and pseudorotaxanes clearly reveals a significant and non-negligible influence of the mechanical bond. At the end, the shuttling is affected by changing interactions between the wheel and the available binding stations as well as steric barriers on its way along the axle and the particular effects of the mechanical bond.

Conflicts of interest

There are no conflicts of interest to declare.

Acknowledgements

Gefördert durch die Deutsche Forschungsgemeinschaft (DFG) – Projektnummer 387284271 – SFB 1349 – und Projektnummer 434455294 (funded by the Deutsche Forschungsgemeinschaft – project-ID 387284271 – SFB 1349 and project-ID 434455294). A.V. kindly acknowledges the Academy of Finland (grant no. 314343) for financial support. We also thank Jennifer Anders for help with the synthesis.

Notes and references

1 J. D. Harris, M. J. Moran and I. Aprahamian, New molecular switch architectures, *Proc. Natl. Acad. Sci. U. S. A.*, 2018, **115**, 9414–9422.
2 J. D. Badjic, V. Balzani, A. Credi, S. Silvi and J. F. Stoddart, A molecular elevator, *Science*, 2004, **303**, 1845–1849.
3 D. Cao, Z. Liu, P. Verwilst, S. Koo, P. Jangjili, J. S. Kim and W. Lin, Coumarin-Based Small-Molecule Fluorescent Chemosensors, *Chem. Rev.*, 2019, **119**, 10403–10519.
4 D. Bleger and S. Hecht, Visible-Light-Activated Molecular Switches, *Angew. Chem., Int. Ed.*, 2015, **54**, 11338–11349.
5 D. Dattler, G. Fuks, J. Heiser, E. Moulin, A. Perrot, X. Yao and N. Giuseppone, Design of Collective Motions from Synthetic Molecular Switches, Rotors, and Motors, *Chem. Rev.*, 2020, **120**, 310–433.
6 A. Coskun, J. M. Spruell, G. Barin, W. R. Dichtel, A. H. Flood, Y. Y. Botros and J. F. Stoddart, High hopes: can molecular electronics realise its potential?, *Chem. Soc. Rev.*, 2012, **41**, 4827–4859.
7 S. Erbas-Cakmak, D. A. Leigh, C. T. McTernan and A. L. Nussbaumer, Artificial Molecular Machines, *Chem. Rev.*, 2015, **115**, 10081–10206.
8 E. R. Kay, D. A. Leigh and F. Zerbetto, Synthetic molecular motors and mechanical machines, *Angew. Chem., Int. Ed.*, 2007, **46**, 72–191.
9 T. Felder and C. A. Schalley, Secondary isotope effects on the deslipping reaction of rotaxanes: high-precision measurement of steric size, *Angew. Chem., Int. Ed.*, 2003, **42**, 2258–2260.
10 E. A. Neal and S. M. Goldup, Chemical consequences of mechanical bonding in catenanes and rotaxanes: isomerism, modification, catalysis and molecular machines for synthesis, *Chem. Commun.*, 2014, **50**, 5128–5142.
11 M. Baroncini, S. Silvi and A. Credi, Photo- and Redox-Driven Artificial Molecular Motors, *Chem. Rev.*, 2020, **120**, 200–268.
12 Z. Liu, S. K. M. Nalluri and J. F. Stoddart, Surveying macrocyclic chemistry: from flexible crown ethers to rigid cyclophanes, *Chem. Soc. Rev.*, 2017, **46**, 2459–2478.
13 A. Carrasco-Ruiz and J. Tiburcio, Electrostatic kinetic barriers in the threading/dethreading motion of a rotaxane-like complex, *Org. Lett.*, 2015, **17**, 1858–1861.
14 P. R. Ashton, P. J. Campbell, P. T. Glink, D. Philp, N. Spencer, J. F. Stoddart, E. J. T. Chrystal, S. Menzer, D. J. Williams and P. A. Tasker, Dialkylammonium Ion/Crown Ether Complexes: The Forerunners of a New Family of Interlocked Molecules, *Angew. Chem., Int. Ed. Engl.*, 1995, **34**, 1865–1869.
15 R. M. Izatt, J. D. Lamb, N. E. Izatt, B. E. Rossiter, J. J. Christensen and B. L. Haymore, A calorimetric titration study of the reaction of several organic ammonium cations with 18-crown-6 in methanol, *J. Am. Chem. Soc.*, 1979, **101**, 6273–6276.
16 P. R. Ashton, I. Baxter, M. C. T. Fyfe, F. M. Raymo, N. Spencer, J. F. Stoddart, A. J. P. White and D. J. Williams, Rotaxane or Pseudorotaxane? That Is the Question!†, *J. Am. Chem. Soc.*, 1998, **120**, 2297–2307.
17 C. J. Bruns and J. F. Stoddart, *The Nature of the Mechanical Bond: From Molecules to Machines*, John Wiley & Sons, Inc., 2016.
18 T. Clifford, A. Abushamleh and D. H. Busch, Factors affecting the threading of axle molecules through macrocycles: binding constants for semirotaxane formation, *Proc. Natl. Acad. Sci. U. S. A.*, 2002, **99**, 4830–4836.
19 J. Groppi, L. Casimiro, M. Canton, S. Corra, M. Jafari-Nasab, G. Tabacchi, L. Cavallo, M. Baroncini, S. Silvi, E. Fois and A. Credi, Precision Molecular Threading/Dethreading, *Angew. Chem., Int. Ed. Engl.*, 2020, **59**, 14825–14834.
20 P. G. Young, K. Hirose and Y. Tobe, Axle length does not affect switching dynamics in degenerate molecular shuttles with rigid spacers, *J. Am. Chem. Soc.*, 2014, **136**, 7899–7906.
21 M. Asakawa, P. R. Ashton, R. Ballardini, V. Balzani, M. Bělohradský, M. T. Gandolfi, O. Kocian, L. Prodi, F. M. Raymo, J. F. Stoddart and M. Venturi, The Slipping Approach to Self-Assembling [n]Rotaxanes†, *J. Am. Chem. Soc.*, 1997, **119**, 302–310.
22 B. Riss-Yaw, C. Clavel, P. Laurent and F. Coutrot, The relationship between the conformational degree of freedom of template-containing threads and slippage in the formation of [2]rotaxane building blocks, *Chem. Commun.*, 2017, **53**, 10874–10877.
23 Y. Yamashita, Y. Saito, S. Kikkawa, Y. Mutoh, S. Hosoya, I. Azumaya and S. Saito, Evaluation of the Steric Bulk of Substituents Utilizing the Shuttling Behavior of [2]Rotaxanes with N-Arylpyrrole Moieties, *Eur. J. Org. Chem.*, 2019, **2019**, 3412–3420.
24 G. Gholami, K. Zhu, G. Baggi, E. Schott, X. Zarate and S. J. Loeb, Influence of axle length on the rate and mechanism of shuttling in rigid H-shaped [2]rotaxanes, *Chem. Sci.*, 2017, **8**, 7718–7723.
25 A. C. Catalan and J. Tiburcio, Self-assembly of pseudorotaxane and rotaxane complexes using an electrostatic slippage approach, *Chem. Commun.*, 2016, **52**, 9526–9529.
26 C. Pezzato, C. Cheng, J. F. Stoddart and R. D. Astumian, Mastering the non-equilibrium assembly and operation of molecular machines, *Chem. Soc. Rev.*, 2017, **46**, 5491–5507.
27 G. Ragazzon, C. Schafer, P. Franchi, S. Silvi, B. Colasson, M. Lucarini and A. Credi, Remote electrochemical modu-

lation of pKa in a rotaxane by co-conformational allostery, *Proc. Natl. Acad. Sci. U. S. A.*, 2018, **115**, 9385–9390.

28 K. Nakazono and T. Takata, Neutralization of a sec-ammonium group unusually stabilized by the "rotaxane effect": synthesis, structure, and dynamic nature of a "free" sec-amine/crown ether-type rotaxane, *Chem. – Eur. J.*, 2010, **16**, 13783–13794.

29 H. V. Schröder, S. Sobottka, M. Nössler, H. Hupatz, M. Gaedke, B. Sarkar and C. A. Schalley, Impact of mechanical bonding on the redox-switching of tetrathiafulvalene in crown ether-ammonium [2]rotaxanes, *Chem. Sci.*, 2017, **8**, 6300–6306.

30 H. Hupatz, M. Gaedke, H. V. Schröder, J. Beerhues, A. Valkonen, F. Klautzsch, S. Müller, F. Witte, K. Rissanen, B. Sarkar and C. A. Schalley, Thermodynamic and electrochemical study of tailor-made crown ethers for redox-switchable (pseudo)rotaxanes, *Beilstein J. Org. Chem.*, 2020, **16**, 2576–2588.

31 A. Crochet, E. Kottelat, A. Fleury, M. Neuburger and K. M. Fromm, Polymorph of Dibenzo-24-Crown-8 and its Mercury Complex, *Z. Anorg. Allg. Chem.*, 2011, **637**, 672–675.

32 H. Nagai, Y. Suzaki and K. Osakada, Thiacrown Ethers with Oxygen and Sulfur for Coordination: Formation of the Pd and Pt Complexes and Pseudorotaxane with Dialkylammonium, *Eur. J. Inorg. Chem.*, 2014, **2014**, 4376–4384.

33 F. Le Derf, M. Mazari, N. Mercier, E. Levillain, P. Richomme, J. Becher, J. Garin, J. Orduna, A. Gorgues and M. Salle, Electroregulated Metal-Binding with a Crown Ether Tetrathiafulvalene Derivative: Toward Electrochemically Addressed Metal Cation Sponges, *Inorg. Chem.*, 1999, **38**, 6096–6100.

34 H. Nagai, Y. Suzaki and K. Osakada, Chemical Modification of a [2]Rotaxane Composed of Dithiacrown Ether and Dialkylammonium with Organic and Inorganic Compounds, *Chem. Lett.*, 2016, **45**, 834–836.

35 A. R. Williams, B. H. Northrop, K. N. Houk, J. F. Stoddart and D. J. Williams, The influence of constitutional isomerism and change on molecular recognition processes, *Chem. – Eur. J.*, 2004, **10**, 5406–5421.

36 S. J. Cantrill, D. A. Fulton, A. M. Heiss, A. R. Pease, J. F. Stoddart, A. J. P. White and D. J. Williams, The Influence of Macrocyclic Polyether Constitution upon Ammonium Ion/Crown Ether Recognition Processes, *Chem. – Eur. J.*, 2000, **6**, 2274–2287.

37 T. Takata, Stimuli-Responsive Molecular and Macromolecular Systems Controlled by Rotaxane Molecular Switches, *Bull. Chem. Soc. Jpn.*, 2019, **92**, 409–426.

38 S. Miyagawa, M. Kimura, S. Kagami, T. Kawasaki and Y. Tokunaga, Utilization of a Crown Ether/Amine-Type Rotaxane as a Probe for the Versatile Detection of Anions and Acids by Thin-Layer Chromatography, *Chem. – Asian J.*, 2020, **15**, 3044–3049.

39 J. Nishiyama, Y. Makita and N. Kihara, Rapid and Efficient Acylative Active Transport on a Rotaxane, *Asian J. Org. Chem.*, 2015, **4**, 1056–1064.

40 H. Sato, D. Aoki and T. Takata, Synthesis and Star/Linear Topology Transformation of a Mechanically Linked ABC Terpolymer, *ACS Macro Lett.*, 2016, **5**, 699–703.

41 S. D. P. Fielden, D. A. Leigh, C. T. McTernan, B. Perez-Saavedra and I. J. Vitorica-Yrezabal, Spontaneous Assembly of Rotaxanes from a Primary Amine, Crown Ether and Electrophile, *J. Am. Chem. Soc.*, 2018, **140**, 6049–6052.

42 H. V. Schröder, F. Witte, M. Gaedke, S. Sobottka, L. Suntrup, H. Hupatz, A. Valkonen, B. Paulus, K. Rissanen, B. Sarkar and C. A. Schalley, An aryl-fused redox-active tetrathiafulvalene with enhanced mixed-valence and radical-cation dimer stabilities, *Org. Biomol. Chem.*, 2018, **16**, 2741–2747.

43 T. Matsumura, F. Ishiwari, Y. Koyama and T. Takata, C-C bond-forming click synthesis of rotaxanes exploiting nitrile N-oxide, *Org. Lett.*, 2010, **12**, 3828–3831.

44 V. N. Vukotic, K. Zhu, G. Baggi and S. J. Loeb, Optical Distinction between "Slow" and "Fast" Translational Motion in Degenerate Molecular Shuttles, *Angew. Chem., Int. Ed.*, 2017, **56**, 6136–6141.

45 K. Hirose, Molecular brake systems controlled by light and heat, *J. Inclusion Phenom. Macrocyclic Chem.*, 2010, **68**, 1–24.

46 J. Dale and P. O. Kristiansen, Cyclic oligo-ethers related to ethylene oxide, *J. Chem. Soc., Chem. Commun.*, 1971, **13**, 670.

47 C. I. Ratcliffe, J. A. Ripmeester, G. W. Buchanan and J. K. Denike, A molecular merry-go-round: motion of the large macrocyclic molecule 18-crown-6 in its solid complexes studied by deuterium NMR, *J. Am. Chem. Soc.*, 1992, **114**, 3294–3299.

48 V. N. Vukotic, K. J. Harris, K. Zhu, R. W. Schurko and S. J. Loeb, Metal-organic frameworks with dynamic interlocked components, *Nat. Chem.*, 2012, **4**, 456–460.

49 K. Zhu, V. N. Vukotic, C. A. O'Keefe, R. W. Schurko and S. J. Loeb, Metal-organic frameworks with mechanically interlocked pillars: controlling ring dynamics in the solid-state via a reversible phase change, *J. Am. Chem. Soc.*, 2014, **136**, 7403–7409.

50 N. D. Suhan, L. Allen, M. T. Gharib, E. Viljoen, S. J. Vella and S. J. Loeb, Colour coding the co-conformations of a [2] rotaxane flip-switch, *Chem. Commun.*, 2011, **47**, 5991–5993.

51 M. Gaedke, F. Witte, J. Anhäuser, H. Hupatz, H. V. Schröder, A. Valkonen, K. Rissanen, A. Lützen, B. Paulus and C. A. Schalley, Chiroptical inversion of a planar chiral redox-switchable rotaxane, *Chem. Sci.*, 2019, **10**, 10003–10009.

52 H. V. Schröder, F. Stein, J. M. Wollschläger, S. Sobottka, M. Gaedke, B. Sarkar and C. A. Schalley, Accordion-Like Motion in Electrochemically Switchable Crown Ether/Ammonium Oligorotaxanes, *Angew. Chem., Int. Ed.*, 2019, **58**, 3496–3500.

Supporting Information

Dual-stimuli pseudorotaxane switches under kinetic control

Marius Gaedke,[a] Henrik Hupatz,[a] Hendrik V. Schröder,[a,b] Simon Suhr,[c] Kurt F. Hoffmann,[d] Arto Valkonen,[e] Biprajit Sarkar,[c] Sebastian Riedel,[d] Kari Rissanen,[e] and Christoph A. Schalley*[a]

[a] Institut für Chemie und Biochemie der Freien Universität Berlin, Arnimallee 20, 14195 Berlin, Germany.

[b] Present address: Department of Chemical and Biological Engineering, Princeton University, Princeton, NJ08544, USA

[c] Lehrstuhl für Anorganische Koordinationschemie, Institut für Anorganische Chemie, Universität Stuttgart, Pfaffenwaldring 55, 70569 Stuttgart, Germany

[d] Institut für Chemie und Biochemie der Freien Universität Berlin, Fabeckstr. 34/36 14195 Berlin, Germany.

[e] University of Jyvaskyla, Department of Chemistry, P.O. Box 35, 40014 Jyväskylä, Finland.

*Corresponding author e-mail: c.schalley@fu-berlin.de

Table of Contents

1. Experimental details

1.1. General methods

All reagents and solvents were obtained from commercial sources and used without further purification. Dry solvents were purchased from Acros Organics (Geel, Belgium) and either directly used or treated with the M. Braun solvent purification system SPS 800. **TTFC8**,[1] 2,6-dimethoxybenzonitrile oxide stopper **St1**,[2] (2,6-dimethylphenyl)methanaminium chloride,[3] (3,5-di-*tert*-butylphenyl)methanamine **1**,[4] 5-hexynyl tosylate **4**,[5] 4-(hex-5-yn-1-yloxyl)benzonitrile **S2**,[6] were synthesised according to literature procedures, naphthalen-2-ylmethanaminium hydrochloride was bought at Fluorochem (Hadfield, U.K.), 3,5-di-*tert*-butylbenzaldehyde, 2-methylbenzylamine hydrochloride, 3-methylbenzylamine hydrochloride, (3-phenylphenyl)methanamine hydrochloride, 2-naphthylmethanamine hydrochloride, 2,3-dimethylbenzylamine, 2,5-dimethylbenzylamine, 2-nitrobenzylamine hydrochloride, 2-ethylbenzylamine hydrochloride, sodium tetrakis[3,5-bis(trifluoromethyl)phenyl]borate ($NaBArF_{24}$), 6-hydroxy-1-naphthoic acid **2**, benzotriazol-1-ol (HOBT), 3-(ethyliminomethyleneamino)-*N*,*N*-dimethylpropan-1-amine hydrochloride (EDC·HCl), *N*-ethyl-*N*-(propan-2-yl)propan-2-amine (DIPEA) and polystyrene-immobilized phosphazene base P2 were bought at Sigma Aldrich (Taufkirchen, Germany) or TCI Chemicals (Eschborn, Germany). Thin-layer chromatography was performed on silica gel-coated plates with fluorescent indicator F254 (Merck KGaA, Darmstadt, Germany). For column chromatography, silica gel (0.04-0.063 mm, Merck), or Biotage (Uppsala, Sweden) SNAP and SNAP Ultra Cartridges were used on a Biotage Isolera One.

^{1}H and ^{13}C NMR experiments were performed on JEOL ECX 400, JEOL ECZ 600, Bruker AVANCE 500 or Bruker AVANCE 700 instruments. Residual solvent signals were used as the internal standards. All shifts are reported in ppm and NMR multiplicities are abbreviated as s (singlet), d (doublet), t (triplet), m (multiplet) and br (broad). Coupling constants *J* are reported in Hertz. Compounds containing the tetrakis[3,5-bis(trifluoromethyl)phenyl]borate ($BArF_{24}^{-}$) anion show ^{13}C NMR spectra with ^{19}F, ^{10}B and ^{11}B couplings. These signals are denoted as one signal.

Melting points were determined on a SMP 30 (Stuart) instrument and are uncorrected.

High-resolution ESI mass spectra were measured on an Agilent 6210 ESI-TOF device. CID experiments were performed on a Synapt G2-S HDMS (Waters Co., Milford, MA, USA) mass spectrometer. HPLC grade solvents were used for sample preparation.

UV/Vis spectra were recorded with a Varian Cary 50 Bio spectrometer equipped with a xenon lamp. Solvents with HPLC grade and Suprasil glass cuvettes with a path-length of 1 cm were used.

CV measurements were carried out with an Autolab PGSTAT302N potentiostat in a 2 mL measuring cell in dichloroethane with 0.1 M n-Bu_4NBArF_{24} as the conducting salt. The working electrode was made of glassy carbon, the reference Ag electrode was etched with conc. aq. HCl. A Pt wire worked as the counter electrode. The cyclic voltammograms were recorded with 10, 25, 50, 100, 250, 500, 1000 and 2500 mV/s scan rates, to ensure that the observed processes are reversible and diffusion-limited. In order to obtain the correct half-wave potentials, $FeCp_2^{*0}/FeCp_2^{*+}$ was used as the pseudo reference. These values were afterwards referenced to $FeCp_2/FeCp_2^{+}$ as described in the literature.[7] The raw data were treated with Nova 1.5 by Metrohm and the plots were made with Origin 2020 by OriginLab.

Bulk electrolysis experiments were conducted in a five-neck cell with a four-electrode set-up (see Figure S54 for a photograph) connected to an Autolab PGSTAT302N MBA potentiostat in bipotentiostat mode, using dry and degassed CH_2Cl_2 as the solvent and n-Bu_4NBArF_{24} as the supporting electrolyte. Electrolysis was performed with a cylindrical GC rod (3 mm diameter) at a potential of 1 V vs. the pseudo-reference. A silver wire was used as the pseudo-reference, a coiled Pt wire as the counter electrode. An additional GC disk electrode was employed to perform CV and DPV measurements every 30 minutes to determine the effect of electrolysis on the electrochemical response. The counter electrode was separated from the rest of the cell by glass wool soaked in analyte solution to suppress diffusion towards the working electrodes. Cyclic voltammograms were recorded at a scan rate of 100 mV/s. Differential pulse voltammograms were recorded with a step size of 0.005 V, a modulation amplitude of 0.025 V and modulation and interval times of 0.05 and 0.5 s, respectively. Measurements and treatment of raw data were performed within the Nova 2.1 software by Metrohm, while plots were made using Origin 2020 by OriginLab. The half-wave and peak potentials in CV and DPV experiments drifted between different measurements when recorded during electrolysis, but the diagnostic potential differences between the characteristic oxidation events remained constant. Potentials were afterwards normalized to the values obtained in regular CV measurements.

1.2. Synthesis of axles PA*n*

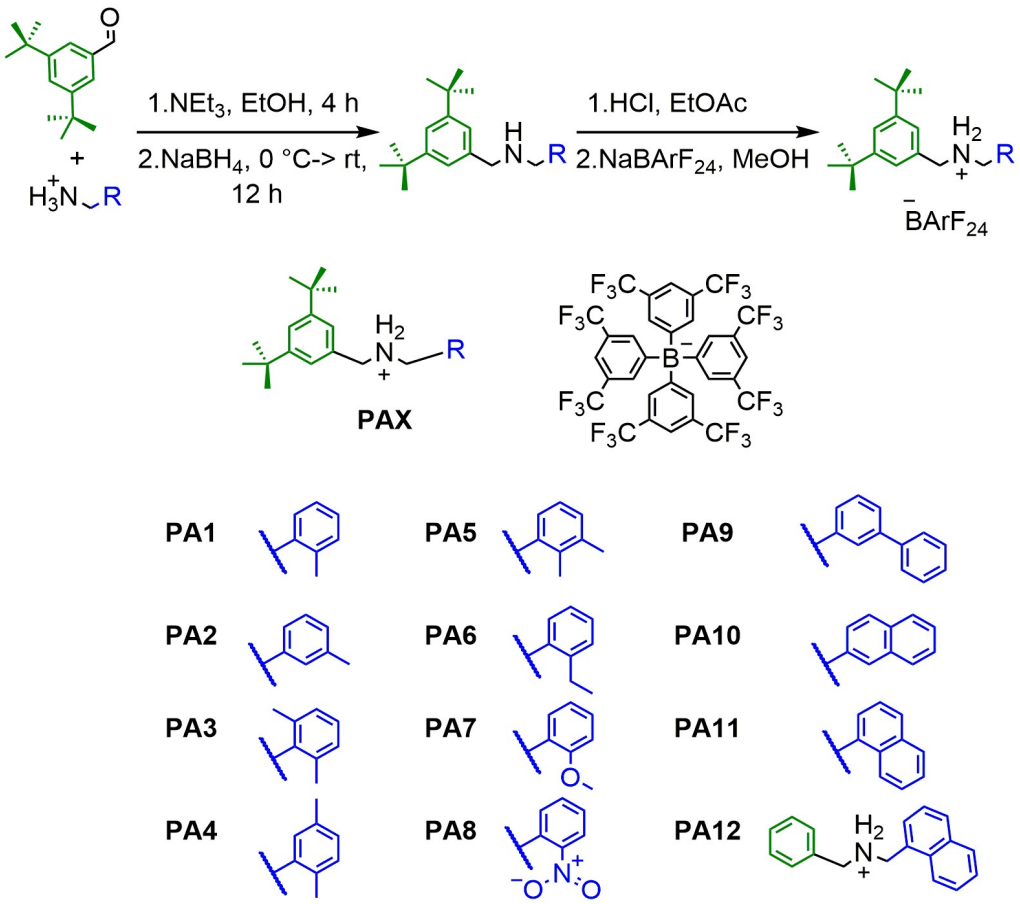

Scheme S1 Synthesis of axles **PA1-12**.

N-(3,5-di-tert-butylbenzyl)-1-(o-tolyl)methanaminium tetrakis(3,5-bis(trifluoromethyl)phenyl)borate

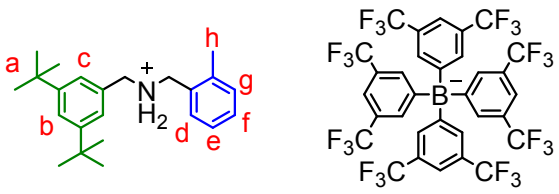

PA1

A solution of 190 mg (1.21 mmol, 1.0 equiv.) 2-methylbenzylamine hydrochloride, 263 mg (1.21 mmol, 1.0 equiv.) 3,5-di-*tert*-butylbenzaldehyde and 150 µL (1.08 mmol, 0.9 equiv.) NEt_3, in dry EtOH (30 mL) were refluxed under argon atmosphere for 4 h. Afterwards, the solution was cooled to 0 °C and 228 mg (6.03 mmol, 5.0 equiv.) $NaBH_4$ were slowly added. The mixture was stirred under argon atmosphere overnight in the thawing ice bath. The reaction was then quenched by slow addition of sat. $NaHCO_3$ solution and filtered. The solvent was removed from the filtrate under reduced pressure and the residue was dissolved in CH_2Cl_2 and then washed with sat. $NaHCO_3$ solution and brine. The organic phase was dried with $MgSO_4$ and the solvent removed again. The crude product was purified by column chromatography (SiO_2, CH_2Cl_2/MeOH = 100:1 -> 50:1, R_f ~ 0.3 in CH_2Cl_2/MeOH (100:1)) to obtain a yellowish oil. The oil was dissolved in EtOAc (5 ml) and acidified with HCl (conc.) until the solution reached pH = 1. The mixture was stirred for 1 h and afterwards the solvent was removed under reduced pressure. The residue was dissolved in MeOH (5 ml) and 195 mg (0.22 mmol, 1.0 equiv.) $NaBArF_{24}$ was added. The solution was left stirring overnight at room temperature, then the solvent was removed. The residue was taken up in CH_2Cl_2, washed with brine/water and dried over $MgSO_4$. The product **PA1** (222 mg, 0.19 mmol, 16 % overall) was obtained as off-white sticky solid.

^{1}H NMR (500 MHz, $CDCl_3$): δ = 1.31 (s, 18H, a), 2.14 (s, 3H, h), 4.26-4.32 (m, 4H, $C\underline{H_2}$-NH_2), 6.24 (s, 2H, $N\underline{H_2}$), 7.09-7.12 (m, 1H, d), 7.14 (d, *J*=1.7 Hz, 2H, c), 7.17-7.27(m, 2H, g), 7.33-7.37 (m, 1H, e), 7.55 (s_{br}, 4H, $BArF_{24}$), 7.66 (t, *J*=1.7Hz, 1H, b), 7.75 (s_{br}, 8H, $BArF_{24}$) ppm. **^{13}C NMR** (176 MHz, $CDCl_3$): δ = 18.4 31.1, 31.2, 31.4, 31.5, 35.2, 50.7, 54.4, 117.7, 117.8, 121.5, 123.3, 123.7, 125.9, 126.2, 126.3, 127.2, 128.1, 129.2, 130.0, 132.1, 132.4, 135.0, 154.3, 161.3, 161.7, 162.1, 162.5 ppm. **HRMS** (MeOH): *m/z* calcd. for $[C_{23}H_{34}N]^+$: 324.2686 $[M]^+$, found: 324.2704.

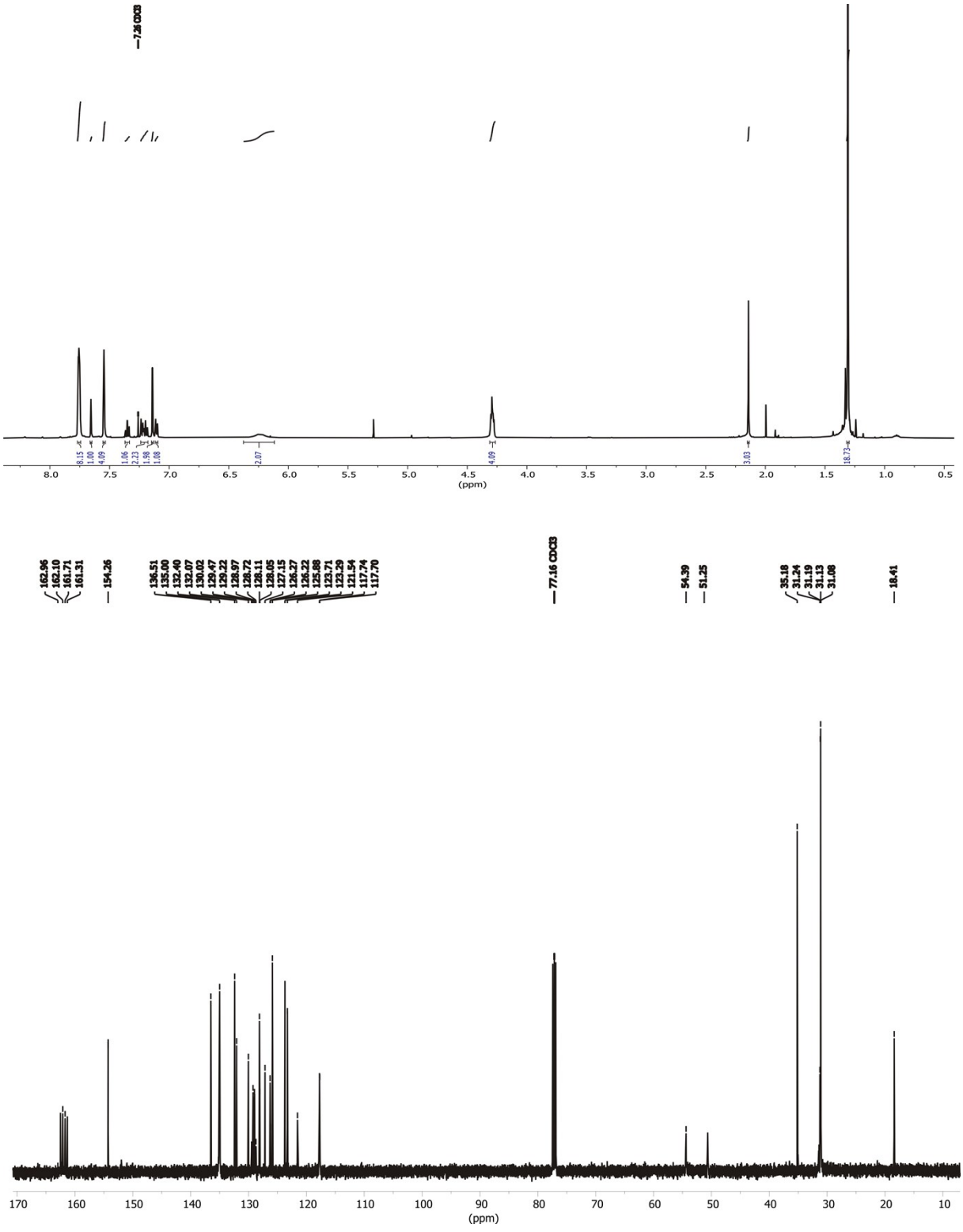

Fig. S1 ^{1}H (top) and ^{13}C (bottom) NMR spectra (500/176 MHz, $CDCl_3$, 298 K) of **PA1**.

N-(3,5-di-tert-butylbenzyl)-1-(*m*-tolyl)methanaminium tetrakis(3,5-bis(trifluoromethyl)phenyl)borate

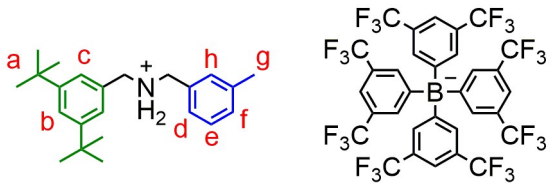

PA2

A solution of 53 mg (0.34 mmol, 1.0 equiv.) 3-methylbenzylamine hydrochloride, 73 mg (0.34 mmol, 1.0 equiv.) 3,5-di-*tert*-butylbenzaldehyde and 31 µL (0.30 mmol, 0.9 equiv.) NEt_3, in dry EtOH (20 mL) were refluxed under argon atmosphere for 4 h. Afterwards, the solution was cooled to 0 °C and 64 mg (1.7 mmol, 5.0 equiv.) $NaBH_4$ was slowly added. The mixture was left stirring under argon atmosphere overnight in the thawing ice bath. The reaction was quenched by slow addition of sat. $NaHCO_3$ solution and then filtered. The solvent was removed under reduced pressure from the filtrate and the residue was dissolved in CH_2Cl_2 and then washed with sat. $NaHCO_3$ solution and brine. The organic phase was dried with $MgSO_4$ and the solvent removed again. The crude product was purified by column chromatography (SiO_2, CH_2Cl_2/MeOH = 100:1 -> 50:1, R_f ~ 0.3 in CH_2Cl_2/MeOH (100:1)) to obtain a yellowish oil. The oil was dissolved in EtOAc (5 ml) and acidified with HCl (conc.) until the solution reached pH = 1. The mixture was stirred for 1 h and afterwards the solvent was removed under reduced pressure. The residue was dissolved in MeOH (5 ml) and 150 mg (0.17 mmol, 1.0 equiv.) $NaBArF_{24}$ was added. The solution was left stirring overnight at room temperature, then the solvent was removed. The residue was taken up in CH_2Cl_2, washed with brine/water and dried over $MgSO_4$. The product **PA2** (200 mg, 0.16 mmol, 47 % overall) was obtained as off-white sticky solid.

^{1}H NMR (500 MHz, $CDCl_3$): δ = 1.30 (s, 18H, a), 2.32 (s, 3H, g), 4.09-4.19 (m, 4H, C$\underline{H_2}$-NH_2), 7.00-7.05 (m, 2H, f,h), 7.09-7.12 (m, 2H, d,e), 7.19 (s, 2H, N$\underline{H_2}$), 7.28-7.30 (m, 2H, c), 7.52 (s_{br}, 4H, $BArF_{24}$), 7.57-7.58 (m, 1H, b), 7.70 (s_{br}, 8H, $BArF_{24}$) ppm. **^{13}C NMR** (176 MHz, $CDCl_3$): δ = 31.3, 35.8, 52.6, 53.3, 117.7, 123.4, 123.7, 125.6, 125.8, 126.2, 127.7, 128.0, 128.3, 129.1, 129.9, 130.2, 132.2, 135.0, 140.7, 153.7 161.8 ppm. **HRMS** (MeOH): *m/z* calcd. for $[C_{23}H_{34}N]^+$: 324.2686 $[M]^+$, found: 324.2708.

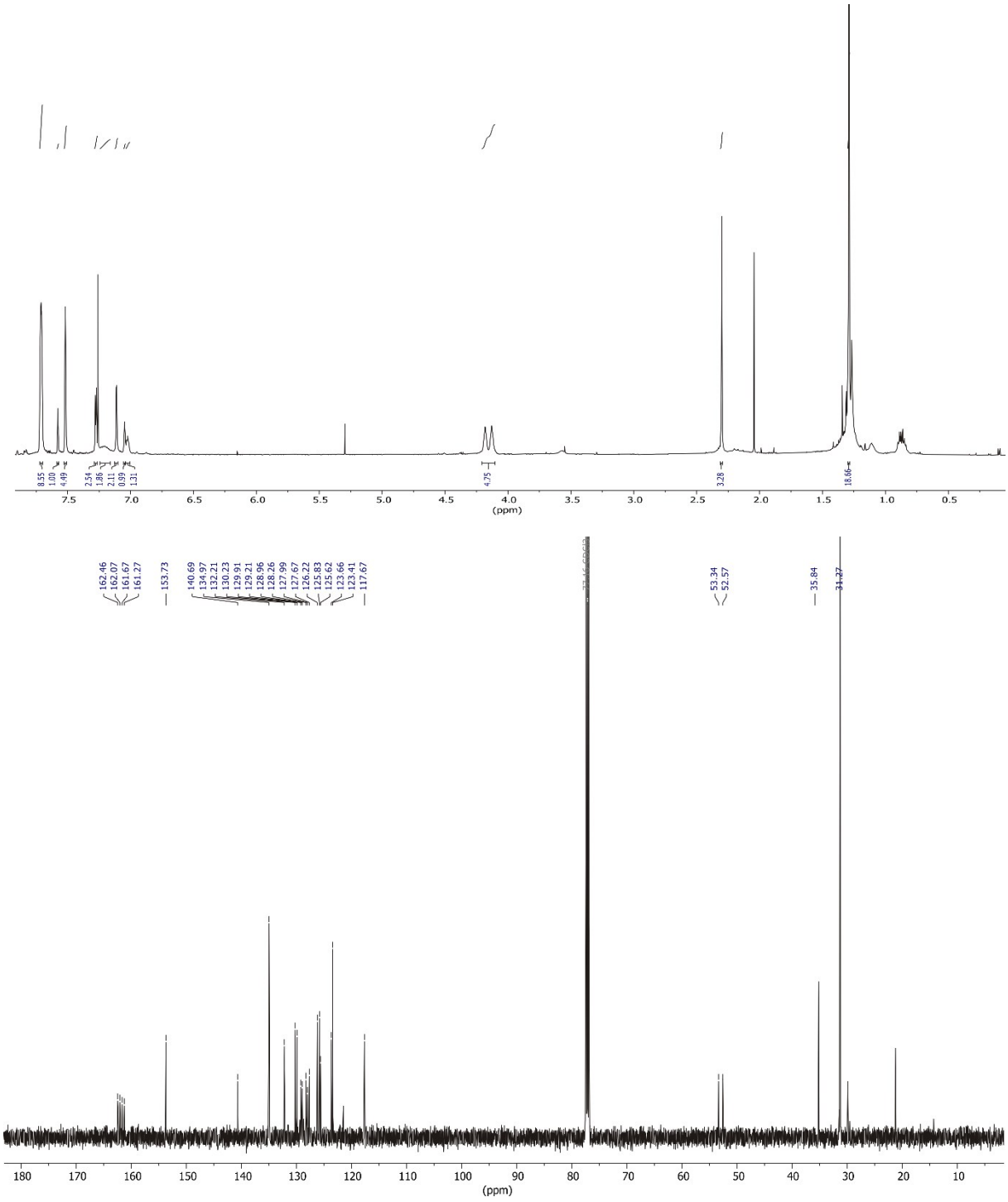

Fig. S2 ^{1}H (top) and ^{13}C (bottom) NMR spectra (500/176 MHz, $CDCl_3$, 298 K) of **PA2**.

N-(3,5-di-tert-butylbenzyl)-1-(2,6-dimethylphenyl)methanaminium tetrakis(3,5-bis(trifluoromethyl)phenyl)borate

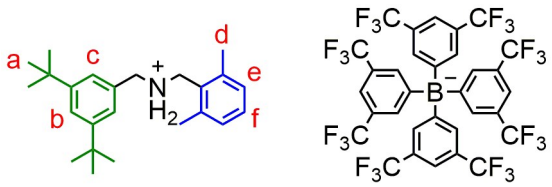

PA3

A solution of 433 mg (2.53 mmol, 1.0 equiv.) (2,6-dimethylphenyl)methanaminium chloride[3], 552 mg (2.53 mmol, 1.0 equiv.) 3,5-di-*tert*-butylbenzaldehyde and 310 µL (2.24 mmol, 0.9 equiv.) NEt_3, in dry EtOH (30 mL) were refluxed under argon atmosphere for 4 h. Afterwards, the solution was cooled to 0 °C and 479 mg (12.65 mmol, 5.0 equiv.) $NaBH_4$ was slowly added. The mixture was left stirring under argon atmosphere overnight in the thawing ice bath. The reaction was quenched by slow addition of sat. $NaHCO_3$ solution and then filtered. The solvent was removed under reduced pressure from the filtrate and the residue was dissolved in CH_2Cl_2 and then washed with sat. $NaHCO_3$ solution and brine. The organic phase was dried with $MgSO_4$ and the solvent removed again. The crude product was purified by column chromatography (SiO_2, CH_2Cl_2/MeOH = 100:1 -> 50:1, R_f ~ 0.3 in CH_2Cl_2/MeOH (100:1)) to obtain a yellowish oil. The oil was dissolved in EtOAc (15 ml) and acidified with HCl (conc.) until the solution reached pH = 1. The mixture was stirred for 1 h and afterwards the solvent was removed under reduced pressure. The residue was dissolved in MeOH (5 ml) and 1.15 g (1.24 mmol, 1.0 equiv.) $NaBArF_{24}$ was added. The solution was left stirring overnight at room temperature, then the solvent was removed. The residue was taken up in CH_2Cl_2, washed with brine/water and dried over $MgSO_4$. The product **PA3** (1.18 g, 0.98 mmol, 39 % overall) was obtained as colorless oil.

^{1}H NMR (500 MHz, $CDCl_3$): δ = 1.31 (s, 18H, a), 2.11 (s, 6H, d), 4.24-4.34 (m, 4H, C$\underline{H_2}$-NH_2), 6.55 (s, 2H, N$\underline{H_2}$), 7.05-7.08 (m, 2H, e), 7.15 (d, J = 1.7 Hz, 2H, c), 7.21-7.25 (m, 1H, f), 7.52 (s_{br}, 4H, $BArF_{24}$), 7.63 (t, J = 1.7 Hz, 1H, b), 7.70 (s_{br}, 8H, $BArF_{24}$) ppm. **^{13}C NMR** (176 MHz, $CDCl_3$): δ = 31.3, 35.2, 45.2, 54.3, 117.7, 122.4, 123.5, 123.6, 123.9, 125.4, 125.5, 125.9, 126.0, 129.0, 130.1, 132.2, 131.2, 134.9, 137.2, 153.1 161.8 ppm. **HRMS** (MeOH): *m/z* calcd. for $[C_{24}H_{36}N]^+$: 338.2842 $[M]^+$, found: 338.2871.

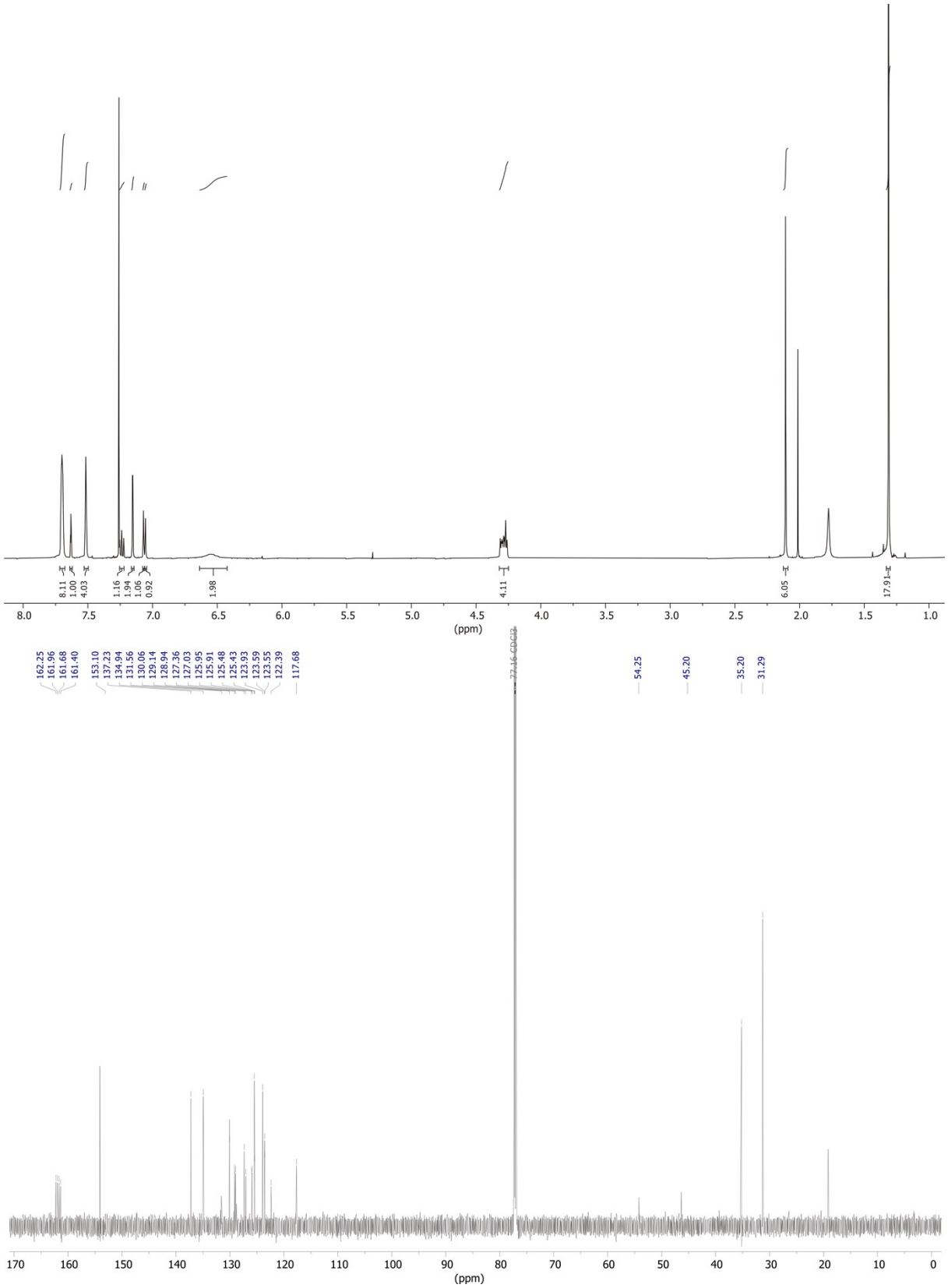

Fig. S3 ^{1}H (top) and ^{13}C (bottom) NMR spectra (500/176 MHz, $CDCl_3$, 298 K) of **PA3**.

N-(3,5-di-tert-butylbenzyl)-1-(2,5-dimethylphenyl)methanaminium tetrakis(3,5-bis(trifluoromethyl)phenyl)borate

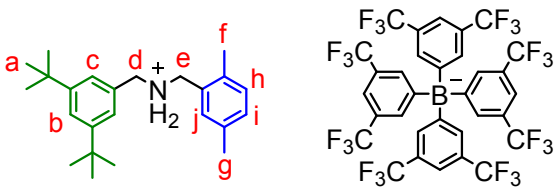

PA4

A solution of 250 mg (1.5 mmol, 1.0 equiv.) (2,5-dimethylphenyl)methanaminium chloride, 319 mg (1.5 mmol, 1.0 equiv.) 3,5-di-*tert*-butylbenzaldehyde and 180 µL (1.3 mmol, 0.9 equiv.) NEt_3, in dry EtOH (60 mL) were refluxed under argon atmosphere for 4 h. Afterwards, the solution was cooled to 0 °C and 275 mg (7.3 mmol, 5.0 equiv.) $NaBH_4$ was slowly added. The mixture was left stirring under argon atmosphere overnight in the thawing ice bath. The reaction was quenched by slow addition of sat. $NaHCO_3$ solution and then filtered. The solvent was removed under reduced pressure from the filtrate and the residue was dissolved in CH_2Cl_2 and then washed with sat. $NaHCO_3$ solution and brine. The organic phase was dried with $MgSO_4$ and the solvent removed again. The crude product was purified by column chromatography (SiO_2, CH_2Cl_2/MeOH = 100:1 -> 50:1, R_f ~ 0.7 in CH_2Cl_2/MeOH (50:1)) to obtain a yellowish oil. The oil was dissolved in Et_2O (15 ml) and acidified with HCl (conc.) until the solution reached pH = 1. The mixture was stirred for 3 h and afterwards the solvent was removed under reduced pressure. A fraction of the residue was dissolved in MeOH (10 ml) and 247 mg (0.27 mmol, 1.0 equiv.) $NaBArF_{24}$ was added. The solution was left stirring overnight at room temperature, then the solvent was removed. The residue was taken up in CH_2Cl_2, washed with brine/water and dried over $MgSO_4$. The product **PA4** (315 mg, 0.26 mmol, 88 % overall) was obtained as colorless oil.

^{1}H NMR (700 MHz, $CDCl_3$): δ = 1.33 (s, 18H, a), 2.12 (s, 3H, f), 2.27 (s, 3H, g), 4.16 - 4.24 (m, 4H, d,e), 6.95 – 6.98 (m, 1H, j), 7.13 - 7.16 (m, 2H, c,h), 7.19 – 7.22 (m, 1H, i), 7.54 (s_{br}, 4H, $BArF_{24}$), 7.62 (t, J = 1.7 Hz, 1H, b), 7.73 (s_{br}, 8H, $BArF_{24}$) ppm. **^{13}C NMR** (176 MHz, $CDCl_3$): δ = 18.1, 20.7, 31.3, 35.2, 49.9, 53.6, 117.7, 122.4, 123.4, 123.9, 125.5, 125.7, 126.6, 127.0, 127.6, 128.8, 129.0, 129.1, 129.3, 130.6, 132.2, 132.5, 133.4, 138.0, 153.9 161.9 ppm. **HRMS** (MeOH): *m/z* calcd. for $[C_{24}H_{36}N]^+$: 338.2842 $[M]^+$, found: 338.2858.

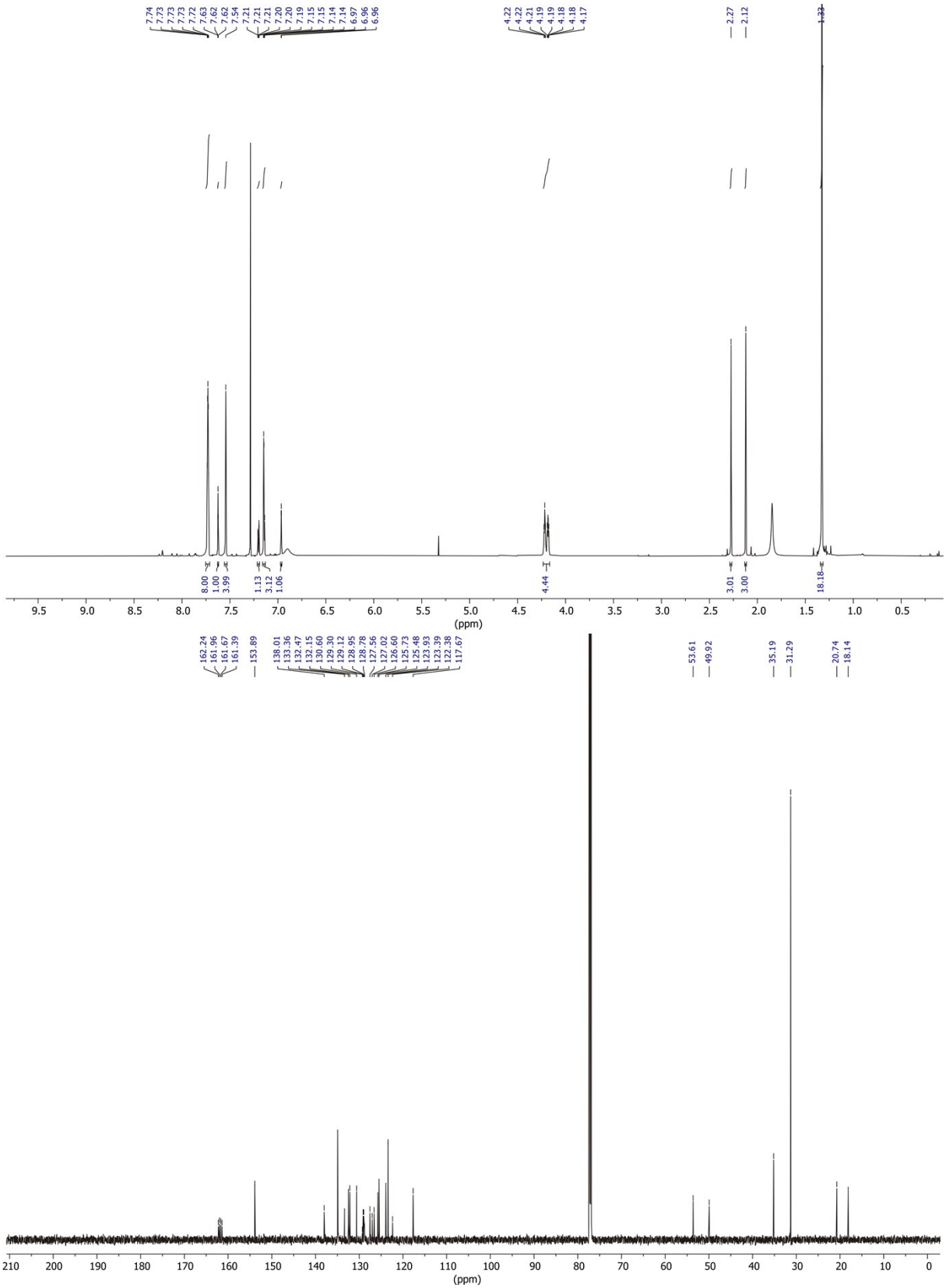

Fig. S4 ^{1}H (top) and ^{13}C (bottom) NMR spectra (700/176 MHz, $CDCl_3$, 298 K) of **PA4**.

N-(3,5-di-tert-butylbenzyl)-1-(2,3-dimethylphenyl)methanaminium tetrakis(3,5-bis(trifluoromethyl)phenyl)borate

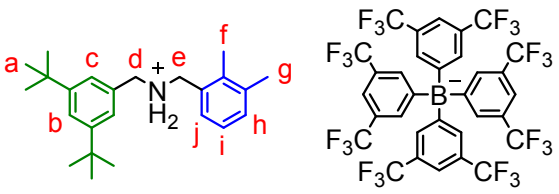

PA5

A solution of 250 mg (1.5 mmol, 1.0 equiv.) (2,3-dimethylphenyl)methanaminium chloride, 319 mg (1.5 mmol, 1.0 equiv.) 3,5-di-*tert*-butylbenzaldehyde and 180 µL (1.3 mmol, 0.9 equiv.) NEt_3, in dry EtOH (60 mL) were refluxed under argon atmosphere for 4 h. Afterwards, the solution was cooled to 0 °C and 275 mg (7.3 mmol, 5.0 equiv.) $NaBH_4$ was slowly added. The mixture was left stirring under argon atmosphere overnight in the thawing ice bath. The reaction was quenched by slow addition of sat. $NaHCO_3$ solution and then filtered. The solvent was removed under reduced pressure from the filtrate and the residue was dissolved in CH_2Cl_2 and then washed with sat. $NaHCO_3$ solution and brine. The organic phase was dried with $MgSO_4$ and the solvent removed again. The crude product was purified by column chromatography (SiO_2, CH_2Cl_2 -> CH_2Cl_2/MeOH = 50:1, R_f ~ 0.7 in CH_2Cl_2/MeOH (50:1)) to obtain a yellowish oil. The oil was dissolved in EtOAc (10 ml) and acidified with HCl (conc.) until the solution reached pH = 1. The mixture was stirred for 3 h and afterwards the solvent was removed under reduced pressure. A fraction of the residue was dissolved in MeOH (5 ml) and 247 mg (0.27 mmol, 1.0 equiv.) $NaBArF_{24}$ was added. The solution was left stirring overnight at room temperature, then the solvent was removed. The residue was taken up in CH_2Cl_2, washed with brine/water and dried over $MgSO_4$. The product **PA5** (324 mg, 0.27 mmol, 58 % overall) was obtained as colorless oil.

^{1}H NMR (700 MHz, $CDCl_3$): δ = 1.30 (s, 18H, a), 2.01 (s, 3H, f), 2.20 (s, 3H, g), 4.11-4.17 (m, 4H, d,e), 6.98 (d, J = 7.6 Hz, 1H, h), 7.08 (t, J = 7.6 Hz, 1H, i), 7.14 (d, J=1.8 Hz, 2H, c), 7.22 (d, J = 7.6 Hz, 1H, j), 7.51 (s_{br}, 4H, $BArF_{24}$), 7.58 (t, J = 1.5 Hz, 1H, b), 7.70 (s_{br}, 8H, $BArF_{24}$) ppm. **^{13}C NMR** (176 MHz, $CDCl_3$): δ = 14.9, 20.5, 31.3, 35.2, 50.0, 53.2, 117.6, 117.6, 117.7, 122.4, 123.5, 123.9, 125.4, 125.5, 127.0, 127.1, 127.9, 128.1, 128.8, 129.0, 129.1, 129.3, 133.0, 134.9, 135.2, 139.4, 153.7 161.9 ppm. **HRMS** (MeOH): *m/z* calcd. for $[C_{24}H_{36}N]^+$: 338.2842 $[M]^+$, found: 338.2847.

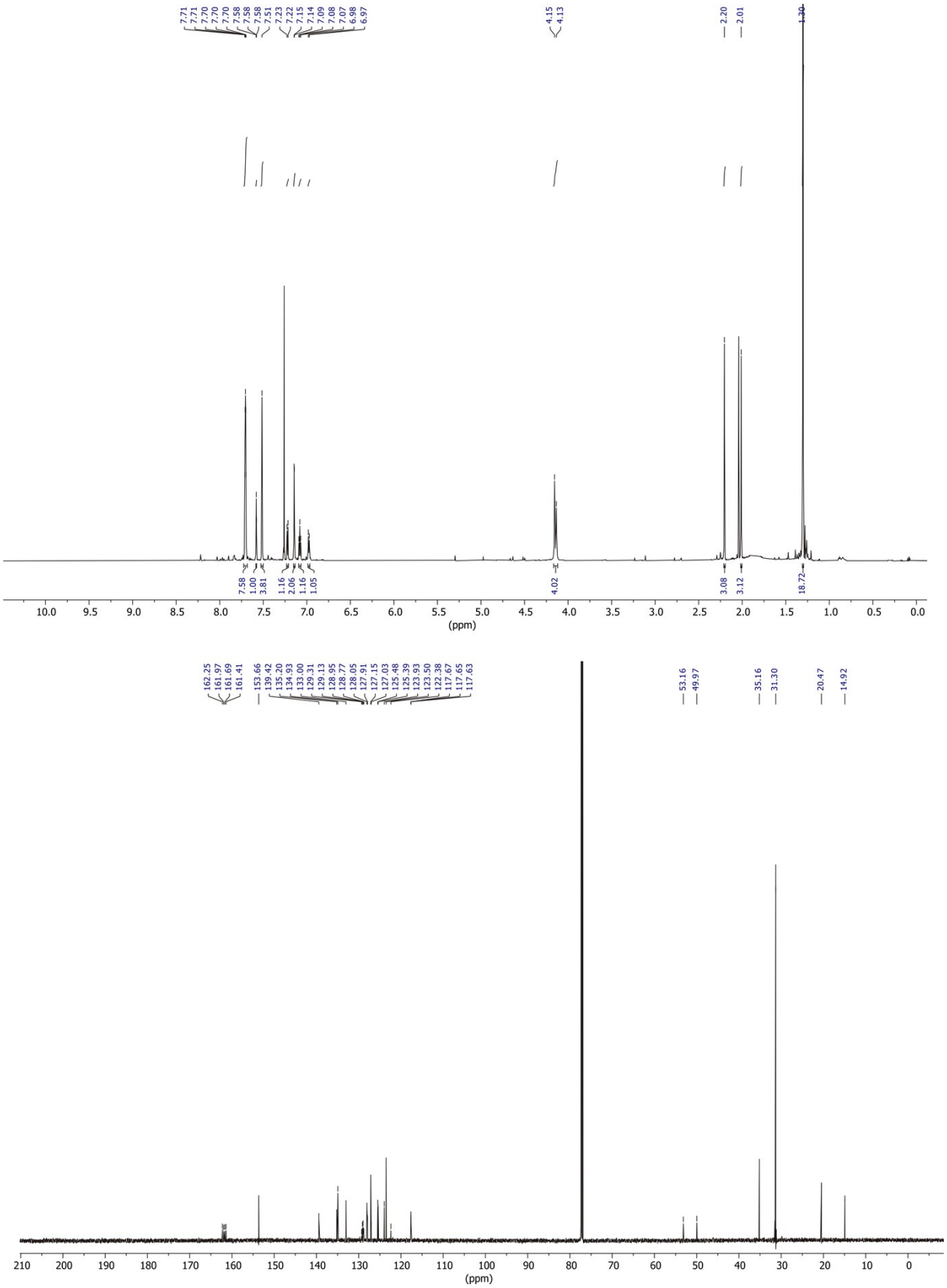

Fig. S5 ^{1}H (top) and ^{13}C (bottom) NMR spectra (700/176 MHz, $CDCl_3$, 298 K) of **PA5**.

N-(3,5-di-tert-butylbenzyl)-1-(2-ethylphenyl)methanaminium tetrakis(3,5-bis(trifluoromethyl)phenyl)borate

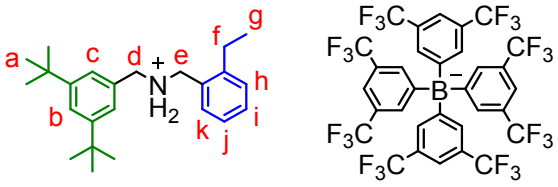

PA6

A solution of 250 mg (1.5 mmol, 1.0 equiv.) (2-ethylphenyl)methanaminium chloride[8], 319 mg (1.5 mmol, 1.0 equiv.) 3,5-di-*tert*-butylbenzaldehyde and 180 µL (1.08 mmol, 0.9 equiv.) NEt_3, in dry EtOH (60 mL) were refluxed under argon atmosphere for 4 h. Afterwards, the solution was cooled to 0 °C and 273 mg (7.3 mmol, 5.0 equiv.) $NaBH_4$ was slowly added. The mixture was left stirring under argon atmosphere overnight in the thawing ice bath. The reaction was quenched by slow addition of sat. $NaHCO_3$ solution and then filtered. The solvent was removed under reduced pressure from the filtrate and the residue was dissolved in CH_2Cl_2 and then washed with sat. $NaHCO_3$ solution and brine. The organic phase was dried with $MgSO_4$ and the solvent removed again. The crude product was purified by column chromatography (SiO_2, CH_2Cl_2 -> CH_2Cl_2/MeOH = 100:1, R_f ~ 0.3 in CH_2Cl_2/MeOH (100:1)) to obtain a yellowish oil. The oil was dissolved in EtOAc (10 ml) and acidified with HCl (conc.) until the solution reached pH = 1. The mixture was stirred for 1 h and afterwards the solvent was removed under reduced pressure. A fraction of the residue was dissolved in MeOH (10 ml) and 239 mg (0.27 mmol, 1.0 equiv.) $NaBArF_{24}$ was added. The solution was left stirring overnight at room temperature, then the solvent was removed. The residue was taken up in CH_2Cl_2, washed with brine/water and dried over $MgSO_4$. The product **PA6** (325 mg, 0.27 mmol, 58 % overall) was obtained as colorless oil.

^{1}H NMR (700 MHz, $CDCl_3$): δ = 1.04 (t, J = 7.6 Hz, 3H, g), 1.31 (s, 18H, a), 2.36 (q, J = 7.5 Hz, 2H, f), 4.13 - 4.22 (m, 4H, d,e), 7.15 - 7.17 (m, 3H, c,i), 7.17 - 7.20 (m, 1H, h), 7.21 - 7.30 (m, 1H, j), 7.36 - 7.39 (m, 1H, k), 7.45 - 7.50 (m, 1H, h), 7.52 (s_{br}, 4H, $BArF_{24}$), 7.59 – 7.60 (m, 1H, b), 7.70 (s_{br}, 8H, $BArF_{24}$) ppm. **^{13}C NMR** (176 MHz, $CDCl_3$): δ = 15.4, 25.5, 31.3, 35.2, 48.7, 53.4, 117.7, 122.4, 123.6, 123.9, 125.5, 125.5, 126.5, 127.0, 127.7, 127.8, 129.0, 129.1, 130.2, 130.3, 131.7, 134.9, 142.9, 153.8, 161.8 ppm. **HRMS** (MeOH): *m/z* calcd. for $[C_{24}H_{36}N]^+$: 338.2842 $[M]^+$, found: 338.2854.

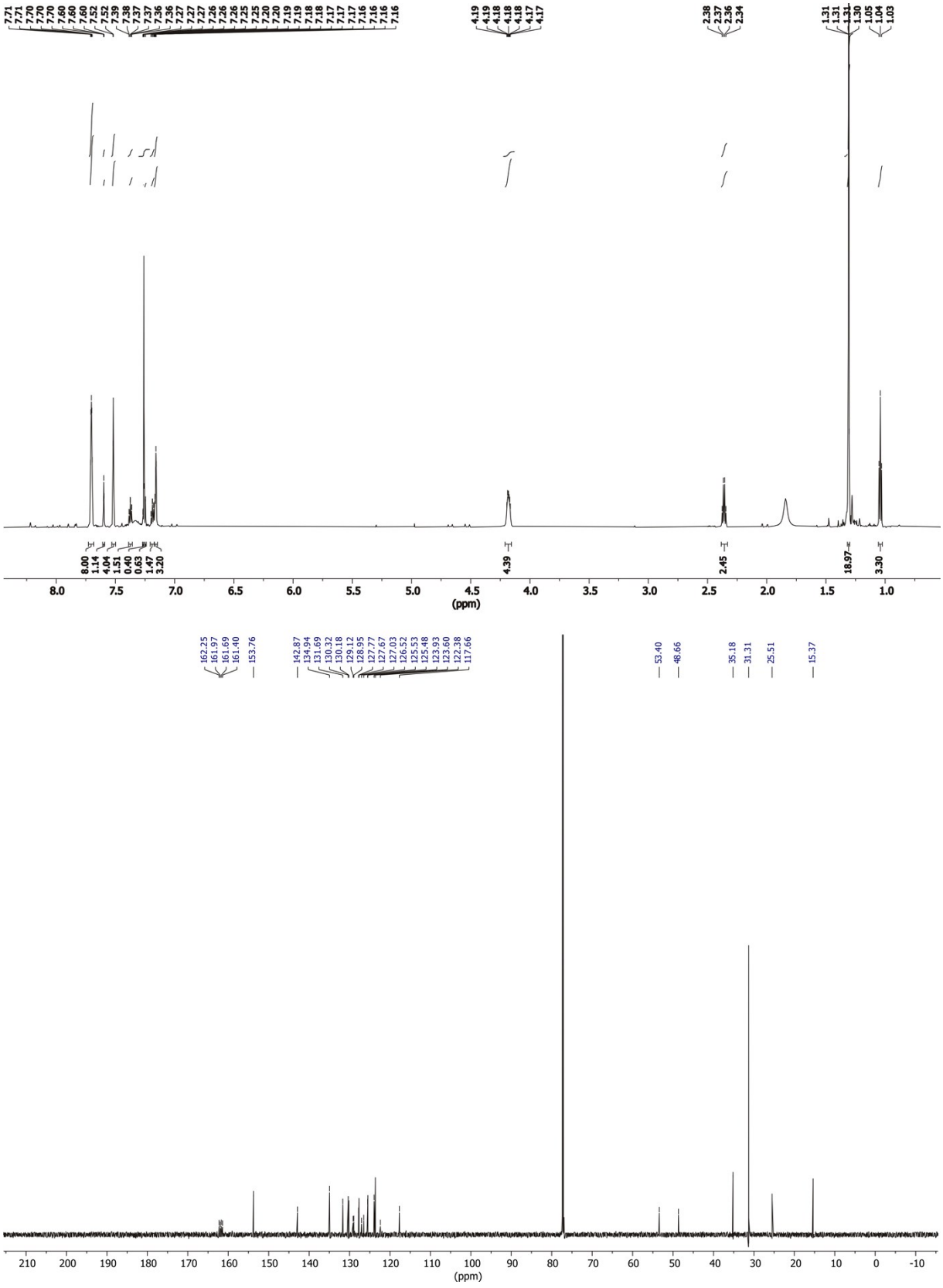

Fig. S6 ^{1}H (top) and ^{13}C (bottom) NMR spectra (700/176 MHz, $CDCl_3$, 298 K) of **PA6**.

N-(3,5-di-tert-butylbenzyl)-1-(2-methoxyphenyl)methanaminium tetrakis(3,5-bis(trifluoromethyl)phenyl)borate

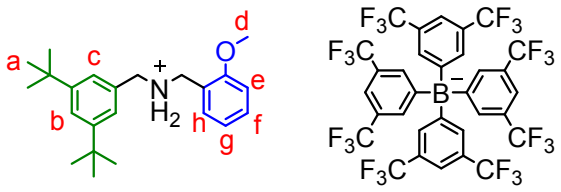

PA7

A solution of 190 mg (1.1 mmol, 1.0 equiv.) (2-methoxyphenyl)methanaminium chloride[8], 240 mg (1.1 mmol, 1.0 equiv.) 3,5-di-*tert*-butylbenzaldehyde and 150 µL (1.08 mmol, 0.9 equiv.) NEt_3, in dry EtOH (30 mL) were refluxed under argon atmosphere for 4 h. Afterwards, the solution was cooled to 0 °C and 207 mg (5.5 mmol, 5.0 equiv.) $NaBH_4$ was slowly added. The mixture was left stirring under argon atmosphere overnight in the thawing ice bath. The reaction was quenched by slow addition of sat. $NaHCO_3$ solution and then filtered. The solvent was removed under reduced pressure from the filtrate and the residue was dissolved in CH_2Cl_2 and then washed with sat. $NaHCO_3$ solution and brine. The organic phase was dried with $MgSO_4$ and the solvent removed again. The crude product was purified by column chromatography (SiO_2, CH_2Cl_2/MeOH = 100:1 -> 50:1, R_f ~ 0.3 in CH_2Cl_2/MeOH (100:1)) to obtain a yellowish oil. The oil was dissolved in EtOAc (10 ml) and acidified with HCl (conc.) until the solution reached pH = 1. The mixture was stirred for 1 h and afterwards the solvent was removed under reduced pressure. The residue was dissolved in MeOH (5 ml) and 478 mg (0.54 mmol, 1.0 equiv.) $NaBArF_{24}$ was added. The solution was left stirring overnight at room temperature, then the solvent was removed. The residue was taken up in CH_2Cl_2, washed with brine/water and dried over $MgSO_4$. The product **PA7** (603 mg, 0.50 mmol, 45 % overall) was obtained as colorless oil.

^{1}H NMR (500 MHz, $CDCl_3$): δ = 1.30 (s, 18H, a), 3.84 (s, 3H, d), 4.11-4.22 (m, 4H, C$\underline{H_2}$-NH_2), 6.84 (s, 2H, N$\underline{H_2}$), 6.95-7.04 (m, 2H, e,f), 7.06 (d, *J*=1.7 Hz, 2H, c), 7.07-7.11 (m, 1H, g), 7.45-7.50 (m, 1H, h), 7.52 (s_{br}, 4H, $BArF_{24}$), 7.59 (t, *J* = 1.7 Hz, 1H, b), 7.70 (s_{br}, 8H, $BArF_{24}$) ppm.

^{13}C NMR (176 MHz, $CDCl_3$): δ = 31.3, 35.2, 50.5, 53.3, 56.3, 111.8, 115.3, 117.7, 122.4, 122.9, 123.1, 123.9, 125.5, 126.0, 127.0, 127.4, 129.1, 131.2, 133.5, 134.9, 154.0, 157.0, 161.8 ppm.

HRMS (MeOH): *m/z* calcd. for $[C_{23}H_{34}NO]^+$: 340.2635 $[M]^+$, found: 340.2643.

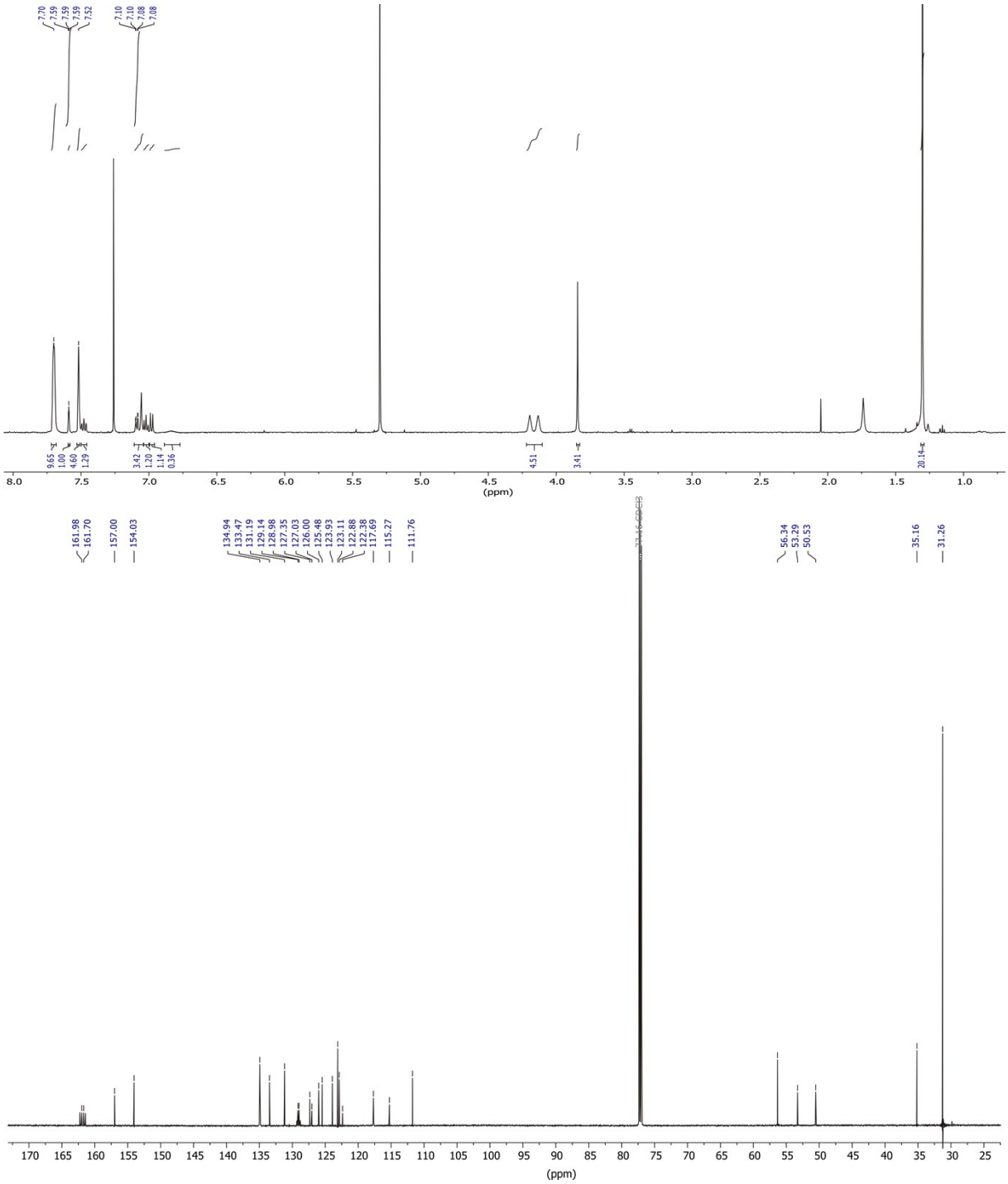

Fig. S7 ^{1}H (top) and ^{13}C (bottom) NMR spectra (500/176 MHz, $CDCl_3$, 298 K) of **PA7**.

N-(3,5-di-tert-butylbenzyl)-1-(2-nitrophenyl)methanaminium tetrakis(3,5-bis(trifluoromethyl)phenyl)borate

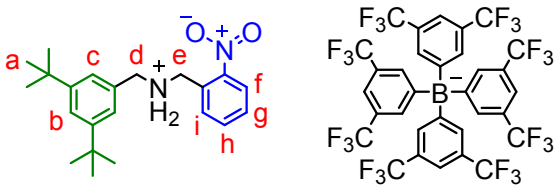

PA8

A solution of 250 mg (1.3 mmol, 1.0 equiv.) (2-nitrophenyl)methanaminium hydrochloride, 290 g (1.3 mmol, 1.0 equiv.) 3,5-di-*tert*-butylbenzaldehyde and 170 µL (0.9 mmol, 0.9 equiv.) dry NEt_3 in dry EtOH (60 mL) was left refluxing under argon atmosphere for 4 h. Afterwards, the solution was cooled to 0 °C in an ice bath and 252 mg (6.7 mmol, 5.0 equiv.) $NaBH_4$ was added. The mixture was left stirring under argon atmosphere in the thawing ice bath overnight. Then, the reaction was stopped by slow addition of sat. $NaHCO_3$ solution until no additional gas development occurred. The solvent was removed under reduced pressure and the residue was taken up in CH_2Cl_2. After washing with water, the organic phase was dried over $MgSO_4$. The crude product was then purified by column chromatography (SiO_2, CH_2Cl_2 → CH_2Cl_2/MeOH = 100:1, R_f ~ 0.2 in CH_2Cl_2/MeOH = 100:1) to get the desired oil, which was directly dissolved in Et_2O (10 mL) and acidified with conc. HCl, until the solution reached pH = 1. Afterwards, the solution was left stirring at r.t. for 3 h, then the solvent was removed under reduced pressure. A fraction of the yellow oil was dissolved in MeOH (10 mL) and 227 mg (0.26 mmol, 1.0 equiv.) $NaBArF_{24}$ was added. The solution was left stirring at r.t. overnight, then the solvent was removed under reduced pressure. Afterwards, the residue was taken up in CH_2Cl_2 and washed with water and dried over $MgSO_4$ to obtain the desired product **PA8** as yellow oil in a combined yield of 80% (327 mg, 0.26 mmol).

^{1}H NMR (500 MHz, $CDCl_3$) δ = 1.30 (s, 18H, a), 4.29 – 4.39 (m, 4H, d,e), 7.20 (d, J = 1.7 Hz, 2H, c), 7.21 – 7.30 (m, 1H, i), 7.34 (s_{br}, 2H, N$\underline{H}_2$), 7.51 (s_{br}, 4H, $BArF_{24}$), 7.52 - 7.55 (m, 1H, h), 7.60 (t, J = 1.8 Hz, 1H, b), 7.62 - 7.66 (m, 1H, g), 7.71 (s_{br}, 8H, $BArF_{24}$), 8.13 – 8.16 (m, 1H, f). ppm. **^{13}C NMR** (126 MHz, $CDCl_3$) δ [ppm] 31.5, 35.2, 50.9, 54.6, 117.7, 121.4, 123.3, 123.4, 123.6, 125.8, 126.0, 127.0, 127.1, 127.9, 128.9, 129.2, 133.4, 134.1, 134.9, 136.0, 149.1, 154.0, 161.9. **HRMS (MeOH):**m/z calcd. for $[C_{22}H_{31}N_2O_2]^+$: 355.2380 $[M]^+$, found: 355.2379.

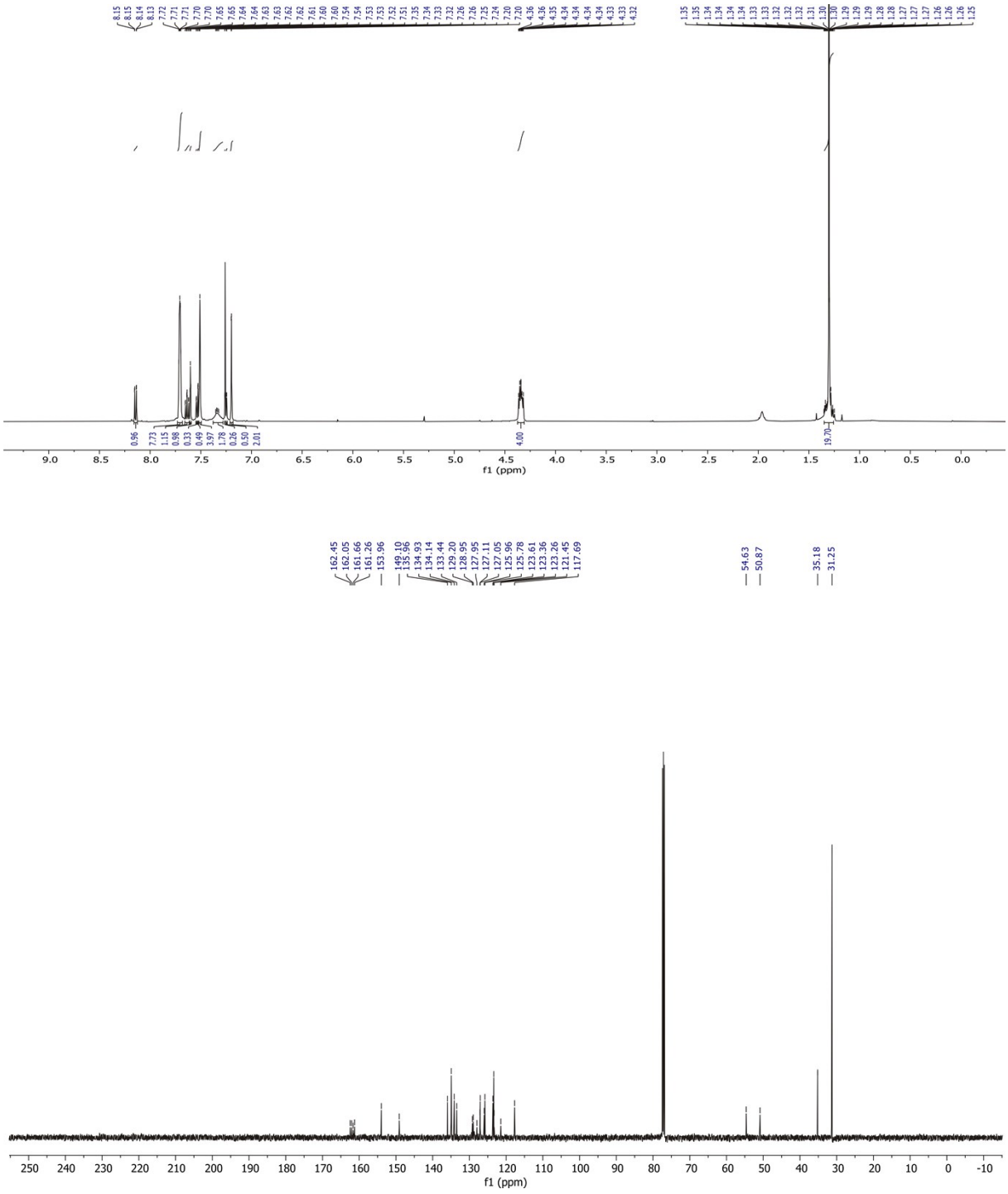

Fig. S8 ^{1}H (top) and ^{13}C (bottom) NMR spectra (500/126 MHz, $CDCl_3$, 298 K) of **PA8**.

1-([1,1'-biphenyl]-3-yl)-N-(3,5-di-tert-butylbenzyl)methanaminiumtetrakis(3,5-bis(trifluoromethyl)phenyl)borate

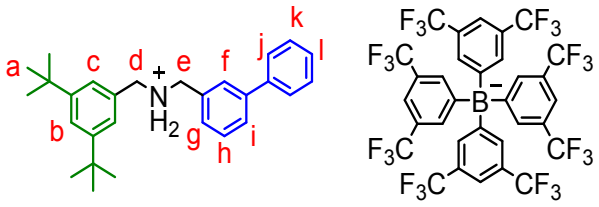

PA9

A solution of 200 mg (0.9 mmol, 1.0 equiv.) (3-Phenylphenyl)methanamine hydrochloride, 218 mg (0.9 mmol, 1.0 equiv.) 3,5-di-*tert*-butylbenzaldehyde and 115 µL (0.8 mmol, 0.9 equiv.) dry NEt_3 in dry EtOH (50 mL) was refluxed under argon atmosphere for 4 h. Afterwards, the solution was cooled to 0 °C in an ice bath and 172 mg (4.6 mmol, 5.0 equiv.) $NaBH_4$ was added. The mixture was left stirring under argon atmosphere in the thawing ice bath overnight. Then, the reaction was stopped by slow addition of sat. $NaHCO_3$ solution until no additional gas development occurred. The solvent was removed under reduced pressure and the residue was taken up in CH_2Cl_2. After washing with water, the organic phase was dried over $MgSO_4$. The crude product was then purified by column chromatography (SiO_2, CH_2Cl_2 → CH_2Cl_2/MeOH = 50:1, R_f ~ 0.2 in CH_2Cl_2/MeOH = 100:1) to obtain a yellowish oil, which was directly dissolved in EtOAc (10 mL) and acidified with conc. HCl, until the solution reached pH = 1. Afterwards, the solution was left stirring at r.t. for 3 h, then the solvent was removed under reduced pressure. The yellow solid was dissolved in MeOH (10 mL) and 361 mg (0.4 mmol, 1.0 equiv.) $NaBArF_{24}$ was added. The solution was left stirring at r.t. overnight, then the solvent was removed under reduced pressure. Afterwards, the residue was taken up in CH_2Cl_2 and washed with water and dried over $MgSO_4$ to obtain the desired product **PA9** as colorless oil in a combined yield of 43% (484 mg, 0.4 mmol).

^{1}H NMR (700 MHz, $CDCl_3$): δ = 1.29 (s, 18H, a), 4.17 - 4.22 (m, 4H, d,e), 7.17 (d, J = 1.8 Hz, 2H, c), 7.17 – 7.19 (m, 1H, j), 7.37 – 7.39 (m, 2H, g,i), 7.43 (t, J = 7.7 Hz, 1H, l), 7.45 - 7.47 (m, 2H, k), 7.52 (s_{br}, 4H, $BArF_{24}$), 7.55 (t, J = 1.9 Hz, 1H, f), 7.57 (t, J = 1.8 Hz, 1H, b), 7.68 (ddd, J = 1.0, 1.8, 7.8 Hz, 1H, h), 7.73 (s_{br}, 8H, $BArF_{24}$) ppm. **^{13}C NMR** (176 MHz, $CDCl_3$): δ = 31.3, 35.2,.1, 52.3, 53.3, 117.6, 117.7, 117.7, 117.7, 117.7, 122.4, 123.6, 124.0, 125.5, 127.1, 127.7, 128.0, 128.3, 128.6, 128.9, 128.9, 129.0, 129.0, 129.1, 129.1, 129.1, 129.1, 129.2, 129.3, 129.8, 129.9, 130.7, 135.0, 139.3, 143.4, 153.6, 161.8 ppm. **HRMS** (MeOH): *m/z* calcd. for $[C_{28}H_{36}N]^+$: 386.2842 $[M]^+$, found: 386.2848.

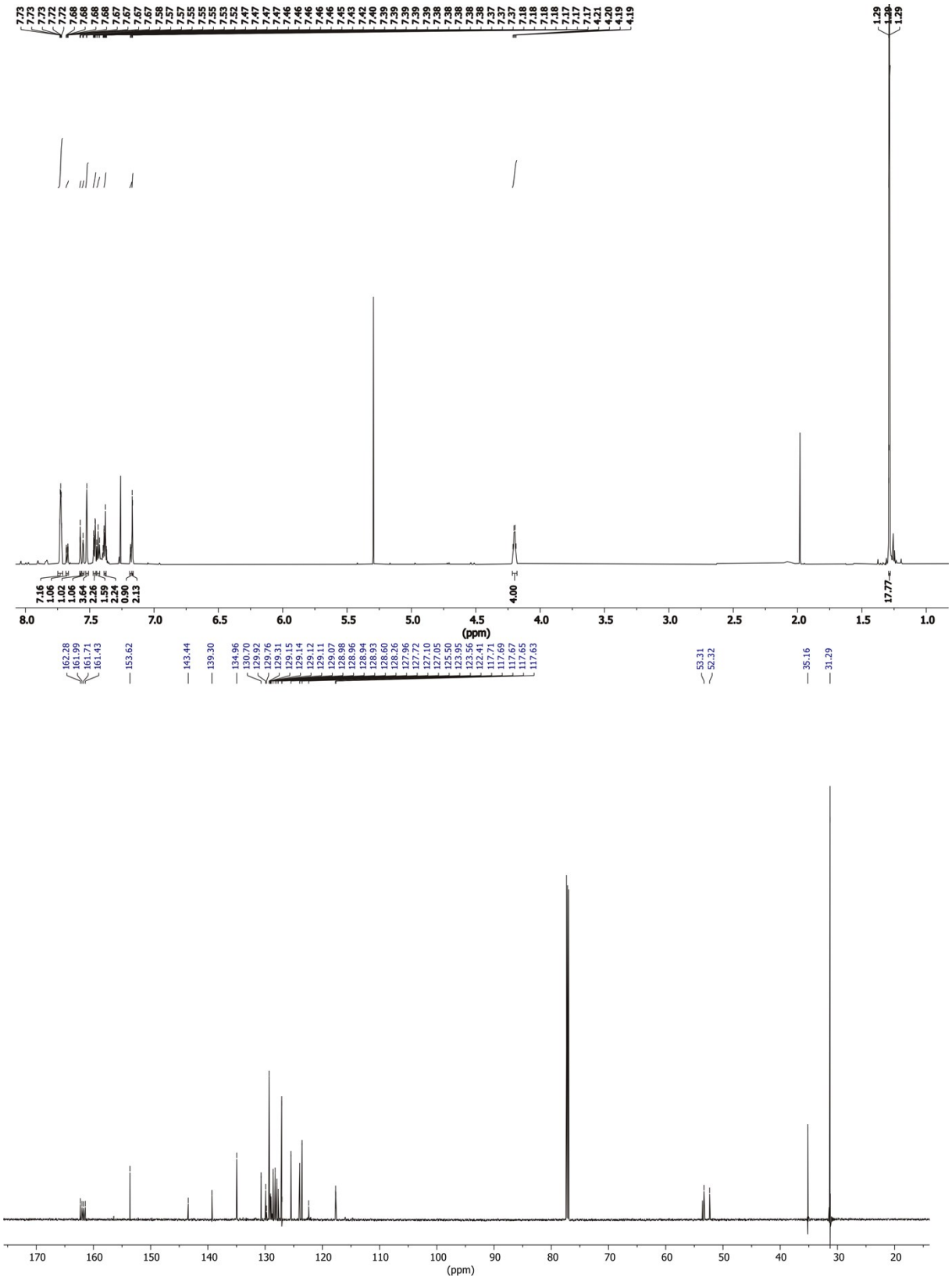

Fig. S9 ^{1}H (top) and ^{13}C (bottom) NMR spectra (700/176 MHz, $CDCl_3$, 298 K) of **PA9**.

N-(3,5-di-tert-butylbenzyl)-1-(naphthalen-2-yl)methanaminiumtetrakis(3,5-bis(trifluoromethyl)phenyl)borate

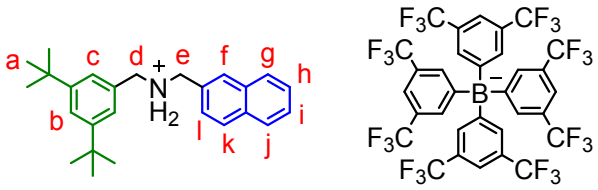

PA10

A solution of 200 mg (1.0 mmol, 1.0 equiv.) naphthalen-2-ylmethanaminium hydrochloride, 226 g (1.0 mmol, 1.0 equiv.) 3,5-di-*tert*-butylbenzaldehyde and 130 µL (0.9 mmol, 0.9 equiv.) dry NEt_3 in dry EtOH (50 mL) was left refluxing under argon atmosphere for 4 h. Afterwards, the solution was cooled to 0 °C in an ice bath and 200 mg (5.2 mmol, 5.0 equiv.) $NaBH_4$ was added. The mixture was left stirring under argon atmosphere in the thawing ice bath overnight. Then, the reaction was stopped by slow addition of sat. $NaHCO_3$ solution until no additional gas development occurred. The solvent was removed under reduced pressure and the residue was taken up in CH_2Cl_2. After washing with water, the organic phase was dried over $MgSO_4$. The crude product was then purified by column chromatography (SiO_2, CH_2Cl_2 → CH_2Cl_2/MeOH = 100:1, R_f ~ 0.2 in CH_2Cl_2/MeOH = 100:1) to get the desired oil, which was directly dissolved in EtOAc (10 mL) and acidified with conc. HCl, until the solution reached pH = 1. Afterwards, the solution was left stirring at r.t. for 3 h, then the solvent was removed under reduced pressure. The yellow solid was dissolved in MeOH (10 mL) and 599 mg (0.7 mmol, 1.0 equiv.) $NaBArF_{24}$ was added. The solution was left stirring at r.t. overnight, then the solvent was removed under reduced pressure. Afterwards, the residue was taken up in CH_2Cl_2 and washed with water and dried over $MgSO_4$ to obtain the desired product **PA10** as yellow oil in a combined yield of 61% (751 mg, 0.6 mmol).

^{1}H NMR (500 MHz, $CDCl_3$) δ = 1.29 (s, 18H, a), 4.19 – 4.25 (m, 2H, d), 4.29 – 4.38 (m, 2H, e), 7.12 (d, J = 1.8 Hz, 2H, c), 7.23 (dd, J = 8.5, 1.8 Hz, 1H, f), 7.52 (s_{br}, 4H, $BArF_{24}$), 7.56 - 7.60 (m, 2H, h, i), 7.60 – 7.64 (m, 1H, b), 7.73 (s_{br}, 8H, $BArF_{24}$), 7.74 – 7.77 (m, 2H, g, j), 7.84 – 7.91 (m, 2H, l, k) ppm.**^{13}C NMR** (176 MHz, $CDCl_3$) δ [ppm] 31.5, 35.2, 49.3, 50.1, 114.5, 116.0, 122.4, 122.8, 123.9, 124.0, 124.3, 125.5, 126.5, 127.1, 127.2, 127.5, 127.7, 127.9, 128.1, 128.7, 129.5, 129.8, 130.2, 132.9, 133.0, 133.1, 133.2, 133.2, 133.3, 133.6, 134.0, 135.0, 140.6, 152.5, 156.7.**HRMS (MeOH):**m/z calcd. for $[C_{26}H_{34}N]^+$: 360.2686 $[M]^+$, found: 360.2677.

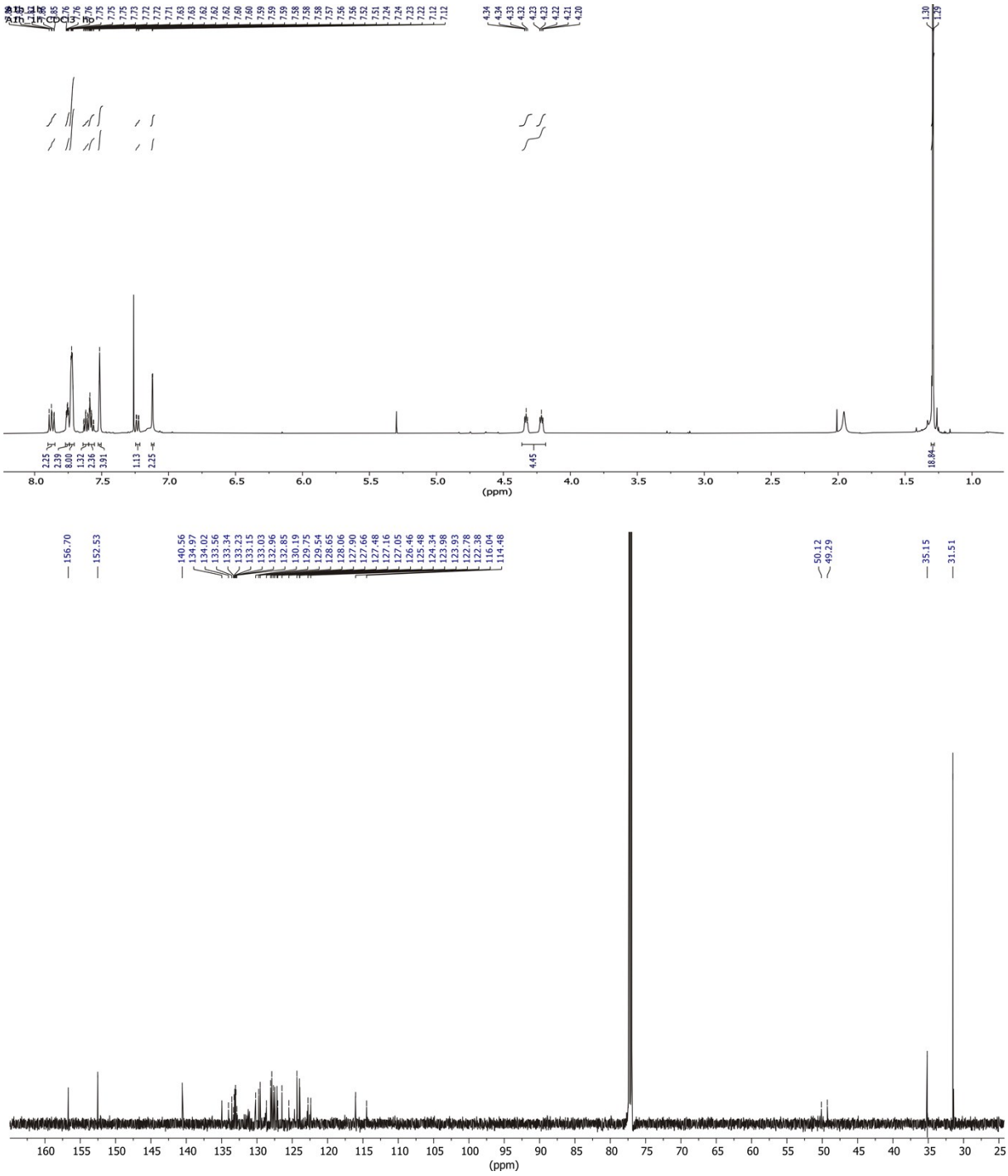

Fig. S10 ^{1}H (top) and ^{13}C (bottom) NMR spectra (500/176 MHz, $CDCl_3$, 298 K) of **PA10**.

N-(3,5-di-tert-butylbenzyl)-1-(naphthalen-1-yl)methanaminiumtetrakis(3,5-bis(trifluoromethyl)phenyl)borate

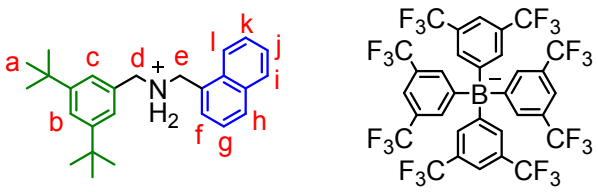

PA11

A solution of 200 mg (1.0 mmol, 1.0 equiv.) naphthalen-1-ylmethanaminium hydrochloride[9], 226 mg (1.0 mmol, 1.0 equiv.) 3,5-di-*tert*-butylbenzaldehyde and 130 µL (0.9 mmol, 0.9 equiv.) dry NEt_3 in dry EtOH (50 mL) was refluxed under argon atmosphere for 4 h. Afterwards, the solution was cooled to 0 °C in an ice bath and 195 mg (5.2 mmol, 5.0 equiv.) $NaBH_4$ was added. The mixture was left stirring under argon atmosphere in the thawing ice bath overnight. Then, the reaction was stopped by slow addition of sat. $NaHCO_3$ solution until no additional gas development occurred. The solvent was removed under reduced pressure and the residue was taken up in CH_2Cl_2. After washing with water, the organic phase was dried over $MgSO_4$. The crude product was then purified by column chromatography (SiO_2, CH_2Cl_2 → CH_2Cl_2/MeOH = 100:1, R_f ~ 0.2 in CH_2Cl_2/MeOH = 100:1) to obtain a yellowish oil, which was directly dissolved in EtOAc (10 mL) and acidified with conc. HCl, until the solution reached pH = 1. Afterwards, the solution was left stirring at r.t. for 3 h, then the solvent was removed under reduced pressure. The yellow solid was dissolved in MeOH (10 mL) and 599 mg (0.7 mmol, 1.0 equiv.) $NaBArF_{24}$ was added. The solution was left stirring at r.t. overnight, then the solvent was removed under reduced pressure. Afterwards, the residue was taken up in CH_2Cl_2 and washed with water and dried over $MgSO_4$ to obtain the desired product **PA11** as reddish oil in a combined yield of 63% (773 mg, 0.6 mmol).

^{1}H NMR (500 MHz, $CDCl_3$): δ = 1.30 (s, 18H, a), 4.20 (s, 2H, d), 4.31 (s, 2H, e), 7.12 (d, J = 1.7 Hz, 2H, c), 7.21 – 7.25 (m, 1H, f), 7.51 (s_{br}, 4H, $BArF_{24}$), 7.56 - 7.64 (m, 3H, b, g, k), 7.72 (s_{br}, 8H, $BArF_{24}$), 7.74 – 7.78 (m, 2H, h, j), 7.86 – 7.91 (m, 2H, l, i). **^{13}C NMR** (176 MHz, $CDCl_3$): δ = 31.5, 31.6, 35.1, 46.1, 51.0, 114.3, 116.0, 116.1, 116.1, 116.1, 121.7, 121.9, 122.4, 122.5, 122.6, 122.8, 122.9, 123.9, 124.0, 124.1, 124.3, 125.5, 125.8, 126.7, 127.6, 127.7, 127.7, 128.9, 129.4, 129.8, 130.0, 130.8, 130.9, 131.0, 131.1, 133.0, 133.8, 134.1, 135.0, 140.6, 152.7, 156.9 ppm. **HRMS** (MeOH): *m/z* calcd. for $[C_{26}H_{34}N]^+$: 360.2686 $[M]^+$, found: 360.2688.

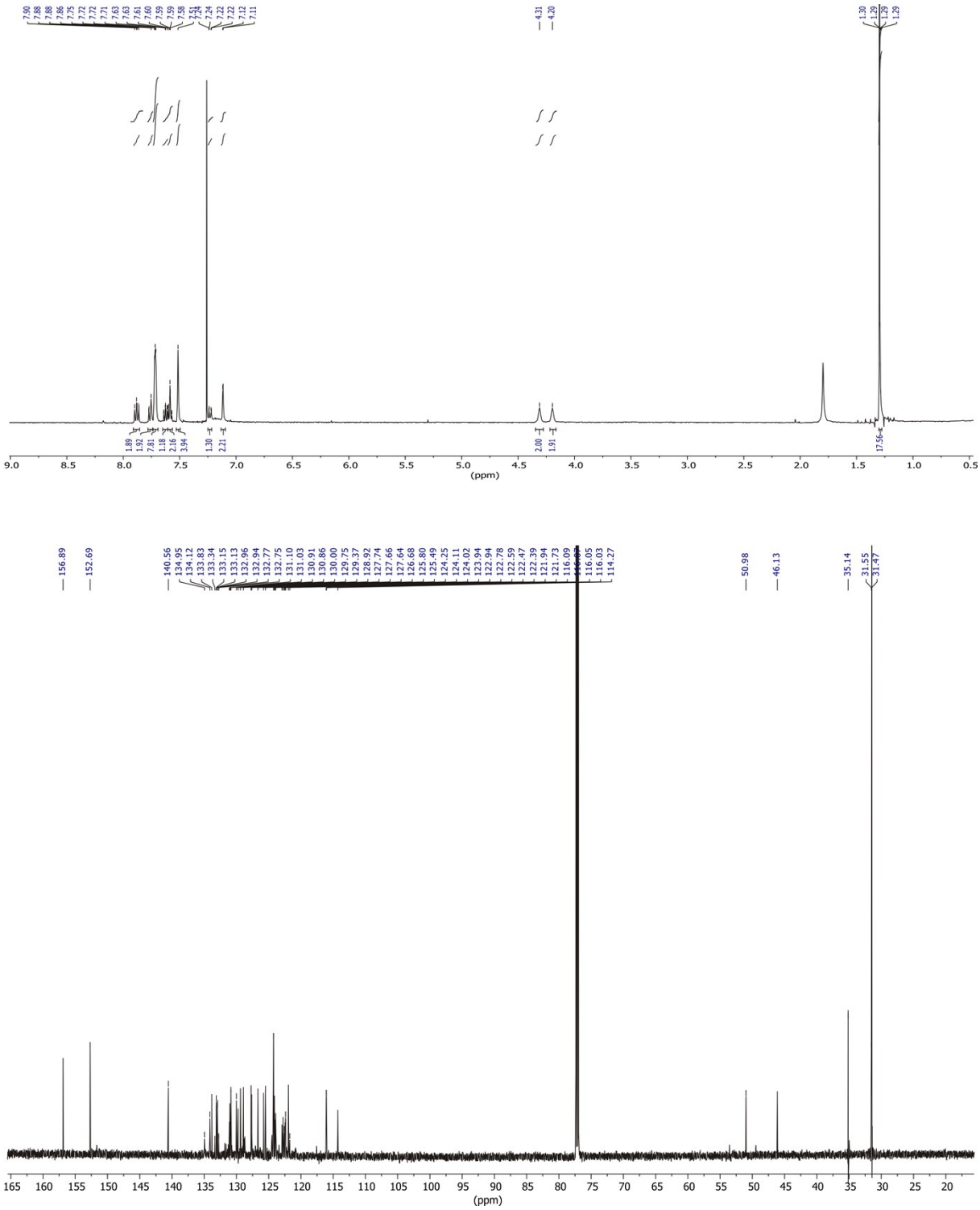

Fig. S11 ^{1}H (top) and ^{13}C (bottom) NMR spectra (500/176 MHz, $CDCl_3$, 298 K) of **PA11**.

N-benzyl-1-(naphthalen-1-yl)methanaminiumtetrakis(3,5-bis(trifluoromethyl)phenyl)borate

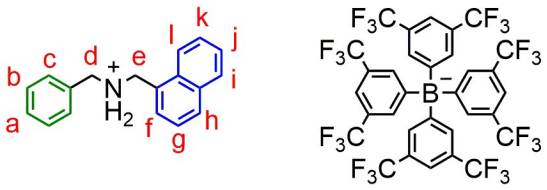

PA12

A solution of 52 mg (0.27 mmol, 1.0 equiv.) naphthalen-1-ylmethanaminium hydrochloride[9], 27 µL (0.27 mmol, 1.0 equiv.) benzaldehyde and 32 µL (0.24 mmol, 0.9 equiv.) dry NEt_3 in dry EtOH (15 mL) was refluxed under argon atmosphere for 4 h. Afterwards, the solution was cooled to 0 °C in an ice bath and 52 mg (1.3 mmol, 5.0 equiv.) $NaBH_4$ was added. The mixture was left stirring under argon atmosphere in the thawing ice bath overnight. Then, the reaction was stopped by slow addition of sat. $NaHCO_3$ solution until no additional gas development occurred. The solvent was removed under reduced pressure and the residue was taken up in CH_2Cl_2. After washing with water, the organic phase was dried over $MgSO_4$. The crude product was then purified by flash column chromatography (spherical SiO_2, CH_2Cl_2 → CH_2Cl_2/MeOH = 6%, R_f ~ 0.3 in CH_2Cl_2/MeOH = 1%) to obtain a yellow oil, which was directly dissolved in EtOAc (10 mL) and acidified with conc. HCl, until the solution reached pH = 1. Afterwards, the solution was left stirring at r.t. for 3 h, then the solvent was removed under reduced pressure. A fraction of the brown oil was dissolved in MeOH (5 mL) and 62 mg (70 µmol, 1.0 equiv.) $NaBArF_{24}$ was added. The solution was left stirring at r.t. overnight, then the solvent was removed under reduced pressure. Afterwards, the residue was taken up in CH_2Cl_2 and washed with water and dried over $MgSO_4$ to obtain the desired product **PA12** as brown oil in a combined yield of 54% (52 mg, 46 µmol).

^{1}H NMR (600 MHz, $CDCl_3$): δ = 4.20 (s, 2H, d), 4.41 (s, 2H, e), 7.08 – 7.11 (m, 2H, c), 7.23 (dd, J = 7.0, 1.2 Hz, 1H, f), 7.33 – 7.39 (m, 4H, g,k,b), 7.42 – 7.46 (m, 1H, a), 7.48 – 7.50 (m, 1H, h), 7.49 – 7.52 (s_{br}, 4H, $BArF_{24}$), 7.57 (m, 1H, j), 7.72 (s_{br}, 8H, $BArF_{24}$), 7.93 – 7.97 (m, 1H, i,l). **^{13}C NMR** (151 MHz, $CDCl_3$): δ = 49.79, 52.99, 117.68, 120.22, 122.01, 123.82, 125.62, 127.46, 128.67, 129.04, 129.34, 130.33, 130.47, 131.19, 132.15, 134.33, 134.95, 161.38, 161.70, 162.04, 162.36 ppm. **HRMS** (MeOH): *m/z* calcd. for $[C_{18}H_{18}N]^+$: 248.1434 $[M]^+$, found: 248.1431.

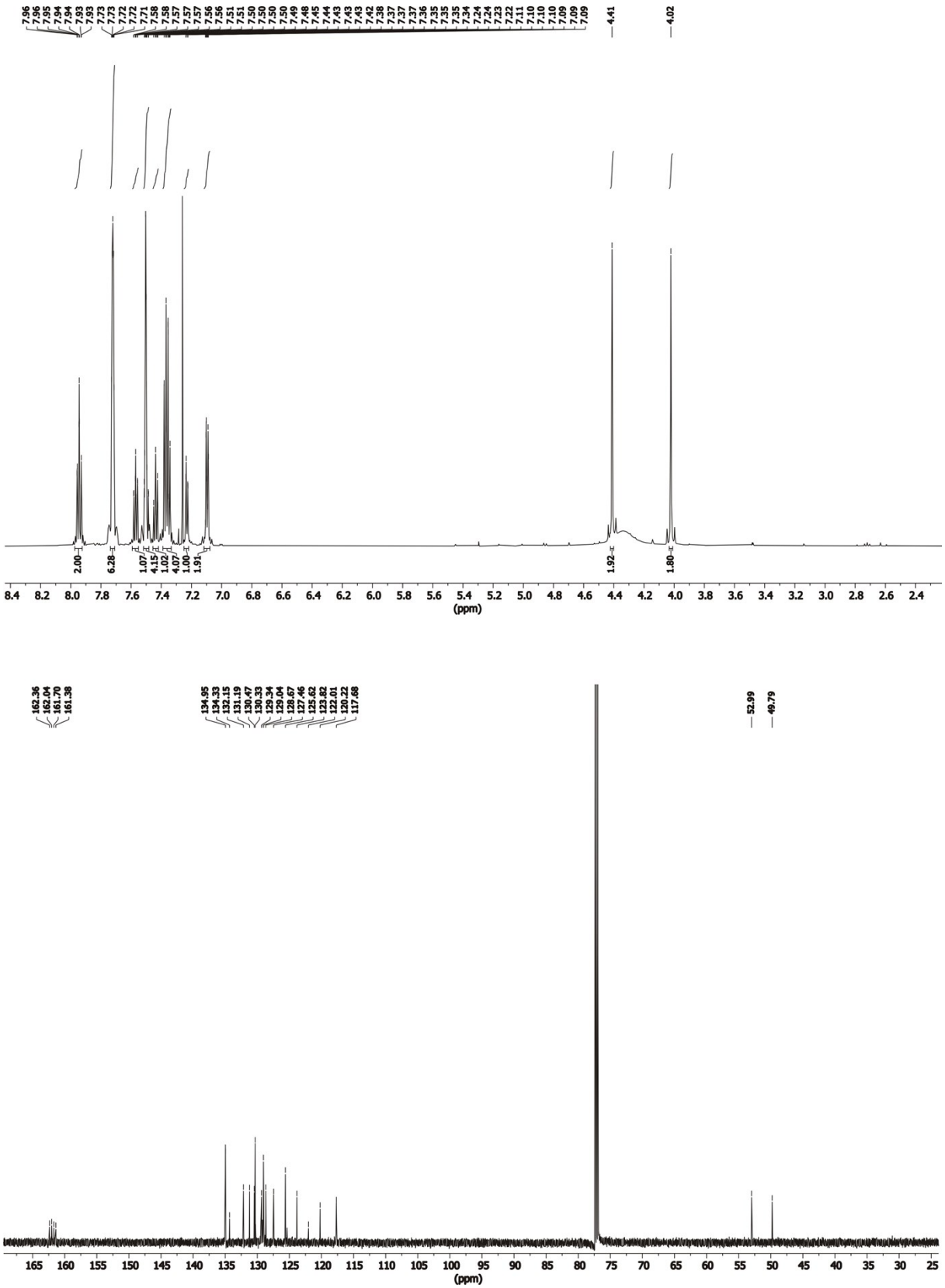

Fig. S12 ^{1}H (top) and ^{13}C (bottom) NMR spectra (600/151 MHz, $CDCl_3$, 298 K) of **PA12**.

1.3. Synthesis of [2]rotaxane R1, R2 and PA11@TTFC8

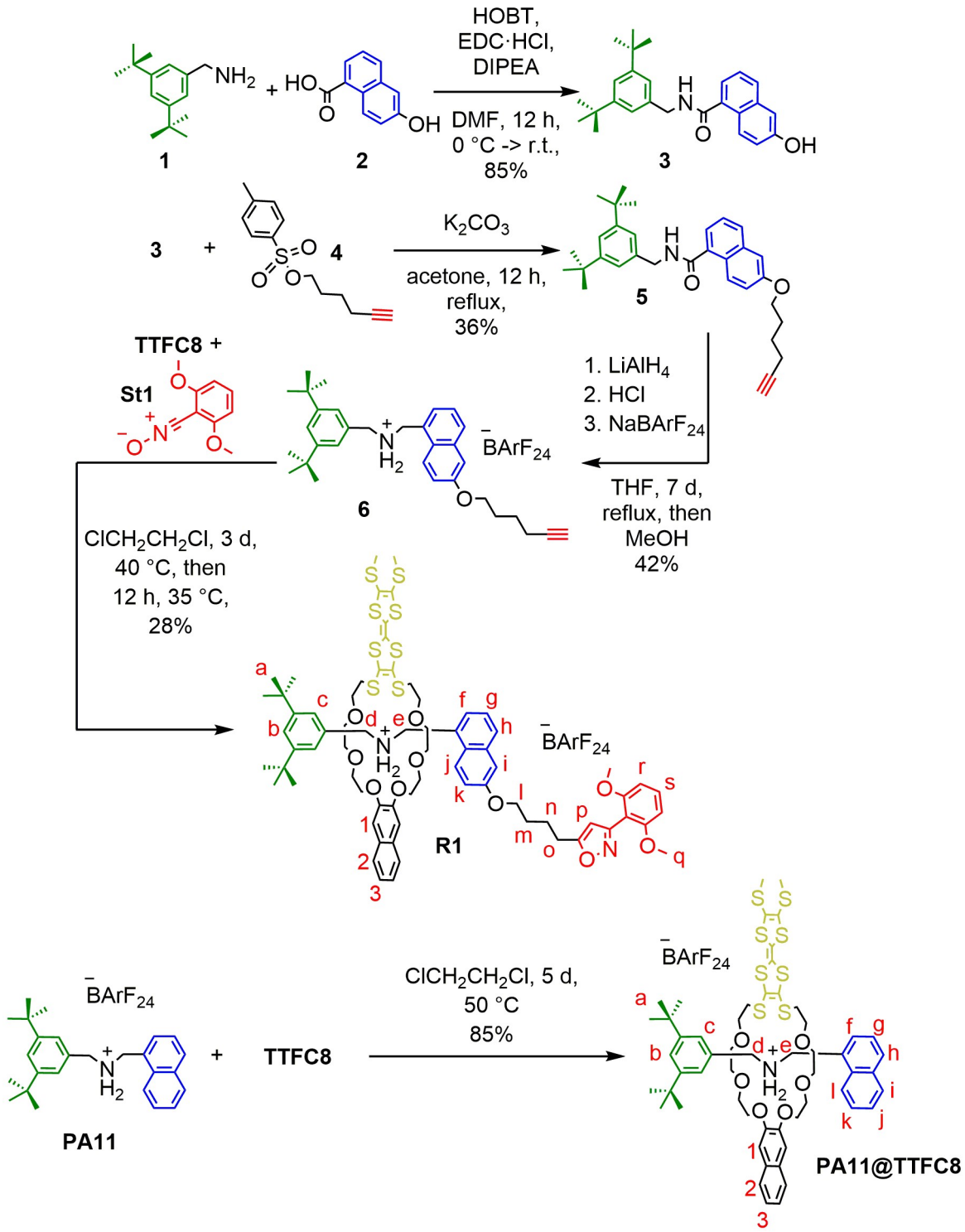

Scheme S2 Synthesis of **R1** and **PA11@TTFC8**.

N-(3,5-di-tert-butylbenzyl)-6-hydroxy-1-naphthamide 3

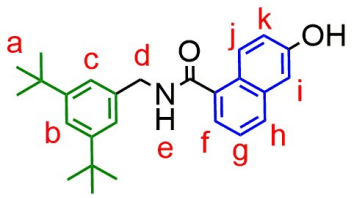

3

A solution of 58 mg (0.27 mmol, 1.0 equiv.) (3,5-di-*tert*-butylphenyl)methanamine **1**, 50 mg (0.27 mmol, 1.0 equiv.) 6-hydroxy-1-naphthoic acid **2** were dissolved in dry DMF (5 mL). In an ice bath 22 mg (0.16 mmol, 0.6 equiv.) HOBT, 66 mg (0.35 mmol, 1.3 equiv.) EDC·HCl and 72 µL (0.43 mmol, 1.6 equiv.) DIPEA were added. The mixture was stirred under argon atmosphere in the thawing ice bath overnight. Then, the mixture was diluted with 30 mL EtOAc and washed with water and brine. After drying over $MgSO_4$, the solvent was removed. Afterwards, the crude product was purified by column chromatography (SiO_2, CH_2Cl_2 -> CH_2Cl_2/MeOH 50:1, R_f ~ 0.4 in CH_2Cl_2/MeOH = 50:1) to get the desired product **3** as yellow sticky solid in 85% yield (85.7 mg, 0.22 µmol).

^{1}H NMR (500 MHz, acetone-d_6) δ = 1.33 (s, 18H, a), 4.68 (d, J = 6.2 Hz, 2H, d), 7.16 (dd, J = 9.1, 2.5 Hz, 1H, k), 7.23 (d, J = 2.5 Hz, 1H, i), 7.35 (d, J = 1.8 Hz, 2H, c), 7.37 – 7.42 (m, 2H, b, h), 7.46 (dd, J = 7.0, 1.3 Hz, 1H, g), 7.72 – 7.76 (m, 1H, f), 8.02 – 8.09 (s_{br}, 1H, e), 8.28 (d, J = 9.2 Hz, 1H, j), 8.83 (s_{br}, 1H, OH) ppm. **^{13}C NMR** (126 MHz, Acetone-d_6) δ = 31.8, 35.4, 44.3, 110.2, 119.8, 121.6, 122.5, 122.8, 126.1, 126.1, 128.4, 129.1, 136.2, 136.4, 139.8, 151.5, 156.4, 169.9 ppm. **HRMS** (CH_2Cl_2/MeOH): m/z calcd. for $[C_{26}H_{31}NO_2]$: 412.2247 $[M+Na]^+$, found: 412.2263.

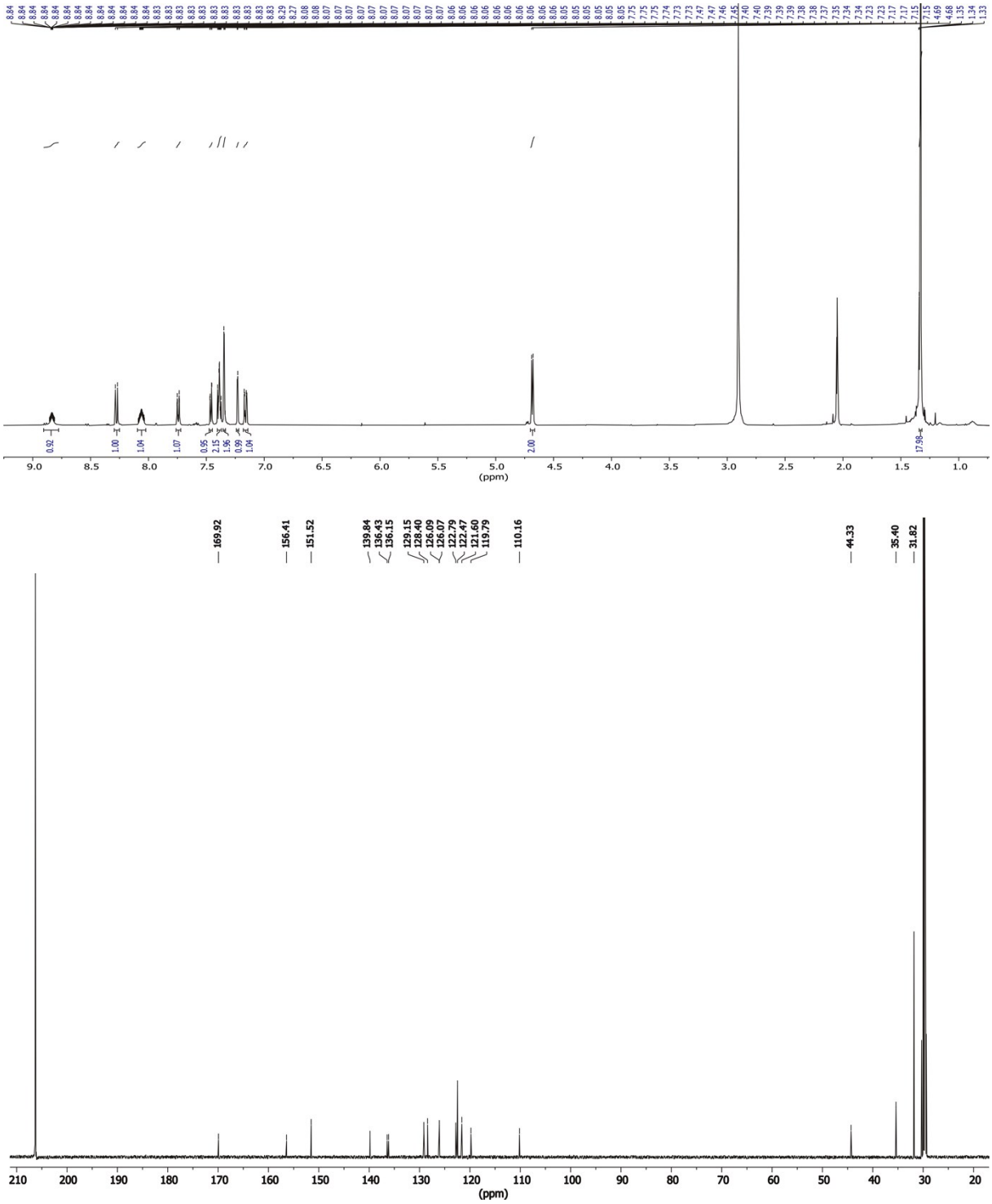

Fig. S13 ^{1}H (top) and ^{13}C (bottom) NMR spectra (500/126 MHz, Acetone-d_6, 298 K) of **3**.

N-(3,5-di-tert-butylbenzyl)-6-(hex-5-yn-1-yloxy)-1-naphthamide 5

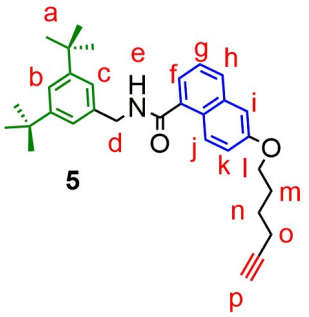

5

A solution of 194 mg (0.77 mmol, 1.2 equiv.) tosylate **4**, 250 mg (0.64 mmol, 1.0 equiv.) amide **3** and 177 mg (1.28 mmol, 2.0 equiv.) K_2CO_3 in acetone (10 mL) was refluxed for 12 h. Then, the mixture was filtered and the solvent was removed, the crude product was dissolved in CH_2Cl_2 and washed with water and brine. After drying over $MgSO_4$, the solvent was removed. Afterwards, the crude product was purified by column chromatography (SiO_2, CH_2Cl_2 -> CH_2Cl_2/MeOH 100:1, R_f ~ 0.8 in CH_2Cl_2/MeOH = 100:1) to get the desired product **5** as yellow sticky solid in 36% yield (108 mg, 0.23 mmol).

^{1}H NMR (500 MHz, $CDCl_3$) δ = 1.34 (s, 18H, a), 1.73 – 1.82 (m, 2H, n), 1.95 – 2.05 (m, 3H, m, p), 2.31 (td, *J* = 7.0, 2.7 Hz, 2H, o), 4.11 (t, *J* = 6.3 Hz, 2H, l), 4.72 (d, *J* = 5.7 Hz, 2H, d), 6.24 (t, *J* = 5.7 Hz, 1H, e), 7.14 (d, *J* = 2.6 Hz, 1H, i), 7.20 (dd, *J* = 9.2, 2.6 Hz, 1H, k), 7.25 (d, *J* = 1.9 Hz, 2H, c), 7.37 – 7.42 (m, 2H, b, g), 7.47 (dd, *J* = 7.1, 1.3 Hz, 1H, h), 7.75 – 7.79 (m, 1H, f), 8.30 (dt, *J* = 9.2, 0.6 Hz, 1H, j) ppm. **^{13}C NMR** (126 MHz, $CDCl_3$) δ = 18.3, 25.2, 28.3, 31.6, 35.0, 44.9, 67.5, 68.9, 84.2, 107.1, 120.2, 121.9, 122.3, 122.6, 125.4, 125.7, 127.2, 129.5, 134.6, 135.3, 137.3, 151.6, 157.4, 169.6 ppm. **HRMS (CH_2Cl_2/MeOH):** m/z calcd. for $[C_{32}H_{39}NO_2]$: 470.3059 $[M+H]^+$, found: 470.3028; 492.2879 $[M+Na]^+$, found: 492.2848; 508.2618 $[M+K]^+$, found: 508.2585.

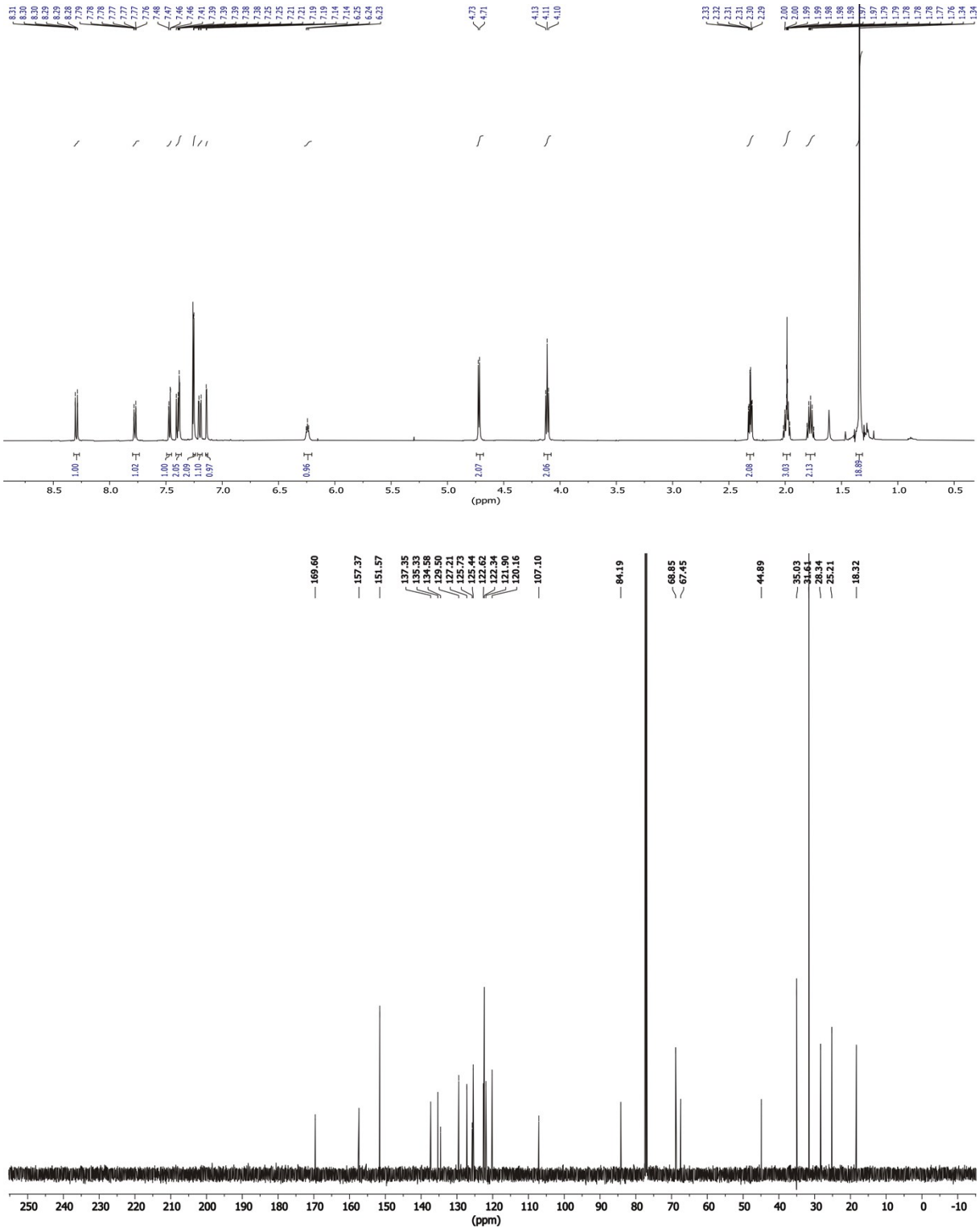

Fig. S14 ^{1}H (top) and ^{13}C (bottom) NMR spectra (500/126 MHz, $CDCl_3$, 298 K) of **5**.

N-(3,5-di-tert-butylbenzyl)-1-(6-(hex-5-yn-1-yloxy)naphthalen-1-yl)methanaminium tetrakis(3,5-bis(trifluoromethyl)phenyl)borate 6

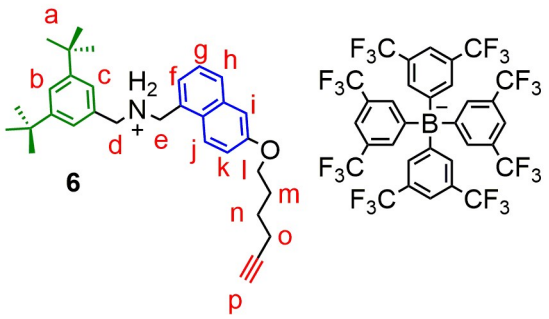

6

Amide **5** (382 mg, 0.813 mmol, 1 equiv.) and $LiAlH_4$ (124 mg, 3.25 mmol, 4 equiv.) were dissolved in 60 mL dry THF and refluxed for 7 days. Afterwards, the reaction was quenched with saturated aq. Na_2SO_4 solution. The white precipitate was filtered off and the solvent was removed. The residue was dissolved in CH_2Cl_2 (50 mL) and washed with brine (3x70 mL). The organic phase was dried over $MgSO_4$ and the solvent was removed. The crude product was purified by column chromatography (SiO_2, CH_2Cl_2 -> CH_2Cl_2/MeOH 100:1, R_f ~ 0.2 in CH_2Cl_2/MeOH = 100:1) to get the desired amine as a yellow oil, which was dissolved in diethylether (20 mL) and protonated with HCl conc. under cooling in an ice bath. The solvent was removed, 100 mg (0.2 mmol) of the brown sticky oil were dissolved in MeOH (10 mL) and $NaBArF_{24}$ (180 mg, 0.2 mmol, 1.0 equiv.) was added. After stirring overnight at room temperature, the solvent was removed, the residue was taken up in CH_2Cl_2 and washed with water (3x50 mL). The organic phase was dried over $MgSO_4$ and the solvent was removed. The crude salt was purified via column chromatography (SiO_2, CH_2Cl_2 -> CH_2Cl_2/acetone 10:1, R_f ~ 0.4 in CH_2Cl_2/acetone = 50:1) to get the desired axle **6** as brown oil in 42% overall yield (112.4 mg, 0.85 µmol).

^{1}H NMR (700 MHz, $CDCl_3$) δ = 1.33 (s, 18H, a), 1.74 – 1.79 (m, 2H, n), 1.97 – 2.02 (m, 3H, m,p), 2.31 (td, *J* = 7.0, 2.7 Hz, 2H, o), 4.10 (t, *J* = 6.3 Hz, 2H, l), 4.14 (s, 2H, d), 4.37 (s, 2H, e), 7.06 – 7.10 (m, 2H, j, f), 7.15 (d, *J* = 1.7 Hz, 2H, c), 7.17 – 7.20 (m, 2H, k, i), 7.26 – 7.29 (m, 1H, g), 7.52 (s, 4H, $BArF_{24}$), 7.61 (d, *J* = 1.8 Hz, 1H, b), 7.71 – 7.74 (m, 8H, $BArF_{24}$), 7.75 (d, *J* = 8.4 Hz, 1H, h) ppm.**^{13}C NMR** (176 MHz, $CDCl_3$) δ = 18.3, 25.1, 28.2, 31.0, 31.4, 35.2, 49.1, 53.5, 67.8, 68.9, 84.0, 108.5, 117.6, 121.4, 122.0, 122.4, 123.40, 123.9, 125.2, 125.5, 125.5, 126.2, 127.0, 129.1, 130.6, 135.0, 153.6, 157.8, 161.9, 212.8 ppm. **HRMS (MeOH):** m/z calcd. for $[C_{32}H_{42}NO]^+$: 456.3261 $[M]^+$, found: 456.3283

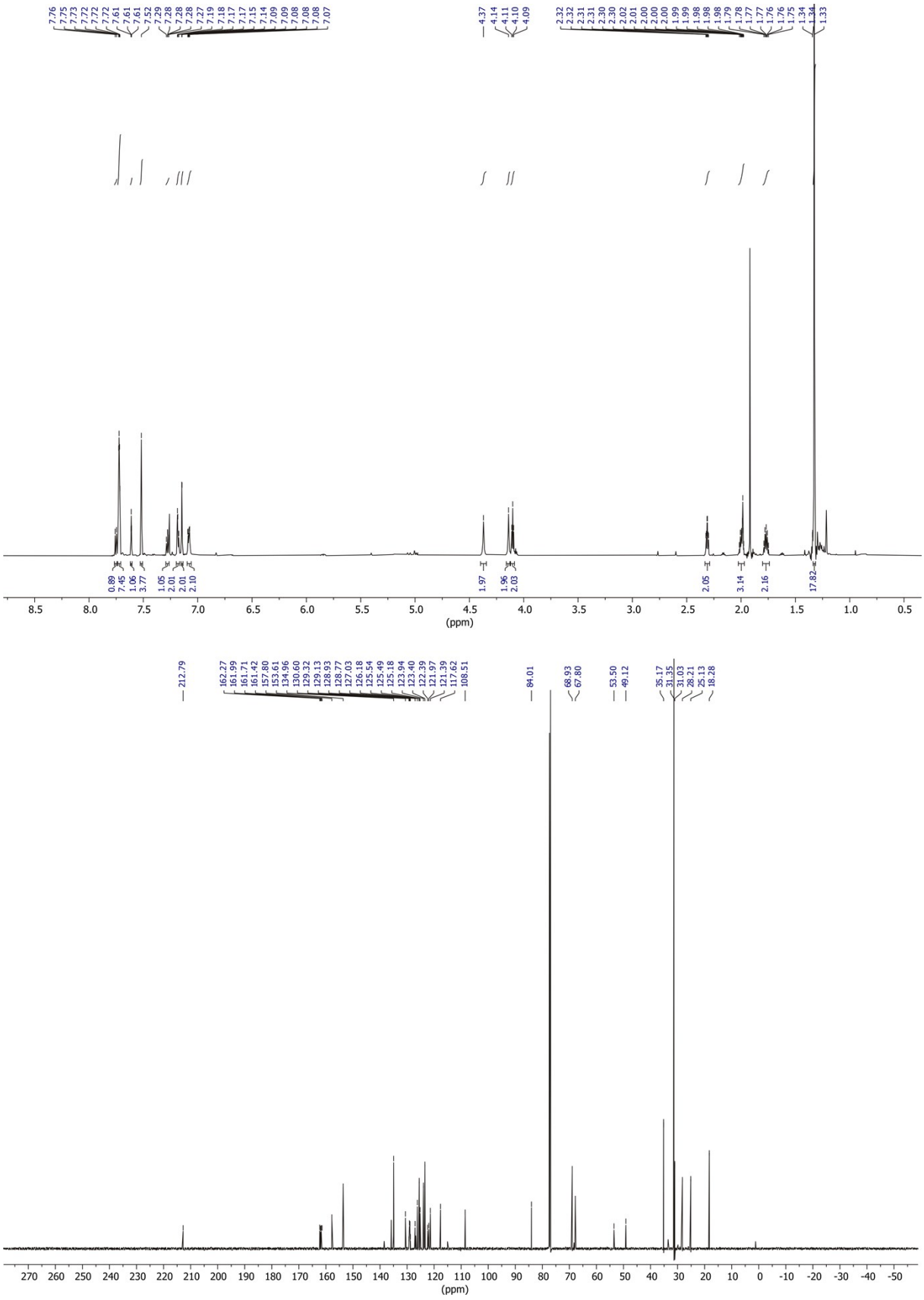

Fig. S15 ^{1}H (top) and ^{13}C (bottom) NMR spectra (700/176 MHz, $CDCl_3$, 298 K) of **6**.

N-(3,5-di-tert-butylbenzyl)-1-(6-(4-(3-(2,6-dimethoxyphenyl)isoxazol-5-yl)butoxy)naphthalen-1-yl)methanaminium tetrakis(3,5-bis(trifluoromethyl)phenyl)borate 7

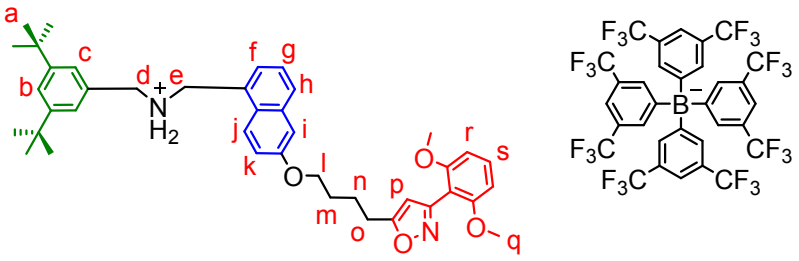

7

The axle **6** (20 mg, 15 µmol, 1.0 equiv.) and stopper **St1** (4 mg, 20 µmol, 1.3 equiv.) was added and the mixture heated to 35°C for 2 days. Then, the mixture was purified by column chromatography (SiO_2, CH_2Cl_2 + EtOH 3%, R_f ~ 0.3 in CH_2Cl_2) to obtain the desired product **7** (8 mg, 5 µmol, 30%) as an brown oil.

^{1}H NMR (400 MHz, CD_2Cl_2) δ = 1.28 (s, 18H, a), 1.80 – 1.92 (m, 4H, m,n), 2.82 (t, J = 7.0 Hz, 2H, o), 3.66 (s, 6H, q), 4.15 (t, J = 5.7 Hz, 2H, l), 4.29 (s, 2H, d,e), 4.59 (s, 2H, d,e), 6.46 (s, 1H, p), 6.65 – 6.69 (d, J = 8.5 Hz, 2H, r), 7.13 – 7.19 (m, 1H, j), 7.20 – 7.25 (m, 4H, c,f,i), 7.29 – 7.35 (m, 1H, g), 7.40 – 7.49 (m, 2H, s,k), 7.55 (s_{br}, 4H, $BArF_{24}$), 7.59 (t, J = 1.8 Hz, 1H, b), 7.71 (s_{br}, 8H, $BArF_{24}$), 7.77 (d, J = 8.3 Hz, 1H, h), 7.97 – 8.05 (s_{br}, 2H, NH_2) ppm. **^{13}C NMR** (176 MHz, CD_2Cl_2) δ = 24.2, 26.7, 28.5, 29.3, 30.1, 31.4, 35.3, 47.2, 49.3, 57.0, 67.9, 105.9, 106.0, 109.4, 117.9, 121.3, 122.7, 123.1, 124.2, 124.2, 125.4, 125.5, 125.8, 126.3, 126.4, 127.3, 127.5, 129.3, 130.7, 135.2, 153.6, 156.5, 157.5, 159.3, 162.2, 173.9 ppm. **HRMS (MeOH):**m/z calcd. for $[C_{41}H_{51}N_2O_4]^+$: 635.3849 $[M]^+$, found: 635.3868.

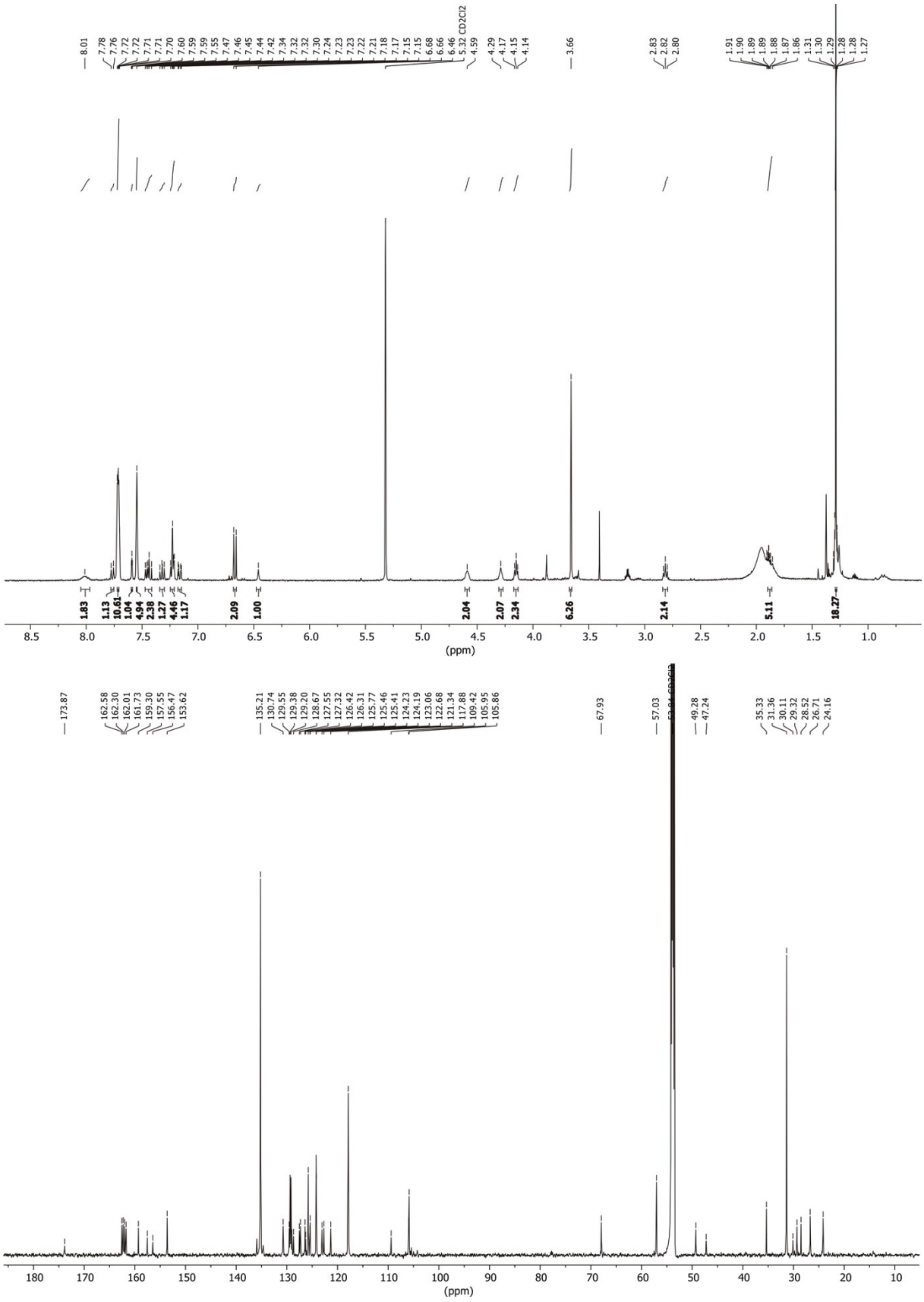

Fig. S16 ^{1}H (top) and ^{13}C (bottom) NMR spectra (400/176 MHz, CD_2Cl_2, 298 K) of **7**.

[2]Rotaxane R1

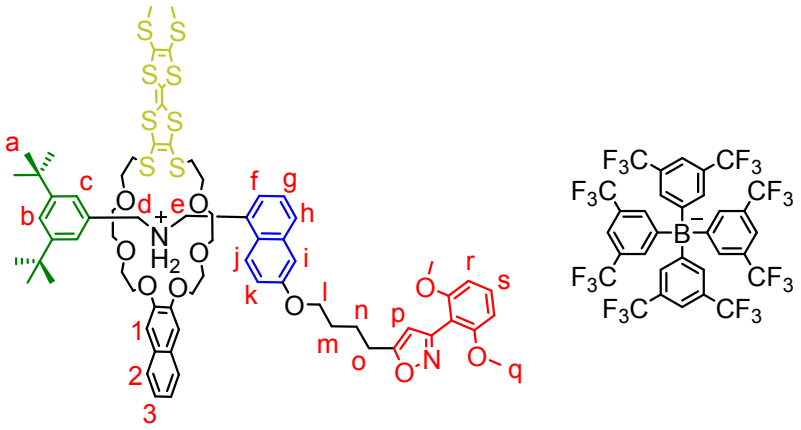

R1

The axle **6** (38 mg, 29 µmol, 1.0 equiv.) and macrocycle **TTFC8** (24 mg, 32 µmol, 1.1 equiv.) were dissolved in $ClCH_2CH_2Cl$ (2 mL) and stirred at 40 °C. for 3 days. Afterwards, the mixture was allowed to cool to room temperature, stopper **St1** (7 mg, 37 µmol, 1.3 equiv.) was added and the mixture heated to 35°C for 2 days. Then, the mixture was purified by column chromatography (SiO_2, CH_2Cl_2/hexane 8:2 -> CH_2Cl_2, R_f ~ 0.5 in CH_2Cl_2) to obtain the desired product **R1** (15 mg, 7 µmol, 23%) as an orange oil.

^{1}H NMR (700 MHz, CD_2Cl_2) δ = 1.28 (s, 18H, a), 1.90 – 1.95 (m, 2H, m), 1.97 – 2.03 (m, 2H, n), 2.40 (s, 6H, S-CH_3), 2.93 – 2.96 (m, 2H, o), 3.17 – 3.25 (m, 4H, S-CH_2-CH_2), 3.42 – 3.49 (m, 5H, O-CH_2-CH_2), 3.55 – 3.59 (m, 3H, O-CH_2-CH_2), 3.60 – 3.68 (m, 5H, O-CH_2-CH_2), 3.75 – 3.77 (m, 2H, l), 3.78 (s, 6H, q), 3.82 – 3.89 (m, 6H, O-CH_2-CH_2), 3.92 – 4.01 (m, 6H, O-CH_2-CH_2), 5.00 – 5.04 (m, 2H, d), 5.06 – 5.11 (m, 2H, e), 6.14 (t, *J* = 0.7 Hz, 1H, p), 6.38 (d, *J* = 2.6 Hz, 1H, j), 6.53 (s, 2H, 1), 6.67 (d, *J* = 8.4 Hz, 2H, r), 7.11 – 7.14 (m, 3H, g,k,i), 7.36 – 7.39 (m, 4H, 2,f,s), 7.50 (t, *J* = 1.7 Hz, 1H, b), 7.52 – 7.54 (m, 4H, 3, c), 7.55 – 7.57 (s_{br}, 4H, $BArF_{24}$), 7.70 – 7.74 (s_{br}, 8H, $BArF_{24}$), 7.98 – 8.01 (d, *J* = 9.2 Hz, 1H, h) ppm. **^{13}C NMR** (176 MHz, CD_2Cl_2) δ = 19.5, 25.0, 27.2, 29.3, 30.3, 31.7, 35.6, 39.1, 51.0, 56.5, 67.8, 68.8, 70.6, 71.2, 71.3, 72.8, 104.2, 104.7, 107.4, 108.0, 108.2, 109.2, 113.9, 118.0, 120.5, 122.8, 122.8, 123.4, 124.4, 124.5, 125.4, 125.8, 125.9, 126.6, 126.7, 127.0, 127.2, 127.5, 128.1, 128.9, 129.4, 129.5, 129.8, 130.1, 131.6, 135.4, 135.5, 147.5, 153.4, 157.4, 157.6, 159.2, 162.3, 173.1 ppm. **HRMS (MeOH):**m/z calcd. for $[C_{71}H_{87}N_2O_{10}S_8]^+$: 1383.4121 $[M]^+$, found: 1383.4156

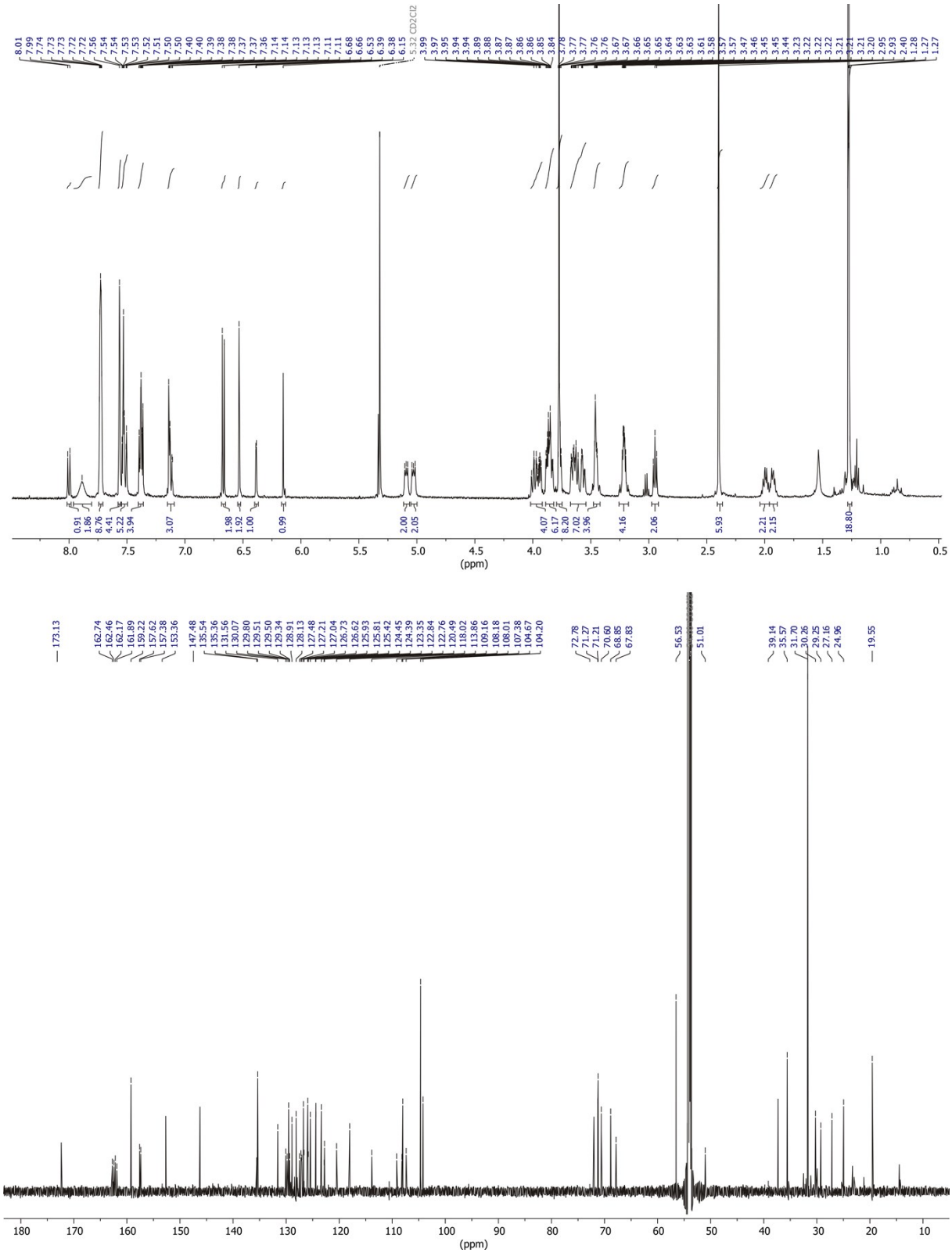

Fig. S17 ^{1}H (top) and ^{13}C (bottom) NMR spectra (700/176 MHz, CD_2Cl_2, 298 K) of **R1**.

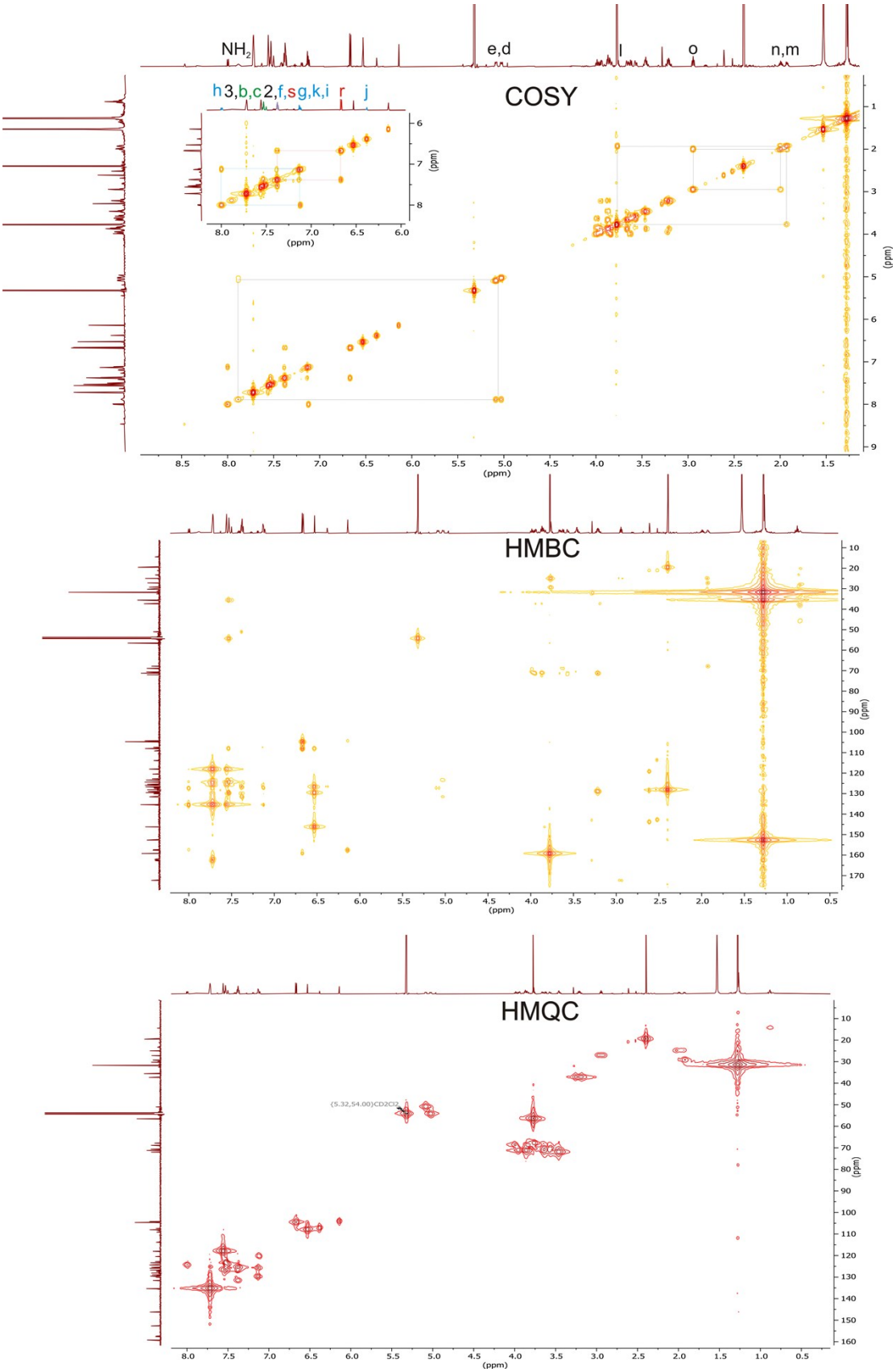

Fig. S18 COSY (top), HMBC (center) and HMQC (bottom) NMR spectra (700/176 MHz, CD_2Cl_2, 298 K) of **R1**.

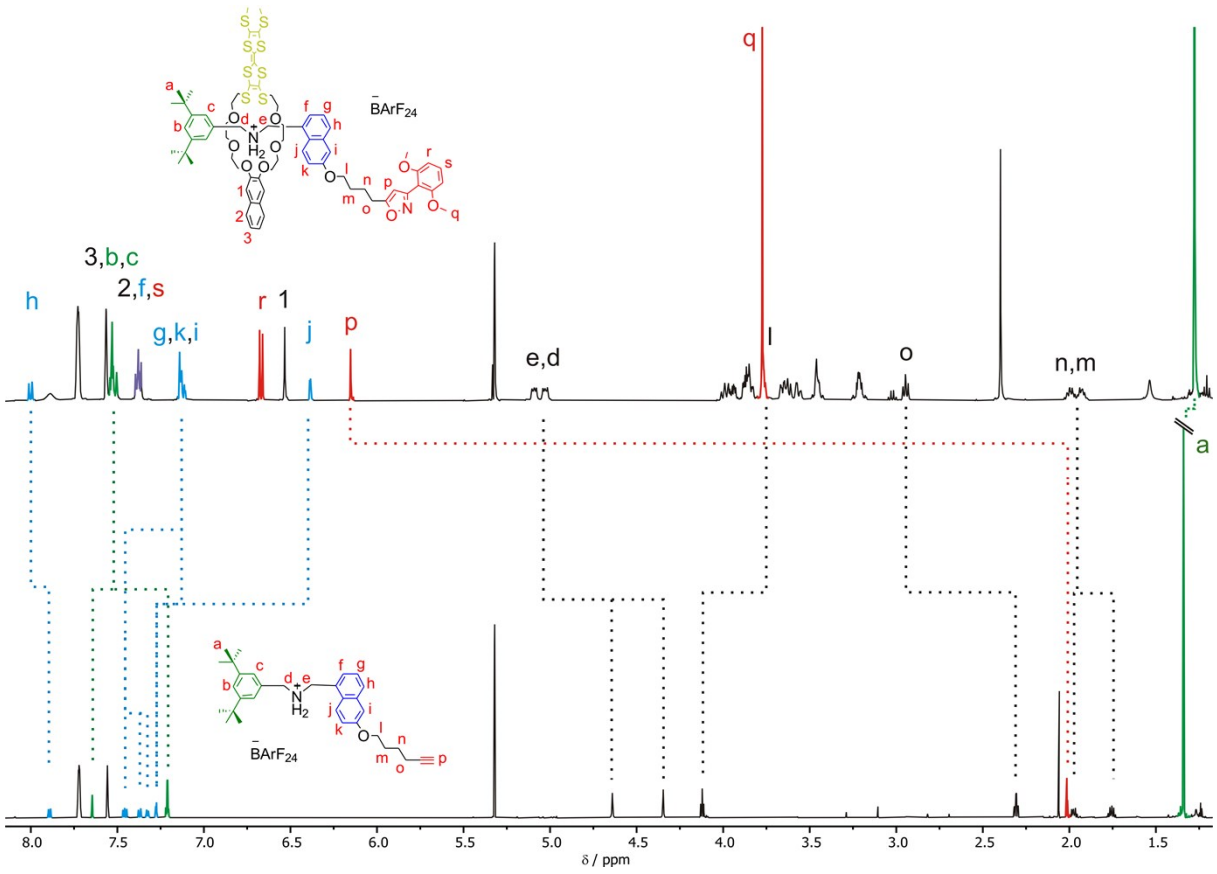

Fig. S19 [2]rotaxane **R1** (top) and axle **6** (bottom) NMR spectra (500 MHz, CD_2Cl_2, 298 K).

Pseudorotaxane PA11@TTFC8

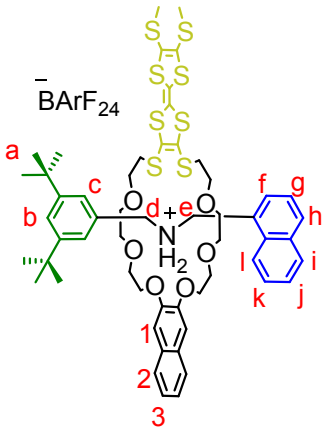

PA11@TTFC8

Axle **PA11** (50 mg, 41 µmol, 1.0 equiv.) and macrocycle **TTFC8** (31 mg, 41 µmol, 1.0 equiv.) were dissolved in $ClCH_2CH_2Cl$ (2 mL) and stirred at 50 °C for 5 days. The mixture was purified by column chromatography (SiO_2, CH_2Cl_2, R_f ~ 0.5 in CH_2Cl_2) to obtain the desired product **PA11@TTFC8** (65.2 mg, 33 µmol, 85%) as an orange sticky solid.

^{1}H NMR (700 MHz, CD_2Cl_2) δ = 1.27 (s, 18H, b), 2.40 (s, 6H, S-Me), 3.16 – 3.24 (m, 4H, S-$C\underline{H}_2$-CH_2), 3.43 – 3.45 (m, 4H, O-CH_2), 3.55 – 3.58 (m, 4H, O-CH_2), 3.61 – 3.68 (m, 4H, O-CH_2), 3.81 – 3.88 (m, 6H, O-CH_2), 3.90 – 3.97 (m, 4H, O-CH_2), 5.02 – 5.06 (m, 2H, d), 5.13 – 5.17 (m, 2H, e), 6.52 (s, 2H, 1), 7.08 (dd, *J* = 8.2, 7.0 Hz, 1H, j), 7.18 – 7.21 (m, 1H, k), 7.27 – 7.29 (m, 1H, f), 7.30 – 7.33 (m, 1H, l), 7.36 – 7.40 (m, 1H, 2), 7.49 (t, *J* = 1.8 Hz, 1H, a), 7.47 – 7.56 (m, 6H, 3, c, g, i), 7.55 – 7.57 (m, 4H, $BArF_{24}$), 7.71 – 7.74 (m, 8H, $BArF_{24}$), 7.91 (s_{br}, 2H, NH_2), 8.10 (d, *J* = 8.5, 0.9 Hz, 1H, h) ppm. **^{13}C-NMR** (176 MHz, CD_2Cl_2) δ = 19.6, 31.7, 35.5, 37.3, 44.5, 50.9, 54.2, 68.8, 70.6, 71.2, 71.3, 72.0, 108.1, 118.0, 122.9, 123.1, 123.4, 124.4, 124.5, 125.2, 125.5, 125.9, 126.7, 126.8, 127.2, 127.5, 127.5, 128.1, 128.8, 129.1, 129.4, 129.5, 130.9, 131.2, 131.5, 134.0, 135.4, 146.2, 152.7, 162.3 ppm. **HRMS (CH_2Cl_2):** m/z calcd. for $[C_{56}H_{70}NO_6S_8]^+$:1108.2963 $[M]^+$, found: 1108.2948

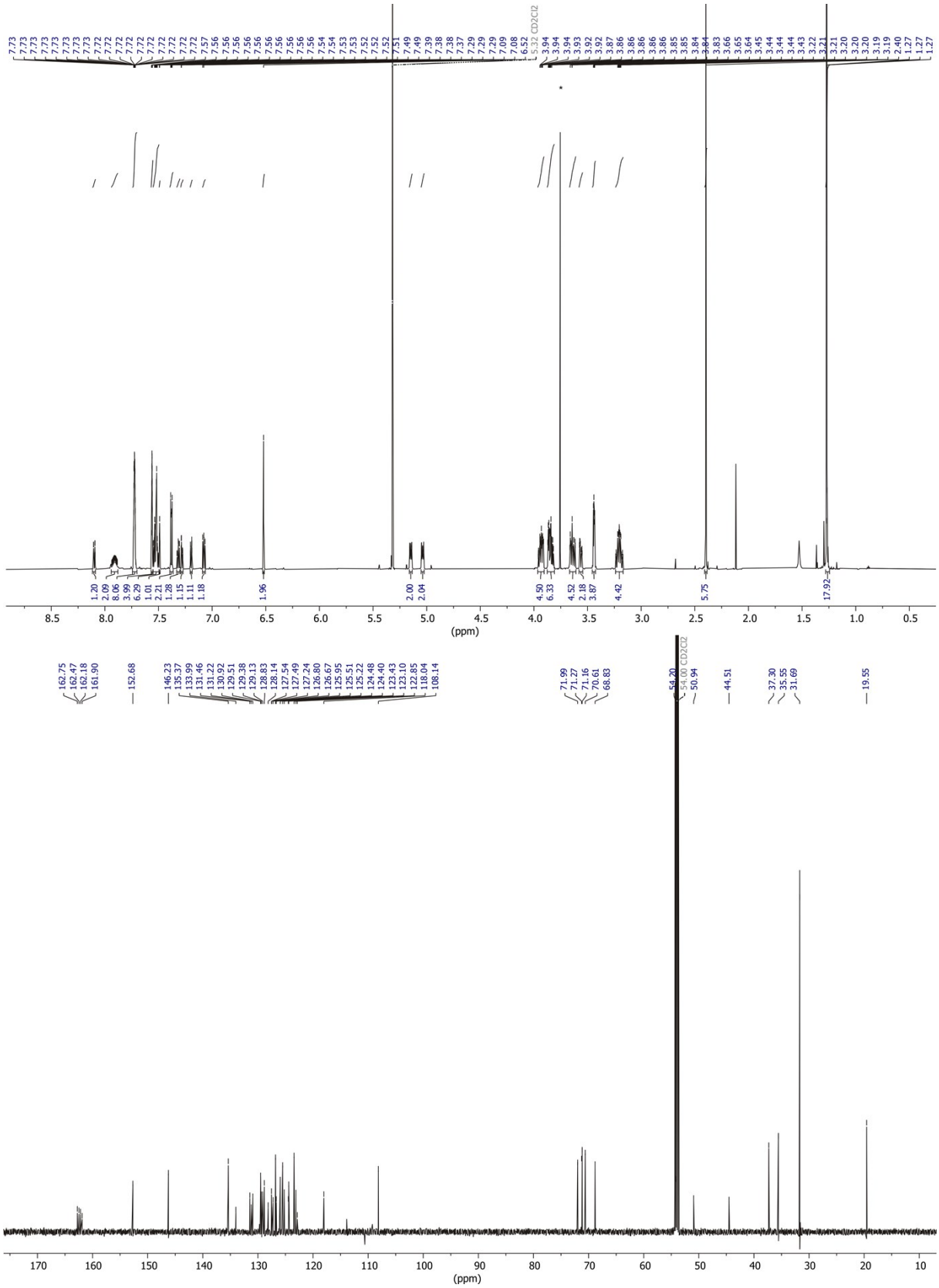

Fig. S20 ^{1}H (top) and ^{13}C (bottom) NMR spectra (700/176 MHz, CD_2Cl_2, 298 K) of **PA11@TTFC8**.

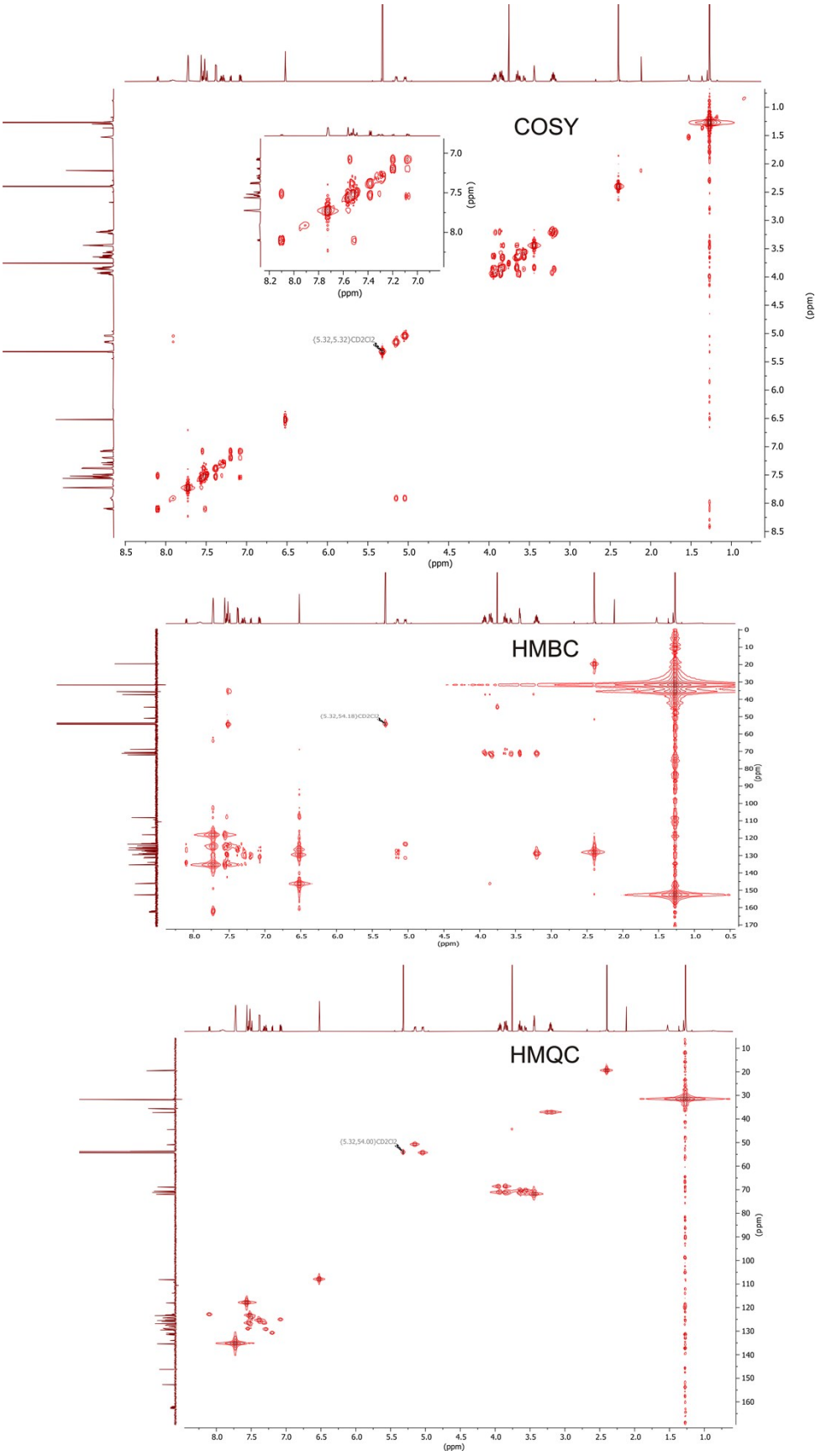

Fig. S21 COSY (top), HMBC (center) and HMQC (bottom) NMR spectra (700/176 MHz, CD_2Cl_2, 298 K) of **PA11@TTFC8**.

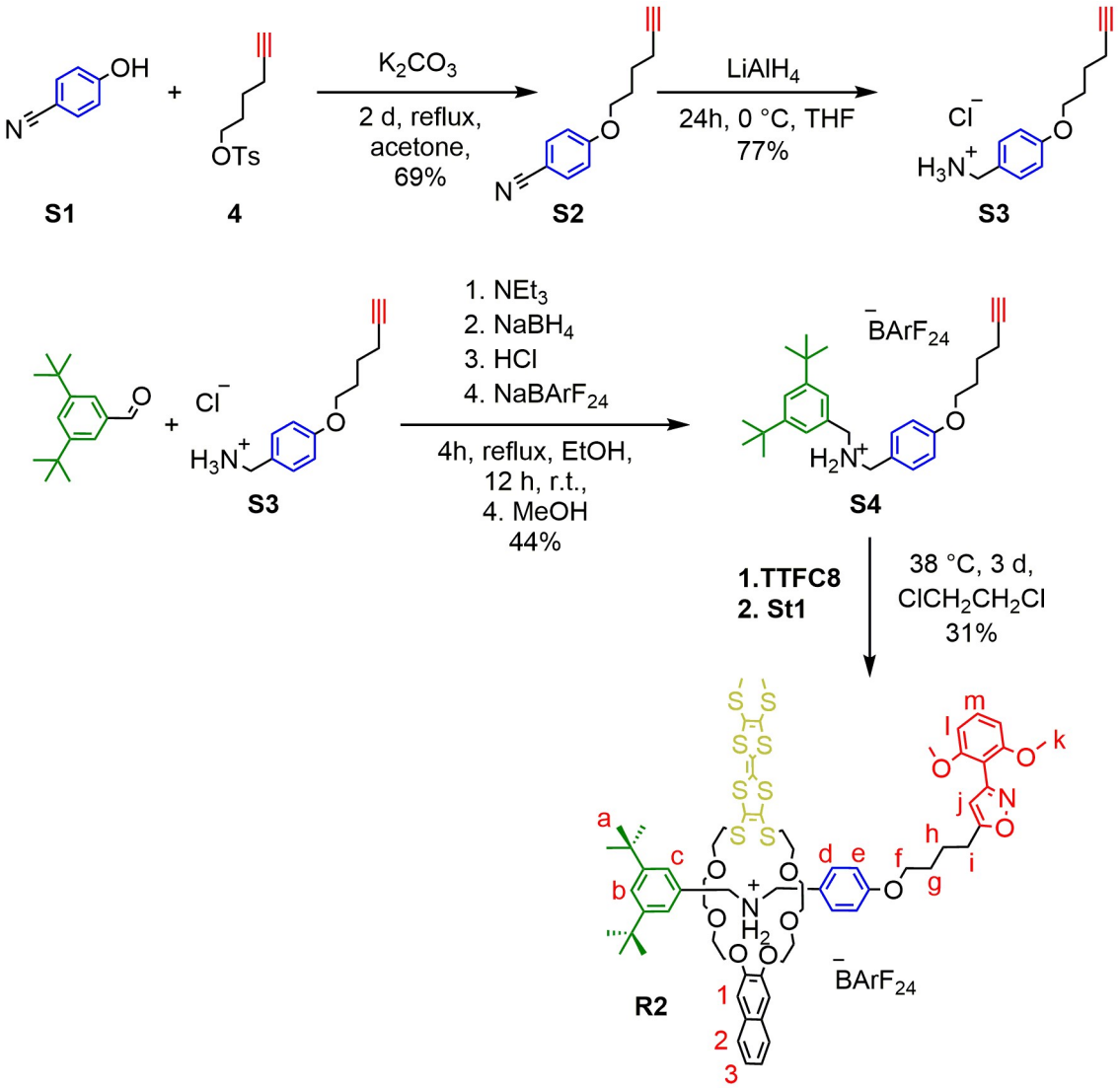

Scheme S3 Synthesis of **R2**.

(4-(Hex-5-yn-1-yloxy)phenyl)methanaminium chloride S3

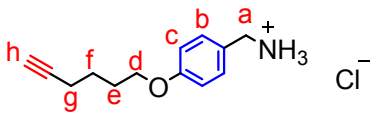

S3

To a solution of 400 mg (2.0 mmol, 1.0 equiv.) 4-(hex-5-yn-1-yloxy)benzonitrile **S2** in dry THF (100 mL), 380 mg (10 mmol, 5.0 equiv.) $LiAlH_4$ was added at 0 °C and stirred for 24 h in the thawing ice bath. The excess $LiAlH_4$ was quenched with saturated Na_2SO_4 solution. The solid parts were filtered off and the solvent was removed under reduced pressure. The oily residue was dissolved in CH_2Cl_2, washed with brine and dried with $MgSO_4$. After removal of the solvent, the crude product was purified by flash column chromatography (SiO_2, CH_2Cl_2 + 1% NEt_3 → CH_2Cl_2 + 1% NEt_3/ 5% EtOH, *Rf* ~ 0.5 in CH_2Cl_2 + 1% NEt_3/ 3% EtOH) to isolate the desired amine, which was dissolved in Et_2O and conc. HCl (aq.) was added until no more solid crushed out. After filtration the white solid was washed with cold acetone. The product is a white sticky solid, which could be isolated in 77% yield (370 mg, 1.5 mmol) over two steps.

^{1}H NMR (700 MHz, DMSO-d_6) δ = 1.55 – 1.61 (m, 2H, f), 1.76 – 1.81 (m, 2H, e), 2.22 (td, *J*=7.1, 2.7 Hz, 2H, g), 2.78 (t, *J*=2.6, 1H, h), 3.92 (s, 2H, a), 3.98 (t, *J*=6.4, 2H, d), 6.92 – 6.98 (m, 2H, c), 7.36 – 7.40 (m, 2H, b), 8.16 – 8.34 (s_{br}, 3H, NH) ppm. **^{13}C NMR** (176 MHz, DMSO-d_6) δ = 17.4, 24.6, 27.7, 41.7, 67.0, 71.4, 84.3, 114.5, 125.8, 130.5, 158.7 ppm. **HRMS (MeOH):** m/z calcd. for $[C_{13}H_{18}NO]$: $[M\text{-}NH_3]^+$, 187.1123 found: 187.1119.

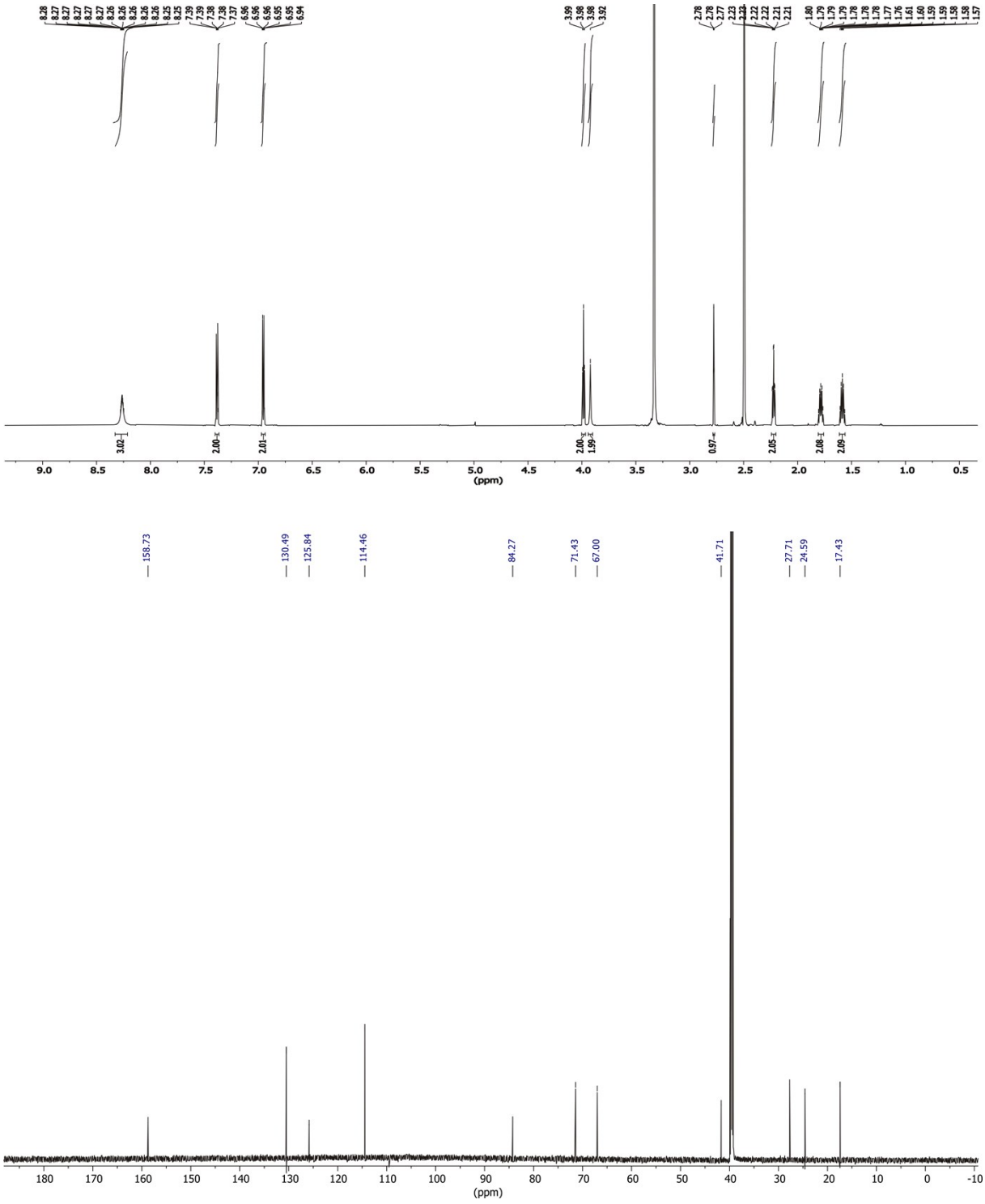

Fig. S22 ^{1}H (top) and ^{13}C (bottom) NMR spectra (700/176 MHz, DMSO-d_6, 298 K) of **S3**.

N-(3,5-di-tert-butylbenzyl)-1-(4-(hex-5-yn-1-yloxy)phenyl)methanaminium tetrakis(3,5-bis(trifluoromethyl)phenyl)borate S4

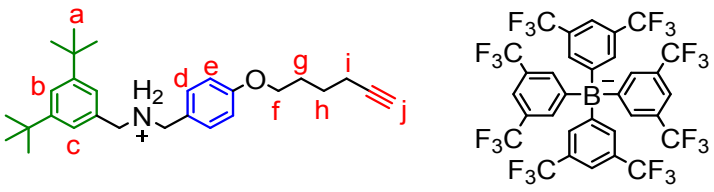

S4

Ammonium compound **S3** (150 mg, 0.63 mmol, 1 equiv.), 3,5-di-*tert*-butylbenzaldehyde (140.0 mg, 0.63 mmol, 1.0 equiv.) and NEt_3 (90 µL, 0.56 mmol, 0.9 equiv.) were dissolved in 30 mL dry EtOH and refluxed for 5.5 h. Then, the mixture was cooled to 0 °C and $NaBH_4$ (150.0 mg, 3.13 mmol, 5 equiv.) was added. The reaction stirred overnight in the thawing ice bath. Afterwards, the reaction was quenched with saturated aq. $NaHCO_3$ solution. The solvent was removed. The residue was taken up with CH_2Cl_2 (40 mL) and washed with Brine (3x50 mL). The organic phase was dried over $MgSO_4$ and the solvent was removed. The crude product was purified via flash column chromatography (SiO_2, CH_2Cl_2 -> CH_2Cl_2 + 10% EtOH, R_f ~ 0.5 in CH_2Cl_2 + 3% EtOH) to get the desired Amine as yellow oil, which was dissolved in EtOAc (10 mL) and protonated with HCl conc. under cooling in an ice bath. The solvent was removed and 60 mg (0.14 mmol) of the brown sticky oil were dissolved in MeOH (5 mL) and $NaBArF_{24}$ (120 mg, 0.14 mmol, 1.0 equiv.) was added. After stirring overnight at room temperature, the solvent was removed, the residue was taken up in CH_2Cl_2 and washed with water (3x50 mL). The organic phase was dried over $MgSO_4$ and the solvent was removed to get the desired axle **S4** as brown oil in 44% yield overall (160 mg, 0.13 mmol).

^{1}H NMR (700 MHz, CD_2Cl_2) δ = 1.32 (s, 18H, a), 1.68 – 1.73 (m, 2H, h), 1.89 – 1.94 (m, 2H, g), 2.00 (t, J = 2.7 Hz, 1H, j), 2.28 (td, J = 7.1, 2.7 Hz, 2H, i), 4.01 (t, J = 6.3 Hz, 2H, f), 4.22 (s, 2H, N-CH_2), 4.24 (s, 2H, N-CH_2), 6.97 – 7.01 (m, 2H, e), 7.15 (d, J = 1.8 Hz, 2H, c), 7.24 – 7.27 (m, 2H, d), 7.56 (s_{br}, 4H, $BArF_{24}$), 7.60 (t, J = 1.8 Hz, 1H, b), 7.72 (s_{br}, 8H, $BArF_{24}$) ppm. **^{13}C NMR** (176 MHz, CD_2Cl_2) δ = 18.6, 25.6, 28.7, 31.6, 35.5, 53.1, 68.4, 69.0, 84.5, 116.4, 118.0, 121.0, 122.9, 123.9, 124.4, 125.9, 125.9, 127.5, 128.9, 129.4, 131.5, 135.4, 153.9, 161.7, 162.3 ppm. **HRMS (MeOH):** m/z calcd. for $[C_{28}H_{40}NO]^+$: 406.3104 $[M]^+$, found: 406.3109

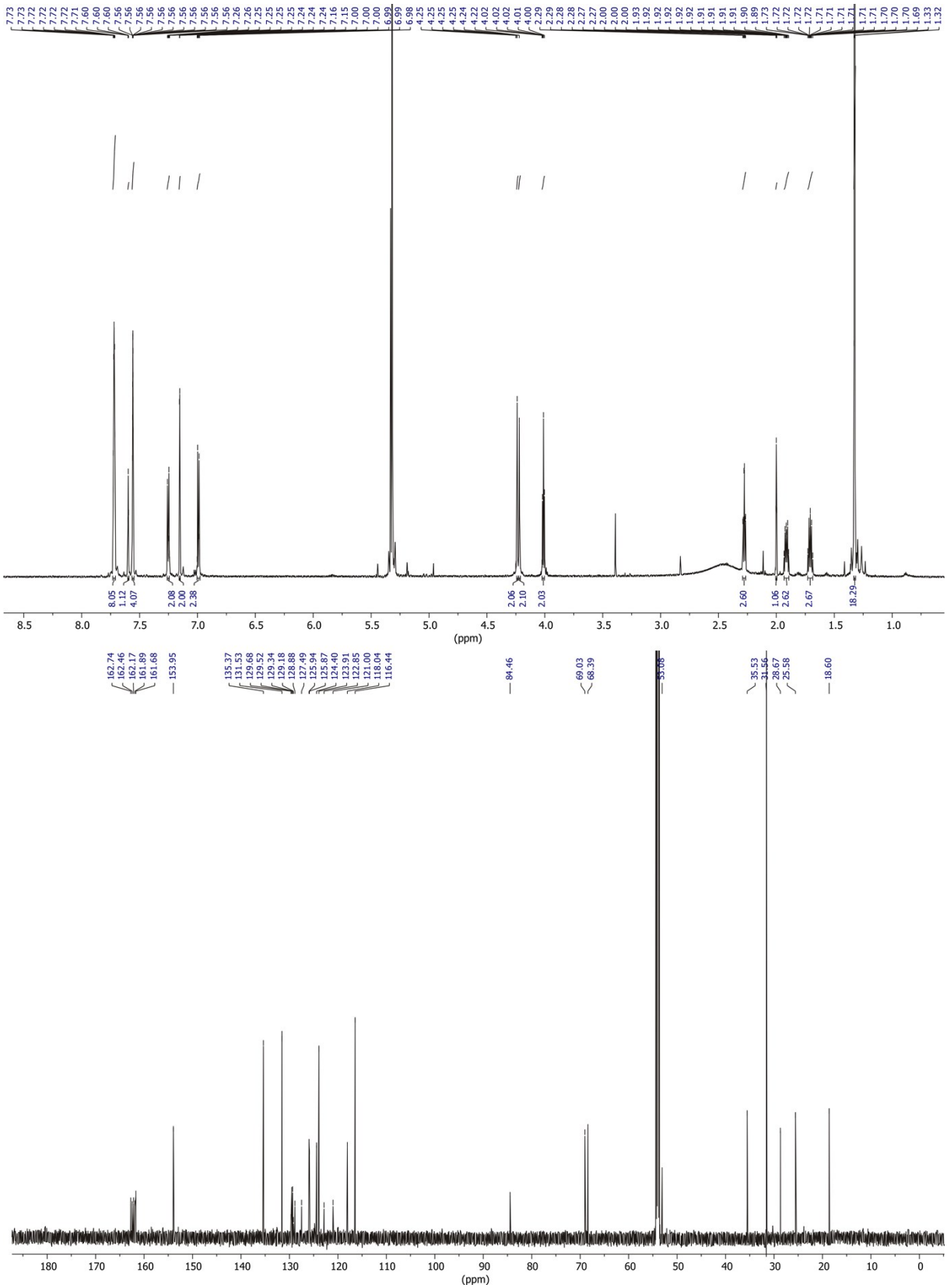

Fig. S23 ^{1}H (top) and ^{13}C (bottom) NMR spectra (700/176 MHz, CD_2Cl_2, 298 K) of **S4**.

[2]Rotaxane R2

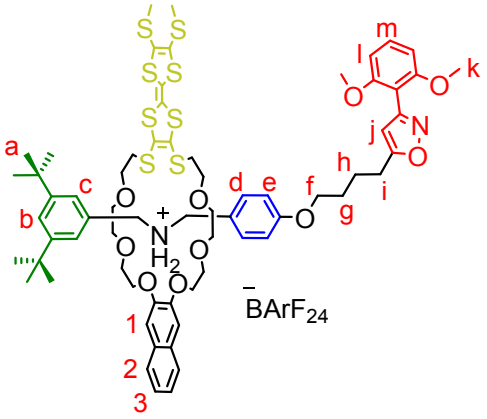

R2

A solution of 50 mg (39 µmol, 1.0 equiv.) axle **S4** and 32 mg (43 µmol, 1.1 equiv.) macrocycle **TTFC8** in $ClCH_2CH_2Cl$ (2 mL) was stirred at 38 °C. for 10 min. Afterwards, the mixture was allowed to cool to r.t. and 9 mg (50 µmol, 1.3 equiv.) stopper **St1** was added and the mixture was stirred at 38 °C for 36 h. Then, the mixture was purified by column chromatography (SiO_2, CH_2Cl_2/hexane 8:2-> CH_2Cl_2, R_f ~ 0.6 in CH_2Cl_2) to obtain the desired product **R2** (27 mg, 12 µmol, 31 %) as orange oil.

^{1}H NMR (700 MHz, CD_2Cl_2) δ = 1.27 (s, 18H, a), 1.54 – 1.59 (m, 2H, g), 1.66 – 1.72 (m, 2H, h), 2.41 (s, 6H, S-CH_3), 2.74 – 2.83 (m, 2H, i), 3.10 (t, *J* = 6.5 Hz, 2H, f), 3.18 (m, 4H, S-CH_2-), 3.46 – 3.54 (m, 4H, O-CH_2-), 3.59 – 3.65 (m, 6H, O-CH_2-), 3.73 – 3.78 (m, 8H, k, O-CH_2-), 3.79 – 3.83 (m, 2H, O-CH_2-), 3.84 – 3.90 (m, 2H, O-CH_2-), 4.00 - 4.04 (m, 2H, O-CH_2-), 4.19 – 4.24 (m, 2H, O-CH_2-), 4.55 – 4.60 (m, 2H, N-CH_2-), 4.78 – 4.82 (m, 2H, N-CH_2-), 6.09 (s, 1H, j), 6.32 – 6.35 (m, 2H, e), 6.67 (d, *J* = 8.4 Hz, 2H, l), 6.93 (s, 2H, 1), 7.10 – 7.12 (m, 2H, d), 7.35 – 7.40 (m, 2H, 3, m), 7.49 (dd, *J* = 7.5, 1.8 Hz, 3H, b, c), 7.56 (s_{br}, 4H, $BArF_{24}$), 7.65 (m, 2H, 2), 7.70 (s_{br}, 2H, NH_2), 7.72 (s_{br}, 8H, $BArF_{24}$) ppm.**^{13}C NMR** (176 MHz, CD_2Cl_2) δ = 19.6, 24.6, 27.0, 29.1, 31.7, 35.5, 37.3, 56.5, 67.5, 69.0, 70.4, 71.1, 71.2, 72.1, 104.2, 104.7, 108.1, 108.3, 114.7, 118.0, 122.8, 122.9, 123.7, 124.4, 124.4, 125.7, 125.9, 126.9, 127.5, 128.1, 129.0, 129.4, 129.6, 131.2, 131.5, 131.6, 135.4, 147.1, 152.7, 157.6, 159.2, 160.3, 162.3, 172.4 ppm. **HRMS (MeOH):** m/z calcd. for $[C_{67}H_{85}N_2O_{10}S_8]^+$: 1333.3964 $[M]^+$, found: 1333.3990 m/z.

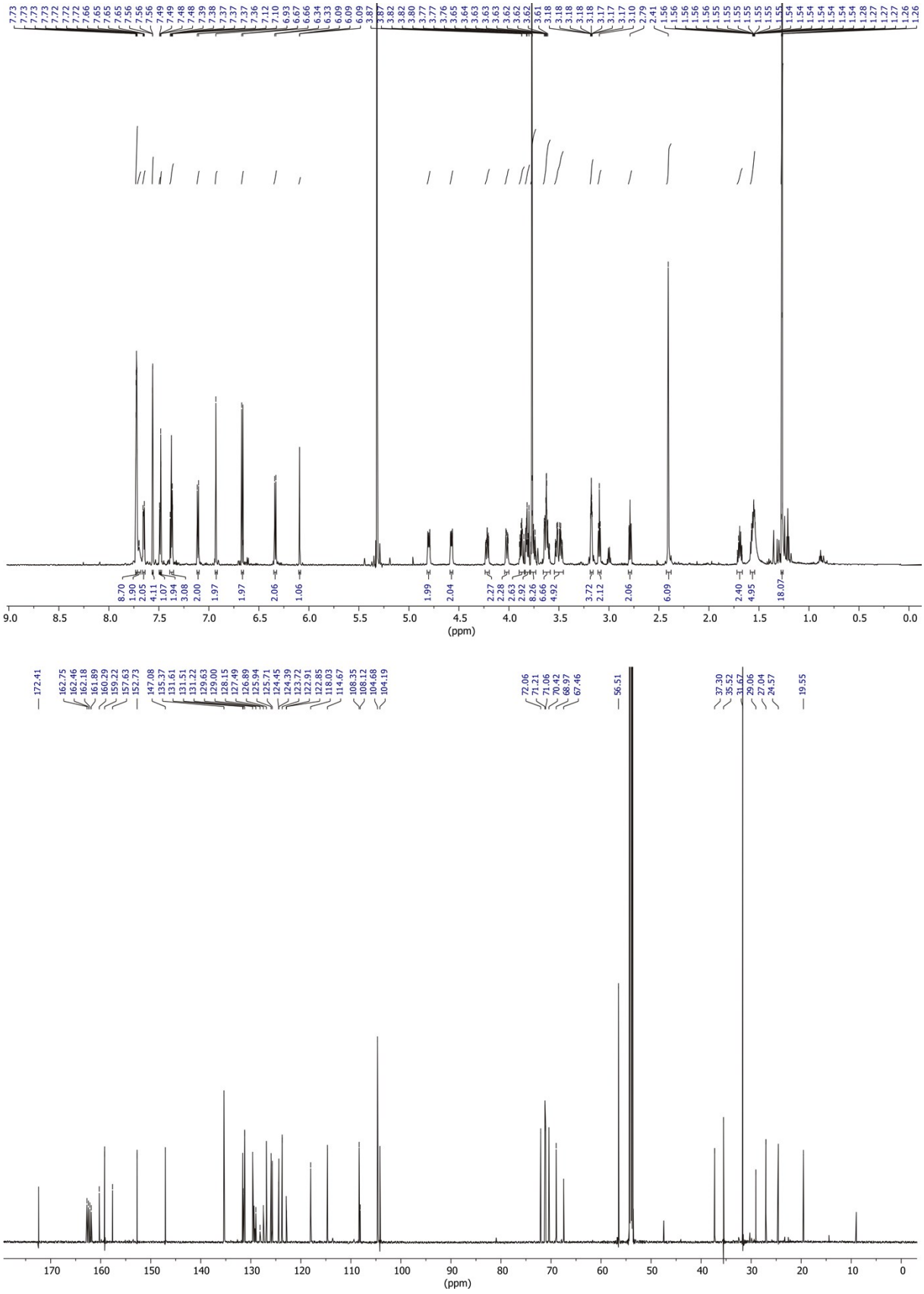

Fig. S24 ^{1}H (top) and ^{13}C (bottom) NMR spectra (700/176 MHz, CD_2Cl_2, 298 K) of **R2**.

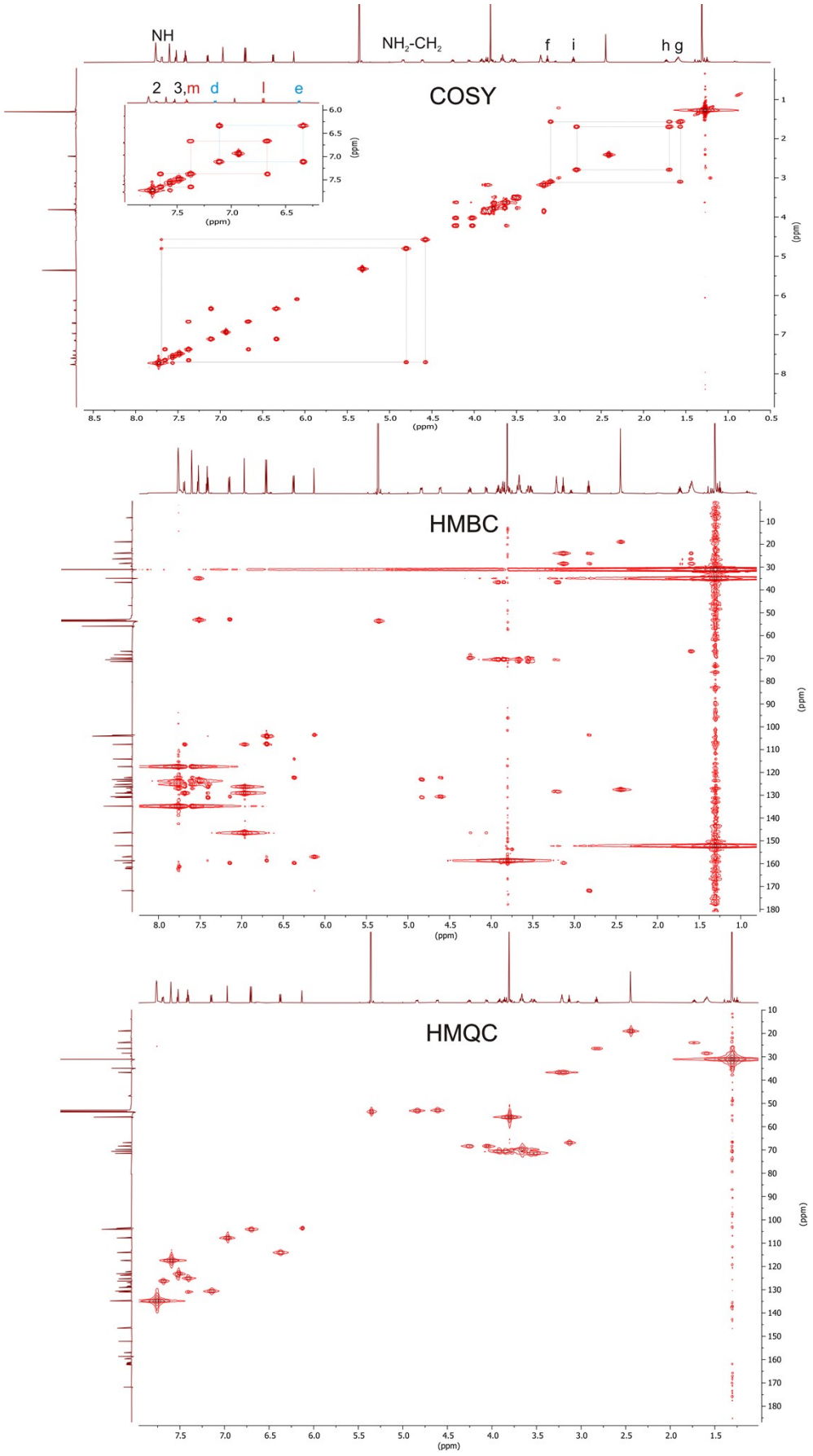

Fig. S25 COSY (top), HMBC (center) and HMQC (bottom) NMR spectra (700/176 MHz, CD_2Cl_2, 298 K) of **R2**.

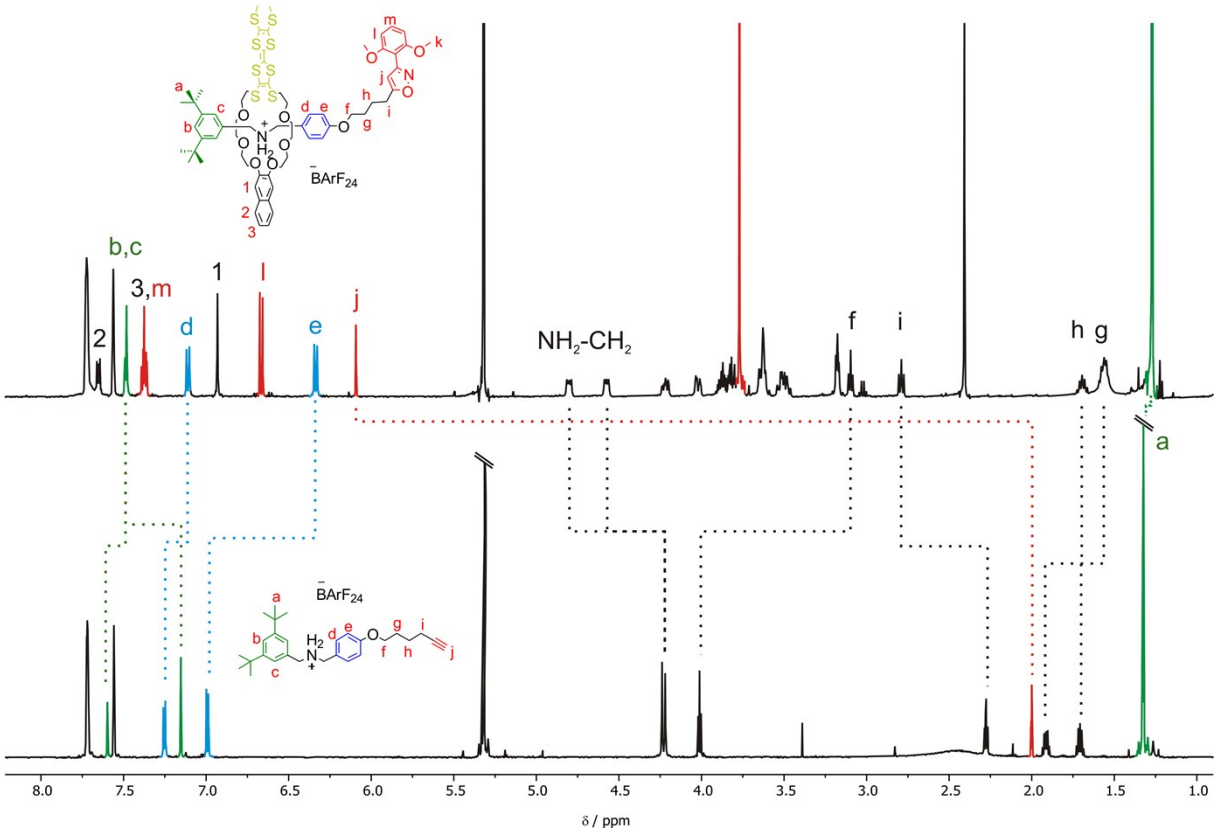

Fig. S26 [2]rotaxane **R2** (top) and axle **S4** (bottom) NMR spectra (500 MHz, CD_2Cl_2, 298 K).

2. Threading and dethreading: ^{1}H NMR experiments

Threading and unthreading experiments were performed at 4 mM concentration, deprotonation/oxidation was performed in dry CD_2Cl_2. Oxidation was performed by adding an excess of $NOSbF_6$ shaking gently, until the solution turned deep blue and subsequent filtration into a J. Young tube under argon atmosphere of residual $NOSbF_6$. Deprotonation was performed by adding an excess of polystyrene-immobilized P2 base, shaking and then filtration into a J. Young tube under argon atmosphere.

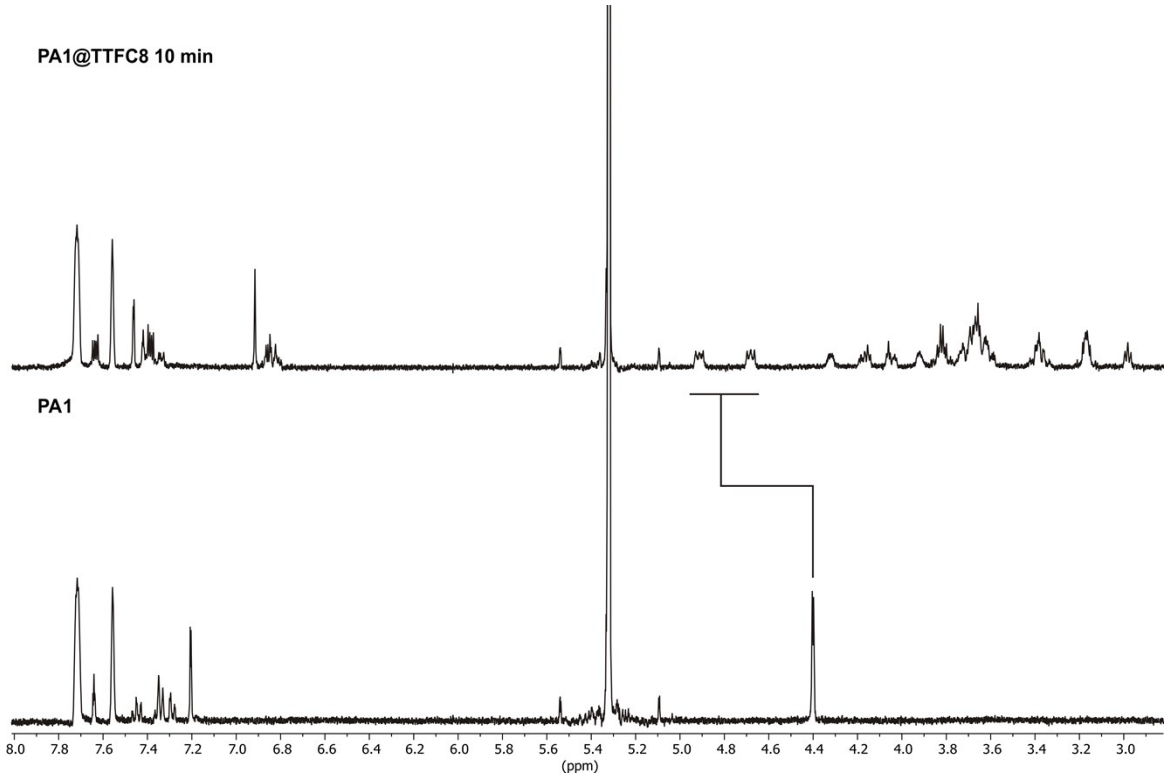

Fig. S27 Partial ^{1}H NMR spectra (400 MHz, CD_2Cl_2, 298 K) of **PA1** before (bottom) and after addition of **TTFC8** (top) the highlighted downfield shift and splitting of the methylene protons next to the ammonium is characteristic for a threaded complex.

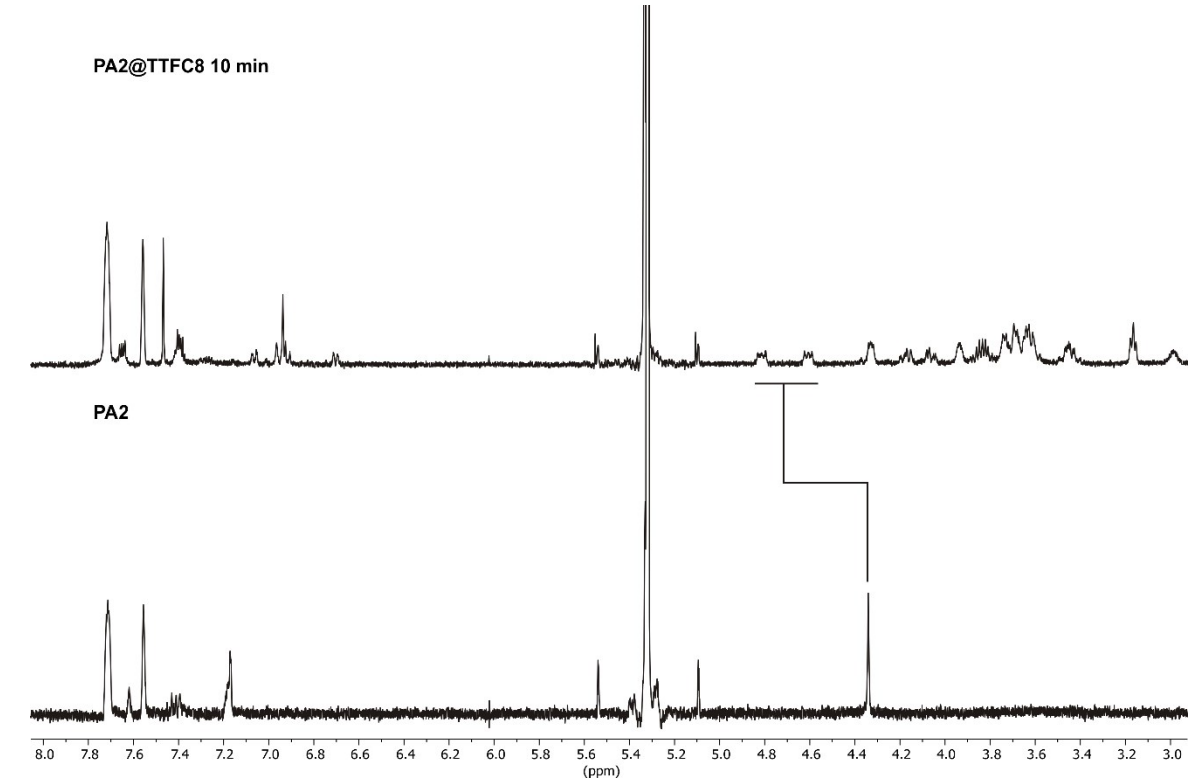

Fig. S28 Partial ^{1}H NMR spectra (400 MHz, CD_2Cl_2, 298 K) of **PA2** before (bottom) and after addition of **TTFC8** (top) the highlighted downfield shift and splitting of the methylene protons next to the ammonium is characteristic for a threaded complex.

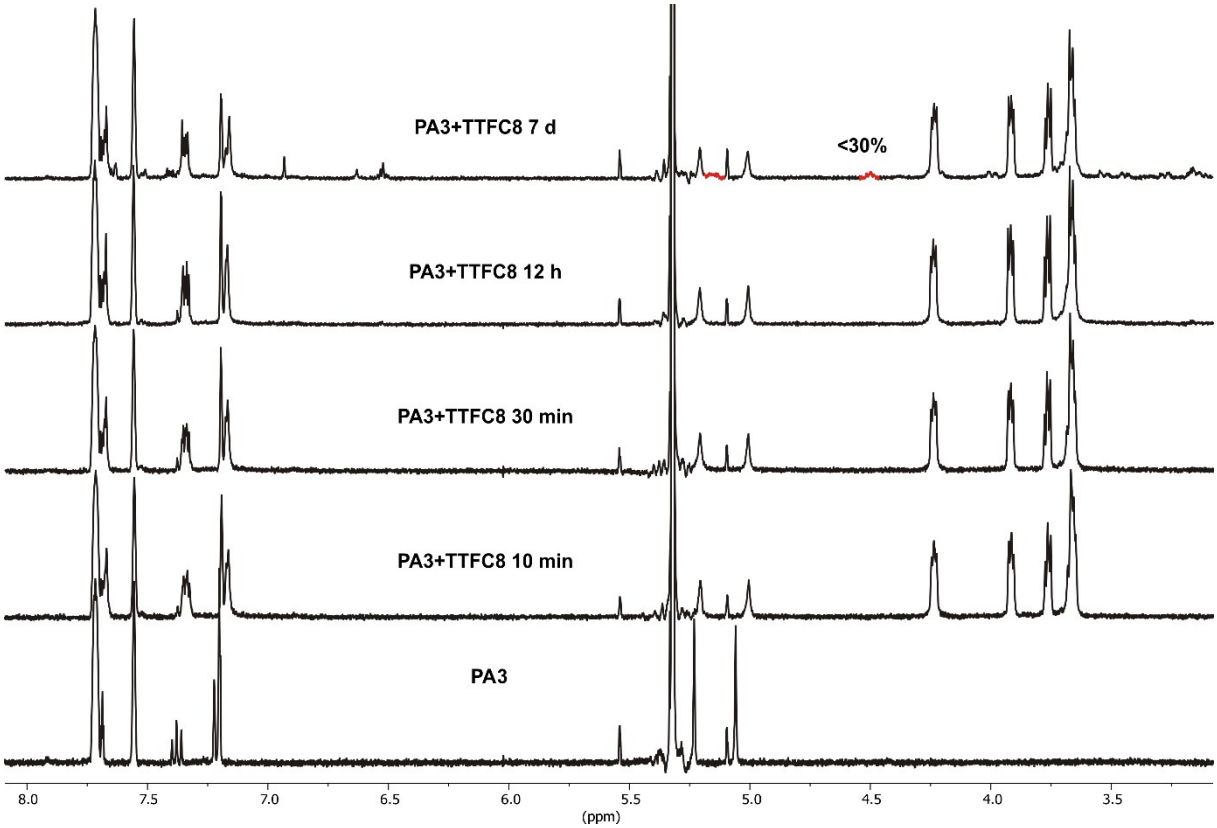

Fig. S29 Partial ^{1}H NMR spectra (400 MHz, CD_2Cl_2, 298 K) of **PA3** before (bottom) and after addition of **TTFC8** (top), the emerging peaks (red) correspond to the threaded complex.

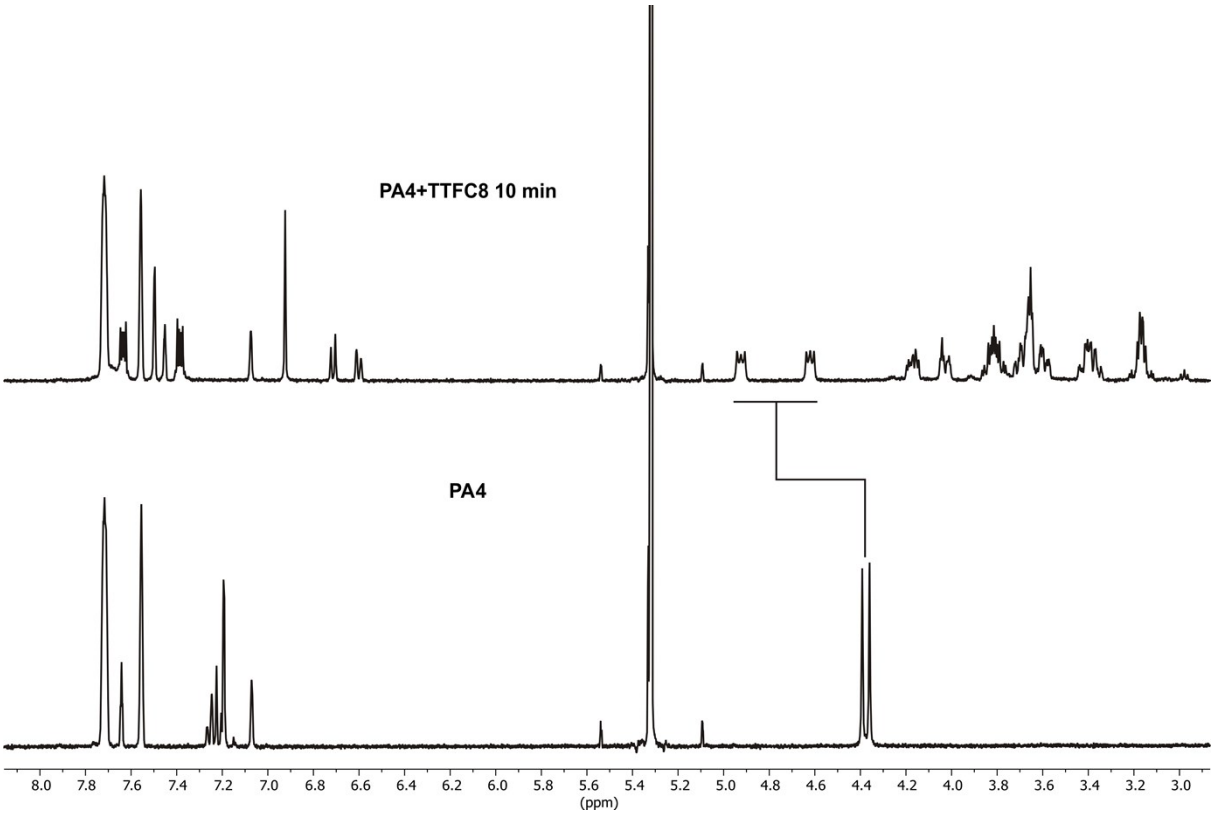

Fig. S30 Partial ^{1}H NMR spectra (400 MHz, CD_2Cl_2, 298 K) of **PA4** before (bottom) and after addition of **TTFC8** (top) the highlighted downfield shift and splitting of the methylene protons next to the ammonium is characteristic for a threaded complex.

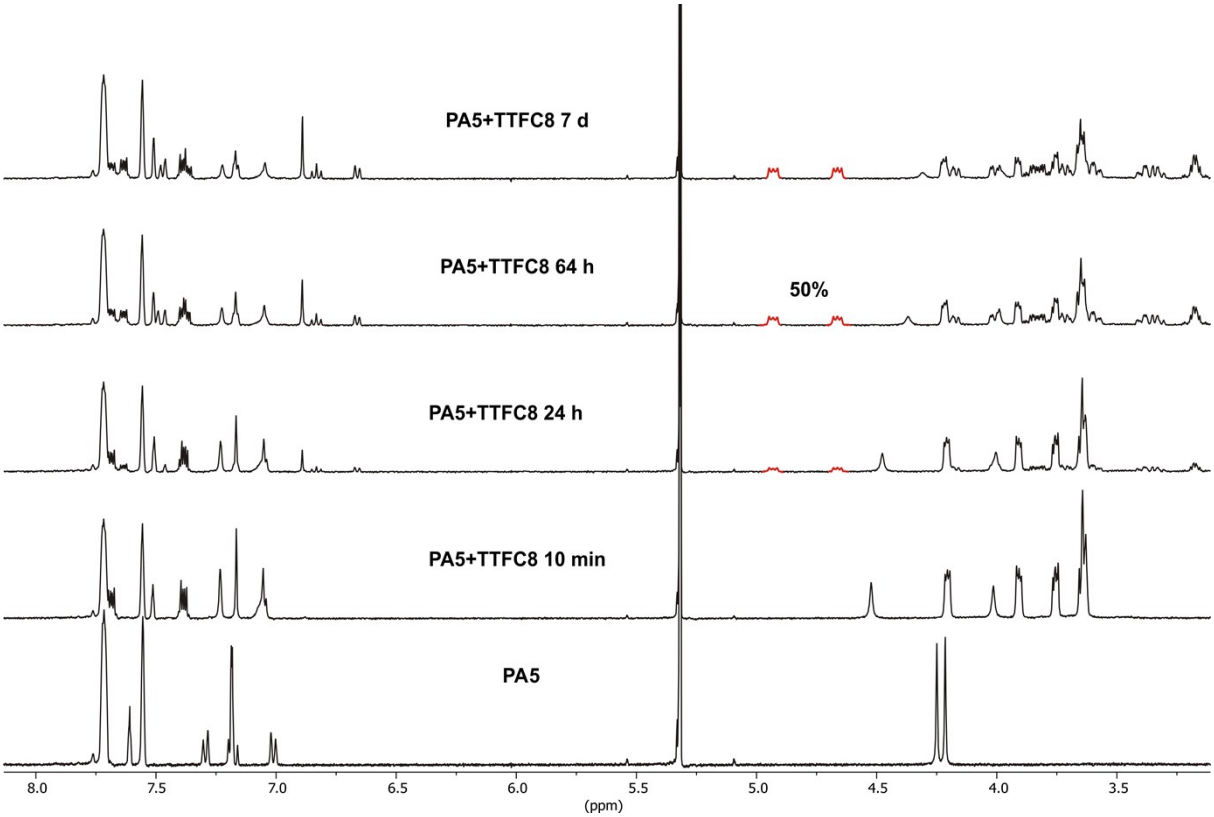

Fig. S31 Partial ^{1}H NMR spectra (400 MHz, CD_2Cl_2, 298 K) of **PA5** before (bottom) and after addition of **TTFC8** (top), the emerging peaks (red) correspond to the threaded complex.

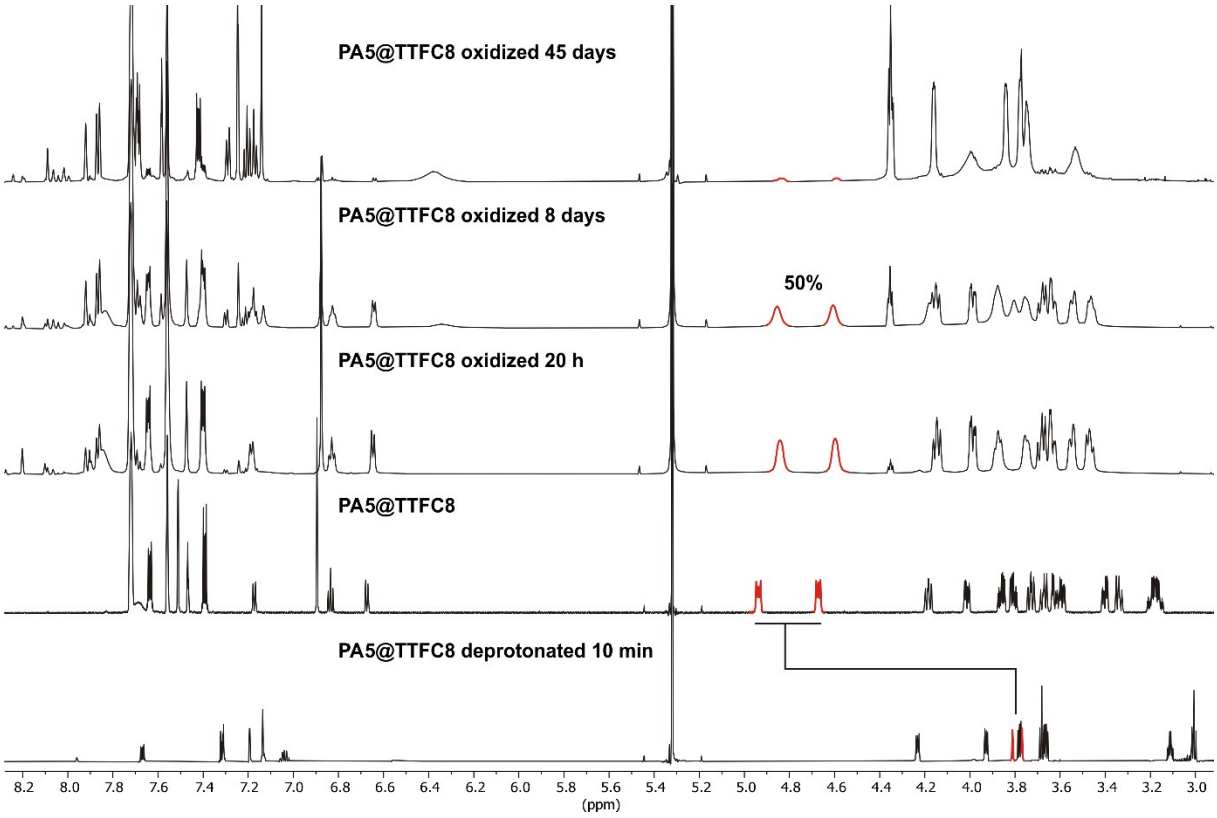

Fig. S32 Partial ^{1}H NMR spectra (700 MHz, CD_2Cl_2, 298 K) of **PA5@TTFC8** (center) after oxidation with $NO^{\cdot+}SbF_6^-$ (top) and after deprotonation with P2 base (bottom). The highlighted peaks in red correspond to the methylene protons next to the nitrogen.

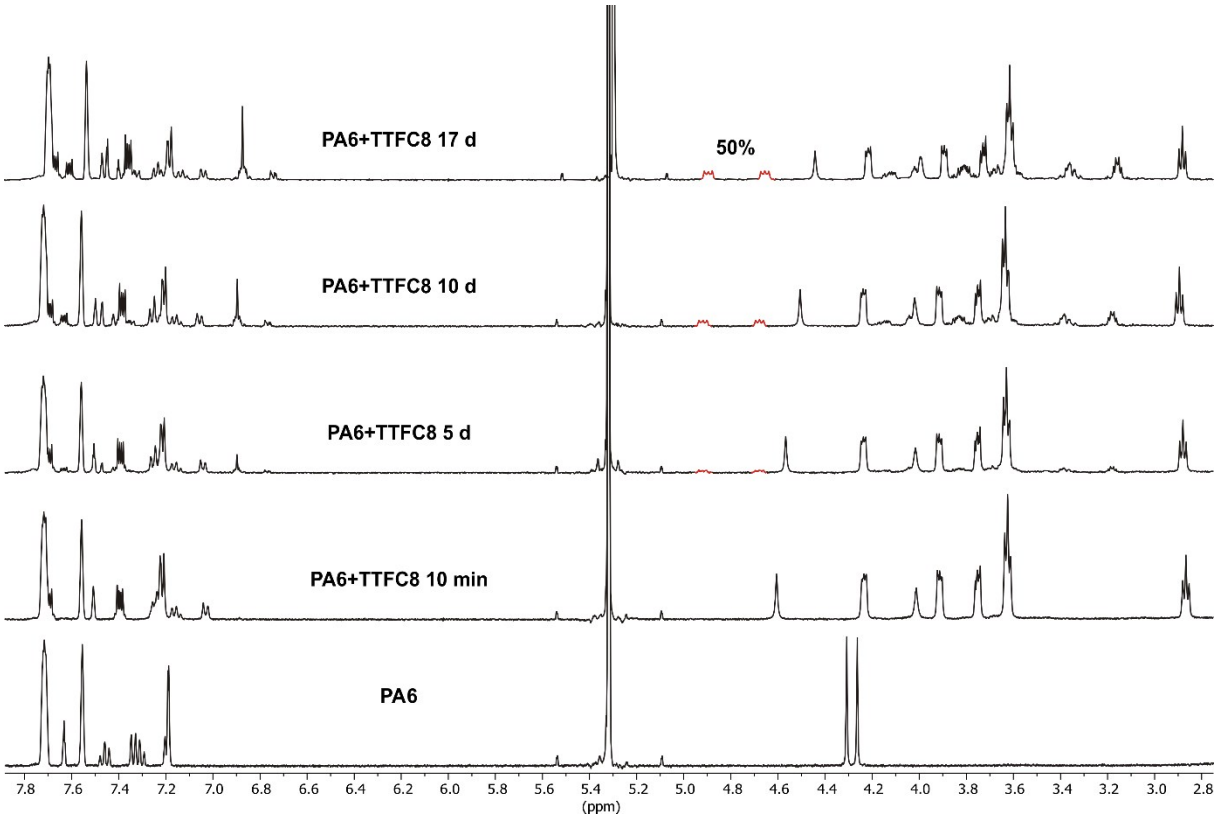

Fig. S33 Partial ^{1}H NMR spectra (400 MHz, CD_2Cl_2, 298 K) of **PA6** before (bottom) and after addition of **TTFC8** (top), the emerging peaks (red) correspond to the threaded complex.

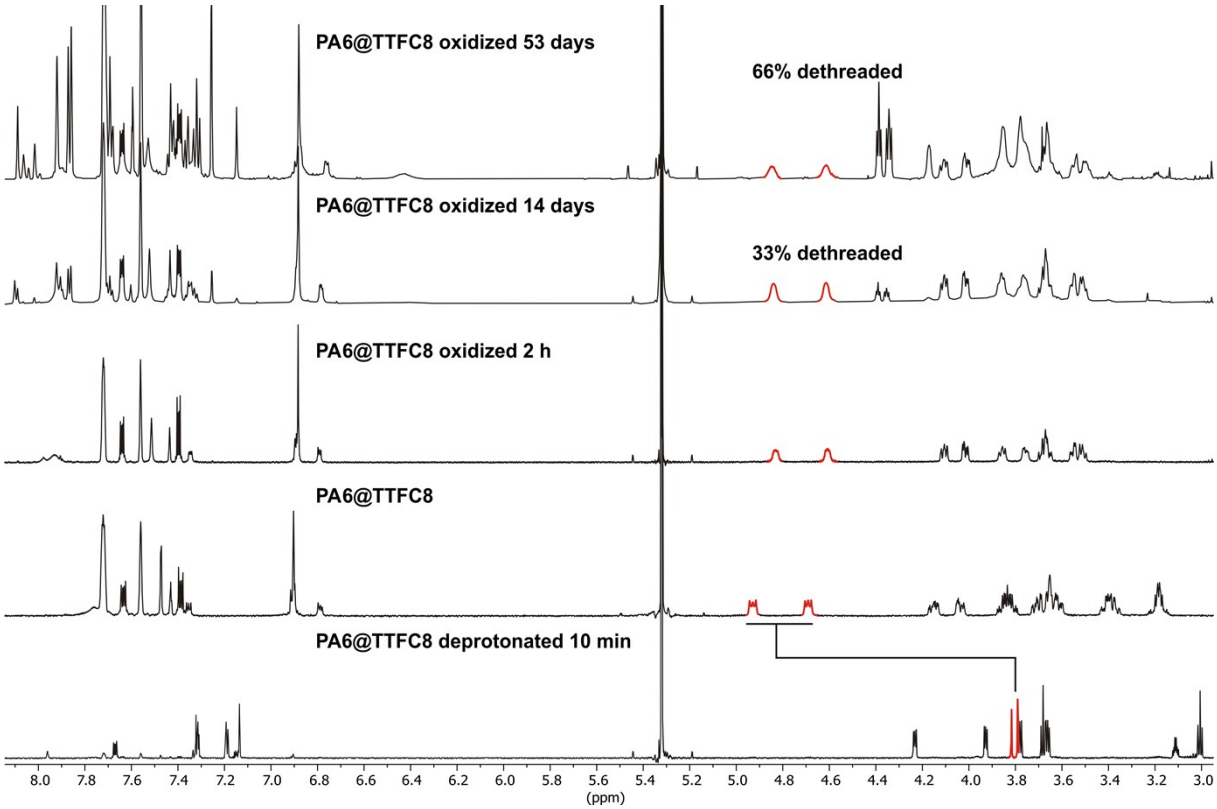

Fig. S34 Partial ^{1}H NMR spectra (700 MHz, CD_2Cl_2, 298 K) of **PA6@TTFC8** (center) after oxidation with $NO^{\cdot+}SbF_6^-$ (top) and after deprotonation with P2 base (bottom). The highlighted peaks in red correspond to the methylene protons next to the nitrogen.

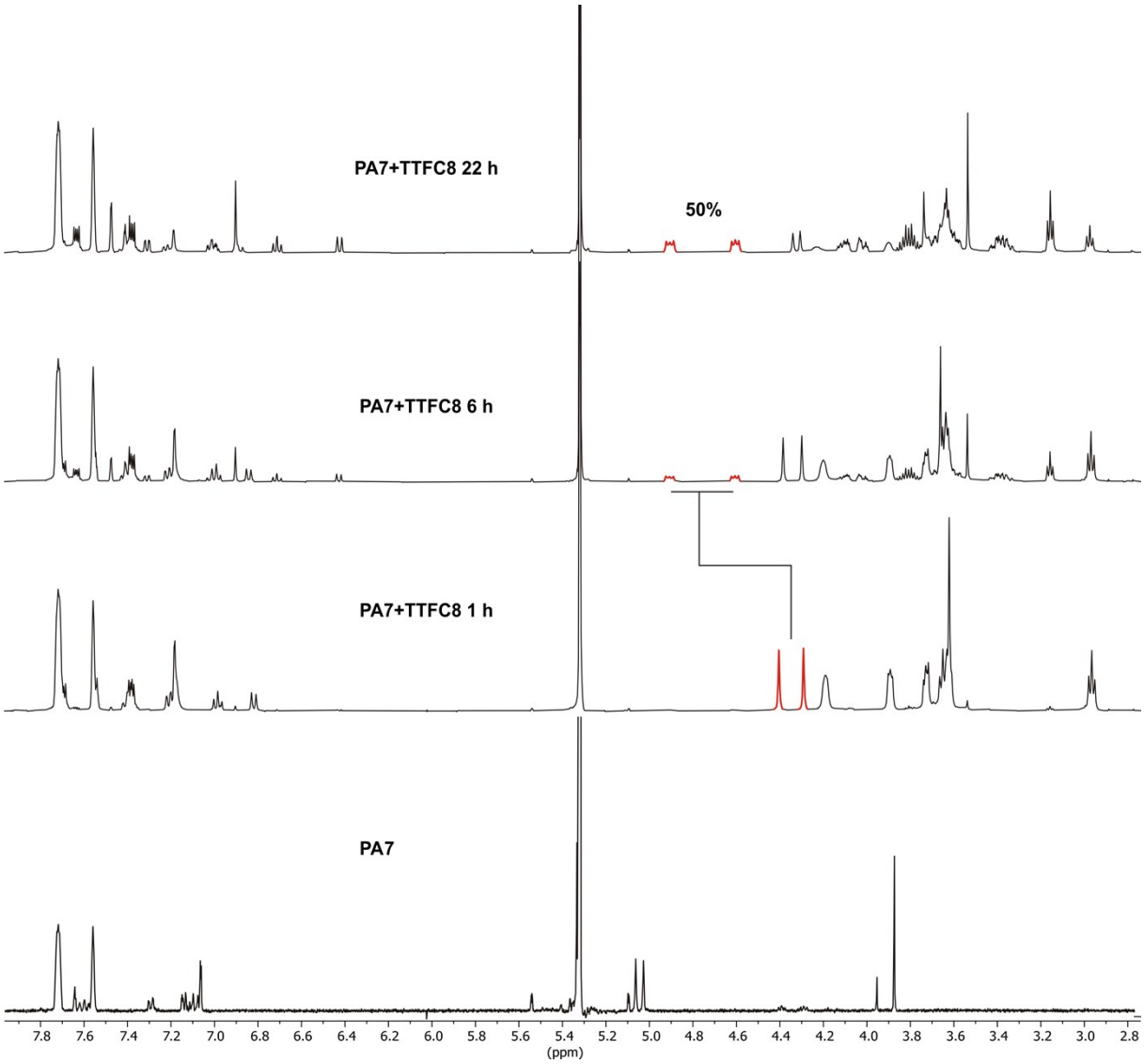

Fig. S35 Partial ^{1}H NMR (400 MHz, CD_2Cl_2, 298 K) spectra of **PA7** before (bottom) and after addition of **TTFC8** (top), the emerging peaks (red) correspond to the threaded complex.

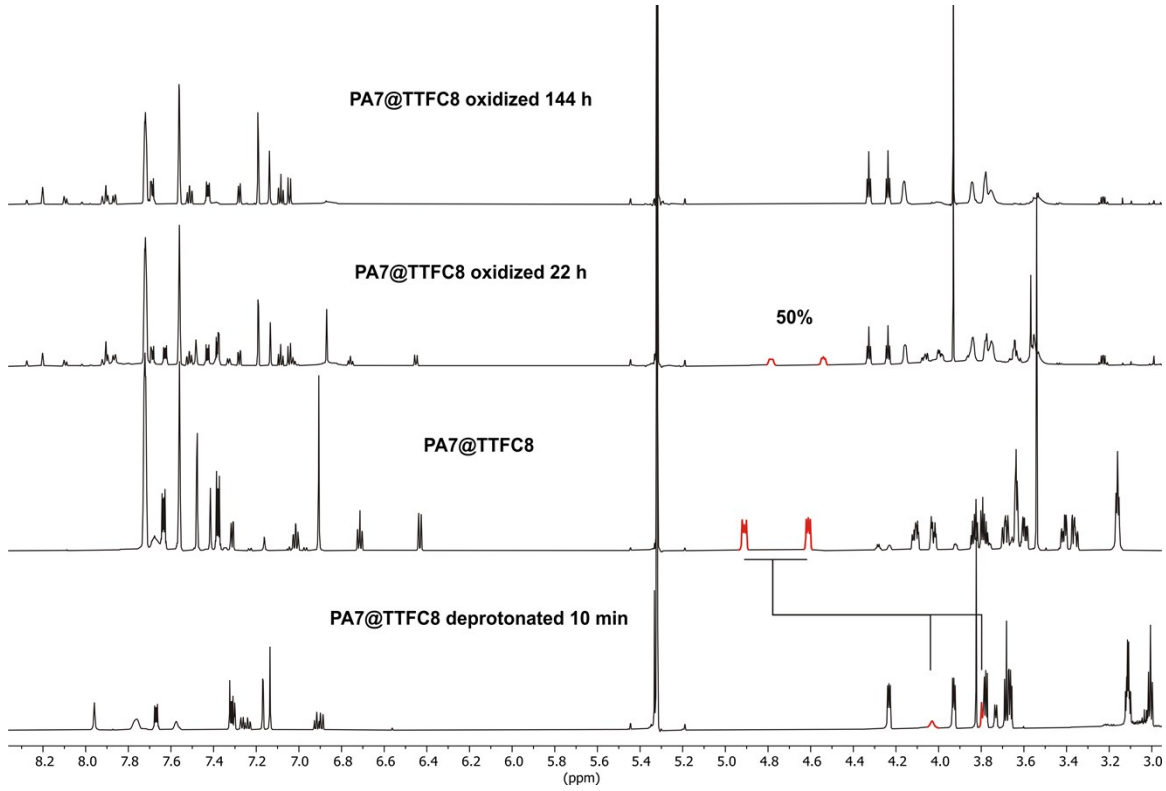

Fig. S36 Partial ^{1}H NMR spectra (700 MHz, CD_2Cl_2, 298 K) of **PA7@TTFC8** (center) after oxidation with $NO^{\cdot+}SbF_6^-$ (top) and after deprotonation with P2 base (bottom). The highlighted peaks in red correspond to the methylene protons next to the nitrogen.

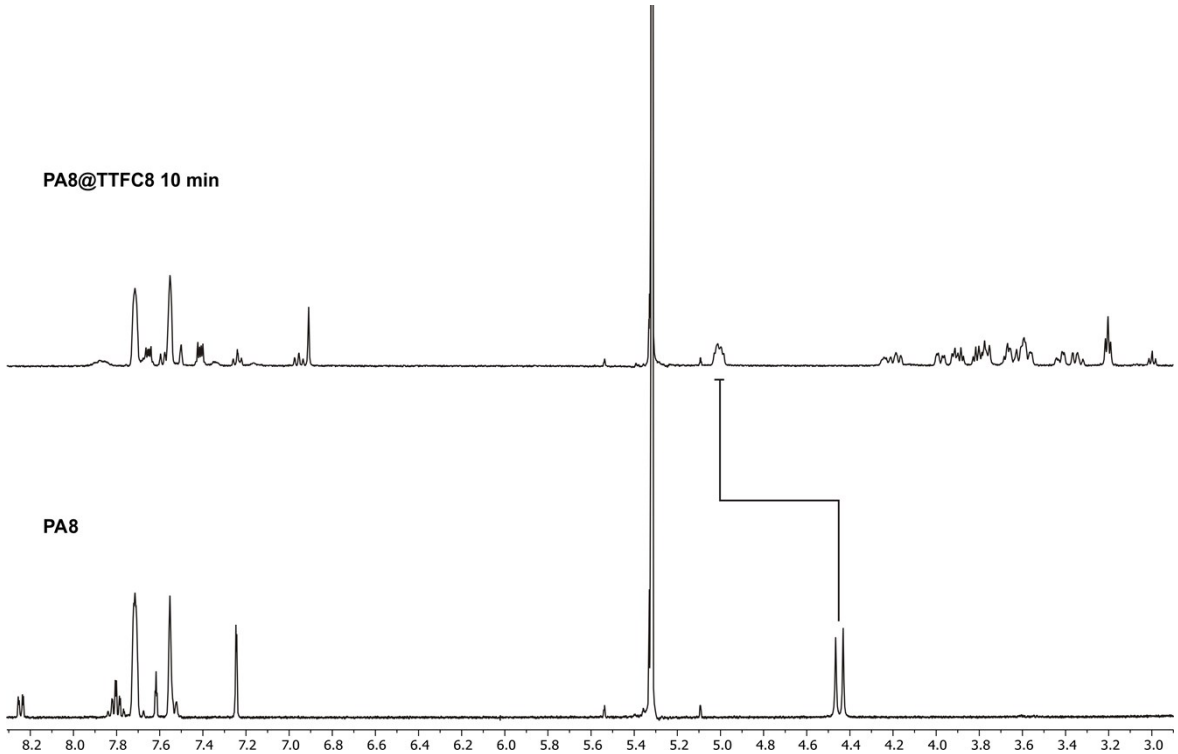

Fig. S37 Partial ^{1}H NMR spectra (400 MHz, CD_2Cl_2, 298 K) of **PA8** before (bottom) and after addition of **TTFC8** (top), the highlighted peaks correspond to the threaded complex.

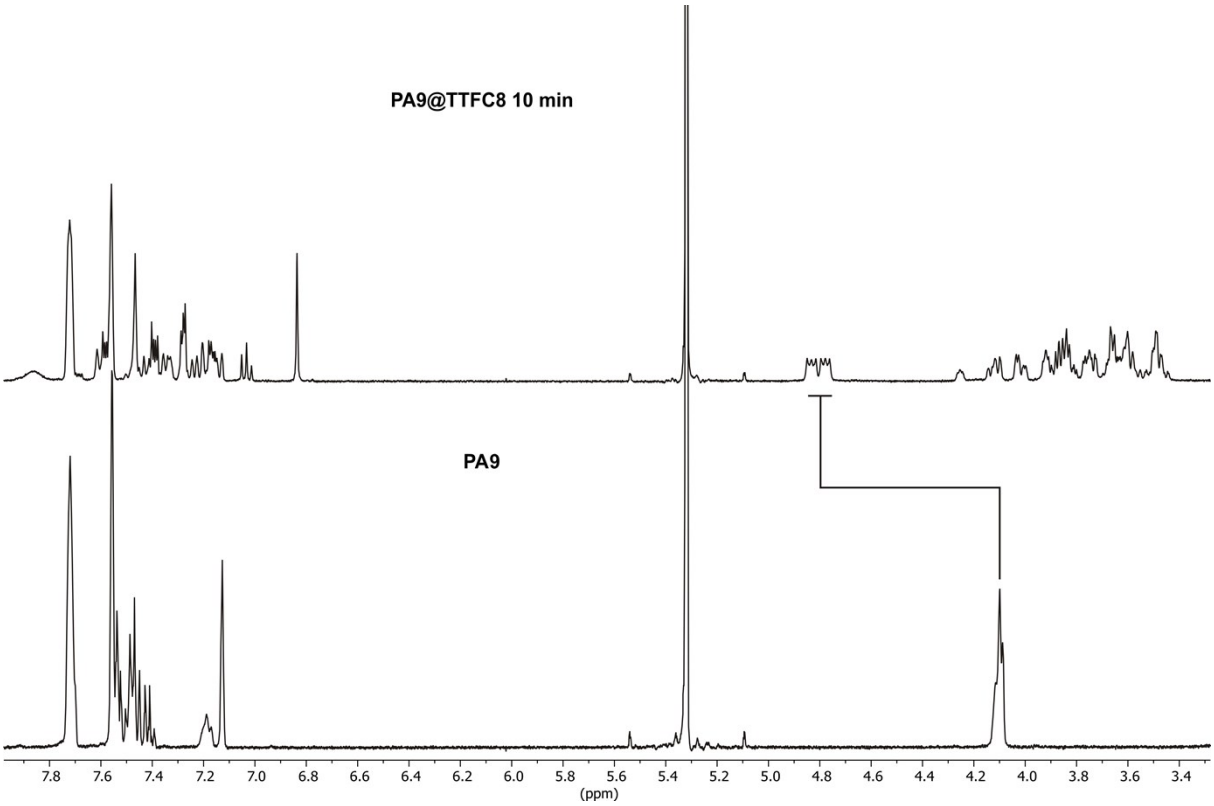

Fig. S38 Partial ^{1}H NMR spectra (400 MHz, CD_2Cl_2, 298 K) of **PA9** before (bottom) and after addition of **TTFC8** (top), the highlighted peaks correspond to the threaded complex.

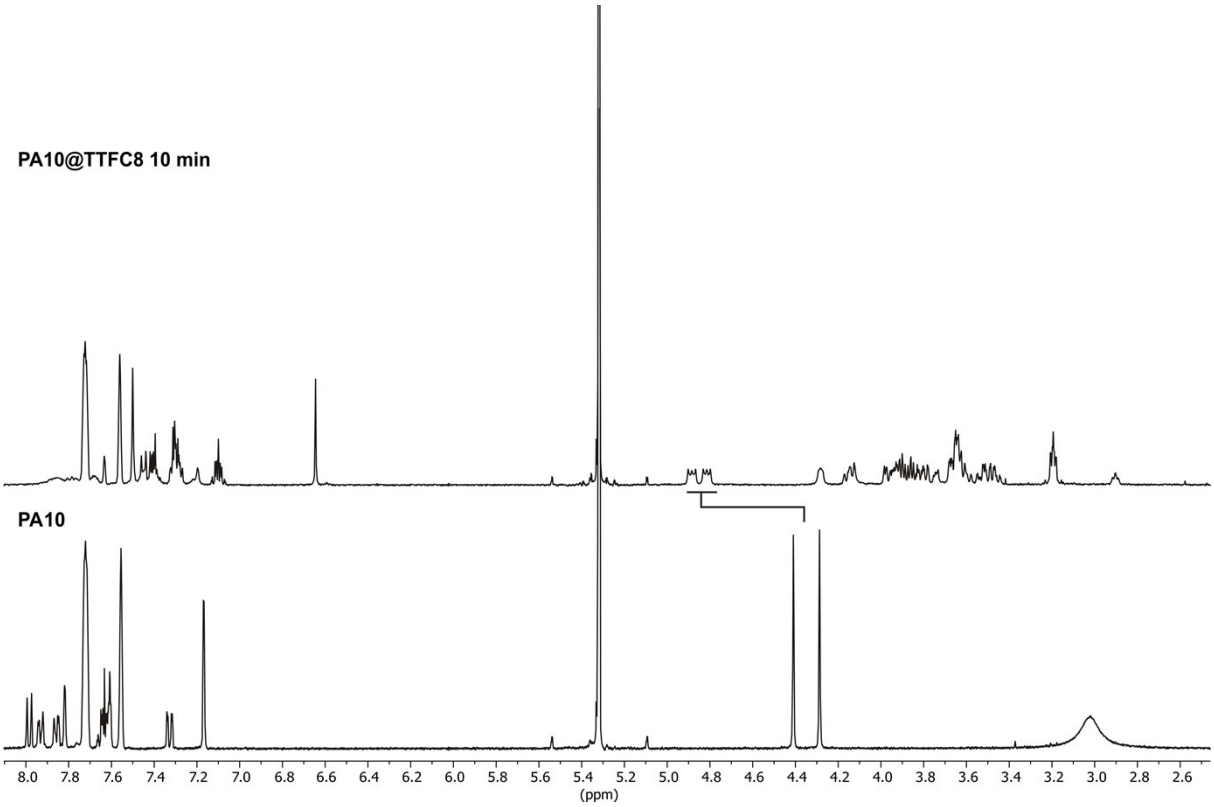

Fig. S39 Partial ^{1}H NMR spectra (400 MHz, CD_2Cl_2, 298 K) of **PA10** before (bottom) and after addition of **TTFC8** (top), the highlighted peaks correspond to the threaded complex

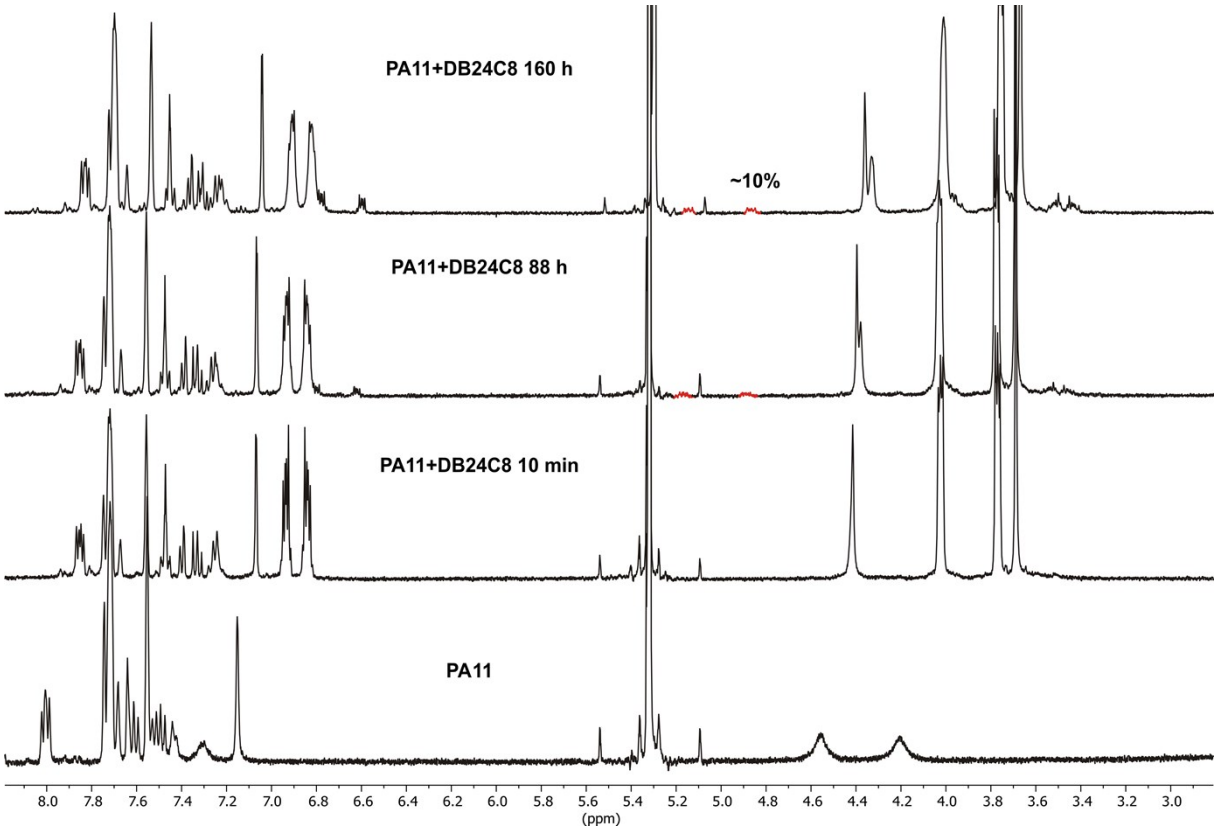

Fig. S40 Partial ^{1}H NMR spectra (400 MHz, CD_2Cl_2, 298 K) of **PA11** before (bottom) and after addition of **DB24C8** (top), the highlighted peaks correspond to the threaded complex.

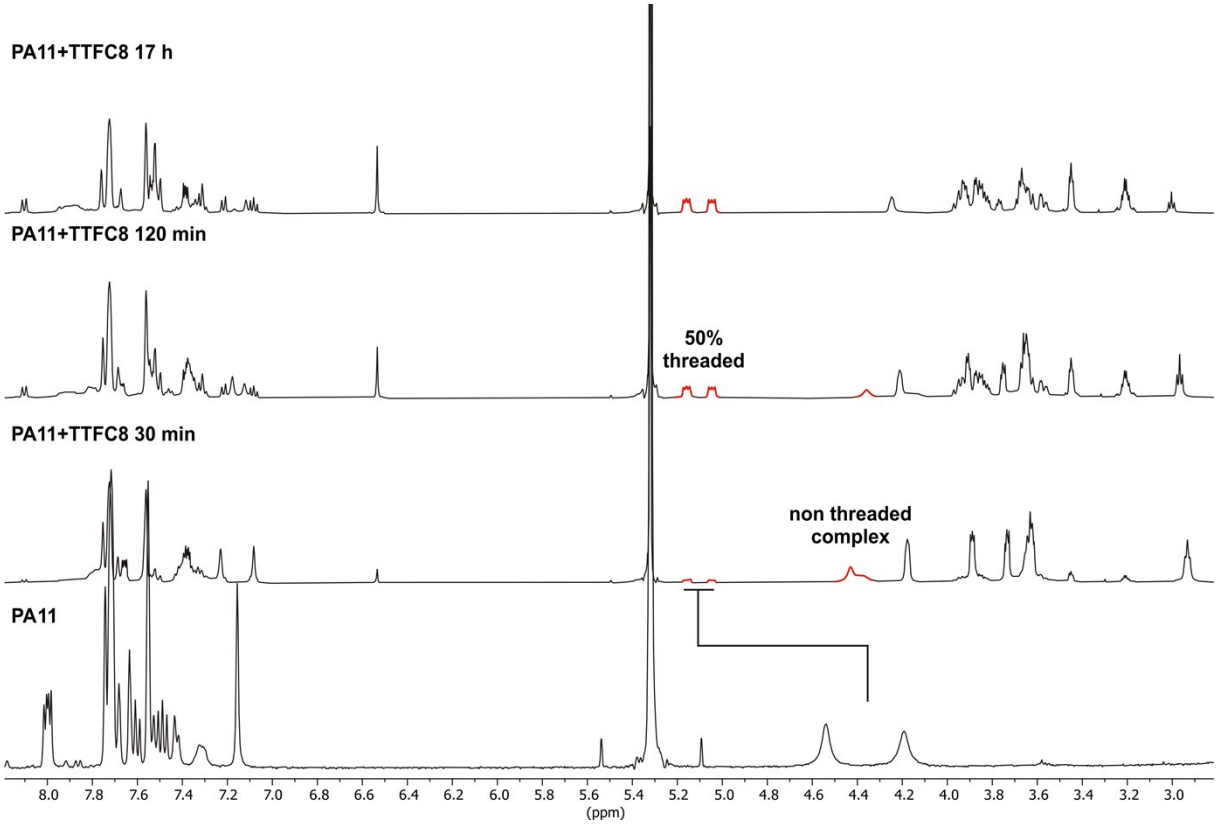

Fig. S41 Partial ^{1}H NMR spectra (500 MHz, CD_2Cl_2, 298 K) of **PA11** before (bottom) and after addition of **TTFC8** (top), the highlighted peaks correspond to the threaded complex.

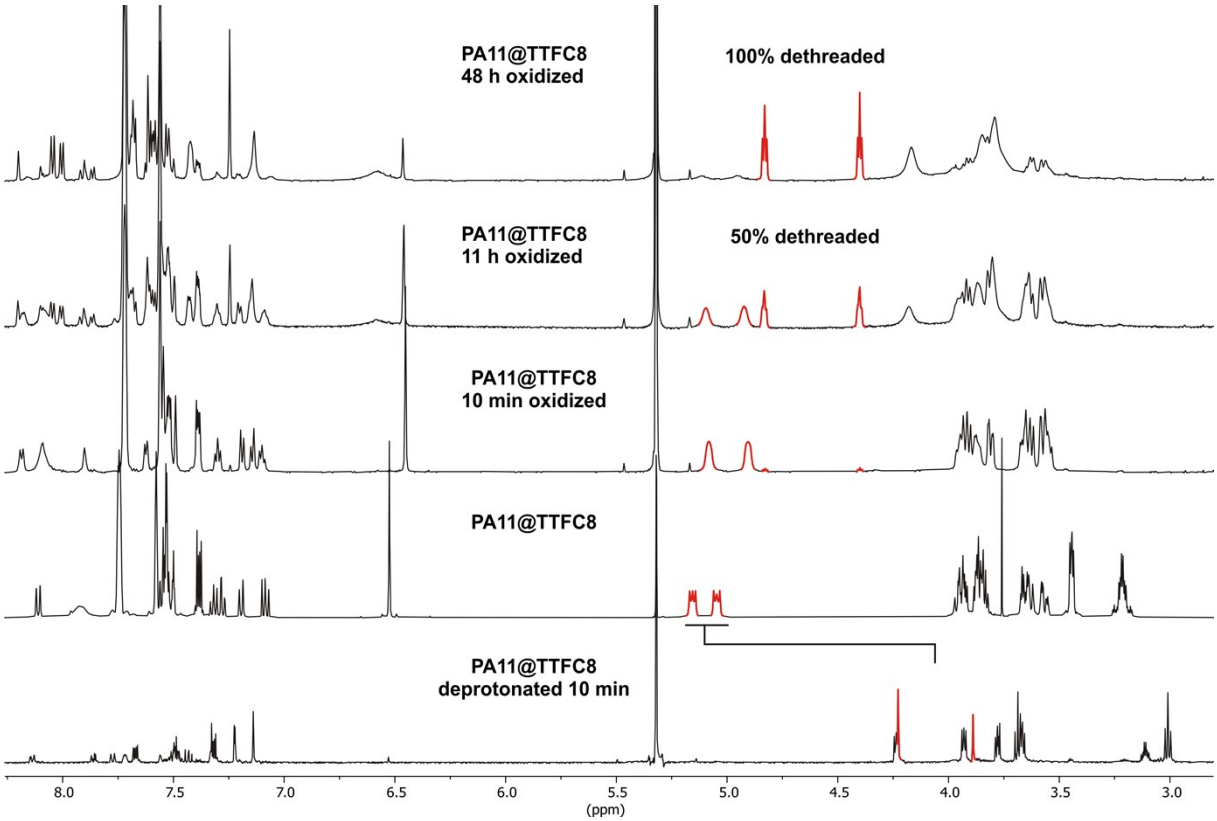

Fig. S42 ^{1}H NMR spectra (600 MHz, CD_2Cl_2, 298 K) of **PA11@TTFC8** (center) after oxidation with $NO^{\cdot+}SbF_6^-$ (top) and after deprotonation with P2 base (bottom). The highlighted peaks in red correspond to the methylene protons next to the nitrogen.

Tab. S1: Dethreading timescales in model pseudo[2]rotaxanes **PA*n*@TTFC8**: $t_{1/2}$, obtained via ^{1}H NMR (2 mM in CD_2Cl_2 400/600/700 MHz at r.t.).

	PA5@TTFC8	**PA6@TTFC8**	**PA7@TTFC8**	**PA11@TTFC8**
deprotonation (P2 base)	< 10 min	< 10 min	< 10 min	< 10 min
oxidation ($NO^{\cdot+}SbF_6^-$)	184 h	> 335 h	22 h	11 h

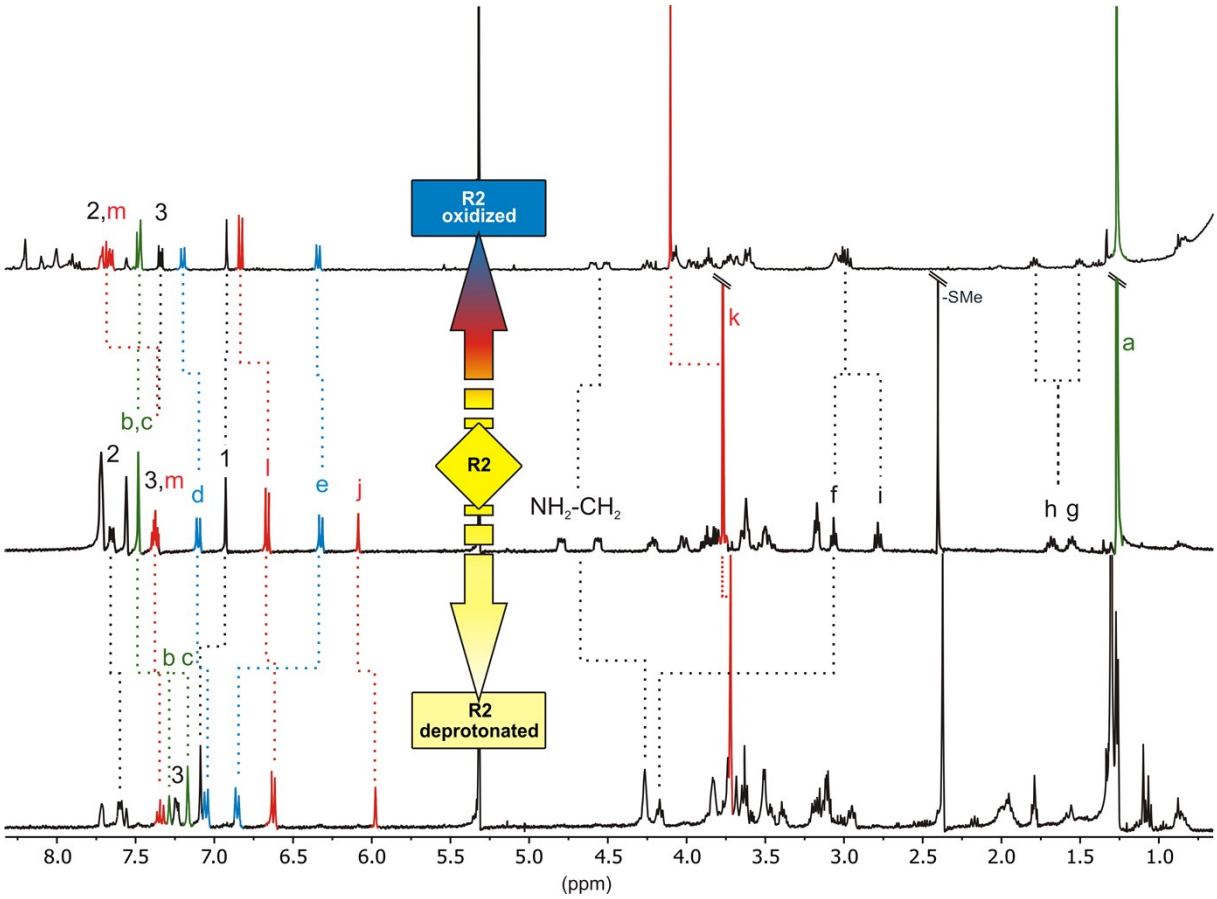

Fig. S43 ^{1}H NMR spectra (400 MHz, CD_2Cl_2, 298 K) with selected shifts highlighted of **R2** (center) 10 min after oxidation with $NO^{\cdot+}SbF_6^-$ (top) and 10 min after deprotonation with polystyrene-immobilized P2 base (bottom).

3. Tandem mass spectrometry

A Synapt G2-S HDMS (Waters Co., Milford, MA, USA) instrument with a quadrupole-time-of-flight high resolution mass detector was used to perform electrospray ionization tandem mass spectrometry. Collision-induced dissociation (CID) experiments of mass-selected ions, were performed using the following settings: flow rate 10 µL min^{-1}, capillary voltage 1.5 kV, sample cone voltage 34 V, source offset 54 V, source temperature 100 °C, desolvation temperature 20 °C, nebulizer gas 5 bar, desolvation gas flow 460 L h^{-1}. For CID, N_2 was used as the collision gas. Fragmentation experiments were conducted in the trap cell of the Synapt G2-S HDMS instrument with collision energies of 2 – 72 V. For the column chromatography isolated sample, 4 V steps were used and for the other samples 2 V steps. Data acquisition and processing was carried out using MassLynx™ (version 4.1).

For plotting of the survival yield curves the spectra were centered. For each spectrum at different collision voltages, the intensity of the ion with the selected mass (m/z 1108) was divided by the total ion intensity (only fragments with an intensity above 1% were considered) and then plotted against the collision voltage. Fitting was done by applying a sigmoidal Boltzmann equation using Origin Pro 2020 to obtain the 50%-survival yield voltages of threaded and non-threaded complex.

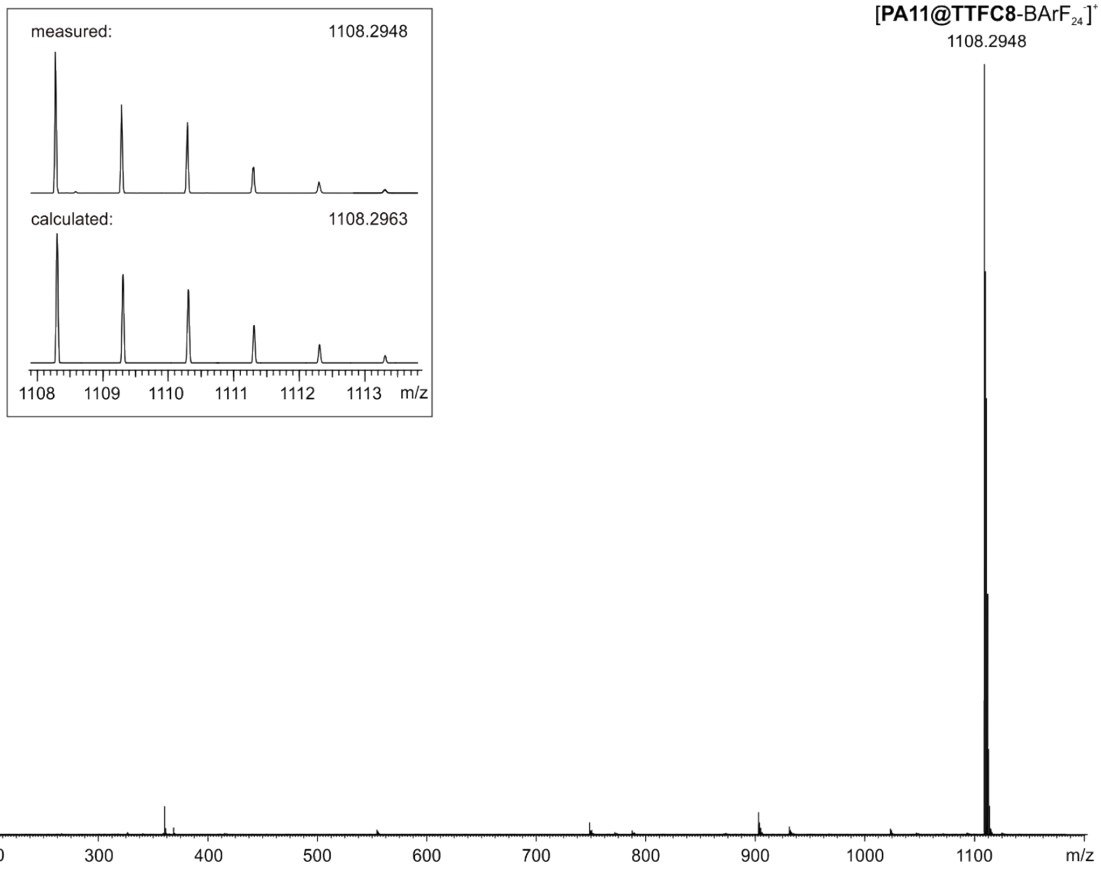

Figure S44 ESI-Q-TOF-HRMS spectrum of **PA11@TTFC8** (5 µM in CH_2Cl_2) isolated after column chromatography; (inset) comparison of measured and calculated isotopic patterns.

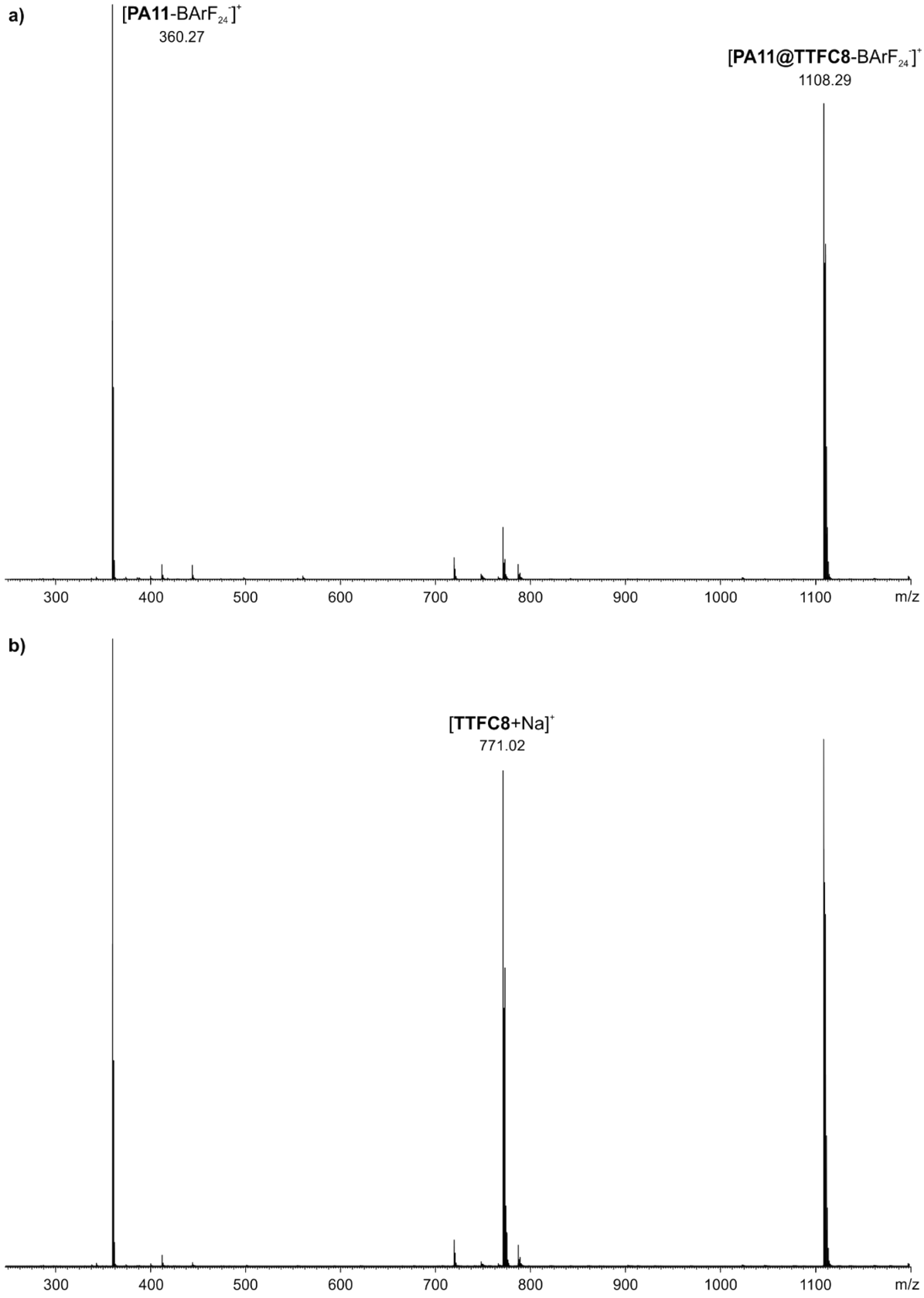

Figure S45 ESI-Q-TOF-HRMS spectrum of a mixture of **PA11** and **TTFC8** (500 µM in CH_2Cl_2), diluted before measuring to 50 µM after 5 min (a) and 135 min (b). Both solutions feature a complex of **TTFC8** and **PA11**, as well as **TTFC8**(+Na) and **PA11** individually. Which indicates that a non-threaded complex is formed within 5 min or during the ionization.

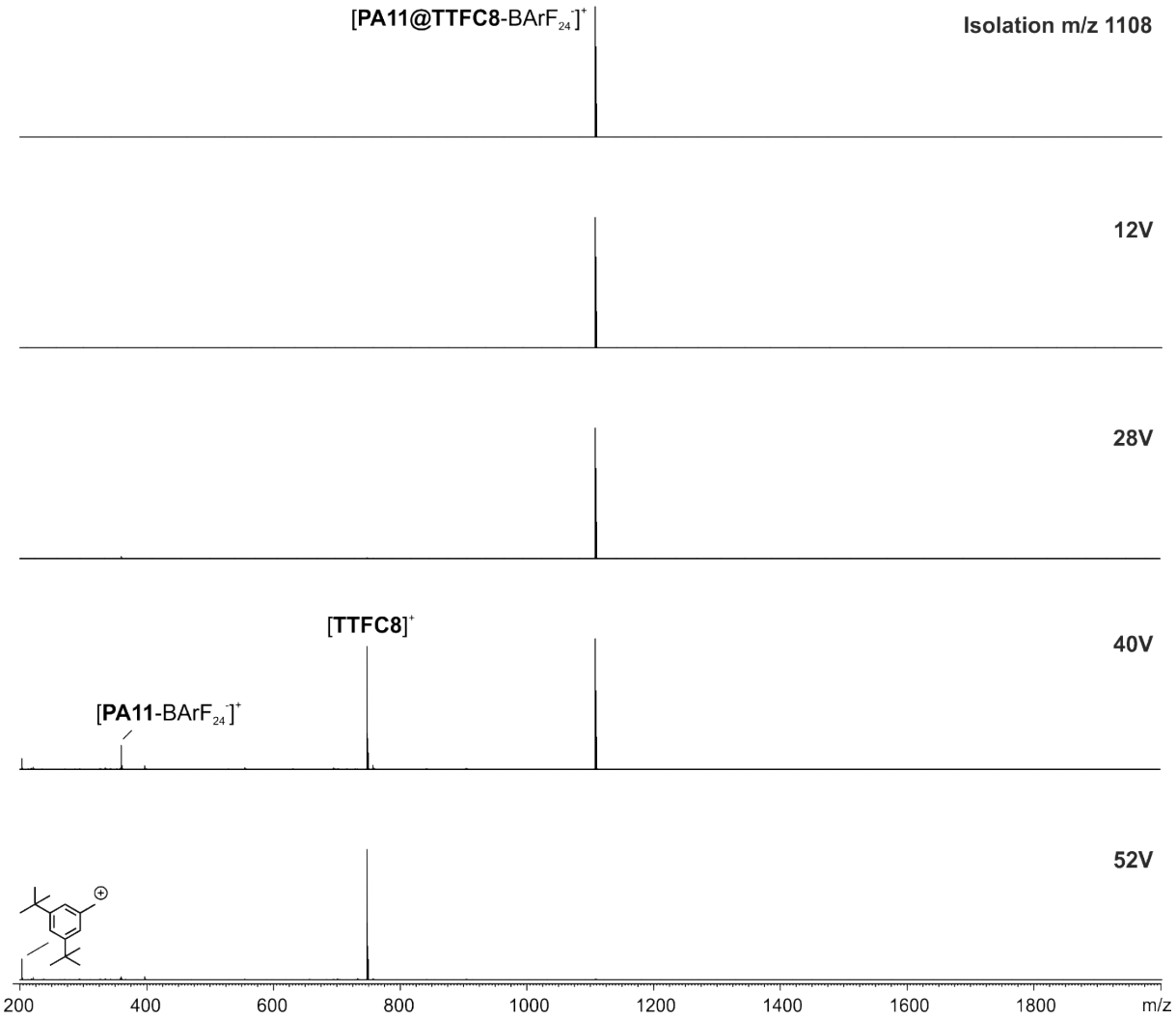

Figure S46 CID experiment with mass-selected ions at *m/z* 1108 obtained from a CH_2Cl_2 solution (50 nM) of **PA11@TTFC8** isolated after column chromatography: (top) after mass-selection; (bottom) after fragmentation at different voltages. Higher voltages are necessary to induce fragmentation and as a major fragment oxidized **TTFC8** is observed. This is diagnostic for a mechanically interlocked structure.[10]

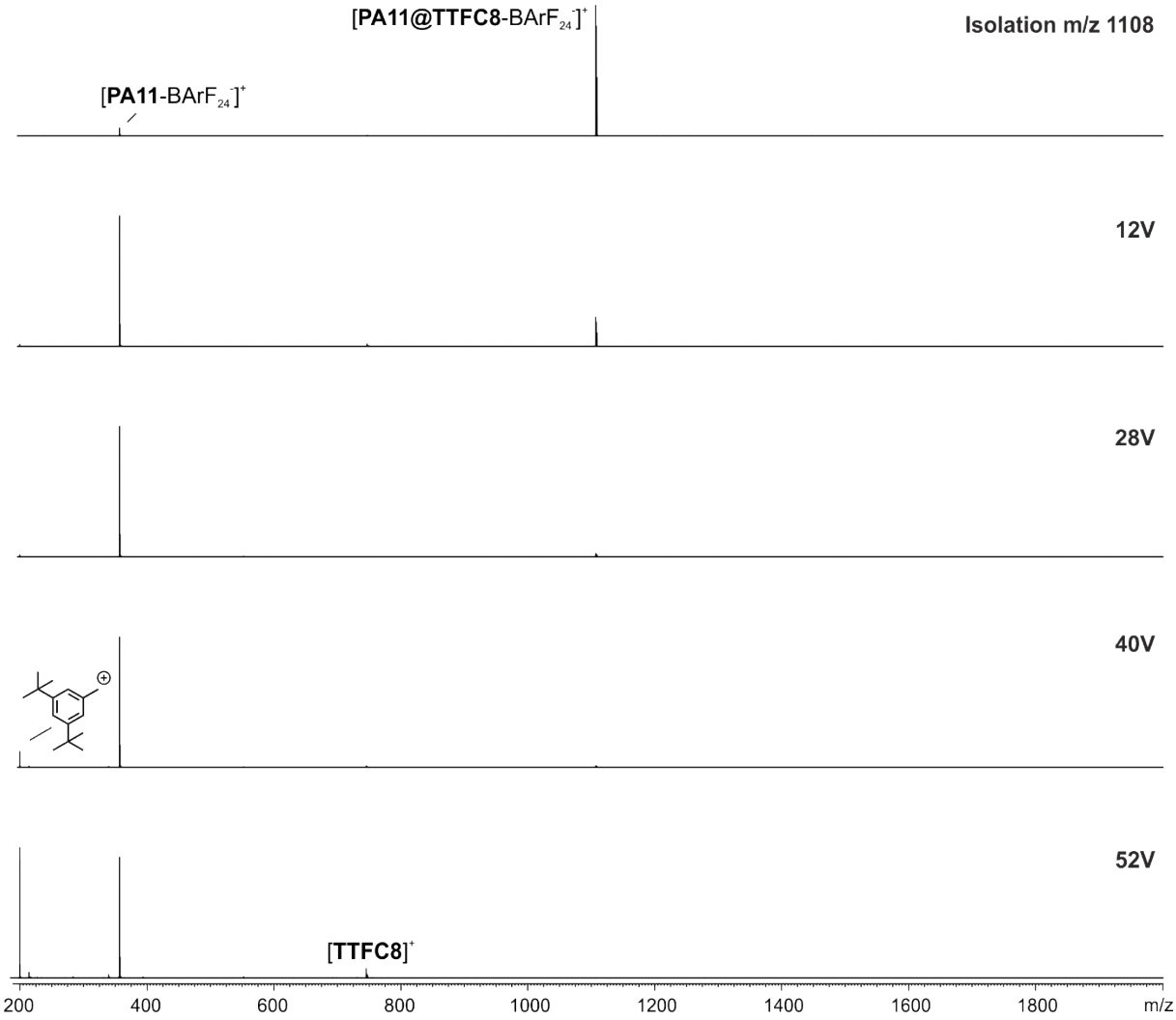

Figure S47 CID experiment with mass-selected ions at *m/z* 1108 obtained from a mixture of **PA11** and **TTFC8** (500 µM in CH_2CCl_2), diluted before measuring to 50 µM after 5 min (top) after mass-selection; (bottom) after fragmentation at different voltages. The complex fragments already appear at low collision voltages, which can be explained by the formation of a non-threaded complex. A minor amount of the complex is still existing at higher voltages (28 and 40 V), which represents the amount of threaded complex.

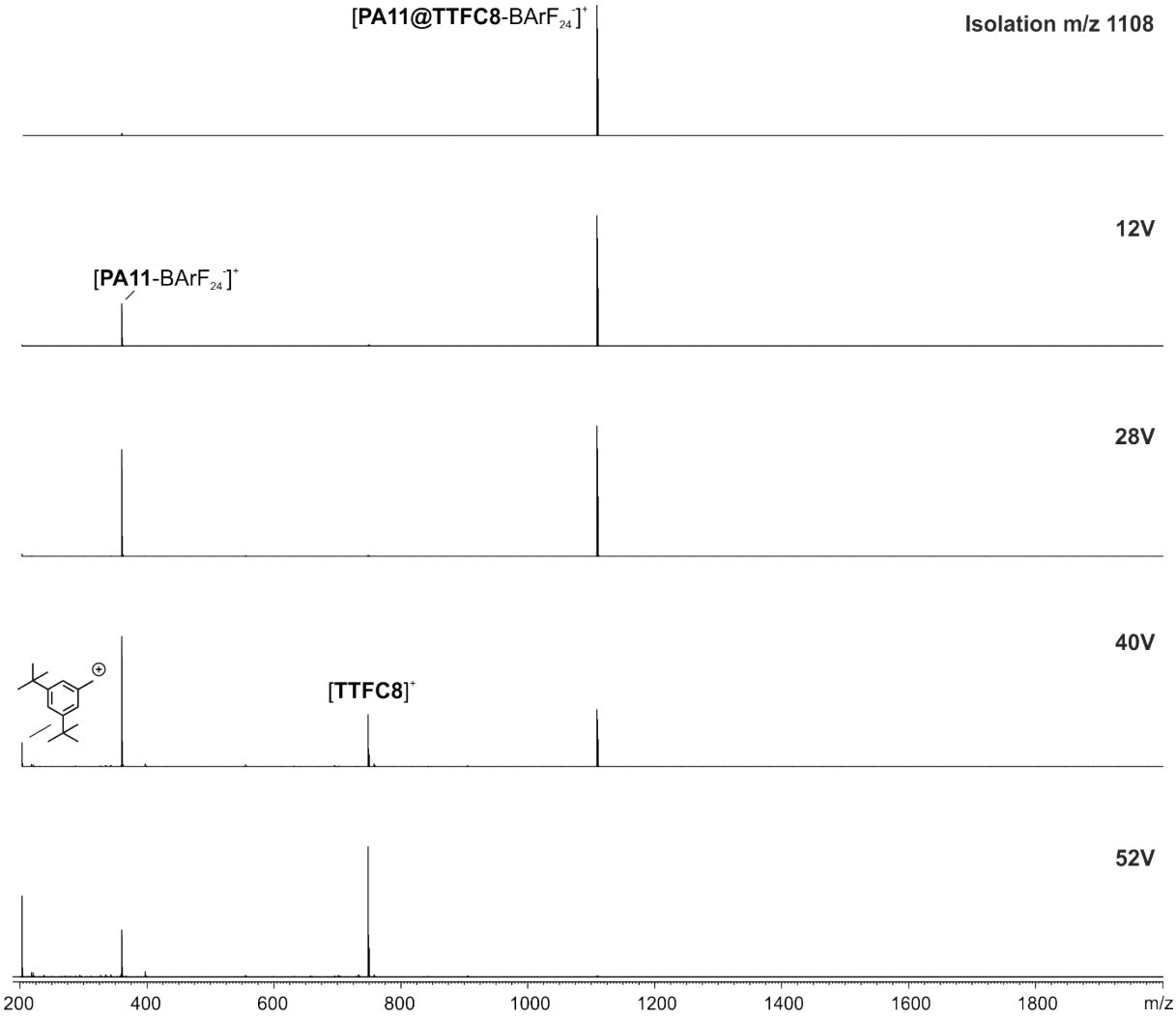

Figure S48 CID experiment with mass-selected ions at *m/z* 1108 obtained from a mixture of **PA11** and **TTFC8** (500 µM in CH_2Cl_2), diluted before measuring to 50 µM after 135 min (top) after mass-selection; (bottom) after fragmentation at different voltages. A fraction of the complex fragments appear already at low collision voltages, which can be explained by the formation of a non-threaded complex. A bigger amount of the complex is still existing at higher voltages (28 and 40 V), which represents the amount of threaded complex.

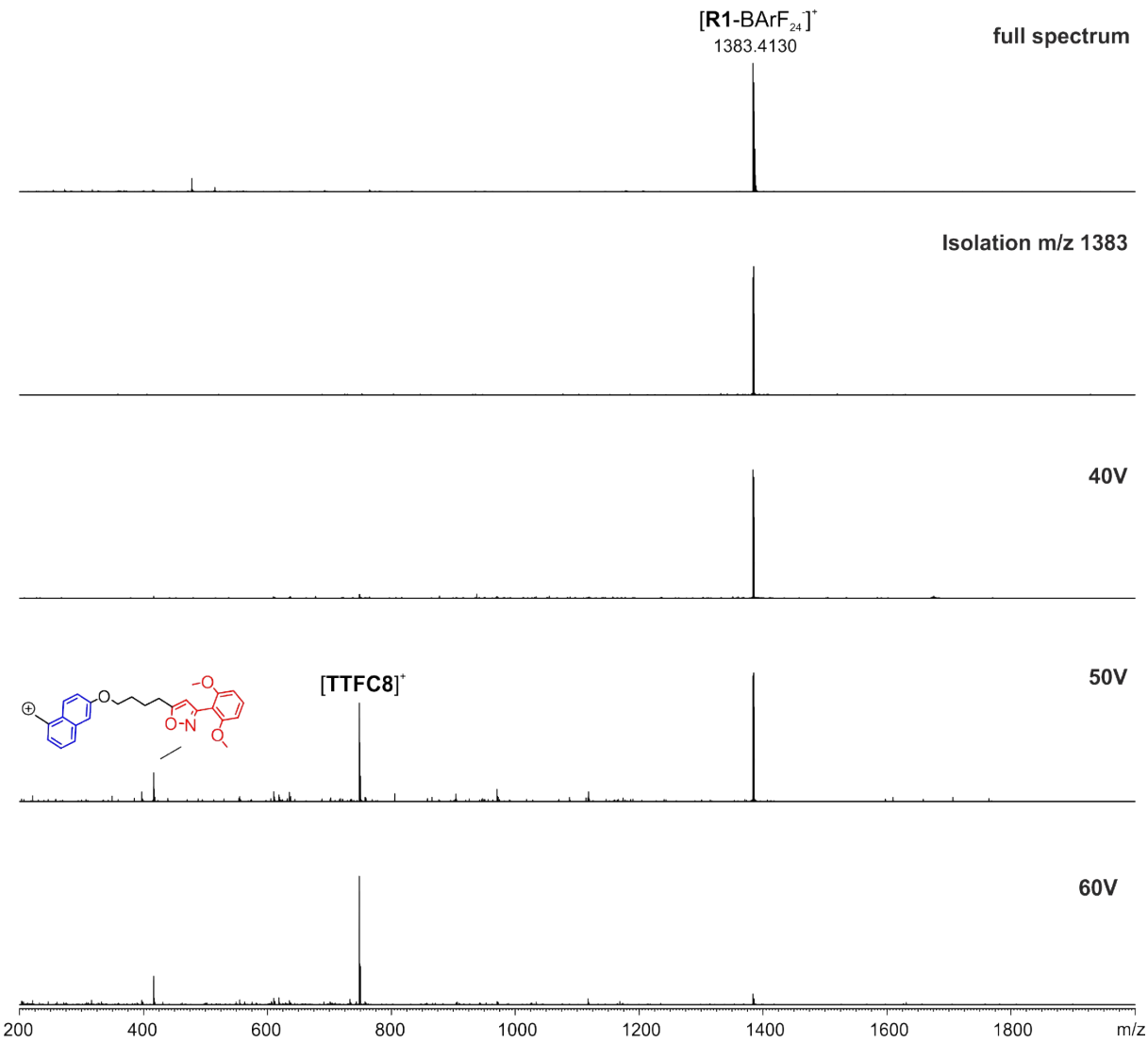

Figure S49 ESI-Q-TOF-HRMS spectrum (top) and CID experiment with mass-selected ions at *m/z* 1383 obtained from solution of **R1** (5 µM in acetonitrile). Higher voltages are necessary to induce fragmentation of **R1** and as major fragments oxidized **TTFC8** and axle fragments are observed. The free axle (m/z 635) is not observed as a fragment. This is diagnostic for a mechanically interlocked structure.[10]

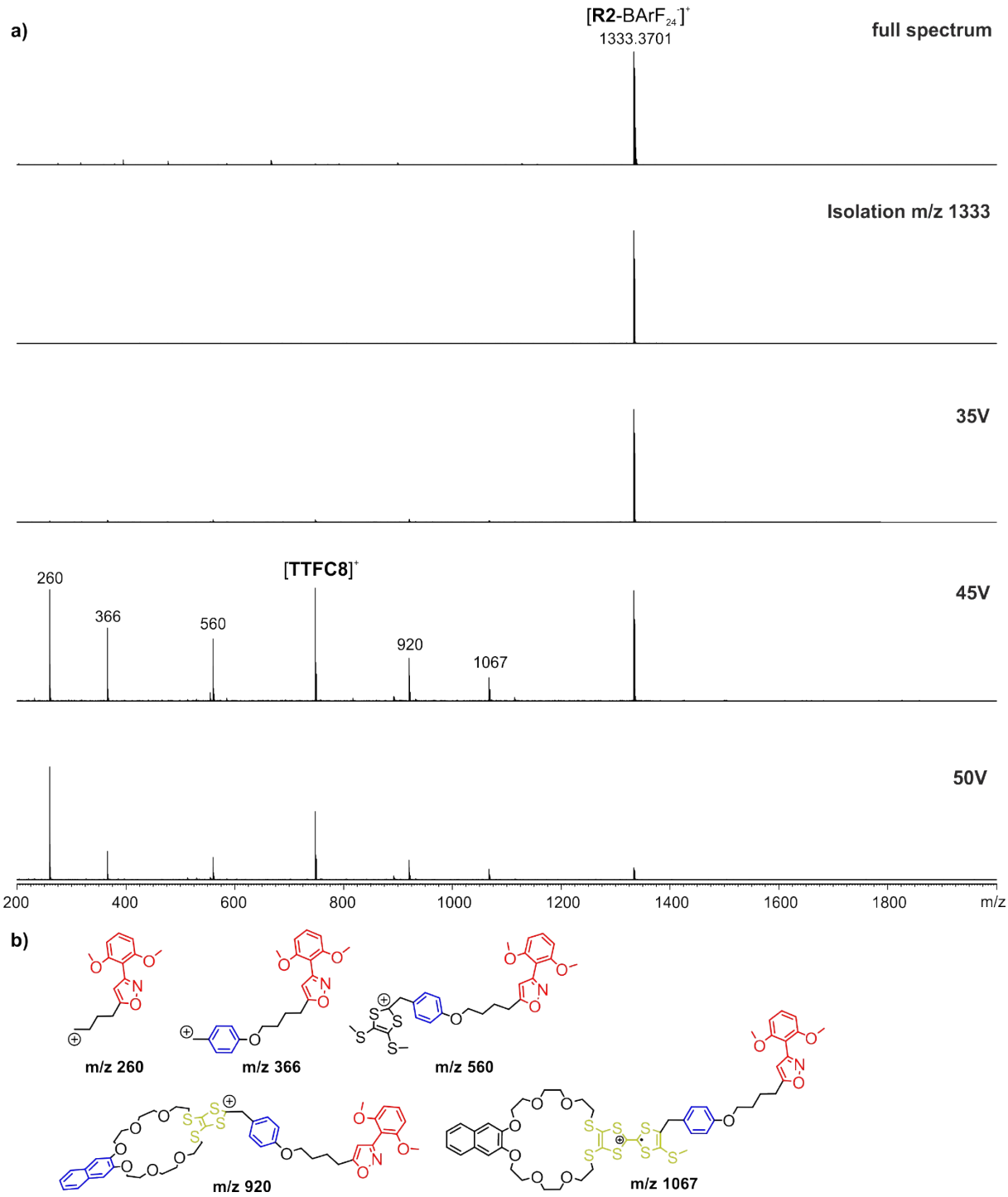

Figure S50 (a) ESI-Q-TOF-HRMS spectrum (top) and CID experiment with mass-selected ions at *m/z* 1333 obtained from solution of **R2** (5 µM in acetonitrile). Higher voltages are necessary to induce fragmentation of **R2** and as major fragments oxidized **TTFC8** and axle fragments are observed. The free axle (m/z 635) is not observed as a fragment. This is diagnostic for a mechanically interlocked structure. (b) Proposed structures for m/z values occurring in the fragmentation spectra. Similar fragments have been observed for other TTF crown/ammonium rotaxane.[10]

4. Variable-temperature ^{1}H NMR spectroscopy

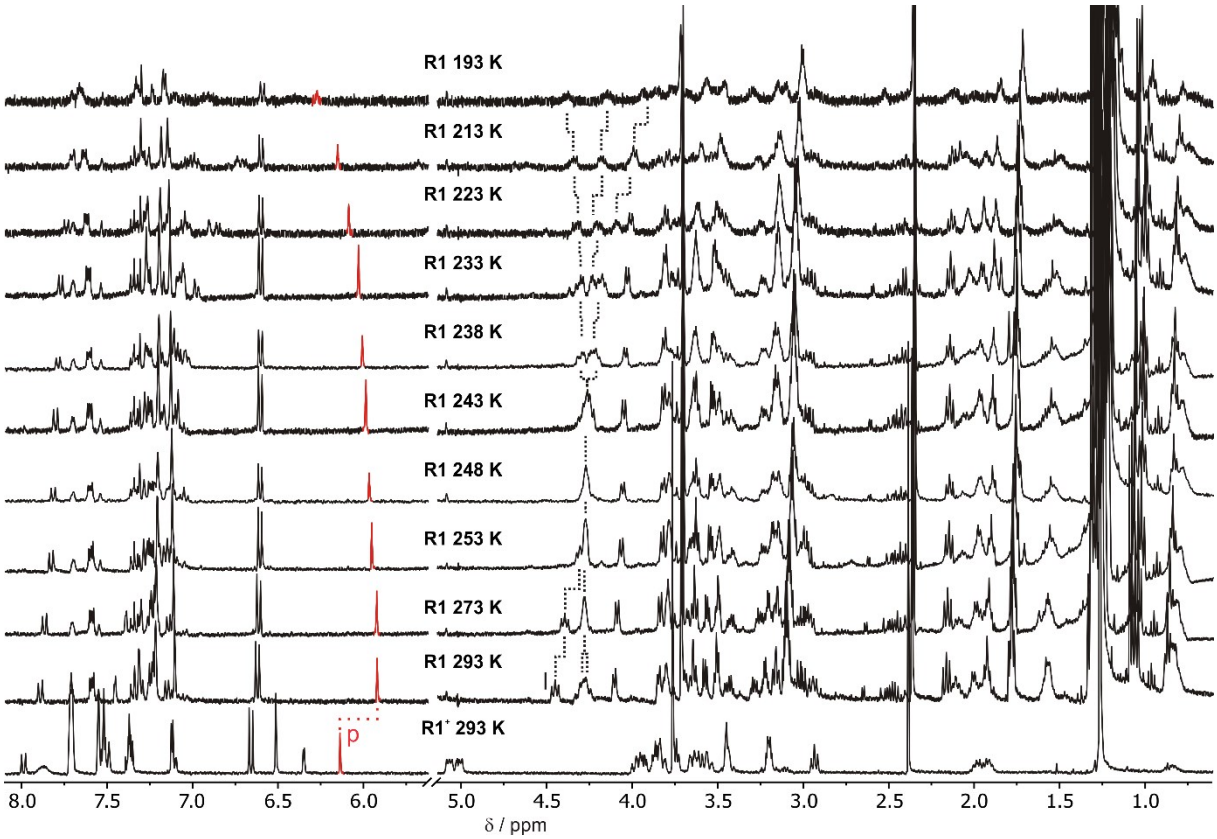

Fig. S51 VT ^{1}H NMR spectra (400 MHz, CD_2Cl_2) of [2]rotaxane **R1** before (bottom) and after deprotonation with P2 base (gradual cooling from 293 to 193 K), showing the shift of H_p (isoxazol).

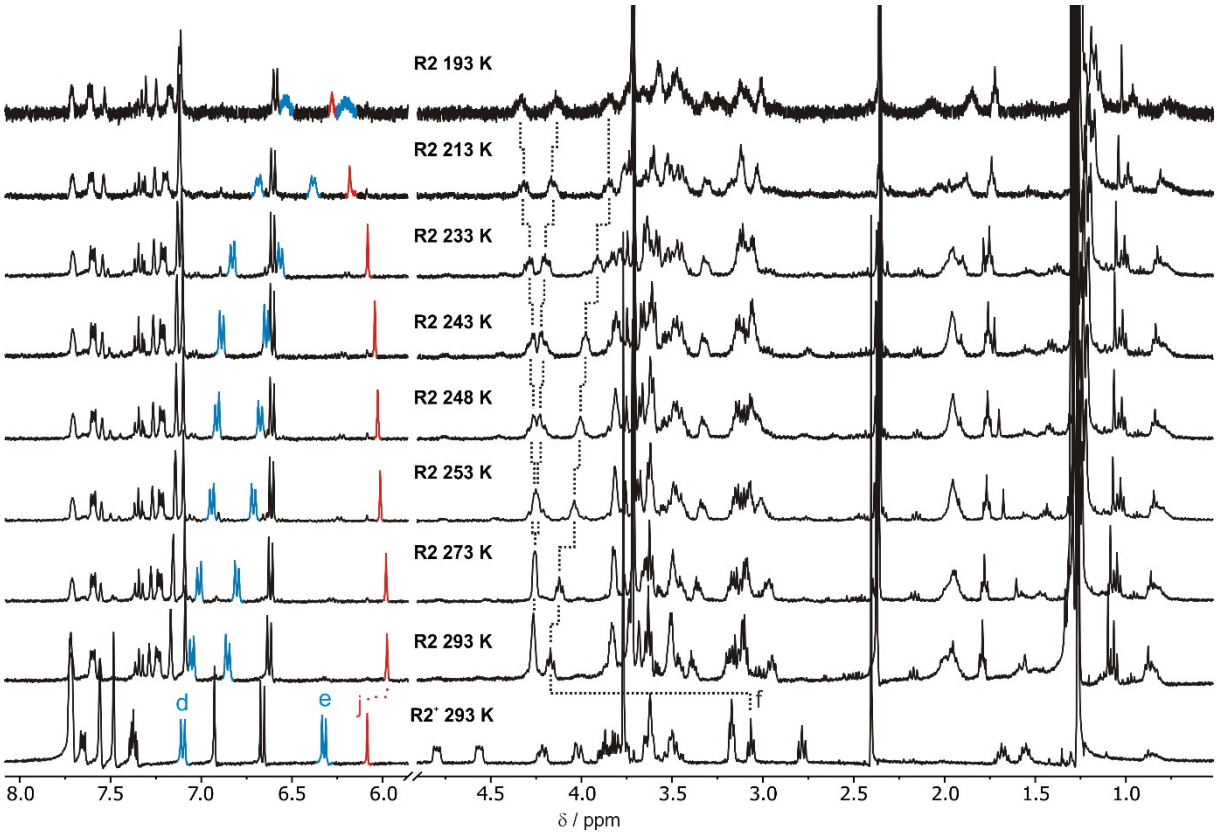

Fig. S52 VT ^{1}H NMR spectra (400 MHz, CD_2Cl_2) of [2]rotaxane **R2** before (bottom) and after deprotonation with P1 base (gradual cooling from 293 to 193 K), showing the shift of H_j (isoxazol), $H_{d,e}$ (phenyl).

5. Isothermal titration calorimetry

ITC experiments were carried out in dry 1,2-dichloroethane at 298 K on a TAM III microcalorimeter (Waters GmbH, TA Instruments, Eschborn, Germany). In a typical experiment, an 800 µL solution of crown ether was placed in the sample cell at a concentration of 1.1 mM, and 250 µL of a solution of the ammonium salt (7.0 mM) were put into the syringe. The titrations consisted of 32 consecutive injections of 8 µL each with a 20 min interval between injections. Heats of dilution were determined by titration of ammonium salt solutions into the sample cell containing blank solvent and were subtracted from each data set. The heat flow generated in the sample cell is measured as a differential signal between sample and reference cell. Hence, an exothermic event results in a positive and an endothermic in a negative heat flow. The data were analysed using the instrument's internal software package and fitted with a 1:1 binding model. Each titration was conducted three times and the measured values for K and ΔH were averaged.

Tab. S2: Thermodynamic data obtained from the ITC experiments.

	K_a /10^4 M^{-1}	ΔG / kJ mol^{-1}	ΔH / kJ mol^{-1}	$T\Delta S$ / kJ mol^{-1}
PA11@TTFC8	1.0 ± 0.3	-22.9 ± 0.6	-28.6 ± 2.0	-5.7 ± 2.6
PA12@TTFC8	39 ± 7	-31.9 ± 0.4	-44.1 ± 1.2	-12.2 ± 1.6
DBA@TTFC8	77 ± 10	-33.6 ± 0.3	-39.8 ± 1.0	-6.2 ± 1.3

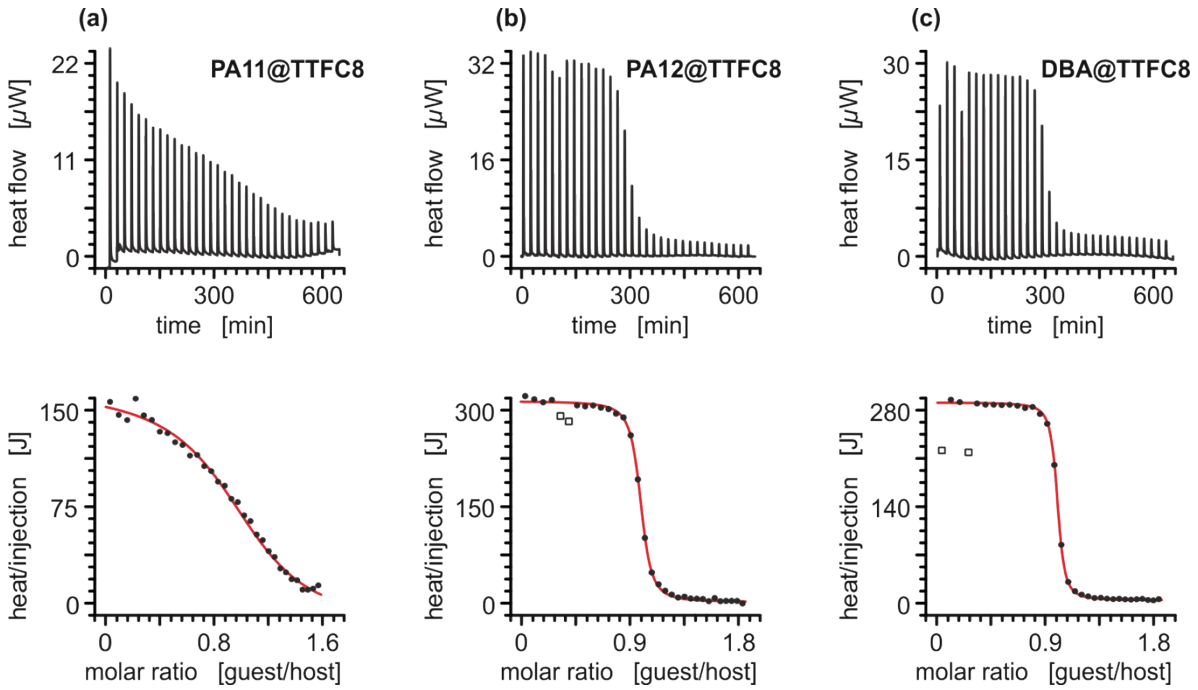

Figure S53. Titration plots (heat flow versus time and heat/volume versus guest/host ratio) obtained from ITC experiments at 298 K in 1,2-dichloroethane**: (a)** vial: **TTFC8**, syringe: axle **PA11**; **(b)** vial: **TTFC8**, syringe: axle **PA12**; **(c)** vial: **TTFC8**, syringe: axle **DBA** (dibenzylammonium $BArF_{24}$). Points marked with non-filled squares were not considered in the fitting process. **PA11@TTFC8** was fitted using a 1:1 binding model. However, for this axle the formation of a threaded complex happens over the course of hours and the formation of a non-threaded complex is observed on a minute timescale. The thermodynamic parameters obtained for this macrocycle/axle combination can therefore be interpreted as a combination of both equilibria (see Figure 3 main text) with the formation of the threaded complex contributing with a less time dependent heat flow. The obtained thermodynamic parameters can therefore be used as an upper limit for the values of K and ΔH of the non-threaded complex.

6. Electrochemical measurements

Redox-potentials reported in this study were obtained by DPV. All measurements were at least conducted twice. Measurements were conducted in CH_2Cl_2 with 0.1 M electrolyte and 2 mM analyte concentration.

Tab. S3 Electrochemical data obtained from DPV measurements (CH_2Cl_2, with n-Bu_4NBArF_{24} as the electrolyte, 298 K).

species	$E^1_{1/2}$ / mV	$E'_{1/2}$ / mV	$E^2_{1/2}$ / mV
TTFC8	594	/	987
PA12@TTFC8	599	987	1294
PA11@TTFC8	695	/	1385
R1	695	/	1380
R2	694	/	1349

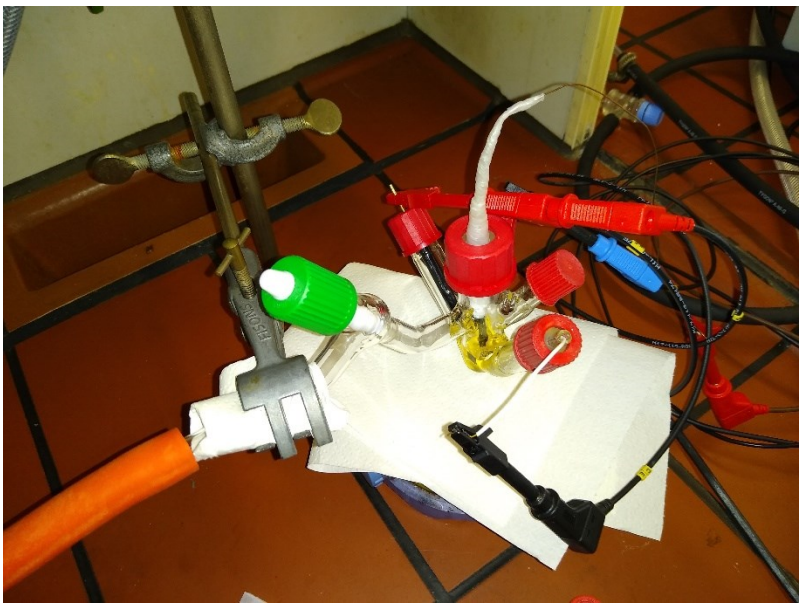

Fig. S54: General set-up for bulk electrolysis experiments.

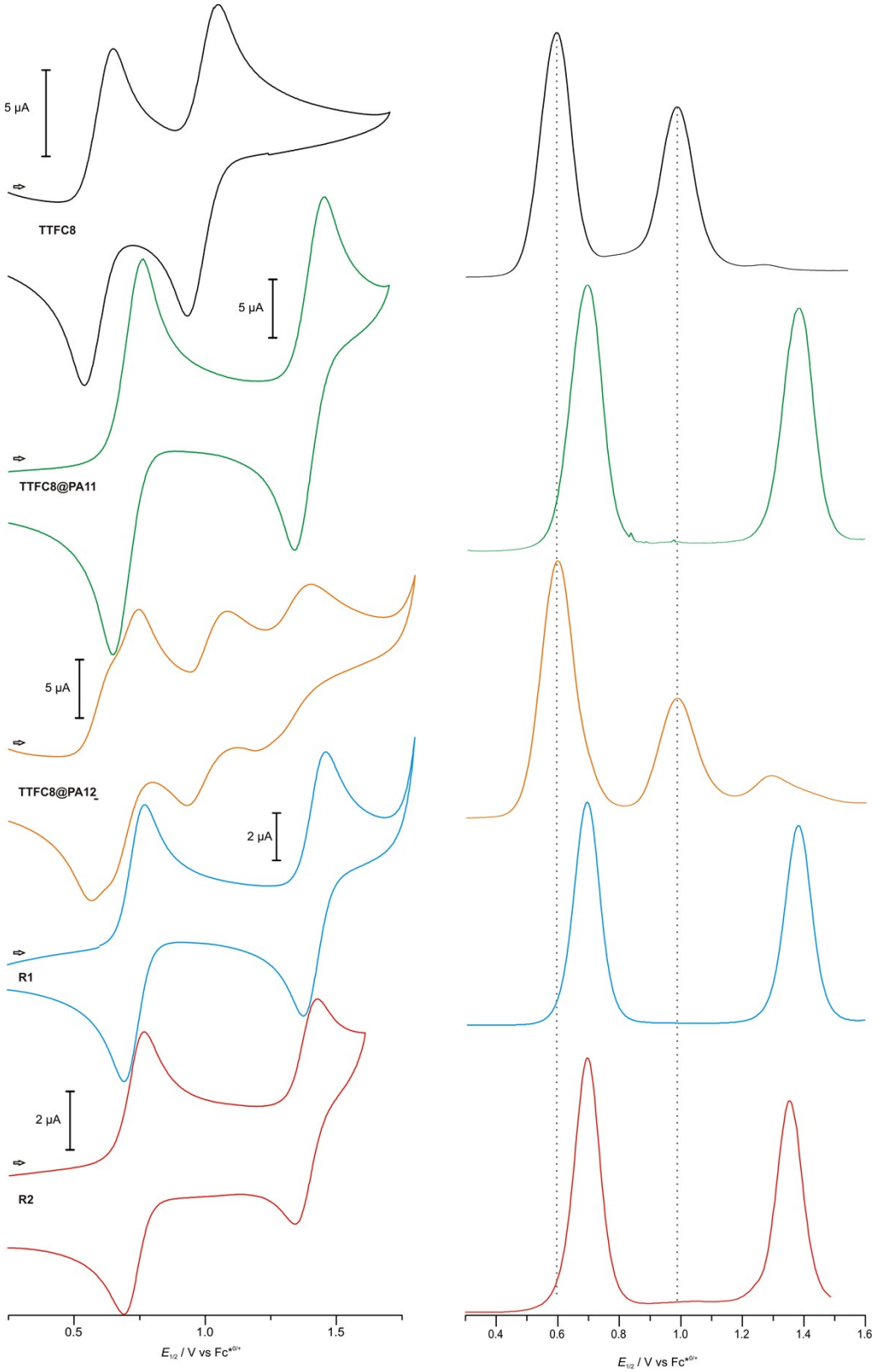

Fig. S55 Stacked cyclic voltammograms (100 mV/s scan rate) with corresponding differential pulse voltammograms (DPV, 10 mV/s scan rate, 25 mV modulation amplitude, 50 ms modulation time, 5 mV step potential, 0.5 s interval time) (CH_2Cl_2, n-Bu_4NBArF_{24}, 298 K) of **TTFC8, PA11@TTFC8, PA12@TTFC8, R1, R2.**

7. UV/Vis experiments

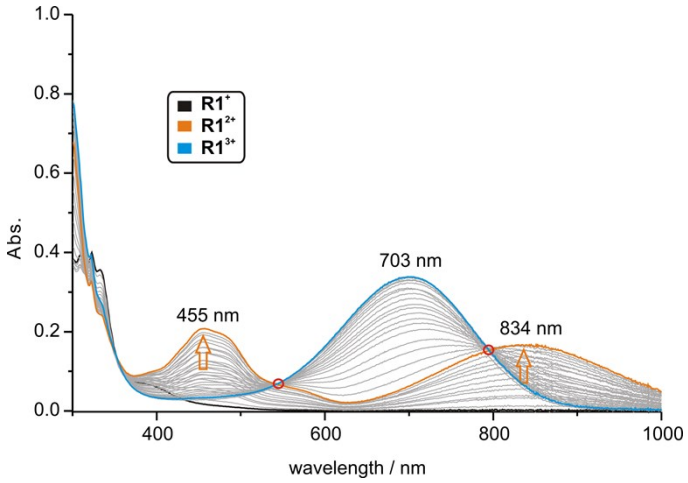

Fig. S56 UV/Vis spectra of **R1** (25 µM in CH_2Cl_2, 298 K, bulk $Fe(ClO_4)_3$ as the oxidant) in the TTF^0 (black), $TTF^{\bullet+}$ (orange) and TTF^{2+} (blue) state. The grey lines correspond to spectra taken in between full conversion to the radical cation or the doubly oxidized species, since the bulk $Fe(ClO_4)_3$ does not dissolve completely in CH_2Cl_2.

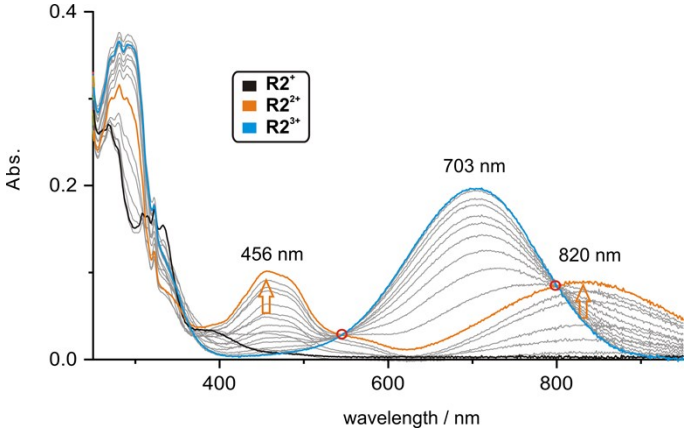

Fig. S57 UV/Vis spectra of **R2** (25 µM in CH_2Cl_2, 298 K, bulk $Fe(ClO_4)_3$ as the oxidant) in the TTF^0 (black), $TTF^{\bullet+}$ (orange) and TTF^{2+} (blue) state. The grey lines correspond to spectra taken in between full conversion to the radical cation or the doubly oxidized species, since the bulk $Fe(ClO_4)_3$ does not dissolve completely in CH_2Cl_2.

8. Crystallographic data

The data for **TTFC8** were collected on an Agilent SuperNova single-source diffractometer equipped with an Eos CCD detector at 123(2) K using mirror-monochromated Mo-Kα (λ = 0.71073 Å) radiation. Data collection (ω scans) and reduction was performed using the program CrysAlisPro. (Version 1.171.38.43, Rigaku Oxford Diffraction 2015) The analytical face-indexing-based absorption correction method was applied. The structure was solved by intrinsic phasing methods (SHELXT[11]) and refined by full-matrix least squares on F^2 using SHELXL-2017/1.[11, 12] Anisotropic displacement parameters were assigned to non-H atoms. All hydrogen atoms were constrained to their idealised positions and refined using riding models with U_{eq}(H) of 1.5U_{eq}(C) for terminal methyl groups and of 1.2U_{eq}(C) for other groups. Moderate geometric and anisotropic restraints were utilized to stabilize the refinement of disordered ethylene group and to make it chemically reasonable. Deposition Number CCDC-2073308 contain(s) the supplementary crystallographic data for this paper. These data are provided free of charge by the joint Cambridge Crystallographic Data Centre and Fachinformationszentrum Karlsruhe Access Structures service www.ccdc.cam.ac.uk/structures.

The slow diffusion of diisopropyl ether into a concentrated solution of **TTFC8** in CH_2Cl_2/CH_3CN (1:1) mixture yielded single crystals suitable for X-ray diffraction study (see Fig. 2). The solid state structure shows planar TTF moiety, as well as, typical bond lengths and angles of neutral TTF derivatives, like characteristically short C=C distance of 1.343(5) Å between the 1,3-dithiole rings and a distance range of 1.749(4) to 1.816(3) Å for C-S bonds.[13, 14] Almost orthogonal distortion of naphthalene unit out of TTF plane with 84.65° interplanar angle is resulting in bent boat-shaped conformation of the molecule. In the crystal packing, the molecules are arranged in columnar stacks with naphthalenes and TTFs on top of each other with plane-to-plane distances of 3.247 Å and 3.415 Å, shifted by 3.908 Å and 3.762 Å, respectively. There is a slight disorder in one ethylene group in the crown ether moiety, which is refined by splitting C and H atoms of that ethylene group over two spatial positions with approximately 63/37 ratio (major/minor).

Crystal data of **TTFC8**: $C_{30}H_{36}O_6S_8$, M = 749.07, triclinic, space group *P*-1 (no.2), a = 5.0805(3), b = 14.9091(10), c = 22.3719(14) Å, α = 98.267(5), β = 91.760(5), γ = 96.811(5)°, V = 1663.2(2) Å^3, Z = 2, ρ_{calc} = 1.496 Mgm^{-3}, μ = 0.579 mm^{-1} (T_{max} = 0.974 and T_{min} = 0.943), F(000) = 784, θ range = 3.27-26.50°, 10254 reflections collected, 6834 unique (R_{int} = 0.0328, I>2σ(I) = 4509), which were used in all calculations (418 parameters, 39 restraints), Goodness-of-fit (F^2) = 1.066. The final R indices [I>2σ(I)]: R1 = 0.0551 and wR2 = 0.1023. R indices (all data): R1 = 0.0947 and wR2 = 0.1248. Largest residual electron densities: 0.531 and -0.398 e.Å^{-3}.

9. References

1. H. V. Schröder, S. Sobottka, M. Nössler, H. Hupatz, M. Gaedke, B. Sarkar and C. A. Schalley, *Chem. Sci.*, 2017, **8**, 6300-6306.
2. T. Matsumura, F. Ishiwari, Y. Koyama and T. Takata, *Org. Lett.*, 2010, **12**, 3828-3831.
3. O. P. S. Rossi, F. Selva, *Farmaco. Ed. Sci.*, 1967, **22**, 172-176.
4. S. Grunder, D. Muñoz Torres, C. Marquardt, A. Błaszczyk, R. Krupke and M. Mayor, *Eur. J. Org. Chem.*, 2011, **2011**, 478-496.
5. J. Bucher, T. Wurm, K. S. Nalivela, M. Rudolph, F. Rominger and A. S. Hashmi, *Angew. Chem. Int. Ed.*, 2014, **53**, 3854-3858.
6. D. Y. Wang, Z. K. Yang, C. Wang, A. Zhang and M. Uchiyama, *Angew. Chem. Int. Ed.*, 2018, **57**, 3641-3645.
7. J. R. Aranzaes, M.-C. Daniel and D. Astruc, *Can. J. Chem.*, 2006, **84**, 288-299.
8. C. Bornschein, S. Werkmeister, K. Junge and M. Beller, *New J. Chem.*, 2013, **37**, 2061.
9. A. R. Salimi, M. Azizpoor Fard, H. Eshtiagh-Hosseini, M. A. M and H. R. Khavasi, *Acta Crystallogr Sect E Struct Rep Online*, 2010, **66**, o509.
10. M. Gaedke, F. Witte, J. Anhäuser, H. Hupatz, H. V. Schröder, A. Valkonen, K. Rissanen, A. Lützen, B. Paulus and C. A. Schalley, *Chem. Sci.*, 2019, **10**, 10003-10009.
11. G. M. Sheldrick, *Acta Crystallogr., Sect. A: Found. Adv.*, 2015, **71**, 3-8.
12. G. M. Sheldrick, *Acta Crystallogr., Sect. C: Struct. Chem.*, 2015, **71**, 3-8.
13. J. Sun, X. Lu, J. Shao, X. Li, S. Zhang, B. Wang, J. Zhao, Y. Shao, R. Fang, Z. Wang, W. Yu and X. Shao, *Chem. Eur. J.*, 2013, **19**, 12517-12525.
14. H. Kobayashi, R. Kato, T. Mori, A. Kobayashi, Y. Sasaki, G. Saito, T. Enoki and H. Inokuchi, *Mol. Cryst. Liq. Cryst.*, 2011, **107**, 33-43.

6.8 Sequence-sorted redox-switchable heterocircuit[3]rotaxanes

M. Gaedke,* H. Hupatz,* F. Witte, S.M. Rupf, C. Douglas, H.V. Schröder, L. Fischer, M. Malischewski, B. Paulus, C.A. Schalley

Org. Chem. Front. **2022**, *9*, 64-74.

*Both M. Gaedke and H. Hupatz contributed equally to this work.

Submitted on October 14, 2021, first published on October 27, 2021 by the Chinese Chemical Society (CCS), Shanghai Institute of Organic Chemistry (SIOC) and the Royal Society of Chemistry.

An electronic version of the articles is available at: https://doi.org/10.1039/D1QO01553B

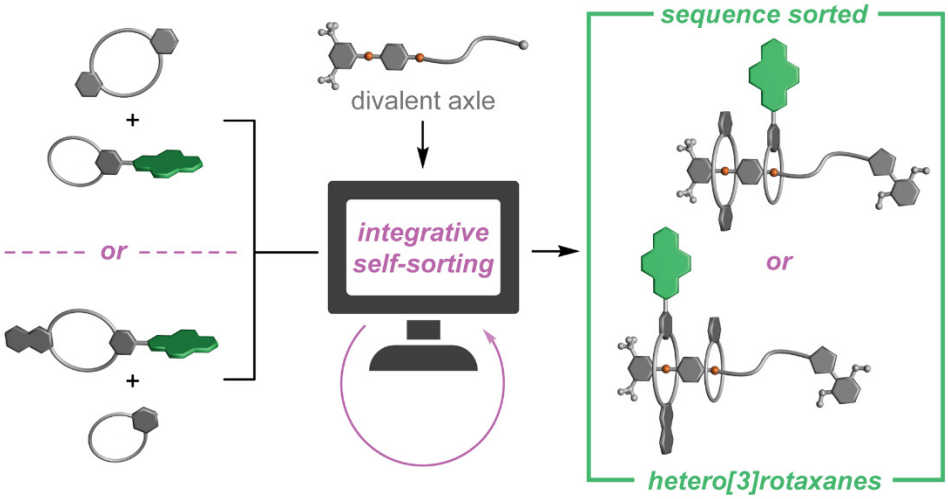

Figure 6.8. Graphical abstract. Reprinted from Gaedke *et al.*[244] with permission from the Chinese Chemical Society (CCS), Shanghai Institute of Organic Chemistry (SIOC), and the Royal Society of Chemistry (published under the CC BY-NC 3.0 licence).

Authors' contributions

The project was developed by Marius Gaedke and me. Marius Gaedke, Christoph A. Schalley, and me wrote the manuscript with main contributions from Marius Gaedke and me. The synthetic work was carried out by Marius Gaedke, Clara Douglas, Sussanne M. Rupf, Lukas Fischer and me with main contributions coming from Marius Gaedke. I conducted and evaluated all time dependent NMR and tandem MS experiments. Marius Gaedke performed further NMR, UV/Vis and CV experiments and prepared the single crystals. Hendrik V. Schröder helped with data evaluation and conception. I measured and analysed the ITC data. All computational work was done by Felix Witte and Beate Paulus. Susanne M. Rupf and Moritz Malischewski measured and solved the SCXRD data. All Authors contributed to the final version of the manuscript.

ORGANIC CHEMISTRY FRONTIERS

RESEARCH ARTICLE

View Article Online
View Journal | View Issue

Cite this: *Org. Chem. Front.*, 2022, **9**, 64

Sequence-sorted redox-switchable hetero[3]rotaxanes†

Marius Gaedke, ‡[a] Henrik Hupatz,‡[a] Felix Witte, [b] Susanne M. Rupf, [c] Clara Douglas, [a] Hendrik V. Schröder, §[a] Lukas Fischer,[a] Moritz Malischewski, [c] Beate Paulus [b] and Christoph A. Schalley *[a]

From a library of five crown ether macrocycles with different ring sizes and redox-active moieties, such as tetrathiafulvalene (TTF) and naphthalene dimiide (NDI), directional heterocircuit[3]rotaxanes were constructed. Using an axle with two binding sites with different steric accessibility, the concept of integrative self-sorting was applied to program the sequence of functional units in heteropseudo[3]rotaxanes. Depending on binding strength and ring size of the smaller macrocycles, different heteropseudo[3]rotaxane selectivities and stabilities were determined by 2D NMR spectroscopy and tandem mass spectrometry. A heteropseudo[3]rotaxane with rotaxane-like behaviour was isolated chromatographically, displaying electrochemically "frustrated" properties. A robust synthetic procedure was developed allowing the synthesis of four new hetero[3]rotaxanes incorporating specific sequences of functional units. Sequence pseudoisomeric rotaxanes which have the naphthalene diimide subunit at two different positions show distinct electrochemical properties. DFT calculations suggest that this differences could arise from a folding of the structure, in which the redox-active moieties stack with a stopper unit. This study presents a blueprint for the construction of hetero[3]rotaxanes with sequential control of the functional units along the track of the axle and paves the way to extend the functionality of mechanically interlocked molecules.

Received 14th October 2021,
Accepted 25th October 2021

DOI: 10.1039/d1qo01553b

rsc.li/frontiers-organic

Introduction

Mechanically interlocked molecules (MIMs) have shown great potential as artificial molecular switches and motors performing various tasks at the nanoscopic level and rudimentarily mimicking functions of natural molecules.[1–3] However, the molecular complexity and thereby accessible functions of MIMs are often limited by their symmetrical structures.[4–7] The asymmetrical and directional structure of functional biomolecules derives not only from the centrochirality of their molecular building blocks originating from a defined structural pool of building blocks, such as DNA nucleotides or amino acids, but also from the specific sequences in which these building blocks are connected. This sequence induces for example the secondary and tertiary structure formation in proteins.[8] The precise positional control of functional units in the natural assembly processes is remarkable. Only minor changes in the sequence can cause a significantly different structure and hence may change function.[9] Therefore, the precise control over the directionality and sequence of subcomponents in molecular assemblies is an important goal when constructing functional molecules.

Most MIMs described in the literature are [2]rotaxanes and some examples incorporate directional axles (Fig. 1, top left). Directional axles have been used to build sophisticated molecular machines which operate in a directional fashion. For example, so-called "ribosomal rotaxanes", incorporate a sequence of amino acids on the track of a directional axle. This amino acid sequence is then sequentially connected to a macrocycle upon chemically induced and directional wheel translation.[10–12]

In a homocircuit[3]rotaxane, two identical macrocycles are threaded onto the axle and a directionality can again only be defined by the axle itself (Fig. 1, top right). Also, oligohomo[*n*]rotaxanes containing more than two macrocycles have been

[a]*Institut für Chemie und Biochemie der Freien Universität Berlin, Arnimallee 20, 14195 Berlin, Germany. E-mail: c.schalley@fu-berlin.de*
[b]*Institut für Chemie und Biochemie der Freien Universität Berlin, Arnimallee 22, 14195 Berlin, Germany*
[c]*Institut für Chemie und Biochemie der Freien Universität Berlin, Fabeckstr. 34/36, 14195 Berlin, Germany*

†Electronic supplementary information (ESI) available: Synthetic procedures and characterization data, results from isothermal titration calorimetry, NMR and UV/Vis spectroscopy, tandem mass spectrometry, electrochemical measurements, crystallography and theoretical calculations. CCDC 2047286. For ESI and crystallographic data in CIF or other electronic format see DOI: 10.1039/d1qo01553b

‡These authors contributed equally to this work.

§Present address: Department of Chemical and Biological Engineering, Princeton University, Princeton, NJ 08544, USA.

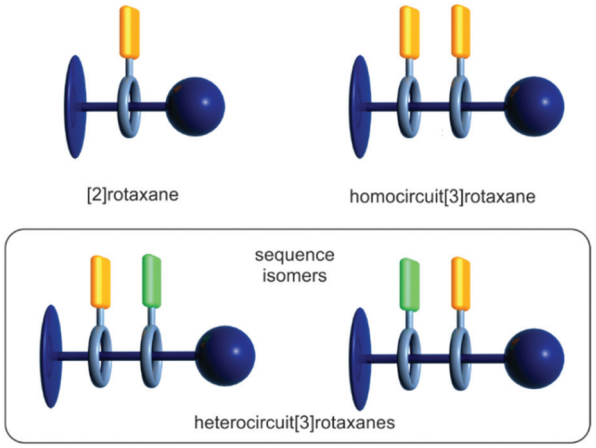

Fig. 1 Schematic representation of [2] and [3]rotaxanes containing a directional axle (dark blue) and one or two macrocycles (grey) carrying functional units (orange and green).

described.[13–16] In particular, molecular pumps, where multiple macrocycles are threaded onto an axle bringing the system to a higher energy state, are fascinating examples for the application of directional homocircuit[*n*]rotaxanes.[17–19]

If the two threaded macrocycles are not identical, a more complex picture arises. In heterocircuit[3]rotaxanes (Fig. 1, bottom), the directionality is additionally described by the order of macrocycles on the directional axle, consequently, sequence isomers may exist.[20–23] As a consequence of their unique structure, the isomer-specific synthesis of heterocircuit [3]rotaxanes is not trivial.[24] Hence, only few examples of heterocircuitrotaxanes have been described yet.[25] In 1995, the first heterorotaxane synthesis was reported by the group of Stoddart applying a sequential threading approach where a [2]rotaxane is synthesised first. In a second step, the second macrocycle is then threaded onto the axle.[26] A decade passed with minor advancements in this field due to the synthetic obstacles. However, in the last 15 years the interest in heterocircuitrotaxanes increased and outstanding examples could be realised *via* new synthetic approaches.[24,27–34] The group of Loeb, for example, utilised a sequential threading–clipping method yielding a [3]rotaxane facilitating a ring-through-ring molecular shuttling.[35]

Fundamentally different are syntheses using the concept of self-sorting. Here, no sequential addition of components defines the sequences, but instead all components are present in one solution, and find their positions in the final structure through the sorting of orthogonal binding motifs.[36] Even though homorotaxanes or sequence isomers could form, the macrocycles and axles are structurally programmed to prefer one of the heterorotaxane isomers. The group of Goldup, for example, developed a kinetic self-sorting method to obtain heterocircuit[3]rotaxanes.[37] In 2008, the concept of integrative self-sorting was introduced by us for constructing heterorotaxanes using sufficiently different crown/ammonium binding motifs.[38,39] This principle allows to program sequences of two macrocycles on one axle, for example by descending ring size accompanying binding site selectivity.[36] Later, it was also applied in the synthesis of a [c2]daisy-chain-containing hetero [4]rotaxane[40] and a hetero[6]rotaxane.[41] In a time-dependent mass spectrometric study of the self-sorting process, the crucial role of error correction and kinetic path selection was demonstrated.[42] So far, all examples of heterorotaxanes have a narrow scope of macrocycle combinations and are mostly complex assemblies, but do not contain functional or stimuli-responsive units. The precise arrangement of functional units would pave the way to new molecular switches with emerging properties.

In our recent work on redox-active crown/ammonium complexes we observed that the combination of electron donor tetrathiafulvalene (TTF) and electron acceptor naphthalene diimide (NDI) in a divalent rotaxane yielded a donor–acceptor complex.[43] Furthermore, homooligorotaxanes incorporating TTF-decorated crown ethers enabled the understanding of new switching modes in donor–donor assemblies, such as synchronised pirouetting motion of two macrocycles[44] and an accordion-like motion of the crown ethers.[15] In a study on TTF- and NDI-decorated crown ethers with different cavity sizes, crown [8] ethers revealed a preference for dibenzylammonium and crown[7] wheels for benzyl alkyl ammonium stations, suggesting integrative self-sorting for more functional wheels.[45]

Herein, we propose a blueprint to sequence-sorted heterocircuit[3]rotaxanes using one directional axle and a library of five macrocycles carrying three different types of functional units. This approach allows for unrestricted selection and combination of the functional units in rotaxane structure. We investigate the influence of different ring sizes and binding strengths of the crown ethers involved on the self-sorting equilibrium and heteropseudo[3]rotaxane properties. We apply these findings to the synthesis of four redox-switchable hetero [3]rotaxanes and study the influence of the sequence of functional units on the spectroelectrochemical properties of the rotaxane assemblies.

Results and discussion

Design of molecular building blocks

The macrocycle library consists of three types of functionalised crown[8] ethers and two types of functionalised crown[7] ethers (Fig. 2): while **TTFC8** contains an electron-rich pro-aromatic tetrathiafulvalene with electron-donor property (yellow, "donor"), **DBC8** and **BC7** exhibit an aromatic system with no significant donor or acceptor properties (grey, "neutral"), and **NDIC8** and **NDIC7** incorporate an electron-poor aromatic system with electron-acceptor properties (green, "acceptor"). The axle **Ax** contains two secondary ammonium binding stations which are separated by a phenyl group to prevent threading of the crown[7] ethers to the dibenzyl ammonium station (Fig. 2).[38] The directionality of the axle is not only described by the two binding stations, but also, the di-*tert*-

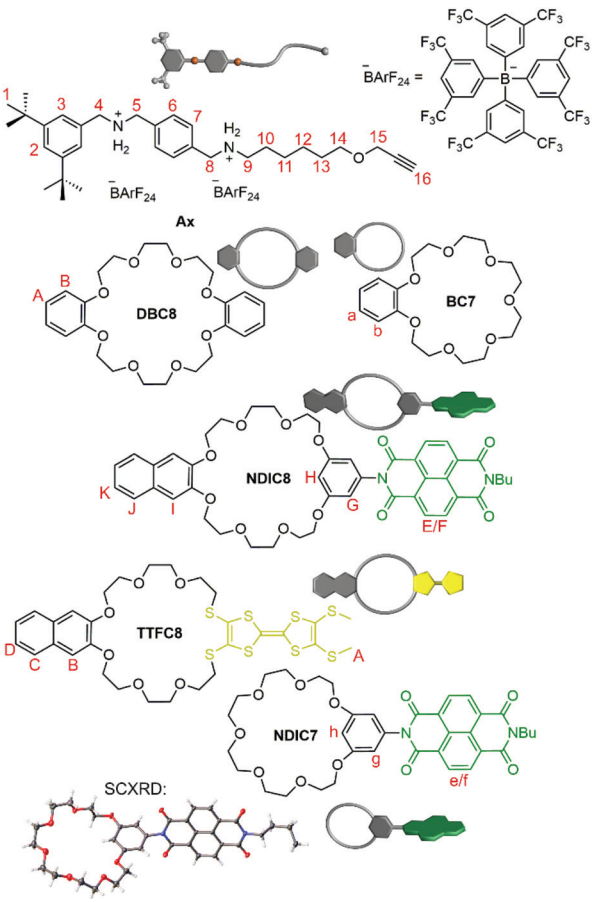

Fig. 2 Molecular Axle **Ax** and crown ether macrocycles used in this work. Protons of crown[8] wheels are denoted with capital letters, whereas crown[7] ether protons are denoted with small letters.

butyl stopper. This stopper prevents any wheel threading from this end of the axle and is crucial for programming the wheel sequence. Weakly coordinating tetrakis[3,5-bis(trifluoromethyl)phenyl]borate ($BArF_{24}^-$) counterions are used to facilitate a stable threaded complex of the weaker binding crown ethers **NDIC8**, **TTFC8** and **NDIC7**. **NDIC7** and axle **Ax** are novel structures and were synthesised along the procedures given in the ESI (ESI section 1†). For **NDIC7** we obtained a crystal structure (ESI section 8†). In the crystal, the dihedral angle between the phenyl group and the NDI is 70.01(11)°, which is considerably flatter than for **NDIC8**[45] (84.18(8)°), in order to facilitate π–π interactions between the NDIs of neighbouring **NDIC7** in the solid state. The ring sizes of **NDIC8**, **NDIC7** and **TTFC8** are wider than those of **DBC8** and **BC7**, respectively, as the 4.766 (6) Å (**NDIC7**)/4.730(4) Å (**NDIC8**) distance of the two phenolic O atoms in the NDI-substituted macrocycles as well as the S–S distance of 3.3136(13) Å in **TTFC8**[46] are substantially larger than the O–O distance of 2.5642(5) Å in **DBC8**.[47]

Recently, we have shown that the spectroelectrochemical properties of redox-active crown ethers are not significantly influenced by the crown ether size.[45] This allows us to use the crown ether sizes to program the position of the functional unit on the axle without changing the spectroelectrochemical properties of the functional units. Therefore, the hetero[3]rotaxane combinations carrying **DBC8**/**NDIC7** and **NDIC8**/**BC7** are considered as "sequence pseudoisomers".

The thermodynamics of pseudorotaxane formation has been studied for monovalent model axles by isothermal titration calorimetry, revealing a 10 times stronger binding for **DBC8** and **BC7** compared to **NDIC8** and **TTFC8**, as well as, **NDIC7**, respectively (for binding data, see ESI Table S1†). Crown[8] ethers bind to the aliphatic ammonium slightly weaker than the crown[7] analogues.

Self-sorting of pseudorotaxanes

The intermediates and products of the self-assembly of equimolar mixtures of divalent axle and the two differently sized generic crown ethers **C8** (pink) and **C7** (blue) are shown schematically in Fig. 3a, where homopseudo[3]rotaxane **PRC8C8** and pseudo[2]rotaxane **PRC7** represent dead-ends on the way to the desired heteropseudo[3]rotaxane **PRC8C7**. Error-correction is necessary to overcome these dead-ends.

For all six combinations of one **C8**, one **C7** and **Ax**, equimolar solutions were equilibrated for 16 days at room temperature after which no further change in the NMR spectra was observed. Although a full assignment of all signals in the highly complex ^{1}H NMR spectra is not straightforward due to severe signal overlap (ESI section 3†), the four methylene signals (H(4), H(5), H(8) and H(9)) can be identified in the COSY spectra and are highly indicative for pseudorotaxane formation (Fig. 3b and e and ESI section 3†). For the mixture containing **TTFC8**, **BC7** and **Ax**, three major species could be identified and assigned by the chemical shift of their methylene protons to the heteropseudo[3]rotaxane **PRTTFC8BC7** (Fig. 3b, blue), homopseudo[3]rotaxane **PRTTFC8TTFC8** (Fig. 3b, red) and pseudo[2]rotaxane **PRBC7** (Fig. 3b, green). Changing the smaller macrocycle to the weaker binding **NDIC7** a higher amount of heteropseudo[3]rotaxane **PRTTFC8NDIC7** (Fig. 3e, blue) is observed. While the pseudo[2]rotaxane **PRNDIC7** cannot be identified, a small fraction of pseudo[2]rotaxane **PRTTFC8** (Fig. 3e, brown) is visible. The other four combinations show similar results (ESI section 3†). As calculated from the integrals of the methylene protons H(4) and H(5), the heteropseudo[3]rotaxanes are preferentially formed with amounts of 56–74% in all six cases (Table 1). For a non-self-sorting system with a directional axle a statistical amount for one specific heteropseudo[3]rotxane of 25% would be expected. The weaker binding macrocycle **NDIC7** forms the corresponding heteropseudo[3]rotaxanes with higher selectivity as compared to **BC7**.

Due to the charge inherent in all pseudorotaxanes under study, electrospray ionisation mass spectrometry (ESI-MS) is a valuable additional analytical technique to study the self-sorting equilibrium (Fig. 3c and f and ESI section 4†). Due to differences in ionisation efficiencies, the overall abundances cannot be directly related to solution concentrations, yet a semiquantitative overview of the formation of the pseudorotaxanes with reaction time can certainly be obtained. A solution

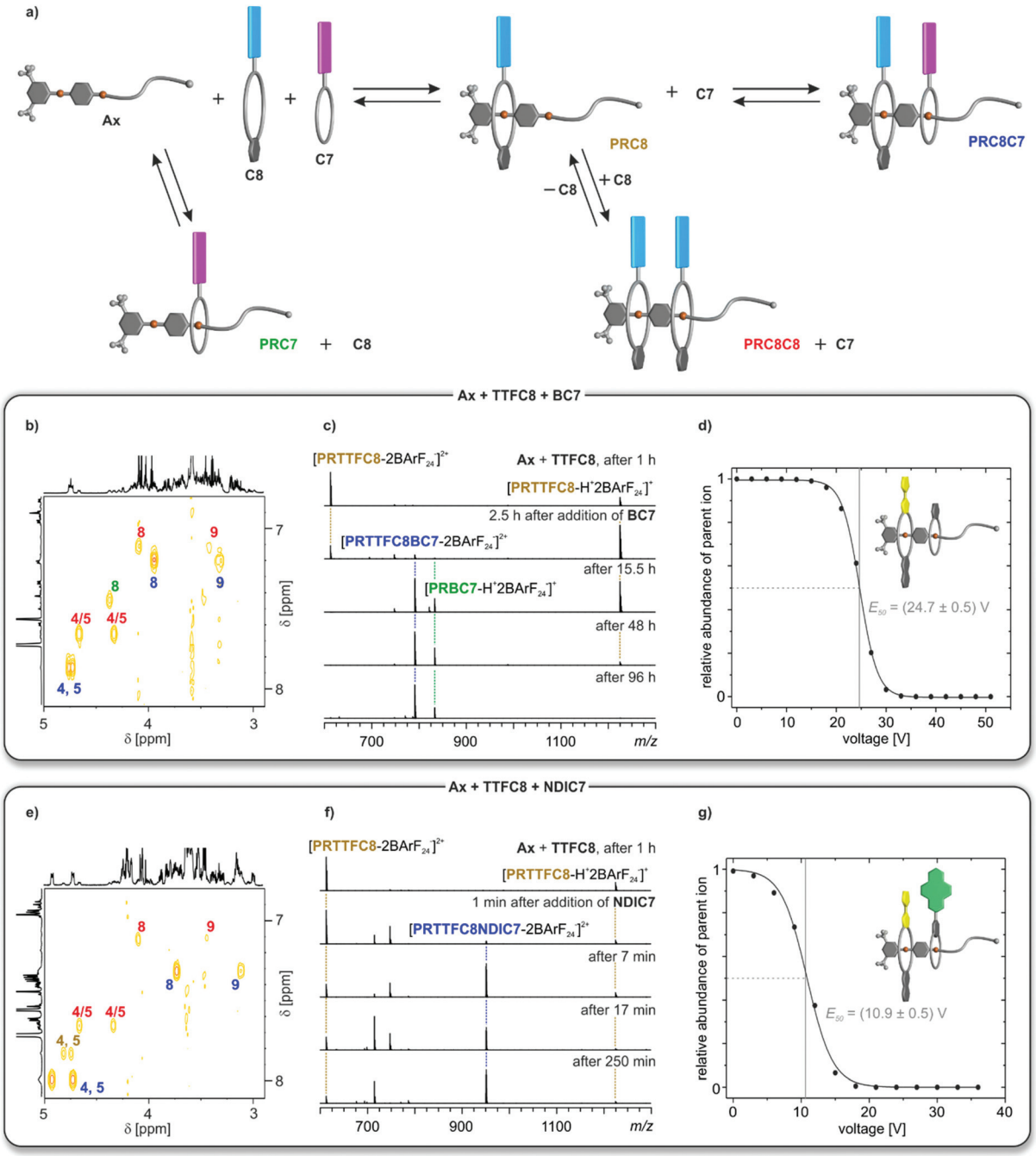

Fig. 3 (a) Schematic representation of the self-sorting equilibrium for two generic crown ethers **C8** (pink) and **C7** (blue). Spectra in (b, c and d) use an equimolar solution of **TTFC8**, **BC7** and **Ax**; and in (e, f and g) of **TTFC8**, **NDIC7** and **Ax**. Signals of protons or ions for the heteropseudo[3]rotaxanes are labeled in blue, for the homopseudo[3]rotaxanes in red, for the pseudo[2]rotaxane **PRTTFC8** in brown and to the crown[7] pseudo[2]rotaxanes in green. (b and e) Partial ^{1}H,^{1}H COSY spectra (700 MHz, CD_2Cl_2, 298 K, 5 mM, 16 d). For full ^{1}H NMR spectra and integration see Fig. S24 and S26.† (c and f) Time-dependent ESI-MS spectra in CH_2Cl_2 at 293 K. Non-labeled peaks correspond to different crown ether ions (ESI section 4†). (d and g) Survival yield curves obtained for mass-selected ions of **PRTTFC8BC7** *m/z* 791 (d) and **PRNDIC8BC7** *m/z* 951 (g) obtained from CID experiments at increasing collision voltages. Solid lines represent a sigmoidal fitting to determine 50% survival yield voltages E_{50} (Table 1 and ESI section 4†).

of **Ax** and **TTFC8** was equilibrated for 1 h. In the ESI mass spectrum, pseudo[2]rotaxane **PRTTFC8** can be observed in the two +1 and +2 charge states (Fig. 3c). The homopseudo[3]rotaxane **PRTTFC8TTFC8** is not observed in the mass spectrum, as it forms **PRTTFC8** rapidly upon dilution and ionisation due to the low thermodynamic and kinetic stability of **PRTTFC8TTFC8**. After addition of **BC7**, heteropseudo[3]rotaxane **PRTTFC8BC7** forms only slowly on an hour time scale, as the threading of **BC7** is a slow process. At the same time, also the dead-end pseudo[2]rotaxane **PRBC7** is formed.

Table 1 Characterisation parameters for the self-sorting equilibrium of six macrocycle combinations with axle **Ax** in equimolar solutions obtained by ^{1}H NMR spectroscopy, time-dependent and tandem mass spectrometry (for full data set and experimental details see ESI sections 3 and 4†)

Macrocycle combination	DBC8 BC7	TTFC8 BC7	NDIC8 BC7	DBC8 NDIC7	TTFC8 NDIC7	NDIC8 NDIC7
Hetero[3]pseudorotaxane amount[a]	58%	56%	57%	72%	70%	74%
Threading timeframe[b]	Days	Days	Days	Hours	Hours	Hours
E_{50} [c]	21.7 V	24.7 V	27.1 V	9.4 V	10.9 V	11.4 V

[a] Calculated from signal integration in ^{1}H NMR experiments (700 MHz, CD_2Cl_2, 298 K, 5 mM, 16 d). Amounts are given as percentages of all identified pseudorotaxane species (estimated error: 5%). [b] Qualitative estimation from time-dependent ESI-MS, when 90% of the maximum heteropseudo[3]rotaxane concentration is reached. [c] Estimated error amounts to 0.5 V.

In marked contrast, hetero[3]pseudorotaxane **PRTTFC8NDIC7** forms already within minutes upon addition of the wider **NDIC7** to the solution of **Ax** and **TTFC8**. After 4 h virtually no changes are observed in the spectrum (Fig. 3f). The same experiments with the other crown[8] ethers revealed that the equilibrium for **NDIC7**-containing mixtures are reached after a couple of hours, while mixtures including **BC7** take several days to equilibrate (Table 1 row 3 and ESI section 4†). This difference can be rationalised by the bigger ring size and thereby faster threading kinetics of **NDIC7**. Slower threading kinetics come together with a slower error correction process, as it can also be seen by the appearance of dead-end **PRBC7** in the mass spectrum as well as the ^{1}H NMR experiments. The different crown[8] ethers do not significantly alter the overall threading kinetics and heteropseudo[3]rotaxane **PRC8C7** selectivity, as their threading is comparably fast.[42]

Collision-induced dissociation (CID) experiments with mass-selected heteropseudo[3]rotaxane ions were used to establish the sequence of the pseudorotaxanes and to exclude non-threaded binding (ESI section 4†). For all heteropseudo[3]rotaxanes incorporating **NDIC7**, the CID mass spectra showed the loss of the crown[7] ether as the first fragmentation step (ESI Fig. S39–S41†). In contrast, **BC7** containing heteropseudo[3]rotaxane ions fragment by breaking of a covalent bond first (ESI Fig. S36–S38†). The 50% survival yield voltages E_{50} obtained from the CID mass spectra allow to compare the gas-phase stabilities of the heteropseudo[3]rotaxane assemblies (Fig. 3d and g, Table 1 and ESI Fig. S42†). **PRTTFC8BC7** exhibits a significantly higher gas phase stability as compared to **PRTTFC8NDIC7** (Fig. 3d and g). Also, E_{50} mainly is impacted by the threaded crown[7] ether (Table 1 row 4). Taking into account, that the isolated ions are doubly charged, the $E_{1/2}$ values of all six heteropseudo[3]rotaxane ions are significantly higher than for a non-threaded crown/*sec*-ammonium complex.[46] Overall, these observations evidence the desired sequence and threaded structures were achieved in all six heteropseudo[3]rotaxane combinations.

These results clearly show that the second, smaller macrocycles **NDIC7** and **BC7** dominate the thermodynamic and kinetic properties of the self-sorting equilibrium. The benefit of faster threading kinetics for a self-sorting process can be highlighted by the observation of a higher selectivity for the **NDIC7** containing heteropseudo[3]rotaxanes. The higher binding constants achieved by using $BArF_{24}^-$ counterions compared to previous studies[38,39,42] where PF_6^- counterions were used, caused a higher kinetic barrier for the dethreading reaction of **BC7**, which is the crucial step for all error-correction processes, resulting in a comparably long equilibration time. Yet, the used conditions are robust and facilitate the formation of heteropseudo[3]rotaxanes for all combinations.

A cascade-stoppered pseudo[3]rotaxane

The slow self-sorting process together with the remarkably high gas phase stability of **BC7**-containing heteropseudo[3]rotaxanes motivated us to study **PRTTFC8BC7** in a greater detail. Although a few exceptions are known,[34,46] crown/ammonium pseudorotaxanes are usually not sufficiently stable to survive column chromatography. Therefore, it is surprising that the pseudorotaxane **PRTTFC8BC7** was chromatographically isolated in 24% yield. For all other combinations of wheels under study here, the formed complexes dissociate on the silica column. Pseudo[3]rotaxanes with **NDIC7** dissociated quickly. The two other **BC7**-containing pseudo[3]rotaxanes required more polar mobile phases, which undermine their stability so that they also dissociate during chromatography. The stronger binding wheel **BC7** on the outer binding site acts as a stopper for the weaker binding wheel **TTFC8** on the dibenzyl ammonium binding site. Pseudo[3]rotaxanes of two **TTFC8** on **Ax** could not be isolated as they fell apart during the purification. This underlines the exceptional importance of the sequence in which the macrocycles are threaded on the one-side stoppered axle for the physico-chemical properties of the assembly.

For comparison, the rotaxane **RTTFC8BC7** was synthesised in 15% yield by adding 1.5 equiv. of 2,6-dimethoxybenzonitrile oxide stopper **St1** and stirring for one day at 35 °C. Fig. 4 shows the ^{1}H NMR shifts of (**P**)**RTTFC8BC7** in comparison to the axle **Ax**. Characteristic shifts include benzylic methylene protons H(4/5) and H(9), which shift downfield ($\Delta\delta \geq$ +0.4 ppm and +0.2 ppm) upon threading of **TTFC8** and **BC7**. Additionally, methylene protons H(8) shift upfield by 0.3 ppm. Both is true for the pseudo[3]rotaxane **PRTTFC8BC7** and the [3]rotaxane **RTTFC8BC7**. A strong downfield shift by 3.9 ppm of the former alkyne proton H(16) is observed, as it is incorporated into the newly formed isoxazole moiety. The methylene group H(15) adjacent to the former alkyne also shifts by 0.4 ppm downfield. Except for the protons on stopper **St1** and H(15,16), the shifts of pseudorotaxane **PRTTFC8BC7** and rotaxane **RTTFC8BC7** are similar.

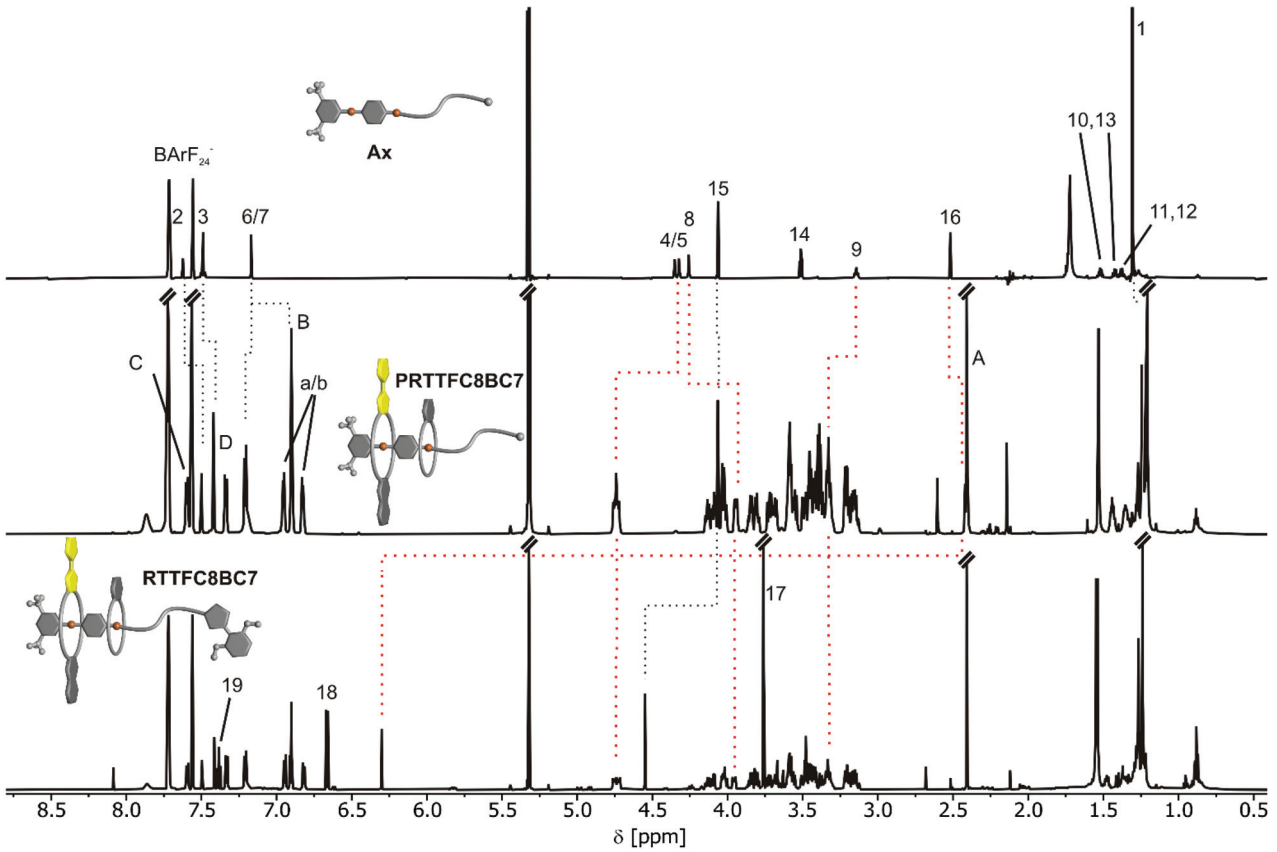

Fig. 4 ^{1}H NMR comparison of free axle **Ax**, **PRTTFC8BC7** and **RTTFC8BC7**. Characteristic shifts are highlighted by red dotted lines (ESI section 1.4† for full signal assignment).

To test the stability in a more polar solvent, chromatographically isolated **PRTTFC8BC7** was dissolved in acetonitrile in high dilution (1 μM). After 6 h a significant amount of threaded **PRTTFC8BC7** could still be observed by ESI-MS (ESI Fig. S43†). It took multiple days to reach thermodynamic equilibrium in which virtually no complex has survived, evidencing the high kinetic stability and nearly rotaxane-like behaviour of **PRTTFC8BC7**.

Electrochemical characterisation of both species (**P**)**RTTFC8BC7**, by cyclic voltammetry (CV) and differential pulse voltammetry (DPV) show similar results (Fig. 5). The two reversible oxidations of TTF are anodically shifted, as expected for wheel **TTFC8** bound to an ammonium site.[48] In previous work, we reported that the ammonium site is expelled upon oxidation due to coulombic repulsion with the oxidised TTF unit. Electrochemically induced dethreading results in a new signal for the $TTF^{\bullet+/2+}$ redox couple of unbound **TTFC8** at ~1 V against decamethylferrocene/decamethylferrocenium ($Fc^{*0/+}$).[48] Sterically demanding end groups can kinetically hamper oxidation-induced dethreading efficiently.[46] However, for both, pseudorotaxane and rotaxane, no dethreading is observed and redox potentials vary only marginally. This underlines the remarkable stability, which is exceptional for a non-interlocked crown/ammonium complex, and rotaxane-like behaviour of **PRTTFC8BC7** as already observed in the CID

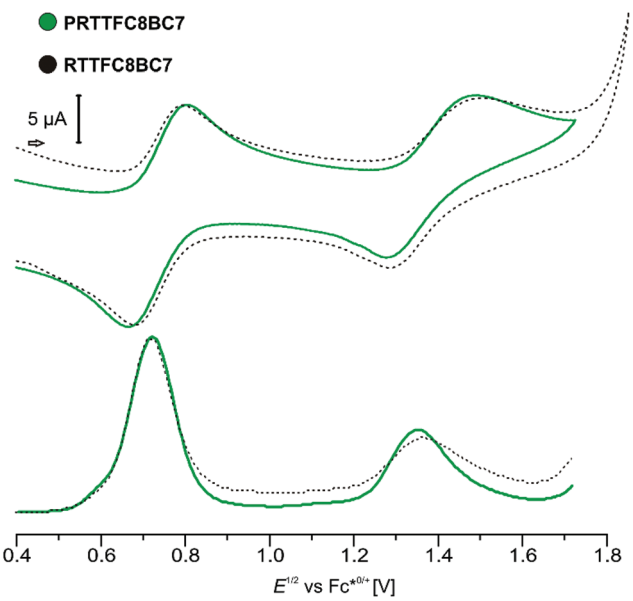

Fig. 5 CV and DPV of (pseudo)hetero[3]rotaxanes (**P**)**RTTFC8BC7** (1,2-dichloroethane with n-Bu_4NBArF_{24} as the electrolyte (0.1 M) 1.5 mM analyte, 25 mV s^{-1} scan rate for CV and 225 mV modulation amplitude, 50 ms modulation time, 5 mV step potential and 0.5 s interval time for DPV).

measurements. The increased TTF oxidation potentials (+126 and 362 mV for first and second oxidation) together with its unability to dethread turn **PRTTFC8BC7** it into an electrochemically "frustrated" pseudorotaxane that is kinetically trapped in a metastable state.

Hetero[3]rotaxane synthesis

The self-sorting experiments show pseudohetero[3]rotaxane formation to be prominent for all **C8**/**C7** macrocycle combinations. We therefore developed a generally applicable synthetic procedure for the synthesis of the corresponding hetero[3]rotaxanes, which does not depend on a prior chromatographic purification of the pseudo[3]rotaxane precursors. The pseudorotaxane mixtures were treated with the 2,6-dimethoxybenzonitrile stopper **St1**. This reaction was optimised by using up to six equivalents of the smaller macrocycle relative to the axle to reduce homo[3]rotaxane formation (for detailed synthetic procedures and characterisation data see ESI section 1.4†). Afterwards, the excess of the smaller macrocycle was recycled. Fig. 6 shows the isolated hetero[3]rotaxanes which all feature the diagnostic ^{1}H NMR shifts upon threading and rotaxanation as well as the diastereotopic splitting of the crown ether methylene groups as described in the previous chapter (ESI Fig. S14, S17 and S20†). The desired macrocycle sequence and the mechanically interlocked structure of the four hetero[3]rotaxanes was confirmed by CID experiments with mass-selected hetero[3]rotaxane ions, where at very high collision energies axle cleavage is observed as the major fragmentation pathway (ESI Fig. S49–S52†). The isolated examples consist of a "donor-neutral" (yellow-grey), "donor–acceptor" (yellow-green) and the pseudo sequence isomers "acceptor-neutral" (green-grey) and "neutral-acceptor" (grey-green) hetero[3]rotaxanes. The isolated yields compare very well to the majority of isolated heterorotaxanes in the literature.[26,28,35,37] Additionally, the isolation of hetero[3]rotaxanes with different wheel combinations without self-sorting would certainly be a very tedious process.

Optoelectronic properties of sequence-sorted rotaxanes

A comparison between isolated hetero[3]rotaxanes and the free macrocycles **TTFC8**, **NDIC7** or **NDIC8** allow an assessment of the influence of the macrocycle sequence on the electrochemical properties. Fig. 7 summarises all peak potentials obtained by DPV measurements in 1,2-dichloroethane with n-Bu_4NBArF_{24} as supporting electrolyte (ESI Table S2†). The potentials are referenced against the $Fc^{*0/+}$ redox-couple. The peaks at positive potentials can be attributed to the two reversible redox waves, $TTF^{(0/\bullet+)}$ and $TTF^{(\bullet+/2+)}$. As previously shown,[48] all species with **TTFC8** bound to an axle are shifted anodically in a comparable fashion. The second macrocycle

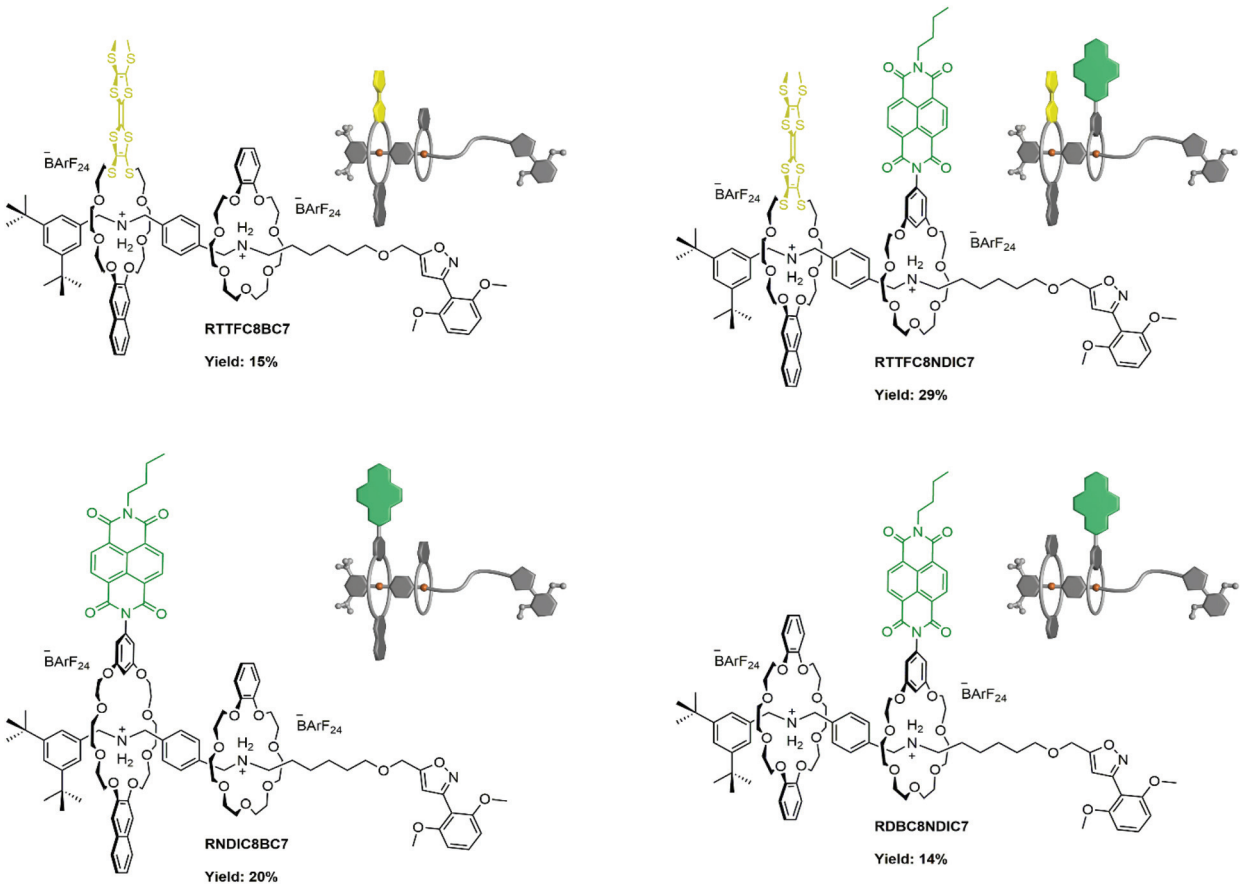

Fig. 6 Hetero[3]rotaxanes synthesised from the pseudorotaxane mixtures and their isolated yields.

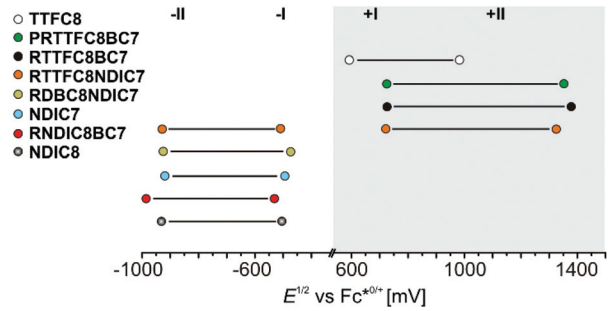

Fig. 7 Correlation diagram of half-wave potentials for hetero[3]rotaxanes and free macrocycles determined by DPV (Table S2,† the error is estimated to be ±10 mV).

does not have strong impact on the oxidation of **TTFC8** in the rotaxane as can be seen on the similar oxidation potentials of donor–acceptor rotaxane **RTTFC8NDIC7** and donor-neutral rotaxane **RTTFC8BC7**.

In contrast, the peaks at negative potentials are the two reversible reductions $NDI^{(0/\bullet-)}$ and $NDI^{(\bullet-/2-)}$. For the free wheels **NDIC7** and **NDIC8** both reduction peaks are similar ($\Delta E^{1/2}$ = 11 mV for $NDI^{(0/\bullet-)}$ and $\Delta E^{1/2}$ = 16 mV for $NDI^{(\bullet-/2-)}$), as expected from their similar structures. For [3]rotaxane **RNDIC8BC7** a significant cathodic shift of 20 mV for $NDI^{(0/\bullet-)}$ and 55 mV for $NDI^{(\bullet-/2-)}$ compared to wheel **NDIC8** is observed. In contrast, [3]rotaxanes **RTTFC8NDIC7** and **RDBC8NDIC7** only show minor differences in the reduction potentials ($\Delta E^{1/2} \leq 10$ mV for $NDI^{(0/\bullet-)}$ and $\Delta E^{1/2} \leq 11$ mV for $NDI^{(\bullet-/2-)}$) compared to wheel **NDIC7**. Consequently, the position of the NDI-unit on the axle indeed has a significant impact on the electrochemical properties. For **NDIC7** we could not determine a significant influence of the second larger macrocycle neither being neutral nor electron donor. The difference of electrochemical properties of the NDI sequence pseudoisomers **RNDCI8BC7** and **RDBC8NDIC7** presumably occurs as a consequence of the sequence rather than the macrocycle combination. Indeed, DFT calculations and conformational analysis at the PBEh-3c level[49] using the COSMO[50] solvation model provide a molecular structure for **RNDIC8BC7**, where the NDI-unit stacks with the dimethoxybenzene stopper (Fig. 8a and ESI section 7†).

For donor–acceptor hetero[3]rotaxane **RTTFC8NDIC7** the calculated structure displays a stacked conformation of TTF- and NDI-unit as well as the dimethoxybenzene stopper (Fig. 8b and ESI section 7†). Even though it is rather difficult to understand the exact reason for the different potential shifts of the NDI-unit, the distance of NDI-bearing crown ether to the stopper unit seems to have an influence. Yet, spin-density plots are TTF-localised for the oxidised species and NDI-localised for the reduced species (ESI Fig. S60 and S61†). Chemical oxidation of **RTTFC8NDIC7** shows similar bands in the UV/Vis spectra as those of the free wheel **TTFC8** for the three redox states of TTF (ESI section 6†). Together with the electrochemical data, these observations demonstrate the spectroelectric properties of **TTFC8** to be retained within the mechanically interlocked assembly.

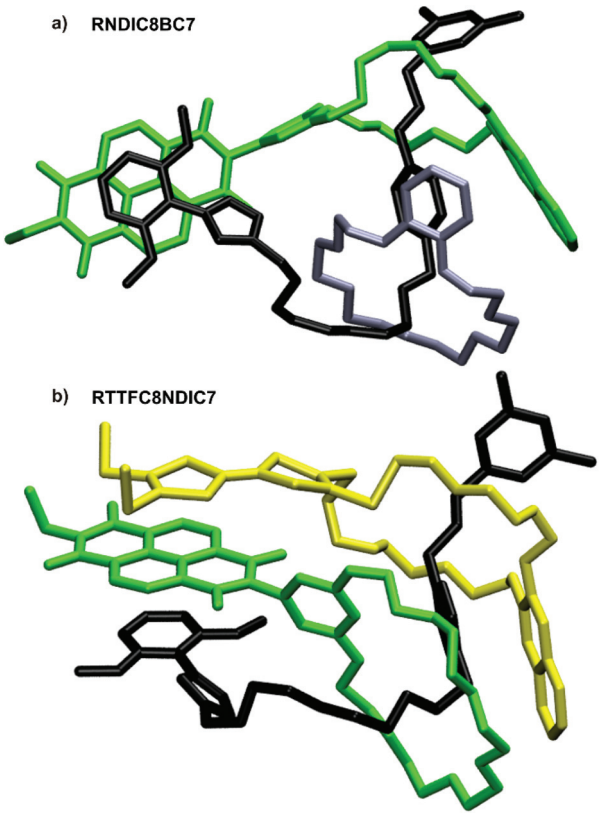

Fig. 8 Calculated structures of (a) **RNDIC8BC7** and (b) **RTTFC8NDIC7**, with the axle denoted in black, **TTFC8** in yellow, **BC7** in grey and **NDIC7** as well as **NDIC8** in green.

Conclusions

We demonstrated how integrative self-sorting can be applied as a molecular programming language to dictate the sequence of redox-switchable units along a molecular track. For the first time, we integrated functional redox-switchable units, namely TTF and NDI, into hetero[3]rotaxanes using this strategy.

The properties of the self-sorting process are dominated by the second macrocycle in the sequence. While the wider and weaker binding **NDIC7** facilitates fast threading kinetics, as well as good hetero[3]rotaxane selectivity, the smaller and stronger binding **BC7** results in slow threading kinetics and a slow error correction as well as in lower selectivities for the heteropseudo[3]rotaxane. The **BC7**-containing heteropseudo[3]rotaxanes show a surprising stability. The pseudorotaxane **PRTTFC8BC7**, could even be isolated by chromatography and thus shows rotaxane-like behaviour with **BC7** being a pseudostopper. Upon TTF oxidation, an electrochemically "frustrated" pseudorotaxane forms, in which the larger wheel experiences charge repulsion with the axle ammonium station, but is unable to dethread.

With the synthesis of four new hetero[3]rotaxanes, we demonstrate that different functional units can be placed in different sequences on the axle, as long as one crown[8] ether and one crown[7] ether is used. While for each individual

hetero[3]rotaxane combination more selective conditions such as counterion, solvent or equilibration time, can be found, our synthetic approach is general and robust and facilitates the synthesis of hetero[3]rotaxanes with varying crown ether sizes, binding strength and functional units. This concept is applicable to other functionalised crown ethers. By the ease to decorate crown ethers[51] with various functional moieties, our approach represents a modular strategy to incorporate and combine a broad variety of such units using hetero[3]rotaxanes as the scaffold.

In our work the functional units were combined to generate a donor-neutral (**RTTFC8BC7**), a donor–acceptor (**RTTFC8NDIC7**), an acceptor-neutral (**RNDIC8BC7**) and a neutral-acceptor (**RDBC8NDIC7**) rotaxane. Studying the electrochemical properties of theses assemblies, we could show that the donor moiety (TTF) was marginally influenced. Instead, the acceptor moiety (NDI) showed shifted redox potentials depending on the position on the axle, probably depending on the availability of interactions to one of the stoppers. Regardless of their sequence, the redox-active units retain their reversible spectroelectrochemical properties upon incorporation into the mechanically interlocked structure. Using these results, highly directional functional molecules bearing different macrocycles can be envisioned and facilitate new switching modes or functions for rotaxane assemblies.

Author contributions

The project was developed by H. H. and M.G. H. H., M. G. and C. A. S. wrote the manuscript with main contributions from H. H. and M. G. The synthetic work was carried out by M. G., C. D., S. M. R., L. F. and H. H. with main contributions coming from M. G. H. H. conducted and evaluated all time dependent NMR and tandem MS experiments. M. G. performed further NMR, UV/Vis and CV/DPV experiments and prepared the single crystals. H. V. S. helped with data evaluation and conception. H. H. measured and analysed the ITC data. All computational work was done by F. W. and B. P. S. M. R. and M. M. measured and solved the SCXRD data. Both M. G. and H. H. contributed equally and have the right to list their name first in their CV. All Authors contributed to the final version of the manuscript.

Conflicts of interest

There are no conflicts to declare.

Acknowledgements

We thank Sebastian Müller for help with the synthesis. We are grateful for funding from the Deutsche Forschungsgemeinschaft (DFG; project number 434455294) and acknowledge the assistance of the Core Facility BioSupraMol supported by the DFG. Furthermore, F. W. and B. P. acknowledge the DFG for funding (PA 1360/16-1) and the North-German Supercomputing Alliance (Norddeutscher Verbund für Hoch- und Höchstleistungsrechnen) for providing computational resources.

Notes and references

1 S. Erbas-Cakmak, D. A. Leigh, C. T. McTernan and A. L. Nussbaumer, Artificial Molecular Machines, *Chem. Rev.*, 2015, **115**, 10081–10206.
2 Y. Feng, M. Ovalle, J. S. W. Seale, C. K. Lee, D. J. Kim, R. D. Astumian and J. F. Stoddart, Molecular Pumps and Motors, *J. Am. Chem. Soc.*, 2021, **143**, 5569–5591.
3 L. Zhang, V. Marcos and D. A. Leigh, Molecular machines with bio-inspired mechanisms, *Proc. Natl. Acad. Sci. U. S. A.*, 2018, **115**, 9397–9404.
4 A. Coskun, M. Banaszak, R. D. Astumian, J. F. Stoddart and B. A. Grzybowski, Great expectations: can artificial molecular machines deliver on their promise?, *Chem. Soc. Rev.*, 2012, **41**, 19–30.
5 M. Xue, Y. Yang, X. Chi, X. Yan and F. Huang, Development of Pseudorotaxanes and Rotaxanes: From Synthesis to Stimuli-Responsive Motions to Applications, *Chem. Rev.*, 2015, **115**, 7398–7501.
6 M. Baroncini, L. Casimiro, C. de Vet, J. Groppi, S. Silvi and A. Credi, Making and Operating Molecular Machines: A Multidisciplinary Challenge, *ChemistryOpen*, 2018, **7**, 169–179.
7 C. A. Schalley, K. Beizai and F. Vögtle, On the Way to Rotaxane-Based Molecular Motors: Studies in Molecular Mobility and Topological Chirality, *Acc. Chem. Res.*, 2001, **34**, 465–476.
8 N. Badi and J. F. Lutz, Sequence control in polymer synthesis, *Chem. Soc. Rev.*, 2009, **38**, 3383–3390.
9 M. Kosloff and R. Kolodny, Sequence-similar, structure-dissimilar protein pairs in the PDB, *Proteins*, 2008, **71**, 891–902.
10 B. Lewandowski, G. De Bo, J. W. Ward, M. Papmeyer, S. Kuschel, M. J. Aldegunde, P. M. Gramlich, D. Heckmann, S. M. Goldup, D. M. D'Souza, A. E. Fernandes and D. A. Leigh, Sequence-specific peptide synthesis by an artificial small-molecule machine, *Science*, 2013, **339**, 189–193.
11 G. De Bo, S. Kuschel, D. A. Leigh, B. Lewandowski, M. Papmeyer and J. W. Ward, Efficient assembly of threaded molecular machines for sequence-specific synthesis, *J. Am. Chem. Soc.*, 2014, **136**, 5811–5814.
12 C. M. Wilson, A. Gualandi and P. G. Cozzi, A rotaxane turing machine for peptides, *ChemBioChem*, 2013, **14**, 1185–1187.
13 A. J. Avestro, D. M. Gardner, N. A. Vermeulen, E. A. Wilson, S. T. Schneebeli, A. C. Whalley, M. E. Belowich, R. Carmieli, M. R. Wasielewski and J. F. Stoddart, Gated electron sharing within dynamic naphthalene diimide-based oligorotaxanes, *Angew. Chem., Int. Ed.*, 2014, **53**, 4442–4449.

14 D. Sluysmans, S. Hubert, C. J. Bruns, Z. Zhu, J. F. Stoddart and A. S. Duwez, Synthetic oligorotaxanes exert high forces when folding under mechanical load, *Nat. Nanotechnol.*, 2018, **13**, 209–213.
15 H. V. Schröder, F. Stein, J. M. Wollschläger, S. Sobottka, M. Gaedke, B. Sarkar and C. A. Schalley, Accordion-Like Motion in Electrochemically Switchable Crown Ether/Ammonium Oligorotaxanes, *Angew. Chem., Int. Ed.*, 2019, **58**, 3496–3500.
16 H. Y. Zhou, Q. S. Zong, Y. Han and C. F. Chen, Recent advances in higher order rotaxane architectures, *Chem. Commun.*, 2020, **56**, 9916–9936.
17 C. Cheng, P. R. McGonigal, S. T. Schneebeli, H. Li, N. A. Vermeulen, C. Ke and J. F. Stoddart, An artificial molecular pump, *Nat. Nanotechnol.*, 2015, **10**, 547–553.
18 C. Pezzato, M. T. Nguyen, D. J. Kim, O. Anamimoghadam, L. Mosca and J. F. Stoddart, Controlling Dual Molecular Pumps Electrochemically, *Angew. Chem., Int. Ed.*, 2018, **57**, 9325–9329.
19 S. Amano, S. D. P. Fielden and D. A. Leigh, A catalysis-driven artificial molecular pump, *Nature*, 2021, **594**, 529–534.
20 H. Y. Au-Yeung and A. W. H. Ng, Mechanical Interlocking of Macrocycles in Different Sequences, *Synlett*, 2020, **31**, 309–314.
21 A. M. Fuller, D. A. Leigh and P. J. Lusby, Sequence isomerism in [3]rotaxanes, *J. Am. Chem. Soc.*, 2010, **132**, 4954–4959.
22 E. A. Neal and S. M. Goldup, Chemical consequences of mechanical bonding in catenanes and rotaxanes: isomerism, modification, catalysis and molecular machines for synthesis, *Chem. Commun.*, 2014, **50**, 5128–5142.
23 C. Talotta, C. Gaeta, Z. Qi, C. A. Schalley and P. Neri, Pseudorotaxanes with self-sorted sequence and stereochemical orientation, *Angew. Chem., Int. Ed.*, 2013, **52**, 7437–7441.
24 E. A. Wilson, N. A. Vermeulen, P. R. McGonigal, A. J. Avestro, A. A. Sarjeant, C. L. Stern and J. F. Stoddart, Formation of a hetero[3]rotaxane by a dynamic component-swapping strategy, *Chem. Commun.*, 2014, **50**, 9665–9668.
25 X. Q. Wang, W. J. Li, W. Wang and H. B. Yang, Heterorotaxanes, *Chem. Commun.*, 2018, **54**, 13303–13318.
26 D. B. Amabilino, P. R. Ashton, M. Bělohradský, F. M. Raymo and J. F. Stoddart, The controlled self-assembly of a [3]rotaxane incorporating three constitutionally different components, *J. Chem. Soc., Chem. Commun.*, 1995, **7**, 747–750.
27 J. E. Lewis, J. Winn, L. Cera and S. M. Goldup, Iterative Synthesis of Oligo[n]rotaxanes in Excellent Yield, *J. Am. Chem. Soc.*, 2016, **138**, 16329–16336.
28 X. Zhao, X. K. Jiang, M. Shi, Y. H. Yu, W. Xia and Z. T. Li, Self-assembly of novel [3]- and [2]rotaxanes with two different ring components: donor-acceptor and hydrogen bonding interactions and molecular-shuttling behavior, *J. Org. Chem.*, 2001, **66**, 7035–7043.
29 A. Joosten, Y. Trolez, V. Heitz and J. P. Sauvage, Use of cleavable coordinating rings as protective groups in the synthesis of a rotaxane with an axis that incorporates more chelating groups than threaded macrocycles, *Chem. – Eur. J.*, 2013, **19**, 12815–12823.
30 X. Hou, C. Ke and J. F. Stoddart, Cooperative capture synthesis: yet another playground for copper-free click chemistry, *Chem. Soc. Rev.*, 2016, **45**, 3766–3780.
31 C. Ke, R. A. Smaldone, T. Kikuchi, H. Li, A. P. Davis and J. F. Stoddart, Quantitative emergence of hetero[4]rotaxanes by template-directed click chemistry, *Angew. Chem., Int. Ed.*, 2013, **52**, 381–387.
32 C. Ke, N. L. Strutt, H. Li, X. Hou, K. J. Hartlieb, P. R. McGonigal, Z. Ma, J. Iehl, C. L. Stern, C. Cheng, Z. Zhu, N. A. Vermeulen, T. J. Meade, Y. Y. Botros and J. F. Stoddart, Pillar[5]arene as a co-factor in templating rotaxane formation, *J. Am. Chem. Soc.*, 2013, **135**, 17019–17030.
33 X. Hou, C. Ke, C. J. Bruns, P. R. McGonigal, R. B. Pettman and J. F. Stoddart, Tunable solid-state fluorescent materials for supramolecular encryption, *Nat. Commun.*, 2015, **6**, 6884.
34 M. A. Soto, F. Lelj and M. J. MacLachlan, Programming permanent and transient molecular protection via mechanical stoppering, *Chem. Sci.*, 2019, **10**, 10422–10427.
35 K. Zhu, G. Baggi and S. J. Loeb, Ring-through-ring molecular shuttling in a saturated [3]rotaxane, *Nat. Chem.*, 2018, **10**, 625–630.
36 Z. He, W. Jiang and C. A. Schalley, Integrative self-sorting: a versatile strategy for the construction of complex supramolecular architecture, *Chem. Soc. Rev.*, 2015, **44**, 779–789.
37 E. A. Neal and S. M. Goldup, A Kinetic Self-Sorting Approach to Heterocircuit [3]Rotaxanes, *Angew. Chem., Int. Ed.*, 2016, **55**, 12488–12493.
38 W. Jiang, H. D. Winkler and C. A. Schalley, Integrative self-sorting: construction of a cascade-stoppered hetero[3]rotaxane, *J. Am. Chem. Soc.*, 2008, **130**, 13852–13853.
39 W. Jiang and C. A. Schalley, Molecular recognition and self-assembly special feature: Integrative self-sorting is a programming language for high level self-assembly, *Proc. Natl. Acad. Sci. U. S. A.*, 2009, **106**, 10425–10429.
40 X. Fu, Q. Zhang, S. J. Rao, D. H. Qu and H. Tian, One-pot synthesis of a [c2]daisy-chain-containing hetero[4]rotaxane via a self-sorting strategy, *Chem. Sci.*, 2016, **7**, 1696–1701.
41 S. J. Rao, Q. Zhang, J. Mei, X. H. Ye, C. Gao, Q. C. Wang, D. H. Qu and H. Tian, One-pot synthesis of hetero[6]rotaxane bearing three different kinds of macrocycle through a self-sorting process, *Chem. Sci.*, 2017, **8**, 6777–6783.
42 W. Jiang, A. Schäfer, P. C. Mohr and C. A. Schalley, Monitoring self-sorting by electrospray ionization mass spectrometry: formation intermediates and error-correction during the self-assembly of multiply threaded pseudorotaxanes, *J. Am. Chem. Soc.*, 2010, **132**, 2309–2320.
43 H. V. Schröder, H. Hupatz, A. J. Achazi, S. Sobottka, B. Sarkar, B. Paulus and C. A. Schalley, A Divalent Pentastable Redox-Switchable Donor-Acceptor Rotaxane, *Chem. – Eur. J.*, 2017, **23**, 2960–2967.
44 H. V. Schröder, A. Mekic, H. Hupatz, S. Sobottka, F. Witte, L. H. Urner, M. Gaedke, K. Pagel, B. Sarkar, B. Paulus and

C. A. Schalley, Switchable synchronisation of pirouetting motions in a redox-active [3]rotaxane, *Nanoscale*, 2018, **10**, 21425–21433.

45 H. Hupatz, M. Gaedke, H. V. Schröder, J. Beerhues, A. Valkonen, F. Klautzsch, S. Müller, F. Witte, K. Rissanen, B. Sarkar and C. A. Schalley, Thermodynamic and electrochemical study of tailor-made crown ethers for redox-switchable (pseudo)rotaxanes, *Beilstein J. Org. Chem.*, 2020, **16**, 2576–2588.

46 M. Gaedke, H. Hupatz, H. V. Schröder, S. Suhr, K. F. Hoffmann, A. Valkonen, B. Sarkar, S. Riedel, K. Rissanen and C. A. Schalley, Dual-stimuli pseudorotaxane switches under kinetic control, *Org. Chem. Front.*, 2021, **8**, 3659–3667.

47 I. R. Hanson, D. L. Hughes and M. R. Truter, Crystal and molecular structure of 6,7,9,10,12,13,20,21,23,24,26,27-dodecahydrodibenzo[b,n][1,4,7,10,13,16,19,22]octaoxacyclotetracosin (dibenzo-24-crown-8), *J. Chem. Soc., Perkin Trans. 2*, 1976, 972.

48 H. V. Schröder, S. Sobottka, M. Nössler, H. Hupatz, M. Gaedke, B. Sarkar and C. A. Schalley, Impact of mechanical bonding on the redox-switching of tetrathiafulvalene in crown ether-ammonium [2]rotaxanes, *Chem. Sci.*, 2017, **8**, 6300–6306.

49 S. Grimme, J. G. Brandenburg, C. Bannwarth and A. Hansen, Consistent structures and interactions by density functional theory with small atomic orbital basis sets, *J. Chem. Phys.*, 2015, **143**, 054107.

50 A. Klamt and G. Schüürmann, COSMO: a new approach to dielectric screening in solvents with explicit expressions for the screening energy and its gradient, *J. Chem. Soc., Perkin Trans. 2*, 1993, 799–805.

51 F. Nicoli, M. Baroncini, S. Silvi, J. Groppi and A. Credi, Direct synthetic routes to functionalised crown ethers, *Org. Chem. Front.*, 2021, **8**, 5531–5549.

Electronic Supplementary Material (ESI) for Organic Chemistry Frontiers.

Supporting Information

Sequence-sorted redox-switchable hetero[3]rotaxanes

Marius Gaedke, ‡[a] Henrik Hupatz, ‡[a] Felix Witte,[b] Susanne M. Rupf,[c] Clara Douglas,[a] Hendrik V. Schröder,[a,d] Lukas Fischer,[a] Moritz Malischewski,[c] Beate Paulus[b] and Christoph A. Schalley*[a]

[a] Institut für Chemie und Biochemie, Freie Universität Berlin, Arnimallee 20, 14195 Berlin, Germany.

[b] Institut für Chemie und Biochemie, Freie Universität Berlin, Arnimallee 22, 14195 Berlin, Germany.

[c] Institut für Chemie und Biochemie, Freie Universität Berlin, Fabeckstr. 34/36 14195 Berlin, Germany.

[d]present address: Department of Chemical and Biological Engineering, Princeton University, Princeton, NJ08544, USA

*Corresponding author e-mail: c.schalley@fu-berlin.de

‡These authors contributed equally to this work.

Table of Contents

1. Experimental details

1.1. General methods

All reagents and solvents were obtained from commercial sources and used without further purification. Dry solvents were purchased from Acros Organics (Geel, Belgium) and either directly used or treated with the M. Braun solvent purification system SPS 800. Wheel **TTFC8**,[1] 2,6-dimethoxybenzonitrile oxide stopper **St1**,[2] monovalent axle **A1**,[3] monovalent axle **A2**,[3] 1-bromo-6-(prop-2-yn-1-yloxy)hexane **S5**,[4] *tert*-butyl (3,5-dihydroxyphenyl)carbamate **S10**,[3] NDI building block **S13**,[5] **BC7**[6] and **NDIC8**[3] were synthesised according to literature procedures, sodium tetrakis[3,5-bis(trifluoromethyl)phenyl]borate ($NaBArF_{24}$), 3,5-di-*tert*-butylbenzaldehyde **S1**, (4-cyanophenyl)methanaminium chloride **S2**, di-*tert*-butyl-dicarbonate, were bought at Sigma Aldrich or TCI Chemicals. Thin-layer chromatography was performed on silica gel-coated plates with fluorescent indicator F254 (Merck). For column chromatography, silica gel (0.04-0.063 mm, Merck), or Biotage SNAP and SNAP Ultra Cartridges were used on a Biotage Isolera One.

^{1}H and ^{13}C NMR experiments were performed on JEOL ECX 400, JEOL ECZ 600, Bruker AVANCE 500 or Bruker AVANCE 700 instruments. Residual solvent signals were used as the internal standards. All shifts are reported in ppm and NMR multiplicities are abbreviated as s (singlet), d (doublet), t (triplet), m (multiplet) and br (broad). Coupling constants *J* are reported in Hertz. Compounds containing the tetrakis[3,5-bis(trifluoromethyl)phenyl]borate ($BArF_{24}^{-}$) anion show ^{13}C NMR spectra with ^{19}F, ^{10}B and ^{11}B couplings. These signals are denoted as one signal.

High-resolution ESI mass spectra were measured on an Agilent 6210 ESI-TOF device or a Synapt G2-S HDMS (Waters Co., Milford, MA, USA) mass spectrometer. HPLC grade solvents were used for sample preparation.

UV/Vis spectra were recorded with a Varian Cary 50 Bio spectrometer equipped with a xenon lamp. Solvents with HPLC grade and Suprasil glass cuvettes with a path-length of 1 cm were used.

CV measurements were carried out with an Autolab PGSTAT302N potentiostat in a 2 mL measuring cell in 1,2-dichloroethane with 0.1 M $n\text{-}Bu_4NBArF_{24}$ as the conducting salt. The working electrode was made of glassy carbon, the reference Ag electrode was etched with conc. aq. HCl. A Pt wire worked as the counter electrode. The cyclic voltammogram traces were recorded with 25, 50, 100, 250, 500, 1000 mV/s scan rates, to ensure that the observed processes are reversible and diffusion-limited. In order to obtain the correct half-wave potentials, $FeCp_2^{*0}/FeCp_2^{*+}$ (decamethylferrocene) was used as the reference. These values were afterwards referenced to $FeCp_2/FeCp_2^{+}$ (ferrocene) as described in the literature.[7] The

raw data were treated with Nova 1.5 by Metrohm and the plots were made with Origin 2020 by OriginLab.

1.2. Synthesis of axle Ax

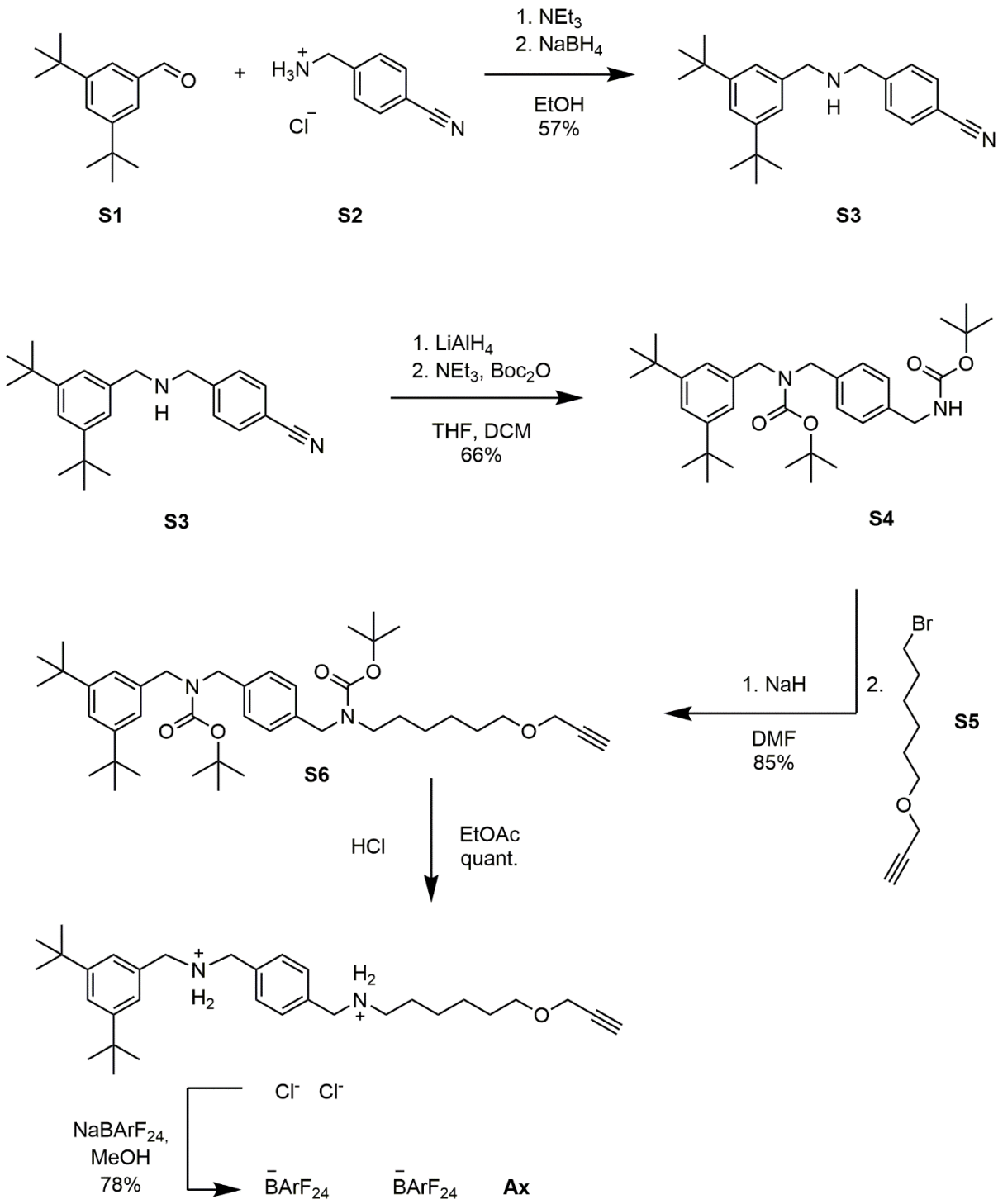

Scheme S1 General procedure for the synthesis of axle **Ax**.

4-(((3,5-di-tert-butylbenzyl)amino)methyl)benzonitrile S3

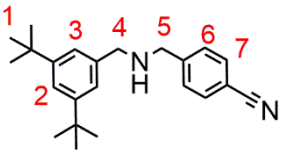

S3

3,5-Di-*tert*-butylbenzaldehyde (2.00 g, 9.16 mmol, 1.00 equiv.) and (4-cyanophenyl)-methanaminium chloride (1.53 g, 9.16 mmol, 1.00 equiv.) were dissolved in dry EtOH (400 ml) under argon atmosphere. Triethylamine (1.15 mL, 8.27 mmol, 0.90 equiv.) was added and the solution was refluxed for 5 h. After it was cooled to 0 °C, $NaBH_4$ (1.73 g, 45.8 mmol, 5.00 equiv.) was added and the solution was stirred under argon atmosphere overnight in the thawing ice bath. The reaction was then quenched by adding a concentrated aq. solution of $NaHCO_3$ until no more gas evolved. The solvent was removed under reduced pressure and the oily residue was dissolved in CH_2Cl_2 (100 ml). The organic layer was washed with brine and dried over $MgSO_4$. The solvent was removed under reduced pressure and the residue was purified by column chromatography (SiO_2, CH_2Cl_2/MeOH 100:1 → 50:1, R_f ~ 0.4 in CH_2Cl_2/MeOH = 50:1) yielding the amine as a white solid (1.76 g, 5.26 mmol, 57%).

^{1}H NMR (500 MHz, CD_2Cl_2): δ = 1.33 (s, 18H, 1), 3.76 (s, 2H, 5), 3.87 (s, 2H, 4), 7.16 (d, J = 1.8 Hz, 2H, 3), 7.32 (t, J = 1.9 Hz, 1H, 2), 7.48 – 7.52 (m, 2H, 6), 7.60 – 7.64 (m, 2H, 7) ppm. **^{13}C NMR** (125 MHz, CD_2Cl_2): δ = 31.8, 35.3, 111.1, 119.6, 121.6, 122.9, 129.2, 132.7, 139.9, 147.2, 151.4.ppm. **HRMS (MeOH)**: m/z calcd. for $[C_{23}H_{31}N_2]$+: 335.2482 [M+H]+, found: 335.2495

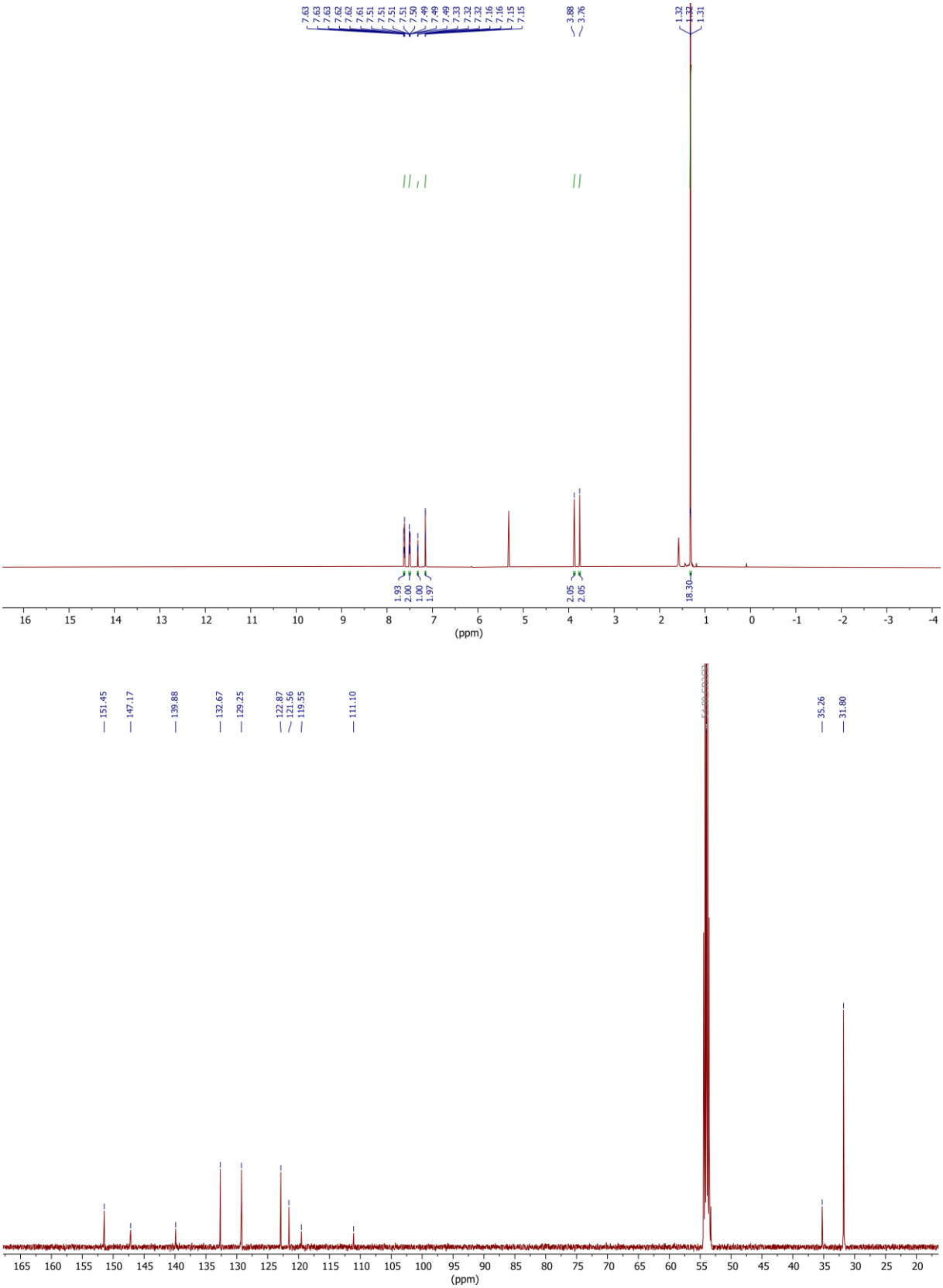

Fig. S1 ^{1}H (top) and ^{13}C (bottom) NMR spectra (500/126 MHz, CD_2Cl_2, 298 K) of amine **S3**.

tert-butyl (4-(((tert-butoxycarbonyl)amino)methyl)benzyl)(3,5-di-tert-butylbenzyl)carbamate S4

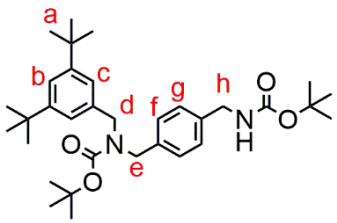

S4

Amine **S3** (1.76 g, 5.26 mmol, 1.00 equiv.) was dissolved in dry THF (400 ml) under argon atmosphere and cooled to 0 °C. $LiAlH_4$ (1.00 g, 26.3 mmol, 5.00 equiv.) was added and the solution was stirred under argon atmosphere for 24 h in the thawing ice bath. The reaction was quenched by adding a concentrated aq. solution of Na_2SO_4 until no more gas evolved. The precipitate was filtered off and the solvent was removed under reduced pressure. The residue was dissolved in CH_2Cl_2 (100 mL), washed with water and brine and dried over $MgSO_4$. The solvent was removed under reduced pressure. The raw product (1.75 g, 5.2 mmol, 1.00 equiv.) was dissolved in CH_2Cl_2 (50 mL) and cooled to 0 °C. Triethylamine (1.26 g, 12.4 mmol, 2.40 equiv.) and di-*tert*-butyl-dicarbonate (2.49 g, 11.4 mmol, 2.20 equiv.) was added. The reaction mixture was stirred overnight in the thawing ice bath. Afterwards, it was quenched by adding a concentrated aq. solution of $NaHCO_3$. The organic layer was washed with water and brine and dried over $MgSO_4$. The solvent was removed under reduced pressure and the residue was purified by column chromatography (SiO_2, CH_2Cl_2/MeOH 100:1 → 20:1, R_f ~ 0.4 in CH_2Cl_2/MeOH = 100:1) yielding the protected diamine as a colorless sticky oil (1.88 g, 3.48 mmol, 66%).

^{1}H NMR (700 MHz, $CDCl_3$): δ = 1.31 (s, 18H, 1), 1.47 (s, 9H, *tert*-butyl), 1.50 (s, 9H, *tert*-butyl), 4.30 (m, 4H, 4,5), 4.40 (s, 2H, 8), 4.40 (s_{br}, 1H, NH), 6.99 – 7.09 (m, 2H, 3), 7.11 – 7.25 (m, 4H, 6, 7), 7.31 (t, J = 1.9 Hz, 1H, 2) ppm. **^{13}C NMR** (176 MHz, $CDCl_3$): δ = 28.6, 31.8, 34.9, 44.6, 48.9, 49.2, 49.7, 50.2, 80.0, 121.3, 122.0, 122.4, 127.8, 128.5, 137.4, 137.9, 151.0, 154.9, 156.2 ppm. **HRMS (MeOH)**: m/z calcd. for $[C_{33}H_{50}N_2O_4]^+$: 577.3403 $[M+K]^+$, found: 577.3436; m/z calcd. for $[C_{33}H_{50}N_2O_4]^+$: 561.3663 $[M+Na]^+$, found: 561.3696.

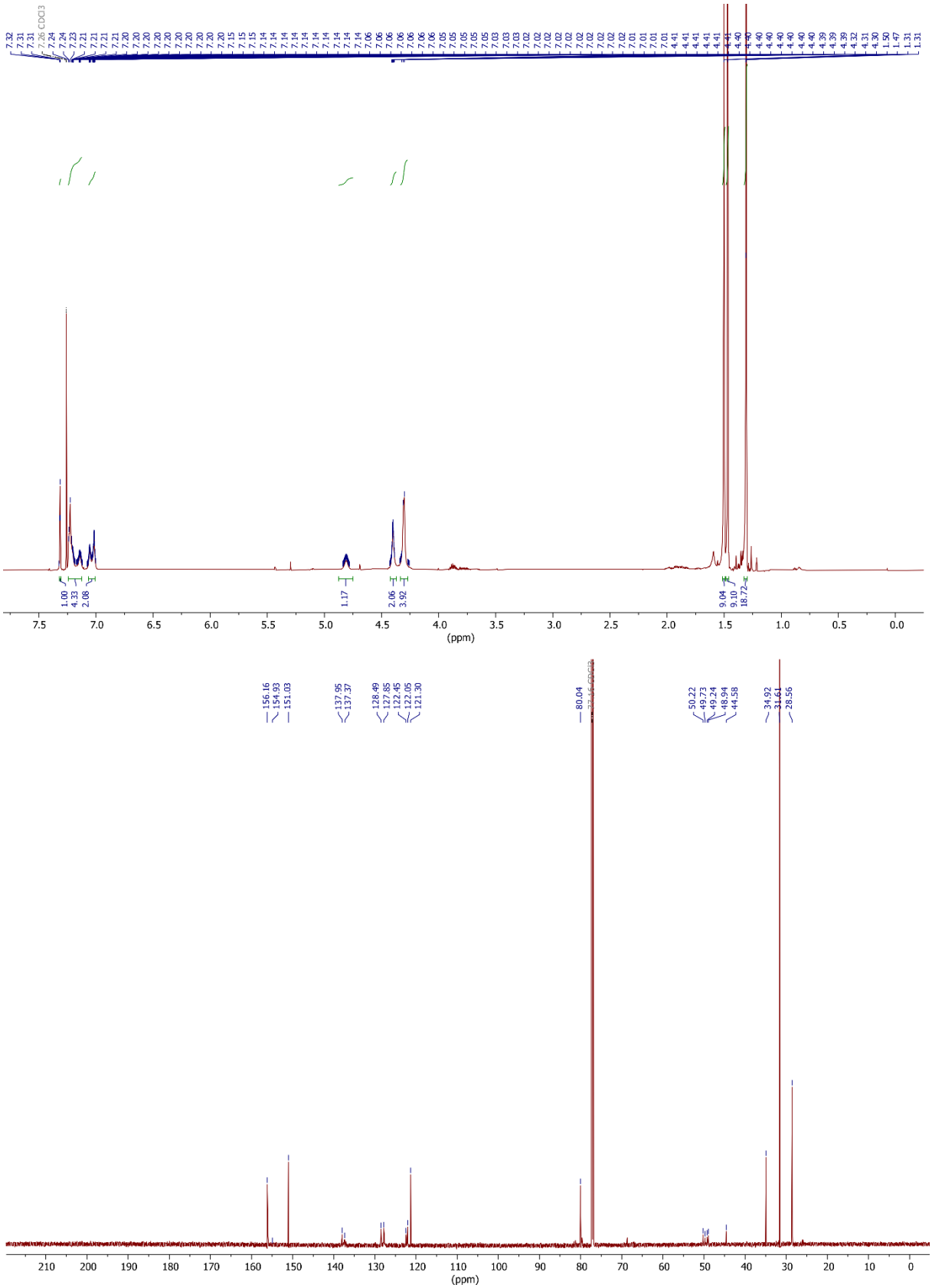

Fig. S2 ^{1}H (top) and ^{13}C (bottom) NMR spectra (700/176 MHz, $CDCl_3$, 298 K) of carbamate **S4**.

***tert*-butyl (4-(((*tert*-butoxycarbonyl)(6-(prop-2-yn-1-yloxy)hexyl)amino)methyl)benzyl)(3,5-di-*tert*-butylbenzyl)carbamate S6**

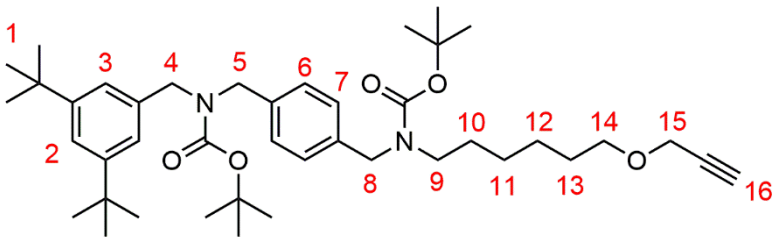

S6

Carbamate **S4** (1.99 g, 3.8 mmol, 1.00 equiv.) was dissolved in dry DMF (50 ml) under argon atmosphere and cooled to 0 °C. NaH (0.2 g, 4.9 mmol, 1.30 equiv.) was added slowly and portion-wise, the mixture stirred for 10 min in the ice bath and became pink. **S5** (1.00 g, 4.5 mmol, 1.20 equiv.) was added and the mixture was stirred under argon atmosphere in the thawing ice bath overnight. The reaction was quenched by adding H_2O (50 mL). The solvent was removed under reduced pressure and the residue was dissolved in CH_2Cl_2 (100 mL), washed with water and dried over $MgSO_4$. The solvent was removed under reduced pressure. The crude product was purified by column chromatography (SiO_2, cyclohexane/Et_2O 9:1 -> 8:2, R_f ~ 0.5 in cyclohexane/Et_2O 8:2) yielding **S6** as a colorless sticky oil (2.19 g, 3.23 mmol, 85%).

^{1}H NMR (700 MHz, $CDCl_3$): δ = 1.24 – 1.29 (m, 2H, 11), 1.31 (s, 18H, 1), 1.33 – 1.39 (m, 2H, 12), 1.42 – 1.53 (m, 20H, *tert*-butyl, 10), 1.55 – 1.62 (m, 2H, 13), 2.40 (t, J = 2.4 Hz, 1H, 16), 3.08 – 3.22 (m, 2H, 9), 3.49 (t, J = 6.6 Hz, 2H, 14), 4.12 (d, J = 2.4 Hz, 2H, 15), 4.25 – 4.33 (m, 2H, 4/5), 4.35 – 4.46 (m, 4H, 8,4/5), 7.00 – 7.08 (m, 2H, 3), 7.11 – 7.22 (m, 4H, 6,7), 7.32 (t, J = 1.9 Hz, 1H, 2) ppm. **^{13}C NMR** (176 MHz, $CDCl_3$): δ = 26.0, 26.8, 28.2, 28.6, 29.6, 30.5, 31.6, 34.9, 47.1, 48.9, 49.3, 50.0, 50.1, 58.2, 70.2, 74.2, 79.7, 80.0, 80.2, 121.3, 122.1, 122.5, 127.2, 127.8, 128.3, 137.1, 137.4, 137.8, 151.0, 156.2 ppm. **HRMS (MeOH)**: m/z calcd. for $[C_{42}H_{64}N_2O_5]^+$: 715.4452 $[M+K]^+$, found: 715.4473; m/z calcd. 699.4713 $[M+Na]^+$, found: 699.4732.

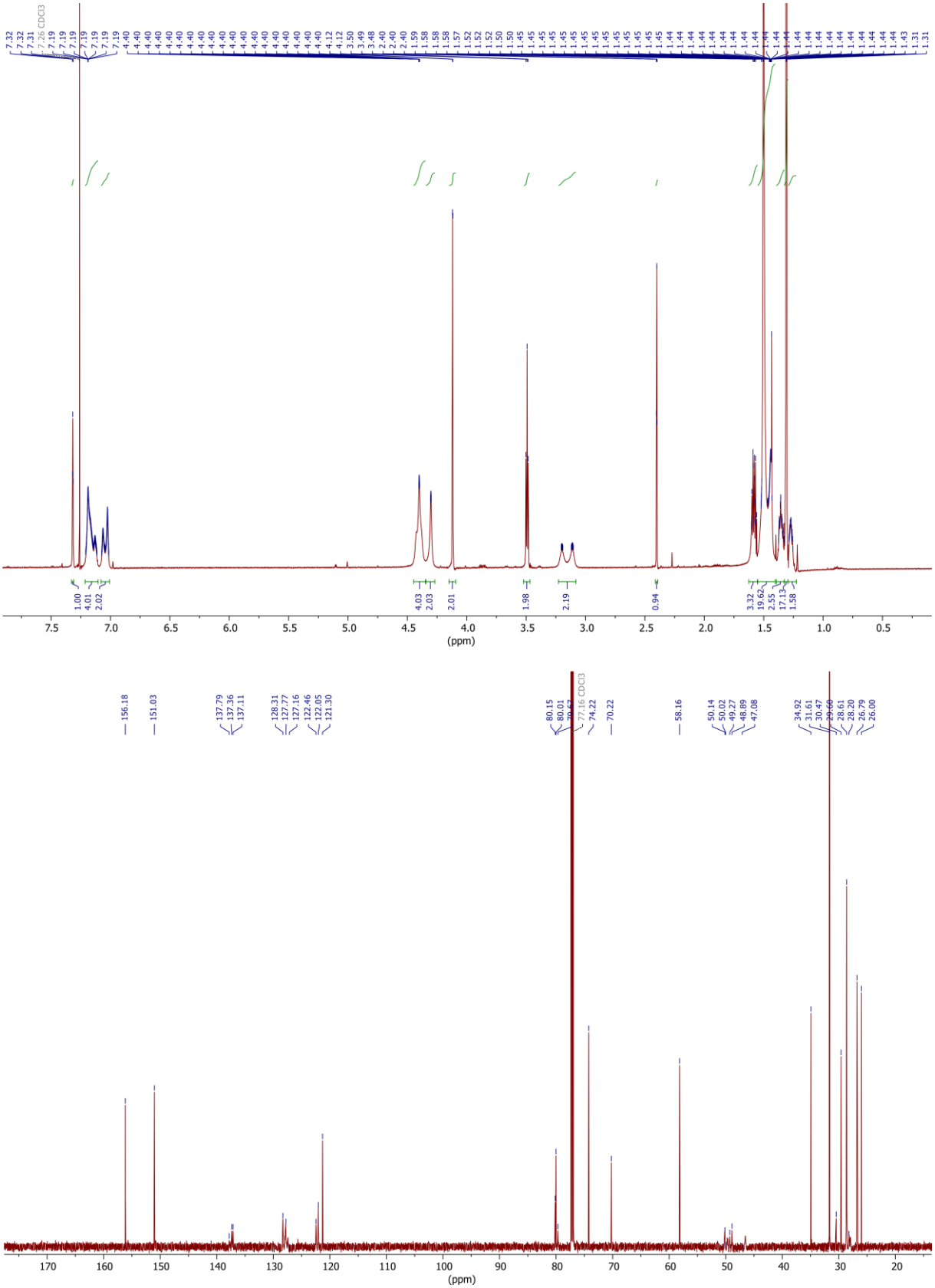

Fig. S3 ^{1}H (top) and ^{13}C (bottom) NMR spectra (700/176 MHz, $CDCl_3$, 298 K) of carbamate **S6**.

N-(4-(((3,5-di-tert-butylbenzyl)ammonio)methyl)benzyl)-6-(prop-2-yn-1-yloxy)hexan-1-aminium tetrakis(3,5-bis(trifluoromethyl)phenyl)borate Ax

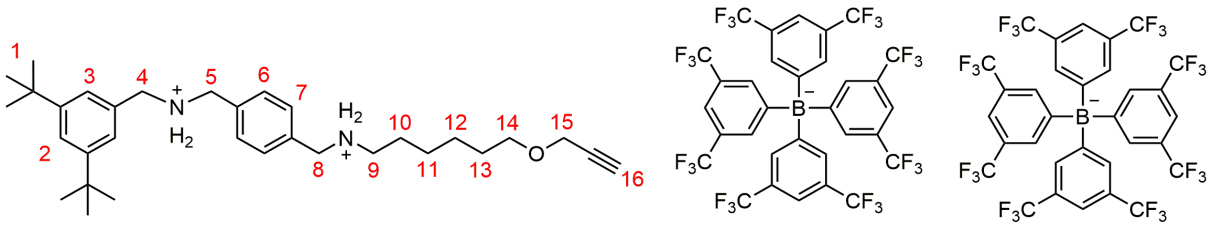

Ax

Carbamate **S6** (0.43 g, 0.61 mmol, 1.00 equiv.) was dissolved in EtOAc (20 ml) and cooled to 0 °C. conc. HCl (3 mL) was added. The mixture was stirred in the thawing ice bath overnight. The solvent was removed under reduced pressure and a portion (0.10 g, 0.18 mmol, 1.00 equiv.) was dissolved in MeOH (20 mL). $NaBArF_{24}$ (0.32 g, 0.36 mmol, 2.00 equiv.) was added and the mixture stirred for 3 h at r.t.. The solvent was removed under reduced pressure, the crude product was dissolved in CH_2Cl_2 (50 mL), washed with water and dried over $MgSO_4$. Removal of the solvent yielded **Ax** as a colorless sticky oil (0.31 g, 0.14 mmol, 78% combined). **^{1}H NMR** (700 MHz, CD_2Cl_2): δ = 1.31 (s, 18H, 1), 1.35 – 1.40 (m, 2H, 12), 1.40 – 1.46 (m, 2H, 11), 1.51 (tt, *J* = 7.0, 5.5 Hz, 2H, 13), 1.74 (m, 2H, 10), 2.53 (t, *J* = 2.4 Hz, 1H, 16), 3.16 (t, *J* = 6.9 Hz, 2H, 9), 3.52 (t, *J* = 5.7 Hz, 2H, 14), 4.06 (d, *J* = 2.4 Hz, 2H, 15), 4.27 (s, 2H, 8), 4.35 (s, 2H, 4/5), 4.37 (s, 2H, 4/5), 7.18 (d, *J* = 1.8 Hz, 2H, 3), 7.49 (m, 4H, 6,7), 7.56 (s_{br}, 8H, $BArF_{24}$), 7.64 (t, *J* = 1.8 Hz, 1H, 2), 7.72 (s_{br}, 16H, $BArF_{24}$). **^{13}C NMR** (151 MHz, CD_2Cl_2): δ = 24.6, 25.2, 25.6, 28.3, 31.4, 35.5, 48.8, 52.3, 52.4, 54.7, 58.2, 71.3, 75.7, 79.8, 118.1, 122.5, 124.0, 125.0, 126.1, 126.4, 127.7, 127.9, 129.4, 131.7, 131.8, 132.0, 132.0, 135.4, 154.2, 162.3 ppm. **HRMS (MeOH)**: m/z calcd. for $[C_{32}H_{50}N_2O]^{2+}$: 477.3845 $[M\text{-}H]^+$, found: 477. 3849.

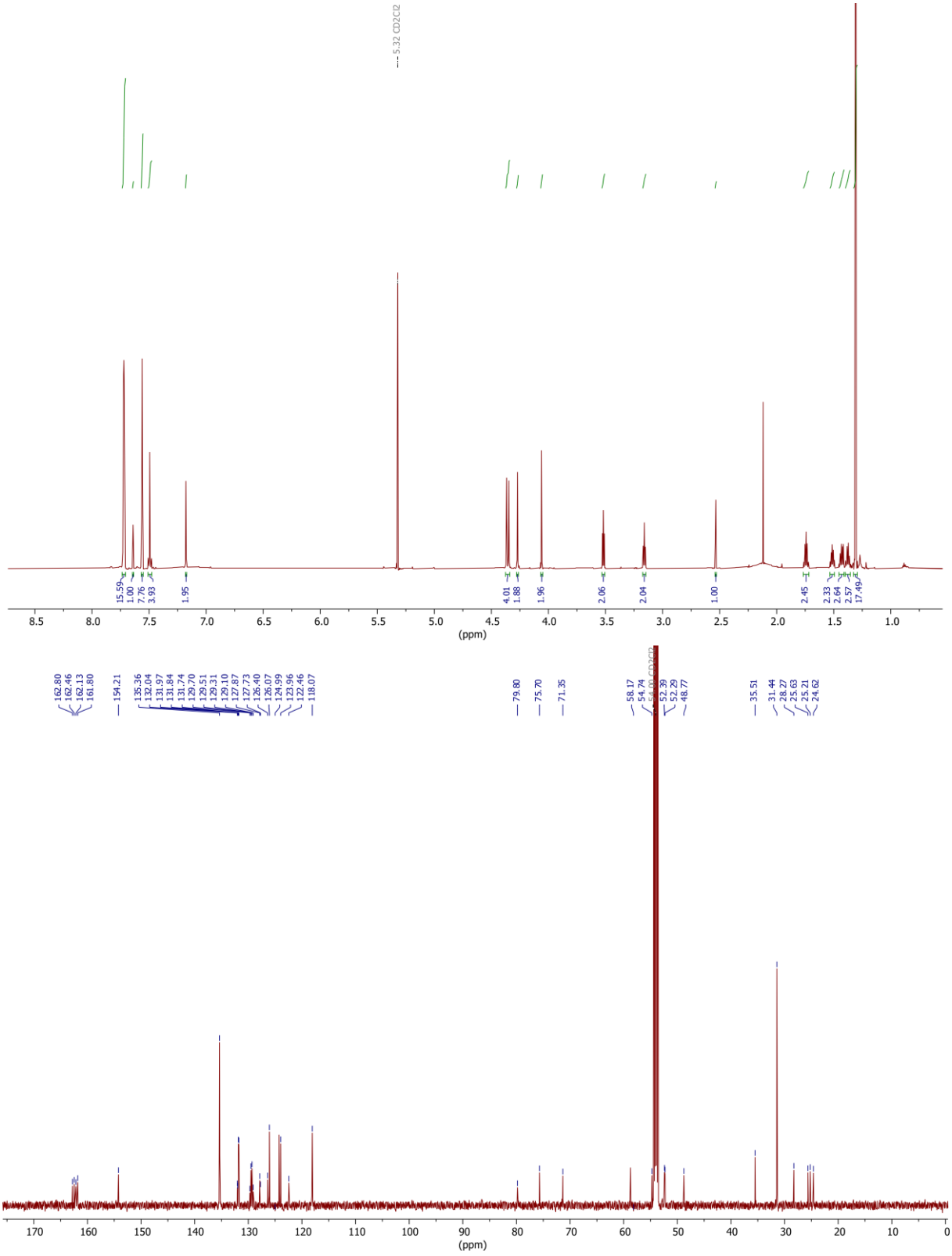

Fig. S4 ^{1}H (top) and ^{13}C (bottom) NMR spectra (700/151 MHz, CD_2Cl_2, 298 K) of axle **Ax**.

1.3. Synthesis of macrocycle NDIC7

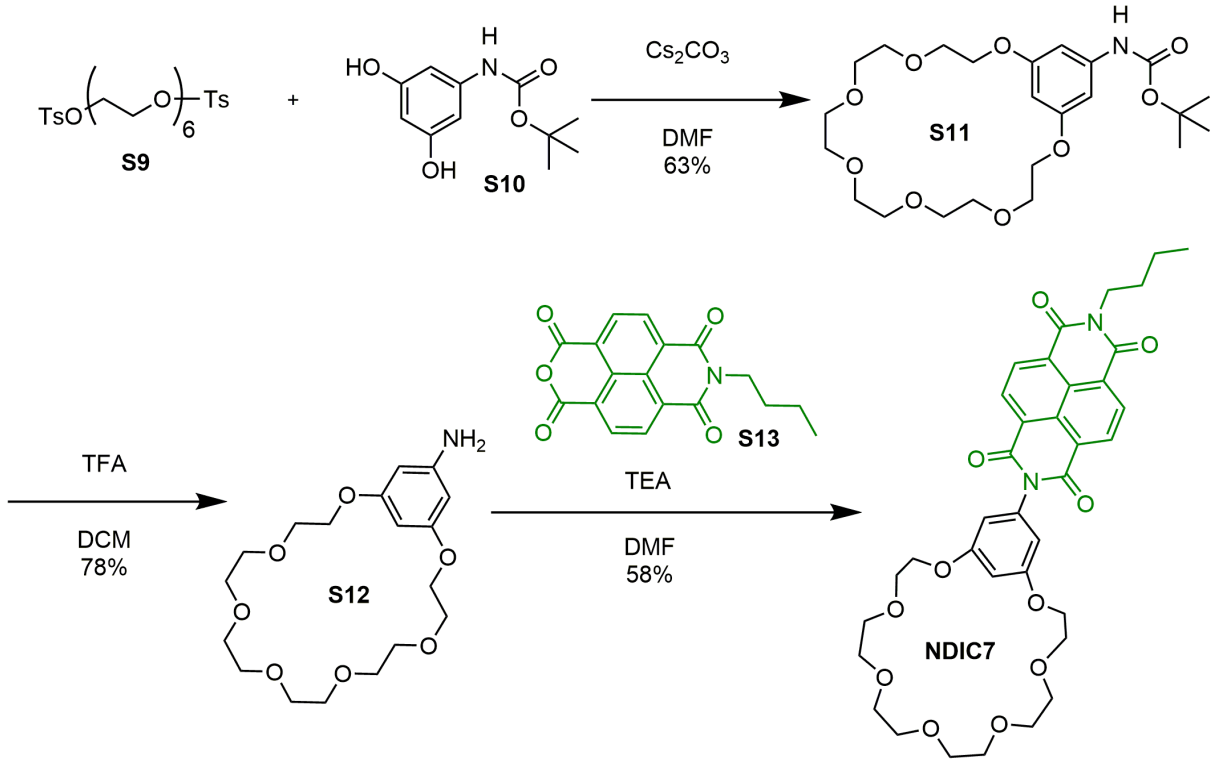

Scheme S2 General procedure for macrocycle **NDIC7**.

***tert*-butyl 2,5,8,11,14,17,20-heptaoxa-1(1,3)-benzenacycloicosaphane-15-ylcarbamate S11**

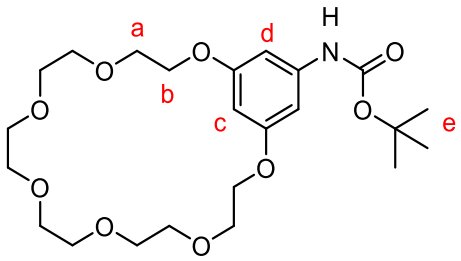

Ditosylate **S9** (525 mg, 0.89 mmol, 1.00 equiv.) was dissolved in dry DMF (100 mL) under argon atmosphere. In a separate vessel, K_2CO_3 (492 mg, 3.56 mmol, 4.00 equiv.) and diol **S10** (201 mg, 0.89 mmol, 1.00 equiv.) were dissolved in dry DMF (200 mL) and stirred at 60 °C under argon atmosphere. The ditosylate solution was added portion-wise over 2 h, afterwards the solution was stirred for 5 days at 80 °C. The solution was cooled to r.t. and filtered. The solvent was removed under reduced pressure. The residue was dissolved in CH_2Cl_2 (100 mL) and washed with water and brine and dried over $MgSO_4$. The solvent was removed under reduced pressure and the residue was purified by column chromatography (SiO_2, CH_2Cl_2/EtOAc 30% → 100% EtOAc, R_f ~ 0.2 in CH_2Cl_2/EtOAc = 1:1) yielding **S11** as a yellowish oil (256 mg, 0.56 mmol, 63%).

^{1}H NMR (500 MHz, $CDCl_3$): δ = 1.49 (s, 9H, e), 3.61 – 3.65 (m, 12H, CH_2-O), 3.68 (m, 4H, CH_2-O), 3.76 – 3.81 (m, 4H, a), 4.12 – 4.16 (m, 4H, b), 6.35 (t, *J* = 2.2 Hz, 1H, c), 6.48 (s, 1H, NH), 6.59 (d, *J* = 2.2 Hz, 2H, d) ppm. **^{13}C NMR** (176 MHz, $CDCl_3$): δ = 28.4, 67.9, 69.7, 70.7, 70.7, 71.1, 71.3, 80.6, 97.9, 98.1, 140.2, 152.6, 160.4 ppm. **HRMS (MeOH)**: m/z calcd. for $[C_{23}H_{37}NO_9]^+$: 494.2366 $[M+Na]^+$, found: 494.2389; 510.2105 $[M+K]^+$, found: 510.2131.

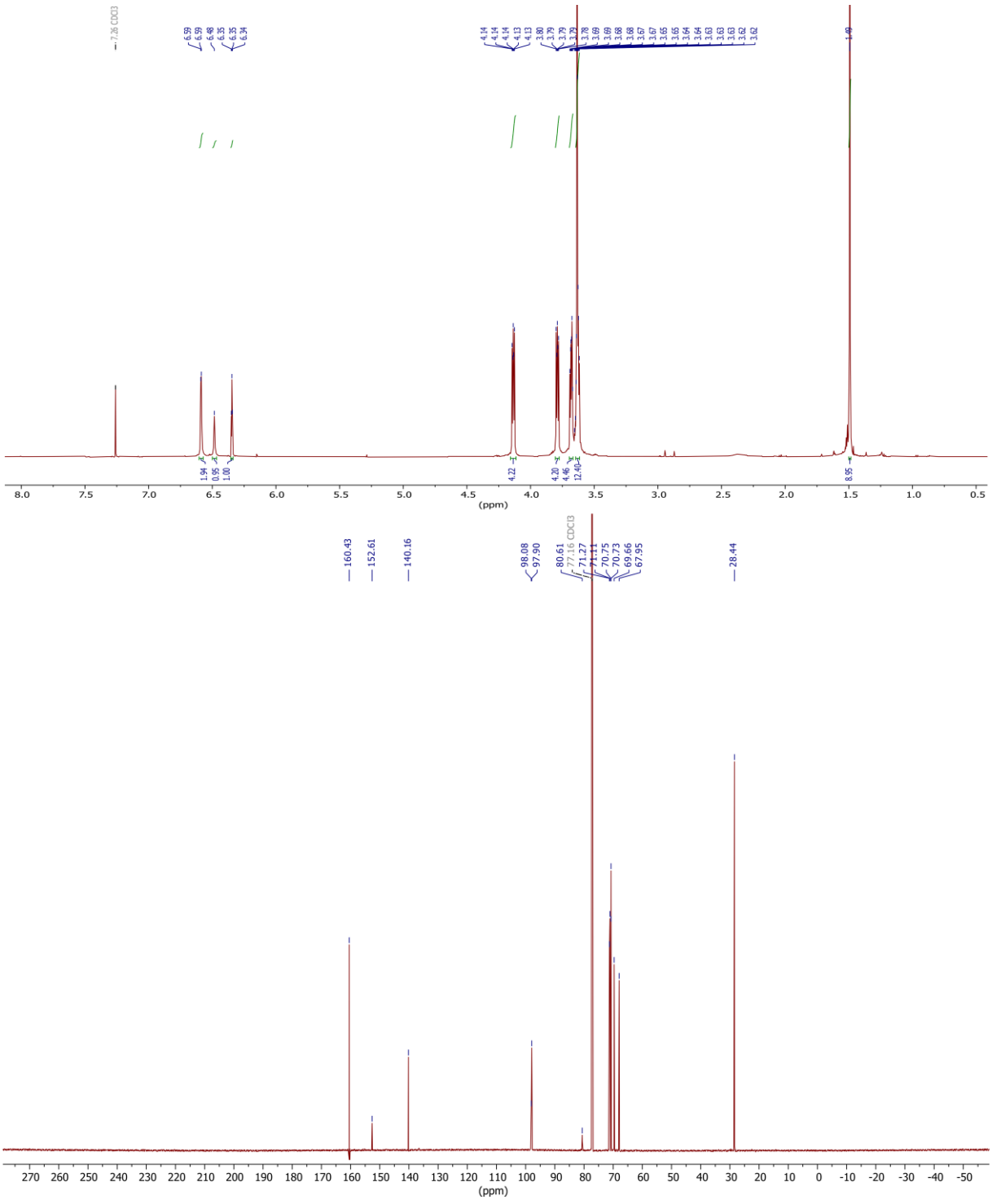

Fig. S5 ^{1}H (top) and ^{13}C (bottom) NMR spectra (500/176 MHz, $CDCl_3$, 298 K) of crown ether **S11**.

***2,5,8,11,14,17,20-heptaoxa-1(1,3)-benzenacycloicosaphan-15-amine* S12**

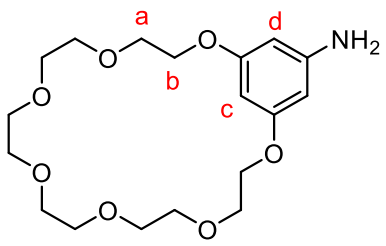

Crown ether **S11** (264 mg, 0.56 mmol, 1.00 equiv.) was dissolved in CH_2Cl_2 (30 mL). After cooling to 0 °C, trifluoroacetic acid (0.86 mL, 11.20 mol, 20.0 equiv.) was added and the mixture was stirred overnight in the thawing ice bath. The solvent was removed and the residue was taken up in aq. sat. $NaHCO_3$ solution. The solution was extracted with CH_2Cl_2 and the combined organic layers were washed with brine and dried over $MgSO_4$. The solvent was removed under reduced pressure and the residue was purified by column chromatography (SiO_2, CH_2Cl_2 → CH_2Cl_2/EtOH 10:1, R_f ~ 0.4 in CH_2Cl_2) yielding **S12** as a brown oil (162 mg, 0.44 mmol, 78%).

^{1}H NMR (700 MHz, $CDCl_3$): δ = 3.65 (d, J = 4.5 Hz, 12H, CH_2-O), 3.69 – 3.71 (m, 4H, CH_2-O), 3.80 – 3.82 (m, 4H, a), 4.10 – 4.13 (m, 4H, b), 5.88 (d, J = 2.1 Hz, 2H, d), 6.10 (t, J = 2.2 Hz, 1H, c) ppm. **^{13}C NMR** (176 MHz, $CDCl_3$): δ = 67.9, 69.8, 70.8, 70.9, 71.2, 71.3, 93.5, 95.3, 125.0, 148.3, 161.1 ppm. **HRMS (MeOH)**: m/z calcd. for $[C_{18}H_{29}NO_7]^+$: 372.2022 $[M+H]^+$, found: 372.2030; 394.1842 $[M+Na]^+$, found: 394.1853; 410.1581 $[M+K]^+$, found: 410.1595.

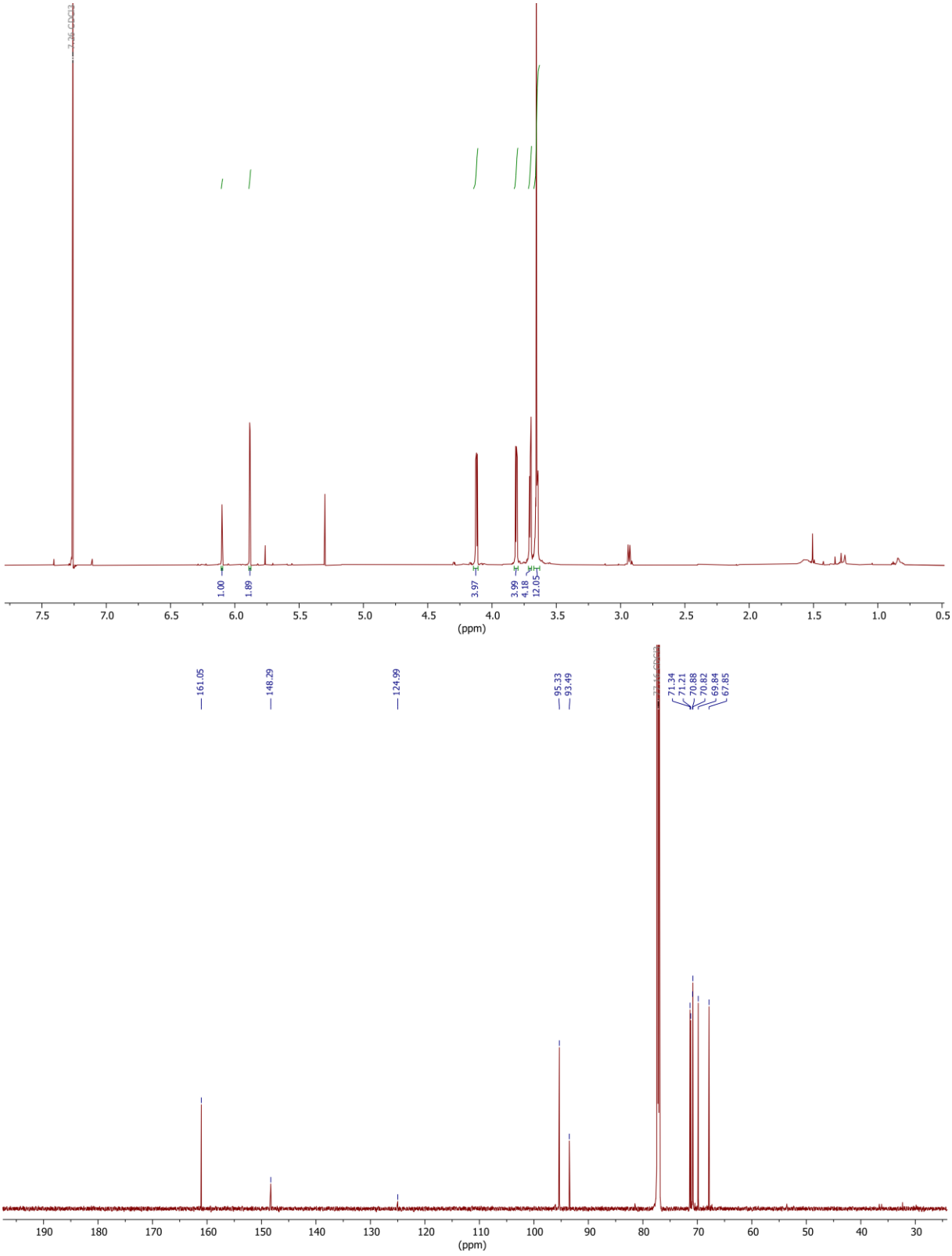

Fig. S6 ^{1}H (top) and ^{13}C (bottom) NMR spectra (700/176 MHz, $CDCl_3$, 298 K) of crown ether **S12**.

2-(2,5,8,11,14,17,20-heptaoxa-1(1,3)-benzenacycloicosaphane-15-yl)-7-butylbenzo[lmn][3,8]phenanthroline-1,3,6,8(2H,7H)-tetraone NDIC7

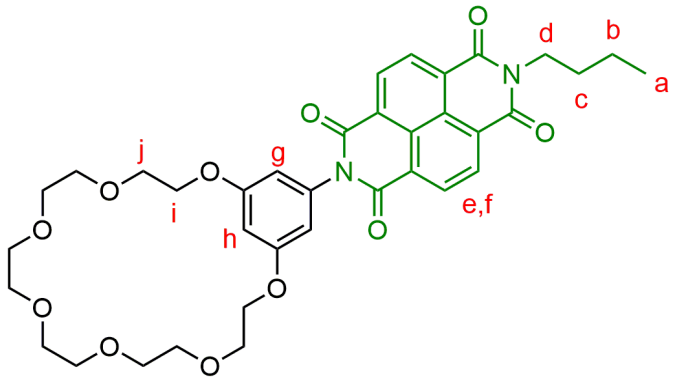

NDI **S13** (146 mg, 0.48 mmol, 1.10 equiv.) was dissolved in dry DMF (18 mL) and stirred for 20 min at 70°C under argon. Triethylamine (0.18 mL, 1.31 mmol, 3.00 equiv.) and crown ether **S12** (162 mL, 0.44 mmol, 1.00 equiv.) were added and the mixture was refluxed overnight. The solvent was removed under reduced pressure and the residue was taken up in CH_2Cl_2 (50 mL). The solution was washed with water and brine and dried over $MgSO_4$. The solvent was removed under reduced pressure and the residue was purified by column chromatography (SiO_2, CH_2Cl_2 → CH_2Cl_2/ACN 2.6:1, R_f ~ 0.3 in CH_2Cl_2) yielding **NDIC7** as a greenish brown solid (170 mg, 0.25 mmol, 58%).

^{1}H NMR (700 MHz, $CDCl_3$): δ = 1.01 (t, J = 7.4 Hz, 3H, a), 1.44 – 1.51 (m, 2H, b), 1.72 – 1.78 (m, 2H, c), 3.66 – 3.74 (m, 16H, CH_2-O), 3.83 – 3.86 (m, 4H, j), 4.19 – 4.21 (m, 4H, i), 4.21 – 4.24 (m, 2H, d), 6.47 (d, J = 2.2 Hz, 2H, g), 6.86 (t, J = 2.2 Hz, 1H, h), 8.80 (s, 4H, e,f) ppm. **^{13}C NMR** (176 MHz, $CDCl_3$): δ = 14.0, 20.5, 30.3, 41.0, 68.3, 69.8, 70.8, 70.9, 71.3, 71.4, 103.6, 108.3, 126.9, 127.1, 131.2, 131.5, 136.1, 160.9, 162.9, 163.0 ppm. **HRMS (MeOH)**: m/z calcd. for $[C_{36}H_{40}N_2O_{11}]^+$: 699.2529 $[M+Na]^+$, found: 699.2507; 715.2269 $[M+K]^+$, found: 715.2252.

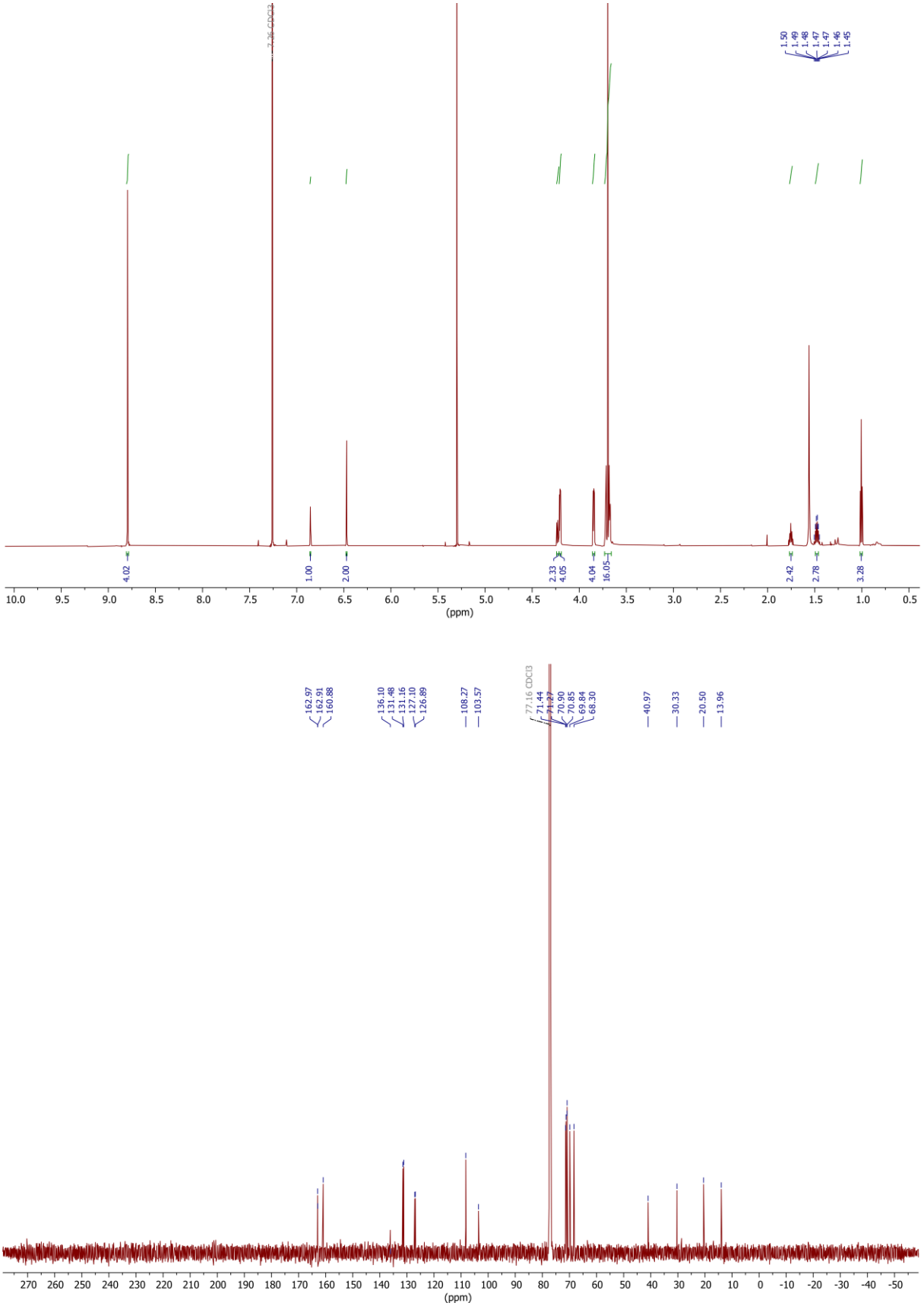

Fig. S7 ^{1}H (top) and ^{13}C (bottom) NMR spectra (700/176 MHz, $CDCl_3$, 298 K) of wheel **NDIC7**.

1.4. Synthesis of (pseudo)[3]rotaxanes

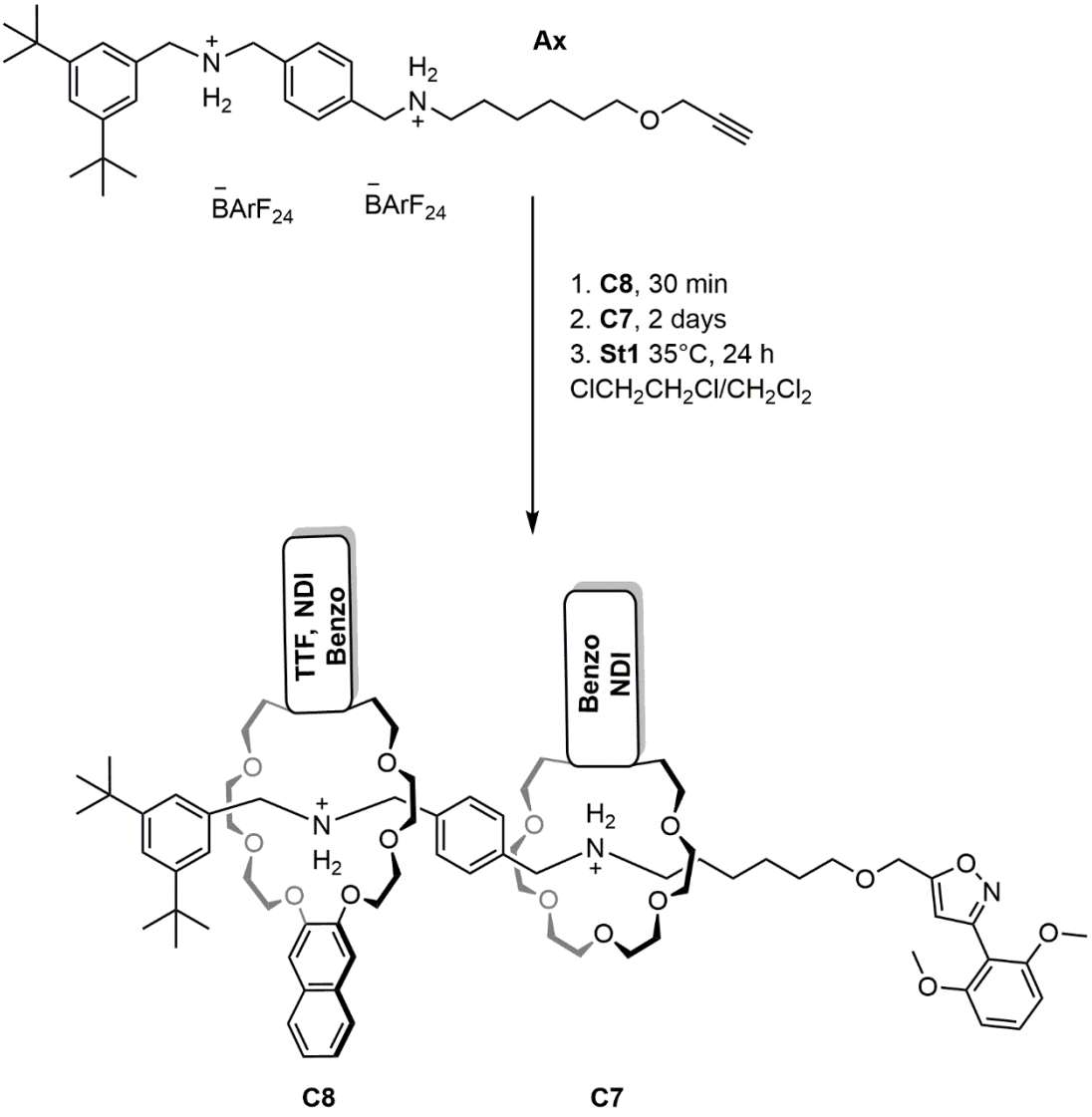

RC8C7

Scheme S3 General synthesis procedure for hetero[3]rotaxanes **RC8C7**.

Pseudo[3]rotaxane PRTTFC8BC7

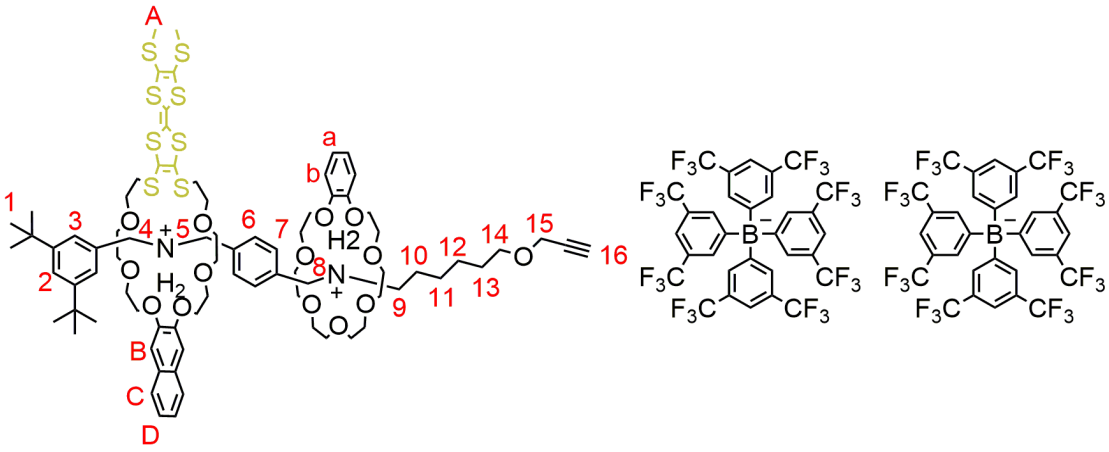

PRTTFC8BC7

The axle **Ax** (50 mg, 23 μmol, 1.00 equiv.) and macrocycle **TTFC8** (15 mg, 20 μmol, 0.90 equiv.) were dissolved in $ClCH_2CH_2Cl$ (2 mL) and stirred for 30 min, then macrocycle **BC7** (49 mg, 136 μmol, 6.00 equiv.) was added. After 2 days, the mixture was purified by column chromatography (SiO_2, CH_2Cl_2, R_f ~ 0.9 in CH_2Cl_2) to obtain the desired product **PRTTFC8BC7** (16 mg, 5 μmol, 24%) as an orange oil.

^{1}H NMR (700 MHz, CD_2Cl_2) δ = 1.23 – 1.25 (s, 18H, 1), 1.25 – 1.32 (m, 4H, 11,12), 1.32 – 1.38 (m, 2H, 10), 1.41 – 1.47 (m, 2H, 13), 2.40 (s, 6H, A), 2.41 – 2.43 (t, *J* = 2.4 Hz, 1H, 16), 3.11 – 3.24 (m, 8H, O-CH_2-CH_2), 3.29 – 3.52 (m, 20H, O-CH_2-CH_2, 9,14), 3.53 – 3.63 (m, 8H, O-CH_2-CH_2), 3.66 – 3.75 (m, 4H, O-CH_2-CH_2), 3.77 – 3.87 (m, 4H, O-CH_2-CH_2), 3.92 – 3.97 (m, 2H, 8), 4.00 – 4.05 (m, 4H, O-CH_2-CH_2), 4.06 (d, *J* = 2.4 Hz, 2H, 15), 4.08 – 4.11 (m, 2H, O-CH_2-CH_2), 4.11 – 4.17 (m, 2H, O-CH_2-CH_2), 4.70 – 4.78 (m, 4H, 4,5), 6.81 – 6.85 (m, 2H, b), 6.88 – 6.92 (m, 4H, B, 6/7), 6.94 – 6.98 (m, 2H, a), 7.17 – 7.23 (m, 4H, 6/7,NH_2), 7.31 – 7.37 (m, 2H, D), 7.42 (d, *J* = 1.8 Hz, 2H, 3), 7.50 (t, *J* = 1.8 Hz, 1H, 2), 7.56 (s_{br}, 8H, $BArF_{24}$), 7.58 – 7.61 (m, 2H, C), 7.70 – 7.77 (s_{br}, 16H, $BArF_{24}$), 7.82 – 7.90 (s, 2H, NH_2) ppm. **^{13}C NMR** (176 MHz, CD_2Cl_2) δ = 19.4, 26.0, 26.9, 27.0, 29.5, 29.6, 31.4, 35.3, 37.2, 47.6, 50.3, 53.1, 58.3, 68.4, 68.9, 70.0, 70.1, 70.1, 70.8, 71.0, 71.2, 71.3, 71.7, 71.8, 74.1, 80.5, 108.2, 108.3, 112.2, 114.5, 117.9, 122.0, 122.7, 123.7, 124.2, 124.8, 125.8, 126.7, 127.3, 128.0, 128.6, 129.3, 130.2, 130.6, 132.7, 134.5, 135.2, 146.9, 147.0, 152.8, 162.2 ppm. **HRMS (CH_2Cl_2):**m/z calcd. for $[C_{80}H_{114}N_2O_{14}S_8]^{++}$: 791.3012 $[M]^{++}$, found: 791.3034.

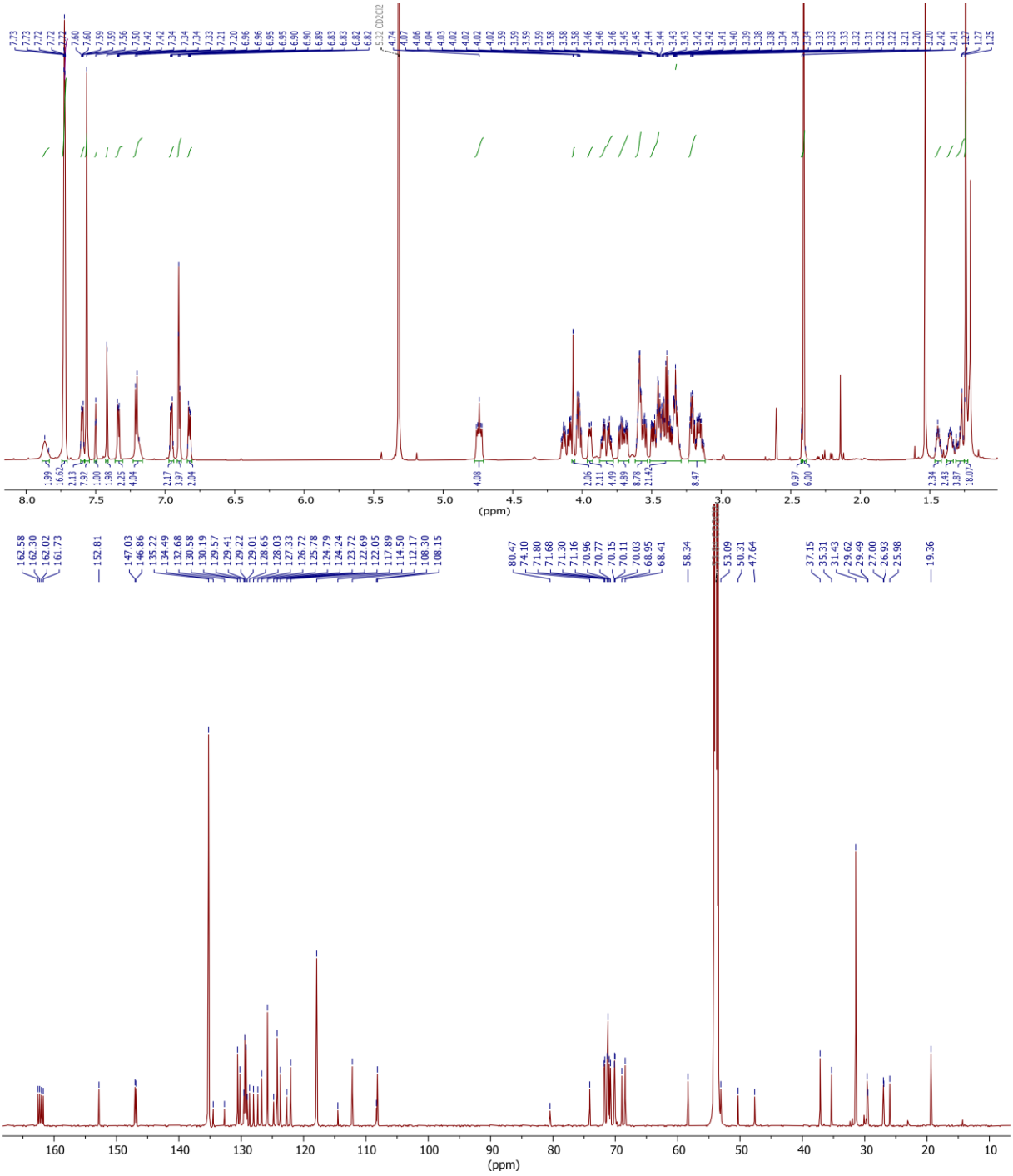

Fig. S8 ^{1}H (top) and ^{13}C (bottom) NMR spectra (700/176 MHz, CD_2Cl_2, 298 K) of pseudo[3]rotaxane **PRTTFC8BC7**.

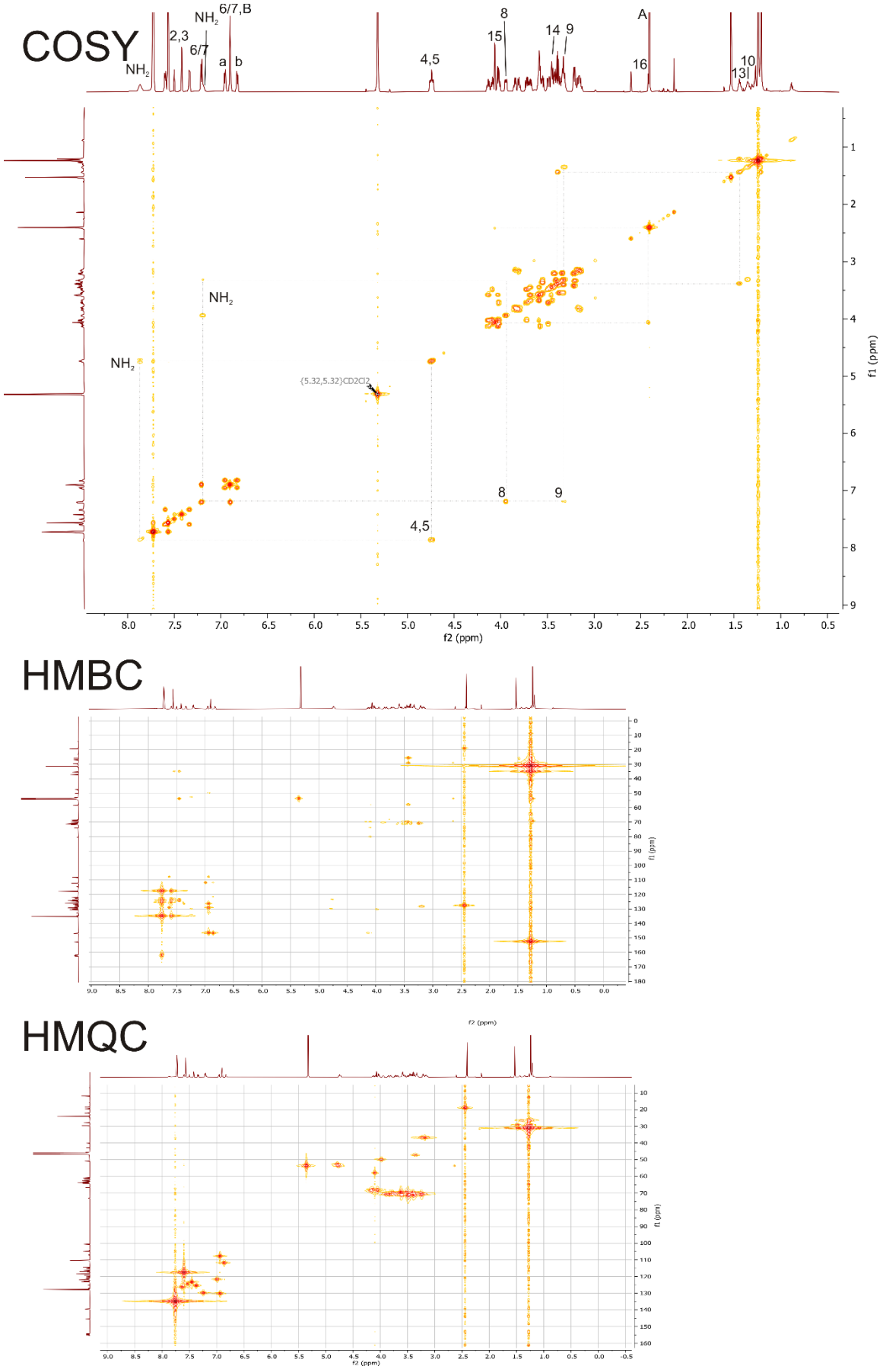

Fig. S9 COSY (top), HMBC (center) and HMQC (bottom) NMR spectra (700/176 MHz, CD_2Cl_2, 298 K) of pseudo[3]rotaxane **PRTTFC8BC7**.

RTTFC8BC7

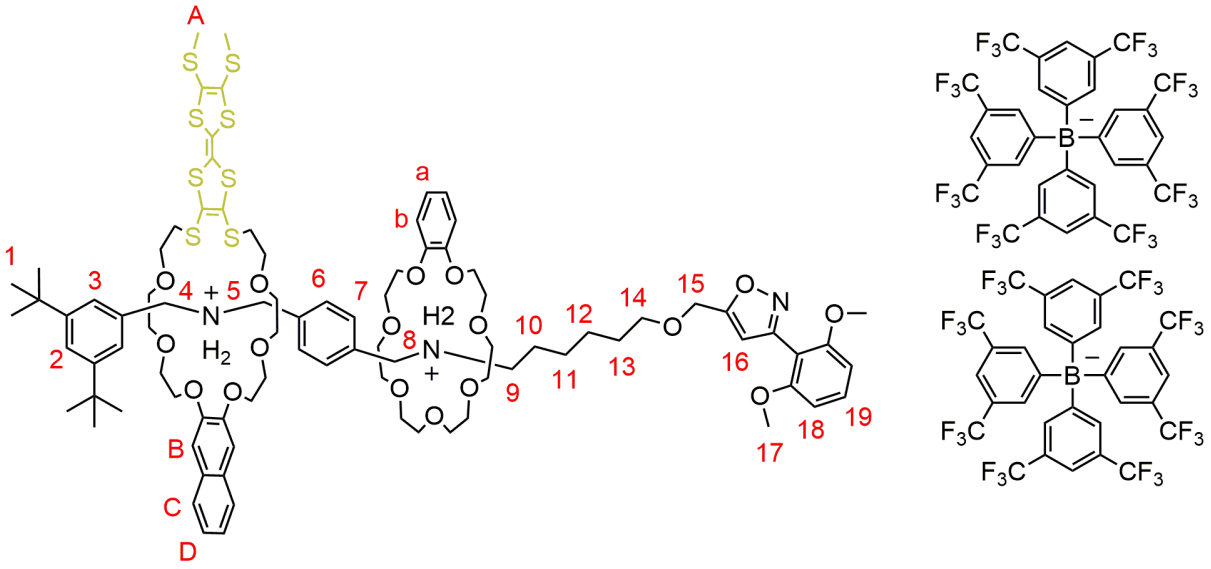

Axle **Ax** (60.0 mg, 27 µmol, 1.00 equiv.) and **TTFC8** (18 mg, 24 µmol, 0.90 equiv.) were dissolved in 1,2-dichloroethane (3 mL) and stirred for 30 min, then **BC7** (58 mg, 163 µmol, 6.00 equiv.) were added and stirred at 35° C. After 2 days, N-oxide **St1** (7 mg, 41 µmol, 1.50 equiv.) was added to the mixture and stirred for an additional 18 h at 35° C. The crude product was purified by preparative thin-layer chromatography (SiO_2, CH_2Cl_2, R_f ~ 0.3 in CH_2Cl_2). The product was obtained as an orange oil (12 mg, 3.6 µmol, 15%).

^{1}H NMR (700 MHz, CD_2Cl_2) δ = 1.23 – 1.25 (s, 18H, 1), 1.34 – 1.39 (m, 6H, 10,11,12), 1.45 – 1.50 (m, 4H, 13), 2.40 – 2.41 (s, 6H, A), 3.11 – 3.23 (m, 8H, O-CH_2-CH_2), 3.28 – 3.39 (m, 10H, 9, O-CH_2-CH_2), 3.40 – 3.52 (m, 14H, 14,O-CH_2-CH_2), 3.54 – 3.64 (m, 10H, O-CH_2-CH_2), 3.66 – 3.71 (m, 4H, O-CH_2-CH_2), 3.71 – 3.75 (m, 3H, O-CH_2-CH_2), 3.75 – 3.76 (s, 6H, 17), 3.76 – 3.83 (m, 3H, O-CH_2-CH_2), 3.83 – 3.88 (m, 3H, O-CH_2-CH_2), 3.93 – 3.98 (m, 2H, 8), 3.99 – 4.05 (m, 4H, O-CH_2-CH_2), 4.08 – 4.16 (m, 4H, O-CH_2-CH_2), 4.55 (s, 2H, 15), 4.70 – 4.77 (m, 4H, 4,5), 6.29 – 6.31 (s, 1H, 16), 6.65 – 6.68 (d, J = 8.5 Hz, 2H, 18), 6.80 – 6.84 (m, 2H, a/b), 6.89 – 6.92 (m, 4H, 7,B), 6.93 – 6.97 (m, 2H, a/b), 7.17 – 7.24 (m, 4H, 6, NH_2), 7.32 – 7.34 (m, 2H, D), 7.36 – 7.41 (t, J = 8.5 Hz, 1H, 19), 7.41 – 7.42 (d, J = 1.8 Hz, 2H, 3), 7.49 – 7.50 (t, J = 1.8 Hz, 1H, 2), 7.55 – 7.57 (s_{br}, 8H, $BArF_{24}$), 7.58 – 7.61 (m, 2H, C), 7.71 – 7.73 (s_{br}, 16H, $BArF_{24}$), 7.81 – 7.90 (s_{br}, 2H, NH_2) ppm. **^{13}C NMR** (176 MHz, CD_2Cl_2) δ = 14.3, 19.4, 23.1, 25.9, 26.9, 27.0, 29.8, 30.1, 31.4, 32.3, 35.3, 37.1, 47.6, 50.3, 53.1, 56.3, 63.9, 68.4, 68.9, 70.0, 70.1, 70.8, 71.0, 71.1, 71.2, 71.3, 71.4, 71.6, 71.8, 104.5, 106.4, 107.4, 108.2, 112.2, 114.2, 114.5, 117.9, 122.0, 122.7, 123.7, 124.2, 124.8, 125.8, 126.7, 127.3, 128.0, 128.6, 129.3, 130.2, 130.6, 131.7, 132.7, 134.5, 135.2, 146.8, 147.0, 152.8, 157.4, 159.0, 162.1, 168.2 ppm. **HRMS (acetonitrile):**m/z calcd. for $[C_{89}H_{123}N_3O_{17}S_8]^{++}$: 881.3319 $[M]^{++}$, found: 881.3325.

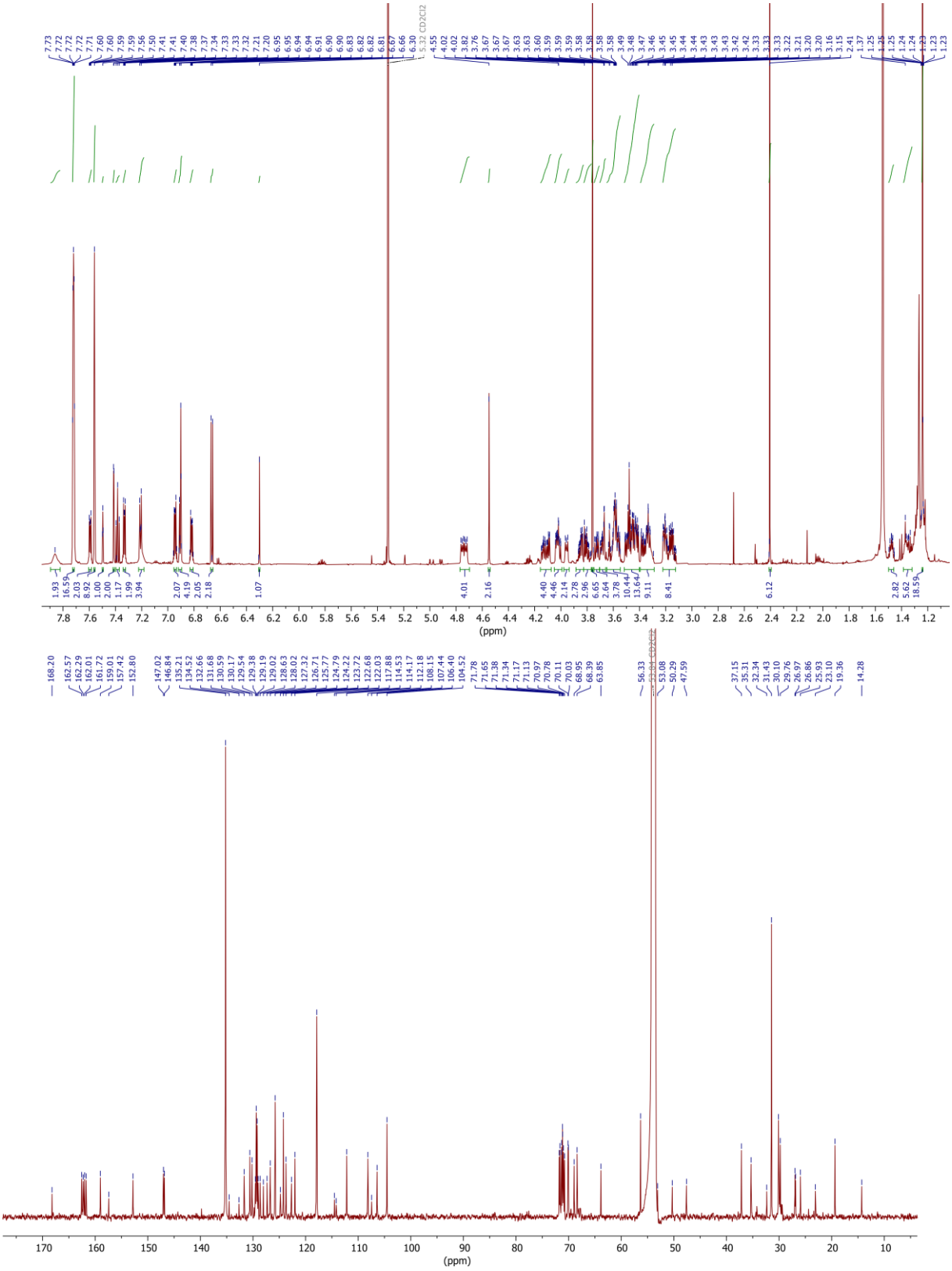

Fig. S10 ^{1}H (top) and ^{13}C (bottom) NMR spectra (700/176 MHz, CD_2Cl_2, 298 K) of [3]rotaxane **RTTFC8BC7**.

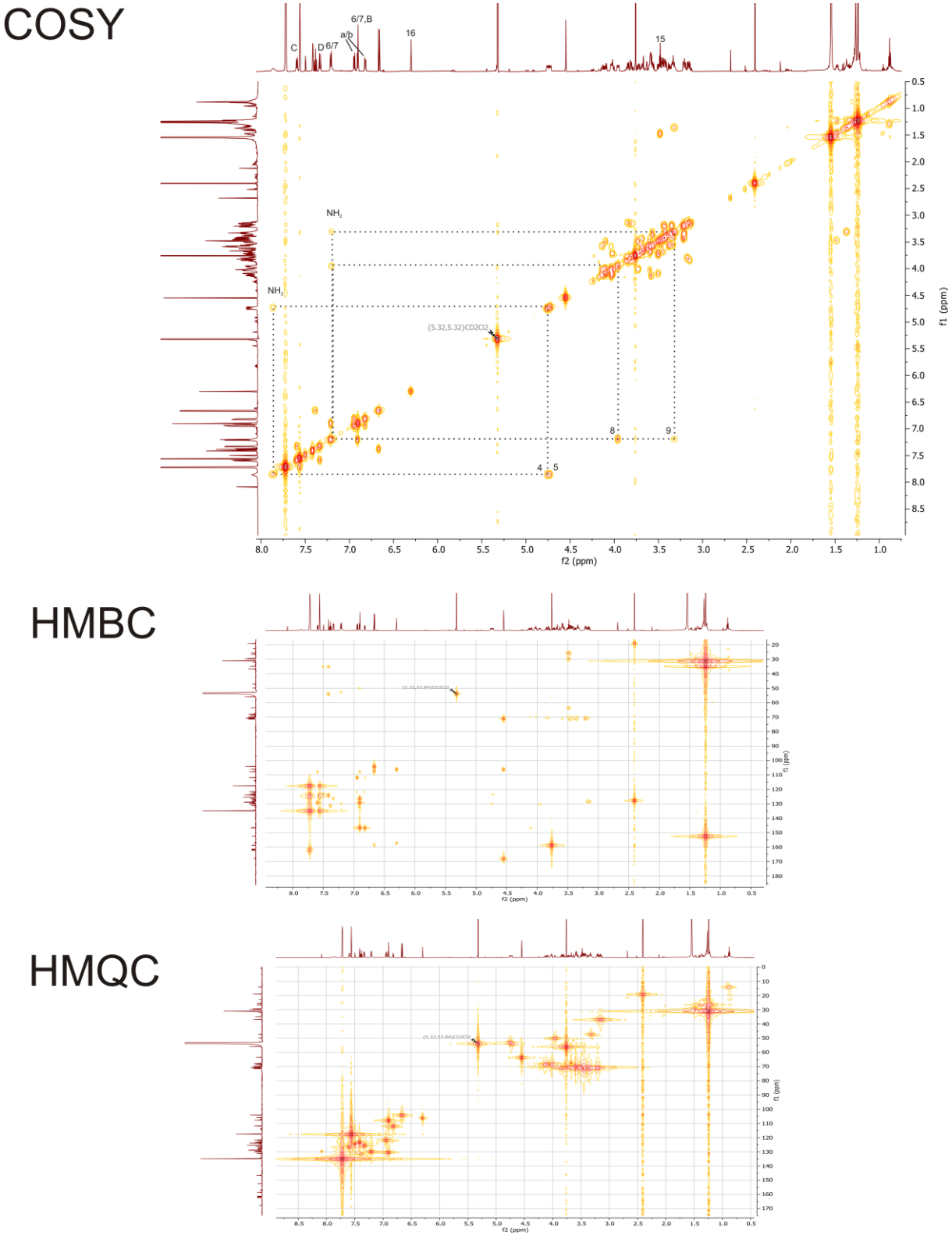

Fig. S11 COSY (top), HMBC (center) and HMQC (bottom) NMR spectra (700/176 MHz, CD_2Cl_2, 298 K) of [3]rotaxane **RTTFC8BC7**.

[3]rotaxane RTTFC8NDIC7

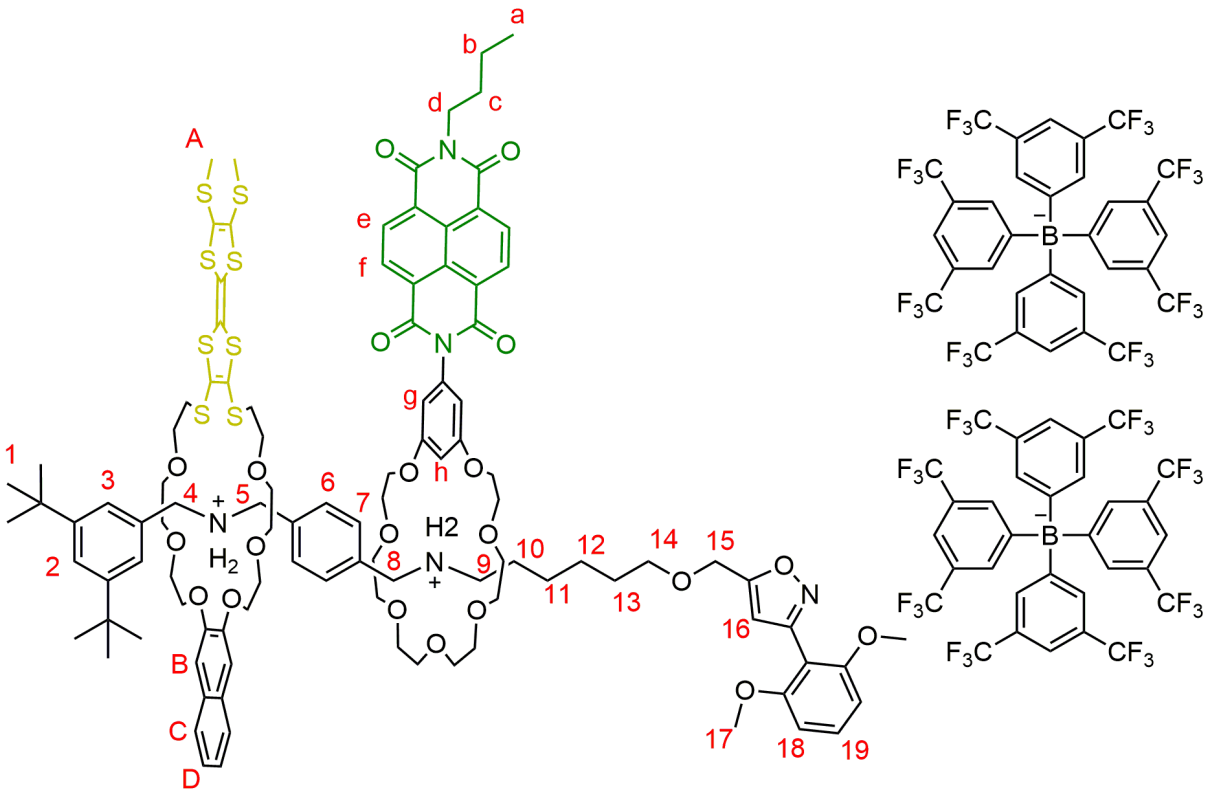

RTTFC8NDIC7

The axle **Ax** (60 mg, 27 µmol, 1.00 equiv.) and **TTFC8** (18 mg, 24 µmol, 0.90 equiv.) were dissolved in CH_2Cl_2 (3 mL) and stirred for 30 min. **NDIC7** (110 mg, 163 µmol, 6.00 equiv.) was added and stirred for another 2 days. Finally, N-oxide **St1** (7 mg, 41 µmol, 1.50 equiv.) was added to the mixture and stirred for an additional 24 h at 35° C. The crude product was purified via preparative thin-layer chromatography (SiO_2, CH_2Cl_2/EtOH 50:1, R_f ~ 0.25 in CH_2Cl_2/EtOH 100:1) The product was obtained as a greenish brown oil (27 mg, 7 µmol, 29%).

^{1}H NMR (700 MHz, CD_2Cl_2) δ =1.00 (t, J = 7.4 Hz, 3H, a), 1.27 (s, 18H, 1), 1.34 – 1.38 (m, 4H, 11,12), 1.42 – 1.45 (m, 2H, 10), 1.45 – 1.49 (m, 2H, b), 1.58 – 1.62 (m, 2H, 13), 1.74 – 1.76 (m, 2H, c), 2.40 (s, 6H, A), 2.96 – 3.03 (m, 4H, O-CH_2-CH_2), 3.07 – 3.19 (m, 10H, O-CH_2-CH_2, 9), 3.26 – 3.30 (m, 2H, O-CH_2-CH_2), 3.32 – 3.35 (m, 2H, O-CH_2-CH_2), 3.38 – 3.42 (m, 2H, O-CH_2-CH_2), 3.46 – 3.50 (m, 4H, O-CH_2-CH_2), 3.50 – 3.56 (m, 10H, O-CH_2-CH_2, 14), 3.58 – 3.67 (m, 16H, O-CH_2-CH_2,), 3.67 – 3.69 (m, 4H, O-CH_2-CH_2), 3.70 – 3.71 (s, 6H, 17), 3.73 – 3.77 (m, 6H, O-CH_2-CH_2, 8), 3.79 – 3.90 (m, 8H, O-CH_2-CH_2,), 4.04 – 4.08 (m, 2H, O-CH_2-CH_2), 4.16 – 4.22 (m, 6H, O-CH_2-CH_2, d), 4.22 – 4.28 (m, 6H, O-CH_2-CH_2), 4.53 (s, 2H, 15), 4.71 – 4.74 (m, 2H, 4/5), 4.90 – 4.94 (m, 2H, 4/5), 6.23 (s, 1H, 16), 6.43 (t, J = 2.3 Hz, 1H, h), 6.56 (d, J = 8.4 Hz, 18H), 6.61 (d, J = 2.2 Hz, 2H, g), 6.94 – 6.97 (m, 4H, B, 6/7), 7.27 – 7.37 (m, 5H, D, 19, NH_2), 7.36 – 7.38 (m, 2H, 6/7), 7.44 (d, J = 1.8 Hz, 2H, 3), 7.54 (t, J = 1.8 Hz, 1H, 2), 7.56 (s_{br}, 8H, $BArF_{24}$), 7.60 – 7.64 (m, 2H, C), 7.72 (s_{br}, 16H, $BArF_{24}$), 7.99 (s_{br}, 2H, NH_2),

8.69 – 8.77 (m, 4H, e,f) ppm. **^{13}C NMR** (176 MHz, CD_2Cl_2) δ = 8.9, 14.0, 14.3, 19.3, 20.8, 23.1, 25.2, 26.1, 26.2, 26.7, 26.8, 26.9, 27.6, 29.5, 29.8, 29.9, 29.9, 30.1, 30.5, 31.4, 31.6, 32.0, 32.3, 33.5, 34.5, 35.4, 37.2, 41.1, 47.1, 48.4, 51.1, 56.2, 63.8, 67.8, 68.0, 68.9, 70.0, 70.2, 70.6, 70.8, 70.9, 71.3, 71.4, 71.9, 103.7, 104.4, 106.5, 107.2, 108.0, 108.2, 108.6, 109.2, 114.7, 117.9, 122.7, 123.5, 124.2, 124.8, 125.8, 126.1, 126.5, 126.7, 126.9, 127.3, 127.4, 127.7, 128.0, 128.8, 129.0, 129.2, 129.4, 129.5, 129.7, 130.1, 130.3, 130.5, 130.6, 130.7, 131.1, 131.4, 131.5, 133.1, 133.5, 135.2, 138.5, 146.6, 152.9, 157.2, 158.9, 159.7, 159.9, 161.7, 162.0, 162.3, 162.6, 163.1, 163.3, 168.0 ppm. **HRMS (acetonitrile):**m/z calcd. for $[C_{107}H_{135}N_5O_{21}S_8]^{++}$: 1041.3719 $[M]^{++}$, found: 1041.3729.

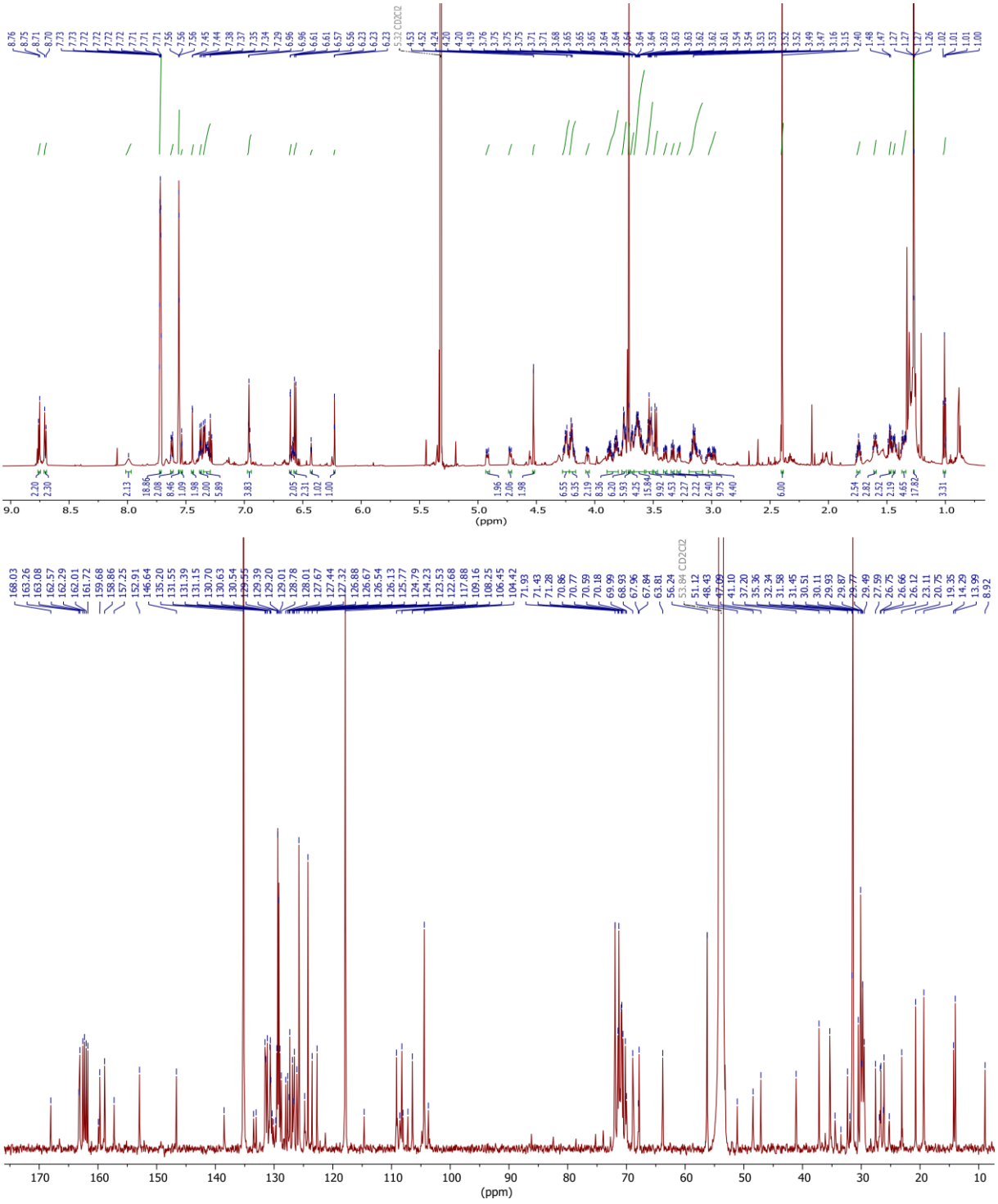

Fig. S12 ^{1}H (top) and ^{13}C (bottom) NMR spectra (700/176 MHz, CD_2Cl_2, 298 K) of [3]rotaxane **RTTFC8NDIC7**

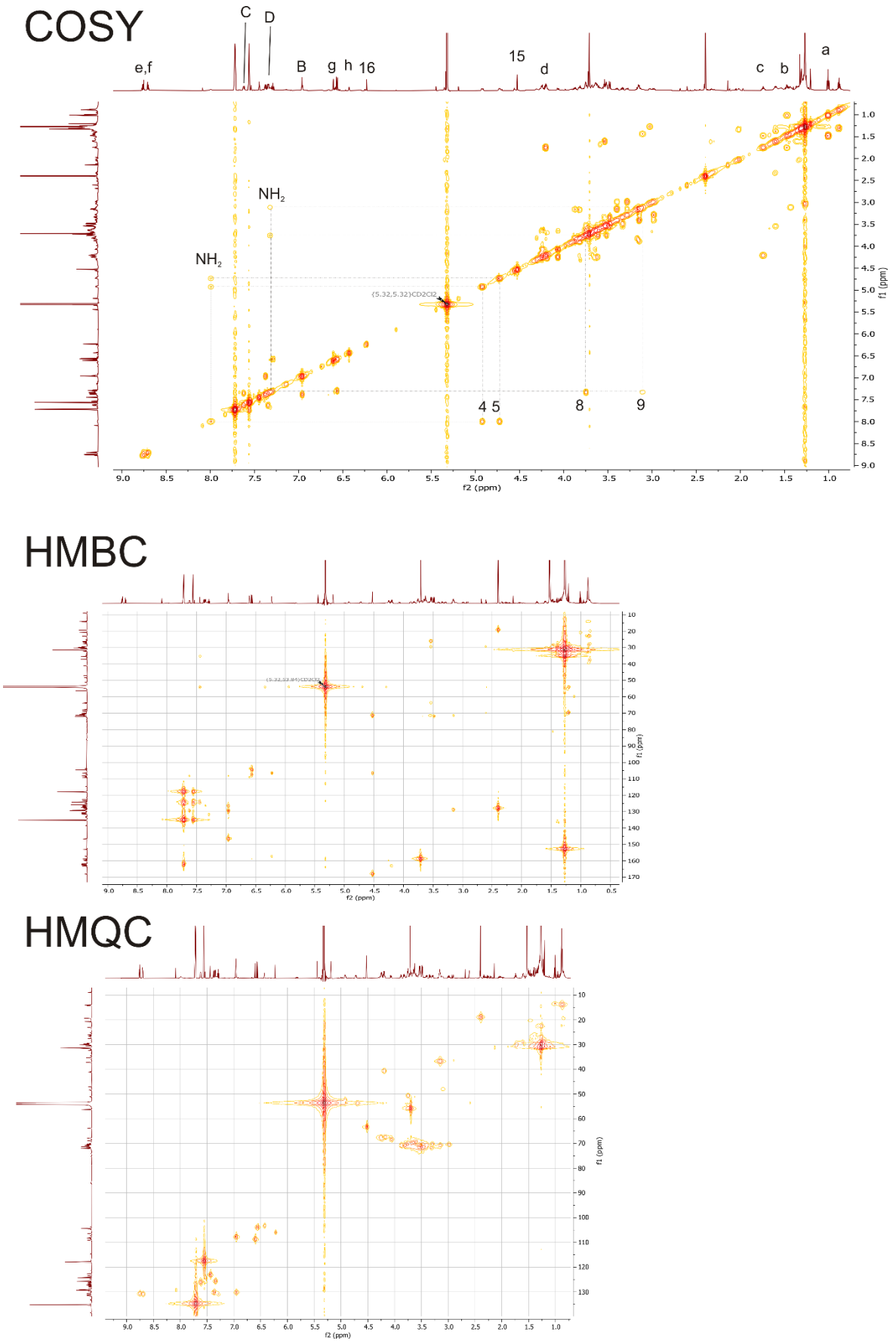

Fig. S13 COSY (top), HMBC (center) and HMQC (bottom) NMR spectra (700/176 MHz, CD_2Cl_2, 298 K) of [3]rotaxane **RTTFC8NDIC7**

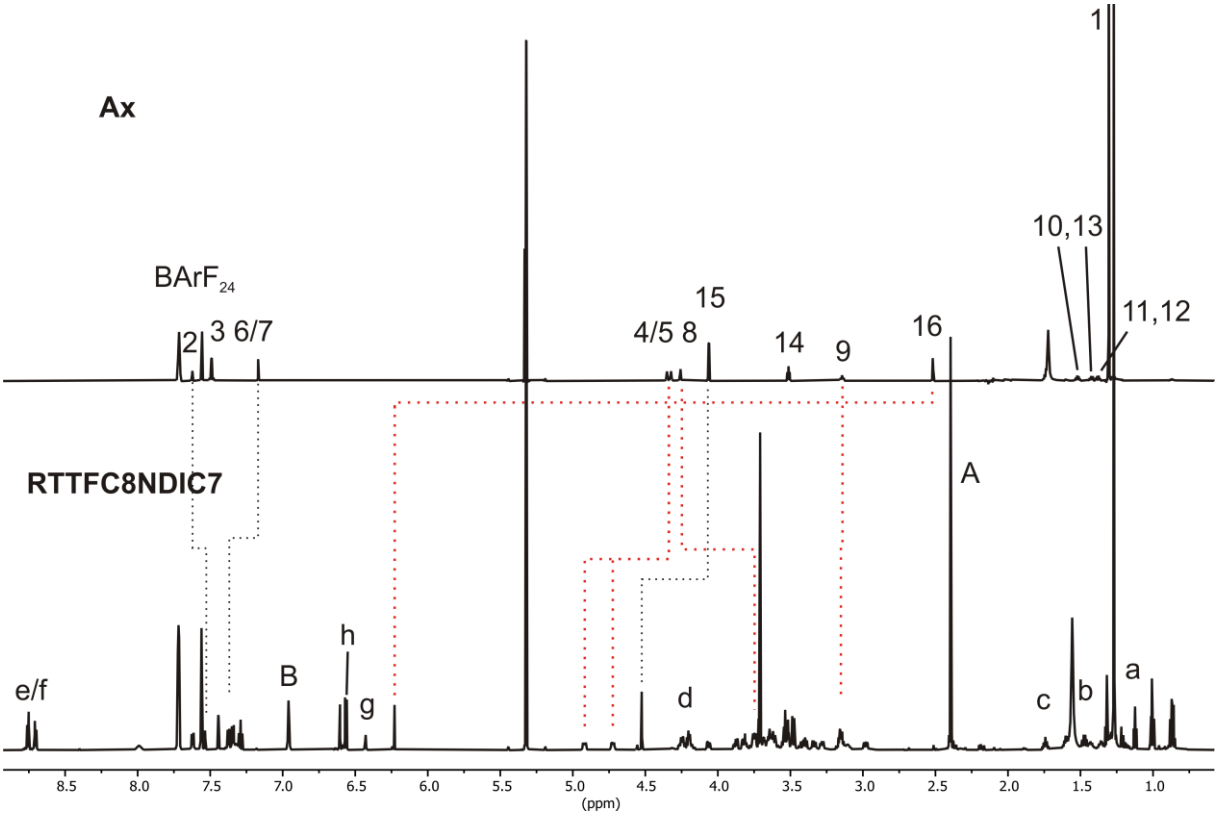

Fig. S14 [3]rotaxane **RTTFC8NDIC7** (bottom) and axle **Ax** (top) NMR spectra (700 MHz, CD_2Cl_2, 298 K).

[3]rotaxane RNDIC8BC7

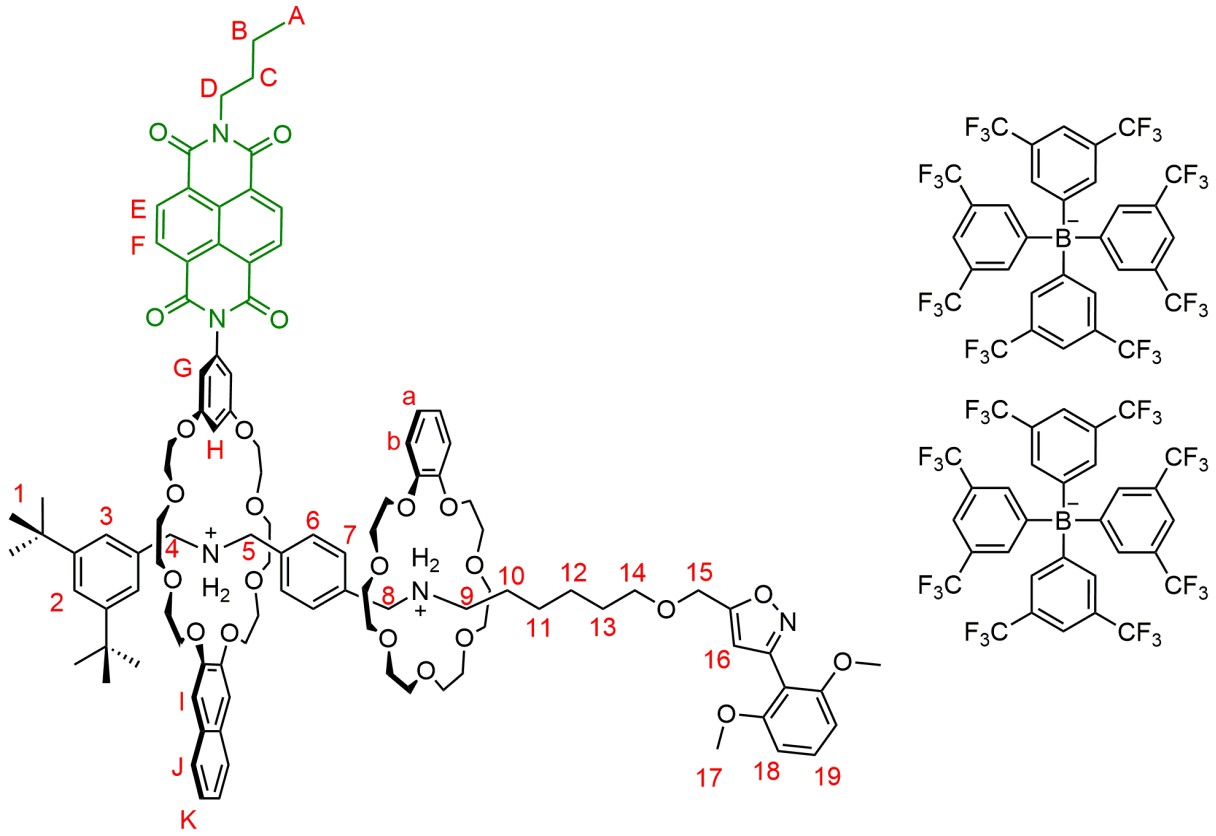

RNDIC8BC7

The axle **Ax** (60 mg, 27 µmol, 1.00 equiv.) and macrocycle **NDIC8** (20 mg, 25 µmol, 0.90 equiv.) were dissolved in CH_2Cl_2 (3 mL) and stirred for 30 min, then macrocycle **BC7** (15 mg, 41 µmol, 1.50 equiv.) was added. After 3 days, stopper **St1** (7 mg, 41 µmol, 1.50 equiv.) was added and the mixture was heated to 35°C for 24 h. Then, the mixture was purified by preparative TLC (SiO_2, 2000 µm, CH_2Cl_2/ACN 10:1, R_f ~ 0.4 in CH_2Cl_2/ACN 10:1) to obtain the desired product **RNDIC8BC7** (17 mg, 5 µmol, 20 %) as yellow oil.

^{1}H NMR (700 MHz, CD_2Cl_2) δ = 0.99 (t, J = 7.4 Hz, 3H, A), 1.24 (s, 18H, 1), 1.33 – 1.40 (m, 6H, 10,11,12),1.43 – 1.46 (m, 4H, B, 13), 1.68 – 1.75 (m, 2H, C), 3.12 – 3.17 (m, 4H, O-CH_2-CH_2), 3.25 – 3.39 (m, 16H, 9, O-CH_2-CH_2), 3.41 – 3.46 (m, 5H, 14, O-CH_2-CH_2), 3.46 – 3.52 (m, 5H, O-CH_2-CH_2), 3.52 – 3.62 (m, 10H, O-CH_2-CH_2), 3.62 – 3.70 (m, 10H, O-CH_2-CH_2), 3.73 (s, 6H, 17), 3.75 – 3.78 (m, 1H, O-CH_2-CH_2), 3.78 – 3.83 (m, 3H, O-CH_2-CH_2), 3.85 - 3.89 (m, 2H, O-CH_2-CH_2), 3.96 – 4.04 (m, 6H, 8, O-CH_2-CH_2), 4.04 – 4.08 (m, 2H, O-CH_2-CH_2), 4.08 – 4.12 (m, 3H, O-CH_2-CH_2), 4.12 – 4.16 (m, 2H, O-CH_2-CH_2), 4.17 – 4.20 (m, 2H, D), 4.21 – 4.27 (m, 3H, O-CH_2-CH_2), 4.53 (s, 2H, 15), 4.60 – 4.64 (m, 4H, 4,5), 6.50 (s, 1H, 16), 6.56 (d, J = 2.2 Hz, 2H, G), 6.63 (t, J = 2.2 Hz, 1H, H), 6.69 (d, J = 8.5 Hz, 2H, 18), 6.78 - 6.82 (m, 2H, a/b), 6.90 – 6.95 (m, 6H, a/b, I, 6/7), 7.22 (s_{br}, 2H, NH_2), 7.29 (dd, J = 8.8, 2.5 Hz, 2H, 6/7), 7.33 – 7.35 (m, 2H, K), 7.37 (t, J = 8.4 Hz, 1H, 19), 7.41 (d, J = 1.8 Hz, 2H, 3), 7.51 (t, J = 1.8

Hz, 1H, 2), 7.55 (s_{br}, 8H, $BArF_{24}$), 7.58 - 7.62 (m, 2H, J), 7.71 (s_{br}, 16H, $BArF_{24}$), 8.00 (s_{br}, 2H, NH_2), 8.67 – 8.80 (m, 4H, E,F) ppm. **^{13}C NMR** (176 MHz, CD_2Cl_2) δ = 1.2, 14.0, 14.3, 20.7, 25.9, 27.0, 27.1, 29.7, 30.1, 30.5, 31.3, 31.4, 32.3, 35.3, 41.2, 47.7, 50.3, 52.4, 57.2, 63.8, 68.4, 68.4, 68.8, 69.5, 70.0, 70.9, 71.1, 71.2, 71.6, 71.7, 71.8, 77.6, 77.7, 77.9, 104.4, 106.2, 106.7, 107.0, 108.1, 108.9, 112.1, 117.9, 122.0, 122.7, 123.9, 124.2, 124.9, 125.8, 126.7, 126.9, 127.3, 127.6, 128.1, 129.3, 130.3, 130.4, 130.7, 131.3, 131.5, 132.6, 134.7, 135.2, 137.9, 146.8, 147.0, 152.8, 157.9, 158.5, 160.6, 162.1, 163.3, 164.8, 168.9 ppm. **HRMS (acetonitrile):** m/z calcd. for $[C_{105}H_{133}N_5O_{23}]^{++}$: 916.4707 $[M]^{++}$, found: 916.4714

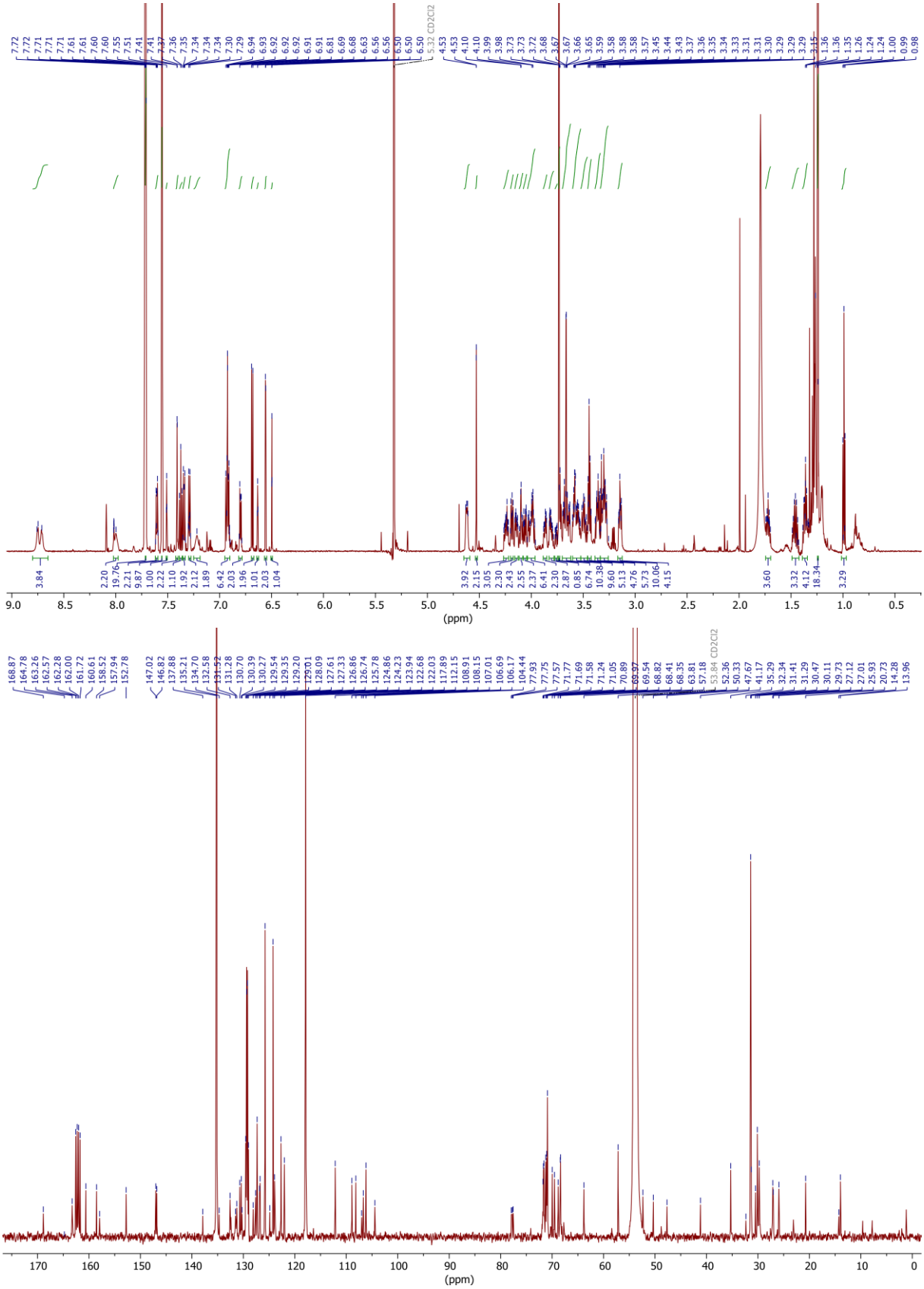

Fig. S15 ^{1}H (top) and ^{13}C (bottom) NMR spectra (700/176 MHz, CD_2Cl_2, 298 K) of [3]rotaxane **RNDIC8BC7**.

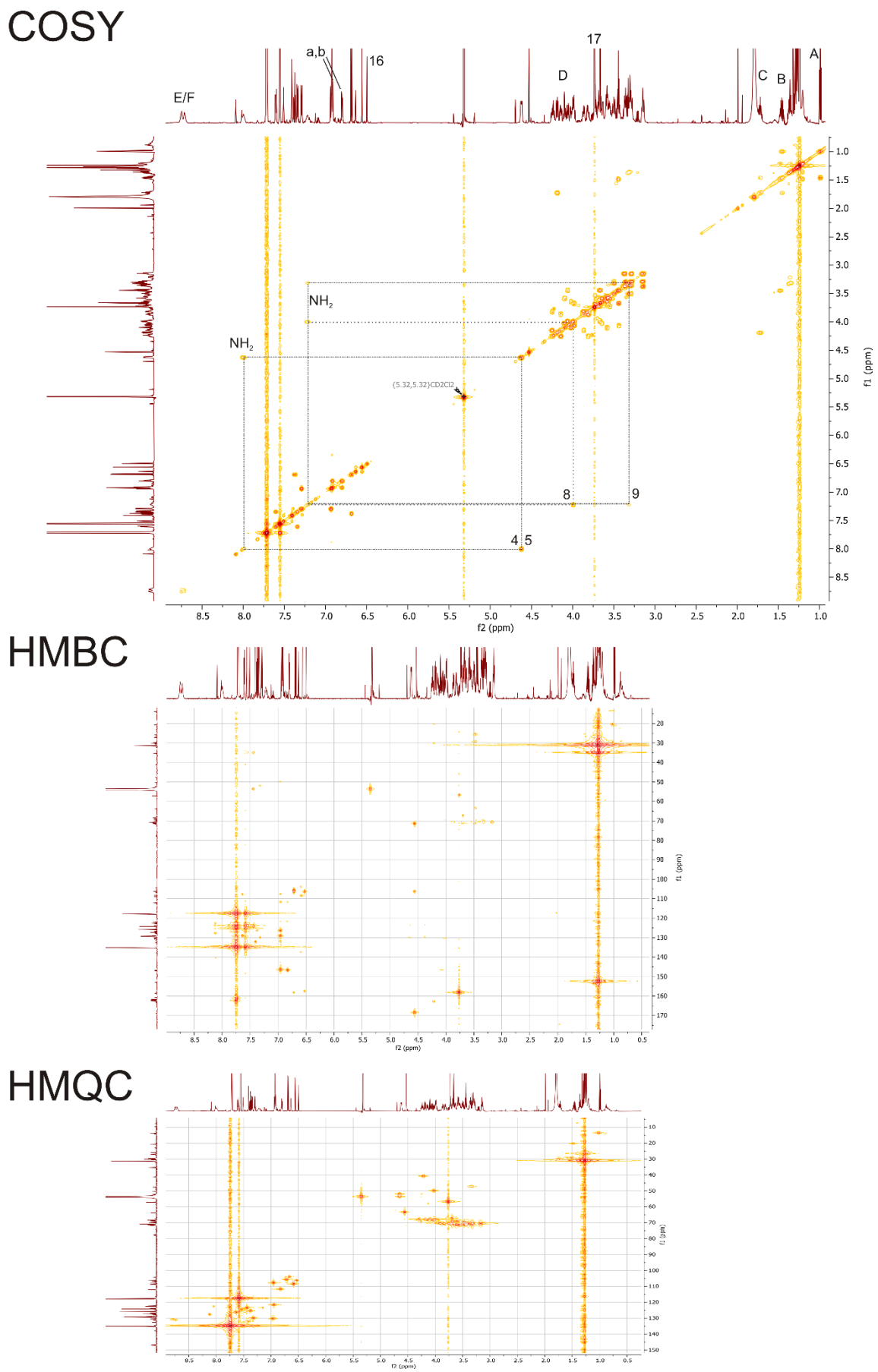

Fig. S16 COSY (top), HMBC (center) and HMQC (bottom) NMR spectra (700/176 MHz, CD_2Cl_2, 298 K) of [3]rotaxane **RNDIC8BC7**.

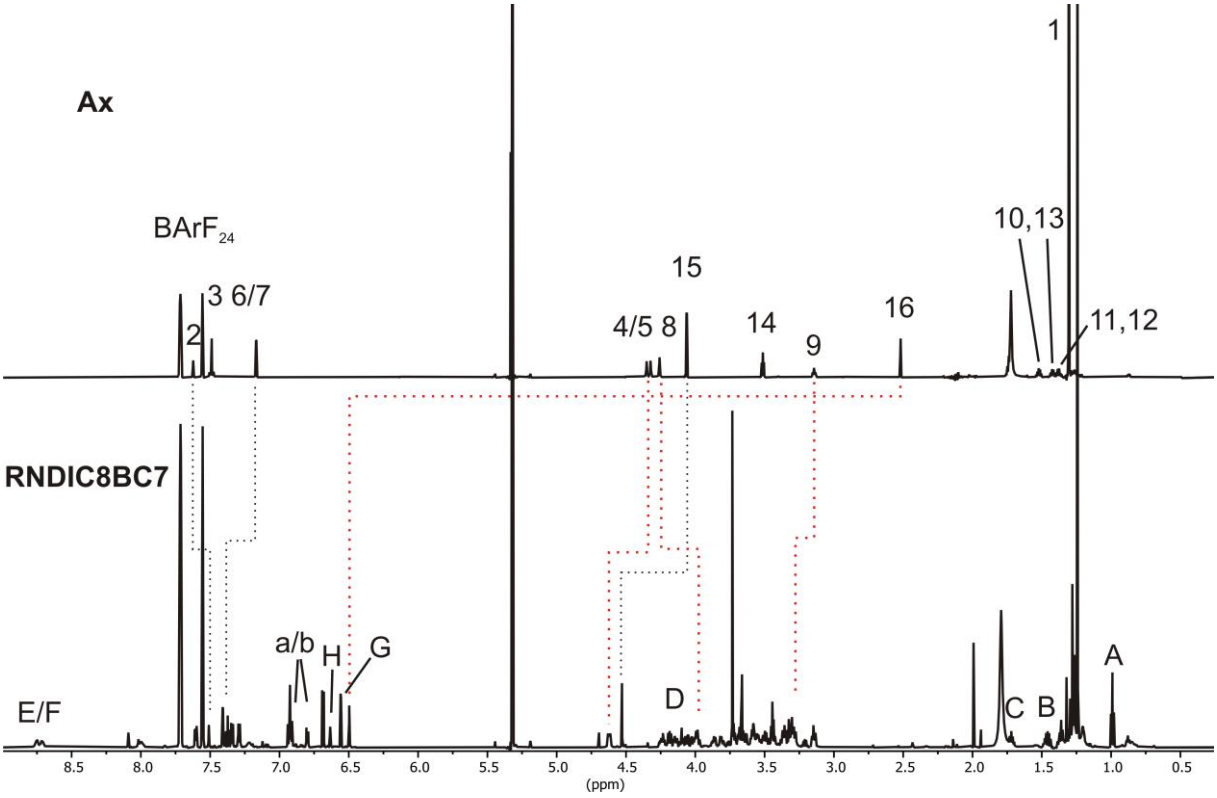

Fig. S17 [3]rotaxane **RNDIC8BC7** (bottom) and axle **Ax** (top) NMR spectra (700 MHz, CD_2Cl_2, 298 K).

[3]rotaxane RDBC8NDIC7

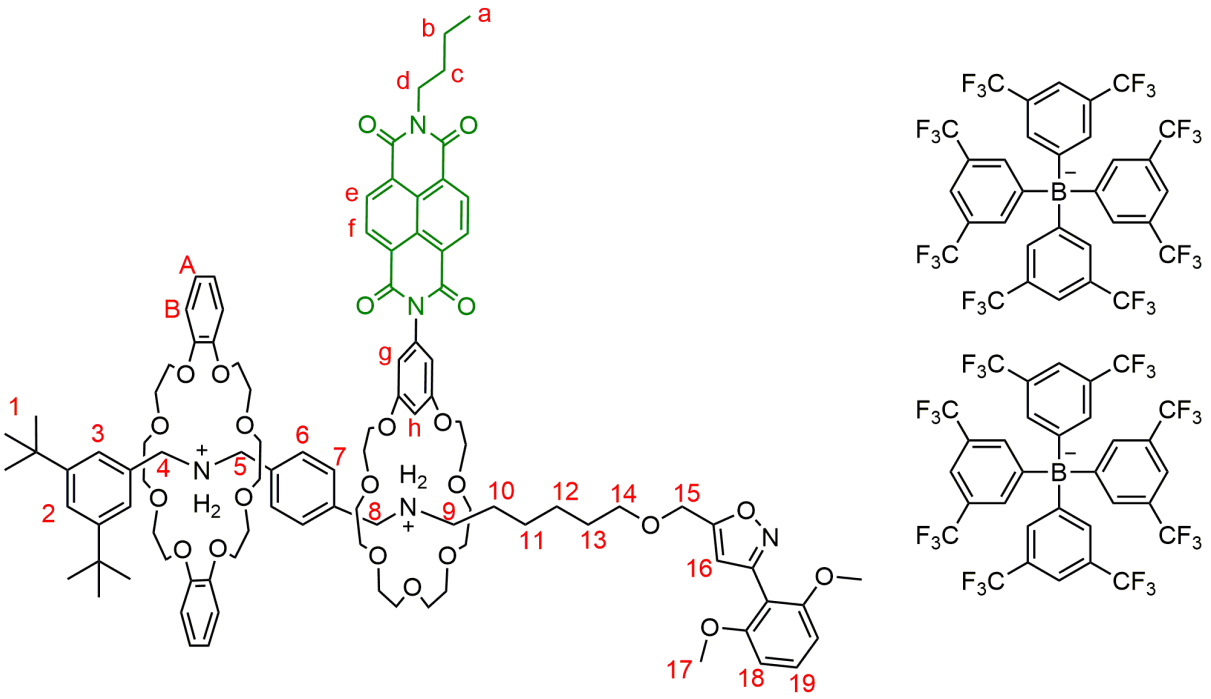

RDBC8NDIC7

The axle **Ax** (60 mg, 27 µmol, 1.00 equiv.) and macrocycle **DBC8** (11 mg, 25 µmol, 0.90 equiv.) were dissolved in CH_2Cl_2 (3 mL) and stirred for 30 min, then macrocycle **NDIC7** (110 mg, 163 µmol, 6.00 equiv.) was added. After 2 days, stopper **St1** (7 mg, 41 µmol, 1.50 equiv.) was added and the mixture was heated to 35°C for 24 h. Then, the mixture was purified by preparative TLC (SiO_2, 2000 µm, CH_2Cl_2/ACN 10:1, R_f ~ 0.4 in CH_2Cl_2/ACN 10:1) to obtain the desired product **RDBC8NDIC7** (12 mg, 3 µmol, 14 %) as yellow oil.

^{1}H NMR (700 MHz, CD_2Cl_2) δ = 0.99 (t, J = 7.4 Hz, 3H, a), 1.24 (s, 18H, 1), 1.33 – 1.38 (m, 1H, c, 11, 12), 1.42 – 1.51 (m, 2H, 10, b), 1.65 (tt, J = 14.3, 6.3 Hz, 2H, 13), 1.69 – 1.75 (m, 2H, c), 2.96 – 3.00 (m, 2H, O-CH_2-CH_2), 3.09 – 3.15 (m, 4H, 9, O-CH_2-CH_2), 3.24 – 3.29 (m, 2H, O-CH_2-CH_2), 3.34 – 3.43 (m, 6H, O-CH_2-CH_2), 3.48 – 3.52 (m, 6H, O-CH_2-CH_2), 3.53 – 3.62 (m, 7H, 14, O-CH_2-CH_2), 3.63 – 3.67 (m, 5H, O-CH_2-CH_2), 3.71 (s, 6H, 17), 3.72 – 3.80 (m, 12H, O-CH_2-CH_2), 4.02 – 4.11 (m, 10H, 8, O-CH_2-CH_2), 4.16 – 4.20 (m, 2H, d), 4.29 – 4.33 (m, 4H, O-CH_2-CH_2), 4.55 (s, 2H, 15), 4.71 – 4.75 (m, 2H, 4/5), 4.79 – 4.83 (m, 2H, 4/5), 6.28 (s, 1H, 16), 6.56 (d, J = 8.5 Hz, 2H, 18), 6.62 (d, J = 2.2 Hz, 2H, g), 6.68 (t, J = 2.3 Hz, 1H, h), 6.74 (m, 4H, A/B), 6.85 (m, 4H, A/B), 6.96 – 7.00 (m, 2H, 6/7), 7.24 – 7.30 (m, 3H, 19, 6/7), 7.33 (d, J = 1.8 Hz, 2H, 3), 7.39 – 7.44 (m, 2H, NH_2), 7.49 (t, J = 1.8 Hz, 1H, 2), 7.54 – 7.57 (m, 8H, $BArF_{24}$), 7.60 (s_{br}, 2H, NH_2), 7.69 – 7.74 (m, 16H, $BArF_{24}$), 8.67 – 8.78 (m, 4H, e/f) ppm. **^{13}C NMR** (176 MHz, CD_2Cl_2) δ = 14.0, 14.3, 19.5, 20.7, 23.1, 26.2, 26.7, 26.9, 29.8, 29.9, 30.1, 30.5, 31.4, 32.3, 35.3, 36.7, 41.1, 48.5, 49.8, 51.4, 52.5, 56.3, 63.8, 68.0, 68.3, 70.6,

70.8, 71.1, 71.2, 71.5, 71.9, 72.0, 103.9, 104.6, 106.6, 107.1, 109.1, 112.9, 117.9, 122.0, 122.7, 123.8, 124.2, 124.3, 125.8, 126.9, 127.3, 127.6, 129.3, 130.4, 130.6, 131.2, 131.4, 131.6, 132.7, 133.9, 135.2, 138.6, 147.9, 152.5, 157.3, 158.8, 159.8, 162.2, 163.1, 163.2, 168.0 ppm. **HRMS (acetonitrile):** m/z calcd. for $[C_{101}H_{131}N_5O_{23}]^{++}$: 891.4629 $[M]^{++}$, found: 891.4639.

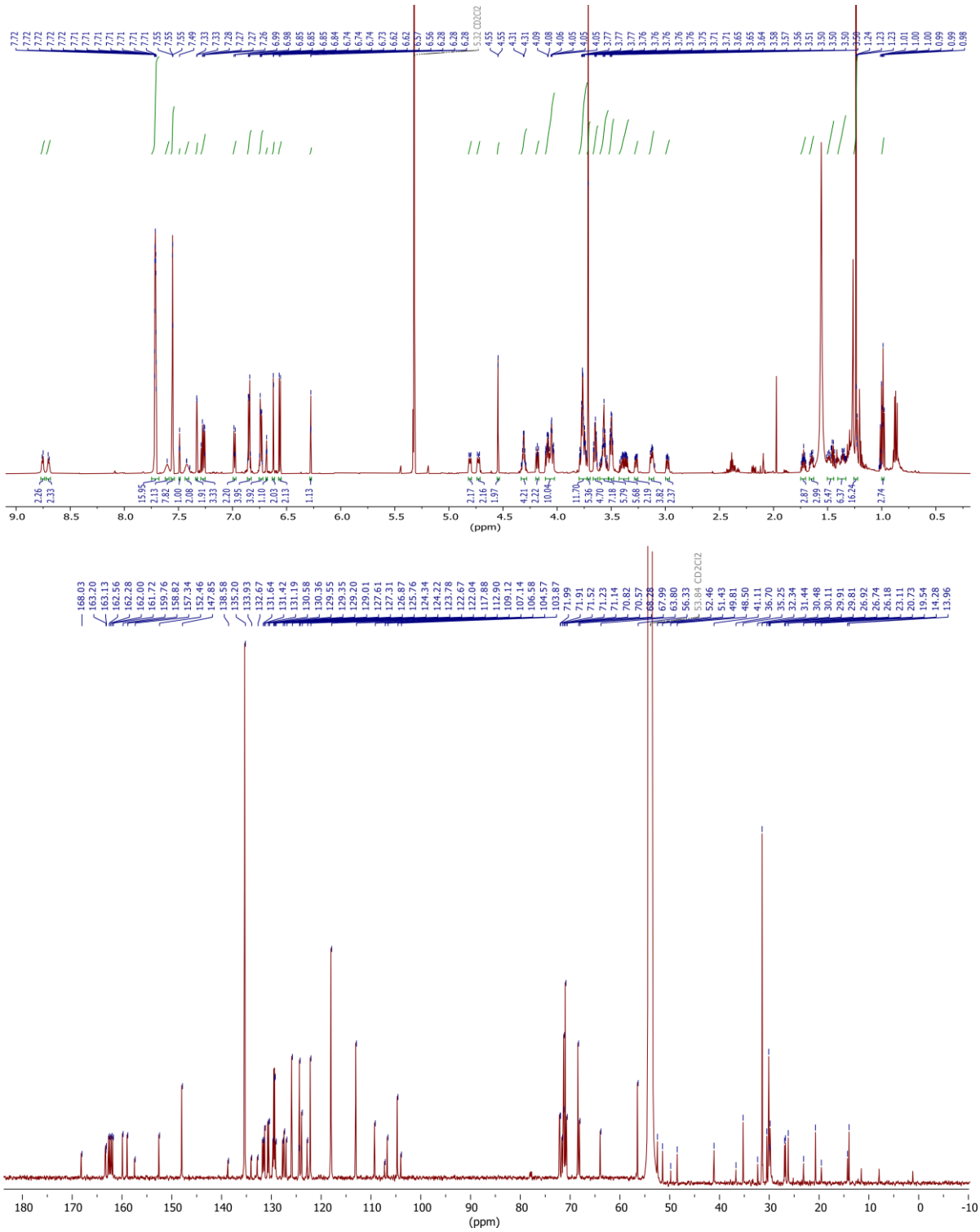

Fig. S18 ^{1}H (top) and ^{13}C (bottom) NMR spectra (700/176 MHz, CD_2Cl_2, 298 K) of [3]rotaxane **RDBC8NDIC7**.

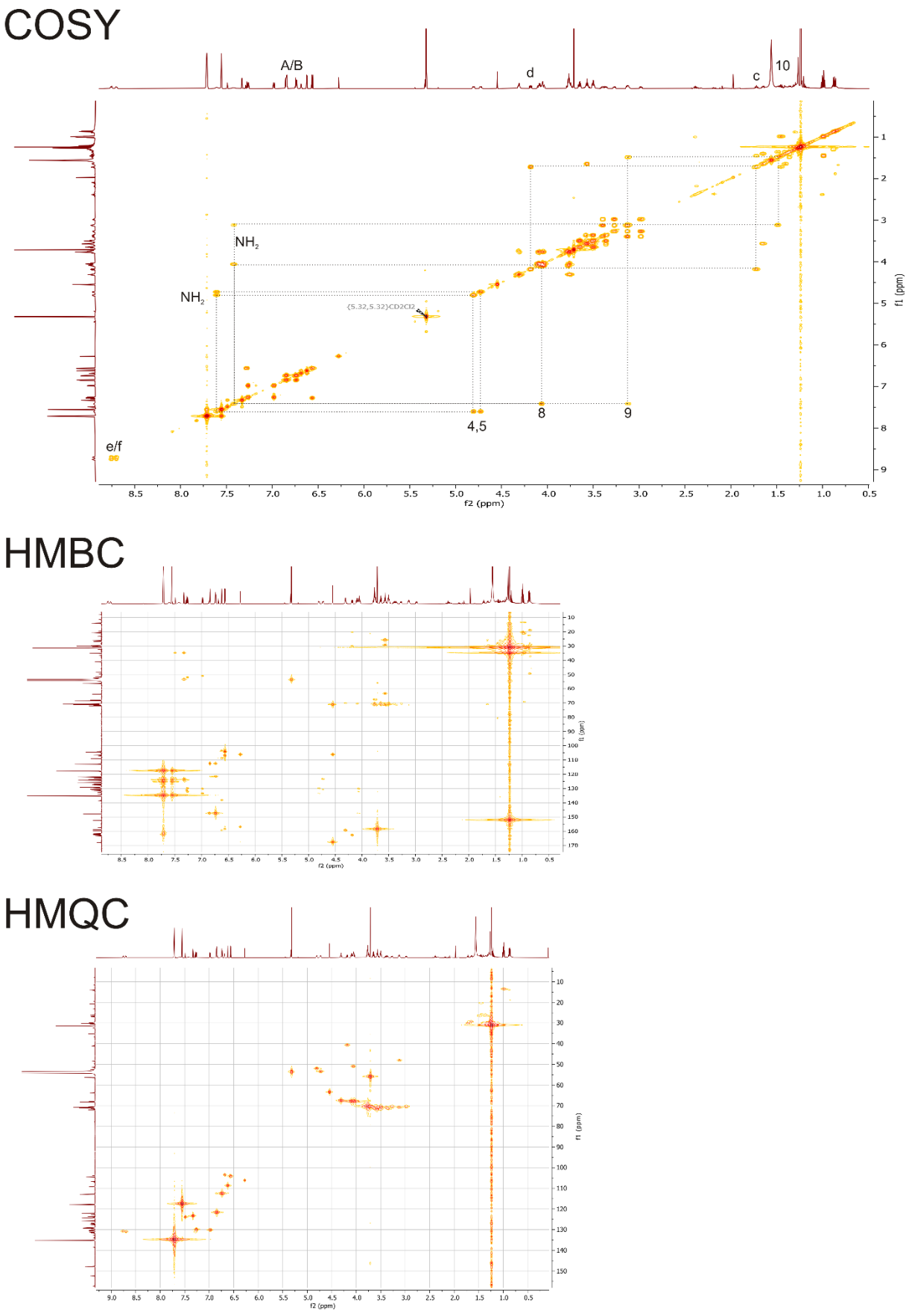

Fig. S19 COSY (top), HMBC (center) and HMQC (bottom) NMR spectra (700/176 MHz, CD_2Cl_2, 298 K) of [3]rotaxane **RDBC8NDIC7**.

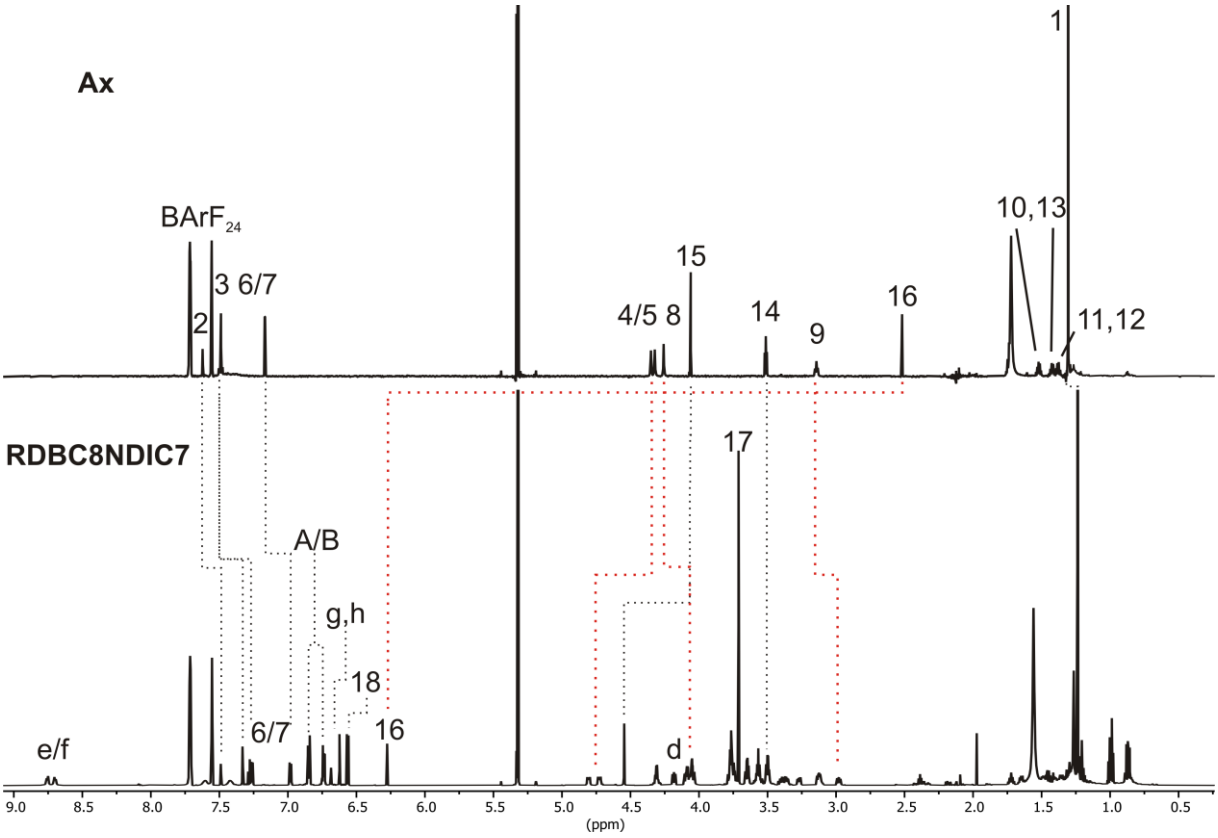

Fig. S20 [3]rotaxane **RDBC8NDIC7** (bottom) and axle **Ax** (top) NMR spectra (700 MHz, CD_2Cl_2, 298 K).

2. Isothermal titration calorimetry

ITC titrations were carried out in dry 1,2-dichloroethane (DCE) at 298 K on a TAM III microcalorimeter (Waters GmbH, TA Instruments, Eschborn, Germany). In a typical experiment, an 800 µL solution of crown ether was placed in the sample cell at a concentration of 1.1 mM, and 260 µL of a solution of the ammonium salt (8.0 mM) were put into the syringe. The titrations consisted of 32 consecutive injections of 8 µL each with a 20 min interval between injections. Heats of dilution were determined by titration of ammonium salt solutions into the sample cell containing blank solvent and were subtracted from each data set. The heat flow generated in the sample cell is measured as a differential signal between sample and reference cell. Hence, an exothermic event results in a positive and an endothermic in a negative heat flow. The data were analysed using the instrument's internal software package and fitted with a 1:1 binding model. Each titration was conducted at least three times and the measured values for K and ΔH were averaged.

Instead of divalent axle **Ax**, two monovalent model compounds **A1** and **A2** were titrated to the five macrocycles (Figure S21) of this study. Hexafluorophosphate PF_6^- was used as counter ion, as the binding constants are too high with $BArF_{24}^-$ anions to be determined with ITC. Earlier studies showed that the binding constant is roughly 15 – 20 times higher with $BArF_{24}$-anions and that trends are similar for both counterions.[3]

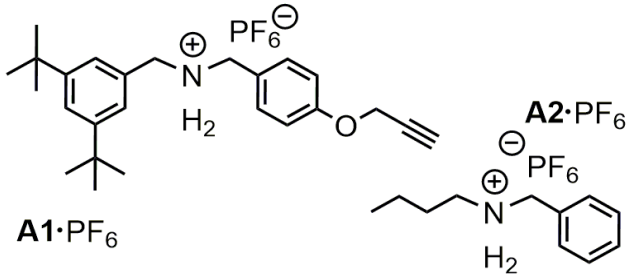

Fig. S21 Chemical structures of the monovalent model ammonium axles used to determine thermodynamic binding data for all five macrocycles.

Table S1. Thermodynamic binding data of different crown ether/secondary ammonium axle complexes obtained by ITC titrations in 1,2-dichloroethane at 298 K.

axle	macrocycle	K_a / 10^3 M^{-1}	ΔG^0 / kJ/mol	ΔH^0 / kJ/mol	$T\Delta S^0$ / kJ/mol
A2·PF_6	**BC7**[a]	1200 ± 100	-34.6 ± 0.2	-63.0 ± 0.5	-28.3 ± 0.7
	NDIC7	7.0 ± 1.0	-22.1 ± 0.2	-51.2 ± 2.0	-29.2 ± 2.2
A2·PF_6	**DBC8**[a]	480 ± 70	-32.4 ± 0.3	-60.4 ± 1.5	-28.0 ± 1.8
	NDIC8[a]	13 ± 1	-23.4 ± 0.2	-48.1 ± 1.0	-24.7 ± 1.2
	TTFC8[a]	7.0 ± 1.0	-22.1 ± 0.2	-50.3 ± 1.0	-28.3 ± 1.2
A1·PF_6	**DBC8**[a]	1300 ± 100	-34.8 ± 0.3	-60.9 ± 2.0	-26.1 ± 2.3
	NDIC8[a]	49 ± 6	-26.7 ± 0.3	-46.6 ± 2.0	-19.9 ± 2.3
	TTFC8[a]	33 ± 3	-25.7 ± 0.2	-51.5 ± 0.9	-25.9 ± 1.1

[a] Taken from a previous report.[3]

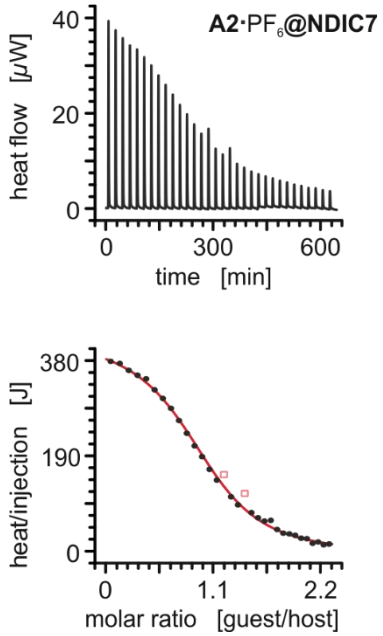

Fig. S22 Titration plots (heat flow versus time and heat/volume versus guest/host ratio) obtained from ITC experiments at 298 K in 1,2-dichloroethane: vial: **NDIC7**, syringe: axle **A2**·PF_6. Points marked with non-filled squares were not considered in the fitting process. Titration plots for the other combinations are part of a previous report. [3]

3. Heteropseudo[3]rotaxane ^{1}H NMR experiments

Equimolar solutions of divalent axle **Ax** and macrocycles gave complex ^{1}H NMR spectra. When a crown ether is bound to ammonium units, the methylene protons (H_4, H_5, H_8 and H_9) exhibit unambiguous cross coupling signals in the COSY spectrum to the corresponding ammonium protons. The characteristic shifts of these methylene protons were used to identify the pseudorotaxane species present in solution and the integrals of these signals were used to calculate the ratio of the species, which is given in percent of all identified pseudorotaxane species. Due to imprecise integration, the given percentages have experimental errors of 5%.

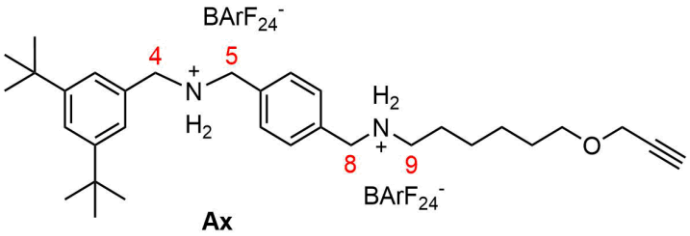

Ax

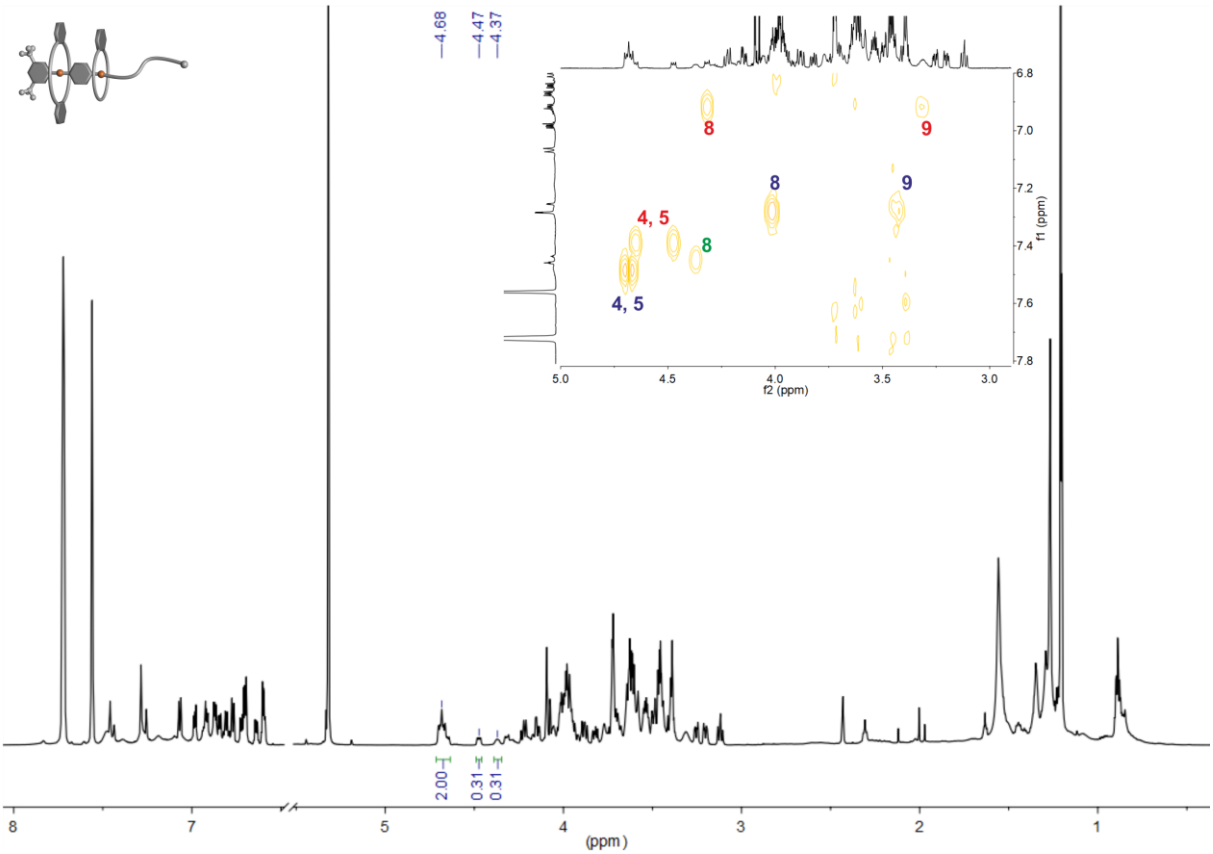

Fig. S23 ^{1}H NMR and partial COSY spectra (700 MHz, CD_2Cl_2, 298 K, 5 mM) of an equimolar solution of **Ax**, **DBC8** and **BC7** 16 d after mixing. Signals of protons corresponding to the heteropseudo[3]rotaxane **PRDBC8BC7** (58%) are labeled in blue, those corresponding to the homopseudo[3]rotaxane **PRDBC8DBC8** (21%) in red and those of the pseudo[2]rotaxane **PRBC7** (21%) in green.

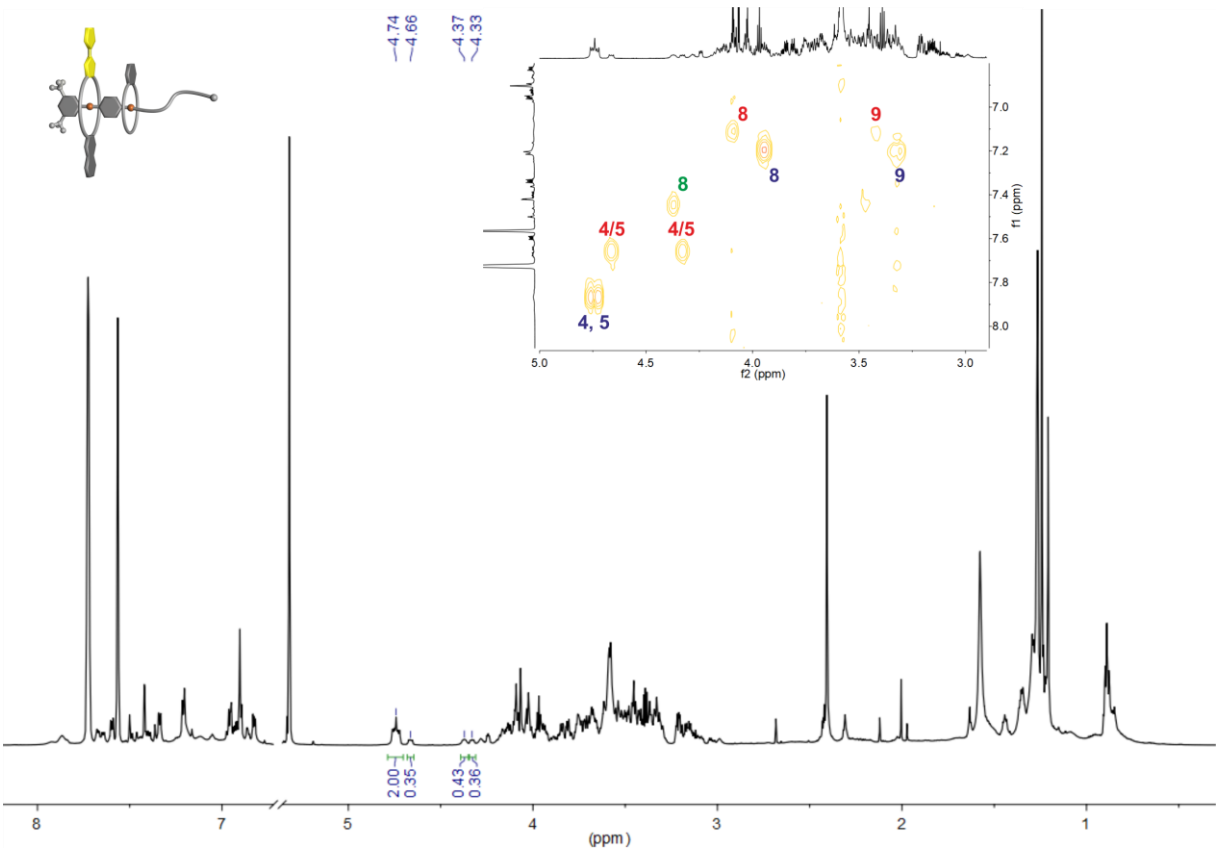

Fig. S24 ^{1}H NMR and partial COSY spectra (700 MHz, CD_2Cl_2, 298 K, 5 mM) of an equimolar solution of **Ax**, **TTFC8** and **BC7** 16 d after mixing. Signals of protons corresponding to the heteropseudo[3]rotaxane **PRTTFC8BC7** (56%) are labeled in blue, those corresponding to the homopseudo[3]rotaxane **PRTTFC8TTFC8** (20%) in red and those of the pseudo[2]rotaxane **PRBC7** (24%) in green.

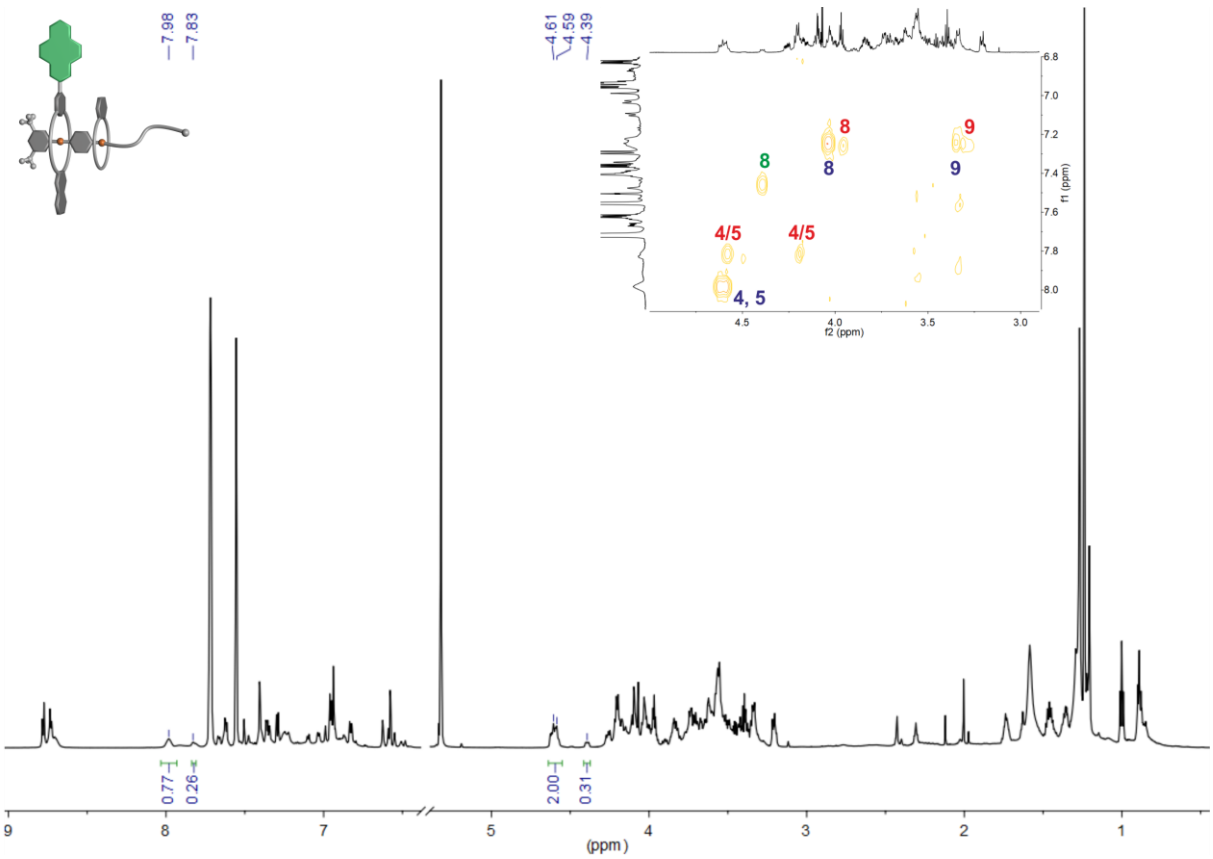

Fig. S25 ^{1}H NMR and partial COSY spectra (700 MHz, CD_2Cl_2, 298 K, 5 mM) of an equimolar solution of **Ax**, **NDIC8** and **BC7** 16 d after mixing. Signals of protons corresponding to the heteropseudo[3]rotaxane **PRNDIC8BC7** (57%) are labeled in blue, those corresponding to the homopseudo[3]rotaxane **PRNDIC8NDIC8** (19%) in red and those to the pseudo[2]rotaxane **PRBC7** (24%) in green. The methylene protons of **PRNDIC8NDIC8** overlap with **PRNDIC8BC7** and crown ether signals, therefore, the integrals of the ammonium protons were used to calculate the ratios.

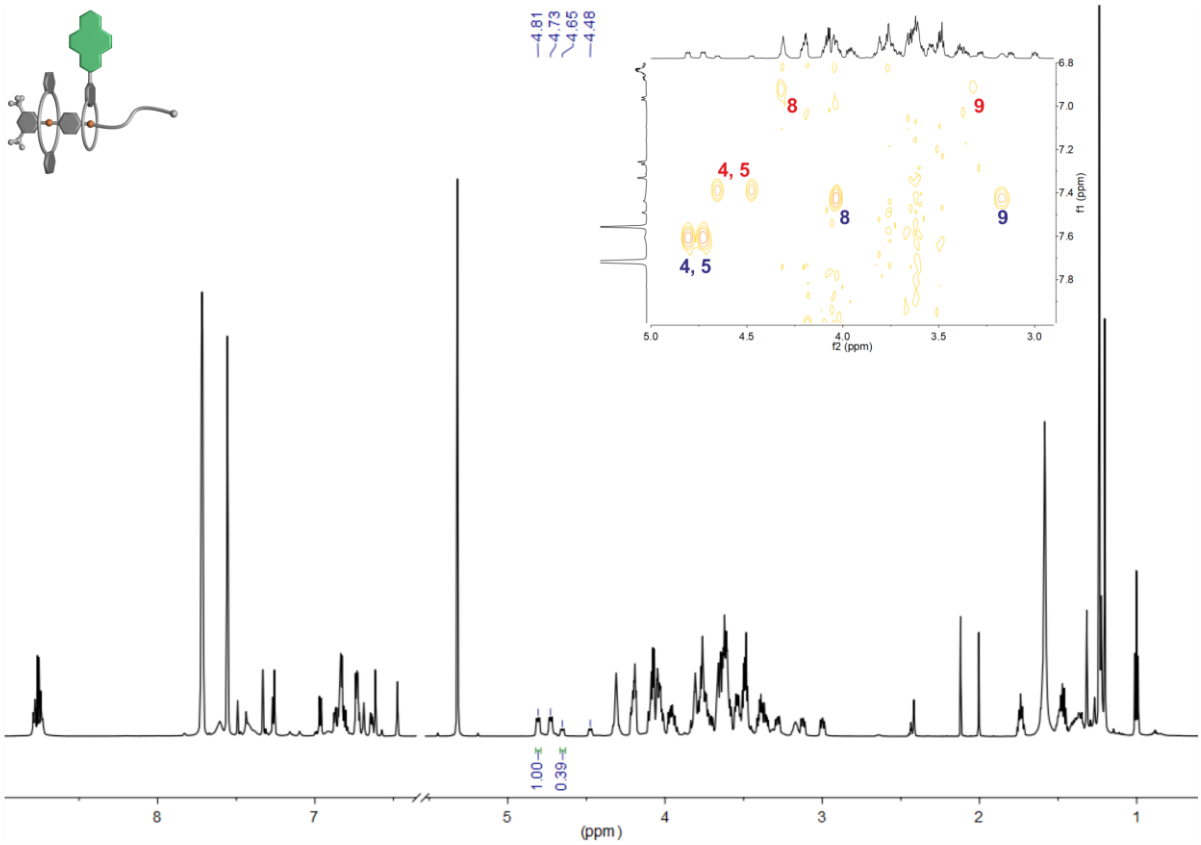

Fig. S26 ^{1}H NMR and partial COSY spectra (700 MHz, CD_2Cl_2, 298 K, 5 mM) of an equimolar solution of **Ax**, **DBC8** and **NDIC7** 16 d after mixing. Signals of protons corresponding to the heteropseudo[3]rotaxane **PRDBC8NDIC7** (72%) are labeled in blue and those corresponding to the homopseudo[3]rotaxane **PRDBC8DBC8** (28%) in red.

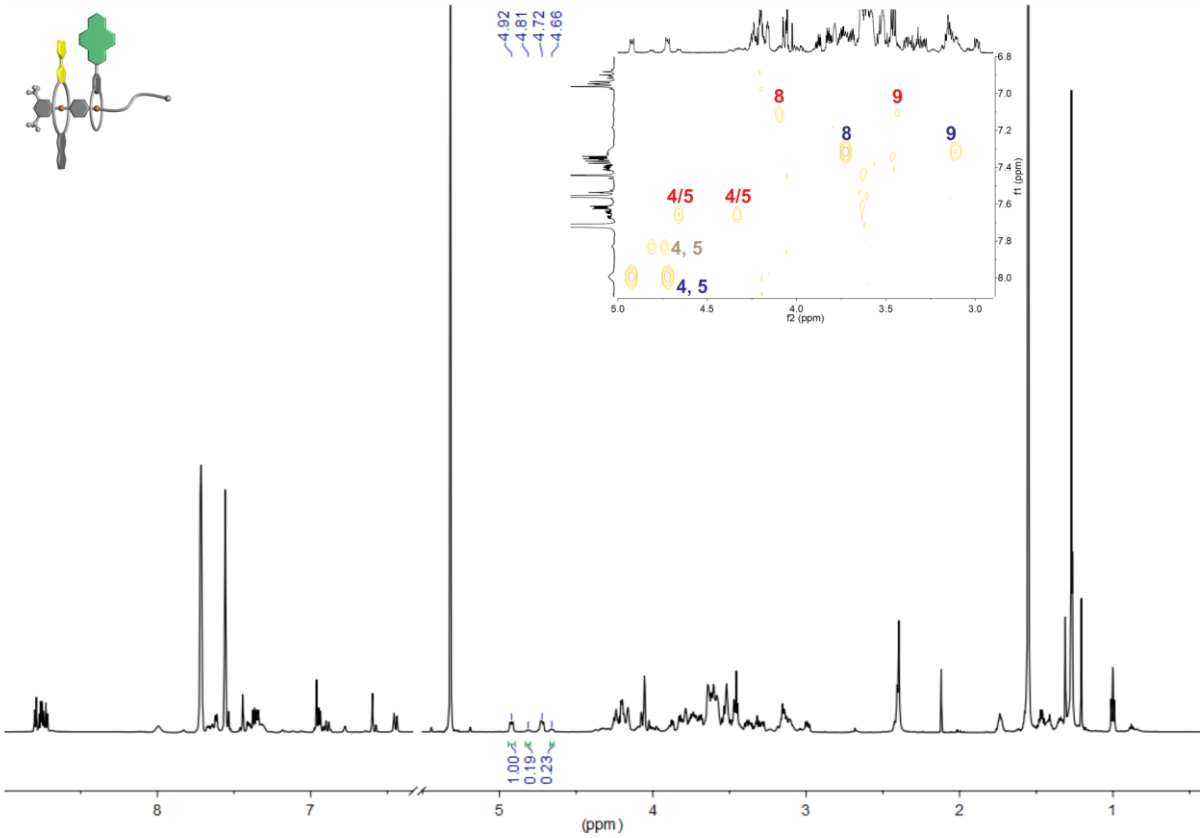

Fig. S27 ^{1}H NMR and partial COSY spectra (700 MHz, CD_2Cl_2, 298 K, 5 mM) of an equimolar solution of **Ax**, **TTFC8** and **NDIC7** 16 d after mixing. Signals of protons corresponding to the heteropseudo[3]rotaxane **PRTTFC8NDIC7** (70%) are labeled in blue, those corresponding to the homopseudo[3]rotaxane **PRTTFC8TTFC8** (16%) in red and those to the pseudo[2]rotaxane **PRTTFC8** (13%) in brown.

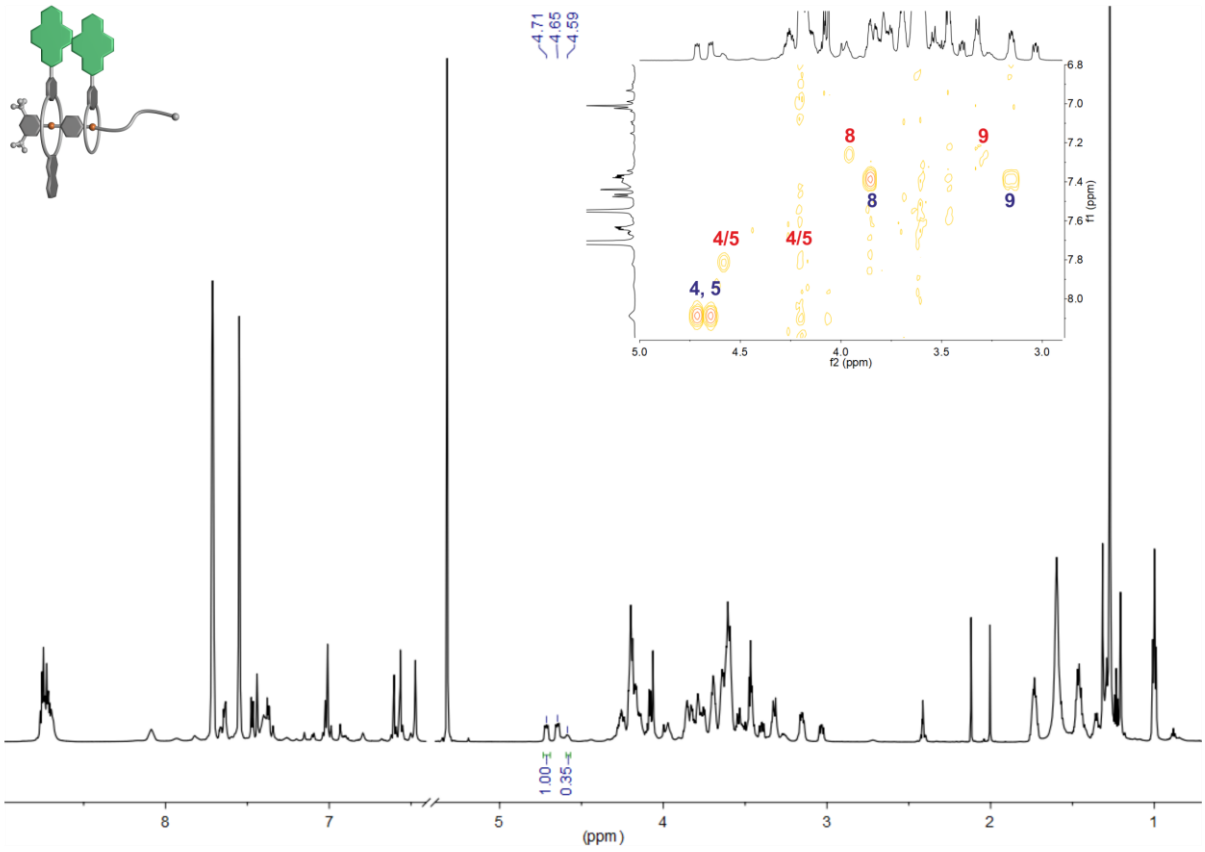

Fig. S28 ^{1}H NMR and partial COSY spectra (700 MHz, CD_2Cl_2, 298 K, 5 mM) of an equimolar solution of **Ax**, **NDIC8** and **NDIC7** 16 d after mixing. Signals of protons corresponding to the Heteropseudo[3]rotaxane **PRNDIC8NDIC7** (74%) are labeled in blue and those corresponding to the Homopseudo[3]rotaxane **PRNDIC8NDIC8** (26%) in red.

4. Tandem mass spectrometry

A Synapt G2-S HDMS (Waters Co., Milford, MA, USA) instrument with a quadrupole-time-of-flight high-resolution mass analyser was used to perform electrospray ionization tandem mass spectrometry. One of the following ionization conditions were used: a) For pseudorotaxane mixtures in dichloromethane or acetonitrile: flow rate 8 µL min^{-1}, capillary voltage 1.5 or 2.5 kV, sample cone voltage 34 V, source offset 54 V, source temperature 100 °C, desolvation temperature 220 °C, nebulizer gas 3.0 bar, desolvation gas flow 450 L h^{-1}. b) For sample solutions of the isolated rotaxane in acetonitrile: flow rate 8 µL min^{-1}, capillary voltage 2.5 kV, sample cone voltage 80 V, source offset 54 V, source temperature 100 °C, desolvation temperature 220 °C, nebulizer gas 2.5 bar, desolvation gas flow 700 L h^{-1}.

For collision-induced dissociation (CID) experiments of mass-selected ions, N_2 was used as the collision gas. Fragmentation experiments were conducted in the trap cell of the Synapt G2-S HDMS instrument with collision energies of 3 – 55 V. For the isolated rotaxane, 5 V steps were used and for the pseudorotaxane mixtures 3 V steps. Data acquisition and processing was carried out using MassLynx™ (version 4.1).

For plotting of the survival yield curves the spectra were centroided. For each spectrum at different collision voltages, the intensity of the ion with the selected mass was divided by the total ion intensity (only fragments with an intensity above 1% were considered) and then plotted against the collision voltage. Fitting was done with applying a sigmoidal Boltzmann function using Origin Pro 2020 to obtain the 50% survival yield voltages.

For time-dependent measurements, a solution of the axle **Ax** and one kind of crown[8] ether was prepared and stirred for 1 h (10 mM, 1,2-dichloroethane, 20 °C). One kind of crown[7] ether was added to yield an equimolar solution of 5 mM. The pseudorotaxane equilibrium in solution was monitored by HRMS. Prior to each measurement the sample was diluted to a concentration of 2.5 µM using dichloromethane. The absolute intensities of the ions do not necessarily correlate with the concentrations of the species in solution, as the ionization efficiencies of the involved species may differ significantly. Especially, all ions involving **BC7** ionize very efficiently at the conditions used in the experiment. For a better visibility of the signals of interest the mass range of these ions (m/z < 450) is not shown. Nevertheless, a good qualitative picture may be derived from these experiments.

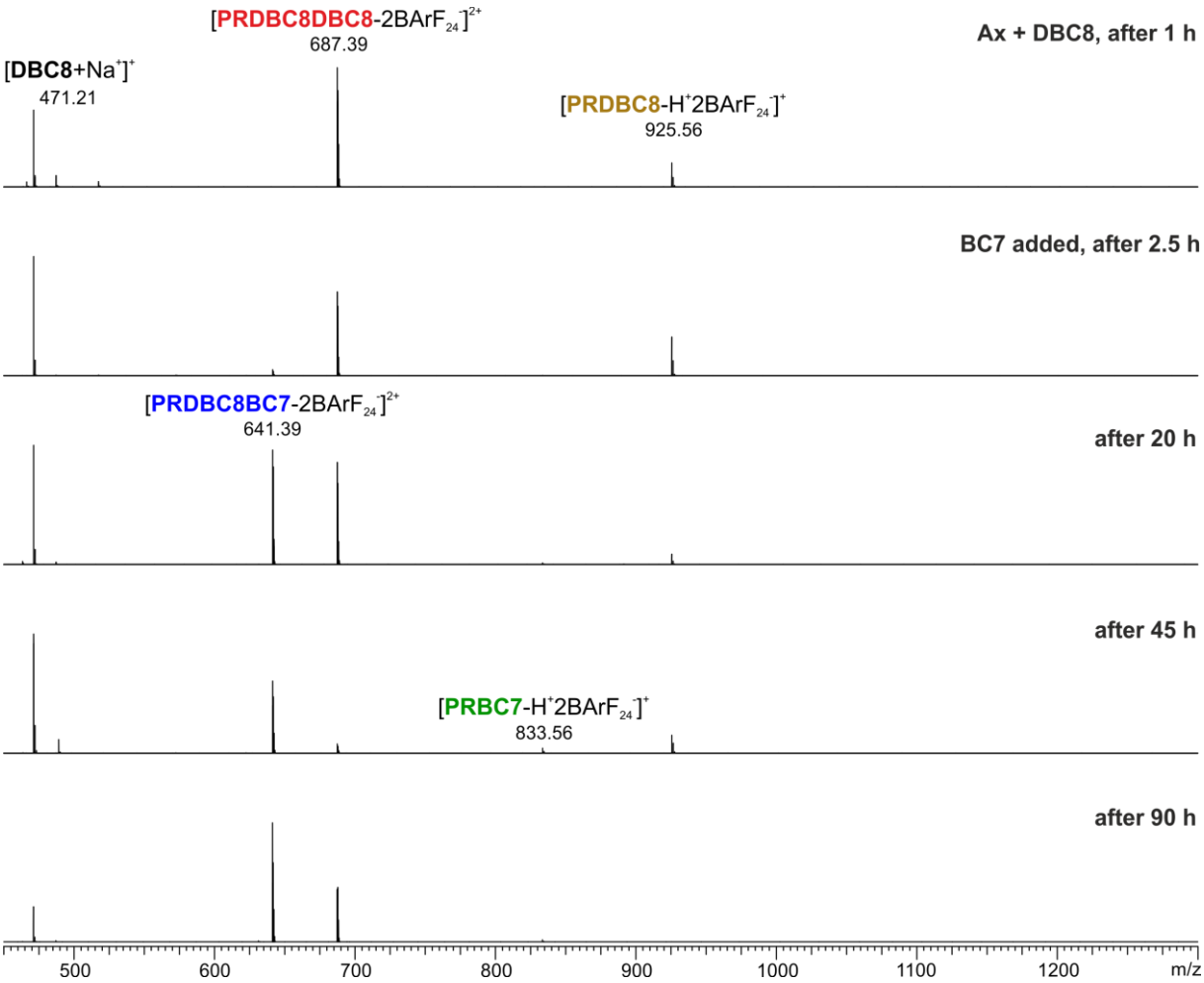

Figure S29 ESI-Q-TOF-HRMS spectra of a solution containing **Ax**, **DBC8** and **BC7** at different times. Prior to each measurement the solution was diluted to 2.5 µM using dichloromethane. Signals belonging to the heteropseudo[3]rotaxane **PRDBC8BC7** are labeled in blue, to the homopseudo[3]rotaxane **PRDBC8DBC8** in red, to the pseudo[2]rotaxane **PRDBC8** in brown and to the pseudo[2]rotaxane **PRBC7** in green.

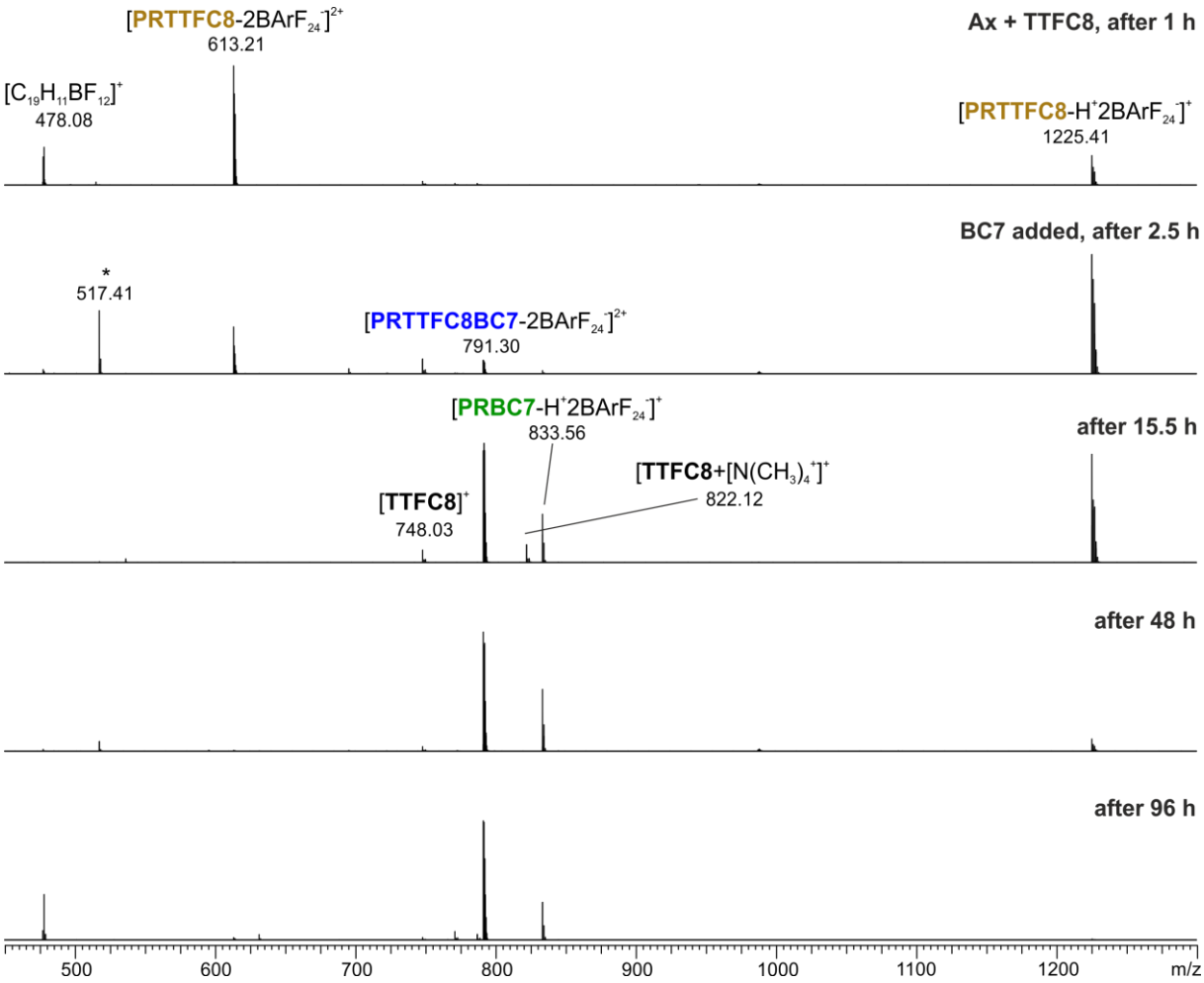

Figure S30 ESI-Q-TOF-HRMS spectra of a solution containing **Ax**, **TTFC8** and **BC7** at different times. Prior to each measurement the solution was diluted to 2.5 µM using dichloromethane. Signals belonging to the heteropseudo[3]rotaxane **PRTTFC8BC7** are labeled in blue, to the pseudo[2]rotaxane **PRTTFC8** in brown and to the pseudo[2]rotaxane **PRBC7** in green. The ion m/z 478.08 represents a fragment of the $BArF_{24}^-$ counterion. Peak marked with a * are impurities present in the instrument.

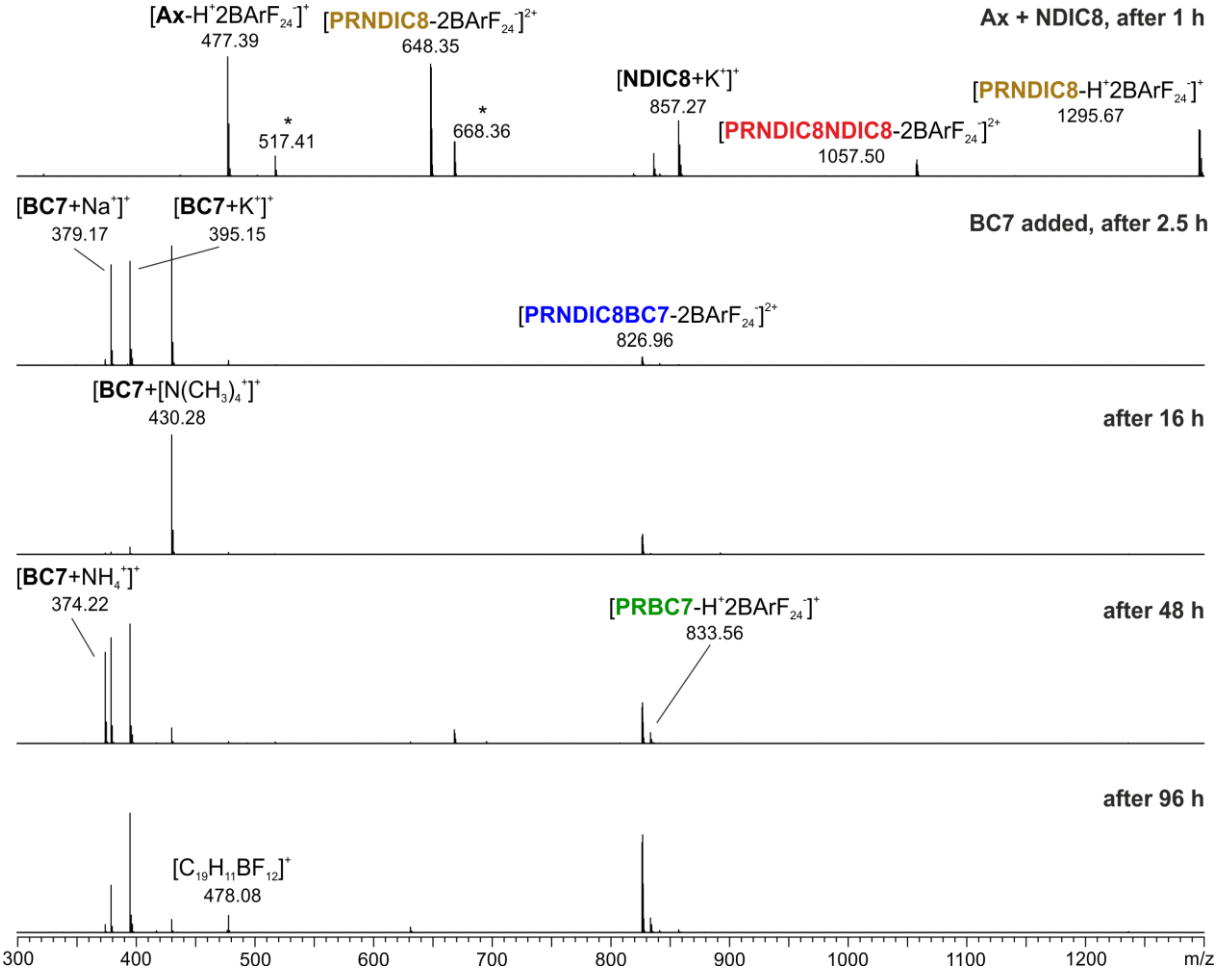

Figure S31 ESI-Q-TOF-HRMS spectra of a solution containing **Ax**, **NDIC8** and **BC7** at different times. Prior to each measurement the solution was diluted to 2.5 µM using dichloromethane. Signals belonging to the heteropseudo[3]rotaxane **PRNDIC8BC7** are labeled in blue, to the homopseudo[3]rotaxane **PRNDIC8NDIC8** in red, to the pseudo[2]rotaxane **PRNDIC8** in brown and to the pseudo[2]rotaxane **PRBC7** in green. The ion m/z 478.08 represents a fragment of the $BArF_{24}$-counterion. Peaks marked with a * are impurities present in the instrument.

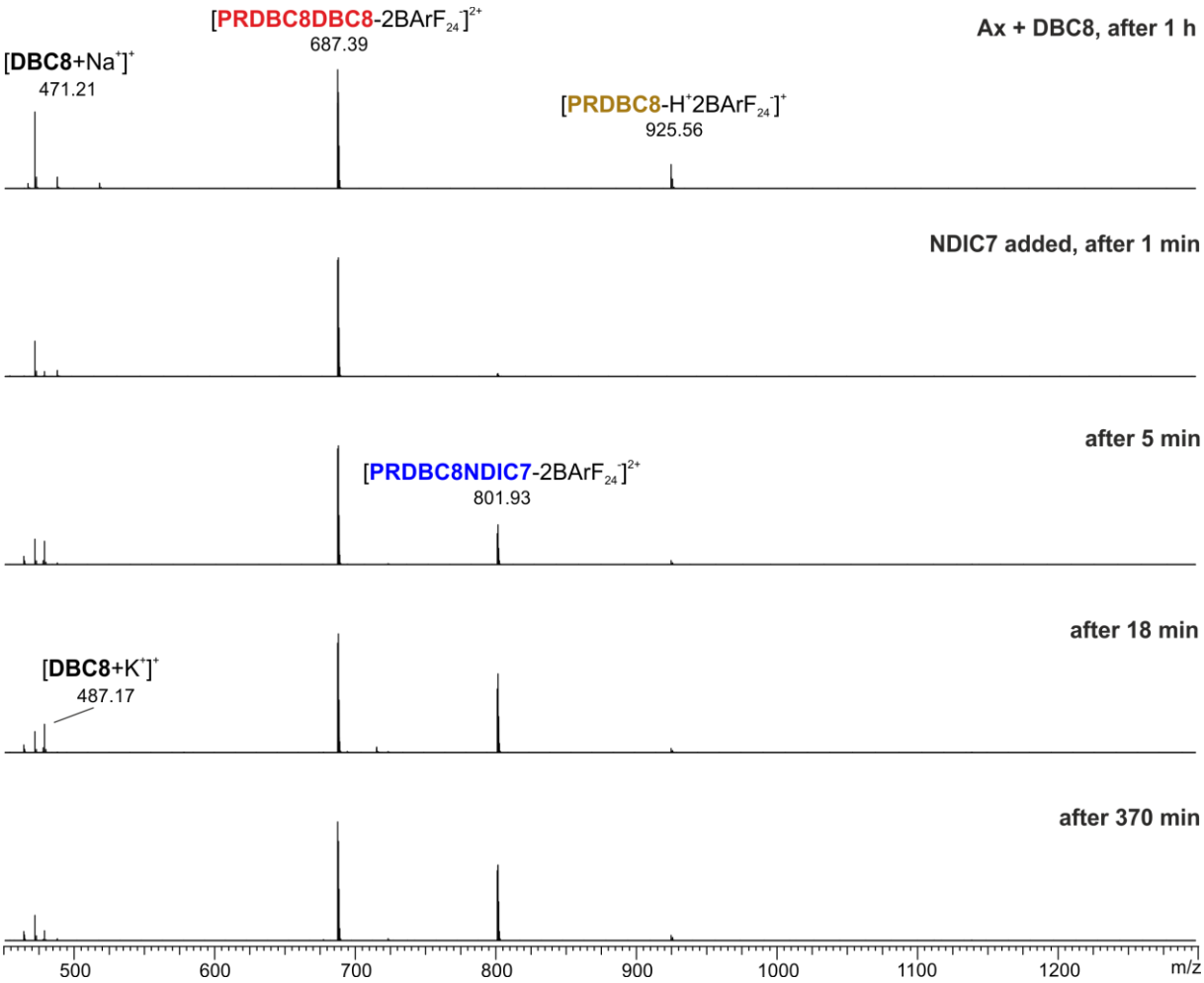

Figure S32 ESI-Q-TOF-HRMS spectra of a solution containing **Ax**, **DBC8** and **NDIC7** at different times. Prior to each measurement the solution was diluted to 2.5 µM using dichloromethane. Signals belonging to the heteropseudo[3]rotaxane **PRDBC8NDIC7** are labeled in blue, to the homopseudo[3]rotaxane **PRDBC8DBC8** in red and to the pseudo[2]rotaxane **PRDBC8** in brown.

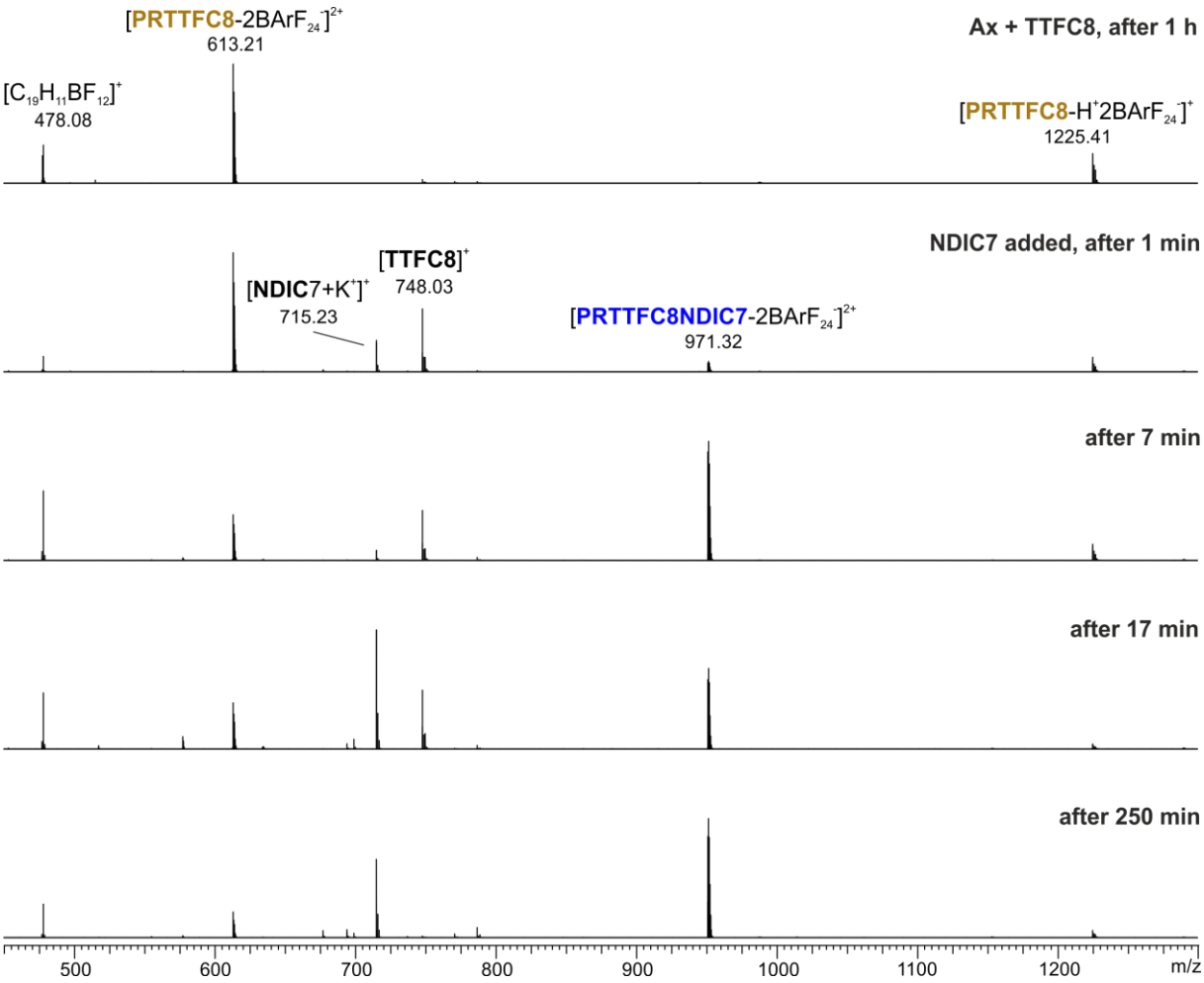

Figure S33 ESI-Q-TOF-HRMS spectra of a solution containing **Ax**, **TTFC8** and **NDIC7** at different times. Prior to each measurement the solution was diluted to 2.5 µM using dichloromethane. Signals belonging to the heteropseudo[3]rotaxane **PRTTFC8NDIC7** are labeled in blue and to the pseudo[2]rotaxane **PRTTFC8** in brown. The ion m/z 478.08 represents a fragment of the $BArF_{24}$-counterion.

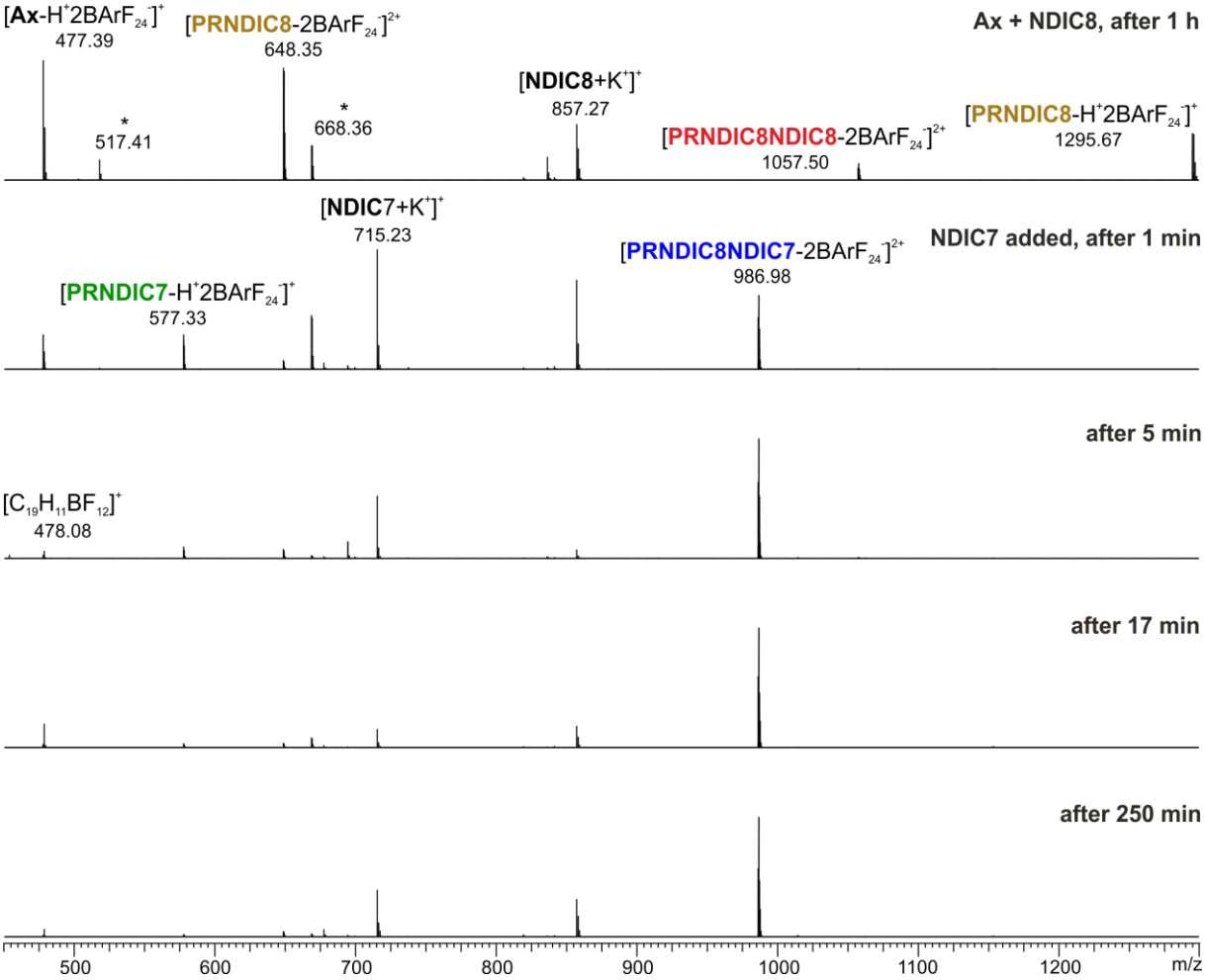

Figure S34 ESI-Q-TOF-HRMS spectra of a solution containing **Ax**, **NDIC8** and **NDIC7** at different times. Prior to each measurement the solution was diluted to 2.5 µM using dichloromethane. Signals belonging to the heteropseudo[3]rotaxane **PRNDIC8NDIC7** are labeled in blue, to the homopseudo[3]rotaxane **PRNDIC8NDIC8** in red, to the pseudo[2]rotaxane **PRNDIC8** in brown and to the pseudo[2]rotaxane **PRBC7** in green. The ion m/z 478.08 represents a fragment of the $BArF_{24}$-counterion. Peaks marked with a * are impurities present in the instrument.

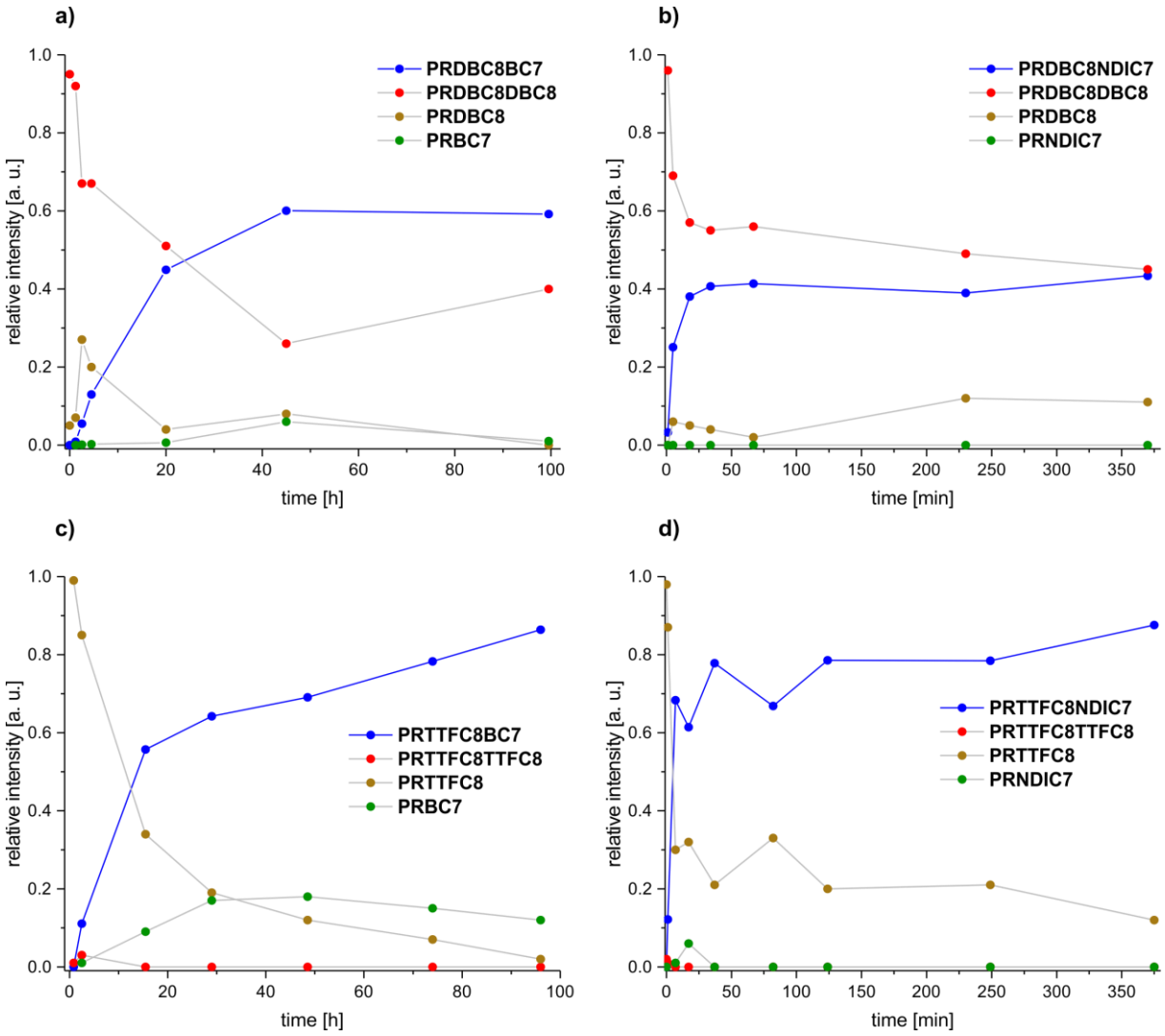

Figure S35 Plots summarising the changes of the hetero- and homopseudo[3]rotaxanes signal intensities and those of their pseudorotaxane precursors over reaction time from equimolar solutions of **Ax**, crown[8] ether and crown[7] ether at 20 °C. The relative intensities are taken from ESI-Q-TOF-HRMS spectra. The absolute intensities of the ions are not representative for the concentrations of the species in solution, as the ionization efficiencies of the involved species differ significantly. For full spetra see above.

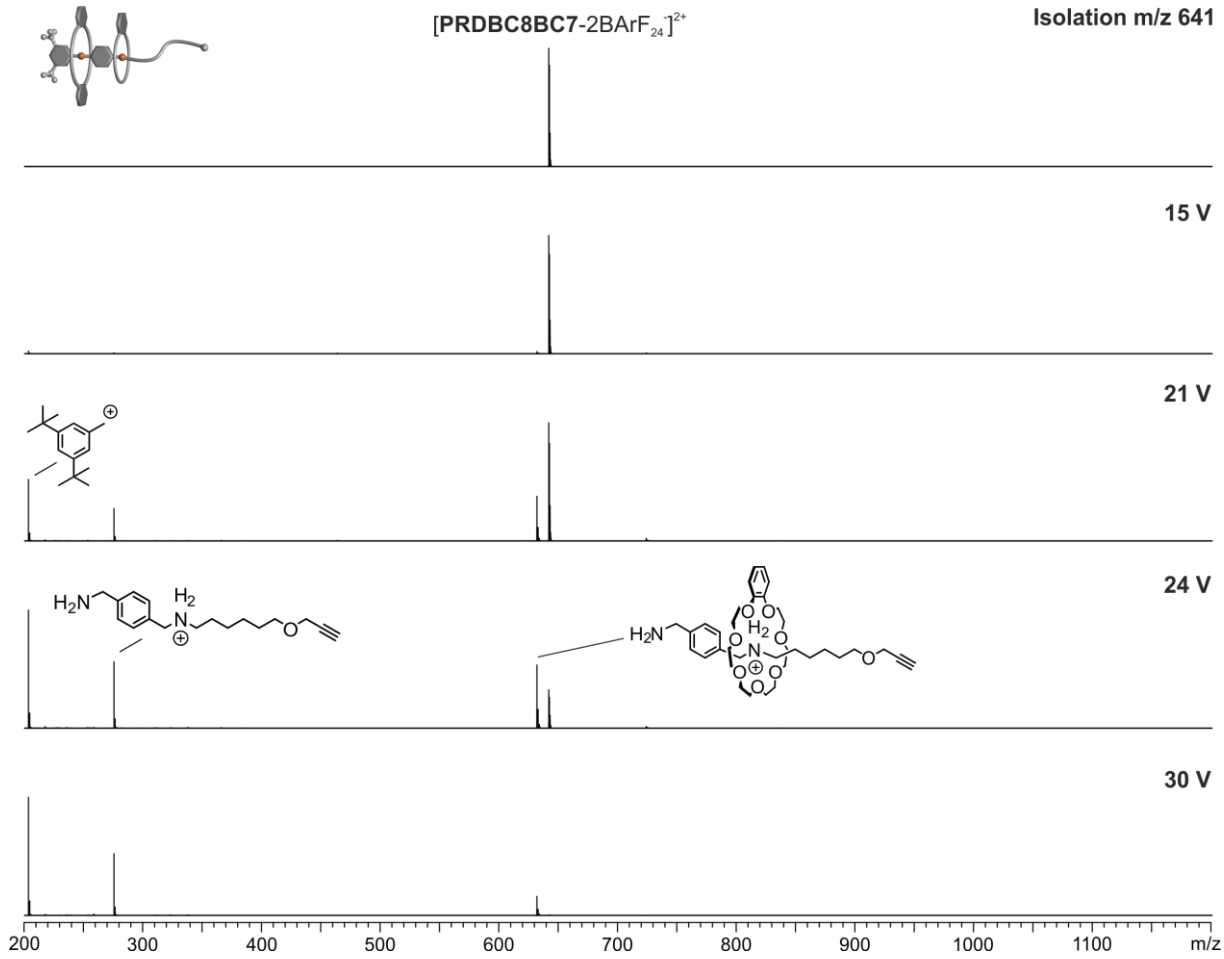

Figure S36 CID experiment with mass-selected [**PRDBC8BC7**-2BArF$_{24}^-$]$^{2+}$ ions at *m/z* 641 obtained from a CH_2Cl_2 solution (2.5 µM). Due to the remarkably strong binding of **BC7**, the first fragmentation at high collision voltages is the cleavage of a covalent bond in the axle rather than dissociation of the crown ether. The loss of **DBC8** upon axle cleavage at the western ammonium station evidences the desired sequence in the **PRDBC8BC7** pseudo[3]rotaxane.

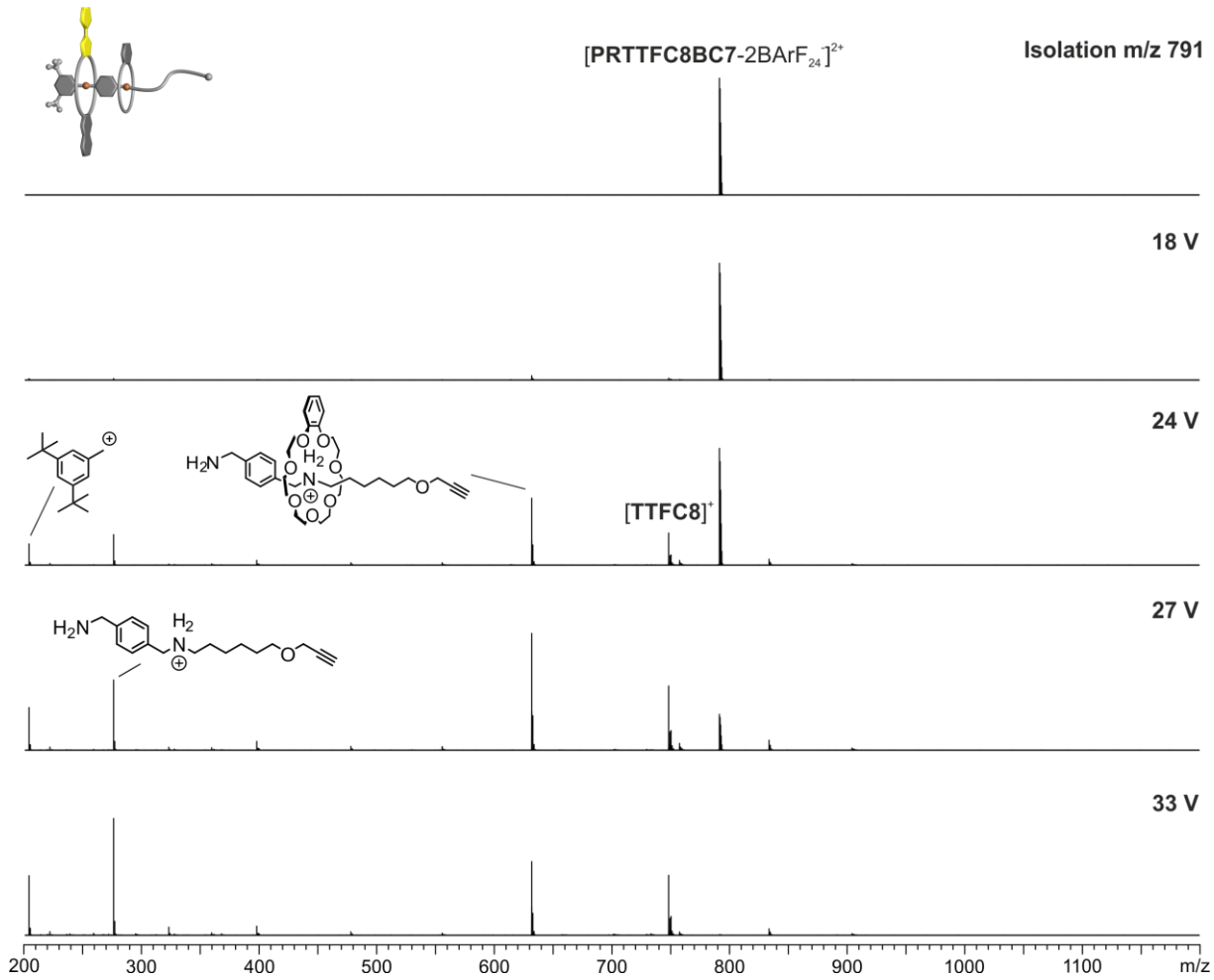

Figure S37 CID experiment with mass-selected [**PRTTFC8BC7**-2BArF$_{24}$$^{-}$]$^{2+}$ ions at *m/z* 791 obtained from a CH_2Cl_2 solution (2.5 μM). Due to the remarkably strong binding of **BC7**, the first fragmentation at high collision voltages is the cleavage of a covalent bond in the axle rather than dissociation of the crown ether. The loss of **TTFC8** upon cleavage of the axle at the western ammonium station evidences the desired sequence in the **PRTTFC8BC7** pseudo[3]rotaxane. The appearance of **TTFC8^{+}** as a fragment has been observed for other mechanically interlocked structures containing **TTFC8.**[1, 8]

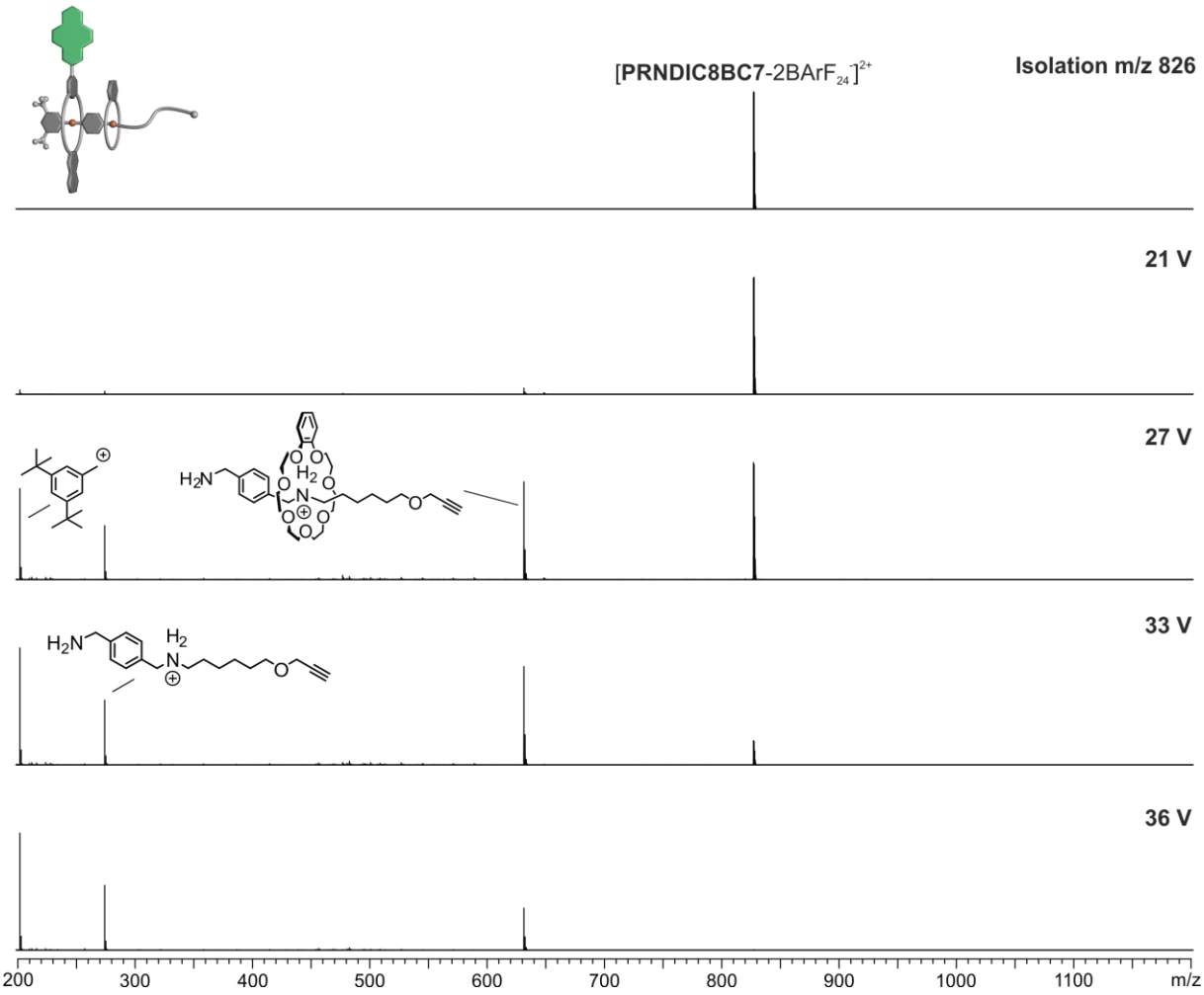

Figure S38 CID experiment with mass-selected [**PRNDIC8BC7**-2BArF$_{24}$]$^{2+}$ ions at *m/z* 826 obtained from a CH_2Cl_2 solution (2.5 µM). Due to the remarkably strong binding of **BC7**, the first fragmentation at high collision voltages is the cleavage of a covalent bond in the axle rather than dissociation of the crown ether. The loss of **NDIC8** upon cleavage of the axle at the western ammonium station evidences the desired sequence in the **PRNDIC8BC7** pseudo[3]rotaxane.

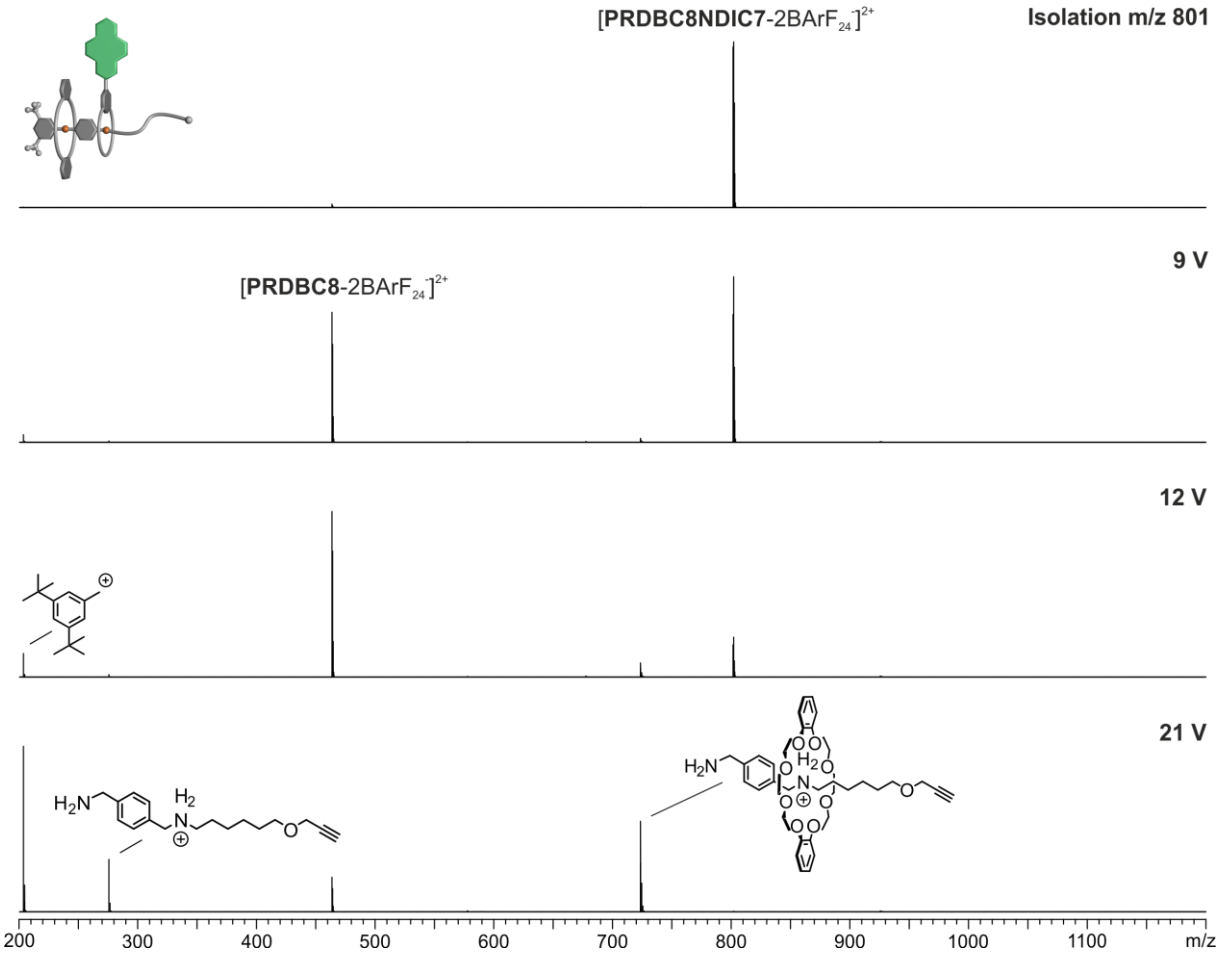

Figure S39 CID experiment with mass-selected [**PRDBC8NDIC7**-2BArF$_{24}^-$]$^{2+}$ ions at *m/z* 801 obtained from a CH_2Cl_2 solution (2.5 µM). The first fragmentation step at lower collision energies is the cleaving of the non-covalent bond to **NDIC7** to form the pseudo[2]rotaxane **PRDBC8**, which evidences the desired sequence in the **PRDBC8NDIC7** pseudo[3]rotaxane.

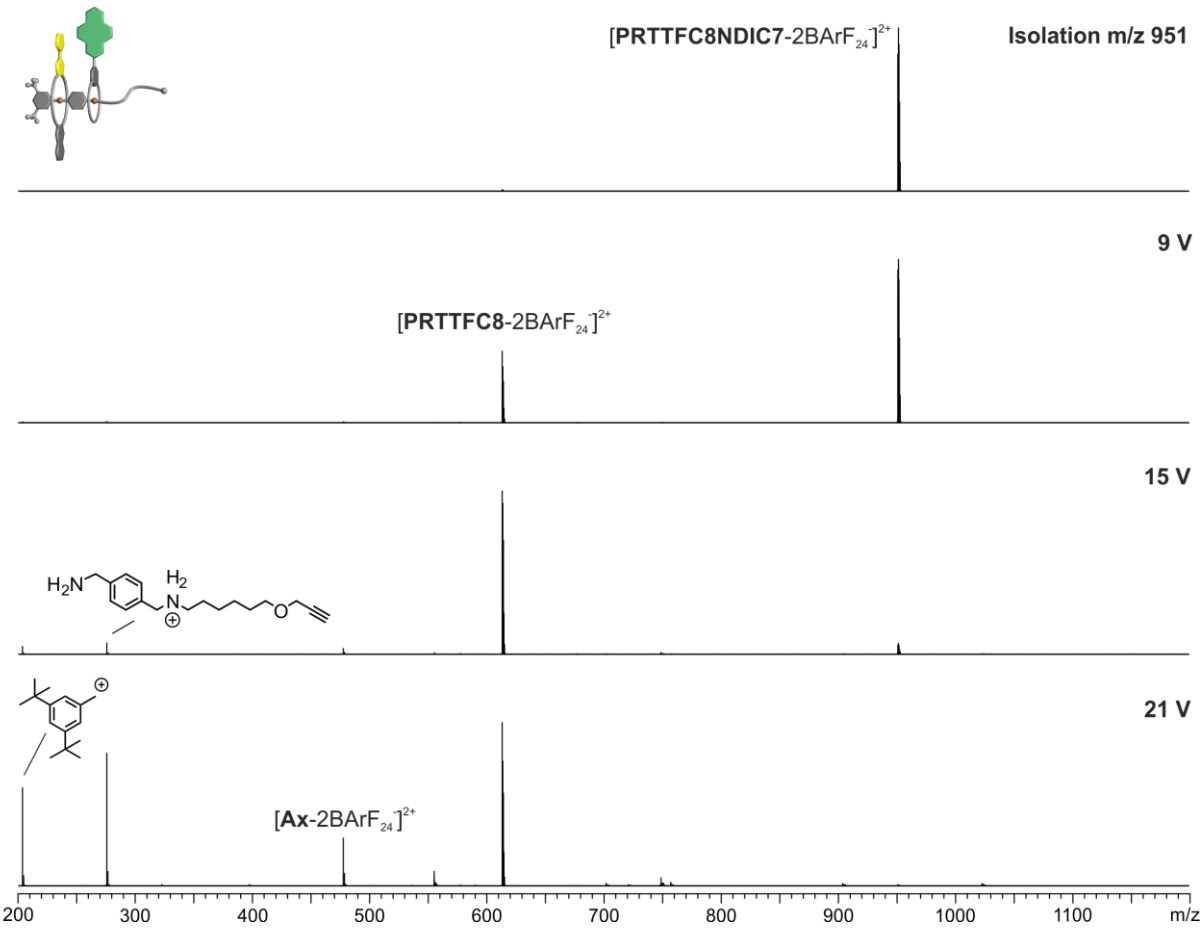

Figure S40 CID experiment with mass-selected [**PRTTFC8NDIC7**-2BArF$_{24}^-$]$^{2+}$ ions at *m/z* 951 obtained from a CH_2Cl_2 solution (2.5 μM). The first fragmentation step at lower collision energies is the cleavage of the non-covalent bond to **NDIC7** to form the pseudo[2]rotaxane **PRTTFC8**, which evidences the desired sequence in the **PRTTFC8NDIC7** pseudo[3]rotaxane.

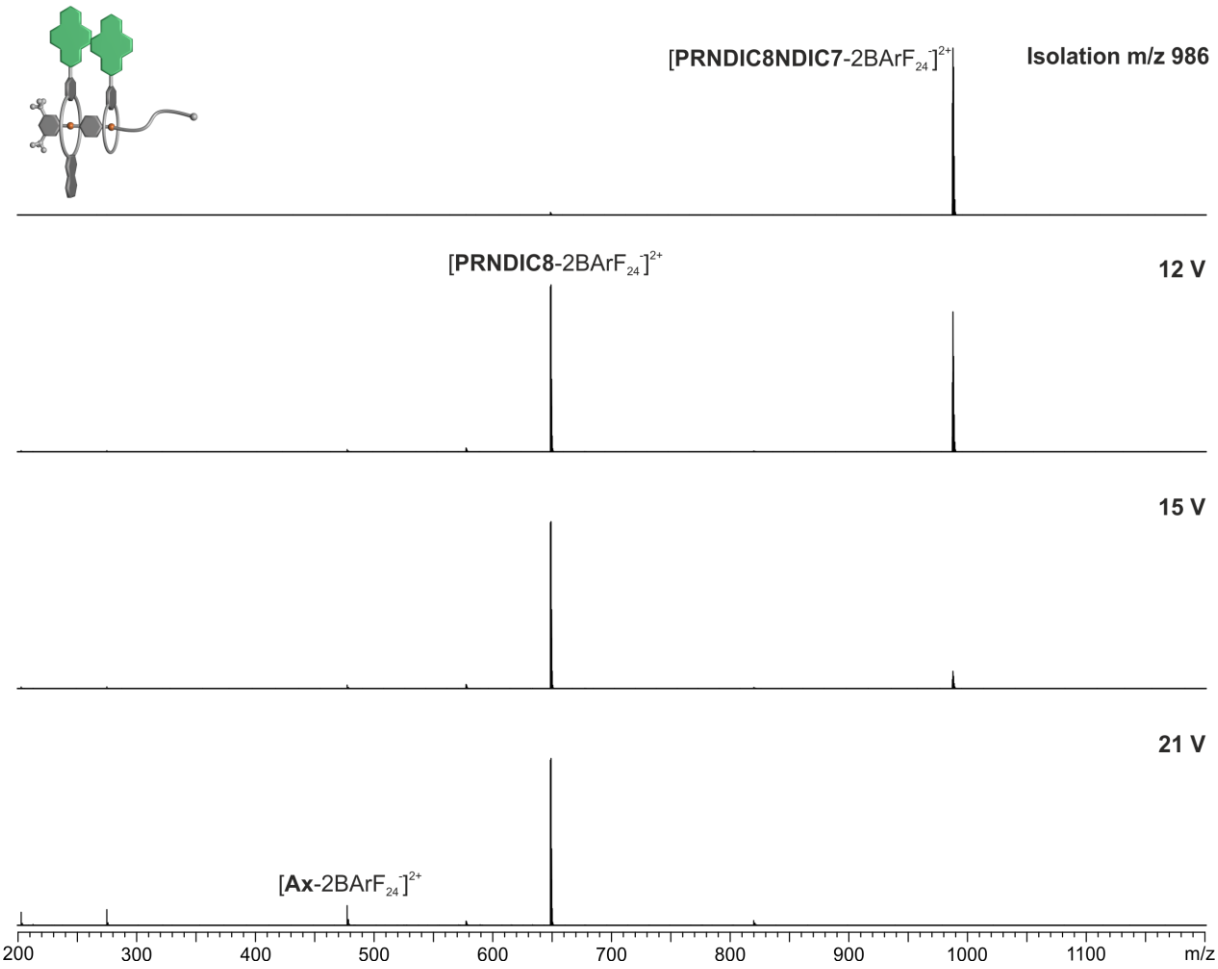

Figure S41 CID experiment with mass-selected [**PRNDIC8NDIC7**-2BArF$_{24}^-$]$^{2+}$ ions at *m/z* 951 obtained from a CH_2Cl_2 solution (2.5 µM). The first fragmentation step at lower collision energies is the cleavage of the non-covalent bond to **NDIC7** to form the pseudo[2]rotaxane **PRNDIC8**, which evidences the desired sequence in the **PRNDIC8NDIC7** pseudo[3]rotaxane.

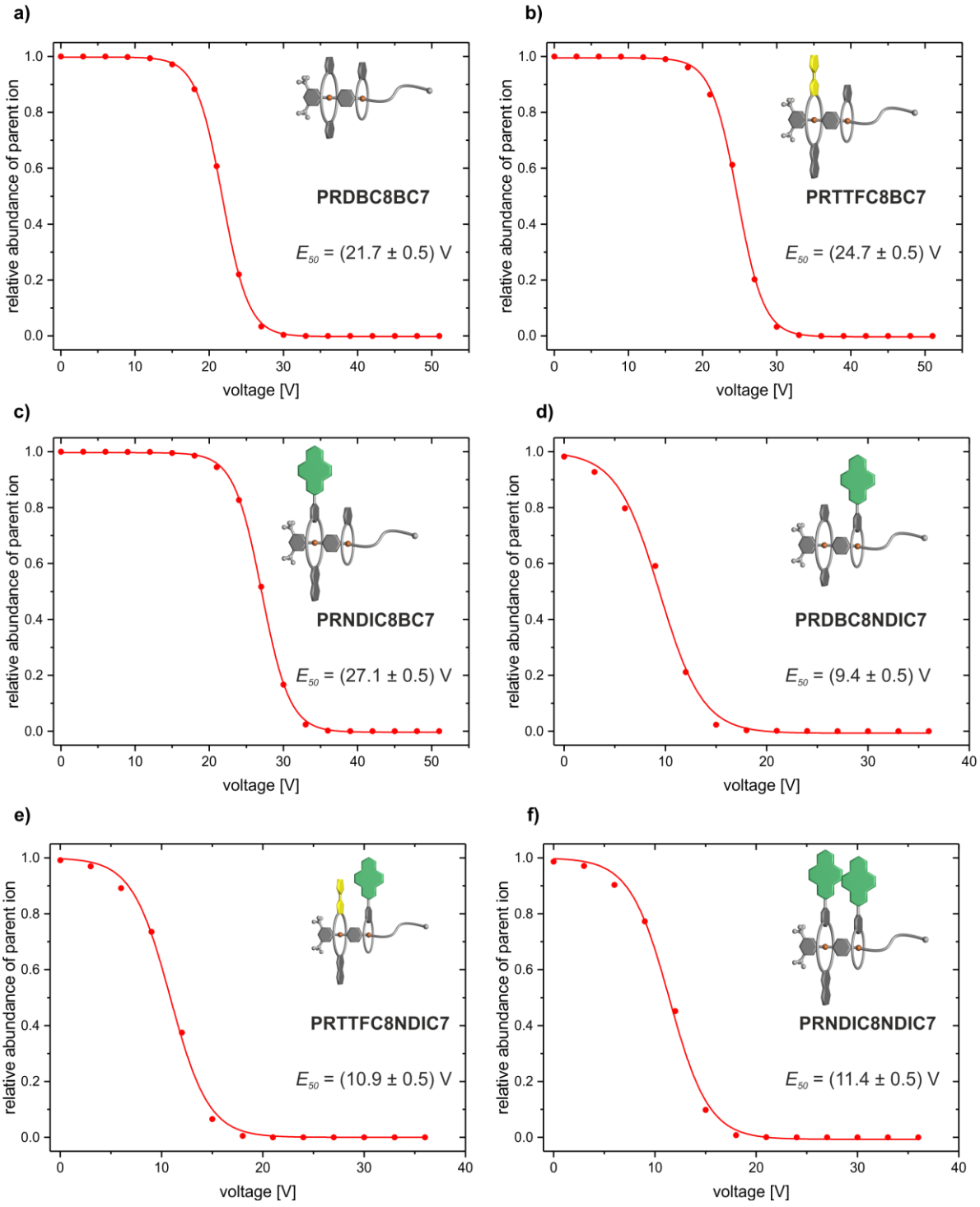

Figure S42 Survival yield curves for the different hetero[3]pseudorotaxane under study. Dications of hetero[3]pseudorotaxanes were mass-selected and fragmented at increasing collision voltages. The solid lines represent a sigmoidal fitting to determine 50% survival yield voltages.

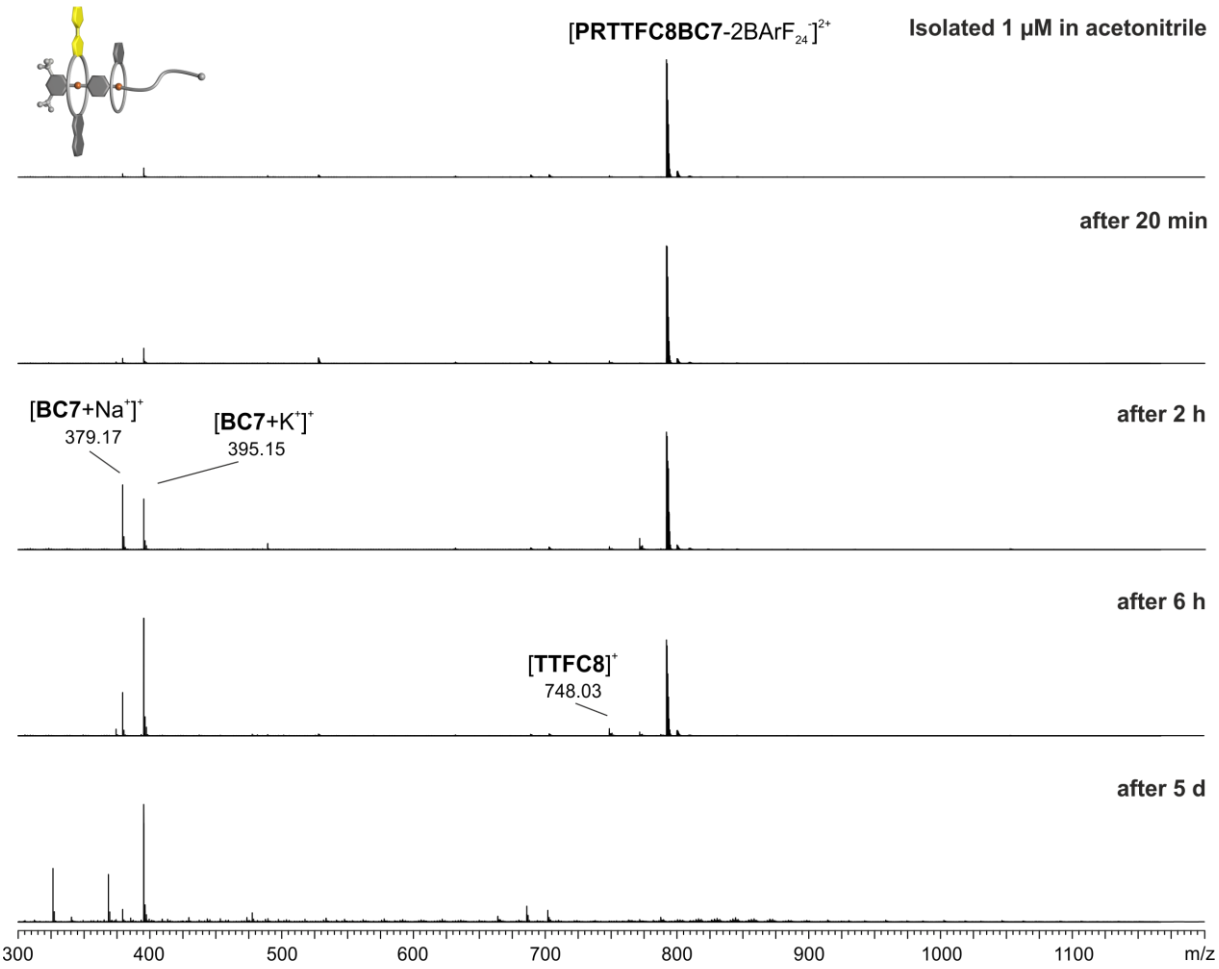

Figure S43 ESI-Q-TOF-HRMS spectra of a **PRTTFC8BC7** solution in acetonitrile at different times (1 µM, 25°C). The pronounced peak of **PRTTFC8BC7** after 6 h indicates the kinetic hinderance for dethreading of **BC7** and the kinetic stability of the pseudorotaxane **PRTTFC8BC7** in acetonitrile at low concentrations.

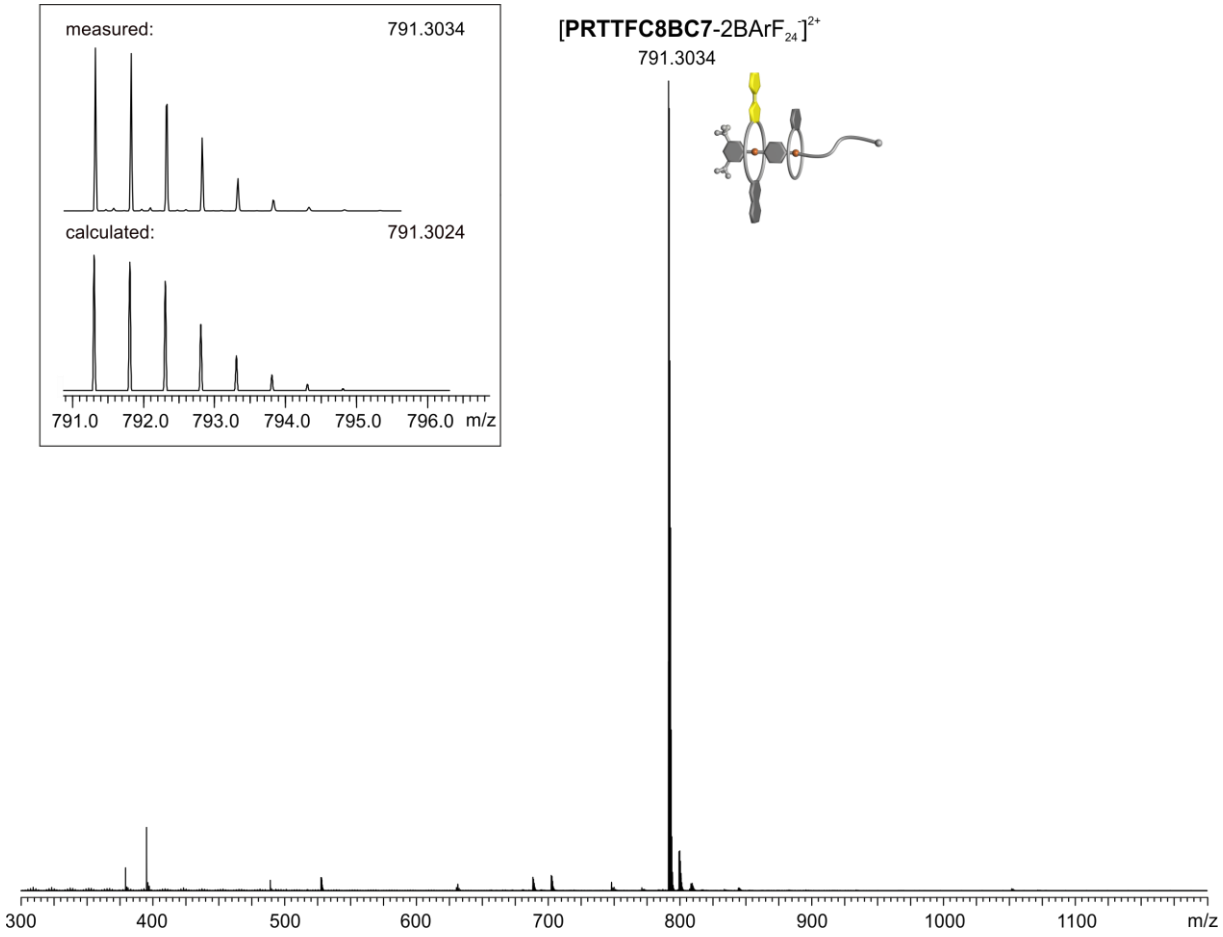

Figure S44 ESI-Q-TOF-HRMS spectrum of **PRTTFC8BC7** (1 µM in acetonitrile) isolated after column chromatography; inset: comparison of measured and calculated isotopic patterns.

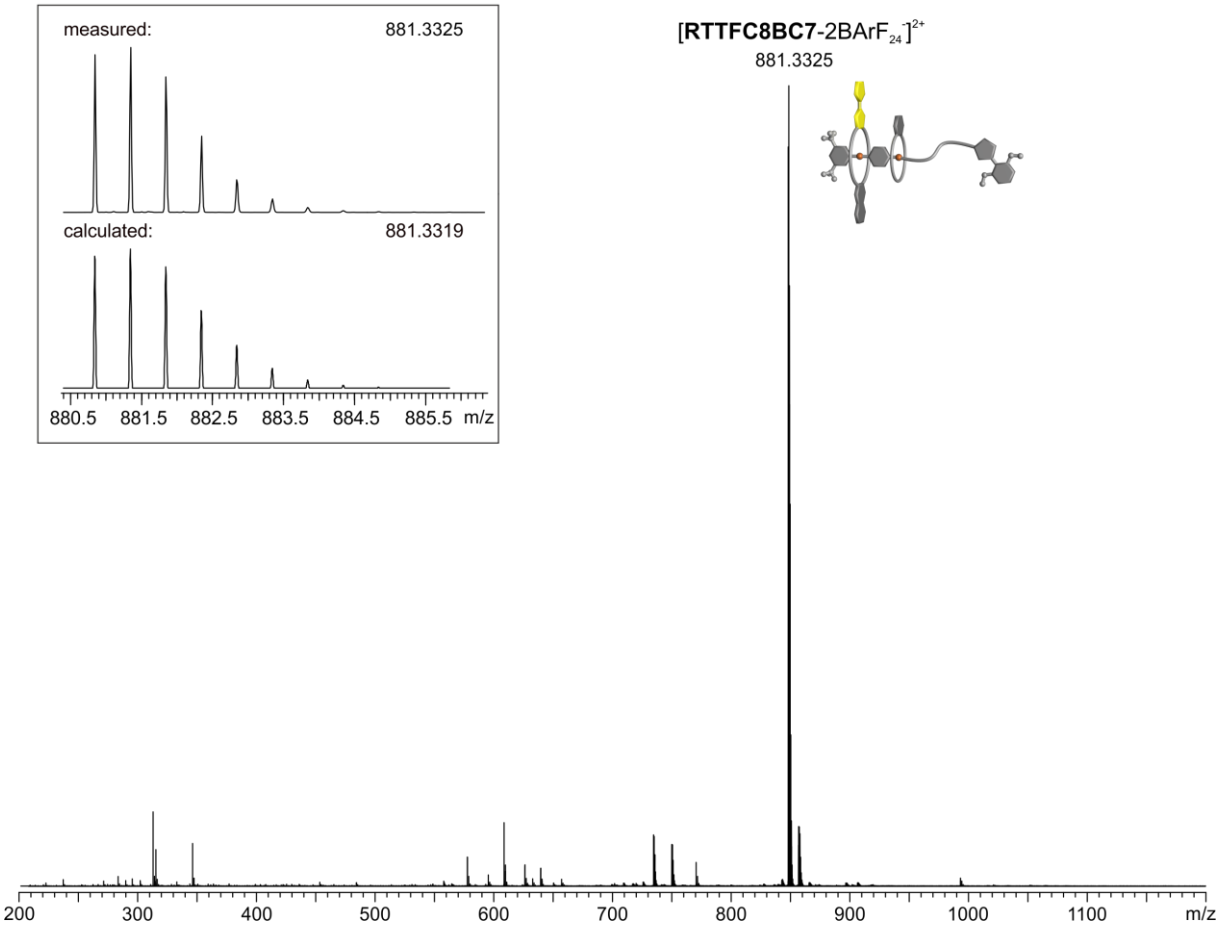

Figure S45 ESI-Q-TOF-HRMS spectrum of **RTTFC8BC7** (1 µM in acetonitrile); inset: comparison of measured and calculated isotopic patterns.

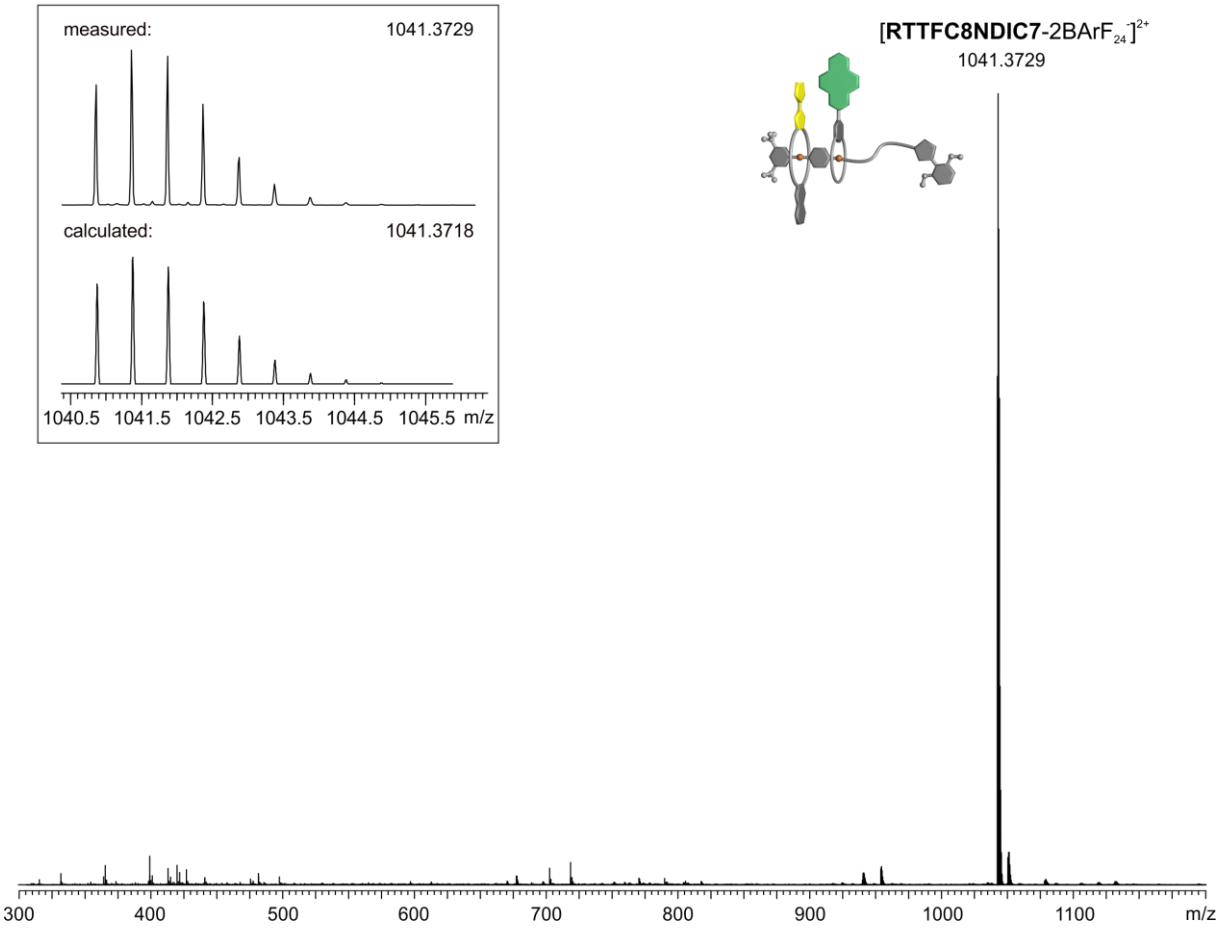

Figure S46 ESI-Q-TOF-HRMS spectrum of **RTTFC8NDIC7** (1 µM in acetonitrile); inset: comparison of measured and calculated isotopic patterns.

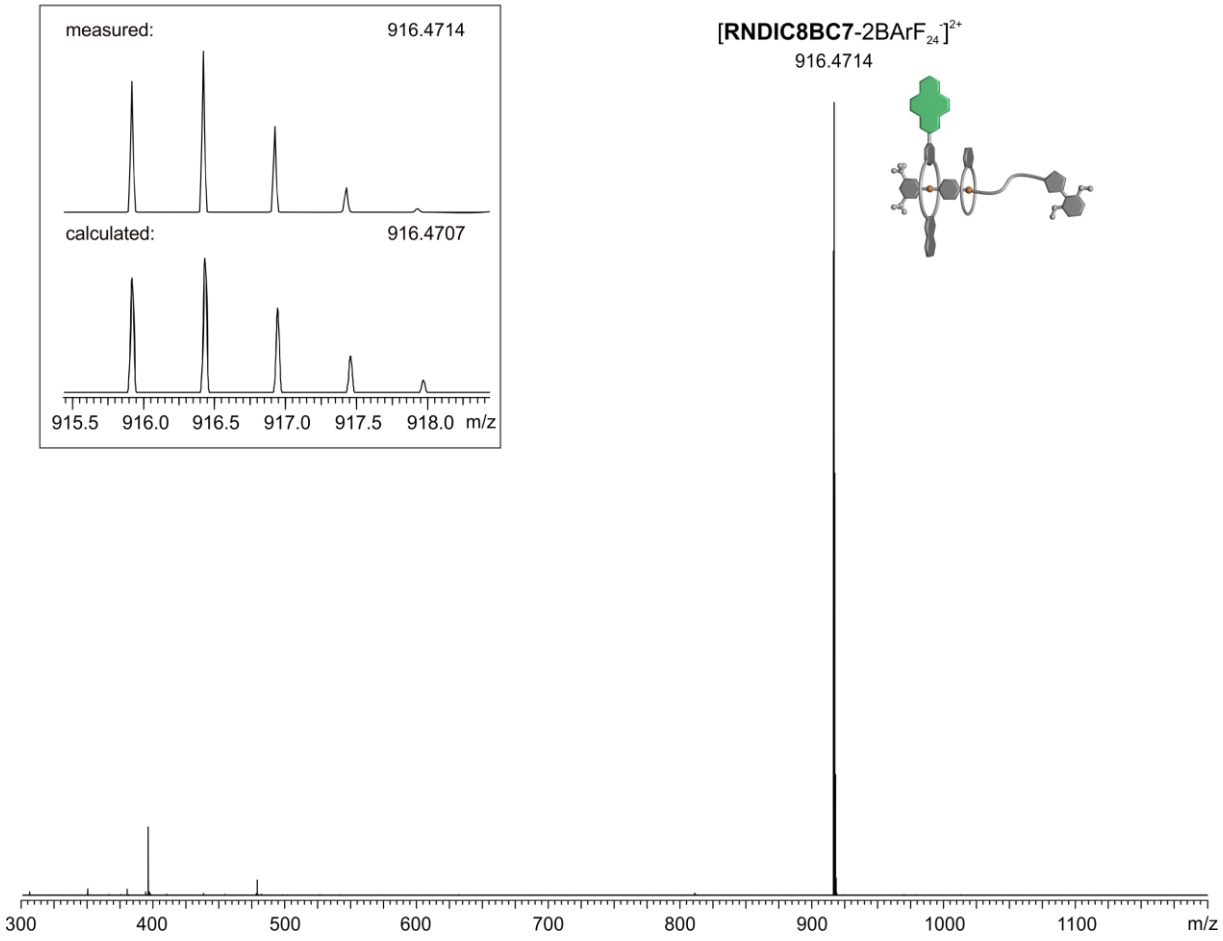

Figure S47 ESI-Q-TOF-HRMS spectrum of **RNDIC8BC7** (1 µM in acetonitrile); inset: comparison of measured and calculated isotopic patterns.

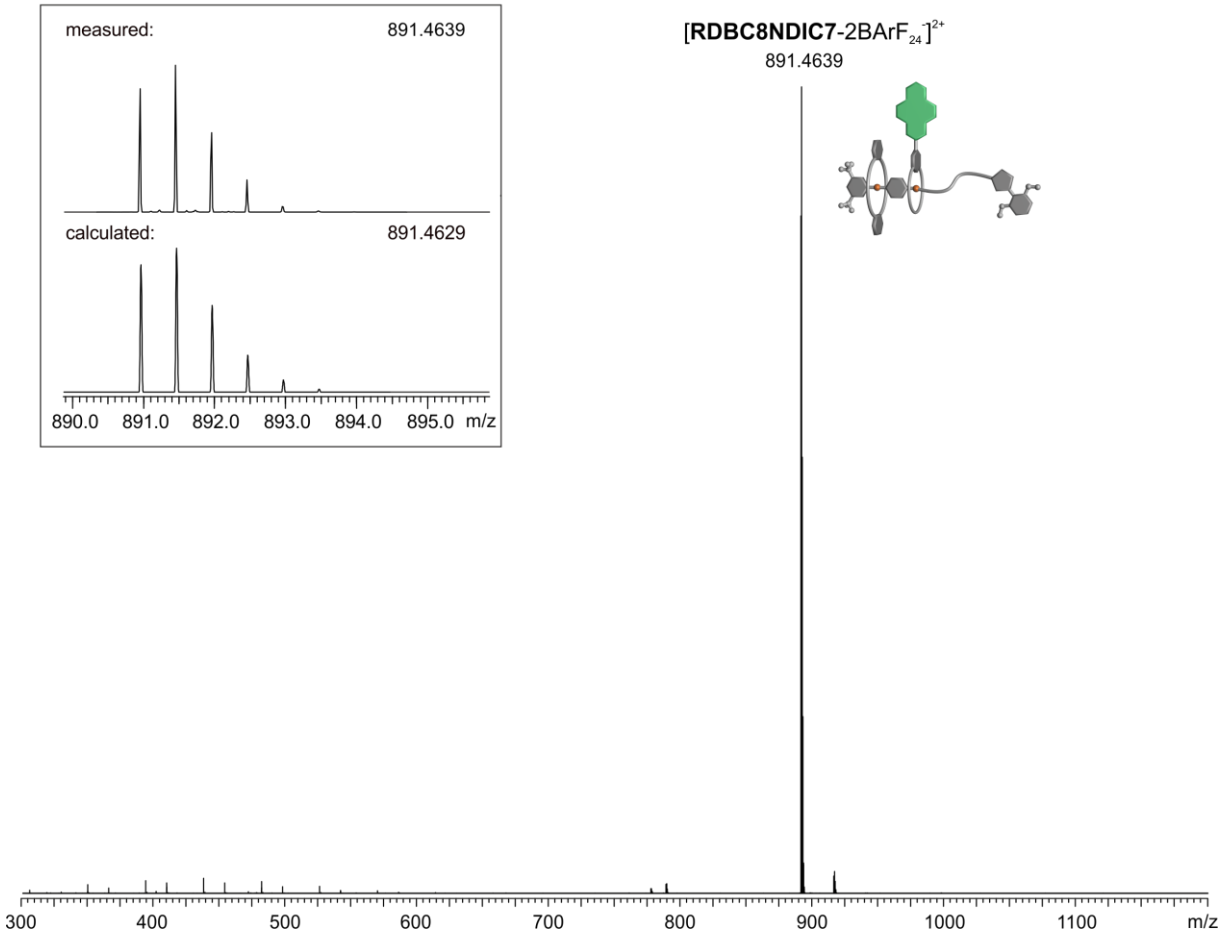

Figure S48 ESI-Q-TOF-HRMS spectrum of **RDBC8NDIC7** (1 µM in acetonitrile); inset: comparison of measured and calculated isotopic patterns.

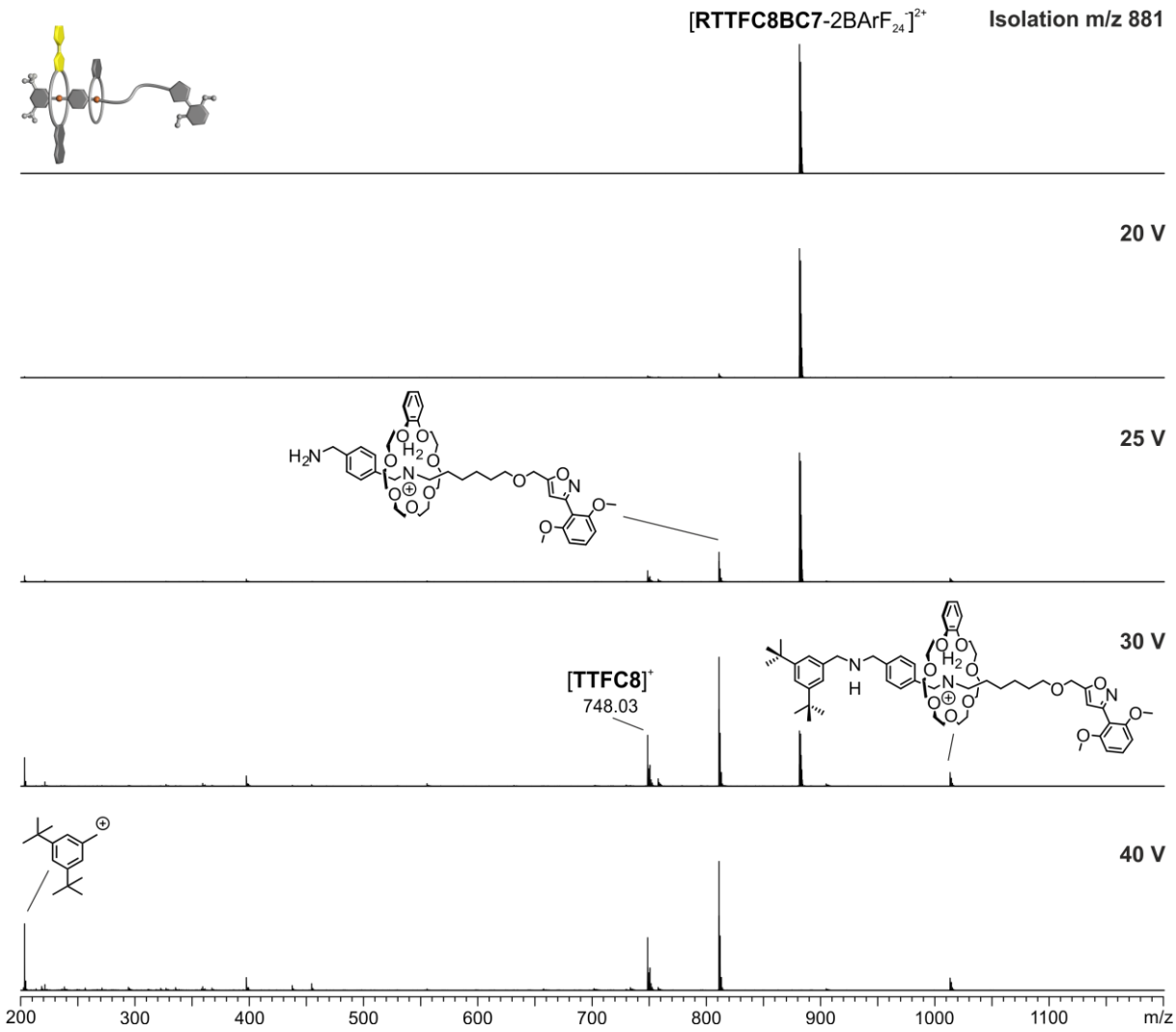

Figure S49 CID experiment with mass-selected ions at *m/z* 881 obtained from solution of **RTTFC8BC7** (1 µM in acetonitrile). Higher voltages are necessary to induce fragmentation of **RTTFC8BC7** and as major fragments oxidized **TTFC8** and axle fragments are observed. This is diagnostic for a mechanically interlocked structure.[8, 9] The small amount of [2]rotaxane fragment at *m/z* 1012 is formed by the opening and loss of **TTFC8** at high collision energies. The loss of **TTFC8** upon cleavage of the axle at the western ammonium station proves the desired sequence in the **RTTFC8BC7** [3]rotaxane.

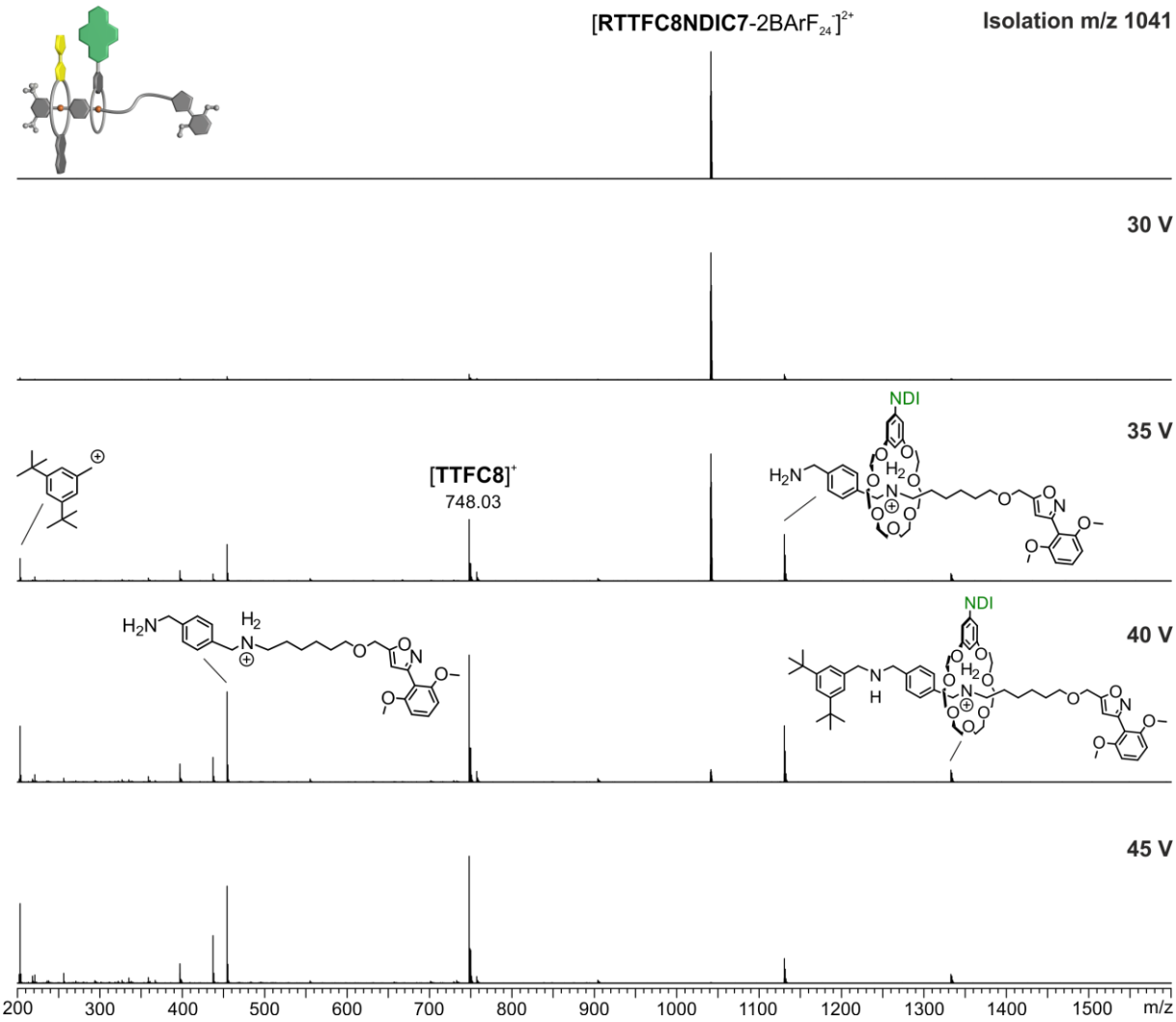

Figure S50 CID experiment with mass-selected ions at *m/z* 1041 obtained from solution of **RTTFC8NDIC7** (1 µM in acetonitrile). Higher voltages are necessary to induce fragmentation of **RTTFC8NDIC7** and as major fragments oxidized **TTFC8** and axle fragments are observed. This is diagnostic for a mechanically interlocked structure.[8, 9] The small amount of [2]rotaxane fragment at *m/z* 1332 is formed by the opening and loss of **TTFC8** at high collision energies. The loss of **TTFC8** upon cleavage of the axle at the western ammonium station proves the desired sequence in the **RTTFC8NDIC7** [3]rotaxane.

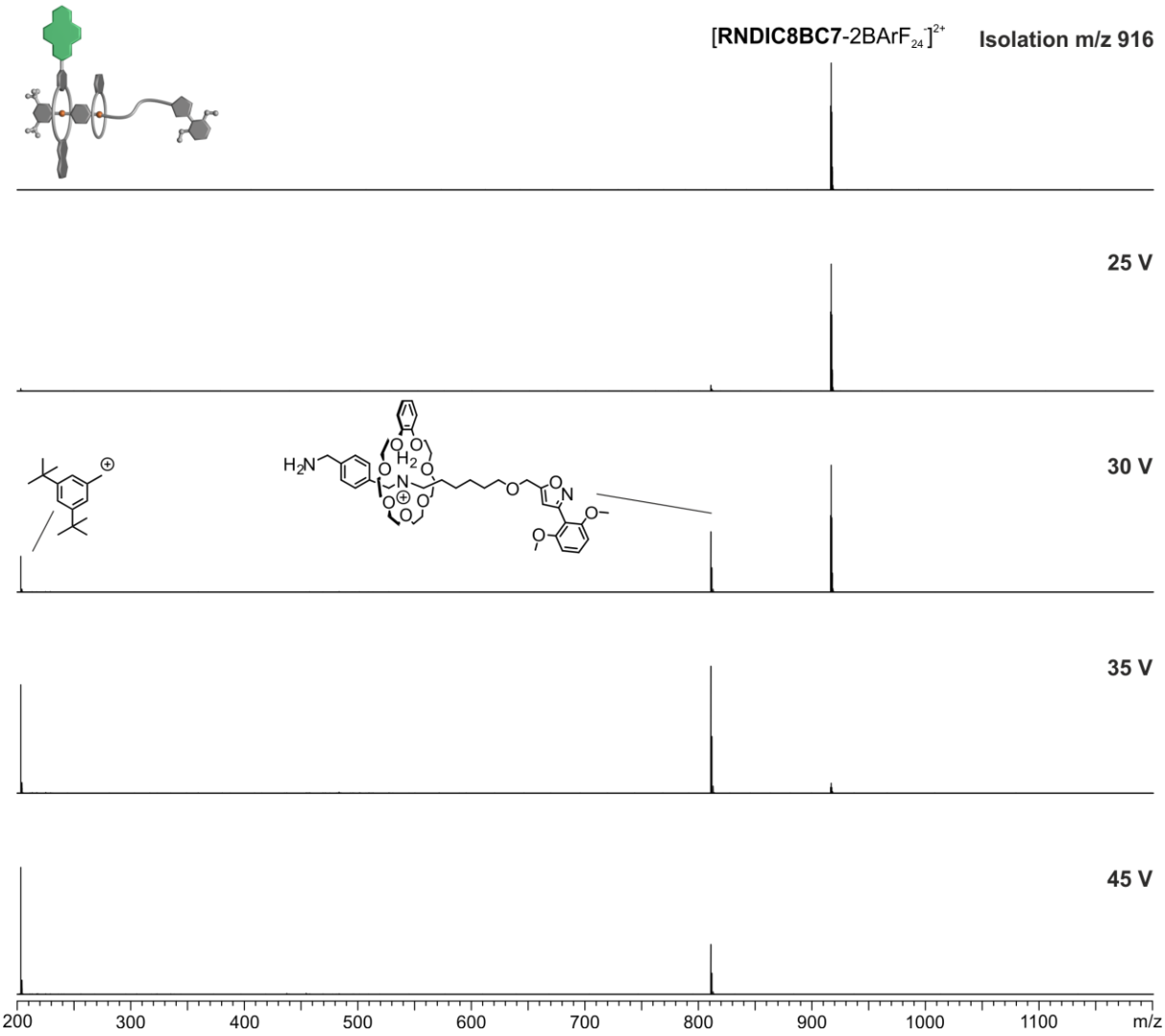

Figure S51 CID experiment with mass-selected ions at *m/z* 916 obtained from solution of **RNDIC8BC7** (1 µM in acetonitrile). Higher voltages are necessary to induce fragmentation of **RNDIC8BC7** and only axle fragments are observed. This is diagnostic for a mechanically interlocked structure.[3] The loss of **NDIC8** upon cleavage of the axle at the western ammonium station proves the desired sequence in the **RNDIC8BC7** [3]rotaxane.

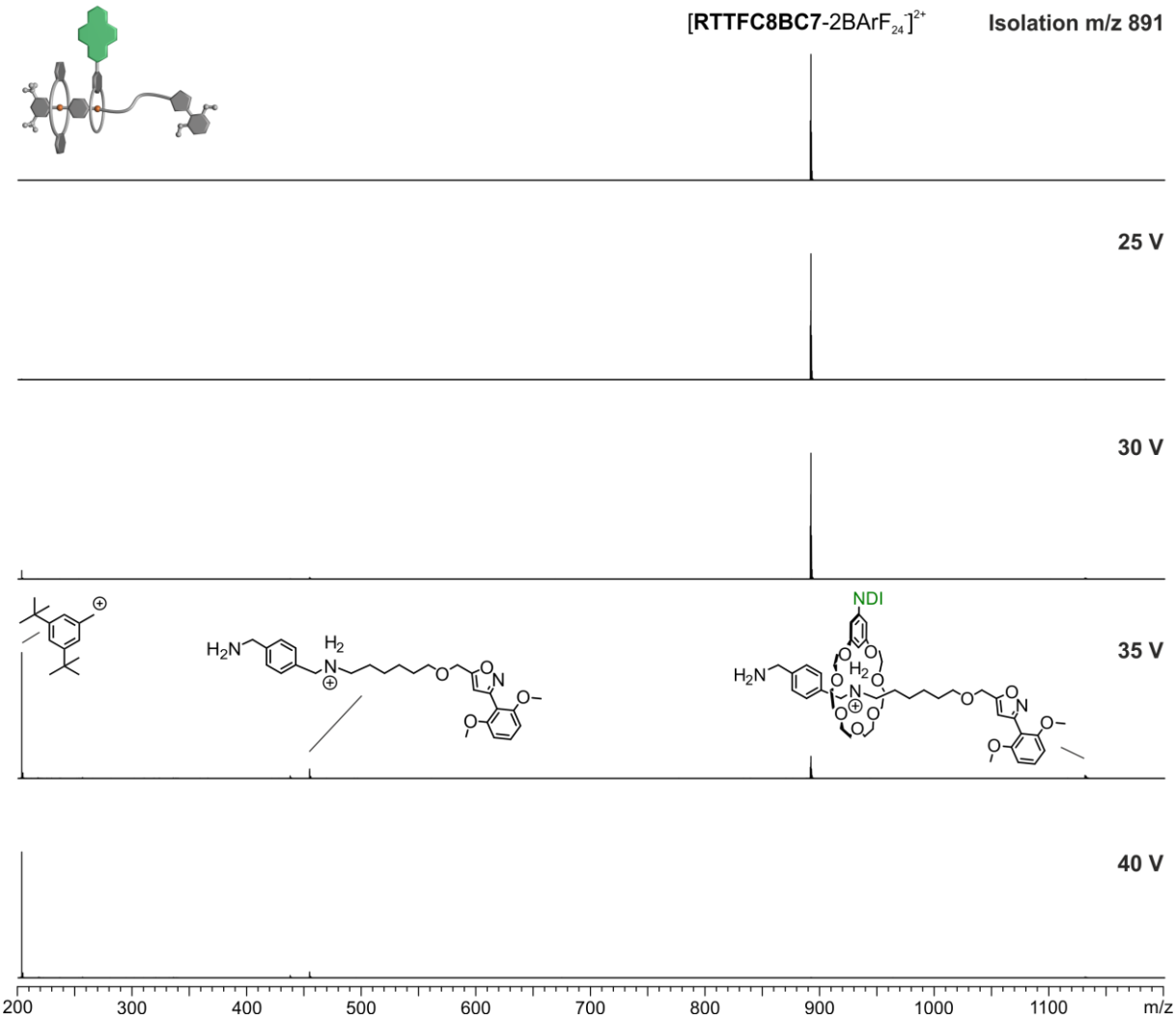

Figure S52 CID experiment with mass-selected ions at *m/z* 891 obtained from solution of **RDBC8NDIC7** (1 µM in acetonitrile). Higher voltages are necessary to induce fragmentation of **RDBC8NDIC7** and only axle fragments are observed. This is diagnostic for a mechanically interlocked structure.[3] The loss of **DBC8** upon cleavage of the axle at the western ammonium station proves the desired sequence in the **RDBC8NDIC7** [3]rotaxane.

5. Electrochemical measurements

Redox-potentials reported in this study were obtained by DPV. All measurements were at least conducted twice. Measurements were conducted in 1,2-dichloroethane (DCE) with 0.1 M electrolyte and 1.5 mM analyte concentration.

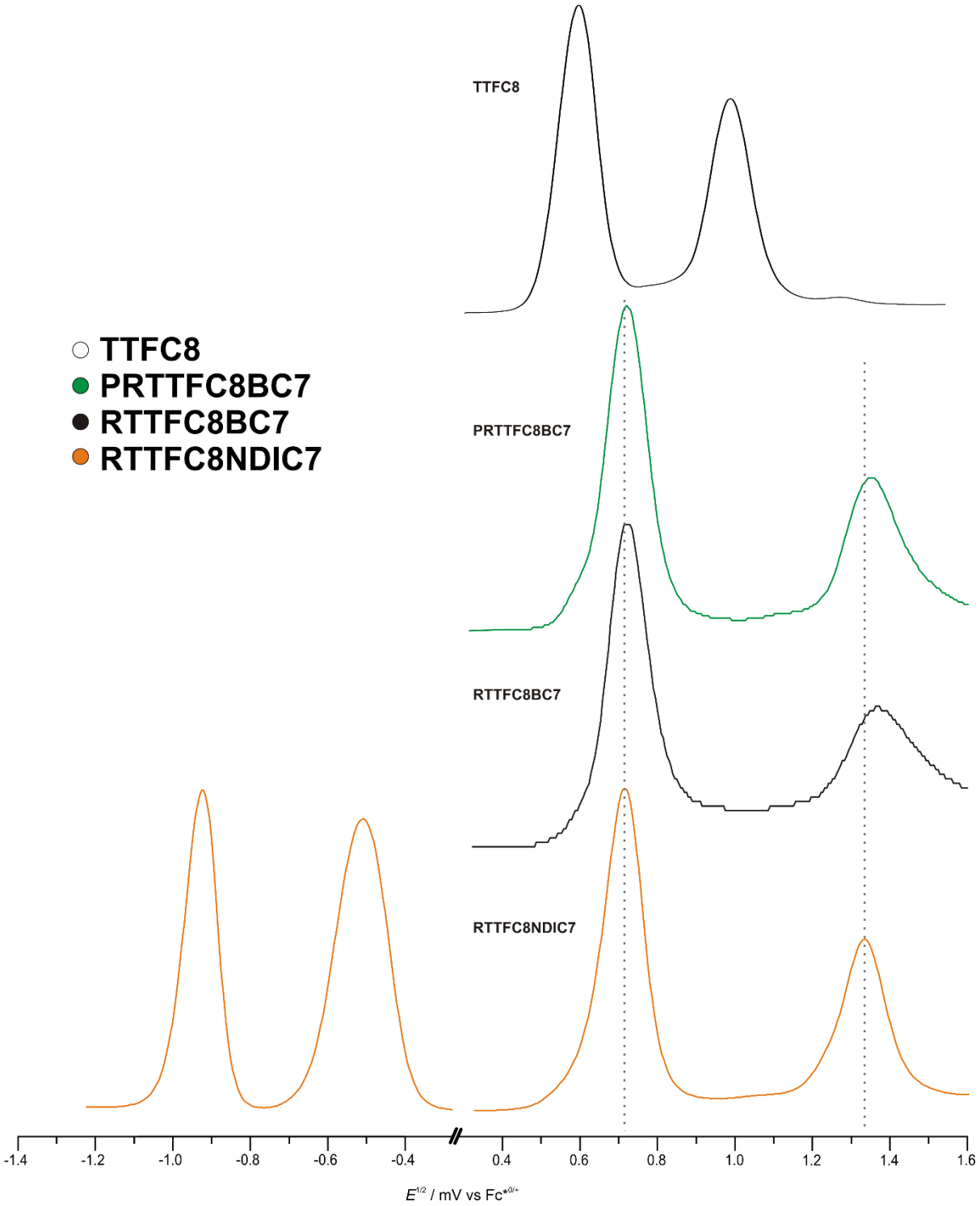

Fig. S53 Stacked differential pulse voltammograms (DPV, 10 mV/s scan rate, 25 mV modulation amplitude, 50 ms modulation time, 5 mV step potential, 0.5 s interval time) (DCE, n-Bu_4NBArF_{24}, 298 K) of **TTFC8**, **PRTTFC8BC7, RTTFC8BC7**, **RTTFC8NDIC7**.

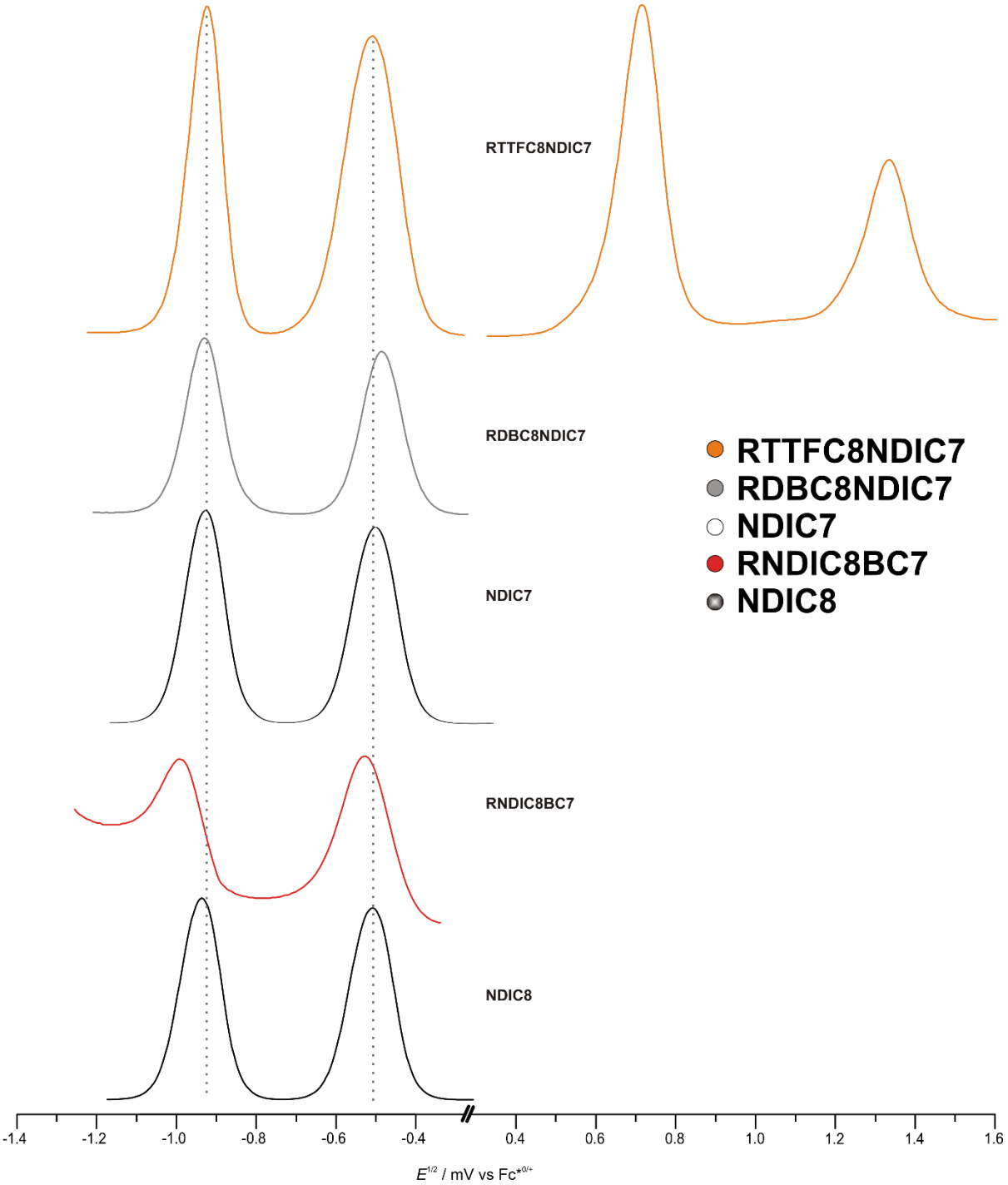

Fig. S54 Stacked differential pulse voltammograms (DPV, 10 mV/s scan rate, 25 mV modulation amplitude, 50 ms modulation time, 5 mV step potential, 0.5 s interval time) (DCE, n-Bu_4NBArF_{24}, 298 K) of **RTTFC8NDIC7**, **RDBC8NDIC7**, **NDIC7**, **RNDIC8BC7**, **NDIC8**.

Tab. S2 Electrochemical data obtained from DPV measurements (DCE, with n-Bu_4NBArF_{24} as the electrolyte, 298 K).

-II / mV	-I / mV	species	+I / mV	+II / mV
		TTFC8	594	987
		RTTFC8[8]	694	1349
		PRTTFC8BC7	720	1349
		RTTFC8BC7	725	1369
-921	-508	**RTTFC8NDIC7**	720	1329
-932	-489	**RDBC8NDIC7**		
-921	-498	**NDIC7**		
-992	-529	**RNDIC8BC7**		
-937	-509	**NDIC8**		

6. UV/Vis experiments

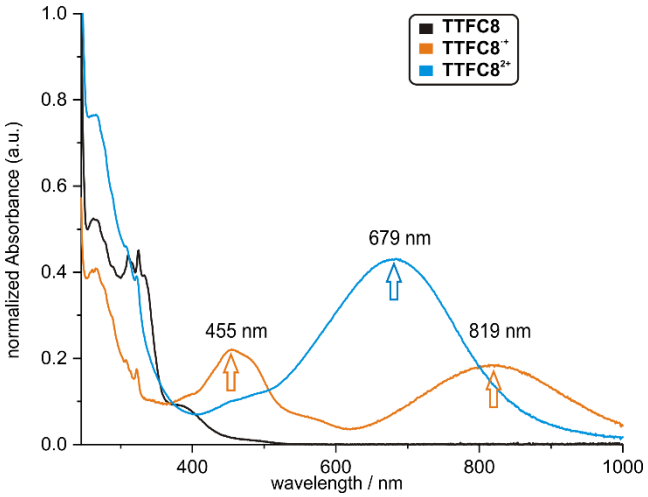

Fig. S55 UV/Vis spectra of **TTFC8** (15 µM in CH_2Cl_2, 298 K, excess bulk $Fe(ClO_4)_3$ as the oxidant) in the TTF^0, $TTF^{\bullet+}$ and TTF^{2+} state.

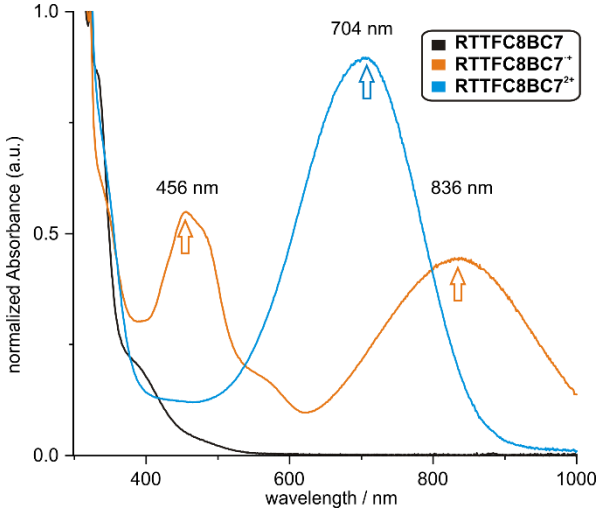

Fig. S56 UV/Vis spectra of **RTTFC8BC7** (15 µM in CH_2Cl_2, 298 K, excess bulk $Fe(ClO_4)_3$ as the oxidant) in the TTF^0, $TTF^{\bullet+}$ and TTF^{2+} state.

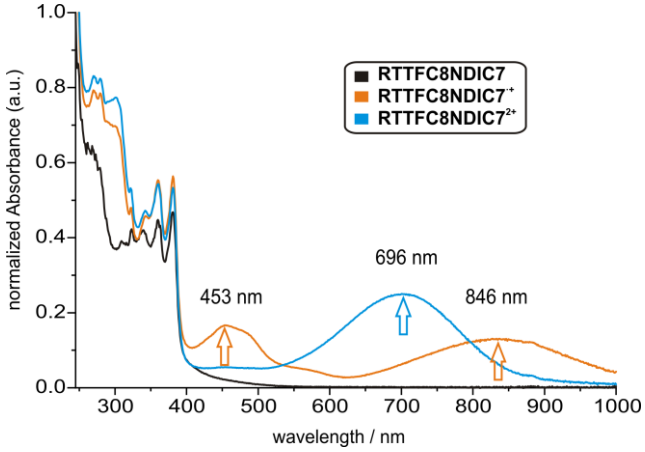

Fig. S57 UV/Vis spectra of **RTTFC8NDIC7** (15 µM in CH_2Cl_2, 298 K, excess bulk $Fe(ClO_4)_3$ as the oxidant) in the TTF^0, $TTF^{\bullet+}$ and TTF^{2+} state.

Tab. S3 Absorption maxima of $TTF^{\bullet+}$ and TTF^{2+} in different species(15 µM in CH_2Cl_2, 298 K, bulk $Fe(ClO_4)_3$ as the oxidant).

species	+I / nm	+II / nm
TTFC8	455, 819	679
RTTFC8BC7	456, 836	704
RTTFC8NDIC7	453, 846	696

The photometric titrations of hetero[3]rotaxanes **RTTFC8BC7** and **RTTFC8NDIC7** with $Fe(ClO_4)_3$ show bands similar to those of free wheel **TTFC8** for the three redox states (TTF, TTF·+ and TTF^{2+}).[10] In contrast to a fixed conformation divalent donor-acceptor rotaxane[11] with TTF and NDI, no intramolecular charge transfer band is observable.

7. Computational details

A conformational scan of the potential energy surface using Grimme's GFN2-xTB code[12] was conducted for compound **RTTFC8NDIC7** and **RNDIC8BC7** to obtain the most stable structures. Compound **RTTFC8NDIC7** was optimised in charge states 1+, 2+, and 3+, respectively, at the PBEh-3c[13] level of DFT in combination with the COSMO[14] solvation model (ε = 8.9 for CH_2Cl_2)[15] employing the Turbomole programm package (Version 7.4).[16] Subsequent single point calculations for an accurate description of the electronic structure were performed at the ωB97X-D3/def2-TZVP[17] level using the CPCM[18] solvent model and the ORCA programm package.[19] Spin densities were generated with ORBKIT.[20]

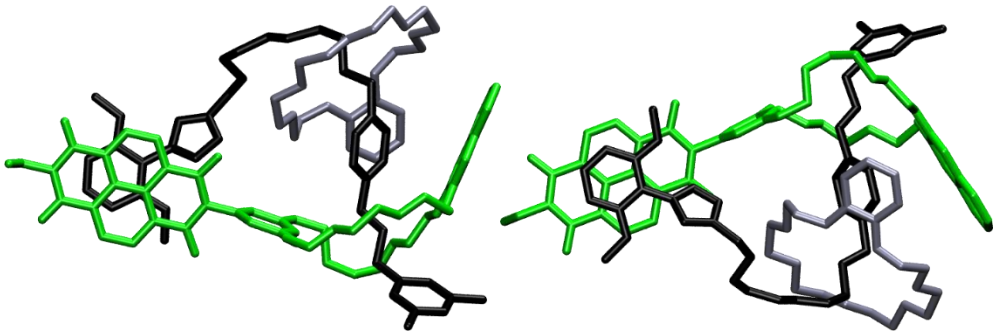

Fig. S58 Optimised structure of compound **RNDIC8BC7** illustrating the efficient stacking between the NDI and stopper moiety.

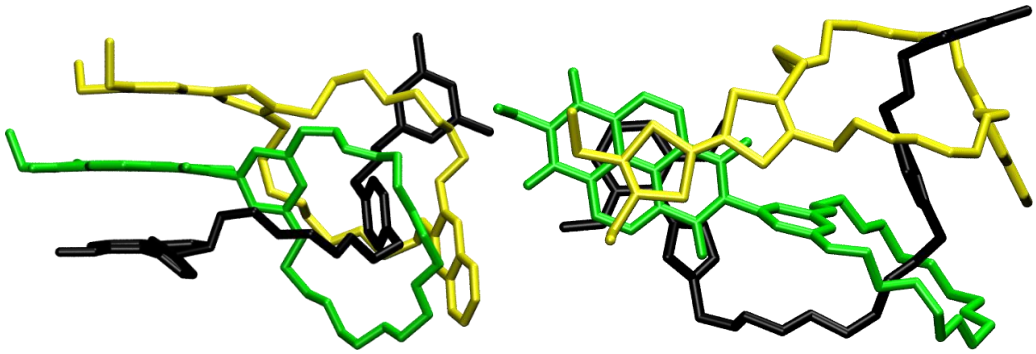

Fig. S59 Optimised structure of compound **RTTFC8NDIC7** illustrating the efficient stacking between the TTF, NDI and stopper moieties.

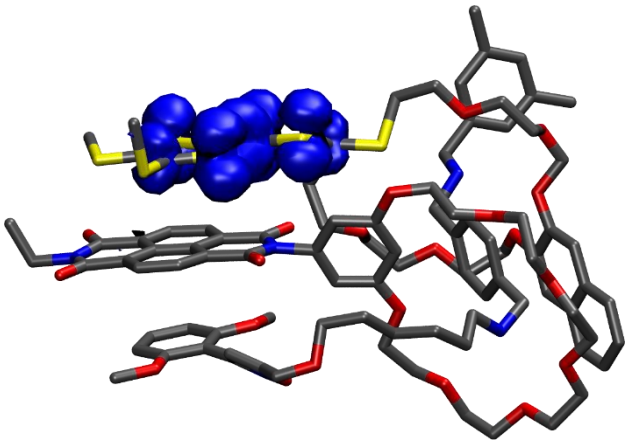

Fig. S60 Spin density of **RTTFC8NDIC7**$^{\cdot+}$ localised on the TTF moiety, isovalue = 0.001 a_0^{-3}.

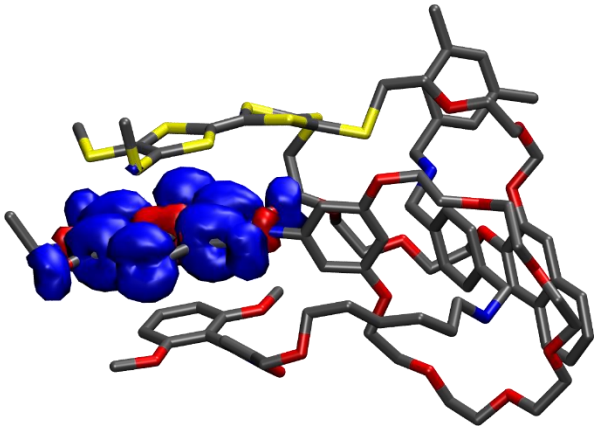

Fig. S61 Spin density of **RTTFC8NDIC7**$^{\cdot-}$ localised on the NDI moiety, isovalue = 0.001 a_0^{-3}.

The spin density plots confirm the retained redox-behaviour of the macrocycles within the rotaxane.

8. Crystallographic data

The crystals were grown by diffusing pentane into a sat. acetonitrile solution of **NDIC7**. X-ray data were collected on a BRUKER D8 Venture system. Data were collected at 100(2) K using graphite-monochromated Mo K_α radiation (λ_α = 0.71073 Å). The strategy for data collection was evaluated by using the Smart software. The data were collected by the standard "*ψ-ω* scan techniques" and were scaled and reduced using Saint+software. The structures were solved by using Olex2,[21] the structure was solved with the XT[22] structure solution program using Intrinsic Phasing and refined with the XL refinement package[23] using Least Squares minimization. Bond length and angles were measured with Diamond Crystal and Molecular Structure Visualization Version 4.6.2.[24] Drawings were generated with POV-Ray.[25] Deposition number CCDC 2047286 contains the supplementary crystallographic data for this paper. These data are provided free of charge by the joint Cambridge Crystallographic Data Centre and Fachinformationszentrum Karlsruhe Access Structures service www.ccdc.cam.ac.uk/structures.

Tab. S4 Crystal data of **NDIC7**.

Compound	**NDI-MC • ACN**
Empirical formula	$C_{38}H_{43}O_{11}N_3$
Formula weight	717.75
Temperature/K	100
Crystal system	triclinic
Space group	$P\bar{1}$
a/Å	8.908(11)
b/Å	8.969(9)
c/Å	26.350(3)
α/°	84.32(7)
β/°	85.34(6)
γ/°	64.95(7)
Volume/Å³	1896(4)
Z	2
ρ_{calc}/g·cm³	1.257
μ/mm^{-1}	0.093
F(000)	760.0
Crystal size/mm³	0.871 x 0.531 x 0.381
Crystal shape	plate
Radiation	MoKα (λ = 0.71073)
2Θ range for data collection/°	4.664 to 50.996
Index ranges	-10 ≤ h ≤ 10, -10 ≤ k ≤ 10, -31 ≤ l ≤ 31
Reflections collected	42858
Independent reflections	6884 [R_{int} = 0.0560, R_{sigma} = 0.0363]
Data/restrains/parameters	6884/0/625
Goodness-of-fit on F^2	1.057
Final R indexes [I>=2σ(I)]	R_1 = 0.0553, wR_2 = 0.1315
Final R indexes [all data]	R_1 = 0.0673, wR_2 = 0.1385
Largest diff. peak/hole / e·Å³	0.26/−0.35

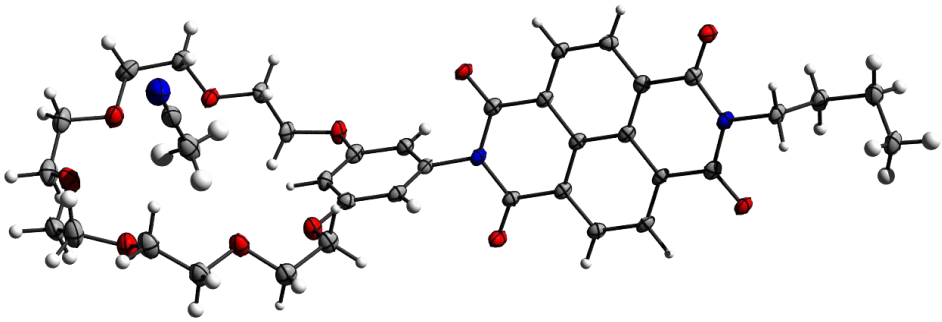

Fig. S62 Asymmetric unit cell of **NDIC7**.

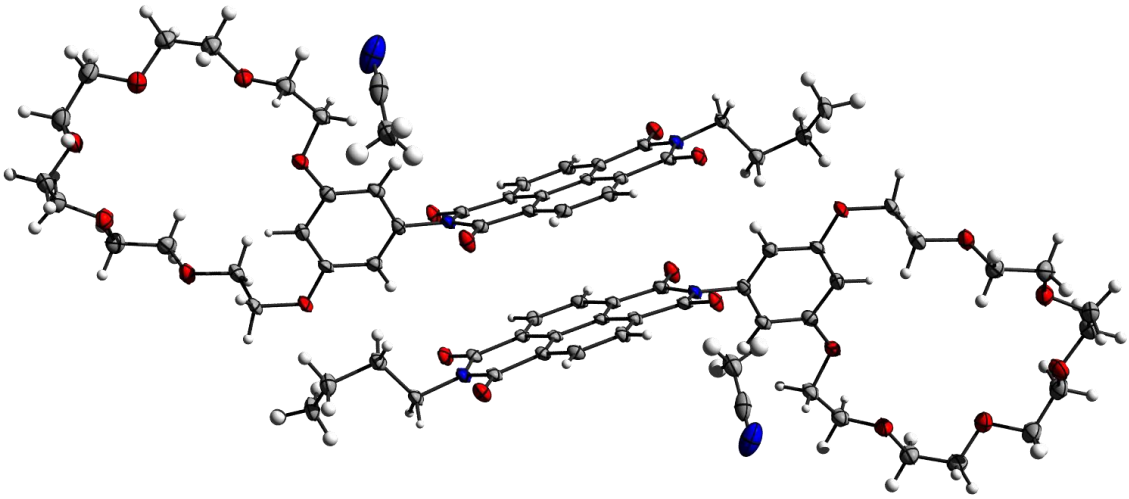

Fig. S63 Crystal packing of two **NDIC7**, with NDI-NDI plane distance of 3.27 Å.

9. References

1. H. V. Schröder, S. Sobottka, M. Nößler, H. Hupatz, M. Gaedke, B. Sarkar and C. A. Schalley, *Chem. Sci.*, 2017, **8**, 6300-6306.
2. T. Matsumura, F. Ishiwari, Y. Koyama and T. Takata, *Org. Lett.*, 2010, **12**, 3828-3831.
3. H. Hupatz, M. Gaedke, H. V. Schröder, J. Beerhues, A. Valkonen, F. Klautzsch, S. Müller, F. Witte, K. Rissanen, B. Sarkar and C. A. Schalley, *Beilstein J. Org. Chem.*, 2020, **16**, 2576-2588.
4. L. Zou and M. J. Webber, *Chem. Commun.*, 2019, **55**, 9931-9934.
5. H. Shao, T. Nguyen, N. C. Romano, D. A. Modarelli and J. R. Parquette, *J. Am. Chem. Soc.*, 2009, **131**, 16374-16376.
6. W. Jiang and C. A. Schalley, *Beilstein J. Org. Chem.*, 2010, **6**, 14.
7. J. R. Aranzaes, M.-C. Daniel and D. Astruc, *Can. J. Chem.*, 2006, **84**, 288-299.
8. M. Gaedke, H. Hupatz, H. V. Schröder, S. Suhr, K. F. Hoffmann, A. Valkonen, B. Sarkar, S. Riedel, K. Rissanen and C. A. Schalley, *Org. Chem. Front.*, 2021, **8**, 3659-3667.
9. M. Gaedke, F. Witte, J. Anhäuser, H. Hupatz, H. V. Schröder, A. Valkonen, K. Rissanen, A. Lützen, B. Paulus and C. A. Schalley, *Chem. Sci.*, 2019, **10**, 10003-10009.
10. S. V. Rosokha and J. K. Kochi, *J. Am. Chem. Soc.*, 2007, **129**, 828-838; M. B. Kirketerp, L. A. Leal, D. Varsano, A. Rubio, T. J. Jørgensen, K. Kilsa, M. B. Nielsen and S. B. Nielsen, *Chem. Commun.*, 2011, **47**, 6900-6902.
11. H. V. Schröder, H. Hupatz, A. J. Achazi, S. Sobottka, B. Sarkar, B. Paulus and C. A. Schalley, *Chem. Eur. J.*, 2017, **23**, 2960-2967.
12. C. Bannwarth, S. Ehlert and S. Grimme, *J. Chem. Theory Comput.*, 2019, **15**, 1652-1671.
13. S. Grimme, J. G. Brandenburg, C. Bannwarth and A. Hansen, *J. Chem. Phys.*, 2015, **143**, 054107.
14. A. Klamt and G. Schüürmann, *J. Chem. Soc., Perkin Trans. 2*, 1993, **5**, 799-805.
15. I. M. Smallwood, *Handbook of Organic Solvent Properties*, Butterworth-Heinemann, Oxford, 1996.
16. R. Ahlrichs, M. Bär, M. Häser, H. Horn and C. Kölmel, *Chem. Phys. Lett.*, 1989, **162**, 165-169.
17. J. D. Chai and M. Head-Gordon, *J. Chem. Phys.*, 2008, **128**, 084106; F. Weigend and R. Ahlrichs, *Phys. Chem. Chem. Phys.*, 2005, **7**, 3297-3305.
18. V. Barone and M. Cossi, *J. Phys. Chem. A*, 1998, **102**, 1995-2001.
19. F. Neese, *WIREs Comput. Mol. Sci.*, 2017, **8:e1327**.
20. G. Hermann, V. Pohl, J. C. Tremblay, B. Paulus, H. C. Hege and A. Schild, *J. Comput. Chem.*, 2016, **37**, 1511-1520.
21. O. V. Dolomanov, L. J. Bourhis, R. J. Gildea, J. A. K. Howard and H. Puschmann, *J. Appl. Crystallogr.*, 2009, **42**, 339-341.
22. G. M. Sheldrick, *Acta Cryst.*, 2015, **A71**, 3-8.
23. G. M. Sheldrick, *SHELXL Version 2014/7, Programm for Crystal Structure Solution and Refinement, University of Göttingen*, 2014; G. M. Sheldrick, *Acta Cryst.*, 2008, **A64**, 112-122.
24. K. Brandenburg, *"Diamond: Crystal and Molecular Structure Visualization" can be found under* http://www.crystalimpact.com/diamond, 2017.
25. *Persistence of Vision. Ltd., retrieved from* http://www.povray.org/download/, 2004.

7 Appendix

7.1 Publication List

1) *Protomer formation can aid structural identification of caffeine metabolits*

   H. Sepman, S. Tshepelevitsh, H. Hupatz, I. Leito, A. Kruve, *Anal. Chem.* **2022**, *94*, 10601-10609.

2) *Sequence-sorted redox-switchable hetero[3]rotaxanes*

   H. Hupatz*, M. Gaedke*, F. Witte, S. M. Rupf, C. Douglas, H. V. Schröder, L. Fischer, M. Malischewski, B. Paulus, C. A. Schalley, *Org. Chem. Front.,* **2022**, *9,* 64-74. (*Authors contributed equally).

3) *Dual-stimuli pseudorotaxane switches under kinetic control*

   M. Gaedke, H. Hupatz, H. V. Schröder, S. Suhr, K. F. Hoffmann, A. Valkonen, B. Sarkar, S. Riedel, K. Rissanen, C. A. Schalley, *Org. Chem. Front.* **2021**, *8*, 3659-3667.

4) *Thermodynamic and electrochemical study of tailor-made crown ethers for redox-switchable (pseudo)rotaxanes*

   H. Hupatz, M. Gaedke, H. V. Schröder, J. Beerhues, A. Valkonen, F. Klautzsch, S. Mülller, F. Witte, K. Rissanen, B. Sarkar, C. A. Schalley, *Beilstein J. Org. Chem.* **2020**, *16*, 2576-2588.

5) *Chiroptical inversion of a planar chiral redox-switchable rotaxane*

   M. Gaedke, F. Witte, J. Anhäuser, H. Hupatz, H. V. Schröder, A. Valkonen, K. Rissanen, A. Lützen, B. Paulus, C. A. Schalley, *Chem. Sci.* **2019**, *10*, 10003-10009.

6) *Naphtocage: A flexible yet Extremely Strong Binder for Singly Charged Organic Cations*

   F. Jia, H. Hupatz, L.-P. Yang, H. V. Schröder, D.-H. Li, S. Xin, D. Lentz, F. Witte, X. Xie, B. Paulus, C. A. Schalley, W. Jiang, *J. Am. Chem. Soc.* **2019**, *141*, 4468-4473.

7) *Switchable synchronization of pirouetting motions in a redox active [3]rotaxane*

   H. V. Schröder, A. Mekic, H. Hupatz, S. Sobottka, F. Witte, L. H. Urner, M. Gaedke, K. Pagel, B. Sarkar, B. Paulus, C. A. Schalley, *Nanoscale* **2018**, *10*, 21425-21433.

8) *An aryl-fused redox-active tetrathiafulvalene with enhanced mixed-valence and radical-cation dimer stabilities*

H. V. Schröder, F. Witte, M. Gaedke, S. Sobottka, L. Suntrup, H. Hupatz, A. Valkonen, B. Paulus, K. Rissanen, B. Sarkar, C. A. Schalley, *Org. Biomol. Chem.* **2018**, *16*, 2741-2747.

9) *Impact of mechanical bonding on the redox-switching of tetrathiafulvalene in crown ether-ammonium [2]rotaxanes*

H. V. Schröder, S. Sobottka, M. Nößler, H. Hupatz, M. Gaedke, B. Sarkar, C. A. Schalley, *Chem. Sci.*. **2017**, *8*, 6300-6306.

10) *A Divalent Pentastable Redox-Switchable Donor-Acceptor Rotaxane*

H. V. Schröder, H. Hupatz, A. J. Achazi, S. Sobottka, B. Sarkar, B. Paulus, C. A. Schalley, *Chem. Eur. J.* **2017**, *23*, 2960-2967.

7.2 Curriculum Vitae

For reasons of data protection, the curriculum vitae is not published in the electronic version.